

# THE DEVELOPMENT OF LOW TEMPERATURE TECHNOLOGY AT STANFORD AND ITS RELEVANCE TO HIGH ENERGY PHYSICS\*

H. Alan Schwettman<sup>†</sup>  
Department of Physics and High Energy Physics Laboratory  
Stanford University  
Stanford, California

## I. INTRODUCTION

In the history of nuclear and high energy physics there have been a few pioneering laboratories which have developed the new technology that has made possible the complex accelerators of today. The High Energy Physics Laboratory (HEPL) at Stanford played this role in the development of the electron linear accelerator and the related microwave technology a little over one decade ago, and this same laboratory is now pioneering the development of the superconducting accelerator (SCA) and the related low temperature technology. The objective of our laboratory is simultaneously to provide modernized facilities to continue basic research at the frontiers of high energy physics and to develop all aspects of this new technology that are required to demonstrate its relevance to the future of low temperature physics and high energy physics.

To make a substantial contribution to this emerging low temperature technology requires the combined efforts of physicists who are both knowledgeable about the fundamental properties of matter at low temperature and willing to explore their applications, and engineers who are prepared to transform these ideas into a viable technology. At HEPL an energetic group of approximately 50 technical personnel are engaged in this effort. As a result, there is now a sizable literature (see for example the HEPL reports referred to in the text) describing the progress in solving the many detailed problems encountered in this development. This paper attempts to outline briefly a few of the major technological innovations that are being developed at HEPL and to indicate their relevance to several applications in high energy physics.

## II. TECHNOLOGICAL INNOVATIONS

### 1. Development of Niobium Cavities

The preparation of a suitable superconducting surface is one of the principal technological problems in the development of the superconducting accelerator. The superconductor must provide extremely high conductivity at microwave frequencies and it must be capable of sustaining high electric and magnetic fields.

Nature has provided a variety of possible candidates among the elemental superconductors and the many "alloys" to satisfy the requirements of this new technology. In the Physics Department at Stanford where there is active research in the problems of low temperature physics we have a strong motivation for understanding the fundamental microwave properties of superconductors over the entire range of physical character-

---

\* Work supported in part by the U.S. Office of Naval Research, Contract [NONR 225(67)].

<sup>†</sup> Alfred P. Sloan Research Fellow.

istics. We are investigating in detail<sup>1-4</sup> materials with small  $\kappa$  values\* which are good type I superconductors, the elemental superconductors with the highest transition temperature where  $\kappa$  values are near unity, and the very high  $\kappa$  value alloys where type II behavior is marked. But among this broad selection of materials that of greatest practical importance is pure niobium.

With pure niobium it should be possible to maintain very high accelerating fields continuously in a SCA. At 1.85°K the lower critical field  $H_{c1}$  for niobium is 1650 G. In a standing wave biperiodic  $\pi/2$ -mode structure this corresponds to an energy gradient of 11 MeV/ft, while for a traveling wave  $\pi/2$ -mode structure the corresponding energy gradient is 19 MeV/ft. It is likely that loading due to field emission of electrons will become important at gradients smaller than the values quoted above since these correspond to a peak electric field of  $1.2 \times 10^6$  V/cm. However, the superior electric breakdown characteristics of niobium are well known and thus it is plausible that this material will provide the very highest attainable energy gradient. We are optimistic that energy gradients as high as 6 MeV/ft in a standing wave structure or 10 MeV/ft in a traveling wave structure can be achieved. In addition, the theoretical conductivity of niobium is sufficient to make continuous operation of a SCA at these high gradients feasible. At 1.3 GHz and 1.85°K the power dissipation in a traveling wave structure at 10 MeV/ft is 2.8 W/ft.

We have made rapid progress in the development of high Q, high field niobium cavities. As shown in Fig. 1, Q's exceeding  $10^{10}$  and energy gradients exceeding 3 MeV/ft in a standing wave structure or 5 MeV/ft in a traveling wave structure have been achieved in cavities fabricated from commercially available niobium<sup>5,6</sup> and it is expected that niobium of greater purity will produce even better results.<sup>†</sup> There is, however, another practical consideration: can niobium cavities be fabricated at reasonable cost? This problem is most acute in considering the application of these techniques to construction of very large, say 1000-2000 GeV, accelerators. When we first achieved high Q in solid niobium cavities through a joint development effort with the Central Research Laboratory of Varian Associates, it was commented that making a linear accelerator of niobium is like making it of platinum. This attitude ignores a wide range of techniques that can be used in fabricating niobium cavities. At Stanford we have investigated a number of these possibilities: electrodeposition, vapor deposition, sputtering, forming of solid niobium and others. Each of these techniques holds real promise as a practical fabrication technique.

The electrodeposition technique as a method for fabricating niobium cavities is particularly attractive, and in cooperation with the Linde Division of Union Carbide

---

\*  $\kappa$  represents the ratio of penetration depth to coherence length.

† Preliminary measurements on very pure electrodeposited niobium cavities using the techniques described below have already yielded similar Q's and still higher gradients.

1. J.P. Turneaure, Thesis, Stanford University (1967).
2. J.M. Pierce, Thesis, Stanford University (1967).
3. J.P. Turneaure and H.A. Schwettman, High Energy Physics Laboratory Report HEPL 553 (1968).
4. J.M. Pierce, High Energy Physics Laboratory Report HEPL 576 (1968).
5. J.P. Turneaure and I. Weissman, High Energy Physics Laboratory Report HEPL 522 (1968).
6. J.P. Turneaure and I. Weissman, High Energy Physics Laboratory Report HEPL 571 (1968).



we are vigorously pursuing its development. The niobium is electrodeposited on a copper mandrel in the geometry of the final accelerator structure. The mandrel is subsequently removed by chemical means leaving a free standing niobium structure. The advantage of the method is that two important steps are taken simultaneously: 1) the niobium is formed in the complicated geometry required, and 2) the niobium is refined in the electrodeposition process. In fact the purity of the electrodeposited niobium exceeds that of triply zone-refined niobium. This, of course, dispels the oft repeated concern about material cost in fabricating niobium cavities. One can start with low grade niobium which in large quantities sells at \$10 per pound and thus for the estimated weight of the accelerator structure at 1.3 GHz (20 lb/ft) the material costs are \$200 per foot.

The development of a practical niobium accelerator structure is progressing rapidly and it is expected that the operation of experimental 20 ft sections will be accomplished within a year.

## 2. Development of Superfluid Refrigeration

Once it was recognized that superfluid helium plays an essential role in the operation of a practical SCA we began serious discussions with interested manufacturers concerning the development of superfluid refrigeration. In describing our plans to accelerator physicists we were frequently told that to develop the first superfluid refrigerator in cooperation with industry would require ten years. Under many circumstances this is probably true. But one unique advantage of a small laboratory engaged in the construction of modernized facilities is that it is possible to talk to industry about the development of important new technology not in terms of the needs of an indefinite future but rather in terms of an immediate requirement. Motivated by the immediate requirement for a 300 W superfluid helium refrigerator Dr. Sam Collins at Arthur D. Little, Inc. modified an existing refrigerator for superfluid operation. Experiments with this 30 W system were performed at company expense and provided design information for the 300 W unit shown in Fig. 2 and now being installed at Stanford just 2½ years after beginning the original discussion.

Operation of the 300 W superfluid refrigerator over an extended period of time will demonstrate the reliability and the economics of large-scale refrigeration. In addition, this unit is an essential part of our plans to demonstrate the feasibility of operating a large and complex laboratory from a central refrigerator. Before discussing the problem of a laboratory using central refrigeration, however, it is advisable to comment on the future of large-scale refrigerators.

Large low temperature refrigerators have most often been used in systems, for instance space simulation chambers, which are required to operate over periods of days. Under these conditions efficiency and reliability have usually been sacrificed in the interest of low initial cost. If cryogenics is to become a viable technology applicable to a broad spectrum of really large-scale problems of practical importance, the questions of efficiency and reliability are in fact the central problems. Also, in the case of superfluid refrigerators where the vapor pressure of helium is low, substantial expense is involved in the room temperature pumping equipment and the space it requires. Thus it is very desirable to recompress the returning helium vapor at low temperature where it is more dense. We are now beginning a cooperative program to investigate the problems of efficiency and low temperature recompression with the expectation of constructing a 1000-2000 W superfluid refrigerator that operates at 25-35% of Carnot efficiency. Such a system would represent a further advance in the state of the art.

### 3. Laboratory with Central Refrigeration

The SCA provides an excellent opportunity to demonstrate the feasibility of operating a large and complex laboratory with central refrigeration. In total our laboratory is 800 ft long, 60 ft wide and 60 ft high and we expect to make refrigeration available throughout this space to serve a large number of separate experimental units. A cryogenic system of this magnitude and this complexity is quite different than any considered previously. It is out of the question to shut down and warm up an entire laboratory in order to replace a single defective component and it is essential that a new experimental unit can be connected into the central refrigeration system at any time.

The SCA itself is illustrative of the problems encountered in a central refrigeration system.<sup>7,8</sup> The accelerator Dewar and the accelerator structure are constructed in 20 ft sections. A single cryogenic unit consists of four of these sections and there are in total six units plus the injector unit. First, it should be recognized that even a single cryogenic unit is quite complex. There are perhaps 100 seals in each unit and even a one percent chance that a seal will fail is intolerable. There is no alternative to reliability and thus we have expended a sizable effort in designing satisfactory seals. Second, in the event of some component failure the relevant cryogenic unit must be isolated from the rest of the system and the defective section must be replaced with a spare section. In order to accomplish this in minimum time without disruption of the central refrigeration system we have made provisions for the necessary manifolding and cryogenic valving and we have demanded interchangeability of components. Third, refrigeration must be provided from the central plant to each of the cryogenic units. In the SCA, superfluid helium is distributed to each of the units via a one inch liquid line that extends the length of the accelerator; the liquid vaporizes and the cold vapor is then transported back to the refrigerator in a 5 in. diameter insulated line. This method of heat transport is consistent with the desire to split the entire low temperature system into smaller units for ease of maintenance and with this method it appears entirely possible to transport 1000 W a distance of 1000 ft and still maintain the temperature constant to within 10-20 m°K.

In addition, we are developing another interesting application of superfluid helium.<sup>9</sup> If two reservoirs are connected by a plug which is porous only to the superfluid, then associated with any temperature difference between the reservoirs there is a large pressure difference known as the fountain pressure. For  $\Delta T \sim 0.2^\circ\text{K}$  this pressure difference can be used to raise the helium level in the "hot" reservoir on the order of 100 ft. Thus, refrigeration can be provided to equipment, for instance a superconducting spectrometer, at elevations far above the normal helium level in the SCA itself and this can be accomplished without the necessity of a cryogenic mechanical pump.

The idea of central refrigeration and the demonstration of its practicality is extremely important to the development of low temperature technology for a broad spectrum of large-scale applications. In high energy physics central refrigeration could be important in a superconducting proton synchrotron, in a superconducting storage ring,

---

7. H.A. Schwettman, J.P. Turneure, W.M. Fairbank, T.I. Smith, M.S. McAshan, P.B. Wilson, and E.E. Chambers, High Energy Physics Laboratory Report HEPL 503 (1967).

8. M.S. McAshan, High Energy Physics Laboratory Report HEPL 526 (1967).

9. C.M. Lyneis and H.A. Schwettman, High Energy Physics Laboratory Report HEPL 577 (1968).

or in a superconducting beam switchyard,\* in addition to the specific application we are considering. Cryogenic technology as it exists today in commercially available equipment is not prepared to cope with the problems of central refrigeration. It is an important objective of our laboratory to take the steps required in its development.

#### 4. Stabilization Using Feedback Control

In a SCA essentially all of the incident microwave power is absorbed by the beam. This situation has prompted questions from accelerator physicists relating to stability in a beam-loaded SCA. But concern about the possibility of achieving stable operation in a SCA is a holdover from conventional linacs. In the conventional linac 80-90% of the microwave power is lost in the structure or in the termination. Thus, fluctuations in the beam loading result at most in modest variations of the load seen by the klystron. As a physical principle, this is a poor way to achieve stability; it has proved adequate in conventional linacs but it is not an appropriate method for the SCA. The SCA, on the other hand, is an ideal system in which to use the more general principle of dynamic stability.

Dynamic stability using feedback control has been used in many systems. An excellent example is provided by electrostatic gyroscopes. It is well known that an electrostatic field does not provide a stable support for a conducting sphere. Yet by sensing the position of the sphere and using feedback to control the voltage on the supporting electrodes, it is possible to hold the position of a gyroscope to one millionth of an inch. The stabilization of the SCA, as illustrated in Fig. 3, is analogous. The fields in the accelerator structure are sampled with a probe and the output from this probe is compared to a reference signal with respect to both amplitude and phase. The error signals are then fed to an electronic phase shifter and a variable attenuator at the input of the klystron to close the feedback loop. The long time constant ( $> 10^{-3}$  sec) for changing the fields in the SCA (due to the high Q) simplifies the feedback problem and stabilization to one part in  $10^4$  in amplitude and to  $0.1^\circ$  in phase has been achieved in preliminary tests.<sup>10</sup>

#### 5. Minimum Radiation Facility

The new technology presently being developed using either low temperature techniques or plasma techniques (in an electron ring accelerator) offer a real opportunity for substantial reduction in the cost of high energy accelerators. Despite this encouraging outlook, the prospects for substantial reduction in the cost of the entire facility is less certain. Smith and Lewin<sup>11</sup> of the Rutherford Laboratory, for example, suggest that a superconducting proton synchrotron could be built for half the cost of its conventional counterpart, but note that this represents only a 20% reduction in total costs. It is clear that one cannot make any real progress without changing the economics of the over-all facility.

One important contributor to the cost of a high energy facility is radiation. The total cost attributable to radiation, including permanent shielding throughout

---

\* The recent report "Refrigeration for Superconducting Magnets in the 200 BeV Accelerator at Weston, Illinois" correctly concludes that with presently available components, superconducting magnets in a beam switchyard would be served best by individual refrigerators. The work in progress at Stanford, however, will change significantly the possibility of using central refrigeration.

10. L.R. Suelzle, High Energy Physics Laboratory Report HEPL 564 (1968).

11. P.F. Smith and J.D. Lewin, Nucl. Instr. Methods 52, 298 (1967).

the facility, movable concrete shielding blocks, radiation resistant materials in various components, large collimators, energy defining slits and so forth, is enormous. In the cost estimate for a conventional proton synchrotron of 200 GeV presented in 1965 to the Joint Committee on Atomic Energy, it was estimated that thirty million dollars would be required for movable shielding alone. In principle there is no reason for generating large amounts of radiation except in the target and in the beam dump. If radiation levels elsewhere were minimal, and there are good reasons to believe that in a SCA this could be achieved, then a high energy facility could be quite different than at present. In a linac, for example, there would be no need for a separate klystron gallery and long rf feed lines. Indeed, for a SCA where the rf power level required is modest it is likely that solid state rf sources will in time be used. Even the accelerator hall itself could be modestly shielded by present standards. Also, with the excellent energy resolution and stability possible in a SCA (one part in  $10^4$ ) the radiation level in the beam switchyard could be held to a minimum. Instead of energy defining slits which are designed to handle 10% of the beam power, beam position monitors could be used supplemented perhaps with slits that are set for several times the inherent width of the beam. Low radiation levels along the accelerator and throughout the beam switchyard could make a significant impact on the cost of a high energy facility. Of course, monitoring devices would be required to shut down the accelerator immediately and automatically in the event that radiation levels increase. But it is expected that this can be accomplished in a simple fashion at relatively small expense. With strict interlocks against increased radiation levels it might appear that initial tune-up of the machine would be difficult. In a fully regulated SCA, however, the initial steering and focusing can be performed at very low intensity. Subsequently, as the current is increased, the feedback stabilization compensates automatically for the increased beam loading.

The suggestion that an accelerator could be operated as a minimum radiation facility is likely to be viewed as fantasy, but if still larger accelerators are to be built, it is probable that all of the traditional ideas of accelerator physics must be re-examined. It is our intention at Stanford to examine carefully this idea and to develop completely the control and interlock systems required.

### III. A FEW APPLICATIONS TO HIGH ENERGY PHYSICS

#### 1. High Resolution CW Linac

One of the frontiers we intended to explore fully at Stanford is the high energy resolution that is possible in a cw SCA. As indicated earlier, the SCA is an ideal system for use of feedback to achieve dynamic stability and it is this fact that has encouraged us to strive for energy resolution of 0.01% in the SCA (100 keV at 1 GeV), as compared to the 1% resolution typical of conventional linacs. This effort is essential to our objective of doing high resolution physics at high energy and to our intention of exploring the feasibility of a minimum radiation facility.

To produce a beam monoenergetic within one part in  $10^4$  requires, in addition to stability of the accelerating fields, that the electrons be confined to a  $1^\circ$  phase bunch. This bunching is accomplished in the injector section and the capture section of the accelerator. As illustrated in Fig. 4, the electrons are emitted from a regulated triode gun and accelerated to 80 kV. The continuous stream of electrons then passes through a chopper cavity and the aperture on the far side stops all electrons except those in a  $20^\circ$  phase bunch. These electrons are injected into a specially designed capture section where they are accelerated to about 2 MeV and where the electron bunch is compressed in phase to  $1^\circ$ . The capture section is a  $\beta = 0.95$  structure of  $2\frac{1}{2}$  wavelengths and the design energy gradient is 1 MeV/ft. The injector section and the capture section complete with electronic stabilization are under construction and

will be tested carefully this fall. Particle motion in the accelerator sections beyond the capture section has been calculated,<sup>12</sup> using the fields in a computer optimized bi-periodic  $\pi/2$ -mode structure,<sup>13</sup> including the effects of radial motion and misalignment of individual accelerator sections.

How far resolution can be pushed in a SCA is not entirely clear. But we are considering even more sophisticated techniques in conjunction with a feasibility study for an electron microscope where energy resolution of one part in  $10^6$  is required at 5-10 MeV.

## 2. High Intensity Linac

From a superficial point of view it would appear that the SCA has little to offer in the design of high intensity linacs such as the meson factory at Los Alamos or the intense neutron generator (ING) proposed at Chalk River. It is easily argued that at high intensity the conventional linac is quite efficient (about 80% of the microwave power is converted to beam power according to the Chalk River design for the ING) and thus superconductivity is simply not required. But this argument misses the essential point; efficiency in the conventional linac is achieved only at great sacrifice. The energy gradient for the meson factory at Los Alamos is about 0.30 MeV/ft (800 MeV in 2600 ft) and for the proposed ING at Chalk River is about 0.2 MeV/ft (1 GeV in 5000 ft). In fact, since the power dissipated in the structure walls is proportional to  $(V/L)^2$  and the power extracted by the beam is proportional to  $(V/L)$ , it is not surprising that for low energy gradient a conventional linac is efficient.

What superconductivity offers in the high intensity linac is a great deal of flexibility in the design of the accelerator. Let us consider just two examples of what this flexibility can provide. First, it is obvious that efficient operation can be achieved at much higher energy gradients. The meson factory at Los Alamos or the ING at Chalk River could be a few hundred feet in length rather than a few thousand feet. Alternatively, the final energy could be increased substantially and it would then be possible to produce K mesons in abundance. Second, the problem of beam loading is simple in the SCA as compared to the conventional linac. In the limit of heavy beam loading the time constant, defined as the ratio of microwave energy stored in the accelerator structure divided by the rate that energy is extracted, is:

$$\tau = \frac{1}{\omega(r/Q)} \cdot \frac{(V/L)}{I},$$

where  $\omega$  is the angular frequency,  $r/Q$  is the shunt impedance per unit length divided by the  $Q$  of the structure,  $V/L$  is the energy gradient, and  $I$  is the beam current. For the conventional intense linac this time constant is a few microseconds, but, principally due to the high energy gradient, the time constant for the SCA is a fraction of a millisecond. Thus feedback stabilization in the SCA even for the heavy beam loading of a meson factory or an ING, is quite simple. It should be added that stability in a proton linac where the velocity of the particle is changing is far more important than in an electron linac where the velocity is constant.

---

12. E.E. Chambers, High Energy Physics Laboratory Report HEPL 570 (1968).

13. T.I. Smith, High Energy Physics Laboratory Report HEPL 527 (1967).

### 3. High Energy Recirculating Linac

From the experience of the past decade it is generally recognized that the cost per GeV for a circular accelerator is substantially less than for a linac. However, if energy gradients of 10 MeV/ft can be achieved in the SCA, and we are confident they can, the economics of the linear accelerator are substantially improved and the question of linacs versus circular accelerators as a means of reaching very high energy must be re-examined.

One interesting possibility in the construction of a high energy accelerator, which is a compromise between the linear and the circular machines, is the recirculating linac. The possibility of recirculating a beam through a linear accelerator has been suggested a number of times in the past. An interesting example is the race track microtron for electrons of a few hundred MeV<sup>14</sup> which is illustrated in Fig. 5. A practical recirculating linac for very high energy particles is different in several respects from the race track microtron mentioned above. First, at very high energy, electrons radiate too much energy to make the scheme useful. But protons even for a final energy of 2000 GeV are not subject to this criticism. Second, for a very high energy accelerator the magnetic deflection system used in the race track microtron is totally impractical. Instead of solid 180° magnets it would be more reasonable to provide separate beam transport systems and arrange that the average radius of curvature for each beam is nearly the same so they could all be placed in a single tunnel. For the special case of three passes through the linac the beam transport system might be particularly simple, since, as illustrated in Fig. 6, recirculation could in principle be accomplished with a single magnet system for two thirds of the final energy.

One can give a crude "existence proof" that on economic grounds the recirculating linac is an interesting alternative for reaching high energy. For this purpose let us compare the superconducting recirculating linac and the superconducting proton synchrotron. It is clear that the rf system represents a minor contribution to the cost of a proton synchrotron while it represents a major cost in a recirculating linac. On the other hand the magnet system is less expensive for a recirculating linac since the magnets used are dc magnets (which eliminates refrigeration for ac losses and large power supplies for pulsing magnets) and since the magnet ring is for  $(2/3)E$ . The question is whether or not these factors balance. The cost estimates below were generated by P.F. Smith of the Rutherford Laboratory and the author based on the assumptions: 1) that development of filamentary superconductor low loss ac magnets will proceed without important complications, and 2) that development of practical niobium rf cavities producing 10 MeV/ft in a traveling wave structure will be accomplished.

Costs in 1000 \$/GeV

	<u>Proton Synchrotron</u>	<u>Recirculating Linac</u>
Magnet system	185	75
Rf system	<u>30</u>	<u>150</u>
	215	225

These figures, of course, do not represent total costs of a high energy facility. They are intended only as comparative costs based on projected developments.

---

14. B.H. Wiik, H.A. Schwettman, and P.B. Wilson, High Energy Physics Laboratory Report HEPL 396 (1966).

Recently crude cost estimates have been generated for a number of "new technology" accelerators: the superconducting proton synchrotron, the cryogenic proton synchrotron, the superconducting recirculating linac, the superconducting FFAG, and the electron ring accelerator. Relatively little significance should be attached to any of these estimates, since all are based on important assumptions about how the relevant technology will develop over the next few years. What is far more significant and encouraging is that several possibilities exist for the construction of future high energy accelerators and these provide alternatives in the technology that must be successfully developed. This flexibility itself is our greatest asset.

#### IV. CONCLUSIONS

The low temperature technology being developed at Stanford can be important in a large number of applications. We have already mentioned the high resolution cw linac, the high intensity linac and the high energy recirculating linac. In addition, this technology is essential to the construction of a superconducting rf separator for use with the large proton synchrotrons, a  $\pi$ -meson accelerator which could be used in conjunction with the meson factory at Los Alamos, and a superconducting race track microtron for electrons of a few hundred MeV. All of these applications are now being given serious consideration by various groups throughout the world. Nor are the applications for this technology restricted to high energy physics. Superconducting cavities may in fact find application in problems as far removed from low temperature physics and high energy accelerators as the generation of electric power by thermonuclear fusion.

At Stanford we are strongly motivated to develop this technology as rapidly and as far as possible so that all of these applications can be pursued in the near future.

#### ACKNOWLEDGEMENTS

As noted in the introduction, to make a substantial contribution to this emerging low temperature technology requires the combined efforts of physicists who are both knowledgeable about the fundamental properties of matter at low temperature and willing to explore their applications, and engineers who are prepared to transform these ideas into a viable technology. The rapid progress in this development at Stanford is due to the enthusiastic efforts of Drs. E.E. Chambers, W.M. Fairbank, E. Jones, M.S. McAshan, T.I. Smith, L. Suelzle, J.P. Turneaure and the entire technical staff of the High Energy Physics Laboratory.

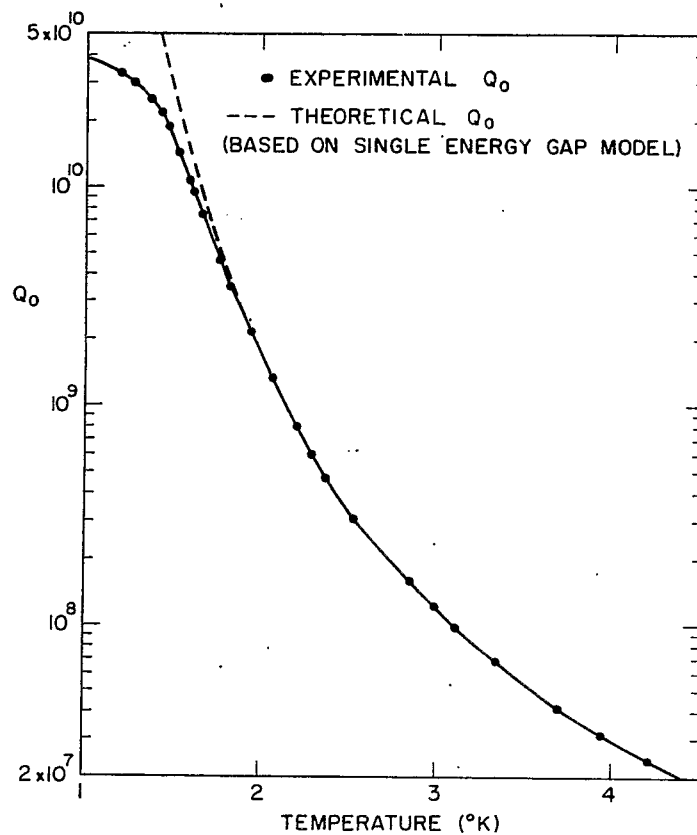


Fig. 1. The unloaded  $Q$  as a function of temperature for an X-band niobium cavity.

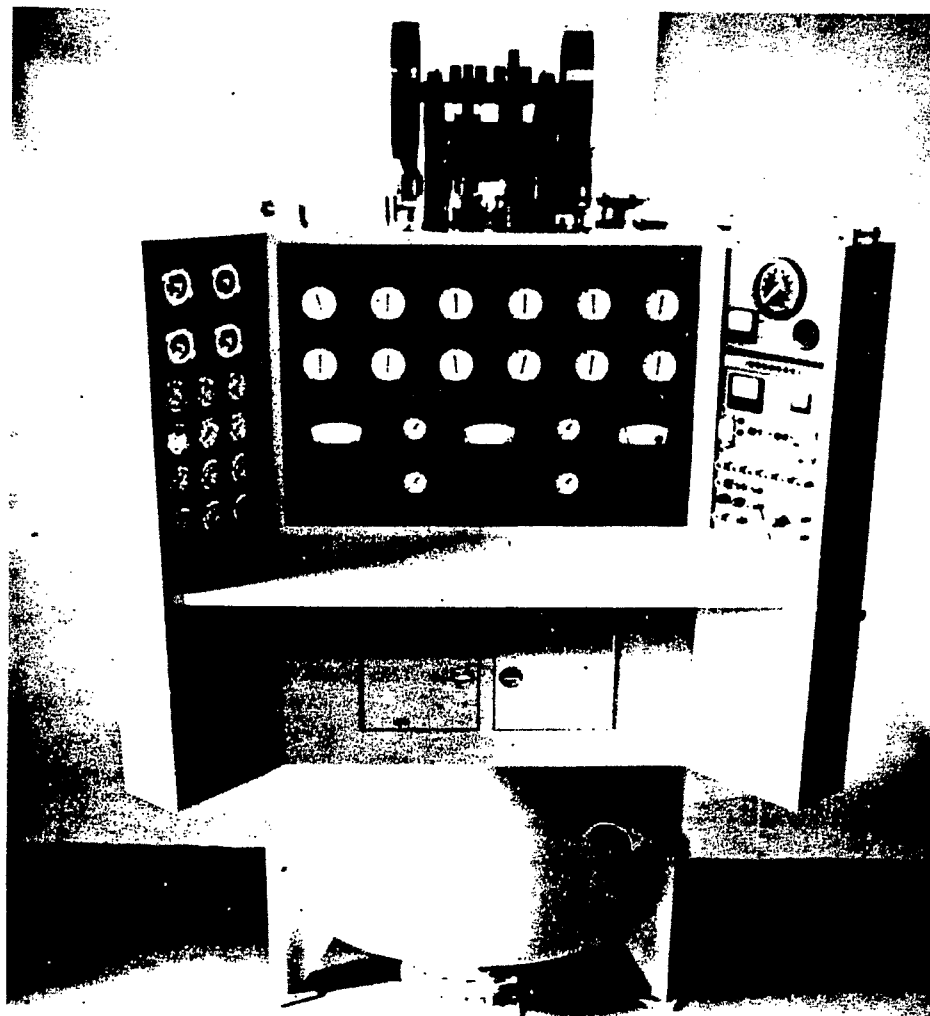


Fig. 2. Control panel and "cold box" of the 300 W superfluid helium refrigerator



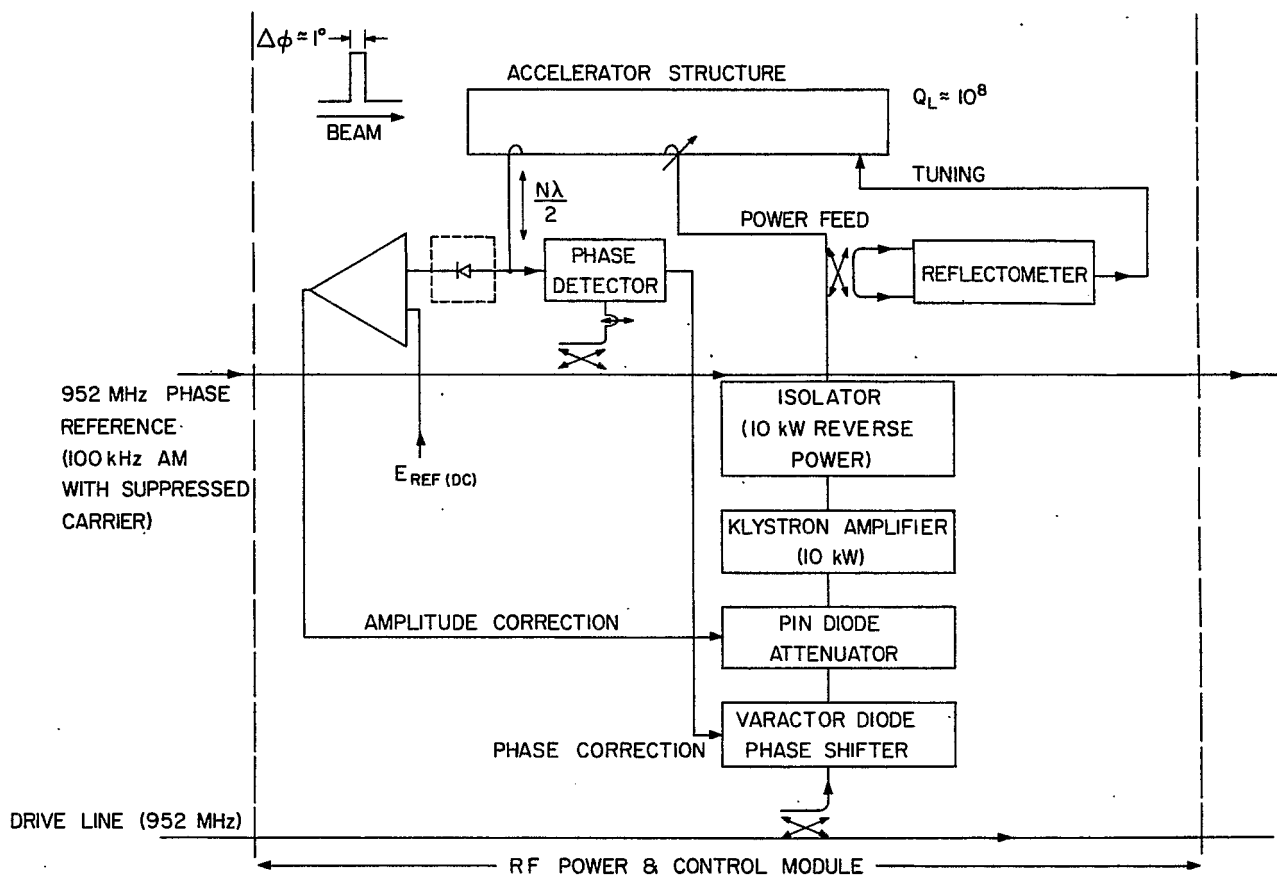


Fig. 3. Block diagram of a feedback stabilized superconducting accelerator section.

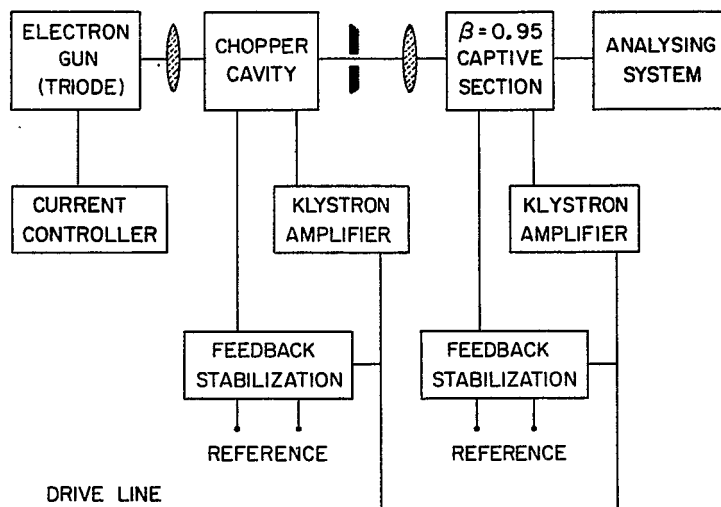


Fig. 4. Block diagram of the injector section and capture section.

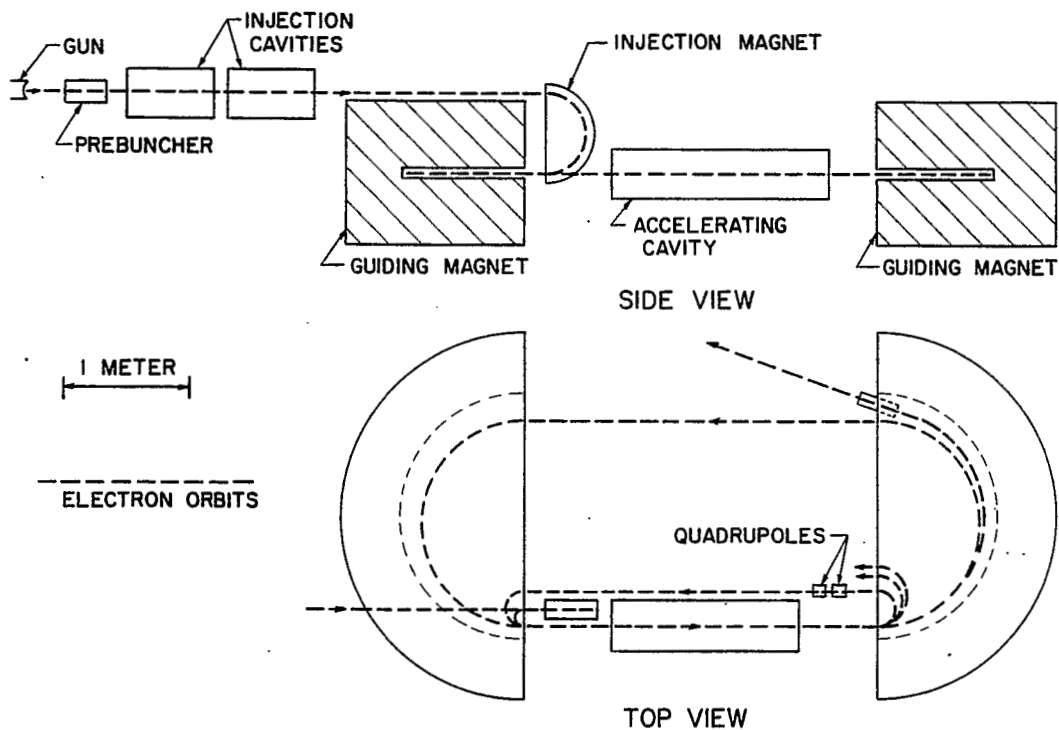


Fig. 5. Schematic drawing of the superconducting race track microtron.

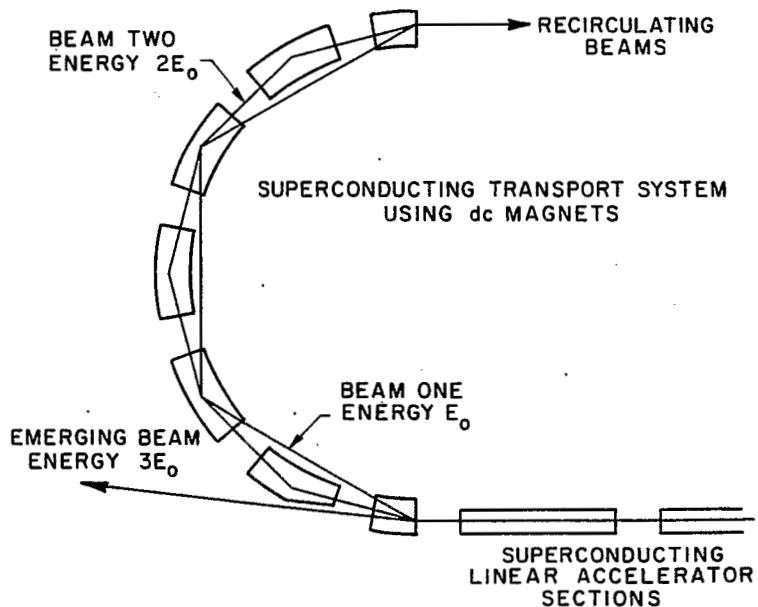


Fig. 6. Schematic drawing of a simple recirculating linac.

# Q MEASUREMENTS ON SUPERCONDUCTING CAVITIES AT S-BAND\*

H. Hahn, H.J. Halama and E.H. Foster  
Brookhaven National Laboratory  
Upton, New York

## I. INTRODUCTION

The investigation of the behavior of superconducting materials was started at this laboratory because of the potential usefulness of these materials for long-pulse rf beam separators which are suitable for counter experiments.<sup>1</sup> The realization of such a device will require the solution of many problems; questions related to the beam optics will be discussed during this Summer Study by Brown, and those related to the microwave system by Halama. Relevant measurements on superconducting lead cavities are the subject of this talk.

The materials of interest to us are pure lead and niobium. The technology of niobium appears to be more difficult, and our investigations have been limited so far to lead, electroplated on OFHC copper. However, cavities have been ordered from Varian which will be machined from electron-beam-melted niobium.<sup>2</sup>

In order to make our results more meaningful for the construction of superconducting deflectors, the investigations were carried out on cavities resonant at 2.87 GHz, which is close to the anticipated operating frequency of the rf beam separator. We also started with a TE<sub>011</sub> cavity which permits the elimination of losses caused by electric fields on the walls. The effects of a normal electric field will be investigated shortly in a TM<sub>011</sub> cavity.

## II. SURFACE IMPEDANCE

The microwave behavior of a superconducting material is conveniently described by the complex surface impedance  $Z = R + jX$ , which is in general a function of material, frequency, temperature and power level. In this paper, the experimental results for the temperature dependence of the surface impedance of superconducting lead at constant frequency and low power levels will be presented.

The measurement of the surface impedance is possible because it is related to the unloaded quality factor  $Q_0$  and the normalized shift of resonant frequency  $\delta\omega/\omega$  of a cavity according to<sup>3</sup>:

$$R + jX \approx \left( \frac{1}{Q_0} - j \frac{2\Delta\omega}{\omega} \right) G Z_0, \quad (1)$$

---

\*Work performed under the auspices of the U.S. Atomic Energy Commission.

1. H. Hahn and H.J. Halama, IEEE Trans. Nucl. Sci. NS-14, No. 3, 356 (1967).
2. J.P. Turneaure and I. Weissman, J. Appl. Phys. 39, 4417 (1968).
3. J.C. Slater, Rev. Mod. Phys. 18, 441 (1946).

with  $Z = c\mu_0$  being the impedance of free space and the geometrical constant  $G$  being defined by

$$G = \frac{\omega \int \vec{H}^* \cdot \vec{H} dV}{c \int \vec{H}^* \cdot \vec{H} dF} \quad (2)$$

For geometrically simple structures, this constant is calculable; it can always be obtained from a  $Q$  measurement on a copper cavity at room temperature, where the surface resistance is known from the classical skin effect. Accurate results, however, require a smooth surface which can be obtained by electropolishing of the surface.<sup>4</sup>

The geometrical constant  $G$  is usually considered to be temperature-independent, which, however, is only true if the surface roughness is small compared to the skin depth. The penetration depth of superconducting lead is about  $0.039 \mu\text{m}$ ;<sup>5</sup> it is therefore possible that a microroughness changes the value of  $G$ . The influence of a surface roughness at unchanged material properties was discussed by Lending,<sup>6</sup> Morgan,<sup>7</sup> and in the case of superconducting lead, by Halbritter.<sup>8</sup> As a result of the microroughness, the observed  $Q$  values will be lower than expected from theory, or, alternatively, the constant  $G$  of a superconducting cavity is not directly measurable. The measurement of the surface impedance of superconductors is, therefore, subject to systematic errors which are not easily corrected. For practical usage it seems preferable to quote the improvement factor, which is defined as the ratio  $I = Q_0/Q_{\text{Cu}, 300^\circ\text{K}}$ , and the variation of the resonant frequency with temperature.

The change of resonant frequency of the test cavity can be caused by a variation of the surface reactance or by dimensional changes with temperature. The selective measurement of the contribution due to the reactance involving the application of a magnetic field to destroy the superconducting state was described by Pippard.<sup>9</sup> The improvement factor is obtained from  $Q$  measurements on the test cavity. The measurement of the quality factor is a classical problem which is, however, somewhat complicated by the extremely high  $Q$  values of superconducting cavities;  $Q > 10^6$  requires some form of decrement method.<sup>10</sup> We found it advantageous to shock-excite a transmission-type cavity by a frequency-swept signal and to observe the decaying eigenoscillations at the cavity output.<sup>11</sup> This method is ideal for low level measurements involving the smallest possible rf heating but it would be less suitable for high power measurements.

- 
4. F. Biquard and A. Septier, Nucl. Instr. Methods 44, 18 (1966).
  5. J.M. Lock, Proc. Roy. Soc. London A208, 391 (1951).
  6. R. Lending, in The Microwave Engineer's Handbook (Horizon House, 1966), p. 84.
  7. S.P. Morgan, Jr., J. Appl. Phys. 20, 352 (1949).
  8. J. Halbritter, Report 3/68-1, Kernforschungszentrum, Karlsruhe, 1968.
  9. A.B. Pippard, Proc. Roy. Soc. London A191, 399 (1947).
  10. C.J. Grebenkemper and J.P. Hagen, Phys. Rev. 86, 673 (1952).
  11. H. Hahn, H.J. Halama, and E.H. Foster, in Proc. 6th Intern. Conf. High Energy Accelerators, Cambridge, Mass., 1967 (available from CFSTI, Springfield, Va.), p. A139.

### III. TEST CAVITY

The test structure is designed as a transmission-type rather than the frequently used reaction-type cavity because of its insensitivity to stray reflections and the possibility of carrying out measurements at very loose coupling. The disadvantage of not being able to use low loss waveguide feed systems is more than compensated for by the ease with which the coupling coefficient is adjusted when coaxial cables are used. The attenuation of radiated signals in the coaxial cables is readily measured and corrected for. Details of the TE<sub>011</sub> test cavity are described in Ref. 12. It should be pointed out here that our biggest problems were caused by vacuum leaks and rf feed-through, that is, a direct power transmission between input and output cable.

The superconducting material is obtained by electroplating a lead film 2.5  $\mu\text{m}$  thick on OFHC copper. Although a correspondence between the microstructure of the superconductor and the quality factor is not established, we feel that one should attempt to deposit the lead in as ideal a form as possible. The criteria by which we evaluate the lead surface are:

- 1) Continuity of the lead surface, i.e. absence of pinholes. This is achieved by the preparation of the copper surface and a proper choice of the plating procedure. Problems caused by trapped air bubbles are alleviated by shaping the geometry of the structure.
- 2) Large grain size as achieved by epitaxial crystal growth. This is achieved by annealing the copper prior to plating and by proper start of the crystal growth (nucleation).
- 3) High purity. This is achieved by using 99.999% pure lead anodes, by immersing the structure in the plating solution under voltage only and by plating the entire surface of the structure. Furthermore, the solution is outplated with slanted electrodes for several hours at very low current densities (0.1 mA/cm<sup>2</sup>).
- 4) Smoothness on microscopic level. This is achieved by comparatively slow electroplating or, better, by slow reverse plating.

The lead deposit is obtained by electroplating from a lead fluoborate bath. The procedure used is similar to industrial methods<sup>13</sup>; certain modifications, however, seem to improve the quality factor. Best results were obtained by adhering to the following procedure:

- 1) Machine the copper surface of the part to be plated to a 16-32  $\mu\text{in.}$  finish. Recrystallization by heating under hydrogen atmosphere is desirable, but has been omitted so far.
- 2) Degrease ultrasonically in vithane and then in safety solvent. Oakite 117 full strength is recommended.<sup>14</sup>
- 3) Soak clean for 3 minutes in Oakite 23 at  $82 \pm 5^\circ\text{C.}$  The concentration is 60 g/l of distilled water.

---

12. H. Hahn, H.J. Halama, and E.H. Foster, J. Appl. Phys. 39, 2606 (1968).

13. Technical Bulletin TA-38351, General Chemical Division, Allied Chemical Corp., Morristown, N.J.

14. Oakite Products, Inc., New York, N.Y.

4) Rinse in water.

5) Electropolish for 6 minutes in Electro-Glo 200.<sup>15</sup> The concentration is 75% by volume of phosphoric acid and 25% Electro-Glo 200. The voltage across the cell is about 7 V. The solution is at room temperature, but not above 27°C. If the surface is not satisfactory, repeat the electropolishing for another 4 minutes. Repeated polishing tends to etch the surface and mechanical polishing may be required.

6) Rinse, first in hot and then in cold water.

7) Anodically electroclean for 3 minutes in Oakite 191. The concentration is 60 g/l of distilled water. The voltage across the cell is about 6 V and the temperature of the solution is  $82 \pm 5^\circ\text{C}$ .

8) Rinse in water. The surface must wet, otherwise repeat electrocleaning.

9) Dip for 10 sec in fluoboric acid. The concentration is 25% by volume of fluoboric acid, 75% distilled water.

10) Dip in distilled water. Drain excess water to avoid streaks.

11) Plate in lead fluoborate bath at a current density of  $2.7 \text{ mA/cm}^2$ , higher during the initial few seconds. The concentration is 22.9% by volume of lead fluoborate concentrate<sup>13</sup> and 77.1% distilled water. Add a small amount of fluoboric acid to achieve  $\text{pH} \leq 1$ ; add 0.4 g/l of extracted bone glue to prevent treeing.<sup>16</sup> Normal plating requires 17 minutes to deposit  $2.5 \mu\text{m}$  of lead. Surface roughness is reduced by reverse plating (20 sec plating, 10 sec polishing<sup>17</sup>) which is done for 30 minutes after 7 minutes of normal plating.

12) Rinse in water.

13) Dip for 3 minutes in Varsene 100. The concentration is 168 g of Varsene 100 with the addition of  $5.3 \text{ cm}^3$  of Duponol per liter of distilled water.<sup>18</sup>

14) Rinse in water.

15) Dip in distilled water.

16) Dip in 200-proof alcohol.

17) Dry under air flow. If watermarks appear, repeat step (13) and on.

---

15. Electro-Glo Company, Chicago, Illinois.

16. Hydroquinone  $\text{C}_6\text{H}_4(\text{OH})_2$  may be used instead of bone glue. D. Gorlé and D. Leroy, private communication.

17. Better polishing is obtained by increasing the current tenfold and reducing the time correspondingly. R.W. Meyerhoff, private communication.

18. Varsene 100 by Dow Chemical Co.; Duponol by E.I. DuPont de Nemours & Co.

- 18) Good parts are stored under vacuum until they are assembled. If the plating is inadequate, the lead is stripped,<sup>13</sup> and the process is repeated starting with step (4). Repeated stripping tends to etch the surface and mechanical polishing is desirable.

#### IV. MEASUREMENTS

The quality factor of the superconducting cavity was measured by a frequency sweep technique. In the case of a fast adiabatic sweep through resonance ( $\dot{\Omega} \ll 1/Q \ll \sqrt{\dot{\Omega}} \ll 1$ ), the power transmission through the cavity may be expressed by<sup>11</sup>

$$\frac{P_{out}}{P_{in}} = \frac{\pi}{2 \dot{\Omega} Q^2} \left\{ \frac{4 \kappa_1 \kappa_2}{(1 + \kappa_1 + \kappa_2)^2} \right\} e^{-\omega_0 t / Q} \quad (3)$$

The loaded  $Q$  follows directly from the time constant of the decaying output signal. The unloaded  $Q_0 = Q(1 + 2\kappa)$  requires the knowledge of the coupling coefficients which are made equal by a symmetric geometry. The coupling coefficient is determined from the amplitude of the output signal and the sweep rate  $\dot{\Omega} = \dot{\omega}/\omega_0^2$ . The transmitted signals refer directly to the cavity input and output and corrections for cable attenuation are necessary.

Errors may be caused by unequal coupling coefficients, FM noise of the source, and stray reflections. The presence of FM modulation would manifest itself by a jitter of the output power and is easily detected. The equality of the coupling coefficients can be verified by comparing the signals reflected from the input port, and from the output port when it serves as an input port. The most accurate measurements, however, are obtained by reducing the coupling coefficients to a few percent. The coupling coefficient is limited by the sensitivity of the detector at the output; the combination of a low noise TWT plus a crystal diode was found to be adequate.

The best results obtained on a  $TE_{011}$  cavity resonant at 2.87 GHz are listed in Table I. The unloaded quality factor of a congruent copper cavity at room temperature is  $Q_{Cu, 300^\circ K} = 56 \times 10^3$ , to which the improvement factor is normalized. The experimental results were compared with the AGK theory and adequate agreement was found.<sup>12</sup>

TABLE I

T ( $^\circ K$ )	$Q_0$	I
4.2	$2.35 \times 10^8$	$4.2 \times 10^3$
3.7	$3.92 \times 10^8$	$7.0 \times 10^3$
3.45	$4.90 \times 10^8$	$8.8 \times 10^3$
3.20	$6.68 \times 10^8$	$1.2 \times 10^4$
2.95	$8.82 \times 10^8$	$1.6 \times 10^4$
2.70	$1.3 \times 10^9$	$2.3 \times 10^4$
2.45	$2.26 \times 10^9$	$4.0 \times 10^4$
2.20	$3.73 \times 10^9$	$6.7 \times 10^4$
1.92	$6.93 \times 10^9$	$1.2 \times 10^5$
1.90	$7.01 \times 10^9$	$1.3 \times 10^5$
1.70	$9.96 \times 10^9$	$1.8 \times 10^5$
1.50	$11.33 \times 10^9$	$2.0 \times 10^5$

It is appropriate to mention that the above results were obtained at small power levels ( $H \ll H_C$ ). Power measurements on  $TE_{011}$  and  $TM_{011}$  cavities are in progress and will be reported as soon as conclusive results are available.

# COUPLING LOSSES IN SUPERCONDUCTING CAVITIES\*

H. Hahn and J.M. Miller<sup>†</sup>  
Brookhaven National Laboratory  
Upton, New York

## I. INTRODUCTION

The nature of the residual losses in superconducting cavities is not yet completely understood. Magnetic flux trapped in the superconducting surface is known to be a source of losses,<sup>1</sup> which can, in practice, be eliminated by proper magnetic shielding. On the other hand, it was shown that losses in the coupling mechanism can, under certain conditions, represent an important contribution.<sup>2</sup>

In this paper we intend to investigate theoretically the losses of a piston-type coupling mechanism which consists of a coaxial cable with a coupling loop and a below-cutoff tube coupled to the TE<sub>011</sub> cavity through an iris. The coupling to the cavity by means of waveguides can be made practically lossless and need not be considered here. It was possible to derive expressions for the maximum measurable quality factor which suggest ways of reducing the residual losses due to the coupling mechanism. Previously published Q measurements<sup>3</sup> are analyzed in regard to coupling losses and it is concluded that the residual losses must have a different origin.

## II. THE UNLOADED QUALITY FACTOR

The unloaded quality factor (no radiation losses) of a cavity is defined by  $Q_0^{-1} = P/\omega W$ , where P represents the wall losses, W the total stored energy, and  $\omega$  the resonant frequency. In the case of a cavity with a homogeneous surface,  $Q_0$  is related to the surface impedance by  $Q_0 R = G$ , where R is the surface impedance, and the geometrical constant, G, is given in natural units by

$$G^{-1} = \frac{\int \vec{B}^* \cdot \vec{B} dS}{k \int \vec{B}^* \cdot \vec{B} dV} \quad (1)$$

with the wave number  $k = \omega$ .

At first we will derive G of the TE<sub>011</sub> cavity coupled to an infinitely long below-cutoff waveguide by an iris in one end plate. The iris is located at the point of maximum magnetic field of the TE<sub>011</sub> cavity and on the axis of the TE<sub>11</sub> guide (Fig. 1).

---

\* Work performed under the auspices of the U.S. Atomic Energy Commission.

<sup>†</sup> Summer student from Queens College of the City University of New York.

1. J.M. Pierce, H.A. Schwettman, W.M. Fairbank, and P.B. Wilson, in Proc. 9th Intern. Conf. Low Temperature Physics, Columbus, Ohio (Plenum Press, New York, 1965), p.396.
2. H. Schopper, to be published in the Proc. of the 1968 Linear Accelerator Conference, Brookhaven.
3. H. Hahn, H.J. Halama, and E.H. Foster, J. Appl. Phys. 39, 2606 (1968). See also these Proceedings, p. 13.



Homogeneous surface properties are assumed, which means that both the cavity and the below-cutoff tube must be lead-plated.

The expressions for the magnetic field in the unperturbed TE<sub>011</sub> cavity (region I) can be written in circular cylinder coordinates as

$$\begin{aligned} B_r^I &= J_1(j'_{01} r/a) \cos \pi z/\ell \\ B_\theta^I &= 0 \\ B_z^I &= \frac{j'_{01}}{\pi} \frac{\ell}{a} J_0(j'_{01} r/a) \sin \pi z/\ell, \end{aligned} \quad (2)$$

where  $a$  is the radius and  $\ell$  the length of the cavity. The following integrals will be needed to evaluate Eq. (1):

$$\int \vec{B}^{I*} \cdot \vec{B}^I dV = \frac{\pi}{2} a^2 \ell J_0^2(j'_{01})(1+g) \quad (3)$$

$$\int \vec{B}^{I*} \cdot \vec{B}^I dS = \pi a \ell J_0^2(j'_{01})(2a/\ell + g), \quad (4)$$

where

$$g = \left( \frac{j'_{01}}{\pi} \frac{\ell}{a} \right)^2.$$

The geometrical constant in the absence of a coupling hole follows as

$$G^{-1} = \frac{4}{k\ell} \frac{1 + \frac{1}{2} g\ell/a}{1+g}. \quad (5)$$

The resonant frequency in the unperturbed case is found from

$$k\ell = \pi(1+g)^{\frac{1}{2}},$$

and finally

$$G^{-1} = \frac{4}{\pi} \frac{1 + \frac{1}{2} g\ell/a}{(1+g)^{3/2}}. \quad (6)$$

In the Brookhaven cavity,<sup>3</sup>  $\ell = 2a$  and  $G^{-1} = 0.483$ .

Due to the iris of radius  $\rho$ , a TE<sub>11</sub> far-field will be excited in the below-cutoff tube with radius  $b$  which can be approximated for  $z > 0$  by

$$\begin{aligned} B_r^{II} &\approx C J_1'(\alpha r) e^{-\alpha z} i e^{-i\theta} \\ B_\theta^{II} &\approx C \frac{J_1(\alpha r)}{\alpha r} e^{-\alpha z} e^{-i\theta} \\ B_z^{II} &\approx -C J_1(\alpha r) e^{-\alpha z} i e^{-i\theta}, \end{aligned} \quad (7)$$

where the attenuation constant  $\alpha^2 = (j'_{11}/b)^2 - k^2$ . In practically important cases where the cutoff tube has a radius  $b \ll a$ ,  $\alpha$  is simply  $\alpha \approx j'_{11}/b$ . The amplitude  $C$

follows from Bethe's small-hole approximation,<sup>4</sup>

$$C = \frac{4}{3\pi} \frac{j_{11}^{'3}}{(j_{11}^{'2} - 1) J_1(j_{11}')} \left( \frac{\rho}{b} \right)^3 \quad (8)$$

or  $C = 1.90 (\rho/b)^3$ . This result can be verified in the case of  $\rho = b$ , for which direct field matching leads to  $C = 2 j_{11}'^2 (j_{11}'^2 - 1)^{-1} = 1.54$ .

To evaluate the geometrical constant in the presence of an iris, we will need the following integrals taken over the infinitely long unperturbed (i.e. open) below-cutoff tube:

$$\int \vec{B}^{II*} \cdot \vec{B}^{II} dv = \frac{\pi}{2} b^3 \frac{(j_{11}^{'2} - 1) J_1^2(j_{11}')} {j_{11}^{'3}} c^2 \quad (9)$$

and

$$\int \vec{B}^{II*} \cdot \vec{B}^{II} dS = \frac{\pi}{2} b^2 \frac{J_1^2(j_{11}')}{j_{11}^{'3}} (1 + j_{11}^{'2}) c^2 \quad (10)$$

Because our analysis neglects near-fields in the vicinity of the iris, Eqs. (9) and (10) are obviously only approximate expressions. This is, however, inconsequential since the geometrical constant of the cavity is practically unaffected by the cutoff tube. To show this, we compare Eqs. (3) and (4) with Eqs. (9) and (10) and find that for  $\ell = 2a$

$$\frac{\int \vec{B}^{II*} \cdot \vec{B}^{II} dv}{\int \vec{B}^{I*} \cdot \vec{B}^I dv} \approx 0.2 \left( \frac{b}{a} \right)^3 \left( \frac{\rho}{b} \right)^6$$

and

$$\frac{\int \vec{B}^{II*} \cdot \vec{B}^{II} dS}{\int \vec{B}^{I*} \cdot \vec{B}^I dS} \approx 0.2 \left( \frac{b}{a} \right)^2 \left( \frac{\rho}{b} \right)^6$$

We conclude that the geometrical constant of the Brookhaven cavity ( $b/a \approx 0.1$ ) is completely determined by the unperturbed  $TE_{011}$  cavity and is given by Eq. (6). Thus the losses of a lead-plated below-cutoff tube are negligible.

The situation changes completely if a coaxial cable with a coupling loop is inserted into the below-cutoff tube. This exposes an area  $A_1$  of normal metal, of which the cable is made, to a magnetic field resulting in additional rf losses:

$$\Delta P \approx \frac{1}{2} R_N A_1 C^2 e^{-2\alpha z} \quad (11)$$

where  $R_N$  is the surface resistance in the normal state. The geometrical constant is now dependent on the loop position according to

---

4. R.E. Collin, Foundations for Microwave Engineering (McGraw-Hill, New York, 1966), p. 190.

$$G^{-1} = \frac{\int \vec{B}^{I*} \cdot \vec{B}^I dS + (R_N/R_S) A_1 C^2 e^{-2\alpha z}}{k \int \vec{B}^{I*} \cdot \vec{B}^I dV} \quad (12)$$

At low temperatures the ratio of normal to superconducting surface resistance,  $R_N/R_S$ , becomes very large and the influence of the coupling loop may not be negligible. A method of eliminating the cable influence by measuring at various loop positions was described by Schopper.<sup>2</sup> This method is rather time consuming and we will investigate in the following section whether the influence of the coupling loop can be eliminated or at least reduced.

### III. THE MAXIMUM MEASURABLE $\hat{Q}_0$

Equation (12) suggests that we may reduce the coupling losses by pulling back the coupling loop from the cavity. This does, however, limit the power which may be coupled out of the cavity, the lower limit being determined by the sensitivity of the instrument used for the rf power measurement. The maximum unloaded quality factor measurable with a given experimental setup is (in natural units) obviously

$$\hat{Q}_0 = \frac{kW}{\Delta P} \quad (13)$$

$\Delta P$  is determined by the minimum power detectable,  $P_{\min}$ , because the radiated power is related to  $\Delta P$  by the loop geometry. Neglecting the inductance<sup>5</sup> and resistance of the loop, the power radiated into the cable is obtained as

$$P_{\text{rad}} = \omega^2 A_2^2 C^2 e^{-2\alpha z} / Z, \quad (14)$$

where  $Z$  is the characteristic impedance of the cable and  $A_2$  the area of the loop. It follows that

$$\hat{Q}_0 = \frac{2 k^3 W A_2^2}{R_N Z A_1 P_{\min}} \quad (15)$$

We see that  $\hat{Q}_0$  can be influenced by the geometry of the coupling loop and by the sensitivity of the power meter. It seems advantageous to work with relatively large loops (reactance about equal to  $Z$ ) and to use a low noise, high gain amplifier at the cable end.

On the other hand, it is worthwhile to point out that the coupling loop hole size  $\rho$  is, in principle, irrelevant to the problem; it determines only the position of the loop at which the measurement is made and consequently the required length of the below-cutoff tube. Because of difficulties with the plating of the superconducting surfaces, the smallest coupling hole is nevertheless desirable.

---

5. The self-inductance of the loop is about equal to its diameter. C.C. Johnson, Field and Wave Electrodynamics (McGraw-Hill, New York, 1965), p. 202. See also S. Ramo, J.R. Whinnery, and T. van Duzer, Fields and Waves in Communication Electronics (John Wiley & Sons, New York, 1965), p. 311.

The Q measurements reported in Refs. 3 and 6 were performed with the same coupling loop. In Ref. 3, the iris hole radius was reduced, and a TWT amplifier with 30 dB gain was inserted between cable output and diode. From the preceding discussion it follows that the maximum measurable  $Q_0$  was increased in Ref. 3 by a factor of 1000 resulting in a  $Q_0 \geq 10^{12}$ . This is much larger than the measured quality factor which permits the conclusion that the residual resistance quoted in Ref. 3 was not caused by position-dependent losses in the coupling mechanism. On the other hand, recent measurements on another cavity of similar geometry show clear evidence of position-independent coupling losses. The analysis of this type of loss is not covered in this paper, and it is not impossible that the residual Q in Ref. 3 is caused by position-independent losses.

#### ACKNOWLEDGEMENTS

The writing of this paper was initiated by a stimulating discussion with Dr. W. Jüngst of Karlsruhe.

- 
6. H. Hahn, H.J. Halama, and E.H. Foster, in Proc. 6th Intern. Conf. High Energy Accelerators, Cambridge, Mass., 1967, p. A-139.

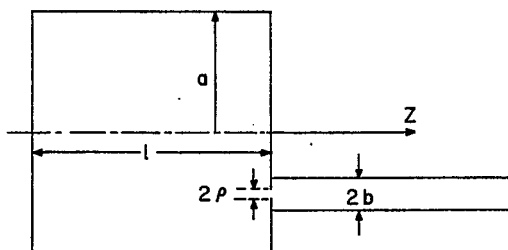


Fig. 1. Geometry of  $TE_{011}$  cavity with below-cutoff tube.

## FABRICATION OF NIOBIUM RF CAVITIES

R.W. Meyerhoff  
Speedway Research Laboratory  
Union Carbide Corporation, Linde Division  
Indianapolis, Indiana

### INTRODUCTION

Experimental studies of the nature and magnitude of ac losses in superconducting niobium were started by the Union Carbide Corporation, Linde Division in 1963. Most of this work was concentrated on niobium produced by the electroplating process developed within Union Carbide by Mellors and Senderoff.<sup>1</sup> Electrical resistivity measurements demonstrated that residual resistivity ratios greater than 20 000, a factor of nearly 10 greater than previously reported for niobium, could be obtained by vacuum outgassing this electroplated niobium.<sup>2</sup> In addition, vacuum outgassed electroplated niobium samples were prepared which showed the most complete magnetic reversibility and the lowest ac losses at magnetic fields up to  $\sim 1400$  G and frequencies up to 10 000 Hz ever observed in niobium.<sup>3</sup>

As the rf field amplitude is increased in a superconducting rf cavity the peak magnetic field at the cavity wall is also increased. Therefore, as the magnetic field at which the superconductor can be operated increases, the maximum energy gradient attainable also increases. Thus in choosing a superconductor for use in an rf cavity, in addition to those factors which influence the energy loss, consideration must be given to the maximum magnetic field at which it will be possible to operate the superconductor. In the case of a type II superconductor the maximum allowable magnetic field will be the thermodynamic critical field,  $H_c$ , while in the case of a type II superconductor it will be the lower critical field,  $H_{c1}$ . The lower critical field,  $H_{c1}$ , for ultra-high purity niobium is greater than either that of any other known type II superconductor or the thermodynamic critical field,  $H_c$ , of any type I superconductor. Thus the highest energy gradients theoretically attainable in a superconducting rf cavity would be in one fabricated of niobium. For this reason niobium is the preferred material for the fabrication of superconducting rf cavities. In addition, the performance of a niobium cavity is not as susceptible to deterioration with time due to oxidation as are lead cavities.

### DISCUSSION

High-purity niobium appears to be the ideal superconductor for use in rf cavities designed for use in linear accelerators and beam separators. In this section some of the problems that have been found to date in fabricating superconducting niobium rf cavities with high Q's are discussed. In addition, a unique new method presently being developed by Union Carbide for fabricating superconducting niobium rf cavities is described.

- 
1. G.W. Mellors and S. Senderoff, J. Electrochem. Soc. 112, 266 (1965).
  2. R.W. Meyerhoff, to be presented at and published in the Proc. of the Electro-Chemical Society Symposium on Preparation and Purification of Ultra-Pure Metals, Montreal, Canada, 1968.
  3. W.T. Beall and R.W. Meyerhoff, to be submitted to J. Appl. Phys.

In principle, all that is required for a superconducting niobium rf cavity is a niobium structure having the desired shape with niobium walls of the order of a few thousand angstroms thick. However, since many of the rf cavities proposed have dimensions of the order of 30 cm or more, such a structure made of niobium only a few thousand angstroms thick would not be self-supporting. Thus, in order to fabricate a superconducting niobium rf cavity there are four alternatives:

- 1) The cavity could be machined from a massive section of niobium with walls sufficiently thick to support the cavity when it is evacuated.
- 2) Deposit the niobium in some manner on a suitable substrate using a thin deposit of niobium as the superconductor with the substrate supplying the mechanical support.
- 3) Deposit niobium on a substrate, which will subsequently be removed, to a thickness sufficient that the niobium will support itself after the substrate is removed.
- 4) Deposit a thin layer of niobium on a substrate which will subsequently be removed and deposit a layer of suitable supporting material onto the niobium before removing the substrate.

The first of the alternatives seems to be impractical for a number of reasons, not the least of which is the prohibitive cost of the niobium required. In addition to the high cost inherent in machining an rf cavity from a solid piece of niobium this method makes it difficult if not impossible in many cases to make a series of complex cavities without one or more joints. For example, cavities such as those shown in Fig. 1 would have to be made in two or more sections since it is not feasible to machine such internal shapes in a solid piece and produce a high quality surface finish.

The second method in which one would fabricate an rf cavity by depositing a thin layer of niobium onto a substrate is more economical. In this case the mechanical support would be provided by the substrate. At first sight the simplest and most direct way of preparing this type of niobium rf cavity would be to use a high thermal conductivity material such as copper as a substrate and then deposit a thin layer of niobium on the inside of this substrate by some technique such as electroplating or vapor deposition. There are, however, two principal problems with this approach. First, rf cavities having complex shapes, such as those shown in Fig. 1, would have to be fabricated in two or more sections because of the difficulty in both machining such shapes and in depositing a niobium film on the inner surface of such shapes.

Second, in order to obtain the required performance in a superconducting rf cavity an extremely smooth superconducting surface is required. At this time the techniques given above do not produce an adequately smooth surface. It is possible to obtain a reasonably good surface by these techniques, if the original deposited niobium surface is then mechanically, chemically or electrically polished. However, this would be very difficult, if not impossible, in most cases because of the complex shapes of rf cavities.

Because of the economic and/or mechanical problems associated with the first two methods discussed above a new technique for manufacturing superconducting niobium rf cavities based on the third and fourth methods listed above is being developed. The steps used in fabricating an rf cavity by this method are illustrated in Figs. 2 and 3 and are described in detail below.

- Step 1. The first step is the fabrication of a copper substrate designed to conform to the shape of the inside of the rf cavity. That is to say, the copper substrate has the same dimensions as will the

empty space within the finished rf cavity. After machining, the copper substrate is first mechanically polished and then electro-polished. In the finished cavity the active niobium surface will be that surface which was originally in contact with the copper substrate and will therefore have a surface finish which is virtually identical to the original surface finish of the substrate.

Step 2A. A coating of niobium having the desired thickness is deposited onto the copper substrate by means of the fused salt plating process developed by Mellors and Senderoff.<sup>1</sup> Since this process is described in detail elsewhere<sup>1</sup> only a brief description is given below. An electrolyte consisting of 26.2 wt% LiF, 10.5 wt% NaF, 47.0 wt% KF and 16.3 wt%  $K_2NbF_7$  is used. During plating this electrolyte is maintained at  $\sim 775^\circ\text{C}$ . Commercial grade niobium is used for the anode and OFHC copper for the cathode substrate although many other materials such as iron, stainless steel, etc. are also suitable as cathodes. Normally niobium is electroplated at a current density of 5-125 mA/cm<sup>2</sup> which corresponds to a deposition rate of 5.08 - 127.0  $\mu\text{h}$ . A typical analysis of the electroplated niobium is as follows: carbon, < 1 ppm; oxygen, 40 ppm; hydrogen, 1 ppm; nitrogen, < 1 ppm; iron, nickel and chromium, 20 ppm each; tantalum, < 8 ppm; tungsten, 2 ppm. The first niobium plated from a new electrolyte will contain < 2 ppm tantalum; however, since this is considerably less than the several hundred ppm tantalum in the commercial purity niobium anodes used, the tantalum content in the electrolyte will increase with time with a concomitant small increase in the tantalum content in the electroplated niobium.

Step 2B. If the niobium deposited in step 2A is not thick enough to be self-supporting, a porous layer of tungsten is then deposited over the electroplated niobium. (While the tungsten can be deposited by plasma plating, powder metallurgy techniques or chemical vapor deposition, plasma plating has been used in the initial cavities prepared by this method.) The tungsten coating serves to support the niobium during the subsequent vacuum outgassing and to provide the mechanical support necessary in the finished rf cavity. In addition, the porosity of the tungsten should enable the helium in the liquid helium bath surrounding the cavity to circulate through it giving rise to an extremely high effective thermal conductivity between the niobium inner cavity wall and the surrounding liquid helium bath.

Step 3. Most of the machining of the plated cavity (machining of o.d. to final size, flanges, mounting holes, etc.) is done prior to the removal of the substrate. Those portions of the substrate used to hold the cavity during plating are also removed in this step.

Step 4. The copper substrate is removed from the electroplated niobium or niobium-porous tungsten composite structure. In the prototype cavities fabricated to date the copper substrate has been removed by dissolving it in dilute nitric acid. The copper substrate could also be removed electrolytically or by melting the copper and pouring most of it out using either nitric acid or an electrolytic method to remove the small quantity of copper left behind by the latter method.

Step 5. The rf cavity, either all niobium or niobium backed with porous tungsten is vacuum outgassed and annealed at a temperature of

$\sim 2200^{\circ}\text{C}$  at a pressure of  $\sim 10^{-8}$  torr. This step will also give rise to both some sintering of the porous tungsten increasing its mechanical strength and improving the quality of the tungsten-niobium bond.

Step 6. The last step consists of final trimming of the rf cavity, vacuum testing of the finished cavity and any other inspection operations necessary to insure that the finished product meets specifications.

#### SUMMARY

In the previous section a new technique for fabricating ultra-high-purity niobium rf cavities was described. It appears that this technique will eliminate the problems associated with the production of rf niobium cavities discussed earlier. The major features of this new fabrication method are discussed below.

- 1) This fabrication method provides a way by which a multiplicity of integrally connected rf cavities of complex shape can be fabricated in a single section free of joints.
- 2) By suitable initial finishing of the surface of the copper substrate an rf cavity can be fabricated which does not require any additional polishing to obtain an adequate surface finish on the niobium.
- 3) When a very high thermal conductivity is required porous tungsten can be used to provide mechanical support for the niobium.

To date, only a few rf cavities have been prepared by this fabrication method. These cavities, both the niobium and niobium backed by porous tungsten variety, have all been X-band cavities designed to be operated at 11.2 GHz. The best results obtained to date were on a  $\text{TE}_{011}$  mode cavity vacuum outgassed at  $2000^{\circ}\text{C}$  for 3 h for which  $Q \approx 2 \times 10^9$  and  $H_{ac} \approx 350 \text{ G}^4$ . A  $\text{TM}_{010}$  mode cavity tested as plated with no additional polishing or heat treating gave  $Q \approx 3 \times 10^7$  and  $H_{ac} \approx 110 \text{ G}^4$ . A  $\text{TE}_{011}$  mode cavity tested as plated gave  $Q \approx 1 \times 10^8$ .<sup>4</sup>

A few typical cavities fabricated by this method are illustrated in Figs. 4 and 5. Future work is planned to further improve the values of  $Q$  and  $H_{ac}$ . Some of the results obtained thus far indicate that by improving the quality of the surface finish on the copper substrate prior to electropolishing niobium higher values of  $Q$  and  $H_{ac}$  can be obtained for both the as-plated and the vacuum outgassed cavities. In fact for some applications, especially at frequencies lower than X-band, it may be possible to prepare cavities with useful  $Q$ 's without the need of any heat treatment subsequent to the electroplating.

---

4. J.P. Turneaure, Stanford University, private communication.



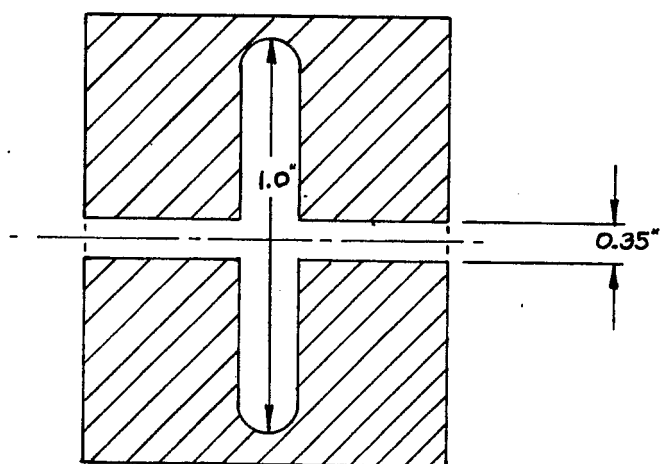
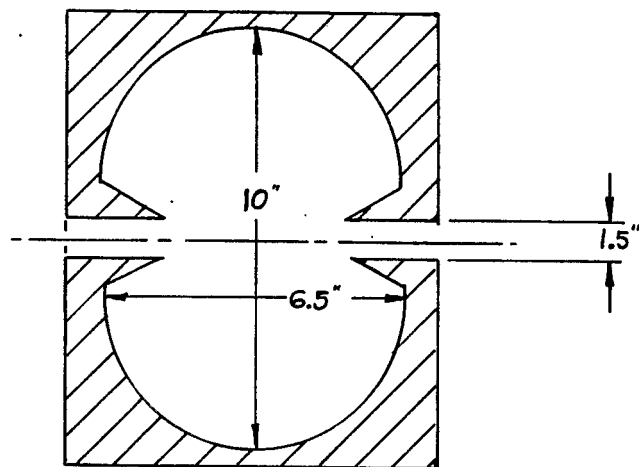
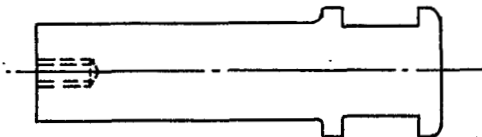
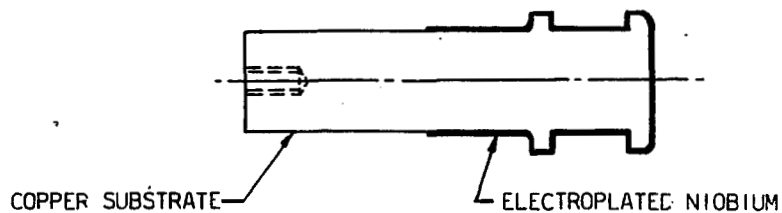


Fig. 1. Typical geometrically complex rf cavities.

**STEP 1 - FABRICATE COPPER SUBSTRATES**



**STEP 2A- ELECTROPLATE SUBSTRATE WITH NIOBIUM**



**STEP 2B- PLASMA PLATE TUNGSTEN**

(THIS STEP IS SKIPPED IF THE ELECTROPLATED NIOBIUM LAYER IS MADE THICK ENOUGH TO BE SELF SUPPORTING)

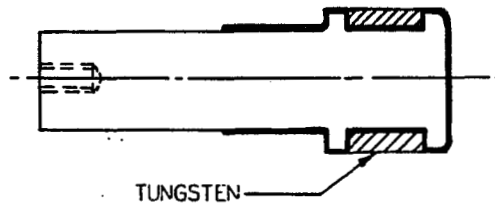
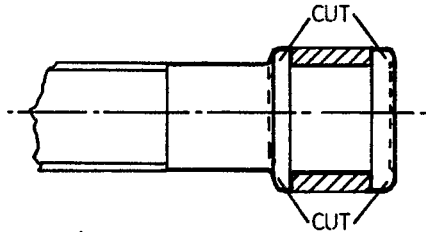


Fig. 2. Steps in the fabrication of rf cavities.

**STEP 3-** CUT OUT CAVITY SECTION



**STEP 4-** REMOVE COPPER

**STEP 5-** OUTGASS

**STEP 6-** FINISH R. F. CAVITY SECTION

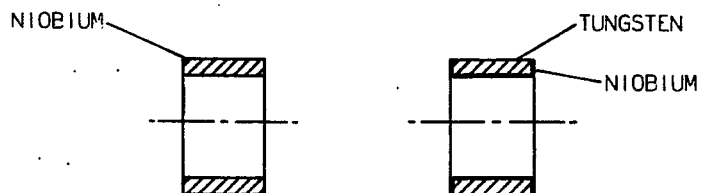


Fig. 3. Steps in the fabrication of rf cavities.

COPPER  
SUBSTRATE

FINISHED  
R.F. CAVITY

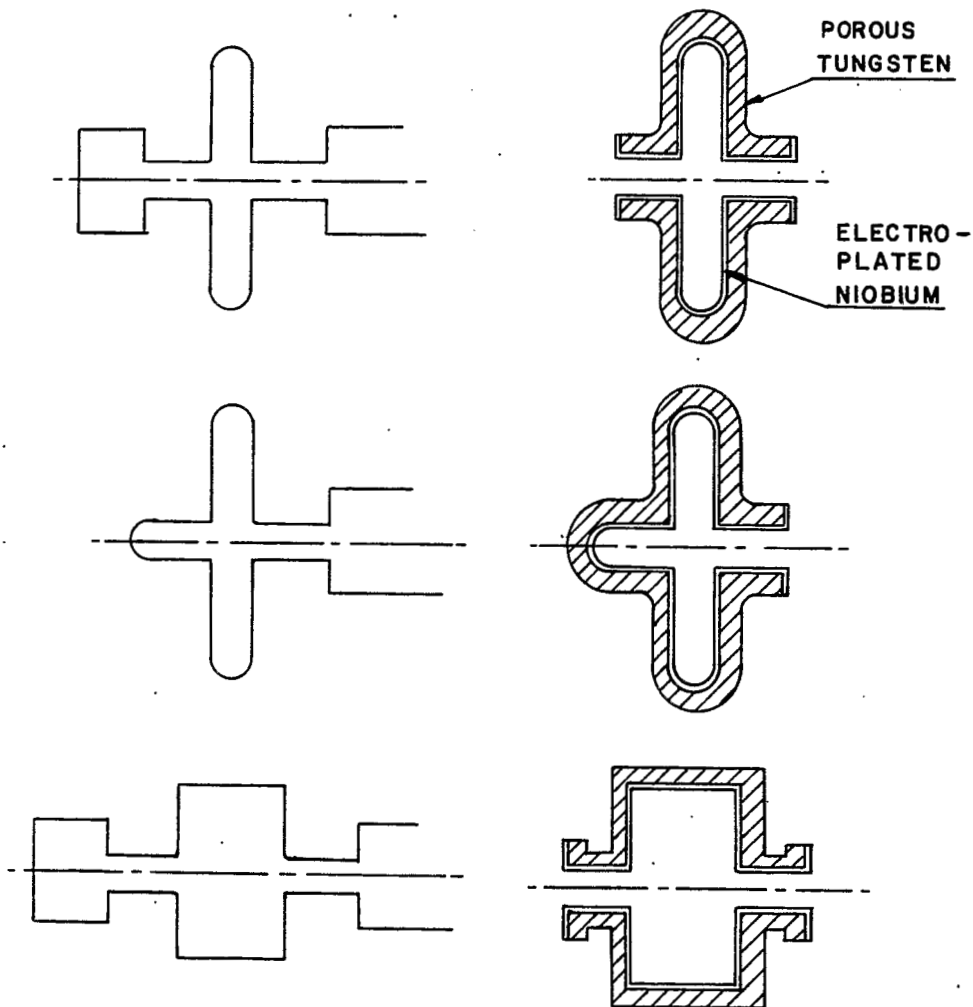


Fig. 4. Examples of easily fabricated geometrically complex rf cavities.

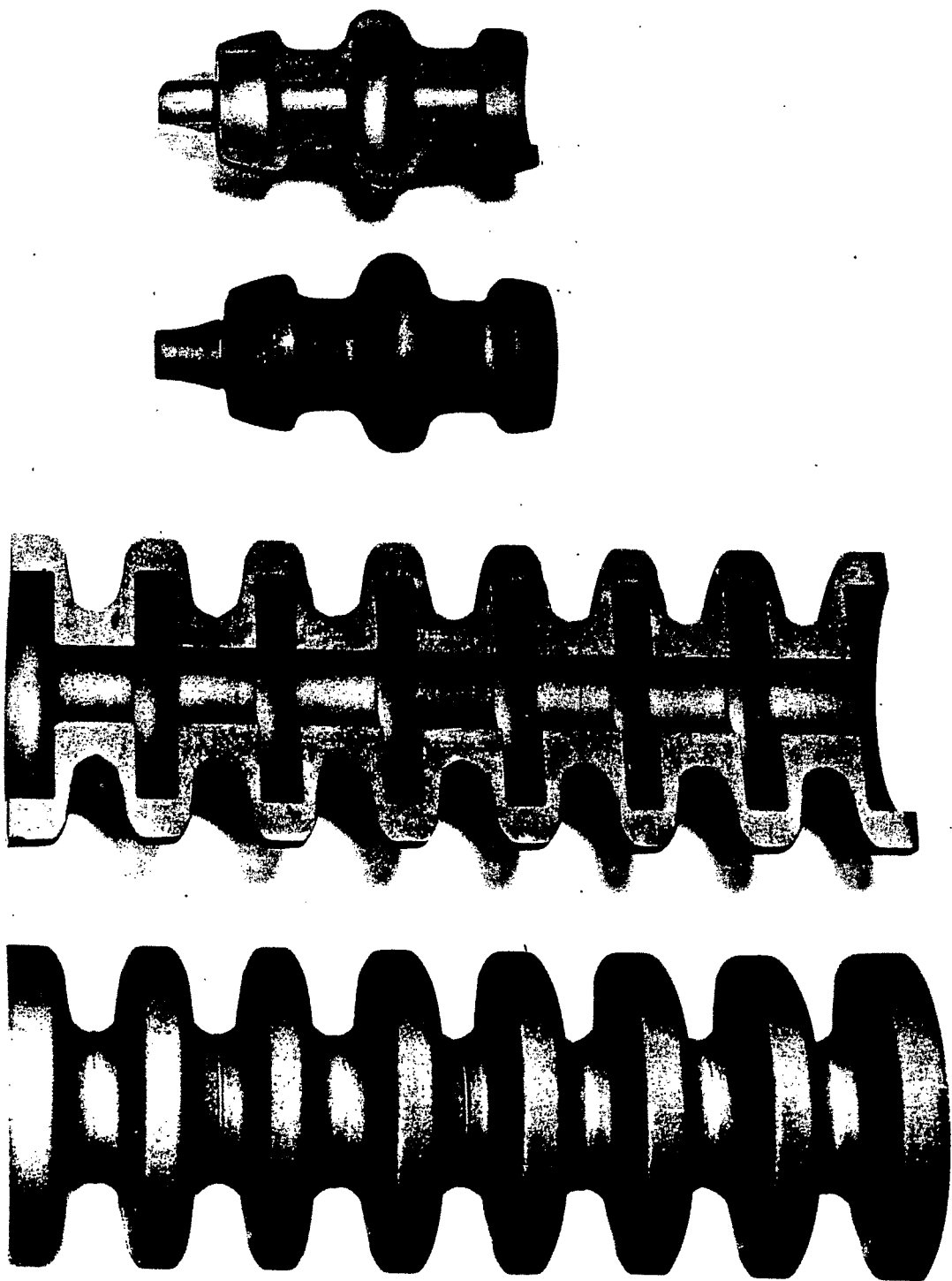


Fig. 5. Examples of easily fabricated geometrically complex rf cavities.

## FABRICATION OF HIGH Q SUPERCONDUCTING NIOBIUM CAVITIES

I. Weissman

Central Research Laboratories  
Varian Associates, Palo Alto, California

X-band superconducting cavities were fabricated by two methods: chemical vapor deposition of niobium onto copper and niobium substrates, and machining from bulk, electron-beam-melted (EBM) solid niobium followed by chemical polishing.<sup>1</sup> The latter method yielded cavities with residual Q's as high as  $3.8 \times 10^{10}$  in the TE<sub>011</sub> mode at 11.2 GHz and  $2.1 \times 10^{10}$  in the TM<sub>010</sub> mode at 8.4 GHz. Both the TM and TE mode solid cavities were limited in power by a critical magnetic field ( $H_c^{ac}$ ) of about 450 G, which is only one-fourth the dc value of  $H_{c1}$  for pure niobium. Subject to high fields the TM<sub>010</sub> mode cavity tested exhibited some Q degradation from its initial high value but it was found that after a sufficient operating period at high fields stable values of  $Q = 1.16 \times 10^9$  measured at low power, and  $1.06 \times 10^9$  measured at high power could be maintained. While these stable values of Q are sufficiently high to make cavities fabricated in this manner from EBM niobium attractive in accelerator and particle separator applications, the cost of fabrication is relatively high and it would be desirable if comparable results could be obtained with plated Nb on some suitable, less costly substrate.

TE<sub>011</sub> mode cavities fabricated by chemical vapor deposition of Nb layers varying in thickness from 5 to 25  $\mu$  onto Cu substrates have been evaluated. The deposition is done in a tube furnace at 950 to 1000°C and the Cu substrates experience considerable grain growth during the predeposition heating. The Nb layers deposit initially as a multitude of large single crystal platelets whose size, orientation and growth are uniquely related to the substrate crystal structure. The surface of the Nb film gets rougher with increasing thickness and at a thickness varying between 10  $\mu$  and 25  $\mu$ , there is a tendency for renucleation at the surface. After renucleation, growth of a dense deposit may be continued, but the as-deposited surface is small grained, duller in appearance and considerably rougher than the surface prior to renucleation. Measurements on as-deposited Nb on Cu TE<sub>011</sub> mode cavities have yielded residual Q's from  $3.3 \times 10^6$  to  $6.3 \times 10^7$  with the value of Q decreasing monotonically as a function of increasing deposit thickness. Polishing of the deposited surface increases the residual Q by between one and two orders of magnitude (in a particular case from  $3.3 \times 10^6$  to  $1.6 \times 10^8$ ). The residual Q thus appears to be critically dependent on surface roughness and the quality of the surface finish. A further increase in residual Q was achieved with cavities consisting of chemically vapor deposited Nb surfaces on Nb rather than Cu substrates. As an example, the as-deposited residual Q would typically be of the order of  $2 \times 10^8$ , increasing to about  $5 \times 10^8$  with abrasive polishing of the deposited surface. This further improvement is attributed primarily to the elimination of differential thermal expansion between deposit and substrate. However, other factors, such as elimination of dissolved Cu from the substrate, in the Nb surface layer, may also be important.

---

1. J.P. Turneure and I. Weissman, J. Appl. Phys. 39, 4417 (1968).

Results to date on cavities fabricated of chemically vapor deposited Nb layers indicate that with additional effort residual Q's comparable to those achieved with solid Nb structures can be realized. The major problem is to find a more compatible substrate-deposit combination. To this end, Elkonite, a copper-impregnated tungsten matrix material, is suggested as a substrate member. With the proper Cu-W ratio (approximately 70% W, 30% Cu) its macroscopic expansion coefficient closely matches that of Nb. Also the thermal conductivity of Elkonite is almost as high as that of Cu, thus making it an ideal substrate material insofar as heat transfer through the cavity walls to the helium bath is concerned.

## MATERIALS INVESTIGATION FOR A TWO-MILE SUPERCONDUCTING ACCELERATOR\*

M.A. Allen and H.A. Hogg  
Stanford Linear Accelerator Center  
Stanford University, Stanford, California

In another paper in these Proceedings, Neal<sup>1</sup> gives the reasons for considering an energy of 100 GeV as the goal for a superconducting SLAC accelerator. This energy corresponds to a gradient of 10 MeV/ft, which is greater than has been achieved to date in any superconducting accelerator structure, either traveling-wave or standing-wave. Gradient limitations are related to the properties of the materials used in the accelerator circuits. An examination of the present day materials situation leads to the conclusion that the materials which come closest to the design requirement are the pure metals, lead and niobium. Cavities which have been constructed to date with lead are limited by field emission loading effects to operating at levels below 4 MeV/ft. Niobium cavities in the accelerating mode have shown sharp reductions due to magnetic field penetration at gradients of about 5 MeV/ft. Both of the above-quoted gradients are for the traveling-wave mode of operation. For both these materials, sufficiently high Q improvement factors have been obtained at superconducting temperatures to qualify them for use in low gradient accelerators. Nevertheless, further work is required before a high gradient superconducting machine can be constructed. The purpose of this paper is to discuss some plans for a materials evaluation program at SLAC.

Materials presently used are either type I or type II, and are operated in the region of perfect diamagnetism — that is, at magnetic fields below the level at which any flux tube penetration takes place. However, the mechanism of microwave loss in type II superconductors operated in the mixed state, where some flux tube penetration occurs, is a subject of current study.<sup>2,3</sup> At low frequencies or dc, the current in a conductor flows in such a manner as to minimize resistive losses, but at high frequencies the stored electromagnetic energy is minimized and the current tends to flow uniformly through the conducting surfaces. When the level of applied magnetic field is such as to establish a mixed state, there will exist a flux tube lattice which is distributed in a manner determined by its interaction with pinning defects in the material. A fraction of the material will be inside the normal cores of the flux tubes, and this fraction is approximately equal to  $H_a/H_{c2}$ , where  $H_a$  is the applied magnetic field and  $H_{c2}$  is the upper critical magnetic field which corresponds to complete flux penetration. It can be shown that, in the mixed state, even currents at microwave frequencies tend to avoid the cores of normal material and flow in the superconducting regions. However, the flux tubes develop displacement — oscillations about the pinning centers, which cause normal currents to flow in the cores and lead to unacceptable losses. This happens even though no pinning constraints are broken. The "pinning frequencies," which are proportional to the pinning forces, are usually quite low (in the low megacycle region), but it might be possible to prepare surfaces with pinning frequencies in the microwave region. In such a case, the effects of flux penetration might be expected to decrease markedly because the interactions which take place at microwave frequencies

---

\* Work supported by the U.S. Atomic Energy Commission.

1. R.B. Neal, these Proceedings, p. 101.
2. J. le G. Gilchrist, Proc. Roy. Soc. A295, 399 (1966).
3. J.I. Gittleman and B. Rosenblum, J. Appl. Phys. 39, 2617 (1968).



are confined close to the surface. However, this is not a very promising approach, because even a very small number of flux tubes having small displacement amplitudes would prevent the achievement of the extremely high Q's desired.

In the above discussion it has been assumed that the flux tubes are established by an externally-applied dc field, and the interaction of a low level probing microwave signal has been considered. If high-level rf magnetic fields (lying between  $H_{c1}$  and  $H_{c2}$ ) are applied to the surface layers of a type II superconductor in the absence of dc magnetic fields, it is not clear how the flux tubes can form because the time of an rf cycle is short compared with the time necessary for a flux tube to become established and to move into the surface. Nevertheless, experimental evidence to date indicates that Q drops sharply as the rf magnetic fields exceed some lower critical field value.<sup>4</sup>

Type II superconductors are thermodynamically reversible and are distinguished from type I superconductors by the value of the Ginsberg-Landau parameter - sometimes called the "disorder parameter,"  $\kappa$ . The value of  $\kappa$  is approximately equal to  $\lambda(0)/\xi$ , where  $\lambda(0)$  is the London penetration depth at absolute zero and  $\xi$  is the coherence length. Materials with values of  $\kappa$  greater than  $1/\sqrt{2}$  are characterized as type II superconductors. An ideal type II superconductor has the type of magnetization curve shown in Fig. 1. The value of  $H_{c2}$  increases with the disorder parameter, but even though  $H_{c2}$  can reach very large values the thermodynamic critical field  $H_c$  stays relatively fixed for a given material. Furthermore,  $H_{c1}$  decreases as  $H_{c2}$  increases. The Abrikosov theory predicts  $H_{c1}/H_{c2}$  values of 0.82, 0.55, 0.32 and 0.2 for  $\kappa$  values of 1, 2, 5 and 10, respectively. Niobium has a  $\kappa$  close to 1 and is a type II superconductor with a relatively high  $H_c$  of about 2000 G, which means that  $H_{c1}$  should be over 1600 G. This has been confirmed by dc magnetization measurements and at present much effort is going into the preparation of surfaces which will yield comparable values of  $H_{c1}$  at microwave frequencies. To date, values about 25% of theoretical have been reported.<sup>4</sup> Most of the work on other type II materials has been directed towards superconducting magnet applications; and the objectives have been both the attainment of high  $H_{c2}$  values and the treatment of materials to yield suitable pinning centers for holding the flux tubes carrying the penetrating flux up to very high currents. Materials have been produced with large disorder parameters and correspondingly very large values of upper critical field  $H_{c2}$ , but nevertheless total flux exclusion is possible only at very low applied magnetic fields. It is reasonable to ask whether type II materials can be prepared with high values of  $H_c$  and low values of  $\kappa$ .

Type II superconductors are usually synthesized as two- or three-phase alloy systems or compounds. A perusal of the literature shows that compounds usually have higher thermodynamic critical magnetic fields than alloys, although the values for alloys do appear to depend quite markedly on the percentage of constituents present. Compounds for magnet technology are normally prepared in polycrystalline form with imperfect stoichiometry. This yields extremely high values of  $H_{c2}$ . Compounds of near-perfect stoichiometry and crystal structure might be expected to yield lower values of  $\kappa$  which would result in higher values of  $H_{c1}$ . Type II superconducting compounds with both high thermodynamic critical field and low intrinsic  $\kappa$  might be good candidates for accelerator applications. Large numbers of intermetallic compounds have been prepared and tabulated, and it is possible that some of these have the desired combination of superconducting parameters. Nevertheless, even if type II materials can be prepared with suitable properties they will be useful to us only if they can be economically formed into a high-Q accelerator structure.

---

4. J.P. Turneure, presented at this Summer Study (unpublished).

At SLAC, a materials research program is being started. Materials and preparation techniques will be studied and rf superconducting properties will be evaluated. It is intended to investigate both niobium and lead with the object of improving surface preparation techniques. For two miles of accelerator structure to be economically feasible it is probable that some deposition technique on copper or a similar substrate will have to be perfected. Niobium test surfaces will be produced by electrodeposition, sputtering, evaporation, and chemical vapor deposition. These surfaces will be further processed in an attempt to obtain consistently the desired properties for use in a high gradient accelerator. We also intend to try coating lead surfaces with thin protective films of other substances.

Following the reasoning outlined in previous paragraphs, a search will be made for intermetallic compounds having suitable rf superconducting properties.

During this Summer Study, it has been suggested by Autler that technetium may be worth consideration as a practical superconductor.<sup>5</sup> While the values of critical temperature and  $H_{c1}$  (Ref. 6) are intermediate between lead and niobium, it has the advantage over lead that it is a hard, oxidation resistant metal, and the advantage over niobium that it can be electroplated from an aqueous solution at room temperature.<sup>7</sup> For these reasons, an attempt will be made to build and test a technetium-plated copper cavity.

Equipment for making sensitive measurements of magnetic susceptibilities at low frequencies is in the process of being assembled. These measurements will be made using samples in the form of rods a few inches long and 1/8 to 1/4 in. in diameter, and will serve as a preliminary selection mechanism in the materials search. Samples will be processed by various techniques such as vacuum annealing, high temperature outgassing, etc. It is anticipated that this approach will be economical, because the use of small samples permits many materials to be investigated in a short time. A sketch of the apparatus is shown in Fig. 2. It is hoped that the sensitivity of the experiment will make it possible to detect penetrations of a few flux tubes, which would be enough to reduce the Q values at microwave frequencies.

Materials which show promise will then proceed to tests at microwave frequencies. It is known that surface conditions are critical at these frequencies. For this reason, it is desirable that the test surfaces should be processed in vacuum and transferred in vacuum to an rf test cavity. Additionally, it is preferable that the sample should be relatively small to ameliorate processing and transferring problems. The sample configuration has to be such that it can become part of a resonant cavity in which the field patterns in the resonant mode do not require currents to flow between the sample and the remainder of the cavity. Making the sample the center conductor of a coaxial cavity supporting the  $TE_{011}$  mode satisfies all these conditions. The diameter of the center conductor can be chosen so that its losses are of the same order as the losses in the rest of the cavity. A preliminary design sketch of the equipment is shown in Fig. 3. A vacuum chamber is mounted directly over the Dewar. It communicates with the cavity at the bottom of the Dewar via a tube along the common vertical axis. The tube diameter is large enough to allow the removable center conductor to slide through it with guides to avoid surface damage. The center conductor is suspended by a stainless-steel wire from a winch actuated through a high vacuum coupling. The upper vacuum chamber is equipped to process the center conductor. After processing the

---

5. S.H. Autler, these Proceedings, p. 49.

6. S.T. Sekula, R.H. Kernohan, and G.R. Love, Phys. Rev. 155, 364 (1967).

7. W.D. Box, Nuclear Applications 1/2, 155 (1965).

sample will be lowered into position in the cavity, which is excited by means of an offset coaxial line in the same way as a simple cylindrical  $TE_{011}$  cavity. Besides the complexity of the whole apparatus, the difficulties anticipated are associated with the cooling and possible cold-welding of the center conductor sample. It is probable that adequate conduction cooling can be obtained by machining a conical recess into the bottom of the center conductor and allowing it to sit over a matching protuberance in the end plate of the cavity. This apparatus will allow an investigation of both  $H_{c1}$  at rf frequencies and Q improvement factors as a function of processing. Materials which perform well in this test will then be used to fabricate end plates or whole rf cavities.

Tests of the most promising materials and surface processing techniques will be continued in cavities resonant in the  $TM_{010}$  or similar mode, to investigate the high power limit imposed by field emission losses. Ultimately, tests will be made on prototype accelerator structures.

#### ACKNOWLEDGEMENT

Useful discussions with E.L. Garwin are gratefully acknowledged.

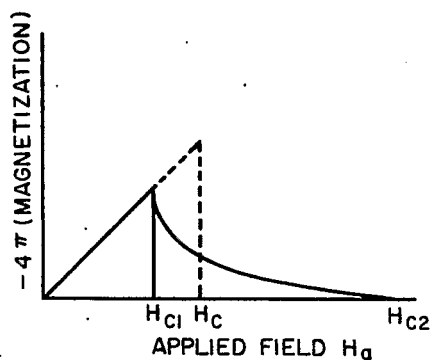


Fig. 1. Magnetization curve for type II superconductor.

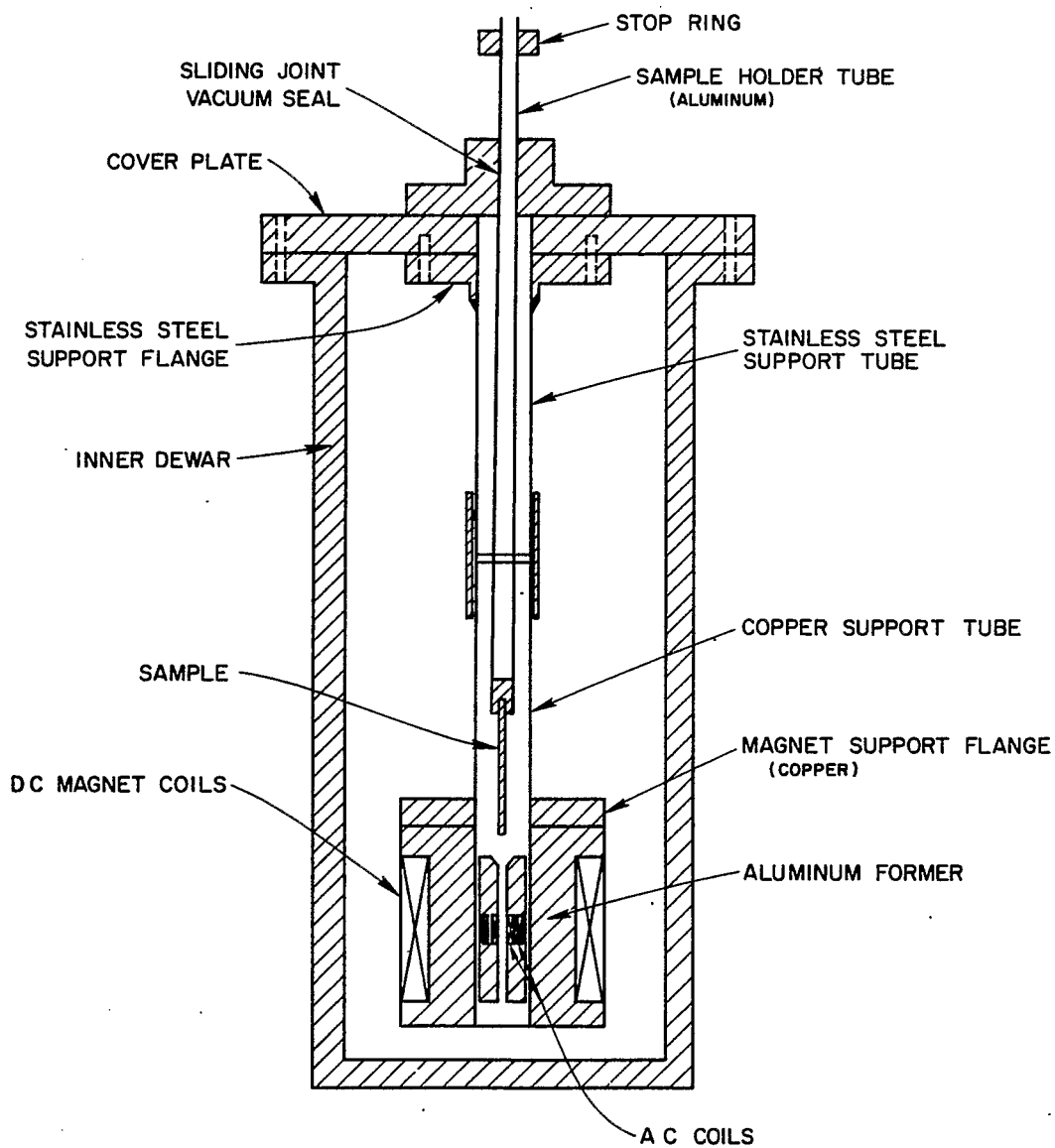


Fig. 2. Magnetic susceptibility measuring equipment.

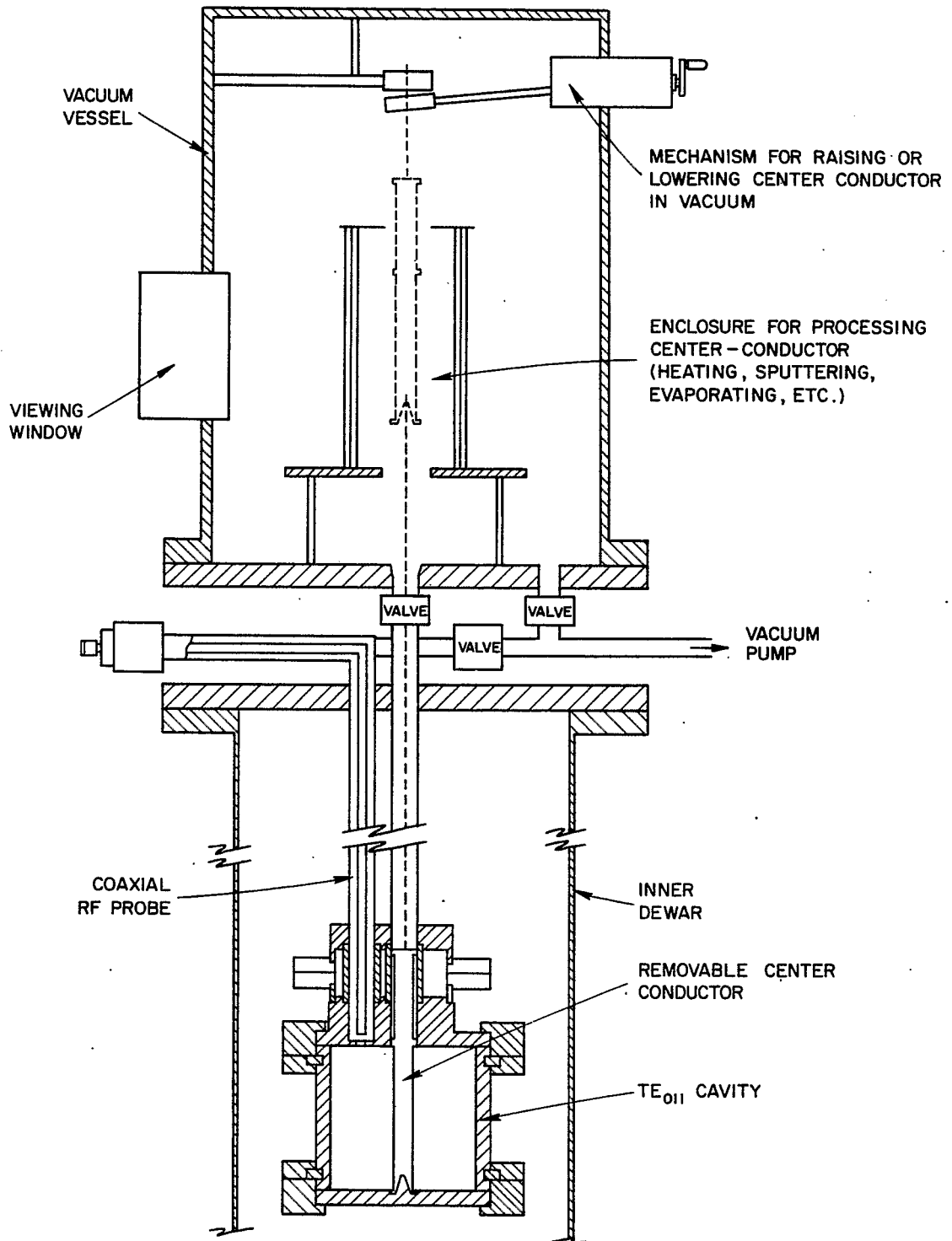


Fig. 3. Equipment for sample processing and rf testing using TE<sub>011</sub> coaxial cavity.

## CHARACTERIZATION OF RESIDUAL RF LOSSES IN SUPERCONDUCTORS

C.R. Haden  
University of Oklahoma  
Norman, Oklahoma

In the design and use of superconducting resonant structures, whether for use in accelerator applications, frequency control, or otherwise, it is desirable to minimize losses and obtain as high a Q as possible. It is theoretically possible to obtain unlimited Q, if temperature limitations are disregarded and if the superconducting surface resistance is the only factor contributing to losses. However, it is always found in practice that some extraneous mechanism limits the Q to finite values. It is seldom easy to determine the sources of such residual loss. The purpose of a portion of the work at the University of Texas has been to characterize the residual losses and, insofar as possible, determine their source. This research was initiated by the author and W.H. Hartwig,<sup>1</sup> but the bulk of the work reported here was performed by Hartwig and J.M. Victor.<sup>2</sup>

On the basis of our previous experience and that of the Stanford group,<sup>3</sup> it seems that trapped magnetic flux can be a very strong source of residual loss. Thus, it is now possible to remove one type of rf loss from the group of undefined losses:

$$\text{Total loss} = \text{Loss in surface resistance} + \text{Loss due to trapped flux} + \text{Other losses} .$$

The "other" group of losses may possibly include dielectric loss, radiation loss, etc., depending on the arrangement of the structure or other unknown factors. The flux-trapping loss can effectively be eliminated by proper design of the circuit and magnetic shielding. However, the Texas group believes it is important to study the flux-trapping effect so that it could be subtracted from the experimental data entirely, thereby leaving the "other" losses for inspection and analysis. Also, it is felt that understanding of the flux-trapping phenomenon might lead to the development of materials such that it can be minimized when magnetic shielding is not feasible.

The experiments were carried out in the frequency range from 30 MHz to 500 MHz on circuits made of foil strips wrapped on Teflon forms and enclosed in superconducting shield cans. The Teflon has been demonstrated to have a very low dielectric loss<sup>4</sup> and was not in a high electric field region. Full details of the experiment are reported in an article published in the Journal of Applied Physics<sup>2</sup> and data reported here are taken from that article with permission of the authors.

- 
1. C.R. Haden and W.H. Hartwig, Phys. Rev. 148, 313 (1966).
  2. J.M. Victor and W.H. Hartwig, J. Appl. Phys. 39, 2539 (1968).
  3. M. Pierce, H.A. Schwettman, W.M. Fairbank, and P.B. Wilson, Low Temperature Physics, LT 9 (Plenum Press, New York, 1964), p. 396.
  4. D. Grissom and W.H. Hartwig, J. Appl. Phys. 37, 4784 (1966).

Flux trapping occurs when the test sample is cooled in an ambient magnetic field. When the sample becomes superconducting, the magnetic field is driven out except for isolated groups of flux tubes which become trapped at sites throughout the material. Due to the collapse of the field, the cores of these tubes may be considered normal, thereby creating a resistive rf loss. This is indicated in Fig. 1. The effective surface resistance is then dependent upon the area of the normal regions, which is proportional to the critical field, and upon the depth of rf field penetration. It thus seems logical to assume a solution for the temperature dependence of the flux-trapping loss which is the product of the temperature dependences of the critical field and the superconducting penetration depth. Using the empirical forms which are widely utilized in the literature, one obtains for the temperature dependence:

$$V(t) = \left[ (1 - t^2) (1 - t^4)^{\frac{1}{2}} \right]^{-1} \quad (1)$$

and

$$r = A(v) f(t) + r_h(0) V(t) + r_o \quad (2)$$

In Eq. (2),  $r$  is the measured surface resistance normalized to the normal value,  $A(v)$  is a frequency-dependent part of the true surface resistance,  $r_h(0)$  is the field-dependent part of the flux-trapping loss,  $r_o$  is the constant residual loss, and  $f(t)$  is the Pippard function for the true surface resistance<sup>5</sup>:

$$f(t) = \frac{t^4 (1 - t^2)}{(1 - t^4)^2} \quad (3)$$

Other temperature dependences for flux-trapping losses are available in the literature.<sup>1,3</sup> In particular, use has been made of the two functions:

$$\lambda(t) = (1 - t^4)^{-\frac{1}{2}} \quad (4)$$

and

$$\varphi(t) = (1 - t^2)^{-1} \quad (5)$$

In deciding which is the correct function, one need realize that, for any given function,  $q(t)$ , elimination of  $r_o$  and surface resistance would yield a curve given by:

$$r = q \frac{dr}{dq} \quad (6)$$

Thus, if the dependence is correct, a "theoretical" curve obtained from (6) should only differ from the experimental data by a negative constant. Inspection of Fig. 2 for  $\lambda(t)$  and Fig. 3 for  $\varphi(t)$  shows that  $r_o$  is not constant and, in fact, changes sign. On the other hand, Fig. 4 gives a constant  $r_o$ . It is thus concluded that  $V(t)$  is the correct temperature dependence.

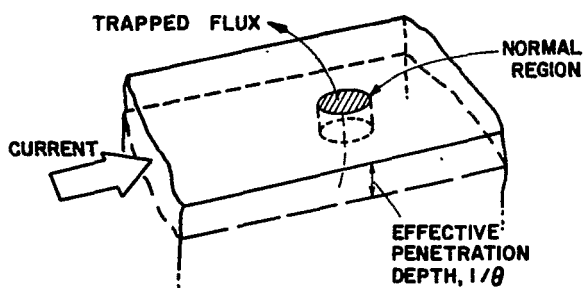
---

5. A.B. Pippard, Proc. Roy. Soc. (London) A203, 98 (1950).

Experiments were run with magnetic field and frequency as variables. The field data are summarized in Fig. 5. It is evident that the loss is proportional to the field intensity as expected. The frequency data for the surface resistance only are summarized in Fig. 6. Agreement with theory seems quite good. The normal material lies somewhere between the classical and anomalous limits. For the flux-trapping loss, the resistance ratio showed little or no frequency dependence, corresponding to normal flux core regions.

Annealing tests were run on a number of samples. This is demonstrated for a 4%In-96%Sn circuit cooled in the earth's field in Fig. 7 and for pure tin at two fields in Figs. 8 and 9. These data indicate that  $A(v)$ ,  $f(t)$  and  $r_o$  are readily reduced by annealing, but that  $r_h(0)$  may not easily be changed. The intercept change in Fig. 7 is due to a change in  $r_o$ . The slope remains constant since the order parameters are controlled by impurities in this sample. In Fig. 8, both the intercept and slope change, indicating that structure now dominates the order parameters. In the higher ambient field of Fig. 9, the normal regions at the flux cores dominate so that the slopes are approximately the same for all annealing times.

In conclusion, the flux-trapping effect definitely exists and may be explained by losses in resistive regions at the flux cores. Also, the remaining residual losses are apparently independent of temperature and magnetic field.



$$\theta = \sqrt{\frac{1}{2\lambda^2} + \sqrt{\frac{1}{4\lambda^4} + \frac{1}{\delta^4}}}$$

$$r = \frac{R_s}{R_n} = A(v)f(t) + r_h(0)V(t) + r_o$$

$$\text{where } r_h = r_h(0)V(t) = \beta(H/H_c) \left[ (1 - t^2)(1 - t^4)^{1/2} \right]^{-1}$$

Fig. 1. Flux-trapping model with an effective depth of penetration.



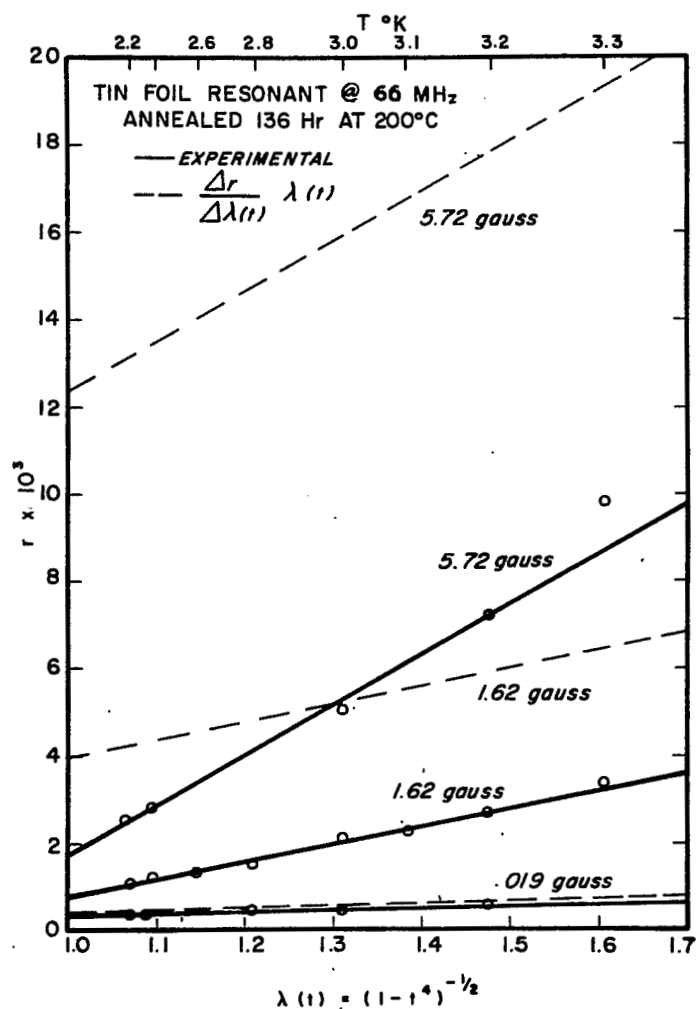


Fig. 2. Relative resistance ratio vs  $\lambda(t)$  (solid lines) and theoretical curves for flux-trapping loss only (dashed). Since the difference is not constant nor positive, as a field- and temperature-independent residual resistance would be,  $\lambda(t)$  is not applicable for the model.

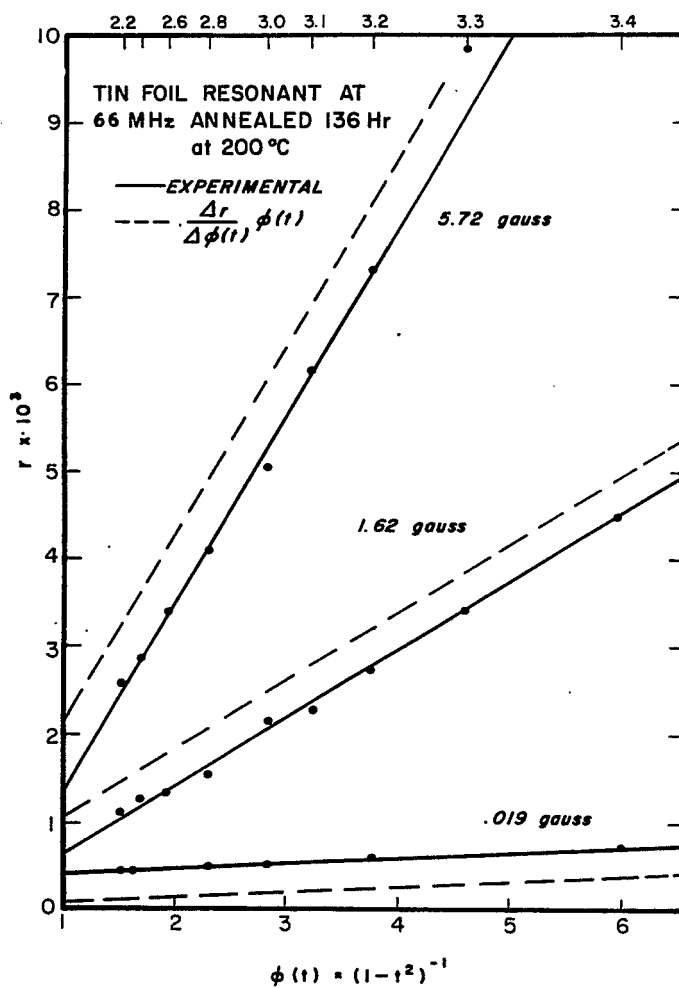


Fig. 3. Relative resistance ratio vs  $\phi(t)$  showing the same disagreement with the model as in Fig. 2.

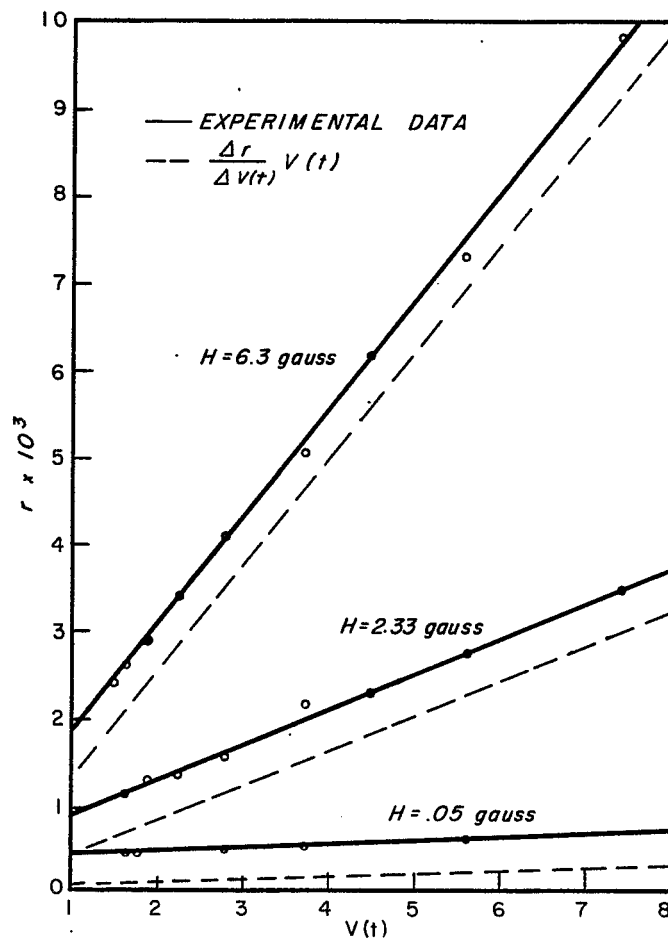


Fig. 4. Relative resistance ratio vs  $V(t)$  showing existence of a constant residual resistance that is independent of  $T$  or  $H$ .

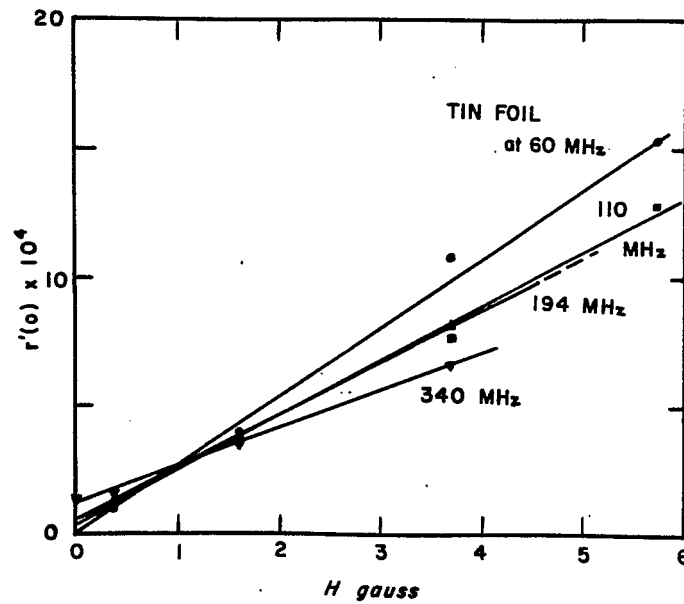


Fig. 5. Magnetic field dependence of  $r'_h(0)$  taken from the slopes of  $r'_h(0) + r'_o$  to eliminate  $r'_o$ . Intercept at  $H = 0$  shows  $KA(v)$  term can be resolved.

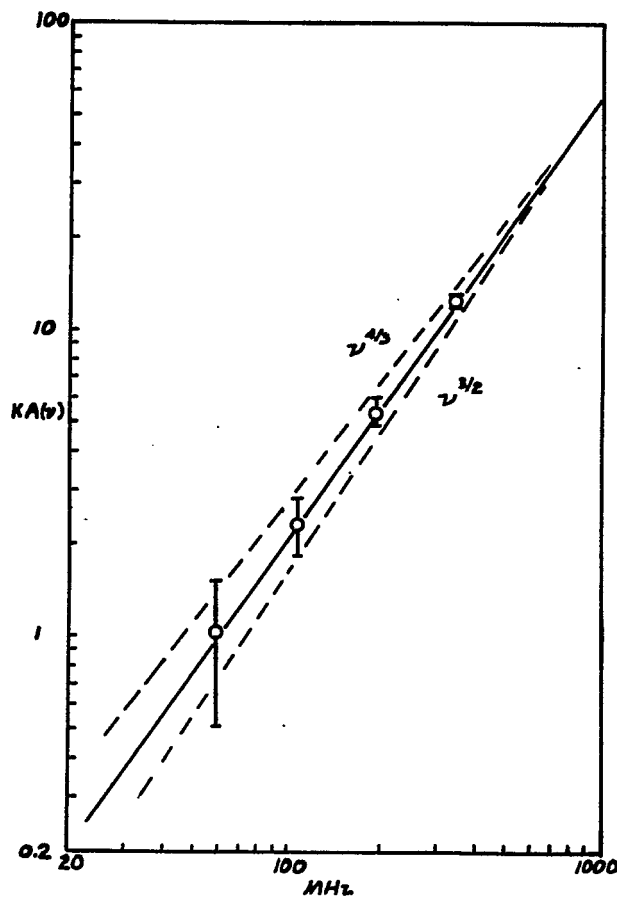


Fig. 6.  $KA(v)$  data from Fig. 5 vs frequency shows tin foil is between the classical skin depth limit and the anomalous limit.

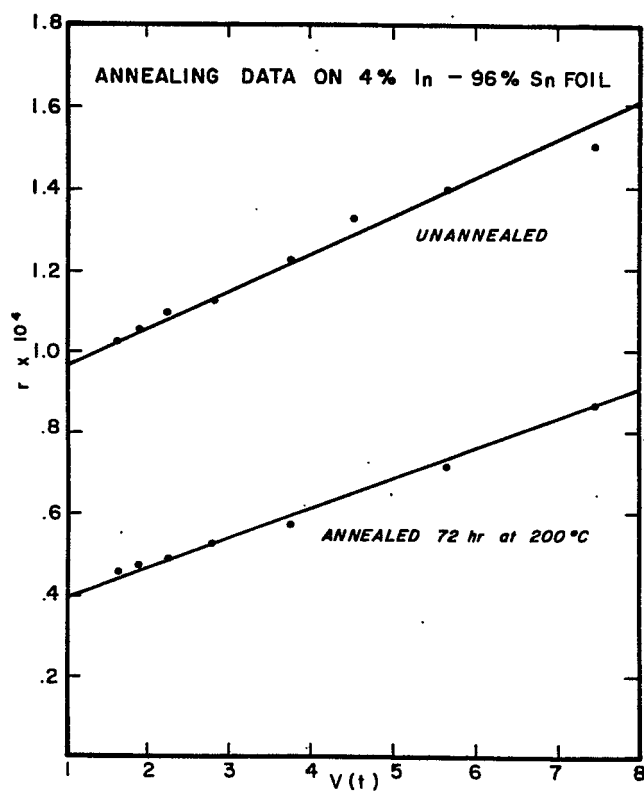


Fig. 7. Annealing 4%In-96%Sn foil shows a large reduction in temperature-independent loss. Data are for earth's field.

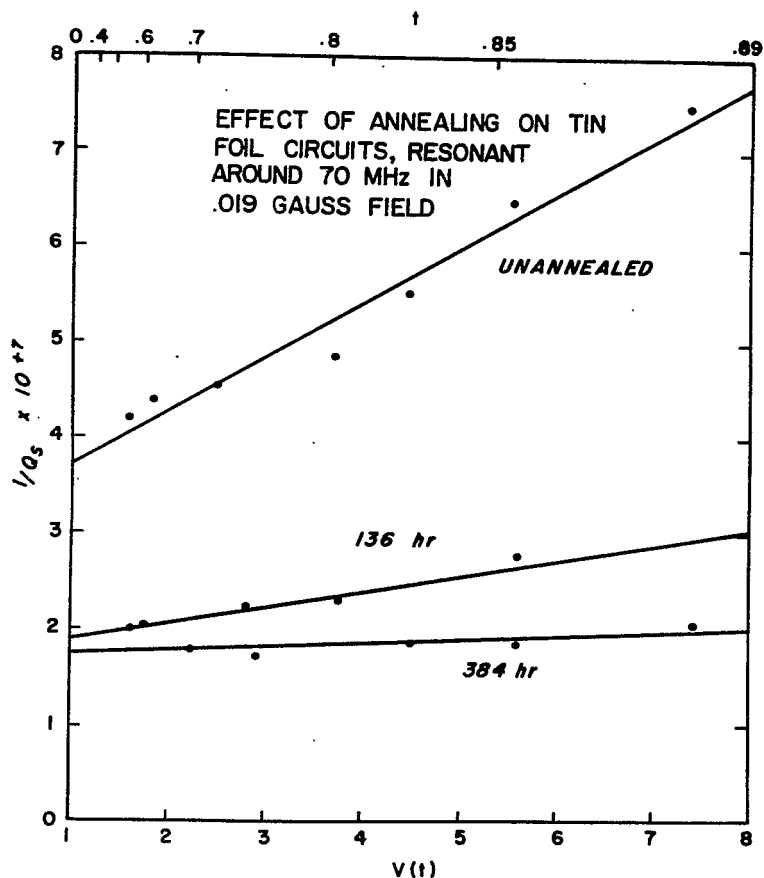


Fig. 8. Annealed pure tin cooled in a magnetic field of 0.019 G shows large change in superconducting resistance in the absence of trapped flux. Annealed loss is attributable to Pippard surface resistance and residual resistance. Straight lines reflect similar shapes of  $f(t)$  and  $V(t)$ .

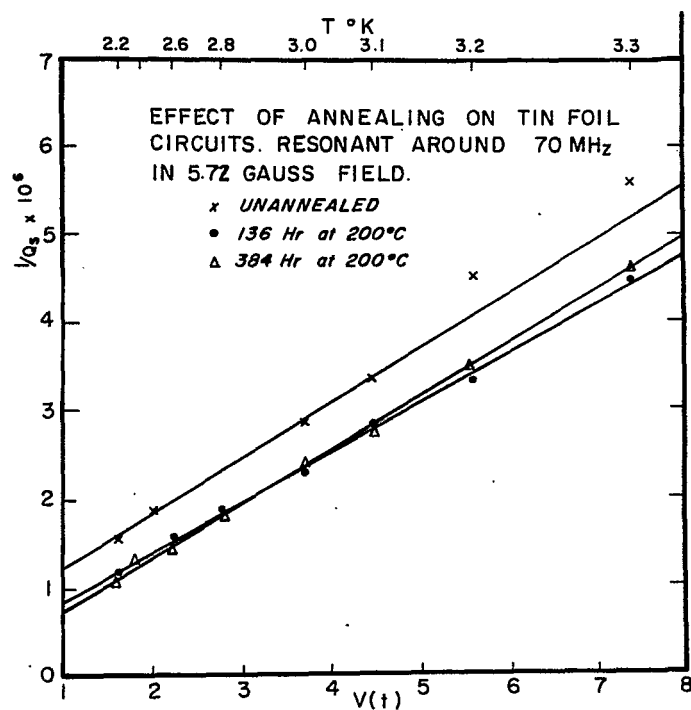


Fig. 9. Annealed tin circuit cooled in a magnetic field of 5.72 G shows small drop in temperature-dependent loss, indicating flux-trapping loss is not readily annealed. Residual resistance annealed out to a minimum.

# TECHNETIUM AS A MATERIAL FOR AC SUPERCONDUCTIVITY APPLICATIONS

S.H. Autler  
NASA Electronics Research Center  
Cambridge, Massachusetts

## INTRODUCTION

The purpose of this note is to expand the impromptu remarks made at the Summer Study, pointing out the fact that the element technetium has some properties which make it worth considering for use in low loss rf circuits, and particularly in cavities intended for use in accelerators or rf separators. Technetium ( $Z = 43$ ) is a refractory metal, melting at  $2140^{\circ}\text{C}$ , which does not exist naturally but is formed as a fission product in nuclear reactors. It is presently available in some quantity by reprocessing nuclear fuel cores. It was formerly thought to have a short radioactive half-life, but the availability of purer samples has shown that  $\text{Tc}^{99}$  has a radioactive half-life of  $\sim 2 \times 10^5$  years. The activity is mainly  $0.29 \text{ MeV } \beta$  particles which can be readily shielded by a thin layer of plastic or metal foil.

## DISCUSSION OF AVAILABLE DATA

Since technetium has been available in sufficient quantity for study for relatively few years, there is not much information on its superconductive properties, and there is still the need for more data. We summarize here some of the existing data.

It has been known for some years that technetium is a superconductor<sup>1</sup> but the originally reported value of transition temperature, which is still being reprinted in some recent textbooks and reviews, is now known to be too high. More recent measurements on much purer samples which have become available indicate a lower transition temperature near  $8^{\circ}\text{K}$ .<sup>2-4</sup> Alloys containing  $\text{Tc}^{2,5}$  are known to have considerably higher transition temperatures, going up to about  $16^{\circ}\text{K}$  for some  $\text{MoTc}$  compositions.<sup>2</sup>

The results of most interest to us here are reported by Sekula, Kernohan, and Love<sup>4</sup> who measured the magnetization properties of fairly pure, partially annealed samples of  $\text{Tc}$ , with  $R(300^{\circ}\text{K})/R(8^{\circ}\text{K}) \sim 100$ .

One of their magnetization curves is reproduced in Fig. 1 and their main conclusions of interest to us may be summarized as follows:

Technetium is a type II superconductor with  $T_c \approx 7.75^{\circ}\text{K}$ . It has a Ginzburg-Landau parameter,  $\kappa$ , of 0.92 at  $T = T_c$ , which is about the same as niobium and indicates  $\text{Tc}$  is barely type II. Annealing at  $2000^{\circ}\text{C}$  for an hour in a moderate vacuum results in a fairly reversible magnetization characteristic such as Fig. 1.

- 
1. J.G. Daunt and J.W. Cibble, Phys. Rev. 92, 507 (1953).
  2. V.B. Compton, E. Corenzwit, J.P. Maita, B.T. Matthias, and F.J. Morin, Phys. Rev. 123, 1567 (1961).
  3. M.L. Picklseimer and S.T. Sekula, Phys. Rev. Letters 9, 254 (1962).
  4. S.T. Sekula, R.H. Kernohan, and G.R. Love, Phys. Rev. 155, 364 (1967).
  5. S.H. Autler, J.K. Hulm, and R.S. Kemper, Phys. Rev. 140, A1177 (1965).

As can be seen in Fig. 1,  $H_{c1} \approx 900$  Oe at  $T = 4.2^\circ\text{K}$ . At other temperatures it can be estimated by assuming the same temperature dependence for technetium as has been measured in niobium by Finnemore, Stromberg, and Swenson.<sup>6</sup> This is justified by the fact that  $\kappa$  happens to be very nearly the same in the two metals. Thus,

$$H_{c1}(t, \text{technetium}) = \frac{H_0(\text{technetium})}{H_0(\text{niobium})} H_{c1}(t, \text{niobium}),$$

where  $t = T/T_c$  and  $H_0 = H_c$  (at  $t = 0$ ).

Using  $H_0(\text{technetium}) = 1400$  Oe,  $H_0(\text{niobium}) = 1990$  Oe, and  $H_{c1}(t, \text{niobium})$  from Ref. 6,  $H_{c1}(t, \text{technetium})$  is plotted in Fig. 2.  $H_c$  and  $H_{c2}$  for technetium as measured by Sekula, Kernohan, and Love are also shown in Fig. 2.

### CONCLUSIONS

Technetium, with  $T_c \approx 7.75^\circ\text{K}$  and  $H_{c1} \approx 1180$  Oe at  $1.8^\circ\text{K}$  has the second highest penetration field of all known superconductors and the second highest transition temperature among the elements. Only niobium excels it (by a small margin) in those properties which promise usefulness for high Q microwave cavities operating at high power levels. Niobium, however, has some disadvantages which impair its applicability; one of these is the fact, discussed at this Summer Study, that in actual niobium cavities field penetration and losses become excessive at field strengths of about 450 Oe instead of the expected 1600 Oe. Also, the preparation of the best niobium surfaces is a difficult, expensive process.

Because technetium might turn out to have an actual penetration field higher than that of niobium, and because some of its metallurgical properties suggest that it may be easier to process than niobium,<sup>7</sup> it would seem to be worthwhile to start a study of its applicability to low loss cavities. Pure technetium is presently available in kilogram quantities with hundreds of kilograms awaiting extraction from reactor fuel cores if a suitable use should develop. If its potential advantages as an ac superconductor should turn out to be real, neither its slight radioactivity nor its relative rarity should be prohibitive obstacles to its use on the surface of high Q cavities.

---

6. D.K. Finnemore, T.F. Stromberg, and C.A. Swenson, Phys. Rev. 149, 231 (1966).

7. For example, it is much easier to remove interstitial oxygen and nitrogen from technetium than from niobium, R. Kemper and C.C. Koch, private communication.



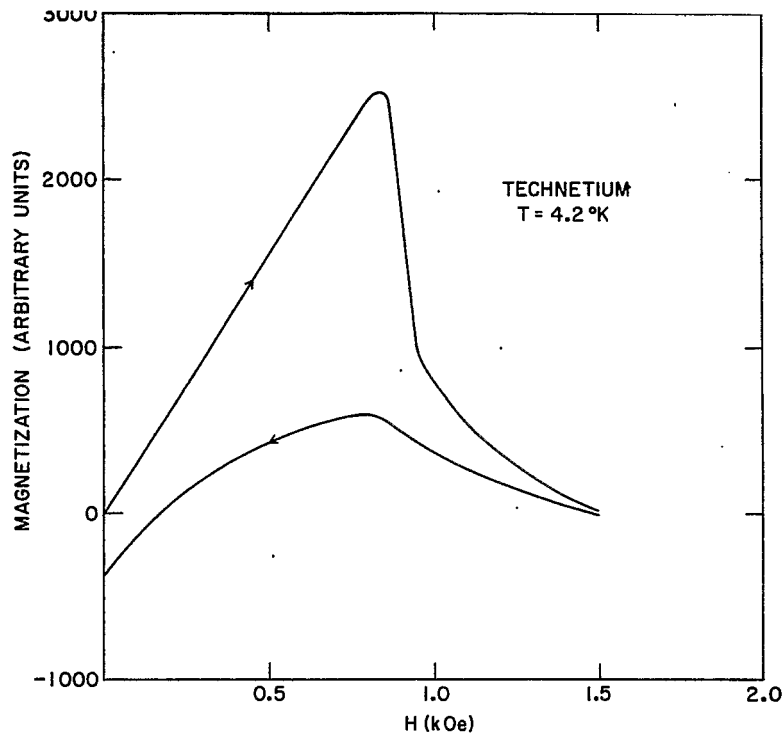


Fig. 1. Magnetization of a sample of technetium annealed at 2000°C for one hour (after Sekula, Kernohan, and Love).  $T_c$  for this sample is 7.75°K.

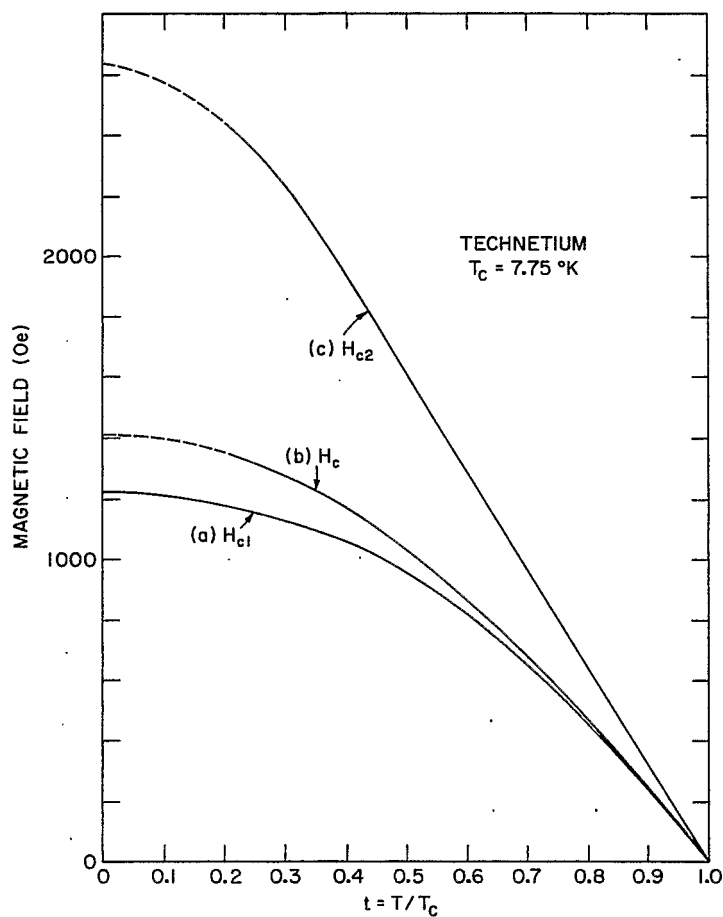


Fig. 2. Critical fields vs reduced temperature for technetium:  
 (a) Lower critical field,  $H_{c1}$ .  
 (b) Thermodynamic critical field,  $H_c$ .  
 (c) Upper critical field,  $H_{c2}$ .  
 Curves (b) and (c) are taken from Sekula, Kernohan, and Love.  
 Curve (a) is estimated by the author.

# APPLICATIONS OF THE FOUNTAIN EFFECT IN SUPERFLUID HELIUM\*

C.M. Lyneis,<sup>†</sup> M.S. McAshan, and H.A. Schwettman<sup>‡</sup>  
Department of Physics and High Energy Physics Laboratory  
Stanford University  
Stanford, California

## INTRODUCTION

If large cryogenic systems using superfluid helium are to be completely practical, simple and efficient methods must be available 1) for providing steady-state refrigeration from a central plant to an individual experiment regardless of its elevation, and 2) for transferring liquid helium in its superfluid state from one reservoir to another. The methods whereby these operations would be accomplished with ordinary liquid helium will not work with superfluid helium. However, the thermomechanical effect, or fountain effect, in superfluid helium can be utilized in the construction of a fountain pressure pump to accomplish both of these objectives.

Consider two superfluid reservoirs connected by a "superleak." If one reservoir is at temperature  $T$  and the other at  $T + \Delta T$ , then in equilibrium there exists a large hydrostatic pressure difference  $\Delta P$ , known as the fountain pressure, which is given by:

$$\frac{\Delta P}{\Delta T} = \rho S \quad , \quad (1)$$

where  $\rho$  is the density and  $S$  is the entropy per gram of liquid helium. Observation of this thermomechanical effect was first reported by Allen and Jones<sup>1</sup> in 1938, and the equation relating its magnitude to the density and entropy of the liquid was derived by H. London<sup>2</sup> in 1939. The magnitude of the fountain pressure is surprisingly large. The hydrostatic pressure difference can be as large as 500 mm of Hg, an order of magnitude greater than the vapor pressure of helium at the lambda point. Combined with the low density of liquid helium, this pressure is sufficient to support a column of helium in excess of 100 ft in height. The thermomechanical effect thus provides the means for constructing a fountain pressure pump that can be used both to provide steady-state refrigeration to elevated experiments and to transfer superfluid helium from one reservoir to another.

## THE IDEAL FOUNTAIN PRESSURE PUMP

For large temperature differences the equation for the fountain pressure [Eq. (1)] must be integrated, since the entropy of helium II is a very strong function of temperature between 1.2°K and 2.1°K.<sup>3</sup> The integrated equation is

---

\* Work supported in part by the U.S. Office of Naval Research, Contract [NONR 225(67)].

<sup>†</sup> National Science Foundation Predoctoral Fellow.

<sup>‡</sup> Alfred P. Sloan Research Fellow.

1. J.F. Allen and H. Jones, *Nature* 141, 243 (1938).
2. H. London, *Proc. Roy. Soc.* A171, 484 (1939).
3. F. London, *Superfluids* (Dover Publications, Inc., New York, 1954), Vol. II. p: 75.

$$P_2 - P_1 = \int_{T_1}^{T_2} \rho(T) S(T) dT \quad , \quad (2)$$

where  $P_1$  and  $P_2$  are the pressures on each side of the reservoir,  $T_1$  and  $T_2$  are the corresponding temperatures,  $\rho$  is the density of helium, and  $S$  is the entropy per gram of helium. This relation has been found to hold within experimental errors up to a temperature difference of 0.6°K and a pressure difference of 500 mm Hg.<sup>4</sup> That pressure difference corresponds to a column of liquid helium 46.8 m in height.

A schematic drawing indicating how the fountain pressure pump could be used to provide refrigeration to an elevated experiment is shown in Fig. 1. If the two reservoirs are at different temperatures  $T_1$  and  $T_2$ , then the pressure difference across the superleak will be

$$P_2 - P_1 = \rho gh + P_v(T_2) - P_v(T_1) \quad , \quad (3)$$

where  $\rho$  is the density of helium,  $g$  is acceleration due to gravity,  $h$  is the difference in height between the two levels, and  $P_v(T)$  is the vapor pressure of helium as a function of temperature. Solving for  $h$  and using Eq. (2) yields

$$h(T_1, T_2) = \frac{1}{\rho g} \left( \int_{T_1}^{T_2} \rho S dT + P_v(T_1) - P_v(T_2) \right) \quad . \quad (4)$$

In Fig. 2 this height is plotted as a function of  $T_2$  for  $T_1 = 1.85^\circ\text{K}$ .

Now consider the effectiveness of the fountain pressure pump in supplying steady-state refrigeration to an elevated reservoir as illustrated in Fig. 1. For a heat input  $\dot{Q}_T$  in the upper reservoir the central refrigerator must provide helium to the lower reservoir at the rate  $\dot{m}_T$ . Part of this helium,  $\dot{m}_2$ , flows through the superleak and evaporates from the upper reservoir at temperature  $T_2$ , and part,  $\dot{m}_1$ , evaporates directly from the lower reservoir at temperature  $T_1$ . The ratio of  $\dot{m}_1$  to  $\dot{m}_2$  is determined by the condition that the heat generated in the lower reservoir by the helium flowing through the superleak must equal the heat removed by vaporization. According to the mechanocaloric effect<sup>5</sup> we have

$$\frac{\dot{m}_1}{\dot{m}_2} = \frac{S(T_1)T_1}{L(T_1)} \quad , \quad (5)$$

where  $T_1$  is the temperature of the lower reservoir, and  $S(T_1)$  and  $L(T_1)$  are the entropy and latent heat of vaporization for helium at temperature  $T_1$ . Using Eq. (5), the helium used is

$$\dot{m}_T = \dot{m}_1 + \dot{m}_2 = \dot{m}_2 \left( 1 + \frac{S(T_1)T_1}{L(T_1)} \right) \quad . \quad (6)$$

---

4. E.F. Hammel, Jr. and W.E. Keller, Phys. Rev. 124, 1641 (1961).

5. F. London, op. cit., Vol. II, p. 69.

The heat input  $\dot{Q}_T$  in the upper reservoir is absorbed in part by the mechanocaloric effect of superfluid flowing through the fountain pressure pump and, in part, by evaporation of helium at the upper reservoir. Thus we have

$$\dot{Q}_T = \dot{m}_2 L(T_2) + \dot{m}_2 S(T_2) T_2 \quad (7)$$

The alternative to using a fountain pressure pump to deliver helium to the upper reservoir from a central refrigerator would be to build a separate refrigerator at the elevated position. To compare the two possible systems, it is useful to consider the ratio

$$R(T_1, T_2) = \frac{\frac{T_1}{T_2} \frac{\dot{Q}_T}{\dot{m}_T}}{\frac{\dot{Q}_r}{\dot{m}_r}} = \frac{T_1}{T_2} \times \frac{1 + \frac{S(T_2) T_2}{L(T_2)}}{1 + \frac{S(T_1) T_1}{L(T_1)}} \quad (8)$$

where  $\dot{Q}_r = L(T_2) \dot{m}_r$  is the cooling supplied by a separate elevated refrigerator.  $\dot{Q}_T/\dot{m}_T$  and  $\dot{Q}_r/\dot{m}_r$  give the ratios of refrigeration to helium evaporation for the fountain pressure pump system and the separate elevated refrigerator respectively, while the factor  $T_1/T_2$  reflects the different temperatures of helium supplied by the two refrigeration systems. The ratio  $R(T_1, T_2)$  is plotted as a function of  $T_2$  in Fig. 3.

The fountain pressure pump can also be used to transfer superfluid helium from one reservoir to another. The superleak only allows the superfluid component to be transferred so that again the mechanocaloric effect is operative. If liquid is transferred at a rate  $\dot{m}_2$ , then heat must be removed from the lower reservoir at a rate

$$\dot{Q}_1 = \dot{m}_2 S(T_1) T_1$$

and heat must be added to the upper reservoir at a rate

$$\dot{Q}_2 = \dot{m}_2 S(T_2) T_2$$

If heat is removed from the lower reservoir by evaporating part of the helium, then the evaporation rate must be

$$\dot{m}_1 = \frac{\dot{Q}_1}{L(T_1)} = \dot{m}_2 \frac{S(T_1) T_1}{L(T_1)}$$

The ratio of helium lost to helium transferred is just

$$\frac{\dot{m}_1}{\dot{m}_2} = \frac{S(T_1) T_1}{L(T_1)} = 5\% \quad \text{at } T_1 = 1.85^\circ \text{K}$$

#### SPECIAL PROBLEMS

In general, a superleak is any passage that permits the flow of the superfluid component of helium II, but prevents the flow of the normal component. For small flow rates the superfluid component can flow through the superleak without a pressure gradient. For flow rates above the superfluid critical velocity,  $v_{sc}$ , various dissipative mechanisms appear. The critical velocity depends on the size of the channel through

which the helium flows and has been found to be as high as 20 cm/sec in some very narrow channels.<sup>6</sup> For large flow rates one very simple type of superleak is a powder-filled plug. It is difficult to compute a critical velocity in the case of a powder superleak since there is no way of knowing the distribution of pore sizes. However, experiments have shown that tubes packed with powder can maintain a flow rate of 1.2 liter/min·cm<sup>2</sup> of tube cross section.<sup>7</sup> Thus a powder superleak one inch in diameter could transport 360 liters per hour.

Care must be exercised so that there is not appreciable conduction of heat across the superleak. Heat can flow by conduction through the walls of the tube, but this can be minimized by using tubes with low conductivity. The normal fluid must be tightly clamped since any back flow of normal fluid would carry heat. There will also be heat conduction by diffusion through the clamped fluid but this should be negligible.

In our previous discussion of the fountain pressure pump (see Fig. 1), where it is used to provide refrigeration to the upper reservoir, we have assumed that the temperature of the upper reservoir is equal to the temperature just above the superleak. Actually there will be a small temperature gradient along the tube due to the large flow rates involved in applications of interest. In steady-state operation the normal fluid will be stationary while the superfluid will have an upward velocity. The flow rate of the superfluid will exceed its critical velocity since as the size of the tube increases, the critical velocity approaches zero.<sup>8</sup> Under these conditions a mutual friction force is operative and must be included in the calculation of the flow. The equations governing the flow are

$$\rho_s \frac{d\vec{v}_s}{dt} = \rho_s S \nabla T - \frac{\rho_s}{\rho} \nabla P - \vec{F}_{ns} - \rho_s \nabla \Phi \quad (10)$$

and

$$\rho_n \frac{d\vec{v}_n}{dt} = -\rho_s S \nabla T - \frac{\rho_n}{\rho} \nabla P + \vec{F}_{ns} + \eta_n \nabla^2 \vec{v}_n - \rho_n \nabla \Phi, \quad (11)$$

where  $\rho_s$  = superfluid density,  
 $\rho_n$  = normal fluid density,  
 $\vec{v}_s$  = superfluid velocity,  
 $\vec{v}_n$  = normal fluid velocity,  
 $\eta_n$  = normal fluid viscosity,  
 $\Phi$  = gravitational potential, and  
 $\vec{F}_{ns}$  = mutual friction force.<sup>9,10</sup>

- 
6. W.M. van Alphen, J.F. Olijhoek, and R. de Bruyn Ouboter, Superfluid Helium (Academic Press, New York, 1966), p. 187.
  7. Ibid., p. 190.
  8. J. Wilks, Properties of Liquid and Solid Helium (Clarendon Press, Oxford, 1967), p. 390.
  9. J. Wilks, op. cit., p. 377.
  10. F. London, op. cit., Vol. II, p. 83.

For use in the fountain pressure pump these equations simplify since

$$\frac{d\vec{v}_s}{dt} = \frac{d\vec{v}_n}{dt} = \vec{v}_n = 0$$

Adding Eqs. (10) and (11) gives

$$\nabla P = -\rho \nabla \Phi \quad (12)$$

and putting this into Eq. (10) yields

$$\rho_s \nabla T = \vec{F}_{ns} \quad (13)$$

The mutual friction force has the form<sup>11</sup>

$$\vec{F}_{ns} = A \rho_s \rho_n (v_n - v_s)^2 (\vec{v}_n - \vec{v}_s),$$

where A is an empirical constant which is a slowly varying function of temperature and geometry. Evaluating Eq. (13) for  $T = 1.9^\circ\text{K}$  and using  $A = 70 \text{ cm}^3 \cdot \text{sec/g}$ ,<sup>12</sup> one finds

$$\nabla T = \frac{6.1 \times 10^{-7} v_s^3}{(\text{cm/sec})^3} \frac{^\circ\text{K}}{\text{cm}}$$

If we require that the  $\Delta T$  in a column of helium 10 m in height be less than  $0.01^\circ\text{K}$ , then we must have  $\vec{v}_s \leq 2.5 \text{ cm/sec}$ . This means that a one-inch diameter column of helium could support the flow of 46 liters of superfluid per hour which represents  $\approx 45 \text{ W}$  of cooling.

The flow velocity can be considerably higher in a system which uses the fountain pressure pump for transfer of liquid helium. In the transfer system, heat can be supplied just above the superleak so that the flow of helium up the tube consists of both normal and superfluid components. Ideally,  $\vec{v}_n = \vec{v}_s$  so that the mutual friction force is zero. Under these conditions calculations show that the temperature gradient along the tube is negligible.

The fountain pressure pump appears to offer a simple and efficient way to provide cooling a distance from a central refrigerator as well as a means for transfer of liquid helium below the lambda point. Experiments are in progress to demonstrate the usefulness of the fountain pressure pump in large-scale systems.

---

11. J. Wilks, op. cit., p. 381.

12. H.C. Kramers, Superfluid Helium (Academic Press, New York, 1966), p. 205.

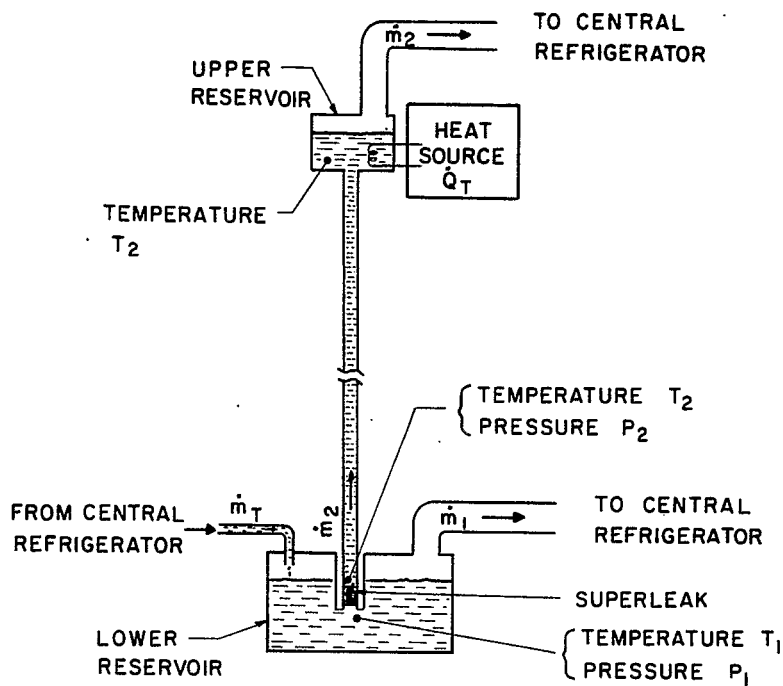


Fig. 1. Schematic drawing of a fountain pressure pump used to provide refrigeration.

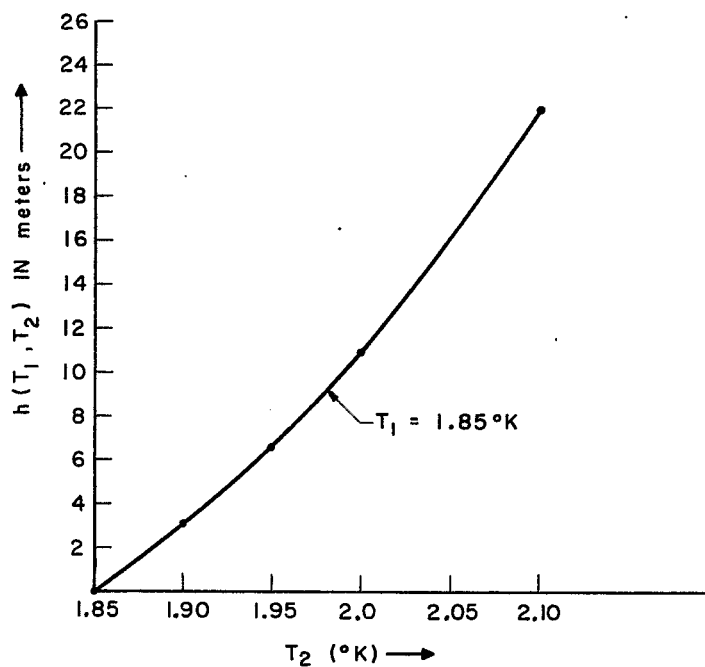


Fig. 2. The difference in height  $h(T_1, T_2)$  as a function of  $T_2$  with  $T_1 = 1.85^{\circ}\text{K}$ .

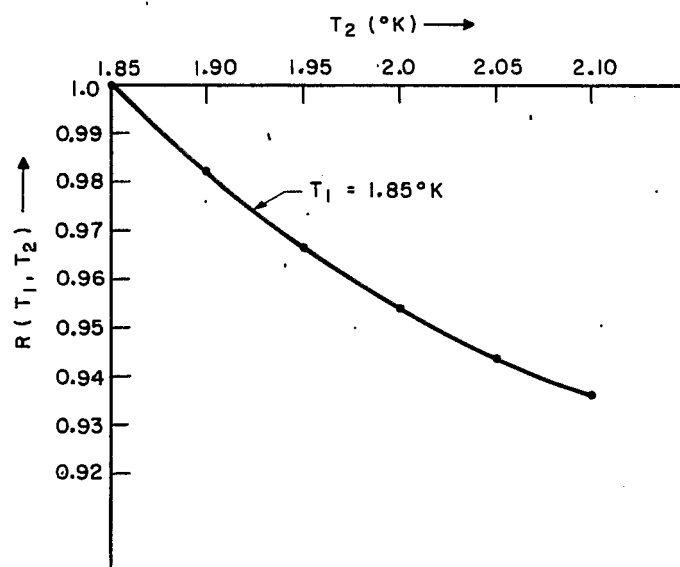


Fig. 3. The ratio  $R(T_1, T_2)$  as a function of  $T_2$  for  $T_1 = 1.85^\circ\text{K}$ .



# REFRIGERATION AT TEMPERATURES BELOW THE BOILING POINT OF HELIUM

S.C. Collins  
500 Inc.  
Cambridge, Massachusetts

## I. INTRODUCTION

The growing need for continuous refrigeration at or near the normal boiling point of helium has led to the practice of coupling a helium liquefier with the apparatus to be cooled in such a manner as to return the cold helium vapor to the heat exchange system of the liquefier and thereby recover substantial amounts of refrigeration.

The value of such an arrangement is demonstrated in Fig. 1. A small liquefier of 4 l/hr capacity containing a somewhat better than average heat exchanger is connected to a liquid storage vessel by means of a two-channel transfer line. The rate of accumulation (or loss) of helium is measured by the rise or fall of an external gas-holder. With the liquefier running and all vapor, that is, the unliquefied portion of the Joule-Thomson stream plus that formed as a result of added heat, returning to the compressor by way of the liquefier, the relation between the rate of heating and the net transfer of helium to or from the storage vessel is given by the upper curve. The lower curve shows the corresponding relation when the liquefier is not in operation and there is no recovery of refrigeration. In the first case the useful refrigeration at 4.4°K varies from 4.8 W·hr/l of liquid at low rates of heating to 3.5 W·hr/l when the heating rate is 38.5 W. In the second case the ratio is 0.78 W·hr/l of liquid helium — about one-fifth as great.

The helium liquefier used for this experiment required a flow of helium of 35 SCFM with adiabatic expansions at two temperature levels from 14 atm to 1 atm. Liquid nitrogen was not used.

It is significant that so long as the average heating rate is below 18 W the rate may be as high as 50 W for a part of the time.

## II. REFRIGERATOR FOR LOWER TEMPERATURES

In response to the need for continuous refrigeration at the 1.85°K by Professors Fairbank and Schwettman of Stanford University for their superconducting accelerator, a small experimental refrigerator was constructed and successfully operated at Arthur D. Little.<sup>1</sup> The refrigeration cycle used in this machine is given in Fig. 2. The heat exchanger for recovering refrigeration from the low-pressure vapor (10-14 mm) represented the chief problem to be solved. The volume of gas to be treated was enormous and the pressure available to drive it through the heat exchanger was very small. The design finally chosen consisted of a vertical stack of pancake coils of finned tubing connected in series in such a manner as to cause the high-pressure stream of incoming helium to flow in a spiral path from the center of one pancake to the periphery and from the periphery of the next pancake to its center and so on. The low-pressure stream flowed vertically upward through the finning which presented a short path of large cross section.

---

1. S.C. Collins, R.W. Stuart, and M.H. Streeter, Rev. Sci. Instr. 38, 1654 (1967).

High-pressure helium enters the special heat exchanger at three temperature levels, room temperature,  $79^{\circ}\text{K}$  and about  $7^{\circ}\text{K}$ . The warmer sections of the heat exchanger are, therefore, unbalanced and the recovery of refrigeration is far from complete. The lowest section in which the mass rate of flow of incoming and outgoing helium was the same was made relatively long for high efficiency so as to conserve refrigeration of high intrinsic value.

During the test continuous refrigeration in the amount of 10 W at  $2.0^{\circ}\text{K}$  and 15 W at  $2.2^{\circ}\text{K}$  was maintained. The major limitation on refrigeration was the capacity of the vacuum pump available for use. For the helium circulated in the special exchanger the refrigeration obtained was approximately 22 J/g, a figure very close to the maximum available.

### III. STANFORD REFRIGERATOR

A large refrigerator of this type has now been made for use in the Stanford accelerator. It has a capacity of 300 W at  $1.85^{\circ}\text{K}$ . The cycle is slightly different (Fig. 3), in that conditions for heat transfer in the range from  $16^{\circ}$  to  $8^{\circ}\text{K}$  were made more favorable by shunting a portion of the high-pressure stream to the main heat exchanger for further cooling by the gas discharged by the No. 2 expansion engine. The heat capacity of helium at 10-15 atm is much higher at the  $16^{\circ}$  to  $8^{\circ}\text{K}$  range than that of the low-pressure outgoing gas.

In Figs. 4, 5 and 6 various stages of the manufacture of the low-pressure heat exchanger for the Stanford refrigerator are shown.

### IV. REFRIGERATOR OF THE FUTURE

Because of the cost of the power to operate a large refrigerator continuously it is readily apparent that any increase in the efficiency of the refrigerator will greatly extend its usefulness.

There is undoubtedly room for improvement in every component of a refrigerator for very low temperatures. The vacuum pump is probably the most inefficient element. A major effort will be required to do much about it but such an undertaking seems well worthwhile.

Industrial compressors use approximately 50% more power than the theoretical minimum but further improvement will likely be slow and costly considering the advanced state of the art.

Only slight improvement in the efficiency of expansion machines seems possible.

Heat exchangers vary greatly in efficiency. In general there is room for much improvement. Such improvement will, of course, add to the cost of the refrigerator.

The most promising possibility for greater efficiency lies in the use of more stages of expansion. This principle is illustrated in Table I. Expanding portions of the stream of high pressure helium at five temperature levels is highly effective.

A flow diagram of a refrigerator having five stages of expansion is given in Fig. 7. Ordinarily the complexity would be considered too great, but recent models of expansion engines have demonstrated a degree of reliability which justifies the use of multiple cylinders. The power produced by the expansion engines should be about equivalent to that required to drive the vacuum pumps. The net power requirement of the system is estimated to be three times that of a Carnot cycle.

TABLE I. Effect of number of thermal stages of expansion on the available refrigeration. Helium flow was 74 SCFM at a pressure of 15 atm.

<u>Number of Stages of Expansion</u>	<u>Refrigeration at 4.4°K (W)</u>
1	12 obs.
2	37 obs.
3½ (N <sub>2</sub> )	58 obs.
5	75 calc..

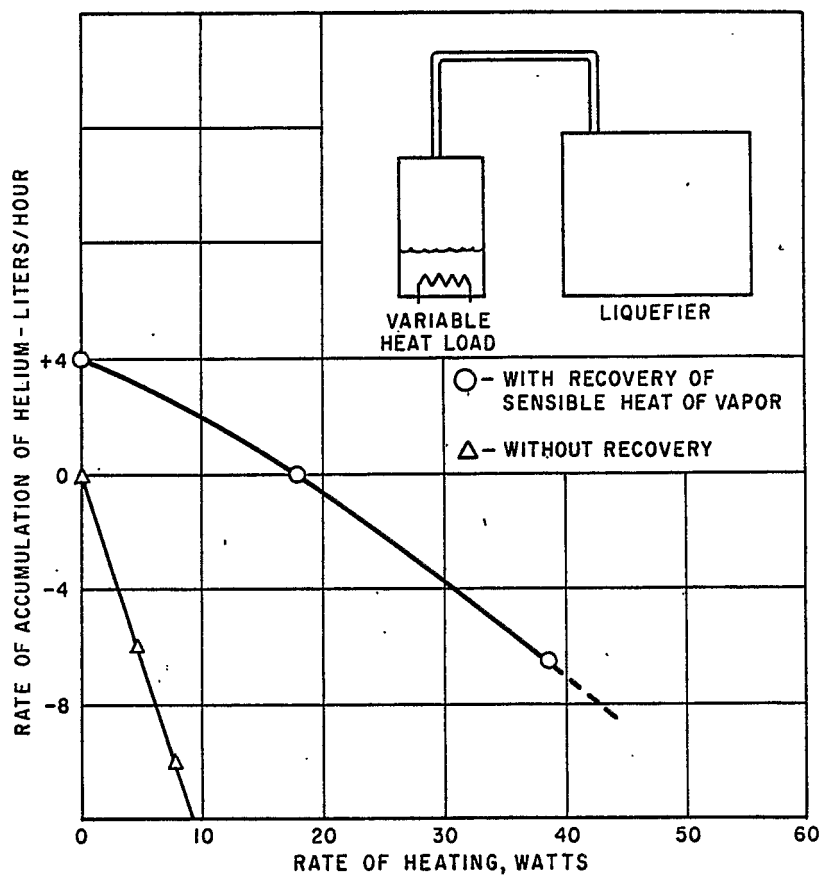


Fig. 1. Refrigeration at 4.4°K.

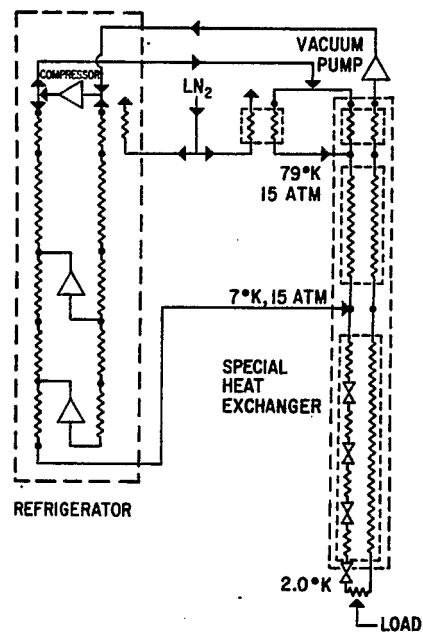


Fig. 2. Flow diagram of experimental refrigerator for 1.85°K.

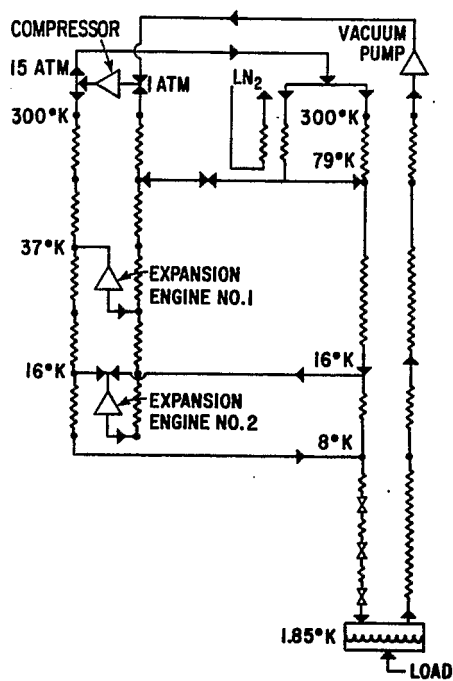


Fig. 3. 300 W, 1.85°K refrigerator cycle.

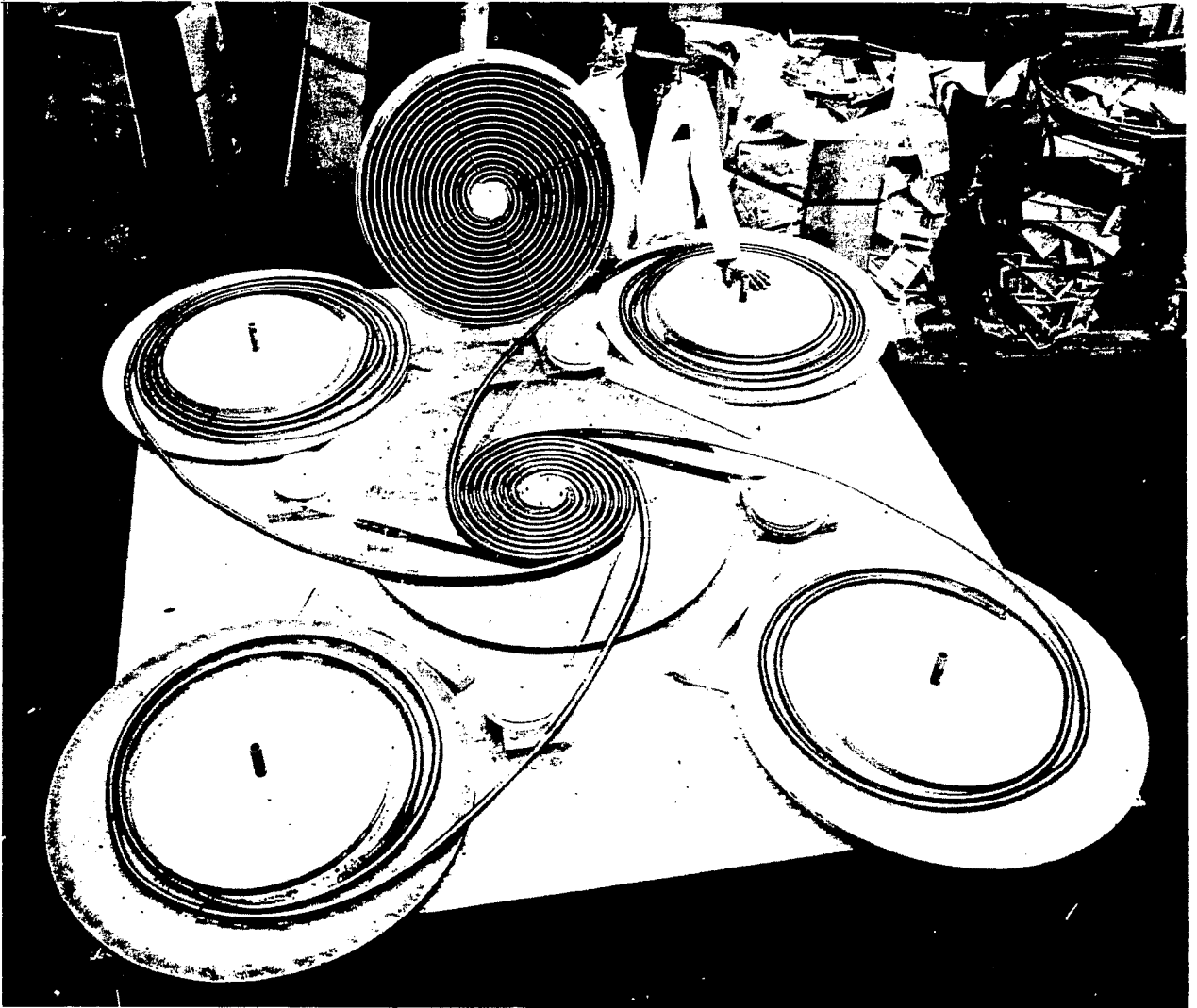


Fig. 4. Heat exchanger pancake under construction.

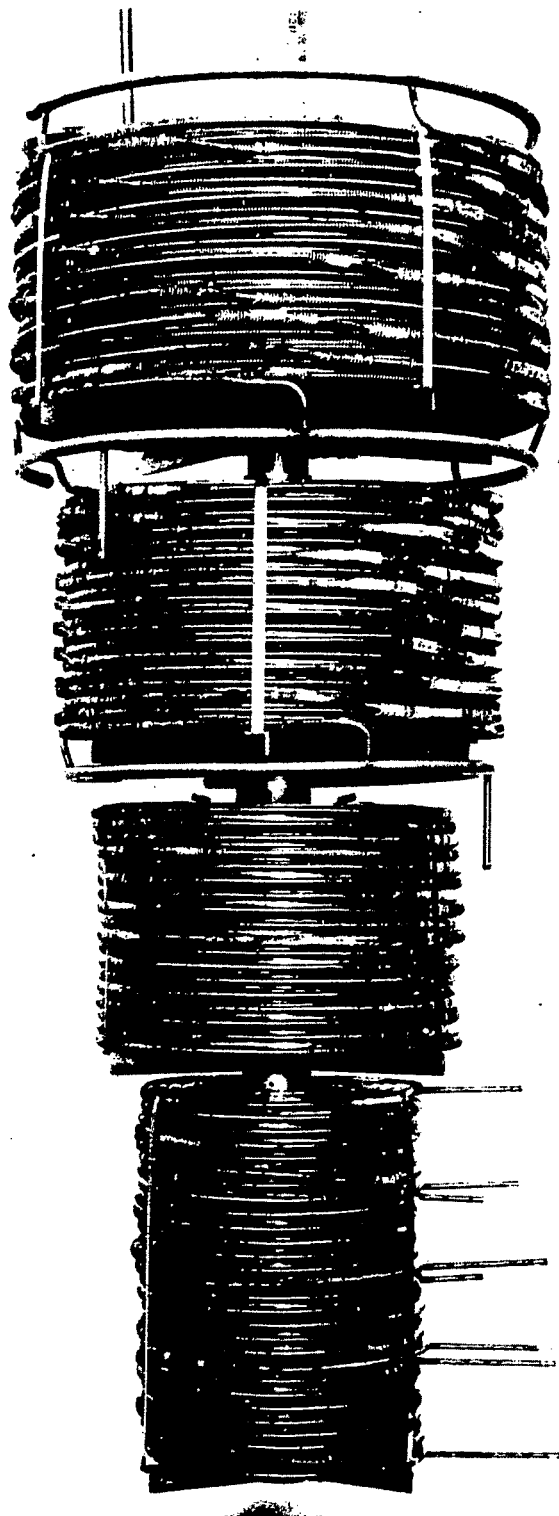


Fig. 5. Low-pressure heat exchanger ready for jacket.

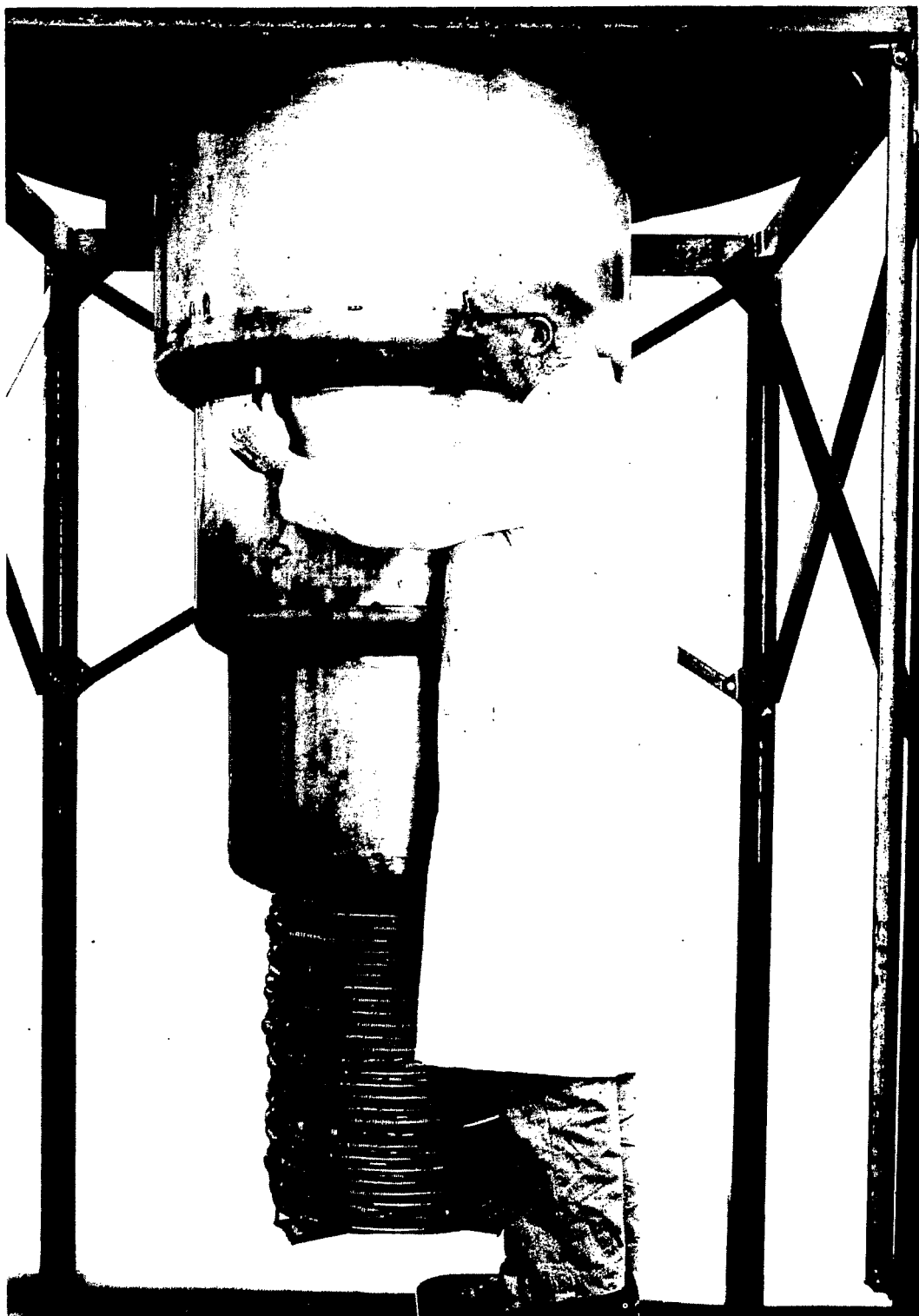
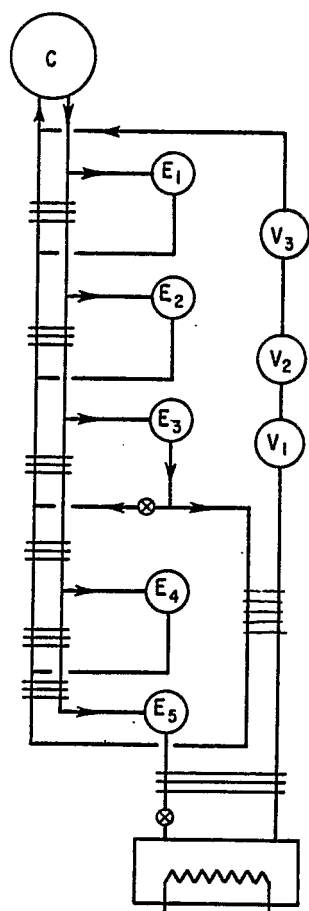


Fig. 6. Low-pressure heat exchanger receiving jacket.



POWER REQUIREMENTS	1.5°K	1.8°K
COMPRESSOR	3050 kW	2410kW
VACUUM PUMP	318	272

Fig. 7. Proposed cycle for 5 kW, 1.5°K refrigerator.



# RF AMPLITUDE AND PHASE STABILIZATION FOR A SUPERCONDUCTING LINEAR ACCELERATOR BY FEEDBACK STABILIZATION TECHNIQUES\*

L.R. Suelzle  
High Energy Physics Laboratory, Stanford University  
Stanford, California

## INTRODUCTION

Of the properties<sup>1,2</sup> of a superconducting electron linac, one of the most important for energy and current stability of the exit beam is the continuous or long-duty-cycle property. Conventional linacs are restricted to short-duty-cycle operation in which case such exit-beam properties as spread in energy are dominated by the transient conditions associated with the short duty cycle. Under these conditions, utilization of feedback stabilization techniques to stabilize the rf accelerating fields in the accelerating structure can be very difficult. In this paper, I would like to discuss some of the feedback stabilization techniques being examined and tested at Stanford and to describe how the high-Q characteristic of a superconducting linac can simplify some of the feedback control problems.

## DRIVING THE ACCELERATOR STRUCTURE

In the superconducting electron linac (SEL), the operating conditions will be typically that of extreme beam loading, where the power supplied to the beam is much larger than the power lost to the cavity structure. In the conventional linac, a beam loading of 50% is considered "heavy loading." The problems of matching the rf sources to the driving-point impedances are therefore very different for the SEL. Other operations such as "drifting" a beam through an unpowered section or such as reverse-phase operation have a very different significance for the SEL.

The beam loading of the accelerating structure can be examined by considering the resonant circuit shown in Fig. 1. It is assumed throughout this discussion that the structure is a standing wave structure. The cavity structure (considering only one mode) is represented by the parallel resonant circuit with admittance

$$Y_c = G_c [1 + j 2Q_0 \delta] \quad , \quad (1)$$

where  $G_c$  is the equivalent shunt conductance,  $Q_0$  is the unloaded quality factor for the structure, and  $\delta$  is the tuning decrement  $(\omega - \omega_0)/\omega_0$ . The power source and transmission line are represented by the voltage source  $\vec{V}_g$  [amplitude  $V_g = |\vec{V}_g|$  and phase  $\text{Arg}(\vec{V}_g)$ ] with impedance  $R_g$  (assumed to be real). The coupling is represented by a

---

\*Work supported in part by the U.S. Office of Naval Research, Contract [NONR 225(67)].

1. P.B. Wilson, Linear Accelerators, P. Lapostolle and A. Septier, editors, Chapter 5.1 (to be published).
2. H.A. Schwettman, J.P. Turneure, W.M. Fairbank, T.I. Smith, M.S. McAshan, P.B. Wilson, and E.E. Chambers, IEEE Trans. Nucl. Sci. NS-14, No. 3, 336 (1967).

transformer of turns-ratio  $n$ .  $\vec{V}_i$  is the voltage of the incident wave and  $\vec{V}_r$  is the voltage of the returning wave.  $P_i$  and  $P_r$ , the incident and returning power, are given by  $P_i = V_i^2/2R_g$  and  $P_r = V_r^2/2R_g$ . The beam effects are represented by the current generator  $\vec{I}_b$ . For a relativistic and well-bunched beam, the amplitude  $I_b$  is approximately equal to  $2I_0$  where  $I_0$  is the dc component of the beam current. The cavity voltage  $\vec{V}_c$  is computed by summing the voltages produced when each of the generators is considered independently. The result is given by

$$\vec{V}_c = n(1 + \Gamma)\vec{V}_i - \frac{n^2 R_g \vec{I}_b}{1 + n^2 R_g Y_c} \quad (2)$$

where

$$\Gamma = \frac{1 - n^2 R_g Y_c}{1 + n^2 R_g Y_c} \quad (3)$$

The coupling coefficient  $\beta$  is given by

$$\beta = (n^2 R_g G_c)^{-1} \quad (4)$$

At resonance ( $\delta = 0$ ),  $\Gamma$  is equal to  $(\beta - 1)/(\beta + 1)$ . The acceleration voltage  $V_a$  is given by

$$V_a = \frac{-\vec{V}_c \cdot \vec{I}_b}{I_b} = -V_c \cos \varphi \quad (5)$$

where  $\varphi$  is the phase angle between the cavity voltage  $\vec{V}_c$  and the current  $\vec{I}_b$ . For a properly phased beam,  $\varphi = 180^\circ$ . From this point on, let us consider only the on-resonance, beam-in-phase case. Let us also assume that  $n^2 R_g G_c \ll 1$ . This is the extremely overcoupled case of  $\beta \gg 1$ . In this case,

$$V_a = 2nV_i - n^2 R_g I_b \quad (6)$$

and

$$V_r = V_i - nR_g I_b \quad (7)$$

Let us further assume that the transformer turns-ratio  $n$  is chosen so that  $V_r = 0$  at  $I_b = I_b(\max)$  and  $V_i = V_i(\max)$ . Remembering that  $I_b = 2I_0$  and  $V_a = nV_i$ ,

$$n^2 = \frac{V_a(\max)}{2R_g I_0(\max)} \quad (8)$$

For this transformer turns-ratio,  $V_a$  and  $P_r$  become

$$V_a = 2V_a(\max) \left[ \frac{P_i}{P_i(\max)} \right]^{\frac{1}{2}} - V_a(\max) \frac{I_0}{I_0(\max)} \quad (9)$$

and

$$P_r = P_i + \left( \frac{I_0}{I_0(\max)} \right)^2 P_i(\max) - 2P_i(\max) \frac{I_0}{I_0(\max)} \left[ \frac{P_i}{P_i(\max)} \right]^{\frac{1}{2}} \quad (10)$$

$V_a$  and  $P_r$  are plotted in Figs. 2a and 2b for the two special cases of  $I_0 = 0$  and  $I_0 = I_0(\max)$ .

From the curves in Figs. 2a and 2b, we see that with  $I_0 = 0$  the power  $P_i$  required to produce the cavity voltage  $V_a(\max)$  is  $P_i = P_i(\max)/4$ . Also, for  $I_0 = 0$ ,  $P_i$  approximately equals  $P_r$ . When  $I_0 = I_0(\max)$ , to obtain  $V_a$  equal to 0,  $P_r$  equals  $P_i$  which equals  $P_i(\max)/4$ . If  $P_i = 0$  (source turned off) and  $I_0 = I_0(\max)$ ,  $V_a$  equals  $-V_a(\max)$  and  $P_r$  equals  $P_i(\max)$ . Therefore, the concept of "drifting" a beam through an unpowered section of accelerator takes on a different significance. It is very important that the source end of the transmission line is always reverse-terminated in a load capable of dissipating a power as large as  $P_i(\max)$  (e.g. an isolator or a circulator plus a load). If a section of the accelerator cannot be powered, it will be necessary to detune the structure so that the energy  $V_a(\max)$  is not lost. The amount of energy lost can also be reduced by increasing the amount of overcoupling.

We also notice from Figs. 2a and 2b that the operation in which the generator is reverse-phased should be avoided since the cavity voltages and return power will become excessive. Reverse phasing is sometimes used with conventional linacs to obtain high currents with low final beam energies.

### RF STABILITY REQUIREMENTS

With the continuous wave or long-duty-cycle capability of the SEL, the transient effects no longer limit the amplitude and phase stability of the accelerating fields. The Stanford group has set a design goal for resolution in energy of the exit beam of  $\Delta E_f/E_f \leq 10^{-4}$ . The design goal for stability of the energy gain in a single accelerating structure has been set at  $\Delta E/E \leq 10^{-4}$ .

The energy gain through a section of the accelerator is described by

$$E = E_0 \cos \varphi, \quad (11)$$

where  $E_0$  is the energy gain when the phasing angle  $\varphi$  is zero. Let us assume that the beam has a phase spread (phase bucket) of  $\Delta\varphi$  centered at a phasing angle  $\varphi_0$ ; then the spread in the energy gain can be approximated by

$$\left[ \frac{\Delta E}{E} \right]^2 \approx \left[ \frac{\Delta E_0}{E_0} \right]^2 + \left[ \frac{(\Delta\varphi + 2|\varphi_0|)^2}{8} \right]^2. \quad (12)$$

With an amplitude stability  $\Delta E_0/E_0 \approx \pm 7 \times 10^{-5}$ , a phase spread  $\Delta\varphi \approx 1^\circ$  (determined by the injector conditions), and a phasing angle  $\varphi_0 \approx \pm 0.2^\circ$ ,  $\Delta E/E$  is approximately  $10^{-4}$ . We are therefore attempting to hold the amplitude of the rf to a stability of  $\pm 7 \times 10^{-5}$  and the phase to a stability of  $\pm 0.2^\circ$ .

### FEEDBACK CONTROL SYSTEM

In order to obtain the desired amplitude and phase stability in the accelerator structure in the presence of large perturbations such as beam loading or frequency shifts, it is necessary to use feedback control. In Fig. 3 a simplified block diagram of the feedback control system that has been constructed and studied at Stanford is shown. The rf field in one of the excited cavities of the accelerating structure is sampled by a pickup probe which couples a relatively small amount of power (0.1 to 1.0 W) to the amplitude and phase detection circuitry. A detector diode, which will be discussed in a subsequent section of this paper, provides a voltage which is proportional to the rf amplitude. This voltage is compared with a reference voltage

which may be a dc or pulse signal. The amplified error signal is then used to control a PIN diode attenuator in the rf input line to a klystron power amplifier.

The phase of the rf is measured relative to a reference signal which is common to the entire accelerator. The phase setting is adjusted by means of a phase shifter located between the reference phase and the phase detector. The problem of selecting the phase angle so that the cavity voltage is in phase with the bunched electron beam will not be discussed in this paper. Once a suitable phase is selected, it is the function of the feedback control system to maintain the phase alignment. The error signal from the phase detector is used to control an electronic phase shifter in the rf input line to the klystron amplifier.

With the large mismatch condition that can exist with the power feed system, it is necessary to provide an isolator (or circulator and load) to absorb the power returning from the structure. As discussed earlier, the isolator must be capable of dissipating the maximum available power from the generator.

The reflectometer shown in Fig. 3 compares the phase of the return signal with the incident signal in the power feed to the accelerator structure. This phase comparison provides a measure of how well the structure is tuned to the driving frequency. The signal from the reflectometer can be used in the automatic tuning of the structure.

Shown in Fig. 4 is the phase shifter circuitry used in our prototype test. A variable reactance at one port of a four-port circulator varies the phase of the reflected rf signal at that port. The variable reactance is produced by varying the reverse bias on a diode. The phase shifting range is expanded by resonating the diode capacitance with an inductance.<sup>3</sup>

#### AMPLITUDE DETECTION

Shown in Fig. 5 is a diagram of the amplitude detection circuit. A coupling probe (magnetic coupling) provides a 0.1 to 1.0 W signal for the amplitude and phase detection circuitry. A Hot Carrier diode operating as a large-signal detector (peak reading with negligible power dissipation in the diode) provides a voltage proportional to the amplitude of the rf signal. The diode is housed in a structure which has a small amount of tuning capability to compensate for the effective capacitance of the diode and is temperature stabilized to better than 0.2°C. The temperature coefficient for the Hot Carrier diode depends on the particular loading conditions and has been measured at approximately 1 mV/°C for our conditions (output voltage of 10 V at the 1 W level). Since our amplitude stability requirements are predominantly short-term requirements of the order of minutes, long-term effects such as diode aging are not considered to be vital problems.

The problems of mismatches or changing impedance of the transmission line affecting the amplitude stability can be minimized by taking advantage of the low output impedance provided by the undercoupled magnetic coupling ( $\approx 0.5 \Omega$ ). This is done by locating the diode at an integer number of transmission-line half wavelengths from the coupling. We have used a PIN diode as a controllable perturbation on the system and have adjusted the line length between the diode and the coupling probe to minimize the amplitude variations produced by the perturbation. Since a change in the amplitude level at the diode will change the reactive loading produced by the diode, the problem of holding the phase constant with changes in amplitude is minimized by locating the diode at this low-impedance point.

---

3. R.H. Hardin, E.J. Downey, and J. Munushian, Proc. IRE 48, 944 (1960).

## PHASE DETECTOR

The phase detector circuitry is summarized in Fig. 6. Signals  $\vec{B}$ , with amplitude  $B$ , and  $\vec{A}$ , with amplitude  $A$  and phase angle  $\varphi$  relative to  $\vec{B}$ , are combined in a four-port, 3 dB hybrid (racetrack hybrid). The vectorial sums  $\vec{A} + \vec{B}$  and  $\vec{A} - \vec{B}$ , which are obtained at the other two ports, are detected by linear detectors with detection efficiencies  $k_1$  and  $k_2$  respectively. The detected signals are subtracted to produce the video signal  $E_v$  where

$$E_v = k_1 [A^2 + B^2 - 2AB \cos \varphi]^{\frac{1}{2}} - k_2 [A^2 + B^2 + 2AB \cos \varphi]^{\frac{1}{2}} \quad (13)$$

With neither  $\vec{A}$  nor the reference signal  $\vec{B}$  modulated,  $E_v$  is a dc signal which, for  $k_1 = k_2$ , is null at  $\varphi$  equal to  $90^\circ$  or  $270^\circ$ . Should the detection efficiencies or detection power law characteristics for one diode change relative to the other diode, the null would be found at a different value of  $\varphi$ . For  $0.1^\circ$  stability, the two diodes must track to about one part in 300.

The problem of the extreme tracking requirement for the diodes can be removed by modulating the reference signal  $\vec{B}$ . For  $B = B_0 + B_1 \sin \omega_m t$ ,  $\varphi = \pi/2 - \alpha$ , and  $A \gg B_0$ ,  $E_v$  becomes

$$E_v = (k_1 + k_2) B_1 \sin \alpha \sin \omega_m t + (k_1 - k_2) \frac{B_0}{A} B_1 \sin \omega_m t + \frac{(k_2 - k_1) B_1^2}{4A} \cos 2\omega_m t + \text{dc terms} \quad (14)$$

If we consider only those terms with frequency  $\omega_m$ , we are left with the first two terms in Eq. (14). If

$$\left( \frac{k_1 - k_2}{k_1 + k_2} \right) \frac{B_0}{A} < 10^{-3} \quad ,$$

then the null in the amplitude of frequency  $\omega_m$  will occur at  $-0.1^\circ < \alpha < 0.1^\circ$ . The ratio  $B_0/A$  is made small by suppressing the carrier ( $B_0 \ll B_1$ ) and by making  $A$  large compared with  $B_1$ . The suppressed carrier reference signal method is referred to as the homodyne phase detection system.<sup>4</sup>

For our tests, we have used a 100 kHz modulation frequency with a doubly-balanced modulator which suppressed the carrier at 952 MHz to -20 dB ( $B_0/B_1 \approx 0.1$ ). The ratio  $B_1/A$  was less than 0.1 and the diode-tracking term  $(k_1 - k_2)/(k_1 + k_2)$  was less than 0.05.

## FEEDBACK DYNAMICS

The high-Q characteristic of the superconducting accelerating structure leads to a great simplification in the feedback control dynamics when the system is compared with the conventional room temperature structure. For a loaded  $Q$  of  $10^8$  at a frequency of 1 GHz, the structure has a time constant of 0.032 sec (video bandwidth of 5 Hz). The time constants of the other elements in the control loops (amplifiers, PIN diode

---

4. S.D. Robertson, Bell System Tech. J. 28, 99 (1949).

attenuator, varactor phase shifters, etc.) will be much smaller than 32 msec, typically in the microsecond range (100 kHz video bandwidth). Consequently, the gain-frequency curve for the control loop can be a -6 dB/octave roll-off with unity-gain crossover at 10 kHz which will be shown later to yield more than an adequate gain-bandwidth product for the control loop.

For the room-temperature linear accelerators, where the loaded  $Q$  may be of the order of  $10^4$  and where pulse lengths are relatively short, the response characteristics of the control loop become more complex because of a much higher gain-bandwidth requirement. A modulated phase reference signal, for example, may not be usable because of the bandwidth limitation of a modulated system. The transient problems are further complicated when the spectrum of video frequencies is sufficiently large that one or more of the adjacent resonant modes of the multicavity accelerating structure can be excited.<sup>5</sup>

For the control loops for the superconducting accelerator at Stanford, we have tentatively selected a gain-bandwidth product of  $10^4$  Hz for both the amplitude and phase control loops. Direct current loop gains of  $10^5$  for the amplitude loop and  $10^3$  for the phase loop will be more than sufficient to handle the perturbations inside the loops.

In Fig. 7 is shown the loop diagram for the amplitude control loop with the appropriate transfer functions.  $A_0$  is the dc loop gain (selected at  $10^5$ ) and  $T_1$  is the dominant pole in the system ( $\approx 1.6$  sec). A zero at  $S = 1/T_2$  and  $T_2 \approx T_c$ , where  $T_c$  is the cavity time constant, maintains the roll-off at -6 dB/octave.  $E_b$  represents the electron beam component to the cavity voltage  $E_c$ . Shown in Fig. 8 are the approximate time responses for the transient conditions from initial turn-on to the maximum operating cavity voltage and beam current. With the initial turn-on of the reference voltage, the power incident to the accelerator structure is turned on to the maximum available power which is assumed, for discussion, to be slightly higher than  $P_i(\max)$ . The cavity voltage  $E_c$  changes exponentially toward the final value  $2V_a(\max)$ . When the voltage reaches the desired value of  $V_a(\max)$  (in approximately 0.7 of a filling time), the control loop comes out of saturation and regulates the cavity voltage to  $V_a(\max)$ . A power of  $P_i(\max)/4$  is required to maintain the voltage of  $V_a(\max)$  with the coupling parameters discussed earlier in this paper.

When the beam current is turned on to  $I_0(\max)$ , the control loop increases the power to the  $P_i(\max)$  level in approximately 16  $\mu$ sec. During this beam turn-on transient, the cavity voltage falls by a part in 2000 and recovers to within a part in  $10^4$  in approximately 100  $\mu$ sec. The transient dip in the cavity voltage when the beam is turned on limits the minimum cavity voltage at which the regulating system can continue to regulate with a step change in the beam current from 0 to  $I_0(\max)$ .

## TEST RESULTS

The amplitude and phase control loops were tested with a room-temperature five-cavity, 952 MHz, copper accelerating structure (power input of 100 W and less). Redundant amplitude and phase detection units were used to check the stability of the system. The desired stabilities in amplitude and phase were achieved even though the mechanical stability of our test coupling probes would not be adequate for the final accelerator. High-stability coupling probes are currently being designed.

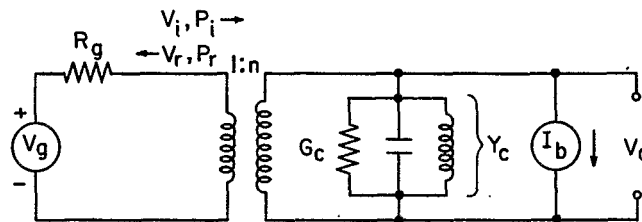
---

5. R.A. Jameson, Los Alamos Scientific Laboratory Report LA-3372 (1965).

A five-cavity, lead-plated-copper, 952 MHz accelerating structure was cooled to 4.2°K and yielded an unloaded Q of  $10^8$ . Shown in Fig. 9 are oscilloscope traces of the cavity voltage, the square root of the incident power, and the square root of the reflected power in response to a pulsed reference signal. The cavity was critically coupled to the generator ( $Q_L = 5 \times 10^7$ ) and stabilized in amplitude and phase. Although this was only the initial test of the system with a superconducting structure (no beam), the performance met our expectations.

#### ACKNOWLEDGEMENTS

The author expresses his appreciation to J. Arnold, G. Ramian, and H. Schwarz for their roles in the designing, developing, and testing of the system presented in this paper. Valuable discussions with J. Weaver were greatly appreciated.



$$\beta = (n^2 G_c R_g)^{-1} \quad I_b \approx 2 I_0$$

$$Y_c = G_c (1 + j 2 Q_0 \delta) \quad \delta = \frac{\omega - \omega_0}{\omega_0}$$

Fig. 1. Equivalent circuit for a standing wave cavity loaded by a relativistic beam.

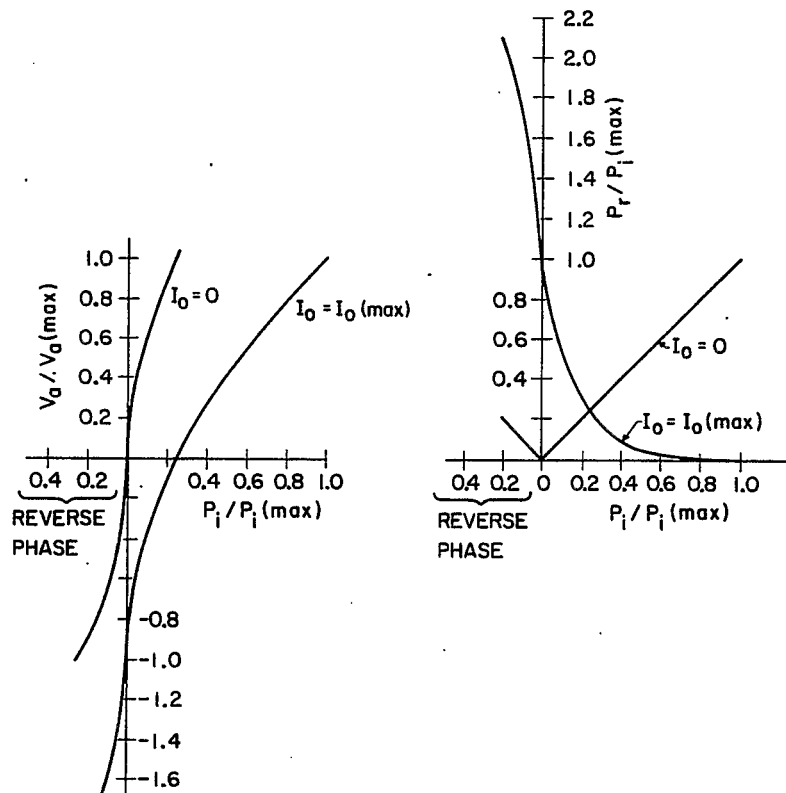


Fig. 2. Voltage gain  $V_a$  and the return power  $P_r$  as a function of the incident power  $P_i$  for values of beam current  $I_0 = 0$  and  $I_0 = I_0(\max)$ . The coupling to the cavity has been selected for optimization at  $V_a = V_a(\max)$  and  $I_0 = I_0(\max)$ .



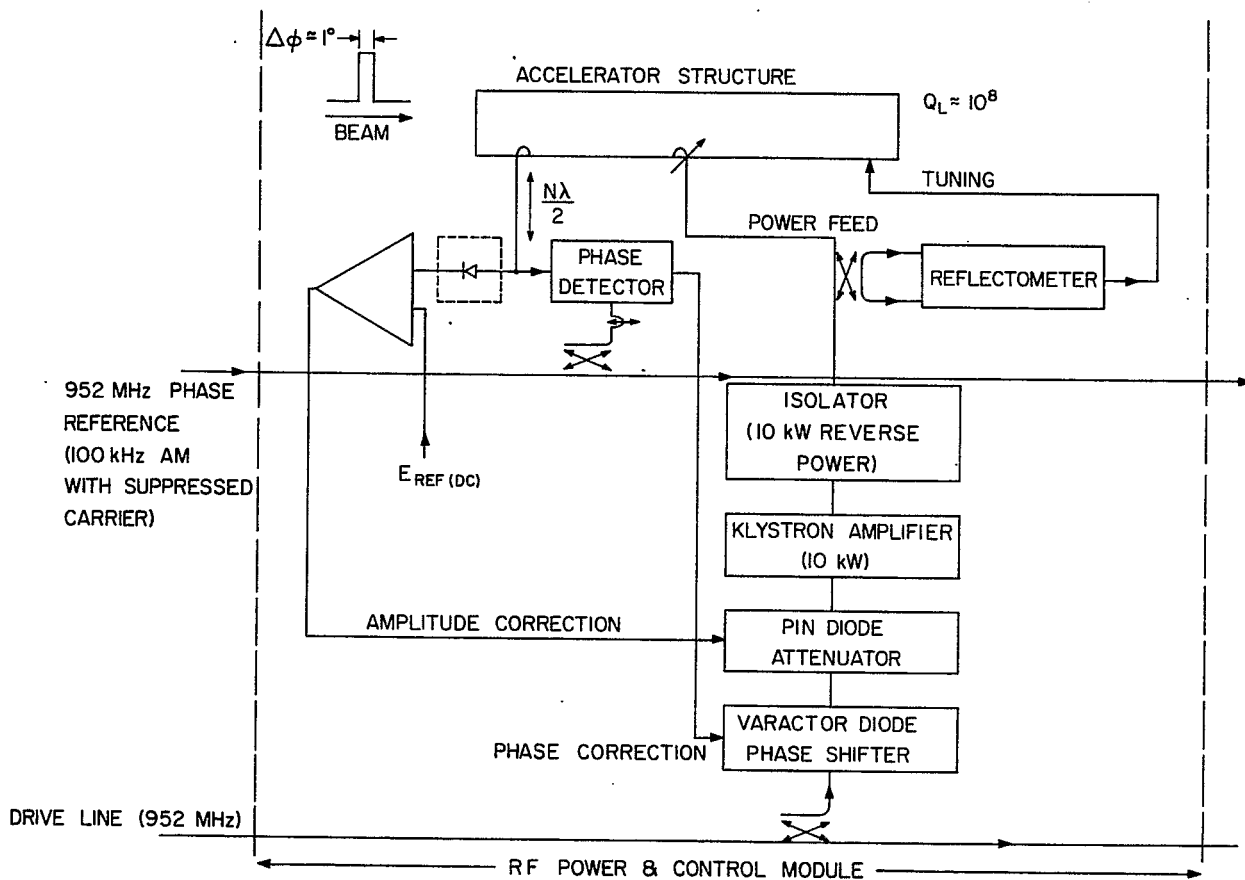


Fig. 3. Block diagram of amplitude and phase control loops.

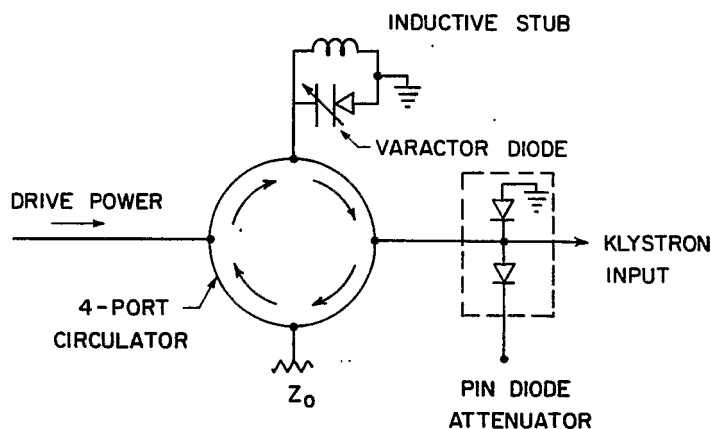


Fig. 4. Prototype varactor diode phase shifter and PIN diode attenuator.

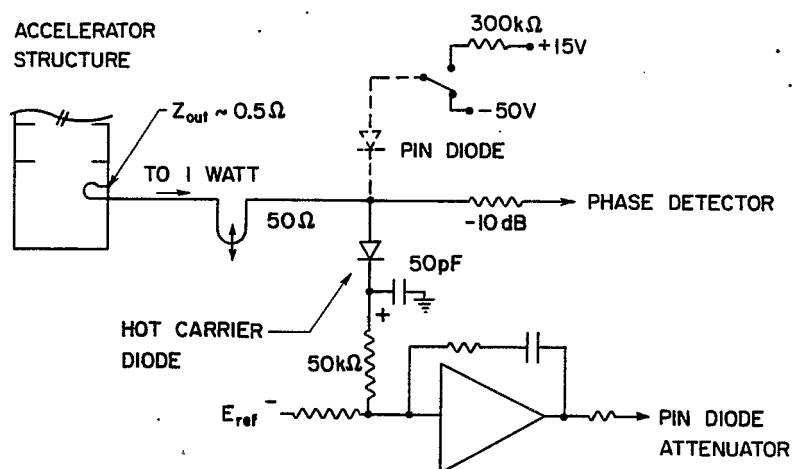


Fig. 5. Amplitude detection circuitry.

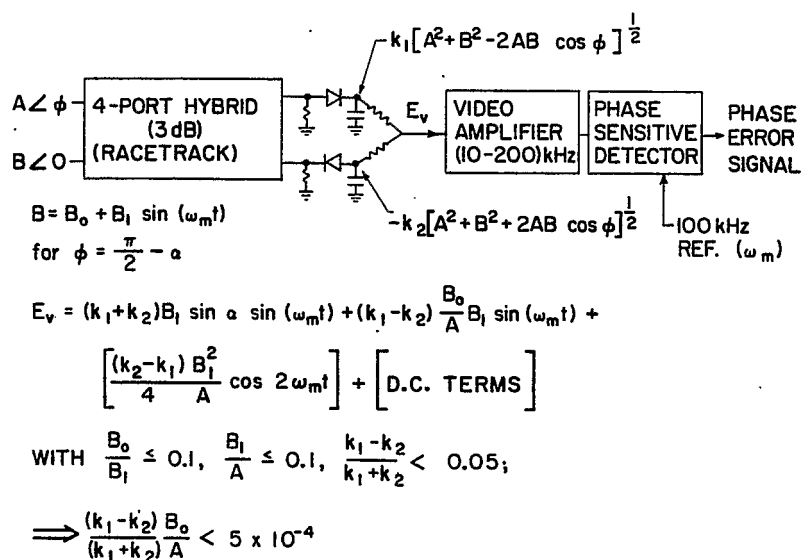
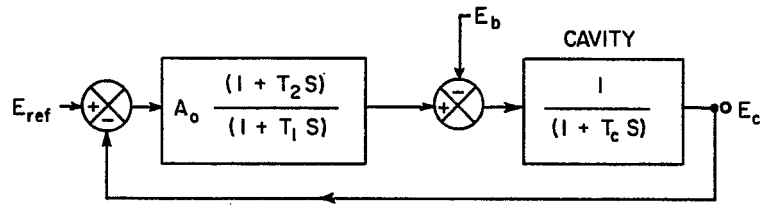


Fig. 6. Summary of the phase detection method.



FOR  $T_2 \approx T_c$

$$E_c \approx \frac{E_{ref}}{(1 + \frac{T_1 S}{A_0})} - \frac{E_b (1 + T_1 S)}{A_0 (1 + \frac{T_1 S}{A_0}) (1 + T_c S)}$$

$$T_c = \frac{.2 Q_L}{\omega_0} \approx 0.032 \text{ sec}$$

$$A_0 \approx 10^5$$

$$\text{GAIN-BANDWIDTH} \approx 10 \text{ kHz} \Rightarrow T_1 \approx 1.6 \text{ sec}$$

Fig. 7. Loop transfer functions for the amplitude control loop. The cavity voltage  $E_c$  is given in terms of the reference voltage  $E_{ref}$  and the beam-induced voltage  $E_b$ .

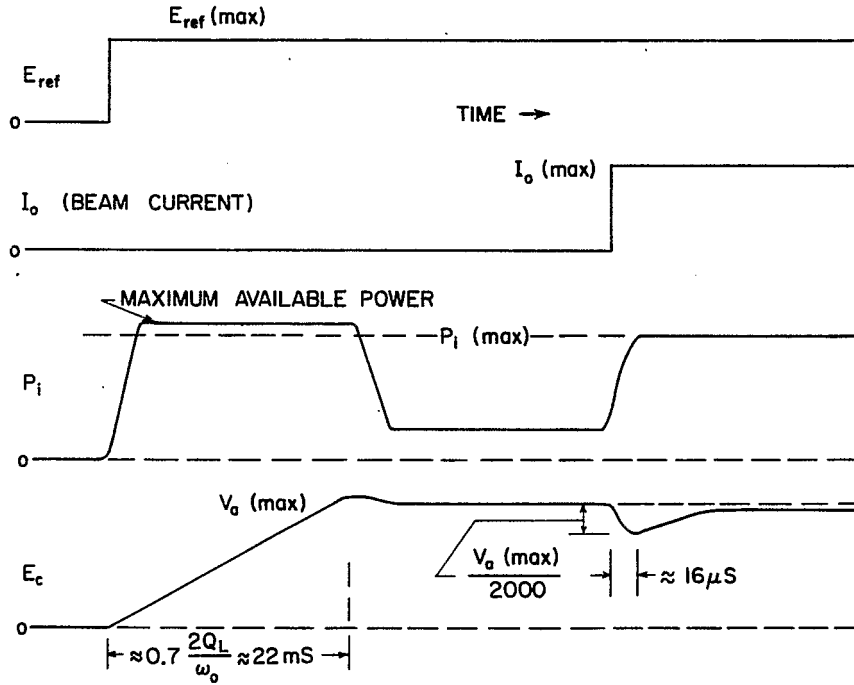


Fig. 8. Expected time response of the cavity voltage  $E_c$  and the incident power  $P_i$  during the turn-on of the reference voltage and beam current. Conditions are shown for the beam current  $I_0(\text{max})$  and the cavity voltage  $V_a(\text{max})$ .

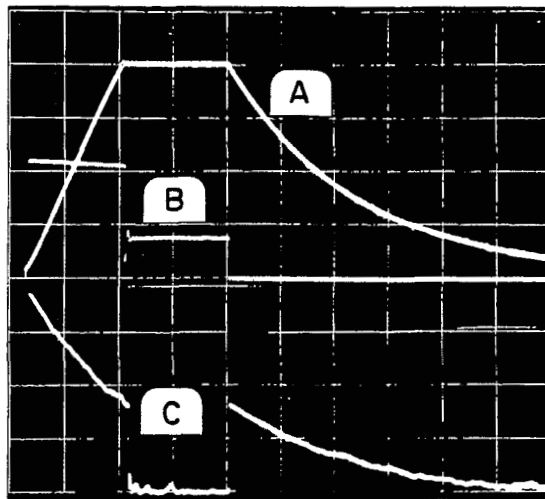


Fig. 9. Oscilloscope traces obtained during a recent test with a pulsed reference voltage on a superconducting cavity structure. Trace (A) is the cavity voltage, trace (B) is the square root of the incident power (linear detectors), and trace (C) is the square root of the reflected power from the cavity structure. The time scale is 5 msec per division.

# PARTICLE MOTION IN A STANDING WAVE LINEAR ACCELERATOR\*

E.E. Chambers  
High Energy Physics Laboratory, Stanford University  
Stanford, California

## I. CASE I: ON AXIS

### 1. Traveling Wave Review

The traveling wave electron accelerator is not simpler than the standing wave machine, but it is better understood. So, with the object of understanding, let us look at the first section of a traveling wave accelerator where the wave velocity  $\beta$  is less than 1.

According to the equations derived in the Appendix, after Slater,<sup>1</sup> the momentum-phase diagram is shown in Fig. 1a. The phase angle,  $\varphi$ , is here defined as the angle by which the electron leads the crest of the traveling wave, and  $P$  is the momentum of the electron. Apparently, Slater chose to call phase zero when the particle is  $\pi/2$  ahead of the wave crest because there is symmetry about the line  $\varphi = \pi/2$  with a traveling wave.

In accordance with Eq. (8) of the Appendix, a function

$$f(\varphi) \equiv H + \frac{\alpha}{2\pi} \sin \varphi = E(P) - \beta P \equiv f(P) \quad , \quad (1)$$

can be defined where  $H$  is the Hamiltonian,  $\alpha$  is the field intensity, and  $E$  and  $P$  are the energy and momentum of the electron, all in dimensionless units.

Figure 1b shows the relationship between  $\varphi$  and  $P$  through the function  $f$ . The shape of the curve depends only on the wave velocity  $\beta$ . The minimum value of  $f(P)$  allowed by

$$\begin{aligned} f(P) &= E(P) - \beta P \\ \frac{df}{dP} &= v - \beta = 0 \quad , \end{aligned} \quad (1a)$$

where  $v$  is the reduced particle velocity, is  $f_1(P_1) = 1/E_1$ , where  $E_1 = (1 - \beta^2)^{-1/2}$  and  $P_1 = \beta E_1$  are the energy and momentum of a particle moving at the traveling wave velocity.

The maximum and minimum values of  $f(\varphi)$ , being  $f_2$  and  $f_3$  respectively, allowed by

$$f(\varphi) = H + \frac{\alpha}{2\pi} \sin \varphi \quad , \quad (1b)$$

are  $f_2 = H + \alpha/2\pi$ , and  $f_3 = H - \alpha/2\pi$ , where  $H$  is determined by the initial condition through

---

\*Work supported in part by the U.S. Office of Naval Research, Contract [NONR 225(67)].

1. J.C. Slater, Rev. Mod. Phys. 20, 473 (1948).

$$H = E - \beta P - \frac{\alpha}{2\pi} \sin \varphi \quad (1c)$$

If  $H$  is less than its critical value,  $H_c = 1/E_1 + \alpha/2\pi$ ,  $f_3 < f_1$ , and the orbit of the particle is like orbit 1 of Figs. 1a and 1b. If  $H > H_c$ ,  $f_3 > f_1$ , and the orbit is like either orbit 2 or 3 of Fig. 1a, depending on the initial conditions.

Figures 2 through 5 show graphs plotted by computer. They are segments of the closed orbits of Fig. 1a. The lines labeled 0 - 0, 1 - 1, etc. show the locus in phase space of electrons at a given distance along the accelerator. The momentum scale was chosen to show desired features best; a constant times  $\log(1 + 2P/mc)$  is plotted. In Fig. 2, fourteen electrons start out along line 0 - 0 at 80 keV. The four starting with  $\varphi \geq 140^\circ$  were approaching  $P = 0$ , and it was not considered fruitful to follow them further. The line 1 - 1 shows where the remaining ten electrons were after passing through  $1/16 \lambda$ . Between the two smallest orbits are contained all the electrons injected between  $70^\circ$  and  $110^\circ$ . If extracted at  $v = \beta$ , they would span  $7^\circ$  in phase; if extracted at the end of a wavelength (on line 4 - 4), they would span  $8^\circ$ . It is also interesting that the electrons injected between  $60^\circ$  and  $90^\circ$  could be extracted in a  $2^\circ$  bunch at the end of  $1 \lambda$ . Figure 3 is for half the accelerating field, Fig. 4 for a more rapidly traveling wave,  $\beta = 0.9$ , and Fig. 5 for  $\beta = 1.0$  ( $P_1 = \infty$ ).

## 2. Standing Wave at Low Energy\*

At low energies, the trajectories in  $P - \varphi$  space of particles which are captured in standing wave linacs (1) cross and recross, (2) have kinks every half wavelength, (3) decrease in momentum at first, and (4) slip about twice as much in phase as one would expect from the corresponding traveling wave case.

Figure 6 shows the orbits in  $P - \varphi$  space for particles accelerated by a standing wave. The graphs do not close on themselves; they do cross. There is hardly a perceptible kink in the curves at the end of  $1 \lambda$  ("2" on the graph) because it just happens that  $v$  very nearly equals  $\beta$  at this point so that the curves are vertical.

Figure 7 gives a very much enlarged view, for 2.5 wavelengths of standing wave accelerator, of a very small segment of a locus such as 4 - 4 in Fig. 4. The locus is the ends of orbits such as those at "10" in Fig. 6. An input of  $\Delta\varphi$  of  $20^\circ$  has been bunched to  $1^\circ$  ( $1 - \cos 0.5^\circ = 0.4 \times 10^{-4}$ ) with an energy spread of  $0.064 mc^2$  (1.5% of present energy, but  $0.3 \times 10^{-4}$  of 1 GeV). A  $9^\circ$  initial  $\Delta\varphi$  ( $69.5^\circ - 78.5^\circ$ ) would give 0.15% of present energy. The curve for 79.9 kV shows that the  $\varphi_0$  of the "bunch" is fairly independent of  $\gamma_0$ , but the point "B" is where "A" would move for 79.0 kV and indicates that a variation of the 80 kV by 1.2% would affect the resolution to the extent that the phase spread contribution to the energy spread would be  $\sim 10^4$ .

In order to establish at least the direction of the gradient of good energy resolution in the multidimensional space of buncher design ( $\alpha$ ,  $\beta_1$ ,  $\beta_2$ , ... length), a large number of calculations were made. Some results for a half wavelength of standing wave accelerator are presented in Fig. 8 whose straight lines attest to the roughness of approximations made in constructing the figure. The trends, however, are not approximate: (1) good bunches are fairly independent of  $\beta$ ; (2) low field strengths give better bunches. Two quantitative conclusions were drawn: (1) since a  $\Delta E/E$  of  $1 \times 10^{-4}$  is the goal,  $\alpha < 2$  would unnecessarily sacrifice fast acceleration where it is most desirable (to arrest transverse velocity); and (2),  $\beta = 1$  eliminates problems that might arise

---

\* As used herein,  $\alpha$  is the effective field.  $2\alpha$  is the maximum field on standing wave axis.

from other choices. (For instance,  $\beta = 1$  makes the accelerating field of the fundamental frequency independent of the distance off axis.)

The calculations leading to Fig. 9 were made in order to design a combination buncher and injector section for a superconducting linac. Notwithstanding the possible advantages of  $\beta = 1$ , the real advantage of increasing the kinetic energy (for  $Z = 2.5 \lambda$ , from 1.6 to 2.6 MeV) by going to  $\beta = 0.95$  was considered worthwhile. The approximate length was determined by how much was needed to become relativistic.

Figures 10 and 11 indicate how the bunch is formed. Continuously injected electrons would be represented at the moment of injection ( $Z = 0$ ) by the line with unit slope. The dotted lines on Fig. 10 show where the electrons are in the first half wavelength when the fundamental rf electric field changes sign. Electrons with  $160^\circ < \phi_0 < 180^\circ$  are stopped at  $Z \geq \lambda/8$ . Electrons with  $-180^\circ < \phi_0 < 100^\circ$  stop before  $\lambda/4$  even though they were initially accelerated. Electrons injected at  $-100^\circ$  ( $180^\circ$  from bunch) would be stopped at  $Z \approx \lambda/4$  and  $\phi \approx 180^\circ$  and presumably would be rejected with 80 kV back at the gun. With continuous injection, 5% ( $\Delta\phi_0 = 20^\circ$ ) will come out in a tight bunch, 25% will come out badly spread in phase and energy, 35% will stop before  $\lambda/4$ , many of which may be "rejected," but the other 35% get beyond  $\lambda/4$  and it is most likely that they will end up as heat in the cavity wall. Figure 11 for  $\beta = 0.95$  shows the bunch gaining on the wave between  $Z = \lambda$  and  $2.5 \lambda$ . It is by proper choice of  $\alpha$ ,  $\beta$  and length that the bunch ends with  $\phi \rightarrow 0$  for maximum energy gain; it is not necessary for good bunching.

There appears to be an understandable characteristic of the bunch. It passes where ( $\lambda/4$ ) the field is maximum when ( $\phi = 0$ ) it is maximum.

### 3. Standing Wave at High Energy

After the energy of an electron is a few MeV, the effect of the backward traveling wave component on the longitudinal coordinates of an electron is completely negligible in a standing wave accelerator.

## II. CASE II: OFF AXIS

### 1. Introduction

In a superconducting accelerator where high energy resolution is possible, the radial motion is particularly important because of its effect on monitoring and controlling the energy of the beam.

Figure 12 is an attempt to show the whole problem at a glance. Radial momentum is plotted against distance off axis. The circle represents a set of particles as they are injected into a short section of accelerator. The dots trace the path in this phase space of a particle started at unit distance off axis. The set of particles at the middle of the first cavity is represented by the fat ellipse, but the dots show that large excursions of momentum have occurred. At the end of the first cavity the set is represented by the long thin ellipse. If the dots were continued they would fill in most of the space between the dots shown. At the end of five cavities, the set is represented by the remaining ellipse. Note that the ellipses represent a set of particles at certain stages of acceleration: the dots represent the orbit of one particle.

Figure 12 represents radial motion in the first accelerator section. It is complicated and will be treated last.

First, the case will be treated in which the particle has its energy much greater

than its rest mass and much greater than the energy gained per wavelength. Next the restriction on the energy gradient will be dropped, and last, an injection section will be considered.

Definitions of symbols are given in the Appendix.

## 2. Very High Energy, Relativistic Particles

The equation of radial motion is

$$\frac{d}{dz} \left( \gamma \frac{dr}{dz} \right) = - 2\pi \alpha r \sin 4\pi z, \quad (2)$$

which is linear in  $r$ ,  $r'$ , and  $r''$  so that all solutions may be scaled. The equation of axial motion integrates to

$$\gamma = \alpha \left( z - \frac{\sin 4\pi z}{4\pi} \right), \quad (3)$$

where a small liberty has been taken with the constants of integration by requiring that  $z_0 = \gamma_0/\alpha$  and  $z_0$  is integer or half integer.

The sine in each of Eqs. (2) and (3) is the result of the backward traveling component of the standing wave. The contribution to the radial force from  $E$  and  $v \times B$  identically cancel in the forward traveling component.

Combining Eqs. (2) and (3) and the definition of radial momentum, and letting  $x = 4\pi z$

$$\frac{dP}{dx} = - \frac{r}{2} \sin x, \quad (4a)$$

$$\frac{dr}{dx} = \frac{P}{x - \sin x} \quad (4b)$$

Equating both the sines in Eq. (4) to zero, the traveling wave solution is found to be

$$P = P_0, \quad (5a)$$

$$r = P_0 \ln \frac{x}{x_0} + r_0. \quad (5b)$$

Using this  $r$  as a first trial solution, and integrating by parts to increase the power of  $x - x_0/x$ , a solution correct to the first order in  $(x - x_0)/x$  was found:

$$P = P_0 \left[ 1 + \frac{\cos x}{2} \ln \frac{x}{x_0} - \frac{\sin x}{2x} \right] + r_0 \left[ - \frac{2 \cos x + 1}{8} \ln \frac{x}{x_0} + \frac{\cos x - 1}{2} + \frac{\sin x}{4x} \left( 1 - \frac{\cos x}{2x} \right) \right] \quad (6a)$$

$$r = P_0 \left[ \ln \frac{x}{x_0} \right] + r_0 \left[ 1 - \frac{1}{2} \ln \frac{x}{x_0} + \frac{\sin x}{2x} \right] \quad (6b)$$

None of the terms in Eq. (6) is a result of the sine in Eq. (4b); that is, the intra-cavity change in mass is not a first order effect.



As indicated in Fig. 12, the gyrations within a cavity may be large compared with the net change across a cavity which is of chief importance. Letting  $x - x_0 = 2\pi$ , and  $x_0 = 2\pi n$ , the effect of the  $(n + 1)^{\text{th}}$  cavity is given by the difference equations:

$$P(n + 1) - P(n) = \frac{1}{2n} P(n) - \frac{3}{8n} r(n) \quad , \quad (7a)$$

$$r(n + 1) - r(n) = \frac{1}{n} P(n) - \frac{1}{2n} r(n) \quad , \quad (7b)$$

which again are good to first order in  $n^{-1}$ .

A solution which satisfies Eq. (7) to first order in  $n^{-1}$  is

$$P(n) = \sqrt{3} P_0 \sin(L + \theta) - 3(8)^{-\frac{1}{2}} r_0 \sin L \quad , \quad (8a)$$

$$r(n) = 2\sqrt{2} P_0 \sin L + \sqrt{3} r_0 \sin(\theta - L) \quad , \quad (8b)$$

where  $L = (8)^{-\frac{1}{2}} \ln n/n_0$  and  $\sin \theta = (3)^{-\frac{1}{2}}$ .

Equation (8) is plotted in Figs. 13 and 14. The solid triangles on each curve indicate the points up to which the curves were checked against a very accurate computer calculation that started with  $Z_0 = 100 \lambda$ . The  $n$ 's of Eq. (8) can be interpreted as energy. The particle will cross the axis after it has increased its energy to 5.7 times its initial energy if its initial radial momentum is zero. From the time the particle crosses the axis, its radial momentum will continue to increase until its energy is increased by a factor of 15 and its radial displacement will increase until its energy is increased by a factor of 85; it will recross the axis again at energy factor  $(85)^2$ .

From the equations, it appears that the maximum radial excursion will be minimized if  $P_0 = \frac{1}{2} r_0$ , and further that a complete cycle of radial motion will be made every time the energy is increased by a factor of  $5 \times 10^7$ .

Comparing the standing and traveling wave radial motion over an energy increase of a factor of  $e$ ,

Standing Wave	Traveling Wave
$P = \frac{3}{2} P_0 - \frac{3}{8} r_0$	$P = P_0$
$r = P_0 + \frac{1}{2} r_0$	$r = P_0 + r_0$

it appears that there is a significant difference from the Lorentz contracted drift tube analogous to the traveling wave accelerator.

As suggested by the eigenvector found during the solution of Eq. (7), let  $Q = 2\sqrt{2/3} P$ ,

$$Q = Q_0 \cos L + (\sqrt{2} Q_0 - \sqrt{3} r_0) \sin L \quad , \quad (9a)$$

$$r = (\sqrt{3} Q_0 - \sqrt{2} r_0) \sin L + r_0 \cos L \quad . \quad (9b)$$

The maximum values of  $Q$  and  $r$  are each equal to  $K$  which is a constant of the motion and  $K^2 = 3Q^2 - 2\sqrt{6} Qr + 3r^2$ . If the axes are rotated  $45^\circ$  and  $K$  is magnified to unity,

$$x = \frac{Q + r}{\sqrt{2} K} \quad \text{and} \quad y = \frac{Q - r}{\sqrt{2} K} \quad .$$

$$x = x_0 \cos L + (\sqrt{3} + \sqrt{2}) y_0 \sin L \quad , \quad (10a)$$

$$y = -(\sqrt{3} - \sqrt{2}) x_0 \sin L + y_0 \cos L \quad . \quad (10b)$$

From this, the constant of the motion is found to be

$$\frac{x^2}{1 + \sqrt{2/3}} + \frac{y^2}{1 - \sqrt{2/3}} = 1 \quad . \quad (11)$$

The ellipse found in Eq. (11) is shown in Qr space in Fig. 15; its area is  $\pi K^2/\sqrt{3}$ . This ellipse is a trajectory as contrasted with the ellipses of Fig. 12 which represented sets of particles.

### 3. Relativistic Particles

If  $\gamma_0$  is not much greater than  $\alpha$ , the analysis of the previous section does not apply, but this can only be the case over only a few wavelengths because  $\gamma = \alpha z$  for relativistic particles.

To investigate this, computer calculations were made over one-half wavelength and the results plotted in Fig. 16. In a drift tube, the particle represented by the dot on the circle would have moved directly to the dot at its right. If  $z_0 = 10\lambda$ , the difference is slight. If  $z_0 = \lambda$ , the difference is significant.

The simple conclusion is that for  $z > 10$  the analysis of the previous section is adequate, for  $z > 100$  it is as good as the computer, and for  $z < 10$  the computer should be used.

### 4. The Injector Section

Consideration of the injector section is not complete, but some calculations have been made. The tentative conclusion is that, in first order, even this section acts like a drift tube if the gyrations within a cavity are not considered. Figure 17 shows the effect of acceleration from 80 keV to 100 MeV. In the injector section, i.e. during the first  $2\lambda$ , besides the drift tube effect of tilting the ellipse forward there is a slight defocusing in that the absolute values of all momenta are increased by about 30%. In the next  $10\lambda$ , after the axial phase is set to zero, the particles (two of which are represented by dots on the curve) move much as would be expected from the analysis of the high energy section. The next two sections of  $20\lambda$  each continue to accelerate as expected. If a  $20^\circ$  axial phase bunch had been injected, the set (in radial phase space) that was first to be injected ( $10^\circ$  early) and the set last to be injected are shown separately at  $52\lambda$ . Clearly, the radial phase space problem in a standing wave injector is soluble.

Figure 18 shows the results of some calculations on another injector section. To get a feeling for the problem the question was asked, "What is necessary to get a parallel beam out of the injector?" Electrons were put in  $\lambda/60$  off axis and the answer depends strongly on axial phase. For an electron in the middle of the axial bunch, the answer is that it should be aimed at a point on the axis  $f = 1.8\lambda$  into the accelerator. For those with different axial phase, the answer is different, as shown in the table:

$\varphi - \varphi_0$	$f/\lambda$
$10^\circ$	0.75
$5^\circ$	1.0
0	1.8
$-5^\circ$	2.7
$-10^\circ$	$\infty$

For a given  $r_0$  in the high energy section, the radial phase space enclosed in an orbit is minimum if  $P_0 = \frac{1}{2} r_0$ , which is to say that it should be diverging with an angle of  $\theta = r_0/2z_0$ . In the case of the injector section of Fig. 18, this would require  $\theta_f = 3$  mrad rather than  $\theta_f = 0$  which was used as a basis for the above table.

This does not conclude the work on the injector, but it does show a way to the solution of radial phase space problems.

## APPENDIX

### I. ONE DIMENSION TRAVELING WAVE

Defining  $\beta c$ ,  $\lambda$ , and  $F$  to be the wave velocity, wavelength, and maximum electric field intensity in the accelerator, respectively, and giving other symbols their usual meaning,

$$\begin{aligned} \frac{dP}{dt} &= qF \cos \left( \varphi_0 + 2\pi \frac{z - \beta ct}{\lambda} \right) , \\ \frac{dz}{dt} &= v \end{aligned} \quad (A-1)$$

which can be put into the form

$$\begin{aligned} \frac{d(P/mc)}{d(\beta ct/\lambda)} &= \frac{qF\lambda}{mc^2 \beta} \cos \left[ \varphi_0 + 2\pi \left( \frac{z}{\lambda} - \frac{\beta ct}{\lambda} \right) \right] \\ \frac{d(z/\lambda)}{d(\beta ct/\lambda)} &= \frac{v}{\beta c} \end{aligned}$$

This immediately suggests simplifying to dimensionless variables. Old symbols are primed:

$$\begin{aligned} \frac{z'}{\lambda} &= z & \frac{v'}{c} &= v \\ \frac{P'}{mc} &= P & \frac{\beta ct'}{\lambda} &= t \\ \frac{E'}{mc^2} &= E & \frac{qF\lambda}{mc^2} &= \alpha \end{aligned} \quad (A-2)$$

The accelerating field parameter,  $\alpha$ , is the electric field intensity in units of particle rest masses/ $q$  (0.511 MV for electrons) per wavelength. Now the equations can be written more simply:

$$\frac{dP}{dt} = \frac{\alpha}{\beta} \cos [\varphi_0 + 2\pi(z - t)] ; \quad \frac{dz}{dt} = \frac{v}{\beta} \quad (A-3)$$

Defining the phase

$$\varphi = \varphi_0 + 2\pi(z - t) , \quad (A-4)$$

which is the amount by which the particle is ahead of the crest of the wave, then

$$\frac{d\varphi}{dz} = 2\pi \left( 1 - \frac{\beta}{v} \right) . \quad (A-5)$$

Now Eqs. (A-3), (A-4), and (A-5) can be combined:

$$\begin{aligned} \frac{dP}{dz} &= \frac{\alpha}{v} \cos \varphi \\ \frac{dP}{d\varphi} &= \frac{\alpha}{2\pi(v - \beta)} \cos \varphi \\ (v - \beta) \cdot dP &= \frac{\alpha}{2\pi} \cos \varphi d\varphi . \end{aligned} \quad (A-6)$$

The equations required from special relativity now have particularly simple forms:

$$\begin{aligned} E^2 &= P^2 + 1 \\ v &= \frac{P}{E} = \frac{dE}{dP} . \end{aligned} \quad (A-7)$$

Equation (A-6) is easily integrated to give

$$E - \beta P = \frac{\alpha}{2\pi} \sin \varphi + H , \quad (A-8)$$

where H is the constant of integration and can be shown to be the Hamiltonian.<sup>1</sup>

The complete solution needs another equation to show the relationship between z or t, and P, E, or  $\varphi$ . Such an equation is (A-5), but it has not been integrated in closed form.

## II. ONE DIMENSION STANDING WAVE

Going back to Eq. (A-3), we can see that the addition of a wave traveling in the opposite direction will give a standing wave

$$\begin{aligned} \frac{dP}{dt} &= \frac{\alpha}{\beta} \cos [\varphi_0 + 2\pi(z - t)] - \frac{\alpha}{\beta} \cos [\varphi_0 + 2\pi(-z - t)] \\ &\equiv \frac{2\alpha}{\beta} \sin(2\pi z) \sin(2\pi t - \varphi_0) \\ \frac{dz}{dt} &= \frac{v}{\beta} . \end{aligned} \quad (A-9)$$

Because of the need to integrate the equations over exactly the same length of accelerator, so that the exit phases be comparable, the equations used were changed to have z as the independent variable

$$\frac{dP}{dz} = \frac{2\alpha}{v} \sin(2\pi z) \sin(2\pi t - \phi_0) \quad (A-10)$$

$$\frac{dt}{dz} = \frac{\beta}{v}$$

These are the equations for a  $\pi$ -mode standing wave accelerator on the axis of its cylindrical symmetry. Phase is defined the same as in the traveling wave case, Eq. (A-4).

### III. CYLINDRICALLY SYMMETRIC STANDING WAVE

Returning to the conventional meaning of symbols for a moment,

$$E_z = F A_z$$

$$A_z = \sum w_n \sin(kz) J_0(\gamma r) \sin(\omega t - \phi_0)$$

$$E_r = F A_r$$

$$A_r = - \sum w_n \frac{k}{\gamma} \cos(kz) J_1(\gamma r) \sin(\omega t - \phi_0) \quad (A-11)$$

$$B_\theta = (F/c) A_\theta$$

$$A_\theta = \sum w_n \frac{\omega}{\gamma c} \sin(kz) J_1(\gamma r) \cos(\omega t - \phi_0)$$

$$\gamma^2 + k^2 = \omega^2/c^2$$

$$k = 2\pi(2n - 1)/\lambda, \quad n = 1, 2, 3, \dots$$

Equations (A-11) describe the field at a particle in a cylindrically symmetric accelerator which has planes of symmetry at the center of each wavelength and anti-symmetry at the ends of each wavelength.

Neglecting the effect of the transverse velocity on the relativistic mass of the particle, the equation

$$\frac{d\vec{p}}{dt} = q\vec{E} + q\vec{v} \times \vec{B} \quad (A-12)$$

can be reduced to one in the  $z$  direction,

$$\frac{dP}{dt} = qE_z + \dot{r}B_\theta, \quad (A-13)$$

and one in the transverse plane,

$$\frac{d\vec{p}_T}{dt} = (qE_r - qvB_\theta)\vec{R} \quad (A-14)$$

where  $\vec{R}$  is the radial unit vector and  $v$  is the velocity in the  $z$  direction, as before.

Still using conventional notation,  $E/c^2$  is the relativistic particle mass, and

$$\begin{aligned}\vec{P}_T &= \dot{\vec{r}}E/c^2 \\ \frac{d\vec{P}_T}{dt} c^2 &= \ddot{\vec{r}}E + \dot{\vec{r}}\dot{E}\end{aligned}\quad (A-15)$$

Invoking some fundamental mechanics where  $\vec{R}$  and  $\vec{\theta}$  are unit vectors,

$$\begin{aligned}\dot{\vec{r}} &= \dot{r}\vec{R} + r\dot{\vec{\theta}} \\ \ddot{\vec{r}} &= (\ddot{r} - r\dot{\theta}^2)\vec{R} + (2\dot{r}\dot{\theta} + r\ddot{\theta})\vec{\theta}\end{aligned}\quad (A-16)$$

Combining (A-14), (A-15), and (A-16),

$$(\ddot{r} - r\dot{\theta}^2) \frac{E}{c^2} + \dot{r} \frac{\dot{E}}{c^2} = qE_r - qvB_\theta ; (2\dot{r}\dot{\theta} + r\ddot{\theta})E + r\dot{\theta}\dot{E} = 0 \quad (A-17)$$

In addition to the simplifying definitions (A-2), add

$$\frac{r'}{\lambda} = r \quad (A-18)$$

To eliminate the second order derivatives, define

$$\begin{aligned}s &= \frac{\dot{r}'}{c} \\ u &= \frac{\lambda\dot{\theta}}{c}\end{aligned}\quad (A-19)$$

Equations (A-7), (A-13), (A-17), and (A-19) reduce, with the definitions in (A-2), (A-11), and (A-18), to:

$$\begin{aligned}\frac{dE}{dz} &= 2\alpha(A_Z + sA_\theta) \\ \frac{dt}{dz} &= \frac{\beta}{v} \\ \frac{ds}{dz} &= \frac{ru^2}{v} - \frac{s}{E} \frac{dE}{dz} + \frac{2\alpha}{vE} (A_r - vA_\theta) \\ \frac{dr}{dz} &= \frac{s}{v} \\ \frac{du}{dz} &= -\frac{2su}{vr} - \frac{u}{E} \frac{dE}{dz} \\ \frac{d\theta}{dz} &= \frac{u}{v} \\ v &= \frac{\sqrt{E^2 - 1}}{E}\end{aligned}\quad (A-20)$$

In accordance with definitions, the arguments of the auxiliary functions in (A-11) can be somewhat simplified:

$$\begin{aligned}
 A_Z &= \sum_{n=1}^N w_n \sin(Z) J_0(R) \sin(T - \varphi_0) \\
 A_r &= -2\pi r \sum_{n=1}^N w_n (2n-1) \cos(Z) \frac{J_1(R)}{R} \sin(T - \varphi_0) \\
 A_\theta &= 2\pi \beta r \sum_{n=1}^N w_n \sin(Z) \frac{J_1(R)}{R} \cos(T - \varphi_0) \quad ,
 \end{aligned} \tag{A-21}$$

where

$$Z = 2\pi(2n-1)z$$

$$R = 2\pi \sqrt{\beta^2 - (2n-1)^2} r$$

$$T = 2\pi t$$

By computer, the evaluation of the functions (A-21) and the integration of Eqs. (A-20) are straightforward.

The coefficients  $w_n$  can be obtained in theory from the Fourier analysis of a known field. The coefficients actually in use are obtained from T.I. Smith<sup>2</sup> who estimated them by numerically solving Maxwell's equations for the accelerator cavity. The first few coefficients are shown in the table:

$n$	$w_n$
1	1.0000
2	-0.0137
3	-0.0106
4	-0.0014
5	+0.0002

---

2. T.I. Smith, private communication.

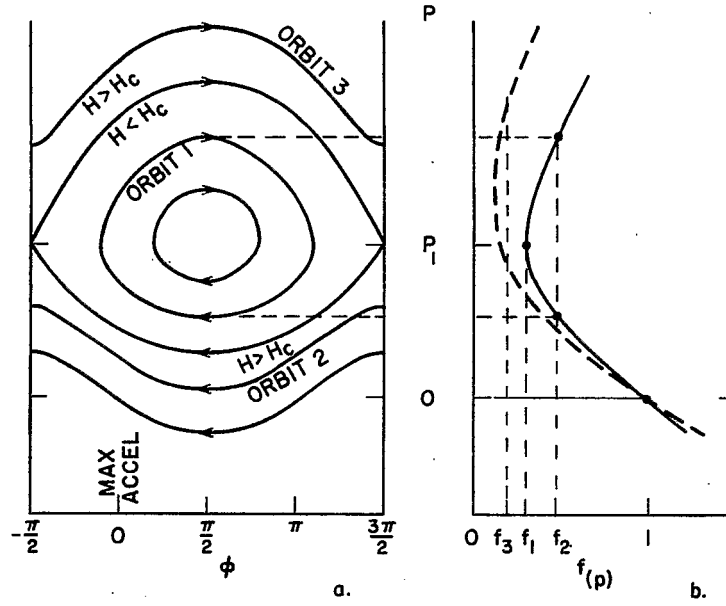


Fig. 1. Orbits in phase space, traveling wave accelerator.

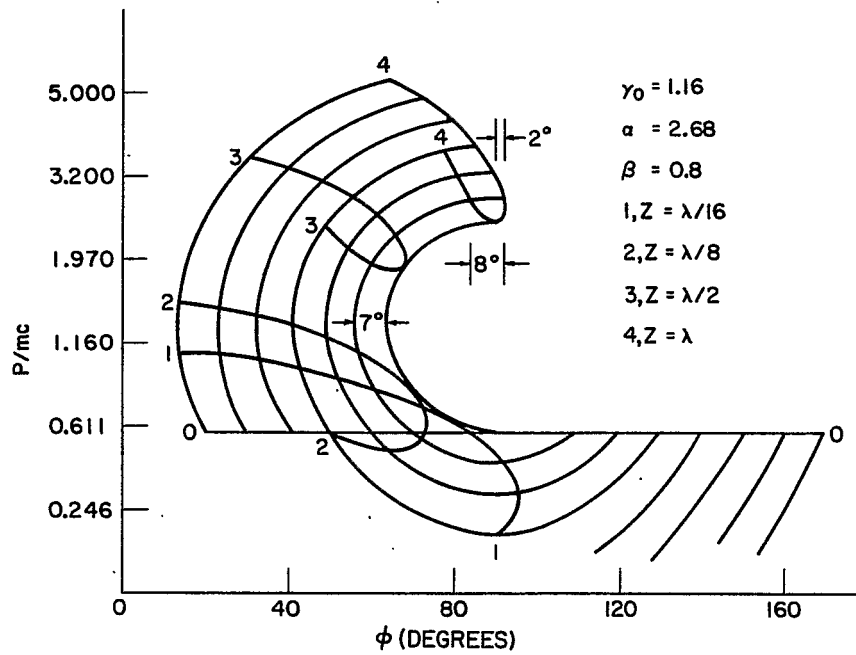


Fig. 2. Computed orbits in phase space, traveling wave accelerator.



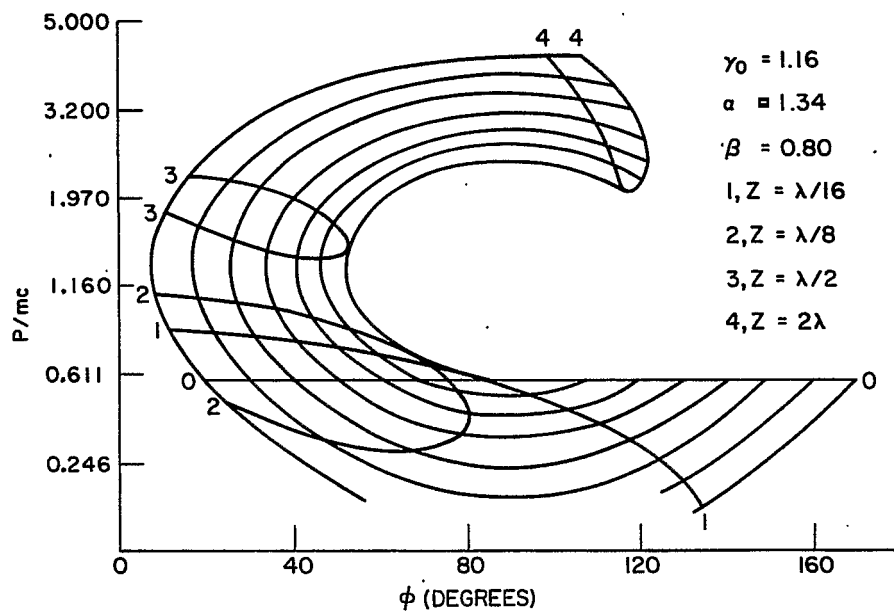


Fig. 3. Computed orbits in phase space, traveling wave accelerator.

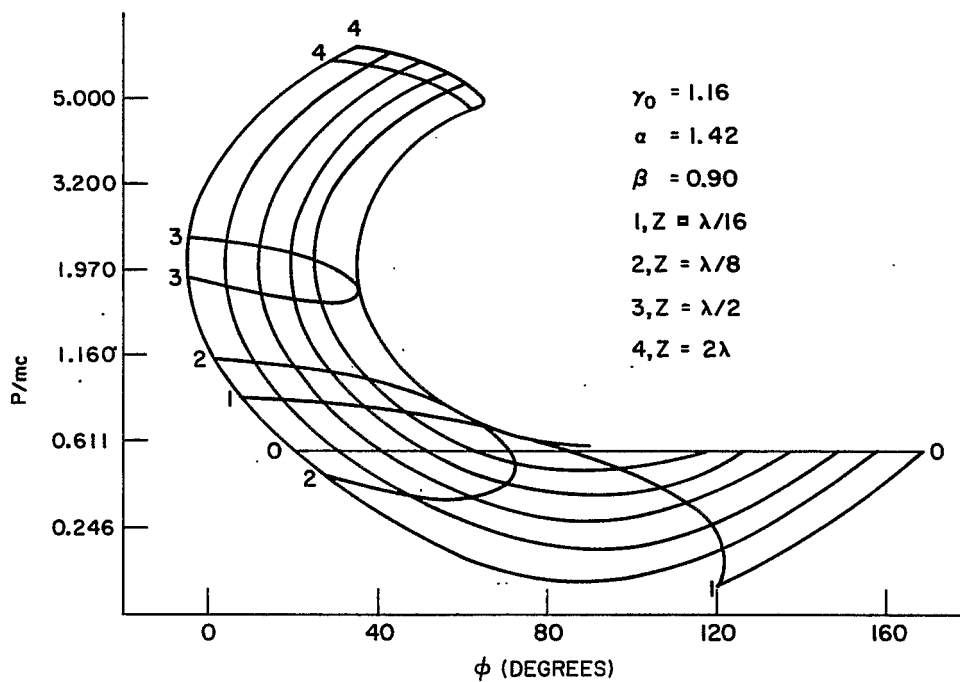


Fig. 4. Computed orbits in phase space, traveling wave accelerator.

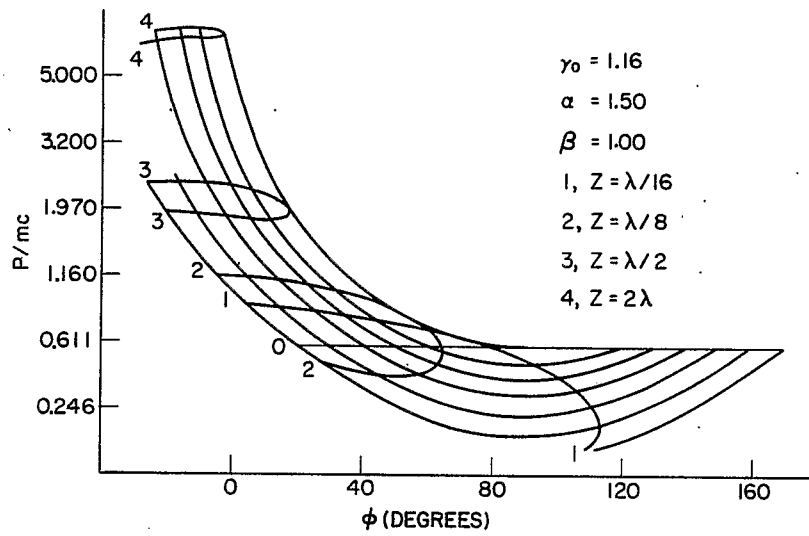


Fig. 5. Computed orbits in phase space, traveling wave accelerator.

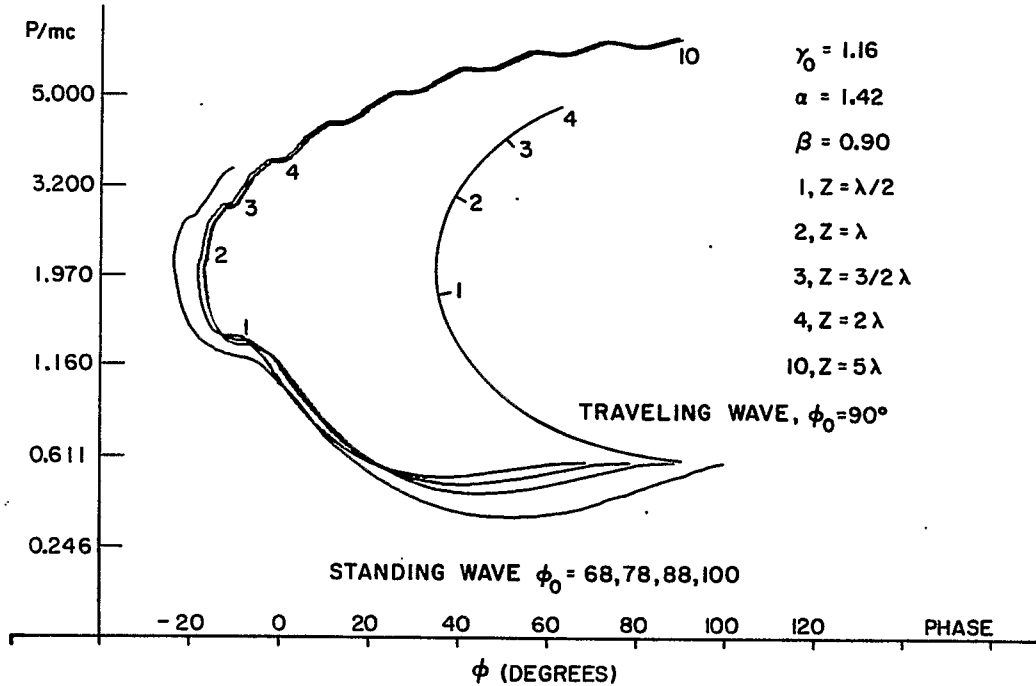


Fig. 6: Computed orbits in  $P - \phi$  space, standing wave accelerator.

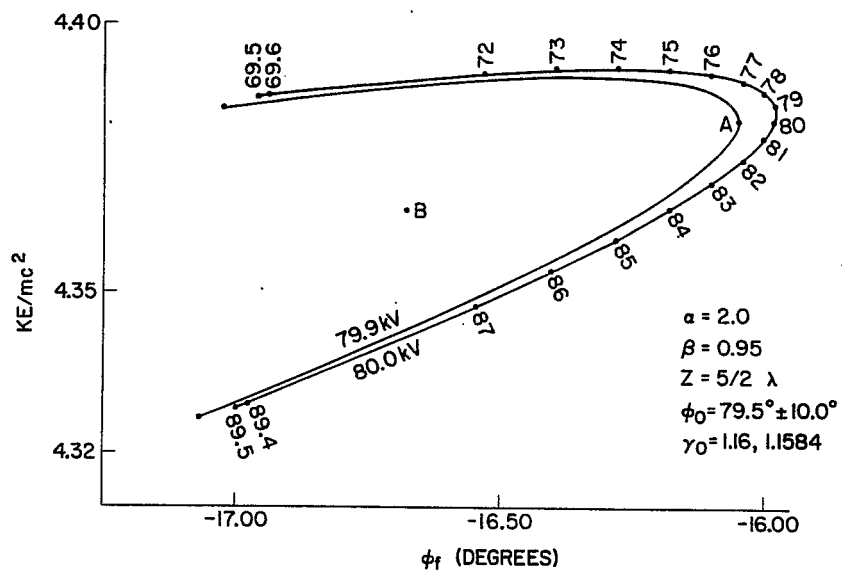


Fig. 7. The bunch of electrons at exit of  $2.5 \lambda$  standing wave accelerator section.

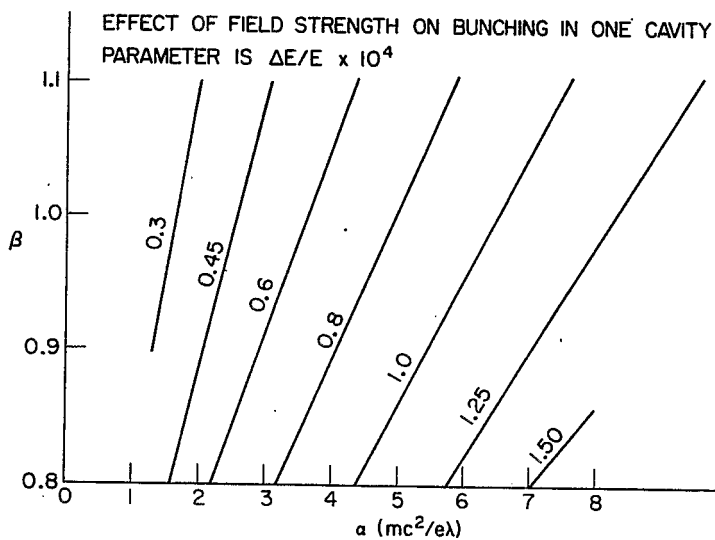


Fig. 8. Effect of  $\alpha$  and  $\beta$  on bunching.

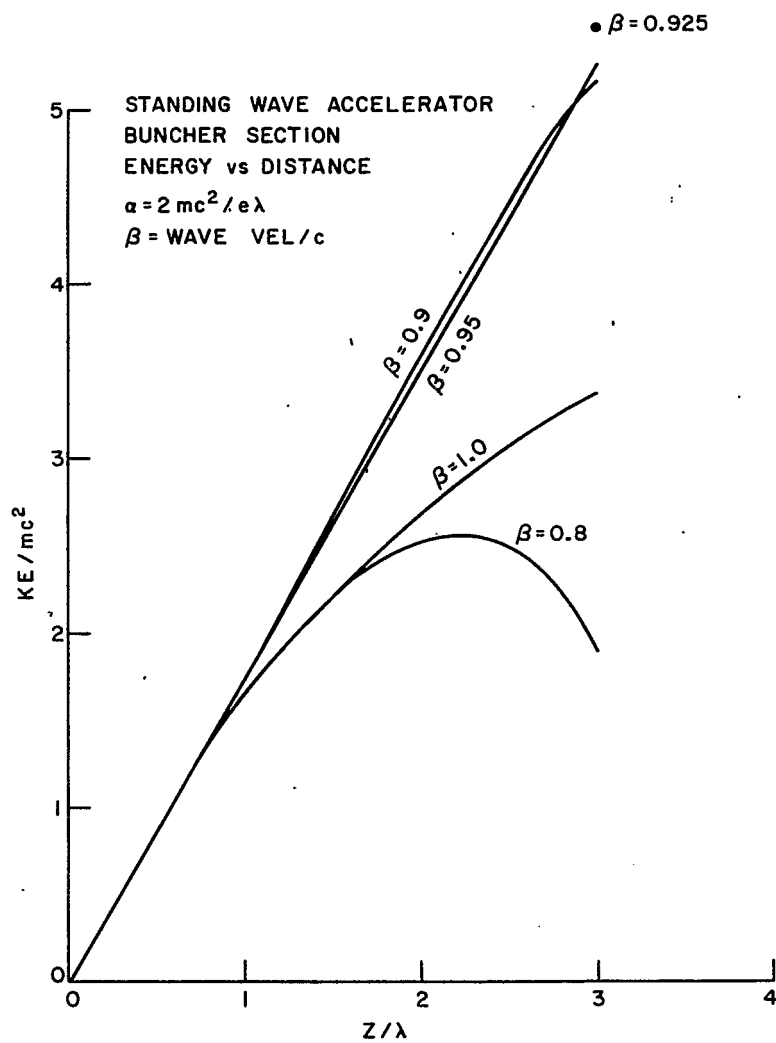


Fig. 9. KE vs Z in buncher section, standing wave.

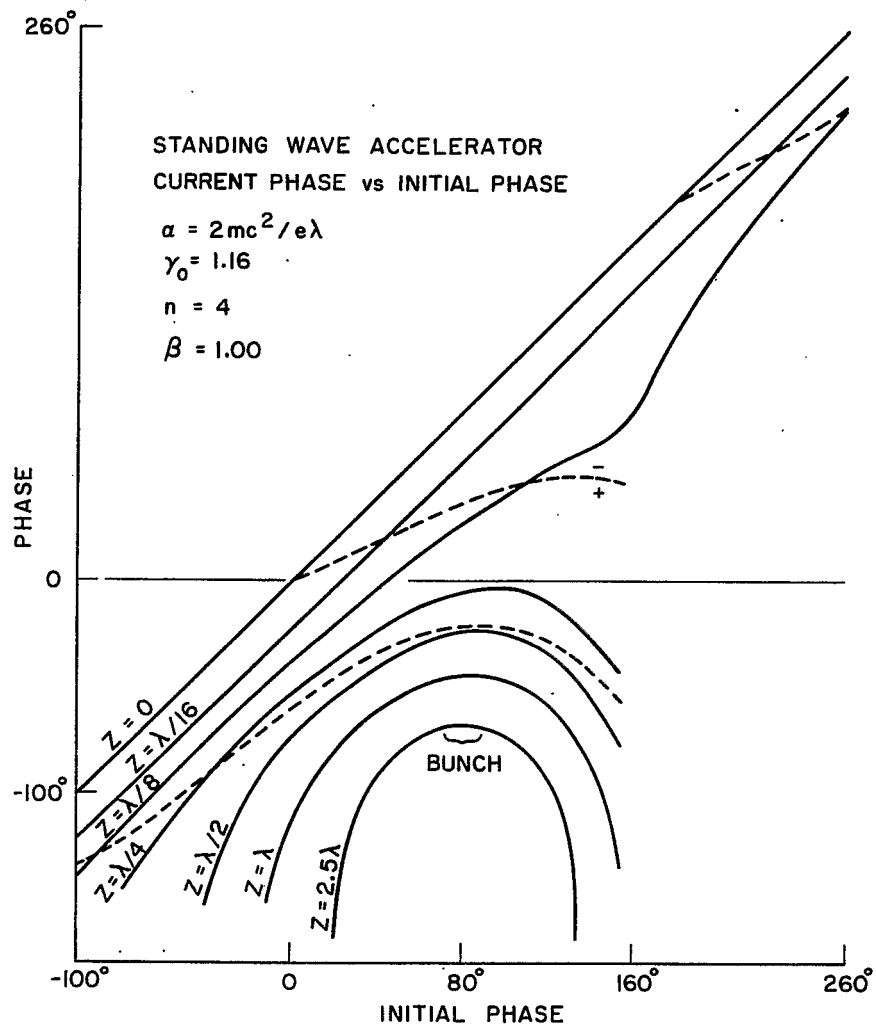


Fig. 10. Bunch forming in standing wave accelerator.

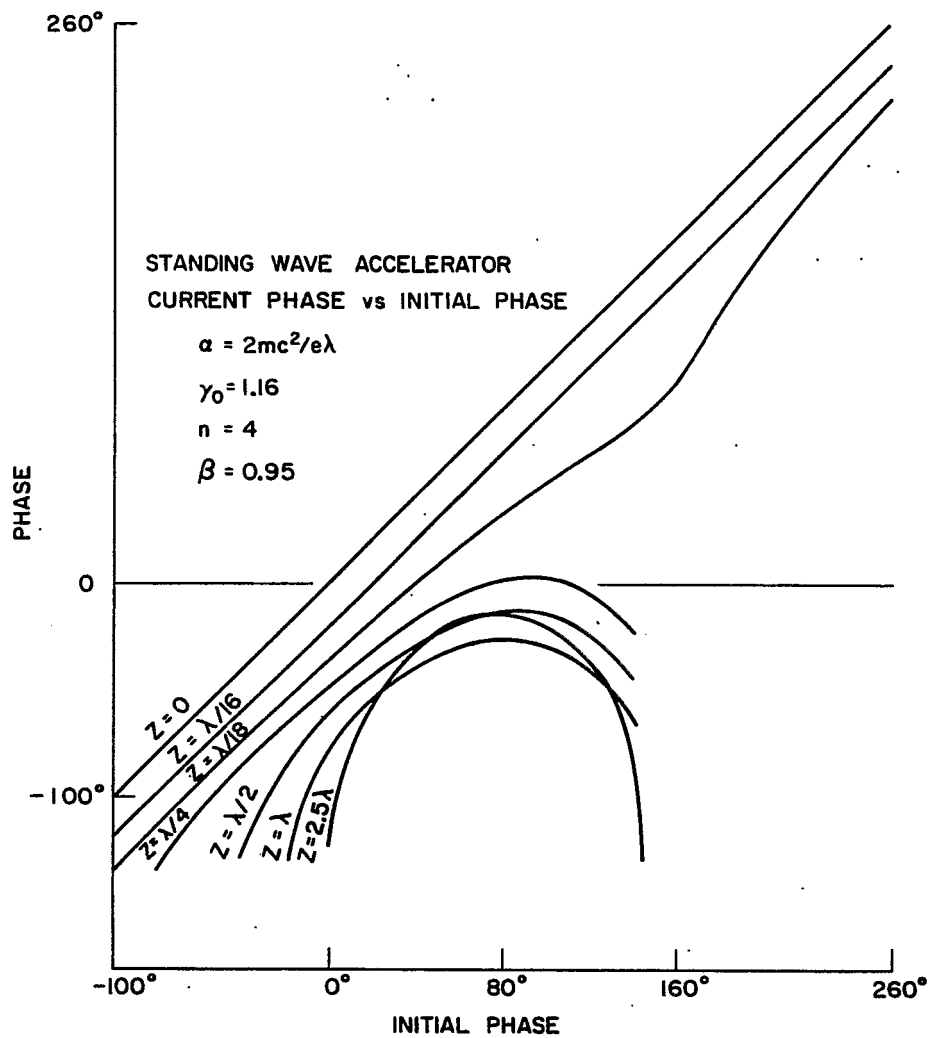


Fig. 11. Bunch forming in standing wave accelerator.

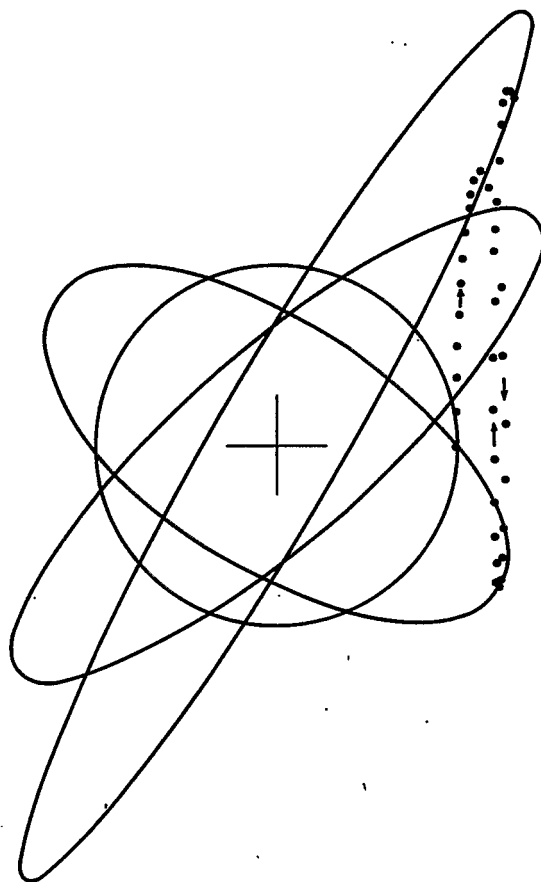


Fig. 12. Orbits and sets in radial phase space.

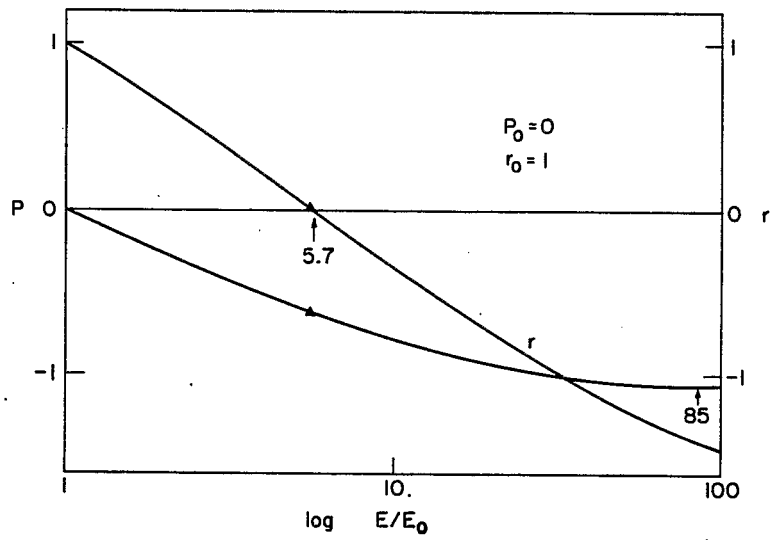


Fig. 13. Radial motion of high energy particles in standard wave accelerator,  $r_0 = 0$ .

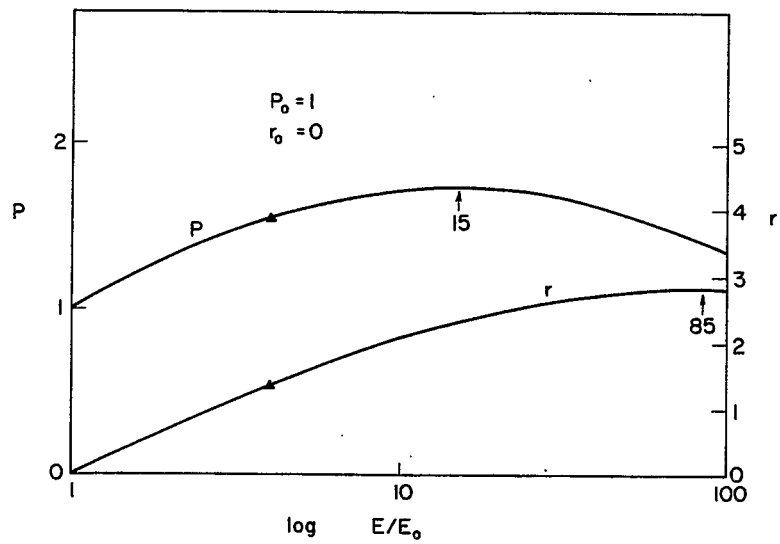


Fig. 14. Radial motion of high energy particles in standard wave accelerator,  $P_0 = 0$ .



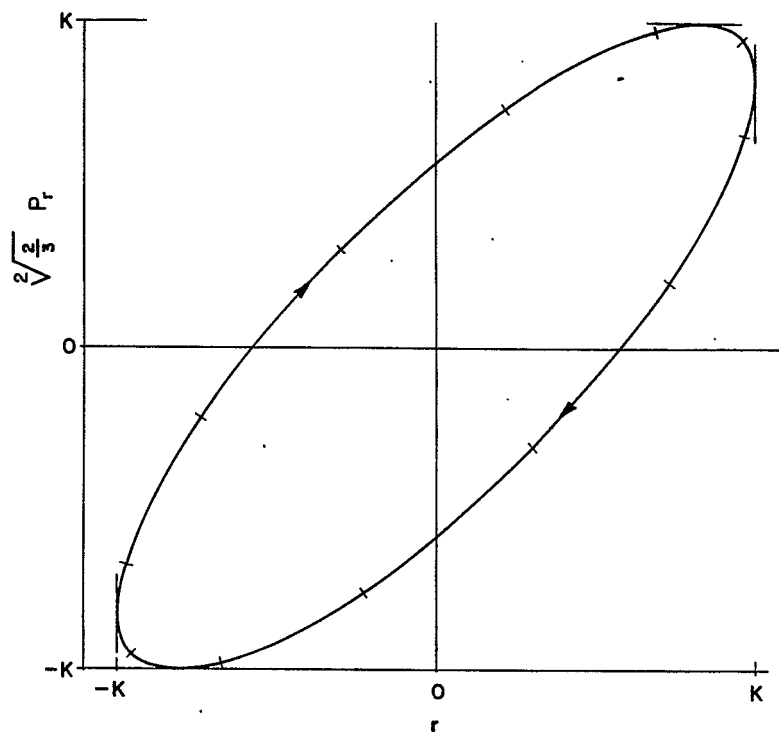


Fig. 15. Radial phase space trajectory in standing wave linac.

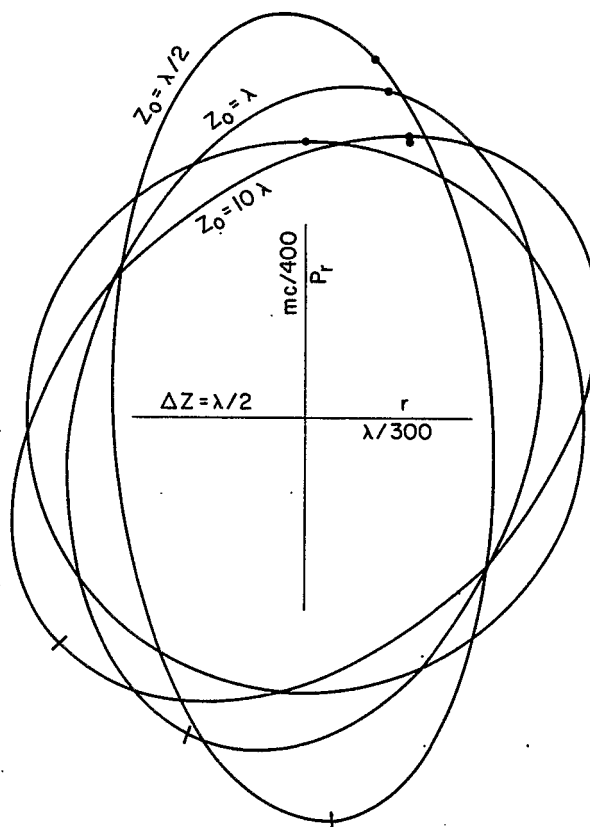


Fig. 16. Sets of relativistic particles in radial phase space,  $E \sim M_0 C^2$

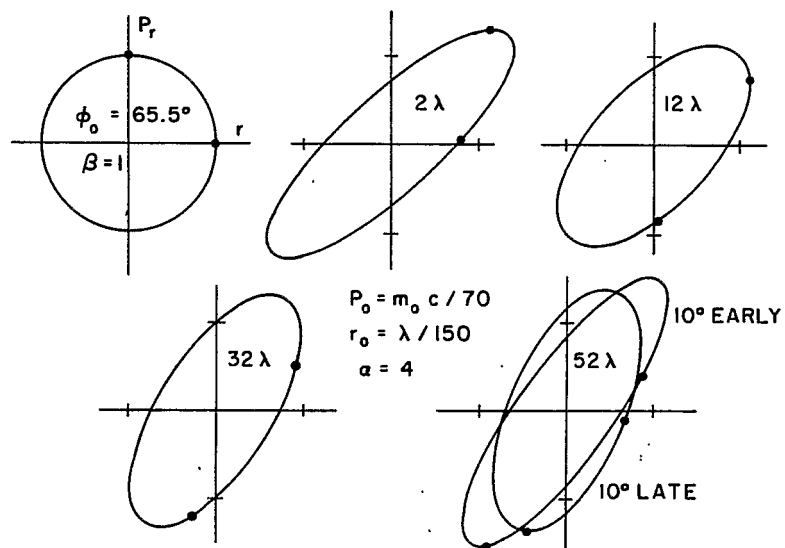


Fig. 17. Set of particles in radial phase space.

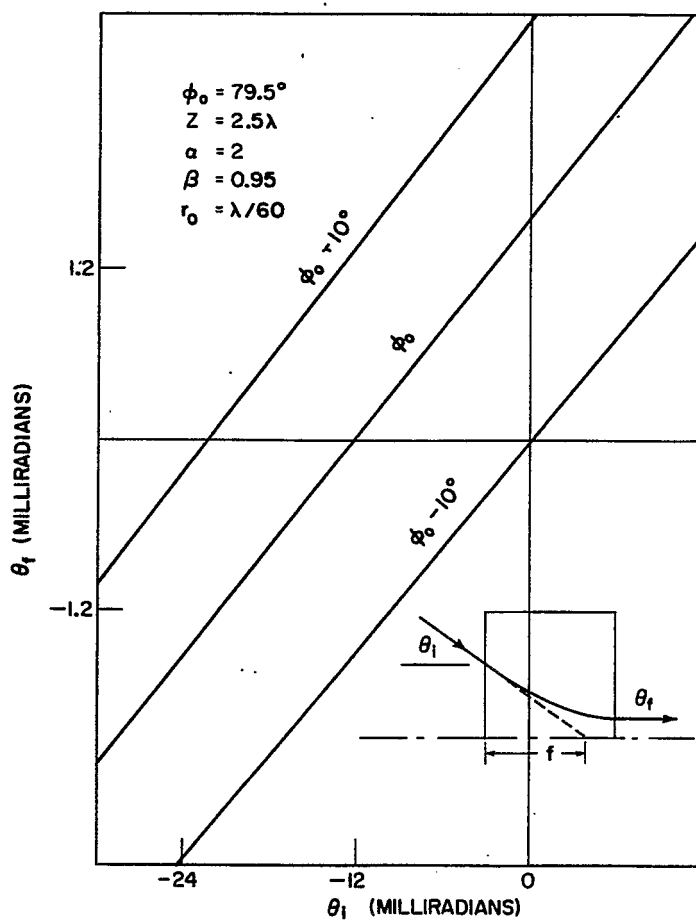


Fig. 18. Lens property of injector section.

## SAMPLE PARAMETERS OF A TWO-MILE SUPERCONDUCTING ACCELERATOR\*†

R.B. Neal  
Stanford Linear Accelerator Center  
Stanford University, Stanford, California

The results derived in Ref. 2 have been used to calculate a sample set of parameters<sup>1</sup> for a superconducting version of the two-mile SLAC accelerator. These calculations have been carried out in order to provide a basis for further technical discussions.

### BEAM ENERGY

The energy goal of 100 GeV (10 MeV/ft) has been chosen since this energy is sufficiently higher than the 20 GeV capability of the present SLAC accelerator to be of great interest in physics research and yet within anticipated fiscal and technical limitations. It should be remarked here that the gradient of 10 MeV/ft is several times higher than the best gradient achieved to date in a superconducting accelerator. However, superconductivity in its application to accelerators is still in its infancy; therefore, in establishing tentative design parameters for a future accelerator it has been assumed that further advances will make the proposed gradient realistic.

### SELECTION OF ACCELERATOR TYPE

As noted in Ref. 2, the ratio of peak-to-average fields in a traveling wave accelerator is significantly less than in a standing wave accelerator (a factor of  $\approx 1.6$  improvement appears to be achievable). For this reason, the tentative decision has been made to adopt a traveling wave design with rf feedback.

### DUTY CYCLE

The possibility of achieving a high duty cycle is one of the attractive features of a superconducting accelerator. However, adopting a 100% duty cycle for the projected 100 GeV two-mile machine would lead to excessive refrigeration costs on the basis of present-day cost experience and estimates. For this reason, the duty cycle of the superconducting machine in this preliminary listing of criteria has been limited to 6%. Even so, this is 100 times the duty cycle of the existing SLAC accelerator and would result in greatly improved experimental statistics.

The filling time of a superconducting accelerator is very long (typically 10 to 100 msec) compared to conventional "room temperature" accelerators ( $\approx 0.5$  to  $5 \mu\text{sec}$ ). The rf pulse length must be many times longer (say 0.3 to 6 sec) in order to allow time for the fields to reach steady state and for particles to be accelerated. Practically speaking, an rf source which is required to produce full power for several

---

\*Work supported by the U.S. Atomic Energy Commission.

†This report is based upon an earlier SLAC Technical Note (Ref. 1).

1. W.B. Herrmannsfeldt, R.B. Neal, and P.B. Wilson, Stanford Linear Accelerator Center Technical Note SLAC-TN-68-9 (1968).

seconds must, for cathode emission and heat dissipation purposes, be designed to operate in a cw manner. Moreover, the existing ac distribution system in the SLAC Klystron Gallery has sufficient capacity to supply the required power on a cw basis. Therefore, the design approach which has been adopted is based on initial operation at a 6% duty cycle but with ac and rf capability for a 100% duty cycle. Then, if at a later date the cost of providing refrigeration decreases, the duty cycle could be increased by adding more refrigeration units to the system.

### CHOICE OF FREQUENCY

Operation of a superconducting accelerator at the lower microwave frequencies is favored<sup>2</sup> because of the higher Q's and the resulting lower dissipative losses at these reduced frequencies. The minimum feasible frequency is probably limited by the increasing physical size of the structure, the increasing filling time, and the more stringent phasing and impedance matching tolerances as the frequency is reduced. Moreover, in the case of the projected superconducting accelerator for SLAC, there is a further consideration which merits attention. There is already in existence an expensive high power waveguide system which operates at a particular frequency, viz., 2856 MHz. Considerable cost savings would obviously result if the same frequency were chosen for the superconducting accelerator so that the existing waveguide system could be used. However, it is not yet clear whether or not this choice of a relatively high frequency would result in sufficiently higher refrigeration costs which would outweigh the cost savings just discussed. For this reason, it has been decided to carry out preliminary design studies and cost analyses at two frequencies, 1428 and 2856 MHz, to determine whether either frequency has a definite technical and/or cost advantage over the other. The parameters shown in Table I have therefore been calculated for both frequencies. The basic beam criteria (beam energy, beam current, beam power, and duty cycle) are the same at each frequency. However, the filling times, pulse lengths, and feedback loop characteristics are different at the two frequencies.

### $r/Q$ , $r$ , AND $Q$

The starting points in determining these parameters are: (1) the expected improvement<sup>3</sup> in  $Q$  at 1300 MHz and 1.85°K by a factor of  $10^6$  compared to the  $Q$  in the same structure at room temperature; and (2) the room temperature values at 2856 MHz of  $Q = 1.3 \times 10^4$  and  $r = 56 \text{ m}\Omega/\text{m}$ . The following scaling laws are then used to calculate the values given in Table I:

$$\begin{aligned}\text{Improvement factor} &\propto \omega^{-3/2} \\ r &\propto \omega^{-1} \\ Q &\propto \omega^{-2}\end{aligned}$$

The room temperature values at 2856 MHz given above can probably be improved by using a somewhat more complicated cavity geometry (e.g., curving the outer walls, etc.) but such potential improvements have not been taken into account in calculating the values given in Table I.

- 
2. R.B. Neal, Stanford Linear Accelerator Technical Note SLAC-TN-68-1 (1968) (also reported to this Summer Study in slightly modified form, p. 111).
  3. P.B. Wilson, private communication.

## AVERAGE BEAM POWER

For initial operation at 6% duty cycle, an average beam power of 0.3 MW has been assumed. This is approximately the same as the maximum average beam power achieved by the present SLAC accelerator. Since a beam conversion efficiency of  $\approx 100\%$  should be achieved in the superconducting version, a total rf power of 0.3 MW average and 4.8 MW peak will be required.

## KLYSTRON POWER

To take maximum advantage of equipment already available in the SLAC Klystron Gallery the same number of klystrons ( $\approx 240$ ) as used with the present SLAC accelerator will be employed. Thus, the rf peak power and average power from each klystron will be 20 kW and 1.2 kW, respectively. However, as noted earlier, each klystron will be rated at 20 kW average power which will permit later increase of duty cycle if desired.

Fortunately, the input section of the existing SLAC modulators (ac transformer, silicon rectifiers, filter, control gear, etc.) has the proper rating to supply a 20 kW klystron on a cw basis. The output of the filter section is  $\approx 20$  kV which means that a tube which has an efficiency of 50% will have a cathode current of 2 A and a perveance of  $0.7 \times 10^{-6}$  amp volt $^{-3/2}$ . It is also fortunate that the existing variable voltage substations along the klystron gallery can be used without modification.

## PEAK BEAM CURRENT

The peak beam current is obtained by dividing the peak beam power by the beam energy, i.e.,

$$i_p = \frac{4.8 \times 10^6}{100 \times 10^9} = 48 \text{ } \mu\text{A} .$$

## POWER DISSIPATED IN ACCELERATOR

From Eq. (4) of Ref. 2, the power dissipated can be written

$$P_d = \frac{V^2}{rL} \times \text{duty cycle} ,$$

where V is the total beam energy, r is the shunt impedance per unit length, and L is the total accelerator length. Thus

$$\text{At 1428 MHz: } P_d = \frac{10^{22} \times 0.06}{3.44 \times 10^{13} \times 3 \times 10^3} = 5800 \text{ W} .$$

$$\text{At 2856 MHz: } P_d = \frac{10^{22} \times 0.06}{1.72 \times 10^{13} \times 3 \times 10^3} = 11\,600 \text{ W} .$$

## COST OF REFRIGERATION

Based on cost estimates<sup>3</sup> made at the W.W. Hansen Laboratories of Physics, the cost of a refrigeration unit capable of cooling to 1.85°K can be approximated by the following formula:

$$C \approx \$12\,000 P^{0.6}$$

where P is the dissipative power in watts which must be removed by the refrigeration unit. Let N be the number of separate refrigeration units, so that  $NP = P_d$  = the total power dissipated in the accelerator and feedback loops. The total cost  $C_T$  can then be written

$$\begin{aligned} C_T &= N \, 12\,000 \left( \frac{P_d}{N} \right)^{0.6} \\ &= \$12\,000 N^{0.4} P_d^{0.6} \end{aligned}$$

Thus, the total cost (neglecting distribution costs) is reduced as the total number of individual refrigeration units is reduced. In this study, it has been assumed that  $N = 15$  since this is the present number of separate power substations along the accelerator and has been found to be a convenient number for control purposes. Then, the estimated costs are:

$$\text{At 1428 MHz: } C_T = (12\,000)(15)^{0.4} (5800)^{0.6} = \$6.4 \text{ M}$$

$$\text{At 2856 MHz: } C_T = (12\,000)(15)^{0.4} (11\,600)^{0.6} = \$9.7 \text{ M}$$

These estimates may change significantly after several more years of cryogenic experience and development and hopefully will be reduced.

#### FILLING TIME

From Eq. (43) of Ref. 2, the filling time of the traveling wave accelerator with feedback to 63.2% buildup of the electric field (at maximum beam conversion efficiency) is

$$t_F = \frac{2Q}{\omega} \frac{V}{irL}$$

Thus,

$$\text{At 1428 MHz: } t_F = \frac{2 \times 1.6 \times 10^{10}}{0.895 \times 10^{10}} \frac{10^{11}}{48 \times 10^{-6} \times 3.44 \times 10^{13} \times 3 \times 10^3} = 72 \text{ msec}$$

$$\text{At 2856 MHz: } t_F = \frac{2 \times 4.0 \times 10^9}{1.79 \times 10^{10}} \frac{10^{11}}{48 \times 10^{-6} \times 1.72 \times 10^{13} \times 3 \times 10^3} = 18 \text{ msec}$$

#### RF PULSE LENGTH

Four of the "filling times" calculated above are required to build up the fields to 98% of the steady-state value. After this buildup, the rf pulse should be on for a period which is long compared to the buildup time in order that the beam duty cycle may be a reasonably large fraction of the rf duty cycle. It will be very desirable to program the beam turn-on during the rf buildup so that the rf and beam loading transients can occur essentially simultaneously. It is not yet clear how successful this technique will be and thus rf pulse lengths in the range of 20 to 80 times the "filling time" are given in Table I.

## TIME OFF BETWEEN PULSES

At a 6% duty cycle, the ratio of "time off" to "time on" is just 0.94/0.06. This ratio is used in calculating the "time off" values shown in Table I.

## BEAM PULSE LENGTH

For criteria purposes, the beam pulse length has been assumed to be the rf pulse length less one "filling time" for the short rf pulse and less four "filling times" for the long rf pulse.

## TEMPERATURE RISE DURING EACH RF PULSE

It is believed that a suitable Dewar capable of enclosing the accelerator and the feedback waveguide at either frequency under consideration would be about 18 in. in diameter and would contain about 20  $\ell$ /ft of liquid helium. The specific heat of liquid helium is 450 J/ $\ell$ /°K giving a heat capacity of  $\approx 10^4$  J/ft/°K. From the calculations of power dissipation made above, the temperature rise per pulse can be calculated as follows:

$$\text{At 1428 MHz: Power dissipation} = 0.58 \text{ W/ft (av)} = \frac{0.58}{0.06} = 9.7 \text{ W/ft (peak)}$$

$$\text{Heat liberated per pulse} = 9.7 \frac{\text{J}}{\text{sec ft}} \times 5.76 \text{ sec} = 56 \text{ J/ft}$$

$$\text{Temperature rise during pulse} = \frac{56}{10^4} = 0.0056^\circ\text{K}$$

$$\text{At 2856 MHz: Power dissipation} = 1.16 \text{ W/ft (av)} = 19.3 \text{ W/ft (peak)}$$

$$\text{Heat liberated per pulse} = 19.3 \frac{\text{J}}{\text{sec ft}} \times 1.44 \text{ sec} = 27.8 \text{ J/ft}$$

$$\text{Temperature rise during pulse} = \frac{27.8}{10^4} = 0.0028^\circ\text{K}$$

## RF FEED INTERVAL

In the present SLAC accelerator, the rf feed interval is 10 ft (the power from each klystron is split into four equal parts). In the superconducting version it has been assumed that the feed interval is 40 ft in order to reduce the total amount of instrumentation and control equipment required. Variation of the principal design parameters with respect to feed interval is shown in Table II. All cases are normalized with respect to the 10 ft feed interval case; all parameters of the 10 ft case are normalized to unity. The same total rf power input and the same beam energy and current are assumed in all cases. Two classes are given in Table II: in class 1 the attenuation parameter  $\tau$  is held constant as the feed interval is varied; in class 2,  $\tau$  is proportional to the feed interval. In class 1 the disk aperture must be increased as the feed interval is increased; this causes a decrease in  $r$ , the shunt impedance per unit length, as shown. In class 2, the cavity geometry is preserved as the feed interval is varied; therefore  $r$  remains constant. The most significant distinctions between the two classes relate to the circulating power  $P_0$  and the bridge ratio  $g$ . In class 1, increasing the feed interval requires a decreasing attenuation per unit length in order to keep the total attenuation  $\tau$  constant; the circulating power must then increase in order to keep the field strength constant. The bridge ratio  $g$  in

class 1 varies only sufficiently to compensate for the variation in  $r$ . In class 2, however, the circulating power  $P_0$  remains constant since the attenuation per unit length remains constant for all feed intervals. The bridge ratio  $g$  varies inversely with feed interval.

In the preliminary listing of criteria shown in Table I it has been assumed that class 2 with a 40 ft feed interval will be adopted. This choice results in reduced instrumentation and control requirements and a relatively small value of the bridge ratio  $g$ . A reduced value of  $g$  eases phasing and matching problems in the feedback loop.

#### ACCELERATOR ATTENUATION FACTOR ( $\tau$ )

In Table I, it has been assumed that each 40 ft section of the superconducting accelerator will consist of cavities of the same geometry as an "average" cavity of the present 10 ft SLAC sections. Each existing 10 ft SLAC section has an attenuation parameter  $\tau = 0.57$  at room temperature. Four of these sections arranged contiguously with a single feed would therefore result in a  $\tau$  of 2.28. At 1.85°K, the  $Q$  of these sections would be improved by the factor  $4.0 \times 10^9 / 1.3 \times 10^4 = 3.08 \times 10^5$ . Thus at 2856 MHz and 1.85°K, the attenuation parameter would be  $\tau = 2.28 / 3.08 \times 10^5 = 74.0 \times 10^{-7}$  nepers. For the same cavity geometry scaled proportional to wavelength,  $\tau \propto \omega^3$ , and thus at 1428 MHz and 1.85°K,  $\tau = 74 \times 10^{-7} / 2^3 = 9.24 \times 10^{-7}$  nepers.

#### FEEDBACK ATTENUATION FACTOR ( $\gamma$ )

In Table I it has been assumed that the loss in the feedback loop is 10% of the accelerator loss. Since the feedback loop consists principally of straight waveguide, this estimate is probably higher than the actual loss will turn out to be.

#### BRIDGE RATIO ( $g$ )

The required bridge ratio can be calculated from the following relation [Eq. (20) of Ref. 2]:

$$g = \frac{P_T}{2\pi i^2 rL}$$

Thus,

$$\begin{aligned} \text{At 1428 MHz: } g &= \frac{4.8 \times 10^6}{18.48 \times 10^{-7} \times (48)^2 \times 10^{-12} \times 3.44 \times 10^{13} \times 3 \times 10^3} \\ &= 1.095 \times 10^4 \end{aligned}$$

$$\begin{aligned} \text{At 2856 MHz: } g &= \frac{4.8 \times 10^6}{148 \times 10^{-7} \times (48)^2 \times 10^{-12} \times 1.72 \times 10^{13} \times 3 \times 10^3} \\ &= 0.273 \times 10^4 \end{aligned}$$

#### CIRCULATING POWER ( $P_0$ )

The normalized circulating power  $P_0/P_s$  at maximum beam conversion efficiency is just equal to  $1 + g$  [Eq. (6) of Ref. 2]. Since the input power per klystron,  $P_s$ , is



20 kW, the circulating powers in the two cases become:

$$\text{At 1428 MHz: } P_o = 1.095 \times 10^4 \times 20 \times 10^3 = 219 \text{ MW}$$

$$\text{At 2856 MHz: } P_o = 0.273 \times 10^4 \times 20 \times 10^3 = 54.6 \text{ MW}$$

#### REQUIRED PHASING ACCURACY IN LOOP

The vector diagram of the voltages in the feedback loop at steady state is shown in Fig. 1. The input from the rf source into the loop is  $V_s/(1+g)^{1/2}$ . The net feedback voltage vector is  $x^{-1} g^{1/2}/(1+g)^{1/2} V_o$ , where  $x$  is the total attenuation due to loss in the walls and to beam loading. At maximum beam conversion efficiency  $x = g^{1/2}/(1+g)^{1/2}$  [Eq. (5) of Ref. 2]. In this case and with  $\varphi = 0$  all the vectors in Fig. 1 lie along the same line and the following relation holds:

$$\frac{V_s}{(1+g)^{1/2}} + \frac{g}{1+g} V_o = V_o$$

or

$$\frac{V_o}{V_s} = (1+g)^{1/2}$$

When  $\varphi \neq 0$ , the following solution of the vector diagram may be obtained using the law of cosines<sup>3</sup>:

$$V_o^2 + \frac{1}{x^2} \left( \frac{g}{1+g} \right) V_o^2 - \frac{2}{x} \left( \frac{g}{1+g} \right)^{1/2} V_o^2 \cos \varphi = \frac{V_s^2}{1+g}$$

Substituting  $x = g^{1/2}/(1+g)^{1/2}$  and  $\cos \varphi \approx 1 - \frac{1}{2} \varphi^2$  yields the result

$$\left( \frac{V_o}{V_s} \right)^2 \approx (1+g)(1 - g^2 \varphi^2)$$

or

$$\frac{\delta V_o}{V_o} \approx - \frac{(g\varphi)^2}{2}$$

Thus, in order for the loop gain to be reduced by no more than 1% by the loop phase error, it is necessary that

$$|g\varphi| \leq (0.02)^{1/2} = 0.1414$$

Using the value of  $g$  calculated above, the required loop phase accuracies become:

$$\text{At 1428 MHz: } \varphi \leq \frac{0.1414}{1.095 \times 10^4} = 1.29 \times 10^{-5} \text{ rad} = 7.4 \times 10^{-4} \text{ deg}$$

$$\text{At 2856 MHz: } \varphi \leq \frac{0.1414}{0.273 \times 10^4} = 5.16 \times 10^{-5} \text{ rad} = 29.6 \times 10^{-4} \text{ deg}$$

## CONCLUSIONS

The tentative parameters calculated in this report and summarized in Table I have been set down to guide further technical and cost studies. It is highly probable that these parameters will be changed as a result of future experience and developments. Many additional questions must be investigated theoretically and experimentally before the basic design framework of a two-mile superconducting accelerator can be considered established.

## ACKNOWLEDGEMENTS

The author is grateful for the many helpful discussions of this subject with his colleagues at SLAC including particularly M. Allen, W. Herrmannsfeldt, H. Hogg, J. Lebacqz, G. Loew, W. Panofsky, R. Taylor, and P. Wilson. Useful advice and background information have also been received from members of the W.W. Hansen Laboratories of Physics at Stanford, including W. Fairbank, R. Hofstadter, and H.A. Schwettman.

TABLE I  
Parameters of a Two-Mile Superconducting  
Accelerator at Two Frequencies

Parameter	f = 1428 MHz	f = 2856 MHz
Length	3000 m	3000 m
$\bar{F}/Q$	$2.15 \times 10^3 \Omega/\text{m}$	$4.3 \times 10^3 \Omega/\text{m}$
$\bar{F}$	$3.44 \times 10^{13} \Omega/\text{m}$	$1.72 \times 10^{13} \Omega/\text{m}$
Q	$16 \times 10^9$	$4.0 \times 10^9$
Loaded energy (max)	100 GeV	100 GeV
V/L	10 MeV/ft	10 MeV/ft
Duty cycle	0.06	0.06
Peak beam current	48 $\mu\text{A}$	48 $\mu\text{A}$
Average beam current	3 $\mu\text{A}$	3 $\mu\text{A}$
Peak beam power	4.8 MW	4.8 MW
Average beam power	0.3 MW	0.3 MW
Number of klystrons	240	240
Peak power per klystron	20 kW	20 kW
Average power per klystron	1.2 kW	1.2 kW
Type of rf structure	TW with rf feedback loop	TW with rf feedback loop
Filling time (to 63.2%)	72 msec	18 msec
Power dissipated in accelerator	5800 W (0.58 W/ft)	11 600 W (1.16 W/ft)
Total cost refrigeration	\$6.4 M	\$9.7 M
Pulse length (rf)	1.44 to 5.76 sec	0.36 to 1.44 sec
Pulse length (beam)	1.37 to 5.47 sec	0.34 to 1.37 sec
Time off between rf pulses	22.6 to 90.3 sec	5.65 to 22.6 sec
Normalized peak current ( $i_n$ ) at $\eta_{\text{max}}$	7.03	4.97
Accelerator attenuation factor ( $\tau$ )	$9.24 \times 10^{-7}$	$74.0 \times 10^{-7}$
Feedback attenuation factor ( $\gamma$ )	$0.924 \times 10^{-7}$	$7.4 \times 10^{-7}$
Bridge ratio (g)	$1.095 \times 10^4$	$0.273 \times 10^4$
Circulating power ( $P_o/P_s$ ) at $\eta_{\text{max}}$	$1.095 \times 10^4$	$0.273 \times 10^4$
Required phasing accuracy in loop for $\delta V_o/V_o \leq 0.01$	$7.4 \times 10^{-4}$ deg	$29.6 \times 10^{-4}$ deg

TABLE II

Variation of Basic Parameters of a Superconducting Accelerator  
as a Function of Feed Interval

Two classes are considered: Class 1 with attenuation parameter  $\tau = \text{constant}$ ; class 2 with  $\tau$  proportional to the distance between fields.

Parameter	Class 1: $\tau = \text{constant}$			Class 2: $\tau$ proportional to distance between feeds		
	Distance between feeds			Distance between feeds		
	10 ft	20 ft	40 ft	10 ft	20 ft	40 ft
Attenuation parameter ( $\tau$ )	1	1	1	1	2	4
Beam energy ( $V_T$ )	1	1	1	1	1	1
Peak beam current ( $i_p$ )	1	1	1	1	1	1
Shunt impedance ( $r$ )	1	0.87	0.77	1	1	1
Total rf input power ( $P_T$ )	1	1	1	1	1	1
Input power per feed ( $P_s$ )	1	2.0	4.0	1	2.0	4.0
Bridge ratio ( $g$ )	1	1.15	1.30	1	0.5	0.25
Normalized circulating power ( $P_o/P_s$ )	1	1.15	1.30	1	0.5	0.25
Circulating power ( $P_o$ )	1	2.3	5.2	1	1	1
Filling time ( $t_F$ )	1	1.15	1.30	1	1	1
Total power dissipated ( $P_d$ )	1	1.15	1.30	1	1	1

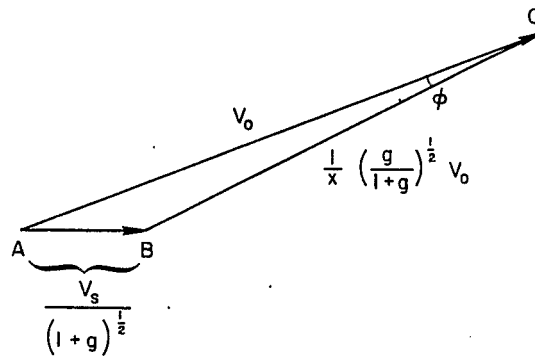


Fig. 1. Steady-state condition in feedback loop with phase error  $\phi$ .

# CONSIDERATION OF THE USE OF FEEDBACK IN A TRAVELING-WAVE SUPERCONDUCTING ACCELERATOR<sup>\*1</sup>

R.B. Neal  
Stanford Linear Accelerator Center  
Stanford University, Stanford, California

## I. INTRODUCTION

In a standing-wave accelerator structure, essentially all of the input rf power is inherently utilized (assuming proper input matching) to set up the accelerating fields and for conversion to beam power. Because of this basic simplicity all of the experimental work on superconducting accelerators carried out to date has employed the standing-wave structure. The theoretical performance of the standing-wave superconducting accelerator under beam loading conditions has been studied by Wilson and Schwettman.<sup>2</sup> (See Section VI of this report for further discussion.) The energy gain in a properly matched standing-wave (SW) accelerator with negligible beam loading is given by<sup>3</sup>

$$V_{SW} = \left( \frac{\tanh \tau/2}{\tau/2} \right)^{\frac{1}{2}} (1 + e^{-2\tau})^{-\frac{1}{2}} (P_s r_o \ell)^{\frac{1}{2}}, \quad (1)$$

where  $P_s$  is the rf power from the source,  $r_o$  is the shunt impedance per unit length,  $\ell$  is the length of the accelerator structure, and  $\tau$  is the attenuation parameter in nepers. For superconducting accelerators, where  $\tau$  is very small, Eq. (1) becomes:

$$V_{SW} \approx \left( \frac{P_s r_o \ell}{2} \right)^{\frac{1}{2}} = \left( \frac{P_d r_o \ell}{2} \right)^{\frac{1}{2}}, \quad (2)$$

where  $P_d = P_s$  is the power dissipated in the accelerator structure.

The energy gain in the traveling-wave (TW) accelerator with negligible beam loading is given by

$$V_{TW} = (2\tau)^{\frac{1}{2}} \left( \frac{1 - e^{-\tau}}{\tau} \right) (P_s r_o \ell)^{\frac{1}{2}}. \quad (3)$$

When  $\tau$  is very small, Eq. (3) becomes:

$$V_{TW} \approx (2\tau P_s r_o \ell)^{\frac{1}{2}} = (P_d r_o \ell)^{\frac{1}{2}}, \quad (4)$$

---

\* Work supported by the U.S. Atomic Energy Commission.

1. This report is based upon an earlier Stanford Linear Accelerator Center Technical Note: R.B. Neal, SLAC-TN-68-1 (1968).
2. P.B. Wilson and H.A. Schwettman, IEEE Trans. Nucl. Sci. NS-12, No. 3, 1045 (1965).
3. G.A. Loew and R.B. Neal, in Linear Accelerators, edited by P. Lapostolle and A. Septier (North-Holland Publishing Company, Amsterdam, The Netherlands) (to be published).

where  $2\pi P_s = P_d$  is the power dissipated in the accelerator structure. In this case,  $P_d$ , which is the power useful in setting up the accelerating fields, is very low and most of the rf power is lost at the output end of the accelerator. To make full use of the available power it is necessary to feed back the residual rf power through an external loop and to combine it in proper phase with the input power. If this is done, the power and fields in the TW structure will build up to a very high level. If the loss in the external loop is negligible compared to the loss in the accelerator structure, essentially all of the input power is available for setting up the accelerating fields, i.e.,  $P_d \approx P_s$ . Comparing Eqs. (2) and (4), it is noted that, for the same no-load energy gain, the power dissipated in the SW structure must be twice the power dissipated in the TW structure with feedback, assuming the structures have the same lengths and shunt impedances. In actual fact, it is possible to compensate largely for this disadvantage in the SW case by using the  $\pi$  mode or the  $\pi/2$  mode in a bi-periodic structure for which the shunt impedances are considerably increased.

From another viewpoint, for a given net energy gain, the ratio of peak to average fields in the standing-wave structure is up to two times as high as this ratio in the traveling-wave structure. This consideration gives an advantage to the traveling-wave structure for superconducting accelerator applications. Again, the relative advantage of the TW structure is reduced when the  $\pi$  mode or the special  $\pi/2$  bi-periodic mode is used in the SW structure.

The original idea of using feedback in conjunction with a traveling-wave linear accelerator was proposed by R.-Shersby-Harvie and Mullett<sup>4</sup> in 1949. This method was used on a number of early low energy British accelerators designed for medical therapy. The use of the feedback principle in resonant rings for the purpose of testing various microwave components such as rf windows was demonstrated by Milosevic and Vautey.<sup>5</sup> Hahn and Halama<sup>6,7</sup> have studied the possibility of using the resonant ring concept in superconducting rf beam separators.

## II. OPTIMUM FEEDBACK IN THE TW ACCELERATOR WITH BEAM LOADING

A schematic of the TW accelerator with feedback is shown in Fig. 1. The residual rf power at the end of the accelerator is fed back to the input end where it is combined with the source power  $P_s$  by means of a suitable waveguide bridge. The combined power  $P_0$  is then fed into the accelerator. The bridge ratio, which will be designated by the symbol  $g$ , is defined as the ratio of the powers which the bridge is designed to combine. When the ratio of the feedback power to the source power is equal to the bridge ratio  $g$  and when the feedback phase is properly adjusted, the power input to the accelerator will be  $(1 + g)$  times the source power and the power  $P_L$  to the external load will be zero.

Suppose that the attenuation due to beam loading and to wall losses in the accelerator structure and feedback loop is such that  $P_F = P_0/x^2$ . Then the condition for maximum power input to the accelerator and zero power to the resistive load is

$$\frac{P_s(1 + g)}{x^2} = g P_s$$

4. R.B. R.-Shersby-Harvie and L.B. Mullett, Proc. Phys. Soc. London B62, 270 (1949).
5. L.J. Milosevic and R. Vautey, IRE Trans. MTT-6, 136 (1958).
6. H.J. Halama and H. Hahn, IEEE Trans. Nucl. Sci. NS-14, No. 3, 350 (1967).
7. H. Hahn and H.J. Halama, IEEE Trans. Nucl. Sci. NS-14, No. 3, 356 (1967).

or

$$g = \frac{1}{x^2 - 1} \quad (5)$$

When the condition of Eq. (5) is met, the steady-state power buildup ratio in the accelerator will be:

$$\frac{P_o}{P_s} = 1 + g = \frac{1}{1 - (1/x^2)} \quad (6)$$

From Eq. (6), it is noted that a large buildup ratio results when  $x^2$  is small (close to 1), i.e., when a large fraction of the input rf power is fed back to the bridge. The design value of the bridge ratio  $g$  must be correspondingly high as also given by Eq. (6).

In the presence of beam loading, the residual power at the output ( $z = \ell$ ) of the accelerator section is<sup>8</sup>:

$$\frac{P_\ell}{P_o} = \left[ e^{-\tau} - \left( \frac{i^2 r_o \ell}{P_o} \right)^{\frac{1}{2}} \frac{1 - e^{-\tau}}{(2\tau)^{\frac{1}{2}}} \right]^2 \quad (7)$$

where  $i$  is the peak beam current and the other terms are as previously defined. The power  $P_F$  fed back to the bridge is  $P_\ell e^{-2\gamma}$ , where  $\gamma$  is the attenuation in the feedback loop expressed in nepers. Thus,

$$\frac{1}{x^2} = \frac{P_F}{P_o} = \left[ e^{-(\tau+\gamma)} - e^{-\gamma} \left( \frac{i^2 r_o \ell}{P_o} \right)^{\frac{1}{2}} \frac{1 - e^{-\tau}}{(2\tau)^{\frac{1}{2}}} \right]^2 \quad (8)$$

Inserting  $1/x^2$  from Eq. (8) in Eq. (6) and solving for  $P_o/P_s$  yields the result:

$$\left( \frac{P_o}{P_s} \right)^{\frac{1}{2}} = \frac{1 + i_n^2 e^{-2\gamma} \frac{(1 - e^{-\tau})^2}{2\tau}}{i_n e^{-(\tau+2\gamma)} \frac{1 - e^{-\tau}}{(2\tau)^{\frac{1}{2}}} + \left[ \left( 1 - e^{-2(\tau+\gamma)} \right) + i_n^2 e^{-2\gamma} \frac{(1 - e^{-2\tau})^2}{2\tau} \right]^{\frac{1}{2}}} \quad (9)$$

where

$$i_n = \left( \frac{i^2 r_o \ell}{P_s} \right)^{\frac{1}{2}}$$

The normalized beam energy with beam loading is given by<sup>8</sup>:

$$V_n = (2\tau)^{\frac{1}{2}} \left( \frac{1 - e^{-\tau}}{\tau} \right) \left( \frac{P_o}{P_s} \right)^{\frac{1}{2}} - i_n \left( 1 - \frac{1 - e^{-\tau}}{\tau} \right) \quad (10)$$

where

$$V_n = \frac{V}{(P_s \ell r_o)^{\frac{1}{2}}}$$

---

8. R.B. Neal, J. Appl. Phys. 29, 1019 (1958).

Substituting Eq. (9) in Eq. (10) yields the result:

$$V_n = \frac{1 + i_n^2 e^{-2\gamma} \frac{(1 - e^{-\tau})^2}{2\tau}}{\frac{i_n e^{-(\tau+2\gamma)}}{2} + \left[ \frac{\tau}{2} \frac{1 - e^{-2(\tau+\gamma)}}{(1 - e^{-\tau})^2} + \frac{i_n^2 e^{-2\gamma}}{4} \right]^{\frac{1}{2}}} - i_n \left( 1 - \frac{1 - e^{-\tau}}{\tau} \right) \quad (11)$$

The beam conversion efficiency  $\eta$  is defined as the fraction of the power from the rf source which is converted into beam power at steady state, i.e.,

$$\eta = \frac{V_i}{P_s} \quad (12)$$

From the definitions of  $V_n$  and  $i_n$ , it is clear that  $\eta$  can also be expressed as  $\eta = V_n i_n$ . Thus,  $\eta$  may be obtained by multiplying both sides of Eq. (11) by  $i_n$ . Two sets of curves of  $V_n$  and  $\eta$  versus  $i_n$  are shown in Fig. 2. One set is based on  $\gamma/\tau = 10^4$  [case (a)] which is typical of feedback through a loop which is at room temperature while the accelerator structure is supercooled. The other set is based on  $\gamma/\tau = 0.1$  [case (b)] which is a rough approximation\* for the case where the feedback loop as well as the accelerator structure is supercooled. From a comparison of these curves, several observations may be made. For fixed rf power input, the theoretical no-load energy is about 95 times higher for case (b) where  $\gamma/\tau = 0.1$  than for case (a) where  $\gamma/\tau = 10^4$ . As the beam current increases,  $\eta$  increases much more rapidly for case (b) than for case (a) and approaches 100% for relatively small values of current. Similarly, the beam energy for case (b) drops off much more rapidly with increasing current. At higher values of beam current, the values of beam energy and  $\eta$  for both cases approach the same values. Case (b) is obviously superior where the attainment of high energy is paramount. However, the very large value of the beam loading derivative requires that the current be maintained constant with high accuracy in order to achieve energy stability.

### III. FIXED BRIDGE RATIO $g$ IN THE TW ACCELERATOR WITH BEAM LOADING

The above discussion is based upon optimum feedback which implies a bridge ratio  $g$  which can be varied to suit any degree of beam loading. While variable ratio bridges have been designed,<sup>9</sup> they are expensive and cumbersome and are of questionable feasibility at cryogenic temperatures. A bridge having a fixed ratio corresponding to a specific value of design current may therefore be required. However, it is desirable to understand the performance of such a system over the entire range of feasible beam currents. To gain insight, it is helpful to study the transient buildup of a feedback system with fixed bridge ratio  $g$ .

The power buildup process is a stepwise affair with intervals between steps equal to the loop transit time. Initially, the voltage  $V_s$  applied to the bridge from the power source will divide, producing a voltage  $V_s/(1 + g)^{\frac{1}{2}}$  in the accelerator arm and a

---

\* At room temperatures, the attenuation in nepers per unit length is typically 50 to 100 times as high in the accelerator structure as in a similar length of ordinaty waveguide. Because of the presence of bends and the recombining bridge in the feedback loop, the more conservative estimate of 10 is being used in this example.

9. C.F. Bareford and M.G. Kelliher, Philips Tech. Rev. 15, No. 1, 11. 1-26 (1953).



voltage  $V_s [g/(1+g)]^{\frac{1}{2}}$  in the resistive load arm. After one transit through the accelerator feedback loop, a voltage  $V_s/[x(1+g)^{\frac{1}{2}}]$  appears in the feedback arm. If the phase is correct, this feedback voltage divides, the fraction  $[g/(1+g)]^{\frac{1}{2}}$  being added to the existing voltage in the accelerator arm and the fraction  $[1/(1+g)]^{\frac{1}{2}}$  being subtracted from the existing voltage in the load arm. Additional transits lead to the series

$$\begin{aligned} \frac{V_o}{V_s} &= \frac{1}{(1+g)^{\frac{1}{2}}} \left[ 1 + \left( \frac{1}{x} \right) \left( \frac{g}{1+g} \right)^{\frac{1}{2}} + \left( \frac{1}{x} \right)^2 \frac{g}{1+g} + \dots \right] \\ &= \frac{x}{x(1+g)^{\frac{1}{2}} - g^{\frac{1}{2}}} \end{aligned} \quad (13)$$

and

$$\begin{aligned} \frac{V_L}{V_s} &= \left( \frac{g}{1+g} \right)^{\frac{1}{2}} - \left[ \frac{1}{x(1+g)} \right] \left[ 1 + \left( \frac{1}{x} \right) \left( \frac{g}{1+g} \right)^{\frac{1}{2}} + \left( \frac{1}{x} \right)^2 \frac{g}{1+g} + \dots \right] \\ &= \frac{xg^{\frac{1}{2}} - (1+g)^{\frac{1}{2}}}{x(1+g)^{\frac{1}{2}} - g^{\frac{1}{2}}} \end{aligned} \quad (14)$$

The squares of Eqs. (13) and (14) give the steady-state values of  $P_o/P_s$  and  $P_L/P_s$ , respectively. From Eq. (14) it is noted that when  $xg^{\frac{1}{2}} = (1+g)^{\frac{1}{2}}$ , i.e.,  $g = 1/(x^2 - 1)$ ,  $V_L$  and  $P_L = 0$ , and all of the power is delivered to the accelerator. In this case  $P_o/P_s = 1+g$  as given in Eq. (6) for the optimum feedback case.

Substituting  $x$  from Eq. (8) in Eqs. (13) and (14), squaring and solving for  $P_o/P_s$  and  $P_L/P_s$  yields the results:

$$\left( \frac{P_o}{P_s} \right)^{\frac{1}{2}} = \frac{1 - g^{\frac{1}{2}} e^{-\gamma} i_n \frac{1 - e^{-\tau}}{(2\tau)^{\frac{1}{2}}}}{(1+g)^{\frac{1}{2}} - g^{\frac{1}{2}} e^{-(\tau+\gamma)}} \quad (15)$$

$$\left( \frac{P_L}{P_s} \right)^{\frac{1}{2}} = \frac{g^{\frac{1}{2}} - (1+g)^{\frac{1}{2}} e^{-(\tau+\gamma)} + e^{-\gamma} i_n \frac{1 - e^{-\tau}}{(2\tau)^{\frac{1}{2}}}}{(1+g)^{\frac{1}{2}} - g^{\frac{1}{2}} e^{-(\tau+\gamma)}} \quad (16)$$

Substituting  $(P_o/P_s)^{\frac{1}{2}}$  from Eq. (15) in the basic energy equation [Eq. (10)] gives the normalized beam energy:

$$(V_n)_{g \text{ fixed}} = (2\tau)^{\frac{1}{2}} \frac{1 - e^{-\tau}}{\tau} \left[ \frac{1 - g^{\frac{1}{2}} e^{-\gamma} i_n \frac{1 - e^{-\tau}}{(2\tau)^{\frac{1}{2}}}}{(1+g)^{\frac{1}{2}} - g^{\frac{1}{2}} e^{-(\tau+\gamma)}} \right] - i_n \left( 1 - \frac{1 - e^{-\tau}}{\tau} \right) \quad (17)$$

The conversion efficiency  $\eta$  is given, as previously stated, by the product of  $V_n$  from Eq. (17) by  $i_n$ . Unlike the case with optimum feedback where  $\eta$  continues to approach unity as  $i_n$  increases, there is, for fixed bridge ratio  $g$ , a value of beam current which results in maximum  $\eta$ . Moreover, for each value of  $i_n$ , there is a value of the bridge ratio  $g$  which results in the maximum values of  $V_n$  and  $\eta$  at that  $i_n$ . Maximizing  $V_n$  in Eq. (17) with respect to  $g$  (holding  $i_n$  constant) gives the optimizing relationship:

$$(1 + g)^{\frac{1}{2}} e^{-(\tau+\gamma)} - g^{\frac{1}{2}} = e^{-\gamma} \left[ \frac{1 - e^{-\tau}}{(2\tau)^{\frac{1}{2}}} \right] i_n . \quad (18)$$

Equation (18) may be used to calculate the optimum design value of  $g$  for given values of the parameters  $\tau$ ,  $\gamma$ , and  $i_n$ .

When  $\eta$  [obtained by multiplying  $V_n$  from Eq. (17) by  $i_n$ ] is maximized with respect to  $i_n$ , the necessary condition is found to be:

$$(i_n) \eta_{\max} = \frac{\left( \frac{\tau}{2} \right)^{\frac{1}{2}} \left( \frac{1 - e^{-\tau}}{\tau} \right)}{\frac{(1 - e^{-\tau})^2}{\tau} g^{\frac{1}{2}} e^{-\gamma} + \left[ (1 + g)^{\frac{1}{2}} - g^{\frac{1}{2}} e^{-(\tau+\gamma)} \right] \left[ 1 - \left( \frac{1 - e^{-\tau}}{\tau} \right) \right]} . \quad (19)$$

When  $\tau$  and  $\gamma$  are small, Eq. (19) reduces to the simple expression:

$$(i_n) \eta_{\max} \approx \frac{1}{(2g\tau)^{\frac{1}{2}}} . \quad (20)$$

Substituting the condition given by Eq. (19) in the equation for  $\eta$  yields the expression for maximum conversion efficiency:

$$\eta_{\max} = \frac{1}{\left[ (1 + g)^{\frac{1}{2}} - g^{\frac{1}{2}} e^{-(\tau+\gamma)} \right] \left\{ 2g^{\frac{1}{2}} e^{-\gamma} + 2 \left[ (1 + g)^{\frac{1}{2}} - g^{\frac{1}{2}} e^{-(\tau+\gamma)} \right] \left[ \frac{\tau - (1 - e^{-\tau})}{(1 - e^{-\tau})^2} \right] \right\}} . \quad (21)$$

When  $\tau$  and  $\gamma$  are both small, Eq. (21) reduces to the expression:

$$\eta_{\max} \approx \frac{1}{1 + 2g(\tau + \gamma)} . \quad (22)$$

When  $(i_n) \eta_{\max}$  from Eq. (19) is substituted in the expression for beam energy [Eq. (17)] the result is

$$(V_n) \eta_{\max} = \frac{\left( \frac{\tau}{2} \right)^{\frac{1}{2}} \frac{1 - e^{-\tau}}{\tau}}{(1 + g)^{\frac{1}{2}} - g^{\frac{1}{2}} e^{-(\tau+\gamma)}} = \frac{V_{no}}{2} , \quad (23)$$

where  $V_{no}$  is the no-load energy which can be obtained by setting  $i_n = 0$  in Eq. (17). Thus, at maximum conversion efficiency, the beam energy is reduced to one-half of the no-load energy as in the case of the simple single feed accelerator without feedback.<sup>8</sup> From the form of Eq. (17), it is clear that  $V_n$  decreases linearly as the beam current increases. In general, as the beam current is varied the beam energy can be expressed as follows:

$$V_n = V_{no} \left( 1 - \frac{i_n}{2(i_n) \eta_{\max}} \right) . \quad (24)$$

When  $\tau$  and  $\gamma$  are small, Eq. (23) becomes:

$$(V_n)_{\eta \max} \approx \frac{\left(\frac{\tau}{2}\right)^{\frac{1}{2}}}{g^{\frac{1}{2}} \left[ \frac{1}{2g} + (\tau + \gamma) \right]} \quad (25)$$

The normalized beam energy  $V_n$  and the beam conversion efficiency  $\eta$  are shown versus  $i_n$  in Fig. 3 for three values of the bridge ratio  $g$  ( $g = 10^4$ ,  $10^5$ , and  $9.08 \times 10^5$ ). The latter value of  $g$  calculated from Eq. (18) gives a maximum no-load energy for the assumed values of  $\tau$  and  $\gamma$ . The same values of  $\tau$  and  $\gamma$  have been taken as for case (b) of Fig. 2. It is noted that a large bridge ratio results in a high value of the no-load energy and a high value of the beam loading derivative. Also, for large  $g$ , the conversion efficiency peaks at a lower value of beam current and the maximum efficiency is less than for smaller values of  $g$ . The dashed curves in Fig. 3 show the values of  $V_n$  and  $\eta$  for the optimum feedback case as given by Eq. (11) for  $V_n$  and by Eq. (11) multiplied by  $i_n$  for  $\eta$ . These dashed curves are the envelopes of all the possible cases of fixed  $g$  for the assumed values of  $\tau$  and  $\gamma$ .

#### IV. POWER DISSIPATED IN THE TW ACCELERATOR, RESISTIVE LOAD, AND FEEDBACK LOOP

The total power dissipated in the accelerator and in the feedback loop including the accelerator and resistive load is just  $P_s(1 - \eta)$ , i.e., the portion of the rf power which is not converted into beam power. The fraction of the rf power which is dissipated in the accelerator structure itself during operation at maximum efficiency can be found by setting Eq. (4) equal to Eq. (23). The result is

$$\left( \frac{P_{d(\text{accel})}}{P_s} \right)_{\eta \max} = \frac{\left(\frac{\tau}{2}\right) \left( \frac{1 - e^{-\tau}}{\tau} \right)^2}{\left[ (1 + g)^{\frac{1}{2}} - g^{\frac{1}{2}} e^{(\tau + \gamma)} \right]^2} \quad (26)$$

When  $\tau$  and  $\gamma$  are small, Eq. (26) becomes:

$$\left( \frac{P_{d(\text{accel})}}{P_s} \right)_{\eta \max} \approx \frac{\tau}{2g \left[ \frac{1}{2g} + (\tau + \gamma) \right]^2} \quad (27)$$

Comparing Eqs. (25) and (27), it is noted that

$$\left( \frac{P_{d(\text{accel})}}{P_s} \right)_{\eta \max} = (V_n)_{\eta \max}^2 \quad (28)$$

Thus, the power dissipated in the accelerator is less (and the power transferred to the beam is greater) when the accelerator is designed for a high value of  $i_n$  (and a corresponding low value of  $V_n$ ).

When the accelerator is designed for a maximum no-load energy, the optimizing relation [Eq. (18)] requires that  $(1/2g) = \tau + \gamma$ . Inserting this relation in Eq. (27) yields the result

$$\begin{array}{l} \text{(Optimum design} \\ \text{for no-load)} \end{array} \quad \frac{P_{d(\text{accel})}}{P_s} = \frac{\tau}{4(\tau + \gamma)} \quad (29)$$

Inserting the same relation in Eq. (22) gives

$$\begin{array}{l} \text{(Optimum design} \\ \text{for no-load)} \end{array} \quad \eta_{\max} = \frac{1}{1 + \frac{\tau + \gamma}{\tau + \gamma}} = 0.5 \quad (30)$$

Thus, the maximum efficiency of an accelerator designed to give maximum no-load energy is 50%. A similar procedure involving Eq. (16) gives

$$\begin{array}{l} \text{(Optimum design} \\ \text{for no-load)} \end{array} \quad P_L/P_s = 0.25 \quad (31)$$

The remaining power is lost in the feedback loop. It is given by

$$\frac{P_{\text{FB Loop}}}{P_s} = \frac{\gamma}{4(\tau + \gamma)} \quad (32)$$

The sum of the fractional powers given by Eqs. (29)-(32) is, as expected, 100%.

#### V. FILLING TIME OF TW ACCELERATOR WITH FEEDBACK

The power flowing in the accelerator and feedback loop may be considered as originating from two sources: (a) the rf power source; and (b) the electron beam. When the accelerator is perfectly phased, the voltages associated with these powers are in opposition and the net voltage at any point in the loop is equal to the difference of these voltages.

The beam-induced steady-state power,  $P_b$ , appearing at the output end of the accelerator can be shown<sup>8</sup> to be equal to

$$P_b = i_o^2 r_o \ell \frac{(1 - e^{-\tau})^2}{2\tau} \quad (33)$$

Thus, the normalized power and voltage due to the beam can be written

$$\frac{P_b}{P_s} = \frac{i_o^2 r_o \ell}{P_s} \frac{(1 - e^{-\tau})^2}{2\tau} = i_n^2 \frac{(1 - e^{-\tau})^2}{2\tau} \quad (34)$$

and

$$\frac{V_b}{V_s} = i_n \frac{1 - e^{-\tau}}{(2\tau)^{\frac{1}{2}}} \quad (35)$$

The voltage given by Eq. (35) is reduced by the factor  $e^{-\gamma}$  in the feedback loop and a fraction  $[g/(1 + g)]^{\frac{1}{2}}$  of the resultant voltage is then sent into the accelerator arm. Thus, after one transit

$$\frac{V_{o(\text{beam})}}{V_s} = i_n \frac{1 - e^{-\tau}}{(2\tau)^{\frac{1}{2}}} e^{-\gamma} \left( \frac{g}{1 + g} \right)^{\frac{1}{2}}$$

During each successive transit through the accelerator and feedback loop the voltage

is attenuated further by the factors  $e^{-\tau}$  and  $e^{-\gamma}$  and the fraction  $[g/(1+g)]^{\frac{1}{2}}$  is added to the existing voltage entering the accelerator. Thus, the voltage entering the accelerator builds up according to the geometrical series

$$\begin{aligned} \frac{V_{o(\text{beam})}}{V_s} &= i_n \frac{1 - e^{-\tau}}{(2\tau)^{\frac{1}{2}}} e^{-\gamma} \left( \frac{g}{1+g} \right)^{\frac{1}{2}} \left\{ 1 + e^{-(\tau+\gamma)} \left( \frac{g}{1+g} \right)^{\frac{1}{2}} + \left[ e^{-(\tau+\gamma)} \left( \frac{g}{1+g} \right)^{\frac{1}{2}} \right]^2 + \dots \right\} \\ &= i_n \frac{1 - e^{-\tau}}{(2\tau)^{\frac{1}{2}}} e^{-\gamma} \frac{g^{\frac{1}{2}}}{(1+g)^{\frac{1}{2}} - g^{\frac{1}{2}} e^{-(\tau+\gamma)}} \end{aligned} \quad (36)$$

Similarly, the voltage from the power source divides with the fraction  $[1/(1+g)]^{\frac{1}{2}}$  going into the accelerator arm; i.e., initially,

$$\frac{V_{o(\text{p.s.})}}{V_s} = \left( \frac{1}{1+g} \right)^{\frac{1}{2}}$$

Successive transits lead to the series

$$\begin{aligned} \frac{V_{o(\text{p.s.})}}{V_s} &= \left( \frac{1}{1+g} \right)^{\frac{1}{2}} \left\{ 1 + e^{-(\tau+\gamma)} \left( \frac{g}{1+g} \right)^{\frac{1}{2}} + \left[ e^{-(\tau+\gamma)} \left( \frac{g}{1+g} \right)^{\frac{1}{2}} \right]^2 + \dots \right\} \\ &= \frac{1}{(1+g)^{\frac{1}{2}} - g^{\frac{1}{2}} e^{-(\tau+\gamma)}} \end{aligned} \quad (37)$$

Subtracting Eq. (36) from Eq. (37) gives the same result obtained earlier [Eq. (15)] using the power flow equation [Eq. (8)].

The same series is summed in obtaining both Eqs. (36) and (37). In studying the buildup of the fields in the accelerator, it is of interest to calculate the fraction of the steady-state field which is reached after  $n$  transits around the loop. Let the series be  $1 + r + r^2 + \dots$ , where  $r = e^{-(\tau+\gamma)} [g/(1+g)]^{\frac{1}{2}}$ . The sums of  $n$  terms and infinite terms are, respectively

$$S_n = \frac{1 - r^n}{1 - r} \quad (38)$$

and

$$S_\infty = \frac{1}{1 - r} \quad (39)$$

Thus,

$$\frac{S_n}{S_\infty} = 1 - r^n \quad (40)$$

The number of transits required to build up to the fraction  $(1 - e^{-1})$ , i.e., 63.2% of the steady-state value ( $S_\infty$ ) may then be calculated as follows:

$$1 - r^n = 1 - e^{-1}$$

or,

$$r^n = e^{-1}$$

or,

$$n = \frac{1}{\ln(1/r)}$$

or, using the definition of  $r$ ,

$$n = \frac{1}{(r + \gamma) + \frac{1}{2} \ln\left(1 + \frac{1}{g}\right)}$$

$$\approx \frac{1}{(\tau + \gamma) + \frac{1}{2g}} \quad (41)$$

Since the time for a single transit is very close to  $\ell/v_g$  and noting that  $\ell/v_g = (2Q/\omega)\tau$ , the time to fill the structure to the fraction  $(1 - e^{-1})$  of the steady-state fields is given by  $n(\ell/v_g)$ ; i.e., using Eq. (41),

$$t_F \approx \frac{(2Q/\omega)\tau}{(\tau + \gamma) + \frac{1}{2g}} \quad (42)$$

When the structure is designed for negligible beam loading, the relationship giving maximum efficiency [see Eq. (18)] is  $(1/2g) = \tau + \gamma$ . Thus, the filling time for this case is  $(2Q/\omega)\tau g = (2Q/\omega)[\tau/(\tau + \gamma)]$ . For heavier design loading,  $g$  is much smaller and  $(1/2g) \gg (\tau + \gamma)$ . Thus, the filling time for the heavy beam loading case approaches  $(2Q/\omega)(2\tau g)$ .

Using Eqs. (20) and (25), the filling time given by Eq. (42) may alternately be written

$$t_F \approx \frac{2Q}{\omega} \frac{(V_n) \eta_{\max}}{(i_n) \eta_{\max}} \quad (43)$$

Thus, the filling time is reduced as the beam current giving maximum conversion efficiency is increased (and the corresponding beam energy decreased). As an example, assuming  $g = 10^5$ ,  $\tau = 5 \times 10^{-7}$  nepers,  $\gamma = 5 \times 10^{-8}$  nepers,  $Q = 10^9$ , and  $\omega = 1.79 \times 10^{10}$  rad/sec ( $f = 2856$  MHz). Then from Eqs. (20) and (25), one obtains  $(i_n) \eta_{\max} = 3.17$  and  $(V_n) \eta_{\max} = 0.285$ . Using these values in Eq. (43), the filling time is found to be  $t_F \approx 0.010$  sec.

Since, as shown previously,  $V_n i_n = \eta \approx 1$  for  $i_n \gg 1$ , it is clear that for  $i_n \gg 1$  the filling time varies as  $(V_n) \eta_{\max}^{-2}$  [or, equivalently, as  $(i_n) \eta_{\max}^{-2}$ ].

The dependence of filling time upon frequency may be determined by recalling that  $Q \propto \omega^{-2}$  and  $r_0 \propto \omega^{-1}$  at superconducting temperatures.<sup>2</sup> Thus,  $V_n/i_n = V/ir_0 \propto \omega$ . Then, from Eq. (43),  $t_F \propto \omega^{-2}$ . The rapid increase of filling time as the frequency is decreased, together with the increasing cross section of the structure, will likely be the principal factors limiting the minimum frequency.

## VI. STANDING-WAVE SUPERCONDUCTING STRUCTURE WITH BEAM LOADING

For purposes of comparison, the standing-wave superconducting structure will now be examined following the results of Wilson and Schwettman.<sup>2</sup> The energy gain in this case in the presence of beam loading is given by<sup>2</sup>:

$$V_{SW} = \frac{2\beta^{\frac{1}{2}}}{1 + \beta} \left( \frac{P_s r_o \ell}{2} \right)^{\frac{1}{2}} - \frac{r_o \ell i}{2(1 + \beta)} \quad (44)$$

where  $\beta$  is the coupling coefficient between the transmission line and the accelerator structure. The first term on the right in Eq. (44) is the no-load energy; the second term is the reduction in no-load energy due to beam loading. Again, for convenience, Eq. (44) will be written in normalized form as follows:

$$V_{n(SW)} = \frac{(2\beta)^{\frac{1}{2}}}{1 + \beta} - \frac{i_n}{2(1 + \beta)} \quad (45)$$

where  $V_n = V/(P_s r_o \ell)^{\frac{1}{2}}$  and  $i_n = [(i^2 r_o \ell)/P_s]^{\frac{1}{2}}$ . The conversion efficiency is then given by<sup>2</sup>:

$$\eta = \frac{V_i}{P_s} = V_n i_n = \left[ \frac{(2\beta)^{\frac{1}{2}}}{1 + \beta} \right] i_n - \frac{i_n^2}{2(1 + \beta)} \quad (46)$$

For a given value of  $i_n$ , there is a value of the coupling coefficient  $\beta$  which results in the maximum values of  $V_n$  and  $\eta$  at that  $i_n$ . Maximizing  $V_n$  in Eq. (45) with respect to  $\beta$  (holding  $i_n$  constant) gives the optimizing relationship:

$$\beta_{(V_n, \eta)_{\max}} = 1 + \frac{i_n^2}{4} + \left[ \frac{i_n^2}{4} \left( 2 + \frac{i_n^2}{4} \right) \right]^{\frac{1}{2}} \quad (47)$$

Equation (47) may be used to calculate the optimum design value of  $\beta$  for a given value of  $i_n$ .

On the other hand, when  $\eta$  is maximized with respect to  $i_n$ , the necessary condition is found to be

$$(i_n)_{\eta \max} = (2\beta)^{\frac{1}{2}} \quad (48)$$

When the condition of Eq. (48) is satisfied, the conversion efficiency and beam energy become<sup>2</sup>:

$$\eta_{\max} = \frac{\beta}{1 + \beta} \quad (49)$$

$$(V_n)_{\eta \max} = \frac{(2\beta)^{\frac{1}{2}}}{2(1 + \beta)} \quad (50)$$

Thus, at maximum conversion efficiency, the beam energy has been reduced by beam loading to one-half of the no-load value. In general, as in the traveling-wave case, the beam energy can be written as:

$$V = V_o \left( 1 - \frac{i}{2i_{\eta \max}} \right) \quad (51)$$

where  $V_o$  is the no-load energy and  $i_{\eta \max}$  is the beam current which results in  $\eta_{\max}$ .

The power dissipated in the structure at maximum conversion efficiency may be found by equating Eqs. (2) and (50). The result is<sup>2</sup>:

$$\left( \frac{P_d}{P_s} \right)_{\eta_{\max}} = \frac{\beta}{(1 + \beta)^2} \quad (52)$$

Comparing Eqs. (52) and (50) it may be noted that  $P_d/P_s$  can also be written as

$$\left( \frac{P_d}{P_s} \right)_{\eta_{\max}} = 2(V_n)^2 \eta_{\max} \quad (53)$$

Thus, for the same value of normalized energy  $V_n$ , twice as much power is dissipated in the standing-wave accelerator structure as in the structure of the traveling-wave accelerator with feedback [see Eq. (28)]. From the conservation of total power, the power reflected ( $P_r$ ) from the input coupler back towards the rf source may be found as follows<sup>2</sup>:

$$\frac{P_r}{P_s} = 1 - \eta_{\max} - \left( \frac{P_d}{P_s} \right)_{\eta_{\max}} = 1 - \frac{\beta}{1 + \beta} - \frac{\beta}{(1 + \beta)^2} = \frac{1}{(1 + \beta)^2} \quad (54)$$

Normalized values of beam energy ( $V_n$ ), beam current ( $i_n$ ), beam conversion efficiency ( $\eta$ ), power dissipated in accelerator structure ( $P_d/P_s$ ), and reflected power ( $P_r/P_s$ ) vs coupling coefficient  $\beta$ , all at maximum conversion efficiency, are shown in Fig. 4. The maximum efficiency obtainable improves as  $\beta$  increases. Other advantages of high  $\beta$  are the smaller fraction of the source power reflected and the smaller fraction of the power dissipated in the accelerator structure. A disadvantage of increasing  $\beta$  is the decreasing magnitude of  $V_n$  at  $\eta_{\max}$ .

## VII. FILLING TIME OF STANDING-WAVE STRUCTURE

For  $\beta \gg 1$ , most of the power is transferred to the beam and the power dissipated in the structure, given by Eq. (52), becomes  $P_d/P_s \approx 1/\beta$ . Thus, the loaded Q,  $Q_L$ , becomes

$$Q_L \approx \frac{Q}{\beta} \approx Q \frac{P_d}{P_s} \approx \frac{Q P_d}{i_{\eta_{\max}} V_{\eta_{\max}}} \quad (55)$$

Combining Eqs. (55) and (2) yields the result<sup>2</sup>

$$Q_L \approx \frac{2V_{\eta_{\max}}/\ell}{i_{\eta_{\max}}(r_o/Q)} = 2Q \frac{(V_n)_{\eta_{\max}}}{(i_n)_{\eta_{\max}}} \quad (56)$$

The time to fill the structure to  $1 - 1/e$ , i.e., to 63.2% of the magnitude of the steady-state field, is  $2Q_L/\omega$ . Thus, the time to fill to this level is:

$$t_F \approx \frac{4Q}{\omega} \frac{(V_n)_{\eta_{\max}}}{(i_n)_{\eta_{\max}}} \quad (57)$$

Comparing Eqs. (43) and (57) one notes that, for equal beam energies, currents, lengths, and  $r_o/Q$ , the filling time of the standing-wave structure is twice that of the traveling-wave structure with feedback. The basic reason for this result is that the standing-wave accelerator is filled by successive reflections in the accelerator structure itself,



whereas the traveling-wave structure is filled by successive feedback of the power through the external loop in which the transit time is negligible compared to the one-way transit time in the accelerator structure.

As in the traveling-wave case, for  $i_n \gg 1$ , the filling time varies as  $(V_n)\eta_{\max}^2$  or, equivalently, as  $(i_n)\eta_{\max}^{-2}$ . Also, with other parameters fixed,  $t_F \propto \omega^{-2}$ .

### VIII. COMPARISON OF TRAVELING-WAVE AND STANDING-WAVE DESIGNS

The normalized beam energy  $V_n$  and beam conversion efficiency  $\eta$  in the standing-wave accelerator are plotted in Fig. 5 vs  $i_n$  for three values of the coupling coefficient  $\beta$  ( $\beta = 1, 10$ , and  $50$ ). Also shown in this figure with dashed lines are the envelopes of the  $V_n$  and  $\eta$  families representing the maximum possible values of these variables at each value of  $i_n$ .

The envelopes of the entire family of  $g$  values for the traveling-wave accelerator with feedback and the  $\beta$  values of the standing-wave accelerator are plotted together in Fig. 6. As noted above, these curves represent the maximum possible values of  $V_n$  and  $\eta$  at each value of  $i_n$  and hence are useful in the theoretical comparison of the various possible designs. It is noted that the traveling-wave accelerator with feedback excels with respect to the maximum beam energy obtainable. At light loading it also has a higher conversion efficiency than the standing-wave accelerator. With increasing beam loading, the energies and efficiencies of both of these basic types approach equality.

The advantages relating to higher energy and higher efficiency stem solely from the reduced loss in the feedback loop compared to the "internal" feedback through the accelerator structure in the standing-wave accelerator. If  $\tau = \gamma$ , i.e., if the losses in the feedback loop are equal to the internal losses, the two accelerator types have the same maximum values of  $V_n$  and  $\eta$  at all values of  $i_n$ . However, the advantage of reduced ratio of peak to average fields for the traveling-wave accelerator with feedback still remains even if  $\tau = \gamma$ .

The practical realization of a superconducting accelerator with feedback may turn out to be quite complicated due to the requirement to supercool the external feedback loop. Also, careful attention must be given to the elimination of rf reflections in the loop in order to prevent the build-up of a backward wave of significant amplitude. This backward wave builds up at the expense of the forward wave and hence would result in a reduction of beam energy and conversion efficiency. A tuner in the feedback loop might be needed to compensate for residual reflections. Ideally, this tuner would be automatically controlled from a signal derived from the backward wave.

In summary, the superconducting traveling-wave accelerator with feedback has the theoretical advantages of somewhat higher energies and efficiencies at light loading as noted above and also the advantage of reduced ratio of peak to average fields in the accelerator cavities. The latter characteristic may be a definite advantage if the maximum energy gradient obtainable is limited by either the critical magnetic field for the superconductor or by field emission. Moreover, for the same values of normalized energies  $V_n$ , the traveling-wave accelerator with feedback has one-half as much rf power dissipated in the accelerator structure as the standing-wave accelerator. Because of the high cost of providing refrigeration at superconducting temperatures, this is an important consideration. In addition, for equal beam energies, beam currents, and  $r_0/Q$ , the traveling-wave accelerator with feedback has one-half the filling time of the standing-wave accelerator. This characteristic may become important if unity duty cycle is not feasible, or if it becomes desirable to turn off the rf power periodically, e.g., while the beam is being switched from one research area to another.

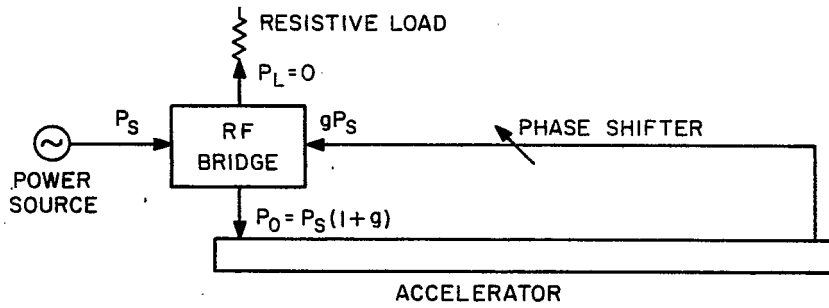


Fig. 1. Schematic diagram illustrating feedback principle. Relations shown represent steady-state conditions with correct bridge ratio.

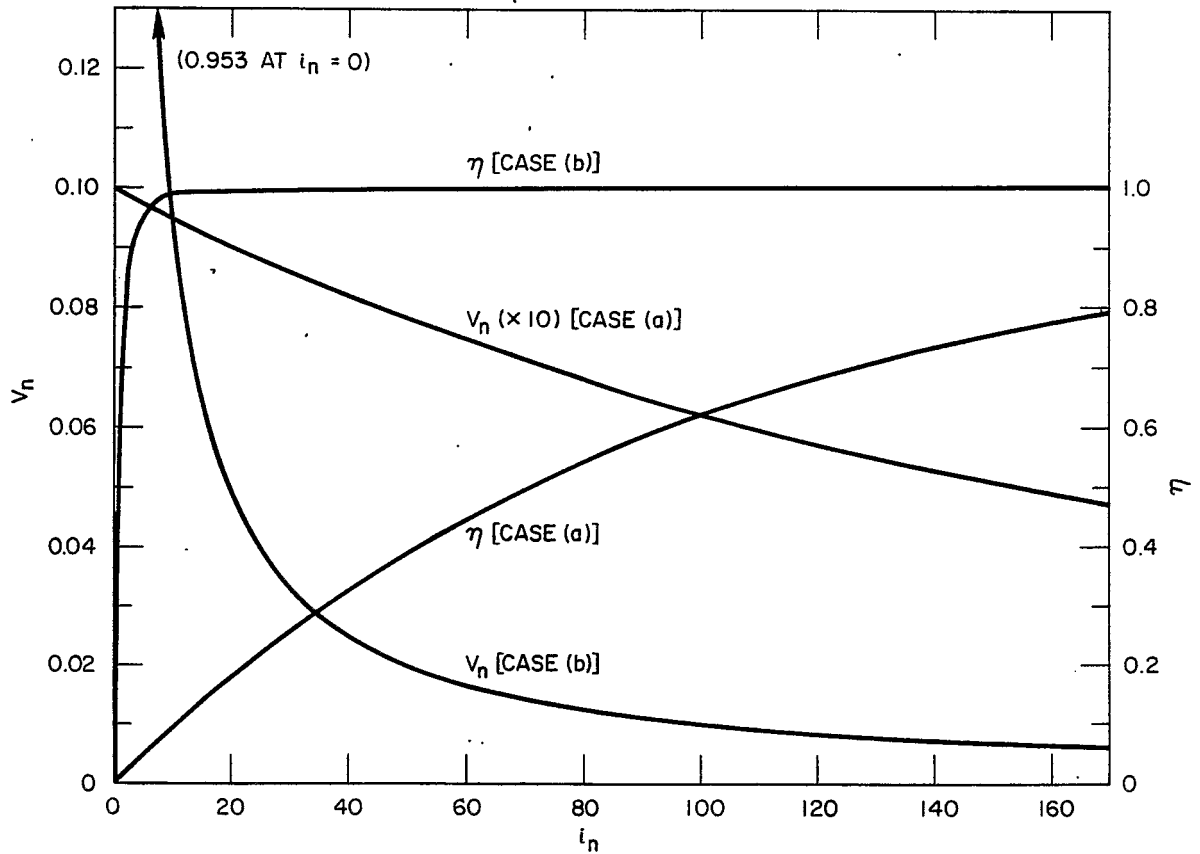


Fig. 2. Normalized beam energy ( $V_n$ ) and beam conversion efficiency ( $\eta$ ) for traveling-wave superconducting accelerator with optimum feedback vs normalized beam current ( $i_n$ ). Accelerator attenuation parameter,  $\tau = 5 \times 10^{-7}$  nepers. Feedback loop attenuation parameter,  $\gamma = 5 \times 10^{-3}$  nepers [Case (a)] and  $\gamma = 5 \times 10^{-8}$  nepers [Case (b)].

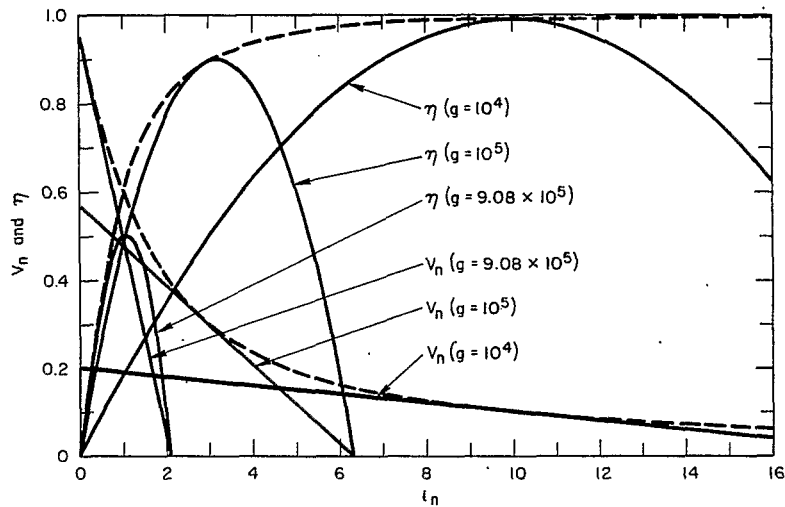


Fig. 3. Normalized beam energy ( $V_n$ ) and beam conversion efficiency ( $\eta$ ) for traveling-wave superconducting accelerator with feedback vs normalized beam current ( $i_n$ ). Curves are shown for three fixed bridge ratios. Accelerator attenuation parameter,  $\tau = 5 \times 10^{-7}$  nepers. Feedback loop attenuation parameter,  $\gamma = 5 \times 10^{-8}$  nepers.

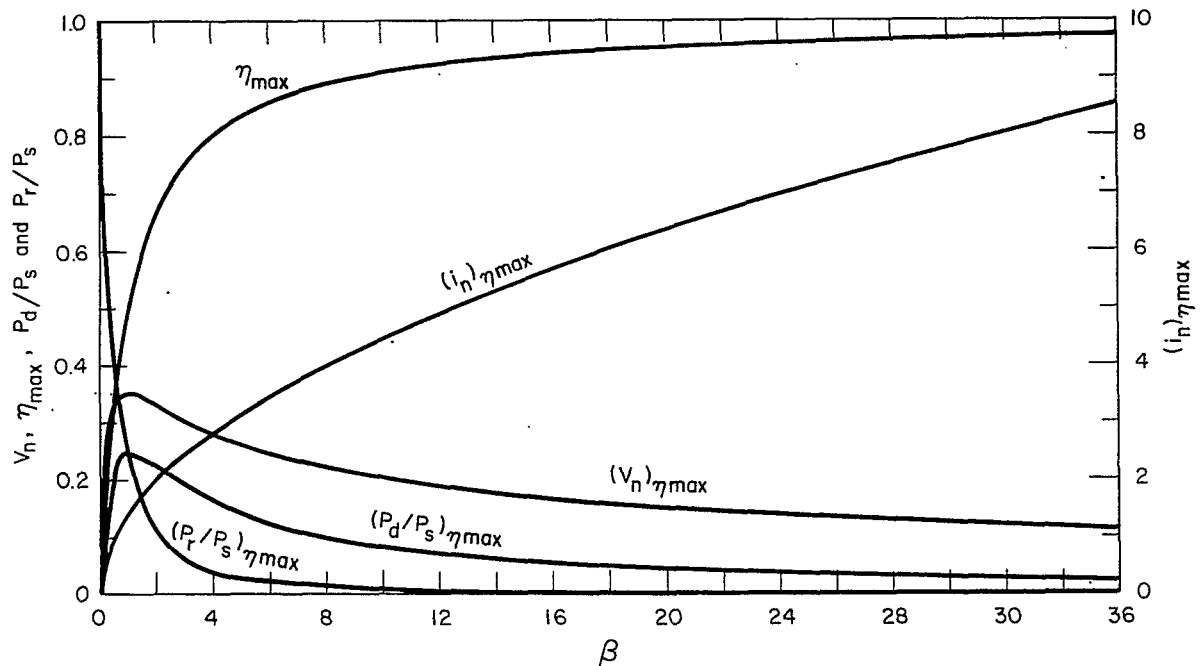


Fig. 4. Normalized values of beam energy ( $V_n$ ), beam current ( $i_n$ ), beam conversion efficiency ( $\eta$ ), power dissipated in accelerator structure ( $P_d/P_s$ ), and reflected power ( $P_r/P_s$ ) in superconducting standing-wave accelerator vs coupling coefficient  $\beta$ , all at maximum beam conversion efficiency.

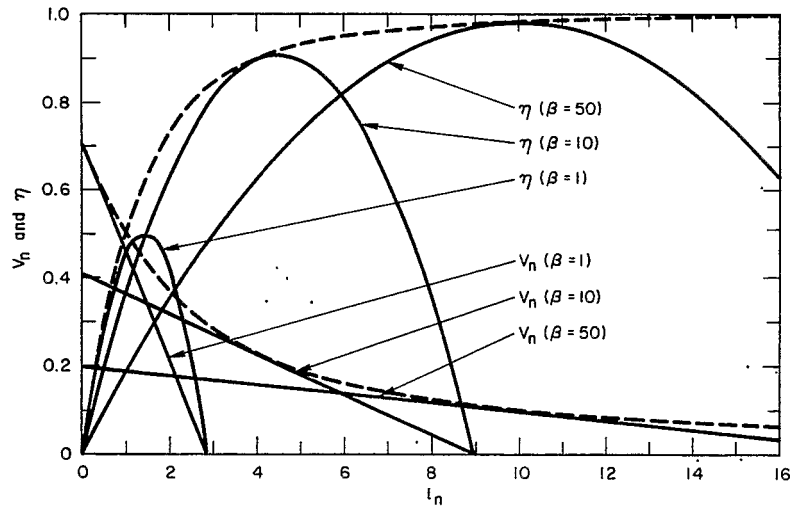


Fig. 5. Normalized beam energy ( $V_n$ ) and beam conversion efficiency ( $\eta$ ) for standing-wave superconducting accelerator vs normalized beam current ( $i_n$ ). Curves are shown for three fixed values of the coupling coefficient  $\beta$ .

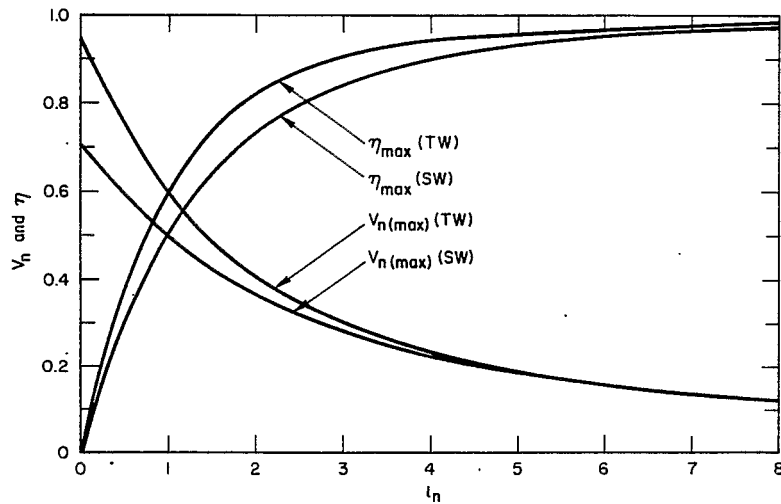


Fig. 6. Comparison of maximum values of normalized beam energy ( $V_n$ ) and beam conversion efficiency ( $\eta$ ) vs normalized beam current ( $i_n$ ) for superconducting traveling-wave and standing-wave accelerators. For traveling-wave accelerator, accelerator attenuation parameter  $\tau = 5 \times 10^{-7}$  nepers and feedback loop attenuation parameter  $\gamma = 5 \times 10^{-8}$  nepers.

# SUMMARY OF RECENT INVESTIGATIONS OF THE KARLSRUHE GROUP ON RF PROPERTIES OF SUPERCONDUCTORS AND ON APPLICATIONS

W. Jüngst  
Universität und Kernforschungszentrum Karlsruhe  
Karlsruhe, W. Germany

The experiments described in this collective report have been carried out by several members of the group. Their names are given in the list of references to more detailed information on the contributions. The reports mentioned there do, moreover, serve as a source of further references which have been omitted in the list.

## I. THE METHOD OF Q MEASUREMENTS

The electromagnetic energy stored in a resonator with walls of finite surface resistance  $R$  decays exponentially with the time constant

$$\tau_o = \frac{Q_o}{\omega} = \mu_o \frac{\int_V |H|^2 dv}{\int_S R |H|^2 ds} ; \quad (\tau_o) R \text{ const} = \frac{G}{\omega R} ,$$

where  $G$  is the so-called geometry factor and  $Q_o$  the rf quality factor of the unloaded resonator. An observation of  $\tau$  is used for the determination of the high  $Q$  values of superconducting cavities. Unfortunately one cannot observe the decay behavior of a resonator without some of its energy coupled into a suitable external instrument. Either the additional losses thus introduced which modify the measured  $\tau$  with respect to  $\tau_o$  have to be kept tolerably small, or they have to be measured and corrected for. The latter method has been investigated in some detail.<sup>1</sup> It turns out that the usual correction  $Q_o = (1 + \beta) Q_M$  applied to the measured  $Q_M$  value with the coupling coefficient  $\beta$  derived from the signal which is reflected from the coupling loop of a pulsed resonator may be insufficient for several reasons. There,  $\beta$  is obtained from the ratio  $P_i/P_e$  of the incident power  $P_i$  and the power  $P_e$  which is emitted from the resonator immediately after  $P_i$  is switched off during the steady state. A residual frequency modulation of the generator of the order of the cavity bandwidth, as well as reflections on the connecting lines due to improper matching, do considerably perturb the  $\beta$  determination. Except from errors in  $\beta$  the above-mentioned correction formula does not cover any extra losses in the coupling region.

A method is used, therefore, which permits the measurement of the  $Q$  value of the unloaded cavity without a  $\beta$  determination.<sup>2</sup> The resonator field is coupled to that of a piece of cut-off waveguide by a small coupling hole and the feeding coaxial line ends in a loop or a pin in this guide (Fig. 1). The distance from loop to hole is adjustable to allow for a large range of coupling coefficients. The individual losses are additive with respect to the observable  $Q_M$  value of the system:

- 
1. J. Halbritter, P. Kneisel, and O. Stoltz, Kernforschungszentrum Karlsruhe Report 3/67-9 (1967).
  2. J. Halbritter, R. Hietschold, P. Kneisel, and H. Schopper, Kernforschungszentrum Karlsruhe Report KFK 758 (1968).

$$Q_M^{-1} \propto P_o + P_{iris} + P_{guide} + P_{loop} + P_{rad}$$

According to the cut-off behavior of the guide, the losses of the loop (in the loop itself and close to it because of its field perturbation),  $P_{loop}$ , and the power  $P_{rad}$  fed into the coaxial line depend on the loop position,  $z$ :

$$P_{loop} + P_{rad} \propto \exp(-2\alpha z),$$

where  $\alpha$  is the attenuation factor of the cut-off fields,

$$\alpha = 2\pi (\lambda_c^{-2} - \lambda^{-2})$$

Usually, the vacuum wavelength  $\lambda$  is several times larger than the critical wavelength  $\lambda_c$  of the guide and  $\alpha$  is, therefore, only weakly frequency dependent.

If the losses  $P_{iris}$  around the coupling hole and  $P_{guide}$  on the walls of the cut-off guide are kept negligibly small by carefully plating these surfaces with the superconducting material,  $P_{loop} + P_{rad}$  can be separated from  $P_o$ . One has to plot  $Q_M^{-1}$  vs the loop position  $z$  which yields a curve that can be fitted by the constant term,  $Q_o^{-1}$ , and an exponential function with the slope,  $-2\alpha$ . Figure 2 shows the result of such a measurement. The experimental value,  $\alpha_{exp} = 0.185$ , is in good agreement with the theoretical attenuation coefficient,  $\alpha = 0.177$ , which corresponds to the  $TE_{11}$  cut-off mode in a 20 mm diameter guide at 2.46 GHz. In cases such as the example of Fig. 2, where a  $Q$  measurement at large  $z$  values (very small coupling coefficients) is possible and directly yields the practically unloaded  $Q_o$  value, there is no necessity to observe all the  $z$  dependence as long as one is sure to be in the region of constant  $Q_M$  values.

If with the same setup the  $\beta$  values are observed simultaneously,

$$\beta = P_{rad} / (P_o + P_{loop})$$

one gets an independent information on the losses  $P_{rad}$ ,  $P_{loop}$ , which, together with the  $z$  dependence measurement, allows the determination of their ratio. It has been found that in our arrangement  $P_{rad}$  and  $P_{loop}$  were of the same order of magnitude.

## II. MEASUREMENTS OF THE SURFACE RESISTANCE OF LEAD AND OF INDIUM

Mainly electroplated  $TE_{011}$  resonators with a diameter-to-length ratio equal to  $\sqrt{2}$  ( $G = 755 \Omega$ ) have been measured (Fig. 1). The results for lead at 2.5 GHz,<sup>1</sup> (IF = improvement factor)

$$Q_o(4.2^\circ K) = 2.8 \times 10^8 \quad Q_o(2^\circ K) = 3 \times 10^9$$

$$IF(4.2^\circ K) = 4600 \quad IF(2^\circ K) = 5 \times 10^4$$

$$R(4.2^\circ K) = 2.7 \times 10^{-6} \Omega$$

do agree with those measured at Stanford and Brookhaven at 4.2°K, whereas at 2°K they are worse.

The frequency of a linear accelerator will be lower. Since the frequency dependence of the surface resistance is not known accurately, measurements at 800 MHz, too,

have been performed.<sup>3</sup> A TE<sub>011</sub> resonator ( $G = 755 \Omega$ ), as well as a TEM coaxial resonator ( $G = 84 \Omega$ ), have been lead-plated and measured. The 800 MHz results were:

$$\begin{aligned} \text{TE}_{011}: Q_0(4.2^\circ\text{K}) &= 1 \times 10^9 & Q_0(2^\circ\text{K}) &= 3 \times 10^9 \\ \text{IF}(4.2^\circ\text{K}) &= 1 \times 10^4 & \text{IF}(2^\circ\text{K}) &= 3 \times 10^4 \\ R(4.2^\circ\text{K}) &= 7.5 \times 10^{-7} \Omega \\ \text{TEM}: Q_0(4.2^\circ\text{K}) &= 2 \times 10^8 \\ \text{IF}(4.2^\circ\text{K}) &= 1.7 \times 10^4 \end{aligned}$$

In Fig. 3 our results for lead at 0.8 and 2.5 GHz as well as the results from other laboratories are plotted vs frequency. With both scales logarithmic, they can be fitted by a straight line which indicates the frequency dependence

$$R \propto \omega^{1.77}.$$

The residual resistance,  $R_{\text{res}}$ , has not been subtracted here from the measured surface resistance. This could, in principle, have been done since  $R_{\text{res}}$  can be obtained from the measured temperature dependence of  $R$  if  $R_{\text{res}}$  is assumed to be temperature independent. Since this assumption is somewhat doubtful and since the accuracy of the measurements is not yet high enough, the correction does not appear worthwhile. It is obvious, however, that the residual resistance becomes more important at lower frequencies in that the slope would be increased.

Although indium surfaces are certainly not of interest for accelerator or separator cavities as their surface resistance is higher by more than a factor of 100 compared to lead, they have nevertheless been investigated.<sup>4</sup> Indium surfaces may possibly serve as protecting layers on top of lead. Indium forms a thin oxide layer and shows practically no aging effect. If the indium surface is thin enough, the superconducting properties of lead will be induced in it. This "proximity effect" will cause it to become superconducting even above its critical temperature ( $3.4^\circ\text{K}$ ) and above its critical magnetic field.

Indium and lead at room temperature form alloys which are known to have rather high critical temperatures, e.g.,  $5^\circ\text{K}$  with only 14% Pb, an effect which acts in the same direction as the proximity effect. We hope, however, to get layers which, although thin, consist mostly of In and are chemically sufficiently resistant.

An indium layer ( $\approx 1000 \text{ \AA}$ ) has been evaporated onto a lead layer, several microns thick, of a 2.5 GHz TE<sub>011</sub> resonator. A  $Q$  value of  $1.3 \times 10^8$  was found at  $4.2^\circ\text{K}$ .<sup>5</sup> With decreasing temperature no special behavior was found at the critical temperature of indium. In contrast to our experience with unprotected lead layers, no significant decrease of  $Q$  could be observed after the resonator had been exposed to air for several weeks. We have to admit that we do not yet know whether the superconducting properties are mainly those of an alloy or mainly due to the proximity effect.

- 
3. P. Flécher, J. Halbritter, R. Hietschold, P. Kneisel, L. List, and O. Stoltz; to be published in the Proc. of the 1968 Linear Accelerator Conference at Brookhaven.
  4. J. Halbritter, P. Kneisel, and L. List, Kernforschungszentrum Karlsruhe Report 3/67-10 (1967).
  5. P. Flécher, private communication.

To gain experience with the electroplating of indium layers, pure indium surfaces have been prepared and measured.<sup>4</sup> The observed temperature dependence of the surface resistance is very close to the theoretical prediction with  $\Delta(0)/kT_c = 1.75$ . The absolute values turned out to be even smaller than the theoretical ones (BCS) with all reasonable sets of parameters.

### III. CALCULATIONS ON SUPERCONDUCTING PROPERTIES

Based on the BCS theory the surface impedance has been computed, with frequency and temperature as free parameters, for a large number of sets of the inherent properties of the material, namely, London's penetration depth,  $\delta_L$ , the coherence length,  $\xi_0$ , and the mean free path,  $\ell$ .<sup>6,7</sup> Examples are given in Figs. 4 and 5.

The temperature dependence of  $R$  for  $T/T_c \leq 0.5$ , the range which is interesting for practical applications, is simply  $R \sim \exp[-\Delta(0)/kT]$ . In the figures  $T/T_c = 0.2$  and  $\Delta(0)/kT_c = 1.75$  are fixed values. Surface impedances for other temperatures or gap/critical temperature ratios can easily be computed with that relation.

The dependence,  $R(\kappa_F, \hbar\nu)$ , where  $\kappa_F = 2\delta_L/(\pi\xi_0)$ , shows (cf. Fig. 4 for  $\ell = \infty$ ) that the surface resistance decreases with decreasing  $\kappa_F$  at low frequencies and that the frequency dependence approaches  $R \sim \omega^2$  for  $\kappa_F \rightarrow 0$  (Pippard's limiting case).

The dependence on the mean free path  $\ell$  can be seen from Fig. 5 in the special case  $\kappa_F = 0.6$  (e.g., niobium). At low frequencies  $R$  is reduced with increasing  $\ell$ . This reduction is significant for large  $\kappa_F$  but amounts to less than 5% at  $\kappa_F \approx 10^{-2}$  (e.g., aluminum).

### IV. MEASUREMENTS AT HIGHER ELECTRIC FIELDS

The goal of these measurements has been to investigate to what extent the  $Q$  values measured at low fields might increase when the field level approaches the design figures required by various applications.

For a TEM resonator the  $Q_0$  value has been measured at various power levels.<sup>8</sup> If  $Q_{00}$  denotes the  $Q_0$  value and  $R_0$  the surface resistance in the limit of very low fields, the fraction of extra losses,  $P_{\text{extra}}$ , beyond those,  $P_0$ , explained by  $R_0$  is given by

$$P_{\text{extra}}(E)/P_0 = Q_{00}/Q_0(E) - 1$$

The first idea has been to attribute these losses to field emission. Using the Fowler-Nordheim relation for the field emission current

$$I_{\text{FE}} \propto E^2 \exp\left(\frac{-2.7 \times 10^7 \varphi^{3/2}}{K E}\right)$$

$\log(P_{\text{extra}}/E^3)$  has been plotted vs  $1/E$  and, indeed, straight lines up to about 6 MV/m result. With the known work function  $\varphi$ , the slope, however, indicated a microscopic

6. J. Halbritter, Kernforschungszentrum Karlsruhe Report 3/67-2 (1967).

7. J. Halbritter, private communication.

8. W. Kühn, to be published in the Proc. of the 1968 Linear Accelerator Conference at Brookhaven.



field enhancement factor K of nearly 7000. Since the highest K values so far observed are about 200 an explanation by mostly field emission becomes rather doubtful.

To get additional information on the field emission from superconducting lead surfaces, a less precise but more specific experiment for the determination of the field emission losses was carried out.<sup>9,10</sup> As it had been done before at Stanford with a warm copper cavity, we measured the X-radiation in the vicinity of the resonator, in our case, outside the cryostat. The various calibrations and corrections which have to be applied before one arrives at the field emission current as function of the electric field do introduce a rather large error, but this mainly influences the absolute values and much less the slope of the curve. The measurements were done with a lead-plated structure with a gap where the field could be raised up to 35 MV/m. The result is plotted in Fig. 6 together with the Stanford results. Regarding the experimental errors, the coincidence of the fitting straight lines can only be called fortuitous. The resulting very normal field enhancement factor,  $K \approx 200$ , however, proves that the extra losses of the Q-value experiment described before have to be explained by effects other than field emission.

One possible explanation would be the imperfect heat conduction which at high power levels may cause a temperature rise of the lead surface. Half a degree would increase the losses by a factor of about two.

Another possible reason for the increased surface resistance may be the increased magnetic field

$$R = R_0 [1 + k (H/H_c)^2 + \dots]$$

where the upper limit for the constant, k, summing up the various contributing effects, has been estimated to be about 5 where the residual resistance is not taken into account.<sup>11</sup> There are theoretical reasons which indicate that an equivalent constant  $k_{res}$  describing the field dependence of the residual resistance can be even much larger.<sup>12</sup> In order to check whether the measured extra losses are in agreement with this relation,  $P_{extra}/P_0$  has been plotted vs  $(H/H_c)^2$  which is expected to yield and, in fact, does yield a straight line. Its slope, which is proportional to k, led to  $k \approx 9$ . We conclude that this effect, too, may be the proper explanation or part of it.

Experiments to elucidate this situation further are being prepared. So far, field emission seems not to be the limiting effect for the field amplitudes since its loading power is far smaller than that of the total of the observed additional losses. There is a chance to reduce these extra losses either by preventing temperature gradients or rf magnetic field concentrations on the surface as far as possible and it is to be expected that, for a surface with a small residual resistance, the field dependence will be less pronounced.

- 
9. W. Kühn and L. Szecsi, in Studie über einen supraleitenden Protonen-Linearbeschleuniger im GeV-Bereich (Kernforschungszentrum Karlsruhe, 1967) p. 202.
  10. H. Schopper, H. Strube, and L. Szecsi, Kernforschungszentrum Karlsruhe Report 3/68-6 (1968).
  11. J. Halbritter, Kernforschungszentrum Karlsruhe Report 3/68-1 (1968).
  12. J. Halbritter, Kernforschungszentrum Karlsruhe Report 3/68-8 (1968).

## V. SPECIAL INVESTIGATIONS IN VIEW OF APPLICATIONS

Two features of linac cavities have to be investigated with a finite length of full-scale accelerating structure instead of only test cavities: the maximum attainable average accelerating field with the associated power requirement, and those effects which are expected to occur under heavy beam loading. An analogue experiment in the superconducting state has therefore been prepared<sup>13</sup> using electrons of the same velocity as the corresponding protons. The reduction of currents and field amplitudes by the electron-proton mass ratio considerably ease the experimental requirements, while the dynamical and beam loading problems remain essentially unchanged. Although it is not necessary for these analogous measurements, the available rf power source is capable of producing rather high fields so that limitations which might influence the design of a proton linear accelerator can be investigated.

A 12-cell structure and the appropriate cryostat have been built but only the room temperature performance tests have been carried out so far. Meanwhile the structure has been lead-plated and results from experiments at 4.2°K are expected soon.

The construction of a superconducting rf particle separator is regarded as a simplified first step on the way towards the construction of a linac. It is short compared to the accelerator and a number of severe difficulties as, for example, beam loading, do not exist here. Even if an improvement factor  $> 10^5$  as is imperative for the accelerator is not achieved in complicated structures, the separator project could still be continued since a few meters of a less economical structure seem tolerable.

The final construction will be a two-cavity separator for around 10 GeV/c kaons at CERN. To gain experience with the operation and optimum layout of the deflectors, a prototype single-cavity separator will precede the final design.<sup>14</sup> The prototype is designed such that, except for the differing deflecting structure itself, practically all components, especially the cryostat, refrigerator and rf system, can later be used for the two-cavity separator. The structure (iris-loaded waveguide, HEM<sub>11</sub> configuration, S-band operated in the  $\pi/2$  mode) will be 3.25 m long with a beam hole diameter of about 4 cm. This rather small diameter has been chosen since it combines the advantages of high shunt impedance and the easier tolerances that are possible with the increased group velocity. The useful momentum range for kaon separation is 1.1 to 1.7 GeV/c and the angular acceptance, including the beam transport system, is  $\geq 500 \mu\text{sr}$ . At an equivalent deflecting field of 3 MV/m, the highest necessary, the power dissipated in the structure will be 25 W if an improvement factor of  $10^5$  is assumed for lead. If the improvement factor should turn out to be much less, one could save cooling power by pulsing the system according to the slow extraction duty cycle of the accelerator. In this case pulsing seems the more feasible as the filling time of the resonator is reduced in proportion to the Q value. Iris-loaded eight-cell resonators have several times been lead-plated and measured. Satisfactory plating turned out to be much more complicated than for structures of simple geometry. Rather tricky anode shapes were necessary which at a sufficiently uniform and not too high current density could still be put in. Another difficulty was raised by the slight surface irregularities at the brazed joints of the individually machined copper parts. The best results<sup>15</sup> which have so far been obtained were  $Q_0 = 2 \times 10^7$  (IF = 2000) at 4.2°K and  $Q_0 = 1 \times 10^8$  (IF =  $10^4$ ) at 2°K.

---

13. W. Jüngst, M. Kuntze, and J. Vetter, Kernforschungszentrum Karlsruhe Report 3/67-15 (1967).

14. W. Jüngst, Kernforschungszentrum Karlsruhe Report 3/67-16 (1967).

15. W. Bauer, H. Eschelbacher, and W. Jüngst, private communication.

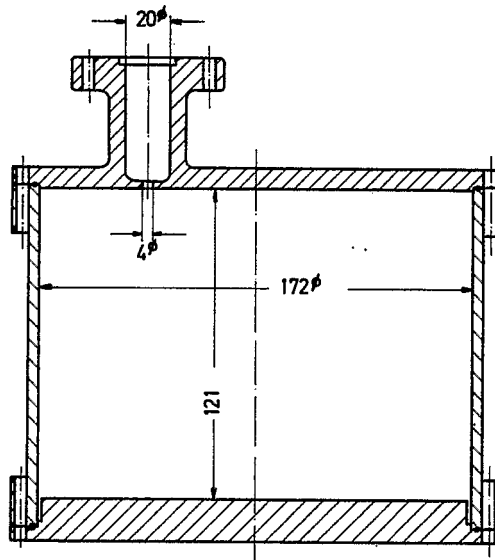


Fig. 1.  $TE_{011}$  test cavity, 2.46 GHz.

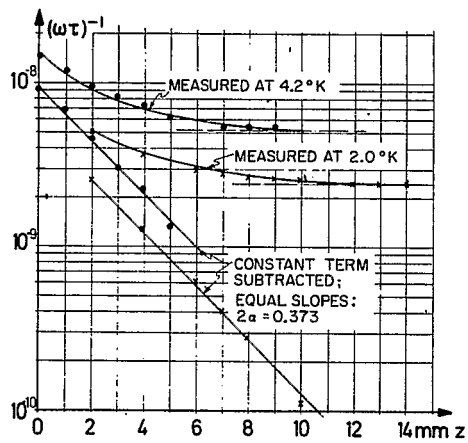


Fig. 2. Examples for the plot of  $1/Q_{\text{meas}}$  as a function of loop position.

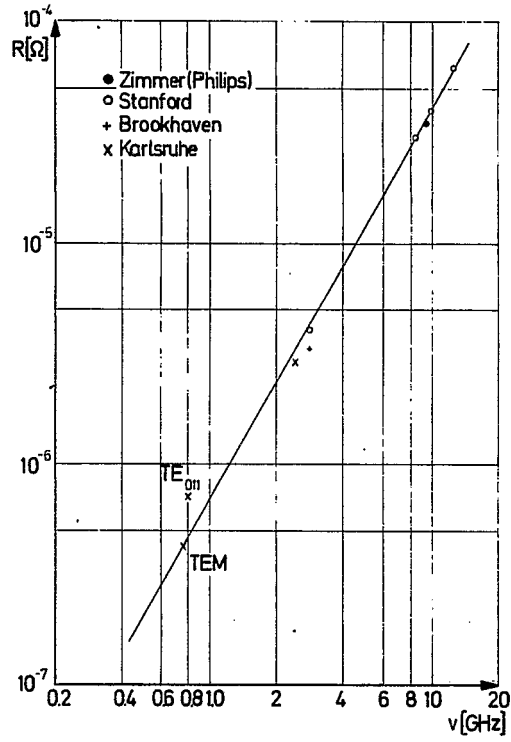


Fig. 3. Surface resistance of lead as function of frequency ( $T = 4.2^\circ\text{K}$ ).

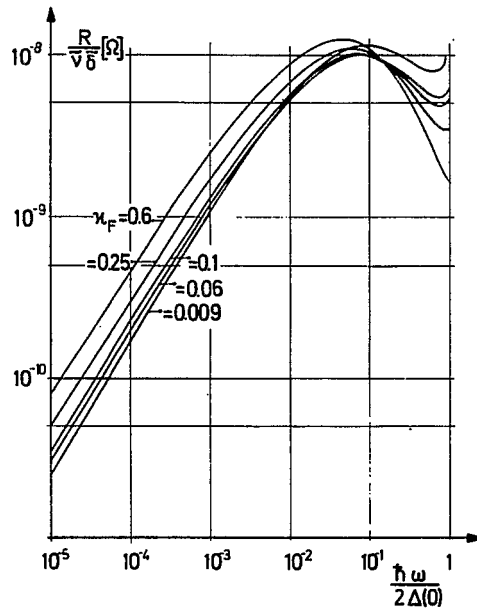


Fig. 4. Surface resistance as function of frequency for various  $\kappa_F$  (diffuse reflection,  $T/T_c = 0.2$ ,  $\Delta(0)/kT_c = 1.75$ ,  $\tilde{\nu} = \nu/\text{GHz}$ ,  $\tilde{\delta} = \delta_L(0)/100 \text{ \AA}$ ).

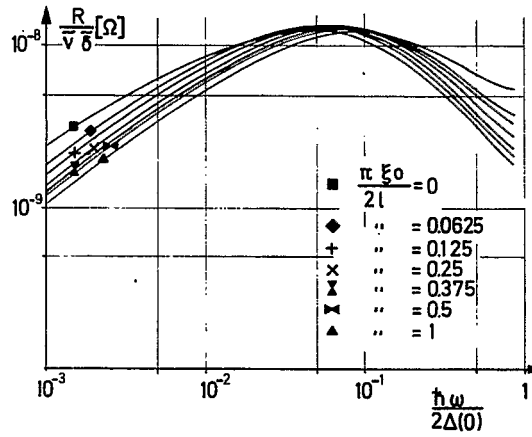


Fig. 5. Surface resistance as function of frequency for various  $\ell$  (diffuse reflection,  $T/T_c = 0.2$ ,  $\Delta(0)/kT_c = 1.75$ ,  $\kappa_F = 0.6$ ,  $\tilde{\nu} = \nu/\text{GHz}$ ,  $\tilde{\delta} = \delta_L(0)/100 \text{ \AA}$ ).

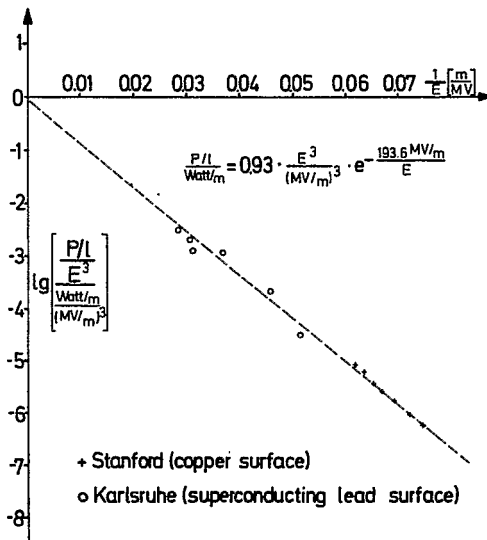


Fig. 6. Fowler-Nordheim plot of field emission losses in a superconducting lead-plated resonator.

# AN ENRICHED PARTICLE BEAM USING SUPERCONDUCTING RF DEFLECTORS\*

H.N. Brown  
Brookhaven National Laboratory  
Upton, New York

Although many in the audience are closely associated with work in high energy physics, there are others who are concentrating more on the physics of superconductors per se, and so it seems appropriate to review briefly the problem of particle separation as it is encountered in high energy physics experiments.

## I. IDENTIFICATION AND SEPARATION OF PARTICLE TYPES

When produced at the target of an accelerator, a beam of secondary particles, directed into the apparatus of a high energy physics experiment, contains several different types of particles. Usually, the experiment concerns the interaction of one particular type (at a given momentum) with the nuclei of a secondary target placed in the beam. These particles differ from one another in numerous characteristics, but unfortunately many of these differences are manifested only in ways which are destructive of the particles themselves. Therefore, the solution to the problem of identifying different particle types in the beam boils down to a determination of the mass of the particle. This is done, indirectly, from the relation  $p = m_i v_i$ . For the given momentum, a velocity determination yields the mass  $m_i$ . Difficulties arise at high momenta, for then this relation becomes

$$p = \frac{m_i v_i}{\sqrt{1 - (v_i/c)^2}}$$

from which

$$\frac{1}{v_i} = \frac{1}{c} \sqrt{1 + \left(\frac{m_i c}{p}\right)^2}$$

and hence, when  $p \gg m_i c$ ,  $v_i$  is only slightly different for two different particles whose rest masses  $m_i$  have a large relative difference. Nevertheless, these small differences in velocity can be detected (e.g., by time-of-flight measurements or Cerenkov counters) and used to identify particle types in flight. However, in a particle beam which may contain 100 times as many  $\pi$ -mesons as K-mesons, it may not be sufficient merely to identify particle types. Physical separation and removal of unwanted particles may be required. This is clearly true in a bubble chamber experiment requiring a K-meson beam - the thousands of superimposed pion tracks in each picture would be intolerable. A counter experiment (by this I mean one which gathers its data by means of detectors such as spark chambers, scintillation counters, Cerenkov counters, etc., which can be triggered after the identification of an incoming beam particle) encounters difficulties when the rates become so high that many wanted and unwanted particles coincide within the resolving time of the apparatus. So here too, actual physical

---

\*Work performed under the auspices of the U.S. Atomic Energy Commission.

separation of particle types becomes desirable in order to detect rare interactions caused by the wanted particle, and it is with this type of experiment that we shall primarily be concerned here.

In order to separate an unwanted particle, we shall wish to subject it to a force which can change its original motion in a way dependent upon its velocity. Proposals have been made to do this by means of longitudinal forces, but let us here restrict the discussion to transverse forces producing an angular change in the direction of flight. First of all, we see that a simple static magnetic field will not suffice, for in this case

$$\frac{d\theta_i}{ds} = \frac{e B(s)}{p}$$

where  $s$  is the coordinate along the trajectory. Thus the deflection depends only on the momentum of the particle and, in fact, it is in this way that the momentum of the beam particles is established to begin with. In a static electric field

$$\frac{d\theta_i}{ds} = \frac{e E(s)}{p v_i}$$

for small angles of deflection. This is quite a practical solution and is employed in the many electrostatic separators now in use at various laboratories. But note that the separation, that is, the difference in angular deflection between two particle types, goes like

$$\theta_i - \theta_j \sim \frac{eE\ell}{p} \left( \frac{1}{v_i} - \frac{1}{v_j} \right)$$

where

$$\left( \frac{1}{v_i} - \frac{1}{v_j} \right) \cong \frac{1}{c} \frac{(m_i c)^2 - (m_j c)^2}{p^2}$$

Hence, the total deflecting capability of the field,  $eE\ell/pv$ , is reduced by the factor  $(1/v_i - 1/v_j)$ , which typically ranges from 0.01 to 0.001 at momenta of interest here. Thus the electrostatic separator rapidly becomes inefficient at high momenta since  $\theta_i - \theta_j \propto 1/p^3$ .

Considering next a time-varying electric field, we may write

$$\frac{d\theta_i}{ds} = \frac{e E(s)}{p v_i} e^{i(\omega s/v_i)}$$

Here, the  $1/v_i$  factor in the amplitude will be unimportant at large momenta, but for high frequencies the phase  $\omega s/v_i$  can now be made to differ by amounts comparable to  $\pi$  for different particle types  $i$ . Therefore, by proper phasing, the separation angle can be on the order of  $eE\ell/pv$  and it decreases only as  $1/p$ . Let us now turn to a practical embodiment of this idea.

## II. PRACTICAL UTILIZATION OF HIGH FREQUENCY DEFLECTING FIELDS

The rf separator arrangement to be considered here was put forward by Panofsky in 1959,<sup>1</sup> and in its simplest form is the basis of the presently operating short pulse, room temperature separators at CERN and Brookhaven.<sup>2,3</sup>

Figure 1 illustrates the principle of this method of separation. The secondary beam, with momentum  $p$  previously determined, enters a first rf resonant cavity whose transverse electric field is in the vertical direction, for example. If the cavity is relatively short, all particle types passing the cavity at time  $t$  will be deflected by an amount

$$\hat{\theta}_i = \frac{eE_i \ell}{p v_i} e^{i\omega t}$$

where  $eE_i$  is the effective transverse force acting upon the particle  $i$  during its passage through the cavity. At high momenta, if the phase velocity of the field in the cavity is close to  $c$ , then the variation of  $E_i$  is slight from one particle type to another. After traversing a distance  $L$ , which includes an imaging section to economize on aperture, the particles encounter another rf deflector whose excitation phase is  $\phi$  with respect to the first. They are therefore left with a net angular departure from their original directions of

$$\theta_i = \frac{eE_i \ell}{p v_i} e^{i\omega t} \left[ e^{i[\phi + (\omega L/v_i)]} - 1 \right].$$

In order to eliminate a certain particle type, say  $\pi$ 's, we choose  $\phi = -\omega L/v_\pi$  so that the second deflector just cancels the effect of the first one to give  $\theta_\pi = 0$ . These unwanted particles then can be caused to strike an absorber or "stopper" and be removed from the beam.

With  $\phi$  as given, another wanted particle type,  $K$ , will have a net deflection of

$$\theta_K = \left[ 2i \frac{eE_K \ell}{p v_K} \sin \frac{1}{2} \omega L \left( \frac{1}{v_K} - \frac{1}{v_\pi} \right) \right] e^{i\omega t} e^{i\frac{1}{2}\omega L(1/v_K - 1/v_\pi)}$$

Thus, if the relative phase slip  $\omega L(1/v_K - 1/v_\pi)$  between wanted and unwanted particles is close to  $(\pi \times \text{odd integer})$ , the wanted ones will emerge with approximately twice the deflection amplitude of a single cavity. Many of them will be able to pass easily above or below the edges of the absorber mentioned above and proceed into the experimental apparatus. Of course, a fraction of the wanted particles which traverse the cavities when the fields are near zero will strike the stopper and be lost. The criterion for best  $\pi$ -K separation then is

$$\frac{L}{\lambda} \left( \frac{1}{\beta_K} - \frac{1}{\beta_\pi} \right) = n + \frac{1}{2}; \quad \{n = 0, 1, 2, \dots\}$$

---

1. See, for example, B.W. Montague, Progr. Nucl. Techn. & Instr. (North-Holland Publishing Co., 1968), Vol. 3, p. 3.

2. W. Schnell, Report CERN 61-5 (1961).

3. H. Hahn, H.J. Halama, and H.W.J. Foelsche, Brookhaven National Laboratory, Accelerator Dept. Report AADD-91 (1965).



where  $\lambda$  is the free space wavelength corresponding to the excitation frequency  $\omega$  of the cavities, and  $\beta_i = v_i/c$ .

Now in a beam of positively charged particles, there are copious quantities of protons as well as pions. In this case it would be desirable to eliminate protons as well to obtain a more pure  $K^+$  beam. By changing subscript K to subscript p, we see that

$$\theta_p = \left[ 2i \frac{eE_p \ell}{p v_p} \sin \frac{1}{2} \omega L \left( \frac{1}{v_p} - \frac{1}{v_\pi} \right) \right] e^{i\omega t} e^{i\frac{1}{2}\omega L(1/v_p - 1/v_\pi)}$$

It is clear that  $\theta_p$  can be made zero too (we have already required  $\theta_\pi = 0$ ) if the  $\pi$ -p relative phase slip is ( $2\pi \times \text{integer}$ ). Hence, to reject both pions and protons (double rejection):

$$\frac{L}{\lambda} \left( \frac{1}{\beta_p} - \frac{1}{\beta_\pi} \right) = n ; \quad \{n = 1, 2, 3, \dots\}$$

Figure 2 is a plot of net deflection amplitude after the second cavity as a function of relative momentum ( $p/p_0$ ). Here,  $p_0$  has been chosen as the highest momentum at which double ( $\pi$ -p) rejection is obtained. Hence, the curve labeled  $\pi$ -p goes to zero at  $(p/p_0) = 1$ . Although, for definiteness, it has been assumed that pions were to be eliminated, this curve applies equally well if protons are the unwanted particle. The only difference will lie in the empirically tuned phase difference  $\phi$  between the two cavities. Maximum kaon deflection, on the same momentum scale, then occurs near  $(p/p_0) = 0.7$ . It should be noted that the net deflection amplitude has been normalized by the factor  $eE\ell/pc\beta$ , i.e., by the deflection amplitude of a single cavity, which varies as  $1/p$ . Hence the absolute deflection amplitude actually obtained would be  $(p_0/p)$  times the ordinate of the appropriate curve.

### III. PROPOSED ENRICHED PARTICLE BEAM

As stated above, the primary concern here is the use of rf cavities to produce separated, or at least enriched, particle beams for use by counter experiments. Because of the limitations encountered due to high flux rates, the duration of the beam entering the detectors must be as long and uniform as possible. Here at the AGS this duration is as much as 0.5 sec out of each 2.4 sec, the common repetition period of the accelerator. It is for this reason that superconducting cavities become attractive, since the rf source required for the very high average power level of a room temperature cavity would be a formidable problem. For example, this might amount to  $10 \text{ MW} \times 0.5/2.4 = 2 \text{ MW}$  average power.

For the initial employment of long pulse, superconducting separators at Brookhaven, we propose to utilize the relatively simple two-cavity arrangement outlined above.<sup>4</sup> The complete beam may conveniently be divided into four sections:

1. Source emittance definition - momentum band, transverse phase space.
2. Angular separation.
3. Purification.
4. Matching to detector.

As indicated in Fig. 3, sections 1 and 2 are distinct, in the present arrangement, but 3 and 4 overlap.

4. H. Hahn and H.J. Halama, IEEE Trans. Nucl. Sci. NS-14, No. 3, 356 (1967).

## 1. Source Emittance Definition

Before defining the source, the admittance of the separation section must be examined. As we have seen, for a given separation condition and momentum (e.g., double  $\pi$ -p rejection at 16 GeV/c), the interdeflector length  $L$  is proportional to the wavelength (e.g.,  $L = 593 \lambda$  for the cited condition). Since our experimental space is not unlimited, we have foregone the gain in flux possible by using large aperture, low frequency cavities,<sup>4</sup> and have chosen the S-band frequency to shorten the beam length and benefit from the easy availability of rf sources and instrumentation in that range. Hence,  $\lambda = 10.5$  cm and we have assumed a conservative iris aperture of  $2a = 0.4 \lambda = 4.2$  cm.

As is commonly done, we restrict the beam in the deflectors to lie within the square circumscribed by the iris aperture to avoid scattering from the edges. Assuming a cavity length of 3 m, we then have the phase-space admittance diagram shown in Fig. 4 for the first deflector. The maximum area fillable by a simple optical system is 14.7 cm·mrad in the horizontal plane. In the vertical plane, the maximum usable admittance is set by the maximum cavity deflection and the desired separation ratio, that is, the ratio of the deflection amplitude to the intrinsic angular spread in the beam at the cavity. The expected transverse impulse imparted by the cavity is about 12 MeV/c. Hence, the deflection amplitude expected is about 0.6 mrad at a momentum of 20 GeV/c. Since we wish to use the enriched beam over a wide momentum range, the separation conditions will not always be optimum, so it would seem advisable to keep the angular width of the beam small. If this is taken as  $0.5 \times$  deflection amplitude, the resulting phase space available is 0.75 cm·mrad. These admittance areas provide bounds to be considered in designing the source emittance section. Again:

$$\begin{aligned} A_H &< 14.7 \text{ cm}\cdot\text{mrad} \\ A_V &\cong 0.75 \text{ cm}\cdot\text{mrad} \end{aligned}$$

This beam would be constructed from a target in the slow external beam of the AGS, with its axis at an angle of  $0^\circ$  with respect to the primary protons. The target will be assumed to be 0.25 cm square. The separator admittances therefore indicate maximum acceptance angles at the target of

$$\left. \begin{aligned} \Delta x'_t &= 59 \text{ mrad} \\ \Delta y'_t &= 3.0 \text{ mrad} \end{aligned} \right\} \text{ full width}$$

It has turned out to be difficult to achieve the full horizontal acceptance. Figure 5 illustrates the source definition section which employs a doublet composed of three N3Q36 quadrupoles immediately following the target to produce a "parallel" beam in both planes at the first turning point. With this arrangement

$$\left. \begin{aligned} \Delta x'_t &= 26 \text{ mrad} \\ \Delta y'_t &= 3.0 \text{ mrad} \end{aligned} \right\} \Delta\Omega = 78 \mu\text{sr} \quad \left. \begin{aligned} f_H &= 0.975 \text{ m} \\ f_V &= 8.71 \text{ m} \end{aligned} \right\} \text{ at central momentum,}$$

where  $f_H$  and  $f_V$  are the horizontal and vertical focal lengths into the bending magnets D1 and D2.

These first two bending magnets, (D1, D2), cause a momentum dispersion which is cancelled by focusing this first turning point upon a second identical point of dispersion at (D3, D4) by the use of four 8Q48 and two 8Q24 quadrupoles. The momentum band passed is determined before dispersion cancellation by a momentum slit at the horizontal target image between the two turning points. The spatial dispersion there is 0.5 cm/%. It is planned to employ a momentum band of up to  $\Delta p/p = 5\%$  full width.

At the first deflector, immediately following (D3, D4), the optical system has again produced a parallel beam with the same horizontal focal length, target into deflector, as before,  $f_H = 0.975$  m.

Vertically, an image of the target is also formed at the momentum slit position, so that a slit there can redefine the vertical width of the source. This slit then also sets the angular width of the "parallel" beam in the first deflector:

$$\begin{aligned} f_{v \text{ mom. slit} \rightarrow \text{RF1}} &= 18.2 \text{ m} \\ f_{v \text{ target} \rightarrow \text{RF1}} &= 8.7 \text{ m} \end{aligned}$$

Thus, with the inclusion of a suitable solid angle defining aperture between Q2 and Q3, the emittance of the source definition section is

$$\begin{aligned} \Delta x_{\text{RF1}} &= 2.5 \text{ cm} & \Delta y_{\text{RF1}} &= 2.6 \text{ cm} \\ \Delta x'_{\text{RF1}} &= 2.6 \text{ mrad} & \Delta y'_{\text{RF1}} &= 0.3 \text{ mrad} \end{aligned}$$

at the central momentum. For off-momentum rays, the chromatic aberration in the horizontal plane is rather pronounced, and so to control the illumination of the iris edges it will be advisable to mask them with an aperture near the point which is imaged onto the cavity (this mask could be at the exit of D2). In addition, a mask should be placed immediately in front of RF1.

## 2. Angular Separation Section

The admittance to the first cavity has been discussed. The next parameter to be fixed is the interdeflector spacing. This has been taken as the shortest distance which will allow double  $\pi$ -p rejection from a K-meson beam at 16.0 GeV/c:

$$\frac{L}{\lambda} = \frac{1}{\left(\frac{1}{\beta_p} - \frac{1}{\beta_\pi}\right)} \doteq \frac{1}{(m_p c)^2 - (m_\pi c)^2} = 592.8$$

$$L = 62.24 \text{ m (for } \lambda = 10.5 \text{ cm) .}$$

As assumed earlier, since the cavities are identical, the deflected particle at RF1 is to be refocused upon the second deflector RF2 with a magnification of -1. As has become common practice, in order to reproduce the phase space of RF1 in RF2 to avoid beam loss, the complete transform between the two cavities has been made equal to the negative unity transform in both planes. (Though not strictly necessary now in the horizontal plane, it will be more important if future improvements allow the RF1 admittance area to be filled more completely.) The optical arrangement chosen for this is a symmetrical sextuplet of 8Q48 quadrupoles shown in Fig. 6. The sextuplet seems to require less power than the quadruplet solution would. It has the added advantages of double horizontal and vertical imaging at the center, which makes instrumentation for focusing the beam simpler, and the transform matrix element  $V_{22} = -1$ , which determines the slope of the deflected particle at RF2, does not depend on momentum to first order.

Referring to Fig. 2, the approximate ranges in momentum available for different particle types have been estimated and are shown in Fig. 7. The dotted lines indicate extended ranges which may be possible if one can tolerate higher impurities. For instance, good  $K^+$  enrichment is obtained only in rather narrow bands, but if single rejection of  $\pi^+$  or  $p^+$  proves to be sufficient the larger  $K^-$  range can be covered.

There are three imperfections in the angular separation section which should be considered. The first is the chromatic aberration in the interdeflector optics. The most important term in the vertical transform matrix is  $V_{22} \cong -1 + 5.6 (\delta p/p)^2$  plus higher order terms, as mentioned previously. (In fact, this is true of  $V_{11}$  also.) Because of this, the cancellation of the pion deflection, for example, is unimpaired. The off-diagonal terms depend on the first power of  $(\delta p/p)$  and cause some mismatch with the admittance of the second deflector, but the loss and scattering from the cavity irises is not serious.

The second possible source of error in phasing of the unwanted particles is due to the increased path length,  $\delta L$ , of off-axis rays in the interdeflector region. Since an increment of path length is

$$ds + (dx^2 + dy^2 + dz^2)^{1/2} = (1 + x'^2 + y'^2)^{1/2} dz \cong dz + \frac{1}{2} (x'^2 + y'^2) dz ,$$

$\delta L$  may be expressed as

$$\delta L \cong \frac{1}{2} \int_0^L (x'^2 + y'^2) dz .$$

The extreme rays in this beam have

$$\delta L \leq 0.0025 L .$$

This is not serious. For double  $\pi$ -p rejection with  $n = 2$  (i.e.,  $4\pi$  phase slip between pions and protons), this corresponds to a phase error of  $1.8^\circ$  and a maximum net deflection error of  $\sim 3\%$  of the single cavity amplitude.

Phase error due to velocity differences within the transmitted momentum band are the most serious. The change in deflection amplitude  $\theta_i$  (in terms of unit single cavity deflection) is

$$\delta \theta_i \cong - \left[ \pi \frac{L}{\lambda} \frac{(m_i c)^2}{p^2} \beta_i \cos \frac{1}{2} \left( \frac{2\pi L}{\lambda \beta_i} + \varphi \right) \right] \frac{\delta p}{p} ,$$

which is clearly largest for protons ( $m_i = m_p$ ). At double  $\pi$ -p rejection,

$$\delta \theta_p \cong 2\pi n \left( \frac{m_p^2}{m_p^2 - m_\pi^2} \right) \beta_p \frac{\delta p}{p} .$$

Table I illustrates the effect of this error on the effective separation ratio for the first three double  $\pi$ -p rejection points.

TABLE I

n =	1	2	3
p (GeV/c)	16.0	11.2	9.3
$\theta_K$ (mrad)	0.65	1.28	1.00
$\eta_0$	2.2	4.3	3.3
$\delta \theta_p$ (mrad)	0.12	0.34	0.62
$(\Delta y')_{\text{prot.}}$ (mrad)	0.42	0.64	0.92
$\eta_{\text{eff.}}$	1.6	2.0	1.1

In the table,  $\theta_K$  is the net kaon deflection,  $\eta_0$  the nominal separation factor ( $\theta_K/0.3$  mrad),  $\Delta y'_{\text{prot.}}$  the increased angular width of the proton beam at the second deflector ( $\Delta y'_{\text{prot.}} = 0.3 + \delta\theta_p$  mrad, a liberal estimate), and  $\eta_{\text{eff.}}$  the effective separation ratio of kaons from protons.

### 3. Purification Section

The angularly separated beam from RF2 is focused in both planes onto the stopper located at the focal plane of the doublet (Q16, Q17) of Fig. 8. This doublet has  $f_H = 5.1$  m and  $f_V = 18.0$  m. A 50 cm length of Hevimet will cause about 90% of any undeflected, unwanted particles hitting it to suffer inelastic collisions and the rest, through ionization, will lose 1.2 GeV or more in energy. Thus, unwanted particles will lose 6% or more in momentum and be scattered, on the average, by 8 mrad or more. A momentum-dispersive system can then separate the wanted particles, with  $\Delta p/p = 5\%$ , from the unwanted particles 6% lower in momentum if the system has a suitable momentum separation ratio, i.e., if the intrinsic beam width corresponds to, say, 2% or less in momentum. The dispersive section may also have an aperture closely matched to the wanted beam so that some unwanted particles are removed quickly as a result of scattering in the stopper.

The rest of the purification section thus consists of an arrangement with  $f_H = 18$  m into the two bending magnets (D5, D6) and out again ( $f_H = 18.0$  m) to the next horizontal focus where the final momentum slit is located. There is also a second stopper here upon which any stubborn vertically focused unwanted particles can be eliminated. The two vertical focal lengths are each 5.1 m.

### 4. Matching Section

As an example, a matching section is included which brings the beam at the end into essentially the same vertical phase space it occupied in RF2, namely  $\Delta y = 2.5$  cm and  $\Delta y' = 0.3 + 2$  mrad or so depending on final net deflections at RF2. There is no "hole" in the spatial distribution. Horizontally the spatial momentum dispersion  $\partial x/\partial p$  is zero, but an angular dispersion remains. It amounts to about a 15 mrad spread. If objectionable, a final set of bending magnets would be required to remove it. The horizontal extent here is about 2.5 cm as in RF2.

## IV. FLUX ESTIMATES

As an example of particle fluxes in this beam, the  $\pi^-$ ,  $K^-$ , and  $\bar{p}$  yields at the end are shown as a function of momentum in Fig. 9. These curves are based on the empirical curves of Sanford and Wang.<sup>5</sup> They have not been corrected for stopper losses. The efficiency of passage around the stopper varies with the separation factor  $\eta_M$  approximately as shown in Fig. 10. This is the result of assuming that the vertical distribution at the stopper is trapezoidal and that the stopper just covers its base width.

## V. PRIMARY PROTON DUMP

In the beam design just described, the primary protons which do not interact in the target pass through the first quadrupoles into the bending magnets D1 and D2. If these magnets should be set for positive secondaries of 6.5 to 20 GeV/c, the 28 GeV/c

---

5. J.R. Sanford and C.L. Wang, Brookhaven National Laboratory, Accelerator Dept. Reports JRS/CLW-1 and JRS/CLW-2 (1967).

(assumed) primaries would pass through and be dumped in an absorber between D2 and Q4. For a negative secondary beam, the dump occurs mostly inside D2. The situation can be helped by offsetting D2 laterally to allow more of the primaries to pass through, but nevertheless the aperture of D2 would have to be packed with absorber to reduce the irradiation of its copper coils as much as possible.

## VI. AREAS FOR IMPROVEMENT

An increased solid angle accepted by the beam would be helpful. In principle, the rf cavities would allow up to 180  $\mu$ sr, using the same 0.25 cm square target assumed. This much would probably be difficult to obtain, but a factor of two increase may be possible. In doing so, the total beam length should not be increased very much, and standard magnet types should be employed.

Although the maximum momentum band of 5% seems to be a reasonable one to retain, improved flexibility would result if the momentum separation factor  $\eta_p$  could be increased. At present it is equal to unity at  $\Delta p/p = 2.5\%$ , which is, therefore, the lower limit on the momentum band. A smaller target, say 0.1 cm, would reduce this to 1.0%, but it would be attractive to get to even lower values, say 0.5 to 0.25%, for certain experiments which might require it. The need for this can sometimes be circumvented by operating with the full 5% band but defining the momenta of individual particles in the enriched beam by employing hodoscopes or wire plane chambers in conjunction with the momentum analysis done in the purification section. Here again, an improved momentum resolution would be needed. As before, we would prefer to keep the beam length to a minimum.

The primary proton beam dumping situation is not ideal. Further investigation should be done to determine if these protons could be absorbed in a place more removed from beam components.

## VII. SUMMARY OF BEAM PARAMETERS

Momentum	16 GeV/c for $\pi$ -p rejection 20 GeV/c maximum
Momentum band	$\pm 1.25\%$ to $\pm 2.5\%$
Acceptance angles	$\pm 13$ mrad horizontal, at $p_0$ $\pm 1.5$ mrad vertical, at $p_0$
Solid angles	78 $\mu$ sr at $p_0$ 56 $\mu$ sr over 5% momentum band
Length, primary to secondary target	162 m
Cavity frequency	2.865 GHz
Iris aperture	4.1 cm diam
Cavity length	3 m
Transverse impulse	12 MeV/c
Number of rf cavities	2
Interdeflector separation	62 m
Magnet complement	3 - N3Q36 6 - 8Q24 16 - 8Q48 6 - 18D72

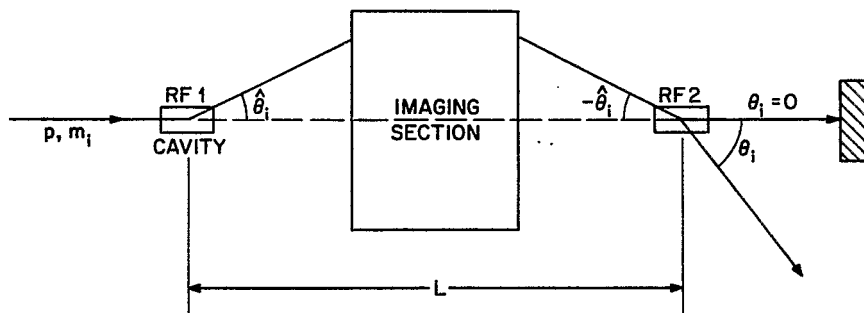


Fig. 1. Schematic rf separation.

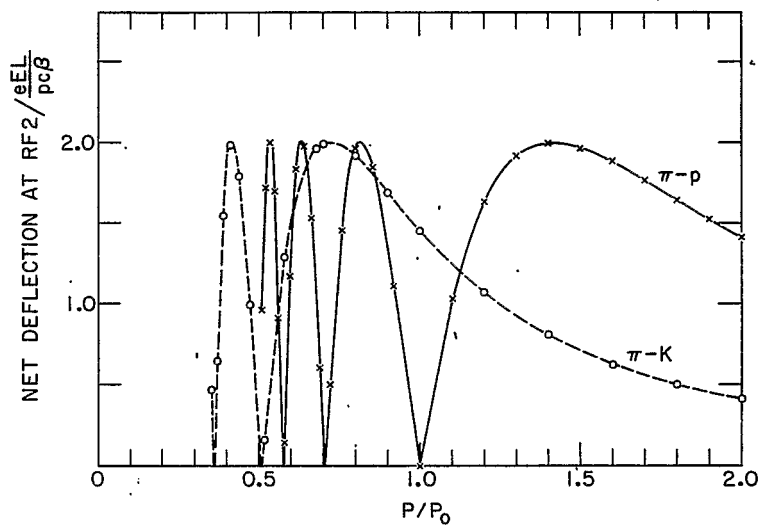


Fig. 2. Net deflection amplitudes following a two-cavity separator vs momentum.

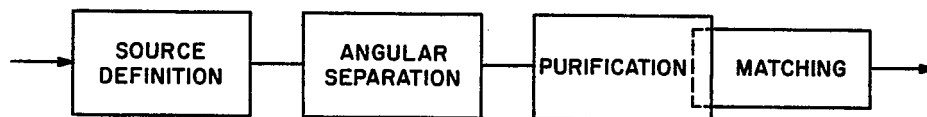


Fig. 3. Block diagram of proposed beam.

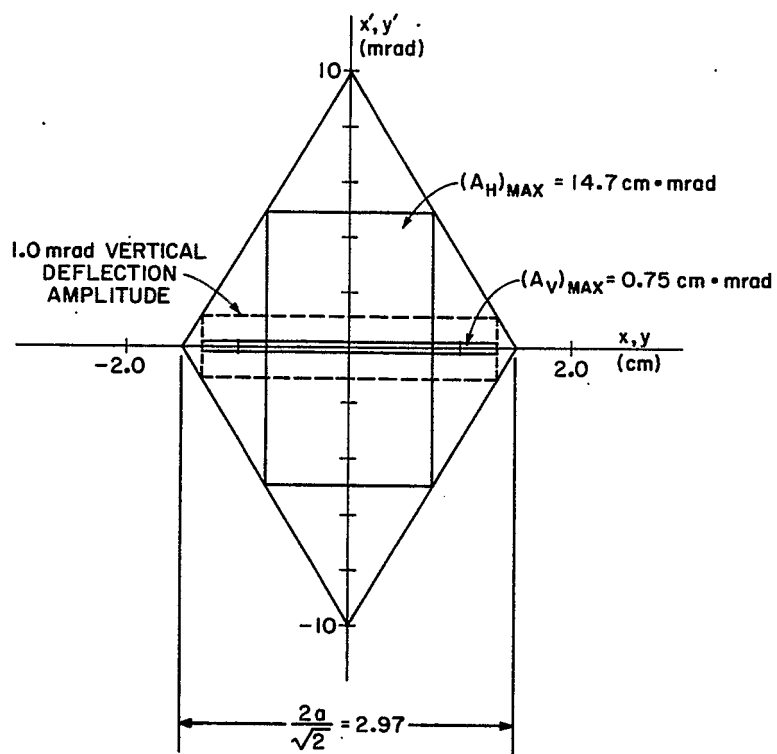


Fig. 4. Rf cavity admittance diagram.



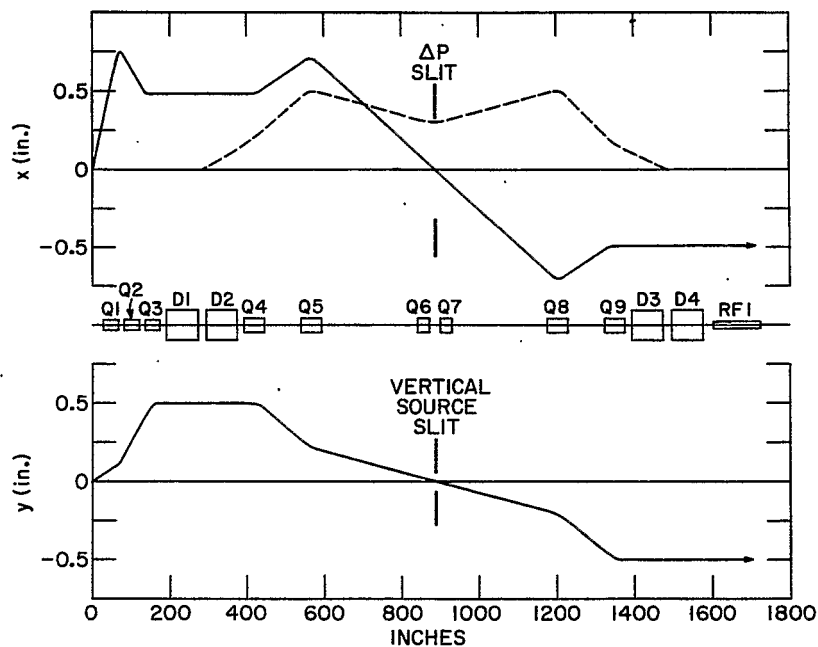


Fig. 5. Component layout and ray trace for source definition section.

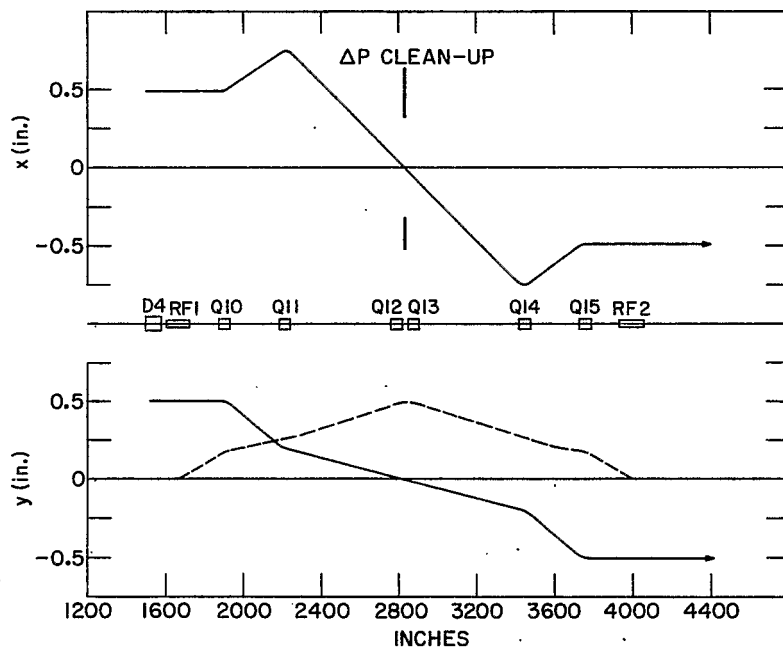


Fig. 6. Component layout and ray trace for interdeflector section.

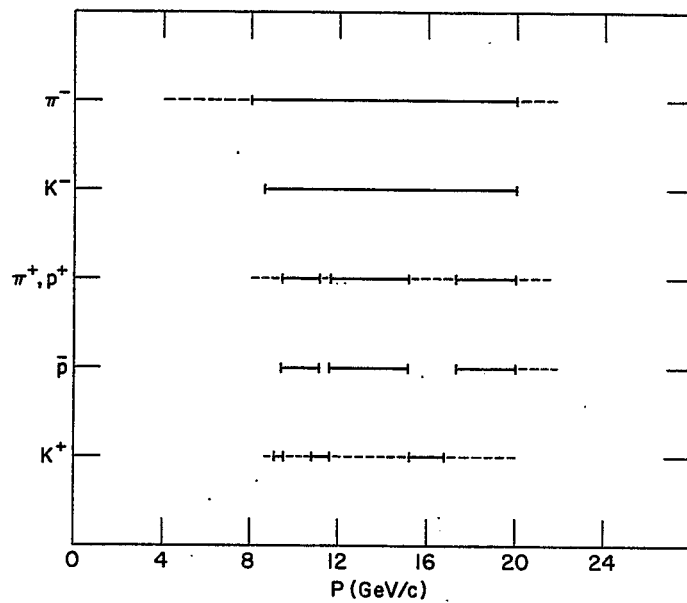


Fig. 7. Operating momentum ranges.

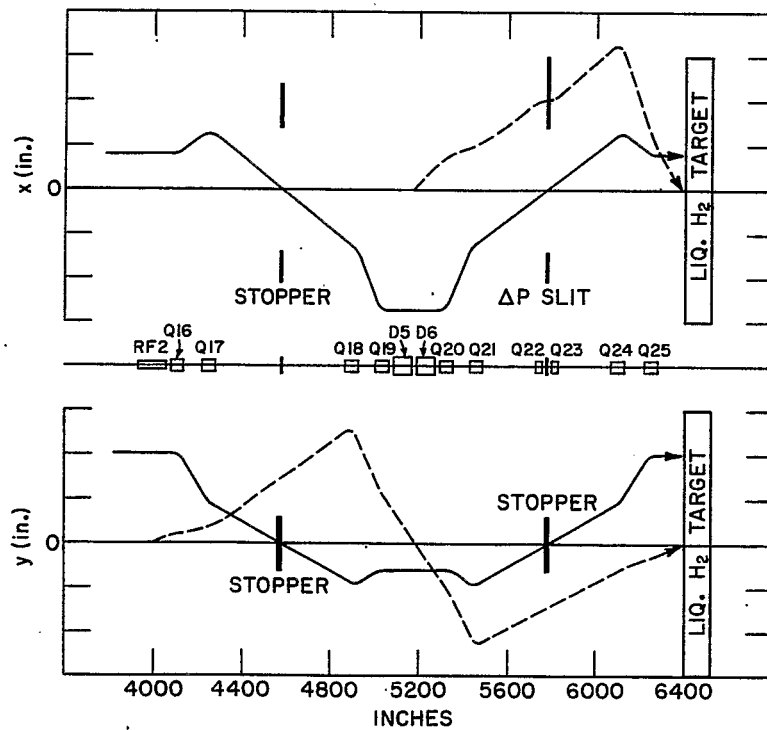


Fig. 8. Component layout and ray trace for purification and matching section.

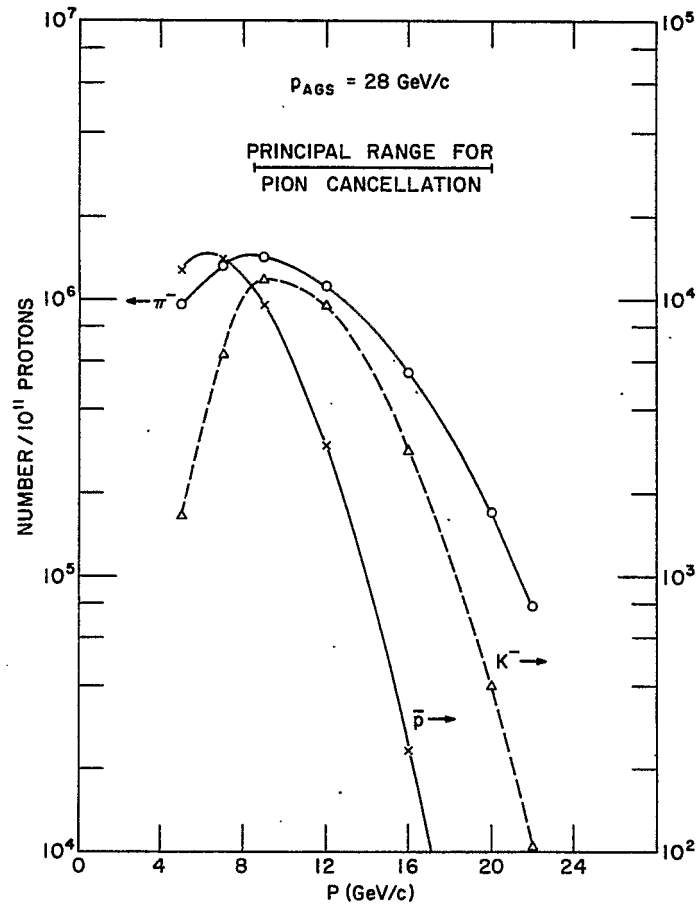


Fig. 9. Particle fluxes at end of beam (stopper passage efficiency not included).

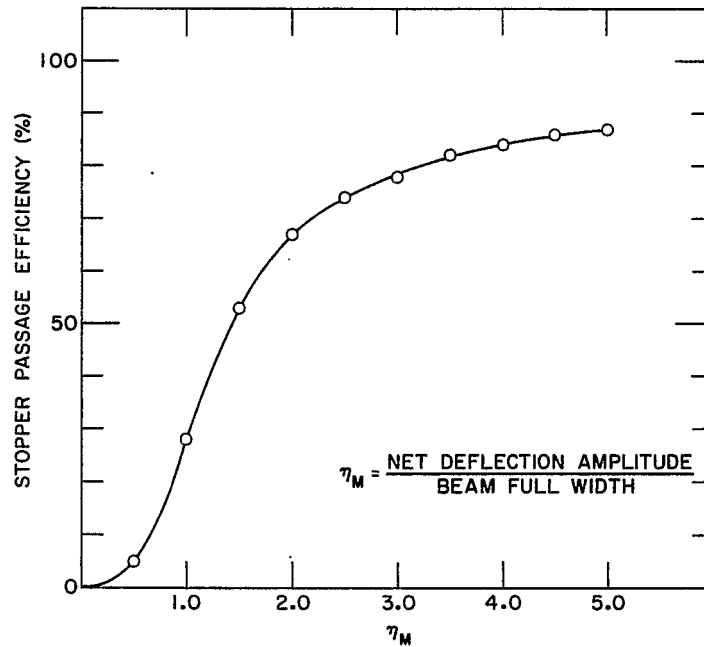


Fig. 10. Stopper passage efficiency vs momentum.

# DESIGN PROBLEMS IN SUPERCONDUCTING RF BEAM SEPARATORS\*

H.J. Halama  
Brookhaven National Laboratory  
Upton, New York

## I. INTRODUCTION

Rf beam separators have now been used in high energy physics research for several years both at Brookhaven and at CERN. They have extended the range of experiments from 6 GeV/c (practical limit of electrostatic separators) to over 20 GeV/c. The magnitude of the deflecting field necessary for successful production of separated beams in this momentum range requires a large amount of microwave power. As a result short pulse operation only is possible, limiting the experiments to bubble chambers. The increased intensity of the converted AGS will make separated counter beams desirable in a few years. Counter experiments require long pulse or CW operation which must be achieved with unconventional techniques. At the present time the very low power losses of pure superconductors appear to provide a unique solution to the problem.

There are several important properties that the superconducting material must possess to be usable in rf separators. The most important are:

- 1) Low surface resistance, which depends on the intrinsic parameters of the material and the metallurgical condition of the surface.
- 2) High ac critical magnetic field.
- 3) High critical temperature.
- 4) High voltage level at which breakdown or appreciable field emission occurs.
- 5) Possibility to construct a complicated iris-loaded structure.

Extensive research on the rf properties of pure lead and niobium has, therefore, been conducted at several laboratories involved in the design studies of either linacs or rf separators. Their results were discussed in previous sessions at this Summer Study. In this paper we shall be concerned primarily with practical problems existing in the Panofsky-Schnell type of rf separator employing two superconducting cavities.

Although there are many similarities between the rf separator and the electron linac the design philosophy differs considerably. The main difference stems from the field configuration of the  $HEM_{11}$  mode as compared to the symmetrical  $TM_{01}$  mode of linear accelerators.<sup>1</sup> A very important practical difference is the absence of beam loading, which permits a simpler design of the coupling mechanism, the transmission line system and the driver amplifier. Furthermore, since the total transverse momentum gain for the proposed separator is about 10 MeV/c per deflector for a period of ~ 200 msec, the device would still be very useful for physics experiments even if the power dissipated were considerably larger than anticipated. Hence the rf separator appears to be the ideal device on which to test superconductivity at high frequencies.

---

\*Work performed under the auspices of the U.S. Atomic Energy Commission.

1. H. Hahn and H.J. Halama, Rev. Sci. Instr. 36, 1788 (1965).

Before we start considering various design approaches of practical systems in some detail, let us write down the principal parameters of the proposed Brookhaven superconducting separator (Table I), for which the beam design is being carried out by Brown.<sup>2</sup> The design momentum  $p_0$  refers here to the highest momentum at which two-contaminant rejection takes place. Useful purified counter beams can, however, be realized up to 20 GeV/c. The selection of a rather high frequency  $f_0 = 2.86$  GHz is dictated primarily by the available space in the AGS experimental area. The choice of the rest of the parameters is the subject of this paper.

TABLE I  
Principal Parameters of Superconducting Rf Beam Separator

Design momentum, $p_0$	16 GeV/c
Design wavelength, $\lambda_0$	10.5 cm
$f_0$	2.86 GHz
Interdeflector spacing, $L$	62 m
Beam hole diameter, $2a$	4.2 cm
Deflector length	3 m
Deflecting field, $E_0$	4 MV/m
Group velocity, $v_g$	- 0.04 c
Shunt impedance, $R_{SW}$	$5 \times 10^{11} \Omega/\text{m}$
Improvement factor, $I$	$5 \times 10^4$
Operating temperature	1.85°K
Duty factor	CW
Dissipated power	100 W
Refrigerator input power	300 kW

## II. GENERAL DESIGN CONSIDERATIONS

In this section we will investigate the effects of operating frequency, improvement factor and peak field on the design of a separator.

The selection of operating frequency plays a very important part in the deflector design and a lower frequency offers some outstanding advantages:

- 1) Since  $Q_0 \propto \lambda_0^2$ , a large saving in the cryostat and operating costs is realized.
- 2) A larger ratio of excited-to-unexcited cell length in the AP structure is possible, resulting in increased shunt impedance and smaller peak fields.
- 3) Larger beam hole results in larger acceptance.
- 4) Larger absolute tolerances.

---

2. H.N. Brown, these Proceedings, p. 136.

- 5) Larger surface area for power dissipation.
- 6) Easier plating.

The disadvantages of a lower frequency would be the higher cost of material which is important if niobium is used, and the required longer interdeflector distance which becomes considerable at high momenta.

The success of the superconducting rf separator will ultimately depend on reducing the rf losses in the deflecting cavities. This reduction is most readily expressed by the improvement factor  $I = Q_o/Q_{cu}$  300. Improvement factors  $> 10^5$  have been achieved in simple structures with either plated lead or solid Nb below 2°K. If the same figures are reached in more complicated structures such as iris-loaded waveguides, the total rf power dissipation in the proposed deflectors will be less than 100 W. Since the surface resistance decreases rapidly as the temperature is lowered below  $T_c$ , the superconducting materials with high  $T_c$  such as Pb, with  $T_c = 7.2^\circ\text{K}$ , and Nb, with  $T_c = 8.8^\circ\text{K}$ , must be selected. Furthermore, the low temperature also improves the frequency stability and insures adequate cooling of the structure due to the superfluid phase of helium below the  $\lambda$ -point ( $2.18^\circ\text{K}$ ).

The equivalent deflecting field is limited either by  $H_{c1}$  or the peak electric field at which a breakdown or appreciable field emission occurs.  $H_{c1}$  depends on temperature,  $T$ , according to

$$H_{c1} = H_c(0) \left[ 1 - \left( \frac{T}{T_c} \right)^2 \right] \quad (1)$$

$H_c(0)$  for Pb  $\approx 800$  G and  $H_c(0)$  for Nb  $\approx 1960$  G. The ac critical field of type I superconductors<sup>3,4</sup> does not differ significantly from  $H_{c1}$ . This is not, however, the case for Nb, a type II superconductor, where significantly smaller values in the range of 261 to 436 G have been measured.<sup>4</sup>

The peak electric field,  $\hat{E}$ , at which appreciable field emission or breakdown occurs, is strongly dependent on the surface condition. No limitation in  $\hat{E}$  was observed in Nb. The only published value for lead-plated iris-loaded cavities is  $\sim 15$  MV/m and will therefore be considered as a limit on the strength of the deflecting field.<sup>5</sup> It should, however, be mentioned that the Karlsruhe group measured no appreciable field emission below 20 MV/m in a coaxial cavity.<sup>6</sup> Until more data are gathered on plated lead, we will adopt the pessimistic limit of 15 MV/m. The ratio  $\hat{E}/E_0 = 5.1$  was measured for the Brookhaven deflector<sup>7</sup> having irises with square edges. The AP structure proposed in the present design reduces  $\hat{E}/E_0$  to  $\sim 3.6$ , limiting the equivalent deflecting field  $E_0$  to 4.2 MV/m for Pb. In the case of Nb the estimated ratio  $\hat{E}/E_0$  yields an equivalent deflecting field of 3.6 MV/m.

- 
3. J.P. Turneaure, Stanford University Report HEPL 507 (1967).
  4. J.P. Turneaure and I. Weissman, J. Appl. Phys. 39, 4417 (1968).
  5. H.A. Schwettman, P.B. Wilson, and G.Y. Churilov, in Proc. V Intern. Conf. High Energy Accelerators, Frascati, 1965, p. 690.
  6. W. Jüngst, these Proceedings, p. 127.
  7. H. Hahn and H.J. Halama, Brookhaven National Laboratory, Accelerator Dept. Report HH/HJH-3 (1963).

### III. DESIGN AND OPTIMIZATION OF THE DEFLECTOR

#### 1. AP Structure

When designing a deflector one has a choice of standing wave (SW), or traveling wave (TW), operation. To take advantage of the very low losses in superconductors the group velocity of TW structures would have to be made extremely small. The resonant ring appears to be the only solution, which entails, however, many mechanical problems. Besides, there is the danger of launching the waves in both directions and the adjustment of the amount of coupling is difficult. The main attraction of the ring is the fact that

$$R_{SW} = \frac{1}{2} R_{TW} , \quad (2)$$

implying that only one-half of the rf power is required for the same deflection

$$P_T = q (R_{SW} P \ell)^{\frac{1}{2}} . \quad (3)$$

A design using a resonant ring system was published earlier where UP (uniform periodic) structures operating at 1.2 GHz were used.<sup>8,9</sup> The complications mentioned put the above system in an unfavorable position as compared to the AP (alternating periodic) cavity approach where significant gains are made in the shunt impedance.<sup>10</sup> Moreover, the existence of unexcited cells makes it very attractive for the construction of superconducting cavities.<sup>11</sup>

The expressions for  $R/Q$ , shunt impedance and peak field in AP deflectors were worked out by Hahn who used a  $TM_{11}$  small pitch approximation with infinitely thin irises.<sup>12</sup> The results are summarized in Figs. 1, 2 and 3. It is apparent that the best  $R$ , as well as  $\hat{E}/E_0$ , are achieved with the smallest beam hole,  $ka$ , and the smallest coupling cell while maintaining the confluent condition. In practice the cell dimensions will be limited by multipactoring distance and manufacturing requirements. Model work based on these data will start shortly to determine the final dimensions.

Due to the narrow bandwidth of superconducting cavities a large group velocity should be selected to decrease the tolerances on the cavity dimensions. Figure 4 shows that this is attained by choosing either a large beam hole,  $ka > \sqrt{3}$ , resulting in a positive group velocity or the maximum negative group velocity. Positive  $v_g$  yields larger acceptance, but smaller shunt impedance, and higher peak fields. Besides, some problems of degeneracy may be encountered in the dispersion diagram and the beam tube terminating the deflector would no longer form a below-cutoff waveguide. In short, the backward wave solution seems preferable.

- 
8. H. Hahn and H.J. Halama, IEEE Trans. Nucl. Sci. NS-14, No. 3, 356 (1967).
  9. H.J. Halama and H. Hahn, *ibid.*, p. 350.
  10. H. Hahn, Brookhaven National Laboratory, Accelerator Dept. Report AADD-139 (1968).
  11. J.N. Weaver, T.I. Smith, and P.B. Wilson, IEEE Trans. Nucl. Sci. NS-14, No. 3 345 (1967).
  12. H. Hahn, to be published in the Proc. 6th Proton Linear Accelerator Conference, Brookhaven National Laboratory, May 1968.

## 2. Optimization

When designing an rf separated counter beam, the maximum number of wanted particles is desirable. An optimization for maximum transmission and most economical operation was performed indicating a beam hole  $2a = 6.4$  cm.<sup>12</sup> In the over-all beam design, however, the acceptance is generally not limited by the deflecting cavities as the particles are in focus when traversing the cavities. The above beam hole would therefore not be filled due to the smaller acceptance of the beam optics; this results in unnecessary power waste. From the point of view of the deflector designer the most important parameters to be optimized are shunt impedance  $R_{SW}$ ,  $\hat{E}/E_0$  and  $v_g$ . As seen from Figs. 2, 3 and 4 maximum  $R_{SW}$  and minimum  $\hat{E}/E_0$  are realized with a smaller beam hole. Maximum negative  $v_g$  of  $\sim 0.04$  occurs at  $2a \approx 4.2$  cm and has been chosen in the present design.

## 3. Stability Considerations

The bandwidth (BW) of a resonant cavity depends on the unloaded  $Q_0$  and the coupling coefficient  $\kappa$  according to

$$BW = \frac{f_0 (1 + \kappa)}{Q_0} \quad (4)$$

Large BW is desirable from the point of view of amplitude stability and large  $Q_0$  is necessary for economical operation. Maximum value of  $\kappa$  is governed by the available power from the driver,  $P_s$ , according to

$$P_s = \frac{(\kappa + 1)^2}{4\kappa} P_{rf} \quad (5)$$

where  $P_{rf}$  is the power dissipated by the cavity. Consulting Table I and assuming a driver power of  $< 1$  kW, we obtain  $\kappa \approx 20$ ,  $Q_0 \approx 4 \times 10^7$  and  $BW \approx 70$  Hz. Obviously the deflectors cannot be produced within the tolerances corresponding to the bandwidth and it must be possible to tune them to the frequency of a common signal source. AP structures, transformed into cavities by placing shorts at either end, are ideally suited for tuning, by adjusting the position of movable shorts (Fig. 6) which changes their over-all length.

Once the cavities are tuned, the principal drift in the resonant frequency will be caused either by a temperature and pressure fluctuation or by mechanical vibrations. The effect of temperature is twofold:

- a) The variation of the surface reactance causes frequency variation according to

$$\frac{\Delta f}{\Delta T} = \frac{1}{2} \frac{r_\infty f_0}{Q r_s} \frac{\Delta(X/r_\infty)}{\Delta T} \quad (6)$$

where  $r_\infty$  is the surface resistance in the extreme anomalous limit and  $\Delta(X/r_\infty)/\Delta T$  is the change of surface reactance with temperature.  $\Delta f/\Delta T$  is plotted in Fig. 5 for 1.3 GHz and 2.85 GHz. It is evident that one must work at temperatures below  $2^\circ\text{K}$  where  $\Delta f/1^\circ\text{K} < 36$  Hz.

- b) Mechanical dimensions also change with temperature, resulting in frequency changes. The expansion coefficient of Cu at  $2^\circ\text{K}$  is  $6 \times 10^{-10}/^\circ\text{K}$ , (Ref. 13), corresponding to 1.7 Hz/ $^\circ\text{K}$ . This value is small compared to the reactive  $\Delta f$  and can safely be neglected.



The frequency shifts caused by changes in pressure will depend on the mechanical rigidity of the structure and will have to be determined experimentally. Schwettman et al.<sup>13</sup> measured  $\sim 0.9 \times 10^{-8} f_0$  for a change of 1 mm Hg at 2°K.

Successful separation of particles will depend on the cancellation of unwanted particles.<sup>14</sup> This is achieved by equal amplitudes of electromagnetic fields and zero phase slip in both deflectors and by the proper phase relationship between the deflectors. Let us permit a variation of 1% in the amplitude, i.e., for  $E_0/E_1 = 1.01$  we obtain

$$\Delta f = \frac{f}{20} \sqrt{\left(\frac{E_0}{E_1}\right)^2 - 1} \approx 5 \text{ Hz} \quad (7)$$

The allowable  $\Delta f$  of 5 Hz requires a temperature control of 0.15°K which can be met without difficulty.

Nonsynchronism between the wave and the traversing particles gives rise to a phase slip,  $\varphi$ , and the deflection is reduced to

$$\frac{\sin \frac{1}{2} \varphi}{\frac{1}{2} \varphi} \approx 1 - \frac{1}{24} \varphi^2 \quad (8)$$

Letting Eq. (8) = 0.99 establishes the limit on  $\varphi \leq 0.5$ .

$\varphi$  is related to the tolerances on the inside diameter  $2b$  by

$$\varphi \approx k\ell \frac{c}{v_g} \frac{\Delta 2b}{2b} \quad (9)$$

resulting in  $\Delta 2b \approx 15 \mu\text{m}$ . It is desirable to hold the tolerances on  $2b$  as close as possible. The difference in the resonant frequency of the excited cells due to an unequal diameter  $2b$  will introduce electric fields in the unexcited cells and thus impose a limit on their width. This in turn will adversely affect both  $R_{SW}$  and  $\hat{E}/E_0$  (Figs. 2 and 3).

Finally, the most stringent tolerances are required by the frequency stability of the individual cells during operation since a mechanical change of 1 Å produces a change of 2 Hz.

#### 4. Practical Considerations

Two materials are being considered for the construction of the iris-loaded cavities, namely solid niobium and lead-plated copper. The material selected will determine not only the method of manufacturing but also some mechanical dimensions, in particular the relative length of the cells. At the present time we favor the lead-plated

- 
13. H.A. Schwettman, J.P. Turneure, W.M. Fairbank, T.I. Smith, M.S. McAshan, P.B. Wilson, and E.E. Chambers, IEEE Trans. Nucl. Sci. NS-14, No. 3, 336 (1967).
  14. H.W.J. Foelsche, H. Hahn, H.J. Halama, J. Lach, T. Ludlam, and J. Sandweiss, Rev. Sci. Instr. 38, 879 (1967).

copper cavities due to easier machining, surface preparation, lower cost and higher ac magnetic field. However, rapid progress in niobium as reported at this Summer Study might soon change the picture.<sup>15-17</sup>

Copper modules consisting of one excited cell plus two small half cells (Fig. 6) will either be electroformed or machined. In the case of Nb much longer sections can be produced. If machining is employed the excited cells will be joined by Cu diffusion under pressure. The modules will be individually measured and brought to the same dimensions by electropolishing. By this method, controlled removal of copper can be achieved in the micrometer range. To prevent the rotation of fields, mode stabilizers in form of flat will be used in electroformed cavities while holes can be employed in brazed cavities. The modules will be plated in a lead fluoborate bath using our standard method.<sup>18</sup>

After the assembly with cryogenic gaskets in the unexcited cells the frequency of both deflectors should be within 20 kHz, which corresponds to a total length change of  $\sim 0.5$  mm. The more closely we can match the resonant frequencies of the deflectors, the less field we shall have in the unexcited cells.<sup>19</sup> When the deflectors reach their operating temperature of  $1.85^\circ\text{K}$ , their resonant frequencies must be adjusted to within 5 Hz. This is accomplished by a variable short  $S_1$  (Fig. 6) which is coupled to the main cavity. By moving the short, the reactance of the last cell is changed, thus changing the over-all resonant frequency of the deflector. At unity coupling a displacement of  $S_1$  by 1 mm corresponds to 40 kHz. With a coupling of  $10^{-2}$  the adjustment range of the resonant frequency of each deflector is approximately 20 kHz.

In a previous section we derived a permissible temperature variation of  $\sim 0.15^\circ\text{K}$  corresponding to a variation of  $\sim 10$  mm Hg at an ambient pressure of  $\sim 15$  mm, which is relatively easy. The most difficult problem rests in the mechanical stability. A pressure change of 1 mm Hg on a long cylinder with comparable dimensions to the deflector corresponds to a frequency shift of  $\sim 28$  Hz.<sup>20</sup> Irises will without doubt stiffen the deflector considerably and alleviate some difficulty in the pressure control. The decoupling of the deflectors from their surroundings to reduce vibrations will require an ingenious mechanical solution.

Most of the variations can be corrected by a servo loop since the shortest time in which they can occur is of the order of the time constant  $\tau > 2$  msec. For this purpose, another short  $S_2$  (Fig. 6) is provided with a coupling of  $10^{-4}$ , having an adjustment capability of  $\sim 200$  Hz. The servo loops will be treated in the next section.

Identical fields in both deflectors will be adjusted for maximum bandwidth by a similar coupling mechanism used in all our superconductive tests,<sup>21</sup> namely a below-cutoff attenuator (A in Fig. 6). A stainless-steel coaxial cable plated with 5-10  $\mu\text{m}$  of Cu (skin depth at 3 Gc  $\approx 1$   $\mu\text{m}$ ) can be adjusted from the outside of the Dewar for

---

15. J.P. Turneure, presented at this Summer Study (unpublished).

16. I. Weissman, these Proceedings, p. 32.

17. R.W. Meyerhoff, *ibid.*, p. 23.

18. H. Hahn, H.J. Halama, and E.H. Foster, *ibid.*, p. 13.

19. T.I. Smith, presented at this Summer Study (unpublished).

20. E.H. Foster, private communication.

21. H. Hahn, H.J. Halama, and E.H. Foster, in Proc. 6th Intern. Conf. High Energy Accelerators, Cambridge, Mass., 1967, p. A-139.

the required amount of coupling. Standard 7/8 in. cable has an attenuation of  $8.5 \times 10^{-2}$  dB/m at 3 GHz, negligible heat leak, and is safely rated for 1 kW operation.

#### IV. MICROWAVE SYSTEM

Several systems were investigated in the course of the last two years.<sup>9</sup> The solution adopted here uses a centrally located signal source common to both deflectors and seems to be the most economical. A stable and yet adjustable frequency source<sup>14</sup> is provided by a phase-locked oscillator shown in Fig. 7. The required frequency stability of  $1 \times 10^{-9}$  is surpassed by more than one order of magnitude in commercial frequency standards. The multiplied output of the standard is mixed with the output of the oscillator which differs in frequency by a predetermined i.f. The i.f. is compared in phase with a variable signal VFO whose stability as well as FM requirements are reduced by the ratio  $f_o/i.f.$  A 2 MHz i.f. with a typical bandwidth of  $\pm 500$  kHz will require a VFO of stability  $\approx 5 \times 10^{-7}$ , which can easily be accomplished by a synthesizer. The detected output from the phase bridge with proper dc amplification and compensation phase-locks the frequency of the oscillator. Here we have a large choice between a BWO, a VTM, a reflex klystron, or a solid-state oscillator. Spurious FM and noise are the most important factors and a narrow bandwidth device is preferable. There are many solid-state sources with excellent specifications as well as low voltage requirements and which are therefore more attractive.

As was pointed out earlier, successful separation depends on the cancellation of unwanted particles.<sup>14</sup> The deflectors must therefore be held in a prescribed phase relationship to within  $\pm 1^\circ$ . The over-all schematic of the microwave system, including the phase loop, is shown in Fig. 8.

The signal from the rf source is amplified (TWT), split ( $H_1$ ), and then transmitted along two phase-stable cables to identical deflector stations located 62 m apart. Here the signals are again amplified in a 1 kW klystron ( $A_5$ ) to a level required by the deflectors. The power amplifier  $A_5$  can either contain its own AGS (automatic gain control) or it can be leveled to a reference signal derived from the deflector.<sup>22</sup> A 1 kW circulator,  $C_3$ , absorbs the reflected power caused by high coupling coefficient. A small portion of the drive is coupled out through a directional coupler DC and is subsequently modulated by 1 kHz in a microwave switch.<sup>9</sup> This signal then travels back through  $C_2$  and  $C_1$  to a phase bridge  $H_2$  where it is compared with a similar signal coming from the other deflector station. The output of  $H_2$  contains the information on the phase error between the deflectors. This error signal is amplified ( $A_4$ ), demodulated ( $D_2$ ), and then used to drive a line stretcher ( $P_2$ ). We thus have a zero-seeking servo which keeps the deflectors in the prescribed phase relationship.<sup>14</sup>

Finally, a signal must be provided to determine the on-resonance condition. This can be accomplished by monitoring either the amplitude of the fields in an excited cell or the phase shift across the deflecting cavity, by coupling out small signals. The difference in phase across the cavity drifting off resonance is sensed in a phase bridge and the error signal is used after proper amplification to actuate a servo circuit which drives a short,  $S_2$  in Fig. 6. For a faster control the short can be replaced by a varactor at room temperature. The reactance of the varactor diode is controlled by the error signal to restore the resonant condition.

The duty factor of the rf separator will be determined by the length of the spill of the AGS beam. The driver power can be reduced by a factor of 10 between the pulses to save refrigeration, while the phase loops can remain operative. A duty factor  $\leq 0.3$  can be anticipated for the converted AGS, which will of course proportionally reduce the power requirements.

22. L.R. Suelzle, these Proceedings, p. 67.

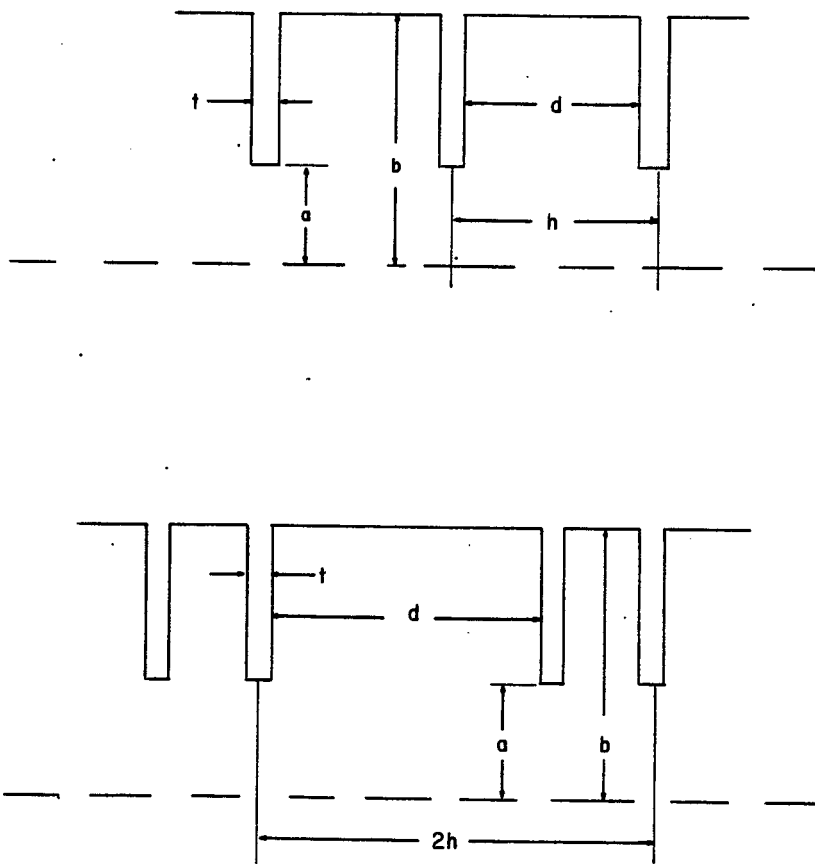


Fig. 1. Geometry of alternating periodic structure.

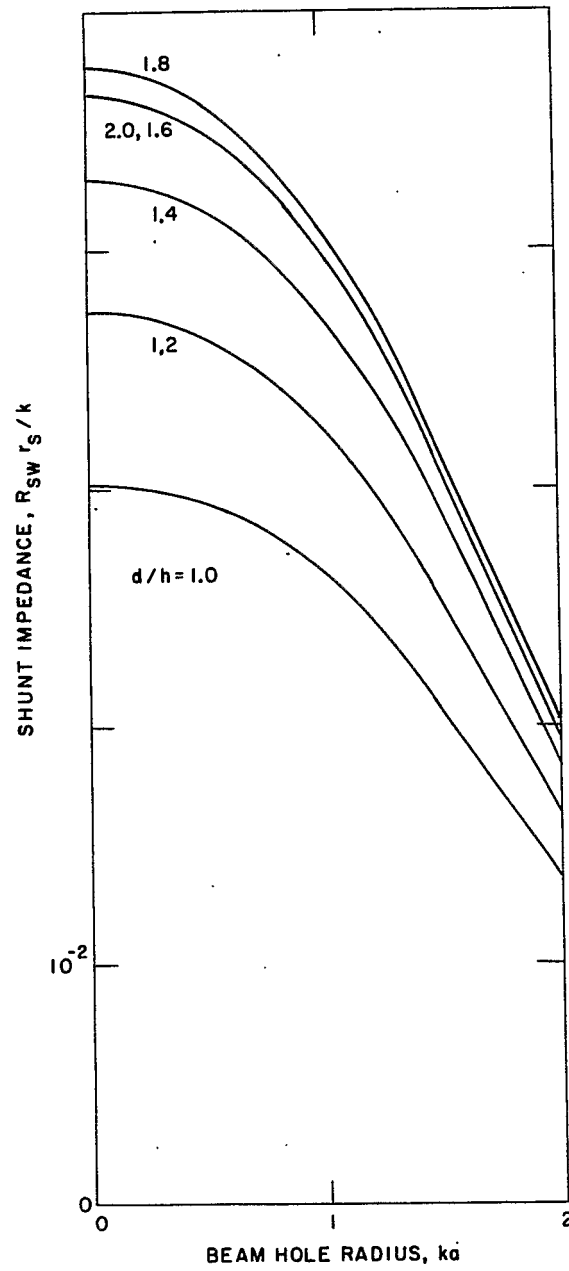


Fig. 2. Shunt impedance of deflector cavity vs beam hole radius.

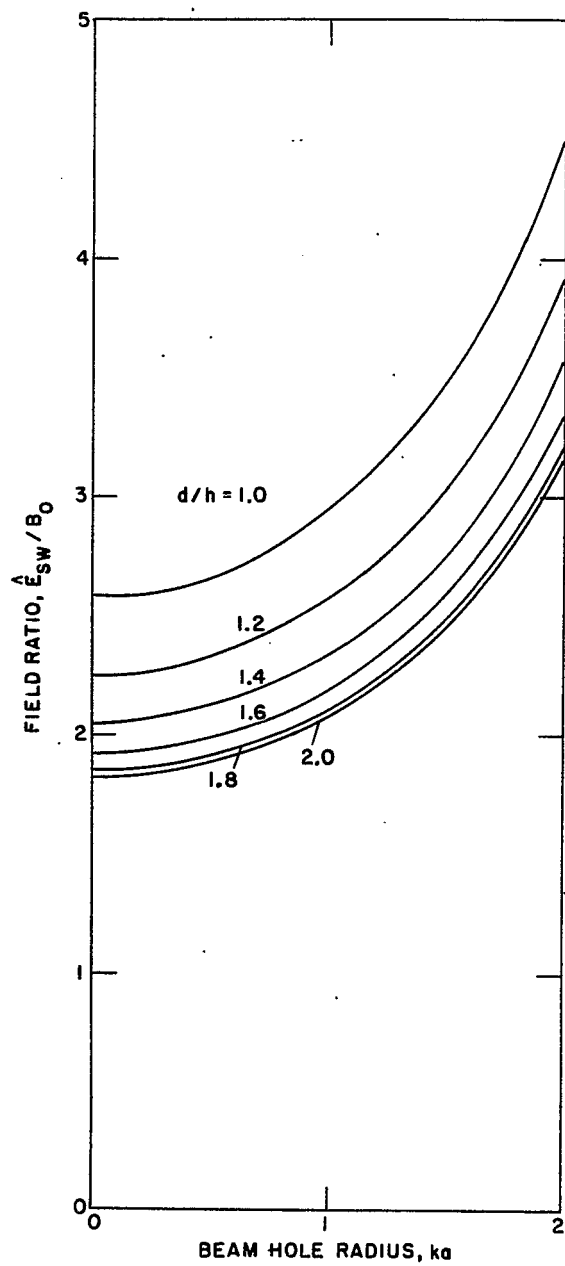


Fig. 3. Ratio of peak electric field to average deflecting field vs beam hole radius.

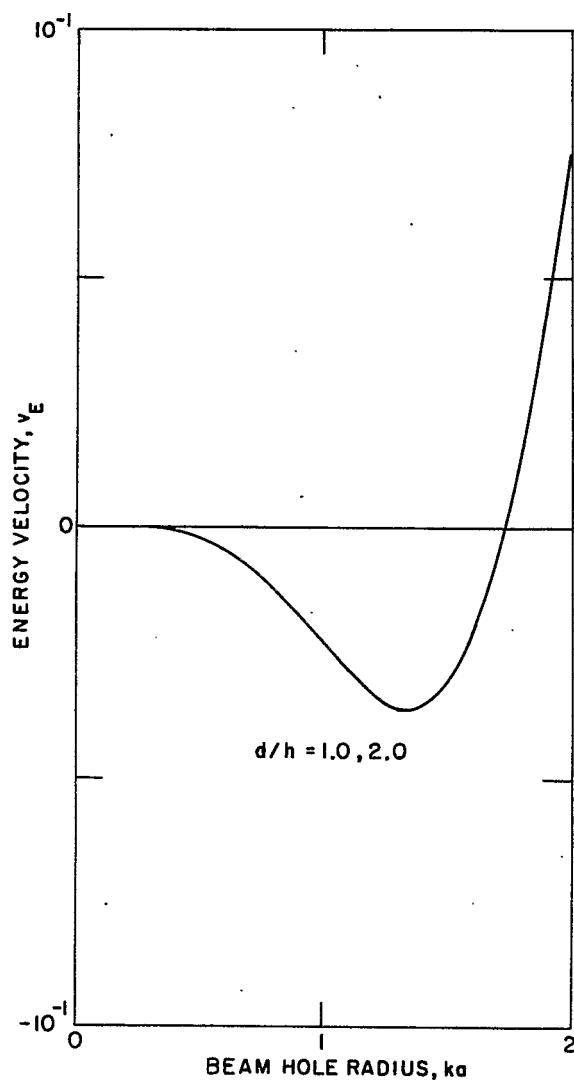


Fig. 4. Group velocity vs beam hole radius.

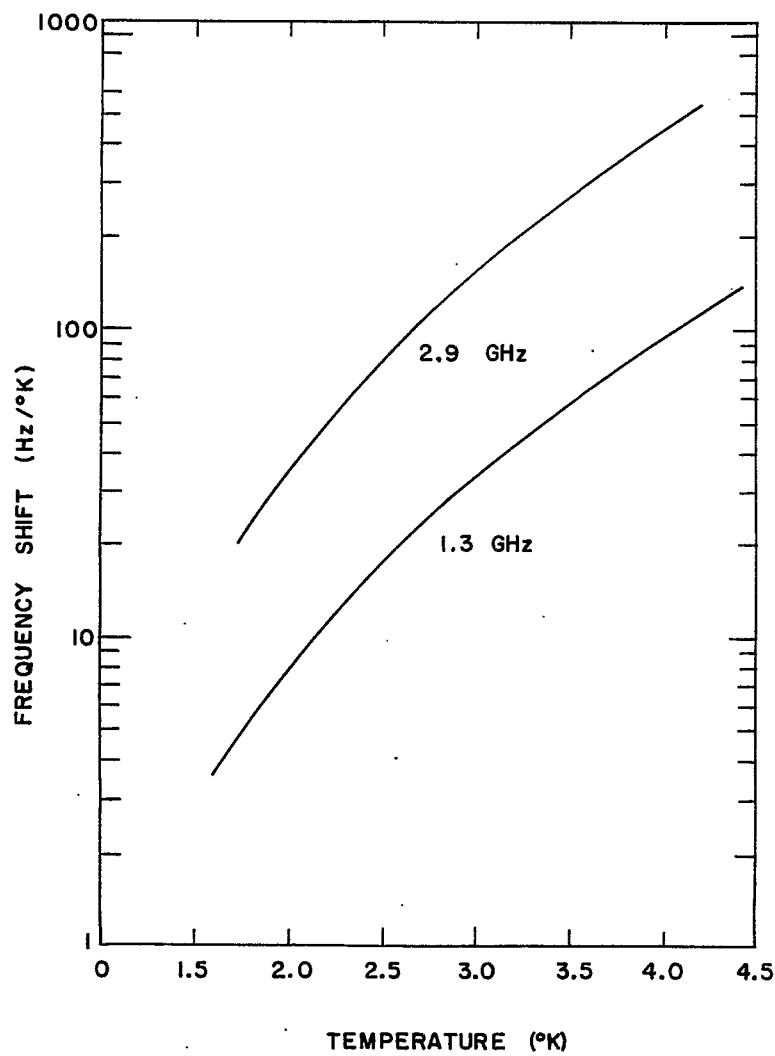


Fig. 5. Frequency shift per  $^{\circ}\text{K}$  vs operating temperature.



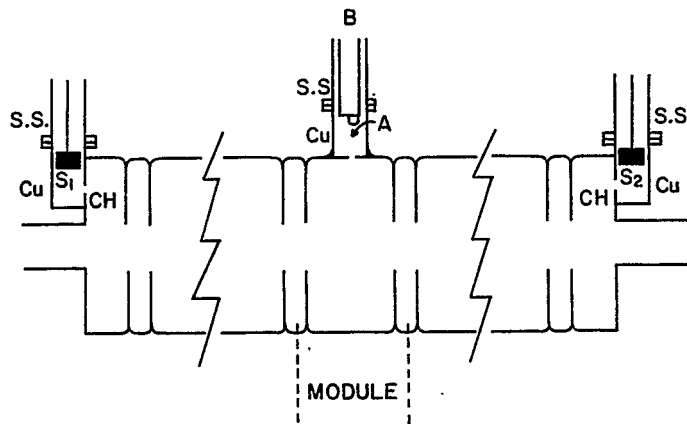


Fig. 6. Schematic of deflecting AP cavity. Legend: SS = stainless steel, Cu = copper, CH = coupling hole, S<sub>1</sub> and S<sub>2</sub> = variable shorts, A = below-cutoff attenuator, B = stainless steel copper-plated cable.

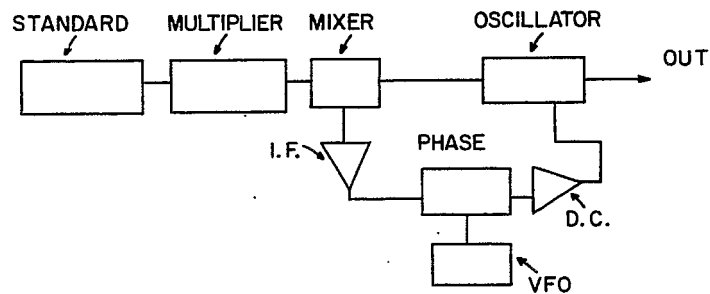


Fig. 7. Block diagram of phase-locked source.

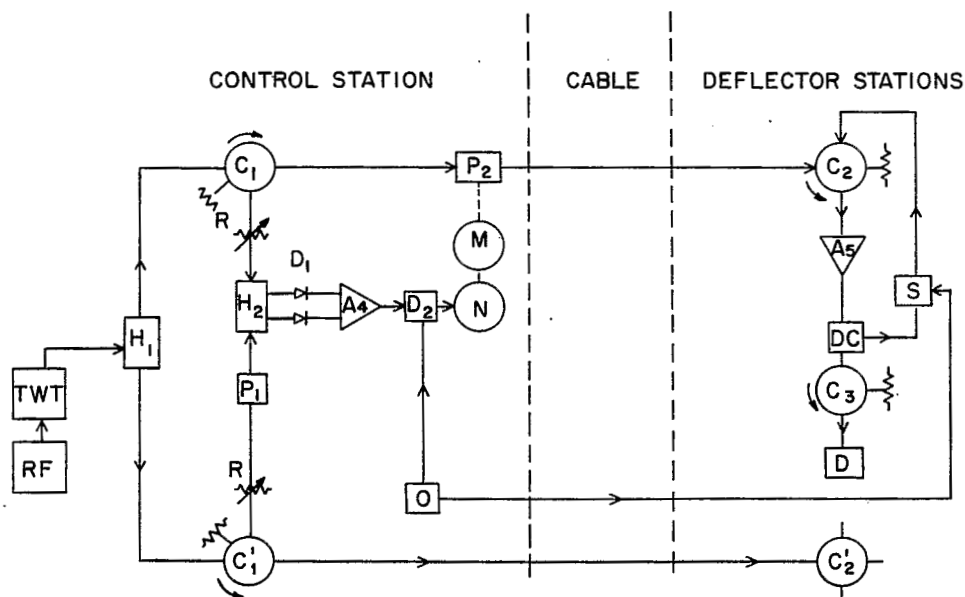


Fig. 8. Block diagram of microwave system for superconducting rf beam separator. Legend:  $A_4$  = differential amplifier,  $A_5$  = klystron amplifier,  $C_1$  and  $C_2$  = four-port circulator,  $C_3$  = circulator,  $D_1$  = crystal diodes,  $D_2$  = synchronous detector,  $D$  = deflector,  $DC$  = directional coupler,  $H_1$  = power splitter,  $H_2$  = phase bridge,  $M$  = motor,  $N$  = polarized relay with snap action,  $O$  = 1 kHz source,  $P_1$  and  $P_2$  = phase shifter,  $R$  = variable attenuator,  $RF$  = signal source,  $S$  = microwave switch,  $TWT$  = traveling wave tube amplifier.

# SUPERCONDUCTING RF SEPARATOR RESEARCH AT THE RUTHERFORD LABORATORY

A. Carne, B.G. Brady, and M.J. Newman  
Rutherford Laboratory  
Chilton, Berks., England

## I. INTRODUCTION

Nimrod at the Rutherford Laboratory is a 7 GeV synchrotron, and compared with the CERN PS or the Brookhaven AGS, produces relatively few kaons. In 1966 a preliminary study was undertaken<sup>1</sup> to compare electrostatic (ES) and rf separators for the momentum range 2-5 GeV/c, and even to consider very low momentum beams of less than 1 GeV/c. The comparison was relevant for both bubble chamber beams using the shortest spill time available at Nimrod of about 200  $\mu$ sec, and also for counter beams of up to about 500 msec duration. The pulse lengths dictate that the rf separators should be superconducting: this is especially obvious for counter beams. Superconducting rf separators operating at L-band frequency offer many advantages over ES beams, in that:

- i) They can separate the maximum emittance beam that can be accepted by conventional quadrupoles (ES separators have too low transmission above 2 GeV/c unless the emittance is reduced).
- ii) They can use the increased acceptance of superconducting quadrupoles when these become available.
- iii) They can provide useful bubble chamber fluxes for momenta up to about 5 GeV/c, and with a larger momentum bite, kaon fluxes of the order  $5 \times 10^3$  per pulse (for an incident proton beam  $\sim 2 \times 10^{11}$  per pulse) for counter beams. Comparison between optimized superconducting and rf beams give the following ratios:

$$\text{Flux rf/ES} = 1.25 \text{ at } 2.0 \text{ GeV/c to } 8.0 \text{ at } 5 \text{ GeV/c.}$$

## II. THE SEPARATOR SYSTEM

The system envisaged is shown in Fig. 1, and is similar to that in use on the CERN PS. The two cavities will operate at L-band frequency (about 1300 MHz), this frequency being chosen as the familiar compromise between physical size and shunt impedance  $R$ , acceptance  $\alpha$ , and cavity separation  $D$ . These latter quantities all favor lower frequencies; even cavity separation, since here we are dealing with beams of low momentum and require space for intercavity beam transport components. For a central momentum of 2.7 GeV/c, an intercavity phase difference of  $180^\circ$  for  $K$ ,  $\pi$  separation requires  $D = 7.5$  m, and the system gives useful separation over the momentum range 2.0 to 4.5 GeV/c. If the distance were increased threefold to give ample space,  $K$  yield would be reduced due to decay, and the useful momentum band would be reduced to 2.4 to 3.0 GeV/c.

Ideally the imaging system between the cavities provides 1:1 imaging in each plane of the phase-space configuration. Due to the comparatively short distance  $D$ , this cannot be achieved unless superconducting quadrupoles are used. If conventional quadrupoles are used, 1:1 imaging can only be achieved in the plane of separation,

---

1. E.J.N. Wilson, Rutherford Laboratory Internal Memo, NIMROD BP 66/26 (1966).

and this can be obtained by using a single symmetrical triplet. In the orthogonal plane the transfer matrix has two solutions, both of which lead to some beam loss due to blowup: this loss is least (about 10%) for a drift length roughly equal to the intercavity length  $D$ .

The choice of L-band frequency results in a large cavity acceptance. Optimization of cavity acceptance alone, based on a maximum equivalent deflecting field of 4 MV/m and a cavity aperture  $2a = 10$  cm, leads to an optimum cavity length of 3.5 m, and a maximum acceptance of 78.5 mm·mrad. Such cavity lengths leave little space ( $\sim 4$  m) for the intercavity beam components; such an acceptance is much greater than the acceptance of the optimum doublet for momentum selection (see Fig. 1), even if it were superconducting. In fact, cavities of length 1.25 m are adequate, and with these it is reasonable to have the beam parallel inside the cavities.

### III. THE SEPARATOR CAVITIES

The cavities themselves will be of disc-loaded waveguide, operating in the uniform-periodic (UP)  $\pi$  mode of the HEM<sub>11</sub> deflecting mode. In  $\pi$ -mode operation the cavities are fundamentally standing wave, for which there are two main advantages:

- i) Resonant chain or ring operation is essential, and for a UP chain,  $\pi$ -mode offers the highest shunt impedance. For a conventional copper structure computed<sup>2</sup> shunt impedances at 1300 MHz,  $\pi$ -mode give 13.2 M $\Omega$ /m ( $2a = 10$  cm) and 11 M $\Omega$ /m ( $2a = 11$  cm).
- ii) The mid-planes of the discs are planes of antisymmetry (i.e., there is zero current) and offer less critical planes for joining cells. An alternative point of view is to regard the structure as an alternating-periodic (AP) structure in  $\pi/2$  mode in which the alternate cavities, which contain zero stored energy, shrink to zero. Practical methods of joining the cells may be:
  - a) A simple compression joint with an indium seal.
  - b) Electron beam welding the lead in the join planes, discussed briefly later.

The disadvantages of  $\pi$ -mode operation in UP structures is the reduced tolerance [proportional to (number of cells)<sup>2</sup> against (number of cells)<sup>1</sup> for AP  $\pi/2$ -mode structures]. But since the cavities are only 10-11 cells long ( $L = 1.25$  meters,  $\ell = \lambda_0/2 = 11.5$  cm), the mode separation is sufficiently large for the tolerances to be manageable. Even though there is a frequency-phase degeneracy for the structure with such large apertures, there is little risk of double-moding, and it can easily be avoided.

The cavities will be of electrodeposited lead on copper, and will operate at 1.85°K. Though the use of niobium offers an exciting alternative, cost precludes its use on this particular project. The theoretical improvement factor  $I(\text{Pb}) \sim 7 \times 10^5$  at 1.85°K, 1300 MHz, and, because of the variability of lead, a practical figure  $I = 10^5$  is aimed at. Field emission limits the maximum equivalent deflecting field to the range 5-7 MV/m: to avoid difficulties a more modest field of 4 MV/m is aimed at.

A deflection of the order 1.5 mrad/cavity is required at 2.7 GeV/c. With  $EL = \theta p$ , this gives for  $E = 4$  MV/m,  $L \sim 1$  m, i.e. 10 cells/cavity. If it is necessary to reduce the field by some small amount because of field emission, then  $L$  must be increased

---

2. H.G. Hereward and M. Bell, CERN Yellow Report CERN 63-33 (1963).

by the same amount to give the same deflection, and the power  $\propto E^2 L$  actually decreases. Because the beam is parallel inside the cavities, and because the cavities already have a much larger acceptance, modifications of this kind will not greatly affect the beam design. With  $I = 10^5$ ,  $2a = 10$  cm,  $P \sim 12$  W/cavity. At a maximum duty cycle of 25% ( $\sim 500$  msec/2 sec), this gives  $(2P)_{av} = 6$  W. To this we add an arbitrary 30% due to cavity end-plate and tuner loss, giving a total 8 W. With total cryostat losses of about 2 W, this gives a total refrigerator load of 10 W.

#### IV. REVIEW OF MEASUREMENTS TO JUNE 1968

Preliminary tests on electron beam welding of lead joints have been made with an outside manufacturer. Electron beam power is seen to be critical (of the order of 30 kV, 8 mA): overheating causes the lead to globulate, underheating does not allow the weld to form. Also the weld does not take if the pressure is allowed to become too high, i.e. greater than  $10^{-5}$  torr. Successful samples show a good uniformity of lead at the join, and are sufficiently encouraging to warrant further study.

It was originally decided to do Q measurements at the final operating frequency to avoid problems with frequency scaling. This view has been changed (mainly due to handling problems) and the major effort is now on S-band cavities. Two copper cavities (one rolled and welded, the other electroformed) have been made for Q tests at 1300 MHz,  $TE_{011}$  mode. Both cavities were originally lead-plated (to a thickness 0.001 in.) by an outside manufacturer by a "standard" commercial process (0.4 g/liter solution of bone glue, 15-20 A/ft<sup>2</sup>). In neither case was the plating good enough for superconducting application: both cavities were somewhat mishandled and were a little distorted (which, however, helped  $TE_{011}$ - $TM_{111}$  mode separation). The cavity  $Q_0$ 's were found to be of the order  $6 \times 10^6$  and  $10^7$  at 4.2°K, with only an improvement of the order 2 at 1.85°K. (These numbers are to be compared with  $Q_0 = 7 \times 10^4$  for copper at 300°K.) Neither cavity was magnetically shielded; both cavities leaked on cool-down at the indium gaskets, particularly at the  $\lambda$ -point of helium.

Because of the above difficulties, we have now established our own plating shop. The two cavities above have been replated, again at 15 A/ft<sup>2</sup>, 0.001 in. thick, and re-tested. Magnetic shielding has been used in the form of a  $\mu$ -metal can 0.040 in. thick. New values of  $Q_0$  have been  $8 \times 10^7$  and  $4 \times 10^8$  at 2°K, respectively, i.e. with I's approaching  $10^4$ . Several new S-band cavities have been prepared and are being tested. With these, experiments can be done more quickly to check plating parameters, e.g. current density (which may well come down to the 2.5 A/ft<sup>2</sup> commonly used in U.S. laboratories) and glue concentrations. Certainly the small quantity of bone glue at present used gives a much smoother surface than with no glue at all. Some conditioning of the copper substrate is being done (e.g. vacuum or reducing-gas furnacing) to produce epitaxis of lead.

Tests are also being done on model structures to investigate field patterns, check R/Q values and develop coupling systems. Other tests are being done to develop components for the rf system. The system envisaged is "conventional" for a superconducting system, but major use is being made of strip-line and solid-state devices. Future work will be aimed at "high power" models to check out limiting E-field values for the  $HEM_{11}$  deflecting wave in  $\pi$  mode; after this the real deflecting cavities will be built.

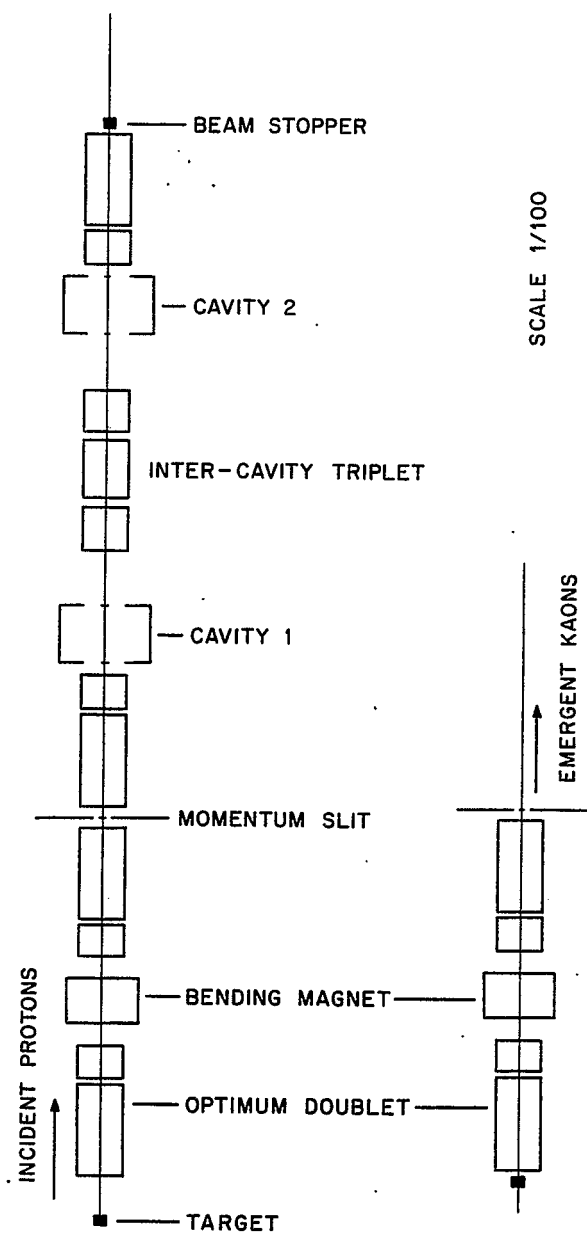


Fig. 1. Rf separated beam.

## BEAM OPTICS DESIGN FOR A 600 MEV MICROTRON

D.C. Sutton and A.O. Hanson  
University of Illinois  
Urbana, Illinois

At the University of Illinois we have studied the feasibility of a racetrack microtron having two  $180^\circ$  bending magnets separated by 6.5 m, a 30 MeV standing wave linac in the common straight section and 19 parallel return paths separated by 14 cm. The problem is similar to that discussed by Wiik and Wilson,<sup>1</sup> except that we call for bending magnets which are about 50% further apart and we have aimed at containing a beam with six times larger emittance: horizontal and vertical extents of  $\pm 2$  mm, divergence angles of  $\pm 0.3$  mrad, and momentum spread of  $\pm 1\%$  at 30 MeV.

We have required that the deviation in position and angle of an electron's path with respect to the linac axis be uncorrelated with its momentum error. Two things are necessary in order to make the position and angle independent of the momentum to first order. First, all of the horizontal focusing of the beam must be done with optical elements which are coaxial with the linac axis. Second, the optical system in each return path should be symmetrical about the plane which is midway between the two bending magnets.

The beam is defocused vertically in the fringe fields of the bending magnets. To provide vertical focusing we have started with two quadrupole pairs on each separate return path, one pair close to each magnet. If one requires an advance in the vertical oscillation phase for each orbit of  $90^\circ$ , which may be greater than necessary, one computes gradients in the quadrupoles which increase monotonically with the orbit number from 0.1 to 0.5 kG/cm for quadrupoles 20 cm long and separated by 10 cm.

Only very weak horizontal focusing powers are required to contain the beam within  $\pm 2$  mm of the linac axis up to 600 MeV. The linac provides some focusing but in the absence of additional horizontal focusing the beam enlarges to about  $\pm 3.5$  mm in the common straight section. We have chosen to use two quadrupole singlets on the linac axis, one near each bending magnet, to provide the horizontal focusing. We have tried focusing powers of 0.68 and 0.13 diopter per singlet at 30 MeV. Both are satisfactory, giving horizontal oscillation phase advances of  $180^\circ$  and  $90^\circ$ , respectively, on the first orbit. The beam profile for the latter case is shown up to 240 MeV in Fig. 1. The focusing power of the singlets decreases as the momentum increases, but so does the emittance of the beam, with the net result that the horizontal extent of the beam remains about the same but the beam becomes more parallel from orbit to orbit. There are some 1 mm waists in the horizontal beam envelope as shown in Fig. 1. The locations and size of these narrow waists imply that the divergence angle of the initial 30 MeV beam could be doubled without changing the maximum horizontal beam size very much.

---

1. B.H. Wiik and P.B. Wilson, Nucl. Instr. and Methods 56, 197 (1967).

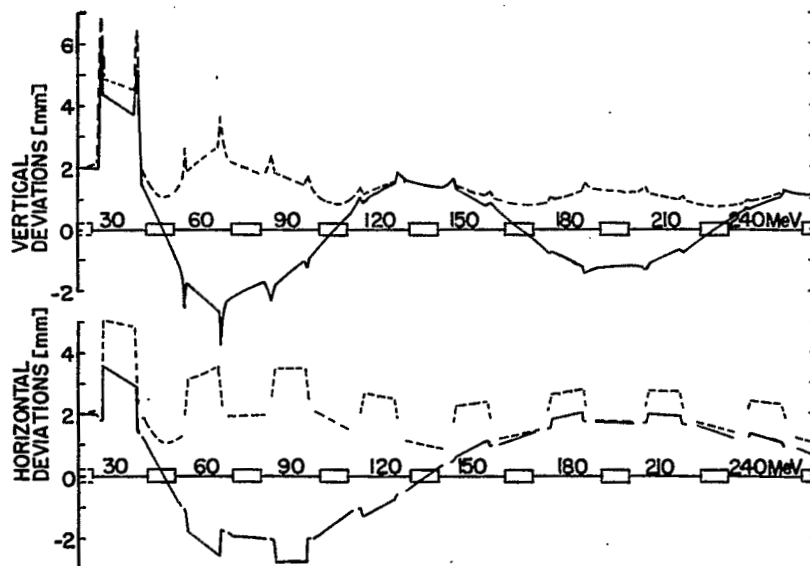


Fig. 1. Vertical and horizontal beam profiles for microtron orbits from 30 to 240 MeV. The boxes indicate the locations of the linac along the path. The dashed lines are beam envelopes. The solid lines are cosine-like principal rays. We have not shown the details of the horizontal beam profile within the  $180^\circ$  bending magnets.



# HIGH STABILITY UHF OSCILLATORS USING A SUPERCONDUCTING CAVITY

F. Biquard, Nguyen Tuong Viet, and A. Septier  
Institut d'Electronique Fondamentale  
Orsay, France

## I. INTRODUCTION

The recent achievement of very high Q factors in superconducting cavities makes possible the realization of powerful microwave oscillators with natural frequency stability as good as that of quartz clocks. This interesting property is a consequence of the Blaquièrre-Townes<sup>1</sup> formula giving the noise bandwidth of a slightly nonlinear oscillator influenced by Johnson noise as:

$$\delta f = \pi k T \frac{(\Delta f)^2}{P}, \quad (1)$$

where  $\Delta f$  denotes the bandwidth of the oscillating circuit and P the microwave power in the circuit.

A superconducting cavity can be used as a part of an oscillator in many ways; we present here two different systems in which the cavity plays, respectively, the role of an active or passive component.

### 1. Monotron

In the monotron oscillator an electron beam is able to transfer a part of its energy to the electromagnetic field in a resonant cavity. Regions of negative conductance appear in the beam loading characteristics of the beam-cavity system, suggesting the possibility of regenerative operation. A general theory of the monotron oscillator has been first given by Muller and Rostas<sup>2</sup> and then by Turner.<sup>3</sup> It turns out that the performance of monotron oscillators can be described correctly in terms of the lumped equivalent circuit shown in Fig. 1, where the admittance  $G_b + j B_b$  represents the effect of the electron beam on the equivalent circuit of the cavity.

In this case the main source of noise is shot noise from the electron beam which is  $10^8$  greater than Johnson noise for a typical case. Replacing Johnson noise power in the cavity,  $P_j = 4kT\Delta f$ , by shot noise coming from the electron beam,  $P_s = M^2 e I_0 \Delta f / G_c$ , and following the Golay<sup>4</sup> method, we find that the effect of noise is adequately described in first approximation by a noise bandwidth  $\delta f$ ,  $\delta f$  being given by:

$$\delta f = \frac{2\pi M^2 e I_0}{G_c} \cdot \frac{f^2}{Q} \cdot \frac{1}{P}, \quad (2)$$

- 
1. A. Blaquièrre, Thèse Paris, Gauthiers Villars, 1953;  
J.P. Gordon, H.J. Zeiger, and C.H. Townes, Phys. Rev. 99, 1264 (1955).
  2. J.J. Muller and E. Rostas, Helv. Phys. Acta 13, 435 (1940).
  3. C.W. Turner, Stanford University Report 830 (1961).
  4. M.J.E. Golay, Proc. IRE 48, 1473 (1960).

where

- $I_o$  = dc beam current crossing the cavity, (A),
- $G_c$  = shunt admittance of the cavity, ( $\Omega^{-1}$ ),
- $D$  = transit angle of electrons through the cavity, (rad),
- $M = \frac{\sin D/2}{D/2}$  = gap coupling coefficient,
- $f$  = frequency of oscillation, (Hz),
- $Q$  = quality factor of the cavity,
- $P$  = microwave power delivered to the circuit, (W).

In the same conditions, the relative standard deviation<sup>5</sup> of the frequency in time  $\tau$  is given by:

$$\frac{\sigma(\langle\dot{\phi}\rangle_{t,\tau})}{2\pi f} = \left( \frac{M^2 e I_o}{8 G_c Q^2 \tau} \right)^{\frac{1}{2}} \quad (3)$$

For an oscillator using a cylindrical cavity working in the  $TM_{010}$  mode, in the best conversion efficiency conditions ( $D = 2.33 \pi$ ), formulas (2) and (3) take the form:

$$\delta f = 2 \times 10^{-14} \frac{f^2}{Q^2 P}, \quad (4)$$

$$\frac{\sigma(\langle\dot{\phi}\rangle_{t,\tau})}{2\pi f} = 2.8 \times 10^{-9} \left( \frac{1}{P Q^2 \tau} \right)^{\frac{1}{2}} \quad (5)$$

Choosing a working frequency of 3 GHz, we could use a cavity having  $Q = 10^7$ . The oscillator may conveniently deliver 0.1 W of microwave power, and the noise bandwidth is then:

$$\delta f = 1.8 \times 10^{-8} \text{ Hz}$$

with

$$\delta f/f = 6 \times 10^{-18} \quad (6)$$

## 2. TWT Oscillator

In the traveling wave tube (TWT) auto-oscillator, the cavity is placed in the external feedback loop of a low noise TWT amplifier to play the role of a frequency-determining circuit. The problem of noise in this type of oscillator has been discussed in detail by Hetland.<sup>6</sup> To compute the noise bandwidth, one can consider the case

---

5. L.S. Cutler and C.L. Searle, Proc. IEEE 54, 136 (1966).

6. G. Hetland, Stanford University, Applied Electronics Laboratory Report No. 40 (1955).

of classical auto-oscillators. When introducing the noise factor and the power gain of the tube, it is possible to derive from the above Blaquièr-Townes formula the following expression for the noise bandwidth of the oscillator output spectrum:

$$\delta f = \frac{\pi k T_o F G f^2}{P Q^2} \quad (7)$$

where

$\delta f$  = bandwidth of output spectrum, (Hz),

$k$  = Boltzmann's constant, ( $1.37 \times 10^{-23}$  J/°K),

$T_o$  = room temperature,

$F$  = noise factor of the TWT at  $f$ ,

$G$  = power gain of the TWT at  $f$ ,

$P$  = output power, (W),

$Q$  = quality factor of the cavity.

In fact, Eq. (7) defines the width of the Fourier spectrum, calculated in principle by integrals running from  $t = -\infty$  to  $t = \infty$ . In practice, we measure  $\delta f$  during a finite observation time  $\tau$  and we have<sup>7</sup>:

$$\delta f_\tau = \left( \frac{\delta f}{2\pi \tau} \right)^{\frac{1}{2}} \quad (8)$$

In the same conditions, the standard deviation of the frequency is given by:

$$\frac{\sigma(\langle \dot{\phi} \rangle_{t,\tau})}{2\pi f} = \left( \frac{k T_o F G}{2 P Q^2 \tau} \right)^{\frac{1}{2}} \quad (9)$$

For  $f = 2.911 \times 10^9$  Hz,  $F = 4.67$  (6.7 dB),  $G = 159$  (22 dB),  $P = 10^{-3}$  W,  $Q = 10^8$  we have:

$$\delta f = 8 \times 10^{-12} \text{ Hz}$$

$$\frac{\delta f}{f} = 2.7 \times 10^{-21}$$

$$\frac{\sigma(\langle \dot{\phi} \rangle_{t,\tau})}{2\pi f} = 1.2 \times 10^{-16} \text{ with } \tau = 10 \text{ sec.}$$

---

7. P. Grivet and A. Blaquièr, in Proc. Symposium on Optical Masers, Brooklyn, 1963, p. 69.

### 3. Comparison Between Oscillators

Table I shows theoretical properties of both oscillators in comparison with the properties of hydrogen and ammonia masers.

TABLE I

	TWT auto-oscillator	Quartz oscillator	Hydrogen maser	Ammonia maser	Monotron
$f_o$ (MHz)	2911	5	1420	23 870	3000
P (W)	$10^{-3}$	$10^{-7}$	$10^{-12}$	$10^{-10}$	$10^{-1}$
Q	$10^8$	$2 \times 10^6$	$2 \times 10^9$	$5 \times 10^6$	$10^7$
$\delta f$ (Hz)	$8 \times 10^{-12}$	$2.7 \times 10^{-12}$	$6.5 \times 10^{-9}$	$3 \times 10^{-3}$	$1.8 \times 10^{-8}$
$\delta f/f$	$2.7 \times 10^{-21}$	$0.54 \times 10^{-18}$	$4.7 \times 10^{-18}$	$1.25 \times 10^{-13}$	$6 \times 10^{-18}$
$\frac{\sigma(\langle \dot{\phi} \rangle_{t,T})}{2\pi f}$ $\tau = 10 \text{ sec}$	$1.2 \times 10^{-16}$	$4.2 \times 10^{-14}$	$7 \times 10^{-15}$	$2.9 \times 10^{-13}$	$3 \times 10^{-16}$

We can foresee that, for both oscillators, frequency stability will not be limited by noise bandwidth but by external factors. Particularly, long-term frequency stability will be influenced by a possible drift of the cavity resonance frequency caused by gas pressure variations in the helium bath.

## II. MONOTRON OSCILLATOR

### 1. Description

An electron beam of velocity  $u_o$  and intensity  $I_o$ , accelerated under a voltage  $V_o$ , flows along the axis of a cylindrical cavity of length  $d$ , oscillating at a frequency  $f$  in the  $TM_{0pq}$  mode. The electron beam exchanges power with the high frequency field in the cavity. If the transit angle of the electrons

$$D = \frac{2\pi f d}{u_o} \quad (10)$$

is well chosen, power can be delivered by the beam to the electromagnetic field and an oscillation can arise in the cavity.

For the  $TM_{010}$  mode (neglecting end perturbations caused by axial holes), the electric field  $E_z$  is uniform along the axis of the cavity and the oscillation condition

is found to be  $D = (2K + \frac{1}{2})\pi$ ,  $K$  being an integer, but other oscillation modes are possible.

The cylindrical cavity resonates in the S band near  $f = 3$  GHz. Our cavities are made of OFHC copper and their inner surfaces are covered with a vacuum deposited or electrolytic thick lead layer (thickness of the order  $5 \mu\text{m}$ ).

Lead is a type I superconductor for temperatures  $T < 7.2^\circ\text{K}$ , and the devices were mainly operated at  $T = 4.2^\circ\text{K}$ . In this first realization (Fig. 2), the cavity is made in two identical pieces, the whole cavity being cut along a plane perpendicular to its axis. This solution is mechanically convenient, but it is a rather bad one from an electrical point of view. Indeed, the indium joint separating the two halves of the cavity causes supplementary H.F. losses, and the  $Q$  reached practically is not higher than  $10^7$  on the average.

Two holes 6 mm in diameter bored in the end plates allow the electron beam to cross the cavity along its axis. The resonant cavity, which is fixed in a special cryostat, constitutes the inner wall of the liquid helium vessel which is surrounded by a copper sheet. This sheet is soldered to four liquid nitrogen reservoirs and reduces radiative heat losses. Two coaxial lines fitted with movable antennas permit variation of the coupling between the cavity and the electrical external circuit at room temperature.

A triode electron gun with a tungsten wire cathode produces the electron beam which is focused by an electrostatic lens; 95% of the electrons reach the collector situated 30 cm from the cathode.

## 2. Properties of the Superconducting Monotron

Steady-state properties. Figure 3 gives experimental curves showing the starting current of the oscillator as a function of accelerating voltage for various oscillating modes of the cavity. We easily obtain oscillations in three different modes, and we give in Table II the measured characteristics of the oscillator.

TABLE II ( $d = 38$  mm)

	$\text{TM}_{010}$	$\text{TM}_{011}$	$\text{TM}_{020}$
Frequency (GHz)	2.970	4.956	6.817
Q factor	$12.25 \times 10^6$	$7.49 \times 10^6$	$10.2 \times 10^6$
Optimum transit angle (radians)	$4.5 \pi$ $6.5 \pi$	$5.5 \pi$	$8.5 \pi$
Optimum accelerating voltage (kV)	7.8 3.5	15	11.9

It is interesting to use modes like  $\text{TM}_{020}$  or  $\text{TM}_{011}$ , in order to reach higher frequencies of operation with the same resonator (X band, for example).  $\text{TM}_{011}$  modes are very promising if we need a high  $Q$  factor at high frequency because the joint in the

lateral wall of the cavity does not disturb the electric current pattern.

From a theoretical point of view it should appear interesting to study the competition between two possible modes for given experimental conditions.

Figure 4 shows theoretical and experimental curves giving the values of the starting current  $I_s$  of the oscillator operating in the  $TM_{010}$  mode, as a function of transit angle, the loaded Q factor being  $2.22 \times 10^6$ . We obtain a good agreement between experiment and theory, if we take into account the fact that theory neglects the action on the beam of the evanescent modes existing in the holes at each end of the cavity (the field repartition along the axis is supposed to be rectangular). More elaborate calculations taking into account the real shape of the leakage field configuration are in progress.

For a given transit angle  $D$ , we have checked that the product  $(Q \times I_s)$  is a constant of the oscillator.

Long-term frequency stability. Figure 5 presents a record of monotron frequency variations during 21 minutes. Experimental working conditions are in this case:

Mode	$TM_{010}$
Loaded Q	$Q_L = 10^7$
Accelerating voltage	$V_o = 7.987 \text{ kV}$
Beam current	$I_o = 1.25 \text{ mA}$
Transit angle	$D = 4.30 \pi$
Helium bath temperature	$T = 4.2^\circ\text{K}$
Output power	$P = 0.15 \text{ W}$
Sampling time	$\tau = 10 \text{ sec}$

Stability of the accelerating voltage is better than 0.01%. We have measured the mean frequency  $f_M = 2969990106.05 \text{ Hz}$  and the mean square value of the error  $\bar{\sigma} = 0.66 \text{ Hz}$ .

The frequency stability is given by:

$$\sigma(\langle \dot{\varphi} \rangle_{t,\tau}) / 2\pi f = 2.2 \times 10^{-10} \quad (11)$$

for  $\tau = 10 \text{ sec}$ . On the same figure we present measurements on short-term frequency stability.

Possible factors governing residual frequency drifts. Two main factors may be of importance for explaining residual frequency instabilities.

- a) These instabilities may be caused by the electron beam accelerating voltage and current fluctuations. Theory shows that:

$$\frac{df}{f} = \frac{1}{Q} \left( \frac{D-1}{4} \frac{dV_o}{V_o} - \frac{1}{2} \frac{dI_o}{I_o} \right) \quad (12)$$

Instability of frequency due to this cause is inversely proportional to  $Q$ . Expectation values for  $dV_o$  and  $dI_o$  are:

$$\frac{d V_o}{V_o} \approx \frac{d I_o}{I_o} \approx 10^{-4} \quad (13)$$

and with an experimental  $Q = 10^7$ , formula (9) gives:

$$\frac{df}{f} \approx 10^{-11} \quad (14)$$

- b) A temperature variation  $\Delta T$  of the liquid helium bath induces a slow drift of the cavity resonant frequency. Indeed, the pressure  $P$  is not yet stabilized and for slow fluctuations the temperature changes with the pressure of the helium gas.

Temperature variations have three different effects:

- i) Thermal expansion of the cavity dimensions; at very low temperatures and for copper walls, this effect is negligible.
- ii) Variations of the surface reactance of the superconductor.
- iii) Mechanical deformation of the cavity walls due to external pressure variations.

In the vicinity of  $T = 4.2^\circ\text{K}$ , adding all preceding effects, we obtain an approximate value of frequency variation:

$$\frac{df}{f} \approx 1.5 \times 10^{-10} \times \Delta P / \text{Torr}$$

where  $P$  is the helium gas pressure in the cryostat.

The limit of useful power. It is possible to increase power from milliwatts to several watts by raising the beam current intensity above the threshold value. However, in order to maintain the frequency stability we are confined by two imperatives:

- a) Beam current has to be sufficiently weak so that it can be well focused and led across the cavity without losses on the walls, thus avoiding local heating of the metal surface.
- b) It is also necessary that high frequency losses in the cavity walls be kept small.

Indeed, too much thermal dissipation in the walls will cause boiling of the liquid helium and thus an elevation of temperature which shifts the oscillator frequency at a rate greater than 20 Hz/min. It has been proven that such "cryogenic" effects limit such an oscillator to an output power of 1 W if the highest frequency stability is required.

#### Short-term frequency stability.

- a) Method of measurement and results:- The short-term frequency stability has been determined by direct comparison with a stable 5 MHz oscillator followed by a multiplying chain to 2910 MHz. The stability of the reference chain is  $9 \times 10^{-13}$  for a 10 sec averaging time and  $6 \times 10^{-11}$  for a 0.01 sec averaging time. Each experimental point on the short-term frequency stability curve (Fig. 5) represents

the relative standard deviation of the frequency  $\sigma(\langle\dot{\varphi}\rangle_{t,\tau})$  of a group of 800 measurements which have been treated in order to eliminate the slow drift coming from the liquid helium bath. In this way, we could evaluate the stability limit defined by (11) as reaching  $2 \times 10^{-10}$  for  $\tau > 0.1$  sec.

- b) Influence of the Q factor:- Several measurements of the short-term frequency stability were made using the same cavity, and varying the Q factor from  $1.66 \times 10^6$  to  $10.1 \times 10^6$ . The experimental results were always in accord with those of Fig. 5 without any noticeable difference, which seems to show that at the present time frequency stability does not depend on Q.
- c) Multipactor effect:- We think that a new phenomenon, not considered above, actually limits the frequency stability of the monotron. We are presently inclined to suppose that field electron emission from cavity walls can be such a possible source of noise. Indeed, high electric field strengths are obtained in the superconducting cavity ( $E > 10^6$  MV/m on the axis). If we still increase the field strength (by raising the beam current) multipactoring effects appear and oscillation vanishes and reappears again as a relaxation process.

These phenomena are especially troublesome in lead electroplated cavities, the lead surface being very rough; sharp crystal corners (visible on relatively low magnification micrographs) enhance the local electric field. The multipactor effect does not appear so easily (even at higher field strength) in cavities where the lead layer is obtained by vacuum deposition. In this case the surface presents better aspect and smoothness. Unfortunately, we are actually unable to obtain Q values higher than  $2.6 \times 10^6$  by this technique. New experiments are now in progress, using a new cavity, lead-plated by an ultra-high-vacuum deposition technique.

### III. TWT AUTO-OSCILLATOR

#### 1. Principle

Figure 7 shows the well-known block diagram of the oscillator.<sup>8,9</sup> A superconducting cavity is introduced in the external feedback loop of a TWT. The loop includes also a variable attenuator and a phase shifter for the purpose of adjusting gain and phase. The device can oscillate if the over-all gain is higher than unity and if the total phase shift is a multiple of  $2\pi$ .

Instabilities in the electrical length of the loop as well as mechanical vibrations, limit the observed frequency stability, but the use of a high Q superconducting cavity is highly efficient in reducing the resulting line width to a low value.

Here, the cavity is made of OFHC copper covered with a lead layer of about 5  $\mu$  in thickness. The oscillating mode is  $TE_{011}$  and the resonance frequency 2911 MHz. External coupling is secured by two small loops of coaxial lines. The resonance frequency is mechanically tunable between the limits  $2911 \pm 10$  MHz. A fine adjustment is provided by a superconducting lead plunger (Fig. 8).

---

8. M.S. Khaikin, Instr. and Experimental Techniques (transl.) 4, 518 (1961).

9. Nguyen Tuong Viet, Compt. Rend. Paris 258, 4218 (1964).



## 2. Frequency Stability

As shown in a previous paper<sup>10</sup> stability is controlled by the helium bath temperature, the room temperature and the high dc voltage applied to the helix of the TWT.

Helium bath temperature fluctuations are due to variations of the pressure of helium vapor; pressure could be well regulated and the temperature can be maintained constant within  $3 \times 10^{-5}$  °K at 2.1°K. Temperature fluctuations cause a change in the surface reactance of the superconductor and in the mechanical dimensions of the cavity (thermal expansion and elastic deformation due to pressure difference between the inside and the outside of the cavity). In any case they result in a slow drift of the resonance frequency.

A great part of the electrical circuit is at room temperature and subject to its variations, which change both mechanical length and dielectric permittivity. Standard precautions are enough to reduce the level of this kind of disturbance to a low level.

Another source of instabilities can arise from fluctuations of the dc voltage applied to the helix of the TWT which change the phase in the loop. The dc voltage used has a relative variation smaller than  $1.5 \times 10^{-5}$ .

Table III shows the frequency fluctuation  $df/f$  obtained by calculation.

TABLE III

TWT CSF/F4107B,  $T = 2.1^\circ\text{K}$ ,  $Q = 3.3 \times 10^7$

		<u><math>df/f</math></u>
Helium bath temperature $ \Delta T  = 3 \times 10^{-5} \text{ }^\circ\text{K}$	Thermal expansion	$1.3 \times 10^{-14}$
	Elastic deformation	$2 \times 10^{-11}$
	Surface reactance	$1.2 \times 10^{-13}$
Room temperature $ \Delta T  = 0.1^\circ\text{C}$	Coaxial length	$6.7 \times 10^{-12}$
	Permittivity (teflon)	$2.4 \times 10^{-11}$
Helix voltage $ dV/V  = 1.5 \times 10^{-5}$		$2.2 \times 10^{-11}$

Frequency fluctuations due to elastic deformation are difficult to reduce for given variations of helium bath temperature, even for higher  $Q$  of the cavity. But fluctuations due to room temperature changes and helix voltage variations can be made as small as possible by increasing  $Q$  (we have realized a cavity having a  $Q$  of  $3.3 \times 10^9$  at 2°K but higher  $Q$ 's have been obtained at Stanford<sup>11</sup> and Brookhaven<sup>12</sup>).

10. Nguyen Tuong Viet, Ann. Phys. (Paris) 2, 225 (1967).

11. J.P. Turneaure, Ph.D. Thesis, Stanford University Report HEPL 507 (1967).

12. H. Hahn, H.J. Halama, and E.H. Foster, J. Appl. Phys. 39, 2606 (1968).

### 3. Experiments Performed

#### Long-term frequency stability.

One milliwatt oscillator (TWT CSF/F4107B):

Figure 9 shows the measured frequency vs time for a 1 mW oscillator having the following parameters:

$$P = 1 \text{ mW}, f = 2911 \text{ MHz}, Q_L = 3.3 \times 10^7, T = 2.1 \pm 3 \times 10^{-5} \text{ }^\circ\text{K}, \\ dV/V = 1.5 \times 10^{-5} \text{ per minute.}$$

Over 6 minutes, the frequency changes by 0.8 Hz and the corresponding stability is  $2.7 \times 10^{-10}$ , i.e.,  $4.5 \times 10^{-11}$  per minute.

Figure 10 shows the influence of helium bath temperature on stability.

One watt oscillator (TWT Huggins HA100C):

In the 1 W oscillator, we have obtained a stability of  $3.4 \times 10^{-10}$  per minute under the following conditions:

$$P = 1 \text{ W}, f = 2911 \text{ MHz}, Q = 4 \times 10^7, T = 1.9 \pm 3 \times 10^{-4} \text{ }^\circ\text{K}, \\ dV/V = \pm 5 \times 10^{-4}.$$

Short-term frequency stability. To have an idea about the short-term frequency stability, the two output signals of the above oscillators are mixed to produce a beat signal whose average frequency is much lower than that of the input signals. The 12 MHz beat signal is mixed again with a frequency synthesizer, whose frequency fluctuations do not degrade the measurement, to get a low frequency signal of 10 kHz. The period of the latter is then measured by a counter and each measurement printed out in a digital recorder. The relative standard deviation of the frequency  $\sigma(\langle \dot{\phi} \rangle_t, \tau) / 2\pi f$  is calculated for different values of  $\tau$ . Figure 11 illustrates the results obtained after removal of slow drifts.

### IV. CONCLUSION

We hope that better long-term stabilities will be obtained in the monotron oscillator after a stabilization of the liquid helium bath temperature; some improvements on voltage source regulation also appear now feasible.

It seems possible to obtain with these oscillators frequency stability as good as that of the best quartz multiplier sets, retaining the advantages of relatively high power and frequency adjustment (in the TWT oscillator).

Much higher frequencies can also be explored, and new experiments are going in this way: in the monotron oscillator, the modulated beam emerging from the superconducting cavity tuned at  $f_0$  is forced to cross a second cavity, resonating at a harmonic frequency  $nf_0$ , and power can be obtained at this frequency.

In the future, one-cavity linear accelerators could be powered by using a high-power amplifier and the accelerator cavity itself.

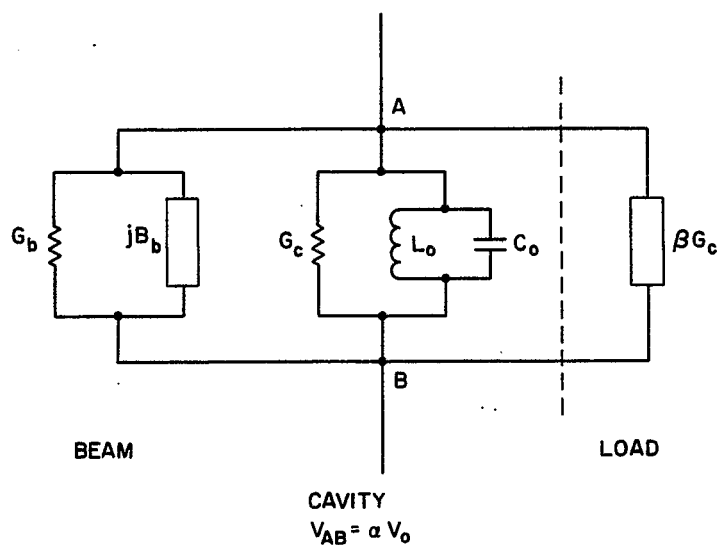


Fig. 1. Equivalent circuit of the monotron.

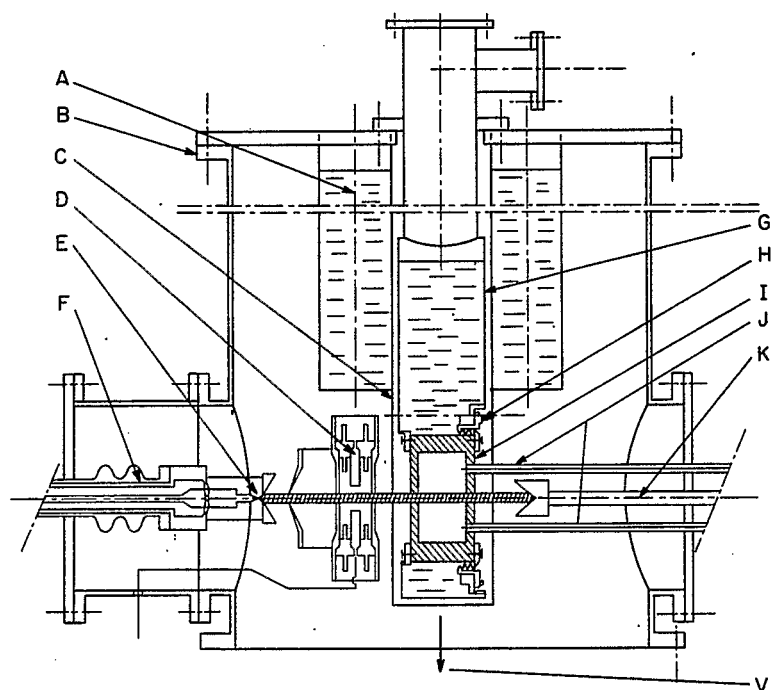


Fig. 2. Arrangement for monotron with superconducting cavity: A, liquid nitrogen vessel; B, vacuum chamber; C, copper sheet; D, electrostatic lens; E, triode electrode gun; F, high voltage isolation of the electron gun; G, liquid helium vessel; H, indium gasket for vacuum; I, superconducting cavity; J, coupling coaxial guide; K, electron collector; V, vacuum pump.

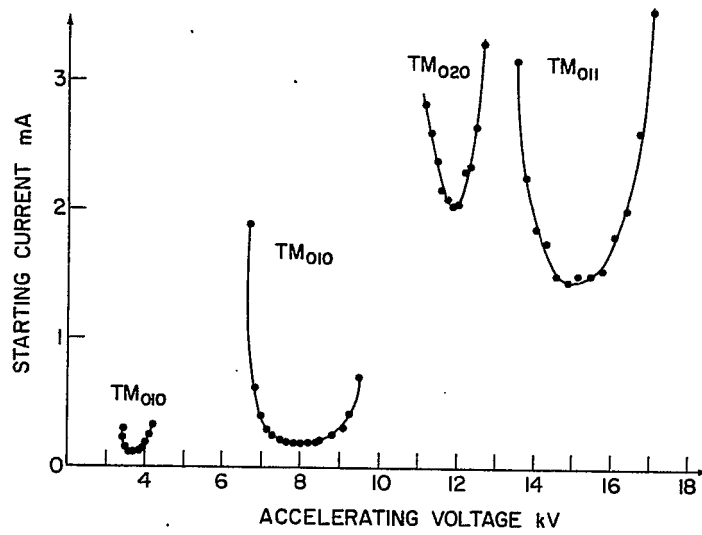


Fig. 3. Starting current in various oscillation modes in cavity with  $Q = 10^7$ .

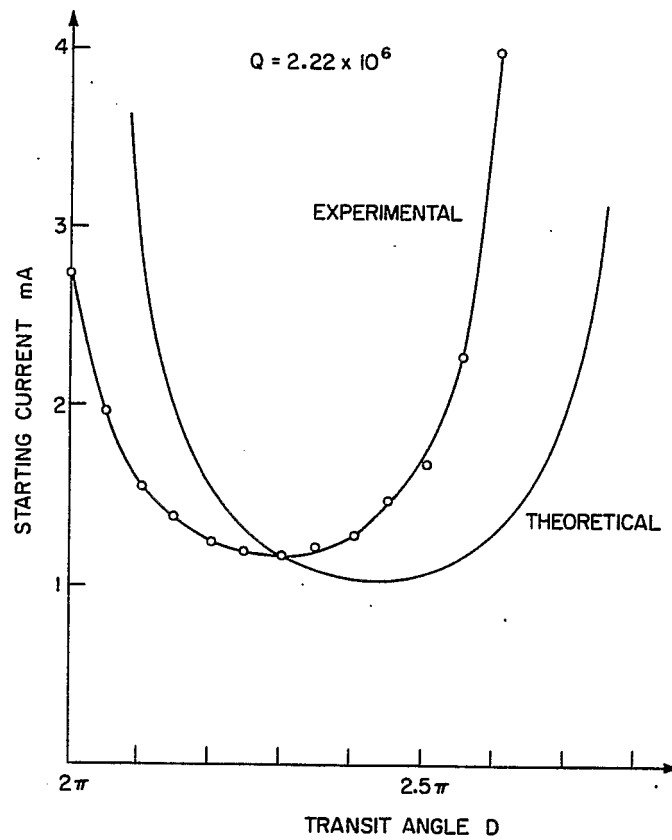


Fig. 4. Starting current of oscillation in  $TM_{010}$  mode at  $Q = 2.22 \times 10^6$ .

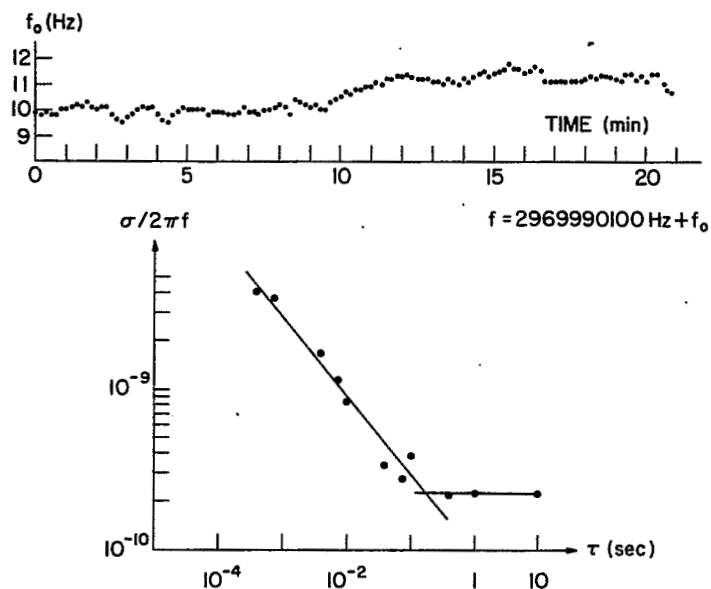


Fig. 5. Oscillator frequency and short-term frequency stability at  $Q = 10^7$ .

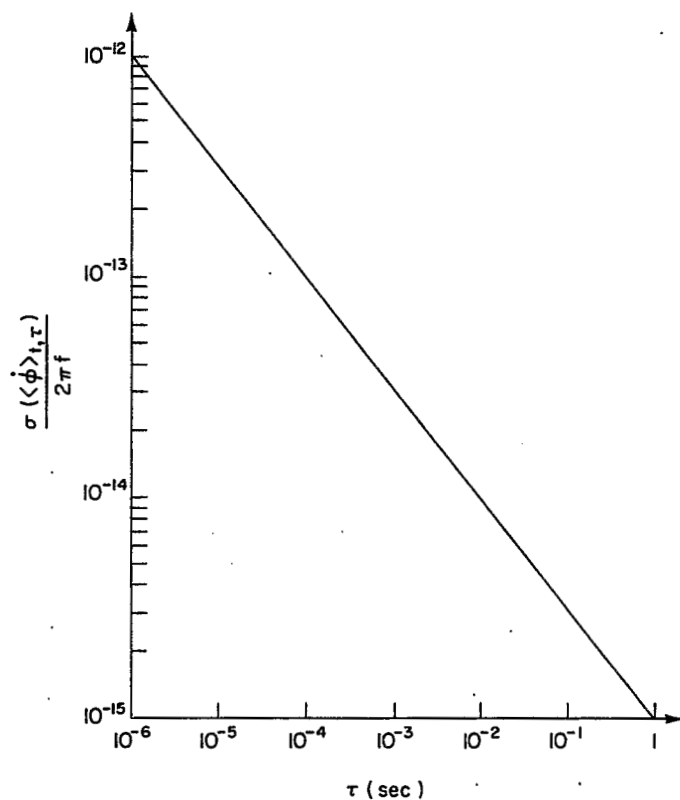


Fig. 6. Theoretical short-term frequency stability:  $f = 3 \text{ GHz}$ ,  $Q = 10^7$ ,  $P = 0.1 \text{ W}$ .

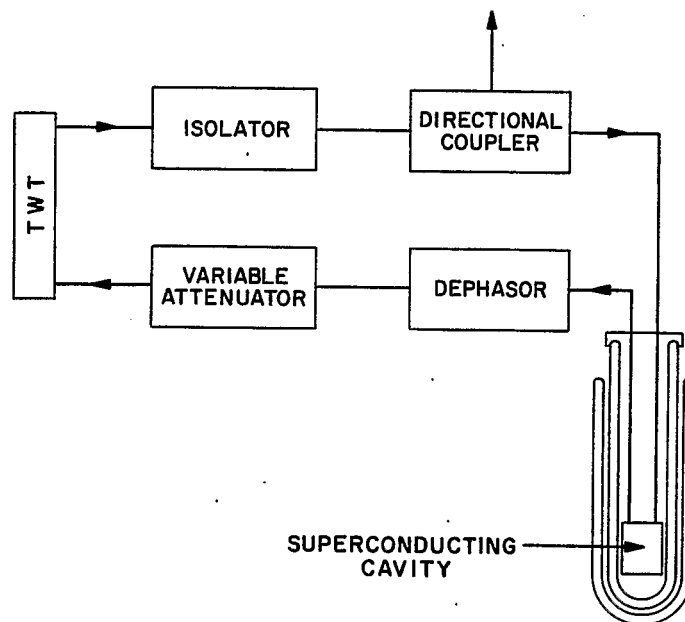


Fig. 7. Block diagram of the TWT auto-oscillator.

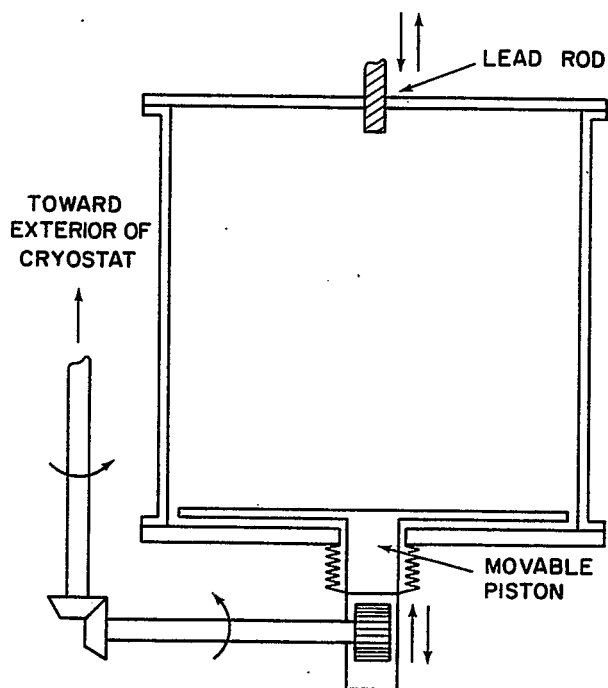


Fig. 8. Tunable cavity.

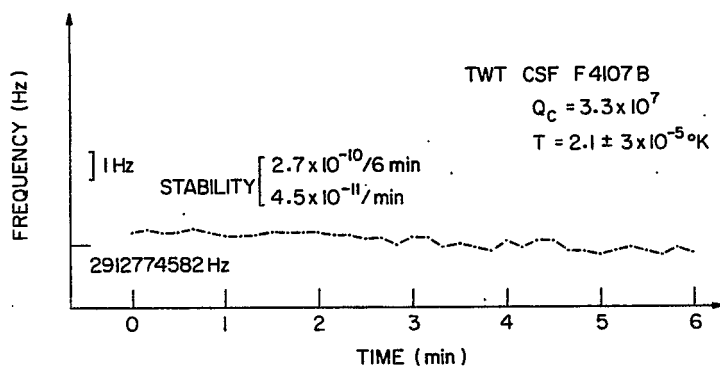


Fig. 9. Frequency vs time.

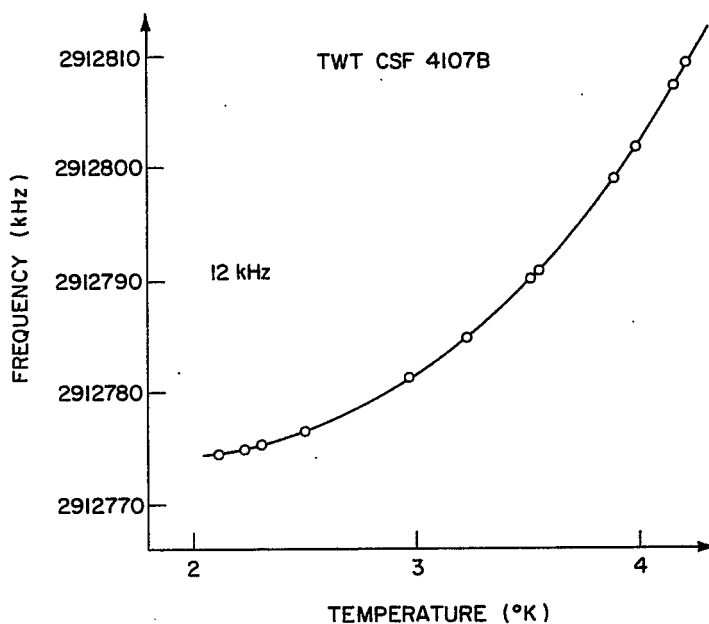


Fig. 10. Frequency vs helium bath temperature.

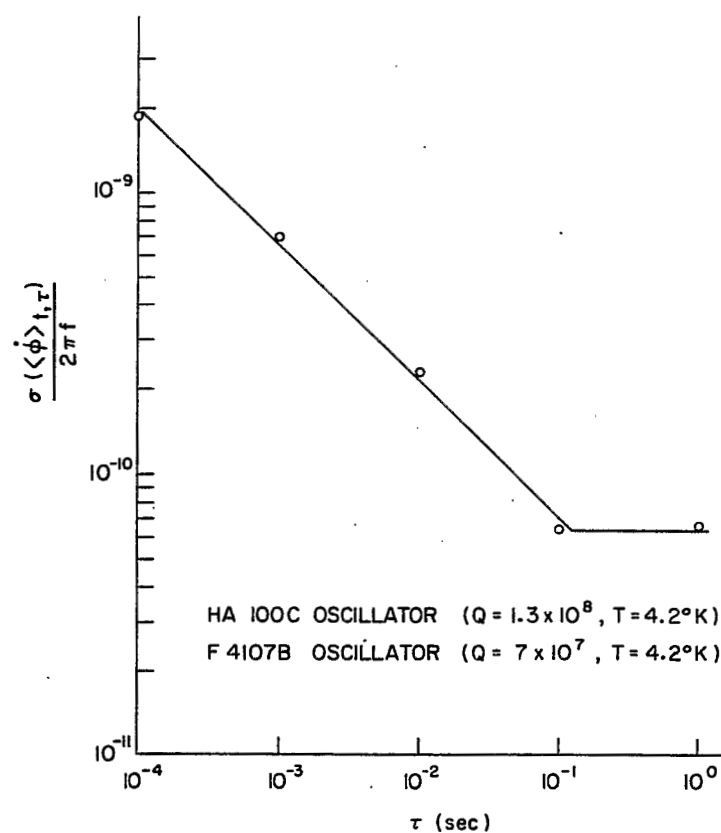


Fig. 11. Short-term frequency stability of TWT oscillator.



## SUMMARY OF FIRST WEEK OF SUMMER STUDY

H.A. Schwettman<sup>†</sup>

Department of Physics and High Energy Physics Laboratory  
Stanford University  
Stanford, California

The first week of the 1968 Summer Study on Superconducting Devices and Accelerators at the Brookhaven National Laboratory dealt with the rf applications of superconductivity and, in addition, with the superfluid helium technology which is essential to this development. The discussion during the week was lively and productive and the sessions were attended by a broad spectrum of physicists from industrial, government, and university laboratories in this country and abroad.

### I. RF PROPERTIES OF SUPERCONDUCTORS AND CAVITY FABRICATION TECHNIQUES

During the first week a great deal of time was given to a careful discussion of recent experiments and planned research on the rf properties of superconductors. This discussion included papers by Hahn from Brookhaven, Turneaure from Stanford, Jüngst from Karlsruhe, Allen and Hogg from SLAC, and Haden from Texas. In addition, because of the particular interest in the recent developments of high Q, high field niobium cavities, Turneaure from Stanford, Meyerhoff from the Linde Division of Union Carbide, and Weissman from Varian Associates described in detail the special techniques involved in the preparation of niobium cavities, and the promising fabrication techniques being developed for construction of practical niobium accelerator structures.

Historically, most of the early experiments by groups interested in superconducting linacs involved measurements on lead cavities. Recently, the greatest emphasis has shifted to niobium, although active experimental work on lead continues. Niobium with a transition temperature of  $9.25^{\circ}\text{K}$ , and lead with a transition temperature of  $7.2^{\circ}\text{K}$  exhibit the very highest transition temperatures and critical magnetic fields among common elemental superconductors. Autler pointed out during the Summer Study, however, that technetium with a transition temperature of  $7.7^{\circ}\text{K}$  should, perhaps, be added to the list of interesting elemental superconductors. The principal disadvantage of technetium is the fact that its nucleus is unstable and beta decays with a half-life of  $5 \times 10^5$  years. There is good reason for the concentration of effort on the development of pure metals for rf applications. Contrary to the case of high field superconducting magnets, high Q, high field superconducting cavities depend on the absence of flux penetration and it is to be expected that this condition can be satisfied best with pure metals. Despite this fact, a few exploratory experiments are planned at Stanford and at SLAC to investigate the fundamental rf properties of some of the superconducting "alloys" which exhibit marked type II behavior.

Extremely high Q's in superconducting cavities were first obtained at Stanford in 1964 using electroplated lead cavities. From the experiments reported by various groups (Brookhaven, Stanford, Karlsruhe) at the Summer Study, it may be concluded that, for lead-plated  $\text{TE}_{011}$  mode cavities, Q's in excess of  $10^9$  are now commonplace and Q's in excess of  $10^{10}$  are frequently achieved. Results reported for TM mode cavities, however, are less encouraging (Stanford, Karlsruhe). Lead surfaces are easily contaminated and in TM mode cavities, where there are large electric fields at the cavity

---

<sup>†</sup> Alfred P. Sloan Research Fellow.

walls, dielectric losses are observed to limit the  $Q$ 's to values that are typically a few times  $10^8$ . In addition, the contamination undoubtedly contributes to enhanced field emission currents when TM mode cavities are operated at high power levels. One interesting approach to this problem is being studied by the group at Karlsruhe. A protective indium layer is plated over the lead. This layer is made sufficiently thin that due to the proximity effect the indium is superconducting even at temperatures above its usual transition temperature. No definitive conclusions have been reached yet in this investigation, but it can be hoped that this method or a similar method will be successful.

Whereas the problem of contamination must yet be solved before lead can be used effectively in accelerator applications, the development of niobium has proceeded well beyond this point. Cavity  $Q$ 's exceeding  $10^{10}$  and energy gradients exceeding 3 MeV/ft in a standing wave structure, or 5 MeV/ft in a traveling wave structure, have been achieved in TM mode cavities fabricated from commercially available reactor grade niobium (Stanford and Varian) and it is expected that niobium of greater purity will produce even better results. Some confidence was expressed at the Summer Study that energy gradients as high as 6 MeV/ft in a standing wave structure or 10 MeV/ft in a traveling wave structure will eventually be achieved. At 1.3 GHz and 1.85°K, the power dissipation in a traveling wave structure at 10 MeV/ft can be as small as 2.8 W/ft, and thus, with pure niobium, it appears that superconducting accelerators operating continuously at very high energy gradients could be possible.

Fabrication techniques for producing superconducting niobium accelerators must be developed with a view toward obtaining not only high energy gradients and low refrigeration requirements, but also low cost. The cost of a niobium accelerator structure differs most markedly from a conventional copper accelerator structure in that niobium is an order of magnitude more expensive. The expense, for instance, eliminates machining of niobium cavities from solid billets as a practical way for producing an accelerator structure. This technique was used in making the TM<sub>010</sub> mode niobium cavity which gave the high energy gradient and  $Q_0$  reported by Weissman and Turneaure. The cost of producing an accelerator structure can be considerably reduced by providing a more efficient means of forming the niobium. Meyerhoff described a technique of electroplating thick layers of niobium from a molten fluoride salt. The niobium could be electroplated onto relatively complicated cathode geometries and in the process considerable refining of the niobium is achieved. The process for producing the niobium accelerator structure consists of making a copper mandrel, electroplating a layer of niobium about 0.150 in. thick on the copper mandrel, chemically dissolving the copper mandrel leaving a niobium shell, and vacuum outgassing the niobium at high temperature ( $\sim 2000^\circ\text{K}$ ). There are other ways in which an accelerator structure could be formed which differ primarily in the technique of producing the niobium layer. One technique is chemical vapor deposition (CVD) which uses the chlorination-hydrogen reduction reaction of niobium. A second technique is forming reactor grade niobium sheet or tubing around a mandrel by hydroforming, explosive forming, or die forming.

An alternative way to reduce the cost of fabricating a niobium accelerator structure is to plate a thin layer of niobium a few microns thick on a less expensive substrate such as copper. This technique would reduce the cost of the niobium to a negligible fraction of the total cost of the accelerator structure.  $Q_0$ 's between  $100 \times 10^6$  and  $500 \times 10^6$  have been measured at Stanford using thin layers of electroplated (Linde), CVD (Varian), and sputtered niobium. To achieve the highest  $Q_0$ 's in these cases, it was necessary to polish the niobium layer with alumina abrasive to the order of 1  $\mu$ . These mechanically polished cavities appear, however, to have a critical field limited to about 100 G. The development of useful thin layer niobium structures probably awaits the development of more sophisticated techniques for degassing, smoothing, and producing suitable crystal size in the niobium layer.

## II. CRYOGENIC SYSTEM USING SUPERFLUID HELIUM

The successful development of large-scale cryogenics using the unique properties of superfluid helium is essential to the operation of a superconducting linac. During the first week of the Summer Study the use of the superfluid properties of helium and the design of a large integrated cryogenic system were discussed by McAshan from Stanford, while developments in superfluid refrigeration were described by Collins from Arthur D. Little, Inc.

As described by McAshan, the special property of helium II that is important in applications is the natural internal circulation of the superfluid component and the normal fluid component which occurs in the presence of thermal differences. For instance, in helium II the superfluid component flows to a heat source and there absorbs a quantity of heat,  $Q = ST$ , in the process of being converted to normal fluid. To maintain constant density the normal fluid component must flow in the opposite direction. This natural convection is responsible for the unique heat transport properties of helium II which are essential to maintaining local thermal equilibrium in a superconducting linac. Further, if two reservoirs of helium II are connected by a superleak which permits the flow of the superfluid component but inhibits the flow of the normal fluid component, then a small temperature difference results in a large pressure difference across the superleak which in turn can be used to support a column of helium greater than 100 ft in height. The pressure across the superleak, known as the fountain pressure, is an osmotic pressure which arises as the helium tries to equalize the superfluid concentrations in the two reservoirs. This phenomenon can be used to construct a fountain pressure pump for transferring helium II from one reservoir to another for providing refrigeration to an experiment located far above the main helium reservoir.

Some of the systems problems which are encountered in the design of a large complicated cryogenic system were also discussed. In a system as large and complicated as the superconducting linac planned at Stanford, it is mandatory that the design be sufficiently flexible that in the event of some component failure the relevant cryogenic subunit can be isolated from the central refrigeration system and can be replaced without disrupting the cryogenic operation of the rest of the system. Such problems as reliability, alignment of the accelerator while at low temperature, and even design of specific components were also described and actively discussed.

In addition to a brief description of the 300 W superfluid refrigerator that was constructed by Arthur D. Little, Inc. and is now being installed at Stanford, Collins discussed two questions which are important in the development of future superfluid refrigerators. One of these questions concerns efficiency and the other concerns the feasibility of using a low temperature pump to replace the large and expensive room temperature pumping system now used. Collins suggested a refrigerator design using a low temperature pump which he felt might operate at 25-35% of Carnot efficiency. Such a system would represent a substantial advance in the state of the art.

## III. STABILIZATION AND ENERGY RESOLUTION IN A SUPERCONDUCTING LINAC

The superconducting linac, due to its relatively high  $Q$ , provides a unique opportunity for the use of feedback to achieve dynamic stability. This fact has encouraged Stanford to strive for energy resolution of 0.01% in the superconducting linac (100 keV at 1 GeV), as compared to the 1% resolution typical of conventional linacs.

Stabilization of the superconducting linac using feedback control was described by Suelzle. In the work at Stanford, the accelerating fields themselves are stabilized so that variations in beam loading do not affect the output energy. The long time constant for changes in the accelerating fields simplifies the feedback problem, and stabilization to one part in  $10^4$  in amplitude and to  $0.1^\circ$  in phase has been achieved in preliminary tests.

To produce a monoenergetic beam within one part in  $10^4$  requires, in addition to stability of the accelerating fields, that the electrons be confined to a one-degree phase bunch. This bunching is accomplished in the injector section and the capture section of the accelerator. In the system at Stanford, the electrons are emitted from a regulated triode gun and accelerated to 80 kV. The continuous stream of electrons then passes through a chopper cavity, and an aperture on the far side stops all electrons except those in a  $20^\circ$  phase bunch. These electrons are injected into a specially designed capture section where they are accelerated to about 2 MeV, and where the electron bunch is compressed in phase to one degree. The capture section is a  $\beta = 0.95$  structure of  $2\frac{1}{2}$  wavelengths, and the design energy gradient is 1 MeV/ft. Chambers from Stanford described calculations of the particle motion in the accelerator sections beyond the capture section, using the actual fields in the biperiodic  $\pi/2$  mode structure. These calculations included the effects of radial motion and misalignment of individual accelerator sections.

The excellent stability and energy resolution that can be achieved in a superconducting linac makes possible high resolution experiments at high energy but, in addition, it suggests possible changes in the design of a high energy facility. With good stability and resolution, there is no reason for generating large amounts of radiation along the accelerator or in the beam switchyard. For instance, in the beam switchyard instead of energy defining slits which are designed to handle 10% of the beam power, beam position monitors could be used, supplemented perhaps with slits that are set for several times the inherent width of the beam. Low radiation levels along the accelerator and throughout the beam switchyard could make a significant impact on the cost of a high energy facility.

#### IV. ACCELERATOR STRUCTURES

Several aspects of structure design for a superconducting linac were discussed during the week by Smith from Stanford, Neal from SLAC and Jüngst from Karlsruhe. Smith discussed in some detail the computer optimization of structures for a superconducting linac with respect to the peak electric and magnetic fields and the shunt impedance, and, in addition, analyzed the effect of individual cell frequency errors on the field profile. Smith also discussed the very important problem of tuning the accelerator sections to the same frequency within one part in  $10^9$  and described several methods of accomplishing this objective that are being studied at Stanford. Neal from SLAC described the calculated properties of a superconducting traveling-wave resonant ring accelerator and, using these properties, presented sample parameters for a two-mile superconducting linac. Jüngst discussed the proton linac structure design work that is in progress at Karlsruhe and described the electron analogue experiments which are being prepared.

#### V. RF PARTICLE SEPARATORS

In addition to accelerator applications, superconductivity can be used to advantage in the construction of rf separators. As in the case of the linac, the high Q that can be achieved with superconducting cavities makes it possible to build a separator that operates at a high duty cycle, matching that of the proton synchrotron, and, as a result, there is great interest in this development. A general discussion of the design of rf separators was presented by Brown from Brookhaven, and this discussion was followed by an outline of the superconducting rf separator programs under way at Brookhaven, Karlsruhe, and the Rutherford Laboratory. Halama described the work at Brookhaven where an S-band superconducting separator for 16 GeV/c is being studied. The program at Karlsruhe was described by Jüngst. The Karlsruhe group plans to construct a separator for 10 GeV/c to be used at CERN. At the Rutherford Laboratory plans are being made to construct a separator for about 3 GeV/c, and this was described by Carne.

## VI. THE RACETRACK MICROTRON AND THE RECIRCULATING LINAC

One interesting possibility in the construction of accelerators, which is a compromise between the linear and the circular machines, is the racetrack microtron or the recirculating linac. Sutton outlined the very interesting program at Illinois to construct a 600 MeV unity duty cycle racetrack microtron that makes use of a superconducting accelerator section. Sutton described the proposed equipment layout for the microtron and presented detailed calculations of beam optics and phase stability.

This type of accelerator also provides an interesting approach to the construction of a very high energy, say 2000 GeV, machine. As pointed out by Schwettman, however, a practical recirculating linac for very high energy particles is different in several respects from the racetrack microtron mentioned above. First, at very high energy, electrons radiate too much energy to make the scheme useful. But protons, even for a final energy of 2000 GeV, are not subject to this criticism. Second, for a very high energy accelerator, the magnetic deflection system used in the racetrack microtron is impractical. Instead of solid  $180^\circ$  magnets, it would be more reasonable to provide separate beam transport systems and arrange that the average radius of curvature for each beam is nearly the same so that they could all be placed in a single tunnel. For the special case of three passes through the linac, the beam transport system might be particularly simple, since recirculation could in principle be accomplished with a single magnet system for two-thirds of the final energy.

Recently crude cost estimates have been generated for a number of "new technology" accelerators: the superconducting proton synchrotron, the cryogenic proton synchrotron, the superconducting recirculating linac, the superconducting FFAG, and the electron ring accelerator. Relatively little significance should be attached to any of these estimates, since all are based on important assumptions about how the relevant technology will develop over the next few years. What is far more significant and encouraging is that several possibilities exist for the construction of future high energy accelerators and these provide alternatives in the technology that must be successfully developed. This flexibility itself is our greatest asset.

## **SECOND WEEK - CRYOGENICS**

**Chairman: T.R. STROBRIDGE, NBS, Boulder**

# REFRIGERATION AT 4°K\*1

T.R. Strobridge  
Cryogenics Division, Institute for Basic Standards  
National Bureau of Standards  
Boulder, Colorado

## I. INTRODUCTION

Refrigeration in the region of 4°K will be necessary for the subject superconducting devices until practical materials with higher transition temperatures become a reality. Even though helium was discovered in the sun's atmosphere one hundred years ago and was identified on earth in 1895, refrigeration technology progressed slowly until the middle of the 1940's. Today, 4°K refrigerators can be obtained in capacities ranging from 1 W to several kilowatts. The scientific literature shows that much early low temperature research was devoted to liquefying the more difficult of the normally gaseous elements. Liquefaction of the lowest temperature fluid, helium, was finally accomplished by H. Kamerlingh Onnes on July 10, 1908.<sup>2</sup> Onnes was awarded the Nobel prize for this contribution to the technology. Many of the succeeding experiments were concerned with the behavior of helium itself and led to the discovery of the lambda transition and the unique, interesting properties of liquid helium II. Investigations rapidly branched out to other materials and superconductivity was observed in mercury by Onnes in April of 1911.<sup>3</sup> Reference 1 is devoted to the refrigeration methods used today - evaporating liquid helium baths, the Simon process, the Joule-Thomson, Brayton, Claude, Stirling and Gifford-McMahon cycles.

## II. THERMODYNAMIC RELATIONSHIPS

The behavior of refrigerators and their components are governed by the laws of thermodynamics. The first law of thermodynamics relates the mass and energy fluxes that occur in natural events. It is used to predict the outcome of the various processes that make up a refrigeration cycle. The first law as given in Eq. (1) and illustrated in Fig. 1 shows that modern nomenclature has clarified the concept of a control volume and a thermodynamic system:

---

\* Contribution of National Bureau of Standards, not subject to copyright.

1. The material on refrigeration presented to the cryogenics session of the Summer Study on Superconducting Devices and Accelerators was selected from:

T.R. Strobridge, in The Technology of Liquid Helium, published as NBS Monograph 111 (1968).

This chapter will be available about the same time that these Proceedings will appear. Therefore, a summary is given here and the reader is referred to Ref. 1 for detail.

2. H. Kamerlingh Onnes, *Communs. Phys. Lab., Univ. Leiden*, No. 108 (1908).
3. H. Kamerlingh Onnes, *Communs. Phys. Lab., Univ. Leiden*, No. 1226 (1911).

$$Q_{c.v.} + \sum m_i \left( h_i + \frac{v_i^2}{2g_c} + z_i \frac{g}{g_c} \right) = W_{c.v.} + \sum m_e \left( h_e + \frac{v_e^2}{2g_c} + z_e \frac{g}{g_c} \right) + \left[ m_2 \left( u_2 + \frac{v_2^2}{2g_c} + z_2 \frac{g}{g_c} \right) - m_1 \left( u_1 + \frac{v_1^2}{2g_c} + z_1 \frac{g}{g_c} \right) \right]_{c.v.} \quad (1)$$

The terms  $Q_{c.v.}$  and  $W_{c.v.}$  are the heat and work crossing the control surface,  $m$  is mass,  $h$  is specific enthalpy,  $u$  is specific internal energy,  $V$  is velocity, and  $Z$  is vertical position. The subscripts  $i$  and  $e$  refer to the incoming and exiting flows, and 1 and 2 refer to states 1 and 2 in the control volume indicated by the subscript  $c.v.$  The proportionality constant that relates force, mass, time, and length in Newton's second law is  $g_c$  and the local acceleration of gravity is  $g$ . (In the SI system,  $g_c = 1 \text{ kg}\cdot\text{m}/\text{N}\cdot\text{sec}^2$ .) The convention is adopted that heat transferred to the system is considered positive as is work done by the system.

The second law of thermodynamics leads to the definition of entropy and is the basis for the concepts of the thermodynamic temperature scale, the Carnot cycle, reversibility, and irreversibility. As stated, the first law predicts the outcome of an assumed process. However, the first law holds equally well for the process proceeding in the reverse direction. The permissible directions for processes are given by the second law.

The second law is useful for rating the performance of processes and cycles. Conventionally, the thermal efficiency of an actual refrigerator is compared to that of a Carnot refrigerator operating between the same temperature levels. The ratio of the amount of power required by a Carnot machine to the refrigeration produced is given by

$$\frac{W_c}{Q_{\text{Carnot}}} = \frac{T_o - T}{T} \quad (2)$$

where  $W_c$  is the net power,  $Q$  is the refrigeration produced,  $T$  is the temperature, on the thermodynamic scale, at which the cycle is producing refrigeration, while  $T_o$  is the temperature at which heat is being rejected by the machine - usually about  $300^\circ\text{K}$ , the nominal temperature of the earth's atmosphere or cooling water supply. Thus, for a helium temperature refrigerator operating between  $4.2$  and  $300^\circ\text{K}$ , the best performance that could be achieved is 70.4 units of power required per unit of refrigeration. As will be seen later, it is not unusual for an actual machine to consume 100 times the Carnot power per unit of usable refrigeration. The efficiencies of various processes are also calculated by comparing them with appropriate, assumed, reversible processes.

### III. REFRIGERATION CYCLES AND METHODS

#### 1. Liquid Helium Baths

By far the most common method of providing cooling at  $4.2^\circ\text{K}$  is by using liquid helium, supplied from a remote liquefier, as the heat sink. Cryostat designs vary widely to accommodate the apparatus or sample that is to be cooled. However, care must be taken to make sure that the vessel can be efficiently cooled down and filled. Adequate pressure relief must be provided and the vent system must prevent atmospheric gases from entering the cold space. The cold saturated helium vapor leaving the vessel has a great deal of refrigeration potential and in some instances the vent pipe is



attached to intermediate temperature shields which reduce the amount of heat transfer from the surroundings to the low temperature space, thus decreasing the liquid evaporation rate. The heat of vaporization of liquid helium is 0.725 Wh/liter at 1 atm pressure. Thus a one watt heat load will evaporate 1.38 liters of liquid per hour and large heat loads require substantial amounts of the relatively expensive liquid. Each new cooling requirement forces a choice between refrigerating with bulk liquid helium or a closed-cycle refrigerator.

## 2. The Simon Process - Adiabatic Expansion

In the years before the development of the Collins liquefier, the Simon process was often used to batch-produce small amounts of liquid helium. When a heavy walled container filled with high pressure gas is allowed to vent, the fluid in the container expands isentropically and its temperature is accordingly depressed as the pressure is lowered. Although the expansion process is isentropic, as the fluid cools there will be heat transferred to it from the warmer walls of the vessel resulting in an entropy increase of the fluid. Fortunately, at liquid helium temperatures the specific heat of most container materials is very low and such entropy contributions may be negligible. In practice, the high pressure helium and the container are cooled to at least 20°K prior to the expansion process to increase the liquid yield. The Simon process has recently been used to refrigerate sodium magnet coils at approximately 7°K by the Lawrence Radiation Laboratory, Livermore, California.<sup>4</sup>

## 3. The Joule-Thomson Process

The lowest temperature stage in virtually all liquid helium temperature refrigerators consists of a counter flow heat exchanger, an expansion valve, and an evaporator. The Joule-Thomson process is defined as the adiabatic isenthalpic reduction in pressure of a fluid flowing through a restriction in a passage. This process takes place only in the expansion valve mentioned above, but its relationship with the energy transferred in the heat exchanger and the evaporator is important. Consider steady state operation of the heat exchanger, expansion valve and evaporator (where the heat load is absorbed) shown in Fig. 2. The saturated liquid in the evaporator changes phase to saturated vapor as heat enters the system from the load. The cold vapor enters the low pressure side of the heat exchanger where energy is transferred to it from the warmer high pressure stream. The high pressure stream enters the warm end of the heat exchanger at a temperature slightly higher than the exiting low pressure stream and is cooled in counterflow heat exchange with the low pressure stream. Expansion through the valve reduces the pressure and temperature of the fluid so that a part of the helium is liquefied. The fraction of the flow that is not liquefied in the expansion process joins the vapor entering the low pressure side of the heat exchanger. Thus the liquid in the evaporator is continuously being depleted by the heat load and supplied at the same rate by the expansion valve. The refrigeration or cooling effect is isothermal because it is obtained by evaporating a saturated liquid and the refrigeration temperature is controlled by the pressure in the evaporator.

Whether a fluid will heat or cool upon expansion in the Joule-Thomson process depends upon the properties of the fluid and the pressure and temperature prior to the expansion. For example, at room temperature, nitrogen will cool in the Joule-Thomson process but helium and hydrogen will heat. Therefore, the system illustrated in Fig. 2 can be made into a closed cycle nitrogen temperature Joule-Thomson refrigerator by supplying a compressor between stations 1 and 5, an insulating enclosure

---

4. C.E. Taylor, in Proc. 1965 Symposium on Engineering Problems of Controlled Thermo-nuclear Research, p. 152.

and the appropriate controls. Because of the heating effect in helium at higher temperatures, a helium refrigerator must have additional cooling means such that the temperature of the gas entering the high pressure side of the low temperature heat exchanger is below about 55°K (the maximum inversion temperature) and preferably much lower. The way in which this precooling is accomplished accounts for the differences in the thermodynamic cycles used for helium temperature refrigerators.

The amount of power required to produce a given amount of refrigeration at a given temperature is always of interest to a potential user for two reasons. First, very low temperature refrigerators require high input power relative to the cooling capacity - operating costs are obviously affected. Second, the capital cost of such equipment is proportional to the installed drive power so low efficiencies mean increases in both purchase price and operating expense. The input power to the Joule-Thomson circuit required per unit of refrigeration decreases for lower precooling temperatures ( $T_1$  in Fig. 2) and better heat exchanger efficiencies as evidenced by smaller temperature differences between the fluid streams at the warmer end of the heat exchanger ( $T_1 - T_5$ ). If a cycle is characterized by a certain precooling temperature and heat exchanger temperature difference, then there is only one high pressure that will give optimum performance, i.e., minimum input power ( $W_c$ ) per unit of refrigeration ( $Q$ ). Dean and Mann<sup>5</sup> have made extensive calculations of the performance of Joule-Thomson refrigerators for low temperatures. Figure 3 is a skeleton diagram illustrating their results. The plot is for a constant heat exchanger temperature difference and shows the input power per unit of refrigeration as a function of the high pressure, for various precooling temperatures. Graphs for other heat exchanger temperature differences form a family of performance surfaces. The line marked optimum is the locus of minima in the curves of constant precooling temperature, the inversion curve is superimposed and the mass flow rate per unit of refrigeration is given. Below and to the right of the line marked second law violation is a region in which the properties of the helium refrigerant will not permit a positive temperature difference between the warm and cold streams throughout the heat exchanger with the assumed precooling temperature and temperature differential ( $T_1 - T_5$ ). The series of performance curves<sup>5</sup> show the effect on performance of changes in the irreversibilities of the heat exchanger, in the precooling temperature, and in the level of the high pressure of the fluid entering the heat exchanger. It must be remembered that the power requirements are for the helium Joule-Thomson circuit only and that additional power will be needed to precool the helium to the inlet temperature of the heat exchanger.

#### 4. The Brayton and Claude Cycles

The cascaded Joule-Thomson helium refrigerator has a nitrogen circuit which pre-cools a hydrogen circuit at about 65°K which in turn pre-cools the helium circuit at about 15°K. The same energy removal necessary to depress the temperature of the helium at the inlet of the final heat exchanger to an acceptable level is often accomplished by using the refrigeration produced by one or more mechanical expanders of either the reciprocating or turbo-machinery varieties. A complete study of the Brayton cycle has been made<sup>6</sup> and the combination of the Brayton cycle with the Joule-Thomson process, known as the Claude cycle, has also been the subject of a complete analysis.<sup>7</sup> The schematic of the Claude cycle in Fig. 4 shows the heat absorber or evaporator thermally connected to the heat load  $Q$ . Heat exchangers III and IV and the two expansion

---

5. J.W. Dean and D.B. Mann, NBS Technical Note No. 227 (1965).

6. R.C. Muhlenhaupt and T.R. Strobridge, NBS Technical Note No. 366 (1968).

7. R.C. Muhlenhaupt and T.R. Strobridge, NBS Technical Note No. 354 (1967).

valves comprise the lowest temperature stages discussed in connection with the Joule-Thomson process. The second expansion valve between stations 4 and 5 is used at times to adjust the temperature profile in the heat exchanger and avoid the region of second law violation shown in Fig. 3. If the expansion valve between stations 4 and 5 is not necessary then heat exchangers III and IV are one unit and the arrangement below stations 3 and 10 is the same as in Fig. 2. In all of the heat exchangers, the low pressure gas returning to the compressor is used to cool progressively the high pressure helium moving toward the low temperature end of the refrigerators. Starting at station 1, the high pressure gas is cooled in HX-I. At station 2, a portion,  $\dot{m}_2$ , of the mass flow through the compressor,  $\dot{m}_1$ , is diverted through the expansion engine. The temperature of the helium decreases as the gas gives up energy by doing work on a piston or turbine blades in the expander (the energy is mechanically or electrically transmitted through the insulating cryostat to the surroundings). The low pressure exhaust of the expander joins the process stream returning to the room temperature compressor at station 10. The refrigeration produced by the mechanical expander is thus made available to precool the high pressure helium flowing toward the low temperature heat exchanger and expansion valve(s). The compressor effectively handles two process streams; the Brayton precooling cycle process path is 1-2-10-12 through the expander and upper heat exchangers, and the path to the low temperature stage is straight through all the heat exchangers. While the two streams can be thought of independently, they are in fact intimately mixed in the compressor, HX-I, and the low pressure side of HX-II.

For any given set of heat exchanger and expansion engine efficiencies and high pressure, there is an optimum engine inlet temperature in terms of over-all cycle performance. In addition, there is an optimum high pressure. The results of Ref. 7 provide a tool for the optimization of the Claude cycle over a wide range of parameters.

## 5. The Stirling Cycle

Low temperature refrigerators operating on the periodic flow Stirling cycle, incorporating one or more regenerators, lend themselves to compact construction with one piston serving for both compression and expansion in a single stage unit. For a thorough discussion of the Stirling cycle itself, see Ref. 8. Stirling cycle refrigerators are not in themselves suitable for refrigeration at liquid helium temperatures because of the rapidly decreasing specific heat of the regenerator materials at low temperatures. The lowest temperatures reported for pure Stirling cycle two-stage refrigerators are about 12°K. However, helium Joule-Thomson circuits are effectively precooled by this type of refrigerator. The precooling stations at two separate temperature levels are shown in Fig. 5, which is a schematic of such a refrigerator suggested by Rietdijk.<sup>9</sup> Energy is transferred from the helium to the Stirling cycle refrigerator through heat exchangers attached to the cold heads of the cooler. The configuration shown is analogous to a two expander Claude cycle. After leaving the lowest temperature precooling station at about 15°K, the helium enters the high pressure side of the Joule-Thomson heat exchanger. An expansion valve and evaporator at the low temperature end of that exchanger would complete the cycle and provide refrigeration at about 4°K if the compressor suction pressure were at one atmosphere. A rather more elegant arrangement is shown in Fig. 5 which allows the compressor suction pressure to be above the vapor pressure of the helium at the refrigeration temperature. The refrigerant is held at three different pressure levels by an expansion ejector. Full compressor flow at the highest pressure enters the nozzle of the ejector where it is accelerated to

---

8. G. Prast, Philips Tech. Rev. 26, 1 (1965).

9. J.A. Rietdijk, in Pure and Applied Cryogenics (Pergamon Press, 1966), Vol. 6, p. 241.

high velocities with a corresponding decrease in pressure. This region of low pressure induces flow,  $\dot{m}_2$ , from the low temperature evaporator through the low pressure side of the final heat exchanger. The two flow streams mix and, as the velocity is decreased, experience a rise in pressure to  $P_2$ . A fraction of the fluid emerging from the ejector may be liquefied. The stream is divided with  $\dot{m}_1$  returning to the compressor through the low pressure side of the heat exchangers and  $\dot{m}_2$  is diverted through the high pressure side of the lowest temperature heat exchanger to an expansion valve and the evaporator. The cooling capacity of a Joule-Thomson system depends only upon the mass flow rate and enthalpy difference at the warm end of the Joule-Thomson heat exchanger and is independent of the refrigeration temperature. Therefore, the expansion ejector can offer advantages in two ways. First, lower refrigeration temperatures can be achieved without any decrease in compressor suction pressure; second, cooling may be produced at 4°K with a compressor suction pressure in excess of two atmospheres. Savings in compressor and heat exchanger size are made in either case. Haisma<sup>10</sup> reports refrigeration temperatures as low as 1.75°K with  $P_1$  at 31 atm and  $P_2$  at 1.15 atm. A production model of this type of refrigerator is not ready as yet, but a 10 liter/h helium liquefier featuring a noncontaminating rolling diaphragm sealed compressor, heat exchangers laminated from metal gauze, paper and resin, and an expansion ejector which permits a 2.5 atm compressor suction pressure has been marketed in Europe (Haarhuis<sup>11</sup>). It should be noted that several thousand Stirling cycle refrigerators are in the field in the United States today for cooling electronic equipment at temperatures higher than liquid helium.

## 6. The Gifford-McMahon Cycle

By itself the Gifford-McMahon refrigeration cycle has about the same low temperature limit as the Stirling cycle since there is periodic reversing flow through one or more regenerators. However, this cycle lends itself very readily to staging and refrigerators precooled at three different temperature levels have been built for liquid helium temperature service. Figure 6 schematically shows a three-stage unit. The three cylinders are made of low conductivity material and are fitted with displacers, sealed against the cylinders at the top, whose movement is controlled from outside the cryostat. The three thermal regenerators are indicated as are the three heat absorption stations at 14, 35 and 80°K. The regenerators are packed with a material such as metal screens to produce the desirable characteristics of high heat capacity per unit volume, low pressure drop, small void volume, and low axial thermal conductivity. Imagine now that all three displacers are in their lowest position and that steady-state operating conditions have been reached so that the proper thermal gradient exists in the regenerator material from room temperature to 80°K in the first regenerator. The compressed gas supply valve is opened, and helium enters the system raising the pressure in the volume at the top of the cylinders above the displacers. When the pressure in the regenerators and the volume above the displacers reaches the maximum pressure, the displacers are all moved to the upper position, forcing the gas above them through the regenerators and into the volumes which now appear below the displacers. The gas is cooled as it gives up heat to the cold regenerators and the decrease in specific volume allows more fluid to enter the system from the compressed gas supply. The supply valve is closed and the exhaust valve is slowly opened. Refrigeration is now produced as each of the elements of fluid do work on preceding elements as they pass out of the system. The fluid is warmed as it passes through the regenerators and through the heat

- 
10. J. Haisma and K. Roozendal, in Proc. 12th Meeting of Commission 1 of the Intern. Inst. of Refrigeration, Madrid, 1967 (to be published), Paper No. 1.37.
  11. G.J. Haarhuis, in Proc. 12th Meeting of Commission 1 of the International Inst. of Refrigeration, Madrid, 1967 (to be published), Paper No. 1.36.

absorption stations. When the pressure in the system reaches its lowest level the displacers are moved to the lower position forcing the remaining cold gas out through the regenerators and to the compressor suction. At this time the temperature distribution in the regenerators has returned to its original profile. This refrigerator inherently has several mechanical advantages. Most of the low temperature apparatus is passive except the displacers which are shown as sealed at room temperature. In later models, the displacers are placed in-line and require seals at low temperatures, but the sealing problem is not serious since the pressure difference across the seals is only that which is required to induce flow through the regenerators. The displacers are operated at low speed, typically less than 100 rpm, and the light duty drive mechanism is used to operate the room temperature inlet and exhaust valves. Difficulties encountered with contaminants in the refrigerant are alleviated somewhat since the exhaust phase of the cycle tends to flush impurities back out of the system.

#### IV. MODERN COMPONENTS AND REFRIGERATORS

Many helium temperature refrigerators which have recently been placed in service feature complete separation of the process gases from petroleum based lubricants to eliminate fouling of the heat exchangers or regenerators and to prevent freezing of the lubricant in other critical areas. Noncontaminating reciprocating compressors can have plastic piston rings, metal diaphragms, or labyrinth seals instead of piston rings. High speed turbine compressors have been developed which have process gas lubricated bearings supporting the shaft. Gas lubricated bearings are also used for high speed turbo-expanders and a variety of reciprocating expanders are operating today. Efforts to improve heat exchanger performance have lead to a proliferation of different designs. Tubes finned both inside and out are extensively used to increase the effective heat transfer surface as are the extended surfaces employed in plate fin exchangers. Accurate prediction of the characteristics of a new heat exchanger design is very difficult and usually heat transfer coefficients and pressure drop friction factors are determined from test models.

Cascaded Joule-Thomson, single and multiple expander Claude, Stirling and Gifford-McMahon cycle  $4^{\circ}\text{K}$  refrigerators are being marketed today. Refrigeration capacities range from about 1 W up to more than 1 kW. Much larger units could be designed and fabricated if necessary. Since dynamic machinery is subject to failure, the reliability of the refrigeration system can be enhanced by providing redundancy in critical areas if continuous operation is required. Modern refrigerator efficiencies range from about 1% of Carnot for capacities of about 1 W to about 16% of Carnot for kilowatt capacity refrigerators. This means that the drive power required per unit of refrigeration ranges from about 10 000 to 500, respectively. The thermal efficiencies at all capacities could be improved, but the refrigerators would be more complex. The capital cost would probably increase to reflect development costs and complexity unless there were a corresponding increase in the size of the market which would lower manufacturing costs.

The most difficult problem in cooling a superconducting accelerator or its supporting superconducting devices will not arise because of a deficiency in refrigeration technology; rather, it is the geometry of the accelerator itself that poses the problem. The total cooling loads suggested are not unusually high, but when it is understood that refrigeration is required in small amounts at widespread locations, then the problem assumes its proper magnitude. A number of small refrigerators could be arranged around the accelerator. Here the disadvantages would be higher capital and operating costs per watt of refrigeration than for one equivalent large refrigerator, and there would be more moving members subject to mechanical failure. On the other hand, a large refrigerator would require a refrigerant distribution system to all parts of the accelerator. This low temperature piping is expensive and the heat leak would increase the refrigeration capacity required. The answer is not at all clear at this time and the problem merits thorough study.

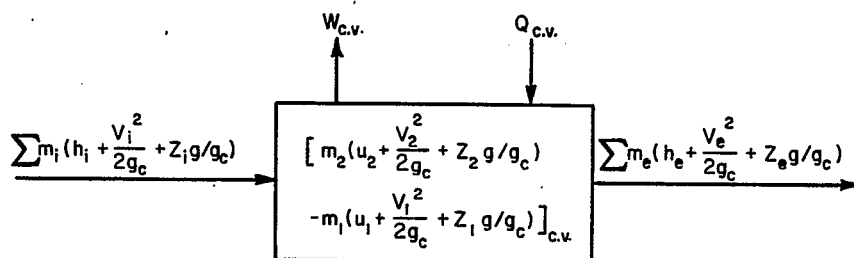


Fig. 1. Pictorial description of first law of thermodynamics for uniform state uniform flow process.

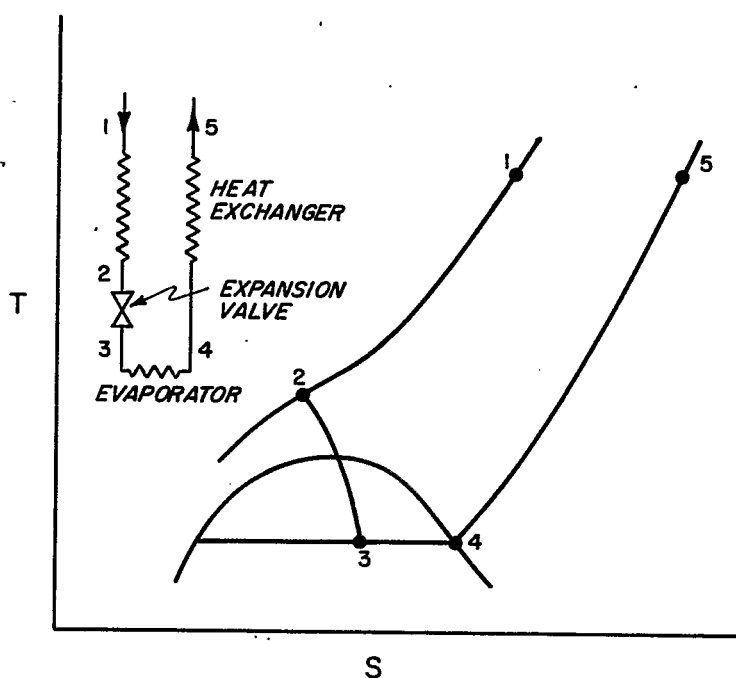


Fig. 2. Schematic of a Joule-Thomson refrigeration system.

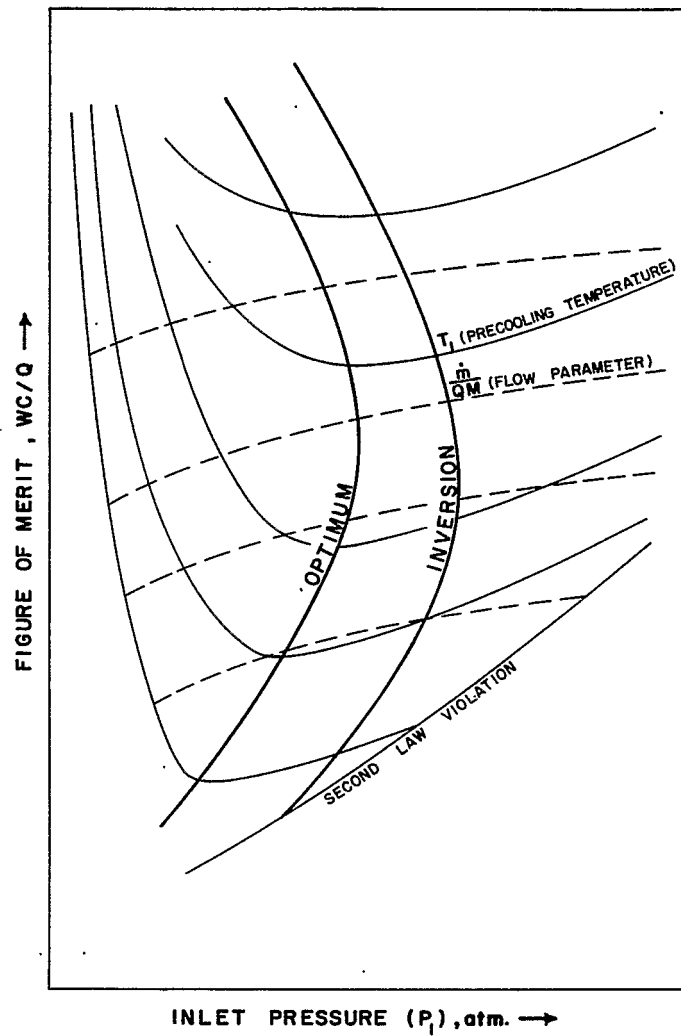


Fig. 3. Generalized performance surface for a Joule-Thomson refrigeration system.

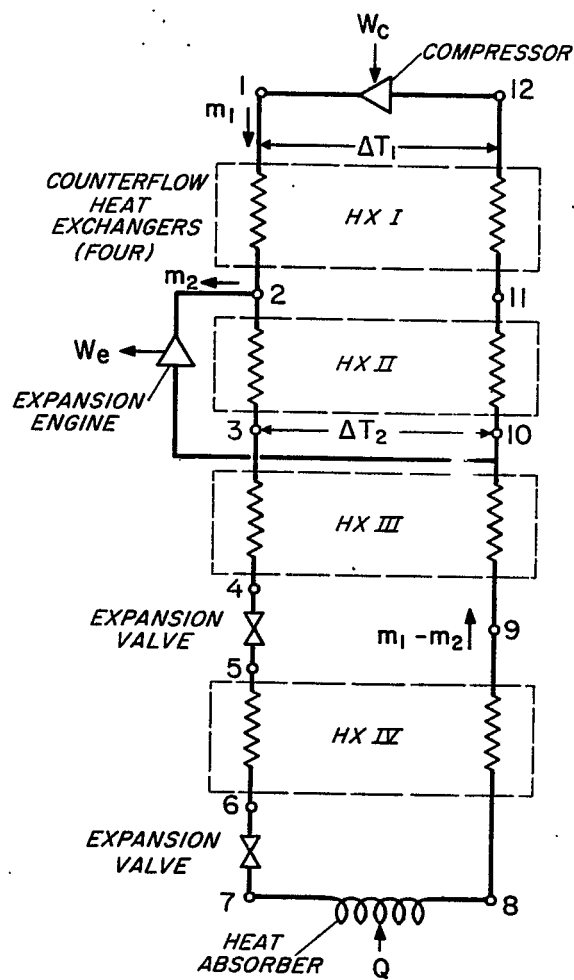


Fig. 4. Schematic of single-engine Claude refrigerator.



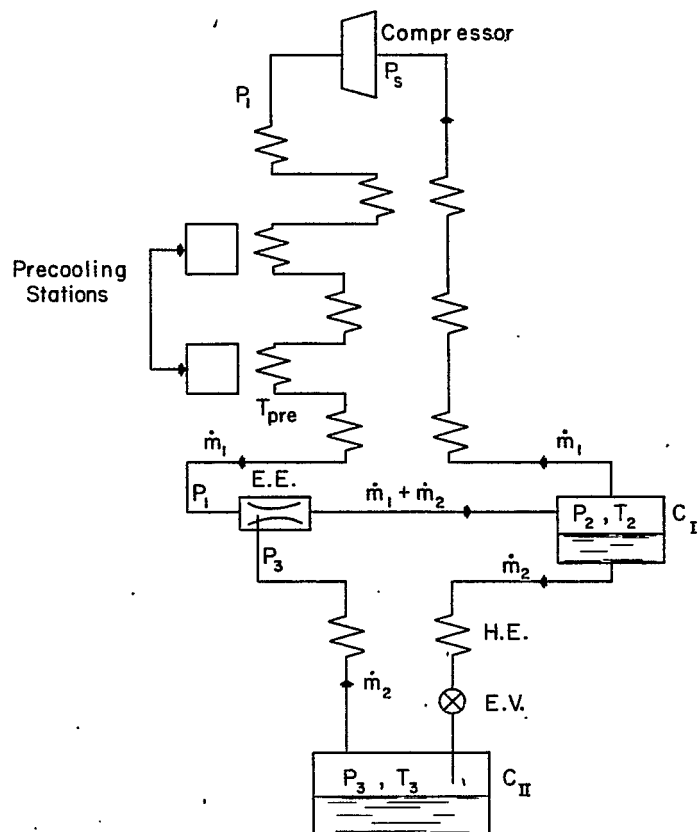


Fig. 5. Schematic of Stirling precooled refrigerator with an expansion ejector.

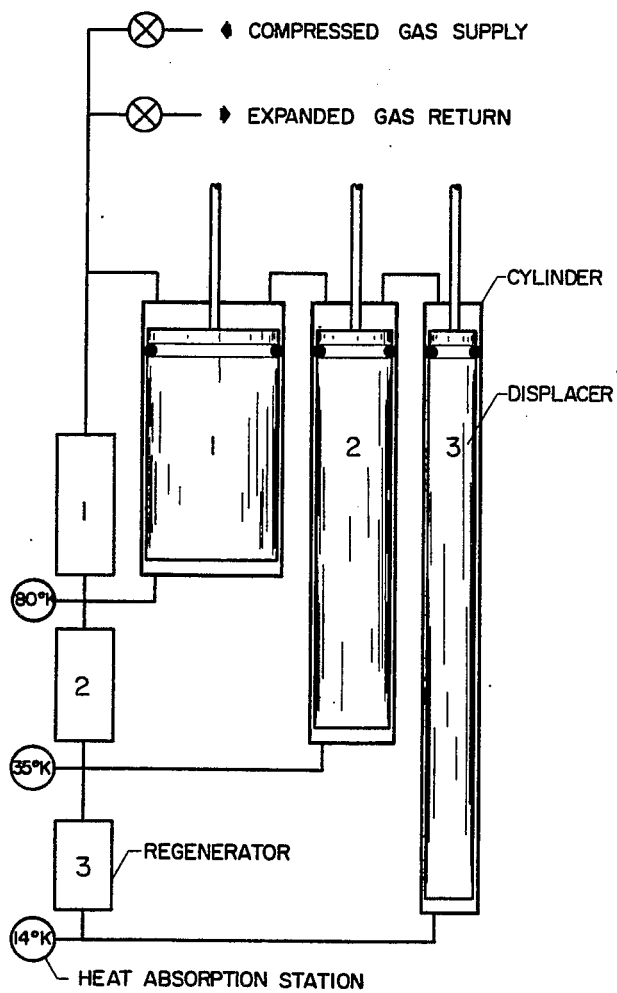


Fig. 6. Schematic of Gifford-McMahon cycle.

## EUROPEAN STATE OF THE ART IN CRYOGENICS

G. Prast  
Philips Research Laboratories  
N.V. Philips' Gloeilampenfabrieken  
Eindhoven, The Netherlands

### INTRODUCTION

To start with, I should like to make two remarks.

First, I have been asked to talk about the European state of the art in cryogenics. Now I certainly do not know enough about the work which is going on in the whole of Europe. I had the luck, however, to receive the invitation from your Chairman just the day before the start of the Cryogenic Engineering Conference in Brighton, England, so I used that conference to learn a bit, and an important part of what I will talk about in this lecture was told in Brighton one month ago.

Second, I may be a European, but I am also working with Philips and therefore I am not objective about the different systems. I will, therefore, devote most of my time to the work we did at Philips, and of course tell you that the Stirling system is by far the best to use for large cryogenic systems. I hope to make this clear in the next hour.

I will divide my talk into three main topics:

- 1) A discussion of what other firms are doing.
- 2) A description of the Stirling refrigerators and some low temperature systems made with it.
- 3) A comparison between systems and a few supplementary remarks.

### CRYOGENIC INDUSTRY IN EUROPE

The title of my lecture, "European State of the Art in Cryogenics," I will primarily understand as the production of low temperatures, and, by restricting myself to the production, I can automatically restrict myself to the industrial firms in Europe and the direction in which their development and fabrication is going.

In Europe there are quite a number of firms working in this field. The most important for this talk are:

British Oxygen Company	England
Air Liquide	France
Linde	Germany
Messer	Germany
Sulzer	Switzerland
Philips	The Netherlands

There are some others such as Hymatic, Oxford Instrument Company, Petrocarbon, and Werkspoor, but these concerns are working on very small systems or in other temperature regions.

The first four of the above list are in the air separation field and mainly produce and sell industrial gases. For this activity they were obliged to fabricate air separation plants and starting from these installations they went into the low temperature region.

Sulzer was probably led into the low temperature field because of its well-known compressors and its knowledge of turbines. They have done quite a bit in deuterium separation and now also produce systems for the 4°K region.

Philips came quite differently into this field. From research on the hot-air engine we also came with the Stirling cycle in the field of refrigeration. For a long time only small laboratory air liquefiers were made, but with a modified Stirling cycle the very low temperatures could also be reached, and we believe that with the Stirling cycle good refrigerators can be made down to very low temperatures.

I will now give you examples of the work the different European companies are doing.

#### BRITISH OXYGEN COMPANY

Mr. Stoll of the British Oxygen Company gave a paper in Brighton about a flexible multipurpose helium refrigerator. They have made one for the Rutherford High Energy Laboratory to operate in conjunction with a 3°K liquid helium bubble chamber. This type of installation can produce 120 W in the 4.3 to 10°K, or 40 liters/hour of liquid helium, or 600 W at 20°K, or a combination of parts of the above-mentioned productions.

The refrigeration system is shown in Fig. 1. It makes use of precooling with liquid N<sub>2</sub>, cooling by one or two gas-bearing expansion turbines down to 9°K, and then, of course, Joule-Thomson expansion for the lowest temperatures.

Automatic control of the installation is by three diverter valves, V<sub>1</sub>, V<sub>2</sub> and V<sub>3</sub>, controlled by temperature sensors or, in the case of V<sub>1</sub>, by a liquid level sensor.

The system is said to be easy to operate and can run unattended for 18 hours per day. BOC hopes to have complete automatic systems in the near future.

A diagram of the complete system is given in Fig. 2.

The main compressor has a capacity of 0.34 m<sup>3</sup>/sec (750 SCFM) with an end pressure of 8.3 atm. The turbines have a capacity of 0.225 m<sup>3</sup>/sec (500 SCFM) at 264 000 rpm. Normally only one turbine is in operation. The second one is only used when a large load has to be cooled down.

#### AIR LIQUIDE

Air Liquide is working in two directions at present. For small systems they make use of our Stirling machine for precooling a Joule-Thomson system. They have, for example, made a 5 W refrigerator with a Philips A20 machine. For bigger systems they have developed a gas-bearing expansion turbine running at 200 000 rpm and with a capacity of 0.083 m<sup>3</sup>/sec (185 SCFM).

With this turbine different systems have been developed. In Brighton, a 25 liter/hour helium liquefier was described. Figure 3 gives a diagram of this system. It uses a Claude refrigeration cycle with liquid N<sub>2</sub> precooling and a combined Joule-Thomson system. The compressor used is a dry Sulzer compressor with a capacity of 0.15 N m<sup>3</sup>/sec (335 SCFM). A cylindrical cold box houses the Hampson-type heat exchangers, the

turbine, Joule-Thomson valve and a liquid helium tank. This cold box has a diameter of 900 mm and is 2.3 m high. This liquefier can run continuously for 100 hours on grade A helium, then regeneration of the purifiers is needed. The production of the installation is 25 liters/hour with a power input of 95 kW and 22 liters/hour of liquid N<sub>2</sub>. This makes a total efficiency of about 5 kW·hour/liter. The liquefier can be transformed into a refrigerator, and then produces about 130 W at 4.2°K.

A larger machine requiring about 125 liters/hour of liquid N<sub>2</sub>, of the same type, has been made.

#### SULZER

Sulzer has made a number of different installations. In Brighton Mr. Pagani reported on two installations set up in the nuclear research establishment in Jülich (Germany). These were:

Installation I :	1000 W at 14.6°K + 200 W at 4.5°K
Installation II :	160 W at 4.5°K + liquefaction of helium, neon or hydrogen.

Sulzer makes use in these installations of two separate circuits, a Joule-Thomson circuit for the load at 4.5°K, and a Claude system for delivering cold at 14.6°K and precooling of the Joule-Thomson circuit.

The Claude system has two expanders in a special circuit, given in Fig. 4 (installation I). The first turbine works around 70°K and expands from 12 to 7 atm; the second works around 14°K and expands from 5.5 atm downwards. The system has been devised like this to make it possible to cool the load in the reactor with high pressure helium gas.

Sulzer dry compressors are, of course, used in the systems. The circuits are operated completely above atmospheric pressure to prevent impurities entering the circuit.

The systems can therefore run unattended for quite long periods.

Figures 5, 6 and 7 show the cold box, the control panel and the compressor station, respectively.

#### LINDE

Linde is making a number of different helium refrigerators and liquefiers.

The smaller ones are based on one or two Doll and Eder valveless piston expanders. These are expanders in which the piston has a very small clearance in the cylinder (average about 1.5 μ) but does not touch the cylinder due to hydrodynamic bearing operation, using the working gas. The piston itself is used to open and close the inlet and outlet ports, so that no separately actuated valves are needed. The expanders run at about 15°K, precooling at 77°K is done with liquid N<sub>2</sub> (Fig. 8).

The bigger systems are equipped with turbines and these do not use liquid N<sub>2</sub> precooling. Most often two turbines are used in a directly-coupled Claude and Joule-Thomson system. These bigger systems are tailor-made. For example, one system for

130 W at 4.7°K plus 700 W at 20°K has been made for a space research institute. Also, a 30 W, 1.8°K system has been made for a research institute in Karlsruhe.

Figures 9, 10 and 11 show the 20 liters/hour liquefier, the heat exchangers for this system, and the 30 W, 1.8°K system.

As you see, all these systems are quite alike. Every firm has developed a turbine expander, most often with gas bearings, and with these combined Claude and Joule-Thomson systems are made. They all have experience with heat exchangers, controls, and cold boxes from their work in the air separation field. No reason can be seen why these systems should not develop into reliable systems.

In this review I did not mention Messer because, as far as I know, they did not develop this type of system. Their work lies mainly in air separation, and at the moment also in liquid natural gas plants (together with American Messer). For helium temperatures they are interested in using Stirling machines for precooled Joule-Thomson loop, and Messer and Philips together made a design for a 300 W, 1.8°K installation for the linac in Karlsruhe.

I will describe that design as an example of the possibilities of the Stirling system, but before I do that I will first describe briefly the Stirling cycle and the Stirling machines we make.

#### STIRLING SYSTEM

The Stirling cycle is performed by alternately compressing and expanding a fixed quantity of gas in a closed cycle. The compression takes place at room temperature; the expansion at a low temperature, for example 77°K. For the purpose of explanation the process may be split up into four phases; they are illustrated in Fig. 12.

This figure shows four positions of the pistons; the Roman figures indicate the four phases referred to. Cylinder I is closed by piston 2 and contains a certain amount of gas. The space is subdivided into two subspaces 4 and 5 by a second piston 3, the displacer. There is open communication between spaces 4 and 5 through an annular channel 6 wherein are located three heat exchangers: the regenerator 7, the cooler 8, and the freezer 9. In position I most of the gas is in space 4 at room temperature and in the first phase this gas is compressed by piston 2. In the second phase this gas is displaced by means of the displacer from space 4 to space 5, which we suppose already to be at a low temperature. During this transport the gas passes through the heat exchangers. In the cooler the heat of compression is discharged to the outside. The regenerator cools the gas nearly to the temperature prevailing in space 5; this will be discussed later on.

Phase III is the phase during which the actual cold production takes place, namely by expanding the gas by moving the displacer and piston together. Finally, by movement of the displacer, the gas is returned to space 4. When passing the freezer its cold is transferred to the outside, and in the regenerator it is reheated to nearly room temperature. The initial situation is now restored and the cycle can be repeated.

Figure 13 explains the working of the regenerator. The regenerator consists of a porous matrix with a high heat capacity. When the machine has run for a certain time, a temperature gradient will prevail in the regenerator, extending from  $T_1$ , room temperature, on the right side, to  $T_2$ , a low temperature, on the left side. During the first phase gas is forced through the regenerator from right to left. Due to the smallness of the pores in the matrix, the heat transfer from the gas to the matrix is extremely high and the gas nearly follows the temperature gradient of the matrix (along the upper dotted curve), so that it issues at the left side at nearly the temperature  $T_2$ . The

heat discharged by the gas during this cool-down is temporarily stored in the matrix and due to the high heat capacity of the latter its temperature does not change very much. In the second phase the gas returns from left to right and the reverse happens; the gas temperature follows the lower dotted curve and issues at the right side at nearly room temperature. For the reheating of the gas the heat that was stored in the matrix during the first phase is used. We see that a regenerator enables us to cool and reheat matter without the need of appreciable amounts of thermal energy. The regenerators to be used in Stirling refrigerators must be of very good quality (99% or more).

### THREE-SPACE STIRLING SYSTEMS

The description above gives the simple Stirling system as invented by Robert Stirling in 1816 and used by us for machines down to about 26°K. Due to the regeneration losses which increase relatively by going to lower temperatures, efficient machines for the region of 20°K can only be made when a change is introduced in the cycle, namely, the introduction of a second, intermediate, expansion space (see Fig. 14). The large amount of cold due to the higher expansion temperature can now cope with the regenerator losses of the first regenerator, and, with this system, relatively high efficiencies can be reached at lower temperatures.

This change was needed in order to reach lower temperatures, but it does more. It has the added advantage that the machine can now also be used for delivering cold at two temperatures, i.e. 80 and 18°K, which is important for a Joule-Thomson system as now the use of liquid nitrogen can be discontinued. The lowest temperature to be reached in our machines now is 12°K. In the laboratory a Stirling machine has worked down to about 8°K.

It is obvious that no Stirling refrigerator down to 4.2°K can be built as the working medium in the cycle is a gas, and no gas is available anymore below that temperature. Therefore all 4.2°K systems make use of the Stirling machines as a precooling system for a Joule-Thomson system.

As can be seen from the above, the Stirling system is a very compact system for producing refrigeration. It has a very high specific output because a high mean pressure and a high speed can be used. Furthermore, the system has very high efficiency. I will come back to this point later.

A number of different types of Stirling machines are available. Important for helium refrigeration are the three-space systems. A one-cylinder (A20) and a four-cylinder system of the same type are in production. A prototype model of the A20 is shown in Fig. 15. Figure 16 gives the production graph of this machine. The machine has two productions,  $Q_E$  at the top and  $Q_m$  at the intermediate freezer, both plotted along the vertical axis, dependent on two temperatures,  $T_E$  and  $T_m$ .  $T_m$  is plotted along the horizontal axis, and  $T_E$  is used as a parameter in the graph.

It can be seen that  $Q_E$  is only slightly dependent on  $T_m$ , which is done so as to have the machine not only useful as a pure refrigerator at, say, 20°K, but also as a precooler or liquefier where both productions are used.

Figure 17 illustrates a B20 machine. This one, of course, has four times the production of the A20. The headers can all be used separately, which means that it could be used with the eight freezers all at different temperatures.

In the near future two machines of this type will be added: the so-called X20, which has about 1/10 of the production of the A20, and a three-space version of our big industrial machine, which now produces 25 kW at 77°K. As a three-space system it will

produce about 2 kW at 20°K, with an efficiency which is about 30% higher than in the A20. It will come to about 20% at 20°K (see Fig. 18).

## INSTALLATIONS

To show what a helium refrigeration system will look like with these machines, I will describe two things: first the helium liquefier we have in production now, and second a design for a 300 W, 1.8°K refrigeration system. The latter we designed together with Messer (Germany) as a proposal to the Karlsruhe Nuclear Research Institute.

## THE LIQUEFIER

The liquefier is a 10 liter/hour system using two of the above-mentioned refrigerators and a special compressor.

The flow diagram is given in Fig. 19. Precooling is done at about 100, 66, 26 and 16°K. This makes the system efficient and furnishes the right temperatures for purifying. The machines can run continuously for 100 hours with helium containing 2% air. Incidentally, it can handle helium containing 10% air. The helium is purified at room temperature with molecular sieves absorbing most of the water, and at 100°K, CO<sub>2</sub> is absorbed. At about 67°K the air is first condensed and taken off as liquid as far as possible, and then with two switching absorbers the rest of the air is taken out. These absorbers use active charcoal. At 16°K an absorber for neon and hydrogen is used.

At very low temperatures a special circuit is used with an ejector instead of the Joule-Thomson valve (see Fig. 20).

The ejector is used to improve the Joule-Thomson system. The basic idea is that in isenthalpic expansion pressure energy is transformed into kinetic energy and kinetic energy is wasted in friction. If one could use the kinetic energy this could not fail to be an improvement. In the ejector kinetic energy is used to compress gas from a second vessel at a lower pressure up to the pressure of the first vessel. By this method, say 0.4 atm absolute can be reached although the sucking pressure of the compressor is 1 atm absolute.

In the liquefier the ejector is used to compress from 1.0 to 2.5 atm absolute. This, of course, makes the return heat exchanger channel and the compressor much smaller.

The compressor used in this system is a so-called "sock compressor." In any helium system, it is an advantage to have a dry compressor. For small systems metal membrane compressors are used, but they have the disadvantage that the membranes only have a life of about 1000 hours.

We had already encountered the problem of a hermetic seal in the Stirling machines. With a normal lubricated piston, oil vapor comes into the system and freezes somewhere in the regenerator. The smaller machines have a maintenance period of about 100 hours for cleaning the regenerator. For the large industrial machine we developed the so-called "sock," a rolling rubber diaphragm between the piston and the cylinder, which is sustained by oil in a constant volume space (see Fig. 21). The average oil pressure is controlled to keep it a few atmospheres below the average gas pressure so as to keep the rubber under a constant tension.

This method is also used in the big machine I showed you (Fig. 18). These membranes can run more than a year, even with a speed of 1500 rpm.



The same system is used now for a small helium compressor used for this liquefier (see Fig. 22).

The control panel and Dewar with the Joule-Thomson system is illustrated in Fig. 23. Roughly, this same unit with two A20 machines and one compressor could be used for about 30 W at about 5°K. For use as a refrigerator the whole purifying unit can be skipped, of course, which makes the unit even more compact.

Apart from the compactness and the advantage of accepting helium with impurities, the liquefier has a high efficiency. The refrigerator and compressor together use 28 kW. For 10 liters/hour of helium this gives 2.8 kW·hours/liter. No liquid nitrogen is needed for precooling, as the intermediate freezers of the A20 machines furnish the cold needed at that temperature. I will compare this figure later with other liquefiers.

### THE 1.8°K SYSTEM

The second system I would like to mention is a design for the Karlsruhe 300 W at 1.8°K refrigerator, which we made together with Messer.

In the design we made use of three B20 machines (a B is four A machines on one crankcase) which furnish the cold and a Joule-Kelvin system, as can be seen in Fig. 24, to transport the cold to the low temperature.

It is an advantage in this Joule-Kelvin system to have two loops, one transporting 150 W down to 5.5°K and one going down to 1.8°K, getting 150 W enthalpy difference at 16°K, and the other 150 at 5.5°K. This is because one tries to have the smallest possible amount of gas in the very low pressure return flow. Therefore, if possible, all the evaporation heat of helium should be used, and this makes precooling to about 6°K necessary. The two high pressure flows of the two loops are, of course, added here in one channel so three-channel heat exchangers can be used, and also the compressors from 2.7 to 20 atm can be combined.

Here again the ejector may be used, although the advantage is not as great as in the helium liquefier. To have always a positive temperature difference in the last heat exchanger, the high pressure helium gas has to be expanded partly in the heat exchanger. At the ejector, then, only part of the total pressure difference is available to be converted into kinetic energy. The result is that a pressure ratio of only about 1.3 can be reached in the ejector. With a pressure of 10 torr at the liquid bath, this remains, nevertheless, an important advantage for the return heat exchanger. The B20 machines are used in a special way in this circuit. In Fig. 24 it can be seen that three precooling temperatures have been used. With a B20 machine, one has eight freezers so, in principle, eight temperatures could be used. For a refrigerator such a large number is no advantage, however, and only three are used, namely 80, 26 and 16°K. Two of the four headers use one freezer at about 80 and 26°K; the other two headers only use the top freezer at 16°K. With this system the double expansion machines are used very efficiently. In practice, probably two B20 machines could do the job. Therefore, the three machines are made identical, and the system is designed so that each machine can be stopped and serviced (or replaced) while the installation remains running. This method can give the system a very long continuous running time, even though the B20 machines have to be stopped and cleaned after about 1000 hours. Also, the reliability of such a system can be made very high in this manner.

In any Joule-Thomson system the compression is a very important factor. Two types of compressors are used in the installation described. Rootes compressors are used for the low pressure region from 13 mm to about 0.2 atm. These Rootes compressors are made by Aerzener in Germany, but, for use with helium, most often delivered by Hereaus.

These Rootes compressors are made in a number of sizes, from very small to quite large, and can be made for any pressure in the vacuum region. For the higher pressures Sulzer dry piston compressors are used.

It is clear that, in cryogenics, the availability of good compressors is very important. I mentioned Aerzener and Sulzer - both have quite a lot of experience in the pumping of dry and clean gases - but there are other firms also who make this type of compressor and all cryogenic firms who make this type of compressor and all cryogenic firms who make units to 4°K can find good dry compressors for them made in Europe.

Apart from this, progress is made in the purification of helium compressed by oil-lubricated piston compressors and that technique may also be used in Joule-Thomson systems.

#### EFFICIENCY COMPARISON

I have yet to make a short comparison between the efficiencies of the different systems. In most descriptions, however, no efficiency figures are given.

The only number I found was for the Air Liquide liquefier, which needed 95 kW and 22 liters/hour of liquid N<sub>2</sub> for a production of 25 liters/hour of helium. If we estimate the nitrogen at 1 kW·hour/liter we arrive at an efficiency of (117/25) kW·hour/liter or 4.7 kW·hour/liter. Our liquefier uses 2.8 kW·hour/liter.

From discussions with the people at Karlsruhe, we know that our proposed system had a much higher efficiency than any other system offered.

Now we have quite often discussed why the Stirling system is so different in efficiency from the Claude system (of course it must be the difference between the Claude and the Stirling systems, because the Joule-Thomson system is always roughly the same). One of the problems in this comparison is that no standard system exists and one can make systems which are extremely good on paper but never manufactured (Keesom cascade for liquid air) because they are too expensive and complicated. A number of years ago Nesselman made a comparison between calculated systems and a measured Stirling machine and found the results shown in Fig. 25. Of course, this comparison is quite old now and expanders may have been improved, but that improvement has not been very large. Also, heat exchangers may be made better than the figures he used in his calculations, but again, even with highly efficient heat exchangers, the Claude systems remain relatively low in efficiency.

The result of our investigation has been that in the Claude systems the efficiency is low due to the low efficiency of the compressors. For the compression there are some differences between Stirling and Claude systems. First the Stirling compression ratio is low (for highly efficient machines less than two) while for the Claude systems much higher ratios are used. Of course, it is possible to use smaller ratios and more compression stages, but that is never done because of the size and price of the installations. Furthermore, in the Stirling systems, the compression is not completely adiabatic as in the compressor for a Claude system. There, all the gas is first compressed and then forced through the cooler which gives quite a loss.

In the Stirling systems, the compression takes place partly in the cylinder, but also in the cooler, regenerator, and freezer. We call our system, therefore, semi-adiabatic, and believe that therein lies the main difference. A third factor is the valve loss, which does not exist in the Stirling systems.

The fact that the regenerator is most often better than a heat exchanger, which we thought earlier to be the main reason for the difference in efficiencies, seems to make no important contribution to this difference.

The calculation of Nesselman was based on 77°K systems. Although, as I said, I have no good figures, I believe for 15 to 20°K systems the same type of difference will be found.

#### SUPPLEMENTARY REMARKS

##### Helium<sup>3</sup>

For the 1.8°K system we looked into the possibility of using helium<sup>3</sup> in the Joule-Thomson system. The difference in vapor pressure around 2°K is a factor 8 to the advantage of He<sup>3</sup> as against He<sup>4</sup>. It is clear that for the heat exchangers and compressors this is quite important.

The use of He<sup>3</sup> has two disadvantages. The Joule-Thomson effect is smaller, so a higher mass flow has to be used (about 30% more). Moreover, in a system at 1.8°K one wants most often to make use of superfluid helium in the liquid bath, so one has to have He<sup>4</sup> there. This means that heat has to be transferred from the He<sup>4</sup> of the liquid bath to the He<sup>3</sup> of the refrigerator, and in this heat transfer some  $\Delta T$  is involved, which means a certain loss.

These disadvantages, however, are small compared to the advantage of the higher vapor pressure. Then, of course, the price of He<sup>3</sup> (about \$85/N liter) is a problem but even with this price a competing system could be built. The main reason which made the use of He<sup>3</sup> impossible was that it cannot be obtained in unlimited quantities at the moment. When it can be shown that for refrigeration around 2°K it is really worthwhile to use He<sup>3</sup> in large quantities, the price might go down and the availability might be improved, resulting in more economic installations in this temperature range.

##### The Ejector (Fig. 26)

I should like to mention some more facts about the ejector. The amount of cold which can be transferred with the ejector loop depends on the pressure ratio. With a very small amount of cold transferred a pressure ratio of 100 has been reached, meaning a temperature of 1.74°K in the second bath, while in the first vessel the temperature was 4.2°K.

This means that if the cooling function of a refrigerator is mainly to compensate for insulation losses, that is, not much dissipation is involved as is the case with a superconducting magnet, a very low temperature can be reached without seeing it on the outside of a system. If the complete magnet is surrounded by a 4.2°K shield, it is probably possible to have about 99% of the needed cold at 4.2°K and only 1% at the lower temperature. With our ejector it is then possible to reach a very low temperature indeed. I have not enough knowledge of magnets but I believe that there are some indications that superconducting magnets could behave much better below the  $\lambda$  point. This is not done, however, because of the added complexity in the cooling system due to the low vapor pressure above the bath. With the ejector system, however, it may be possible to do this sort of thing. Due to the added 4.2°K shield, the cryostat design may be more complicated, but the refrigerator remains simple, because no very low pressure in the return heat exchanger is needed, nor are the low pressure compression stages.

## CONCLUSION

I hope I have succeeded in telling you that the cryogenics industry in Europe has the know-how and the potential to build cryogenic systems, and has, indeed, produced quite a number of installations. To reach the state where a low temperature environment can be used without any problems, however, requires more experience which can only be gotten by just doing it.

I am sorry that I could tell you only little about other firms than my own, and, therefore, had to use quite a bit of your time to tell what our group is doing. We are trying to do things a bit differently from all others, and you may have found it interesting to hear about that.

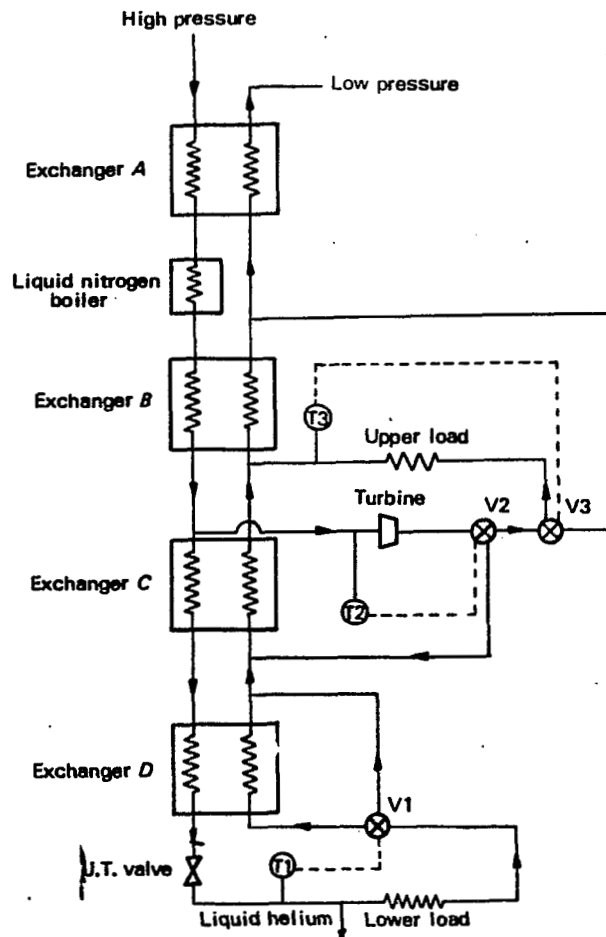


Fig. 1. Schematic layout of cold box and control system of a multipurpose helium refrigerator of the British Oxygen Company.

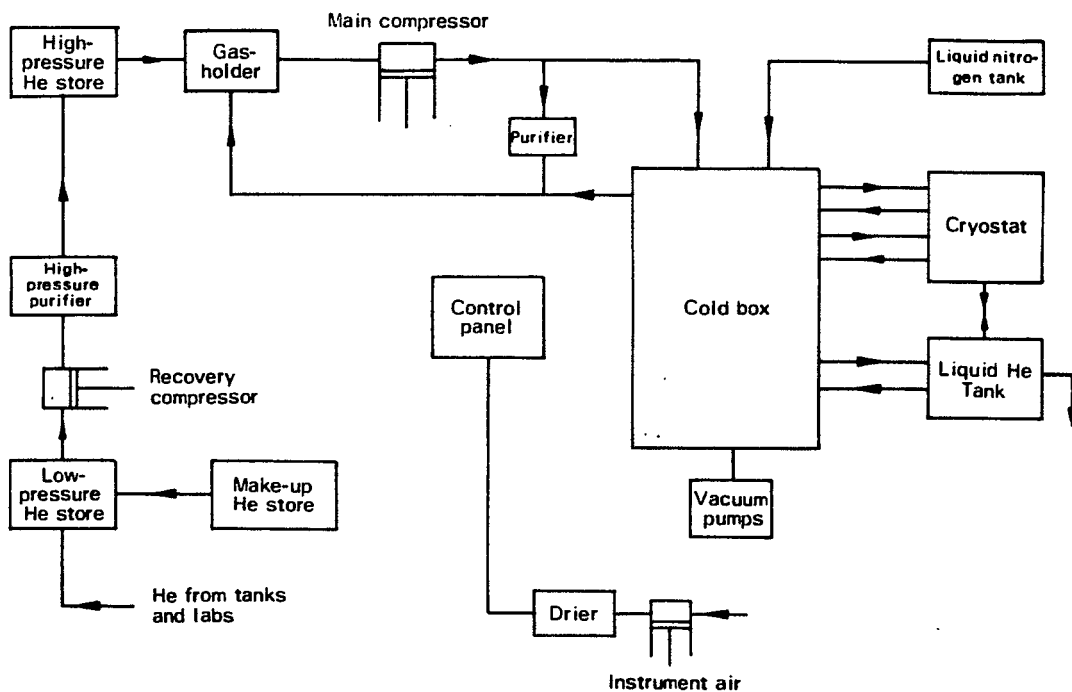


Fig. 2. General plant layout of refrigerator/liquefier system of the British Oxygen Company.

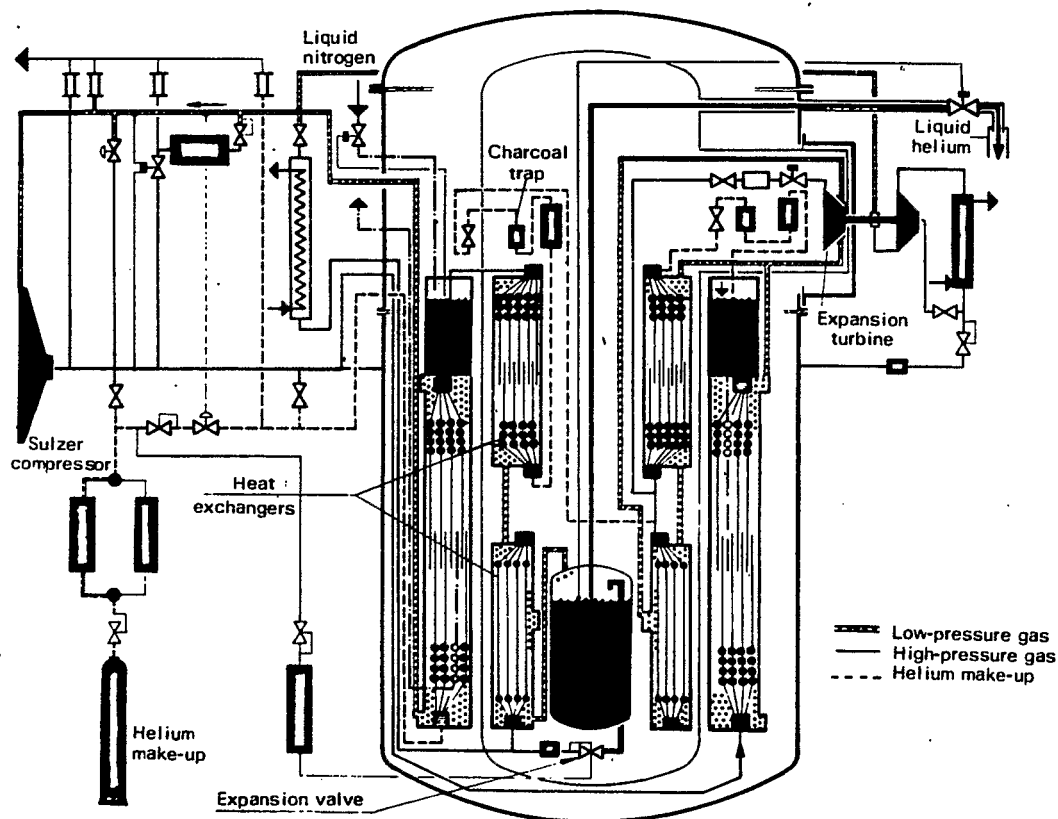


Fig. 3. Flow diagram of Air Liquide 25 liter liquefiers.

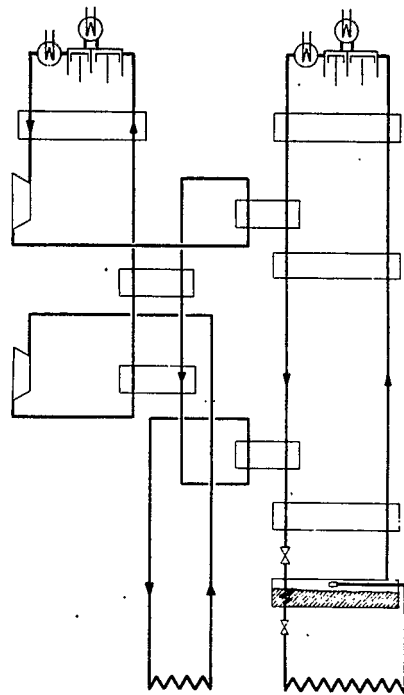


Fig. 4. Flow diagram of Jülich I refrigerator (Sulzer).

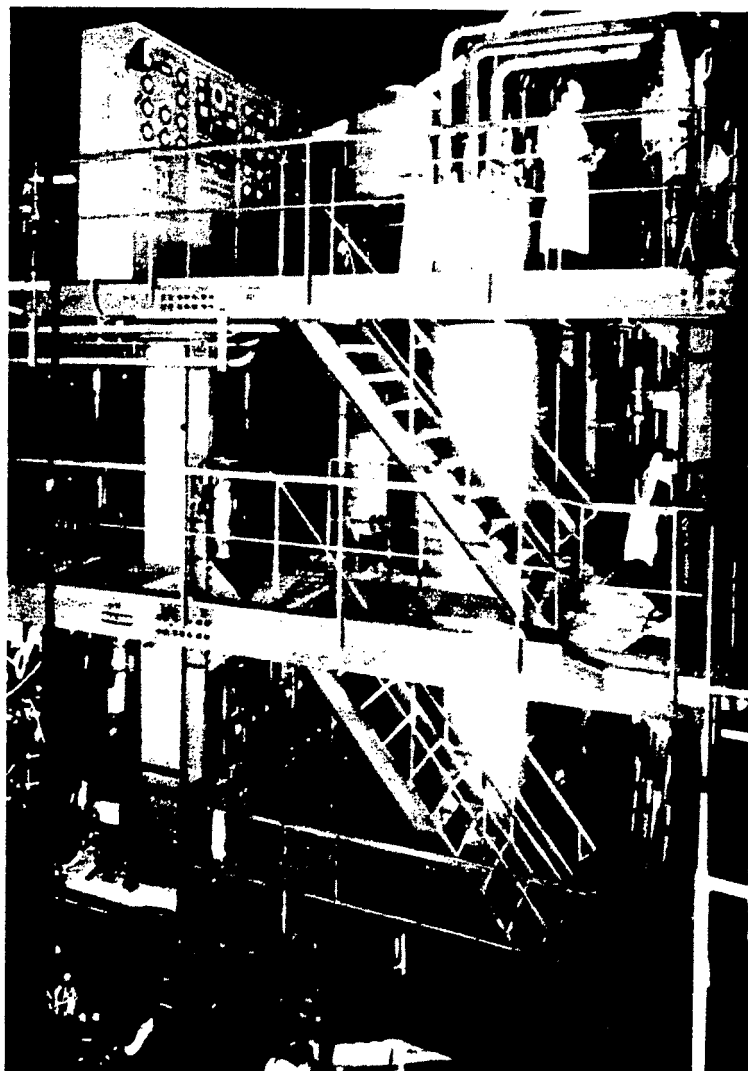


Fig. 5. Cold box of Jülich refrigerator.

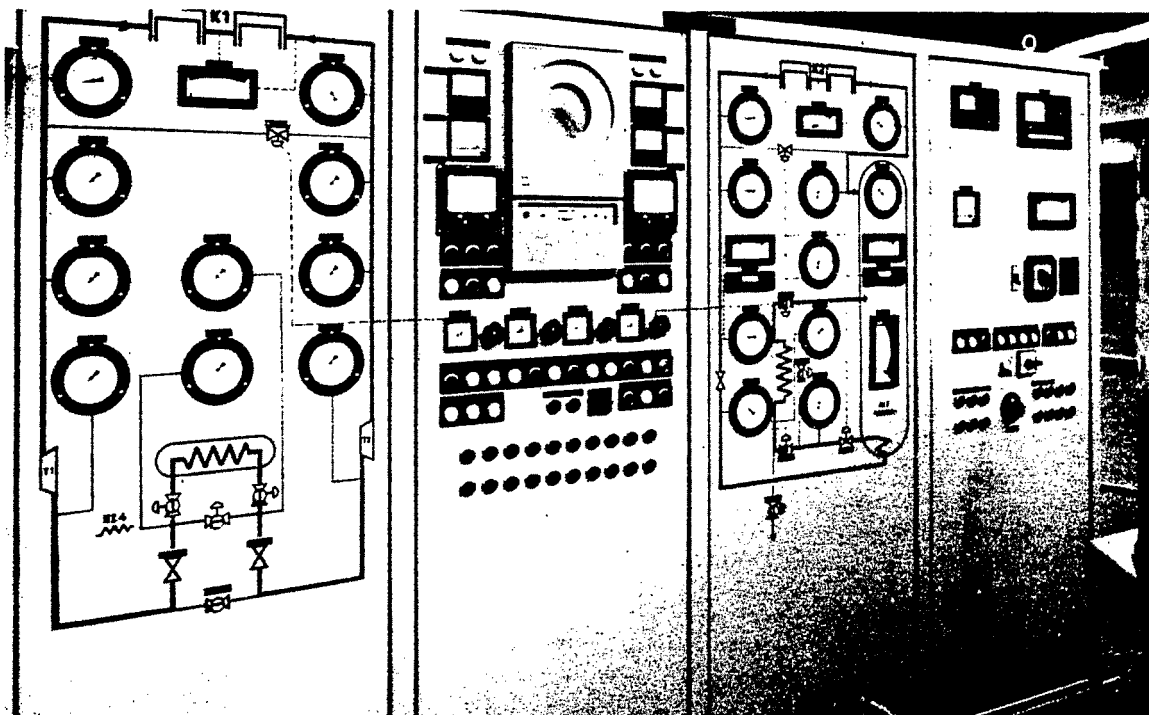
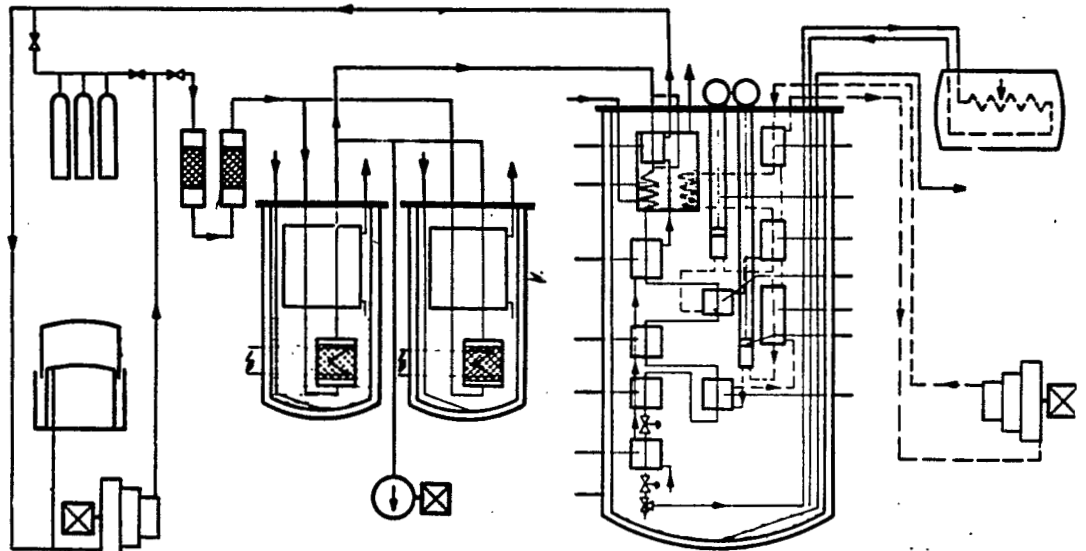


Fig. 6. Control panel of Jülich refrigerator.



Fig. 7. Compressor room of Jülich refrigerator.

# Helium Liquefier V 20



- 1 Compressor for pre-cooling cycle
- 2-4 Heat exchangers of pre-cooling cycle
- 5-6 Valveless piston expanders (Doll-Eder)
- 7-8 Heat exchangers for pre-cooling
- 9 Nitrogen evaporator

- 10-14 Heat exchangers of liquefaction cycle
- 15 Vacuum jacket for insulation
- 16-17 Interchangeable purifiers with heat exchanger, low temperature adsorber and metallic dewar for insulation
- 18 Vacuum pump for regeneration of adsorber

- 19 Oil separator
- 20 Dryer
- 21 Compressor of liquefaction cycle
- 22 Gas holder
- 23 High pressure storage vessel for impure helium

Fig. 8. Flow diagram of Linde V liquefier.

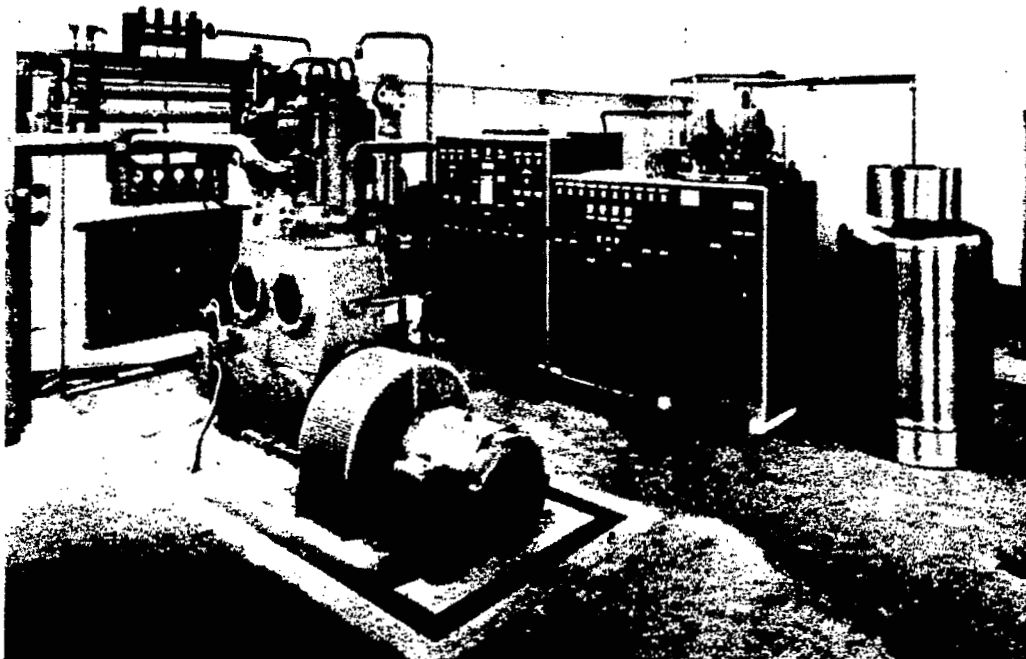


Fig. 9. Linde V20 liquefier.



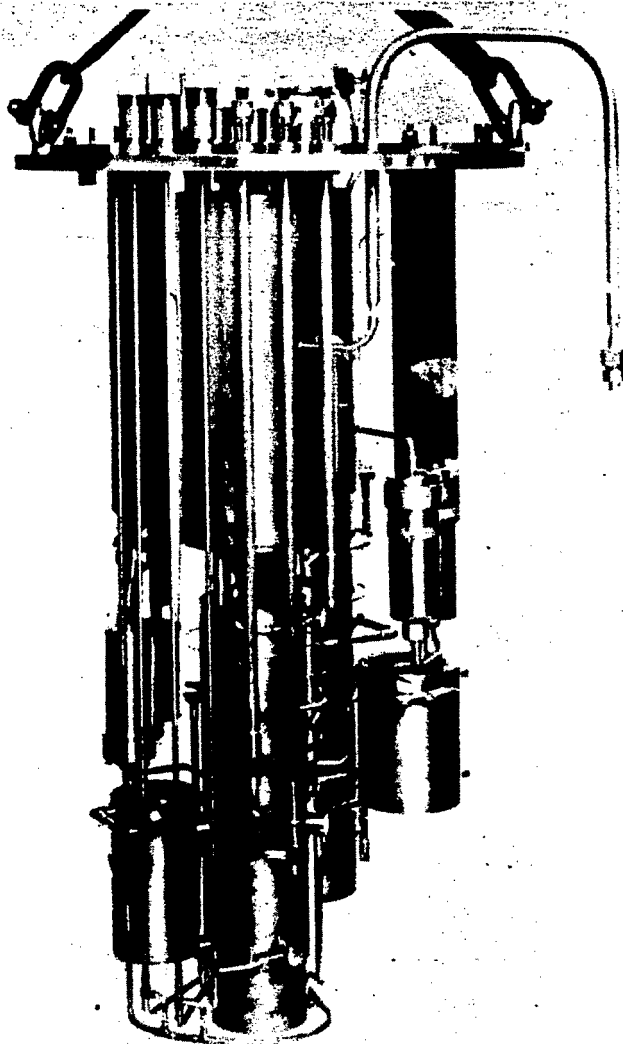


Fig. 10. Heat exchangers of V20 liquefier.

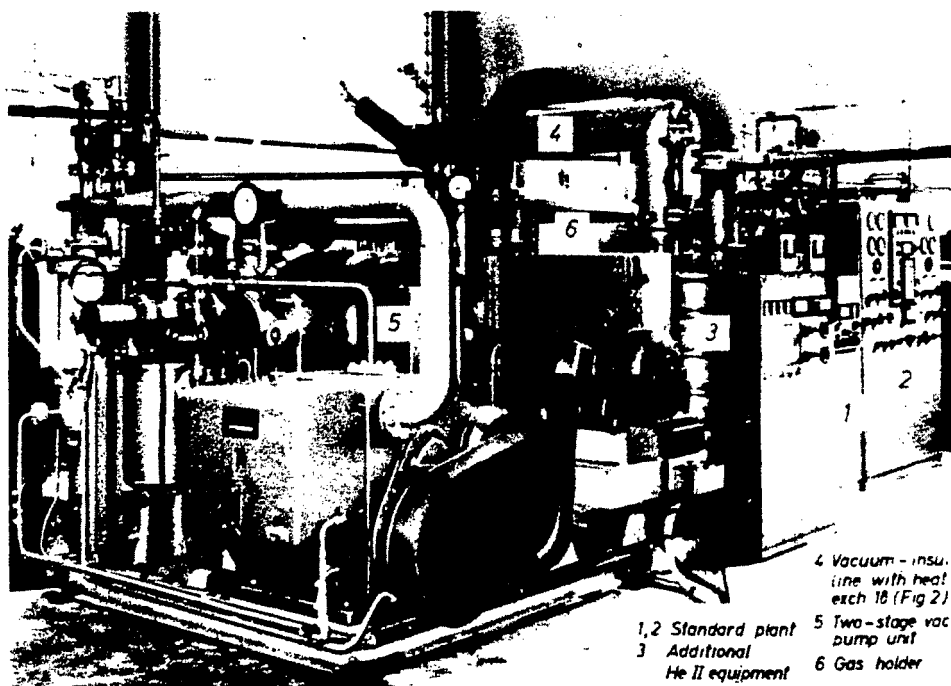


Fig. 11. Helium II refrigerator (Linde).

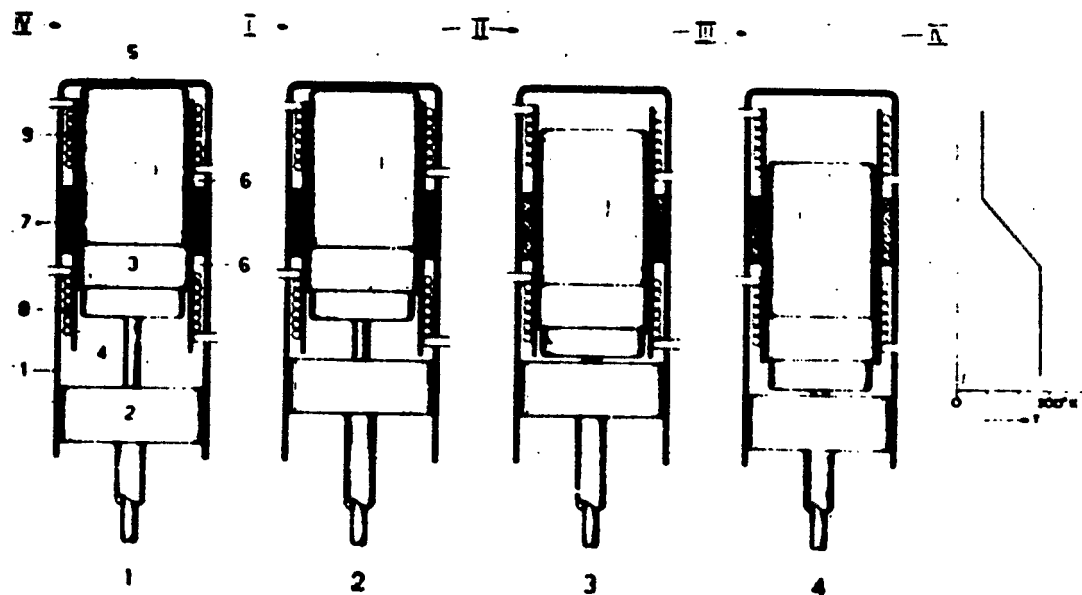


Fig. 12. Schematic phases of Stirling process.

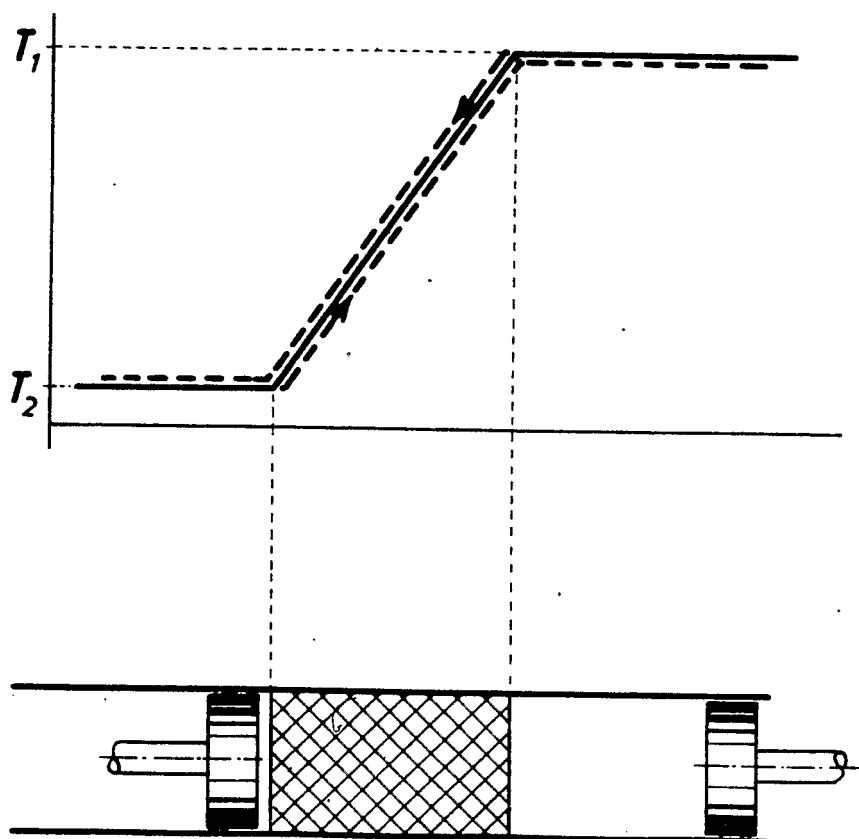


Fig. 13. Regenerator temperatures in Stirling process.

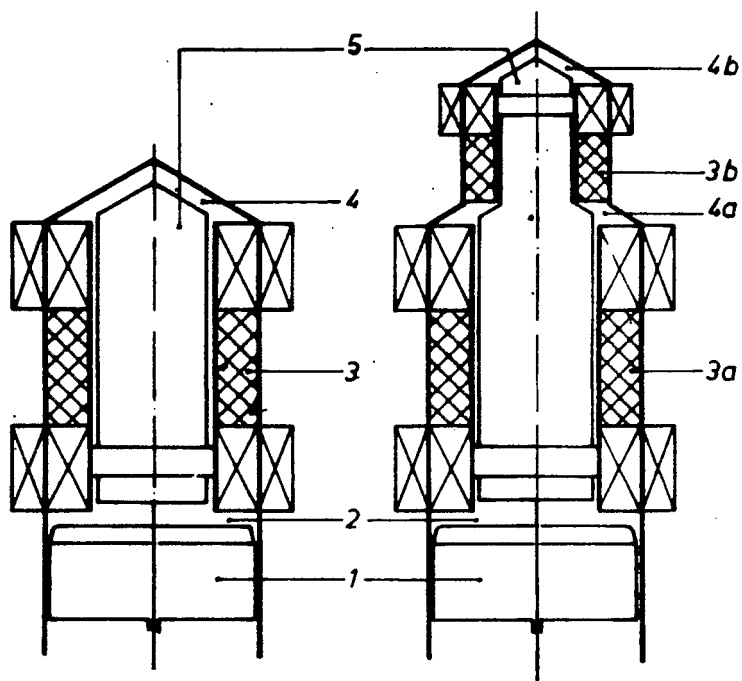


Fig. 14. Two- and three-phase Stirling process.

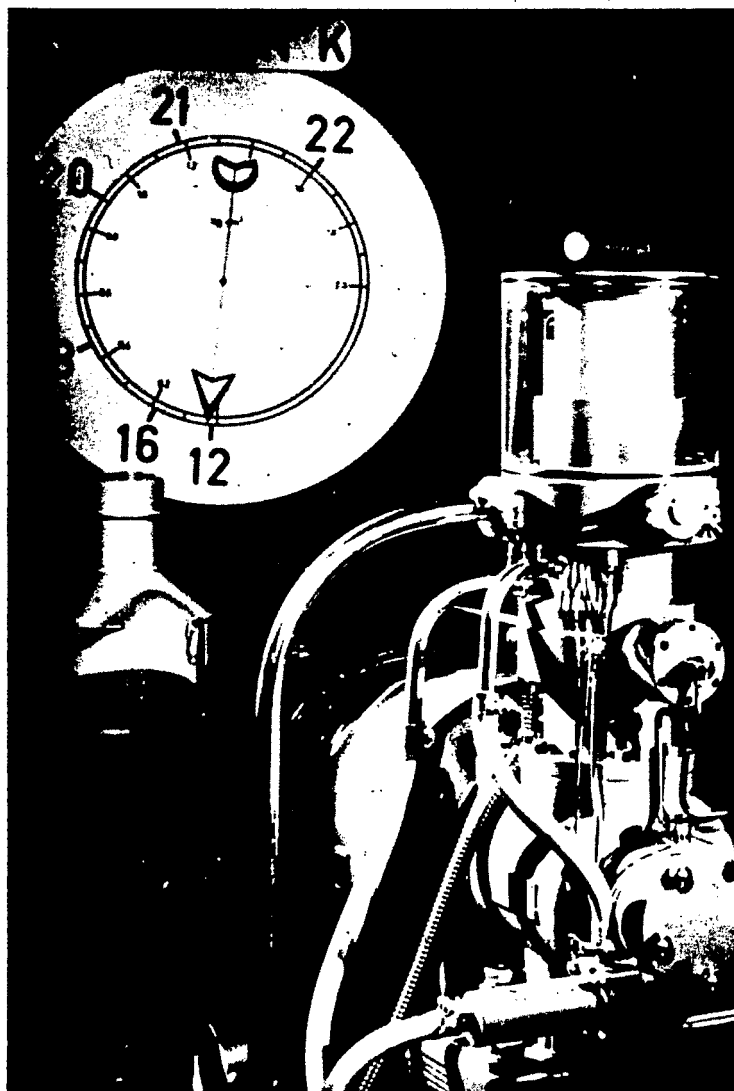


Fig. 15. Prototype A20 Stirling machine, with bar magnet floating above superconducting plate.

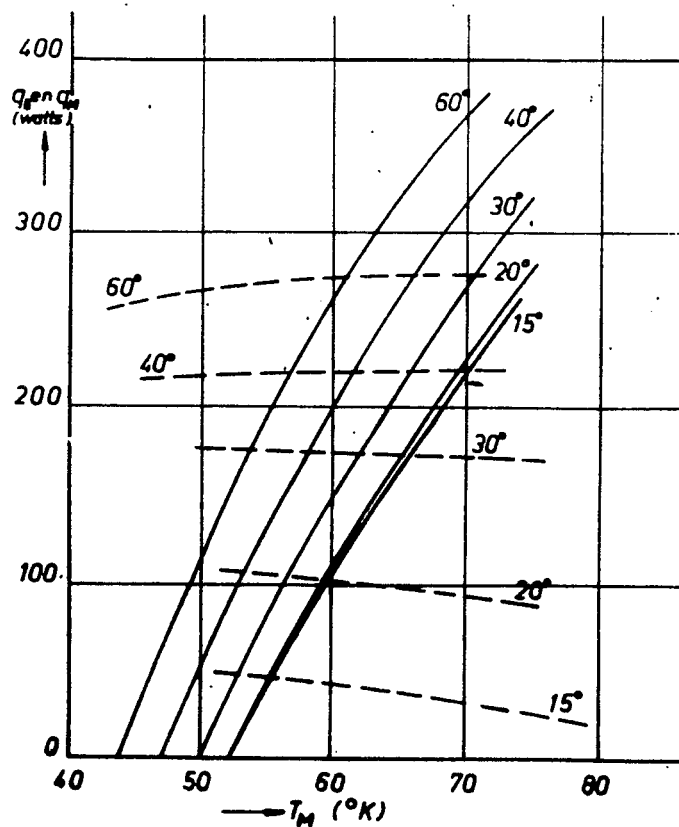


Fig. 16. Cold productions of prototype A20 Stirling refrigerator.

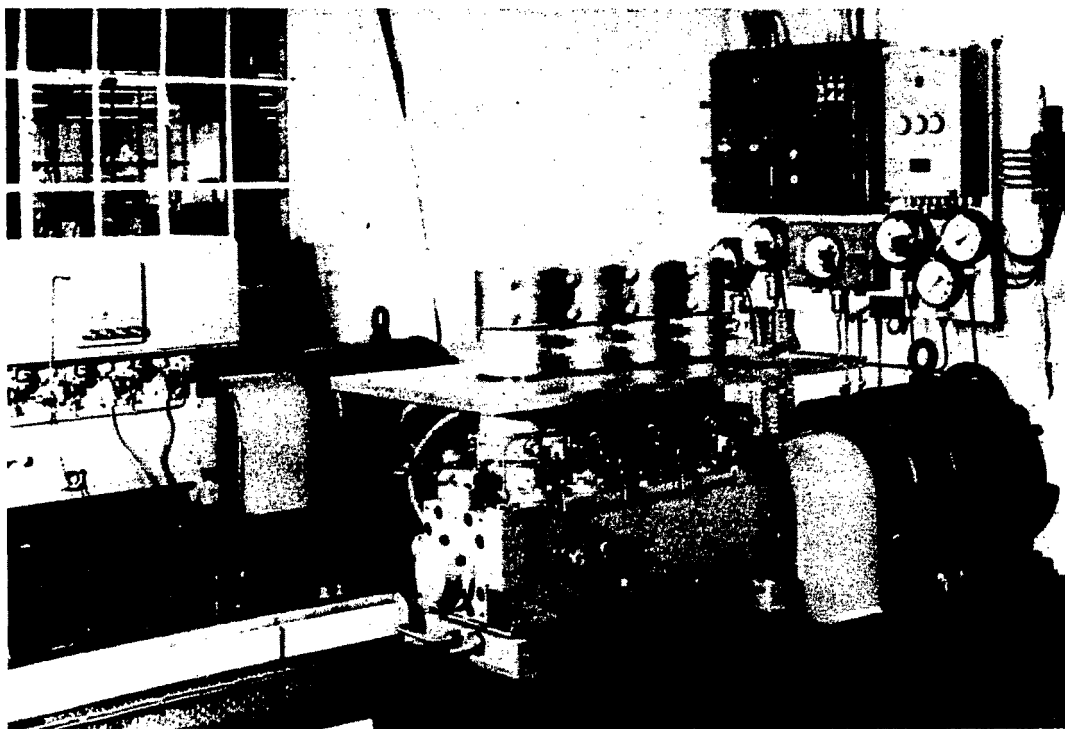


Fig. 17. Four-cylinder Stirling refrigerator.

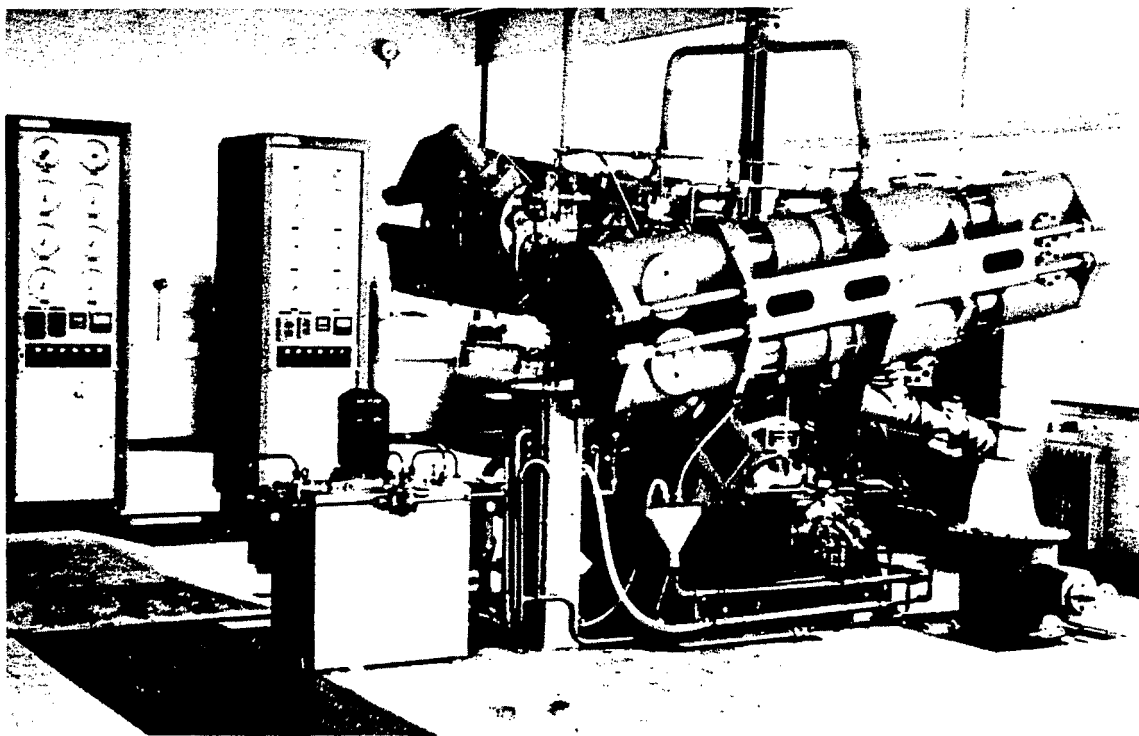


Fig. 18. Stirling refrigerator for 25 kW at 77°K.

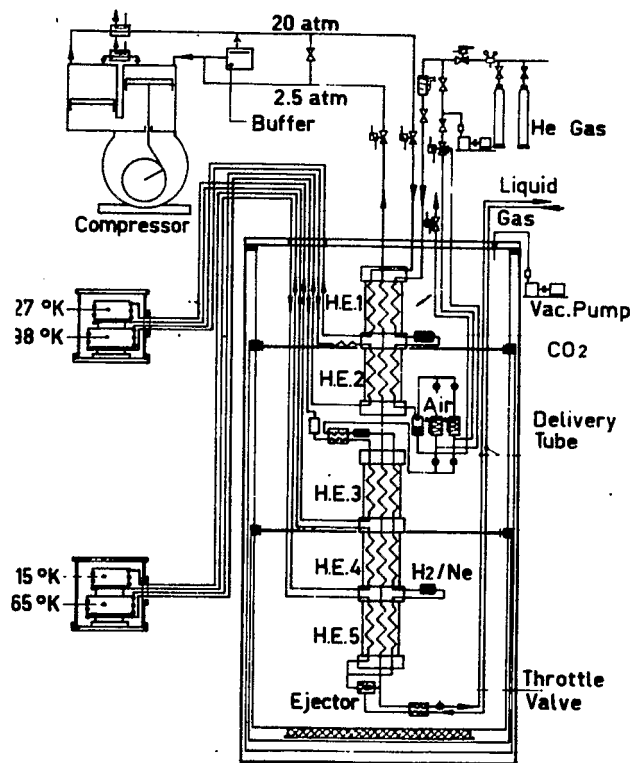


Fig. 19. Flow diagram of Philips helium liquefier.

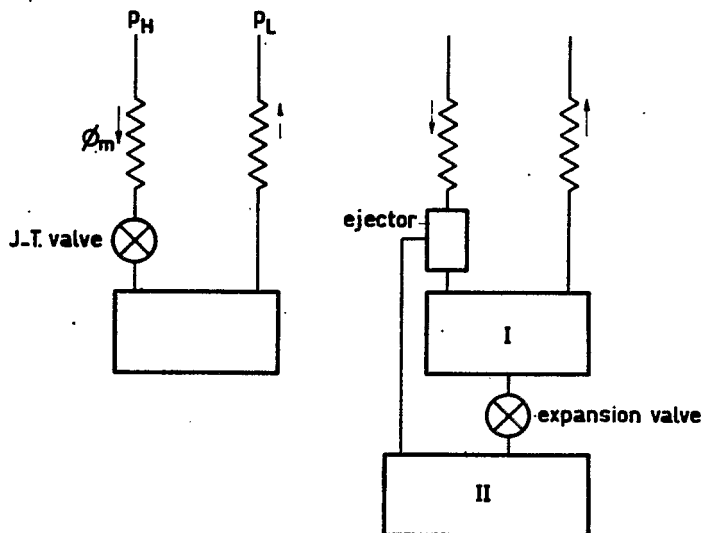


Fig. 20. Ejector system in Joule-Kelvin process.

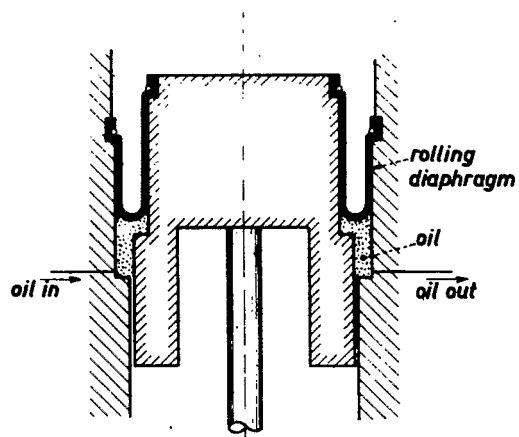


Fig. 21. Schematic of oil-supported rolling diaphragm.

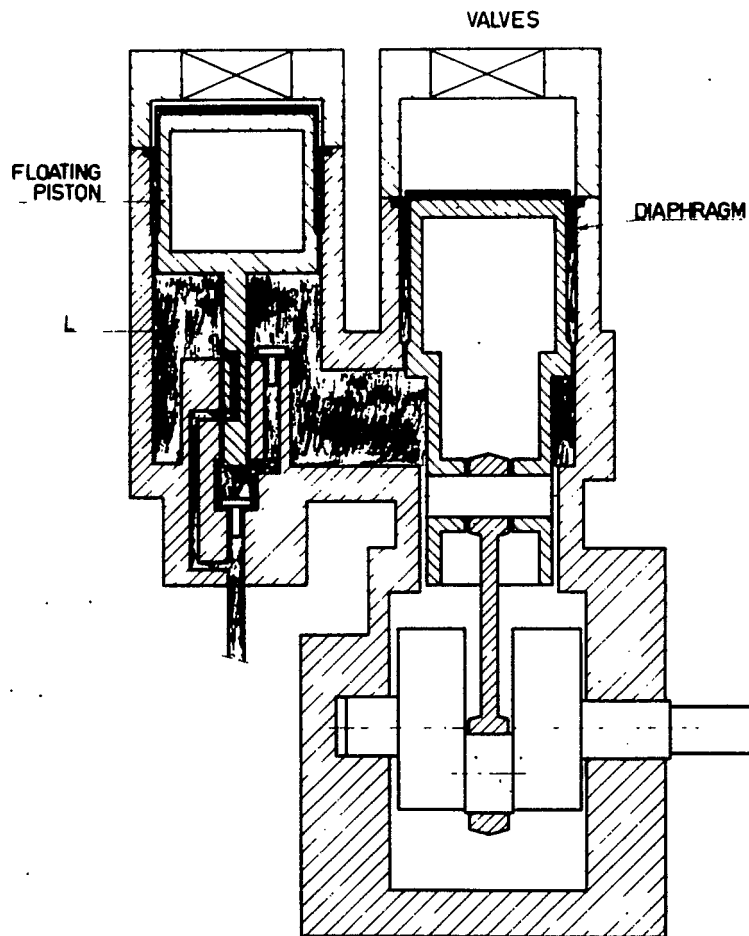


Fig. 22. Oil-free compressor with rolling diaphragms.

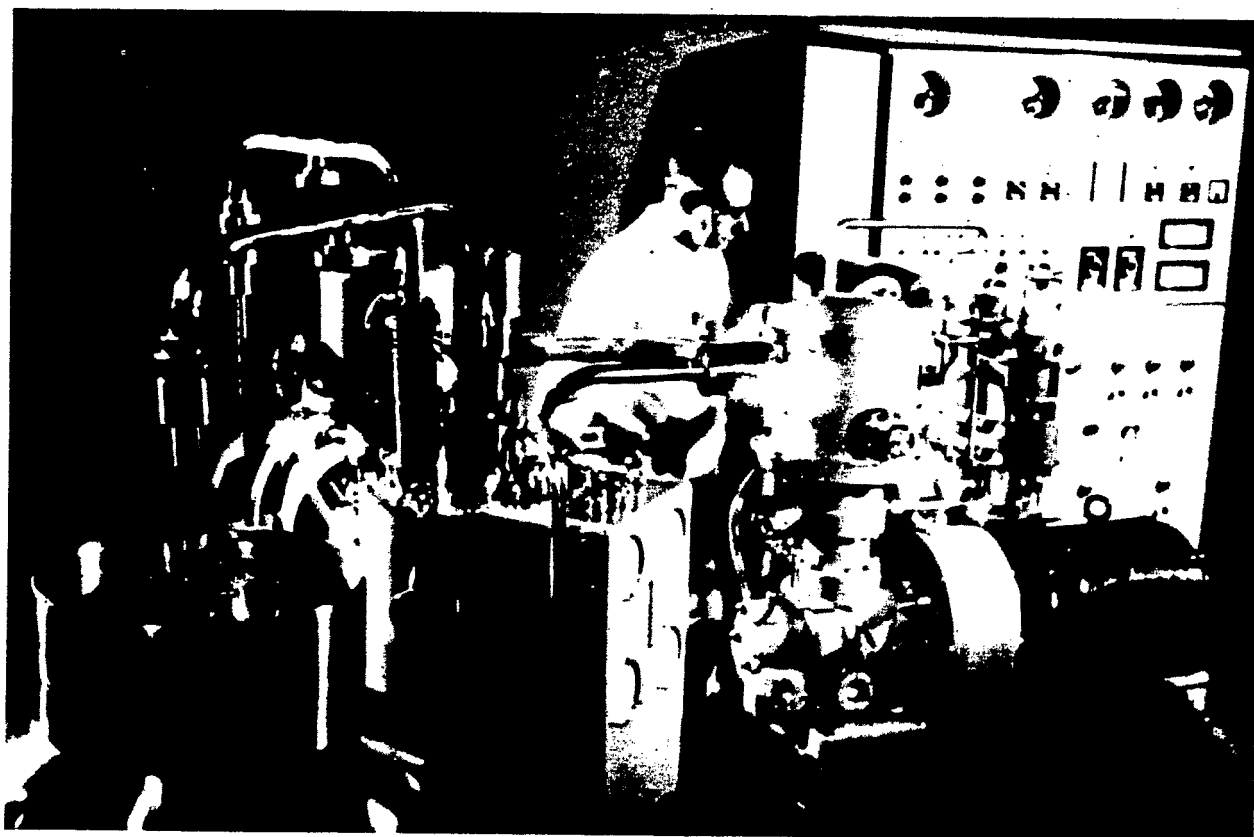


Fig. 23. Philips helium liquefier.



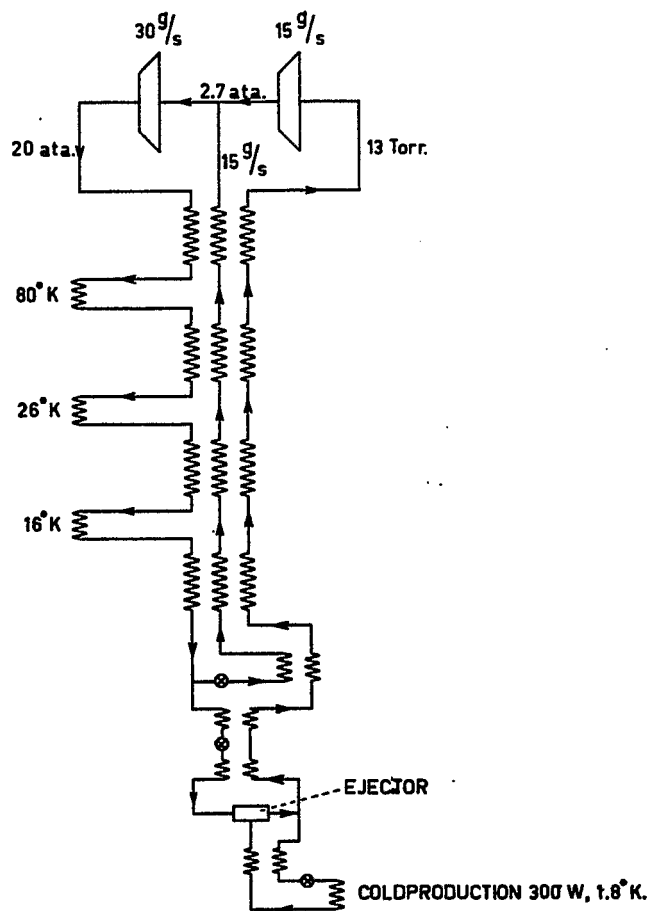


Fig. 24. Flow diagram of proposed 300 W, 1.8°K system.

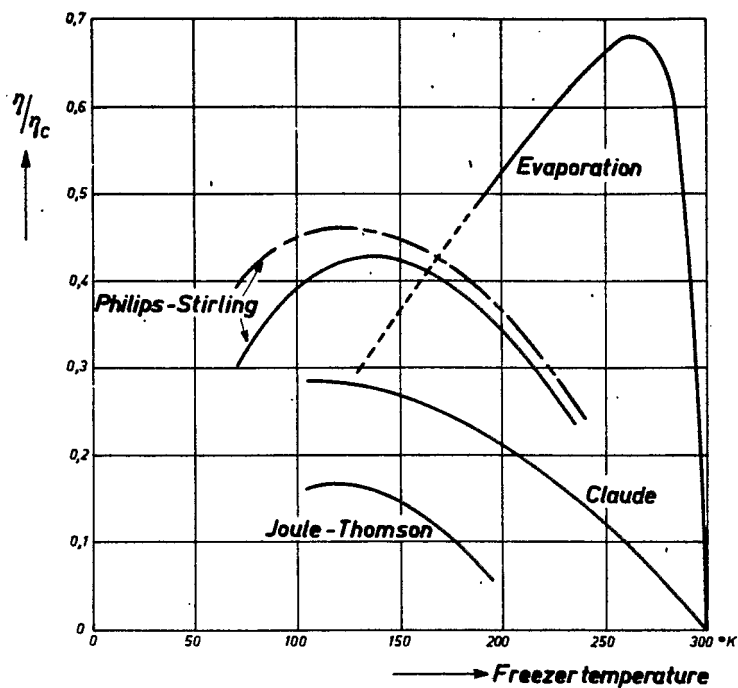


Fig. 25. Comparison of efficiencies of different systems.

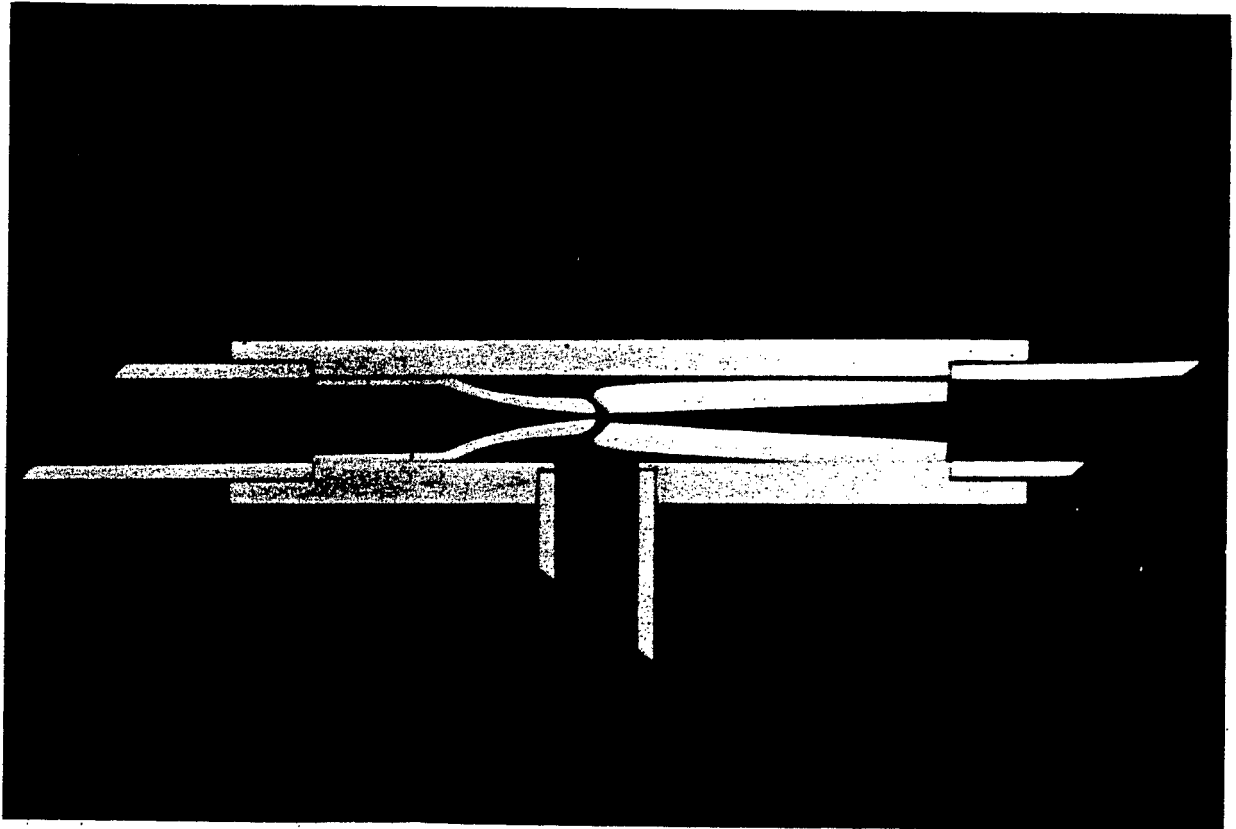


Fig. 26. Ejector.

## CRYOGENIC SAFETY\*

Michael G. Zabetakis  
Explosives Research Center  
Bureau of Mines  
Pittsburgh, Pennsylvania

### ABSTRACT

In any cryogenic system, we must first consider the hazards associated with the materials, processes, and procedures of interest. These can be divided into three general areas: physiological, physical, and chemical. The first includes frostbite, respiratory ailments, and the specific effects of certain materials such as oxidizers on body tissues. The second includes the effects of phase changes, low temperatures, oxygen enrichment, and hydrogen embrittlement. The third includes the ignition of flammable mixtures, the propagation of deflagrations and detonations, and the initiation of destructive fires. A knowledge of these hazards and the applicable basic principles then permits one to design a suitable facility for the production, storage, handling and disposal of cryogenic fluids in the laboratory, plant and test site.

---

\*This talk was based on the author's monograph Safety with Cryogenic Fluids (Plenum Press, New York, 1967).

## CRYOPUMPING

C. Barnes  
CVI Corporation  
Columbus, Ohio

### I. INTRODUCTION

Cryopumping<sup>1</sup> is the removal of gas from a system by condensation onto a cold plate. The phenomenon of cryopumping is not new, but it has received much emphasis in the last few years because of the need for very great pumping speeds in space simulation work.<sup>2</sup> As cryogenic liquids and low temperature refrigerators become more readily available, cryopumps are used in more and more facilities not related to space simulation. The use of liquid helium and liquid hydrogen in particle accelerator programs makes the use of cryopumping quite natural in these facilities.

### II. THE CONCEPT OF CRYOPUMPING

The requirement for effectively cryopumping a gas is that the vapor pressure of the condensate shall be quite low, and that gas molecules shall stick to the cold surface upon impact (at least for the majority of impacts).

The change of vapor pressure with temperature follows the Clausius-Clapeyron equation:

$$\frac{dp}{dT} = \frac{L}{T (V'_f - V'_i)}$$

where  $L$  = latent heat of the phase change,

$V'_f$  = final specific volume,

$V'_i$  = initial specific volume,

$T$  = absolute temperature.

If  $L$  is approximately constant, if the specific volume of the gas is much greater than that of the solid, and if the gas approximately follows the ideal gas law, then  $\ln p = A - (B/T)$ , or  $p = C e^{-B/T}$ . It is clear that a substantial reduction in temperature can produce a drastic reduction in vapor pressure. For example, hydrogen vapor pressure varies approximately as:

$T$ °K	5	4.2	3.5	3
$p$ ( $H_2$ ) torr	$1.5 \times 10^{-5}$	$3 \times 10^{-7}$	$1 \times 10^{-9}$	$1 \times 10^{-11}$

1. B.M. Bailey and R.L. Chuan, Trans. Fifth National Symposium on Vacuum Technology (Pergamon Press, 1959), p. 262.
2. D.J. Santeler et al., National Aeronautics and Space Administration Report NASA SP-105 (1966).

and nitrogen vapor pressure varies approximately as:

T °K	50	40	30	20
p (N <sub>2</sub> ) torr	4	$5 \times 10^{-2}$	$3 \times 10^{-5}$	$1 \times 10^{-11}$

The dependence of vapor pressure on temperature<sup>3</sup> for a wider range, and for other gases, is shown in Fig. 1.

The effectiveness of cryopumping, assuming a sufficiently low vapor pressure for the condensate, is determined by the fraction of those molecules incident on a cold "pumping" surface which stick to the surface. Only a limited number of sticking fraction experiments have been done,<sup>4,7-9</sup> and the results are not particularly clear. However, the sticking fraction will, in general, increase with surface roughness and with decreasing temperature. This is expected, because the accommodation coefficient (Fig. 2) is influenced in the same ways,<sup>5,6</sup> and a high sticking fraction implies a high accommodation coefficient. As a good general rule, nitrogen and oxygen have a high coefficient of sticking (in excess of 0.9) for impact on 20°K or lower temperature surfaces. Water vapor and carbon dioxide have a high coefficient of sticking when contacting 80°K or lower temperature surfaces. Hydrogen has a high coefficient on contacting 4.2°K surfaces. All cryopumping surfaces which have been in operation long enough to build up a film of condensate will be "rough" from a molecular standpoint, and will have relatively high values for accommodation coefficient and for sticking fraction, provided the temperature is low enough.

### III. PUMPING SPEEDS AND ULTIMATE PRESSURE

The condensation pumping speed of cold surfaces depends on a number of factors such as (1) sticking fraction at the surface, (2) temperature of the gas being pumped, (3) molecular weight of the gas being pumped, and (4) system geometry, including the presence or absence of thermal (and mechanical) shielding. Also, the ultimate pressure attainable in a cryopumped chamber depends on (1) the magnitude of the introduced gas load, as well as the outgassing load, (2) the temperature of the gas being pumped, (3) the system geometry, (4) the vapor pressure of the condensate, and (5) the amount of "noncondensable" gas present, which must be removed by other pumping methods.

- 
3. R.E. Honig and H.O. Hook, RCA Review 21, 360 (1960).
  4. J.P. Dawson, J.D. Haygood, and J.A. Collins, Jr., in Advances in Cryogenic Engineering (Plenum Press, 1964), Vol. 9, p. 443.
  5. W.H. Keesom and G. Schmidt, Physica 3, 590 (1936); 3, 1085 (1936); 4, 828 (1937).
  6. H.Y. Wachman, Am. Rocket Soc. J. 32, 2 (1962).
  7. B.A. Buffham, P.B. Henault, and R.A. Flynn, Trans. Ninth National Vacuum Symposium (MacMillan Co., 1962), p. 205.
  8. R.F. Brown and E.S.J. Wang, in Advances in Cryogenic Engineering (Plenum Press, 1965), Vol. 10, p. 283.
  9. J.A. Collins and J.P. Dawson, Arnold Engineering Development Center Report AEDC-TDR-63-51 (1963).

The calculation of pumping speeds and ultimate pressures is in general quite complicated, but there are several very simple geometries for which the analysis is direct and exact. The results for these give indications of what to expect for other, more realistic, systems.

### 1. Spot Cryopumping

First consider a small condensation spot of area  $A$  at some low temperature  $T_c$  in a chamber of otherwise uniform conditions. Because the spot is very small, nearly all of the gas is at the wall temperature  $T_w$ , and has a corresponding average molecular speed  $\bar{v}_w$ . However, if the entire wall were at a temperature  $T_c$ , then the gas would all be at temperature  $T_c$  in equilibrium with the evaporation from the "condensing spot." If, therefore, we imagine the spot to be replaced by an opening with a chamber at temperature  $T_c$  on the other side of the opening, Fig. 3, the resulting imaginary system may be treated by the same analysis as the real system. In particular, the molecules in the imaginary system travel through the opening at different speeds ( $\bar{v}_w$  or  $\bar{v}_c$ ) depending on their origin, so the ultimate pressure in the actual chamber (with no gas addition) is given by the classic thermal transpiration analysis,  $p_u = p_v (T_w/T_c)^{1/2}$ , where  $p_v$  is the vapor pressure of the condensate and also the pressure in the imaginary chamber at temperature  $T_c$ , and where molecular speed is proportional to the square root of the absolute temperature. If the condensing spot is at 20°K, the vapor pressure of nitrogen is  $10^{-11}$  torr and the ultimate pressure in the chamber for nitrogen gas alone (no outgassing from the walls and no inleakage) is  $10^{-11} (300/20)^{1/2} = 3.87 \times 10^{-11}$  or almost four times the condensate vapor pressure.

The pumping speed is determined by the difference between condensing rate and evaporation rate. However, at pressures significantly higher than ultimate, the amount of evaporation is insignificant as compared to the amount of condensation, so the volumetric pumping speed is (assuming unity sticking fraction)  $S = (\bar{v}_w/4)A$ , which is the "orifice speed" for gas at temperature  $T_w$ . For 300°K nitrogen gas, the orifice speed per unit area is approximately 75 liter/sec for each square inch.

### 2. Parallel Wall Cryopumping

Next consider the case of two parallel walls,<sup>10</sup> Fig. 4. One is at temperature  $T_c$  and condenses a fraction  $f$  of all the gas which strikes it. The other wall is at a warmer temperature  $T_w$  and reflects all incident gas. For simplicity of calculations, we assume unity accommodation coefficient at both walls. The gas molecules leaving a wall in random directions are different from a normal random gas in that there is no component of velocity back toward the wall. The volumetric flow of such a gas is therefore given by  $\bar{v}/2$  rather than the usual  $\bar{v}/4$ , where  $\bar{v}$  is the average speed of the molecules. Consider the mass flow of evaporated vapor from the cold wall to be  $\dot{m}_c$  and the mass flow of outgassing from the warm wall to be  $\dot{m}_w$ . Define  $\dot{m}_c$  as the total flow of gas from the cold wall, and  $\dot{m}_w$  as the total flow of gas from the warm wall. Then the total gas flow leaving the warm wall is the outgassing plus the reflected gas from the cold wall, i.e.,  $\dot{m}_w = \dot{m}_w + \dot{m}_c$ . Similarly, the total gas leaving the cold wall is the fraction from the warm wall which is reflected at the cold wall, plus the rate of condensate vaporization. That is,  $\dot{m}_c = (1 - f) \dot{m}_w + \dot{m}_c$ . Solving these two equations gives:

---

10. R.W. Moore, Jr., Trans. Eighth National Vacuum Symposium and Second International Congress on Vacuum Science and Technology (Pergamon Press, 1962), Vol. 1, p. 426.

$$\dot{m}_c = \frac{\dot{w}_w (1 - f) + \dot{w}_c}{f},$$

$$\dot{m}_w = \frac{(\dot{w}_w + \dot{w}_c)}{f}.$$

The mass flow rate is simply the density multiplied by the volumetric flow rate:

$$\dot{m} = [\rho(\bar{v}/2)A],$$

thus

$$\rho_{tot} = \rho_w + \rho_c = \frac{2\dot{m}_w}{\bar{v}_w A} + \frac{2\dot{m}_c}{\bar{v}_c A}.$$

Substituting the expressions for  $\dot{m}_w$  and  $\dot{m}_c$ , we get an expression for total density in terms of the rates of evaporation and outgassing (or other gas introduction). The net gas load being pumped is that introduced at the warm wall, i.e.,  $\dot{w}_w$ , and if this is divided by the density, we get a volumetric "speed"  $S$ . When we carry out the substitutions, we get

$$\frac{S}{A} = \frac{\dot{w}_w}{\rho A} = \frac{f(\bar{v}_w/2)}{[1 + (1 - f)(T_w/T_c)^{1/2}] + (\dot{w}_c/\dot{w}_w)[1 + (T_w/T_c)^{1/2}]}$$

For  $f = 1$ , i.e., complete capture, the expression reduces to

$$\left(\frac{S}{A}\right) = \frac{(\bar{v}_w/2)}{1 + (\dot{w}_c/\dot{w}_w)[1 + (T_w/T_c)^{1/2}]}$$

and, if the introduced gas load is much greater than the rate of evaporation (which is true in most practical applications), then

$$(S/A) = (\bar{v}_w/2)$$

which is twice the so-called "orifice speed."

Although the basic expression derived for speed in terms of  $\dot{w}_w$  and  $\dot{w}_c$  is satisfactory, it is interesting to develop an alternate expression for speed in terms of chamber pressure and condensate vapor pressure.<sup>10,11</sup> First, we note that when a gas leaves a wall in random directions, the averaged component of molecular velocity normal to the wall is  $\bar{v}/2$ , where  $\bar{v}$  is the average speed of the molecules. Then the mass flow rate away from a wall section of area  $A$  is  $\dot{m} = A\rho(\bar{v}/2)$ , where  $\rho$  is the density of that part of the gas which is leaving the wall. The same sort of expression exists for that part of the gas which is incident on the wall. Dividing the difference in mass flow (between incident and evaporated gas) by the total density,  $\rho_{tot} = \rho_w + \rho_c$ , gives the volumetric pumping speed. That is,

$$\frac{S}{A} = \frac{\rho_w(\bar{v}_w/2) - \rho_c(\bar{v}_c/2)}{\rho_w + \rho_c}.$$

---

11. E.L. Garwin, in Advances in Cryogenic Engineering (Plenum Press, 1963), Vol. 8, p. 37.

In order to convert the "partial densities" in this expression to pressures, we define  $Mp = \rho RT$ , where

$M$  = molecular weight of the gas

$p$  = "pressure"

$\rho$  = density

$R$  = universal gas constant

$T$  = absolute temperature.

This definition agrees with the "pressure" as measured by a nude ion gauge, where the gauge actually measures gas density. Then

$$\rho_w = Mp_w / RT_w,$$

and

$$\rho_c = Mp_c / RT_c,$$

and using

$$\bar{v}_c / \bar{v}_w = (T_c / T_w)^{1/2},$$

$$\frac{S}{A} = \frac{\bar{v}_w}{2} \left[ \frac{p_w - p_c (T_w / T_c)^{1/2}}{p_w + p_c (T_w / T_c)} \right].$$

By using the concept of total pressure,  $p = p_w + p_c$ , and vapor pressure,  $p_v = 2p_c$  (that is, the true vapor pressure includes equal flows toward and away from the wall), we get

$$\frac{S}{A} = \left[ \frac{p - (p_v/2)(1 + (T_w/T_c)^{1/2})}{p - (p_v/2)(1 - T_w/T_c)} \right] \left( \frac{\bar{v}_w}{2} \right).$$

Clearly, when  $p \gg p_v$ , we have a constant speed (twice the orifice speed) independent of pressure. However, we know that at some ultimate pressure the net speed must be zero. Setting  $(S/A) = 0$  gives the ultimate pressure

$$p_u = (p_v/2) [1 + (T_w/T_c)^{1/2}].$$

If we consider the initial fall-off in low pressure speed to occur when  $(S/A) = 0.9 (\bar{v}_w/2)$ , i.e., when 10% decrease in speed has occurred, then the "fall-off pressure"  $p^*$  is given by

$$0.9 = \frac{p^* - (p_v/2) [1 + (T_w/T_c)^{1/2}]}{p^* - (p_v/2) [1 - T_w/T_c]}.$$

The following values are obtained:

$T_w$ °K	$T_c$ °K	$p^*$
300	100	22.65 $p_v$
300	20	87.4 $p_v$



Therefore, in order to maintain full pumping speed the cryoplate temperature must be cold enough that the condensate vapor pressure is well below the operating pressure.

It is interesting to use the ultimate pressure in this same expression for the "fall-off" pressure, to get

$$0.9 = \frac{p^* - p_u}{p^* - \left[ \frac{p_u}{1 - (T_w/T_c)^{1/2}} \right]}$$

$$\frac{p^*}{p_u} = 10 \left[ 1 + \frac{0.9}{(T_w/T_c)^{1/2} - 1} \right]$$

This shows that speed falls off for pressures at least one order of magnitude greater than ultimate.

### 3. Concentric Sphere Cryopumping

There are few true "spot cryopumps" and even fewer parallel wall (two-dimensional) pumping systems. The simplest model for a "three-dimensional" cryopumping situation is that of two concentric spheres, and such pumping situations do exist. The most extensively studied of these (because of its direct application to space simulation work) is that of a warm outgassing sphere concentrically surrounded by a cold cryopumping sphere.<sup>12,13</sup> The method of determining pumping speed for this situation has the same basis as the methods used for spot cryopumping and for parallel wall cryopumping. That is, the speed is defined as the ratio of mass capture to total gas density  $\rho$  at the point of pumping. In a closed system, the mass capture rate (at equilibrium) is simply the rate at which gas is introduced, or in our example, the warm outgassing rate,  $\dot{w}_w$ . Therefore,  $S = \dot{w}_w/\rho$ . The density is obtained as follows. We note, from Fig. 5, that gas which leaves the warm inner sphere at temperature  $T_w$  (assuming an accommodation coefficient of unity at all surfaces) will definitely strike the outer surface. The gas leaving the cold wall at temperature  $T_c$  may go to the warm inner sphere, or it may bypass the inner sphere and go to another part of the cold wall. Therefore, the gas at any point adjacent to the cryopumping sphere comes from three different sources. These are: (1) gas leaving the cold surface in random directions at average speed  $\bar{v}_c$ , (2) gas approaching the cold surface from the warm sphere, moving at an average speed  $\bar{v}_w$  within an angle  $\varphi$  to the normal, and (3) gas approaching the cold surface from other parts of the cold wall, moving at an average speed  $\bar{v}_c$  and at an angle to the normal greater than  $\varphi$ . The normal component of velocity for any molecule moving toward a surface at a speed  $v$  and at an angle  $\theta$  to that surface is  $v \cos \theta$ . Averaging over all permitted directions (within some total solid angle  $\Omega$ ), the average normal molecular component of speed toward the surface is given by

$$\frac{1}{\Omega} \int \bar{v} \cos \theta \, d\Omega$$

---

12. C.B. Hood and C.B. Barnes, J. Vacuum Sci. Tech. 2, 302 (1965).

13. J.D. Pinson and A.W. Peck, Trans. Ninth National Vacuum Symposium (MacMillan Co., 1962), p. 406.

The mass flow per unit area toward the surface is the product of gas density and average normal component of velocity, so

$$\frac{\dot{m}}{A} = \rho \left[ \frac{1}{\Omega} \int \bar{v} \cos \theta \, d\Omega \right] .$$

Consider the molecules moving away from the cold surface in all directions within an angle  $\pi/2$  to the normal. Then

$$\begin{aligned} \frac{\dot{m}_c}{A_c} &= \rho_c \left[ \frac{1}{2\pi} \int_0^{\pi/2} \bar{v}_c \cos \theta \, 2\pi \sin \theta \, d\theta \right] \\ &= (\rho_c \bar{v}_c / 2) , \end{aligned}$$

where  $\rho_c$  is that part of the total density attributed to the molecules under discussion, i.e., those leaving the cold surface. Next consider the molecules moving toward the cold surface from the warm inner surface at all angles  $0 < \theta < \varphi$  measured from the normal:

$$\begin{aligned} \frac{\dot{m}_{wc}}{A_c} &= \rho_{wc} \left[ \frac{\int_0^{\pi/\varphi} \bar{v}_w \, 2\pi \sin \theta \cos \theta \, d\theta}{\int_0^{\varphi} 2\pi \sin \theta \, d\theta} \right] \\ &= \frac{\rho_{wc} \bar{v}_w}{2} \cdot \left[ \frac{\sin^2 \varphi}{1 - \cos \varphi} \right] . \end{aligned}$$

Finally, consider the molecules moving toward the cold surface from other parts of the cold surface (at all angles  $\varphi < \theta < \pi/2$ ):

$$\frac{\dot{m}_{cc}}{A_c} = \rho_{cc} \bar{v}_c \left[ \frac{\cos \varphi}{2} \right] .$$

The total density is then

$$\begin{aligned} \rho &= \rho_c + \rho_{wc} + \rho_{cc} \\ &= \frac{2}{\bar{v}_w A_c} \left[ \dot{m}_c \left( \frac{T_w}{T_c} \right)^{\frac{1}{2}} + \dot{m}_{wc} \left( \frac{1 - \cos \varphi}{\sin^2 \varphi} \right) + \frac{\dot{m}_{cc}}{\cos \varphi} \left( \frac{T_w}{T_c} \right)^{\frac{1}{2}} \right] . \end{aligned}$$

There remains to express the mass flow in terms of the total outgassing rate  $\dot{w}_w$ , and the total evaporation rate  $\dot{w}_c$ . This is done by noting that the amount of gas leaving any surface is the sum of gas emitted by that surface and the gas reflected from it. Mass balance gives:

$$\begin{aligned} \dot{m}_c &= \dot{w}_c + (\dot{m}_{wc} + \dot{m}_{cc}) (1 - f) \\ \dot{m}_{wc} &= \dot{w}_w + F \dot{m}_c \\ \dot{m}_{cc} &= \dot{w}_c (1 - F) + (\dot{m}_{wc} + \dot{m}_{cc}) (1 - f) (1 - F) \\ &= \dot{m}_c (1 - F) , \end{aligned}$$

where  $f$  is the capture fraction at the cold surface, and  $F$  is the view factor from the outer surface to the inner surface, i.e.,  $F$  is the fraction of molecules which will strike the inner surface  $A_w$  after diffusely leaving the outer surface  $A_c$ . Solving the equations and substituting into the expression for total density gives

$$\left( \frac{\bar{v}_w A_c}{2 \dot{w}_w} \right) \rho = \left( \frac{T_w}{T_c} \right)^{\frac{1}{2}} \left\{ \frac{\dot{w}_c}{\dot{w}_w} \cdot \frac{1}{f} + \left( \frac{1-f}{f} \right) + (1-F)^{\frac{1}{2}} \left[ \frac{\dot{w}_c}{\dot{w}_w} \cdot \frac{1}{f} + \left( \frac{1-f}{f} \right) \right] \right\} \\ + [1 - (1-F)^{\frac{1}{2}}] \left\{ \frac{\dot{w}_c}{\dot{w}_w} \cdot \frac{1}{f} + \frac{1}{F} + \frac{1}{f} - 1 \right\} ,$$

where the substitution  $\cos \varphi = (1-F)^{\frac{1}{2}}$  has been made also. The speed of pumping is therefore

$$S = \dot{w}_w / \rho \\ = \frac{(\bar{v}_w / 2) A_c}{[1 - (1-F)^{\frac{1}{2}}] \left[ \frac{\dot{w}_c}{\dot{w}_w} \cdot \frac{1}{f} + \frac{1}{F} + \frac{1}{f} - 1 \right] + [1 + (1-F)^{\frac{1}{2}}] \left( \frac{T_w}{T_c} \right)^{\frac{1}{2}} \left[ \frac{\dot{w}_c}{\dot{w}_w} \cdot \frac{1}{f} + \left( \frac{1-f}{f} \right) \right]}$$

The additional complications of the three-dimensional analysis are obvious.

The equation just developed for speed may be put into a better form for practical solutions. For spheres,

$$(A_w / A_c) = F$$

and

$$\frac{\dot{w}_c}{\dot{w}_w} = \frac{\dot{w}_c / A_c}{\dot{w}_w / A_w} \cdot \frac{1}{F} .$$

Then, using the symbol  $R$  to represent the ratio of evaporation per unit area of the cold wall to outgassing rate per unit area of the warm sphere,

$$(\dot{w}_c / \dot{w}_w) = R / F ,$$

and

$$\frac{S}{A_c} = \frac{\bar{v}_w}{4} \left\{ \frac{2F}{[1 - (1-F)^{\frac{1}{2}}] \left[ \frac{R}{f} + 1 + \frac{F}{f} - F \right] + [1 + (1-F)^{\frac{1}{2}}] \left( \frac{T_w}{T_c} \right)^{\frac{1}{2}} \left[ \frac{R}{f} + \left( \frac{1-f}{f} \right) \right]} \right\}$$

which is orifice speed per unit area multiplied by a correcting factor. For  $F = 1$  (indicating that the two spheres are nearly equal size) this expression reduces to

$$\frac{S}{A_c} = \frac{f(\bar{v}_w / 2)}{(1+R) + (T_w / T_c)^{\frac{1}{2}} (1-f+R)} .$$

This is the same expression developed earlier for parallel walls.

#### 4. Arguments in the Definition of Speed and Pressure

The analysis for cryopumping speed in the system of an infinitesimal warm sphere (or outgassing source) at the center of a perfectly condensing spherical cryopumping surface gives (for  $F \rightarrow 0$  and  $f = 1$ )  $S = 4(\bar{v}_w/4)A$ , which is a factor of four greater than orifice speed. Most vacuum texts imply that orifice speed is an upper limit to pumping rates, and represents a "perfect system." This apparent contradiction is really only a conflict in initial assumptions. The classical analysis of orifice speed is the determination of the volumetric rate at which gas strikes a perfectly reflecting surface in a closed system in equilibrium. If a pinhole orifice in this surface allows gas to escape to a perfect vacuum, the volumetric rate of escape out of the orifice is given by  $(S/A) = (\bar{v}/4)$ . The orifice is so small that equilibrium is only slightly disturbed. If the orifice size is increased, equilibrium is disturbed, completely random motion no longer exists, and the definition of volumetric pumping speed becomes ambiguous. However, we can think of at least one completely nonequilibrium case in which volumetric speed seems clearly indicated. In this case, a perfectly collimated beam of molecules is completely captured by a surface perpendicular to the direction of motion. If the average molecular speed is  $\bar{v}$ , then the volumetric speed of molecular capture per unit area of capturing surface is  $\bar{v}$ . It seems reasonable, therefore, to define pumping speed at a point in terms of the gas conditions at that point.<sup>14,15</sup> Such a definition always gives a unique speed if we simply divide mass capture rate by gas density, both measured at the point in question. This definition gives the true volumetric speed, and has been used throughout the present discussion.

There have been objections to a definition of pumping speed based on nonequilibrium conditions. However, we note that "beaming" of molecules, i.e., collimated motion, does usually cause an increase in the molecular capture rate. It seems only reasonable to say that increased capture rate indicates increased "speed," and the definition of volumetric speed as mass capture rate divided by density certainly seems better than any alternate proposals.

There is also some confusion concerning the definition of pressure. The basic definition is, of course, the force per unit area on a surface, this definition is satisfactory for an equilibrium gas. When a gas is not in equilibrium, then true pressure becomes directional. However, in most cases we are really interested in "how much" gas is present in a given volume, i.e., in the density. It is for that reason that the foregoing analysis used  $p = \rho RT/M$  as the definition of gas pressure, regardless of directions. If a nude, or nontubulated, gauge is used, then it is actually density rather than true pressure that is being measured. Therefore, we must add the qualification, in our analyses, that the theoretical results will correspond to measured results only if a nude gauge is used to measure pressure.

#### IV. MASS CAPTURE RATES

The mass capture rate of a cryopumping system is sometimes quite difficult to calculate. For the simplest geometries, discussed in Sections III.1, III.2, and III.3, it is sufficient to separate the gas leaving each surface into the gas originating from that surface and the gas reflected from it.<sup>10</sup> Then a set of equations may be set up which are solved for the total gas leaving each surface, expressed in terms of the gas originated at all other surfaces. This method is, in principle, adequate for all

---

14. C.B. Barnes, Vacuum **14**, 429 (1964).

15. W.W. Stickney and B.B. Dayton, Trans. Tenth National Vacuum Symposium (MacMillan Co., 1963), p. 105.

analysis, but in fact it becomes difficult to use if the systems are very complicated. For that reason, we present three other techniques for determining mass flows (or throughput flows) in general systems.

### 1. Network Analogy

There is an analogy between free molecular gas transfer and radiant energy transfer which is quite striking. For example, a variation of the Oppenheim network method for radiant transfer may be used to determine the free molecular mass gas flow between arbitrary surfaces.<sup>14</sup> In this technique,

$$Q_{\text{net}} = (J - G)A$$

where  $G$  = incident mass rate per unit area on the surface,

$J$  = mass rate per unit area leaving the surface.

Also,  $J = W' + (1 - f)G$ ,

where  $W'$  = outgassing (or evaporation) mass rate per unit area,

$f$  = capture fraction of incident molecules.

The last equation may be written

$$(1 - f)(J - G) = f \left( \frac{W'}{f} - J \right)$$

from which

$$Q_{\text{net}} = \frac{\left( \frac{W'}{f} - J \right)}{\left( \frac{1 - f}{fA} \right)}$$

The "electrical" analogy is that the "potential difference" corresponds to  $(W/f) - J$  and the "resistance" corresponds to  $(1 - f)/fA$ . For any two surfaces  $A_i$  and  $A_j$ , the net free molecular mass flow between them is

$$(Q_{\text{net}})_{ij} = A_i F_{ij} J_i - A_j F_{ji} J_j = A_i F_{ij} (J_i - J_j),$$

where the view factor  $F_{ij}$  is the fraction of diffusely emitted molecules which leave  $A_i$  and strike  $A_j$ . Here, "potential difference" corresponds to  $J_i - J_j$ , while the "resistance" corresponds to  $(A_i F_{ij})^{-1}$ . For example, consider the simple two-surface system of Fig. 6 where the total potential difference is divided by the sum of the resistances to get the net gas transfer:

$$Q_{\text{net}} = \frac{\frac{W'_1}{f_1} - \frac{W'_2}{f_2}}{\frac{1 - f_1}{f_1 A_1} + \frac{1}{A_1} + \frac{1 - f_2}{f_2 A_2}}$$

In our treatment of two infinite planes, the warm surface did not capture, and therefore the net mass flow was simply the outgassing of the warm, noncapturing surface. In the equation above, this is obtained by setting  $f_1 = 0$ , so that  $Q_{\text{net}} = W'_1 A_1$ .

The basic technique may be extended to any number of surfaces in a closed system. The network for a four-surface system is shown in Fig. 7, where the net gas flow is determined just as is current in an electrical system.

## 2. Adopted Gebhart Method

Another, and probably better, technique of determining mass flow to arbitrary surfaces is an adoption of the Gebhart method of matrix solution to radiant heat transfer. In the adopted Gebhart method, we define  $B_{ij}$  as the fraction of molecules which diffusely leave a surface  $A_i$  and are captured by another surface  $A_j$ . The fraction includes not only direct motion from  $A_i$  to  $A_j$ , but also motion from  $A_i$  to other surfaces and then, after reflection(s), capture by  $A_j$ . In a closed system, the fraction of molecules which leave  $A_i$  and are eventually captured by  $A_j$  can be expressed as a sum of terms, of which a typical one is  $F_{ik}R_kB_{kj}$ . In this term,  $F_{ik}$  is the fraction of molecules going directly from  $A_i$  to  $A_k$ , where a fraction  $R_k$  is reflected. Of these reflected molecules (from surface  $A_k$ ) a fraction  $B_{kj}$  will eventually be absorbed by  $A_j$ , going there by whatever paths are available. This expression of  $B_{ij}$  as a sum of terms is:

$$B_{ij} = F_{i1}R_1B_{1j} + F_{i2}R_2B_{2j} + \dots + (F_{ij}R_jB_{jj} + F_{ij}f_j) + F_{in}R_nB_{nj}$$

The term  $F_{ij}f_j$  represents the fraction of molecules captured by  $A_j$  after a direct flight from  $A_i$ . This basic equation may be rewritten as:

$$-F_{ij}f_j = F_{i1}R_1B_{1j} + F_{i2}R_2B_{2j} + \dots + (F_{ii}R_i - 1)B_{ij} + \dots + F_{in}R_nB_{nj}$$

Fixing  $j$  and allowing  $i$  to vary from 1 to  $n$  gives  $n$  equations, which can be solved by Cramer's rule:

$$\Delta = \begin{vmatrix} (F_{11}R_1 - 1) & F_{12}R_2 & F_{13}R_3 \dots & F_{1n}R_n \\ F_{21}R_1 & (F_{22}R_2 - 1) & F_{23}R_3 \dots & F_{2n}R_n \\ F_{31} & & & \\ \vdots & & & \\ F_{n1}R_1 & F_{n2}R_2 \dots & & (F_{nn}R_n - 1) \end{vmatrix}$$

$$B_{kj} = -\frac{f_j}{\Delta} \begin{vmatrix} (F_{11}R_1 - 1) & F_{12}R_2 \dots & F_{1,k-1}R_{k-1} & F_{1j} & F_{1,k+1}R_{k+1} \dots & F_{1n}R_n \\ F_{22}R_1 & (F_{22}R_2 - 1) \dots & F_{2,k-1}R_{k-1} & F_{2j} & F_{2,k+1}R_{k+1} & F_{2n}R_n \\ \vdots & & & & & \\ F_{n1}R_1 & F_{n2}R_2 \dots & F_{n,k-1}R_{k-1} & F_{nj} & F_{n,k+1}R_{k+1} \dots & (F_{nn}R_n - 1) \end{vmatrix}$$

If we restrict the meaning of  $B_{ij}$  (whatever the values of  $i$  and  $j$ ) to the fraction of molecules emitted by  $A_i$  (that is, originating at  $A_i$ ) and captured by  $A_j$ , then we have a direct and comparatively simple method of determining capture fractions for systems of many surfaces, including partly shielded cryopumping surfaces. The advantage of the adopted Gebhart method over the network method is the direct solution of the former. In the network method, equations must still be set up and solved even after the network itself has been drawn.

### 3. Monte Carlo Technique

Finally, the molecular capture fraction of a cryopumping system may be determined by Monte Carlo techniques.<sup>13</sup> Possible paths of molecules are traced by mathematical expressions in a computer program; many such computed paths determine the approximate capture fraction of the system. The Monte Carlo technique has been used extensively in determining free molecular conductance fractions,<sup>16,17</sup> i.e., Clausing factors, and may also be used for any closed system where the geometry and sticking fraction are known. One great advantage of the Monte Carlo technique over most others is that nondiffuse reflection may be programmed into the solution. In the adoptions of the Oppenheim and Gebhart methods to free molecular gas flow, it is essential that all reflections be diffuse and therefore that molecules do not have a "memory" after striking a surface.

### 4. Shielded Array Capture Fractions

Cryopumping may be used even in the presence of high temperature surfaces which radiate great amounts of thermal energy. In such situations, the cryopumping surfaces are shielded by cool panels, which panels absorb the majority of the thermal radiation load. For example, the array shown in cross section in Fig. 8 has been used in many space simulation systems. The 20°K plates are separated from each other by one plate width, and are separated from the back-up sheet by at least one plate width. The front shields and the back-up sheet are cooled to between 77°K and 100°K. The back-up sheet is painted with a highly absorptive material (for absorbing thermal radiation). Radiant energy incident on the array will be partly reflected (or absorbed) by the front shields and partly transmitted to the back-up sheet. If the spaces and plates are exactly equal in width, then half of the incident radiation will pass between the shields through the back-up plate, where 10% will be reflected. Half of the reflected radiation will strike the 20°K plates, and half will return to the openings. If these plates are "bright" so that about 90% of the incident radiation is reflected, then the total fraction of incident radiation which is eventually absorbed at the 20°K plates is  $(\frac{1}{2})(0.1)(\frac{1}{2})(0.1) = 0.0025$ , or a quarter of one percent. On the other hand, if the sticking fraction for molecules is unity on the 20°K plate (and zero on the other sheets), the array capture fraction for incident molecules is  $(\frac{1}{2})(1)(\frac{1}{2})(1) = 0.25$  or 25%. The 20°K plates in the array, therefore, capture molecules rather well, but are shielded from the thermal radiation. This simple situation was easily analyzed, but most other geometries are more complicated<sup>18,19</sup> and usually require the use of a network solution, the Gebhart method, or a Monte Carlo analysis as described in the preceding sections.

- 
16. L.L. Levenson, N. Milleron, and D.H. Davis, Trans. Seventh National Symposium on Vacuum Technology (Pergamon Press, 1961), p. 372.
  17. D.W. Jones and C.A. Tsonis, J. Vacuum Sci. Tech. **1**, 19 (1964).
  18. F.C. Hurlbut and P.J. Mansfield, in Advances in Cryogenic Engineering (Plenum Press, 1963), Vol. 8, p. 46.
  19. C.B. Barnes and C.B. Hood, in Advances in Cryogenic Engineering (Plenum Press, 1962), Vol. 7, p. 64.

It is important to note that there is no simple, direct relation between cryoplate area and pumping speed. A small perfectly capturing plate of area  $A$  inside a large chamber will pump gas at the rate  $(\bar{v}/4)A$ , where  $\bar{v}$  is the average molecular speed. This is a direct application of the orifice speed concept, and shows that for this simple situation, speed is directly proportional to pumping area. However, for the shielded array which we analyzed, the speed is  $\frac{1}{4}[(\bar{v}/4)A]$ , where  $A$  is the frontal area of the array. Actually, the cryoplate has two sides so that the cryoplate surface area is as much as the frontal area, but shielding has reduced the plate effectiveness to one fourth. If we were to use wider cryoplates, simultaneously reducing the space between the plates, we would have even more cryoplate area for a given frontal area, but the pumping speed would actually be reduced.

Also, it is important to distinguish between cryoplate sticking fraction and cryopumping array capture fraction. The sticking fraction is the fraction of molecules which will stick to a cold plate upon striking it. The cryopumping array capture fraction is the capture fraction of molecules incident on the frontal area (not plate area) of an array of cryoplates and shields.

## V. CONDENSATE PROPERTIES

The thermal and physical properties of cryogenic condensates can be important. For example, the amount of radiant heat transfer to a cryopanel from surrounding warmer surfaces is dependent on the surface emissivities. When the condensate is sufficiently thick to obscure the base material, emissivity values are those of the condensate<sup>20,21</sup> and obviously are not dependent on the base material. Experiments with deposits of water vapor on 77°K surfaces receiving nominal 300°K radiation shows emissivity values of 0.9 or greater<sup>22</sup>; this is for thickness of 0.001 in. and more. On the other hand, the emissivity of CO<sub>2</sub> deposits is less than that of water vapor deposits, assuming equal thicknesses. The emissivity of many heavy cryodeposits receiving high temperature thermal radiation (composed of wavelengths in the low micron region) is in the range  $\epsilon = 0.4$  to  $\epsilon = 0.6$  although, naturally, there are exceptions. The effect of changing the cryosurface emissivity is to change the heat load to the cryogenic refrigeration system. This is usually of economic importance because the cost of refrigeration increases greatly with decreasing temperatures.

The presence of a thick cryodeposit can also prevent cryopumping at low pressures. Whatever heat load is absorbed at the deposit outer surface must be transferred across the deposit to the cold metal substrata. The temperature change across the deposit thickness is

$$\Delta T = \frac{t}{K} (\dot{Q}/A) ,$$

where  $(\dot{Q}/A)$  = heat load per unit area,

$t$  = deposit thickness,

$K$  = thermal conductivity.

- 
- 20. T.M. Cunningham and R.L. Young, in Advances in Cryogenic Engineering (Plenum Press, 1963), Vol. 8, pp. 85-92; Discussion, p. 92.
  - 21. R.P. Caren, A.S. Gilcrest, and C.A. Zierman, in Advances in Cryogenic Engineering (Plenum Press, 1964), Vol. 9, p. 457.
  - 22. B.C. Moore, Trans. Ninth National Vacuum Symposium (MacMillan Co., 1962), p. 212.



For example, solid nitrogen at 20°K has a thermal conductivity of about 4 mW/cm °K. If the condensate vapor pressure must remain below  $10^{-7}$  torr (a typical value), then the condensate outer surface must not be warmer than 25°K. Under such conditions,

$$(\dot{Q}/A)t = K \Delta T = 0.02 \quad \text{W/cm} \quad .$$

The radiant heat load from a "black" 300°K surface is 0.045 W/cm<sup>2</sup>. If a nominal 20°K cryoplate with nitrogen condensate were in a relatively large chamber surrounded with 300°K radiation surfaces, then the maximum allowed condensate thickness (with 25°K surface temperature) would be

$$\begin{aligned} t &= \frac{0.02}{0.045} \text{ cm} \\ &= 4.3 \text{ mm} \quad . \end{aligned}$$

Therefore, it is not absolutely essential to shield nitrogen pumping cryopanel in a system where none of the surroundings are warmer than 300°K, unless a condensate thickness greater than a few millimeters is present, or unless the total heat load on the refrigeration system is excessive.

The physical properties of cryogenic solids<sup>23</sup> are, in general, not well known. The properties of solid cryodeposits are even less well known. Values given for condensate density, for example, are usually only educated conjectures. For example, cryopumped nitrogen<sup>24</sup> may have a specific gravity near unity, but it may also be much less dense, depending on whether it was formed with an ice-like structure or a snow-like structure. Other properties, such as brittleness, tensile or compressive strength, and hardness (as several examples) are known only to within orders of magnitude.

## VI. CRYOSORPTION AND CRYOTRAPPING

Condensation pumping is the simplest cryogenic vacuum-pumping technique, but other techniques do exist. Cryosorption pumping, for example, offers advantages in refrigeration requirements. If activated charcoal or a zeolite (whether artificial or natural) is cooled to low temperatures, gases may be absorbed, to low pressures, at their normal boiling temperature.<sup>25-28</sup> For example, nitrogen gas may be sorbed to sub-micron pressures by Molecular Sieve 5A cooled to 77°K. Ordinary condensation pumping would require a cryoplate temperature of less than 34°K to achieve the same result. Similarly, helium can be pumped to very low pressures (in the range  $10^{-6}$  to  $10^{-10}$  or lower depending on conditions) at temperatures around 3.5°K to 4°K. As is well known,

- 
23. V.J. Johnson (ed.), National Bureau of Standards Technical Report WADD 60-56 (1960).
  24. R.L. Chuan, University of Southern California Report USCEC 56-201 (1957).
  25. R.A. Hemstreet et al., Arnold Engineering Development Center Report AEDC-TDR-64-100 (1964).
  26. S.A. Stern et al., Arnold Engineering Development Center Report AEDC-TDR-62-200 (1962).
  27. F.T. Turner and M. Feinleib, Trans. Eighth National Vacuum Symposium and Second International Congress on Vacuum Science and Technology (Pergamon Press, 1962), Vol. I, p. 300.
  28. J.E.A. John and W.F. Hardgrove, Am. Inst. Aeron. Astronaut. Publication CP-11 (1964), p. 1.

helium does not solidify under vacuum conditions, and ordinary cryopumping techniques can never be used to pump helium gas. Although cryosorption pumping has much to recommend it, there are numerous disadvantages. Gases which freeze on the sorption surface are obviously not absorbed; and for such gases there is no advantage over ordinary cryopumping. Also, if frozen gas covers the surface, then the blockage will prevent all gases from being absorbed. Examples of troublesome freezing situations are moist air being sorption pumped at 77°K, and nitrogen contaminated hydrogen being sorption pumped at 20°K. Even if the gas being pumped is appropriate for the sorbent and for the sorbent temperature, the rate of pumping is strongly history dependent. If the sorbent pumps long enough, in a closed container, an equilibrium will be established between the "saturated" gas in the cold sorbent and the gas at reduced pressure in the container. Equilibrium exists when the net pumping speed is zero. This equilibrium condition will occur at higher pressures for greater total absorption. It would seem logical that pumping speed should decrease at lower pressures, and should depend in some way on the difference between actual system pressure and the "equilibrium pressure" corresponding to the amount of gas absorbed. Such dependence does indeed occur. However, it is usually masked by another effect, which is: speed is reduced by high rates of absorption. That is, if the mass absorption rate is high, the pumping speed (indicating molecular capture fraction) will continuously decrease; if the throughput is reduced, the molecular capture fraction (and therefore the volumetric speed) will increase as the sorbent material "recovers." The net result of these effects is that pumping speed varies in a complicated way with both the total amount of gas absorbed and rate at which it is being absorbed.

Another technique of cryogenic pumping is cryotrapping. In this technique, rapid cryopumping of one gas results in trapping of a "noncondensable" gas impurity into the condensate. For example, limited amounts of helium can be cryotrapped in the process of cryopumping relatively large amounts of nitrogen at 20°K. The disadvantage of cryotrapping is its gross inefficiency, which prevents pumping of more than trace amounts of gas.

## VII. CRYOGENIC PUMPING, PRO AND CON

The disadvantages of a cryogenic pumping system are primarily:

- a) The cryogenic liquids and/or refrigerators are so expensive that usually only high speed systems can be justified economically.
- b) Cryogenic pumping, whether by condensation or sorption, is quite selective in the gases pumped. The same gas can be cryosorbed at a higher temperature than it is cryopumped, for example, but then the sorption material must be protected from higher freezing point gases freezing on the surface.
- c) Cryopumping is not economically justified at pressures high enough that the heat of condensation is a major part of the heat load.
- d) Cryosorption systems do not maintain constant pumping speeds; the speed varies both with the total amount of gas absorbed and with the mass rate of absorption.

On the other hand, cryogenic pumping has three great advantages over other pumping systems. First, the total area which can be cryogenically cooled is large relative to the pumping orifices of most pumps; consequently, speeds of as high as several millions of liters per second are attained in very large chambers, while speeds of as high as a few tens of thousands of liters per second are attained in chambers containing several square feet of cryopumping sheets. Second, cryogenic pumping is "clean" pumping; a failure of the pumping system will raise the chamber pressure but will not cause

contamination such as that from back diffusion by oil diffusion pumps. Third, the cost of cryopumping in terms of dollars per liter/sec is lower than for any other vacuum pumping system, provided that the system is large enough (and the heat load low enough) that the basic fixed costs (engineering, etc.) are not the major costs. At the present time, simple 20°K cryopumping systems compete economically with other vacuum pumping systems for system speeds of around 50 000 liter/sec or more (free molecular region). Special purpose cryosorption systems (particularly those using liquid nitrogen cooling) can compete even at very low speeds if the total amount of the gas to be absorbed is not too great. Finally, various systems which already contain low temperature liquids or other means of cryogenic refrigeration may sometimes be adapted to cryopumping with a minimum of effort. One example is that of vacuum jacketed, cryogenic tankage in which the cold inner tank surface may be used, with proper engineering, for cryopumping and/or cryosorption.

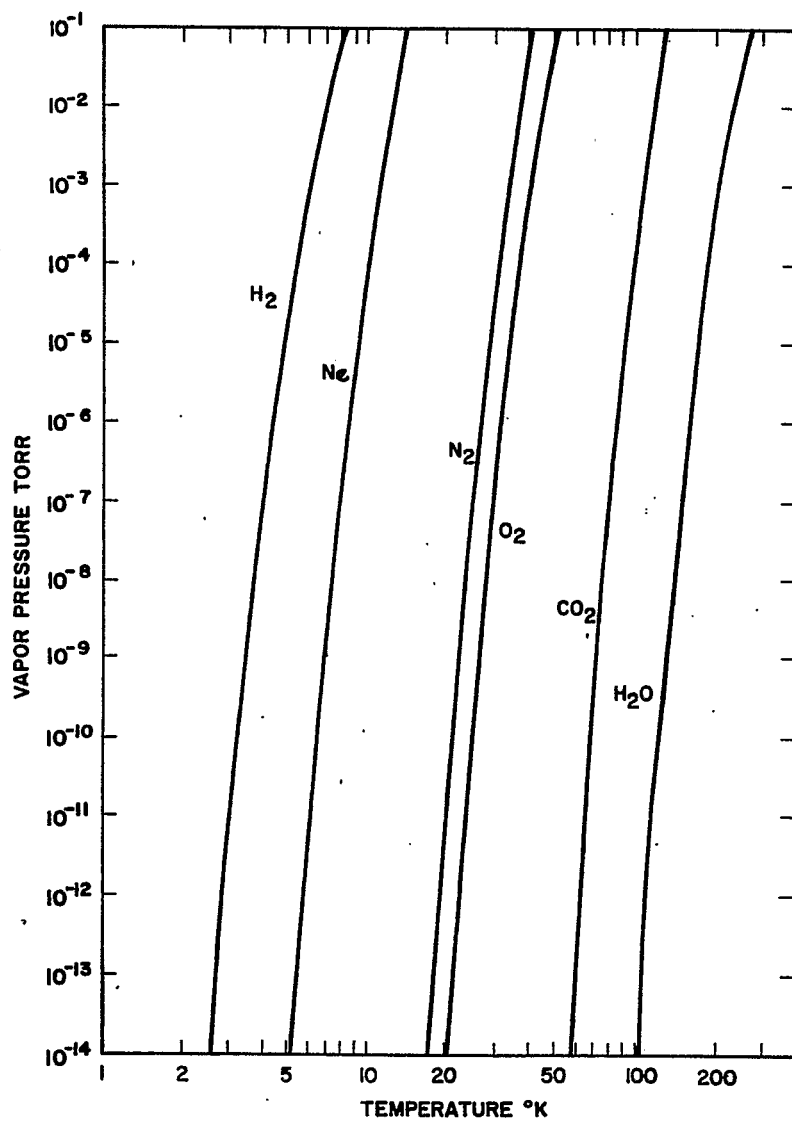


Fig. 1. Vapor pressure vs temperature of condensate.

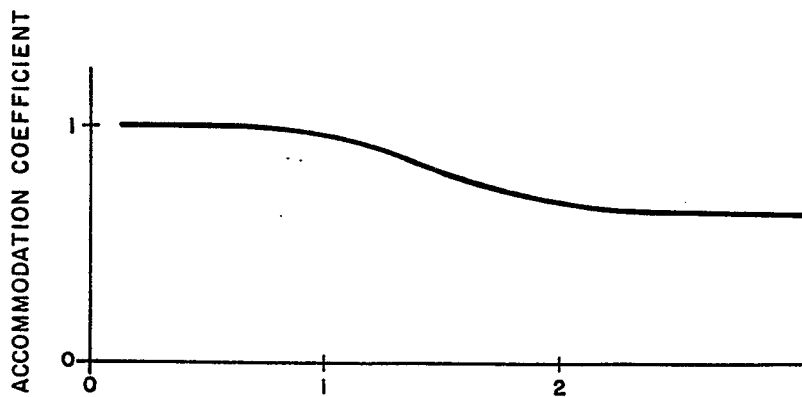


Fig. 2. Reduced temperature  $T/T_c$

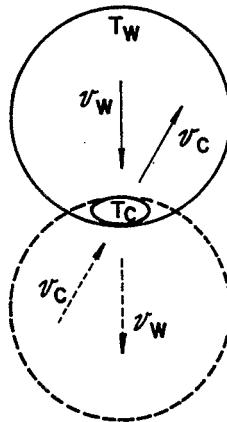


Fig. 3. Schematic of spot cryopumping

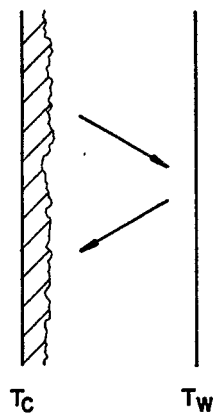


Fig. 4. Parallel plate.

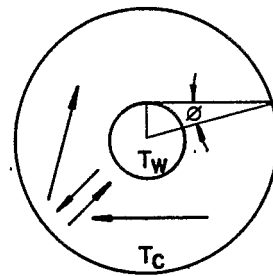


Fig. 5. Spherical cryopumping systems.

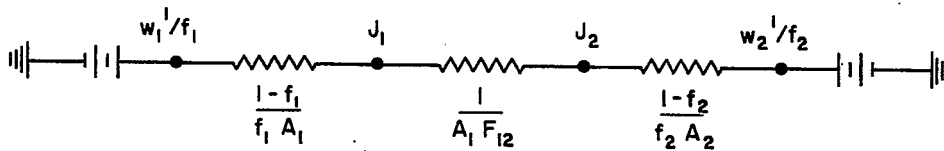


Fig. 6. Two-surface network.

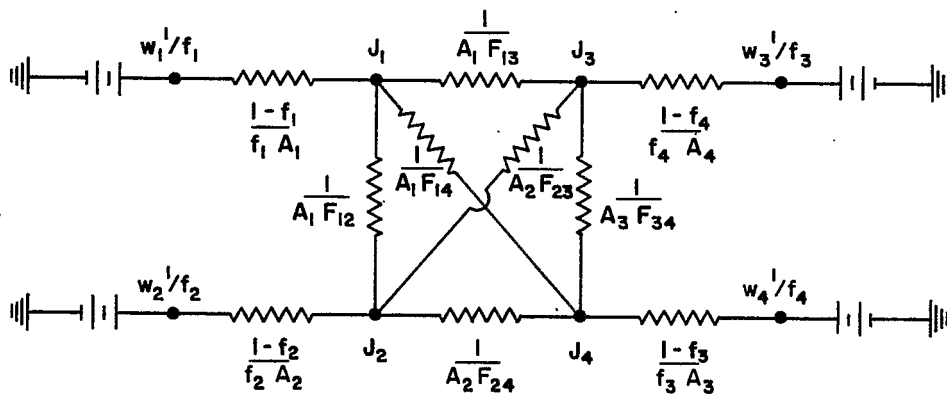


Fig. 7. Four-surface network.

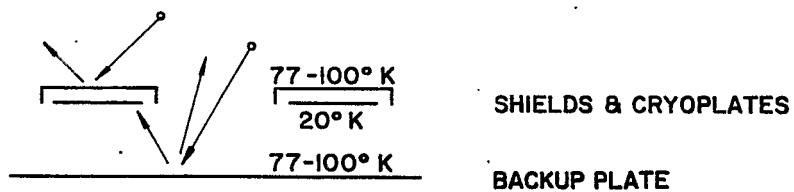


Fig. 8. Shielded cryopumping array.

# REVIEW OF HEAT TRANSFER TO HELIUM I\*

R.V. Smith  
Cryogenics Division  
NBS Institute for Basic Standards  
Boulder, Colorado

## I. INTRODUCTION

The purpose of this paper is to collect, compile, and to make useful recommendations on information with respect to heat transfer to helium I. The collection section of the paper considers all the relevant information with respect to helium heat transfer. This includes not only data on heat transfer coefficients but also appropriate properties data and heat transfer data, from systems using fluids other than helium, that should be useful to this study. The purpose of the compilation section of the paper will be to present these data in a concise manner which is optimally useful for engineering or design studies. The recommendations section of the paper will be concerned both with making recommendations for engineering and design practices on the basis of the findings of the first two sections of the paper and also with recommending future studies which are needed so that optimum design may be achieved.

## II. HELIUM VERSUS CONVENTIONAL FLUID

At the outset, it might be well to consider the differences one may encounter between heat transfer studies with conventional fluids, such as air or water, and with a cryogenic fluid. First, as shown in Fig. 1 for helium, small pressure and temperature ranges enclose a given fluid phase or condition. Thus, for the pressure and temperature ranges required by some cooling systems one may encounter the helium fluid in a number of phases or states. Also, with helium the designer may be unable to avoid the regions around the critical point where the fluid behavior has some undesirable characteristics and where the heat transfer phenomena are not well understood. Therefore, when dealing with liquid helium, one must expect to encounter heat transfer problems which involve the liquid, the supercritical fluid, and also fluid in the two-phase condition. Certainly, the two phase and the supercritical fluid regions are among the more difficult heat transfer regions to study for any fluid. At helium temperatures there are no alternative fluids available.

Secondly, perhaps as great or even greater differences may be noted in comparing transport properties of a conventional and of a cryogenic fluid in which there is some quantum influence for any given phase. Figure 2 from Corruccini<sup>1</sup> shows the general differences in behavior of a conventional and a quantum fluid. In particular, one should note the behavior of the lower pressure liquid where the slope of the conductivity curve is reversed. The behavior might be expected to require, at least, a modification of a correlation developed for conventional liquids.

Even greater evidence of the difficulties of heat transfer studies with helium may be found on examination of Figs. 3, 4, and 5,<sup>2</sup> which show the viscosity and conductivity data available for helium at the present time. In considering helium heat transfer studies, one immediately notices the large regions indicated by the dashed lines where

---

\*This work was carried out at the National Bureau of Standards under the sponsorship of the U.S. Atomic Energy Commission Contract Agreement AT(49-2)-1165.

there are no reliable experimental or theoretical guides and where values for properties must be considered to be crude estimates with a poor degree of reliability. Except for data in the saturated region and in the vicinity of 1 atm, the reliability of the data shown by the solid lines is marginal for use in heat transfer studies. Figures 4a and 5a show the data with constant-pressure parameters for engineering use. Thirdly, the values of the properties are relatively different from those of a conventional fluid. For example, at the normal boiling point the viscosity of water is about 100 times that of helium, the specific heat about equal to that of helium, and the density about eight times as great. Therefore, in considering the conventional heat transfer correlations which involve Reynolds ( $uD\rho/\mu$ ) and Prandtl ( $c_p\mu/k$ ) numbers, one can quickly see that, with helium, quite different combinations of values of these dimensionless groups will be encountered. Since the correlations themselves are not based on rigorous theory but are, indeed, primarily empirical relationships of dimensionless groups, the extensions of these expressions into regions where the fluid properties differ by such a margin cannot be justified without some experimental verification.

In summary, with respect to transport properties, heat transfer studies are more difficult because the properties vary significantly in value from those of conventional fluids, and extrapolation of the correlations are not justified without experimental verification. Further, the transport properties for the liquids behave quite differently from those of conventional fluids except at very high pressures, and the reliability of all of the properties data leaves a great deal to be desired in pursuing heat transfer studies. Finally, heat transfer studies with helium are substantially more difficult than those dealing with conventional fluids because one must deal with the difficult regions for heat transfer with respect to phase changes and pseudo-phase changes. The problem is additionally complicated by marked differences in behavior and in values of the transport properties from those of conventional fluids, and by a poor reliability of data for these transport properties.

### III. DIVISION INTO REGIONS OF PHASE AND TRANSPORT PROPERTY BEHAVIOR

In general, one might say that heat transfer phenomena are influenced by two sets of conditions. One set of conditions has to do with the physical properties and the other with the flow structure. With respect to the flow structure, one is primarily concerned with the behavior in the boundary layer. That is, one would first want to know whether the boundary layer is laminar or turbulent and, if turbulent, the nature of the turbulence. Since the flow structure is very much a function of a specific system, it was decided not to make any divisions in this study with respect to this phenomenon. Therefore, the heat transfer study of helium will be divided into regions with respect to the transport property and phase behavior, and the characteristics of the flow structure will be discussed in these regions where appropriate. The divisions are shown in Fig. 6.

Region 1 and Region 2 differ from each other primarily because in Region 2 phase separation with equilibrium will be distinct whereas in Region 1 phase separation is either not distinct or not possible. The liquid region and the gaseous region are Regions 3 and 4, respectively.

The line of maximum specific heats, which separates Region 1 from Region 4, is quite significant because, on the left of the line, one has what is often called a pseudo-liquid. In this region then, quite close to the saturated liquid line or the line of maximum specific heats, one does experience pressure and density oscillations and other phenomena which are usually associated with the two-phase region.

The data from which these curves were constructed may be seen in Fig. 7a.<sup>3</sup> In Fig. 7a the constant-pressure lines show distinct peaks or humps in the specific heat behavior for pressures reasonably close to the critical pressure. The maximum points



of these peaks constitute the locus of points used to construct the maximum specific heat or "transposed critical" curve. The dashed line in Fig. 6 representing this condition is drawn with shorter dashes as the pressure is increased to indicate a weaker tendency toward critical-point behavior. In drawing the line in this manner it was meant to show that, as the peaking of the specific heat curve became less distinct, the line, while still indicating the maximum specific heats, was recording a phenomenon which was becoming less and less important. Fluid in conditions falling to the left of this maximum specific heat curve is often called a pseudo-liquid, with fluid on the right of this maximum specific heat curve similarly named a pseudo-gas. Further two-phase analogy is seen in Fig. 7b,<sup>4</sup> from which large density changes associated with the crossing of the transposed critical line can be deduced.

Looking at the regions from the point of view of heat transfer knowledge obtained from other fluids, one might make some general statements as to the expected behavior for each of the regions selected. In Region 4, the gas region, one would expect the conventional correlations to be generally effective although some modification may be required because of the properties behavior previously discussed. In Region 3, the liquid region, the properties behavior with respect to that of conventional fluids is quite different; however, the conventional correlations should still form the basis by which one may make reliable heat transfer predictions. Heat transfer phenomena in Region 2, the two-phase region, is not well understood for any fluid. This means that almost any extension of the use of conventional expressions to the helium region should be accompanied by a rather complete experimental verification if any substantial reliability is required in the use of the data. In Region 1 the pseudo-liquid or supercritical region near the line of maximum specific heats, a poor understanding exists, at best, for the heat transfer behavior. Here again, a good deal of experimental data will be required for helium if reliable heat transfer predictions are to be achieved.

#### IV. REGION 1 - SUPERCRITICAL NEAR THE TRANSPOSED CRITICAL LINE

##### IV.1. Region Boundaries

Referring to Fig. 6, one may see that the best defined boundary for Region 1 is that made by the line of maximum specific heats or the transposed critical line. The transport properties of viscosity and conductivity are generally believed to go through a similar peaking phenomenon as shown in Fig. 7a when the critical point is approached for any fluid. Therefore, it would be expected that curves similar to Fig. 7a could be generated, for helium, for the transport properties of conductivity and viscosity. However, no experimental data have been generated to verify this concept.

The left boundary of this region is more difficult to define. It is meant to describe the boundary such that the fluid on its left shows no evidence of maxima singularities in its properties nor associated tendencies toward pressure oscillations. One might conclude, therefore, that the left boundary of this region should fall along a pressure line where the specific heat curve as shown in Fig. 7a no longer exhibits a peaking behavior or the density curve shown in Fig. 7b no longer has a steep slope. For helium, this would appear to be along a constant pressure line in the region of roughly 15 atm.

It might be reasoned that Region 1 should extend to the right of the transposed critical line as well as to the left. This area includes the right half of the property "hump" behavior shown in Fig. 7a. For this paper, it was decided not to include this area in Region 1 for two reasons. First, the slope of the curves describing property behavior are less steep on this side of the maxima. Secondly, almost all heat transfer processes which seem likely with helium involve pressure reduction. Consequently processes will generally run from left to right in Fig. 6. Therefore, the variable property region is unlikely to be approached from the right of the transposed critical line.

The lower boundary of the curve which extends across the liquid-vapor dome is also reasonably difficult to define in a precise or distinct manner. The curve is intended to form a boundary such that fluid which falls above the curve will have properties, particularly density properties, for the liquid and the gas such that a separation of the phases is fairly slow or difficult.

#### IV.2. Behavior of Conventional Fluids in Region 1

In Region 1, the special problem encountered in the heat transfer analysis is that of the fluid property, particularly the transport and density property, behavior in the boundary layer. These variations are shown in Figs. 7a and 7b. If the wall temperature is above the transposed critical temperature for the fluid and the bulk temperature of the fluid below that value, some fluid in the boundary layer must be in Region 1. This means that there will be widely varying values for the properties and, also, situations where some of the properties will go through maximum values within the boundary layer. Most heat transfer correlations assume the use of constant or effective property values. Correlations using this system are known to be ineffective for conditions where there are wide variations in the fluid boundary layers. This would occur either when there are high temperature differences between the wall and the fluid or when there are large property variations with relatively small variations in temperature such as those conditions in Region 1.

##### IV.2.1. Oscillations

Perhaps the most important physical phenomenon which has been associated with this region has been that of pressure and flow oscillations. This behavior has been similar to that of a two-phase fluid. Some authors have chosen to label this as a boiling-like or a pseudo-boiling region. Among these are Dickinson and Welch,<sup>5</sup> Dubrovina and Skripov,<sup>6</sup> and Griffith and Sabersky.<sup>7</sup> One might very easily associate this phenomenon with the presence of a heavy and light species in this region; however, this has not been completely experimentally documented at this time. Some understanding of these oscillations has been obtained by the use of treatments that are modifications of rather conventional mechanics developed to describe specifically the oscillating systems. That is, the fluid system has been treated as one which is analogous to a more conventional oscillating system. Among those papers that have recently reported studies primarily dealing with oscillations in this region are the following: Hendricks et al.<sup>8</sup> for hydrogen, Thurston et al.<sup>9</sup> and Thurston<sup>10,11</sup> for hydrogen, and Cornelius<sup>12</sup> for Freon 114.

##### IV.2.2. Temperature profiles in the boundary layer

Some further insight into the behavior in the fluid in this region may be obtained by consideration of the temperature profiles one might expect to find in the boundary layer. This was investigated by Wood and Smith<sup>13</sup> using carbon dioxide. First of all, one does not expect to find these phenomena occurring except when the transposed critical temperature falls between the temperature of the wall and the temperature of the bulk of the fluid. When these conditions are met, then, of course, the extreme behavior of the fluid properties will be found in the region of the boundary layer. Most papers record that this special behavior indeed does occur only when these temperature conditions are met. Some further insight into the behavior of the temperature profiles in the boundary layer may be found by first considering the expression for turbulent heat transfer which is as follows:

$$q/A = (k + \epsilon_h \rho C_p) \frac{dT}{dy} \quad (1)$$

In the parentheses, the first term describes heat transfer coefficient of the temperature

gradient that would exist if the boundary layer were completely laminar, while the group of terms in the parentheses represents the coefficient of the gradient for the turbulent condition. Remembering that in all flow there is a laminar-like sublayer, one might speculate that, in this region where the conductivity term controls, and where this value will be expected to be enhanced generally, the resistance to heat transfer would be decreased and the temperature profile would be less steep than usual in this region. If the turbulent level or scale of turbulence is assumed to be essentially constant, then the resistance to heat transfer in this region will be inversely proportional to the density times the specific heat. In examining the terms in this region one would generally expect the resistance to decrease. This is because the specific heat would be expected to increase more rapidly than the compensating density decrease near the critical point.

Another possible change in the heat transfer in this region might be brought about by a change in the level of turbulence shown by  $\epsilon_h$ . Such a change may be possible because the large density changes shown in Fig. 7b would create a rather large fluid acceleration. Under such circumstances the turbulent eddies might change such that the level of turbulence would be reduced.

#### IV.2.3. Behavior of the heat transfer coefficient

Then, looking at these two regions of the laminar sublayer and the turbulent core, one finds that the resistance in the net is decreased in the laminar sublayer and in the turbulent core so that the conventional temperature profile would be somewhat flattened for this heat transfer condition. Considering these circumstances alone, one might expect the heat transfer in the net to be enhanced because of these changes in this region. After the bulk temperature reaches the transposed critical temperature, however, the opposite would be expected to be true and one would expect to find a degradation of the heat transfer rate. This is indicated by property behavior and confirmed by experiment.

An example of this behavior of the heat transfer coefficient near the transposed critical is shown in Figs. 8a and 8b as reported by Dubrovina and Skripov.<sup>6</sup> These figures show that the heat transfer coefficient follows the property behavior rather closely, with a substantial enhancement near the transposed critical and considerably lower values on either side. It should be noted, however, that Fig. 8b shows that the enhancement occurs only for very small temperature differences between the wall and the fluid.

#### IV.3. Analytical Work

Finally, one may consider the analytical work which has been reported to describe the heat transfer in this region. One may generally arrange this work into two sections divided by the general method of approach which was used. One set of analyses has concerned itself with an integration through the boundary layer for the case of variable fluid properties. This method involves the use of universal parameters for the flow variables. A review of universal velocity distribution functions may be found in Spalding.<sup>14</sup>

Deissler<sup>15,16</sup> has presented a series of papers employing this method. Figure 9 shows the relationship between the temperature,  $T_x$ , at which properties are evaluated to produce the proper relationship between the Nusselt number and the Reynolds number for supercritical water. These curves are for a Prandtl number of one. Of course, some function of the Prandtl number can be found to bring the curves nearer to a single curve. One may also see that if the proper temperature,  $T_x$ , is chosen the same form of the conventional correlation which employs constant properties may be used.

The other method of analyzing experimental data reported in this region is to seek a satisfactory modifying parameter for the conventional correlations. In almost all the cases, this modifying parameter contains the ratio of the wall to bulk temperature or the ratio of properties which are primarily a function of this temperature ratio, such as kinematic viscosity. Thus,

$$Nu = 0.023 (Re)^{0.8} (Pr)^{0.4} (\text{modifying parameter})$$

where

$$(\text{modifying parameter}) = (T_w/T_b)^{(a)} \text{ or } f(\nu_w/\nu_b)$$

where  $a$  is an exponent determined empirically.

Hendricks et al.<sup>17</sup> show a ratio of the Nusselt number over a Nusselt number calculated by an analogous procedure to a two-phase Nusselt number correlated with the Martinelli and Nelson<sup>18</sup> parameter as

$$\frac{Nu}{Nu_{calc}} = f(x_{tt})$$

Again, the correlations produced by this method have been shown to be superior to those simply using the conventional single-phase heat transfer correlations.

Although the two methods of approach previously discussed appear to be quite different, the resulting correlations are fairly similar in form. Some examples of these predictive correlations and their use follow:

Bringer and Smith<sup>19</sup> Forced Convection  $CO_2$  (no humps)

$$Nu = 0.0266 (Re)_{T_x}^{0.77} (Pr)_{T_x}^{0.55} (\text{Deissler}^{15})$$

Wood and Smith<sup>13</sup> Forced Convection  $CO_2$  - Two resistance concept - Enhanced near transposed critical

Miller et al.<sup>20</sup> and Miller<sup>21</sup> Forced Convection  $H_2$  (no humps)

$$Nu = 0.0204 \left( \frac{\rho_{0.4} u_b D}{\mu_{0.4}} \right)^{0.8} (Pr)_{0.4}^{0.4} (1 + 0.00983 \nu_w/\nu_b)$$

where the subscript indicates the location of the boundary layer temperature for the property evaluation as proposed by Deissler and Pressler<sup>22</sup> and the modifying parameter is of the form proposed by Hess and Kunz.<sup>23</sup>

#### IV.4. Helium I in Region 1

Three papers have reported on systems which involved heat transfer to supercritical helium. These are: Kolm et al.<sup>4</sup>, Klipping and Kutzner,<sup>24</sup> and Brechna.<sup>25</sup> Because the actual boundaries of Region 1 are yet to be determined, it cannot be said whether or not these data actually have fallen in what has been termed Region 1 for this paper. Additionally, all of these papers which do report data are handicapped because reliable property data are lacking in this general region for helium. Kolm et al.<sup>4</sup> reports a system using the supercritical helium I for heat transfer but does not report experimental heat transfer data. Klipping and Kutzner<sup>24</sup> report a study of heat transfer to supercritical helium by free convection. The heated surface was a horizontal cylinder,

2 cm long and 0.4 cm in diameter. Since property data were not available, they reported the data in a form as shown in Fig. 10. Here, one can see that, as Kolm et al.<sup>4</sup> had previously suggested, heat transfer with supercritical helium is competitive with boiling heat transfer from other fluids and also with boiling heat transfer from helium. Brechna<sup>25</sup> shows some results from forced convection heat transfer using superconductor cable material. These results indicate that the helium heat transfer in this region is about 1.7 times that which would be expected using conventional single-phase heat transfer correlations. This work is also discussed for Region 3.

The very limited reported data for heat transfer to supercritical helium I do not allow any conclusions except that more work is certainly needed in this region. For optimum design of any system employing heat transfer to supercritical helium, one first needs the necessary transport property data, and secondly, one needs reliable predictive heat transfer correlations for the fluid. It would appear that these correlations will be modifications of the correlations applied to conventional fluids. Additionally, the boundaries of Region 1 need to be defined rather specifically. This is particularly important with respect to pressure and temperature oscillations. In heat transfer to cool superconductors, stability is much more important than in ordinary heat transfer situations. Therefore, the unstable regions where pressure oscillations might occur with supercritical helium need to be well defined.

## V. REGION 2 - TWO-PHASE, BOILING HEAT TRANSFER REGION

The accepted divisions of boiling studies into that of pool boiling and forced convection boiling will be made.

### V.1. Pool Boiling

#### V.1.1. Boundaries of regions

The boundaries of this region seem reasonably well defined. Referring again to Fig. 6, the left boundary is in the vicinity of a liquid-vapor saturation line. Some further discussion of the point of inception of bubbles will be carried out in the subsequent examination of the boiling curves. The lower limit of the region is in the vicinity of the lambda line. The right hand division of the region is distinct, as the vapor saturation line. Finally, the upper limit of the region has been discussed previously since it forms the boundary of the lower part of Region 1.

#### V.1.2. Behavior of conventional fluids - pool boiling

The general boiling curve exhibited for all fluids may be divided into four sections of study. These are:

- The nucleate boiling curve.
- The maximum nucleate boiling flux.
- The film boiling curve.
- The minimum film boiling flux.

Following the pattern set in Region 1, the behavior of other fluids in these various boiling divisions will be discussed first. This will allow some insight into the peculiarities of helium boiling and allow estimates for helium behavior where data have not been previously obtained or have been obtained in very small quantities without the confirmation of subsequent studies.

### V.1.2.1. Nucleate boiling

Typical nucleate boiling curves may be seen in Figs. 11, 13, and 14. The lower portion of the curve is defined by the inception of the formation of bubbles and on a plot such as in Figs. 13 and 14 where the heat transfer per unit area is plotted against the temperature difference between the bulk of the fluid and its surface, the inception of bubbles causes a sharp rise in the slope of the curves. This slope remains generally constant on such a plot and is proportional to about the third power of the temperature difference. The analytical curves then developed to express the nucleate boiling phenomena will be of the general form

$$q/A = f_{(\text{properties})} (T_w - T_{\text{sat}})^3 \quad (2)$$

It seems reasonably well established at this time that, in many cases, the multiplier of the temperature difference is a function of the heated surface as well as the fluid. This aspect of boiling will be discussed in a later section.

A number of nucleate boiling curves, evaluated for hydrogen at 1 atm, are shown in Fig. 11 along with the regions of reported experimental data. In general, the correlations are dependent upon fluid properties alone, and that will be the basis on which these curves will be discussed. The state of knowledge regarding the boiling phenomena has not advanced to the point where the primary or controlling influences in the process have been established in a manner generally accepted as that one which is correct. Therefore, all of the correlations may be said to owe some of their development to dimensional or similarity concepts. A number of the correlations that have been more recently proposed involve the number of nucleation sites. Since these data are not generally available on an engineering or design basis, these correlations are not yet useful for design use. In a previous report on boiling of cryogenic fluids by Brentari and Smith,<sup>26</sup> the Kutateladze<sup>27</sup> correlation was recommended as one that represented the behavior of hydrogen reasonably well. Obviously, from an examination of Fig. 11, one can see that several other correlations could be said to represent the data with equal reliability. The general requirements for a successful correlation are to express the properties data in such a way that the curve will have a point with the approximately correct horizontal location and then from that point have the slope expressed as about the third power of a temperature difference. Since the Kutateladze correlation is reasonably successful for the cryogenic fluids it will be used as a reference in the subsequent discussion of helium boiling. This expression is

$$\begin{aligned} \frac{h}{k_l} \left( \frac{\sigma}{g \rho_l} \right)^{\frac{1}{2}} = 3.25 (10)^{-4} \left[ \frac{(q/A) (C_p)_l \rho_l}{h_{fg} \rho_v k_l} \left( \frac{\sigma}{g \rho_l} \right)^{\frac{1}{2}} \right]^{0.6} \\ \left[ g \left( \frac{\rho_l}{\mu_l} \right)^2 \left( \frac{\sigma}{g \rho_l} \right)^{3/2} \right]^{0.125} \left[ \frac{P}{(\sigma g \rho_l)^{\frac{1}{2}}} \right]^{0.7} \end{aligned} \quad (3)$$

### V.1.2.2. Maximum nucleate boiling flux

As the temperature of the heated surface is increased during nucleate boiling a point is reached where the nucleate boiling curve essentially becomes discontinuous. Physically, this might be very roughly visualized as the point at which the vapor removal procedure during the boiling becomes such that a wetting cycle during that process is no longer possible. The boiling is then said to enter the film boiling regime where essentially a vapor film is maintained between the heated surface and the bulk of the liquid. This point is almost always associated with a very rapid increase in the temperature of the heated surface. The point is of particular interest to many

design situations because, very often, if this condition is allowed to occur, it will result in the system's failure. This would almost certainly be the case for a helium-cooled superconductor. In separate studies, both Kutateladze<sup>27</sup> and Zuber<sup>28</sup> have produced expressions which are reasonably successful in predicting this maximum flux. This expression is as follows:

$$(q/A)_{\max} = 0.16 h_{fg} \rho_v^{1/2} \left[ \sigma g (\rho_\ell - \rho_v) \right]^{1/4} \quad (4)$$

Again, it will be noted that this expression is a function of a fluid properties alone and not of the relationship between the fluid and the boiling surface conditions or of the surface conditions. Deviations which may occur as a result of the surface conditions will be discussed subsequently in this section. It should be pointed out that although the maximum heat flux can be predicted to a reasonable degree of accuracy, the temperature difference at which this flux will occur is much more difficult to predict. One may estimate this temperature difference by using the value of the maximum heat flux substituted in the nucleate-boiling-curve correlation.

Figure 12 shows the values obtained from (4) compared with experimental data from cryogenic fluids. The agreement is reasonably good except for lower values of the abscissa which correspond to higher values of  $p/p_c$ .

#### V.1.2.3. Film boiling

Typical film boiling curves produced from experimental and analytical data may be seen in Fig. 13. Again, in a previous review by Brentari and Smith,<sup>26</sup> the Breen and Westwater<sup>29</sup> correlation was found to describe the behavior of cryogenic fluids boiling in the film region reasonably well. Therefore, most of the discussion relating analytical to experimental work in this paper will be referred to that correlation. In order to calculate the heat transfer in the film boiling region one must know something of the characteristics of the film or make some assumptions regarding these characteristics. Most of the more recently proposed analyses study the stability of the liquid-vapor interface of this film. This was the approach of Bromley<sup>30</sup> and subsequently of Breen and Westwater<sup>29</sup> who presented the following correlation:

$$h \left( \frac{\sigma}{g(\rho_\ell - \rho_v)} \right)^{1/8} \left[ \frac{\mu_v (T_w - T_{\text{sat}})}{k_v \rho_v (\rho_\ell - \rho_v) g h'_{fg}} \right]^{1/4} = 0.37 + 0.28 \left( \frac{\sigma}{g D^2 (\rho_\ell - \rho_v)} \right)^{1/4}, \quad (5)$$

where

$$h'_{fg} = \frac{[h_{fg} + 0.34 C_{p,\ell} (T_2 - T_\ell)]^2}{h_{fg}}$$

It should be noted that a diameter effect does occur in the correlation, but otherwise surface effects are considered negligible.

#### V.1.2.4. Minimum film boiling flux

In proceeding downward along the film boiling curve, as  $(T_w - T_{\text{sat}})$  is reduced, there will be a point reached when the boiling mechanism will return to nucleate boiling. This point at which that change occurs is known as the minimum film boiling flux. This point is also of considerable interest to designers because it represents the minimum heat flux which would be expected in the temperature range of nucleate and film boiling except, perhaps, for cases of very low temperature differences on the nucleate boiling curve. Several authors, among them Zuber,<sup>28</sup> and Lienhard and Wong,<sup>31</sup> have produced predictive equations for the minimum film boiling. This point is quite difficult

to obtain experimentally, and specific experimental information on this heat flux is reasonably scarce for any fluid. The point, however, can be generally determined for most fluids from a knowledge of the necessary shape of the general boiling curve and from data regarding the nucleate and film boiling regions. The correlation proposed by the two authors previously mentioned has been shown to be reasonably successful for other cryogenic fluids. This correlation for a cylinder with  $D > 1.0$  cm or for a flat plate is:

$$(q/A)_{\min} = 0.16 h_{fg} \rho_v \left[ \frac{g \sigma (\rho_l - \rho_v)}{(\rho_l + \rho_v)^2} \right]^{1/4} \quad (6)$$

#### V.1.2.5. General discussion of the boiling correlations

In many cases, additional factors should be considered before the previously discussed correlations are used to predict the behavior of a system. The correlations are primarily limited because, for wider variations in fluid properties, the correlations have not been thoroughly tested and some tests show poor reliability at high values  $p/p_c$ ; further, they do not account for the geometry or the properties of the solid surface.

##### V.1.2.5.1. Nucleate boiling correlations - pressure effects

Both the expressions for the nucleate boiling flux (3) and the maximum nucleate flux (4) appear to be unreliable at  $p/p_c > 0.6$ . (See Figs. 15 and 16.)

##### V.1.2.5.2. Subcooling

When temperatures of the liquid are below the saturation temperatures, the boiling fluxes are changed from those indicated in the previous discussion where only saturated liquid conditions were considered. Four expressions have been proposed as a correction to the expressions that consider saturated liquids. The correction is simply

$$(q/A)_{\substack{\text{subcooled} \\ \text{max}}} = (q/A)_{\substack{\text{sat} \\ \text{max}}} F_{\text{sub}} \quad (7)$$

These expressions are:

Kutateladze I<sup>27</sup>:

$$F_{\text{sub}} = 1.0 + 0.040 \left( \frac{\rho_l}{\rho_v} \right)^{0.923} \left( \frac{C_p}{h_{fg}} \right) (T_{\text{sat}} - T_{\text{sub}}) \quad (8)$$

Kutateladze II (from Gambill<sup>32</sup>):

$$F_{\text{sub}} = 1.0 + 0.065 \left( \frac{\rho_l}{\rho_v} \right)^{0.800} \left( \frac{C_p}{h_{fg}} \right) (T_{\text{sat}} - T_{\text{sub}}) \quad (9)$$

Ivey and Morris<sup>33</sup> (from Gambill<sup>32</sup>):

$$F_{\text{sub}} = 1.0 + 0.102 \left( \frac{\rho_l}{\rho_v} \right)^{0.750} \left( \frac{C_p}{h_{fg}} \right) (T_{\text{sat}} - T_{\text{sub}}) \quad (10)$$



Zuber et al.<sup>34</sup>:

$$F_{\text{sub}} = 1.0 + 12.326 \left[ \frac{(C_{p,k})_{\ell}^{0.500} (\Delta p)^{0.125}}{h_{fg} \rho_v^{0.750} \sigma^{0.375}} \right] (T_{\text{sat}} - T_{\text{sub}}) \quad (11)$$

There are no experimental data to test these expressions for cryogenic liquids.

#### V.1.2.5.3. Surface conditions

While it is known that surface conditions have a significant effect on the boiling phenomena, the specific influence of any given surface variable is not well understood. Enough data have been acquired, however, to permit a qualitative discussion of the effects of specific surface variations. Considered here are surface history, surface temperature variations as affected by the heated material mass and properties or by the type of heat source, surface roughness, and surface-fluid interface phenomena as influenced by the surface and fluid chemical composition.

##### V.1.2.5.3.1. Surface history

A heating surface immediately after immersion in liquid will produce a higher heat transfer coefficient than one which has been immersed for a reasonable period of time (Kutateladze<sup>27</sup>). This is presumably due to additional nucleation centers provided by factors such as dissolved air and oxidation of the heating surface. Graham et al.<sup>35</sup> reported that for nucleate boiling of hydrogen, boundary layer history has a significant effect on the boiling incipient point. The apparent incipient point for nucleate boiling occurred at a much lower  $\Delta T$  when a boiling run was immediately repeated rather than begun with a fresh supply of hydrogen surrounding the heating surface; the two curves then join at higher heat fluxes. The authors speculate that some residue of the thermal layer remained to change the incipient point for the succeeding test.

Vliet and Leppert<sup>36</sup> studied the effect of aging or boiling for a period of time at about half peak flux. They found that with water flowing over a stainless-steel tube, aging of about 90 min was necessary before reproducible peak fluxes could be obtained. Aging for about one-third that time produced peak fluxes only slightly greater than half the fluxes produced using the longer aging procedure.

##### V.1.2.5.3.2. Surface temperature variations

It is possible that surface temperature differences can occur which may be attributed to properties of the heater surface and not entirely to the fluid boiling phenomena. Heaters with a small mass per unit of heater surface such as very thin materials may produce temperature variations and, subsequently, a lower peak flux. Vliet and Leppert,<sup>36</sup> however, reported that there were no surface effects down to a thickness of 0.006 in. for a cylinder with water cross-flow.

The source of energy for the heater may also influence surface temperature variations. Kutateladze<sup>27</sup> reports that electrically heated surfaces have slightly different heat transfer characteristics than those heated by vapor condensation, probably because condensation droplets cause surface temperature differences.

Of course, the boiling phenomena also produce temperature variations at the surface, and these are reported, for example, by Kutateladze,<sup>27</sup> Hendricks and Sharp,<sup>37</sup> and Moore and Mesler.<sup>38</sup> Sharp<sup>39</sup> studied the microlayer film at the base of nucleate bubbles and found that the flux from this microlayer appeared to vary with  $k/\alpha$  for

the surface material. Cummings and Smith,<sup>40</sup> and Bowman,<sup>41</sup> have shown some boiling variations which are a function of the properties of the substrate material, and in turn, may be attributed to changes in these properties during temperature fluctuations.

#### V.1.2.5.3.3. Surface roughness

Rougher surfaces generally produce higher fluxes for the same  $\Delta T$ . Mikhail<sup>42</sup> reported work with oxygen using nickel surfaces with different roughness values, and his data were similar to others who investigated higher temperature fluids. Rougher surfaces cause incipient nucleate boiling to occur at a lower  $\Delta T$ , and then the  $h$  vs  $\Delta T$  curves rise abruptly from that point. Thus the rougher surfaces produce markedly higher coefficients for the same  $\Delta T$  - in Mikhail's work as high as a factor of 4. Lyon,<sup>43</sup> working with cryogenic and other liquids, indicates, however, that although the nucleate boiling flux curve is changed by roughness, the peak flux does not change. Surface roughness would be expected to show a much smaller effect in the film boiling region, and work such as that of Class et al.<sup>44</sup> indicates essentially no effect of roughness for film boiling.

Tuck,<sup>45</sup> in experimental work with hydrogen, found that  $\Delta T$  for inception was less than  $0.1^\circ\text{K}$  for a rough surface but could be as great as  $3^\circ\text{K}$  for a surface finished to  $1.25 \mu\text{in. rms}$ . The Tuck experiments were at zero gravity condition; however, the results would be expected to be applicable generally under other gravitational fields, although at or near zero gravity the inception point seems to be time dependent and that time a function of the gravitational field.

#### V.1.2.5.3.4. Surface chemistry

The surface chemical effect is often difficult to separate from other surface effects such as roughness. Wetting characteristics would appear to be a major influence. Cryogenic fluids will wet almost all surfaces except those with a very low surface energy; this is illustrated, for example, in a hydrogen study by Good and Ferry<sup>46</sup> and perhaps further substantiated by the reasonably effective use of a single wetting coefficient in the Rohsenow<sup>47</sup> correlation for cryogenic fluids. Lyon<sup>43</sup> studied nucleate boiling with oxygen and nitrogen using clean copper and gold surfaces and surfaces with various chemical films. He found that the different surfaces produced somewhat different nucleate boiling curves and differences as much as 25% in the peak flux.

Young and Hummel<sup>48</sup> have shown that higher coefficients in the lower region of the nucleate boiling regime are made possible by providing poorly wetted spots on the metal surface. Sharp<sup>39</sup> has studied the microlayer at the base of bubbles and has found that nonwetting surfaces tend to destabilize the layer. Costello et al.<sup>49</sup> found that the burnout heat flux was increased by a factor of 2.3 if tap water rather than distilled water was used.

#### V.1.2.5.4. Geometry

The correlations essentially describe systems of simple geometry with surfaces which are vertical or facing upward. The data from the surfaces facing downward and of vertical channels are shown in Figs. 18 and 19 which will be discussed later. Other variations with geometry have been reported; for example, Costello et al.<sup>49</sup> have reported that for pool boiling burnout heater size is quite significant. They found that 0.067 in. diameter semi-cylinders burned out at fluxes 2.7 times greater than for flat plate heaters with no liquid in-flow from the sides. This suggested to the authors that such difference may be a result of different convective effects for the various heated surfaces. They show that the convective component may be approximately one-half the total flux in some cases.

### V.1.3. Pool boiling - helium I

#### V.1.3.1. Comparison of data with results from correlations

Figure 13 shows experimental and analytical pool boiling data for helium. The figure indicates that agreement between the predictive correlations and the experimental work is approximately as good as that for other fluids. In order to show most of the reported experimental work, some of the data have been corrected by means of the property variations indicated by (3) to the case for  $\frac{1}{2}$  atm pressure. These data are for simple geometries with surfaces facing upward or vertical.

Figure 16 shows the comparison of the results of the maximum nucleate flux comparisons. Here, as with the other cryogenic fluids, the agreement is good except for higher values of  $p/p_c$ . It would appear that a safe upper limit for the correlation would be  $p/p_c = 0.6$ .

#### V.1.3.2. Pool boiling - additional factors to consider with the correlations

##### V.1.3.2.1. Hysteresis

Figure 14 shows the hysteresis effect as reported by three investigators. The difference in the curves with increasing flux and decreasing flux is generally regarded as being associated with the point of initial bubble inception and its requirements for higher temperatures than that for subsequent bubbles. Also, as the temperature differences and the heat fluxes are increased the behavior of the curve must indicate the activation of new boiling sites.

Bankoff<sup>50</sup> has shown that, in general, the theoretical superheat requirements to form new vapor nuclei are considerably higher than those observed. Therefore, one might conclude that nucleation usually occurs at nonwetted sites on the surface, usually in cavities. This hypothesis could be used to explain the additional hysteresis for helium because at helium temperatures all gases which might serve to create nonwetted sites will be condensed, except helium itself.

##### V.1.3.2.2. Geometry effects

Figure 17 shows data from two sources for surfaces facing downward. In both cases the data appear to follow the same general nucleate boiling behavior except that the maximum flux is reduced very substantially.

The work of Sydoriak and Roberts<sup>51</sup> for narrow channels shows that for this special geometry, the helium boiling problem must be handled quite differently. They developed an expression for the maximum flux which, for this case, is limited by the outflow rate from the channel. Figure 19 shows the predicted results from this theory compared with experimental data from Wilson.<sup>52</sup> The agreement appears reasonably good, particularly for a problem as complex as this one.

Figure 13 indicates that the film boiling correlation (5) does not properly account for boiling behavior with small wire sizes.

##### V.1.3.2.3. Substrate effects

Figure 20 shows the results of Cummings and Smith<sup>40</sup> which demonstrate significant effects traceable to the behavior of the properties of the substrate. These properties are conductivity, density, and specific heat. The authors show that these properties, together with a frequency term (representing boiling bubble frequency), can be made to

form a function that will correlate boiling data from different substrates. This behavior could well be most significant for helium because the properties will tend to vary more with small temperature changes (such as those encountered in boiling) at helium temperatures.

Bowman<sup>41</sup> has shown that radiation has a significant influence on the pool boiling of helium by decreasing the thermal conductivity of the substrate and by inducing residual radioactivity in the substrate.

#### V.1.3.3. Additional factors to consider with correlations - significant but apparently no different for helium than for other fluids

##### V.1.3.3.1. Pressure

Figure 15 shows the nucleate boiling data of Lyon<sup>53</sup> taken at different pressures. The lower pressure data appear to behave essentially as predicted, but the higher pressure data are quite different from a reasonable extrapolation of lower pressure data or from the apparent prediction using (3). It may be that the property values used in (3) near the critical would be quite unreliable, but even with a reasonable allowance for that, one must conclude that the behavior indicates an approach quite different from (3) should be taken to predict the higher pressure behavior. As in the case of the maximum nucleate flux data (Fig. 12), it would appear that the correlations are only reliable to  $p/p_c = 0.6$ .

##### V.1.3.3.2. Surface roughness and chemistry

There are no reported studies which have considered surface chemistry effects. As previously discussed, Lyon<sup>43</sup> found significant effects for other cryogenic fluids.

Figure 17 shows surface roughness effects reported by Boissin et al.,<sup>54</sup> and Cummings and Smith.<sup>40</sup> The work of Boissin et al.<sup>54</sup> indicates that only polished surfaces are markedly different for the nucleate boiling curve. Cummings and Smith<sup>40</sup> show that ice crystals did not influence the nucleate boiling curve for their surface. They did, however, very significantly influence the curve in the region of transition from nucleate to film boiling.

##### V.1.3.3.3. Subcooling

There are no data to show the influence of subcooling (fluid temperatures below saturation) on helium boiling. Some indication of the possible effect can be obtained by evaluating (8)-(11) previously discussed. These evaluations are shown in Fig. 21.

#### V.2. Forced Convection Boiling

##### V.2.1. Behavior of conventional fluids

The general treatment of forced convection boiling is simply to extend the method used in the single-phase case. The systems employed may be divided into two general categories. In the first category a two-phase Nusselt number is calculated from a Dittus-Boelter<sup>55</sup> form of the equation

$$(\text{Nu}_{\text{calc}})_{\text{tp}} = 0.023 (\text{Re})_{\text{tp}}^{0.8} (\text{Pr})^{0.4}$$

In this equation the two-phase aspect is introduced by some sort of a two-phase modification of the density term in the Reynolds number. This Nusselt number does not yield

the proper film coefficient to describe the forced convection boiling process, however. Instead, it is used as the denominator of a Nusselt number ratio with the numerator representing the experimental or in the case of a predictive use of the correlation, the predictive Nusselt number. In this system the Nusselt number ratio is assumed to be a function of some correlating parameter. The most common correlating parameter employed is the Martinelli-Nelson parameter  $\chi_{tt}$  which was originally proposed to correlate a similar pressure drop, or essentially a momentum transport process:

$$\text{Nu}/(\text{Nu}_{\text{calc}})_{\text{tp}} = f(\chi_{tt})$$

Hendricks et al.<sup>17</sup> have reported a very thorough study employing this type of correlation using hydrogen as the working fluid. Figure 22<sup>56</sup> shows that the correlation is relatively successful for hydrogen.

The second analytical method, which is employed to describe forced convection boiling processes, is usually called the superposition method. Here, the concepts are very simple. The heat flux which would be indicated for the pool boiling case is simply added to the heat flux which would be indicated by a conventional correlation for the single phase fluid:

$$(q/A)_{\text{Forced conv. boiling}} = (q/A)_{\text{Pool boiling}} + (q/A)_{\text{Forced conv. single phase}}$$

For the case of nucleate boiling the single-phase fluid would be assumed to be a liquid, and for the film boiling case the single-phase fluid would generally be assumed to be a gas. Although this method is extremely simple and makes no provision at all for the interplay between the two energy transport processes, it has been shown to be reasonably successful for a number of fluids including hydrogen. Giarratano and Smith<sup>57</sup> have reported a comparative study of these methods using previously reported data for hydrogen heat transfer.

#### V.2.2. Forced convection boiling with helium I

There has only been one paper on forced convection boiling with helium. This is by de La Harpe et al.<sup>58</sup> who employed a long coiled tube. The authors used the method of a Nusselt number ratio correlated with the Martinelli parameter for their data with higher quality, higher vapor content, runs. Their results are shown in Fig. 23. This method produced an empirical line which correlated the data to within  $\pm 20\%$ . For the low quality region (where the quality was approximately 0.2 and less), the method of superposition was employed as the Nusselt number ratio appeared to be insensitive to changes in the Martinelli parameter for the low quality case. When the superposition method for the lower quality region was used, the data were correlated within  $\pm 20\%$  for the range of experimental data produced. This dividing point between the apparent wet-wall and dry-wall regions is at a considerably higher quality than that which would be expected for other fluids. This is because the density ratio (of liquid to gas) at the normal boiling point for helium is much lower than that for other fluids. For example, for hydrogen this ratio is about 53 and for helium about 7.5. Wright and Walters<sup>59</sup> report wet-wall boiling data for a similar case of forced convection with hydrogen showing a maximum quality of about 0.05. In a separate, but related study, the authors report that although the Martinelli parameter was successful in correlating heat transfer data, it was not at all successful in correlating the pressure drop data which they obtained from this long helical tube. Instead, they found that the use of a homogeneous model described the pressure drop data reasonably well.

## VI. HELIUM I, REGION 3

Since Region 3 is devoted entirely to the single-phase fluid where a good deal of heat transfer work has been done for other fluids, one might expect less difficulty in extending the conventional correlations to the helium case. It may be, however, that the extreme property differences for helium and the property behavior for liquid helium, particularly, would make the helium behavior significantly different from the conventional fluids. For conventional fluids the Dittus-Boelter<sup>55</sup> correlation to produce the Nusselt number as

$$Nu = 0.023 (Re)^{0.8} (Pr)^{0.4} ,$$

is generally satisfactory. The only experimental work for helium reported in Region 3 is that of Dorey.<sup>60</sup> Dorey employed a test section of a small flat plate and investigated the cases of both free and forced convection. In cases of both free and forced convection, Dorey's experimental data were obtained at Reynolds numbers which were in the general transition region between laminar and turbulent flow. He compared his data with respect to both the laminar and turbulent heat transfer predictions of the conventional correlations. For the free convection case, a difference between the analytical expression for the two flow regimes is expressed in the power (a) to which the product of the Grashof and Prandtl number is raised in the following expression:

$$Nu = (\text{const}) (Gr \cdot Pr)^{(a)} .$$

Although the constant coefficient in the expression varies between the two flow regimes, the exponent (a) is a better indicator of the flow regime. In this transition region for free convection, Dorey found that the exponent conventionally used for the turbulent case more nearly described his experimental data. He recommended the following expression for the heat transfer coefficient for free convection for helium in the Reynolds number range which is transition between laminar and turbulent flow:

$$h = 0.16 \left( \frac{P_{\ell}^2 k_{\ell} g \beta C_p (T_w - T_b)}{\mu_{\ell}} \right)^{1/3} . \quad (12)$$

For forced convection, Dorey investigated two equations for laminar and turbulent flow. These expressions were recommended by Jacob<sup>61</sup> for flat-plate flow rather than the more conventional case of flow inside tubes considered previously. These two expressions are

$$Nu = 0.664 Re^{0.5} Pr^{0.5} \text{ (laminar)} \quad (13)$$

$$Nu = 0.36 Re^{0.8} Pr \text{ (turbulent)} . \quad (14)$$

Again as shown in Fig. 24, Dorey's data in a transition region between the two flow modes fell between predictions of the analytical exponents of the two modes.

Brechna<sup>25</sup> has reported some forced convection, liquid helium data discussed previously in Region 1. He finds that the coefficient in the conventional turbulent, forced convection equation is increased by a factor of about 1.7 for the case of helium heat transfer. It is not clear at this time whether the data of Brechna were obtained for Region 1 or Region 3; however, it is presumed that some of these data were obtained in Region 3.

## VII. REGION 4

A full discussion of helium heat transfer in Region 4 is not considered in this paper. There are two reasons for this. First, helium in this region would not be expected to behave differently than another gas. Some small modifications might be required by the rather significant properties differences, particularly that of viscosity; however, the author is not aware of any investigators who have reported the need for such modifications. Most of the helium gas studies, however, have been carried out at considerably higher temperature than those shown or considered in this paper. The second reason for omission of the Region 4 is that for the most part the temperatures in Region 4 are presumed to be too high for cooling superconductors.

## VIII. SUMMARY AND RECOMMENDATIONS

### VIII.1. Region 1 - Supercritical Near Transposed Critical

- a) This region should be avoided, if at all possible, if oscillations in pressure and temperature are undesirable.
- b) The region boundary appears to be generally defined by the transposed critical line and the minimum constant pressure line which does not exhibit the "hump" or rapidly changing property behavior similar to that at the critical point. This pressure is at about 15 atm.
- c) The conventional heat transfer correlation using constant properties,

$$Nu = 0.023 (Re)^{0.8} (Pr)^{0.4}, \quad (15)$$

can probably be used as a general guide to predict the heat flux for forced convection, turbulent heat transfer inside conduits. Enhancement is theoretically possible but, since heat transfer behavior is unknown and property values are uncertain, one should not expect to obtain enhancement unless a development program is undertaken. Degradation is perhaps more likely for systems in this region.

- d) Heat transfer and property data are urgently needed in this region. First studies should be to:
  - i) Define the region boundaries.
  - ii) Establish the magnitude and nature of the oscillations in the region.
  - iii) Investigate arrangements to minimize the oscillations.
  - iv) Establish a heat transfer predictive system better than a constant property correlation.

### VIII.2. Region 2 - Boiling, Two Phase

#### VIII.2.1. Pool boiling

- a) For pool boiling, it would appear that the correlations for conventional fluids can be used with approximately the same degree of reliability as for other cryogenic liquids.

Nucleate - Kutateladze,<sup>27</sup> Eq. (3).

Maximum nucleate - Kutateladze,<sup>27</sup> Zuber et al.,<sup>34</sup> Eq. (4).

Film - Breen and Westwater,<sup>29</sup> Eq. (5).

Minimum film - Lienhard and Wong,<sup>31</sup> Eq. (6).

- b) These correlations do not consider some of the significant variables and should be used with caution. Among these variables which seem to have a more pronounced influence with helium are:

- i) Hysteresis - Lyon,<sup>53</sup> Cummings and Smith,<sup>40</sup> Thibault et al.<sup>62</sup>
- ii) Geometry effects - Lyon,<sup>53</sup> Sydoriak and Roberts.<sup>51</sup>
- iii) Substrate effects - Cummings and Smith.<sup>40</sup>

- c) Other variables, not accounted for in the correlations, but which have been shown to have a significant influence with other cryogenic liquids are:

- i) Surface roughness - Boissin et al.,<sup>54</sup> Cummings and Smith.<sup>40</sup>
- ii) Surface chemistry - Lyon.<sup>43</sup>
- iii) Pressure effects for the nucleate boiling curve are reasonably well accounted for by the nucleate correlations for

$$p/p_{\text{crit}} < 0.6.$$

For pressures above this value the correlations do not appear to be reliable.

- iv) Subcooling effects are unknown (see Fig. 21 for estimates).

#### VIII.2.2. Forced convection boiling

For forced convection boiling, the single reported work, de La Harpe et al.<sup>58</sup> indicated behavior similar to conventional fluids. The nucleate boiling or wetted surface region appears to be extended in quality.

#### VIII.2.3. Recommendations for further work

Further work in this region appears to be less critically needed than in the other areas. Perhaps the regions of surface and substrate effects, geometry effects, pressure effects and forced convection should have first priority for future investigations.

#### VIII.3. Regions 3 and 4

- a) The very limited data of Brechna,<sup>25</sup> and Dorey,<sup>60</sup> indicate the use of conventional correlations, Eqs. (12), (13), (14), and (15) may be conservative.
- b) Fluid property data would indicate that the conventional correlations can be used with reasonable confidence except, perhaps, for liquid helium at lower pressures where the transport properties have the opposite slope of that for other liquids.
- c) Some further work is rather urgently needed, however, to establish more positively whether or not conventional correlations may be used without modification.



## NOMENCLATURE

### Latin Letters

$a$	= Empirically determined exponent.
$C_p$	= Specific heat capacity at constant pressure.
$D$	= Diameter.
$F_{sub}$	= Multiplying factor for peak heat flux due to subcooling $(q/A)_{sub} = (q/A)_{sat} F_{sub}$ .
$h$	= Convective heat transfer coefficient.
$h'_{fg}$	= "Effective" latent heat vaporization, defined by Eq. (5).
$h_{fg}$	= Latent heat of vaporization at saturation.
$g$	= Acceleration of gravity.
$Gr$	= Grashof's number, $\rho g \beta (T_w - T_b) y^3 / \mu^2$ , dimensionless.
$k$	= Thermal conductivity.
$Nu$	= Nusselt number, $(hD/k)$
$Nu_{calc}$	= Calculated Nusselt number, dimensionless.
$P$	= Pressure.
$Pr$	= Prandtl number, $(c\mu/k)$ .
$q/A$	= Rate of heat transfer per unit area.
$Re$	= Reynolds number, $(uD\rho/\mu)$ .
$T$	= Temperature.
$u$	= Average fluid velocity.
$x$	= Quality, (mass vapor/mass mixture), dimensionless.
$y$	= Length dimension.

### Greek Letters

$\beta$	= Thermal coefficient of volumetric expansion.
$\epsilon_h$	= Eddy diffusivity of energy.
$\mu$	= Newtonian coefficient of viscosity.
$\rho$	= Density
$\nu$	= Kinematic viscosity.
$\sigma$	= Surface tension between the liquid and its own vapor.
$x_{tt}$	= Martinelli parameter, dimensionless.

### Subscripts

$b$	= Indicates bulk property.
$l$	= Subscripted liquid property.
$w$	= Wall or solid surface conditions.
$x$	= Proportional location in thermal boundary layer to establish temperature for property evaluation.

sat = Saturated conditions.  
v = Vapor or gas condition.  
c = Critical condition.  
tp = Two phase.

#### REFERENCES

1. R.J. Corruccini, in Liquid Hydrogen (Inst. Intern. Froid, Paris, 1965), p. 65.
2. H.J.M. Hanley and G.E. Childs, to be published.
3. O.V. Lounasmaa, D. Phil. thesis, Oxford University (1958).
4. H.H. Kolm, M.J. Leupold, and R.D. Hay, in Advances in Cryogenic Engineering (Plenum Press, 1966), Vol. 11, p. 530.
5. N.L. Dickinson and C.P. Welch, Trans. ASME 80, 746 (1958).
6. E.N. Dubrovina and V.P. Skripov, in Proc. 2nd All-Soviet Union Conference on Heat and Mass Transfer, Vol. I (translation by Rand Corp., R-451-PR) (1966).
7. J.D. Griffith and R.H. Sabersky, Am. Rocket Soc. Journal, 289 (1960).
8. R.C. Hendricks, R.W. Graham, Y.Y. Hsu, and R. Friedman, National Aeronautics and Space Administration Technical Note NASA TN D-3095 (1966).
9. R.S. Thurston, J.D. Rogers, and V.J. Skoglund, in Advances in Cryogenic Engineering (Plenum Press, 1966), Vol. 12, p. 438.
10. R.S. Thurston, in Advances in Cryogenic Engineering (Plenum Press, 1965), Vol. 10, p. 305.
11. R.S. Thurston, Los Alamos Scientific Laboratory Report LA-3616 (1966).
12. A.J. Cornelius, Argonne National Laboratory Report ANL-7032 (1965).
13. R.D. Wood and J.M. Smith, A. I. Ch. E. J. 10, 180 (1964).
14. D.B. Spalding, J. Appl. Mech. 28, 455 (1961).
15. R.G. Deissler, Trans. ASME 76, 73 (1954).
16. R.G. Deissler, J. Heat Transfer, Trans. ASME 82C, 160 (1960).
17. R.C. Hendricks, R.W. Graham, Y.Y. Hsu, and A.A. Medeiros, Am. Rocket Soc. Journal 244 (1962).
18. R.C. Martinelli and D.B. Nelson, Trans. ASME 70, 695 (1948).
19. R.P. Bringer and J.M. Smith, A. I. Ch. E. J. 3, 49 (1957).
20. W.S. Miller, J.D. Seader, and D.M. Trebes, in Pure and Applied Cryogenics (Pergamon Press, 1966), Vol. 4, p. 173.
21. W.S. Miller, presented at Am. Inst. Astronaut. Aeron. 2nd Propulsion Joint Specialist Conference, Colorado Springs, Colo., 1966, Paper No. 66-580.
22. R.G. Deissler and A.F. Presler, in International Developments in Heat Transfer (ASME, 1963), p. 579.

23. H.L. Hess and H.R. Kunz, J. Heat Transfer, Trans. ASME 87C, 41 (1965).
24. G. Klipping and K. Kutzner, in Pure and Applied Cryogenics (Pergamon Press, 1967), Vol. 6, p. 97.
25. H. Brechna, Stanford Linear Accelerator Center Report SLAC-PUB-274 (1967).
26. E.G. Brentari and R.V. Smith, in International Advances in Cryogenic Engineering (Plenum Press, 1965), Vol. 10, p. 325.
27. S.S. Kutateladze, State Sci. and Tech. Pub. of Lit. on Machinery, Moscow (Atomic Energy Commission Translation 3770, Tech. Info. Service, Oak Ridge, Tennessee).
28. N. Zuber, U.S. Atomic Energy Commission Report AECU-4439 (AEC, Oak Ridge, Tennessee, 1959).
29. B.P. Breen and J.W. Westwater, Chem. Eng. Progr. 58, No. 7, 67 (1962).
30. L.A. Bromley, Chem. Eng. Progr. 46, No. 5, 221 (1950).
31. J.H. Lienhard and P.T.Y. Wong, J. Heat Transfer, Trans. ASME 86C, 220 (1964).
32. W.R. Gambill, Brit. Chem. Engr. 8, No. 2, 93 (1963).
33. H.J. Ivey and D.J. Morris, AEEW-R137 (1962).
34. N. Zuber, M. Tribus, and J.W. Westwater, in International Developments in Heat Transfer (ASME, 1963), p. 230.
35. R.W. Graham, R.C. Hendricks, and R.C. Ehlers, in International Advances in Cryogenic Engineering (Plenum Press, 1965), Vol. 10, p. 342. Also: National Aeronautics and Space Administration Technical Note NASA TN D-1883 (1965).
36. G.C. Vliet and G. Leppert, J. Heat Transfer, Trans. ASME 86C, 59 (1964).
37. R.C. Hendricks and R.R. Sharp, National Aeronautics and Space Administration Technical Note NASA TN D-3095 (1964).
38. F.D. Moore and R.B. Mesler, A. I. Ch. E. J. 7, 620 (1961).
39. R.R. Sharp, National Aeronautics and Space Administration Technical Note NASA TN D-1997 (1964).
40. R.D. Cummings and J.L. Smith, Jr., in Pure and Applied Cryogenics (Pergamon Press, 1967), p. 85.
41. H.F. Bowman, Ph.D. thesis, Massachusetts Institute of Technology (1968).
42. N.R. Mikhail, Ph.D. thesis, Imperial College of Science and Technology, London (1952).
43. D.N. Lyon, Intern. J. Heat and Mass Transfer 7, No. 10, 1097 (1964).
44. C.R. Class, J.R. DeHaan, M. Piccone, and R.B. Cost, in Advances in Cryogenic Engineering (Plenum Press, 1960), Vol. 5, p. 254.
45. G. Tuck, General Dynamics/Astronautics Report No. 55D, 859 (1962).
46. R.J. Good and G.V. Ferry, in Advances in Cryogenic Engineering (Plenum Press, 1963), Vol. 8, p. 306.
47. W.M. Rohsenow, Trans. ASME 74, 969 (1952).
48. R.K. Young and R.L. Hummel, presented at A. I. Ch. E. Meeting, Boston, Mass. (1964).
49. C.P. Costello, C.O. Buck, and C.C. Nichols, Heat Transfer Conference, Cleveland, Ohio (A. I. Ch. E., 1964).
50. S.G. Bankoff, A. I. Ch. E. J. 4, 24 (1958).

51. S.G. Sydoriak and T.R. Roberts, in Pure and Applied Cryogenics (Pergamon Press, 1966), Vol. 6, p. 115.
52. M.N. Wilson, *ibid.*, p. 109.
53. D.N. Lyon, in International Advances in Cryogenic Engineering (Plenum Press, 1965), Vol. 10, p. 371.
54. J.C. Boissin, J.J. Thibault, J. Roussel, and E. Faddi, in Advances in Cryogenic Engineering (Plenum Press, 1968), Vol. 13, p. 607.
55. F.W. Dittus and L.M.K. Boelter, Univ. Calif. (Berkeley) Publ. Eng. 2, 443 (1930).
56. E.G. Brentari, P.J. Giarratano, and R.V. Smith, National Bureau of Standards Technical Note No. 317 (1965).
57. P.J. Giarratano and R.V. Smith, in Advances in Cryogenic Engineering (Plenum Press, 1966), Vol. 11, p. 492.
58. A. de La Harpe, S. Lehongre, J. Mallard, and C. Johannes, presented at Cryogenic Engineering Conference, Cleveland, Ohio, 1968.
59. C.C. Wright and H.H. Walters, Wright Air Development Center Technical Report WADC 59-423 (1959). Also: H.H. Walters, in Advances in Cryogenic Engineering (Plenum Press, 1961), Vol. 6, p. 509.
60. A.P. Dorey, Cryogenics 5, 146 (1965).
61. M. Jacob, Heat Transfer (Wiley, 1949).
62. J.J. Thibault, J. Roussel, and E. Faddi, in Pure and Applied Cryogenics (Pergamon Press, 1966), Vol. 4, p. 249.

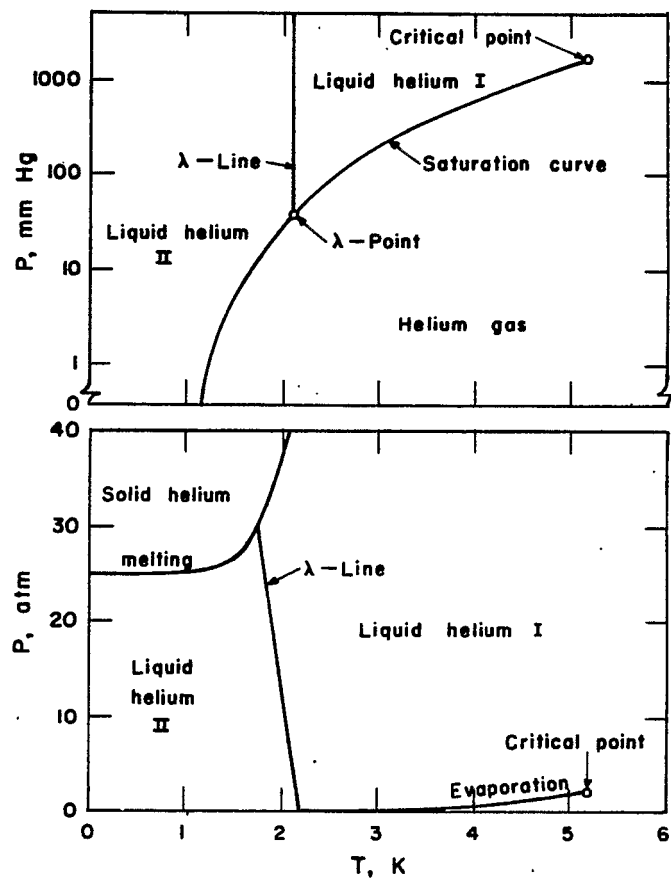


Fig. 1. Pressure-temperature diagrams for helium.

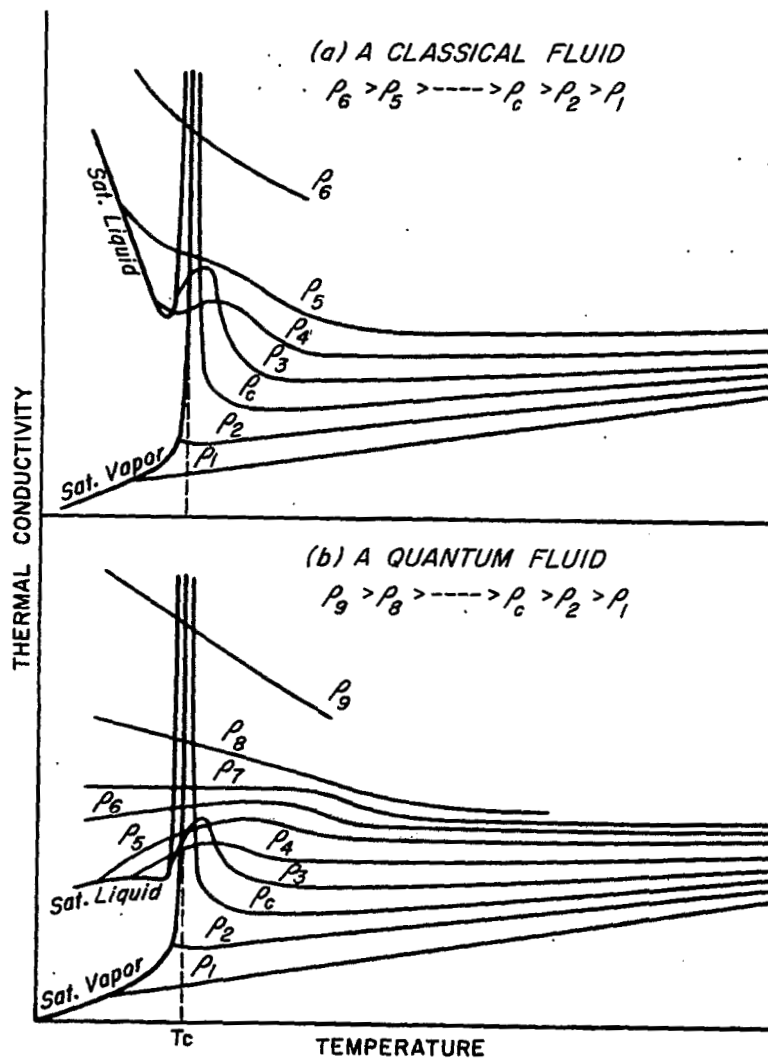


Fig. 2. Comparison of the behavior of thermal conductivity for a classical and for a quantum fluid from Corruccini (Ref. 1).

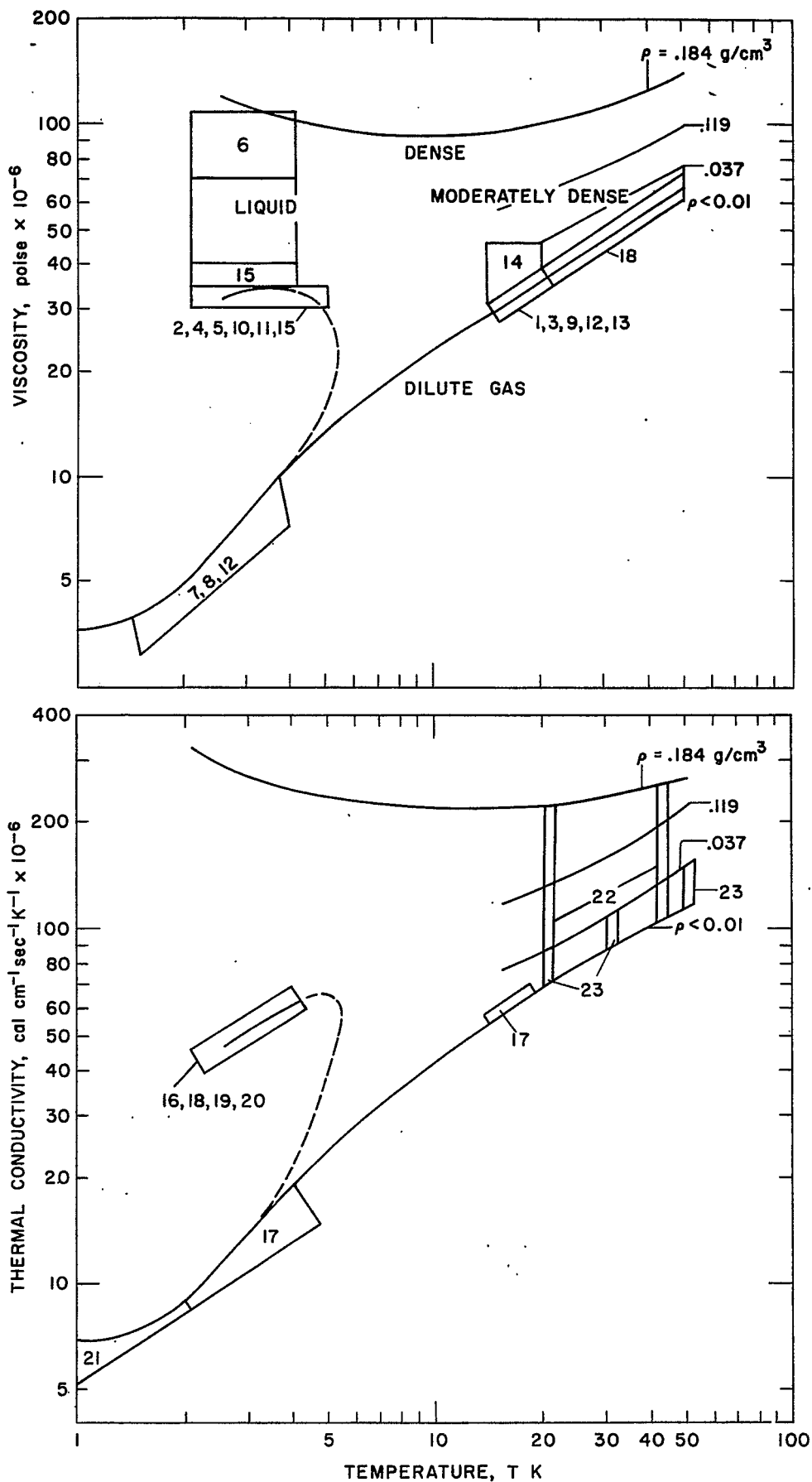


Fig. 3. Viscosity and thermal conductivity diagrams for helium showing regions of reported experimental data from Hanley and Childs (Ref. 2). Lines are for conditions of constant density.

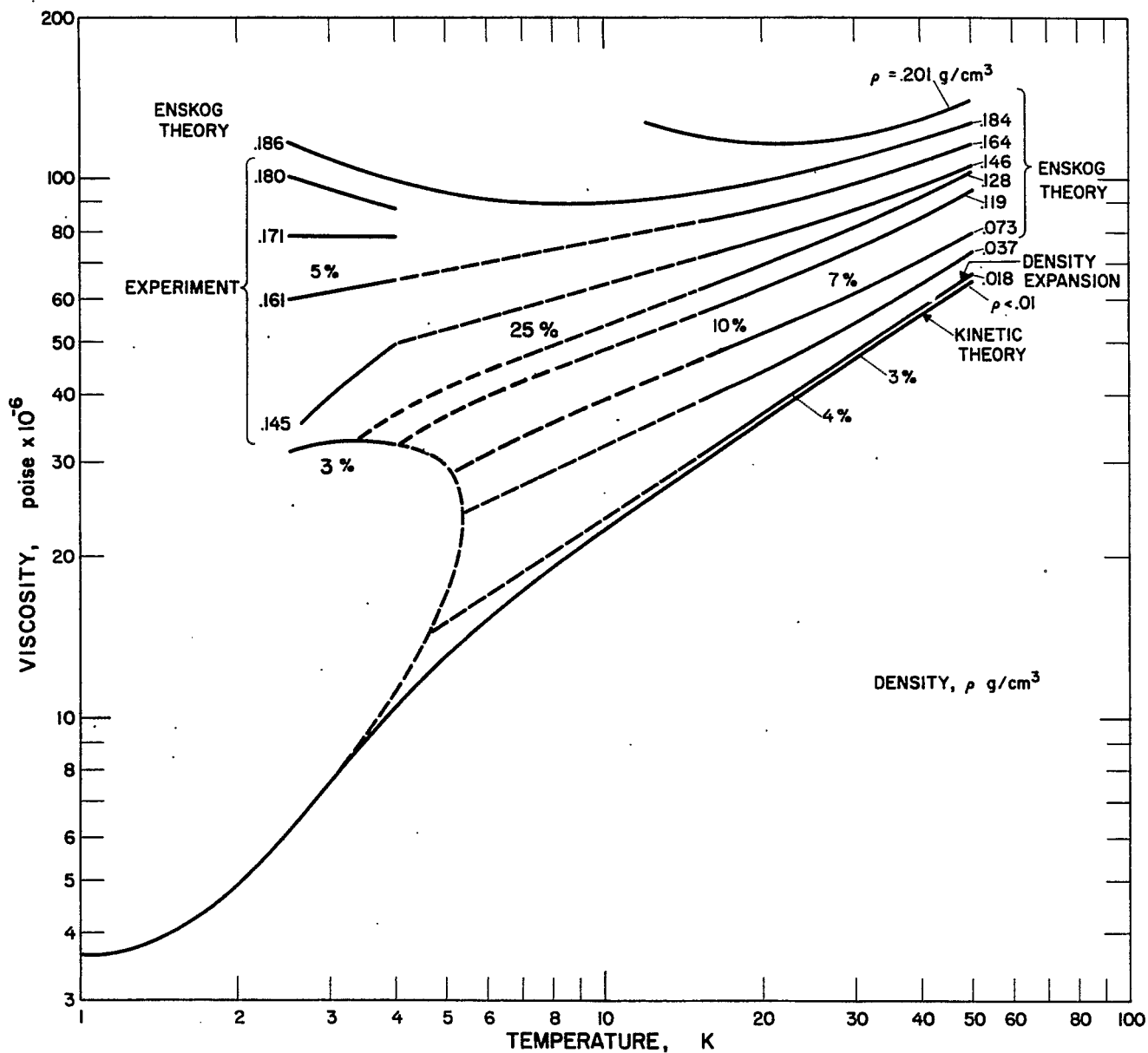


Fig. 4. The viscosity of helium at constant density. Solid lines represent data from theory or experiment which have the approximate reliability shown. Dashed lines indicate regions where there are no reliable data. From Hanley and Childs (Ref. 2).



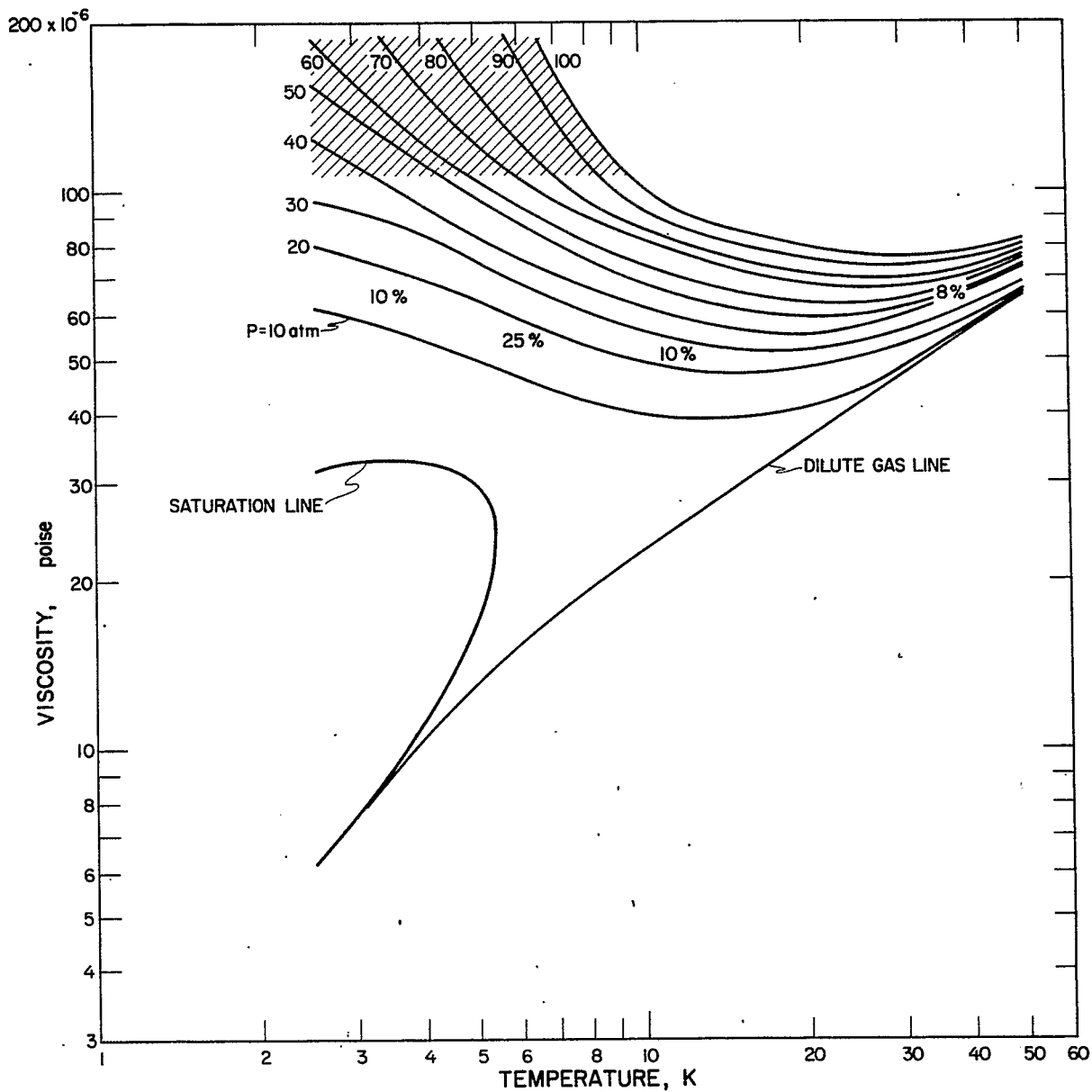


Fig. 4a. Viscosity of helium at constant pressure. Data are from Fig. 4. Conversion was made by use of properties in NBS TN 154 by D.B. Mann (1962). Crosshatched area indicates regions where data are considered unreliable.

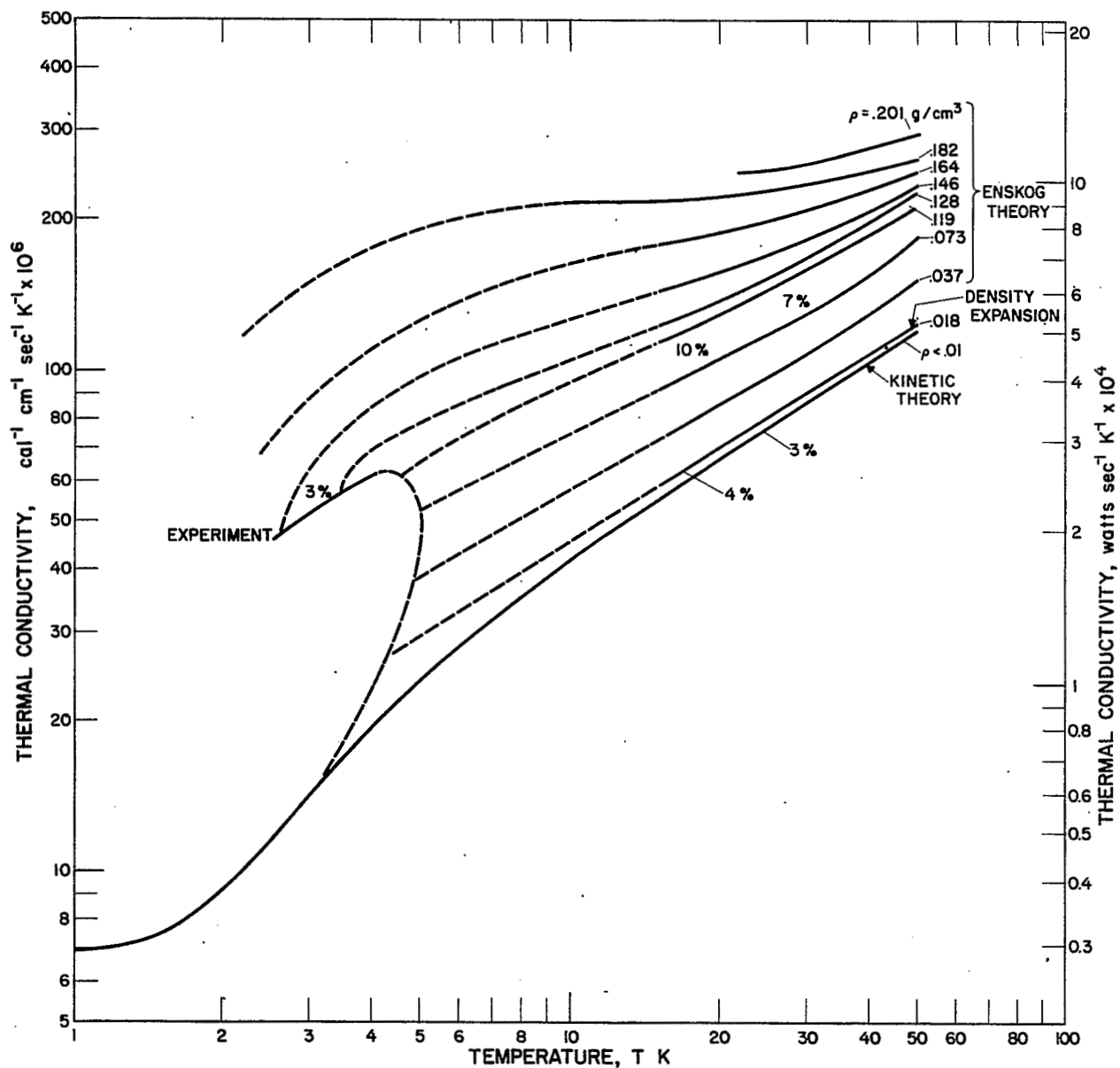


Fig. 5. The thermal conductivity of helium at constant density. Solid lines represent data from theory or experiment which have the approximate reliability shown. From Hanley and Childs (Ref. 2).

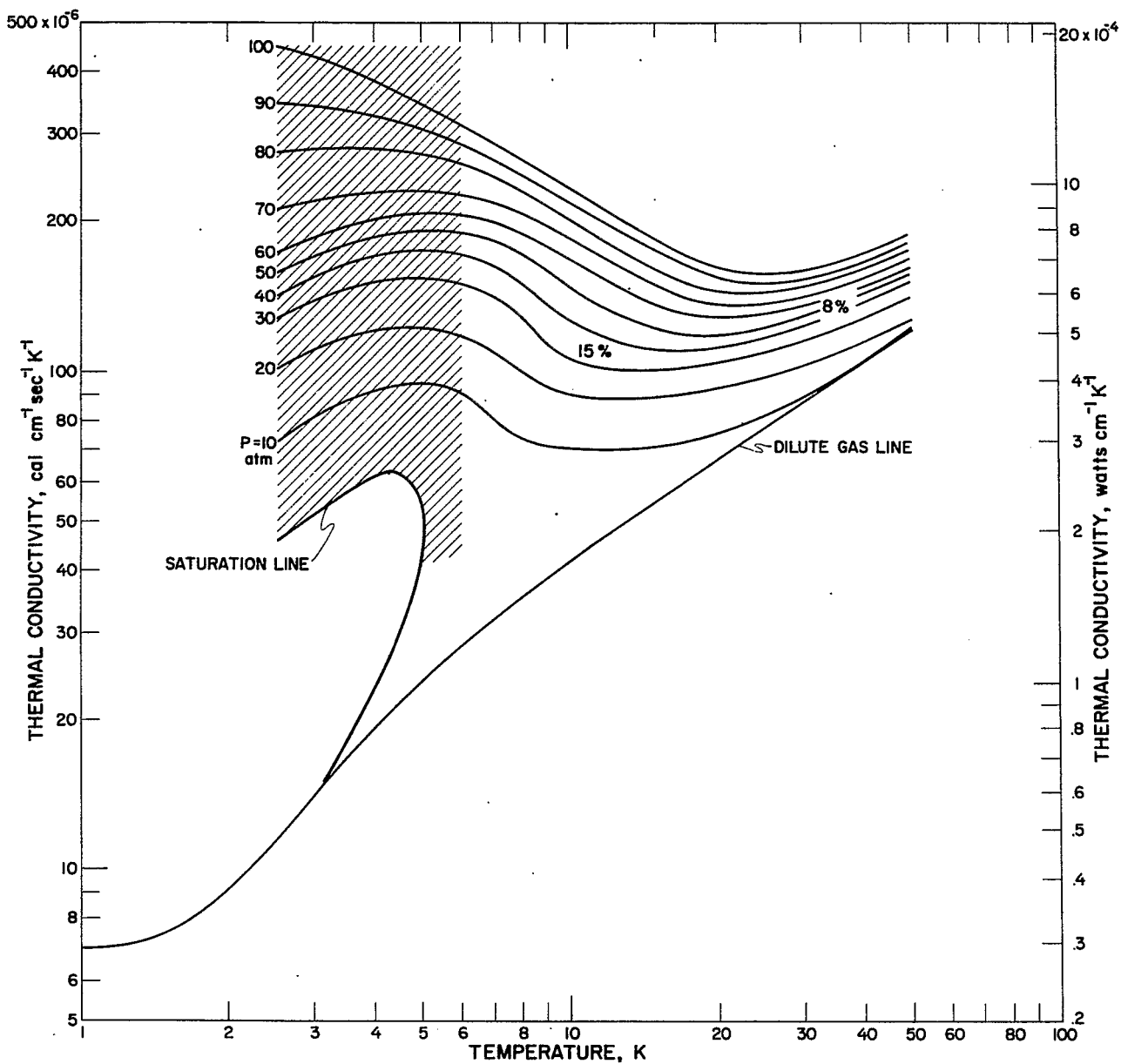


Fig. 5a. Thermal conductivity of helium at constant pressure. Data are from Fig. 5. Conversion was made by use of properties in NBS TN 154 by D.B. Mann (1962). Crosshatched area indicates regions where data are considered unreliable.

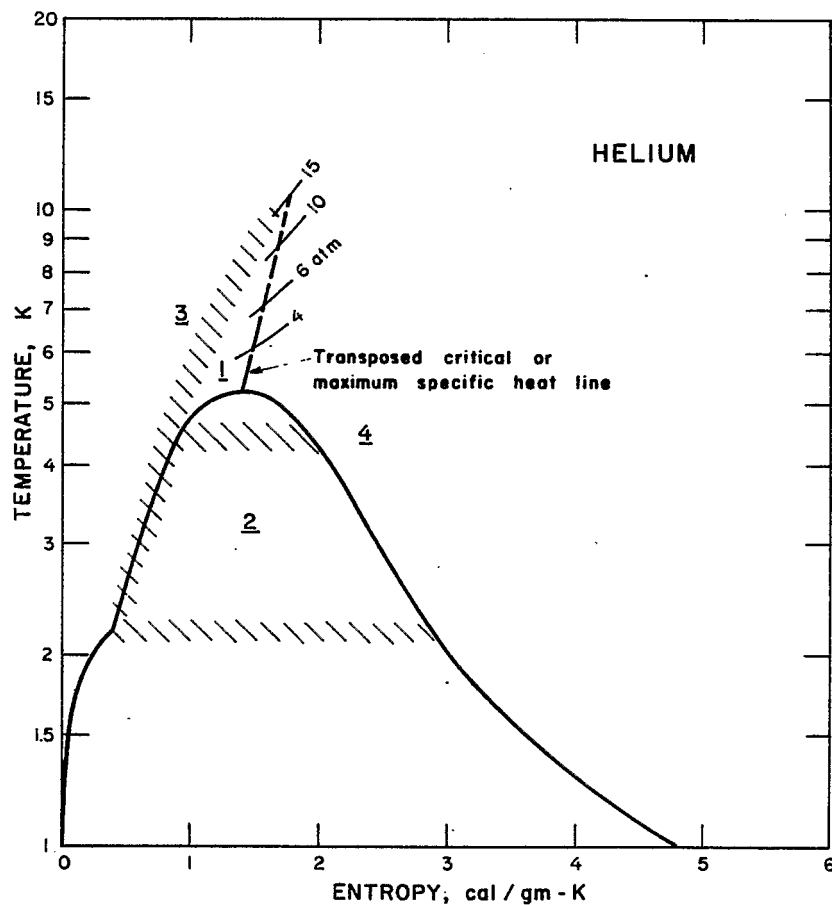
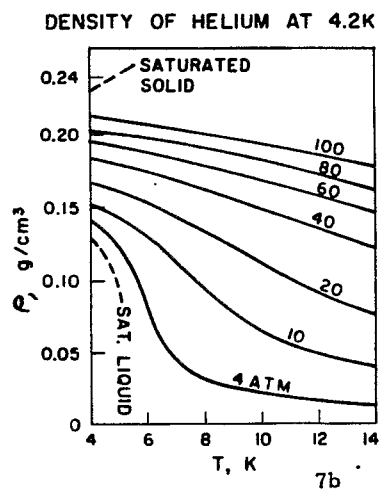
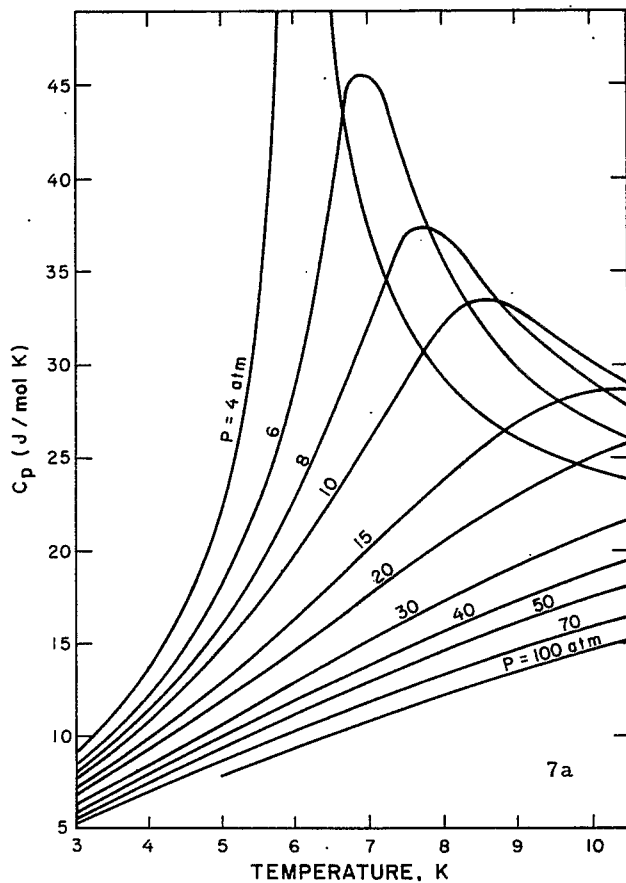


Fig. 6. Temperature-entropy diagram for helium showing the regions of similar property and heat transfer behavior.



Figs. 7a & 7b. Specific heat data from Lounasmaa (Ref. 3) and density from Kolm et al. (Ref. 4) for helium showing the large property changes with temperature in the region of the critical and the transposed critical.

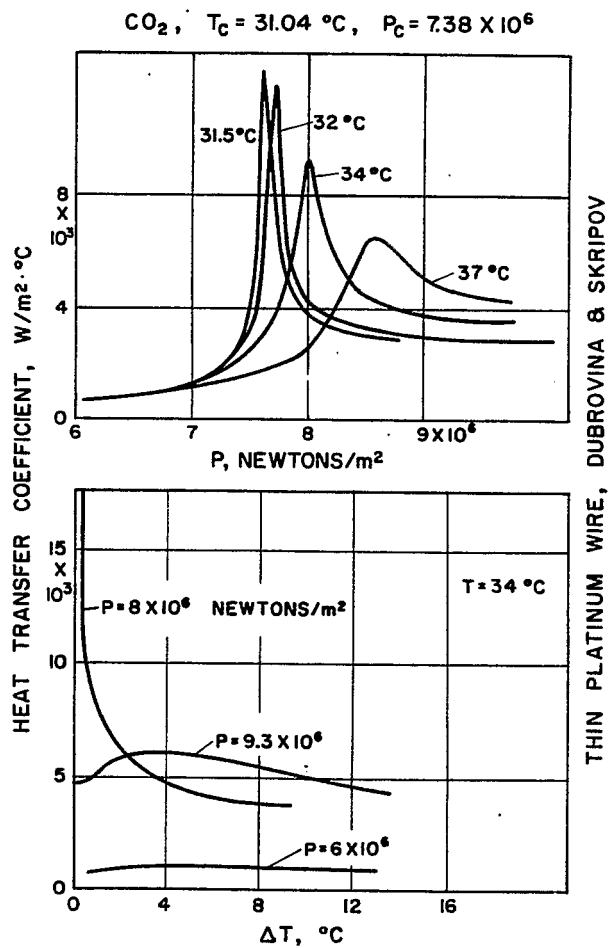


Fig. 8. Heat transfer coefficients from Dubrovina and Skripov (Ref. 6). Data show the coefficient behaves as the properties near the critical or transposed critical if the temperature differences are very small.

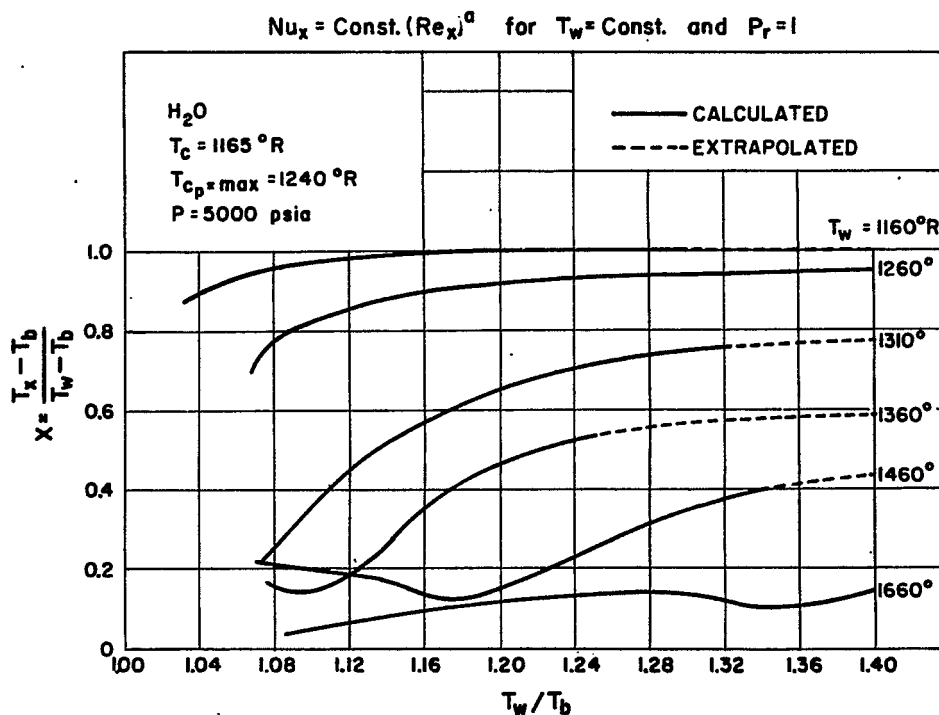


Fig. 9. Diagram showing reference temperature locations for property evaluation in the Nusselt and Reynolds numbers relationship. From Deissler (Ref. 15).

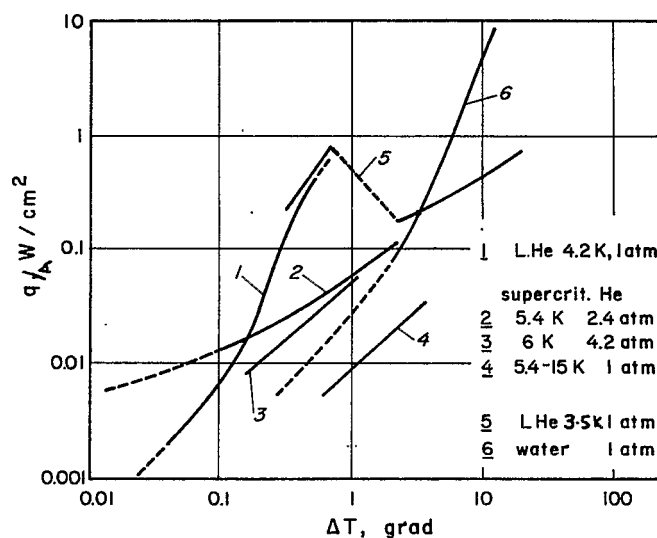


Fig. 10. Heat transfer to supercritical helium, boiling helium and boiling water at 1 atm. From Klipping and Kutzner (Ref. 24).

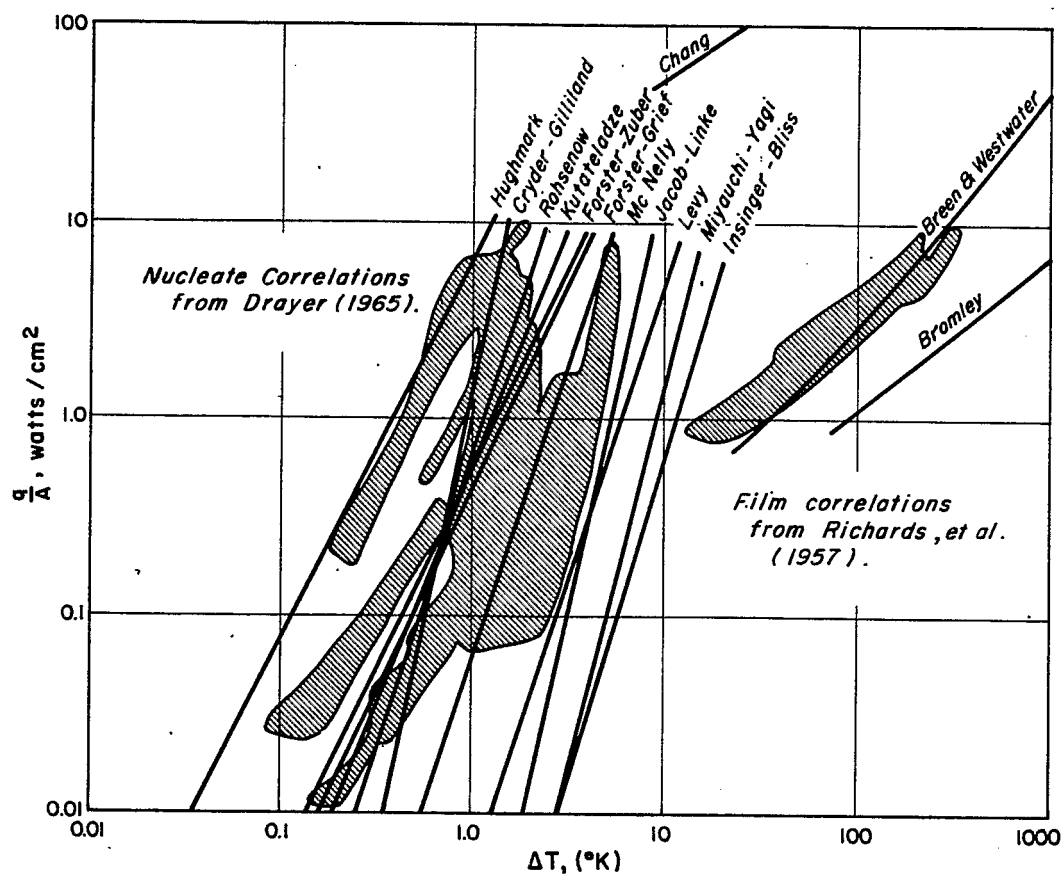


Fig. 11. Comparison of various boiling heat transfer correlations from the literature for hydrogen at 1 atm pressure with the reported experimental data shown as crosshatched areas. From Brentari et al. (Ref. 56).



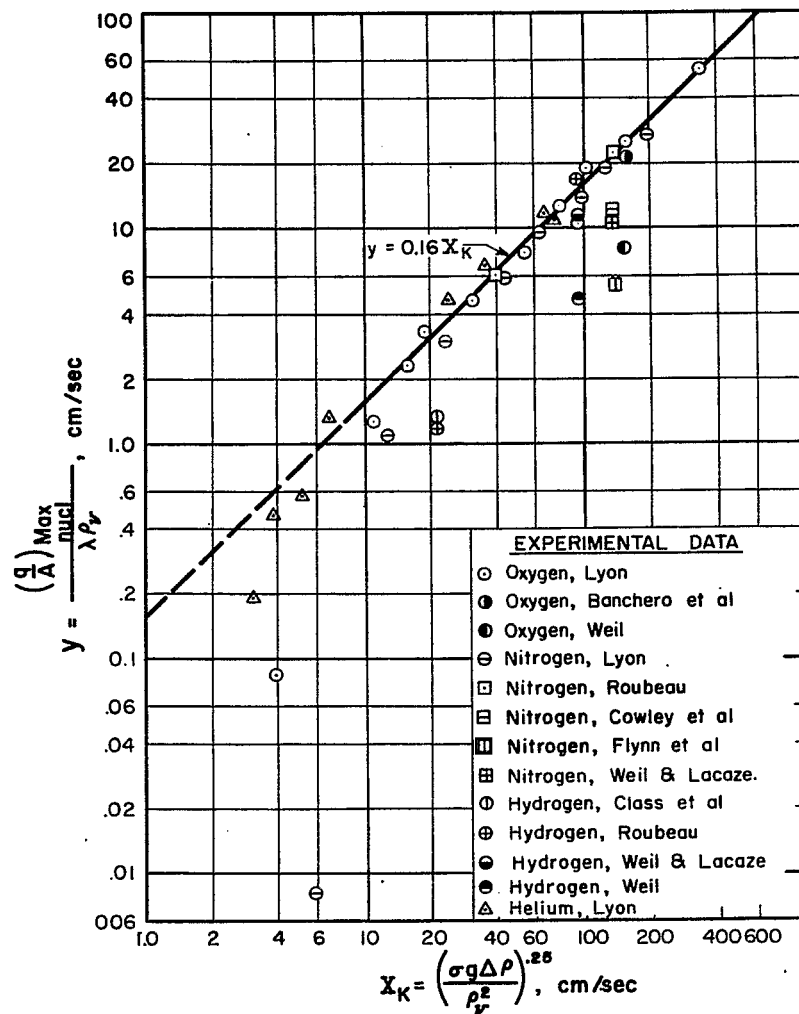


Fig. 12. Comparison of the experimental maximum nucleate heat transfer fluxes for cryogenic liquids with the Kutateladze maximum correlation. From Brentari et al. (Ref. 56).

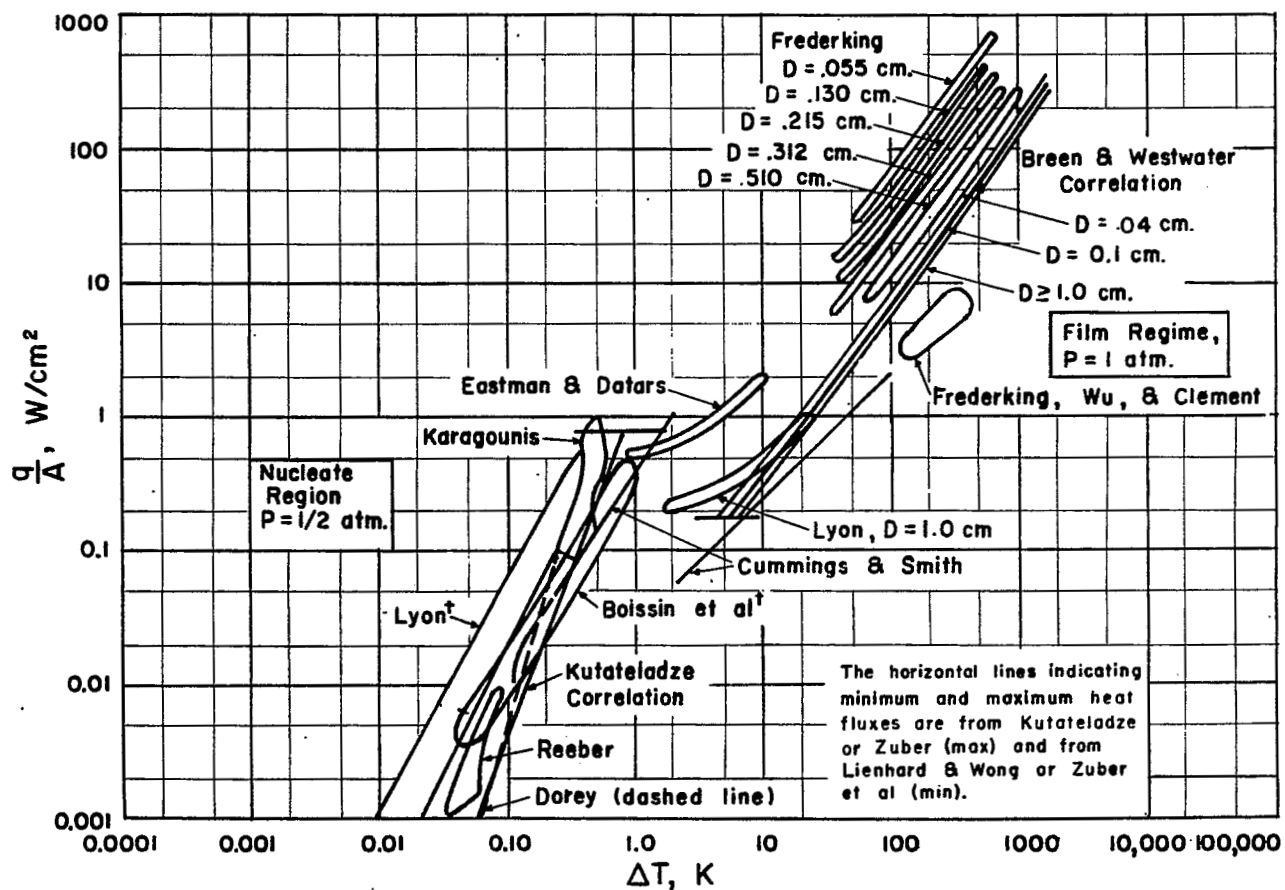


Fig. 13. Pool boiling of helium compared with results from correlations. Data identified by <sup>†</sup> has been corrected to values for the  $\frac{1}{2}$  atm case by use of the pressure dependence implied from the Kutateladze correlation.

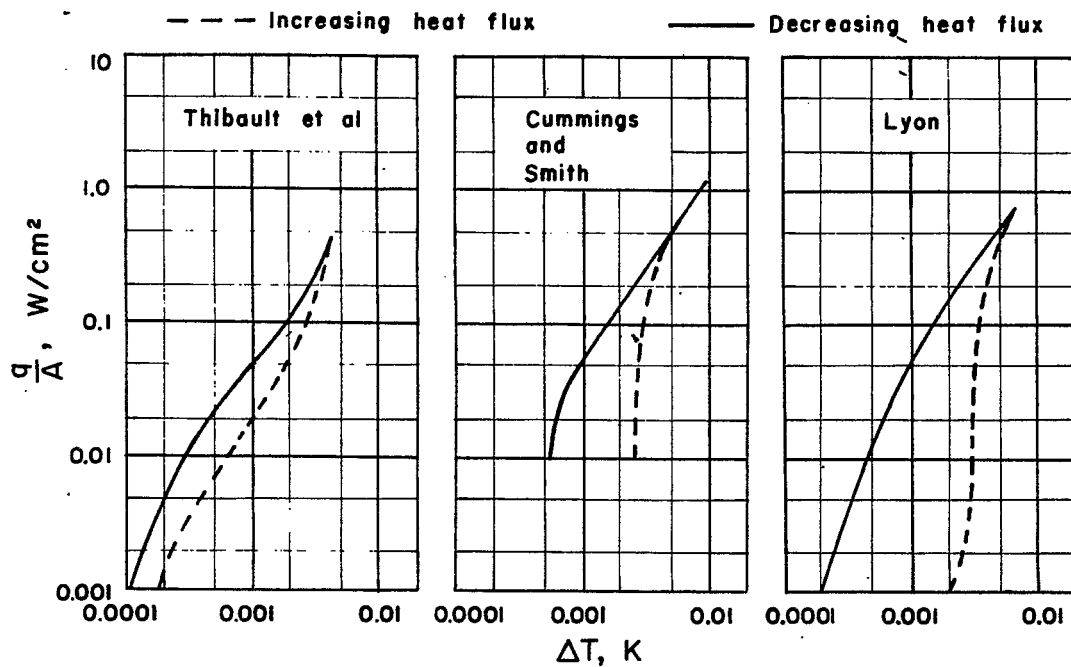


Fig. 14. Hysteresis or the effect of delayed bubble inception in the nucleate boiling region for helium as reported by three investigators.

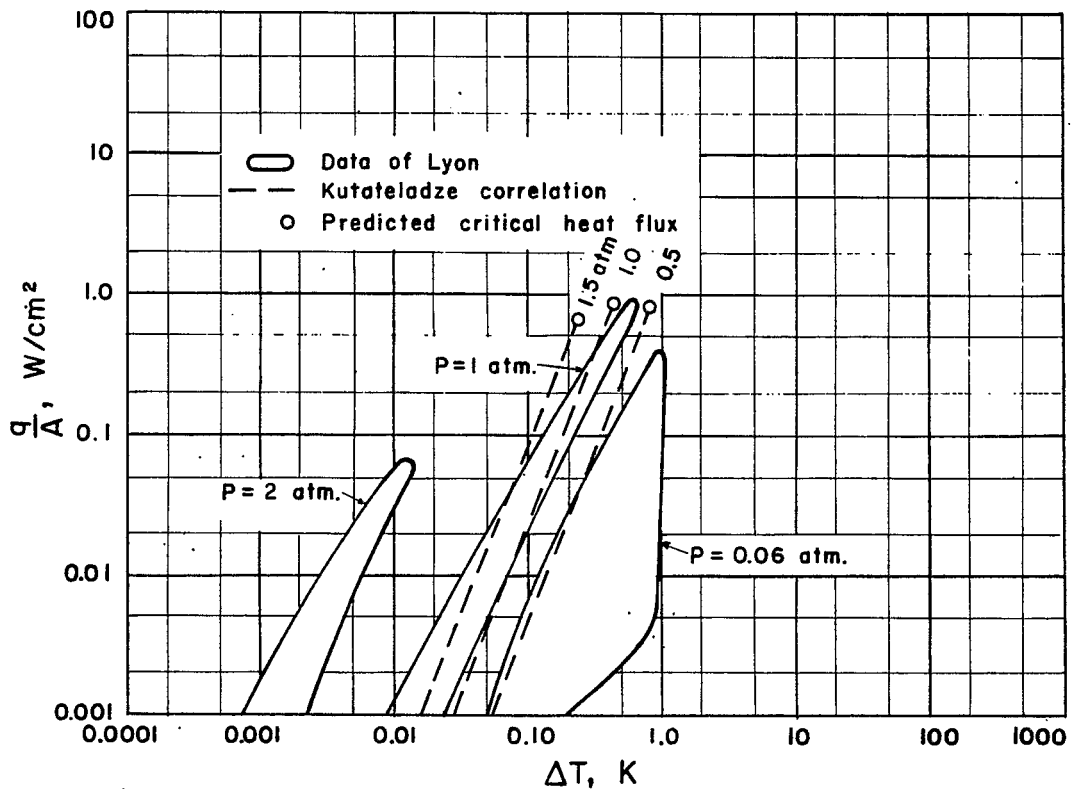


Fig. 15. Predicted nucleate boiling results from the Kutateladze correlation compared with experimental data from Lyon (Ref. 53) to show the reliability of the correlation at different pressure levels.

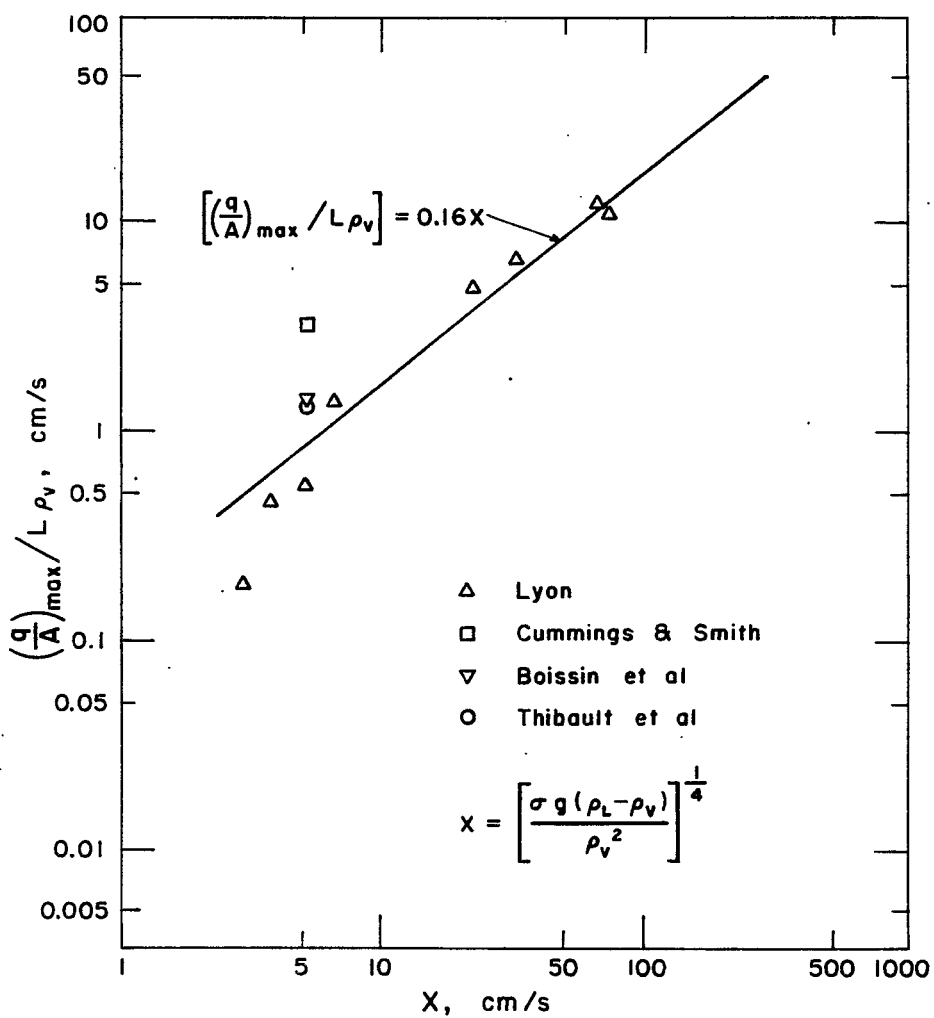


Fig. 16. Experimental data of maximum nucleate boiling fluxes compared with predictive results from the Kutateladze or Zuber correlation (Refs. 27 and 28).

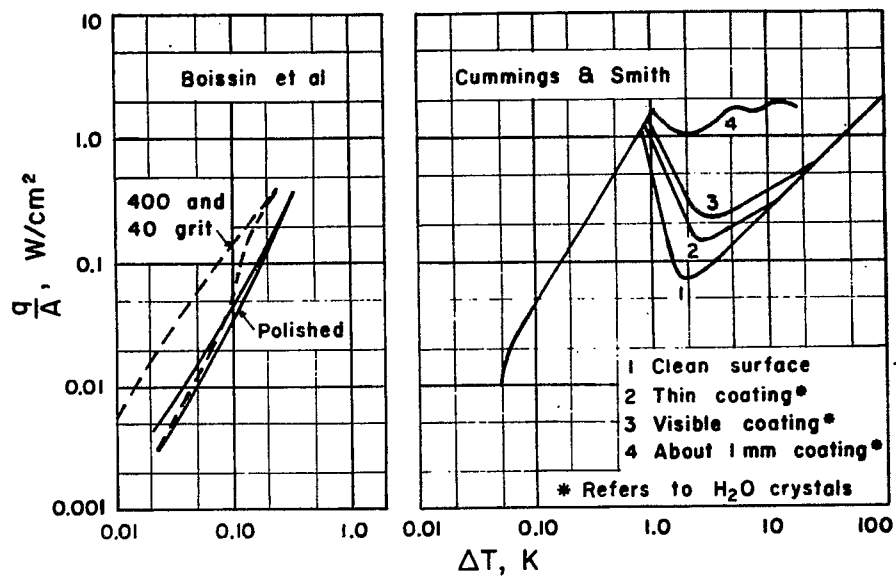


Fig. 17. Surface roughness effects for pool boiling with helium as reported by two investigators.

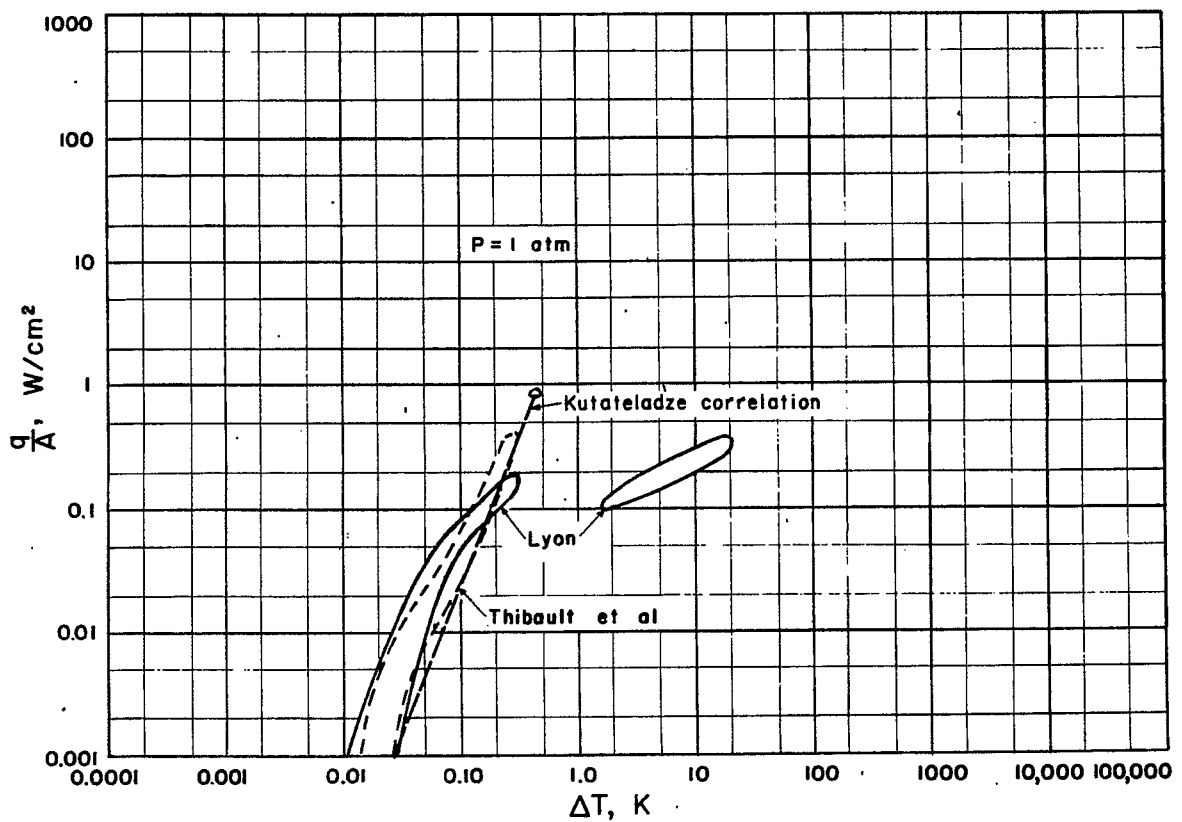


Fig. 18. Pool, nucleate boiling of helium from heated surfaces facing downward. Circle indicates predicted burnout condition.

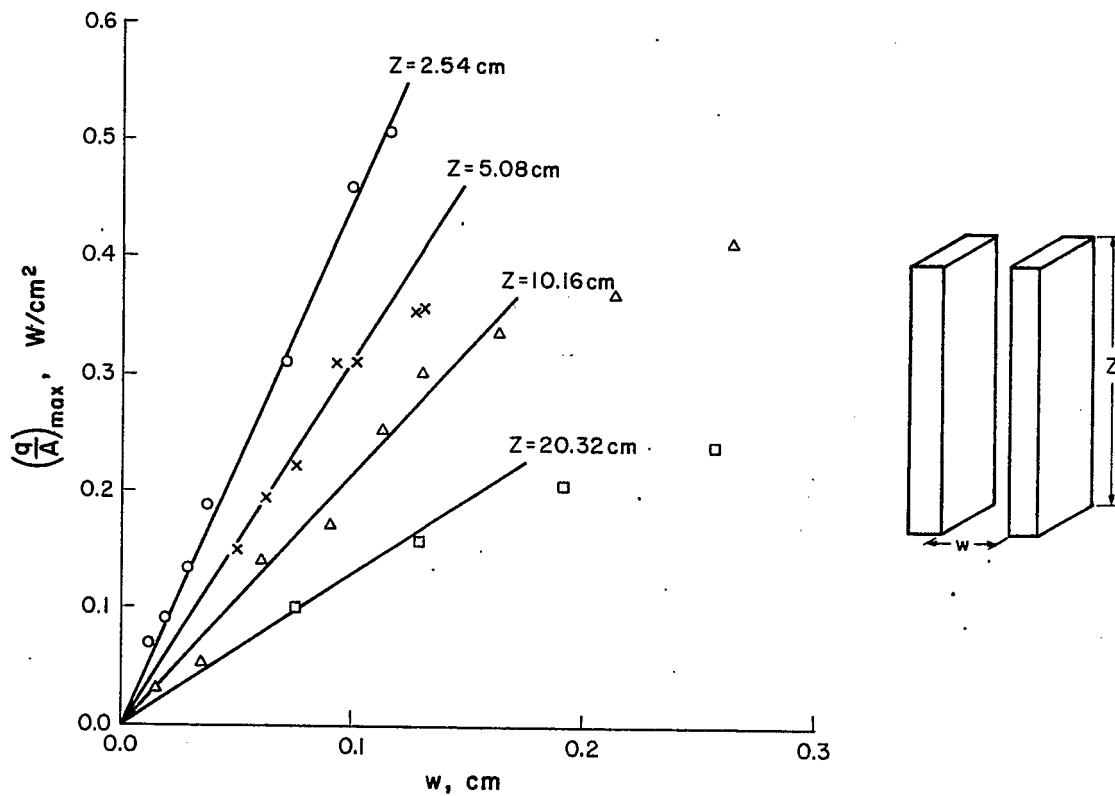


Fig. 19. Experimental data on helium boiling in vertical channels from Wilson (Ref. 52). Solid lines are maximum heat flux prediction from Sydoriak and Roberts (Ref. 51).

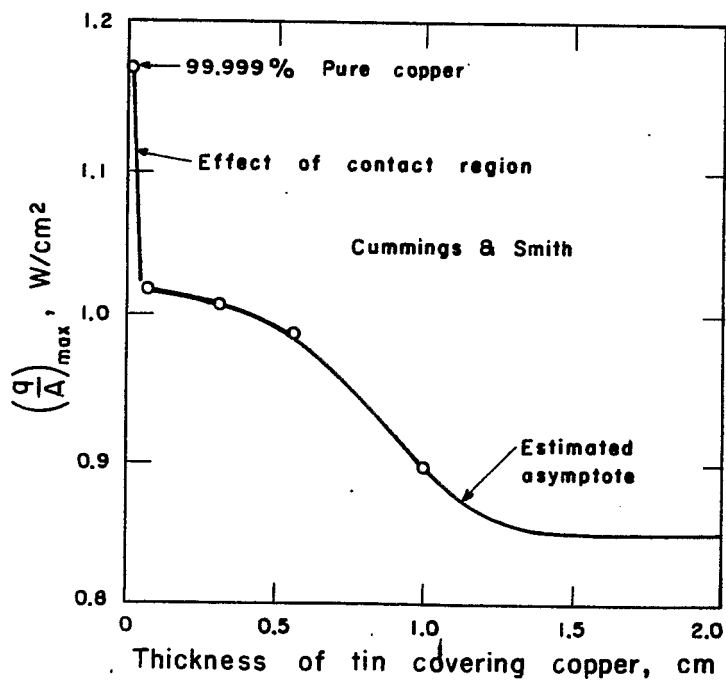


Fig. 20. Data for pool boiling of helium showing the effect of variations in the substrate material from Cummings and Smith (Ref. 40).

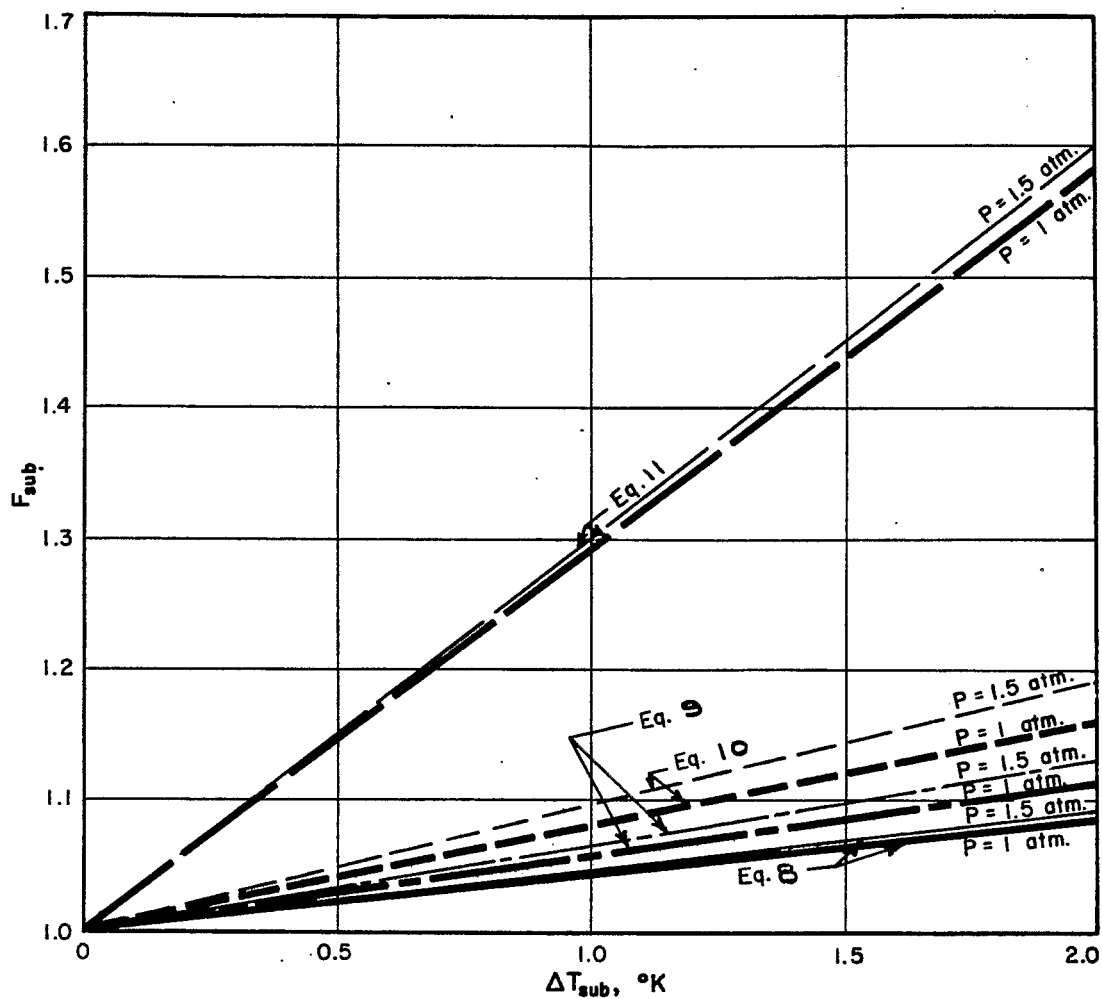


Fig. 21. Correction factor for maximum nucleate boiling flux for subcooled helium.

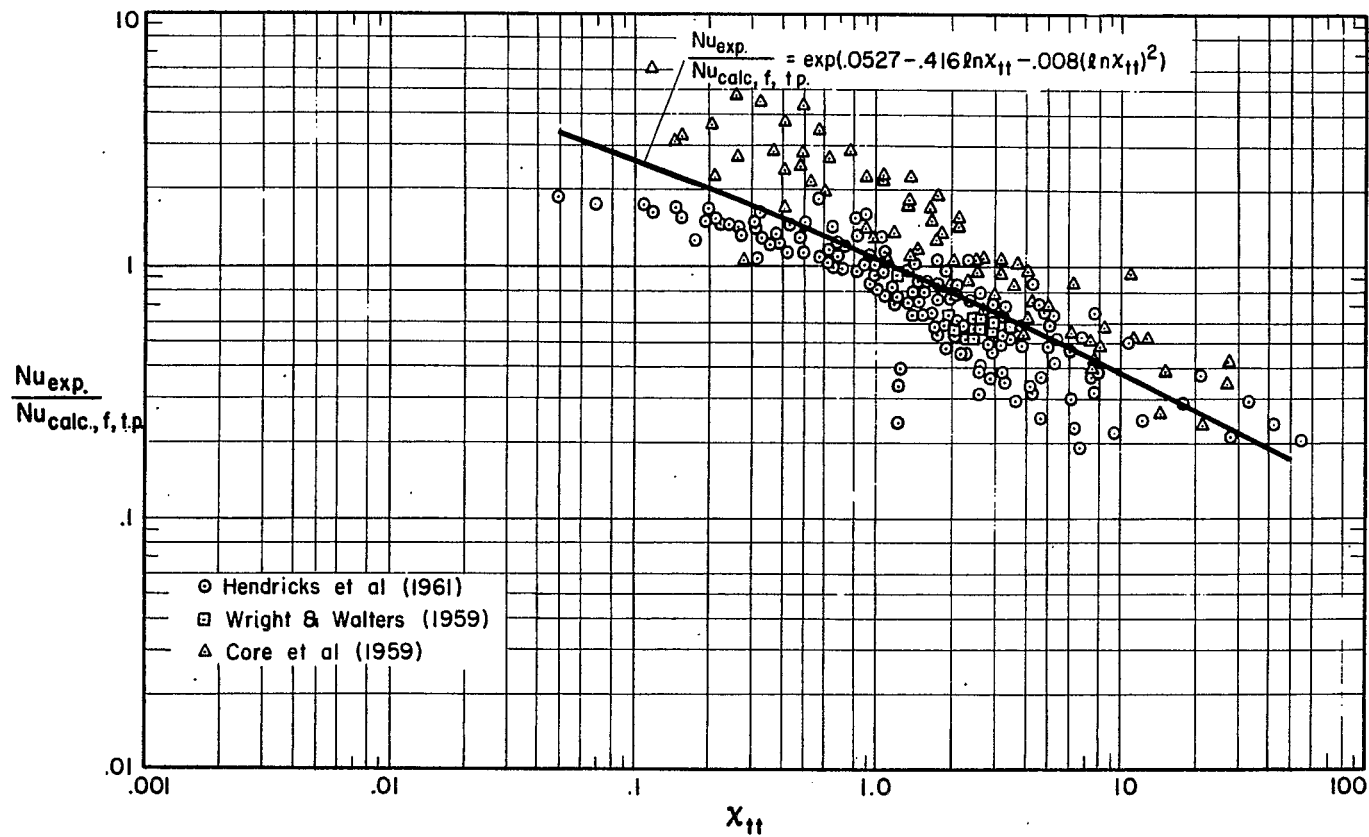


Fig. 22. Two-phase Nusselt number ratio vs  $x_{tt}$  for hydrogen. Correlation from Hendricks et al. (Ref. 17), figure from Brentari et al. (Ref. 56).



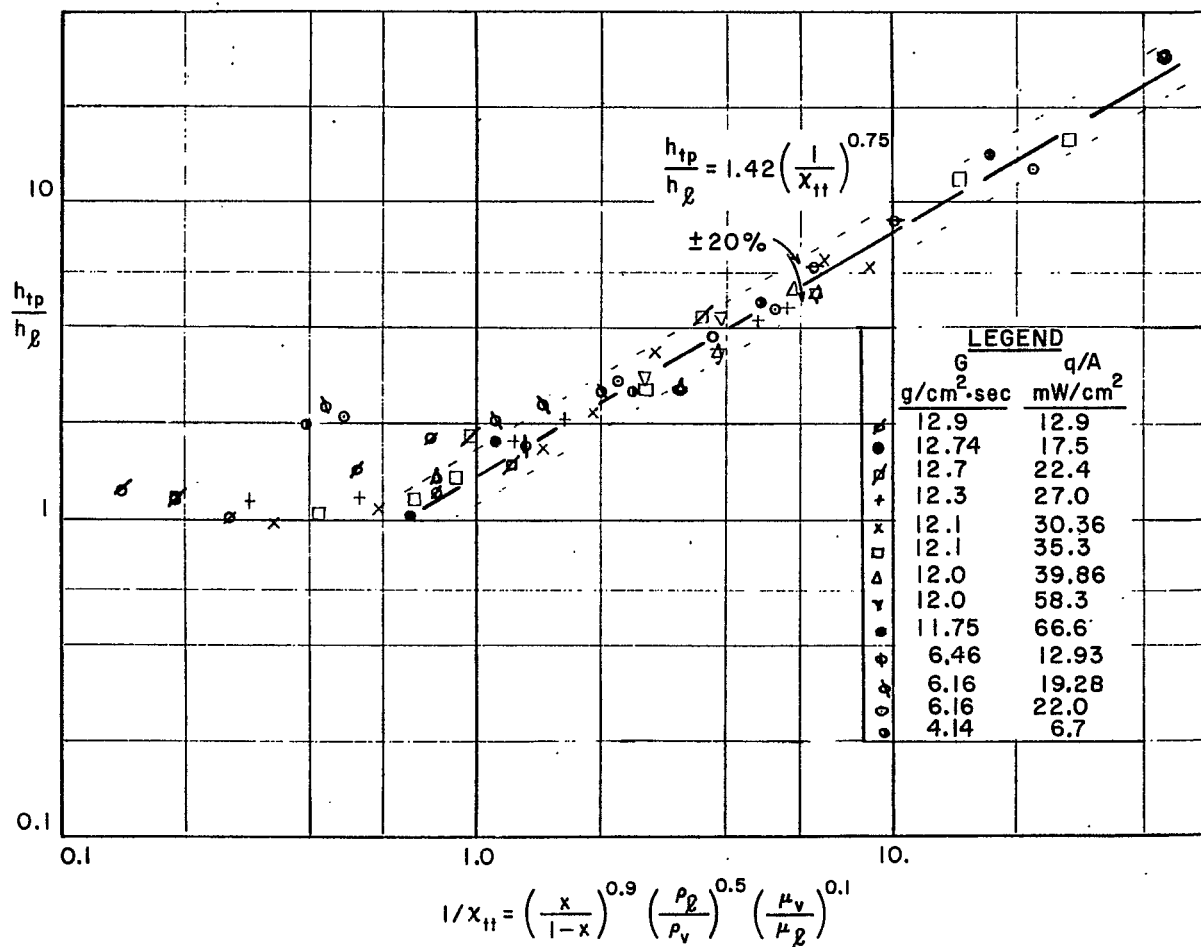


Fig. 23. Data for forced convection boiling of helium compared with a Martinelli-type correlation from de La Harpe et al. (Ref. 58).

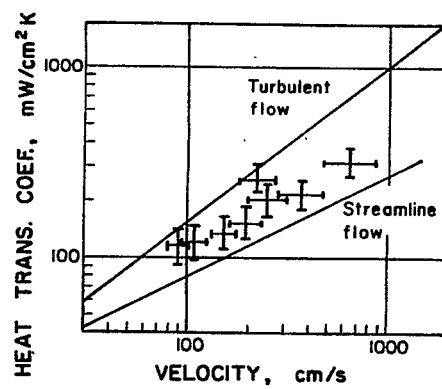


Fig. 24. Forced convection heat transfer data for liquid helium from Dorey (Ref. 60). Experimental data are compared with predicted results for streamline and turbulent flow.

AN EXAMINATION OF A LIQUID HELIUM REFRIGERATION  
SYSTEM FOR SUPERCONDUCTING MAGNETS IN  
THE 200 GEV EXPERIMENTAL AREA\*

M.A. Green  
Lawrence Radiation Laboratory  
Berkeley, California

G.P. Coombs and J.L. Perry  
500 Incorporated  
Cambridge, Massachusetts

## I. INTRODUCTION

It has been suggested that the dc experimental area transport magnets for the 200 GeV machine be superconducting. The primary advantages of dc superconducting magnets are the elimination of large power supplies and cooling towers, and a drastic decrease in the consumption of electric power and cooling water. Although the need for power and cooling water is drastically reduced, capital and operating expenditure is required to maintain the superconducting magnets at liquid helium temperature (4.2°K).

The first analysis of this refrigeration problem was done by Strobbridge, Chelton and Mann<sup>1</sup> of the National Bureau of Standards in Boulder, Colorado. A second more detailed report on the refrigeration system was published<sup>2</sup> in June 1968 by 500 Incorporated, a subsidiary of Arthur D. Little, Cambridge, Massachusetts. This second report is summarized in this paper. The second report differs considerably from the first in several respects. First, a specific experimental area model is analyzed; second, the refrigeration systems analyzed are all helium systems (no liquid nitrogen is used); third, simplicity, reliability, and flexibility are important considerations in the study; fourth, gas compression, storage, and purification are centralized; finally, the cost reduction resulting from quantity production is considered.

Three basic refrigeration concepts are analyzed in the second report<sup>2</sup>: 1) central liquefier, liquid delivery, 2) central refrigerator, cold gas supply and return, and 3) many small refrigerators with warm gas supply and return from central compressor stations. Several versions of the small refrigerator concept are investigated.

## II. THE EXPERIMENTAL AREA

The experimental area model used is a modified version of one found in the National Accelerator Laboratory design report.<sup>3</sup> The approximate dimensions of the experimental area are 300 m by 1600 m. The over-all design is divided into three smaller areas, one for each of the three target stations.

---

\* Work performed under the auspices of the U.S. Atomic Energy Commission.

1. T.R. Strobbridge, D.B. Mann, and D.B. Chelton, NBS Report 9259 (1966).
2. M.A. Green, G.P. Coombs, and J.L. Perry, 500 Incorporated Report (1968).
3. National Accelerator Laboratory Design Report (1968).

TABLE I. The parameters of secondary beams used in the LRL-500 Inc. refrigeration study.

	Beam length (m)	Number of beam magnets	Beam life (yr)	Radiation shielding required
<u>Beams off Target A</u> (Fig. 1)				
Beam A-1a	55	9	< 1	Moderate
Beam A-1b	230	14	< 1	Moderate
Beam A-2	120	18	< 1	Moderate
<u>Beams off Target B</u> (Fig. 2)				
Beam B-1	140	10	< 1	Moderate to heavy
Beam B-2	233	14	< 1	Moderate to heavy
Beam B-3	232	12	< 1	Moderate to heavy
Beam B-4	463	24	1 - 3	Light
<u>Beams off Target C</u> (Fig. 3)				
Beam C-1	1590	64	> 3	Light
Beam C-2	1590	68	> 3	Very heavy
Beam C-3	746	19	1 - 3	Moderate

Two hundred and fifty-two magnets are to be found within the experimental area. A future complication is the constant change in the experimental area beam layout. The model used in the 500 Incorporated report<sup>2</sup> only exists at one point in time. Table I presents detailed parameters of the beam lines found within the experimental area model used for the refrigeration study.

Several types of secondary beams are not represented in the experimental area model. The elimination of these beams does not affect the validity of the model because many of the beams will be similar to beams that were included in the model.

### III. THE MAGNETS AND THEIR CRYOSTATS

The dipoles and quadrupoles housed in the magnet cryostats are assumed to have field strengths at the windings of the order of 40 kG. The dipole central fields are assumed to be 35-40 kG, the 4 in. quadrupole gradients 6-7 kG/cm, and the 8 in. quadrupole gradients 3-3.5 kG/cm. The length of the quadrupole and dipole fields given in the 500 Incorporated report is based on the above numbers.

The helium temperature mass is assumed to be 250-500 kG. The magnet stored energy will vary from  $3 \times 10^5$  J for a 4 in. quadrupole to  $2 \times 10^6$  J for an 8 in. dipole. It is assumed that a magnet quench is an infrequent phenomenon.

The cryostat design will be as simple as possible. It is assumed that the magnet cryostat will have only an inner vessel and an outer vacuum jacket which are separated by multilayer superinsulation and a tension-rod support system. The 1000 A electrical leads are assumed to be gas cooled. The total heat leak into the Dewar is assumed to be 5 W. The liquid storage capacity of the Dewar varies from 70 to 2000 liters depending on the type of refrigeration system used.

The simple high heat loss cryostat design seems to be contrary to normal cryogenic practice. However, the elimination of intermediate temperature shields and retractable leads has several important advantages, which are: 1) the Dewar design has less plumbing to fail, hence the Dewar will be more reliable; 2) the amount of money saved on the cryostat construction more than compensates for the increased refrigeration cost (reduced total system cost); 3) operational simplicity - there is no nitrogen filling process, a simple orifice at room temperature regulates the lead cooling gas flow. Considerable development work is required on the magnet cryostat before the simplified low-cost cryostat becomes a reality.

#### IV. THE REFRIGERATION SYSTEMS AND THEIR COST

The 500 Incorporated study<sup>2</sup> presents a number of cases for providing 4.2°K refrigeration to the experimental area superconducting magnets. Three basic types of systems are presented: 1) a central liquefier providing liquid in portable Dewars with warm gas return (Case 1); 2) a small number of central refrigeration units providing cold gas through transfer lines and cold gas return (Case 2); 3) a large number of small refrigerators run off a small number of large compressor stations with gas transport at ambient temperature (Cases 3a, 3b, 4a, 4b, and 5). The small-refrigerator concept has a number of cases represented because it appears to be feasible from both an economic and operational standpoint. Table II presents a comparison between all of the refrigeration concepts studied in the 500 Incorporated report.

The large-liquefier concept (Case 1, see Fig. 4) has a number of advantages as follows: 1) high "process plant" reliability can be achieved in the liquefier, 2) storage and distribution Dewars can be made with a long life and little required maintenance, and 3) replaced magnet can be changed and cooled quickly. There are a number of important disadvantages that cannot be overlooked: 1) clear access to the magnet Dewar fill line must be provided at all times, 2) the system has a high labor input, and 3) gas storage is a problem during a liquefier failure.

The advantages and disadvantages of the central refrigeration system (Case 2, see Fig. 5) are as follows: Advantages - 1) large refrigerators are more efficient and less costly per watt than either liquefiers or small refrigerators; 2) less labor is required during operation; and 3) less space is required on the experimental area floor either for refrigerators or for fill vehicles. Disadvantages - 1) transfer line reliability is questionable today; it is difficult and expensive to move and install helium temperature transfer lines; and 2) when one refrigerator fails a large amount of liquid must be provided to a large number of magnets.

The advantages and disadvantages of each of the small-refrigerator cases (Cases 3a to 5, see Figs. 6 and 1) are discussed in detail in the 500 Incorporated report.<sup>2</sup> The following general statements can be made: Advantages - 1) the systems are flexible; warm compressed gas piping is easy to move and is reliable; 2) the refrigerator design can be simplified - mass production techniques can be used; and 3) the systems have a low operating labor output. Disadvantages - 1) the system reliability goes down because of a large number of small refrigerator units; regular maintenance will increase reliability; and 2) the refrigeration efficiency goes down as the size decreases and refrigerator cost per watt is increased.

TABLE II. A comparison of various 4.2°K refrigeration systems for the 200 GeV experimental areas.

Case	System description	Location of refrigerator	Refrigerator or liquefier size	Number of refrigerators	Number of compressor stations
1	Central liquefier, portable Dewar, liquid distribution and warm gas return	A location accessible to all three target areas	2200 liters/h	1	1
2	Central refrigerators with cold gas supply and return	Four locations near the three target areas	800 W, 1800 W, 2100 W, and 2300 W	4	4
3a	One refrigerator per magnet Dewar, central compressor station, warm gas supply and return	On top of the magnet Dewar inside shielding	10 W	252	4
3b		Near the magnet outside the shielding	10 W	252	4
4a	Two magnet Dewars per refrigerator when possible, central compressor station, warm gas supply and return	Near the magnet pair inside the shielding	20 W	140	4
4b		Near the magnet pair outside the shielding	20 W	140	4
5	Mixed 80 W and 20 W refrigerators, central compressor station, warm gas supply and return	Near the magnets outside the shielding	20 W and 80 W	7 - 80 W 115 - 20 W	4

The central compressor station concept is an important one. The central compressor station has the following advantages over individual compressors: 1) the gas storage and purification is removed from the experimental floor; 2) the central compressor station costs less than many small compressors; 3) the over-all system reliability increases because the largest cause of failure in today's small refrigerators is their compressors; 4) a number of types of refrigerator, including helium II and supercritical helium, can be run off the same compressor station.

A detailed cost analysis of each of the cases can be found in the 500 Incorporated report.<sup>2</sup> The cost factors used to calculate refrigeration may be found there also. Table III presents a summary of the capital and operating costs for each case.

TABLE III. The refrigeration system cost summary (costs in thousands of dollars).

	Refrigeration system capital cost	Refrigeration system 10-yr operating cost (continuous operation)	Total system cost
Case 1	2980	13 405	16 385
Case 2	5200	6590	11 790
Case 3a	5400	4090	9490
Case 3b	5575	4090	9665
Case 4a	5015	3890	8905
Case 4b	4835	3890	8725
Case 5	5125	3885	9010

There is approximately a 12% variation in capital cost in Cases 2 through 5. Case 1 has a low capital cost but is extremely expensive to operate. The costs given for Case 2 will change considerably with changes in transfer line technology. It is clear that careful design work is required if the small refrigeration systems are to be reliable.

The capital cost of the refrigeration system will be 25-30% of the total magnet system cost. Over half of the system operating costs will be associated with the refrigerators.

## V. CONCLUDING REMARKS

A few concluding remarks can be made about the following concepts: 1) the no-nitrogen simplified-Dewar concept, 2) the small refrigerator vs large refrigerator, and 3) the central compressor station vs small individual compressors.

The no-nitrogen simplified-Dewar concept is valid when the following conditions apply: 1) small refrigerators are used to supply helium to the Dewar; 2) large refrigerators are used, but the Dewar heat leak is not the major part of the refrigeration load; and 3) many Dewars are widely separated. The no-nitrogen simplified-Dewar concept may not be valid under the following conditions: 1) when a laboratory Dewar is used; 2) when cooling is supplied by liquid (both nitrogen and helium transfer can be made at the same time); and 3) when large refrigerators are used and the Dewar heat leak is the major part of the heat load.

Many small refrigerators supplying a helium system appear to be attractive when: 1) the loads are scattered over a wide area, 2) transfer line losses exceed Dewar losses in a large system, and 3) flexibility of the system is required. Large refrigeration units become attractive when: 1) the loads are concentrated in a small area, 2) the loads greatly exceed the transfer line losses, and 3) when the system position is fixed. Many small refrigerators appear to be attractive for an accelerator experimental area, but large refrigerators would clearly be best for a large superconducting synchrotron.

Central compressor station seems to be most attractive when: 1) the refrigerator and load contain a large volume of helium, 2) piping is not the major part of the compressor station cost, and 3) system reliability is important. The small compressor is useful for temporary machines and machines that would require large amounts of piping if they were tied into a central system.

The transformation of superconductivity from a laboratory to a useful tool for the high energy physicist requires an extensive analysis of the whole system. There appear to be a number of refrigeration systems which can apply to the experimental area of the 200 GeV accelerator. Changes in technology will affect the final solution to the problem.



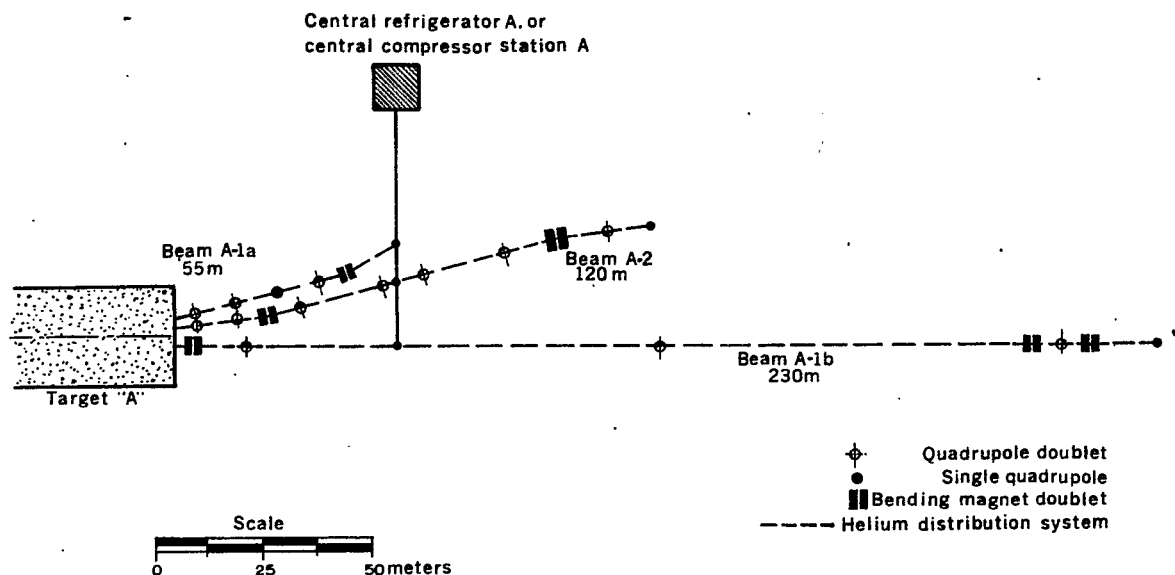


Fig. 1. Experiments from Target Station "A".

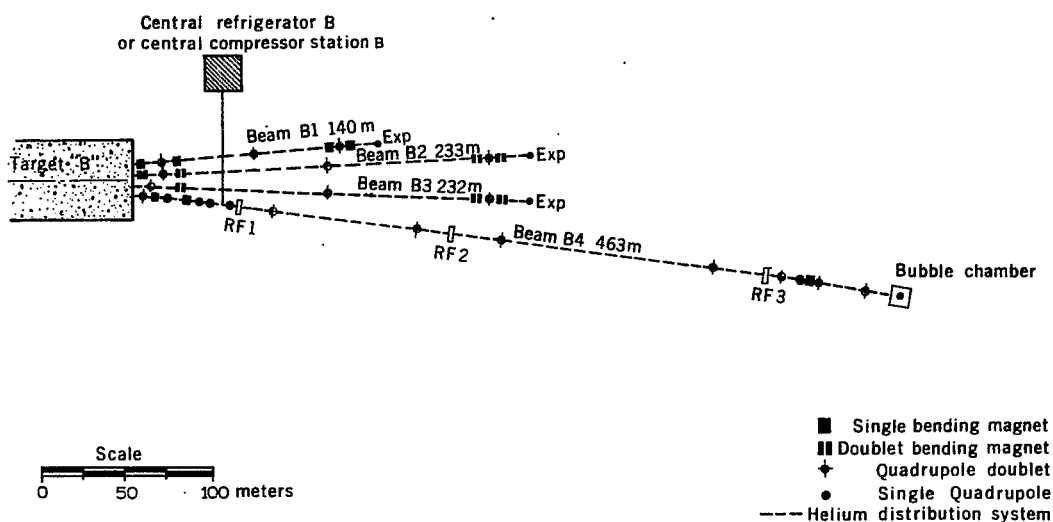


Fig. 2. Experiments from Target Station "B".

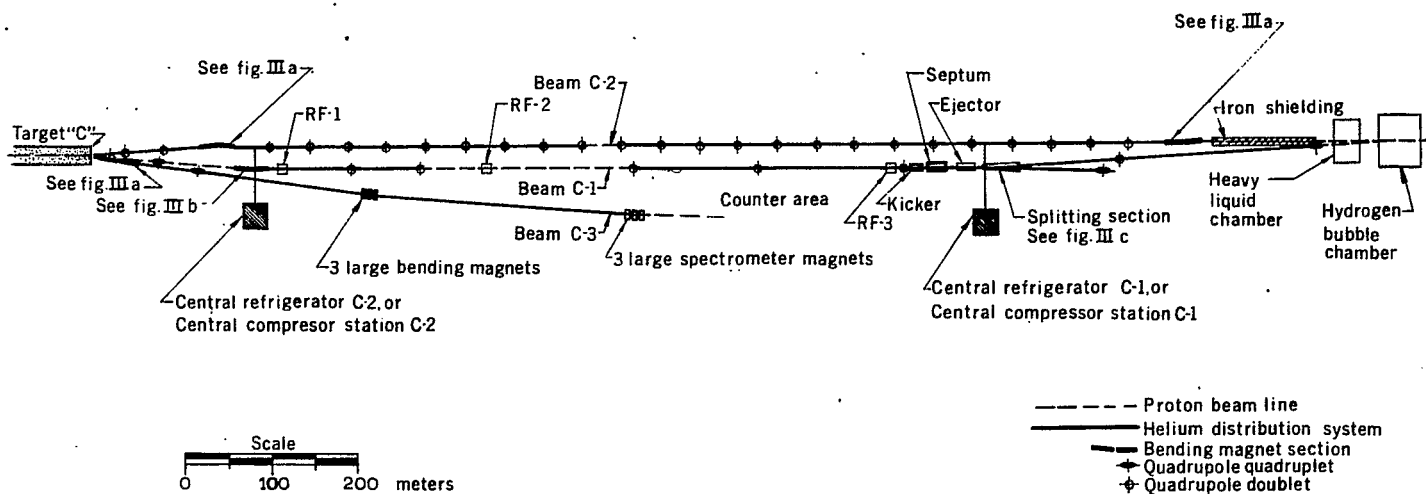


Fig. 3. Experiments from Target Station "C".

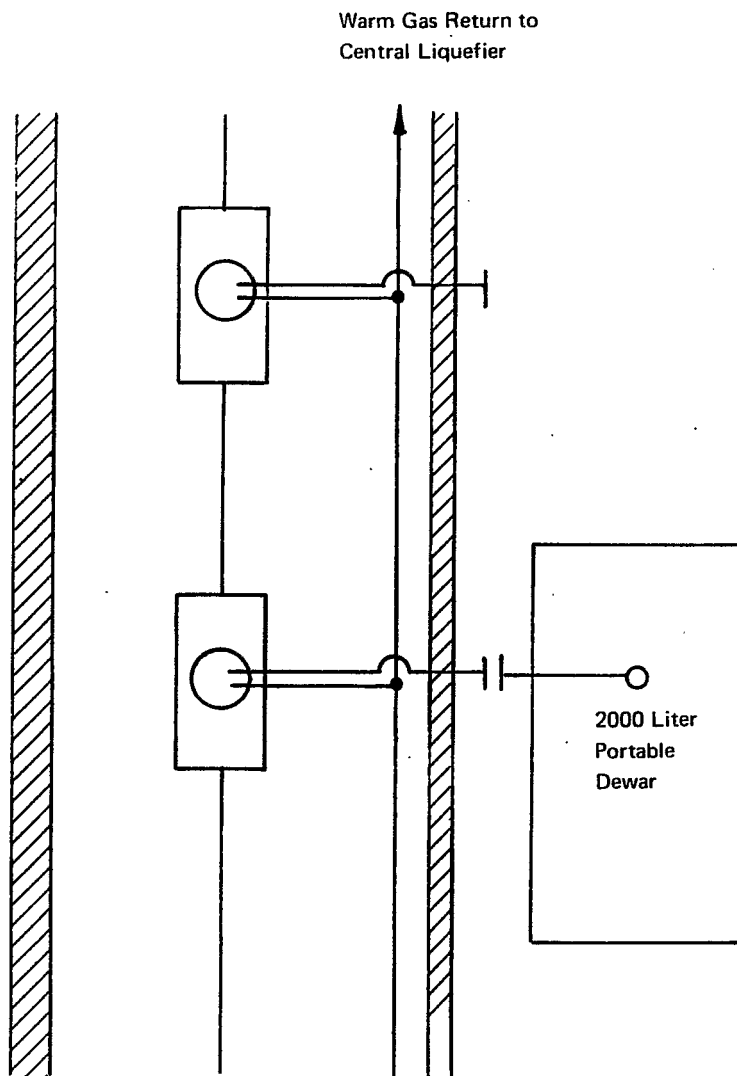


Fig. 4. Case 1 — central liquefier with transport of liquid in portable Dewars.

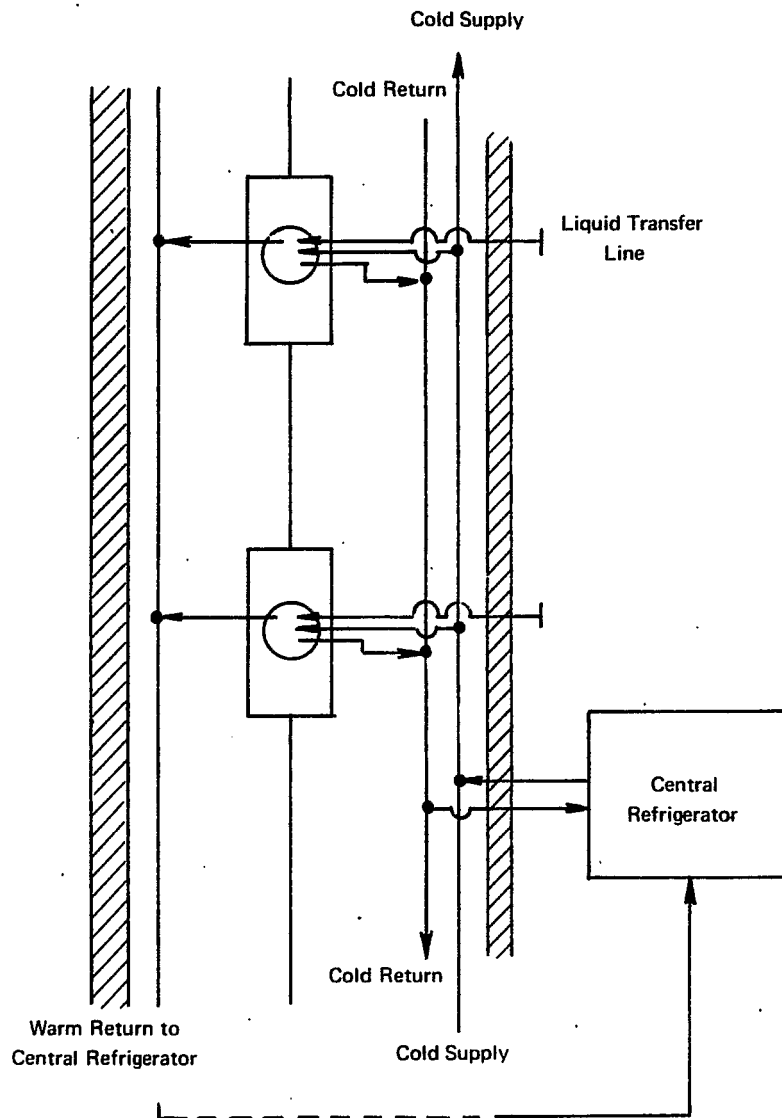


Fig. 5. Case 2 — four central refrigerators with continuous transfer of cold gas.

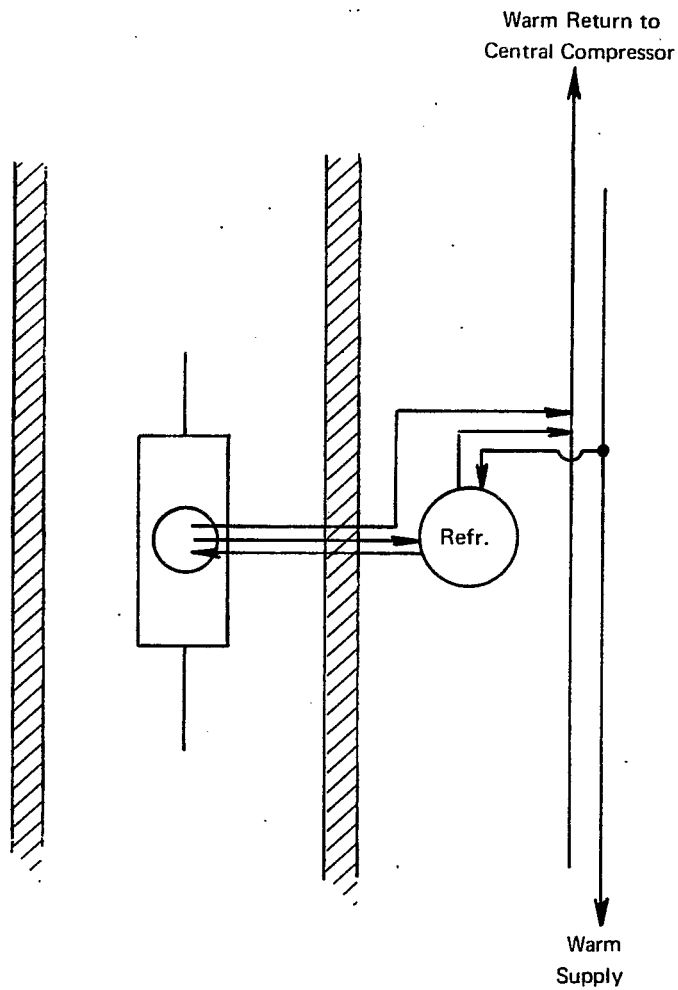


Fig. 6. Case 3b - individual refrigerator for each magnet; the refrigerator is located outside of the shielding.

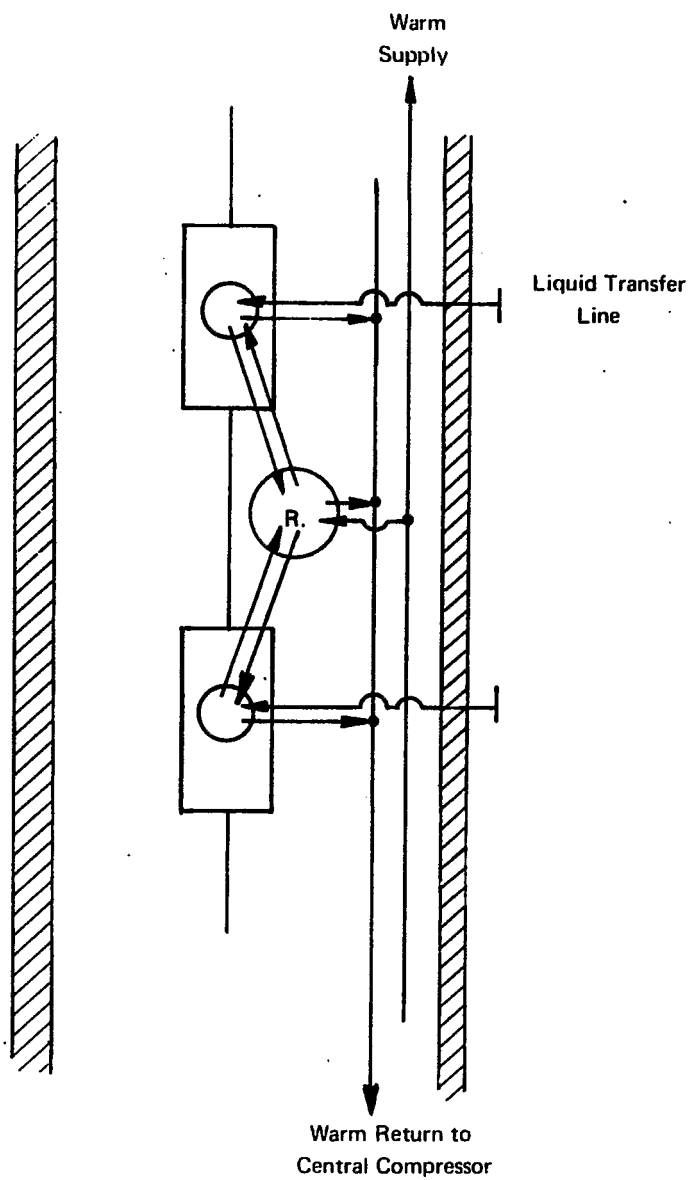


Fig. 7. Case 4a - small refrigerator servicing two magnets; the refrigerator is located within the shielding.

## CRYOGENIC ELECTRICAL LEADS\*

C.D. Henning  
Lawrence Radiation Laboratory  
Livermore, California

### INTRODUCTION

Recent developments in superconducting magnets and power transmission lines have prompted an interest in electrical leads to carry large currents into a liquid helium environment. These electrical leads allow an influx of heat to the low-temperature region both by conduction and by joule heating, causing evaporation of the cryogen. Accordingly, several attempts have been made to minimize this heat flux by adjusting the lead design and composition.<sup>1-13</sup> McFee<sup>1</sup> theoretically determined that an optimum length-to-area ratio exists for a thermally insulated lead - a short and heavy lead will conduct excessive heat, but a long and thin one will produce excessive joule heating. Mallon<sup>2</sup> presented design data for aluminum and sodium leads to supplement the data for copper given by McFee. Then Mercoureff<sup>3</sup> discussed the expected efficiency of leads made of materials which deviated from the Wiedemann-Franz law relating thermal and electrical conductivities.<sup>†</sup>

The first experimental data on cryogenic electrical leads were published by Sobol and McNichol<sup>4</sup> for small copper wires. They found that heat conduction from the copper wires to the surrounding helium gas greatly reduced the heat leak into the liquid helium. These results inspired Williams,<sup>5</sup> Fournet and Mailfert,<sup>6,7</sup> and Pippard<sup>8</sup> to make further studies on the effects of heat exchange between the conductor and evaporated gas. The first large electrical leads (150 A) were constructed by Deiness,<sup>9</sup> who further emphasized the importance of a large heat-exchange area between the conductor and effluent gas. Mathews et al.<sup>10</sup> pointed out the advantage of attaching the superconductor to the submerged portions of the electrical lead, thereby eliminating a source of joule heating. Extending this idea, Keilin and Klimenko,<sup>11</sup> and Henning<sup>12</sup> experimentally demonstrated the advantage of soldering superconductor along the lower portion of the electrical leads. The current could then transfer to the superconductor below the critical temperature, further reducing joule heating. Finally, Efferson<sup>13</sup> has presented design data on a very efficient lead which carried an optimum current of 1300 A.

The present trend clearly points to the development of larger electrical leads with increased efficiency. Full utilization of the refrigeration available in the effluent helium gas, a proper choice of conductor materials, and the attachment of superconductors to the lower portion of the leads should produce the greatest efficiency.

### GAS-COOLED LEADS

Many, and sometimes conflicting, analyses have been made to determine the optimum dimensions and performance of gas-cooled leads. Often the solution was unduly complicated, and without exception the observed heat leak was many times higher than that predicted. Now sufficient experimental data are available (Table I) to substantiate

---

\*Work performed under the auspices of the U.S. Atomic Energy Commission.

†Thermal conductivity times electrical resistivity equals  $2.45 \times 10^{-8}$  times the absolute temperature ( $W\Omega/^{\circ}K^2$ ).

clearly several conclusions. For each pair of leads, the helium loss from a Dewar was measured as a function of current. As shown in Fig. 1, the line drawn tangent to the data line C locates the point at which the least liquid helium is lost per ampere. Note that the optimum is very broad and that a current twice the optimum would not increase the loss unreasonably. Curves A and B in Fig. 1 demonstrate the advantage of increased gas flow. Both curves reflect the disadvantage of not having a superconductor attached to the lower portion. Whenever possible, all the effluent gas should be used to refrigerate the leads, and superconductors should be used when current is transported below the liquid level.

In Table I the liquid helium loss per kiloampere of optimum current was listed for two conditions: (1) with no current; and (2) with the optimum current in the leads. Note that the ratio of these two helium loss rates is near 0.6 on the average; Deiness<sup>9</sup> analytically predicted a ratio of 0.5, which is quite close to the observed value. Also note that the helium loss rate is independent of the warm-end temperature, as predicted by Keilin and Klimenko.<sup>11</sup> Cooling the upper end of the leads with liquid nitrogen enables the leads to be shortened, but does not affect the resulting helium loss.

Very seldom is the helium loss rate of the least efficient gas-cooled lead more than twice that of the most efficient. However, in all cases the observed helium loss was several times that predicted by analysis. When the average surface heat flux given in Table I is plotted against the helium loss rate a definite trend is evident; the helium loss rate decreases with decreasing surface heat flux. Those leads which have the greatest surface area in contact with the effluent gas introduced the least heat into the liquid helium. The conclusion is that present leads are not sufficiently good heat exchangers. Further evidence was supplied by a quick experiment with aluminum foil. Five 18 in. wide, 48 in. long sheets of 0.001 in. thick aluminum foil were rolled up and pushed into a 1 in. stainless-steel tube. The cross-sectional area was 0.58 cm<sup>2</sup> which was enough to carry 1000 A. (Normally 0.4 cm<sup>2</sup> of copper will carry 1000 A, but aluminum has a slightly higher room-temperature resistivity.) The helium loss measured for the aluminum foil was 0.49 liter/hr·kA at zero current. By multiplying by two (for a pair of leads) and dividing by 0.6 (ratio of  $m_0/m$ ), the predicted result in Fig. 2 was obtained, which is consistent with the general trend of decreasing helium loss with increasing conductor surface area.

In nearly every case, the Reynolds number for the effluent gas in a lead indicates laminar flow. As such, the Nusselt number for constant-wall heat flux does not vary with flow rate, and the mode of heat transfer from the conductor is pure conduction to the gas. Large surface areas in contact with the gas will improve the heat transfer process and the lead efficiency. Of course, mechanical mixing of the effluent gas by extended surfaces on the conductor will improve the heat transfer rate, as well.

Rather simple design equations can be obtained by interpreting the mathematical formulation of a gas-cooled electrical lead together with the experimental data in Table I. First, consider the mathematical formulation. As heat is conducted toward the liquid helium region, cold effluent gas abstracts some heat, depending upon the surface area, the local temperature difference, and the heat-transfer coefficient. It would be desirable to include the local heat-transfer rate in any analysis, but this would greatly complicate the solution. Keilin and Klimenko<sup>11</sup> included a parameter,  $\beta$ , in their analysis to crudely account for incomplete heat exchange. However, they then concluded that  $\beta$  was of minor importance.

For a lead of constant area A, the governing differential equation is written

$$\frac{d}{dx} \left( k \frac{dT}{dx} \right) - \frac{mc}{2A} \frac{dT}{dx} + \frac{I^2 \rho}{A^2} = 0$$

$$T = T_1 \text{ at } x = 0$$

$$T = T_h \text{ at } x = L, \quad (1)$$

where  $T_h$  and  $T_l$  are the high and low temperatures;  $x$  is distance;  $I$  is electrical current;  $k$ ,  $\rho$ ,  $A$ , and  $L$  are the thermal conductivity, electrical resistivity, cross-sectional area, and total length of the lead, respectively; and  $c$  and  $m$  are the heat capacity and total mass flow rate of the effluent gas. As a first approximation, we can integrate each term in Eq. (1) between the high and low temperatures. However, the integral of the first term, representing conducted heat, is relatively small. Very little heat is conducted into the liquid helium at one end, and it has been shown<sup>12</sup> that for an optimum lead the temperature gradient is zero at the upper end, corresponding to zero heat conduction. Then the remaining terms (joule heating and heat carried away by the gas) are nearly equal over the integrated length of the lead. This conclusion is experimentally substantiated by comparing the values in Table I of the joule heating and available refrigeration:

$$I^2 L/A = \frac{m}{2} \int_{T_l}^{T_h} \frac{c}{\rho} dT \quad (2)$$

The above equation can be simplified by substituting an average resistivity  $\bar{\rho}$ , and taking the specific heat of helium gas  $c$  to be constant; also, the helium loss rate  $m$  varies directly with the current, so that the right side of the following equation should be constant for a given lead material and temperature difference:

$$I L/A = \frac{(m/I)}{2\bar{\rho}} c (T_h - T_l) \quad (3)$$

In view of the noncritical nature of the optimum current and the unpredictable efficiency of a new lead design, the above equation is adequate for calculating lead dimensions. The helium loss rate for the leads can be estimated from Table I, although the efficiency will increase somewhat when the effluent gas caused by other system losses is significant.

A typical design procedure would be to estimate the helium loss due to the leads by checking Table I. Add to this helium loss the other losses in the system to determine a total mass flow rate to be used in Eq. (3) along with the average resistivity of the lead material. Alternately, the ratios of the second-to-last column in Table I can be used to calculate the length-to-area ratio for the optimum current. This is possible only if the average resistivity is the same and the helium loss is largely due to the leads. Generally, an area of  $0.4 \text{ cm}^2/\text{kA}$  of copper has been found to be adequate for leads around 3 to 4 ft long. The area needed for other materials may be adjusted according to their room-temperature resistivity.

Another interesting relationship can be derived from Eq. (3) for the voltage drop across a lead, which should be nearly constant for a given lead efficiency and temperature difference:

$$E = I \bar{\rho} \frac{L}{A} = \left( \frac{m}{2I} \right) c (T_h - T_l) \quad (4)$$

This constant voltage drop is closely approximated in Table I.

#### FUTURE DEVELOPMENTS

From the preceding discussion it is evident that the lead dimensions are easily calculated and are not particularly critical. Even a simple copper or nickel tube approaches the minimum helium loss rate of the most sophisticated lead. For a small experiment the most simple configuration may be best, but for large leads careful design is mandatory. Superconducting magnets are using leads of 6000 A capacity at present.<sup>14</sup> In the future, superconducting power transmission lines may require even larger leads.<sup>15</sup>



Certainly these two applications alone are sufficient to inspire new efforts.

Possible areas for future exploration include the use of new materials of high electrical and low thermal conductivity. Also, increasing the conductor surface area exchanging heat with the effluent gas should be attempted; the aluminum foil leads discussed earlier may represent such an improvement. Keilin and Klimenko<sup>11</sup> predict a 50% reduction in the helium loss rate by attaching superconductor along the lower portion of the leads. This improvement was not fully realized experimentally,<sup>11,12</sup> possibly because of the inefficiency of the leads. More efficient leads with greater heat-exchange area may use superconductors to greater advantage.

Another area to explore is off-optimum design. Systems with short duty cycles use less liquid helium if the leads are operated at more than the optimum current. When the operation time is quite short, transient effects may prove to be useful. Experimentally we observe that a pair of leads will require 5 to 30 min to reach equilibrium. It is possible to overload greatly a lead for a short time without damage or excessive helium loss, and that may be useful for special systems.

The advent of the gas-cooled electrical lead has reduced the liquid helium loss by a factor of thirty when transporting electrical current into a low-temperature environment. Future improvements should further reduce the helium loss, but probably not to the same degree.

#### ACKNOWLEDGMENT

Thanks are expressed to R.L. Nelson, A.R. Taylor, C. Ward, and C. Gilmore for their helpful suggestions and assistance with experiments.

#### REFERENCES

1. R. McFee, Rev. Sci. Instr. 30, 102 (1959).
2. R.G. Mallon, Rev. Sci. Instr. 33, 564 (1962).
3. W. Mercouroff, Cryogenics 3, 171 (1963).
4. H. Sobol and J.J. McNichol, Rev. Sci. Instr. 33, 473 (1962).
5. J.E.C. Williams, Cryogenics 3, 234 (1963).
6. G. Fournet and A. Mailfert, Compt. Rend. (Paris) 257, 4153 (1963).
7. G. Fournet and A. Mailfert, Compt. Rend. (Paris) 258, 103 (1964).
8. A.B. Pippard, Cryogenics 5, 81 (1965).
9. S. Deiness, Cryogenics 5, 269 (1965).
10. P.W. Mathews, T.L. Khoo, and P.D. Neufeld, Cryogenics 5, 213 (1965).
11. V.E. Keilin and E. Yu. Klimenko, Cryogenics 6, 222 (1966).
12. C.D. Henning, Lawrence Radiation Laboratory, Livermore, Report UCRL-14775 (1966).
13. K.R. Efferson, Rev. Sci. Instr. 38, 1776 (1967).
14. A.G. Prodell, private communication.
15. J.K. Hulm, Chem. Engr. 72, 109 (1965).

TABLE I. PERFORMANCE OF ELECTRICAL LEAD PAIRS

Optimum Current	Lead Description	Helium Loss No. Current $m_0$	(1 liters/hr-kA)*		Voltage Drop Pair (mV)	Joule Heating (watts)	Refrigeration Available*** $mc(T_h - T_1)$ (watts)	Avg. Surface Heat Flux (watts/cm <sup>2</sup> )	I L/A (kA/cm)	Reference
			Optimum Current m	Ratio $m_0/m$						
1	#34 AWG copper wire, 25 cm long; LN precooling	1.9	3.3	0.58	-----	----	0.2	----	125 LN precooled	4
10	Helical Cu strip, 0.79 cm wide, 0.018 cm thick, lead length 23 cm	2.04	4.75	0.43	-----	----	2.9	----	----	5
150	High-purity Ni tubes, 22 cm long; 0.42 cm i.d., 0.56 cm o.d.	1.46	2.86	0.51	50	7.5	26	0.06	33 Ni tube	9
100	10 - #22 AWG Cu wires; length unknown	3.15	4.5	0.70	-----	----	27	----	----	11
200	1/4-in. o.d. phos-deox Cu tube, 0.030-in. wall, 55-in. long; superconductor attached and only half boil-off through leads	2.88	5.76	0.50	-----	----	70	0.19	210	12
200	Cu screen of 0.01-in. wire; 200 wires vertical and horizontal; 32-in. long; superconductor attached	2.3	3.25	0.70	195	39	40	0.05	162	Present
2000	Folded Cu sheet in sq. stn. steel tube; 0.01-in. thick, 12-in. wide, 48-in. long. Superconductor attached.	3.1	4.7	0.66	210	420	550	0.056	315	Present
500	1920 Cu wires, #38 gage and 60 cm long; superconductor attached	1.74	2.72	0.64	225	113	110	0.012	200	13
1300	5120 Cu wires, #38 gage and 60 cm long; superconductor attached	1.62	2.71	0.60	225	293	286	0.012	195	13

\* The helium loss for insulated copper leads is 84 liters/hr-kA (McFee<sup>1</sup>).

\*\*\* The upper temperature  $T_h$  was greater than room temperature in several cases because the power cable heated the top of the lead.

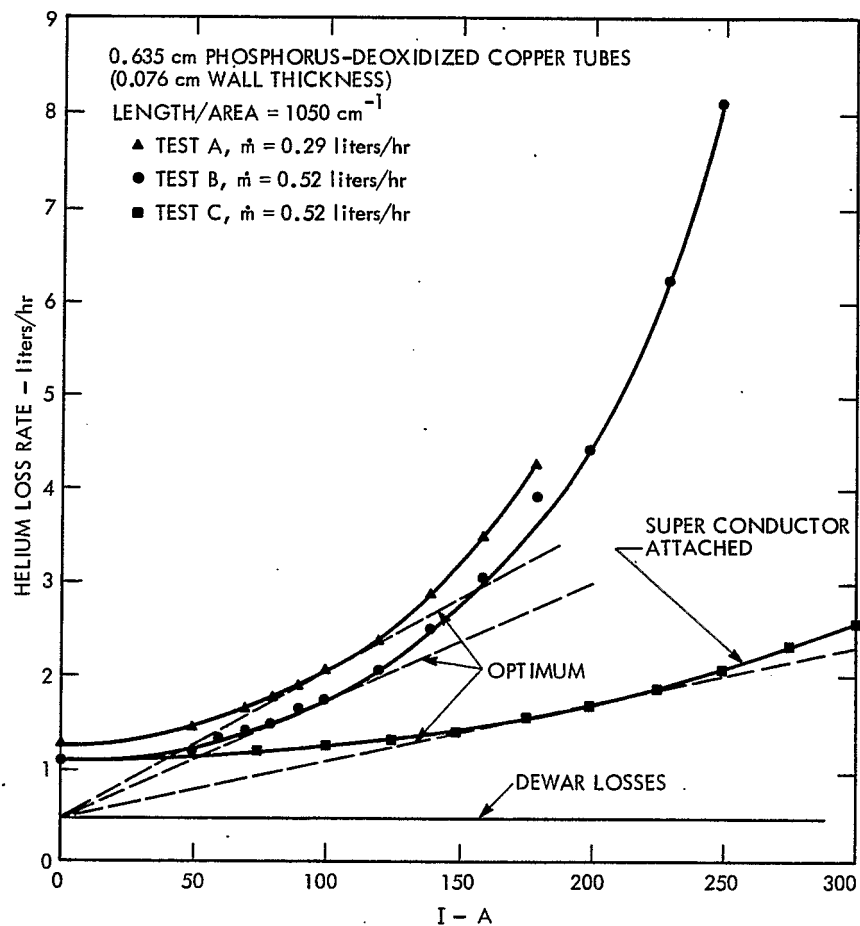


Fig. 1. Experimental determination of the optimum current for an electrical lead.

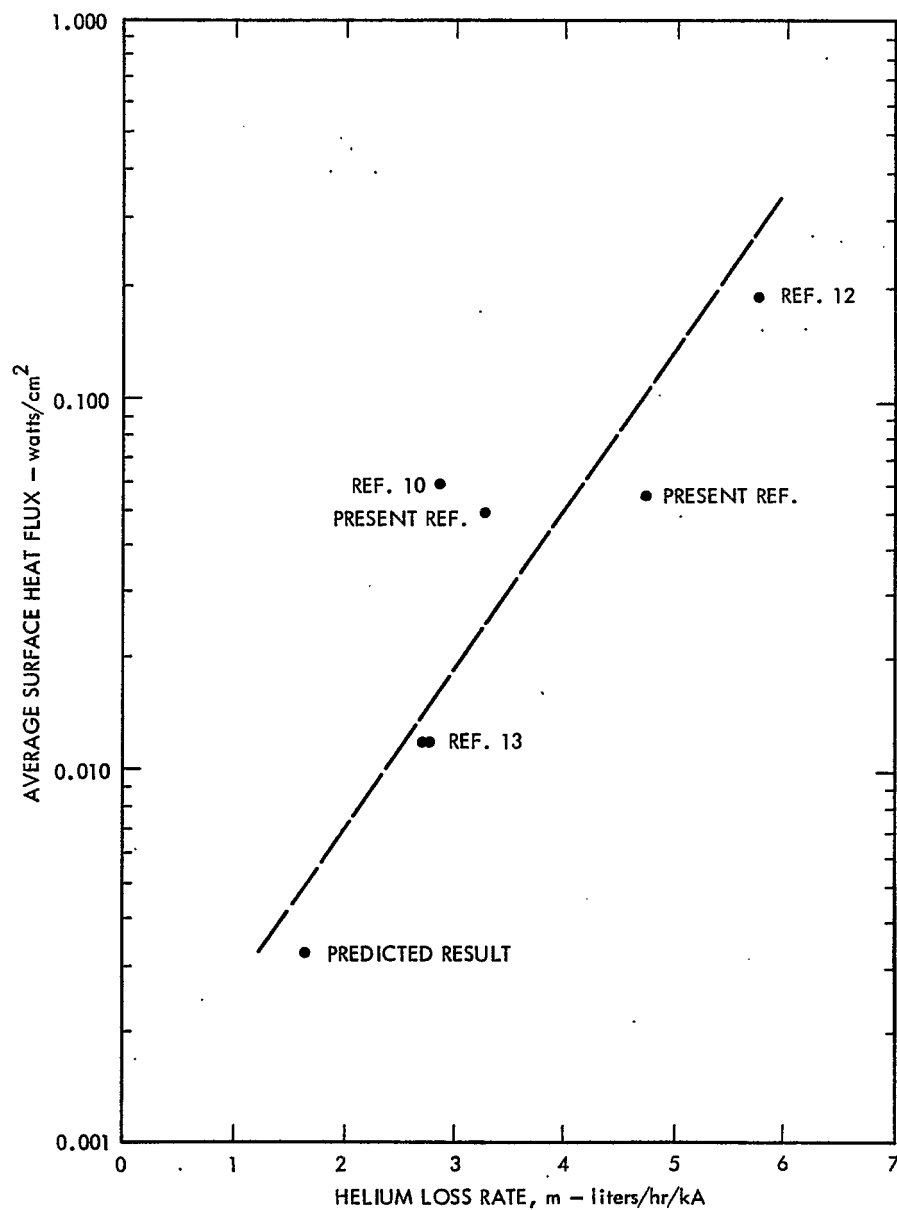


Fig. 2. Helium loss rate as a function of average surface heat flux.

## LOW TEMPERATURE METALS\*

A. Hurlich  
General Dynamics/Astronautics  
San Diego, California

Before we consider how low temperatures affect the engineering properties of specific metals and alloys, we should review the general effects of low temperature upon the properties of metals. As the temperature is lowered, the hardness, yield strength, tensile strength, modulus of elasticity, and fatigue resistance of almost all metals and alloys increase.

Unfortunately, many engineering metals and alloys become embrittled at reduced temperatures so that structures fabricated from them fracture or shatter unexpectedly at low temperatures when loaded to stress levels at which performance would be satisfactory at normal temperatures. Brittle fracture is generally characterized by little or no deformation of the metal in the vicinity of the fracture, or by a distinctive fracture having bright crystalline appearing facets.

Considerable confusion has, unfortunately, existed about the nature of the behavior that is the opposite of brittle. Some refer to this as "ductile," while others use the term "tough." Although both terms are correct, they do not describe the same characteristic of a material's behavior.

Ductility is commonly expressed in terms of percentage elongation in gauge length, and reduction in area, of a tensile specimen that is tested to fracture. Ductility is thus a measure of the deformation undergone by a smooth test specimen of uniform cross section that is slowly and uniaxially stressed until fracture occurs. Toughness, on the other hand, is a characteristic that permits a metal to absorb energy by undergoing plastic deformation rather than fracturing in the presence of high stress concentrations (cracks or notches) and multiaxial stress distributions, under high rates of loading, or at low temperatures.

It is possible for a metal to exhibit high ductility in a tension test, yet behave in a catastrophically brittle fashion in service at moderate temperatures; witness the plague of fractures in Liberty ships during World War II, when many ship plates broke apart with virtually no deformation anywhere near the fracture, and yet tensile test coupons removed from adjacent areas exhibited 40% elongation and 60% reduction in area.

While ductility is measured as deformation occurring in a tension test of a uniaxially loaded smooth specimen, toughness is commonly measured in terms of the energy absorbed in breaking, under impact loading, a test specimen that is notched with a circular or sharp groove on the side where fracture initiates. At a given test temperature, a metal may manifest high ductility in the tensile test and practically no toughness in a notched-bar impact test. Consequently any statement regarding the effects of low temperature upon the tendency of metal to behave in a ductile or brittle fashion must be qualified by the conditions under which the fracture is produced.

In general, metals fall into two distinct classes with respect to the influence of low temperatures upon their ductility and toughness: a relatively small class of

---

\* Reprinted with permission from Chemical Engineering, November 25, 1963, copyright 1963, McGraw-Hill Publishing Co., Inc.

metals that retain a high order of ductility and resistance to brittle fracture down to very low temperatures, and a much larger class of metals that, at some temperature or in some range of temperature, undergo a transition from ductile to brittle behavior. As pointed out above, the temperature level where this transition in fracture behavior occurs is influenced by the test conditions.

The metals that remain ductile at extreme subzero temperatures include nickel, copper, aluminum, lead and silver, among others. These metals all have a face-centered cubic crystal structure, and ductility at low temperatures appears to be a characteristic common to them. The explanation of this phenomenon is as yet obscure. Metals having a body-centered cubic structure (iron, chromium, molybdenum, tantalum, tungsten, etc.) undergo a marked decrease in ductility over a range of temperatures (upper chart of Fig. 1) and the range of transition temperatures may occur from well above boiling-water temperature to several hundred degrees below 0°F. Several common metals - for instance, magnesium, zinc, titanium and beryllium - have a hexagonal crystal structure, and these metals, except for titanium, are generally brittle or have limited ductility at room and at moderately elevated temperatures. Titanium and several of its alloys may exhibit high ductility and toughness down to very low temperatures.

The different effects of low temperatures upon the ductility of metals is explained in terms of the influence of low temperatures upon two characteristics of the metal. These are the flow strength (stress level at which plastic yielding starts) and the fracture strength (stress level at which undeformed metal fractures). Low temperatures cause an increase in both flow and fracture strengths of metal, but they may increase at characteristically different rates. In the cases of aluminum and copper, as well as other face-centered cubic metals, the fracture strength increases at a rate equal to or greater than the flow strength. Greater spreads between the flow and fracture strengths permit more deformation to occur prior to fracture; hence these metals retain or increase their ductility at low temperatures.

Iron, however, exhibits a more rapid increase in flow strength than in fracture strength as the temperature is lowered. As the spread between flow and fracture strengths decreases, less plastic deformation occurs. Finally, at some reduced temperature, fracture takes place with no plastic deformation, and the flow and fracture strengths coincide. The two charts of Fig. 1 show how the low temperature affects the ductility and flow strength of several metals.

In the metals that undergo a transition from ductile to brittle performance with decreasing temperature, it is found that a large number of factors may have a marked influence on the temperatures where this transition occurs. As discussed earlier, at a given test temperature a metal may be ductile in the tension test and brittle in an impact test.

In the case of mild steel, Fig. 2a shows the wide variations in transition temperature revealed in torsion, tensile and impact tests. Heindlhofer<sup>1</sup> explained the difference in transition behavior in the three tests in terms of the ratios between maximum principal and shearing stresses.

Other mechanical factors that influence the temperature level where brittle fracture transitions occur are geometry of test specimen, rate of load application, and the presence and sharpness of notches. Large or wide specimens, as illustrated in Fig. 2b, tend to raise the temperatures of brittle fracture because of the greater degree of restraint imposed upon the deformation capabilities of the material. Increasing the rate of load application also raises the temperature of transition from ductile to brittle behavior, as shown in Fig. 2c.

---

1. K. Heindlhofer, Trans. AIMME 116, 232 (1935).

Armstrong and Gagnebin<sup>2</sup> studied the effect of increasing the sharpness of notches upon the transition from ductile to brittle fracture in notched-bar impact tests. The notched-bar impact test, by combining complex stress distributions, high rates of loading and a sharp notch, provides a sensitive index of the tendency of materials to perform in a brittle fashion at extreme subzero temperatures.

In addition to crystal structure, a considerable number of metallurgical factors influence the low-temperature toughness of alloys; for example, increasing amounts of nickel up to 13% significantly raise the notched-bar impact properties of low-carbon steels (Fig. 3a). For this reason, low-carbon alloy constructional steels containing up to 9% nickel are commercially employed for cryogenic-fluid storage tanks and transport equipment. Similarly, increasing the carbon content of alloy steels lowers the toughness and raises the ductile-to-brittle transition temperature of alloy steels as shown in Fig. 3b.

Microstructure also greatly affects the low-temperature mechanical properties of alloys, especially toughness. In the case of heat-treatable low- and medium-alloy steels, heat treatment to a tempered martensitic microstructure develops the best combination of strength and toughness at subzero temperatures, with tempered bainite being less tough, and tempered pearlite still less tough, at temperatures below approximately 50°F (see Fig. 3c).

Nonmetallic inclusions, intermetallic compounds, and other impurity constituents that may form or precipitate at grain boundaries, will reduce the toughness of metals, especially at low testing temperatures.<sup>3</sup> We have determined at General Dynamics/Astronautics that impurity levels causing no apparent embrittlement in titanium alloys when tested at room temperature may cause excessive embrittlement at extreme subzero temperatures.

The embrittlement effects of oxygen, nitrogen, sulfur and phosphorus in carbon and alloy steels have been long recognized<sup>4-6</sup> and attempts are made to keep these impurities at low levels in quality steels intended for critical service applications.

Grain size also has a marked effect upon the toughness of metals at reduced temperatures. At any given strength level, fine-grained metals and alloys generally possess significantly higher notched-bar impact properties than coarse-grained metals. They also retain higher toughnesses down to lower testing temperatures. The effect of grain size upon the impact resistance of a heat-treated low-alloy steel is shown in Fig. 4.<sup>7</sup>

Many other factors also influence the notch-toughness of metals. Wrought products (sheet, plate, forgings, etc.) are generally tougher in the direction longitudinal to the direction of hot or cold working than in the transverse direction. However, in thick plates or forgings, the toughness in the direction through the thickness (short transverse) is often considerably reduced. Tensile ductility generally parallels this

- 
2. T.N. Armstrong and A.P. Gagnebin, Trans. ASM 28, 1 (1940).
  3. S.A. Herres and C.H. Lorig, Trans. ASM 40, 775 (1948).
  4. C.H. Lorig and A.R. Elsea, Trans. AFA 55, 160 (1947).
  5. C.E. Sims and F.B. Dahle, Trans. AFA 46, 65 (1938).
  6. F.T. Sisco, Alloys of Iron and Carbon, Vol. II, Properties, p. 468 (Mc-Graw Hill, New York, 1937).
  7. L.D. Jaffe, Trans. ASM 40, 805 (1948).

same behavior. Cast metals and alloys generally exhibit somewhat lower toughness than wrought products at the same strength levels, but are less prone to directional effects.

The lower toughness of cast metals is attributable to the generally coarser grain structure, segregation of alloys, intermetallic compounds and nonmetallic inclusions around grain boundaries (or around the primary solidification structure) and to casting defects. Hot working generally eliminates these casting defects, refines and homogenizes the structure and improves the ductility and toughness.

Similarly, heat treatments can drastically affect both ductility and toughness at given strength levels by changing grain size and the size, shape and distribution of phases and intermetallic compounds.

As should be evident from the preceding discussions, welding produces a cast structure and can exert a profound effect upon the ductility and toughness of metals. This is especially true at reduced temperatures. Welding introduces geometrical factors that promote brittle behavior, notches and stress concentrators. It also causes complex stress distributions resulting from weld undercutting, changes in section thickness at the weld crown on one or both surfaces, and from slag entrapment, porosity, or weld cracks. Some of the metallurgical structures thus formed may be very notch-brittle and prone to crack propagation, especially if minute flaws occur in such zones.

Another possible source of weld embrittlement is contamination by atmospheric gases in contact with the hot solid or liquid metal in the weld zone. Titanium, for example, can be severely embrittled by the absorption of oxygen and nitrogen during welding. This metal and its alloys must be welded either in vacuum or inert atmosphere chambers, or with inert atmosphere shielding applied to both sides of the weld joint when welding in air.

Steel weldments may undergo severe reductions in ductility and become prone to cracking by absorption of hydrogen resulting from the decomposition of moisture in organic electrode coatings or in the welding atmosphere. Special low-hydrogen electrode coatings have been developed for the welding of steels subjected to critical service applications. Post-welding stress-relieving heat treatments are often applied to weldments not only to relieve stresses but also to temper or to age brittle, heat-affected zones to improve their toughness.

#### TESTS FOR MATERIAL SELECTION

While the standard tensile test, if conducted at sufficiently low temperatures, shows the effect of reduced temperatures upon the behavior of metals, it is not by itself sufficient or satisfactory for use in selecting materials for low-temperature applications. As described previously, the simple, uniaxial stress distribution, absence of stress concentrators, and low rate of loading, enhance the tendency toward ductile behavior in the tension test. A number of other tests were consequently developed to evaluate the embrittlement of metals as influenced by metallurgical, mechanical, and physical conditions of the test. Practically all of these tests possessed at least two features in common: stress concentrators and multiaxial stress distributions, both of which result from notches located within the test section.

The earliest tests (between the turn of the century and World War I) generally involved impact since at that time high-speed loading was considered to be a major factor in brittle fracture. The keyhole and V-notch Charpy and the Izod impact tests are representative of the early tests used to evaluate the effects of low temperature upon the behavior of metals.

The V-notch Charpy impact test is the most widely used of the three tests and



finds extensive use to this day. Here a 60° V-notch is machined across one face of the specimen. The bar is broken by being supported at both ends and struck by a pendulum-supported weight impacting the face opposite the notch. The energy absorbed in rupturing the bar is determined by measuring the loss in kinetic energy of the pendulum.

The notched-bar impact test is generally considered to be qualitative in nature. Materials specifications incorporating notched-bar impact-test requirements have been developed for many critical applications. Generally, requirements have been established on the basis of experience gained by correlating notched-bar impact properties with simulated or actual service behavior of full-size or scale-model structures.<sup>8,9</sup>

A group of researchers at Watertown Arsenal<sup>10</sup> has attempted to employ the V-notch Charpy impact test quantitatively in materials specifications covering low- and medium-alloy steels required for critically stressed applications at room and moderately low temperatures. The approach is based upon the equivalence of low temperature and high strain rate in causing transition from ductile to brittle fracture (Fig. 2c). From an estimation of the maximum strain rate and lowest service temperature to which an engineering structure or part will be subjected, it is possible to calculate, or pick off from a special graph the temperature at which a V-notch Charpy impact-test specimen should be tested to behave the same as regards ductile or brittle fracture as the part in question. Several Army Ordnance specifications based on this approach have since withstood the searching test of time.

While the notched-bar impact test is very useful for evaluating the toughness of forgings, plate, and bar stock, it is not applicable to very thin sheet materials such as are often employed in aerospace vehicles and airborne pressure vessels. Another type of test specimen that has been employed to evaluate the brittle-fracture tendency of heavy sections of steel, and more recently of sheet alloys, is a tensile test specimen notched on both sides. In round specimens, the notch is circumferential.

A variety of notches has been employed by various investigators, with stress concentrations ranging from 3 for mild notches to as high as 18 for severely notched specimens (ASTM and NASA standard specimens). At General Dynamics/Astronautics, we have standardized on a notched tensile-test specimen having a stress concentration factor of 6.3, since this specimen has been found to yield results that correlate with the fracture behavior of full-scale, thin-skinned cryogenic pressure vessels and with the behavior of large specimens containing complex welded joints.<sup>11,12</sup> With materials that are notch-tough, the effect of the biaxial stress distribution at the notched section is to increase the effective strength of the material, and the notched tensile strength may range from 1.0 to approximately 1.5 times the smooth tensile strength. In notch-brittle or notch-sensitive steels, the effect of the notch is to induce premature brittle fracture, and the notched tensile strength will be less than the smooth tensile strength. The ratio of the two strengths thus serves as an index of the brittle fracture characteristics of materials.

- 
8. A. Hurlich, ASTM Special Tech. Publ. No. 158, p. 262 (1954).
  9. A. Hurlich and A.F. Jones, Metal Progress 71, 65 (1957).
  10. L.D. Jaffe et al., SAE Journal 59 (Mar. 1951).
  11. J.F. Watson, J.L. Christian, T.T. Tanalski, and A. Hurlich, ASTM Special Tech. Publ. No. 302, p. 129 (1961).
  12. A. Hurlich, ASTM Special Tech. Publ. No. 287, p. 215 (1960).

More recently, with the development of the concepts of fracture mechanics,<sup>13,14</sup> it has become possible to employ notched tensile tests in a quantitative manner to determine the critical crack-extension force, the critical crack length beyond which catastrophically rapid crack propagation ensues, or the stress level where a cracklike flaw or defect will propagate to result in failure.

Other tests of importance in evaluating the mechanical properties of materials at reduced temperatures include both notched and unnotched fatigue tests, bend tests (particularly of weld joints), and notched and unnotched tensile tests of fusion weldments.

Notched and unnotched tensile fatigue, bend and impact tests can be readily performed over a range of temperatures down to the boiling point of liquid helium ( $-452^{\circ}\text{F}$ ) to evaluate the effect of low temperatures upon the brittle fracture characteristics of metals. For the sake of convenience and economy, low-temperature mechanical-property tests are generally conducted at some of the following temperatures:  $-100^{\circ}\text{F}$  (dry ice and alcohol);  $-320^{\circ}\text{F}$  (liquid nitrogen); or  $-423^{\circ}\text{F}$  (liquid hydrogen).

Temperatures between room and  $-100^{\circ}\text{F}$  can be achieved and maintained constant by adding appropriate amounts of dry ice to the alcohol as may be needed.

A typical test facility for conducting tensile tests at temperatures down to that of liquid hydrogen is shown in Fig. 5. The liquid hydrogen is contained in a double-walled, vacuum-jacketed Dewar, surrounded by a liquid-nitrogen bath that in turn is insulated with polyurethane foam. Pull rods extend through Teflon-sealed holes in the bottom and top cover of the liquid-hydrogen Dewar. Hydrogen gas boil-off is vented through a flexible steel hose attached to the cover. The test equipment is located in a room fitted with a sealed sheet-steel ceiling pierced with vents fitted with explosion-proofed motors and fans to provide rapid air changes within the room. All electrical connections more than a few feet off the floor are explosion-proofed, while a sheet-steel room having positive air pressure is erected round the console of the tensile machine since the many electrical connections in this unit could not be explosion-proofed. More than 15 000 tests have been performed with liquid hydrogen in this facility at General Dynamics/Astronautics since 1959 without a single serious incident.

A large outdoor liquid-hydrogen test facility is shown in Fig. 6. This installation includes a tensile-test facility (far left), larger bend and compression-test fixtures (center) fitted with double-walled vacuum-jacketed liquid-hydrogen chambers, and a cryogenic test setup for cyclic fatigue testing of the large coupons of thin materials used for cryogenic propellant storage. In all of these test fixtures, loading is applied by means of hydraulic load cells calibrated to read loads directly.

---

13. G.R. Irwin, Naval Res. Lab. Report 4763 (1956).

14. G.R. Irwin, J.A. Kies, and H.L. Smith, Proc. ASTM 58 (1958).

## METALS FOR CRYOGENIC APPLICATIONS

References 15 to 20 give data on a variety of low-temperature materials. A very comprehensive compilation of data on the mechanical and physical properties of a large number of metallic alloys, as well as nonmetallic materials, is included in the "Cryogenic Materials Data Handbook." This handbook was initially compiled by the Cryogenic Engineering Laboratory, National Bureau of Standards, Boulder, Colorado, but it now being kept up to date by the Martin Co., at Denver, under contract to the Aeronautical Systems Division, Air Force Systems Command, Wright-Patterson Air Force Base, Dayton, Ohio.

Typical of such data is the accompanying table of results obtained at General Dynamics/Astronautics on sheet nickel alloys.

Figure 7 lists the more important steels, aluminum, nickel, and titanium-base alloys that are suitable for critically stressed applications at reduced temperatures. It places them in order corresponding to the lowest temperatures at which they may be reliably used. This method of presentation, borrowed from J.M. Hodge,<sup>21</sup> provides a ready reference to the comparative usefulness of metallic alloys at low temperatures. It should be borne in mind, however, that high toughness is not always an essential requirement for low-temperature applications. Many parts subjected to extreme subzero temperatures are not subjected to high stresses, multiaxial stress distributions, or impact loading. Magnesium-alloy castings, which are extremely notch brittle, have served very satisfactorily as pump housings, valve bodies, and in other applications at liquid-hydrogen temperatures. The alloys listed in Fig. 7 were selected on the basis of their suitability for critically stressed applications where notches, sharp changes in section, complex stress distributions, and high rates of loading may be involved in addition to the reduced operating temperatures. Another factor that entered into their placement in Fig. 7 was consideration of the alloys' weldability, and toughness of the weld joints at reduced temperatures.

The various alloys will be briefly discussed in the following sections where the low-temperature ranges are divided into four classifications for uses down to -50°F, to -150°F, to -320°F, and below -320°F.

Metals for use to -50°F. The temperature range from ambient down to -50°F is of interest because it essentially encompasses the minimum temperatures encountered on the earth's surface - as well as the boiling temperatures of ammonia, propane and freon, materials that are of considerable interest to the chemical processing and refrigeration industries.

Most of the standard constructional carbon steels such as the ASTM A7, A36, or A373 grades cannot be reliably used at temperatures down to -50°F. These steels are

- 
15. M.P. Hanson, G.W. Stickley, and H.T. Richards, ASTM Special Tech. Publ. No. 287, p. 3 (1960).
  16. J.F. Watson, J.L. Christian, and J. Hertz, Electro-Technology (Sept.-Nov. 1961).
  17. J.L. Christian and A. Hurlich, ASD-TDR-62-258, Part II (1963).
  18. J.L. Christian and J.F. Watson, Advances in Cryogenic Engineering, Vol. 7 p. 490 (Plenum Press, New York, 1962).
  19. J.L. Christian, ASD-TDR-62-258 (1962).
  20. J.E. Campbell and L.P. Rice, ASTM Special Tech. Publ. No. 287 (1960).
  21. J.M. Hodge, ASTM Special Tech. Publ. No. 302, p. 96 (1961).

not subject to notched-bar impact test requirements and may or may not be aluminum-killed to develop fine grain sizes. Their cooling rates during processing are not controlled. They may vary from tough to brittle at ambient temperatures. There are, however, several fine-grained carbon steels available for low-temperature applications down to  $-50^{\circ}\text{F}$ . These are the ASTM A334-61T, A333-61T and A420-61T grades that are required to meet  $-50^{\circ}\text{F}$  notched-bar impact-test requirements. In addition, silicon-killed fine-grained carbon steels of the ASTM A-201 and A-212 grades have good toughness properties down to  $-50^{\circ}\text{F}$ , but are not required to meet notched-bar impact tests except when specified to meet the test requirements of A-300. In the latter case, they may be and are widely used in refrigeration and transport equipment.

Quenched and tempered low-alloy steels are, of course, applicable at temperatures down to  $-50^{\circ}\text{F}$ , and many of them are suitable for use at temperatures down to  $-100^{\circ}\text{F}$  or  $-150^{\circ}\text{F}$ , but these will be discussed more fully in the next section.

Practically all aluminum and titanium alloys may be used in critically stressed applications at temperatures down to  $-50^{\circ}\text{F}$ , except for some of the highest-strength aluminum alloys such as 7178-T6 and 7075-T6. These are not recommended, especially where sharp changes in section, complex stress distributions or impact loads are involved. Similarly, the all-beta 13V-11Cr-3Al-titanium alloy (120VCA) and the 8 Mn-titanium alloy tend to be notch-brittle at moderately reduced temperatures.

Nickel and copper-base alloys are virtually all suitable for use at temperatures down to  $-50^{\circ}\text{F}$ , and generally much lower.

Metals for use to  $-150^{\circ}\text{F}$ . Low-alloy steels suitable for use at temperatures down to  $-150^{\circ}\text{F}$  fall into two categories: quenched and tempered steels having essentially fine-grained, tempered, martensitic microstructures, and nickel-alloyed ferritic steels. Most of the lower carbon (0.20 to 0.35% C) low-alloy steels having sufficient hardenability to achieve martensitic microstructures through the section thickness when either water- or oil-quenched are, after tempering at appropriate temperatures, sufficiently tough for most critical service applications at temperatures down to at least  $-100^{\circ}\text{F}$ . Many of these steels contain several alloying elements such as manganese, nickel, chromium, molybdenum and vanadium. Several contain small quantities of zirconium or boron, the latter having a potent effect on increasing hardenability. These steels include proprietary grades such as T-1 and N-A-XTRA, among others, as well as standard grades such as AMS 6434, 4130, 4335, etc.

Although the above steels are usable to at least  $-100^{\circ}\text{F}$ , they may, depending upon steel-making practice, tempering temperature, etc., undergo the tough-to-brittle transition at some temperature between  $-100^{\circ}\text{F}$  and  $-150^{\circ}\text{F}$ . For more reliable performance at the lower end of this temperature range, it is necessary to employ somewhat more highly alloyed quenched and tempered steels such as HY-80 or HY-TUF, both of which are proprietary steels.

Low-carbon  $3\frac{1}{2}\%$  nickel steel is widely used in large land-based storage tanks to contain liquefied gases at temperatures down to  $-150^{\circ}\text{F}$ . This steel falls under ASTM A203, Grades D and E, and is subject to impact tests in accordance with the requirements of A-300.

As shown in Fig. 7, a large number of aluminum, nickel, and titanium-base alloys are suitable for critically stressed applications at temperatures down to  $-150^{\circ}\text{F}$  and lower. The high-strength 7079-T6 aluminum alloy may be used down to  $-200^{\circ}\text{F}$ , but is not recommended for lower-temperature applications. In the case of titanium alloys, the 6Al-6V-2Sn-Ti alloy in the heat-treated condition may be used at temperatures down to  $-40^{\circ}\text{F}$ , and the 16V-2.5Al-Ti alloy may be used down to  $-100^{\circ}\text{F}$ , but neither is recommended for use at temperatures lower than these.

Metals for use at -320°F. Increasing the nickel content of low-carbon steel progressively reduces the temperature of transition from ductile to brittle fracture as shown in Fig. 3a. In the normalized and tempered condition, a steel with 9% nickel has a keyhole-notch Charpy impact energy of 30 ft-lb at -320°F. In the quenched and tempered condition the same steel will show 50 ft-lb impact energy at this temperature. ASTM A353-58 covers the 9% nickel grade and requires the normalized and tempered heat treatment. Revision of current pressure-vessel codes to permit quenched and tempered steel of this grade for pressure vessels will result in improved reliability of low-temperature storage tanks.

The austenitic stainless steels of the Type 300 series are all suitable for use at -320°F, as is the heat-treatable A-286 stainless steel. Precipitation-hardenable stainless steels of the PH series are not recommended for subzero temperature applications since they evidence notch embrittlement at temperatures between 0°F and -40°F.

The recently developed maraging steels of the 20% and 25% nickel varieties, with various amounts of cobalt, molybdenum, titanium, aluminum and columbium added, exhibit notch toughness at temperatures down to at least -320°F, and possibly down to liquid-hydrogen temperature. The maraging steels are readily formable and weldable, and are hardened by a relatively low-temperature aging at 900°F.

A large number of aluminum alloys, including 2024-T6, 7039-T6, 2014-T6, and 5456-H343 have excellent resistance to brittle fracture at -320°F, although weld joints in the 2014-T6 alloy tend to exhibit brittle behavior at low temperatures. Other aluminum alloys of the 5000 series aluminum-magnesium type are also tough at -320°F and at lower temperatures, as are the 6061-T6 and 2219-T87 alloys.

Nickel-base alloys are almost all tough at -320°F, as shown in Fig. 7. Titanium alloys such as the 6Al-4V-Ti (both in the annealed and heat-treated conditions), the 8Al-2Cb-1Ta-Ti, and the 5Al-2.5Sn-Ti alloys are ductile and tough at -320°F. It has been found that impurity elements such as oxygen, nitrogen and carbon, as well as iron, can embrittle these alloys at low temperatures; care should be taken to keep these impurities as low as possible in materials intended for critical applications at very low temperatures. Cooperative work at General Dynamics/Astronautics and Titanium Metals Corp. of America led to the development of the ELI (extra low impurity) grades of the 6Al-4V-Ti and 5Al-2.5Sn-Ti alloys.

Metals for use below -320°F. There is a large gap between the temperature of liquid nitrogen, -320°F, and that of the next lower-temperature liquefied gas of importance, liquid hydrogen, which boils at -423°F. Liquid helium, boiling at -452°F, is the only other cryogen that fills this low-temperature range. Liquid hydrogen, because of the space program, has become of wide commercial significance, and a production capacity in the tens of thousands of tons per year has been established here within the past few years.

Among the steels, only the more highly alloyed austenitic stainless steels are suitable for use at liquid-hydrogen or helium temperatures. Types 304 and 310 stainless steels fall within this classification, and the low-carbon grades of these steels are recommended, especially when welding is to be performed. There are a number of low-carbon stainless-steel casting alloys containing generally 18 to 21% chromium and 9 to 14% nickel that may be used for piping, valve bodies, flanges, etc., at -423°F or lower.

The aluminum alloys that may be safely used at liquid-hydrogen temperatures include several of the 2000 and 5000 series, as well as the 6061-T6 alloy. Weldments of the 2219-T87 alloy have demonstrated excellent resistance to brittle fracture at -423°F, while the lower-strength 5052-H38 and 5083-1138 alloys have also showed good notch-toughness at this temperature.

Monel, K-Monel, both annealed and aged, electroformed nickel, TD (thorium dispersion hardened) nickel, and heat-treatable nickel-base alloys such as Inconel X, Inconel 718, and René 41, and cold-rolled-to-strength Hastelloy B, all exhibit excellent ductility and notch toughness down to  $-423^{\circ}\text{F}$ .

In titanium, only the very low interstitial unalloyed titanium, Ti45A (AMS 4902), and the 5Al-2.5Sn-Ti ELI grades are recommended for use at  $-423^{\circ}\text{F}$  or lower. Both base metal and weld joints exhibit good ductility at very low temperatures.

While the preceding discussion was confined to steel and aluminum, nickel, and titanium-base metals, other metals and alloys are used in many cryogenic-temperature applications. Copper and its alloys are used for bushings, valve components, and other parts subjected to lower temperatures. Most copper alloys retain their ductility and toughness down to very low temperatures. These include 70-30 brass, beryllium copper, and aluminum and iron-silicon bronzes. Magnesium alloys are generally a little more brittle at subzero temperatures than at room temperature, with some tendency for lower elongation at extreme subzero temperatures. As stated previously, magnesium alloys can be used in low-stress application at reduced temperature with care in design to reduce stress concentrations and multiaxial stress distributions.

#### CORROSION RESISTANCE

Metals used in the chemical processing industry must often exhibit a high order of resistance to corrosion by chemicals. The higher chromium-nickel base alloys and stainless steels exhibit somewhat lower resistance to corrosion but still provide a high order of corrosion resistance. Aluminum alloys are resistant to corrosion attack by organic acids, halogenated hydrocarbons, ethers, esters, amines and ketones, and hence are widely used in the chemical processing industry. The cryogens listed in Fig. 7 are all compatible with aluminum alloys insofar as chemical attack is concerned. Nickel and nickel-base alloys also exhibit a generally high degree of corrosion resistance.

Carbon and low-alloy steels, as well as the high-nickel maraging steels, have generally poor corrosion resistance; there may be cases where, despite good mechanical properties at subzero temperatures, these alloys will be eliminated because of poor corrosion resistance.

## Mechanical Properties of Nickel Alloys at Cryogenic Temperatures

(Tests on sheet material 0.015 to 0.050 in. thick. Notched specimens were double edge-notched with  $K_t = 6.3$ )

Alloy	Test Temp., °F.	Base Metal				Weld Joint		
		Yield Point, M Psi.	Ult. Tens. Strength, M Psi.	Elong., %	Notched Ult. Tens. Strength, M Psi.	Notched/Unnotched Ratio	Ult. Tens. Strength, M Psi.	Elong., %
K-Monel (aged)	75	97.3	154	22	144	0.93	141	11
	-100	107	166	24	155	0.93	154	14
	-320	120	183	30	174	0.95	170	15
	-423	136	200	28	198	0.98	190	14
Inconel 718 (Cold rolled and aged)	75	183	204	13.2	226	1.11	114	5.0
	-320	214	254	21.0	262	1.03	151	5.3
	-423	228	281	22.0	286	1.02	174	3.5
Hastelloy R-235 (aged)	75	118	171	18.0	148	0.87	164	12.7
	-100	124	184	18.3	154	0.84	154	8.0
	-320	138	189	11.7	166	0.88	181	6.7
	-423	144	188	9.0	183	0.97	187	7.7
Electroformed Nickel	75	85.9	139	7.5	169	1.21	...	....
	-423	109	184	15.9	216	1.17	...	....
TD Nickel	75	58.6	79.7	12.0	89.5	1.12	...	....
	-320	70.4	111	27.5	112	1.01	...	....
	-423	72.9	132	31.5	125	0.95	...	....
Rene 41 (aged)	75	131	189	21.3	168	0.88	132	3.0
	-100	139	205	20.0	176	0.86	154	4.6
	-320	155	229	17.0	192	0.84	174	4.8
	-423	171	255	14.9	209	0.82	192	3.3
Hastelloy B (40% cold rolled)	75	177	191	3	220	1.15	107	2
	-100	207	222	5	245	1.10	...	....
	-320	208	228	12	265	1.16	...	....
	-423	240	283	16	308	1.09	145	2

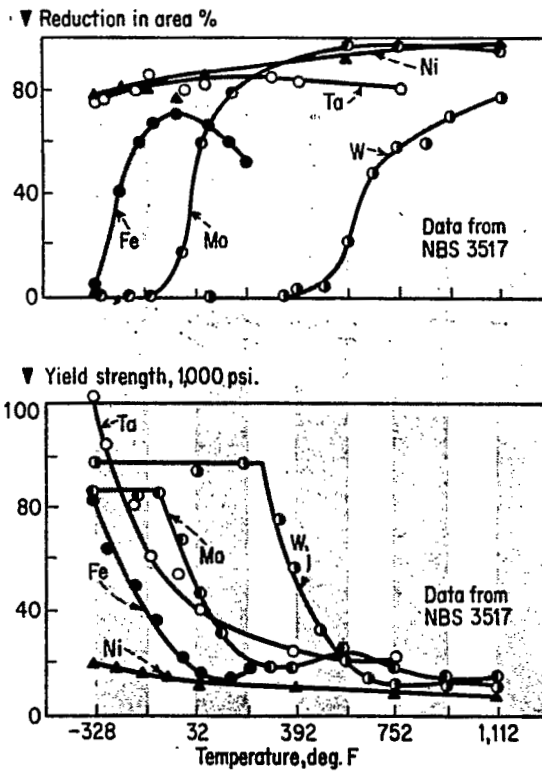


Fig. 1. How temperature affects ductility (top) and yield strength (bottom) of body-centered cubic metals compared with Ni, a face-centered cubic metal.

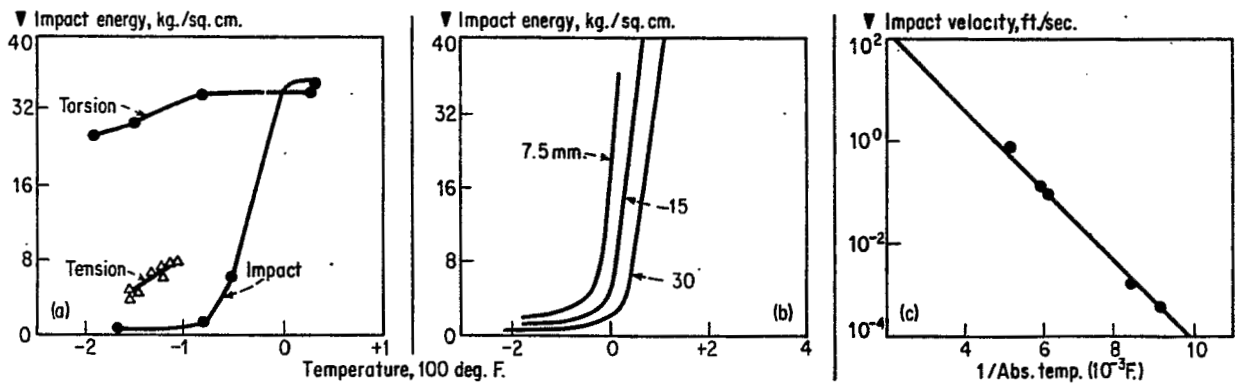


Fig. 2. Effect of mechanical factors (a, plastic displacement; b, specimen width; and c, impact velocity) on embrittlement of ferritic steels.



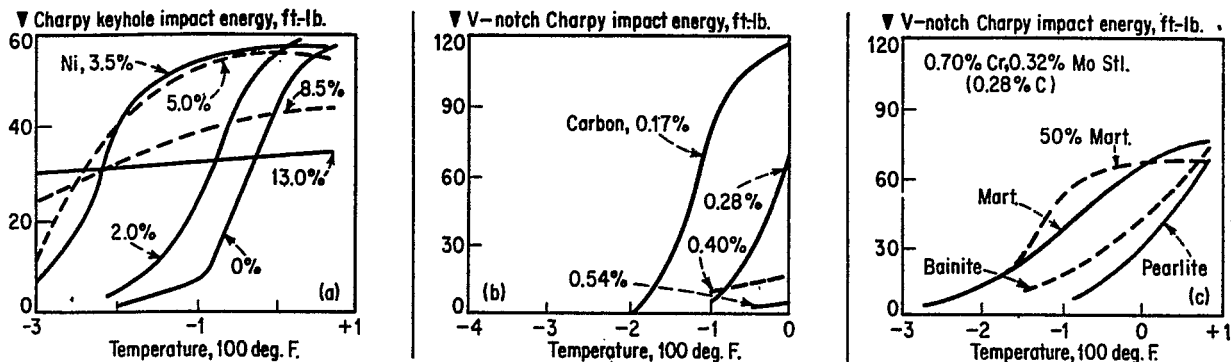


Fig. 3. How chemical composition and microstructure (a, nickel; b, carbon; and c, microstructure) affect the toughness of wrought steels.

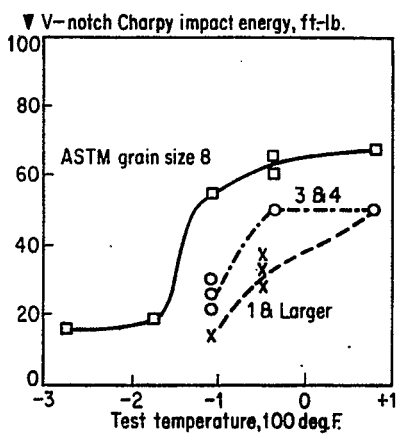


Fig. 4. Influence of grain size on toughness of 8640 steel, heat treated to  $R_{\text{O}} 34$ .

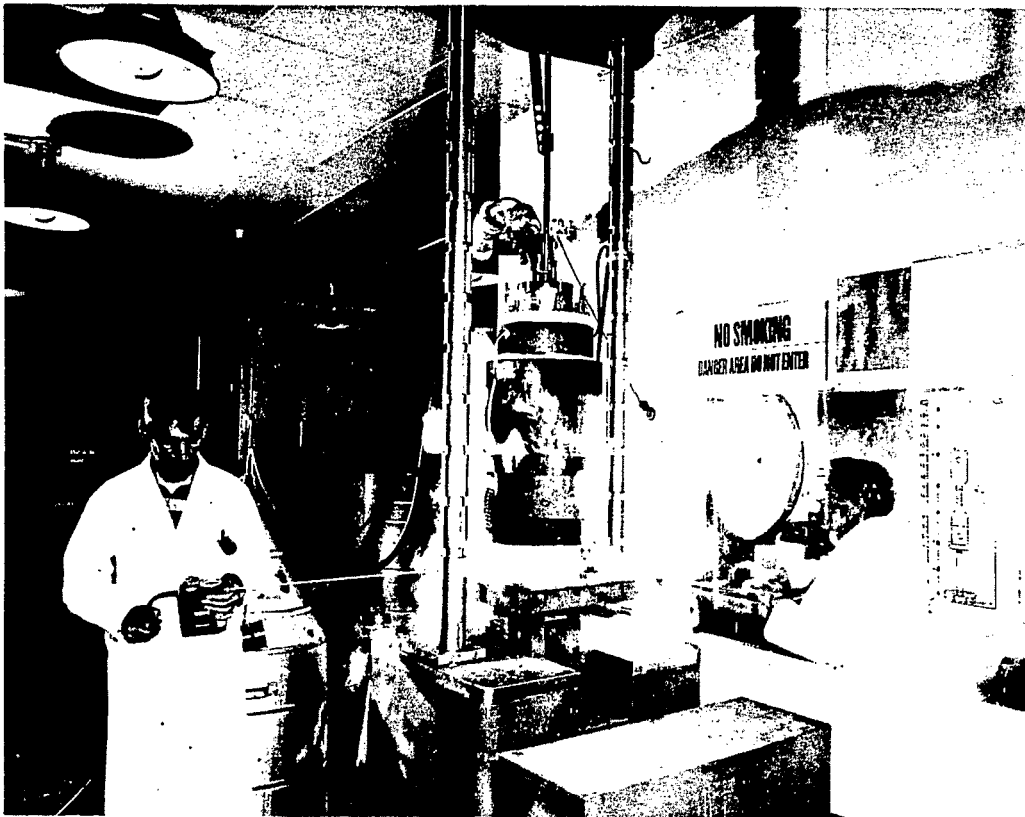


Fig. 5. Indoor test facility with liquid hydrogen cooling requires careful design to avoid explosions.

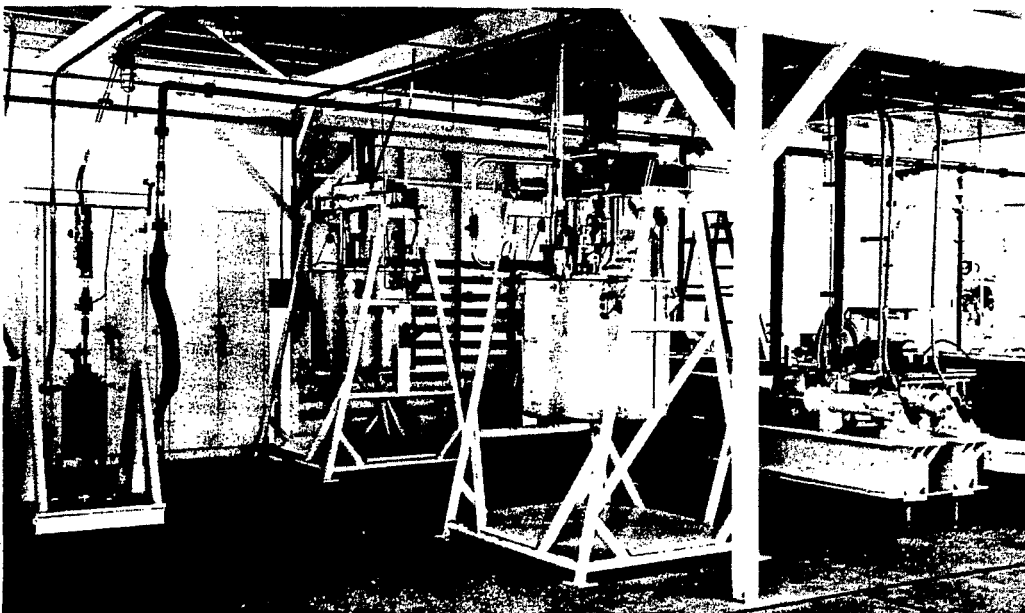


Fig. 6. Outdoor test facility permits tensile, bending and fatigue testing of specimens at  $-423^{\circ}\text{F}$ .

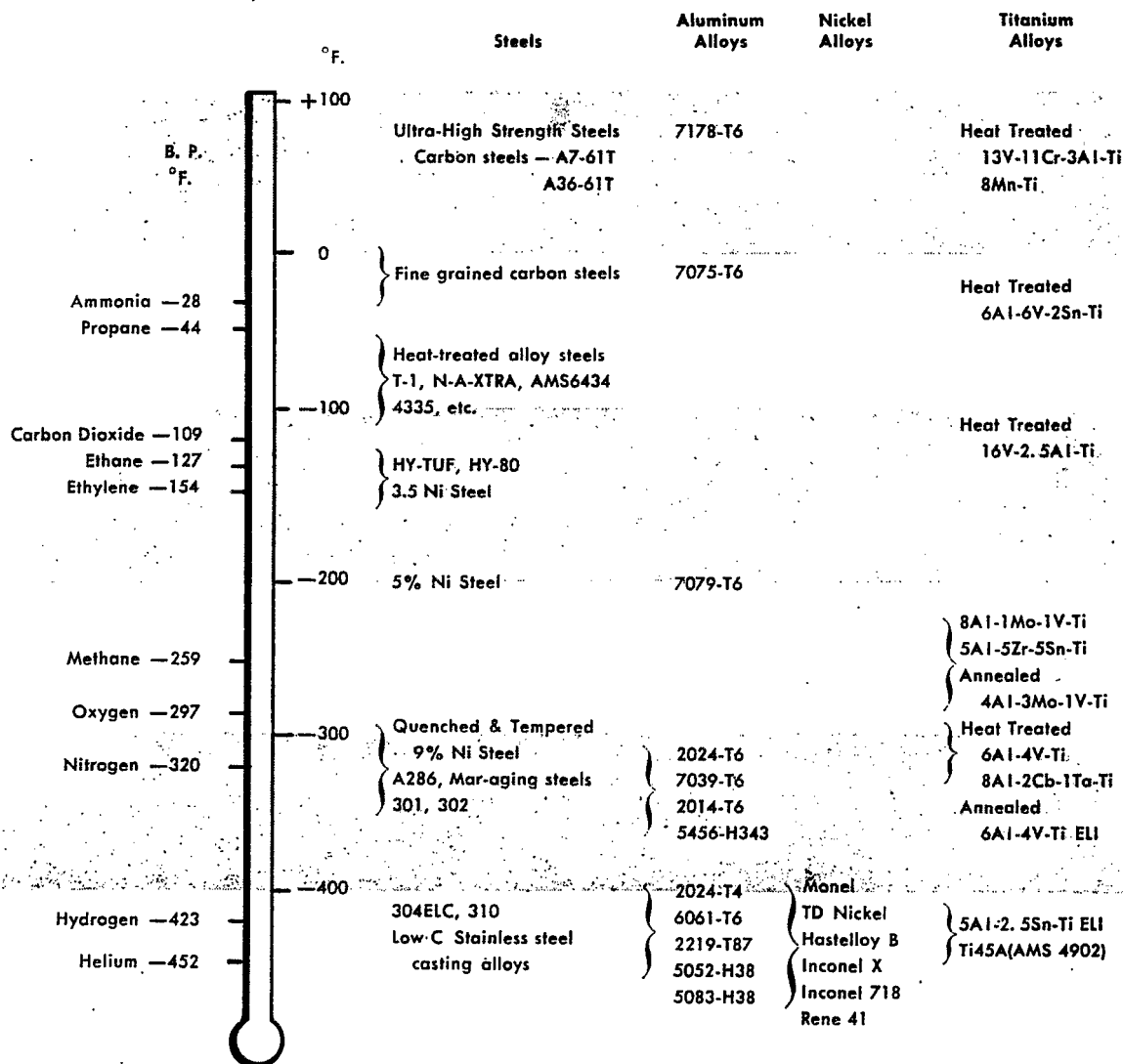


Fig. 7. Metals suitable for use from atmospheric temperature to the lowest available are here spotted at lowest applicable temperatures.

## PROPERTIES OF NONMETALLIC MATERIALS AT CRYOGENIC TEMPERATURES

R. Mowers  
Rocketdyne  
A Division of North American Rockwell Corporation  
Canoga Park, California

### SUMMARY

This paper presents property data and information describing the various cryogenic applications for nonmetallic materials. Until very recently, this classification of materials was usually ignored for structural applications at cryogenic temperatures.

Basically, there are three reasons for the reluctance of designers to use this family of materials. First, there were essentially no cryogenic mechanical and physical property data available. Few standards for samples or test methods existed to determine the properties, which made it extremely difficult to compare data obtained with the meager data available. Second, stress analysis of the most attractive structural materials, the filament-wound, fiber-reinforced composites, was extremely complex and specialized, and the concepts utilized to arrive at design analyses were still under development. Third, variations in the constituents and their effect on end-item properties made it less than attractive to utilize this type of material for cryogenic structural applications, although preliminary data indicated these materials had a great potential because of their high strength-to-weight ratio.

The impetus necessary to overcome this lack of information was provided by the aerospace industries' urgent requirements for structural materials with high strength-to-weight ratios capable of operating over wide temperature ranges. Minimum weight has always been important for aircraft applications, but is of the utmost necessity for hardware used in upper stage vehicles, satellites, and spacecraft.

Contract funds were provided to various organizations to obtain cryogenic property data, to develop sophisticated design analysis techniques, and to improve the materials available for use in manufacturing structural nonmetallic hardware for cryogenic service.

Today the results of these programs are being reduced to common practice. Other scientific disciplines, such as high-energy physics, which work in the cryogenic temperature region, are benefiting from the results obtained in the programs initiated for cryogenic aerospace applications.

### INTRODUCTION

Many nonmetallic materials are either being used or evaluated for structural or semistructural applications at cryogenic temperatures. Some advantages that are considered when evaluating these nonmetallic materials for cryogenic temperatures include the following characteristics:

1. High strength-to-weight ratios.
2. Low thermal conductivities.
3. Low specific heats.
4. Ease of orthotropic fabrication.
5. Corrosion resistance.

6. Durability.
7. Self-lubricating properties of some materials.
8. Fatigue resistance.

However, these potential advantages are not achieved without simultaneously accepting certain design problem areas which result from the following characteristics of nonmetallic materials:

1. High coefficients of thermal expansion.
2. A tendency towards brittleness at low temperatures.
3. Complexities of the stress analysis of heterogeneous composite resin-fiber structures.
4. Lack of generally standardized test techniques for developing design data.
5. Variations in resins and fibers used to fabricate composite structural elements.

Some typical cryogenic applications for nonmetallic materials of construction can be separated into five classifications:

1. Reinforced plastic structures.
2. Adhesives, sealants, and coatings.
3. Bearings and dynamic seals.
4. Gaskets and static seals.
5. Film materials used as diaphragms, vapor barriers, etc.

A sixth major use classification for nonmetallic materials, cryogenic thermal insulation, has not been considered for this paper.

A short description of typical examples from each classification is presented below. This overview will be followed by a presentation of cryogenic property data available at the present time for materials from each of these classifications. More complete descriptions of current and potential applications will be presented in each section. Limitations of the data available and a discussion of the data not yet obtained will also be presented.

#### CLASSIFICATION OF NONMETALLIC MATERIAL USES

The first category of nonmetallic materials includes glass-fiber reinforced-plastic structures such as filament-wound pressure vessels used for storage of cryogens or as the basic structural element of liquid hydrogen bubble chambers (although fiber-glass is the principal current reinforcement, high modulus fiber reinforcements such as boron and graphite are being evaluated with various resin combinations in an attempt to develop a composite laminate material with a modulus at least as great as aluminum). Another cryogenic application for fiber-reinforced plastic materials is structural insulators and supports used between the insulation and outer walls of cryogen containing vessels. Sandwich constructions of fiber-reinforced plastic face materials in combination with honeycomb, foam core systems, and foam-filled honeycombs have also been used in various cryogenic systems. These combinations of materials are used as composite structural members of insulation systems where the heat leak through a honeycomb core must be tolerated to prevent structural failure of the foam insulation caused by thermal shock and strain.

The second category of nonmetallic materials for structural applications at cryogenic temperatures consists of adhesives, sealants, and coatings. The effects of cryogenic temperatures on the strengths of adhesive joints have recently been examined by many investigators. Sections of large cryogenic tanks have been successfully joined using adhesive bonding techniques. Dissimilar metallic materials are bonded together to prevent galvanic corrosion, and integral linings for filament-wound cryogenic storage vessels are adhesively bonded into place. The most critical problem to be overcome before filament-wound tanks can be used for multiple cryogenic pressure cycles is associated with the development of an adhesive system to attach the liner to the filament-wound wall. Adhesive sealants are also used at cryogenic temperatures to provide pressure-tight structural seals. Some organic coatings have been evaluated for reducing to zero the tolerances between rotating members in cryogenic turbomachinery applications. Thin coatings of some of these same insulating materials have been shown to alter the boiling characteristics of hydrogen so as to enhance the heat transfer from cryogenic fluid to the structural members, and in this manner to reduce the time required to achieve thermal equilibrium.

The third category for structural applications of nonmetallic materials at cryogenic temperatures includes dynamic seals and bearings. Typical cryogenic shaft-riding face seals utilize various proprietary compositions of carbon-graphite or ceramic oxide materials as the primary seal. A compromise is made between the amount of friction, face wear, and the leakage allowed past the seal face.

The fluorocarbon plastics, in particular, have inherently low friction coefficients at all temperatures. Many cryogenic bearings utilize various types of fluorocarbon resins, alone or in combination with other materials. These specialized items form a very small but important portion of many cryogenic devices.

Static gaskets and seals comprise the fourth category of nonmetallic materials used in cryogenic applications. Gaskets used at cryogenic temperatures, however, become harder as the temperature decreases. To maintain the sealing capacity accomplished at ambient temperatures, the gasket should maintain flexibility or compressibility. A further problem with most organic gasket materials evolves from their inherently larger thermal contraction coefficients compared to the joining metal surfaces. This results in a decrease in sealing force as the device cools to cryogenic temperatures and increases the potential for leakage past the gasket. Various special nonmetallic gaskets, composite metal-plastic gaskets, and special design techniques have been developed to meet cryogenic sealing requirements.

Many types of nonmetallic materials are used as static structural seals at cryogenic temperatures. These seals are used to control the flow of cryogenic fluids and gases under high and low pressures and from flowrates small enough to be measured with a mass spectrometer to those measured in tons/second. Many of these cryogenic seals have utilized fluorocarbon plastic materials. This family of materials maintain some ductility at extreme cryogenic temperatures even at extremely high strain rates.

A fifth category of nonmetallics used in cryogenic applications includes the film materials that are used as diaphragms and vapor barriers. Regulators with nonmetallic pressure sensing diaphragms have been used in cryogenic environments (fluid and pneumatic) at high and low pressures. High pressure differentials over small areas are common, and multi-ply polyester film diaphragms have been used effectively at high- and low-frequency rates at temperatures as low as 20°K. Over two-million cycles have been completed successfully at 20°K using this multi-ply type of diaphragm as a small R&D positive displacement pump for liquid hydrogen.

Representative cryogenic test programs pertaining to all five use categories of nonmetallic materials are presented in the following sections. Each section includes the title of the program, its source, its objectives, the materials tested, the properties measured, the data obtained, and the conclusions drawn.

## Reinforced Plastic Laminates

Reinforced plastic laminate materials have received the most experimental attention because their potential structural properties are very attractive to a designer. Comprehensive test programs have been completed by various organizations pertaining to the effects of cryogenic temperatures on mechanical and physical properties of reinforced plastic laminates.

Data from five programs have been selected for this report. One program was established to determine if reproducible data could be obtained for fiber-reinforced plastic materials at cryogenic temperatures; a second presents data obtained for glass fabric laminates utilizing a variety of resin systems; a third shows data for unidirectional filament-wound laminates; a fourth indicates the combined effects of nuclear radiation and cryogenic environments; and a fifth presents property data for filament-wound laminates being considered for liquid hydrogen bubble chambers.

Title. "An Assessment of Test Specimens and Test Techniques Useful to the Evaluation of Structural Reinforced Plastic Materials at Cryogenic Temperatures" (NAS 8-11070).

Source. Goodyear Aerospace Corporation, Akron, Ohio.

Objectives. The primary objective of this program was to establish industry standards for reinforced plastic test specimens and test techniques applicable to cryogenic temperatures. The ultimate objective was to obtain a design handbook containing data for a variety of reinforced plastic materials at cryogenic temperatures.

Materials. To minimize variables, two S/HTS glass fabric styles, 1543 and 1581, were used in this program. A single epoxy resin was preimpregnated onto both fabrics.

Properties. Tensile strength, elongation, and modulus; compressive strength, flexural strength, and modulus; shear strength and bearing strength; were measured parallel, normal, and at 45° to the warp direction of the fabric.

Test temperatures. Test temperatures were 298, 197, 77, and 20°K.

Data. Some of the data obtained in this program are presented in Table I. These data show that the mechanical properties of fiberglass-reinforced plastics increase substantially at lower temperatures over the room temperature values. The specific strengths (stress-density) of the materials were found to be exceptionally high.

Conclusions. The spread of the data, expressed as the coefficient of variation, obtained during the program for samples cut parallel to the principal reinforcement direction were:

Tension	4.8%
Compression	9.6%
Flexure	5.6%
Shear	9.6%
Bearing strength	9.4%

These coefficients of variation were based on a small number of samples and include the rather large variation obtained in the strength of the S/HTS glass fibers themselves. It was concluded, therefore, that the test values appear in general to be within acceptable limits.

Title. "Determination of the Performance of Plastic Laminates Under Cryogenic Temperatures" [AF 33(616)-8289].

Source. Narmco Research and Development, San Diego, California.

Objectives. The objective of this program was to determine the mechanical properties for a wide variety of plastic laminate materials at cryogenic temperatures.

Materials. Glass fabric (181 style) laminates were fabricated using epoxies, phenolics, polyesters, high-temperature polyesters, silicones, flexible polyurethanes, polybenzimidazol, fluorinated ethylene propylene, phenyl-silanes, and nylon epoxies.

Properties. Tensile, compressive, and flexural strengths and moduli; tensile fatigue, and bearing strength tests were performed.

Test temperature. Tests were performed at 298, 195, 77, and 20°K.

Data. The data indicated that reinforced plastics generally increase in strength as temperatures decrease. Based on static test data, it was found that epoxy resins were best for cryogenic use; polyesters and phenolics were second. When subjected to tensile fatigue, however, the epoxies and phenolics continued to show good life while the polyesters fell behind. Average tensile strength of the glass-reinforced laminates is shown in Fig. 1. Average tensile, compressive, and flexural property data are shown in Figs. 2, 3, and 4. Bearing strength and tensile fatigue data are shown in Figs. 5 and 6.

Conclusions. It was concluded that decreasing the test temperature from 77°K to 20°K had little effect on properties, although decreasing from ambient to 77°K resulted in marked increases in strength. Further, it was concluded that modulus values did not increase as rapidly as strength data as test temperatures were reduced. Finally, the tensile fatigue strengths of fiberglass-reinforced plastics were higher at cryogenic temperatures than at room temperatures.

Title. "Cryogenic Properties of High Strength Glass-Reinforced Plastics" [AF 33(657)-9161].

Source. Martin Company, Denver, Colorado.

Objectives. The objectives were to determine the behavior of a variety of unidirectional filament-wound resin/glass combinations at cryogenic temperatures.

Materials. Ten resin systems and two glass types were used. Resins included four epoxies, an epoxy novolac, a phenolic, two polyesters, a silicone, and a phenyl-silane. E and S glasses were used.

Properties. Tensile strength, modulus, and static tensile fatigue data were obtained.

Test temperatures. Tests were performed at ambient, 77, and 20°K.

Data. The strength data for the various resin systems are shown in Figs. 7 and 8. Modulus data is shown in Fig. 9. These data show a general increase in strength as temperature is decreased from ambient to 77°K. Below 77°K, strength shows a tendency to level off or decrease. Modulus data show a continued increase down to 20°K as opposed to the strength data. Static fatigue did not occur at cryogenic temperatures, which adds evidence that ambient temperature static fatigue is in reality a stress corrosion process resulting from absorbed water vapor onto the glass.



Conclusions. The conclusions drawn from this study were: first, the resin made a large contribution to the tensile strength of NOL ring samples at cryogenic temperatures, and second, the effect of reinforcement type on the tensile modulus was significant. The E-glass material shows a much lower modulus than the S-glass.

Title. "Effect of Nuclear Radiation and Liquid Hydrogen on Mechanical Properties of Three Phenolic Materials."

Source. Aerojet-General Corporation, Sacramento, California.

Objectives. The objectives were to investigate the mechanical properties of three phenolic based materials in a combined environment of liquid hydrogen and nuclear radiation.

Materials. Phenolic asbestos-cloth laminates (Grade AA - MIL-P-8059A), phenolic linen-cloth laminates (Grade L - MIL-P-15035B, Type FBI), and phenolic glass-cloth laminates (MIL-F-9084, Type VIII impregnated with 91-LD phenolic resin) were used in this study.

Properties. Ultimate tensile strength and elongation data were obtained.

Test temperatures. Tests were performed at 20°K plus one series at ambient temperatures.

Data. The data obtained in this study are presented in Table II. The data show that tensile strength for all three materials is not appreciably affected by the combined environment of cryogenic temperature and nuclear radiation. However, loss of ductility was significant after nuclear radiation.

Conclusions. Care should be exercised in selecting any of the three types of materials tested for a combined cryogenic-radiation environment if any appreciable strain must be sustained by the materials.

Title. "Physical Properties of Filament-Wound Glass-Epoxy Structures as Applied to Possible Use in Liquid Hydrogen Bubble Chambers."

Source. Stanford Linear Accelerator Center, Stanford, California.

Objectives. The objectives were to determine the feasibility of using filament-wound laminates for a structural, liquid hydrogen pulse system bubble chamber where eddy current heating makes a metal chamber impractical.

Materials. Materials tested were S/HTS roving impregnated with ERL 2256 epoxy and MPDA hardener. H-film sheets were incorporated into the structure to reduce permeability.

Properties. Fatigue (flexural), flexural strength and modulus, shear strength, low-temperature permeability, and thermal contraction were measured.

Test temperatures. Tests were performed at ambient to 4.2°K.

Data. Thermal contraction data obtained in this program are shown in Fig. 10. It is shown that the laminate contraction is basically that of the glass filaments. Flexural fatigue data are shown in Table III. The data indicate that inclusion of H-film in the structure had no adverse effects on the integrity of the laminate under flexural fatigue conditions. Flex and shear strength data of samples with Mylar,

Tedlar, and beryllium film showed a weakening of the matrix. Shear strength losses on the order of 50% were measured for all samples with barriers other than H-film. H-film resulted in  $\approx 5\%$  loss in shear strength.

Conclusions. Glass-filament epoxy structures exposed to cryogenic temperatures, particularly liquid hydrogen, are equal to or superior to stainless-steel bubble chambers with dc field or transient magnetic fields. Problems such as feed-through tubing into the chamber and sealing of the chamber must be investigated in more detail. The filament-wound chamber was lighter than a stainless-steel unit and had considerably less static heat loss than stainless steel.

## Adhesives, Sealants, and Coatings

### Structural adhesives

Structural adhesive evaluations for cryogenic temperature environments have been reported in the literature since the middle 1950's. The early reports were limited to descriptions of paste and liquid adhesive systems and usually to temperatures down to 77°K. Recent programs have considered the basic problems associated with bonded joints at cryogenic temperatures. Most of these problems have been attributed to stress concentrations and gradients developed within the bond. Some of the principal causes for these concentrations include:

1. Differences in the thermal coefficient of expansion between adhesive and adherends..
2. Shrinkage of the adhesive on curing.
3. Trapped gases or volatiles evolved during bonding.
4. Differences in elastic moduli and strength between adhesives and adherends.
5. Residual stresses in joints as a result of releasing bonding pressures.

For example, a low modulus adhesive may readily relieve stress concentrations at room temperatures by deformation, but at cryogenic temperatures it may become so brittle that these concentrated stresses are only relieved by fracture of the adhesive.

The results of two review papers from the same organization are presented to describe some of the recent information developed for cryogenic structural adhesives. The later report presents information obtained through 1964; the earlier report includes data obtained as early as 1961. Differences in the conclusions indicate continued increase in knowledge regarding adhesives for cryogenic temperatures.

Title. "Development of Adhesives for Very Low Temperatures" (NAS 8-1565).

Source. Narmco Research and Development, San Diego, California, 1961-1963.

Objectives. The objectives were to search the literature and evaluate various commercially available adhesives for cryogenic applications.

Materials. Research efforts were concentrated on nylon-epoxy, epoxy-polyamides, polyurethane, and fluorocarbon film systems. Aluminum and stainless-steel adherends were used.

Properties. Tensile shear, tee peel, mechanical shock, and butt tensile strengths were determined.

Test temperatures. Tests were performed at room temperature, 77, and 20°K.

Data. Tensile lap shear strength data for the commercial adhesives evaluated at the beginning of this program are shown in Fig. 11. These data indicate the general superiority of nylon-epoxy adhesive systems at cryogenic temperatures.

Conclusions. The nylon powder-filled epoxy-polyamide paste was the best system evaluated during this program. A polyurethane elastomer adhesive showed superior strength and toughness at extremely low temperatures. However, it tended to absorb moisture from the air, which caused it to foam during bonding and resulted in unsatisfactory joints.

Title. "Adhesive Bonding of Insulation for Temperature Extremes - Cryogenic to Re-entry."

Source. Narmco Material Division, Costa Mesa, California, 1964.

Objectives. The objectives were to determine mechanical property data for a variety of structural adhesives at temperatures from 20 to ~800°K. The advantages of adhesives, design considerations, fabrication techniques and variables, and recommended steps for selecting an adhesive were also summarized.

Materials. Nylon epoxies, modified epoxies, silicone phenolics, epoxy-phenolics, polyaromatics, and polyurethane adhesives were investigated.

Properties. Tensile shear, tee peel, mechanical shock, and butt tensile strengths were determined.

Test temperatures. Tests were performed at 20 to 850°K.

Data. The effect of temperatures on the lap shear strength of different types of adhesives is presented in Fig. 12. These data show that at extreme cryogenic temperatures, the polyurethane adhesives are stronger than all others. However, at ambient temperatures the strength of the polyurethane adhesive is less than most of the other adhesive types. Figure 13 shows the lap shear strengths of eight different types of adhesive systems at a temperature of 20°K.

Conclusions. Polyurethane adhesives are very good for extremely low temperatures, but their strength decreases very quickly as they approach ambient temperatures. The nylon-epoxy materials, on the other hand, have a rather uniform strength at temperatures from 20 to 373°K.

#### Adhesive sealants

NASA has sponsored programs to develop adhesive sealants for use at cryogenic temperatures. These programs were directed toward finding materials that would be flexible down to a temperature of 20°K. However, preliminary screening tests indicated that even the most flexible materials were incapable of meeting the bending requirements described in MIL-S-8516 at liquid nitrogen (77°K) temperatures. Further testing indicated that the low-temperature sealing characteristics of polyurethanes and methyl-phenyl silicone elastomers could be improved by using them in conjunction with nylon or glass-fabric reinforcements. The higher modulus fabric reinforcements minimized the thermal strains in the sealants at low temperatures by accepting a larger portion of those thermal strains and transmitting them to the metal substrate rather than concentrating them in the sealant.

Various informal programs have been performed to evaluate specific cryogenic sealant requirements. One of these programs was directed toward the development of a sealant system to prevent moisture from penetrating into rigid polyurethane-foam-insulated liquid hydrogen lines. A polyurethane elastomer impregnated into circumferentially wrapped open weave nylon tape was satisfactory for this purpose, even when attached directly to the outer metal wall of the hydrogen line.

Very little quantitative data are available pertaining to sealants for use at cryogenic temperatures. Evaluation tests have to be tailored to the solution of particular problem areas. One of the few reports available is summarized below.

Title. "Development of Cryogenic Sealants for Applications at Cryogenic Temperatures" (NAS 8-2428).

Source. Hughes Aircraft Company, Culver City, California.

Objectives. The objectives were to develop organic sealants that may be used to seal or repair containers for cryogenic fluids.

Materials. Eight different polymer systems were investigated:

1. Polysulfide.
2. Silicone.
3. Epoxy.
4. Polyurethane.
5. Fluorosilicone.
6. Epoxy-silicone.
7. Butyl formal, butyl ether, and polysulfide blend.
8. Carboxyl terminated polybutadiene and epoxy blend.

Properties. Low-temperature bend characteristics, thermal contraction, and resistance to vibration were determined.

Test temperatures. Tests were performed at ambient to 77°K.

Data. Only reinforced silicones and polyurethanes met vibration and bend test requirements at 77°K.

Conclusions. The woven fabric provided reinforcement continuity throughout the structure, and was capable of transmitting loads to the metal substrate during the bend tests. Further, the reinforcement lowers the over-all thermal contraction to a level where thermal stress at the sealant-substrate interface is reduced to a minimum.

#### Structural coatings

Structural coatings have been considered for cryogenic turbomachinery applications. These coatings were evaluated for dual use as an internal wearing surface and as an internal thermal insulation. Investigations performed by several manufacturers of liquid propellant rocket engines indicated that some filled fluorocarbon plastic materials might be effectively utilized for this dual (wearing and insulating) purpose. Unknown factors included the possibility that thermal strains could be large enough to cause the coating to separate from the metallic substrate at cryogenic temperatures, and determination of the effects of fluid erosion on the adhesion of the coatings. Some

of the systems evaluated were quite promising, even though only preliminary tests were completed. One of these preliminary programs is described below.

Title. "Evaluation of KX635 for Turbomachinery Applications."

Source. Rocketdyne, a division of North American Rockwell Corporation, Canoga Park, California.

Objectives. The objectives were to determine if a filled fluorocarbon plastic, (KX635) might be developed for an insulating internal wearing surface for cryogenic turbomachinery.

Materials. Metallic substrates were K-monel and Tens-50 aluminum casting alloy. Coating material was KX635, a glass microballoon-filled Kel-F dispersion material.

Properties. Bond strength between coating and substrates at ambient and cryogenic temperatures was determined by static tensile tests and flexural fatigue tests. Thermal contraction and thermal conductivity were measured from ambient to cryogenic temperatures.

Test temperatures. Tests were performed at ambient, 77 and 20°K.

Data. Tensile tests indicated that the coating adhered to metallic substrates at all temperatures until metal failure occurred. Flexural fatigue tests at cryogenic temperatures showed that the coating adhered to substrates at total deflections up to 0.300 in. without coating-to-metal separation. Erosion rates of the coating material caused by fluid flow were not determined.

Conclusions. The various data generated were promising enough that further efforts could be justified to evaluate this type of internal insulation-wearing surface for cryogenic applications.

#### Dynamic Seals and Bearings

Nonmetallic materials are used as semistructural elements in many dynamic seal and bearing applications at cryogenic temperatures. Bearings and seals are required for any application with movement or where flow of cryogenic fluids or gases must be controlled. Examination of the literature reveals that materials from one polymer family, the fluorocarbons, are widely used for these applications. The fluorocarbon plastics have characteristics that make them very attractive for cryogenic sealing and wear applications. Some of these are:

1. Some ductility at cryogenic temperatures.
2. Adequate mechanical properties at cryogenic temperatures.
3. Chemical inertness.
4. Low coefficients of friction over total useful temperature range.

Many cryogenic seal applications utilize unmodified fluorocarbon plastics as sealing elements. Generally, cryogenic bearing applications have used fluorocarbons (particularly TFE Teflon) to achieve the appropriate friction, wear, and durability characteristics necessary for prolonged, trouble-free operation at cryogenic temperatures under widely varying stress conditions.

Data from four programs pertaining to fluorocarbon plastics have been selected

for this report. The first two describe efforts performed to develop self-lubricated bearings for cryogenic temperatures. The third describes a comprehensive program initiated to obtain design properties of various thermoplastic materials at temperatures down to 20°K. The fourth program presents information pertaining to strain rate, temperature, crystallinity, and surface smoothness on the mechanical properties of PCTFE plastics.

Title. "Bearing Lubrication at Low Temperatures."

Source. British Oxygen Research and Development, Ltd., London, England.

Objectives. The objectives were to determine the effectiveness of various Teflon-containing materials as solid lubricants in liquid oxygen and liquid nitrogen against stainless steel and lead-bronze shafts.

Materials. Shaft and bushing materials investigated were:

1. Shafts - Two types of shaft material were used.
  - a. S.80 stainless steel.
  - b. 20% lead-bronze.
2. Bushings - Three types of bushing were used.
  - a. Porous bronze (0.010 in. thick) filled with TFE to a thickness of 0.0005 in. (Glacier DP).
  - b. TFE, with graphite and bronze powder added (Glacier DQ).
  - c. Porous bronze containing 80% bronze and 20% TFE (Bound Brook Polyslip).

Properties. Wear of bearings (measured as increase in diameter of bushing) was determined after 1.5 hours running time at stresses from 100 to 900 psi.

Test temperatures. Tests were performed at 90 and 77°K.

Data. Wear data for the three Teflon-containing bushing materials against the two shaft materials in liquid oxygen are shown in Fig. 14. The data indicate all three materials were essentially equivalent when running against a 20% lead-bronze shaft. The bearing material with the least quantity of exposed Teflon had the least wear against S.80 stainless steel.

Conclusions. It was concluded that a shaft with good thermal conductivity used in conjunction with TFE Teflon-containing bearing material was suitable for service in liquid oxygen and liquid nitrogen. The design of the bearing is such that adequate "dry lubrication" is maintained under operating conditions, and a free flow of liquid passes through the bearing for cooling.

Title. "Evaluation of Ball Bearing Separator Materials Operating Submerged in Liquid Nitrogen."

Source. CEL, National Bureau of Standards, Boulder, Colorado.

Objectives. The objectives were to develop a reliable, high-load-capacity (axial and thrust) bearing operating at moderate speeds.

### Materials.

1. Ball and Race - ball and race materials were 440C.
2. Separators - separators were three types:
  - a. Metallic coated with TFE.
  - b. Filled TFE.
  - c. Phenolic.

Properties. Bearing life (hours vs torque in in.-oz) was measured while operating under constant environmental conditions of thrust load, speed, and temperatures.

Test temperature. Tests were performed at 77°K.

Data. Sample identification information is shown in Table IV. Bearing life data in liquid nitrogen for all samples tested are shown in Fig. 15. These data indicate that the filled TFE separator (sample No. 8) had a much longer bearing life than all other materials tested. Torque decreased with time for this material. Torque for all others increased with time.

Conclusions. It was concluded that filled TFE separators were superior to the other separator materials when operating in liquid nitrogen.

Title. "Final Report, Program of Testing Nonmetallic Materials at Cryogenic Temperatures" [AF 04(611)-6354].

Source. Rocketdyne, a division of North American Rockwell Corporation, Canoga Park, California.

Objectives. The objectives were to determine the mechanical properties of a variety of thermoplastics at cryogenic temperatures. The study included the determination of the effect of thermal treatments on the crystallinity levels of certain materials and the resultant effect on mechanical properties.

Materials. Materials tested were TFE and FEP Teflon, Kel-F, Mylar, and nylon, as well as fabric, fiber, and powder-reinforced TFE and FEP Teflons.

Properties. Tensile yield, ultimate, modulus and elongation; flexural strength and modulus; compressive strength and modulus; impact strength, modulus of rigidity, and coefficient of thermal expansion were determined.

Test temperatures. Tests were performed at 300, 194, 144, 77, and 20°K.

Data. A summary of the data from this program is presented in Figs. 16-20 and Table V.

Conclusions. The conclusions are separated into the five types of materials tested:

1. Kel-F (PCTFE) - Ambient yield strength variations between the three crystallinity levels was  $\approx 20\%$  (5500 psi/amorphous, 6500 psi/crystalline). At a temperature of 20°K, the spread was  $\approx 60\%$  (28 600 psi/amorphous, 18 000 psi/crystalline). At ambient temperatures the amorphous material was slightly weaker than the crystalline, but at cryogenic temperatures the more amorphous was much stronger than the crystalline.

The notched Izod impact strength of Kel-F remained relatively constant over the test temperature range. However, the amorphous samples had slightly higher impact strength than the crystalline.

2. Teflon (TFE) - The effect of crystallinity on the low-temperature properties of TFE was very similar to Kel-F. The crystalline materials had higher properties than the amorphous at room temperatures, but at cryogenic temperatures, the reverse was true. The effect, however, was less pronounced than for Kel-F.
3. Teflon (FEP) - Normal processing variables had little effect on crystallinity of material. FEP Teflon has about 50% higher impact strength than Kel-F at cryogenic temperatures. Cryogenic elongation of FEP Teflon was also higher than Kel-F; however, it had lower flexural and compressive properties than Kel-F. In addition, the contraction of FEP Teflon is greater than Kel-F at cryogenic temperatures.
4. Powder and Fiber-Filled Teflons - Advantages of powder and fiber-filled TFE and FEP Teflons were found to be less evident at cryogenic temperatures than those usually described for ambient and moderately elevated temperatures. Results obtained in this program indicate that these materials were usually inferior to the unfilled materials. Coefficient of expansion of filled materials was less than the unfilled.
5. Glass-Fabric Reinforced Teflons - Glass-fabric reinforced Teflons are used where the mechanical properties of the glass are combined with the lubricity of the Teflon. The materials are very strong and can be used in applications involving tensile and flexural strength, as well as compression and shear. The room temperature mechanical properties of these reinforced Teflons, both FEP and TFE, are controlled in great part by the strength of the glass fabric, rather than the resin. However, the increase in mechanical properties for these materials at cryogenic temperatures is much greater than normal for fiberglass reinforced plastic laminates. The great increase in the strength of the Teflon resins at cryogenic temperatures is seen in the strength of the laminates at these low temperatures.

Title. "Effects of Strain Rate, Temperature, Crystallinity, and Surface Smoothness on the Tensile Properties of PCTFE Plastics."

Source. Rocketdyne, a division of North American Rockwell Corporation, Canoga Park, California.

Objectives. The objectives were to determine by statistical analysis the independent and interacting effects of strain rate, temperature, crystallinity, and surface finish on the tensile properties of PCTFE (Kel-F) plastic.

Material. Test material was PCTFE (Kel-F).

Properties. Tensile yield, maximum and ultimate, elongation at maximum strength, and ultimate elongation properties were measured.

Test temperatures. Tests were performed at ambient and 77°K.



Data. Tensile data obtained over six decades of loading rates 0.02 to 10 000 in./min) at two temperatures (ambient and 77°K) using molded and machined surfaces on the samples are presented in Tables VI and VII. These data indicate that the maximum tensile strength at ambient temperatures increases in direct proportion to the strain rate, but at cryogenic (77°K) temperatures, the maximum strength was much less at 10 000 in./min loading rate than at the 1000 in./min rate. In fact, the maximum tensile strength of the material at 10 000 in./min loading rate was less at cryogenic temperatures than at ambient temperatures.

Conclusions. At the very high (1000 and 10 000 in./min) loading rates the effects of surface finish and crystallinity on the tensile properties of PCTFE plastic materials were much less apparent than at more conventional testing rates. At low and medium strain rates, the effects of crystallinity and surface were also found to be dependent on the loading rate at which the tests were performed. Further, strain rate effects were more significant at cryogenic temperatures than at ambient temperatures.

### Gaskets and Static Seals

Until recently, flat gaskets were almost universally used for detachable flange seals. For cryogenic applications where flanges can be heavy, gaskets may still be the logical solution to a sealing problem. Gaskets used in cryogenic applications should not be brittle at use temperatures. Flanges and bolts must be selected so that cooling will not cause an excessive decay in sealing force as the gasket (because of its higher contraction) tries to shrink away from them. A further requirement, chemical inertness with liquid oxygen, must be met by gasket materials used in some aerospace cryogenic applications.

Very little thought has been given to the definition and standardization of cryogenic static seals. Generally, seals have been used that did an adequate job in a specific application, without regard to past or future seal designs or needs. Because of this history, there are many varieties of static cryogenic seals available today, and each claims superiority over rival designs.

A review of two specialized static seals has been selected for inclusion in this report. One is a gasket designed specifically for use in liquid oxygen, and the other, a plastic-coated-metal pressure-actuated seal, which is typical of the many new commercially available static seals on the market.

Title. "The Development of a New Cryogenic Gasket for Liquid Oxygen Service" (NAS 8-5053).

Source. Narmco Research and Development, San Diego, California.

Objective. The objective was to develop a superior flat gasket material for service in liquid oxygen.

Materials. The material tested was a laminated gasket composed of alternate layers of TFE Teflon film and glass cloth, encapsulated with FEP Teflon.

Properties. Compressibility and leakage measurements were performed.

Test temperatures. Tests were performed at ambient and 77°K.

Data. Laminate constructions that indicated higher energy absorption values at 77°K, with the least fall-off in the repetitive compressive energy absorption tests, were judged to be superior in compressibility. Figures 21 and 22 show the laminate

construction and the 77°K cyclic energy absorption data for the laminated Teflon-glass gasket construction compared to an asbestos-rubber gasket previously used in liquid oxygen applications. Leakage tests were performed by compressively loading the gaskets in a special flanged fixture to 3000 psi, and pressurizing the internal volume to 200 psi. Flange loads were reduced until leakage occurred to determine the ASME gasket m-factor. (Factors less than 1 only attained with pressure-actuated seals.) The same procedures were followed at ambient and cryogenic temperatures. The laminated material had m-factors as low as 1.31 at ambient and 1.56 at 77°K. The currently used asbestos-rubber gasket had values of 1.30 at ambient temperature, but at 77°K no seal was obtained at 3000 psi flange pressure.

Conclusions. The laminated TFE Teflon-glass fabric gasket material was superior to the currently used asbestos-rubber gasket in compressibility and sealing characteristics at 77°K.

Title. "Static and Dynamic Seals Used on Rocketdyne Engines."

Source. Rocketdyne, a division of North American Rockwell Corporation, Canoga Park, California.

Objectives. The objectives were to describe the various sealing concepts utilized in Rocketdyne liquid propellant rocket engines.

Materials. Test materials were various plastic, elastomeric, metal-plastic, and metal-elastomeric materials.

Properties. Detail seal performance was not given; sealing concepts were emphasized.

Test temperatures. Tests were performed at temperatures from ambient to 20°K.

Data. Data given are pertinent to the Naflex pressure-actuated seal. Rocketdyne designed and developed the Naflex seal in 1958 for the Atlas engine system. Many improvements have been made to the original design with the assistance of digital computers. The basic metal cup is made from steel alloys. The primary and secondary sealing surfaces are dispersion coated with Teflon resins fused to the metal substrate, Fig. 23. Leakage can be monitored between the primary and secondary seals. The Teflon coating provides the soft sealing surface and the metal portion, the spring force necessary to achieve a seal at pressures of 15 to 1500 psi at temperatures from 20 to 373°K.

### Film Materials

High-strength plastic film materials have been used in a variety of structural and semistructural applications at cryogenic temperatures including diaphragms, bladders, and filament-wound tank liners. Shaft-riding lip-seals used at temperatures down to 20°K are often fabricated from multiple plies of various plastic films. Film materials are also used to form vapor barriers between cryogenic fluids and internal tank insulation materials such as polyurethane foams.

Liners for filament-wound pressure vessels designed for cryogenic temperature service must have enough biaxial ductility at cryogenic temperatures to be able to expand with the pressurized reinforced plastic shell. Not only must the liner materials have enough elongation at cryogenic temperatures to move with the shell, but the material must have enough additional low-temperature elongation to compensate for the higher thermal contraction of the liner over that of the filament-wound tank. These two additive requirements are very difficult to meet at cryogenic temperatures. Cryogenic

fluid vapor barriers for internally insulated cryogenic tanks have some of the same problems associated with liners for filament-wound tanks (although working pressure strains for large cryogenic metal storage tanks are considerably less than those of high-pressure filament-wound tanks). Further, a small leak of hydrogen through the vapor barrier into the internal polyurethane foam insulation greatly increases the thermal conductivity of the foam, reducing its efficiency.

Information presented from two papers pertaining to film materials as liners for filament-wound tanks for cryogenics and as vapor barriers is outlined in the paragraphs below.

Title. "Structural Properties of Glass-Fiber Filament-Wound Cryogenic Pressure Vessels" (NAS 3-2562).

Source. Douglas Aircraft Company, Santa Monica, California, and NASA-Lewis Research Center, Cleveland, Ohio.

Objectives. The objective was to obtain a suitable liner for a filament-wound high-pressure tank for cryogenic service.

Materials. Materials tested were Mylar, Tedlar, H-film, and Seilon UR29E polyurethane.

Properties. Thermal contraction, biaxial cyclic tests, and uniaxial tensile tests were performed.

Test temperatures. Tests were performed at 297, 77, and 20°K.

Data. Uniaxial tensile data for the four film materials is shown in Figs. 24-27. These data show Mylar to have the highest strength at 20°K and Tedlar to have the greatest elongation. Thermal contraction data are shown in Fig. 28. The data show Mylar, of the four plastic film materials, to have the lowest contraction and UR29E polyurethane to have a contraction rate approximately four times as great. Table VIII shows the combined effects of the contraction differentials between the laminate, the liner, and the residual elongation of the liner at 20°K.

Conclusions. If the total theoretical elongations were realized by tank liners at cryogenic temperatures, the shell would only be carrying between 25 and 49% of its predicted ultimate load, not a very attractive limit. Only the Mylar-lined tank failed at its predicted stress. Other liner materials failed at stresses considerably lower than predicted. Because of this, the emphasis was switched to metallic foil liners.

Title. "Low Temperature Tensile, Thermal Contraction, and Gaseous Hydrogen Permeability Data on Hydrogen-Vapor Barrier Materials" (NAS 8-5600).

Source. Lockheed Missiles and Space Company, Sunnyvale, California.

Objectives. The objectives were to determine promising gaseous hydrogen vapor barrier materials.

Materials. Three film materials, two impregnated glasses, and three impregnated quartz types were evaluated.

Properties. Permeation, contraction, and tensile properties were measured.

Test temperatures. Tests were performed at 297, 77 and 20°K.

Data. Average permeation rates for films and impregnated fabrics are shown in Table IX. These data show the laminate films to be less permeable than the unsupported films. Contraction data are shown in Fig. 29 for film and laminate materials. Film materials had more contraction than the impregnated fabrics. Tensile properties of the film materials, Tables X, XI, and XII, show the mechanical properties of the film and impregnated fabrics.

Conclusions. Although the ultimate strengths of the impregnated fabrics were higher than those of the film materials at cryogenic temperatures, the strain carrying abilities of the films were much better than the laminates. A further disadvantage of the impregnated fabrics was their poorly defined transition stresses in the 45° direction.

TABLE I  
MECHANICAL PROPERTIES OF TWO TYPES OF EPOXY-GLASS CLOTH LAMINATES  
WOUND ON FLAT MANDRELS AT AMBIENT AND CRYOGENIC TEMPERATURES

Laminate	Specimen Direction	Temperature, K	Tension, psi	Compression, psi	Flexure, psi	Shear, psi	Bearing Yield/Ultimate, psi	Tensile Elongation, percent	Tensile Modulus, percent	Flexural Modulus, psi
1581 Cloth (37.61% resin)	Parallel	298	92 506	62 587	104 186	8 237	45 925 79 017	3.37	3 286 670	3 328 300
		197	115 540	79 663	134 650	10 003	48 208 107 183	4.11	3 496 330	3 334 000
		77	144 543	103 202	170 638	13 495	67 330 121 530	5.01	3 980 000	3 911 500
		20	137 770	109 097	180 325	11 542	65 283 123 367	4.81	4 266 000	3 664 000
	Normal	298	84 474	59 161	96 297	7 638	44 433 76 333	3.30	3 166 000	3 127 200
		197	98 752	74 089	126 103	10 028	48 383 104 600	3.96	3 340 670	2 976 000
		77	128 010	94 826	157 132	12 240	65 933 121 200	4.64	3 974 000	3 589 333
		20	118 110	100 847	170 221	10 869	74 700 131 533	4.50	4 178 000	3 785 000
	45 degrees	298	32 716	31 370	48 529	6 186	41 750 86 200	10.0	1 498 670	1 631 900
		197	46 034	45 939	72 274	7 241	41 387 110 167	10.57	2 108 670	1 809 667
		77	50 684	69 935	105 156	9 442	67 733 121 300	6.71	2 730 670	2 600 667
		20	46 613	77 689	103 330	8 686	68 700 129 600	4.84	2 834 000	2 911 000
	Parallel	298	169 316	89 503	133 264	9 861	54 358 82 625	3.27	5 495 000	5 194 900
		197	186 190	106 620	167 701	12 440	56 608 103 183	3.51	5 565 830	5 108 333
		77	232 385	122 448	207 525	15 966	81 158 138 780	4.48	5 858 330	5 405 000
		20	220 683	128 171	217 897	13 848	73 500 132 667	4.09	5 997 857	5 561 000
1543 Cloth (32.59% resin)	Normal	298	28 613	35 753	43 665	*	36 567 83 917	3.71	2 144 670	2 060 900
		197	35 008	49 318	55 480	*	37 333 98 200	4.98	2 463 330	2 212 000
		77	42 190	69 359	76 035	*	61 750 104 200	5.58	3 237 330	2 845 000
		20	37 554	65 480	74 688	*	61 016 104 200	5.68	3 287 330	2 992 000
	45 degrees	298	19 937	31 245	44 824	*	42 200 90 017	5.48	1 894 670	1 876 700
		197	23 607	45 471	61 222	*	47 416 109 367	4.47	2 154 000	2 122 330
		77	27 861	66 456	75 756	*	67 900 114 900	1.11	3 011 330	2 815 330
		20	27 490	68 476	81 668	*	64 683 118 000	1.21	3 531 330	3 250 000

\*Failure occurred in flexure instead of shear

TABLE II

NUCLEAR RADIATION EFFECT ON MECHANICAL PROPERTIES\* AT  $-423^{\circ}\text{F}$ 

Control Test at $-423^{\circ}\text{F}$					Cryogenic Test											
					First Irradiation Test at $-423^{\circ}\text{F}$ Average Dose: $4 \times 10^6$ ergs/g(C)				Second Irradiation Test at $-423^{\circ}\text{F}$ Average Dose: $5 \times 10^8$ ergs/g(C)				Third Irradiation Test; Irradiated at $-423^{\circ}\text{F}$ , Tested at Room Temperature Average Dose: $5 \times 10^8$ ergs/g(C)			
Material	Ultimate Strength, psi	Standard Deviation	Elongation, percent	Standard Deviation	Ultimate Strength, psi	Standard Deviation	Elongation, percent	Standard Deviation	Ultimate Strength, psi	Standard Deviation	Elongation, percent	Standard Deviation	Ultimate Strength, psi	Standard Deviation	Elongation, percent	Standard Deviation
Phenolic Asbestos	13 470	999	6.5	0.6	14 182	2381	2.0	0.14	12 444	903	1.0	0.14	8 921	1770	1.5	0.3
Phenolic Linen	16 598	1162	6.3	0.3	16 342	538	1.8	0.07	16 102	364	1.5	0.07	11 550	569	4.1	1.24
Phenolic Glass	42 099	1653	3.7	1.3	42 752	3663	4.2	0.78	40 579	2735	0.4	0.001	24 816	570	0.8	0.04

\*Average data for five specimens.

TABLE III

## UNIDIRECTIONAL FATIGUE TESTS ON FLAT SPECIMEN

Sample Structure	Maximum Flexural Stress, psi	Maximum Deflection, inch	Fatigue Test Temperature, °K	Number of Cycles	Deviation From Original Value
HTS--Filament structure (no film barrier)	±3000	±0.024	77.8	5x10 <sup>6</sup>	None
HTS--Filament epoxy structure with H-film barriers	±3000	±0.024	77.8	10x10 <sup>6</sup>	None
HTS--Filament epoxy structure with H-film barriers	±6000	±0.058	77.8	16.7x10 <sup>6</sup>	None
HTS--Filament epoxy structure with H-film barriers	±9000	±0.089	77.8	4x10 <sup>6</sup>	None
HTS--Glass cloth-epoxy structure (no film barrier)	±3000	±0.024	77.8	6.5x10 <sup>6</sup>	None

TABLE IV

## TYPES OF BEARINGS TESTED

Bearing No.	Bearing Type	Ball and Race Material	Separator Type	Separator Material	Internal Clearance x 10 <sup>-4</sup> in.
1	Radial*	52100	Riding inner ring	Phenolic	5.0 to 9.8
2	Radial*	440C	Riding inner ring	Phenolic	5.5 to 7.5
3	Radial*	440C	Riding balls	Phenolic	4.3 to 5.3
4	Radial**	440C	Riding outer ring	Phenolic	5.3 to 12.5
5	Radial**	440C	Two-piece, aluminum armored, riding outer ring	Phenolic	5.6 to 7.0
6	Radial**	440C	Two-piece pressed	Steel, PTFE Coated	8 to 18
7	Radial*	440C	None	Alternate undersized 440C balls	4.8 to 5.5
8	Radial**	440C	Riding outer ring	Filled PTFE	4.4 to 5.8
9	Radial**	440C	Riding outer ring	Phenolic	2.5 to 4.5
10	Radial**	440C	Riding outer ring	PTFE coated, Grade A, phosphor bronze	4.6 to 5.5
11	Radial**	440C	Riding outer ring	Grade A phosphor bronze	4.1 to 5.5
12	Angular Contact**	52100	Riding inner ring	Phenolic	2.5 to 4.5

\*Full shoulder on both sides of inner ring and a counterbore on one side of outer ring.

\*\*Full shoulder on both sides of outer ring and a low shoulder on one side of inner ring.

TABLE V

## MECHANICAL AND THERMAL PROPERTIES OF FLUOROCARBON RESINS OF VARYING CRYSTALLINITIES

Mechanical Property	Temperature, °F	Kel-F Crystallinity, percent				FEP Teflon Crystallinity, percent			TFE Teflon Crystallinity, percent				
		40	55	60	70	44	49	51	47	49	52.5	66.2	71
Notched Izod Impact Strength, ft-lb/in.	-423	—	—	1.4	1.2	—	1.95	1.7	—	—	1.25	—	1.55
	-320	—	—	1.3	1.1	—	1.9	1.5	—	—	1.17	—	1.35
	(-297)	—	—	(1.25)	(1.07)	—	(1.9)	(1.5)	—	—	(1.15)	—	(1.39)
Modulus of Rigidity, psi x 10 <sup>3</sup>	-423	262	222	—	230	935	—	695	267	—	275	377	—
	-320	232	197	—	203	305	—	305	224	—	190	200	—
	(-297)	(229)	(192)	—	(195)	(275)	—	(275)	(216)	—	(175)	(175)	—
Tensile Yield Strength, psi x 10 <sup>3</sup>	-423	28.5	20.5	—	18.0	23.8	23.5	—	—	20.0	19.0	15.6	—
	-320	24.9	17.5	—	15.3	19.1	18.8	—	—	16.0	15.4	10.6	—
	(-297)	(24.4)	(17.0)	—	(15.0)	(17.9)	(17.6)	—	—	(14.2)	(14.1)	(9.0)	—
Ultimate Tensile Strength, psi x 10 <sup>3</sup>	-423	29.0	22.5	—	17.95	24.0	23.6	—	—	20.05	19.0	15.7	—
	-320	24.9	17.6	—	15.8	18.1	17.9	—	—	17.9	15.4	11.8	—
	(-297)	(24.1)	(17.5)	—	(15.3)	(17.0)	(16.8)	—	—	16.0	14.2	11.0	—
Tensile Modulus, psi x 10 <sup>6</sup>	-423	1.26	0.975	—	0.830	0.825	0.620	—	—	0.600	0.645	0.625	—
	-320	1.11	0.802	—	0.760	0.700	0.450	—	—	0.500	0.520	0.435	—
	(-297)	(1.08)	(0.800)	—	(0.750)	(0.652)	(0.430)	—	—	(0.465)	(0.480)	(0.400)	—
Elongation, percent	-423	ca 2	ca 1	—	1	ca 5	ca 5	—	—	ca 4	ca 3	ca 2	—
	-320	ca 4	2.5	—	ca 1	ca 7	ca 7	—	—	ca 9	ca 8	ca 4	—
	(-297)	(ca 4.5)	(3)	—	(ca 1)	(ca 8)	(ca 7)	—	—	(9)	(8)	(ca 5)	—
Flexural Strength, psi x 10 <sup>3</sup>	-423	74.0	55.5	—	50.5	35.9	39.6	—	—	33.8	25.7	22.8	—
	-320	58.0	42.7	—	37.0	25.7	27.7	—	—	30.0	24.0	21.5	—
	(-297)	(53.5)	(41.0)	—	(35.0)	(24.0)	(25.5)	—	—	(28.0)	(23.0)	(20.5)	—
Flexural Modulus, psi x 10 <sup>6</sup>	-423	2.09	1.94	—	1.84	0.78	0.75	—	—	0.778	0.72	0.695	—
	-320	1.83	1.70	—	1.64	0.68	0.68	—	—	0.720	0.70	0.64	—
	(-297)	(1.70)	(1.64)	—	(1.59)	(0.67)	(0.66)	—	—	(0.690)	(0.64)	(0.61)	—
		50*	55	60	70	44	49	51	47	50*	56*	68*	71
Compressive Strength, psi x 10 <sup>3</sup>	-423	42.5	—	44.5	28.8	36.3	35.2	—	—	30.4	32.5	33.2	—
	-320	35.0	—	37.5	38.8	30.0	30.0	—	—	20.0	21.2	22.0	—
	(-297)	(34.0)	—	(36.0)	(38.8)	(28.5)	(28.5)	—	—	(18.5)	(20.0)	(21.5)	—
Compressive Modulus, psi x 10 <sup>6</sup>	-423	1.67	—	1.76	1.48	1.01	1.04	—	—	0.81	0.90	0.97	—
	-320	1.48	—	1.52	1.65	0.91	0.91	—	—	0.75	0.79	0.84	—
	(-297)	(1.27)	—	(1.40)	(1.65)	(0.90)	(0.89)	—	—	(0.72)	(0.76)	(0.81)	—
Coefficient of Thermal Expansion (Total contraction from 70°F) in./in.	-423	0.011	—	—	—	0.017	—	—	—	0.0214	—	—	—
	-320	0.0093	—	—	—	0.0157	—	—	—	0.0205	—	—	—
	(-297)	(0.0090)	—	—	—	(0.0154)	—	—	—	0.0201	—	—	—

The above values were obtained by PLASTEC by reading off data points from the original data curves. The values in parentheses() were obtained by interpolation. No actual data was obtained with liquid-oxygen temperatures in the original study.

Note change in crystallinity, indicated by asterisk (\*)



TABLE VI

## MEAN VALUES OF TENSILE STRENGTH FOR PCTFE TEST SAMPLES

Sample and Strain Rate, in./min	Mean Value of Maximum Tensile Strength, psi				Mean Value of Tensile Stress at Failure, psi			
	Temperature				Temperature			
	-320°F		75°F		-320°F		75°F	
	Molded Surface	Machined Surface	Molded Surface	Machined Surface	Molded Surface	Machined Surface	Molded Surface	Machined Surface
40-Percent Crystallinity Sample								
0.02					20 939	21 290	4 710	5 165
0.2					24 345	24 155	4 818	5 884
2.0					26 533	24 241	4 208	4 661
20.0					22 924	22 211	4 808	5 572
1 000.0	22 507	22 799	8 548	9 294	22 500	22 800	6 210	6 890
10 000.0	9 313	8 496	13 698	13 296	4 020	4 120	7 830	6 800
55-Percent Crystallinity Sample								
0.02					19 833	19 835	5 264	4 933
0.2					23 119	22 732	5 313	5 684
2.0					24 581	24 174	5 068	5 306
20.0					22 247	21 192	5 400	6 007
1 000.0	22 293	21 417	9 016	9 431	22 290	21 400	6 380	6 820
10 000.0	9 816	8 179	13 618	13 226	4 700	3 440	12 770	15 230

TABLE VII

## MEAN VALUES OF PERCENT ELONGATION FOR PCTFE TEST SAMPLES

Sample and Strain Rate, in./min	Mean Value of Percent Elongation at Maximum Tensile Strength				Mean Value of Percent Elongation at Failure			
	Temperature				Temperature			
	-320°F		75°F		-320°F		75°F	
	Molded Surface	Machined Surface	Molded Surface	Machined Surface	Molded Surface	Machined Surface	Molded Surface	Machined Surface
40-Percent Crystallinity Sample								
0.02					6.2	6.9	125.0	141.0
0.2					5.8	5.2	120.0	137.0
2.0					9.3	8.4	130.0	152.0
20.0					5.0	3.9	70.0	88.0
1 000.0	6.45	6.53	13.30	14.00	6.45	6.53	71.50	58.75
10 000.0	5.32	4.65	14.35	12.67	11.55*	11.50*	47.00*	37.50*
55-Percent Crystallinity Sample								
0.02					7.0	7.7	180.0	139.0
0.2					4.6	4.5	189.0	90.0
2.0					9.2	8.8	214.0	92.0
20.0					6.5	3.8	59.0	53.0
1 000.0	6.90	6.62	15.35	14.70	6.90	6.62	63.30	42.75
10 000.0	5.30	4.30	11.13	11.00	12.25*	10.27*	23.30*	24.00*

\*Failure appeared to be a two-step process

TABLE VIII

## POLYMER LINER BEHAVIOR AT 20°K

Mechanical Property	Tedlar BG-50-WH	H-Film	Mylar A	Polyurethane Seilon UR29E
Contraction of Liner, $10^{-5}$ in./in.	9.16	5.26	3.86	16.31
Chilldown Differential, percent (difference in contraction between liner and fiberglass cylinder)	0.73	0.34	0.20	1.44
Average Ultimate Elongation of Liner, percent	2.16	1.69	0.82	2.20
Residual Elongation of Liner, percent	1.43	1.3	0.62	0.76
Predicted Liner Failure, psi percent of cylinder ultimate	786 48	742 45	345 21	418 25
Actual Liner Failure, psi percent of cylinder ultimate	184 11	355 to 388 21 to 24	360 22	Not tested

TABLE IX

AVERAGE PERMEATION ( $\rho$ ) RATES (std  $\text{cm}^3\text{-cm/cm}^2\text{-sec-cm Hg}$ )

Material	No. of Samples	Room Temperature*	Liquid Nitrogen Temperature*	Liquid Hydrogen Temperature*
H-Film, 1 mil thick	3	$\rho < 1.2 \times 10^{-10}$	$\rho < 1.8 \times 10^{-13}$	$\rho < 1.8 \times 10^{-13}$
Mylar Film, 1 mil thick	3	$\rho < 3.9 \times 10^{-11}$	$\rho < 1.1 \times 10^{-13}$	$\rho < 1.1 \times 10^{-13}$
Aluminized Mylar, 1 mil thick	3	$\rho < 1.6 \times 10^{-12}$	$\rho < 1.3 \times 10^{-13}$	$\rho < 1.3 \times 10^{-13}$
181EE-Glass Cloth, 828/Z, 43.9% Resin, 0.011 in. thick	4	$\rho < 1.7 \times 10^{-12}$	$\rho < 1.9 \times 10^{-12}$	$\rho < 1.5 \times 10^{-12}$
181 Quartz Cloth, 828/Z, 43.1% Resin, 0.012 in. thick	3	$\rho < 1.6 \times 10^{-12}$	$\rho < 1.6 \times 10^{-12}$	$\rho < 1.5 \times 10^{-12}$
S-Glass Cloth, 828/Z, 46.7% Resin, 0.012 in. thick	3	$\rho < 7 \times 10^{-13}$	$\rho < 6.1 \times 10^{-13}$	$\rho < 6 \times 10^{-13}$

\* < Denotes that the permeability was at or below the least readable count of the output meter of the mass spectrometer detector, and hence lies at or below the noted permeability values.

TABLE X

## THIN FILMS\*

Material Type	Test Temperature	Modulus, x 10 <sup>-7</sup> psi	Ultimate Stress, x 10 <sup>3</sup> psi	Maximum Strain, ΔL/L	Average Thickness, x 10 <sup>3</sup> in.
Plain Mylar (M-Series)	Room	0.80 (3.8%)	17.5 (21%)	0.160 (8.8%)	0.70 ±0.05
	LN <sub>2</sub>	1.47 (4.1%)	43.5 (8%)	0.038 (10%)	0.50 ±0.05
	LH <sub>2</sub>	1.40 (12%)	34.3 (6.7%)	0.030 (23%)	0.60 ±0.05
Aluminized Mylar (R-Series)	Room	0.86 (4.7%)	23.6 (27%)	0.140 (29%)	0.45 ±0.05
	LN <sub>2</sub>	1.60 (2.5%)	38.7 (8.0%)	0.034 (17.7%)	0.50 ±0.05
	LH <sub>2</sub>	1.57 (5.7%)	29.1 (8.6%)	0.020 (15%)	0.50 ±0.05
H-Film (H-Series)	Room	0.48 (7.1%)	16.5 (20%)	0.110 (19%)	0.90 ±0.05
	LN <sub>2</sub>	1.09 (4.6%)	30.7 (3.3%)	0.033 (3.0%)	0.80 ±0.05
	LH <sub>2</sub>	0.96 (4.4%)	27.3 (16%)	0.033 (27%)	0.90 ±0.05

\*Percentage values are the maximum deviation from average of three tests.

TABLE XI

## EPOXY IMPREGNATED QUARTZ CLOTH PROPERTIES IN THREE DIRECTIONS

(1 Ply # 181)\*

Direction of Pull	Test Temperature	Initial Modulus, x 10 <sup>-6</sup> psi	Ultimate Stress, x 10 <sup>3</sup> psi	Maximum Strain, ΔL/L	Secondary Modulus, x 10 <sup>-6</sup> psi	Transition Stress, x 10 <sup>-3</sup> psi
Warp (A-Series)	Room	2.71 (3.3%)	44.6 (3.6%)	0.037 (3.0%)	2.06 (6.8%)	13.0 (13%)
	LN <sub>2</sub>	2.78 (8.6%)	73.3 (2.3%)	0.040 (10%)	1.85 (1.6%)	11.2 (15.2%)
	LH <sub>2</sub>	3.87 (14.5%)	71.4 (8.0%)	0.034 (8.8%)	1.97 (6.6%)	11.1 (12.6%)
Woof (C-Series)	Room	2.52 (4.4%)	45.5 (9.0%)	0.023 (8.7%)	1.89 (4.8%)	9.7 (1.0%)
	LN <sub>2</sub>	2.82 (2.1%)	57.2 (4.5%)	0.038 (10.5%)	1.48 (5.4%)	6.3 (17.5%)
	LH <sub>2</sub>	2.99 (6.4%)	68.5 (16.8%)	0.041 (5.0%)	1.59 (12.6%)	6.6 (16.7%)
45 Degrees to Warp (B-Series)	Room	1.62 (14.0%)	15.0 (4.7%)	0.029 (15%)	---	---
	LN <sub>2</sub>	2.51 (9.2%)	21.2 (30%)	0.019 (88%)	---	---
	LH <sub>2</sub>	2.88 (11.8%)	19.2 (2.1%)	0.014 (28.6%)	---	---

\*Percentage values are the maximum deviation from average of three tests.

TABLE XII

## EPOXY-IMPREGNATED CLOTHS

(1 Ply # 181)\*

Material Type	Test Temperature	Initial Modulus, x 10 <sup>-6</sup> psi	Ultimate Stress, x 10 <sup>-3</sup> psi	Maximum Strain, ΔL/L	Secondary Modulus, x 10 <sup>-6</sup> psi	Transition Stress, x 10 <sup>-3</sup> psi
Fiberglass (E-Series)	Room	3.14 (6.4%)	31.4 (7.0%)	0.013 (17.0%)	2.10 (11.0%)	10.1 (21%)
	LN <sub>2</sub>	4.25 (3.5%)	51.0 (1.6%)	0.024 (8.3%)	1.78 (9.5%)	11.3 (7.1%)
	LH <sub>2</sub>	5.02 (11.6%)	52.4 (4.6%)	0.023 (8.7%)	1.77 (13.0%)	8.0 (10%)
S-Glass (D-Series)	Room	2.83 (4.2%)	58.9 (12.0%)	0.12* (8.5%)	2.25 (9.3%)	17.7 (13%)
	LN <sub>2</sub>	3.92 (8.2%)	92.0 (1.4%)	0.045 (8.9%)	1.97 (6.6%)	16.0 (13.1%)
	LH <sub>2</sub>	3.60 (4.7%)	85.6 (1.9%)	0.052 (77.7%)	1.73 (6.4%)	12.6 (12.7%)
Quartz (A-Series)	Room	2.71 (3.3%)	44.6 (3.6%)	0.037 (3.0%)	2.06 (6.8%)	13.0 (13.0%)
	LN <sub>2</sub>	2.78 (8.6%)	73.3 (2.3%)	0.040 (10.0%)	1.85 (1.6%)	11.2 (15.2%)
	LH <sub>2</sub>	3.87 (14.5%)	71.4 (8.0%)	0.034 (8.0%)	1.97 (8.8%)	11.1 (12.6%)

\*Averages of three tests along with maximum deviation from average expressed as percent.

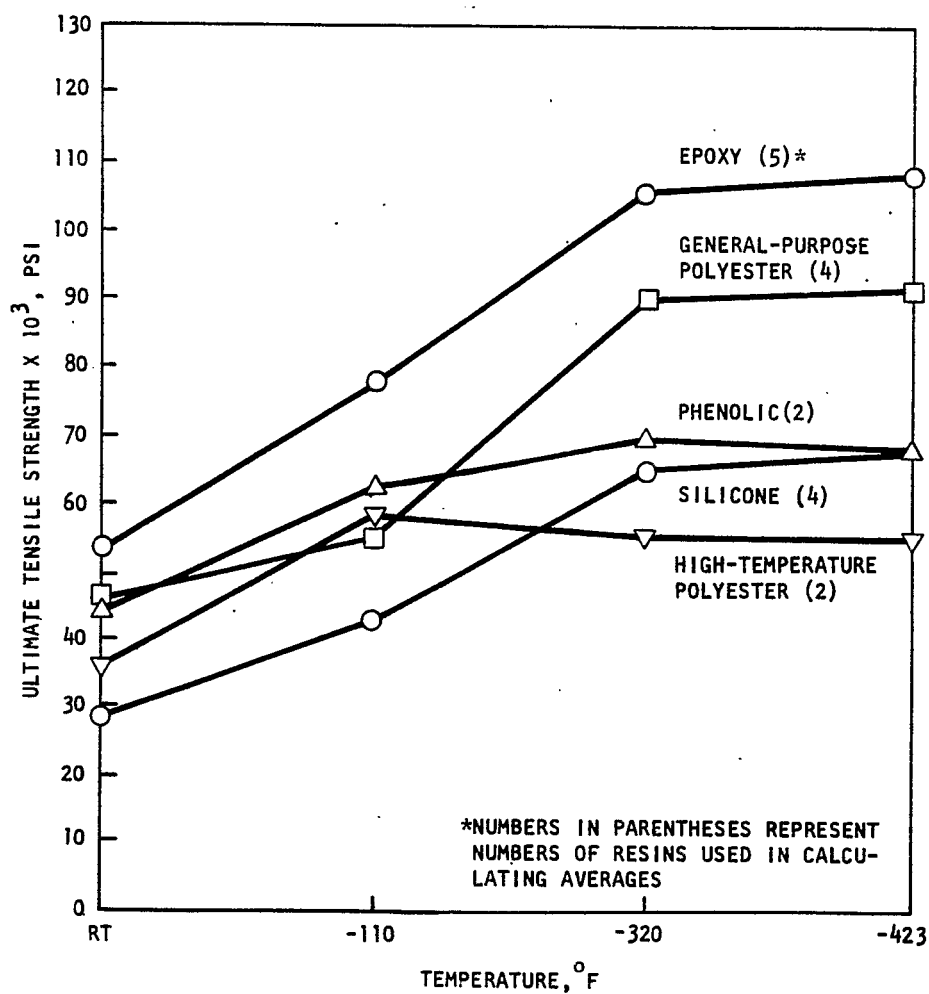


Fig. 1. Average tensile strength of glass-reinforced plastic laminates laminated with 181 glass cloth.

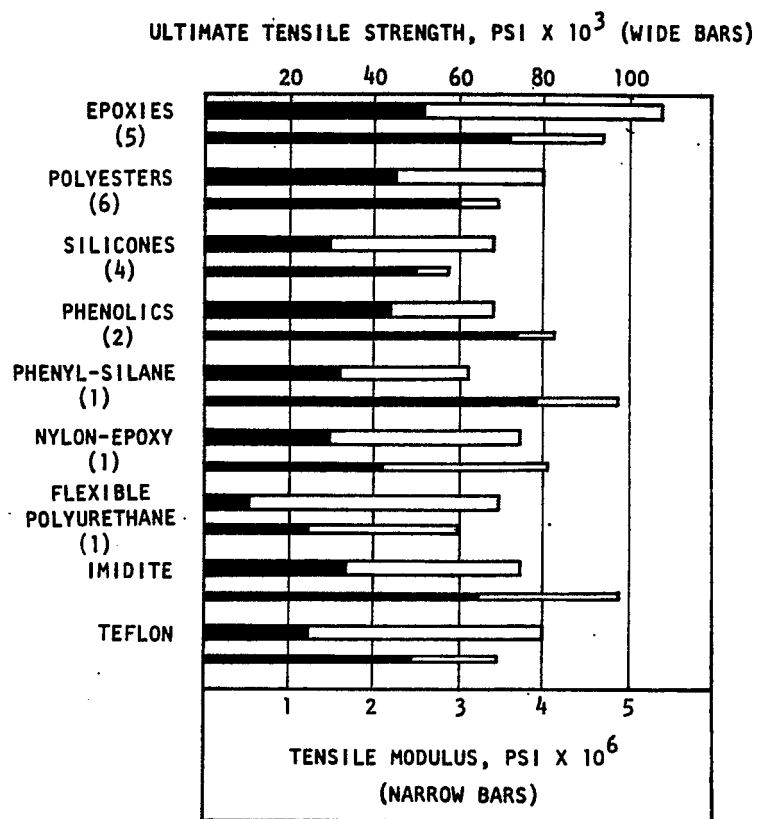


Fig. 2. Average ultimate tensile strength and modulus of laminates at room temperature (shaded bars) and at 20°K.

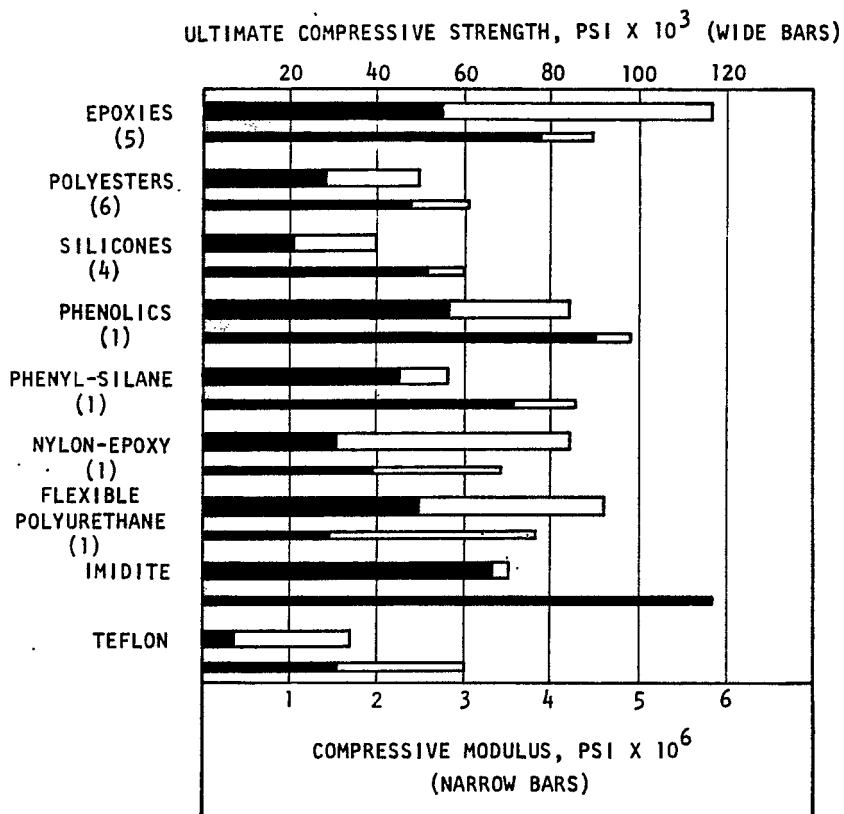


Fig. 3. Average ultimate compressive strength and modulus at room temperature (shaded bars) and at 20°K.

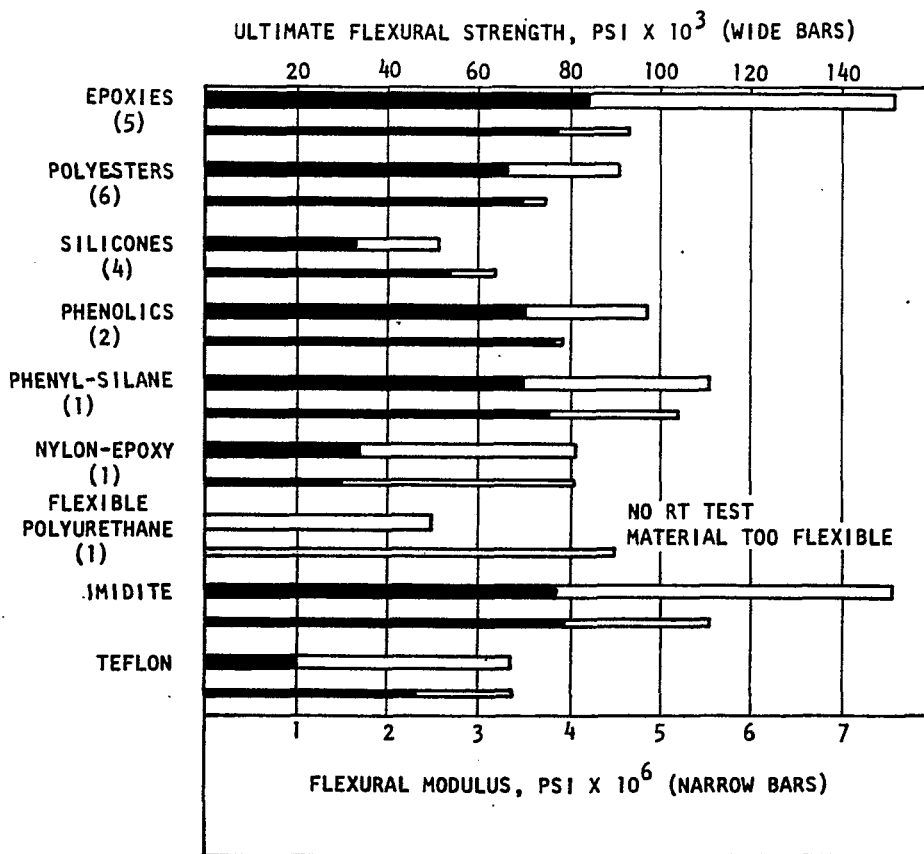


Fig. 4. Average flexural strength and modulus at room temperature (shaded bars) and at 200°K.

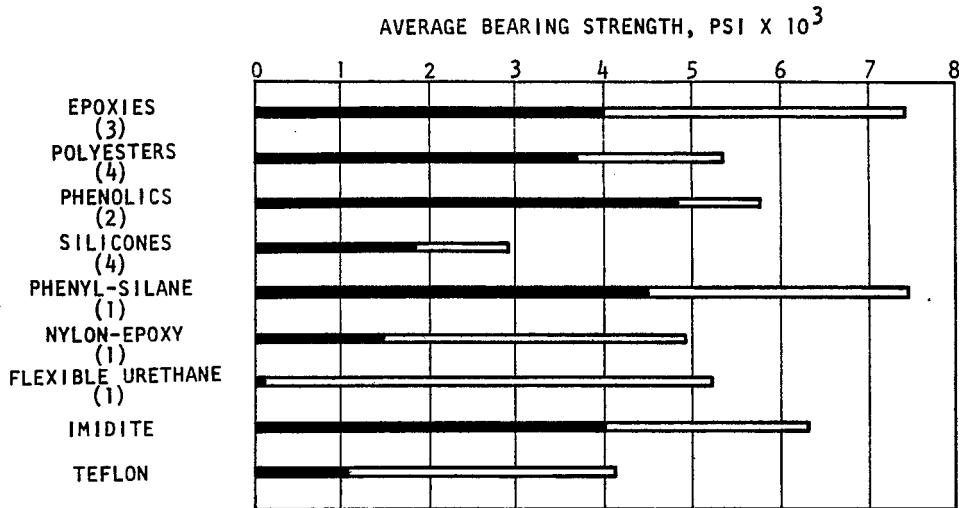


Fig. 5. Average bearing strength of 1/8 in. thick laminates on a 3/16 in. diameter pin at room temperature (shaded bars) and at 77°K.

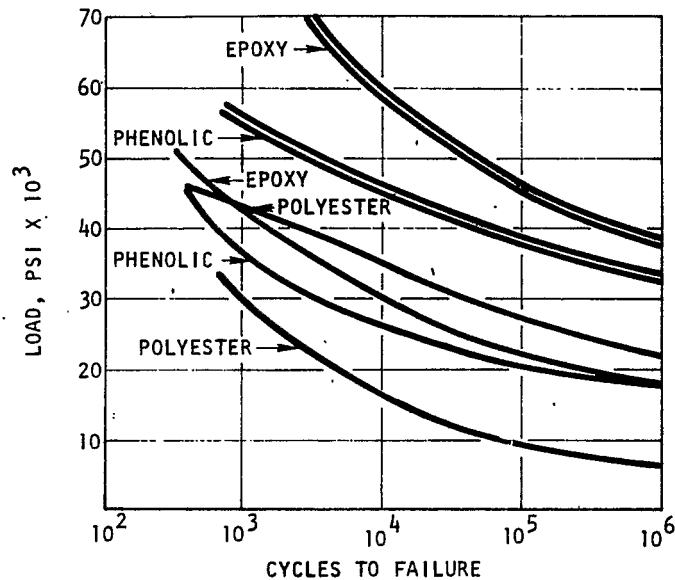


Fig. 6. Composite S-N curves derived from average fatigue strength values at room temperature (lower in each case) and at 20°K.

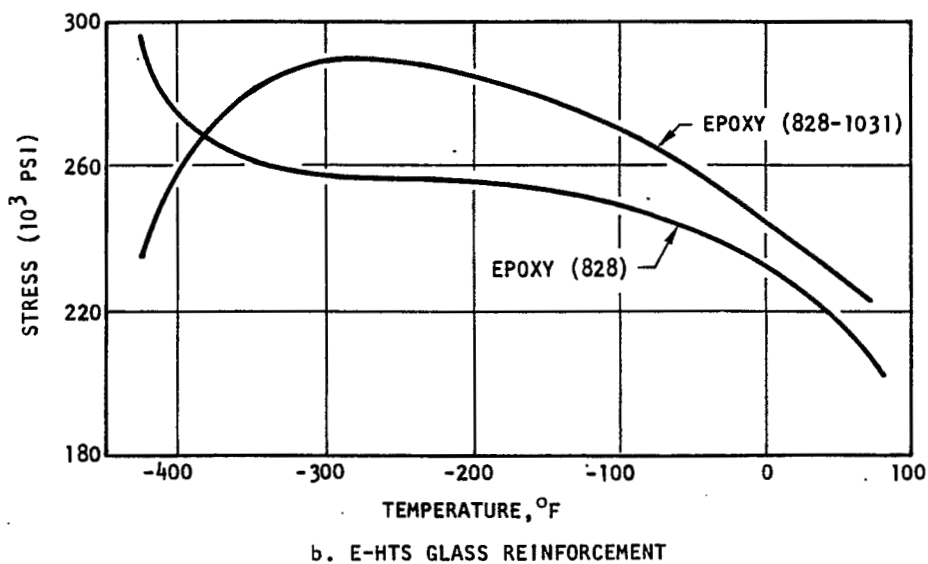
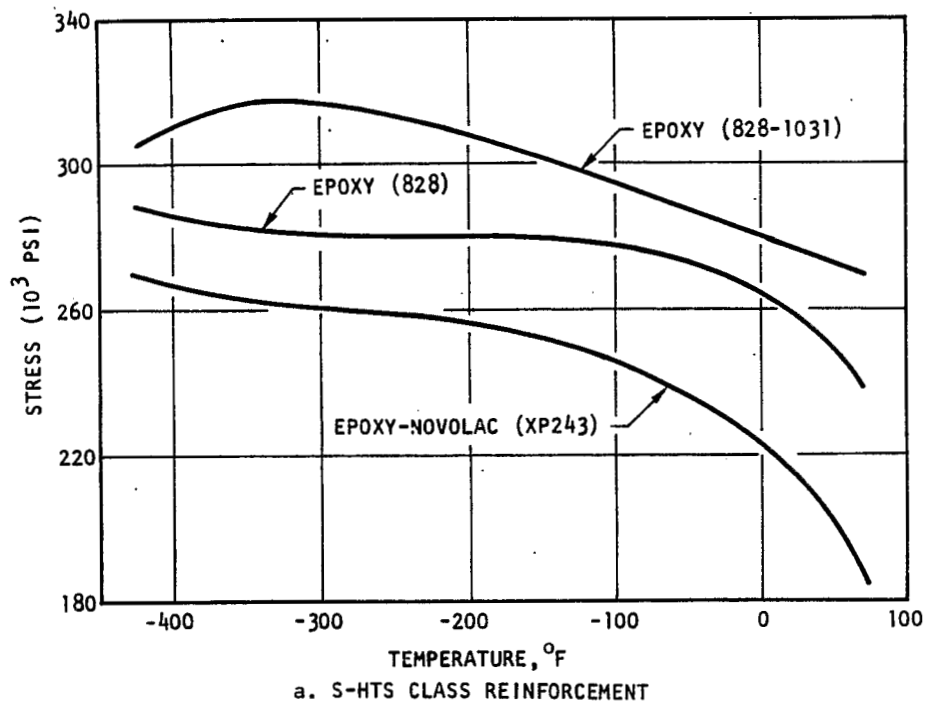


Fig. 7. Strength of epoxy filament-wound rings at cryogenic temperatures.



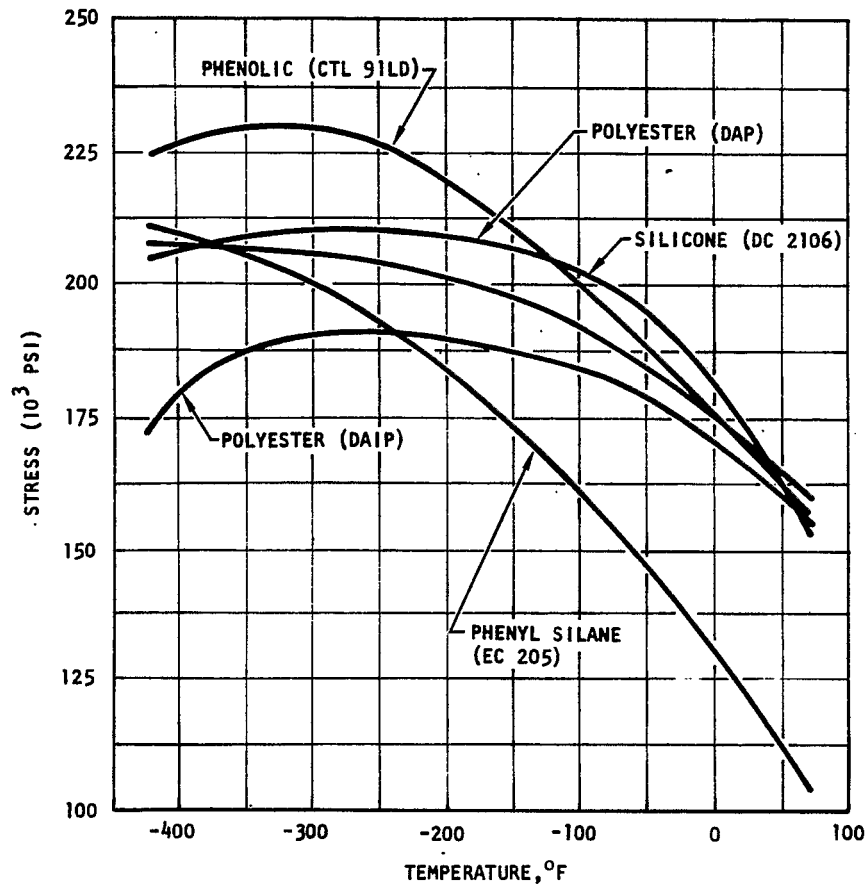


Fig. 8. Strength of filament-wound rings at cryogenic temperatures.

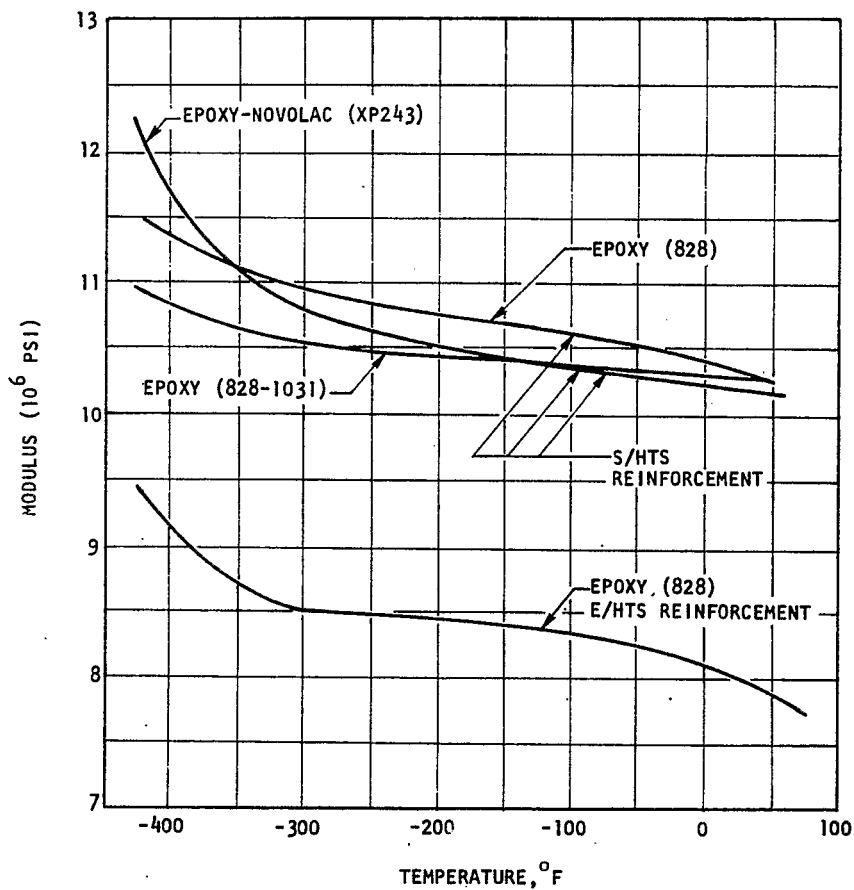


Fig. 9. Modulus of elasticity of epoxy filament-wound rings at cryogenic temperatures.

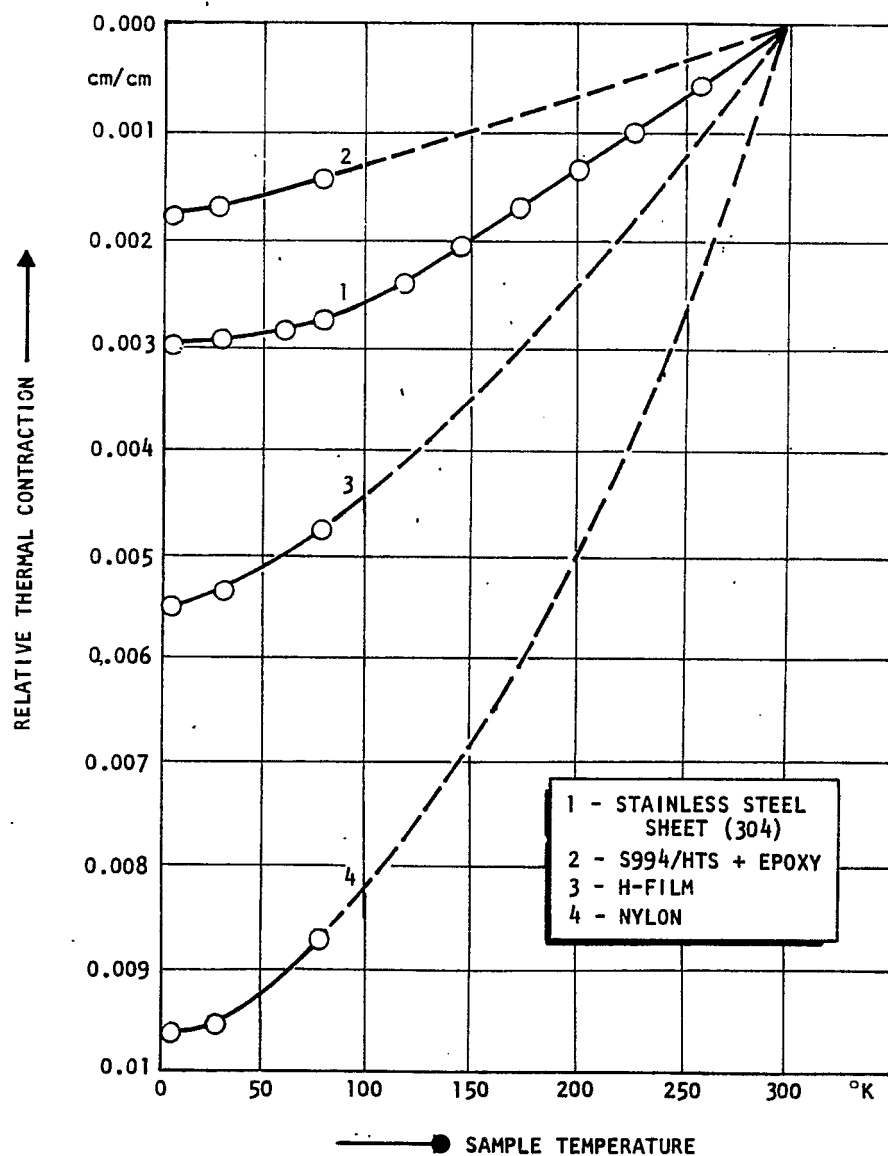
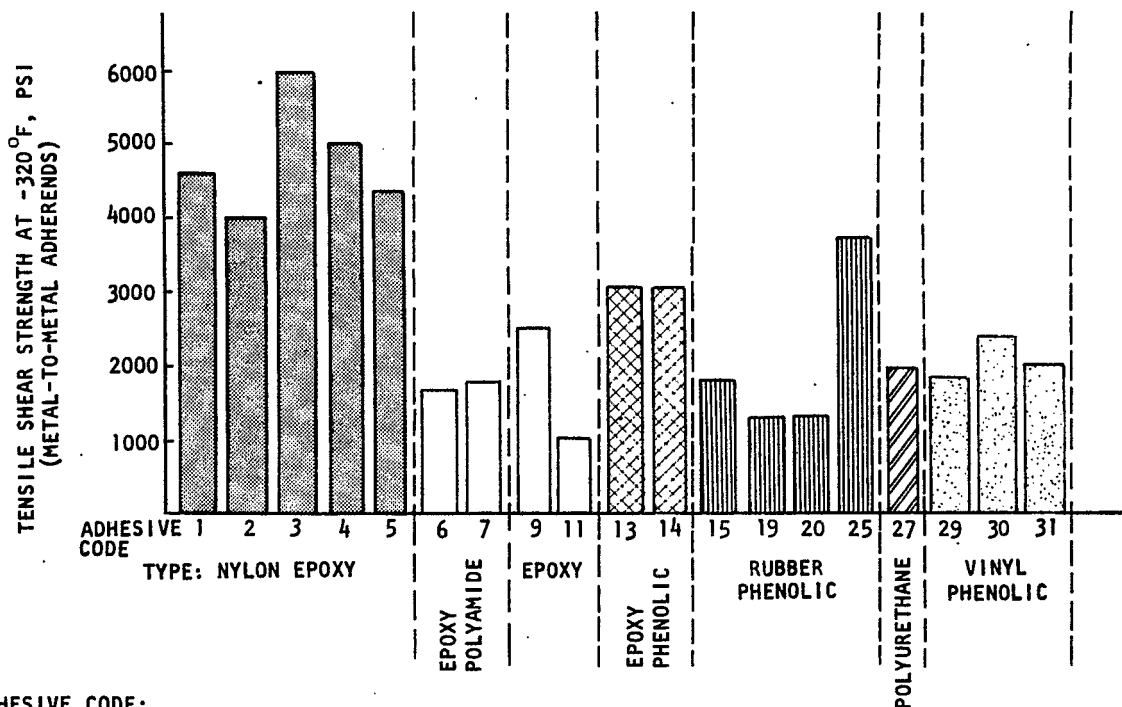


Fig. 10. Linear thermal contraction vs bath temperature.



#### ADHESIVE CODE:

- |                 |                                |                     |                        |
|-----------------|--------------------------------|---------------------|------------------------|
| 1. METLBOND 406 | 6. RESIN 3135 AND CURING AGENT | 13. METLBOND 302    | 25. METLBOND 303(MN3C) |
| 2. METLBOND 408 | 7. EC/1933B/A                  | 14. EPON 422J       | 27. APCO-1261          |
| 3. AF-40        | 9. EC-1469                     | 15. METLBOND 4021   | 29. SWEDLOW 371W       |
| 4. AF-41        | 11. ALUMINA-FILLED EPOXY       | 19. AF-5930         | 30. FM-47              |
| 5. FM-1000      |                                | 20. BONDMASTER M24B | 31. REDUX 775          |

Fig. 11. Tensile shear strength at  $-320^{\circ}\text{F}$  of existing adhesive types with metal-to-metal adherends.

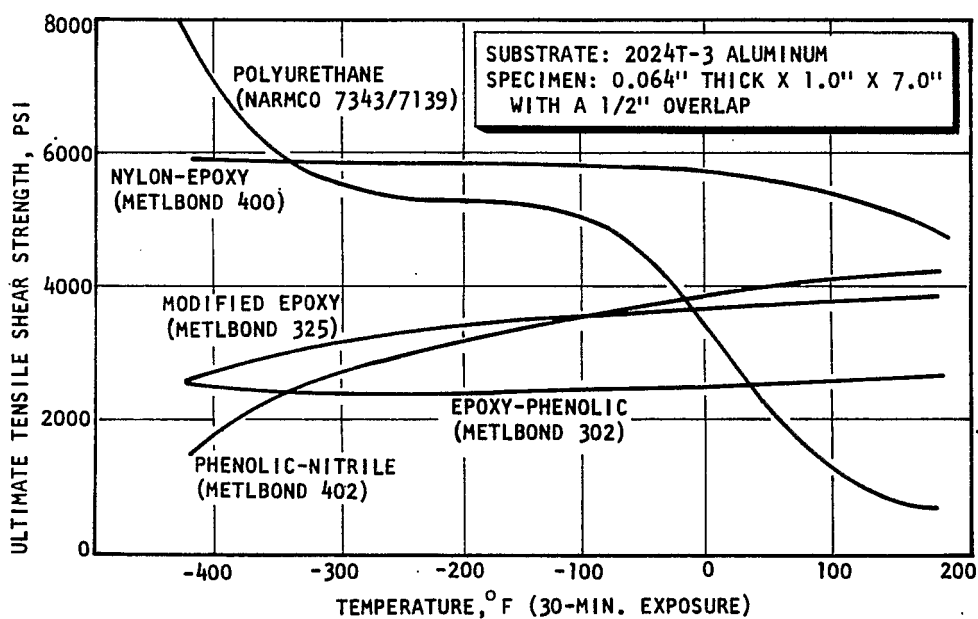


Fig. 12. Effect of temperature on ultimate tensile shear stress of different classes of structural adhesives.

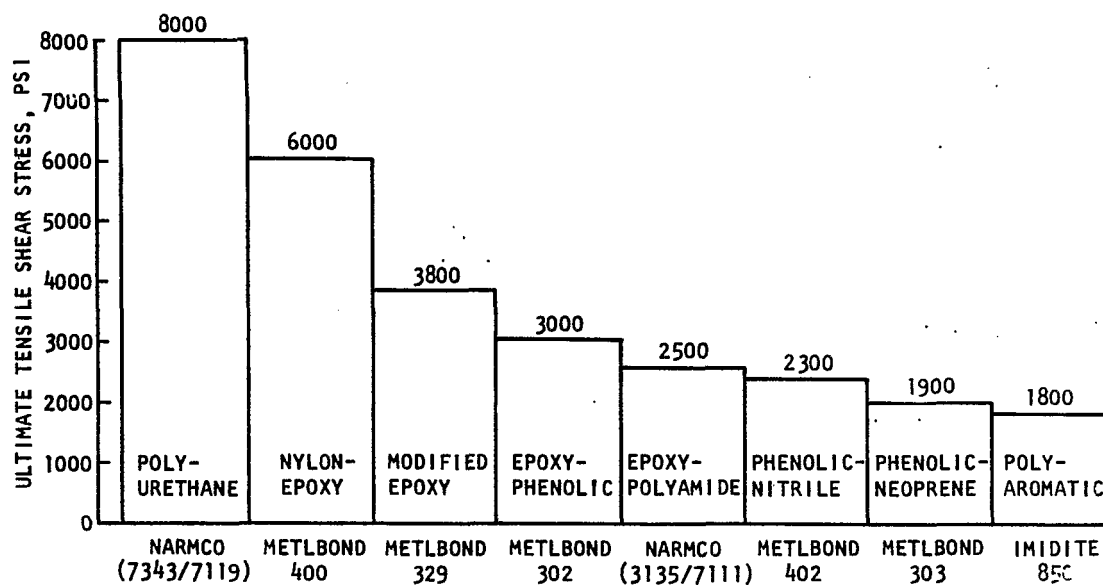


Fig. 13. Effect of liquid hydrogen temperature ( $-423^{\circ}\text{F}$ ) on the tensile shear strength of several different classes of structural adhesives.

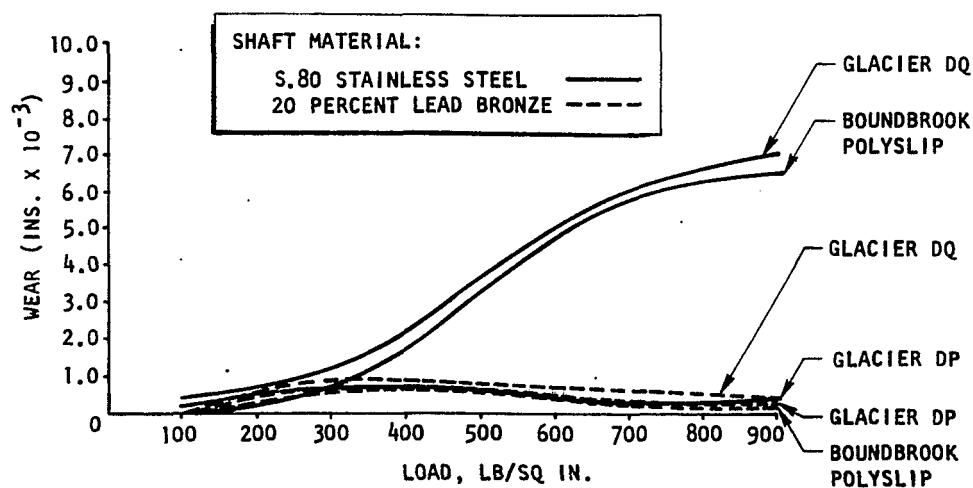


Fig. 14. PTFE-containing bearings in liquid oxygen.

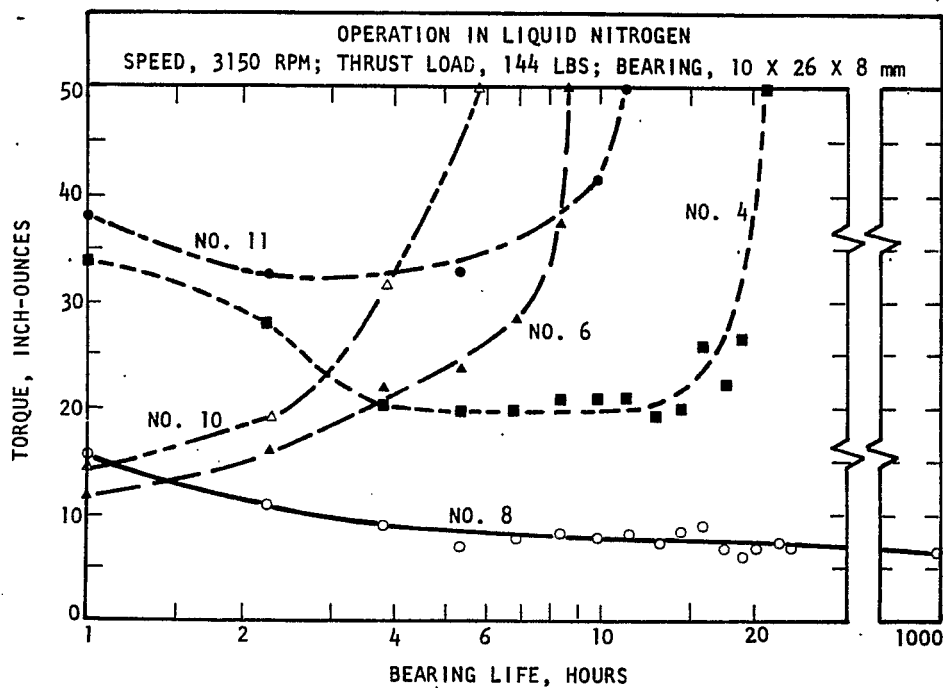


Fig. 15. Bearing torque history.

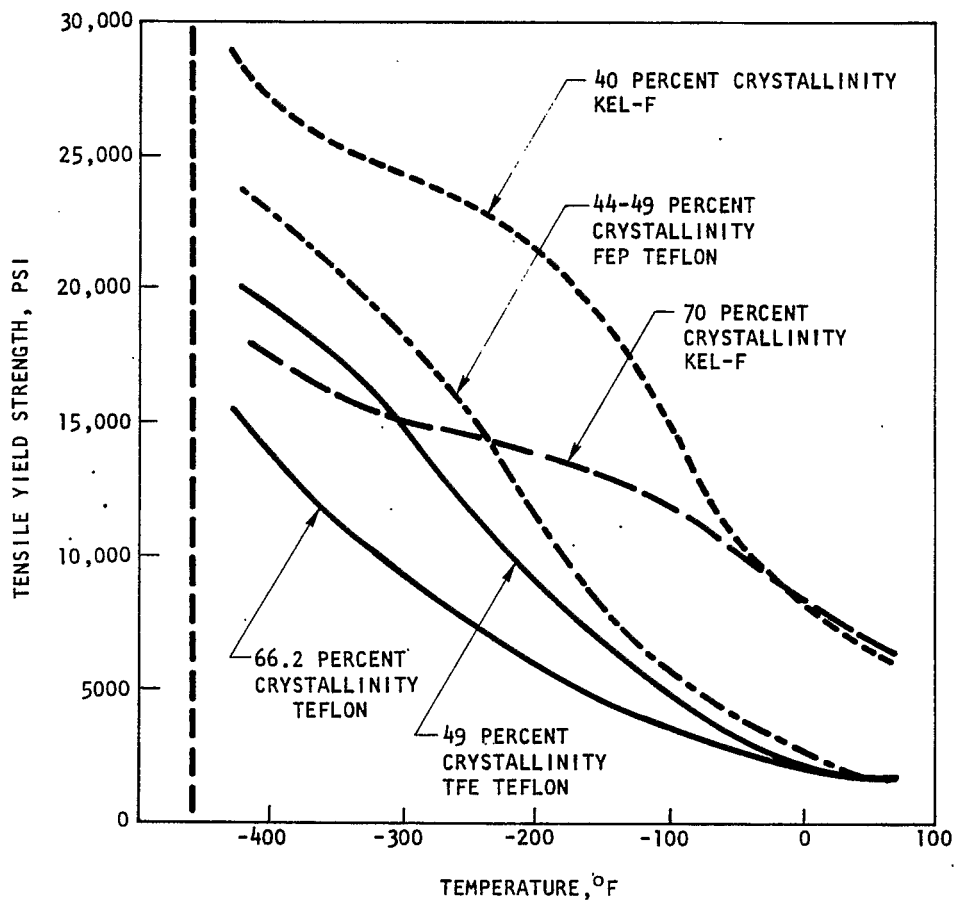


Fig. 16. Effect of temperature on the tensile yield strength of fluorocarbon plastics of different crystallinities.

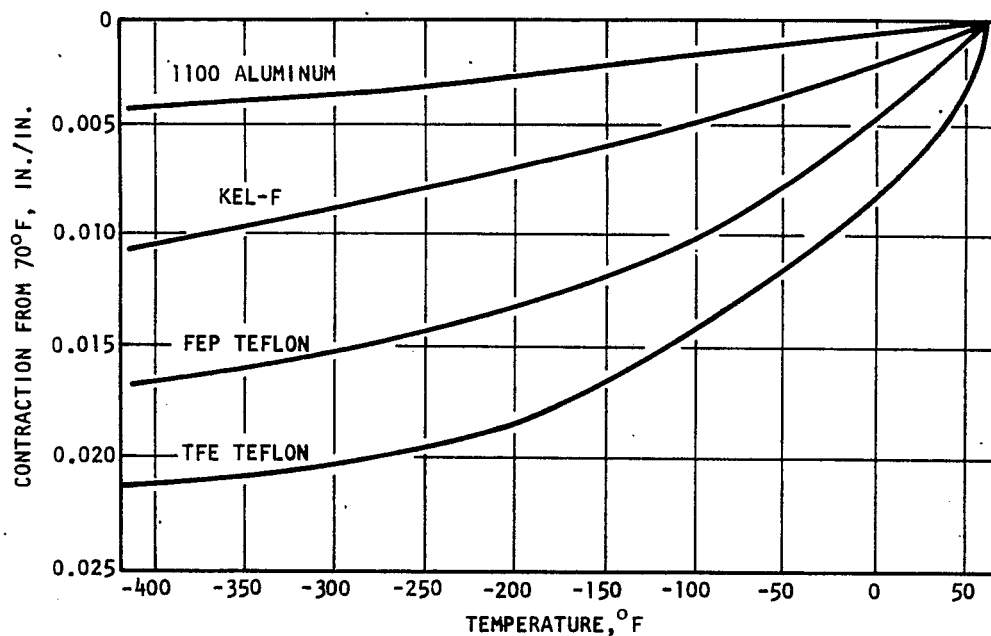


Fig. 17. Total contraction of Kel-F, FEP Teflon, TFE Teflon and aluminum from 70 to -423°F.

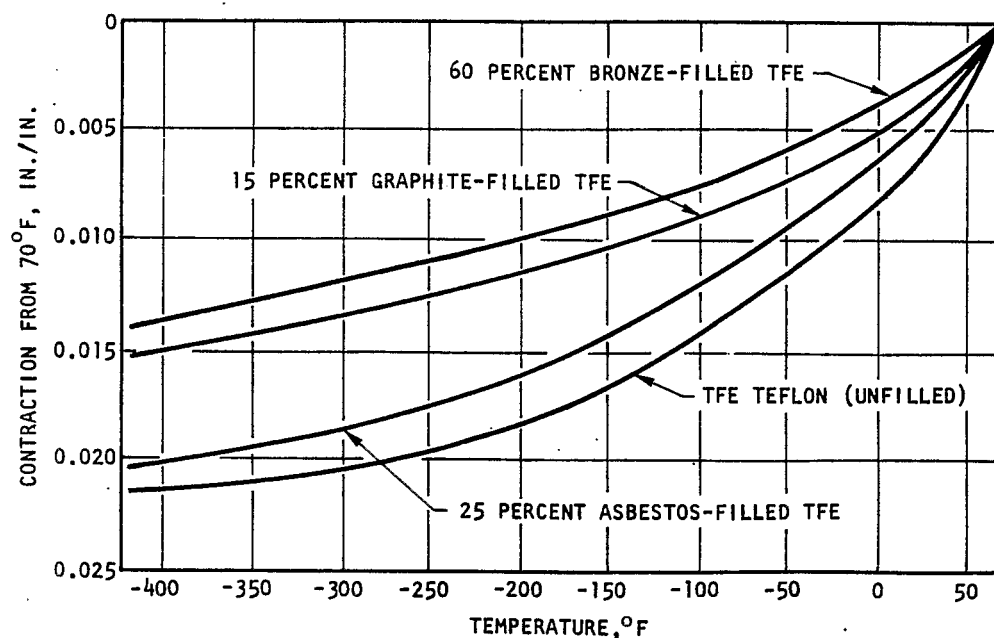


Fig. 18. Total contraction of powder-filled and unfilled TFE Teflons from 70 to -423°F.

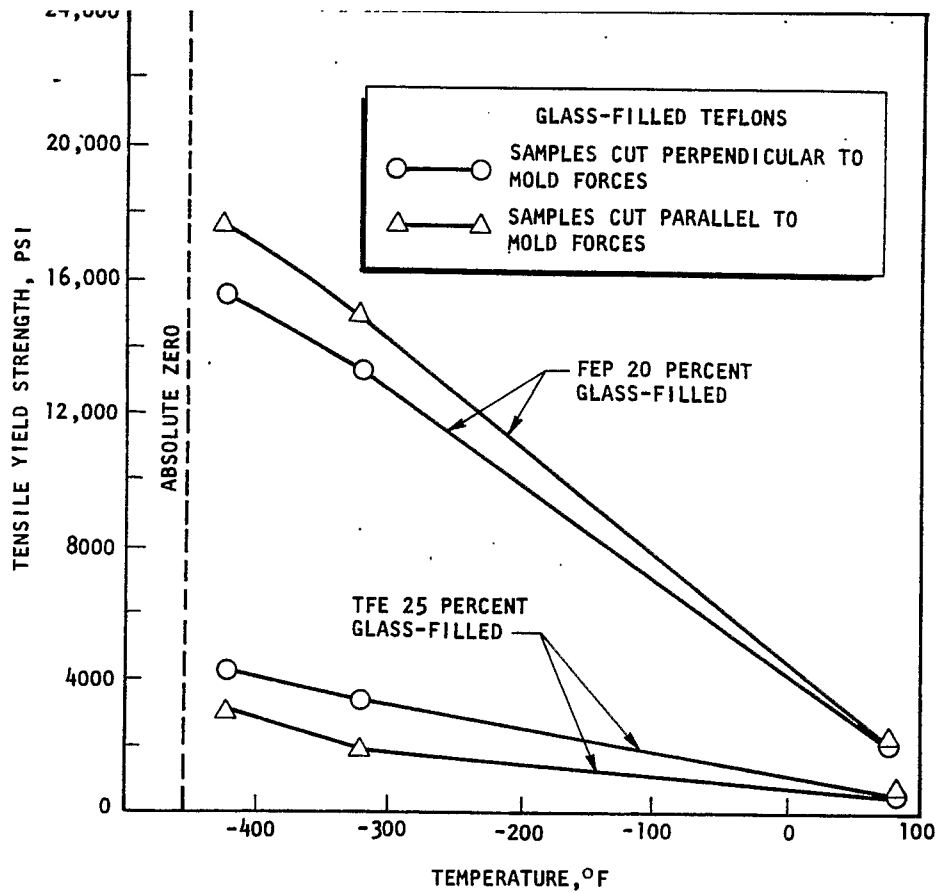


Fig. 19. Effect of temperature on the tensile yield strength of glass-fiber-filled Teflons.

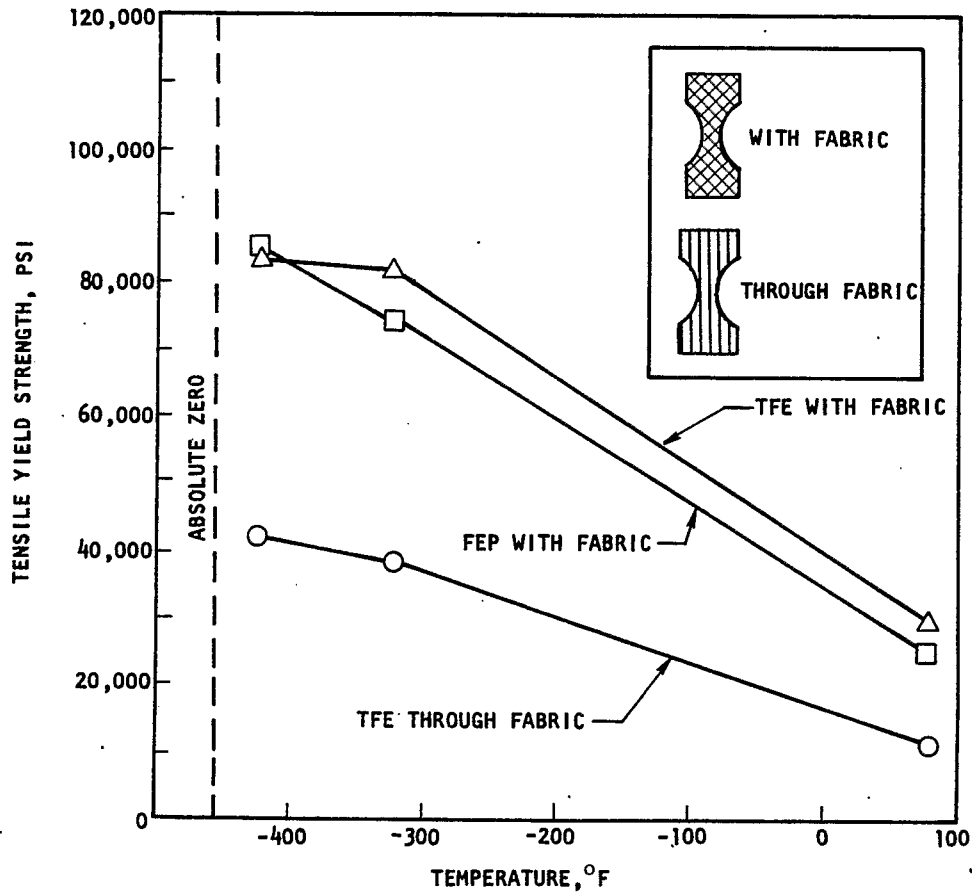


Fig. 20. Effect of temperature on the tensile yield strength of glass-fabric-reinforced Teflons.

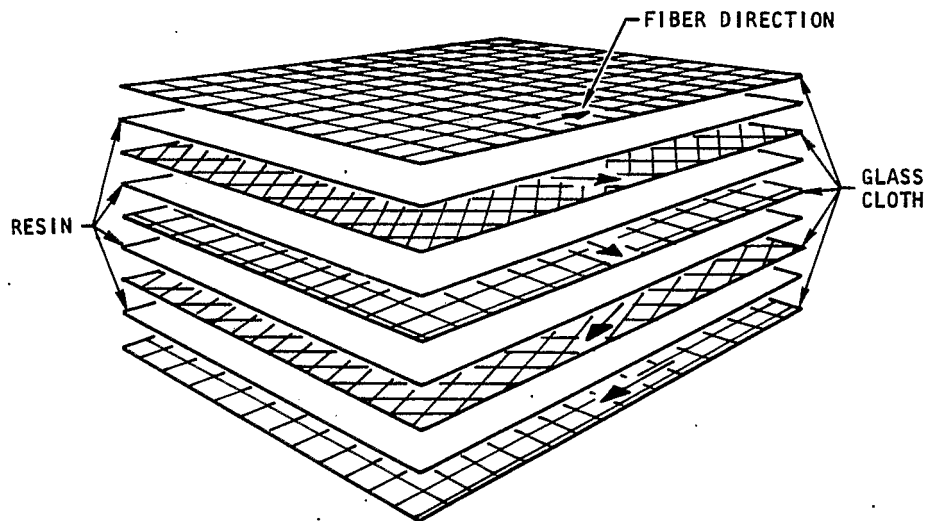


Fig. 21. Laminate lay-up.

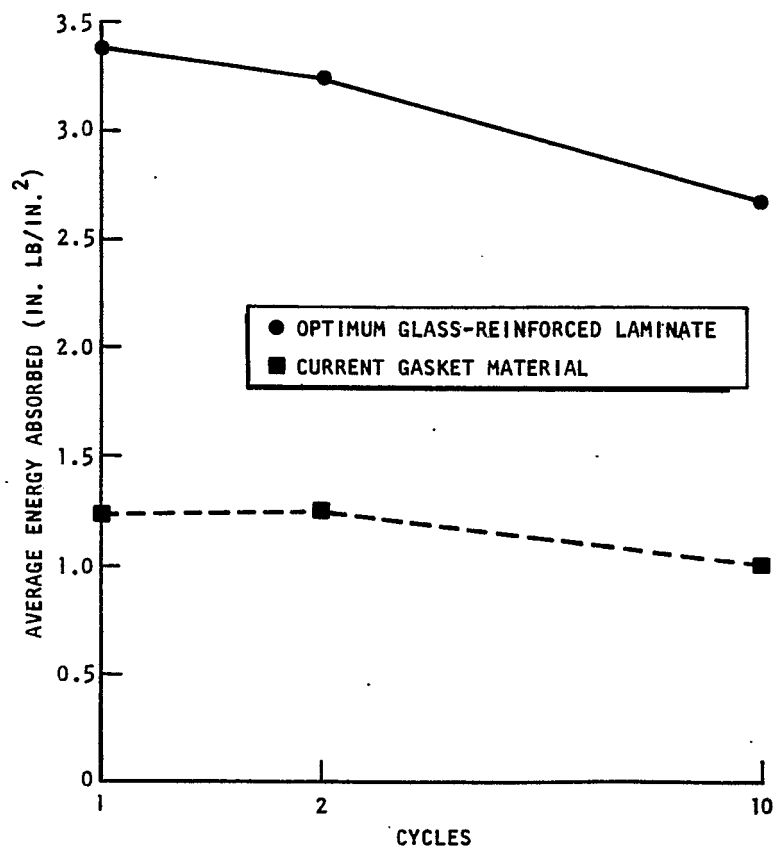


Fig. 22. Energy absorption of glass-reinforced laminate and current gasket material.



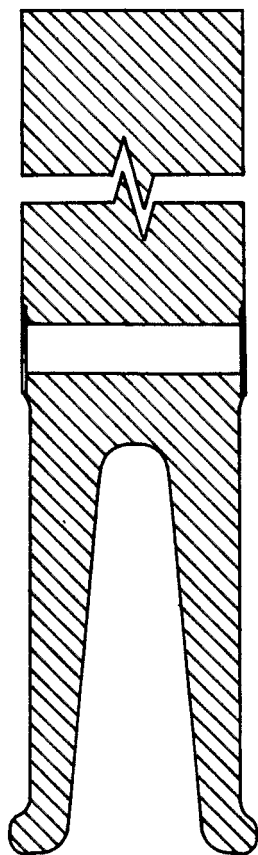


Fig. 23. Cross section of Naflex seal.

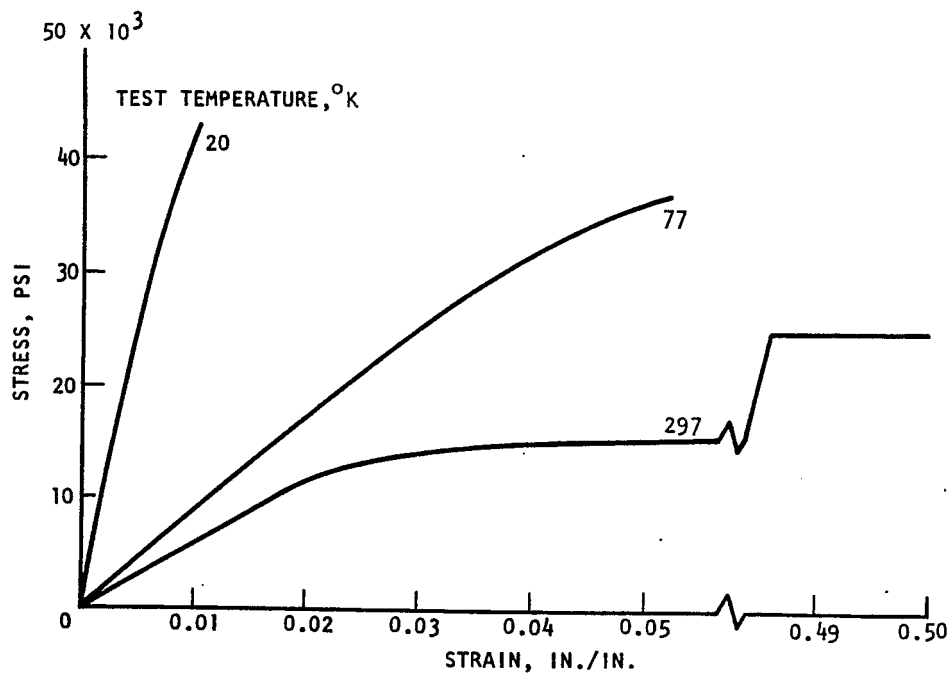


Fig. 24. Temperature-strength behavior - Mylar A film.

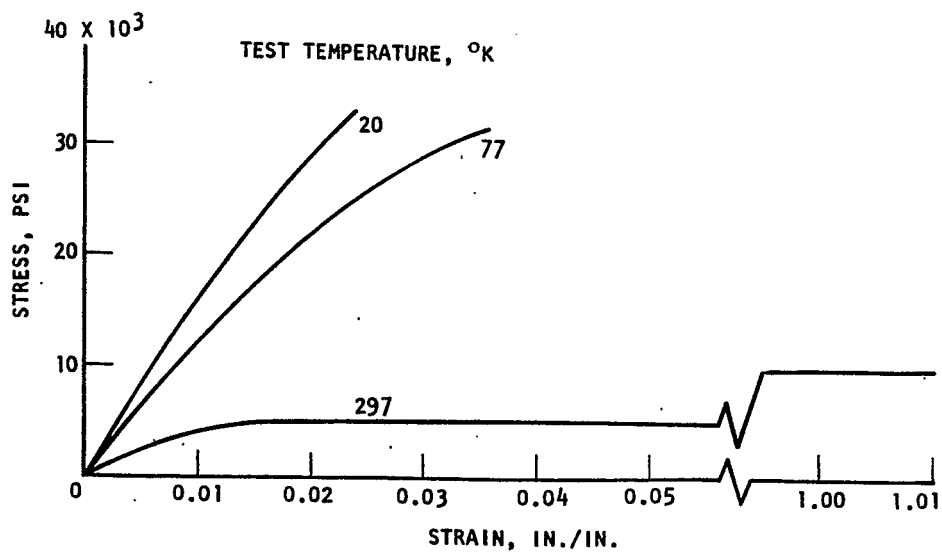


Fig. 25. Temperature-strength behavior - Tedlar BG-30-WH film.

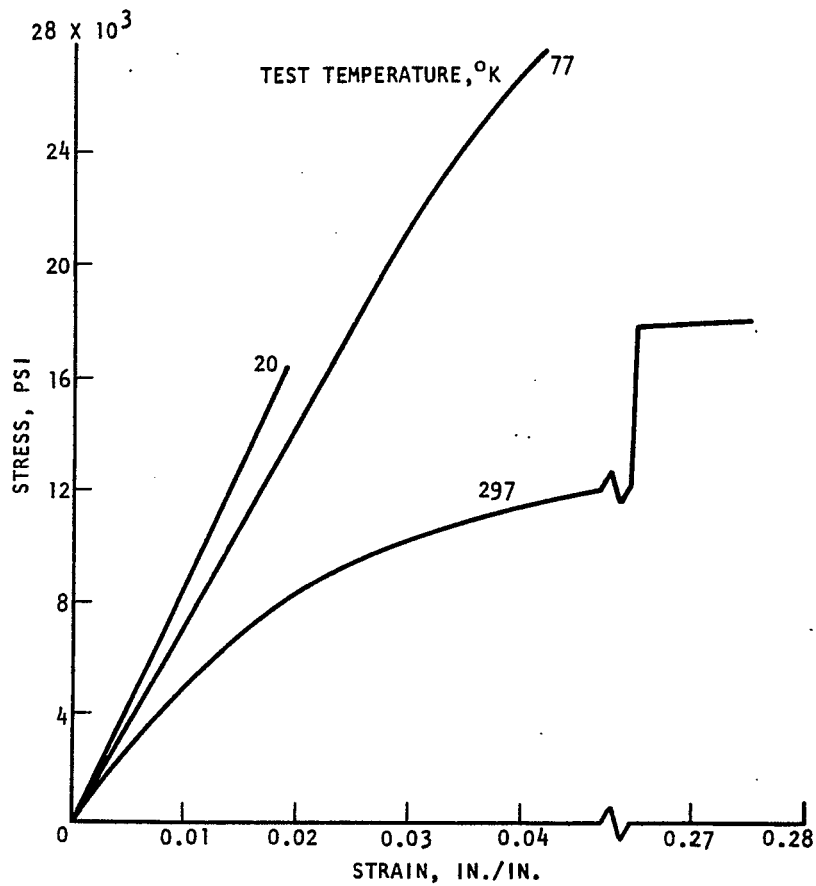


Fig. 26. Temperature-strength behavior - H film.

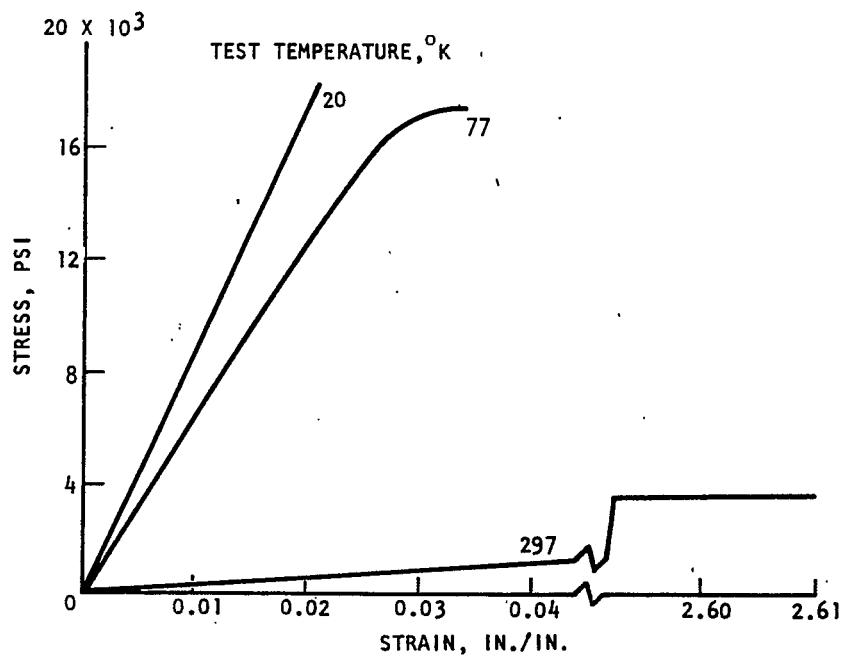


Fig. 27. Temperature-strength behavior - polyurethane Seilon UR29E.

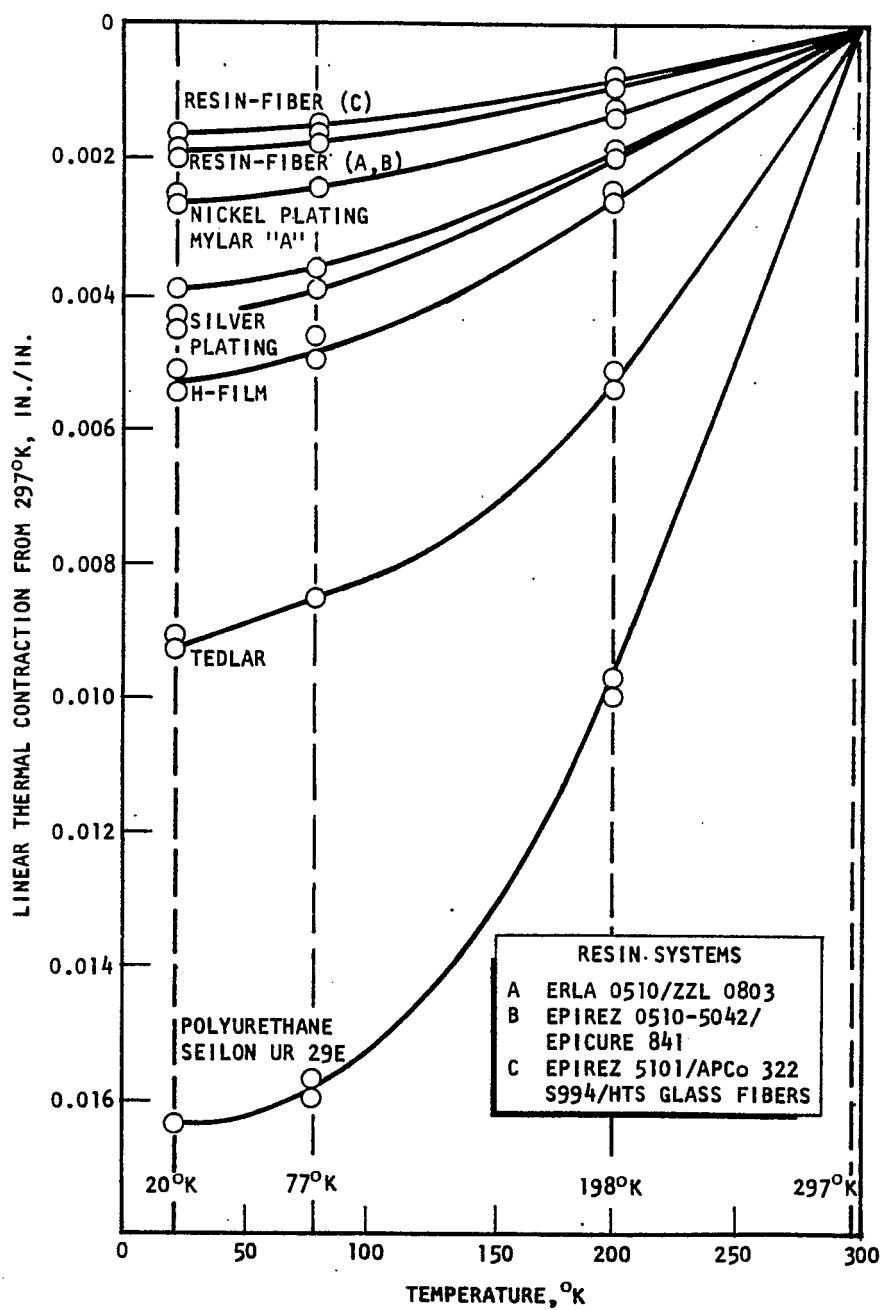


Fig. 28. Contraction curves of candidate liner materials.

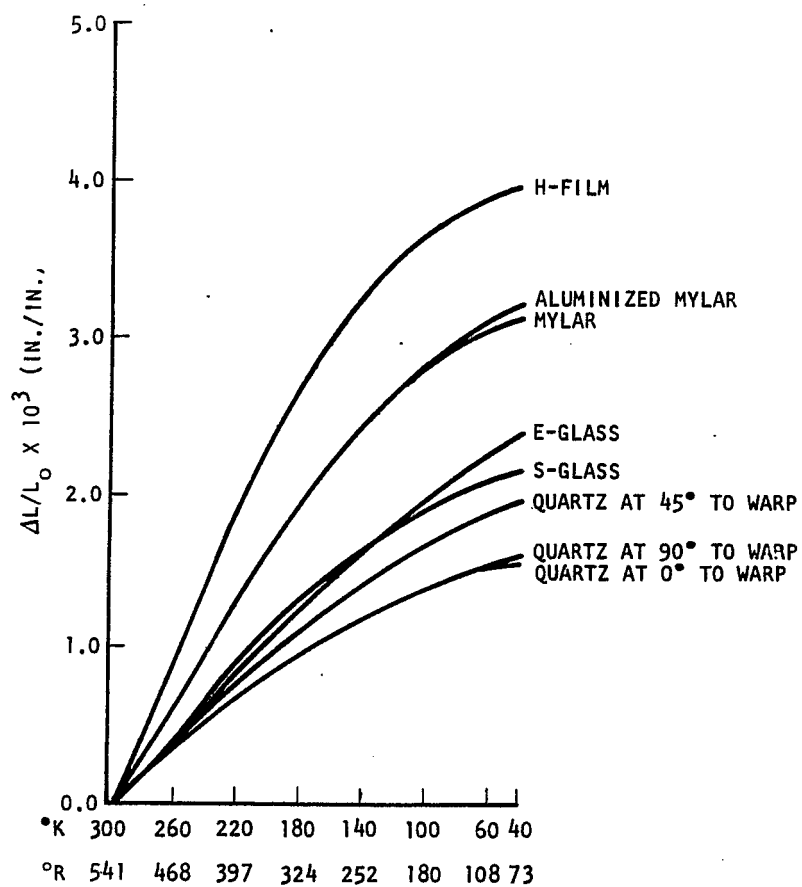


Fig. 29. Thermal contraction of films and laminates.

REVIEW OF THE CRYOGENICS SESSION - SECOND WEEK OF THE BROOKHAVEN  
SUMMER STUDY ON SUPERCONDUCTING DEVICES AND ACCELERATORS\*

T.R. Strobridge  
Cryogenics Division, Institute for Basic Standards  
National Bureau of Standards  
Boulder, Colorado

Although low temperature research and industrial installations are becoming more numerous each year, none approach in cooling capacity at 4°K or in complexity of the heat load distribution the requirements of the high energy physics research facilities which were under discussion at these meetings. To some, helium has become an industrial commodity with the advent of the large liquefiers that are operational today. The bulk transportation of helium in the liquid phase is a routine common carrier matter. To others, liquid helium means low temperatures and the benefits that high energy physics can accrue from the superconductivity phenomenon.

From a cryogenics viewpoint, a superconducting accelerator has poor geometry and physical characteristics (high surface-to-volume ratio, large masses that must be cooled down and that require heavy supports which conduct heat to the low temperature space, and small cooling passages). Furthermore, the superconducting devices which require refrigeration may be separated by kilometers. The fact remains that neither a comparable cooling requirement nor a refrigeration system to meet such a requirement exists today. Yet, the cryogenics support has been referred to as (and should fall into the category of) a utility which is economic and which must be reliable.

Therefore, the lecture topics for the cryogenics section were selected, with these problems in mind, to attempt an assessment of the state of the art directly related to the proposed programs, and to see how closely the utility image can be approximated. In the end, the achievement of utility status for superconducting devices would give great impetus for more widespread application of the technology. This review will give the lecture topics, then outline the experts' opinions, and list the areas which most urgently require further research and development.

The lecture topics were:

- 1) The low temperature mechanical properties of metallic structural materials.
- 2) Properties of nonmetallic materials at cryogenic temperatures.
- 3) Cryostat design.
- 4) Cryopumping.
- 5) Cryogenic electrical leads.
- 6) Cryogenic safety.

---

\* Contribution of National Bureau of Standards, not subject to copyright. The appearance of trade names was required to identify those who presented the material reviewed. Such appearance in no way implies approval, endorsement, or recommendation of a specific product by the National Bureau of Standards.

- 7) Superfluid helium as a refrigerant.
- 8) Heat transfer to helium I.
- 9) Refrigeration.
- 10) The European state of the art.
- 11) Refrigeration for superconducting magnets in the 200 GeV accelerator, Weston, Illinois.

The following is a narrative summary of the lectures.

#### THE LOW TEMPERATURE MECHANICAL PROPERTIES OF METALLIC STRUCTURAL MATERIALS<sup>1</sup>

Although many common metals and alloys may not be used as load-bearing structural members at low temperatures because they become brittle, there are a number of materials which are suitable for liquid helium temperature service. The result of a transition from ductile to brittle behavior at low temperatures can be the sudden catastrophic failure of a part under conditions that would not be excessive at ordinary temperature. Such fractures usually occur with little or no deformation. A distinction should be made between the terms ductility and toughness. Ductility is the ability to deform plastically without fracturing under stress while toughness is the ability to absorb energy through deformation under stress and the resistance to fracture propagation. Metals may be relatively ductile in a tensile test but brittle when broken in a test to measure toughness - each test conducted at the same temperature. Investigation of the suitability of new materials for low temperature service must include measurements to determine toughness.

In general, larger grain size will result in a higher temperature for the ductile-brittle transition. Therefore, cast structures which tend to have larger grains may have lower toughness. Hot working generally improves the characteristics of cast metals. Welding leads to larger grains in the welded area. The brittleness and crack propagation tendencies in welds can be alleviated by stress relieving and by welding in vacuum or in proper inert atmospheres which preclude adsorption of detrimental gases (atmospheric, including water which may decompose into hydrogen). Selection of the proper welding rod is essential. The importance of the brittle fracture at low temperatures should not be overlooked since it may be desirable to move equipment which is at liquid helium temperature - for example, superconducting beam transport magnets. Fortunately, there are a number of metals and alloys suitable for liquid helium temperature service in complex or welded structures. Representative materials include 300 series austenitic stainless steels (low carbon grades), and certain alloys of aluminum, nickel, and titanium. Copper and many of its alloys are also suitable.

The developments in fracture mechanics, a relatively new field that is attracting considerable attention, should be of value in determining the critical crack length or stress level beyond which rapid failure will occur. Testing techniques are well established and low temperature testing facilities exist both in industry and in government laboratories.

#### PROPERTIES OF NONMETALLIC MATERIALS AT CRYOGENIC TEMPERATURES<sup>2</sup>

Structures fabricated from nonmetallic materials may be attractive for several reasons especially since significant progress in understanding the mechanical properties

- 
1. A. Hurlich, these Proceedings, p. 311.
  2. R.E. Mowers, these Proceedings, p. 326.

of these materials has been made in the recent past. This progress is attributed to standardization of test techniques and sample preparation, development of stress analysis of the composites - a difficult and complex field, and a reduction in the variations of the constituents of these materials. High strength-to-weight ratios, low thermal conductivities, low specific heats, and ease of fabricating complex shapes are characteristic advantages of the reinforced plastic structures. As a class, they tend to have high coefficients of thermal expansion, a tendency towards brittleness at low temperatures and as stated, stress analysis is difficult. Eddy current heating in the presence of changing magnetic fields is, of course, eliminated and the feasibility of constructing liquid hydrogen bubble chamber bodies from filament-wound laminates has been investigated. Ports and piping penetrations and the sealing of the vessel present problems, but the savings in weight and elimination of eddy currents should lead to lower static heat losses. Filament-wound pressure vessels are promising but the key to success is a suitable nonpermeable liner which can be matched to the high thermal contraction and low elastic modulus of the material. Adhesives have been the subject of research since the bonding of low temperature structures could be very useful and tests have shown that satisfactory joints can be made. The low coefficients of friction of some of the fluorocarbons are utilized in dynamic seals and bearings and laminated flat gaskets have been found superior to certain other low temperature seals. The effects of radiation damage must always be taken into account when considering the use of the organic materials.

### CRYOSTAT DESIGN<sup>3</sup>

Cryostat design will depend to a large extent on information which must be provided by the physicist about the device to be protected thermally from the surroundings. The support structure will be determined by the size and weight of the cold apparatus, magnetic forces, orientation, need for precise alignment, the space envelope, whether or not there must be a warm bore, and the possible necessity for periodic disassembly. The electrical lead size and how they are to be cooled are important as is the method of refrigerating the entire assembly. There are many subtle interactions between the insulation system, the scheme for electrical lead cooling, the supply of refrigeration and the cooldown requirements (for example, if cold helium gas can be tapped from the process stream, intermediate temperature gas-cooled shields may be used to reduce heat leak). There is a cost trade-off between cryostat sophistication and liquid helium or refrigeration consumption. The forces which are anticipated due to shipping and handling are very important. Ordinary shipping loads are predictable, but problems have been encountered during user handling or in unusual transportation situations. Designs conforming to ASME Code are adequate using ordinary textbook relations. There are several insulations to choose from and that choice is influenced again by the availability of cold gas, liquid nitrogen, lead cooling, and the maximum heat leak that can be tolerated which is directly related to operating expense. The problems which may be encountered are vacuum leaks, lower than expected insulation performance, and inadequate provision for containment of the effluent gas which leads to long cooldown times.

### CRYOPUMPING<sup>4</sup>

Space simulation has been responsible for the development of large cryopumping systems, but the features of cryopumping - high pumping speeds, low ultimate pressures

---

3. G.E. McIntosh, Cryogenic Engineering Company, presented at this Summer Study (unpublished).

4. C. Barnes, these Proceedings, p. 230.



(below  $10^{-8}$  N/m<sup>2</sup>), and noncontamination of the pumped volume — can also be attractive to high energy physics. In fact, the proposal for a heavy particle accelerator, the Omnitron, which requires very low pressures in the beam path, includes cryopumping at liquid helium temperatures. Cryopumping (to be distinguished from cryosorption and cryotrapping) condenses gas molecules striking a low temperature surface. For highest efficiency, the cold surface must have a wide view of the pumped volume. However, this would mean that a large radiation heat exchange would take place with warm surfaces and the heat load on the cryosurface would become excessive. Therefore, it is common to shroud the condensing surfaces with higher temperature shields at about 80°K. The geometry of these shields is important and calculation of the effects of geometries on both heat load and capture coefficient, though complicated, are handled by Monte Carlo techniques or view factor analysis. A number of different geometries have been used in operating systems, so pumping performance and refrigeration needs are well known and can be predicted for other applications.

#### CRYOGENIC ELECTRICAL LEADS<sup>5</sup>

Electrical leads are planned for most of the superconducting magnets being considered. These electrical connections are used for charging the magnet, and trimming the field since, although in principle persistent dc operation is possible, joint resistance would degrade the current if energy was not supplied. The most compelling reason for using these leads is the large amount of energy in the magnetic field which must be dissipated outside of the cryostat if there is a failure or quench. Some of the conductors are large — carrying up to 7000 A. This means that large thermal conduction paths exist between the superconductor at liquid helium temperatures and the ambient surroundings, causing the liquid helium to evaporate at a rapid rate. In addition, there is joule heating in the conductor which, upon conduction toward the lower temperatures, imposes an additional heat load on the refrigerant. This may not be a significant problem for small magnets with many turns and low currents, but is costly for larger magnets. The objective is to design leads with the smallest heat introduction per ampere of current carried. A survey of the literature shows that, over the years, numerous analyses and designs have evolved to remedy the high heat loads evidenced by rapid helium boiling. The first solution was to use the cold effluent vapor to intercept the energy above the 4°K level through heat exchange with the lead. The next was to attach superconducting material extending from the lowest temperature end some distance toward the warmer end. The object is that in any portion of the conductor that is below the critical temperature of the superconductor the current will switch to the path of zero resistance and the joule heating will be eliminated. The problem still remains that accurate solutions of the relation describing the flow of energy along the lead, the temperature distribution, and the heat transfer, taking into account the temperature variations of the electrical and thermal properties of the lead material, and the heat transfer coefficient, are difficult. A simplified relation for lead design has been developed from which lead dimensions for optimum performance can be calculated. Although gas cooling and the alternate superconducting current path have reduced the heat reaching the 4°K level by a factor of thirty, further improvement should be possible. It is suggested that materials of higher electrical conductivity and lower electrical resistivity should be investigated. The Reynolds number in all leads has been so low that the helium flow has been laminar. A higher heat transfer coefficient could be induced by increasing the Reynolds number. Off-optimum operation should be investigated for it may be of benefit during charging or for short duty cycles.

---

5. C.D. Henning, these Proceedings, p. 304.

## CRYOGENIC SAFETY<sup>6</sup>

The safety hazards associated with the usual laboratory amounts of liquid helium are most often minor, but the amounts of liquid which may be required and the stored energy in the superconducting devices may raise the potential for physical and physiological damage following an accident. Hazards are associated with some cryogens because of their potential for chemical activity; for example, hydrogen, oxygen, and fluorine. All of these fluids including the nonreactive elements can cause damage not related to toxicity, burning, or detonation. Frostbite or deep freezing of tissue occurs rapidly on contact with either the liquids, cold vapor or surfaces at low temperatures. A large spill of a cryogen can, because of the approximate 600-fold increase in specific volume upon warming to ambient temperature, displace the surrounding air and deplete the oxygen supply to a fatally low level. This same high change of specific volume from liquid to room temperature gas means that liquid trapped in a vessel or a line between two valves can build destructively high pressures if there is any heat leak to the system. The solutions to these potential hazards are obvious and simple, but must be implemented. The amounts of liquid helium present in a superconducting accelerator and the stored energy in the magnets are a combination which requires careful study. The damage potential can be predicted and the structures designed accordingly.

Prevention is the best design for accidents. Adequate training, the establishment of well-thought-out emergency procedures and an understanding that bad accidents are caused by seemingly improbable cascading of events are essential to a safe operation. In regard to operational procedures, check lists and alternative actions in case of trouble should be planned well in advance and any plant modifications should be subject to review by those responsible for safety.

An accident resulting from a lack of information is regrettable, but an accident caused by willfully ignoring well-known safety procedures for the sake of economy or expediency is inexcusable. Criteria for accident-free operation of cryogenic facilities are well known, and have been established through bitter experience.

## SUPERFLUID HELIUM AS A REFRIGERANT<sup>7</sup>

Superfluid helium has attracted the attention of experimental and theoretical physicists for many years and workable models have been developed to explain some of its truly unique properties. These models, commonly used for the design of small experiments, are by and large adequate; perhaps because research of this nature is amenable to trial solutions. The lecture given by the chairman (H.A. Schwettman) of the previous session on superconducting rf devices and linacs was opened by a statement to the effect that there must be cooperation between physicists and engineers if very low temperature technique is to come out of seclusion in the physics laboratory and become at least a specialized technology. This is a heartening attitude for superfluid helium is a liquid whose engineering potential has not been tapped. Very low temperature is necessary to improve the duty cycle of the superconducting linear accelerator and many liters of superfluid will be used. It is anticipated that the very high thermal conductivity of the superfluid will maintain the temperature constant to within  $0.020^{\circ}\text{K}$  over a 152 m accelerator length. This operation will be watched with great interest not only by physicists interested in the research, but by engineers as well, for the experience gained in this large-scale use of superfluid will be valuable indeed. The cooling arrangement selected for the superconducting cavities calls for heat transfer from the cavities to the liquid-vapor interface where evaporation occurs. The cold vapor will

---

6. M.G. Zabetakis, these Proceedings, p. 229.

7. H.A. Schwettman, these Proceedings, p. 1.

then be returned to the refrigerator through subatmospheric insulated piping. It has been suggested that long lines filled with superfluid could be used to conduct energy away from remotely located heat sources to refrigeration stations. This would not require the separate low pressure vapor return lines which introduce further energy into the system and are another potential source of leaks. There may be real advantage to this scheme and it should be investigated. It was noted that the Kapitza resistance between the superfluid and the superconducting surface of the cavities is not known.

## HEAT TRANSFER TO HELIUM I<sup>8</sup>

An understanding of the mechanisms of heat transfer to helium I is critical. The operation of a superconducting magnet may typically involve heat transferred to dense gas during cooldown, to liquid during steady state, and to two-phase mixtures of liquid and gas during a quench. The helium may be single phase at super or subcritical pressures or may be saturated as either liquid or vapor. The cooling passages must be designed to transfer the required energy under any of these circumstances at a rate sufficient to assure predictable behavior and to prevent damage to the coil, cryostat, and personnel. Unfortunately, there are regions where the transport properties of helium required to make correlations of experimental heat transfer data have not been measured. Experimental heat transfer coefficients are also lacking. With respect to transport properties, heat transfer studies are more difficult because the properties vary significantly in value from those of conventional fluids and extrapolation of the correlations are not justified without experimental verification. In the gas region, one would expect the conventional correlations to be generally effective although some modification may be required because of the properties behavior previously discussed. In the liquid region, the properties behavior with respect to that of conventional fluids is quite different; however, the conventional correlations should still form the basis by which one may make heat transfer predictions. Heat transfer phenomena in the two-phase region is not well understood for any fluid. This means that almost any extension of the use of conventional expressions to the helium region should be accompanied by a rather complete experimental verification if any substantial reliability is required in the use of the data. In the pseudoliquid or supercritical region near the line of maximum specific heats, a poor understanding exists, at best, for the heat transfer behavior. Here again, a good deal of experimental data will be required for helium if reliable heat transfer predictions are to be achieved. This paper collects together all of the relevant information with respect to helium heat transfer. The data were reviewed for each of the regions for all modes of heat transfer in those regions and recommendations from among the available correlations were given. Further, recommendations for experimental properties and heat transfer studies were made. It should be noted that some of these experimental programs are now under way.

## REFRIGERATION<sup>9</sup>

### THE EUROPEAN STATE OF THE ART<sup>10</sup>

#### REFRIGERATION FOR SUPERCONDUCTING MAGNETS IN THE 200 GEV ACCELERATOR, WESTON, ILLINOIS<sup>11</sup>

A general review of 4°K refrigeration was given including some of the appropriate thermodynamics, the process cycles that can be used, the types of components available

8. R.V. Smith, these Proceedings, p. 249.
9. T.R. Strobridge, these Proceedings, p. 193.
10. G. Prast, these Proceedings, p. 205.
11. M.A. Green, G.P. Coombs, and J.L. Perry, these Proceedings, p. 293.

and some of the complete units that are on the market. The description of the progress in Europe showed that refrigerators there are distinctly competitive with those manufactured here. Witness to that are some of the coalitions that have been recently formed between U.S. and European manufacturers. Two points may be germane to this meeting — the distinction between a refrigerator and a liquefier and the input power requirements of existing units. First, most if not all  $4^{\circ}\text{K}$  refrigerators produce liquid in the process stream. Energy from the heat load evaporates the liquid and the cold gas (which has high refrigeration potential) is returned to the refrigerator where it is used to cool the incoming gas stream. Thus, refrigeration is produced only at one temperature. In a liquefier, part of the process fluid stream is removed as liquid. Therefore, the return stream in the liquefier is depleted and this means that additional refrigeration is required at all temperatures to cool the unbalanced flow in the inlet stream. The result is that a liquefier with a capacity to provide liquid to a device with a specified heat load at a rate just matched to that load will require approximately 5 or 6 times the input power of a refrigerator just matched to the same load. The second point regards the efficiency of  $4^{\circ}\text{K}$  refrigerators. Data on existing refrigerators show that at 1 kW capacity about 500 W of input power are required per watt of refrigeration. At 10 W capacity, about 1000 W/W are required and the specific power requirement increases further for smaller units. About 15 to 18 percent of Carnot efficiency is the best performance recorded for contemporary  $4^{\circ}\text{K}$  refrigerators. It is entirely possible that improvements can be made but the refrigerators are likely to be more complex and costly. Since the design of contemporary refrigerators took into account economic factors, it may be that increased efficiency and the resulting reduction in input power may not be justified when the increased purchase price is considered.

It is clear that a reliable supply of cooling is absolutely necessary because the proposed accelerators will be inoperable at higher temperatures. Refrigerators and liquefiers are mechanical devices which are subject to failure. Redundant components and/or reserve liquid supplies are a necessity. A study of how to best refrigerate superconducting beam transport magnets in the experimental area of the 200 GeV machine was made some time ago. The results of another more recent effort were presented to this meeting. Both studies made allowance for failure of the regular cooling supply, but more important, serve to show the logistical problems inherent with such an installation. It is a far different matter to construct a large helium liquefier in the Midwest to fill transportation Dewars than it is to design a  $4^{\circ}\text{K}$  refrigeration system for hundreds of small distributed heat loads. The cooling can be done by oversized, crude systems, but the reason for utilizing low temperature phenomena is primarily economic and a system which causes downtime and requires many man-hours will not be economic. The problem posed is certainly not insurmountable, but the solution will require careful study in the selection of the system, and good design with an emphasis on reliability.

## CONCLUSIONS

In summary then, although there is the brittle fracture problem with metals, there are a number which may be safely used for structural load bearing members. Testing and evaluation techniques are well established to investigate new metals and alloys. Nonmetallic materials of various kinds are coming of age for use in cryogenic environments. Some of their properties may be very useful and here also testing and evaluation criteria are becoming better defined. Cryostat design is an established field with many choices in approach available. Cryopumping techniques should present no problems. Safety practices in the use of large quantities of liquid helium are well known.

There still seem to be some questions concerning electrical leads and their rôle in large systems. Further work here seems appropriate since lead design will affect

cryostat design and refrigeration requirements. If superfluid helium is to play a larger role in high energy physics research, then engineering data are desperately needed and the design practices should be established at an early date. The need for helium heat transfer data is serious and an experimental program is in the first stages of equipment design. The logistics problem of supplying refrigeration to widespread superconducting devices needs serious consideration. The decision on one method or another is virtually irreversible and is important. The choice of cooling method will affect many aspects of the system - including cryostat design and refrigeration capacity.

The conclusion to be drawn is that cryogenic technology is far enough advanced to provide support for almost any superconducting facility. Experience in all aspects of cryogenic engineering is well documented and competent personnel are active in the field. The key to success is to realize and accept the fact that there must be cooperation between the disciplines and that the cryogenics will be an integral part of the system and therefore must be considered in the planning from the very beginning. Just as in superconducting technology, there is research to be done in cryogenic technology. However, there is reason to believe that by careful, long-term planning, the utility concept of cryogenics support can be realized. A poorly thought-out system will lead to enormous waste and refitting.



# STRUCTURE AND PROPERTIES OF HIGH-FIELD SUPERCONDUCTORS

J.D. Livingston  
General Electric Company  
Research and Development Center  
Schenectady, New York

## I. INTRODUCTION

The intent of this paper is to review recent literature on the relation between structure and properties in high-field superconductors. Critical temperatures and fields will be discussed briefly, but emphasis will be on critical currents and flux pinning, where metallurgical microstructure plays its major role. For a comprehensive review of earlier structure-properties studies in superconductivity, see Livingston and Schadler.<sup>1</sup>

## II. CRITICAL TEMPERATURES AND FIELDS

### High-Field Materials

Most elemental superconductors are type I superconductors with maximum critical fields below 1000 Oe. Most alloy and compound superconductors are type II superconductors, but only a limited number have very high critical fields. If we arbitrarily define "high-field" superconductors as those having critical fields greater than 50 kOe, high-field materials known today fall into three structural classes:

1) Body-centered-cubic alloys, such as NbZr and NbTi. Most superconducting magnets have been, and are being, made with these materials. NbTi appears to be superseding NbZr because of higher critical fields and easier fabrication.

2) Interstitial compounds with the NaCl (B1) crystal structure, such as NbN. Difficulties in producing and handling these compounds have so far precluded any commercial application. However, the recent observation of high critical currents obtained by a thin-film sputtering technique<sup>2</sup> is promising.

3) Compounds of the "β-tungsten" (A15) structure, such as Nb<sub>3</sub>Sn and V<sub>3</sub>Ga. Superconducting magnets producing fields of 100 kOe and higher are already being produced with several varieties of commercially-available Nb<sub>3</sub>Sn.

### Critical Temperatures

High values of the critical temperature,  $T_c$ , are of interest not only in themselves, but also because they directly influence the thermodynamic critical field  $H_c(T)$ , which is proportional to  $T_c[1 - (T/T_c)^2]$ , and which in turn limits our ultimate critical currents.

Critical temperatures of superconducting materials have been tabulated by Roberts.<sup>3</sup> For bcc alloys, the highest known  $T_c$  is near 14°K, but the commercially-available alloys are generally in the range of 9-11°K. Extensive study of the interstitial compounds<sup>4</sup> has revealed compositions in the NbCN and NbTiN systems with critical temperatures near 18°K.

Several A15 compounds, including Nb<sub>3</sub>Sn, have critical temperatures near 18°K.<sup>5</sup> A ternary compound of approximate composition Nb<sub>3</sub>Al<sub>0.8</sub>Ge<sub>0.2</sub> was reported last year<sup>5</sup>

to have a critical temperature of 20°K. More recent work, in which composition and order in this ternary system were believed to be optimized, has produced a critical temperature of 20.7°K.<sup>6</sup> This  $T_c$ , slightly above the boiling point of liquid hydrogen (at a pressure of one atmosphere), is the highest known critical temperature.

Our fundamental understanding of what determines  $T_c$  in a particular superconductor is very limited. The BCS theory indicates that  $T_c$  increases very sensitively with the product  $NV$ , where  $N$  is the density of states at the Fermi surface, and  $V$  is the electron-electron interaction parameter. However, the high- $T_c$  materials have complex band structures, and even their normal-state properties are not well understood. The parameter  $N$  is, in principle, obtainable from the zero-temperature limit of the normal-state specific heat. (Experimental limitations, however, require considerable extrapolation in high-field materials.) The parameter  $V$  remains essentially underivable from first principles, and thus is generally inferred from  $T_c$ , rather than vice versa.

Broadly, it appears that the  $\beta$ -tungsten compounds with high  $T_c$  have a high  $N$  (and low  $V$ ), while the high- $T_c$  interstitial compounds have a low  $N$  (and high  $V$ ).<sup>7</sup> Much more theoretical and experimental work is necessary to improve our understanding of the electron structure of these materials. From the viewpoint of metallurgical structure, the major need is more information on the effect of stoichiometry, alloying, and order on  $T_c$ . The relation between the cubic-tetragonal martensitic transformation observed in some of these materials and their superconducting critical temperature also remains obscure.<sup>8</sup>

### Critical Fields

The major basis for our understanding of the critical fields of type II superconductors is the GLAG (Ginzburg-Landau-Abrikosov-Gorkov) theory. According to this theory, the bulk upper critical field is given by  $H_{c2} = \sqrt{2}\kappa H_c$ . The dimensionless Ginzburg-Landau parameter  $\kappa$  can be written approximately as  $\kappa_\ell + \kappa_0$ , where the "extrinsic" part,  $\kappa_\ell$ , is proportional to  $N^2\ell^{-1}$  ( $\ell$  is the electron mean free path), and the "intrinsic" part,  $\kappa_0$ , is proportional to  $T_c N^{3/2}$ , and independent of  $\ell$ . In many high-field superconductors, the upper critical field does not fully reach the GLAG  $H_{c2}$  because of paramagnetic effects. The various factors affecting critical fields are reviewed in depth by Cody.<sup>9</sup>

For bcc alloys<sup>10</sup> and the interstitial compounds,<sup>11,12</sup> the maximum upper critical fields appear to be roughly 150 kOe. In these materials,  $\kappa_\ell \gg \kappa_0$ ,<sup>13</sup> and they may be called "extrinsic" high-field superconductors. Several  $\beta$ -tungsten compounds, in particular Nb<sub>3</sub>Sn, have critical fields approaching 250 kOe. Because of their high  $N$ , these materials appear to have  $\kappa_0 \gg \kappa_\ell$ , and are believed to be "intrinsic" high-field superconductors.<sup>14,15</sup> Hake<sup>16</sup> has recently suggested that their critical fields could perhaps be increased even further if they could be produced with shorter mean free paths, i.e., with both  $\kappa_0$  and  $\kappa_\ell$  large. He suggested an ultimate upper limit for Nb<sub>3</sub>Sn of about 830 kOe.

Recent preliminary measurements using pulsed fields show that a NbAlGe compound, prepared after the prescription described by Matthias et al.,<sup>5</sup> was still superconducting at 4.2°K and 265 kOe.<sup>17</sup> It is interesting that this material has a higher critical field than Nb<sub>3</sub>Sn despite a significantly smaller  $N$ , which implies a smaller  $\kappa_0$ . It is possible that ternary alloying has produced a shorter mean free path and increased  $\kappa_\ell$ .

More work is needed to clarify the effect of mean free path on upper critical field in the  $\beta$ -tungsten compounds. The major effect of metallurgical structure on critical fields is through the effect of defects on  $\ell$ , and, hence, on  $\kappa_\ell$ . It perhaps should also be mentioned that, at surfaces between superconductors and nonconducting phases, a superconducting "sheath" can persist to  $H_{c3} \approx 1.7 H_{c2}$ . It is possible that the effective critical field of some superconductors could be increased by producing a large amount



of such internal surfaces, perhaps with oxide inclusions, for example. Critical fields for nucleation of superconductivity at internal surfaces have recently been considered theoretically by Boyd<sup>18</sup> and Tilley.<sup>19</sup>

### III. CRITICAL CURRENTS

Critical currents in the mixed state (between  $H_{c1}$  and  $H_{c2}$ ) are controlled by the interaction between the metallurgical and magnetic microstructures. As in the analogous fields of mechanical and ferromagnetic properties, commercially interesting "hard" properties result not from homogeneous, well-annealed specimens, but from internally heterogeneous microstructures. To see why, we first consider a relatively homogeneous type II superconductor.

#### The Flux Lattice

Until very recently, the magnetic microstructure of the mixed state was known only from theory and from indirect experiments such as neutron diffraction<sup>20</sup> and nuclear magnetic resonance.<sup>21</sup> However, in a beautiful series of experiments, Trüble and Essmann<sup>22-25</sup> have succeeded in directly observing the flux lattice of the mixed state (Fig. 1). As predicted by theory, a hexagonal lattice of flux threads containing one flux quantum ( $\Phi_0 = 2 \times 10^{-7}$  G·cm<sup>2</sup>) each is observed. The lattice, however, is found to be highly imperfect, the major defects observed being "dislocations" in the flux lattice (Fig. 2).<sup>24,26</sup>

The equilibrium flux lattice spacing, and, hence, the internal flux density  $B$ , is determined by a balance between the magnetic pressure of the externally applied field and the mutual repulsive forces between flux threads. The repulsive force between flux threads increases rapidly as the interthread spacing  $d$  decreases, eventually varying as  $1/d$  at small  $d$ . In a homogeneous sample, these interthread forces lead to a uniform  $B$  throughout the sample (except in the immediate vicinity of the surface).

If one attempts to impose a bulk current of density  $J$  transverse to the flux threads, the threads experience a force transverse to both  $B$  and  $J$ , commonly called a Lorentz force. From the flux lattice point of view, this force can be looked upon as resulting from the gradient in  $B$  that is necessitated by  $J$  through Maxwell's equations. (A flux thread in a flux gradient, of course, experiences more repulsive interthread forces from one side than the other, yielding a net force directed down the flux gradient.) In a homogeneous specimen, flux threads will move in response to this force, producing losses and therefore electrical resistance. Thus a homogeneous specimen can carry no lossless bulk current in the mixed state.

In an inhomogeneous sample, however, variations in flux thread line energy from point to point can yield "pinning forces" that can resist the "Lorentz forces" resulting from flux gradients. Thus internal flux gradients, i.e., bulk currents, can occur, and can be observed (Fig. 3). It is found that the gradient in lattice parameter (gradient in  $B$ ) can be related through standard lattice theory to the net density of flux lattice dislocations of one sign.<sup>25</sup>

When the surface fields of a sample in the mixed state are changed by changing applied currents or fields, flux threads will move in response only as long as the resulting flux gradient forces (Lorentz forces) are greater than the local pinning forces. Thus, when static conditions are reached, the two forces will be locally in balance. The flux gradient force in dyn/cm<sup>3</sup> is given approximately by  $JB/10$ , if  $J$  is in A/cm<sup>2</sup>, and  $B$  is in gauss. The static flux distribution expected, therefore, in an inhomogeneous type II superconductor in the mixed state, will everywhere exhibit a critical current density  $J_c = 10 F_p/B$ , where  $F_p$  is the net pinning force per unit volume. If we consider instead the net pinning force  $f_p$  per flux thread per unit length, we get

$J_c = 10 f_p / \phi_0$ , since each flux thread contains one flux quantum  $\phi_0$ . Thus  $J_c = 5 \times 10^7 f_p$ , where  $f_p$  is in dyn/cm. We defer the question of the B dependence of  $f_p$  (or  $F_p$ ) to a later section.

### The Critical State (Bean Model)

We have seen that the balance between pinning forces and "Lorentz" forces (actually a flux-gradient force produced by interthread repulsive forces) yields a bulk critical current density  $J_c$ . The existence of this parameter  $J_c$  is the basis of the critical state model for high-field superconductors, first introduced by Bean,<sup>27</sup> independently conceived by London,<sup>28</sup> and subsequently developed by Anderson and Kim.<sup>29-31</sup>

The detailed verification of this model has been extensive in recent years. The theory is supported, for example, by quantitative relations between magnetization curves and transport current data,<sup>32,33</sup> by the influence of transport current on magnetization,<sup>34-36,\*</sup> by specimen-size-dependent effects,<sup>27,38-40</sup> and by detailed experiments with alternating fields and currents.<sup>41-44</sup> Perhaps the most dramatic experiments, however, are those which directly probe the macroscopic flux distribution within inhomogeneous high field superconductors in the mixed state.<sup>45,46</sup> For example, the results in Fig. 4 are much like the schematic diagrams of flux penetration appearing in Bean's early papers.

The data in Fig. 4 demonstrate two other significant points. First, it is clear that the critical internal flux gradient, and, therefore,  $J_c$ , decreases with increasing B. Although Bean's first paper assumed  $J_c$  constant for mathematical simplicity, the B-dependence of  $J_c$  was recognized by him and is generally accounted for by workers using the critical state model. Some of the forms for the B-dependence of  $J_c$  appearing in the literature are  $B^{-1}$  (which results if  $F_p$  is constant),<sup>29,47,48</sup>  $B^{-1/2}$ ,<sup>36</sup>  $B^{-1/3}$ ,<sup>49</sup>  $(B+B_0)^{-1}$ ,<sup>30,31</sup>  $(H_{c2}-B)$ ,<sup>50</sup> and  $B^{-1/2}(H_{c2}-B)$ .<sup>33,51,52</sup> No single form for  $J_c(B)$  applies generally all the way from  $H_{c1}$  to  $H_{c2}$ . This complicates, but in no way invalidates, application of the critical state model.

Another feature of Fig. 4, however, shows a serious limitation of the application of the simple critical state model to real materials. At five different occasions as the field was increased, magnetic flux abruptly penetrated the specimen completely, as if the specimen had temporarily lost all flux-shielding capability. These flux jumps result from a thermal instability that cannot be treated by the simple isothermal Bean model. Extensions of the Bean model to include the heating produced by flux motion have been made, however, and are reviewed by Hart.<sup>53</sup>

Schweitzer and co-workers<sup>54-56</sup> have recently challenged the critical state model, suggesting that surface contributions to hysteresis and critical currents are more significant than bulk effects. This was true in some of their samples, which were low- $n$  superconductors with little bulk pinning. Hysteresis only appeared to be surface-controlled in others, in which bulk pinning was so great that internal flux gradients were very steep, and the Bean penetration depth remained small compared with specimen dimensions until fields near  $H_{c2}$ .<sup>46,47</sup> Several other results they incorrectly used to reject the critical state model can easily be interpreted in terms of it.

The existence of surface contributions to hysteresis and critical currents in the mixed state had been noted earlier,<sup>57</sup> and has since been well documented by many workers. This requires, however, not rejection of the critical state model, but incorporation into it. These effects can be treated by modifying the surface boundary conditions

---

\* Although most experiments deal with the case of field transverse to the transport current, the critical state model has also been successful in the more complicated case of longitudinal field.<sup>37</sup>

applied to the critical state model, and can be experimentally separated from bulk effects by varying specimen size or with certain ac measurements.<sup>58</sup> For inhomogeneous high-field (high  $\kappa$ ) superconductors of ordinary dimensions, however, most experiments indicate that bulk currents are much more important than surface currents. Why this is true is noted below under the discussion of surface pinning.

In summary, macroscopic electrical and magnetic properties of high-field superconductors are explainable on the Bean critical state model, and depend on the parameter  $J_c(B)$ . This parameter in turn depends on the bulk pinning forces on flux threads produced by structural defects. We therefore turn to detailed consideration of flux pinning by various types of defects.

### Flux Pinning

We will consider first the basic element of flux pinning, the interaction between a single defect and a single flux thread. The line energy of an isolated flux thread has several components. Each flux thread contains a quasi-normal core roughly a coherence length in radius, which contributes a condensation core energy of roughly  $H_c^2 \xi^2/8$  per unit length. The surrounding supercurrent vortex, extending to distances of roughly a penetration depth,  $\lambda$ , contributes a vortex energy mostly produced by the kinetic energy of the supercurrents. For  $\kappa \gg 1$ , the vortex energy of an isolated flux thread is large compared with the core energy, and therefore roughly equals the total line energy,  $\Phi H_{c1}/4\pi$ .<sup>59</sup> However, because the vortex extends over a much larger distance than the core, the maximum possible energy gradients (forces) related to the core and vortex may be comparable.<sup>33</sup> Furthermore, vortex forces will decrease as flux density increases and neighboring vortices overlap, whereas core forces may remain relatively unchanged until near  $H_{c2}$ , when cores begin to overlap.

Before making crude calculations of possible pinning forces, we must consider the various types of defects that may serve as pinning centers. Flux pinning by various pinning centers has been reviewed by Dew-Hughes.<sup>60</sup>

Classification of pinning centers. A great variety of microstructural features can interact with flux threads. It is convenient<sup>33</sup> to classify them according to the number of dimensions of the pinning entity that are large compared with  $d$ , the flux thread spacing. Note that a given element of microstructure may change classification as  $B$  increases, since  $d$  decreases as  $(\Phi_0/B)^{1/2}$  (For  $B = 20$  Oe,  $d = 1 \mu$ ; for  $B = 2000$  Oe,  $d = 1000$  Å; for  $B = 200\ 000$  Oe,  $d = 100$  Å.)

- A. Zero: "Point" pins - The major classes here are voids, second-phase particles, and defect clusters (such as produced by radiation damage).
- B. One: "Line" pins - The major defect in this category is the dislocation. However, several metallurgical processes can produce rod-like second-phase particles, and some radiation damage tracks may have this dimensionality.
- C. Two: "Surface" pins - This category includes stacking faults, grain and subgrain boundaries, twin and transformation boundaries, and inter-phase boundaries. For completeness, we can also include the external surface of the specimen as a special case of surface pinning.
- D. Three: "Volume" pins - Large voids or particles could easily be larger than  $d$  in all dimensions.

"Point" pins. Critical currents in NbTi alloys are enhanced by a dispersion of fine precipitates produced by heat treatment.<sup>61</sup> A commercially-available Nb<sub>3</sub>Sn material is believed to derive its current-carrying capacity, at least in part, from an intentionally-introduced dispersion of fine ZrO<sub>2</sub> particles.<sup>62</sup> Thus point pins are of

practical as well as fundamental interest. We will find, however, that most clear-cut structure-properties experiments have been done on "model" type II superconductors, rather than on practical high-field superconductors.

We will first consider the significance of the nature of the pinning center, and will later consider the importance of the size and spacing of the pins.

A variety of second-phase particles can be used for pinning centers. The particle can itself be a superconducting metal, a normal metal, a semiconducting material, or a nonconducting material. A void can be considered as an extreme example of the last case. Another special case of interest is a paramagnetic or ferromagnetic particle.

Theoretical considerations and several experimental results suggest that the greater is the difference between the superconducting or electronic properties of the particle and those of the matrix, the greater will be the pinning force. That is, a normal particle will provide stronger pinning than a superconducting particle, and an oxide particle or void would provide still stronger pinning.

The distinction between normal and superconducting pins is supported by the observations of Levy et al.<sup>63</sup> on eutectic alloys, but was most clearly demonstrated in an experiment on PbInSn alloys.<sup>64</sup> Here the tin-rich pinning centers were superconducting, but had a lower critical temperature and critical field than the PbIn matrix. Thus as temperature or field was increased, the particles become normal. Critical currents were found to increase with increasing field and temperature, in contrast to usual behavior, proving that normal particles pin more strongly than superconducting particles. [This result also provides an approach to control the temperature and field dependence of critical currents. This may be significant in controlling magnetic instabilities (flux jumps), in which  $dJ_c/dT$  plays an important role.<sup>53</sup>]

Returning to voids, we can make a rough calculation of the pinning forces involved. Consider a spherical void of diameter  $D \approx \xi$ . The condensation energy of the core will completely disappear where it intersects the void, producing a decrease in energy of  $(H_c^2 \xi^2/8) \times D$  over a distance  $D$  of flux thread motion, yielding a pinning force of roughly  $H_c^2 \xi^2/8$ . If  $H_c = 3000$  Oe and  $\xi = 100$  Å, the force is roughly  $10^{-6}$  dyn. If the flux thread intersects one such void each  $1000$  Å along its length,  $f_p = 10^{-1}$  dyn/cm, and  $J_c = 5 \times 10^6$  A/cm<sup>2</sup>. Larger voids can produce larger forces per void by also decreasing much of the vortex energy,<sup>45,47,48</sup> but intervortex spacing would necessarily be larger, and achievable critical current densities would be of the same order of magnitude.

The calculated interaction force between a ferromagnetic particle and flux thread<sup>51</sup> is comparable to that produced by a void, but the weakening of superconductivity in the surrounding matrix produced by large magnetic fields and a strong proximity effect probably greatly weakens the net effect on  $J_c$ . The major interesting feature of ferromagnetic pinning centers is the ability to change the pinning force from attractive to repulsive by varying the direction of magnetization. Because attractive forces produce a higher  $J_c$ , ferromagnetic pins can produce critical currents dependent on the sense of the applied magnetic field.<sup>51</sup>

Turning now to the optimum size for pinning centers, it is generally agreed that pinning decreases for pinning centers smaller than a coherence length,  $\xi$ , and for centers bigger than the interthread spacing,  $d$ . Since  $d$  approaches  $\xi$  near  $H_{c2}$ , it follows that optimum pinning center size is roughly a coherence length. There is some experimental verification of this concept. The decrease in  $J_c$  with the coarsening of pinning centers larger than a coherence length has been observed in several systems.<sup>33,57,65</sup> Where pinning centers are smaller than a coherence length, coarsening should increase  $J_c$ , and this has been observed in an AlZn alloy.<sup>66</sup> The quantitative interpretation of these results, however, is complicated by the fact that both size and spacing of pinning

centers change during coarsening, and more careful experiments are necessary to separate these effects.

Considering spacing separately, it seems obvious that  $J_c$  will increase with increasing density  $N$  of pins per unit volume. If one assumes that every pin produces a force  $f$ , then  $J_c = 10 Nf/B$ . However, several factors will work against this linear increase with  $N$ . First, as an increasing volume fraction of the sample becomes occupied by pinning centers, let us say voids, the amount of superconducting matrix available to carry supercurrent of course decreases. Thus, there will eventually be a maximum in  $J_c$  with increasing volume fraction of voids.<sup>67</sup>

Second, as the density of pins increases, it becomes increasingly difficult for the flux threads to utilize all the available pinning forces. For example, if the intervaid spacing is less than  $d$ , a flux thread may be able to move so that some voids are pinning its core, but others will be distributed throughout the vortex, producing weaker forces directed in various directions. Furthermore, strong interthread forces make it impossible to deflect each flux thread independent of its neighbors. Anderson and Kim<sup>30</sup> reasoned that these interthread forces were large to distances of the order of  $\lambda$ , so that a flux-thread lattice would remain virtually undistorted over a "flux bundle" of this size.\* One quantitative approach to account for this effect is to assume that the net pinning experienced by the flux bundle will be proportional to the statistical imbalance of forward and reverse pinning forces over the flux bundle volume.<sup>51,70</sup> This will lead to a  $J_c$  proportional not to the pinning center density  $N$ , but to  $\sqrt{N}$ . (This statistical weakening of the net pinning force would be less significant if pinning centers had a regular spacing that matched the flux-thread spacing. The match, however, would occur only at one sharply-defined flux density. Furthermore, such structural regularity is very unlikely, except for artificially-produced structures, or structures produced by spinoidal decomposition<sup>71</sup> or two-phase directional solidification.<sup>72</sup>)

There is a clear-cut need for better data on the effect of pinning center density and distribution on  $J_c$ . Radiation damage is perhaps the most promising way of achieving such data, although there is some uncertainty as to the nature of the radiation damage centers themselves. Several experimenters have demonstrated an increase in  $J_c$  with increasing radiation damage. Such work is reviewed by Cullen.<sup>73</sup>

"Line" pins. The major new feature here is the possibility of anisotropic properties if the rod-like pins are all parallel. If the pins produce attractive forces, as would voids, maximum pinning would be expected with the field directed parallel to the rods. If the forces were repulsive, optimum forces may be expected with fields normal to the rods. Under certain assumptions,<sup>36</sup> the geometric nature of this transverse case can lead to  $J_c$  proportional to  $B^{-1/2}$ , a behavior approximately observed in some materials.

The major line defect in materials, of course, is the dislocation. The effects of dislocations on superconducting properties have been reviewed by van Gorp and van Ooijen.<sup>74</sup> Experiments on many superconducting alloys show that the production of dislocations during cold work can greatly increase  $J_c$ . Calculation of the elastic dislocation-flux thread interaction has been attempted by several authors.<sup>75-78</sup> It is here found convenient to consider the effect of a flux thread on the line energy of a dislocation, rather than vice versa. The flux thread core is viewed as a normal filament with slightly different interatomic distances and elastic modulus than the superconducting matrix. These calculations yield a force of about  $10^{-8}$  dyn for a single dislocation-flux thread intersection.

\* Although early experiments by Träuble and Essmann<sup>68</sup> appeared to observe flux bundles directly, these observations are now believed to be artifacts.<sup>69</sup>

Whereas these elastic effects can be related to the effect of the dislocation's stress field on  $H_c$ , another possible interaction is through the effect of a locally decreased mean free path on  $\kappa$ . This has not yet been rigorously calculated, but the resulting force may be significantly greater.<sup>74</sup> An even larger effect might be expected if the dislocation were "decorated" by impurity segregation which further decreased the local mean free path. The pinning force still, of course, will be much less than would be produced by a rod-like void.

After remarking that "none of these treatments comes even close to a satisfactory solution" to the problem of the interaction between the dislocation microstructure and the flux lattice, Seeger and Kronmüller<sup>79</sup> have recently set up complex "micromagnetic" equations to treat this problem. We must await further work, however, to see if these equations can produce useful results.

Experimental determination of the dislocation-flux thread pinning force has been attempted,<sup>80-82</sup> but several complications in the interpretation of the data remain, including the question of flux lattice rigidity and statistical cancellation of forces discussed earlier. A recent paper<sup>82</sup> concludes that the elementary dislocation-flux thread interaction force is roughly  $10^{-7}$  dyn.

Several experimental results<sup>83,84</sup> suggest that a given number of dislocations produces a higher  $J_c$  when clustered into sub-boundaries than when isolated. Dislocations in cold-worked metals often form structures of low-dislocation-density cells separated by high-dislocation-density cell walls. (Because precipitates can play a significant role in controlling this cell structure, they may have both a direct and indirect effect on flux pinning.) It has been suggested<sup>74,83,84</sup> that the decreased mean free path in the cell walls, and the corresponding increase in  $\kappa$ , is the major source of the pinning forces. In our classification, of course, these cell walls, or dislocation sub-boundaries, are "surface" pins between two regions of different  $\kappa$ .<sup>60</sup>

"Surface" pins. Again, anisotropy is expected. Optimum  $J_c$  is expected when both field and current are parallel to the pinning surface, i.e., when the "Lorentz force" is normal to it. Anisotropy has been demonstrated for external surfaces,<sup>85</sup> grain boundaries,<sup>84</sup> and martensitic transformation boundaries.<sup>86</sup> In samples where most of the internal boundaries are parallel to each other and not perfectly perpendicular to the Lorentz force, flux travels across the sample by moving parallel to the boundaries rather than intersecting them. This "guided flux motion" produces controllable transverse voltages.<sup>87</sup>

An alteration in flux thread density near grain boundaries in thin foils has been directly observed by Essmann and Träuble.<sup>23</sup> These workers have not yet studied type II superconductors carrying transport current. However, they have studied the effect of transport current on thin foils of type I superconductors, in which the intermediate state consists of a flux lattice of multi-quantum flux tubes.<sup>88</sup> Current induces motion of the tubes, and the interference of grain boundaries and slip planes with flux motion is directly observed.

Campbell et al.<sup>33</sup> have found that  $J_c$  in various PbBi alloy samples was proportional to the total interphase surface area. They also found that a given amount of internal surface carried the same current as the same amount of external surface. Since most metallurgical two-phase microstructures have much more internal than external surface, this demonstrates that bulk currents will usually far exceed surface currents.

Campbell et al. also present a detailed model of surface pinning that predicts  $J_c(B)$  proportional to  $M_r(B)/B^{1/2}$ , where  $M_r(B)$  is the reversible magnetization expected for a homogeneous sample. This was the dependence observed experimentally. A discrepancy in the constant of proportionality, however, suggests that surface roughness may be significant. Other workers have suggested that pinning of transverse flux at

surface irregularities may control the magnitude of surface currents.<sup>85</sup>

Levy et al.<sup>63</sup> have also demonstrated a proportionality between  $J_c$  and interphase surface area in a variety of eutectic alloys. Kramer and Rhodes<sup>89</sup> correlated  $J_c$  and internal surface area, but did not find simple proportionality.

Several workers have observed a dependence of  $J_c$  on grain size<sup>90,91</sup> and related this to pinning by grain boundaries. Although this is a possible interpretation, it also should be noted that the procedures that were used to produce samples of different grain size were also likely to produce different dislocation densities within the grains, which may have been the major source of variations in  $J_c$ . Witcomb et al.<sup>92</sup> report that both grain boundaries and mechanical twin boundaries are relatively ineffective at pinning flux in MoRe alloys.

Surface pinning should be greatest when the surface lies between the superconductor and a void or nonconducting particle. Such a surface also produces a sheath of enhanced superconductivity. Extremely high  $J_c$  would be obtained in a multiple-layer sample of alternating superconductor and oxide, where the sample approaches an assembly of thin films.

"Volume" pins. It was pointed out by Campbell et al.<sup>33</sup> that although the line energy of a flux thread would be lowered anywhere within a large void or normal precipitate, the changes in energy, or pinning forces, are only associated with entry and exit of the flux thread, i.e., its surfaces. Thus "volume" pins are really "surface" pins, and therefore become less effective as they coarsen.

Flux pinning was originally discussed<sup>29,30</sup> in terms of the pinning of "flux bundles" by volume pins, and a similar model has recently been employed by Maxwell et al.<sup>93</sup> to explain a striking "peak effect" in NbN.

Flux lattice effects. Although we have discussed primarily the interaction forces between a single flux thread and a single defect, we have noted that the strong interaction between flux threads can play a major role in influencing the net pinning forces per unit volume, hence  $J_c$ , particularly when the distance between pinning centers becomes less than  $\lambda$ . In a recent paper, Träuble and Essmann<sup>25</sup> purport to show that the individual defect-flux thread interaction force is two orders of magnitude greater than the average net force inferred from the flux gradient. Although the validity of their calculation of the individual pinning force is in doubt, a substantial reduction in net effect probably generally occurs because of a statistical cancellation of individual pinning forces. This is expected to be true particularly when the density of pinning centers is high.

The real physical case, the interaction between defects and a flux lattice, is a very complicated problem. Several approaches to the problem have been attempted (Refs. 51,70,94-96). One interesting approach<sup>69</sup> is to focus attention on the flux-lattice dislocations (FLD's) (Figs. 2 and 3). We have noted the relation between FLD's and flux gradients. It has also been suggested<sup>97</sup> that flux motion down flux gradients may be accomplished by FLD motion. This suggests that defect pinning of FLD's may be an appropriate model for flux pinning. This approach has not yet been fully evaluated.

Our major hope for improved understanding of this complex problem probably lies with experiments that directly observe the flux lattice, how it is altered in the presence of specific defects, and how it moves under applied currents. Only preliminary observations of defect-flux interactions have been made to date with the Träuble-Essmann fine-powder technique.<sup>23,88,98</sup> Additional experiments will certainly be forthcoming. More suitable for studying dynamic effects, however, would be the Faraday technique. This technique has recently been greatly improved in resolution,<sup>99</sup> and may eventually be able to resolve individual flux threads in motion.

Thermal stability. In actual use of high-field superconductors in high-field magnets, it has been found that thermal instabilities (flux jumps) make it impossible to use the full current-carrying capability of the superconductor. Large amounts of normal metal must be included for stability, and this greatly decreases the over-all current density of the windings. In considering flux pinning, therefore, it is significant to ask how the basic nature of the pinning centers may influence thermal instabilities. It seems likely that pinning centers designed from this point of view, even though they may not yield maximum pinning forces or maximum  $J_c$  in a short-sample test, may give a material with higher usable  $J_c$  in magnet applications.

One factor already mentioned is the ability to control  $dJ_c/dT$  using weakly superconducting pinning centers.<sup>64</sup> High-specific-heat centers would also contribute to stability. Also helpful might be high-conductivity pinning centers, that increase magnetic time constants and decrease thermal time constants. Finally, improved uniformity of pinning center distribution would be very desirable. None of these approaches has yet been evaluated in practical materials.

#### IV. SUMMARY

Critical temperatures and critical fields of high-field superconductors are less influenced by metallurgical structure than are critical currents. However, for high-field superconducting compounds, particularly of the  $\beta$ -tungsten structure, there is need for more study of the effect of order, stoichiometry, and alloying on critical temperatures and fields.

Critical currents are controlled by interaction between the metallurgical microstructure of the sample and the magnetic microstructure (flux thread lattice) of the mixed state. The balance between flux pinning forces and flux gradient forces (Lorentz forces) determines  $J_c$ . A great variety of metallurgical defects have been shown to produce flux pinning.

Consideration of "point" pinning centers suggests that voids or nonconducting particles roughly a coherence length in size may provide optimum pinning forces. Critical currents will no longer increase appreciably with increasing pinning center density when the spacing between centers becomes less than a penetration depth. More experiments with carefully-controlled pinning centers are necessary to test these conclusions.

Although there is ample experimental and theoretical evidence that dislocations can provide flux pinning, it remains in doubt whether the basic interaction is primarily an elastic or a mean free path effect. Several experiments suggest that dislocations are most effective when clustered into sub-boundaries.

Rod-like or lamellar pinning centers may have certain advantages, but properties will depend sensitively on field orientation. If pinning centers are large, only their surfaces contribute to pinning forces, leading to critical currents proportional to internal surface area. External surfaces can also carry current, but bulk currents usually dominate.

A major problem in quantitative understanding of flux pinning is to relate single defect-flux thread pinning forces to the net pinning force exerted on the flux lattice as a whole. Direct-observation experiments are expected to throw light on this problem.

In considering the most desirable pinning centers, it may not be best to optimize net pinning forces and  $J_c$ . Because thermal instabilities play such a major role in limiting the applications of high-field superconductors, more thought should be given to the effect of the nature and distribution of pinning centers on thermal instabilities.



## REFERENCES

1. J.D. Livingston and H.W. Schadler, Prog. Mater. Sci. 12, 183 (1964).
2. H. Bell, Y.M. Shy, D.E. Anderson, and L.E. Toth, J. Appl. Phys. 39, 2797 (1968).
3. B.W. Roberts, in Progress in Cryogenics (Academic Press, New York, 1964), Vol. 4, p. 159.
4. N. Pessall and J.K. Hulm, Physics 2, 311 (1966).
5. B.T. Matthias, T.H. Geballe, L.D. Longinotti, E. Corenzwit, G.W. Hull, R.H. Willens, and J.P. Maita, Science 156, 645 (1967).
6. S. Foner, E.J. McNiff, Jr., B.T. Matthias, and E. Corenzwit, in Proc. 11th Intern. Conf. Low Temperature Physics, St. Andrews, 1968.
7. T.H. Geballe, B.T. Matthias, J.P. Remeika, A.M. Clogston, V.B. Compton, J.P. Maita, and H.J. Williams, Physics 2, 293 (1966).
8. T.R. Finlayson, E.R. Vance, and W.A. Rachinger, Phys. Letters 26A, 474 (1968).
9. G.D. Cody, these Proceedings, p. 405.
10. T.G. Berlincourt and R.R. Hake, Phys. Rev. 131, 140 (1963).
11. L.E. Toth, C.M. Yen, L.G. Rosner, and D.E. Anderson, J. Phys. Chem. Solids 27, 1815 (1966).
12. C.M. Yen, L.E. Toth, Y.M. Shy, D.E. Anderson, and L.G. Rosner, J. Appl. Phys. 38, 2268 (1967).
13. L.E. Toth, Report on Air Force Grant AFOSR 1012-66 (1967).
14. B.B. Goodman, Phys. Letters 1, 215 (1962).
15. G.D. Cody, J.L. Cooper, and G.W. Cullen, U.S. Air Force Technical Report AFML-TR-65-169, p. 96 (1965).
16. R.R. Hake, Appl. Phys. Letters 10, 189 (1967).
17. I.S. Jacobs and J.D. Livingston, unpublished results (1967).
18. R.G. Boyd, Phys. Rev. 153, 444 (1967).
19. D.R. Tilley, J. Phys. C (Proc. Phys. Soc.) 1, 293 (1968).
20. D. Cribier, B. Jacrot, B. Farnoux, and L. Madhav Rao, J. Appl. Phys. 37, 952 (1966).
21. W. Fite, II, and A.G. Redfield, Phys. Rev. Letters 17, 381 (1966).
22. U. Essmann and H. Träuble, Phys. Letters 24A, 526 (1967).
23. U. Essmann and H. Träuble, Phys. Letters 27A, 156 (1968).
24. H. Träuble and U. Essmann, Phys. Stat. Sol. 25, 373 (1968).
25. H. Träuble and U. Essmann, J. Appl. Phys. 39, 4052 (1968).
26. R. Labusch, Phys. Letters 22, 9 (1966).
27. C.P. Bean, Phys. Rev. Letters 8, 250 (1962); Rev. Mod. Phys. 36, 31 (1964).
28. H. London, Phys. Letters 6, 162 (1963).
29. P.W. Anderson, Phys. Rev. Letters 9, 309 (1962).
30. P.W. Anderson and Y.B. Kim, Rev. Mod. Phys. 36, 39 (1964).
31. Y.B. Kim, C.F. Hemstead, and A.R. Strnad, Phys. Rev. 129, 528 (1963).
32. W.A. Fietz, M.R. Beasley, J. Silcox, and W.W. Webb, Phys. Rev. 136, A335 (1964).
33. A.M. Campbell, J.E. Evetts, and D. Dew-Hughes, Phil. Mag. 18, 313 (1968).

34. W.F. Druyvesteyn, Phys. Letters 14, 275 (1965).
35. M.A.R. LeBlanc, Phys. Rev. Letters 11, 149 (1963).
36. K. Yasukochi, T. Ogasawara, N. Usui, and S. Ushio, J. Phys. Soc. Japan 19, 1649 (1964); J. Phys. Soc. Japan 21, 89 (1966).
37. B.C. Belanger, Ph.D. Thesis U.S.C. (1968); Bull. Am. Phys. Soc. 13, 361 (1968); to be published.
38. J.E. Evetts, D. Dew-Hughes, and A.M. Campbell, Phys. Letters 16, 113 (1965).
39. P.S. Swartz, Phys. Rev. Letters 9, 448 (1962).
40. J.J. Hauser, Phys. Rev. Letters 9, 423 (1962).
41. T.W. Grasmehr and L.A. Finzi, IEEE Trans. on Magnetics MAG-2, 334 (1966).
42. C.P. Bean, R.L. Fleischer, P.S. Swartz, and H.R. Hart, Jr., J. Appl. Phys. 37, 2218 (1966).
43. H.R. Hart, Jr., and P.S. Swartz, U.S. Air Force Technical Report AFML-TR-65-431 (1966).
44. Reviewed by S.L. Wipf, these Proceedings, p. 511.
45. H.T. Coffey, Cryogenics 7, 73 (1967).
46. H.E. Cline, R.M. Rose, and J. Wulff, J. Appl. Phys. 37, 1 (1966).
47. J. Friedel, P.G. deGennes, and J. Matricon, Appl. Phys. Letters 2, 119 (1963).
48. J. Silcox and R.W. Rollins, Appl. Phys. Letters 2, 231 (1963).
49. F. Irie and K. Yamafuji, J. Phys. Soc. Japan 23, 255 (1967).
50. S.H. Goedemoed, P.H. Kes, F. Th. A. Jacobs, and D. deKlerk, Physica 35, 273 (1967).
51. T.H. Alden and J.D. Livingston, J. Appl. Phys. 37, 3551 (1966).
52. H.T. Coffey, Phys. Rev. 166, 447 (1968).
53. H.R. Hart, Jr., these Proceedings, p. 571.
54. D.G. Schweitzer and B. Bertman, Phys. Letters 20, 339 (1966).
55. D.G. Schweitzer, M. Garber, and B. Bertman, Phys. Rev. 159, 296 (1967).
56. D.G. Schweitzer and M. Garber, Phys. Rev. 160, 348 (1967).
57. J.D. Livingston, Rev. Mod. Phys. 36, 54 (1964).
58. H.A. Ullmaier, Phys. Stat. Sol. 17, 631 (1966).
59. A.A. Abrikosov, J. Phys. Chem. Solids 2, 199 (1957).
60. D. Dew-Hughes, Mater. Sci. Eng. 1, 2 (1966).
61. D. Kramer and C.G. Rhodes, Trans. AIME 236, 1612 (1967).
62. M.G. Benz, Trans. AIME 242, 1067 (1968).
63. S.A. Levy, Y.B. Kim, and R.W. Kraft, J. Appl. Phys. 37, 3659 (1966).
64. J.D. Livingston, Appl. Phys. Letters 8, 319 (1966).
65. J.D. Livingston, J. Appl. Phys. 34, 3028 (1963).
66. G.A. Beske, P. Hilsch, and J. Wulff, Trans. AIME 239, 890 (1967).
67. J.A. Catterall and I. Williams, J. Less-Common Metals 12, 258 (1967).
68. H. Träuble and U. Essmann, Phys. Stat. Sol. 20, 95 (1967).
69. H. Träuble, private communication.

70. J.I. Gittleman and B. Rosenblum, J. Appl. Phys. 39, 2617 (1968).
71. J.W. Cahn, Trans. AIME 242, 166 (1968).
72. G.A. Chadwick, Prog. Mater. Sci. 2, 2 (1963).
73. G.W. Cullen, these Proceedings, p. 437.
74. G.J. van Gorp and D.J. van Ooijen, J. Physique 27, C3-51 (1966).
75. R.L. Fleischer, Phys. Letters 3, 111 (1962).
76. W.W. Webb, Phys. Rev. Letters 11, 191 (1963).
77. E.J. Kramer and Ch. L. Bauer, Phil. Mag. 15, 1189 (1967).
78. K. Yamafuji, F. Irie, and C.L. Bauer, Phys. Rev. Letters 20, 658 (1968).
79. A. Seeger and H. Kronmuller, Phys. Stat. Sol. 27, 371 (1968).
80. E. Nembach, Phys. Stat. Sol. 13, 543 (1966).
81. E. Nembach, H. Freyhardt, and P. Haasen, Phys. Stat. Sol. 18, 807 (1966).
82. H. Freyhardt and P. Haasen, Z. Metallk. 58, 856 (1967).
83. A.V. Narlikar and D. Dew-Hughes, J. Mater. Sci. 1, 317 (1966).
84. G.J. van Gorp, Philips Res. Repts. 22, 10 (1967).
85. P.S. Swartz and H.R. Hart, Jr., Phys. Rev. 137, A818 (1965); Phys. Rev. 156, 412 (1967).
86. G.J. van Gorp, Phys. Stat. Sol. 17, K135 (1966).
87. A.K. Niessen, J. van Suchtelen, F.A. Staas, and W.F. Druyvesteyn, Philips Res. Repts. 20, 226 (1965).
88. H. Träuble and U. Essmann, Phys. Stat. Sol. 25, 395 (1968).
89. D. Kramer and C.G. Rhodes, J. Inst. Metals 94, 261 (1966).
90. J.J. Hanak and R.E. Enstrom, in Proc. Tenth Intern. Conf. Low Temperature Physics, Moscow, 1966, Vol. 2B, p. 10.
91. K.J. Gifkins, C. Malseed, and W.A. Rachinger, Scripta Met. 2, 141 (1968):
92. M.J. Witcomb, A. Echarri, A.V. Narlikar, and D. Dew-Hughes, J. Mat. Sci. 3, 191 (1968).
93. E. Maxwell, B.B. Schwartz, H. Wizgall, and K. Hechler, J. Appl. Phys. 39, 2568 (1968).
94. K. Yamafuji and F. Irie, Phys. Letters 25A, 387 (1967).
95. R. Labusch, to be published.
96. W.W. Webb, these Proceedings, p. 396.
97. F.C. Frank, unpublished (1963).
98. N.V. Sarma, Phil. Mag. 17, 1233 (1968).
99. H. Kirchner, Phys. Letters 26A, 651 (1968).

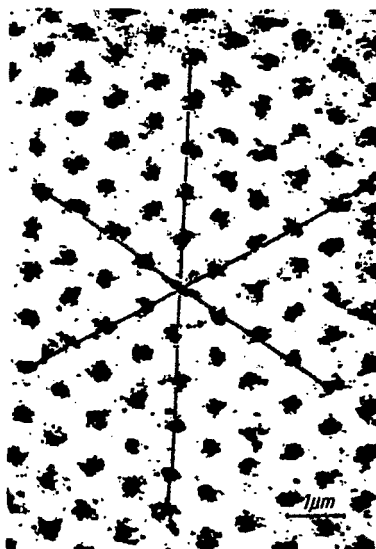


Fig. 1. Flux thread lattice in Pb-6.33 at.% In at 1.2°K. Remanent state,  $B = 70$  Oe. Flux threads are made visible by deposition of fine ferromagnetic particles. (After Träuble and Essmann, Ref. 24.)

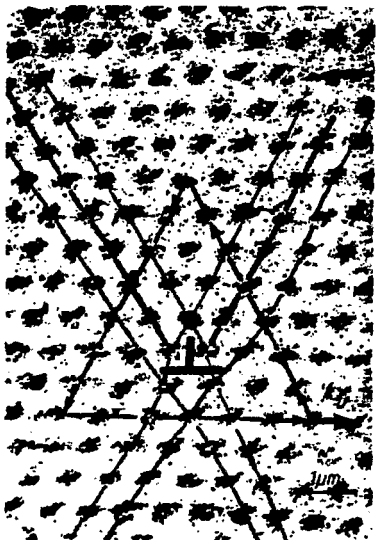


Fig. 2. Edge dislocation in the flux thread lattice. (After Träuble and Essmann, Ref. 24.)

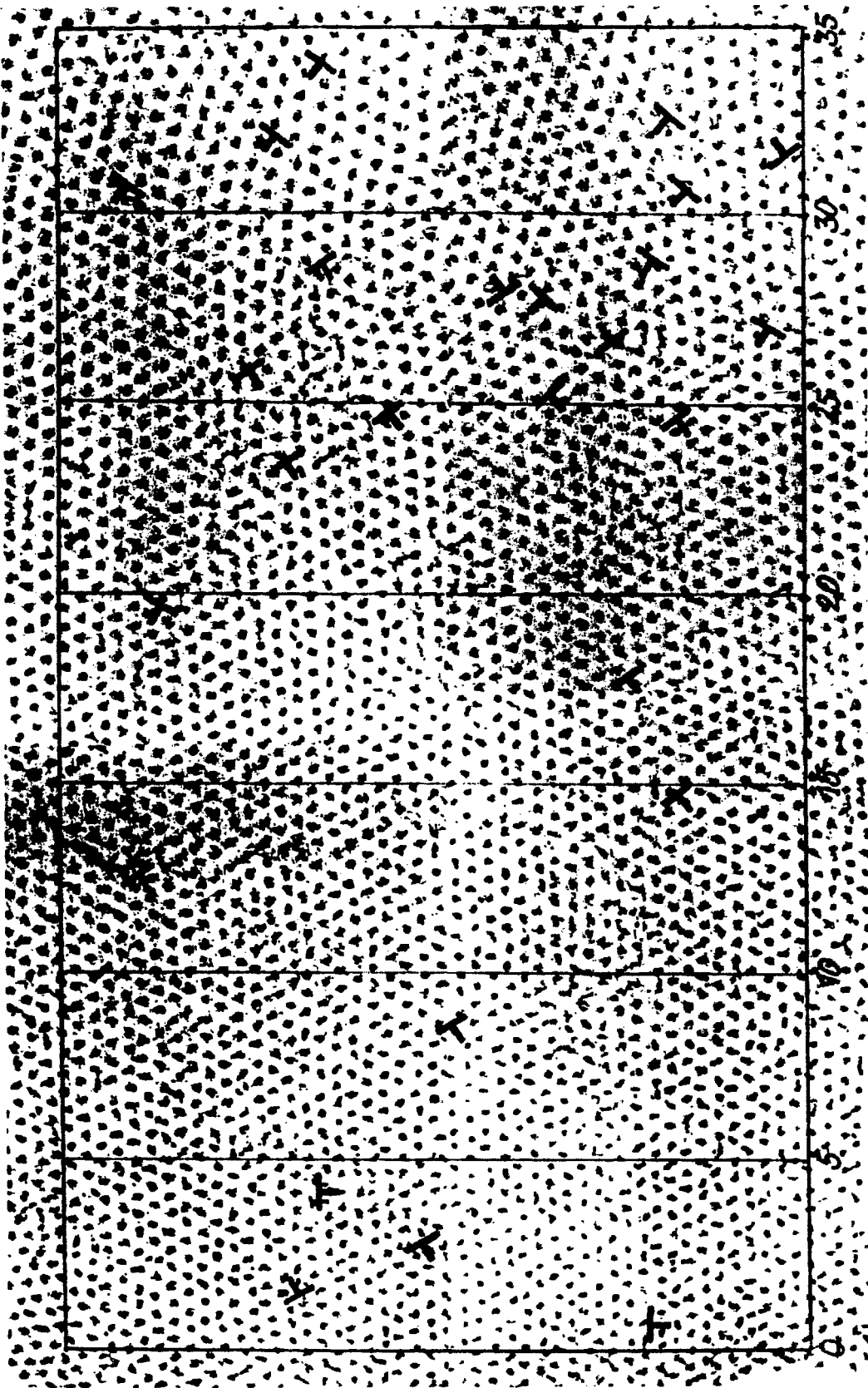


Fig. 3. Flux lattice with flux density gradient from right to left. Dislocation cores are indicated by the symbol 1. (After Träuble and Essmann, Ref. 25.)

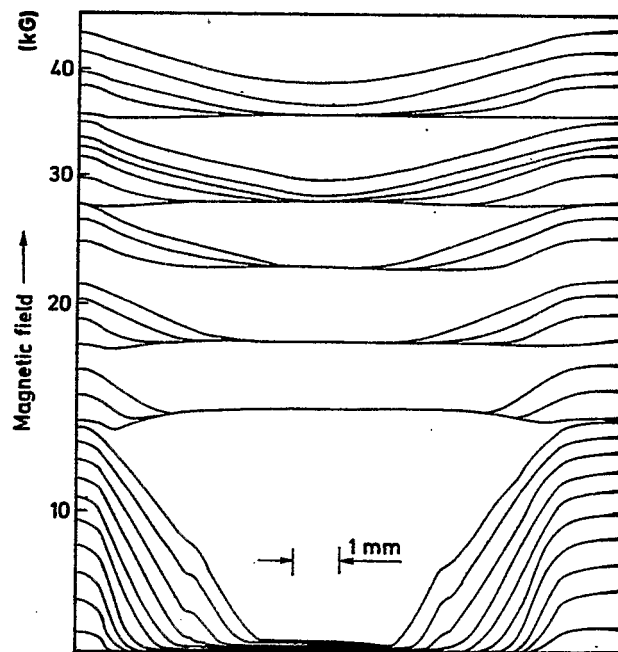


Fig. 4. Field distribution in a NbTi sample in increasing field, as measured by driving a Hall probe through a fine transverse gap in the sample. (After Coffey, Ref. 45.)

## INSTABILITY COMMENTS

S.L. Wipf  
Atomics International  
A Division of North American Rockwell Corporation  
Canoga Park, California

There has been considerable confusion in discussions of instabilities. This is mainly because the problem is rather complex and somewhat ill defined. I should like to summarize quickly a simplified way of looking at the whole complex without going too deeply into any specific detail.

The term magnetic instability or "flux flow instability" relates to the movement of flux lines into or out of a superconductor due to the changing external field (which may be the self-field of a current flowing through the superconductor). If this flow is stable (flux flow or flux creep) the flow velocity  $v_{dr}$  is proportional to the rate of change of the external field

$$v_{dr} \propto dH/dt \quad (1)$$

(The proportionality factor would depend mainly on geometry and  $j_c$ .) We should talk about an instability as soon as this relation is no longer valid.

The following picture may illustrate what can happen (see Fig. 1): Starting with  $H$  from 0 one would encounter stable flux flow up to a threshold field  $H_{fi}$ ; formulae for  $H_{fi}$  have been given by Hancox,<sup>1</sup> Swartz and Bean,<sup>2</sup> Lange,<sup>3</sup> and Wipf.<sup>4</sup> They are of the form  $H_{fi} = A c^{1/2} f(T)$ , where  $A$  is a constant,  $c$  the specific heat per unit volume, and  $f(T)$  is  $\{-F_p/(\partial F_p/\partial T)\}^{1/2}$  which is usually a temperature function independent of  $F_p$  itself ( $F_p$  = pinning strength per unit volume).

Above  $H_{fi}$  we encounter flux jump activity until a field  $H_{GT}$  is reached, above which stability is reached again.  $H_{GT}$  has not been calculated in general, but, roughly, it may be proportional to  $D \cdot j_c$ , where  $D$  is a characteristic distance given by the geometry. There is also a dependence on  $dH/dt$ , a large value of  $dH/dt$  may raise  $H_{GT}$ .

A real or catastrophic flux jump is an event which makes the whole or portions of the superconductor temporarily normal. In a coil this gives the degraded critical current while other instabilities or "limited flux jumps" give voltage spikes or noise at the terminals. The flux jump field,  $H_{fj}$ , again is very difficult to calculate.\*

How do we improve our materials with regard to instabilities? There are several methods either proposed or actively pursued in the fabrication of materials now used for magnet construction.

\*For small  $dH/dt$ , i.e., thermal diffusivity  $D_{th} >$  magnetic diffusivity  $D_{mag}$  (which is proportional to  $dH/dt$ ), we have  $H_{fj} \propto \text{const} - \log(dH/dt)$ , and a large  $D_{th}$  increases the constant.<sup>4</sup>

1. R. Hancox, Appl. Phys. Letters 7, 138 (1965).
2. P.S. Swartz and C.P. Bean, to be published.
3. F. Lange, Cryogenics 6, 176 (1966).
4. S.L. Wipf, Phys. Rev. 161, 404 (1967).

1. Obviously the simplest idea is to produce a material which is inherently stable (a trivial case being a low field superconductor whose critical field  $H_c < H_{fi}$ ). The solution to the problem is a material with  $\partial F_p / \partial T > 0$  (or  $\partial j_c / \partial T > 0$ ); then the function  $f(T)$  mentioned above becomes imaginary and  $H_{fi}$  does not exist. Livingston<sup>5</sup> mentioned this method in his talk.
2. A less radical method consists in raising  $H_{fi}$  or lowering  $H_{ST}$  or both, thus narrowing down the instability region or making it disappear altogether.  $H_{fi}$  is raised by reducing  $\partial F_p / \partial T$ , or by increasing  $c$ . The porous  $Nb_3Sn$  cylinder of Corsan and Hancox<sup>6</sup> has a  $c$  which is two orders of magnitude larger due to the presence of liquid He in the pores.  $H_{ST}$  can be lowered by decreasing the diameter of the superconductor and this is partly the reason for the popularity of the multifilament conductors.
3. Most magnet builders have successfully tackled the problem of preventing the catastrophic jump by efficiently limiting the instabilities, while they got used to the idea of living with instabilities. The methods developed have different reasoning for a background. The instabilities are accompanied by the growth of various interdependent quantities:  $d\Phi/dt$ , flux admitted to the superconductor, or to the coil;  $\partial T / \partial t$ , rise in temperature;  $\partial \rho / \partial t$ , rise in the resistivity (electromagnetic diffusivity) of the superconductor. By controlling, or limiting any of these quantities the catastrophic flux jump is prevented. The practical solutions are summarized in the table:

Controlled Quantity	Remedy	Practical Terms
$\frac{d\Phi}{dt}$	Provide shorts	Shorting strips in RCA <sup>7</sup> coils
$\frac{\partial \rho}{\partial t}$	Cu bypass	"Stabilization" (AI, <sup>8</sup> Stekly <sup>9</sup> ) (full or partial) "Current Sharing"
$\frac{\partial T}{\partial t}$	High specific heat High thermal conductivity (by adding liquid He or Pb, Cd)	"Enthalpy Stabilization" <sup>10</sup> "Adiabatic Stabilization" "Transient Stabilization" <sup>11</sup> (Hancox) "Dynamic Stabilization"

5. See also J.D. Livingston, Appl. Phys. Letters 8, 319 (1966).
6. J.M. Corsan, G.W. Coles, and H.J. Goldsmid, Brit. J. Appl. Phys. 15, 1383 (1964).
7. E.R. Schrader, P.A. Thompson, and W. Coles, J. Appl. Phys. 39, 2652 (1968).
8. C.N. Whetstone and R.W. Boom, in Advances in Cryogenic Engineering (Plenum Press, 1968), Vol. 13, p. 68.
9. A.R. Kantrowitz and Z.J.J. Stekly, Appl. Phys. Letters 6, 56 (1965).
10. R. Carruthers, D.N. Cornish, and R. Hancox, in Proc. First Intern. Cryogenic Engineering Conference, Kyoto, 1967 (Heywood-Temple, London, 1968), p. 107; R. Hancox, to be published in Proc. Intermag Conference, 1968.
11. J.R. Hale and J.E.C. Williams, J. Appl. Phys. 39, 2634 (1968).



Naturally this table only provides a very sketchy summary of a very complex situation which also includes the cooling process and the thermal diffusivity.

Using the third method one still has instabilities in the sense that Eq. (1) is not fulfilled. But they may be so small or so slow as not to be detectable in practical cases.

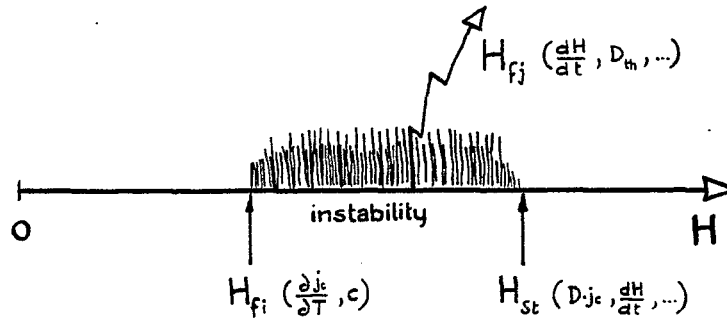


Fig. 1. Instability in a superconductor as a function of applied field.

# CRITICAL CURRENT BEHAVIOR OF HARD SUPERCONDUCTORS

W.W. Webb

Department of Applied Physics and  
Laboratory of Atomic and Solid State Physics  
Cornell University  
Ithaca, New York

## I. INTRODUCTION

For many applications it is not enough that a superconductor have a high critical temperature  $T_c$  and high upper critical magnetic field  $H_{c2}$ ; often a high critical current density  $J_c(B,T)$  in high magnetic fields and at reasonable temperatures is also essential. High critical current density in the presence of a transverse magnetic field is not an intrinsic property of superconductors. Instead the critical current density in the presence of a transverse field is a nonequilibrium property that is closely analogous to the permanent magnetism of a hard ferromagnet, hence the designation hard superconductor. Just as the coercive force of a permanent ferromagnet depends on the strength of pinning of ferromagnetic domain walls, the critical current densities, or corresponding field gradients, in hard superconductors depend on pinning of the flux distribution in the fluxoid lattice against Lorentz-like electromagnetic forces.

The Lorentz force density is<sup>1</sup>

$$\mathbf{F} = \frac{\gamma}{c} \mathbf{J} \times \mathbf{B} \approx \frac{JB}{c}, \quad (1)$$

where the effect of the equilibrium magnetization is included by introduction of the factor  $\gamma = [\partial B(H)/\partial H]_{eq}$ . In sufficiently high fields  $\gamma \approx 1$ . The approximate scalar form on the right of Eq. (1) holds for  $\mathbf{J}$  and  $\mathbf{B}$  mutually perpendicular. The critical force density  $F_c$  or corresponding critical force density  $J_c \approx cF_c/B$  is loosely defined as the value of  $F(B)$  or  $J(B)$  at which dissipation becomes significant so that persistent currents decay at a significant rate, or a voltage appears along a wire carrying a transport current. Since Maxwell's equations give  $\mathbf{J} = (c/4\pi) \nabla \times \mathbf{B}$ , or in simplified scalar form,  $J = (c/4\pi) dB/dx$ , magnetic cycling of a hard superconductor should produce a distribution of induced currents of magnitude up to  $J_c$  with corresponding nonuniform magnetic field distribution. The condition in which the current density is everywhere equal to the critical current density is designated as the "critical state" although it is not a uniform equilibrium state in the thermodynamic sense.

The magnitudes of the critical current density can be determined either by analysis of hysteretic magnetization curves produced by magnetic cycling or by the measurement of the transport current densities at which losses become appreciable in ribbons exposed to magnetic fields.

This explanation of critical currents was advanced by Bean<sup>2</sup> and by London,<sup>3</sup> and developed by Kim, Hempstead, and Strnad,<sup>4</sup> and has been amply substantiated by many

- 
1. J. Friedel, P.G. deGennes, and J. Matricon, Appl. Phys. Letters 2, 119 (1963).
  2. C.P. Bean, Phys. Rev. Letters 8, 250 (1962).
  3. H. London, Phys. Letters 6, 162 (1963).
  4. Y.B. Kim, C.F. Hempstead, and A.R. Strnad, Phys. Rev. Letters 9, 306 (1962).

subsequent experiments. Of interest amongst the earlier experiments are direct observations of the predicted field gradient by Coffey,<sup>5</sup> and a direct comparison of the critical transport current density with the current density deduced from magnetization measurements by Fietz, Beasley, Silcox and Webb,<sup>6</sup> in addition to various experiments by Kim and co-workers.<sup>7</sup> At least for large values of the Ginzburg-Landau parameter,  $\kappa$ , and internal fields well above the lower critical field but with  $B < H_{c2}$ , critical state concepts appear to describe adequately hard superconductors. However, in low  $\kappa$  materials and very thin filaments, hysteretic surface currents make significant contributions if the bulk  $J_c$  is small.

At temperatures above absolute zero Anderson<sup>8</sup> predicted that thermal activation assisted by the Lorentz force would lead to creep of flux in the neighborhood of the critical state. The general ideas of a thermally activated process suggest a flux creep rate

$$R = R_0 \exp^{-U/kT}, \quad (2)$$

where  $R_0$  is a very large pre-exponential and  $U$  is an activation energy which in this case is approximately

$$U = U_p - JB\gamma VX/c, \quad (3)$$

where  $U$  is composed of an interaction energy between the pinning inhomogeneities and the fluxoid lattice,  $U_p$ , reduced by the Lorentz force per unit volume  $JB\gamma/c$  times an activation volume  $V$  and a pinning length  $X$ . It turns out that  $U \gg U_p$  and  $U_p \approx JB\gamma VX/c$ , and the rate  $R$  is appreciable only if  $J > J_c$ , so the critical state is reasonably well defined by putting  $J = J_c$  such that

$$F_c = J_c B\gamma/c = \frac{U_p - kT \ln R_0/R_c}{VX}, \quad (4)$$

where  $R_c \ll R_0$  is a creep detection limit characteristic of experiments used to determine the critical current. Beasley, Labusch and Webb<sup>9</sup> have found that  $U_p \gg kT \ln R_0/R_c$  so that the temperature dependence of  $F_c$  is dominated by the temperature dependence of various material parameters rather than by the explicit linear term in  $T$ .

## II. CURRENT STATUS

In the present state of knowledge about critical currents in hard superconductors, the critical state concepts are well established and a great deal of practical data on critical currents in many hard superconductors have been obtained. The inhomogeneities that give rise to pinning of the fluxoid lattice have been explored in some detail and

---

5. H.T. Coffey, *Cryogenics* 7, 73 (1967).

6. W.A. Fietz, M.R. Beasley, J. Silcox, and W.W. Webb, *Phys. Rev.* 136, A335 (1964).

7. See, for example, Y.B. Kim, C.F. Hempstead, and A.R. Strnad, *Phys. Rev.* 129, 528 (1963).

8. P.W. Anderson, *Phys. Rev. Letters* 9, 309 (1963).

9. M.R. Beasley, Ph.D. Thesis, Cornell University, 1968 (available as Materials Science Center Report 921 or AEC Report NYO-3029-29).

at least qualitative information is available about them. Dr. Livingston has thoroughly reviewed this information in the preceding lecture<sup>10</sup> and earlier in a review article with Schadler.<sup>11</sup>

A development has also appeared at this Summer Study that refocuses attention on the critical current problem. In recent, practical, high field superconducting devices, performance has been limited by instabilities that cause flux jumps that often cause catastrophic heating and loss of superconductivity. However, as reported here by Brechna, Hart, Wipf, and Smith in various contributions, there has been substantial recent progress in controlling this problem through appropriate geometric design. Thus, there is now again good reason to try to develop higher pinning force materials to obtain higher critical current densities.

However, a serious problem remains in applying the well established critical state concepts to hard superconductors. This problem is the lack of a satisfactory basis to calculate the critical current density to be obtained from even a simple array of localized pinning points. Livingston has described in some detail the various types of effective pinning points and our knowledge of their properties. The fact that we cannot simply add the pinning forces of all of the pinning points in a material to obtain  $F_c$  is clear. Instead we must take into account cooperative action amongst adjacent pinning points and fluxoids. Anderson<sup>8</sup> recognized this problem in 1963 in his formulation of flux creep by incorporating a sort of activation volume which he called the flux bundle. However, little subsequent progress with this problem has appeared in the literature.

### III. SOME RECENT RESEARCH

At Cornell, M.R. Beasley, W.A. Fietz, R. Labusch, and I have been trying to understand the problem of determining the quantitative connection between  $J_c$ , or  $F_c$ , and the properties of the array of pinning points. This connection is complicated by the fact that the pinning process involves the cooperative interaction between a quasi-random array of pinning points and a nominally regular array of fluxoids. We have carried out systematic measurements of flux creep and critical current densities in alloys over a wide range of  $T$ ,  $B$ , and  $\kappa$  using crystal dislocations as the pinning entities. It has been possible to calculate the pinning properties of dislocations better than other pinning entities so these otherwise complex objects were chosen as the best pinning entities to study.<sup>12-15</sup> From this work we have been able to extract information about the pinning process that has guided us in developing a simple model that seems to make the appropriate connection between the critical current density and the pinning points. This research is nearly complete, but manuscripts describing it are still in preparation. I will present here a preliminary summary of the essential ideas of the pinning model and the results of some of our pinning experiments.

---

10. J.D. Livingston, these Proceedings, p. 377.

11. J.D. Livingston and H.W. Schadler, Prog. Mat. Sci. 12, 183 (1964).

12. W.W. Webb, Phys. Rev. Letters 11, 191 (1963).

13. E.J. Cramer and C.L. Bauer, Phil. Mag. 15, 1189 (1967).

14. R. Labusch, Phys. Rev. 170, 470 (1968).

15. J.S. Willis, J.F. Schenck, and R.W. Shaw, Appl. Phys. Letters 10, 101 (1967).

#### IV. PINNING MODEL

If we were to assume that the pinning force density is given simply by a linear superposition of the contribution of all the effective pinning points we would have a pinning force density

$$F_p = f_p N_p, \quad (5)$$

where  $N_p$  is an effective density of pinning points and  $f_p$  is the maximum pinning force for each interaction. Since flux creep introduces negligible changes in the current density, the pinning force density  $F_p$  is essentially equal to the critical force density so we may take  $F_p = F_c$ .

Assuming that the pinning points consist of individual fluxoid-dislocation interactions, that the fluxoids are relatively stiff, and that their range of interaction with the dislocations is a distance  $d$  less than the fluxoid spacing, the effective density of interactions  $N_p$  becomes just the density of interactions with individual pinning points  $N_1$ , which is just the product of the length of fluxoid per unit volume  $B/\varphi_0$ , the effective area per unit length  $d$ , and the density  $\rho$  of dislocations threading the area, that is:

$$N_1 \approx (B/\varphi_0)\rho d. \quad (6)$$

Typical magnitudes for our cases give  $N_1 \approx 10^{11} \times 10^{11} \times 10^{-6} \approx 10^{16} \text{ cm}^{-3}$ . Figure 1 depicts the geometrical model leading to Eq. (6).

If the fluxoid lattice were perfectly rigid, no net pinning could accrue from interaction with a random array of pinning points because in this case the total energy of the system would be independent of the position of the fluxoid lattice with respect to the pinning points. This astonishing result disappears if the lattice is even slightly deformable and a net pinning force is found, but the strength of the resulting pinning depends strongly on the magnitude of the deformation of the lattice introduced by the pinning interaction. In fact the ratio  $\delta/d$  of the distance  $\delta$  that a fluxoid can be displaced by the pinning potential to the width of the pinning potential  $d$  can be interpreted as the fraction of the points of interaction between fluxoids and obstacles that can become effective in pinning against an applied (Lorentz) force. This result is equivalent to replacing  $d$  by  $\delta$  in Eq. (6).

The maximum deformation,  $\delta$ , due to a single pinning point, depends on the strength of the interaction force per pinning point,  $f_1$ , and the effective stiffness of the fluxoid lattice represented by an elastic constant  $C$  times the nominal fluxoid spacing  $(\varphi_0/B)^{1/2}$ . Thus we can obtain, following the elasticity calculation of Labusch<sup>16</sup>

$$\delta \approx f_1 \frac{a}{C} \left( \frac{B}{\varphi_0} \right)^{1/2}, \quad (7)$$

where  $a$  is a constant of order unity. Using<sup>12,17</sup>  $f_1 \approx 10^{-8} \text{ dyn}$ , and  $C/a \approx 10^6 \text{ dyn}\cdot\text{cm}^{-2}$ , we find the extremely small displacement  $\delta \approx 10^{-9} \text{ cm}$ . A similar calculation in the low field limit using the line energy or tension of a single fluxoid as the restoring force yields essentially the same kind of result. Thus the fluxoid lattice is very rigid and

---

16. R. Labusch, private communication.

17. R. Labusch, Phys. Stat. Sol. 19, 715 (1967); additional results for  $H \sim H_{c2}$  to be published.

the pinning process must involve a statistical average over all of the interaction forces sampled by this relatively rigid net.

Using Eq. (7) for  $\delta$ , an efficiency factor  $W = \delta/d$  can be defined as follows:

$$W = (f_p/d)(a/C)(B/\varphi_0)^{\frac{1}{2}}, \quad (8)$$

where  $f_p = f_1$  is the maximum pinning force of an individual dislocation-fluxoid interaction.

Thus, the pinning force density given by Eq. (5) is simply reduced by the efficiency factor  $W$  giving

$$F_p = f_p N_p W. \quad (9)$$

Assuming  $f_p = f_1$ ,  $N_p = N_1$  as given by Eq. (6), and  $W$  as given by Eq. (8), the effective pinning force density is

$$F_p = f_1^2 \rho (B/\varphi_0)^{3/2} (a/C). \quad (10)$$

Thus we find the remarkable result that the pinning force density is proportional to the square of the strength of individual pinning points because of the appearance of  $f_1$  in the efficiency factor of Eq. (9).

However, Labusch has carried out a detailed statistical analysis of this many-body problem<sup>16</sup> indicating that to lowest order in the pinning point density there is no pinning, i.e.,  $F_p = 0$ , unless the quantity that we call an efficiency factor  $W$  is greater than 1. In other words, the elementary calculation indicates that it is necessary that distortions of the fluxoid lattice be larger than the width of the pinning potential for pinning to occur, or  $\delta > d$ . However, in usual materials  $f_1 \sim 10^{-8}$  dyn, and  $d \sim 10^{-6}$ , and we have  $\delta \sim 10^{-8}$ , so  $W \sim 10^{-2}$ . Nevertheless, consideration of the effect of fluctuations in the pinning point distribution leads to pinning by even a random array as a first order effect. Assuming that only groups of pinning points strong enough that  $W \geq 1$  are effective, we seek fluctuations that provide a net local excess of  $n$  favorable pinning points providing a net strength  $f_p \rightarrow f_n \geq n f_1$ , where the number  $n$  is determined by the requirement that  $W \geq 1$ . This configuration should occur with random probability  $1/n^2$  so that the effective density of these pinning coefficients is  $N_p \rightarrow N_n \geq (B/\varphi_0) \rho d/n^2$ . The criterion that  $W \geq 1$  yields

$$n \geq \left[ \frac{f_1}{d} \left( \frac{B}{\varphi_0} \right)^{\frac{1}{2}} \frac{a}{C} \right]^{-1}. \quad (11)$$

The new values of  $N_p$  and  $f_p$  can be inserted in Eqs. (8) and (9) to obtain the pinning force density  $F_p$ . However, inserting  $N_p = N_n$  and  $f_p = f_n$  yields precisely the same pinning strength given by Eq. (11) since  $n$  cancels out exactly in the expression for  $F_p$ .

If the pinning points are not randomly arrayed, the pinning force is enhanced by the clustering since the number of favorable fluctuations then varies more like  $1/n$  instead of  $1/n^2$ . In our measurements on severely cold-worked alloys we found  $10^{-8} < f_1 < 10^{-7}$  dyn, while the calculated value is  $f_1 \sim 10^{-8}$ , suggesting that some dislocation ordering occurs as is expected.

The collective pinning represented by the pinning force  $f_p = n f_1$  in a volume containing between  $n$  and  $n^2$  pinning interactions seems to be simply an explicit description

of a property of the "flux bundle" hypothesized by Anderson in his original theory of flux creep.<sup>8</sup> The size of this bundle can be estimated from our measurements on niobium-titanium alloys<sup>18</sup> using Eq. (6), which give  $n \sim 10^2$ . Thus,  $n^2 = 10^4$ , and the "bundle volume"  $V_p \approx N_p^{-1} n^2 \approx n^2 / [(B/\phi_0)\rho d] \approx 10^{-12} \text{ cm}^3$ . From measurements of flux creep in PbTi alloys subjected to severe plastic deformation at low temperatures to produce pinning structures similar to ours, Beasley, Labusch and Webb<sup>19</sup> observed volumes  $\sim 10^4$  times the volume per pinning point and pinning energies  $\sim 10^2$  times the energy per pinning point under comparable conditions. This comparison suggests that the cooperative pinning in our analysis of the critical pinning force really corresponds to the activation volume or "flux bundle" invoked by Anderson to understand flux creep.

## V. RESULTS OF CRITICAL PINNING FORCE MEASUREMENTS

We have deduced critical pinning force densities from hysteretic magnetization curves on niobium alloys over a wide range of the Ginzburg-Landau parameter,  $\kappa$ , magnetic field,  $H$ , and temperature,  $T$ . A sample of this data is shown as a logarithmic critical current density plot in Fig. 2, and as a critical pinning force density plot in Fig. 3. The fields have been normalized by dividing by the temperature dependent upper critical field  $H_{c2}$ . Although the critical currents show the usual plateau on a logarithmic scale, the pinning force invariably peaks at  $B/H_{c2} = 0.6$  in these materials. This and all other features of the results support a well-defined set of scaling laws in which the pinning force density is given, the separable product of factors depending on temperature, normalized field and  $\kappa$ . The temperature dependence is accurately represented in terms of the temperature dependence of  $H_{c2}$ . Thus we found

$$F_p \propto k(\kappa) H_{c2}^{5/2} g(B/H_{c2}) \quad (12)$$

where the function  $g(B/H_{c2})$  has the shape shown in Fig. 3 and  $k(\kappa)$  is something like  $\kappa^{-\gamma}$  with  $1 < \gamma < 3$ . The factor  $[H_{c2}(T)]^{5/2}$  is established with high precision,  $g(B/H_{c2})$  is determined to better than  $\pm 15\%$  for  $0.2 < B/H_{c2} < 0.9$ , but  $k(\kappa) = \kappa^{-\gamma}$  is only a qualitative form. The most remarkable result is the precise temperature dependence fit given by the factor  $[H_{c2}(T)]^{5/2}$ . This is illustrated by the logarithmic plots in Fig. 4 where straight lines with slope 5/2 are drawn through the data.

To compare these data with the pinning model previously described, it is necessary to work out the temperature and field dependence of the fluxoid lattice stiffness, represented by the factor  $a/c$ , and of the pinning force,  $f_1$ , that appear in Labusch's<sup>17</sup> calculation of  $a/c$  and Webb's<sup>12</sup> second order elastic calculation of  $f_1$ . Combining the field, temperature, and  $\kappa$  dependence of all of the factors we find that the pinning model gives the proportionality

$$F_p \propto H_{c2}(T)^{5/2} \cdot \begin{cases} (B/H)/\kappa^2 & : B \text{ small} \\ 1/\kappa^2 & : B \sim H_{c2}/2 \\ (B/H_{c2})(1 - B/H_{c2})/\kappa^3 & : 1 - B/H_{c2} \ll 1 \end{cases} \quad (13)$$

in satisfactory agreement with the experiments.

18. W.A. Fietz and W.W. Webb, submitted for publication.

19. M.R. Beasley, R. Labusch, and W.W. Webb, private communication.

## VI. DISCUSSION AND SUMMARY

Clearly the empirical model for critical pinning force that has been suggested by Fietz and Webb,<sup>18</sup> on the basis of Labusch's theoretical investigations,<sup>16</sup> fits the wide range of data they collected. It also fits data obtained by Coffey on a magnet wire alloy<sup>20</sup> and seems to be consistent with a great deal of earlier data on materials with other types of pinning points except that the detailed shape of the field dependence of  $F_p$  given by the factor  $g(B/H_{c2})$  depends on materials preparation.

For example, T. Hall (unpublished) annealed some of Fietz's niobium alloys at various temperatures and found that a new maximum of  $F_p$  developed at  $B/H_{c2} \cong 0.4$  as the peak at  $B/H_{c2} \cong 0.6$  decreased, until even the new peak became very weak as annealing was made more complete. During this change the factor  $[H_{c2}(T)]^{5/2}$  represented the temperature dependence of the first peak rather well, although the exponent for the second peak may be as low as about two.

Although the temperature dependence of  $a/C$  should remain the same for most superconducting alloys, various pinning entities should give different temperature dependences for  $f_1$ . This is yet to be tested systematically.

In the case of the superconducting intermetallic compounds, such as  $V_3Si$  and  $Nb_3Sn$ , based on the beta-tungsten structure, the situation seems to be different. It has been suggested that grain boundaries or nonsuperconducting inclusions provide the observable pinning and that the critical current is limited by Silsbee's hypothesis in part of the measured range.<sup>21</sup> Brand and Webb found that in  $V_3Si$  pinning is also enhanced by the occurrence of the martensitic phase transformation to a tetragonal structure.<sup>22</sup> Some uncertainties about pinning in these compounds remain.

Special pinning properties may lead to "peak effects" in the pinning strength<sup>10</sup> with unique temperature dependence, and it may be useful to exploit them or to look to the sort of models described here for ways of decreasing the temperature dependence of  $F_p$  in order to reduce thermal instabilities, and for ways of increasing the critical current density. Composite superconductors may provide some of these properties.

## ACKNOWLEDGMENTS

We are pleased to acknowledge the support of the United States Atomic Energy Commission through the Materials and Metallurgy Branch of the Division of Research for this research including the work attributed to M.R. Beasley, W.A. Fietz, R. Brand, and much of that attributed to R. Labusch. This effort also benefited from the use of facilities provided by the Advance Research Projects Administration at Cornell.

---

20. H.T. Coffey, Phys. Rev. 166, 447 (1968).

21. See contribution by G.D. Cody, these Proceedings, p. 405.

22. R. Brand and W.W. Webb, to be published in Solid State Communications.



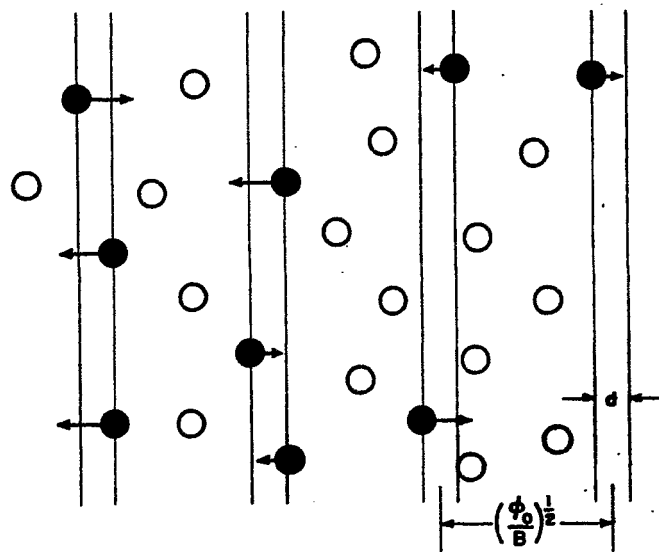


Fig. 1. Schematic diagram of the interaction of fluxoids with localized pinning points. The interaction range of pinning potential is represented by the effective width  $d$  of the fluxoids which are spaced a distance  $(\phi_0/B)^{1/2}$ . The pinning points are supposed to be repulsive potential lines perpendicular to the paper. Thus the direction of the interaction force on the fluxoids is indicated by the arrows. Only the blackened pinning points are close enough to interact in this section. On the average in this rigid lattice model the net force on the fluxoid lattice is zero.

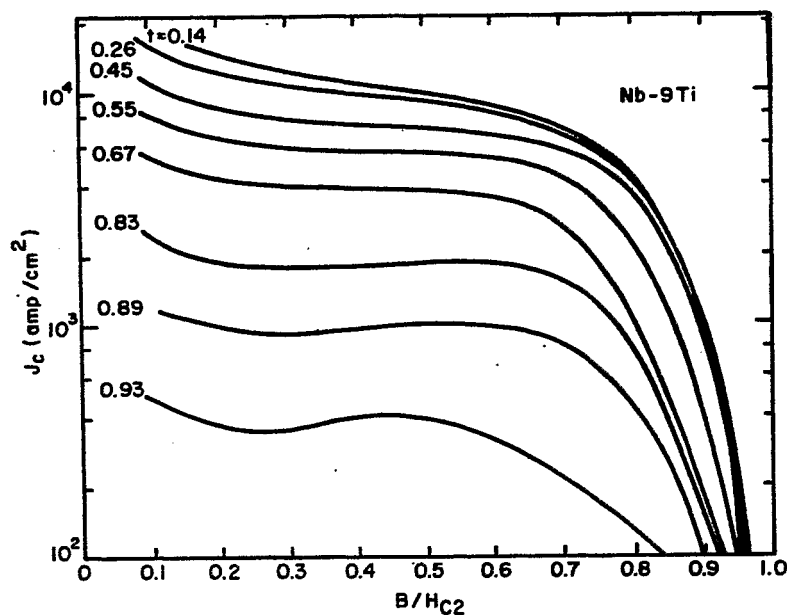


Fig. 2. Logarithmic plot of the critical current density as a function of normalized field  $B/H_{c2}$  in severely plastically deformed alloy of niobium with 9% titanium at various normalized temperatures  $t = T/T_c$ .

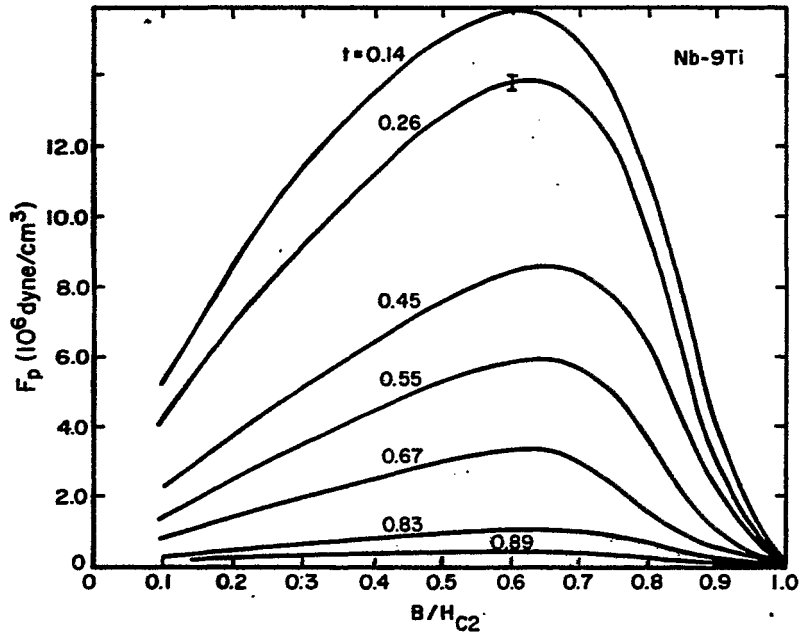


Fig. 3. Pinning force density as a function of normalized field  $B/H_{c2}$  in a severely plastically deformed alloy of niobium with 9% titanium at various normalized temperatures  $t = T/T_c$ . The normalizing value of  $H_{c2}$  is taken as  $H_{c2}(t)$ .

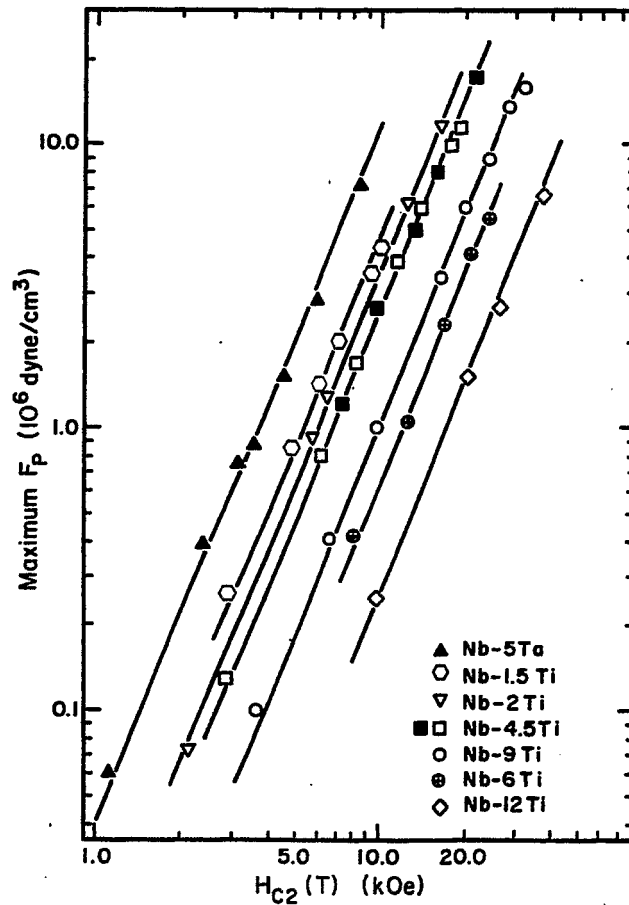


Fig. 4. Logarithmic plot of maximum value of the volume pinning force  $F_p(\max)$  as a function of  $H_{c2}(t)$ . Lines have slope  $5/2$ .

## CRITICAL FIELDS OF TYPE II SUPERCONDUCTORS

G. Cody  
RCA Laboratories  
Princeton, New Jersey

### INTRODUCTION

The purpose of this paper is to discuss the critical fields of type II superconductors. In order to develop a physical basis for the concept of the critical field, we start with a discussion of the magnetic behavior of type I superconductors, and particularly the intermediate state. The approach to type II behavior will be through the vortex model of deGennes which follows naturally from a consideration of surface energies in a type I superconductor. Finally, we will cover recent results from the Gor'kov microscopic Ginsburg-Landau equation which accurately predicts the effects of temperature, purity, normal electron spin paramagnetisms and variable coupling on the critical field behavior of a large class of type II superconductors. The exceptions to this theory and possible sources of their unique behavior will be discussed. Finally, we will consider recent experimental observations of critical field behavior in materials of practical interest.

### MAGNETOSTATICS AND THERMODYNAMICS OF TYPE I SUPERCONDUCTORS

Superconductors exhibit zero resistance below the transition temperature,  $T_c$ , but when relatively defect free, exhibit a diamagnetism that is field dependent and reversible.<sup>1</sup> This last fact, although of little practical utility, is the basis for the theoretical treatment of the superconducting state. For a uniformly magnetized ellipsoid three fields are introduced in addition to the microscopic local field  $h(r)$  and the applied field  $H_0$ . These three fields are  $B$ , the flux density or average local field  $h(r)$ ,  $M$ , the dipole moment per unit volume or magnetization, and  $H$ , the internal field. From magnetic theory:

$$B = H + 4\pi M = H_0 + 4\pi (1 - D) M \quad (1)$$

In Eq. (1),  $D$  is the demagnetization coefficient of the ellipsoid. For a long cylinder, a sphere and a disk,  $D = 0$ ,  $1/3$  and  $1$ , respectively, where the applied field,  $H_0$ , is along the symmetry axis of the ellipsoid.

From considerations of the magnetic work, we are led to consider the specific Gibbs free energy  $g$ , which is a function of  $H_0$  and  $T$ , and is a minimum under equilibrium at constant field and temperature. From the thermodynamic treatment,

$$dg = -s dT - M dH_0 \quad (2)$$

In Eq. (2),  $s$  is the specific entropy. The Gibbs free energies of two phases in equilibrium can be shown to be equal, and this criterion for phase equilibrium is critical for understanding the gross features of field effects in superconductors.

For type I superconductors, when  $D = 0$ , it is observed experimentally that  $M_s = -H_0/4\pi$  up to a critical field  $H_c(T)$ .<sup>2</sup> Thus  $B = 0$  in the superconducting state. Above this field the magnetization of the superconductor,  $M_s(T)$ , is the same as that of the normal state,  $M_n(T) = \chi_n H$  (the paramagnetic susceptibility,  $\chi_n$ , is of the order of  $20 \times 10^{-6}$  for transition metals, but is considerably less for nontransition metals).

The discontinuous change of magnetization at  $H_c(T)$  defines a type I superconductor, as well as the thermodynamic critical field  $H_c(T)$ .

If we consider Eq. (2) we can arrive at another view of  $H_c(T)$  which explains its nomenclature. From simple integration and use of the equilibrium criteria we see that

$$g_n(H_c, T) \approx g_n(0, T) = g_s(0, T) + \frac{H_c^2}{8\pi} = g_s(H_c, T) \quad (3)$$

and thus  $H_c^2/8\pi$  represents the free energy difference between the normal and superconducting state. Figure 1 shows the free energy and the magnetization  $[M = -(\partial g/\partial H_0)_T]$  of a type I superconductor and illustrates the content of Eq. (3). The effect of the field on the free energy of the superconductor is to destroy the energy gained by the initial condensation to the ordered superconducting state ( $H_c^2/8\pi$ ). From Eqs. (3) and (2) one can obtain the entropy  $s [s = -(\partial g/\partial T)_{H_0}]$  and it can easily be seen that the superconducting state is the more ordered state ( $s_s < s_n$  for  $T < T_c$ ). Furthermore, in zero field  $s_s(T_c) = s_n(T_c)$ , which implies a second order transition. In a finite field the entropy remains at its zero field value, up to  $H_c(T)$ , but jumps discontinuously at  $T[H_0 = H_c(T)]$  to the normal entropy (a first order transition).

The absence of a field dependence to the entropy is accounted for by the observation that since  $B = 0$  up to  $H_0 = H_c(T)$ , the field plays no role in changing the order of the superconductor. Of course, this ignores the fact that there cannot be a discontinuity in the field at the surface of the superconductor. The field extends a distance into the superconductor, given by the penetration depth  $\lambda(T)$ . A penetration depth,  $\lambda_L$ , was first introduced by London, who derived on the basis of a dissipationless fluid the following equation for the field penetration, which when combined with Maxwell's equations are in semiquantitative agreement with experiment:

$$\lambda_L^2 \nabla \times (\nabla \times H) = -H, \quad (4)$$

where

$$\lambda_L^2 = \left( \frac{mc^2}{4\pi ne^2} \right) = \left( \frac{3c^2}{4\pi N v_F^2 e^2} \right). \quad (5)$$

In Eq. (5)  $m$  and  $n$  are the mass per particle and the density of the fluid, respectively; in the second form of  $\lambda_L$ ,  $N$  and  $v_F$  are the total density of states and Fermi velocity, respectively. This second form is of greater generality than the fluid model. It is interesting to note that Eq. (5) is invariant under the transformation to pairs appropriate to the BCS theory of superconductivity ( $m \rightarrow 2m$ ,  $e \rightarrow 2e$ ,  $n \rightarrow n/2$ ).

From Eqs. (4) and (5) we can associate  $H_c(T)$  with the kinetic energy of the shielding currents that maintain the condition  $B = 0$  in the bulk. It is simple to show that the kinetic energy density  $K$  is given by

$$K = \frac{1}{2} nm v_d^2 = \frac{1}{2} \frac{mJ^2}{ne^2} = \frac{4\pi}{2c^2} \lambda_L^2 J^2 = \frac{H^2}{8\pi}, \quad (6)$$

where  $v_d$  is the drift velocity and we have used the solution for Eq. (4) at a plane boundary:  $J = cH/4\pi \lambda_L$ . At  $H = H_c(T)$ , the kinetic energy density of the shielding electrons equals the quantity  $g_n - g_s(0, T)$  and the material goes normal.

It clearly costs the superconductor to expel a magnetic field. Consider Fig. 2 where again we show the free energy of a type I superconductor. If there were a way

to achieve a lower magnetization  $[M = - (\partial g / \partial H_0)_T]$  as shown by the dashed curve, the material could achieve a lower free energy and would presumably remain superconducting to considerably higher fields. Experimentally such a situation has been known since the thirties for systems where one dimension approached a size of the order of  $\lambda$  ( $\approx 300$ - $600 \text{ \AA}$ ). Under these conditions, field exclusion is not complete,  $B = \bar{h} \neq 0$ , and  $M$  is appreciably smaller than for bulk materials. Indeed, critical fields considerably higher than  $H_c(T)$  were observed and were correlated with the London expressions with qualitative and semiquantitative agreement.<sup>3</sup> From these experiments, an important question emerges: namely, why a bulk specimen did not subdivide into domains of the order of  $\lambda$ , and hence remain superconducting to fields much higher than  $H_c(T)$ .

#### INTERMEDIATE STATE OF TYPE I SUPERCONDUCTORS

A model for such a domained structure was developed in the thirties to explain magnetization data on ellipsoidal specimens where  $D \neq 0$ . While neither the experiments nor the model led to critical fields higher than  $H_c(T)$ , it led through the work of Pippard<sup>4,5</sup> to what might be described as the physical basis of type II superconductivity. Curve (1) in Fig. 3 shows the magnetization and free energy of a bulk specimen with  $D \neq 0$ . The magnetization in the state for which  $B = 0$  (the Meissner state) is of the form  $M = - H_0 / 4\pi (1 - D)$ , and hence the free energy rises considerably faster than the curve (2) for  $D = 0$ : If this high moment state persists, the specimen would enter the normal state at a field considerably less than  $H_c(T)$ . In fact the material follows the curve (3), branching off from (1) at  $H_0 = H_c (1 - D)$  and finally enters the normal state close to  $H_c(T)$ . In this new state, the intermediate state,  $M = (-1/4\pi D)(H_c - H_0)$  and

$$g(H, T) = g_s(0, T) + H_c^2 / 8\pi - (H_c - H)^2 / 8\pi D. \quad (7)$$

In the new state Peierls<sup>6</sup> suggested that the system is subdivided into normal domains where  $h = H_c$ , and superconducting domains where  $h = 0$ . Thus if  $x$  is the concentration of normal domains

$$x = \frac{B}{H_c} = -\frac{1}{D} \left( 1 - \frac{H_0}{H_c} \right), \quad (8)$$

and  $x$  goes from 0 at  $H_0 = H_c(1 - D)$  to 1 at  $H_0 = H_c$ . It is easily shown that the entropy of the intermediate state is a continuous function of field and it, as well as  $M$ , goes continuously to normal state values at  $H = H_c$ . In view of the presence of normal domains this is not a surprising effect.

Given the possibility of domains, it is not apparent why they cannot reduce in size to such a degree that  $M \rightarrow 0$ , as for thin films which would permit the intermediate state to persist to fields above  $H_c$ . However, far from this being the case, a careful examination of the magnetic transition of the intermediate state shows that the critical field,  $H_I$ , is slightly less than  $H_c(T)$ .

In order to understand this phenomenon, an additional property has to be introduced, the surface energy. In the intermediate state with many normal-superconducting interfaces, it is clear that there may be surface tension or surface energy effects resisting the increase of the interface. If the surface energy is  $\alpha$ , an additional free energy  $\alpha f(x)$  will be lost to the superconductor and the critical field will be less than  $H_c(T)$ , as shown in Fig. 4.

Pippard<sup>4</sup> gave a physical picture of the source of this surface energy. Consider the superconducting state to be associated with an order parameter,  $n_s$ . The order parameter may be identified with the density of superconducting electrons, or with the

energy gap. In either case it is a quantity that varies from its full value at  $T = 0^\circ\text{K}$ , to zero at  $T_c$ . We consider a normal-superconducting boundary to be defined by  $n_s = 0$ , but we cannot permit  $n_s$  to change discontinuously at the interface. As in the case of field penetration, we are led to consider a fundamental length  $\xi^*$ , over which the order parameter can vary.

In Fig. 5, we consider a normal-superconducting boundary where  $H = H_c(T)$  in the bulk of the normal metal ( $n_s = 0$ ) and  $H = 0$  in the bulk of the superconductor [ $n_s = n_s(T)$ ]. It is easy to see that there is a gain of energy of order  $\lambda H_c^2/8\pi$  per unit area due to flux penetration. Conversely, there is a loss of condensation energy of the order  $\xi^* H_c^2/8\pi$  per unit area, where  $\xi^*$  is the distance over which the order parameter varies. Thus the surface energy is given by  $\alpha = (\xi^* - \lambda) H_c^2/8\pi \equiv \Delta H_c^2/8\pi$ . For a positive surface energy ( $\xi^* > \lambda$ ) we cannot gain energy by infinite subdivision. The minimum size of a domain is of the order of  $\xi^*$ , and the limit of  $x \rightarrow 1$  for the intermediate state corresponds to the vanishing of the last domain, not its shrinking in size. For thick disks ( $D \approx 1$ ) in a perpendicular field, one can show that the critical field  $H_{L1}$ ,<sup>7</sup> is given by

$$H_{L1}/H_c \approx [1 - (\Delta/d)^{\frac{1}{2}}] \quad (9)$$

and this relation, as well as the slope of  $(\partial M/\partial H)_H = H_{L1}$ , can be used to determine  $\Delta$ .

Pippard<sup>8</sup> further suggested a relationship for pure metals between  $\xi^*$  and the transition temperature and Fermi velocity. As later given by BCS<sup>9</sup> this is

$$\xi^* \approx \xi_0 = \hbar v_F / \pi \Delta \quad , \quad (10)$$

where  $2\Delta$  is the energy gap ( $2\Delta = 3.56 k T_c$ ). Calculations show that for most pure metals,  $\xi_0 \approx 2000 - 10\,000 \text{ \AA}$ , whereas  $\lambda \approx 200 - 600 \text{ \AA}$ . Hence  $\Delta > 0$ .

From these considerations we have been led to consider two fundamental lengths for a superconductor,  $\xi^*$  and  $\lambda$ . If we define their ratio as  $\sqrt{2}\kappa = \lambda/\xi^*$ , we see that for  $\sqrt{2}\kappa > 1$ ,  $\Delta < 0$ , and one might expect a general depression of the free energy below even the Meissner curve for  $D = 0$ . Furthermore, the experience with the intermediate state suggests that such a negative surface energy state might be a proper thermodynamic phase — homogeneous and reversible.

## THE MIXED STATE OF TYPE II SUPERCONDUCTORS

It is one of the triumphs of solid state physics that the negative surface energy state was predicted mathematically before there was any recognition of experimental justification. However, it remains a paradox, that the experimental evidence for such a state was largely ignored both prior to the theory and to its eventual experimental "verification." The theory, of course, is the Ginzburg-Landau theory<sup>10</sup> published in 1950, "discovered" in 1961,<sup>11</sup> and which has received numerous verifications since that time, but some of whose predictions were observable in the experiments of Shubnikov et al.<sup>12</sup> in 1937. The G-L theory, the theory of the microstructure of the negative surface energy state due to Abrikosov,<sup>13</sup> and the microscopic theory of Gor'kov<sup>14</sup> (the GLAG theory) have all been the subject of numerous reviews, and only the results will be considered in detail in the present paper.

In its original form the theory was based on an expansion of the free energy close to  $T_c$  in terms of an order parameter, and was explicitly designed to take into account spatial variations of the order parameter as occur in the intermediate state and in thin films. It was shown by Gor'kov to be a natural consequence of the BCS microscopic theory when the energy gap was permitted spatial variations. As developed

by Abrikosov,<sup>13</sup> Gor'kov,<sup>14</sup> deGennes,<sup>15</sup> Maki,<sup>16,17</sup> Helfand and Werthamer,<sup>18-21</sup> Eilenberger<sup>22</sup> and others, it is a sophisticated nonlinear highly mathematical theory which is in very good agreement with experiment.

Despite the mathematical complexity of the theory, there is a physical approach to the magnetic behavior of type II superconductors that follows naturally from our previous discussions of surface energy. As developed by deGennes,<sup>23</sup> this approach considers a specific domained structure - a vortex of circulating superconducting electrons around a normal state core. In the following sections we will follow this approach, and will later make contact with the exact mathematical results of Maki,<sup>17</sup> Helfand and Werthamer<sup>18-19</sup> and Eilenberger.<sup>22</sup>

The laminellar domains<sup>24</sup> of the intermediate state are clearly not the only configuration appropriate to a domained structure. Again the task is to lower the magnetic energy while doing minimum damage to the condensation energy. Let us consider a normal core of radius  $\xi^*$ , with a field dropping off from its maximum value at the center as in Fig. 6. To proceed further we require a generalization of the London equations to take into account the normal core, and the circulation electrons about that core.

The usual form of London's equation [Eq. (4)], when combined with the Maxwell Equation  $\nabla \times H = 4\pi J/c$ , can be written as

$$\nabla \times v = - \frac{q}{mc} H \quad , \quad (11)$$

where  $v$ ,  $q$ , and  $m$  are the velocity, charge and mass of the superconducting fluid ( $J = nqv$ ). If we write  $P = mv + (q/c)A$ , where  $P$  is the quantum mechanical momentum, we can write Eq. (11) as

$$\nabla \times P = 0 \quad . \quad (12)$$

However, from the presence of the normal core and the electron circulation, we know that Eq. (12) cannot hold everywhere. A suitable generalization of Eq. (12) is

$$\nabla \times P = \frac{q}{c} \Phi \delta(r) \quad , \quad (13)$$

where  $\delta(r)$  is a two-dimensional  $\delta$  function and  $\Phi$  is the flux in the core. Consideration of the circulation  $\oint P \cdot dS$  about the core suggests  $\Phi$  to be quantized in units of  $hc/2e$  ( $q = 2e$ ), where  $\Phi_0 = (hc/2e) (= 2 \times 10^{-7} \text{ G}\cdot\text{cm}^2)$  is the unit of flux quantization. From Maxwell's Equations and Eq. (2) we obtain as a generalization<sup>25</sup> of Eq. (4)

$$\lambda_L^2 \nabla \times (\nabla \times H) + H = \Phi_0 \delta(r) \quad . \quad (14)$$

Using cylindrical symmetry, a solution of Eq. (14) for  $\xi^* < r < \lambda_L$  is

$$H = \frac{\Phi_0}{2\pi\lambda^2} \log \frac{\lambda_L}{r} \quad . \quad (15)$$

We next calculate the magnetic and kinetic energy,  $F$ , of the vortex, per unit length of vortex [the core energy  $(H_c^2/8\pi) \pi \xi^{*2}$  can be shown to be less than 12% of the magnetic and kinetic energy]

$$F = \int da \left( \frac{H^2}{8\pi} + \frac{1}{2} nmv^2 \right) = \int da \left( \frac{H^2 + \lambda^2 (\nabla \times H)^2}{8\pi} \right) \quad . \quad (16)$$

Using the vector identity,

$$\nabla \cdot [\mathbf{H} \times (\nabla \times \mathbf{H})] = (\nabla \times \mathbf{H})^2 - \mathbf{H} \cdot [\nabla \times (\nabla \times \mathbf{H})]$$

and Eq. (14) we obtain

$$F = \frac{\lambda_L^2}{8\pi} \int_{r=\xi^*} ds \mathbf{H} \times (\nabla \times \mathbf{H}) = \left( \frac{\varphi_0}{4\pi \lambda_L} \right)^2 \log \frac{\lambda_L}{\xi^*} \quad (17)$$

Noting that the flux density  $B$  is given by  $n\varphi_0$ , and neglecting the interaction between vortices, we have for the total free energy

$$nF = B \frac{\varphi_0}{(4\pi \lambda_L)^2} \log \frac{\lambda_L}{\xi^*} \quad (18)$$

at equilibrium

$$H_0 = 4\pi n \frac{\partial F}{\partial B} = \frac{\varphi_0}{4\pi \lambda_L^2} \log \frac{\lambda_L}{\xi^*}$$

Thus vortices will penetrate at  $H_0 = H_{c1}$  where

$$H_{c1} = \frac{\varphi_0}{4\pi \lambda_L^2} \log \frac{\lambda_L}{\xi^*} \quad (19)$$

We will find that the condition for  $H_{c1} < H_c$  will be related to the previous negative surface energy requirement  $\xi^* < \lambda_L$ . We can further estimate the transition field where  $M = 0$ , ( $H_{c2}$ ) as that field ( $B \approx H$ ) where the vortices overlap. Thus

$$H_{c2} \approx B \approx \frac{\varphi_0}{4\pi \xi^{*2}} \quad (20)$$

The next step is to relate the fields  $H_{c1}$  and  $H_{c2}$  to  $H_c$ . In the G-L equations a parameter  $\kappa$  is introduced such that, as suggested previously,  $\xi^* = \lambda/\sqrt{2\kappa}$ . Furthermore

$$\kappa = \lim_{T \rightarrow T_c} \frac{2\sqrt{2\pi} \lambda^2 H_c}{\varphi_0} \quad (21)$$

If we ignore the restriction to temperatures close to  $T_c$  (and consider local superconductors where  $\lambda \approx \lambda_L$ ) we can rewrite Eqs. (19) and (20) as

$$H_{c1} = \frac{H_c}{\sqrt{2\kappa}} (\ln \kappa + 0.3) \quad (22)$$

and

$$H_{c2} = \sqrt{2\kappa} H_c \quad (23)$$

Thus if  $\kappa > 1/2$ ,  $H_{c1} < H_c$  and  $H_{c2} > H_c$ , and we expect the superconductor to make a gradual magnetic transition from the state where  $B = 0$  (Meissner state) at  $H_{c1}$  to the normal state at  $H_{c2}$  where a second order transition occurs. Materials for which  $\kappa > 1/2$  are called type II superconductors and the region between  $H_{c1}$  and  $H_{c2}$  where



vortices penetrate is called the mixed state. Figures 7 and 8 show the magnetization, free energy and phase diagram of this state.

The resemblances to the gross features of the intermediate state are obvious, however it must be emphasized that there are fundamental differences. The intermediate state is only macroscopically second order; the last superconducting domain vanishes discontinuously at  $H_1$ . However, the mixed state is microscopically second order at  $H_{c2}$ . In the intermediate state one expects supercooling, i.e., a lowering of the field until the volume free energy can overcome the positive surface energy. In the mixed state there can be no supercooling due to the negative surface energy. Indeed, in the original work of Ginsburg-Landau,  $H_{c2}$  ( $\sqrt{2}\kappa < 1$ ) is defined as the minimum field to which one can supercool a type I superconductor. As we shall see, this is only true for certain field orientations.

It is interesting to note that the vortex approach described here led Tinkham to consider the question of what happens to thin disks of type I superconductors in a perpendicular field. For example, for low  $\kappa$ ,  $\Delta \approx \xi^*$  and, given Eq. (9), one expects  $H_1$  to approach zero as  $d \approx \xi^*$ . Tinkham,<sup>26</sup> from energy consideration, suggested that a vortex state at  $H_1 = \sqrt{2}\kappa H_c$  might be energetically favorable and replace the intermediate state. The transition field  $H_1$  has been observed for lead,<sup>27</sup> tin,<sup>28</sup> and indium.<sup>28</sup> Figure 9 shows experimental data for lead films. In this figure the rise in  $H_1$  for low thicknesses is related to a thickness dependence of  $\kappa$ . However, the bulk value of  $\kappa$  ( $< 1/\sqrt{2}$ ) can be obtained by extrapolation. This technique can be used instead of supercooling for the determination of  $\kappa$  in type I material.

#### EXACT THEORIES OF THE MIXED STATE

The picture of the type II superconductor is physically that of the reduction of magnetization due to the penetration of vortices with normal cores. The exact calculations of the Gor'kov equation leads to the following expressions for  $H_{c1}(T)$ ,  $H_{c2}(T)$  and the slope of the magnetization curve close to  $H_{c2}$ :<sup>17</sup>

$$H_{c1}(T) = \frac{H_c(T)}{\sqrt{2}\kappa_3(T)} \ln \kappa_3(T) \quad , \quad (24)$$

$$H_{c2}(T) = \sqrt{2}\kappa_1(T) H_c(T) \quad , \quad (25)$$

$$\left( \frac{\partial M}{\partial H} \right)_{H_{c2}} = - \frac{1}{(1.16)} \left( \frac{1}{4\pi} \right) \frac{1}{(2\kappa_2^2 - 1)} \quad , \quad (26)$$

where  $\kappa_1(T)$ ,  $\kappa_2(T)$ , and  $\kappa_3(T)$  approach  $\kappa$  as  $T \rightarrow T_c$  and<sup>29,30</sup>

$$\kappa \approx 0.96 \frac{\lambda_L}{\xi_0} + 0.7 \frac{\lambda_L}{\ell} \quad (27)$$

$$= 0.96 \frac{\lambda_L}{\xi_0} + 7.53 \times 10^3 \rho_0 \gamma^{\frac{1}{2}} \quad . \quad (28)$$

In Eq. (27)  $\ell$  is the mean free path, and in Eq. (28)  $\rho_0$  is the residual resistivity ( $\Omega \cdot \text{cm}$ ) and  $\gamma$  ( $\text{erg/cm}^3 \text{ } ^\circ\text{K}^2$ ) is the coefficient of the linear term in the electronic specific heat. It should be emphasized that Eqs. (24)-(28) take band structure effects into account only in terms of a one-band effective mass model. In this sense they are restricted in the same sense as BCS. However, the two terms for  $\kappa$  permit

one to define an intrinsic type II superconductor ( $\ell \gg \xi_0$ ) and an extrinsic type II superconductor ( $\ell \ll \xi_0$ ). This classification coincides with the distinction between "clean" and "dirty" superconductors, and hence one expects poorer agreement with theory for clean materials where anisotropy and multiple band effects have not been washed out by scattering.

Equations (27) and (28) permit one to give a more precise definition of  $\xi^*$ . Using the BCS results that, for  $T \rightarrow T_c$

$$\lambda \rightarrow \frac{\lambda_1}{\sqrt{2}} (1 - t)^{-\frac{1}{2}} \left( \frac{\xi_0}{\xi} \right)^{\frac{1}{2}}, \quad (29)$$

where

$$\frac{1}{\xi} = \frac{1}{\xi_0} + \frac{0.7}{\ell}, \quad (30)$$

we obtain

$$\xi^* \approx \frac{\xi_0}{\sqrt{2}} (1 - t)^{-\frac{1}{2}}, \quad (31a)$$

$$\xi^* \approx \frac{(\xi_0 \ell)^{\frac{1}{2}}}{\sqrt{2}} (1 - t)^{-\frac{1}{2}}, \quad (31b)$$

in the clean and dirty limit, respectively. From Eq. (31b) one notes that for impure metals  $\xi^* \approx (\xi_0 \ell)^{\frac{1}{2}} \approx (v_F \ell)^{\frac{1}{2}}$  and is related to a diffusion length.<sup>15</sup>

The original theory of G-L and Abrikosov was confined to temperatures close to  $T_c$ , where the order parameter was small and the free energy expansion might be expected to be valid. However, the order parameter is also small close to  $H_{c2}$ , and one might expect the theory to have a wider range of validity. Calculations of Gor'kov,<sup>14</sup> Maki,<sup>16,17</sup> Helfand and Werthamer,<sup>18-21</sup> and Eilenberger,<sup>22</sup> have shown that the temperature dependence of either  $\kappa_1(T)$ ,  $\kappa_2(T)$  or  $\kappa_3(T)$  is quite weak, and is of the order of 20% from 0 to  $T_c$  for extrinsic type II superconductors. However, this result is correct only for low  $\kappa$  material. The general temperature and impurity dependence of  $\kappa_1(T)$  and  $\kappa_2(T)$  is quite complicated, and an additional physical mechanism, the magnetic nature of the normal state has to be included before it can be discussed.

#### PARAMAGNETIC AND IMPURITY EFFECTS ON $H_{c2}$

Up to the present we have neglected the magnetic properties of the normal state. For transition metals such as Nb, or intermetallic compounds such as Nb<sub>3</sub>Sn, V<sub>3</sub>Si or V<sub>3</sub>Ga the paramagnetic susceptibility,  $\chi$ , is of the order of  $20 \times 10^{-6}$ , with about equal orbital and spin contributions.<sup>31</sup> For a BCS superconductor the ground state consists of pairs of electrons with opposite spins, and hence the spin susceptibility is zero in the superconducting state. The unequal assignment of spin magnetic energy between the normal and superconducting states is the additional factor that has to be included to account in detail for the high field behavior of type II superconductors.

In the original suggestion of Clogston<sup>32</sup> and Chandrasekhar<sup>33</sup> the paramagnetic limiting field  $H_p$  was obtained by equating the magnetic energy of the normal state to the condensation energy, i.e.,

$$\frac{1}{2} \chi_N H_P^2 = \frac{H_c^2}{8\pi}. \quad (32)$$

Using  $\chi_N = N\mu^2$ , and the BCS relations  $H_{c2}^2/8\pi = N\Delta^2/4$ ,  $2\Delta = 3.5 kT_c$ , we obtain

$$H_P = 18.4 \times 10^3 T_c \quad (33)$$

In these papers the prediction was made that  $H_{c2}$  could not exceed  $H_P$ . A slightly more realistic calculation (although still incorrect) utilizes Fig. 10 to calculate the effect of normal state spin paramagnetism.

If we ignore spin contributions in the superconducting state we have for the magnetization  $M = \chi_S(H - H_{c2}^*)$ , where  $\chi_S \approx 1/8\pi\mu^2$  and therefore:

$$g_s(H) = g_n^0(H_{c2}^*) - \chi_S \frac{(H - H_{c2}^*)^2}{2} \quad (34)$$

In Eq. (34)  $g_n^0(H_{c2}^*)$  is the normal state free energy without the spin paramagnetism,  $\chi_N H$ . The quantity  $H_{c2}^*$  is the upper critical field in the absence of the paramagnetic limitation. If we include the spin paramagnetism in the normal state we have

$$g_n(H) = g_n^0(H_{c2}^*) - \frac{\chi_N H^2}{2} \quad (35)$$

Equating Eqs. (35 and (34) at the transition field  $H_{c2}$ , we obtain

$$\frac{H_{c2}^* - H_{c2}}{H_{c2}} = \left( \frac{\chi_N}{\chi_S} \right)^{1/2} = \frac{\sqrt{2}\kappa}{H_P} H_c = \frac{H_{c2}^*}{H_P} \quad (36)$$

where we have utilized Eq. (32). For a superconductor where  $H_{c2}^* > 100$  kG,  $T_c \approx 10^\circ K$ , we estimate  $(H_{c2}/H_{c2}^*) \approx 0.6$ . Figure 11 shows the magnetization curve resulting from the above treatment and one notes the first order transition to the paramagnetic normal state at  $H_{c2}$ .

There are two objections to the above treatment. First, it is not clear how the normal cores will modify the free energy of the superconducting state. In terms of the simple vortex model, the essentially normal material of the core will have a tendency to lower the superconducting free energy, and lead to a magnetization that approaches that of the normal state at  $H_{c2}$ . Figure 12 shows the expected free energy curve and magnetization. One notes that the transition is second order, and that  $M$  crosses the  $H$  axis at a field where  $g_s(H, T)$  has a maximum. Despite the change in the order of the transition, the magnitude of  $H_{c2}$  is not very different from the simple relation Eq. (36). A second more significant effect arises from the fact that in highly disordered alloys there may be appreciable spin scattering in the superconducting state leading to a depairing of the spins in the superconducting state. This last effect, which is the dominant one, leads to a reduction of the paramagnetic effect on  $H_{c2}^*$  due to an equalization of the spin paramagnetism in the normal and superconducting states.

The parameter to measure the effect of spin-orbit scattering can be estimated by comparing the energy uncertainty introduced by such scattering with the energy gap. If  $\tau_{so}$  is the spin-orbit scattering time, from the uncertainty principle one expects depairing effects to be large when  $[\hbar/\tau_{so}(3.5 kT_c)] \geq 1$ . The exact theories<sup>17,19</sup> to be discussed introduce two parameters to describe scattering effects:

$$\lambda_{so} \equiv (\hbar/3\pi kT_c \tau_{so}) \quad (37)$$

$$\lambda \equiv (\hbar/2\pi kT_c \tau) \quad (38)$$

where  $\tau_{so}$  is the spin-orbit scattering time, and  $\tau$  is the spin independent scattering time. In the work of Maki<sup>17</sup> and of Helfand, Werthamer, and Hohenberg,<sup>18,19</sup>  $\tau$  is identified with the transport scattering time. As suggested by Eq. (36), the basic parameter of the paramagnetic effect is

$$\alpha \equiv [\sqrt{2} H_{c2}^*(0)/H_p] \quad (39)$$

and Maki<sup>17</sup> introduces a mixed parameter  $\beta_0$  to characterize the paramagnetic effect, and its reduction by spin orbit scattering,

$$\beta_0^2 \equiv \frac{\alpha^2}{1.78 \lambda_{so}} \quad (40)$$

To summarize the discussion to the present, we note that the results of the GLAG theory, Eqs. (24)-(28), are only exactly valid near  $T_c$ . Close to  $H_{c2}$ , at lower temperatures and when spin paramagnetism can be neglected, Eqs. (24)-(28) retain approximate validity, and departures from the exact theory will be measured by the parameter  $\lambda$  [Eq. (38)]. For high  $\kappa$  dirty materials the parameters  $\alpha$  [Eq. (39)],  $\lambda_{so}$  [Eq. (37)], and  $\beta_0$  [Eq. (40)], determine the upper critical field and its temperature dependence.

Before we discuss the formal theories and their comparison with experiment it will be helpful to make three general observations about experimental results. First, it is important to note that in all of the theories, paramagnetic effects vanish at  $T_c$ . Physically, this arises because close to  $T_c$  quasi-particle excitations dominate the superconductor, and hence the mixed state is depaired. Thus if we use the notation:

$$H_{c2}(\alpha, \lambda, \lambda_{so}, T) \equiv H_{c2}(T)$$

$$H_{c2}(0, \lambda, \lambda_{so}, T) \equiv H_{c2}^*(T)$$

we obtain

$$\left( \frac{dH_{c2}}{dT} \right)_{T_c} = \left( \frac{dH_{c2}^*}{dT} \right)_{T_c} = \sqrt{2\kappa} \left( \frac{dH_c}{dT} \right)_{T_c} \quad (41)$$

where  $\kappa$  is given by Eqs. (27) and (28). Second, in the dirty limit, the parameter  $\alpha$  does not have to be fit to the data, but can be obtained independently. This observation follows from the theoretical temperature dependence of  $H_{c2}^*$ , which will be discussed presently, and Eqs. (41) and (28) plus some results from BCS. In the dirty limit one obtains

$$\alpha = 2.35 \rho \gamma \quad (42a)$$

where  $\rho$  is in  $\Omega \cdot \text{cm}$  and  $\gamma$  has been defined below Eq. (28). Further algebra shows that

$$\alpha = 5.33 \times 10^{-5} \left( - \frac{dH_{c2}}{dT} \right)_{T_c} \quad (42b)$$

Hake<sup>34</sup> has presented an admirable review of the effect of spin paramagnetism on the mixed state, and this review has an appendix which lists a variety of formulae showing relationships between experimental and theoretical quantities.

The third observation is the most important and must be taken into account before any discussion of experiment. In general there are two ways of presenting experimental

data. One can use the usual relation  $H_{c2} = \sqrt{2}\kappa_1 H_c$  and show  $\kappa_1$  as a function of temperature. For greater generality it is convenient to introduce a normalized quantity

$$\kappa^*(t) \equiv \kappa^*(t, \alpha, \lambda, \lambda_{so}) \equiv \frac{\kappa_1(T, T_c, \alpha, \lambda, \lambda_{so})}{\kappa} \quad (43)$$

This mode of presentation presents two difficulties: first, it combines two quantities  $H_{c2}$  and  $H_c$ , and hence couples the mixed state with the zero field state; second, it requires the experimentalist to have data on  $H_c(T)$  for the specimen under consideration, and these data often are not available. Werthamer, Helfand and Hohenberg<sup>19</sup> suggest the use of the normalized field

$$h^* = \frac{H_{c2}(T)}{-T_c \left( \frac{dH_{c2}}{dT} \right)_{T_c}} \quad (44)$$

for comparisons between theory and experiment, and they present data on impurity effects as well as spin paramagnetic effects in terms of  $h^*$  (to be distinguished from  $H_{c2}^*$ ).

Figure 13 shows the results of the calculation of Helfand and Werthamer<sup>18</sup> for  $h^*$  as a function of  $T/T_c$  for  $\alpha = 0$ , and for two values of  $\lambda$ . Figure 14 shows the same results expressed in terms of  $\kappa^*(t)$ . One notes the weak impurity dependence of  $h^*$  and  $\kappa^*$ . However, it must be emphasized that the calculations shown in Fig. 14 are based on BCS values for  $H_c(T)$ , and the small variation in  $\kappa^*(t)$  with temperature holds only for BCS-like superconductors.

This observation can be seen more clearly if we note that

$$\begin{aligned} \kappa^*(t) &= -h^* [T_c (dH_c/dT)_{T_c} / H_c(T)] \\ \kappa^*(t) &= -h^* \varphi(T) \end{aligned} \quad (45)$$

For all superconductors, from the normalization of  $h^*$ ,  $\kappa^* \rightarrow 1.0$  as  $T \rightarrow T_c$ . However,  $\kappa^*(0)$  will depend strongly on the value of  $\varphi(0)$ . Table I shows values of  $\varphi(0)$  for Sn, Pb, V, Nb<sub>3</sub>Sn and Nb. It also shows the value of  $\varphi(0)$  predicted by BCS, and  $\kappa^*(0)$  for pure ( $\lambda = 0$ ) and dirty ( $\lambda = \infty$ ) materials.

TABLE I  
 $\kappa^*(0)$  for BCS and Non-BCS Superconductors

	<u><math>\varphi(0)</math></u>	<u><math>[\kappa^*(0)]</math> pure</u>	<u><math>[\kappa^*(0)]</math> dirty</u>
Sn	1.855	1.35	1.28
Pb	2.132	1.56	1.47
V	1.773	1.29	1.22
Nb <sub>3</sub> Sn	2.000	1.46	1.38
Nb	2.000	1.46	1.38
BCS	1.737	1.27	1.20

From Table I we see that the variation in  $\kappa^*(0)$  between different materials is much larger than the variation induced by changing from completely pure to impure materials. Clearly the simple statement that  $\kappa^*(0) > 1.27$  does not in itself constitute a departure from theory. For completeness we note that

$$H_{c2}(T) = h^* (\sqrt{2}\kappa) [-T_c (dH_c/dT)_{T_c}] \quad (45a)$$

and again any comparison between theory and experiment has to include a knowledge of  $(dH_c/dT)_{T_c}$ .

The results shown in Figs. 13 and 14 are in excellent agreement with low  $\kappa$  materials where paramagnetic limitations are inoperative, and where impurity effects dominate. There is not good agreement for clean type II superconductors such as V and Nb.<sup>35,36</sup> Figure 15 shows the departures from theory for Nb, and similar departures are seen for V. For type I material such as Sn and In,<sup>27,28</sup> where measurements have been made of the transition fields of thin films in a perpendicular field, similar departures are noted. It is interesting to note that in all cases the departure from theory is expressed by the experimentalist as a preference for the two-fluid temperature dependence of  $\kappa$  (Eq. 21), i.e.,  $\kappa = \kappa_0 [1 + (T/T_c)^2]^{-1}$ . For V, Nb and Sn use of the theory leads to  $h^*(0) = 0.85, 0.83$  and  $0.85$ , respectively, whereas the maximum value of Fig. 13 is about  $0.72$ . The discrepancy ( $\approx 20\%$ ), although small, is well outside experimental and theoretical uncertainty. It cannot be accounted for on the basis of strong coupling effects, and according to Hohenberg and Werthamer<sup>21</sup> may arise from Fermi surface anisotropy effects. Before we leave the area of nonparamagnetically limited type II superconductors, it is of interest to point out the extensive numerical calculations of Eilenberger<sup>22</sup> for  $\kappa_1$  and  $\kappa_2$  as a function of purity including both S-S and S-P scattering.

Although the small departures from theory for clean type II superconductors are sufficiently large to bother theoreticians and experimentalists, the paramagnetically limited alloys (i.e. the dirty limit) appear to be well understood. Figure 16 shows the comparison between  $h^*$  for Ti(0.56)Nb(0.44) and the predictions of the theory of Werthamer, Helfand, and Hohenbert.<sup>19</sup> In fitting the data,  $\alpha$  is fixed by Eqs. (42) and  $\lambda_{so}$  is chosen as a free parameter. The fit is excellent.

Maki<sup>17</sup> has expressed his results in terms of  $\kappa_1/\kappa$  and  $\kappa_2/\kappa$  as a function of  $t$  and  $\beta_0$  as shown in Figs. 17 and 18, and one notes the depression of  $\kappa_2(T)$  as well as  $\kappa_1(T)$  below  $\kappa$  where the paramagnetic effect is operative. In this connection it is important to note that  $\kappa_2(T)$  is defined by  $-4\pi(M_s - M_n) = (H_{c2} - H)/[2\kappa_2^2(T) - 1](1.16)]$ . Figure 19 shows a comparison between the Maki theory for  $\kappa_2(T)$  and the experimental results of Hake.<sup>34</sup> The agreement appears satisfactory. Figure 20 is an impressive example of the effect of spin paramagnetism from the work of Hake,<sup>34</sup> where the free energy as well as the magnetization is plotted as a function of field for a Ti16%Mo alloy with an  $H_{c2}^*$  of about 100 kG, paramagnetically reduced to about 40 kG.

Figure 21 from the paper of Hake shows a comparison of the Werthamer, Helfand, and Hohenberg<sup>19</sup> (WHH) computer solutions for  $h^*$  ( $t = 0$ ) as a function of  $\alpha$  and  $\lambda_{so}$ , compared to the analytic approximate form derived by Maki. The Maki<sup>17</sup> expression, corrected from the original paper, as quoted by Hake, is

$$h^*(t) = 1.39 h_{c2} [1 + (1 + \beta_0^2 h_{c2}^2)^{\frac{1}{2}}]^{-1}, \quad (46)$$

where  $\beta_0$  is given by Eq. (4) and  $h_{c2} = H_{c2}^*(t)/H_{c2}^*(0)$ . A condition to be met for both theories is that the spin flip scattering time  $\tau_{so}$  be large compared to the transport scattering time  $\tau$ ; a condition which is physically realizable in high  $\kappa$  transition metal alloys. As shown in the paper of Hake, one can get about equally good fits to

either the Maki or WHH theory within the experimental uncertainties.

Finally, it is important to note that for  $\lambda_{so} \rightarrow \infty$ , there is no paramagnetic limitation of  $H_{c2}$ , and  $H_{c2} \rightarrow H_{c2}^*$ . Since  $\lambda_{so} \propto (Z^4)$ , where  $Z$  is the average atomic number, one might expect high  $Z$  alloys to have less paramagnetic limitations and hence achieve the upper critical field predicted from Eq. (28).

## CRITICAL FIELDS OF INTERMETALLIC COMPOUNDS

From the previous discussion it is apparent that dirty type II superconductors (extrinsic) are in excellent agreement with theory for both the paramagnetically limited and nonparamagnetically limited regime. Clean (intrinsic) type II superconductors exhibit characteristic departures from theory at low temperatures. Intrinsic high  $\kappa$  materials (if they exist) have yet to be critically examined in the paramagnetic regime, although the theory exists. The departure from theory for low  $\kappa$  materials has been ascribed to band structure and anisotropy effects, but no quantitative calculations have been made.

It is an interesting question whether similar departures from theory might be expected for the intermetallic compounds  $Nb_3Sn$ ,  $V_3Si$  and  $V_3Ga$ . These materials show significant departures from "normal-metal" behavior<sup>31</sup> above  $T_c$ , and there has been little success in correlating their superconducting behavior with existing free electron theories. One is inclined to believe that these materials exhibit band anisotropy and strong coupling, but they present experimental difficulties for both sample characterization and experiment. They are difficult to prepare in single crystal form, and the high critical fields and transition temperatures make it difficult to extract such parameters as the residual resistivity and electronic specific heat.

Table II gives data for  $(dH_{c2}/dT)_{T_c}$ ,  $(dH_c/dT)_{T_c}$ ,  $\gamma$ ,  $\rho$  and  $\kappa$  for  $Nb_3Sn$ ,  $V_3Si$  and  $V_3Ga$ , as well as a calculation of  $\kappa_\ell$  ( $\kappa_\ell = 0.7 \lambda_L/\ell$ ). Unfortunately, except in the case of  $Nb_3Sn$ , the  $H_{c2}$  data do not necessarily refer to the same specimen for which the  $\rho$  is given. Moreover, resistivity data on sintered specimens are often overestimated due to the problems of porosity. From the Table one notes that  $Nb_3Sn$  and  $V_3Si$  are intrinsic ( $\kappa > 2\kappa_\ell$ ). However, the apparent insensitivity of  $(dH_{c2}/dT)_{T_c}$  to sample preparation for  $Nb_3Sn$ ,  $V_3Si$  and  $V_3Ga$  suggests that all are intrinsic and more so than

TABLE II  
Parameters of Type II Intermetallic Compounds

	$T_c$	$\rho$	$\gamma$	$(dH_{c2}/dT)_{T_c}$	$(dH_c/dT)_{T_c}$	$\kappa^b)$	$\kappa_\ell^a)$
	(°K)	( $10^{-5} \Omega \cdot \text{cm}$ )	( $10^4 \text{ erg/cm}^3 \text{ } ^\circ\text{K}$ )	( $\text{kG}/^\circ\text{K}$ )	( $\text{G}/^\circ\text{K}$ )		
$Nb_3Sn$	18	$1.0^{31}$	$1.18^{37}$	$-18.0^{37}$	$-590^{37}$	$22^{37}$	8.2
$V_3Si$	17	$0.4^{39}$	$2.4^c)$	$-19.0^{41}$	$-720^{40}$	19	5.0
$V_3Ga$	16	$4.0^{38}$	$2.7^c)$	$-45.0^{41}$	$-870^{42}$	37	<49.0

a) Eq. (28).

b) Eq. (25) at  $T_c$ .

c) Best values derived by L. Vieland from Ref. 40 and Ref. 42.

is suggested by the calculation of  $\kappa_L$  from Eq. (28). For example, doubling the resistivity of Nb<sub>3</sub>Sn has no measurable effect on the slope  $(dH_{c2}/dT)_{T_c}$ .<sup>43</sup> Another example is the invariance of  $dH_{c2}/dT$  under large changes in stoichiometry for V<sub>3</sub>Ga.<sup>41</sup> Furthermore, both V<sub>3</sub>Si and Nb<sub>3</sub>Sn (and perhaps V<sub>3</sub>Ga) exhibit specific heat anomalies at low temperatures that cast some doubt on the quoted  $\gamma$ 's. Since this Table includes two materials of practical interest, and three of great theoretical interest, it is of some importance to obtain critical field data on well characterized specimens.

Before leaving the intermetallic compounds, it may be of value to consider two-band effects. Roger Cohen of our laboratory has made some preliminary calculations of the dependence of  $\kappa$  on the material properties of a two-band system with two energy gaps (e.g., an s gap and a d gap). Similar calculations have been made by Tilley<sup>44</sup> and Moskalenkov.<sup>45</sup> Cohen expresses his results as a function of  $N_i$ , the density of states in the  $i$ th band ( $i = 1, 2$ );  $v_{Fi}$ , the Fermi velocity;  $T_c$ ; and the energy gap,  $\Delta$ . A basic parameter is the quantity  $r$ , where near  $T_c$

$$\Delta_1^2 / \Delta_{BCS}^2 = [1 + (N_2/N_1)r^2] / [1 + (N_2/N_1)r^4] \quad (47)$$

$$\Delta_2^2 = r^2 \Delta_1^2 \quad (48)$$

and  $\Delta_{BCS} = \Delta_{BCS}(T)$ , and  $\Delta_{BCS}(0) = 3.5 kT_c$ . The result for  $\kappa$  in the clean limit is

$$\kappa = \kappa_{01}^2 \frac{[1 + (v_{F1}^2/v_{F2}^2)r^2]}{[1 + (N_2 v_{F2}^2/N_1 v_{F1}^2)r^2]} \quad (49)$$

where

$$\kappa_{01}^2 = \left( \frac{9\pi}{7\xi(3)} \right) \left( \frac{ckT_c}{\hbar e} \right) \left( \frac{1}{N_1 v_{F1}^4} \right) = \left( \frac{0.96 \lambda_{L1}}{\xi_{01}} \right) \quad (50)$$

Figure 22 shows an approximately self-consistent variation of  $\kappa$  with  $r$  for Nb<sub>3</sub>Sn as a function of various d-band Fermi velocities. The curves are based upon paramagnetic susceptibility, Hall data, specific heat data for Nb<sub>3</sub>Sn. Unfortunately, it is not possible to fit all the existing data, in particular  $\lambda$  and  $\kappa$ , with this model. It is clear that more data are required to satisfactorily understand  $\beta$ -W intermetallic compounds.

## SURFACE SUPERCONDUCTIVITY

Up to now, we have not touched upon the third critical field,  $H_{c3}$ . This field arises from a peculiar boundary condition of the G-L equations for a field parallel to the surface. Under these conditions a superconducting sheath of thickness  $\approx \xi^*$  can exist up to a field  $H_{c3} = 1.695 H_{c2}$  (Fig. 23). Furthermore, for type I superconductors  $H_{c3}$  is the supercooling field. There is good experimental agreement with the ratio  $H_{c3}/H_{c2}$  when there is proper control of the surface. Calculations by Eilenberger and Ambegaokar<sup>46</sup> in the strong-coupling limit for pure superconductors close to  $T_c$  show that the ratio is maintained. Recent calculations of Lüders<sup>47</sup> for clean superconductors suggest that  $H_{c3}/H_{c2}$  at low temperatures can be as large as 2.2 due to the effect of electron reflection. Fischer<sup>48</sup> has interpreted microwave data for lead along these lines, and derived an  $H_{c2}(T)$  for Pb which is in good agreement with the calculations of Werthamer and Helfand. However, in these measurements ( $\kappa < 1/\sqrt{2}$ ,  $1.695/\sqrt{2}\kappa > 1$ )  $H_{c2}$  is not directly measurable and there is some question of interpretation. Moreover,



given the disagreement of Nb and V with the calculations of Helfand and Werthamer,<sup>18</sup> there is a question as to whether one should expect good agreement for Pb. Finnemore et al.<sup>36</sup> measured  $H_{c3}/H_{c2}$  for Nb, for samples with a residual ratio of 280 and 2000, and found  $H_{c3}/H_{c2}$  of 1.69 and 1.50 respectively. However, the transitions were broad and extended to  $H_{c3}/H_{c2}$  of 1.8 and 2.0 respectively.<sup>49</sup>

Saint-James<sup>50</sup> has derived the modification of  $H_{c3}$  when there are paramagnetic effects with the following expression at  $T = 0^\circ\text{K}$ :

$$\frac{H_{c3}(0,\alpha)}{H_{c2}(0,\alpha)} = \frac{1.695 (1 + \alpha^2)^{\frac{1}{2}}}{[1 + (1.695 \alpha)^2]^{\frac{1}{2}}} \quad (51)$$

As before, paramagnetic effects vanish close to  $T_c$ . When one includes spin orbit scattering one obtains

$$H_{c3}(T, \alpha, \lambda_{so}) = 1.69 H_{c2}(T, 1.69\alpha, \lambda_{so}) \quad (52)$$

and, as Saint-James points out, simultaneous measurement of  $H_{c2}$  and  $H_{c3}$  should permit direct determination of  $\alpha$  and  $\lambda_{so}$ . Equation (52) does not appear to have received any experimental verification. Equation (51) for  $\alpha \approx 1$  suggests  $H_{c3}(0,\alpha) \approx 1.2 H_{c2}(0,\alpha)$ , which is in fair agreement with measurements of Kim et al.<sup>51</sup>

Finally, I present some recently measured data on practical materials made by Saur and Wiggall<sup>52</sup> (Fig. 24). Table III summarizes the results as well as giving some predictions of Hake<sup>53</sup> on possible values for  $H_{c2}$  if their properties could be maintained under massive alloying to raise  $\rho$ . As noted, since I believe the intermetallic compounds are inherently intrinsic, this part of the Table should be considered with some discretion. In my own opinion the critical field of these materials is intimately related to their  $T_c$ , and poorly understood band structure and electronic interactions. It is quite possible that large enhancements in  $H_{c2}$  beyond that realized today will only follow the understanding that leads to increases in  $T_c$  above  $20^\circ\text{K}$ .

TABLE III  
Upper Critical Fields of Intermetallic Compounds

Material	$H_{c2}(0)$ (kG)	$H_{c2 \text{ max}}$ (kG) (after Hake <sup>53</sup> )
Nb <sub>3</sub> Sn	245	880
V <sub>3</sub> Si	235	850
V <sub>3</sub> Ga	210	810
NbN	153	250

#### REFERENCES

1. An excellent review of superconductivity is E.A. Lynton, Superconductivity (Methuen, London, 1964), 2nd ed.
2. Ibid., p. 27.
3. Ibid., p. 76.
4. A.B. Pippard, Proc. Camb. Phil. Soc. 47, 617 (1951); Phil. Mag. 43, 273 (1952); Phil. Trans. Roy. Soc. A248, 97 (1955).

5. P.R. Doidge, Phil. Trans. Roy. Soc. A248, 553 (1956).
6. R. Peierls, Proc. Roy. Soc. A155, 613 (1936).
7. E. Guyon, C. Caroli, and A. Martinet, J. Phys. Radium 25, 683 (1964).
8. A.B. Pippard, Proc. Roy. Soc. A216, 547 (1953); T.E. Faber and A.B. Pippard, Proc. Roy. Soc. A231, 336 (1955).
9. J. Bardeen, L.N. Cooper, and J.R. Schrieffer, Phys. Rev. 108, 1175 (1957); J. Bardeen and J.R. Schrieffer in Prog. in Low Temp. Phys., Vol. 3, C.J. Gorter, Ed. (North Holland, Amsterdam, 1961), p. 170.
10. V.L. Ginzburg and L.D. Landau, J. Expt. Theor. Phys. (U.S.S.R.) 20, 1064 (1950). An excellent review of the theory is B.B. Goodman, Reports on Progress in Physics 29, II, 445 (1966).
11. B.B. Goodman, IBM J. Research and Development 6, 631 (1962).
12. L.W. Shubnikov, W.I. Khotkevich, J.D. Shepdev, and J.N. Riabinin, J. Expt. Theor. Phys. (U.S.S.R.) 7, 221 (1937).
13. A.A. Abrikosov, J. Phys. Chem. Solids 2, 199 (1957).
14. L.P. Gor'kov, Sov. Phys. JETP 9, 1364 (1959); Sov. Phys. JETP 10, 593 (1960); Sov. Phys. JETP 10, 998 (1960).
15. P.G. deGennes, Rev. Mod. Phys. 36, 225 (1964); Phys. Kondens. Materie 3, 79 (1964).
16. K. Maki, Physics 1, 127 (1964); Physics 1, 21 (1964).
17. K. Maki, Phys. Rev. 148, 362 (1966).
18. E. Helfand and N.R. Werthamer, Phys. Rev. 147, 288 (1966).
19. N.R. Werthamer, E. Helfand, and P.C. Hohenberg, Phys. Rev. 147, 295 (1966).
20. N.R. Werthamer and W.L. McMillan, Phys. Rev. 158, 415 (1967).
21. P.C. Hohenberg and N.R. Werthamer, Phys. Rev. 153, 493 (1967).
22. G. Eilenberger, Phys. Rev. 153, 584 (1967).
23. P.G. deGennes, Unpublished Lecture Notes, Herzengnovi Summer School; P.G. deGennes and J. Matricon, Rev. Mod. Phys. 36, 45 (1964).
24. T.E. Faber, Proc. Roy. Soc. A248, 460 (1958).
25. B.B. Goodman, Reports on Progress in Physics 29, II, 445 (1966).
26. M. Tinkham, Phys. Rev. 129, 2413 (1963); Rev. Mod. Phys. 36, 268 (1964).
27. G.D. Cody and R.W. Miller, Phys. Rev. Letters 16, 697 (1966); Phys. Rev. Sept. 1968 (to be published).
28. G.K. Chang and B. Serin, Phys. Rev. 145, 274 (1966).
29. B.B. Goodman, Rev. Mod. Phys. 36, 12 (1964).
30. T.G. Berlincourt, Rev. Mod. Phys. 36, 19 (1964).
31. R.W. Cohen, G.D. Cody, and H. Halloran, Phys. Rev. Letters 19, 840 (1967).
32. A.M. Clogston, Phys. Rev. Letters 9, 266 (1962).
33. B.S. Chandrasekhar, Appl. Phys. Letters 1, 7 (1962).
34. R.R. Hake, Phys. Rev. 158, 356 (1967).
35. R. Radebaugh and P.H. Keesom, Phys. Rev. 149, 209 (1966); Phys. Rev. 149, 217 (1966).
36. D.K. Finnemore, T.F. Stromberg, and C.A. Swenson, Phys. Rev. 149, 231 (1966).

37. L.J. Vieland and A.K. Wicklund, Phys. Rev. 166, 424 (1968).
38. L.J. Montgomery and H. Wizgall, Phys. Letters 22, 48 (1966).
39. J.J. Hauser, Phys. Rev. Letters 13, 470 (1964).
40. J.E. Kunzler, J.P. Maita, H.J. Levinstein, and E.J. Ryder, Phys. Rev. 143, 390 (1966).
41. J.H. Wernick, F.J. Morin, F.S.L. Hsu, D. Dorsi, J.P. Maita, and J.E. Kunzler, in High Magnetic Fields, ed. Kolm, Lax, Bitter, Mills (The M.I.T. Press, 1962), p. 609.
42. F.J. Morin, J.P. Maita, H.J. Williams, R.C. Sherwood, J.H. Wernick, and J.E. Kunzler, Phys. Rev. Letters 8, 275 (1964).
43. J.L. Cooper, RCA Review 25, 405 (1964).
44. D.R. Tilley, Proc. Phys. Soc. 84, 573 (1964).
45. V.A. Moskalenkov, Sov. Phys. JETP 24, 780 (1967).
46. G. Eilenberger and V. Ambegaokar, Phys. Rev. 158, 332 (1967).
47. G. Lüders, Z. Physik 202, 8 (1967).
48. G. Fischer, Phys. Rev. Letters 20, 268 (1968).
49. For recent work on niobium, see G. Webb, Sol. State Comm. 6, 33 (1968).
50. D. Saint-James, Phys. Letters 23, 177 (1966).
51. Y.B. Kim, C.F. Hempstead, and A.R. Strnad, Phys. Rev. 139A, 1163 (1965).
52. E. Saur and H. Wizgall, in Proc. Intern. Conf. High Magnetic Fields, Grenoble, 1966, p. 223.
53. R.R. Hake, Appl. Phys. Letters 10, 189 (1967).

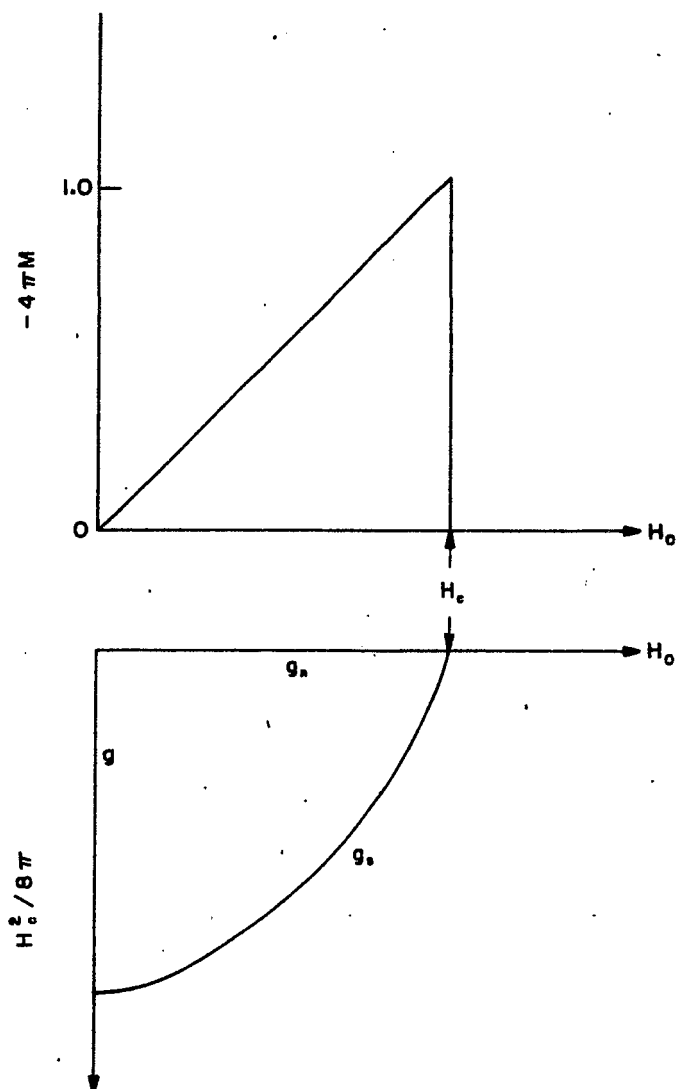


Fig. 1. Magnetization and free energy (type I).

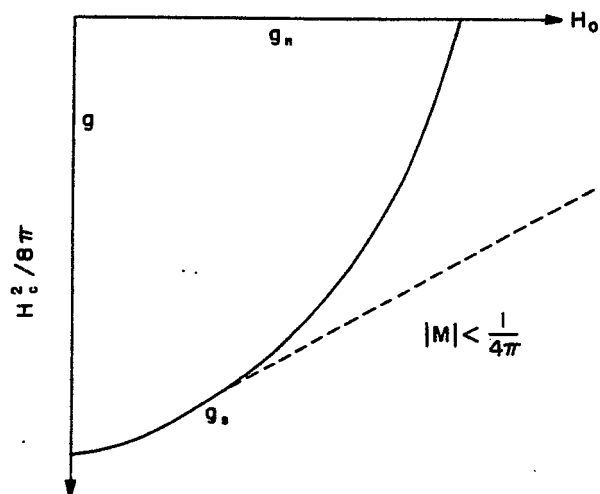


Fig. 2. Effect of reduction of magnetization on free energy.

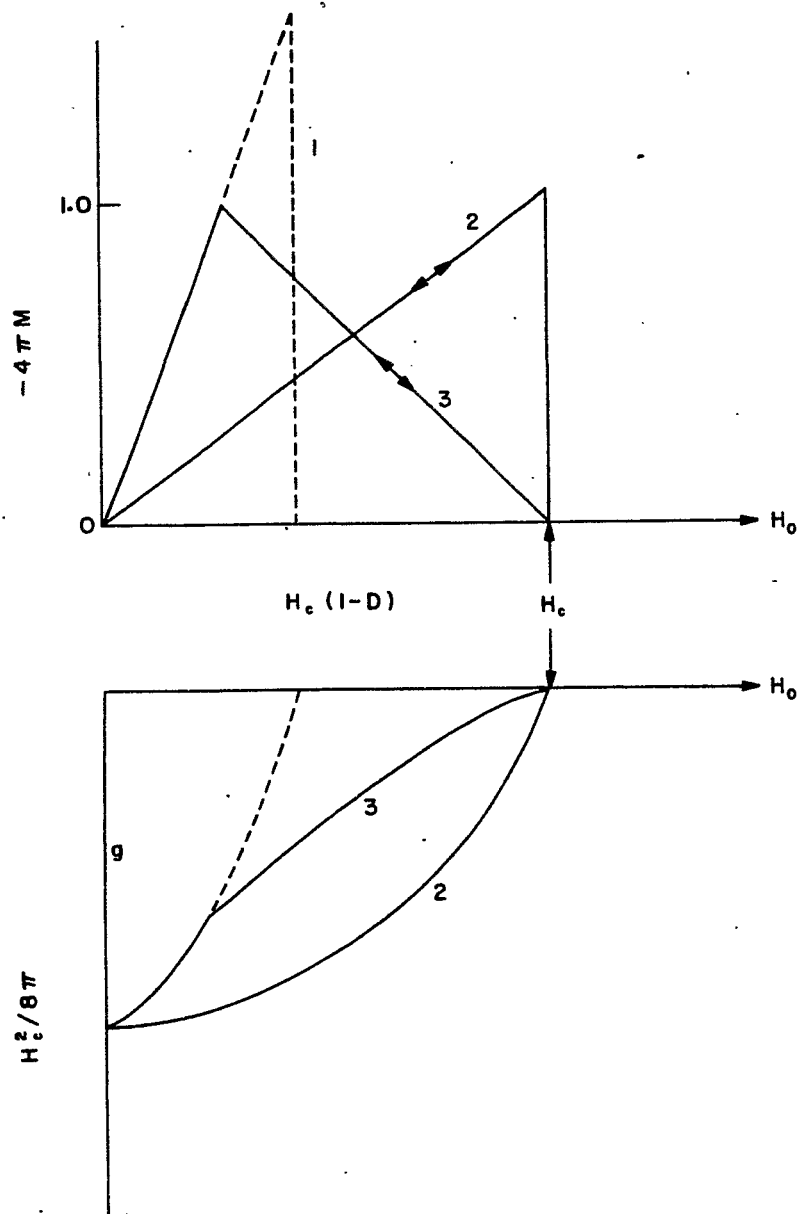


Fig. 3. Magnetization and free energy intermediate state.

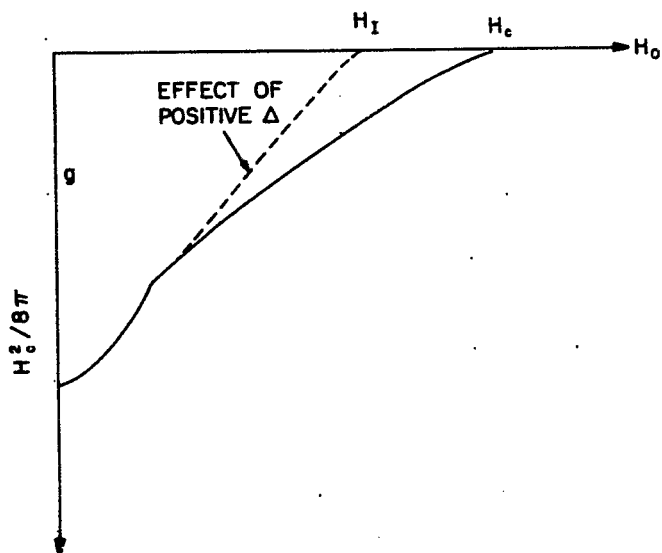


Fig. 4. Effect of positive surface energy on free energy of intermediate state.

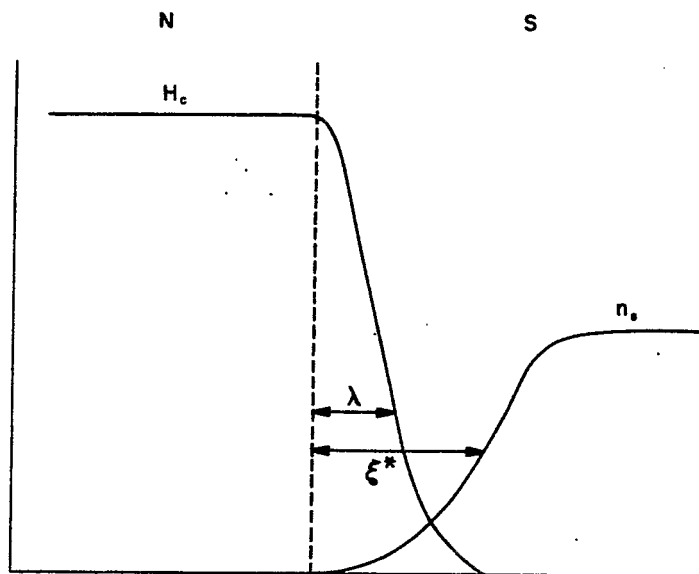


Fig. 5. Normal-superconducting boundary.

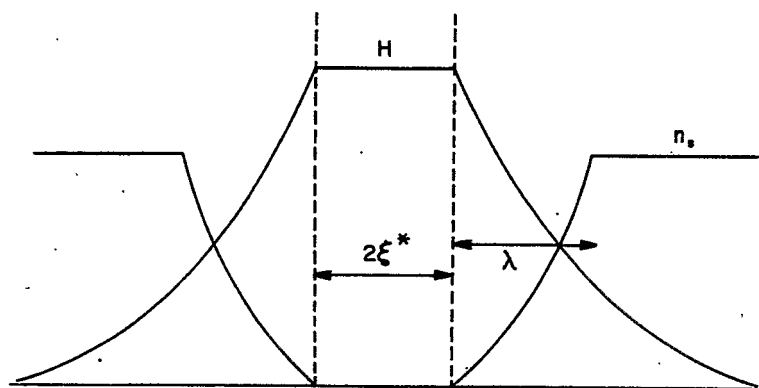


Fig. 6. Schematic of vortex structure.

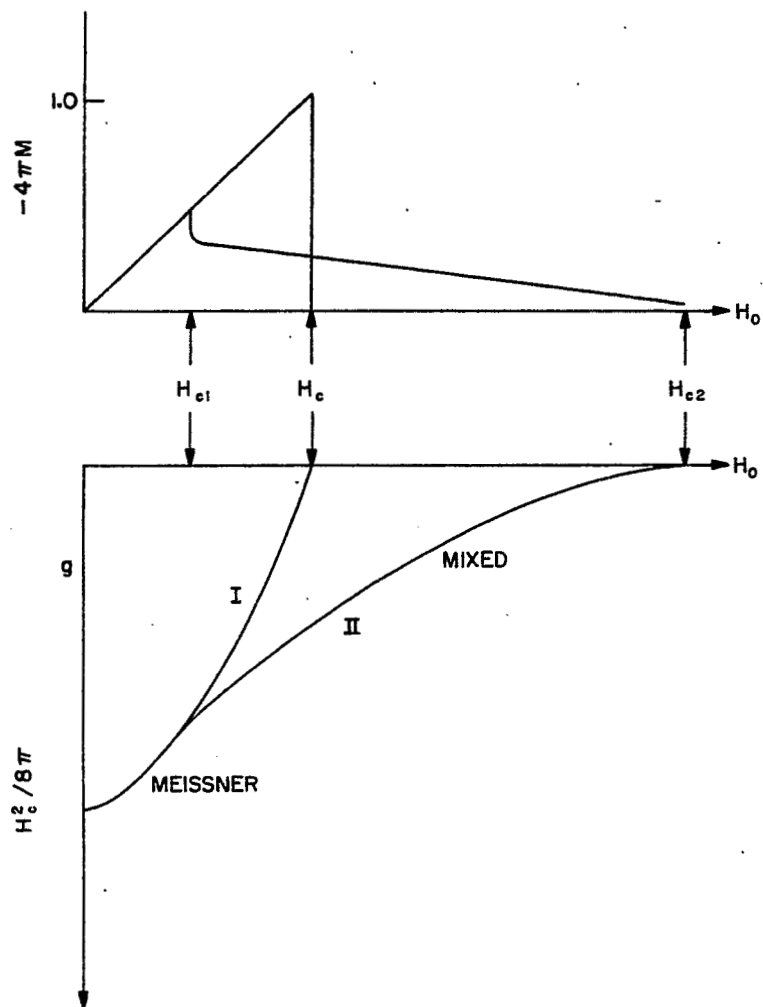


Fig. 7. Magnetization and free energy of type I and type II superconductors.

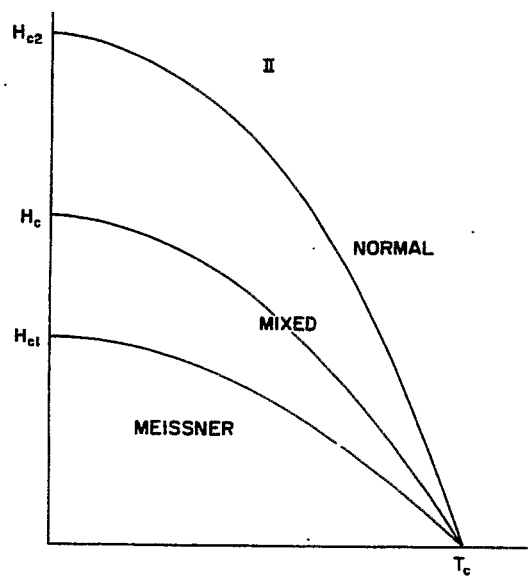
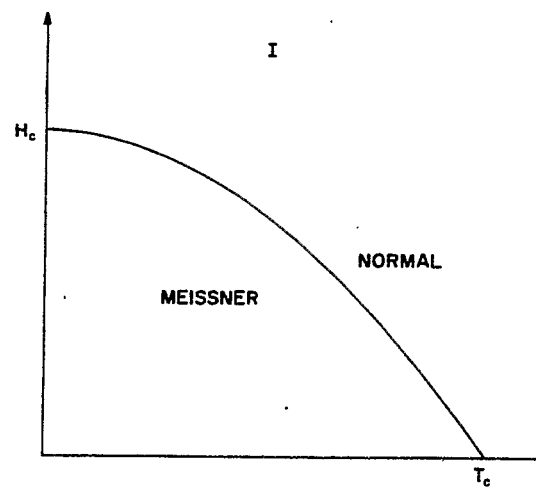


Fig. 8. Phase diagrams of type I and type II superconductors.



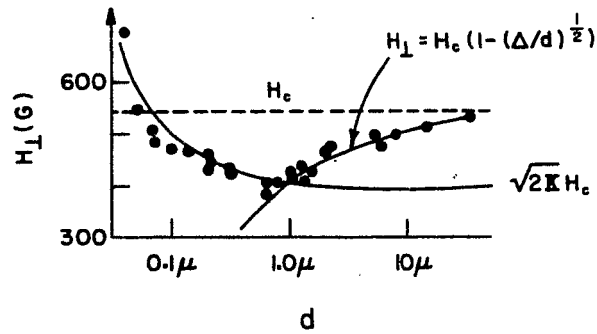


Fig. 9. Thickness dependence of perpendicular critical fields in thin Pb films and foils.

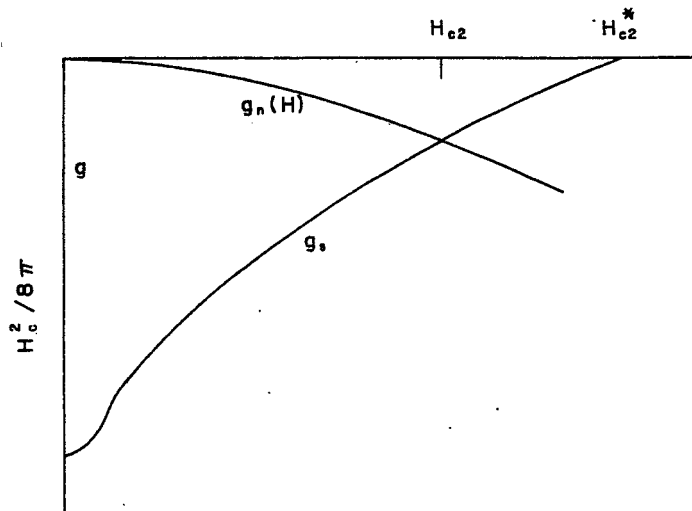


Fig. 10. Free energy, including spin energy, of normal state - first order transition.

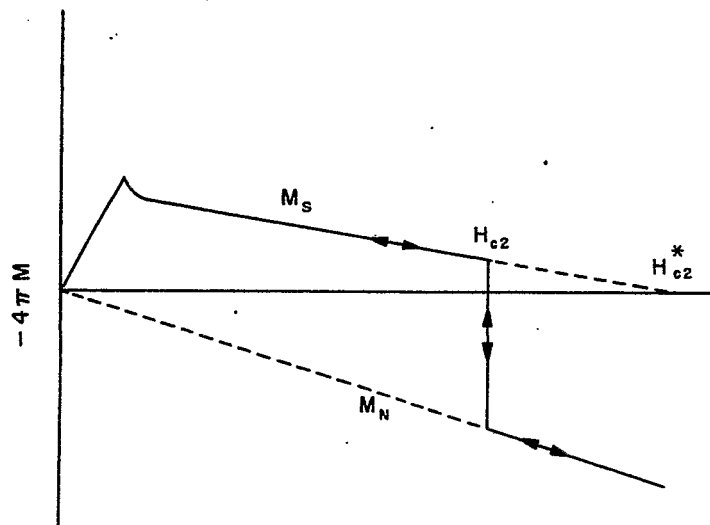


Fig. 11. Magnetization corresponding to free energy of Fig. 10 - first order transition.

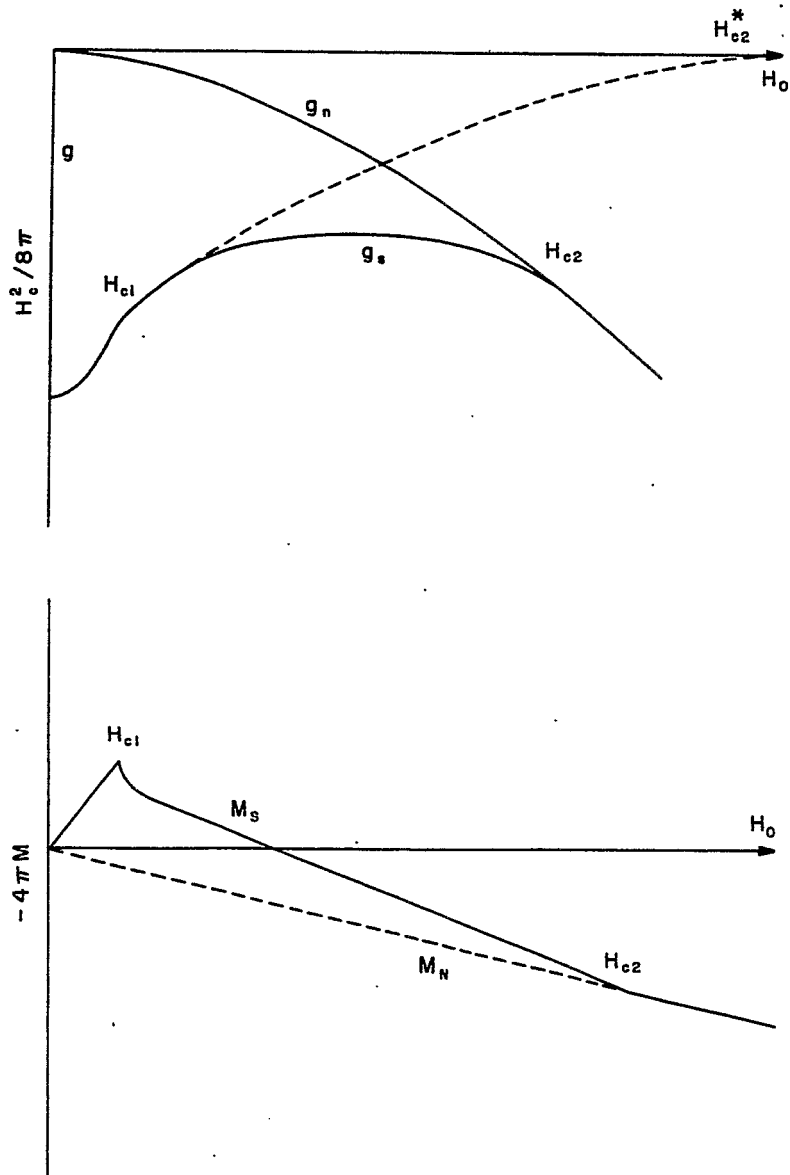


Fig. 12. Free energy and magnetization, including spin energy, of normal and superconducting states - second order transition.

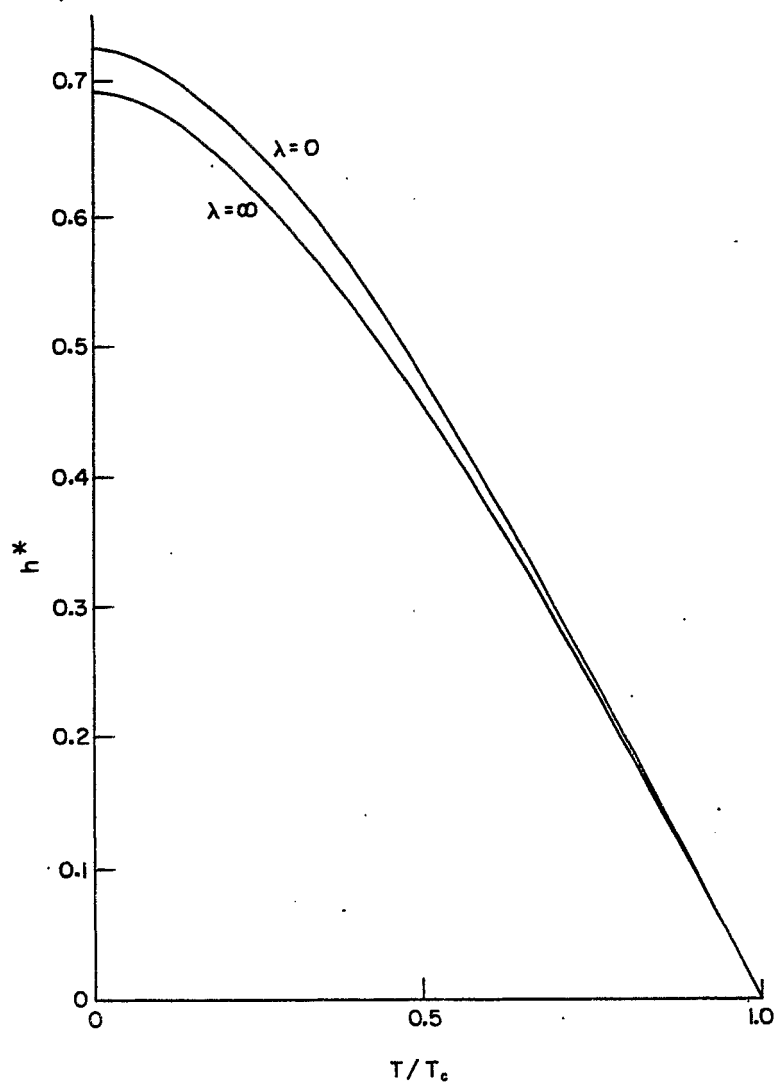


Fig. 13. Reduced field  $h^*$  as a function of  $T/T_c$ , after Ref. 18.

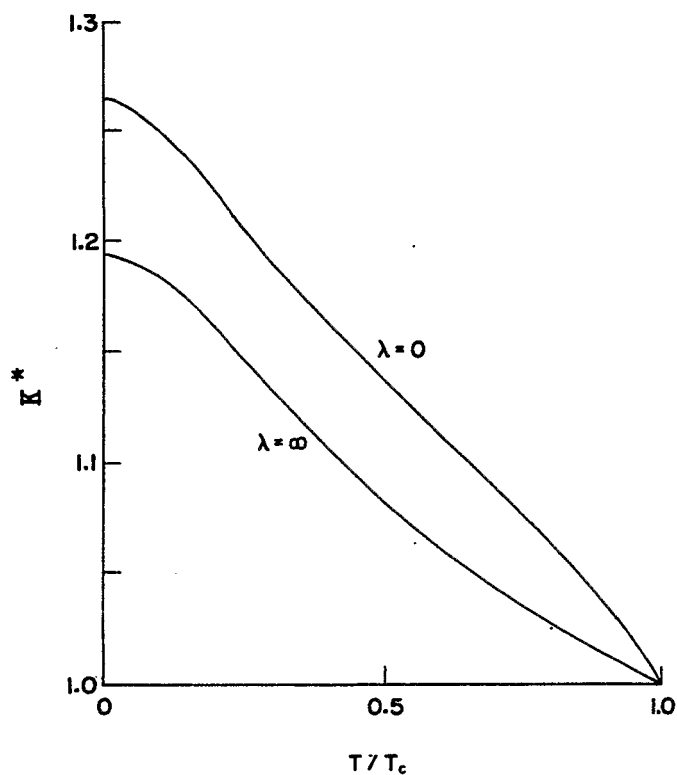


Fig. 14. Reduced parameter  $\kappa^*$  as a function of  $T/T_c$ , after Ref. 18.

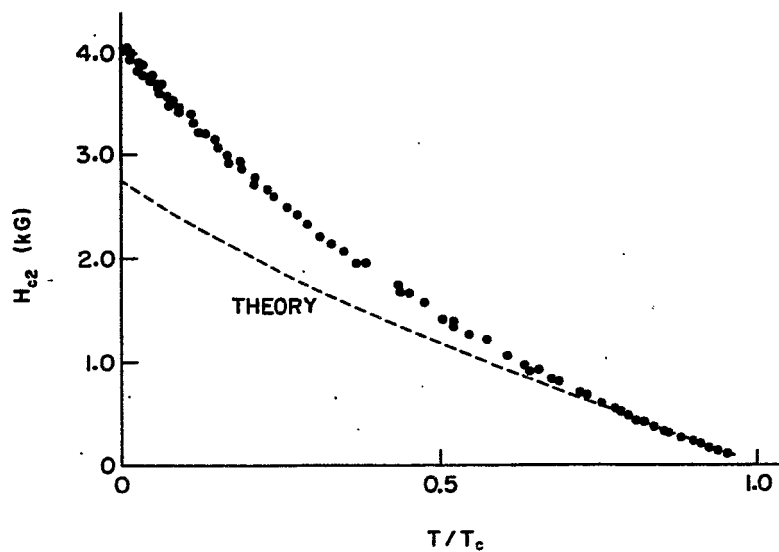


Fig. 15. Measured  $H_{c2}$  for Nb compared with theory of Hohenberg and Werthamer, after Ref. 36.

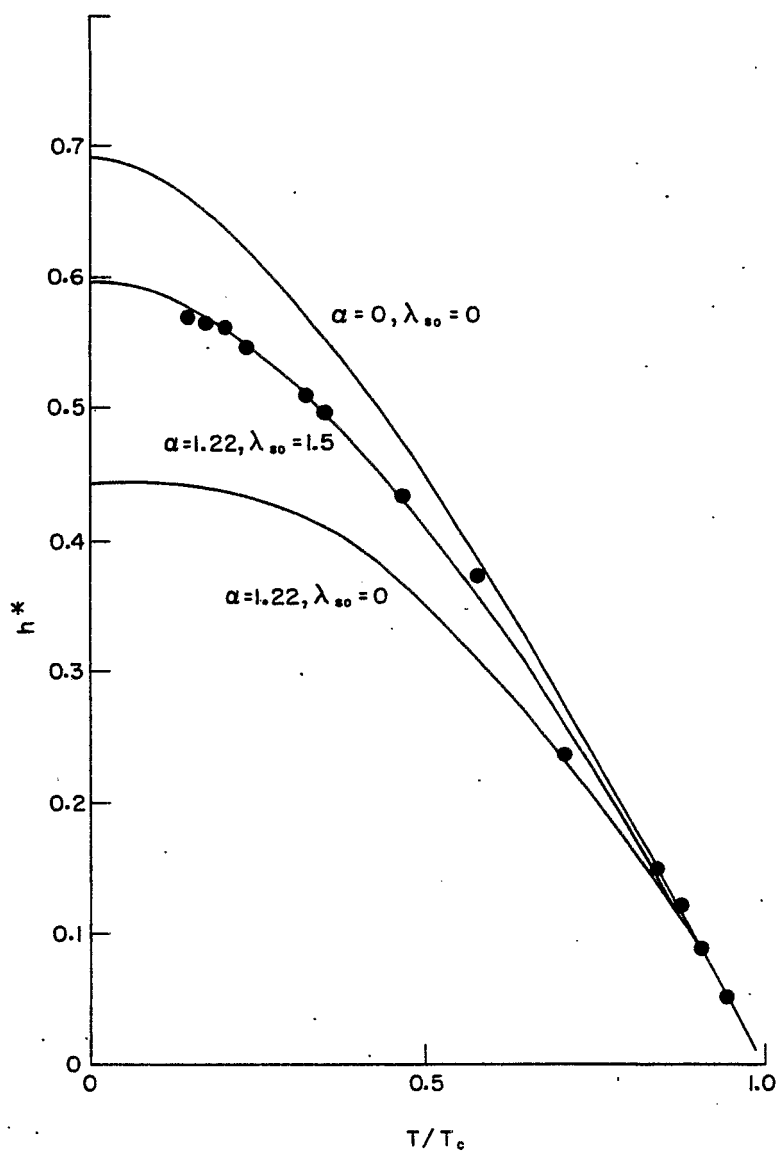


Fig. 16. Reduced field  $h^*$  as a function of  $T/T_c$  for  $\text{Ti}(0.56)\text{Nb}(0.44)$ , after Ref. 17.

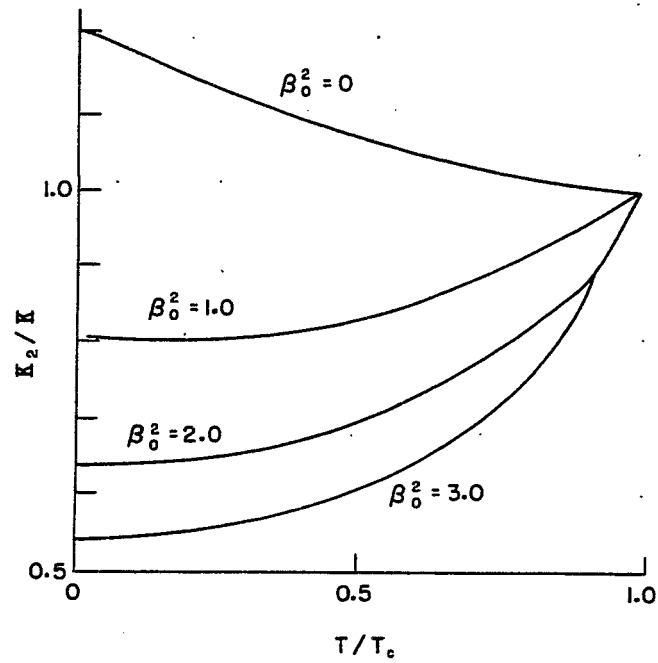


Fig. 17. Reduced parameter  $\kappa_2/\kappa$  as a function of  $T/T_c$ , after Ref. 17.

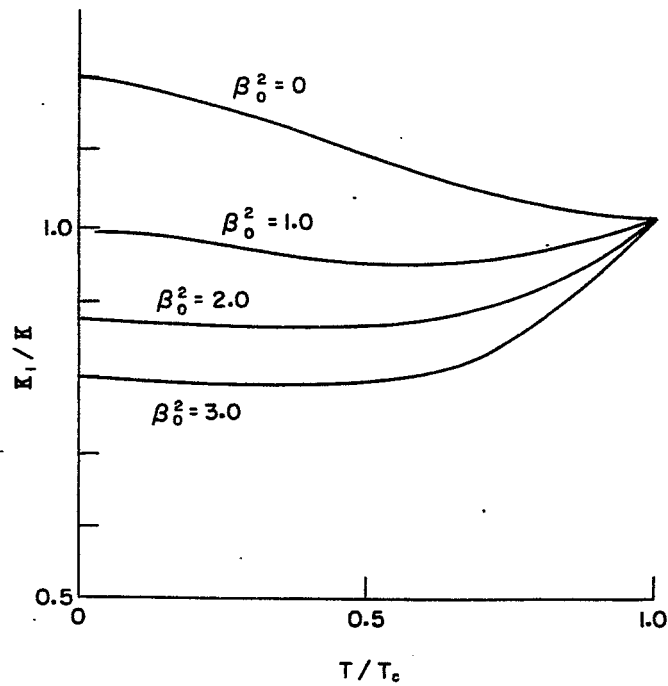


Fig. 18. Reduced parameter  $\kappa_1/\kappa$  as a function of  $T/T_c$ , after Ref. 17.

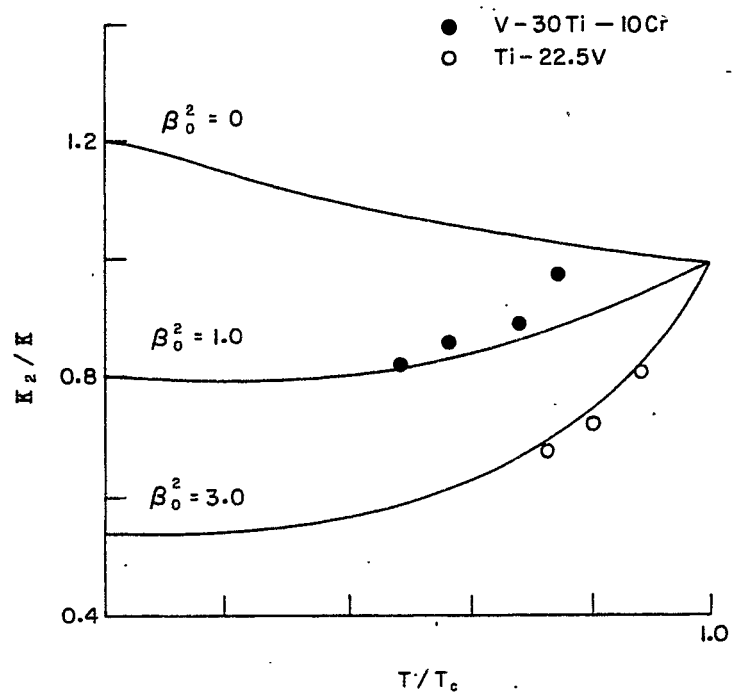


Fig. 19. Reduced parameter  $\kappa_2/\kappa_1$  for two alloys as a function of  $T/T_c$  compared to Maki theory after Ref. 34.

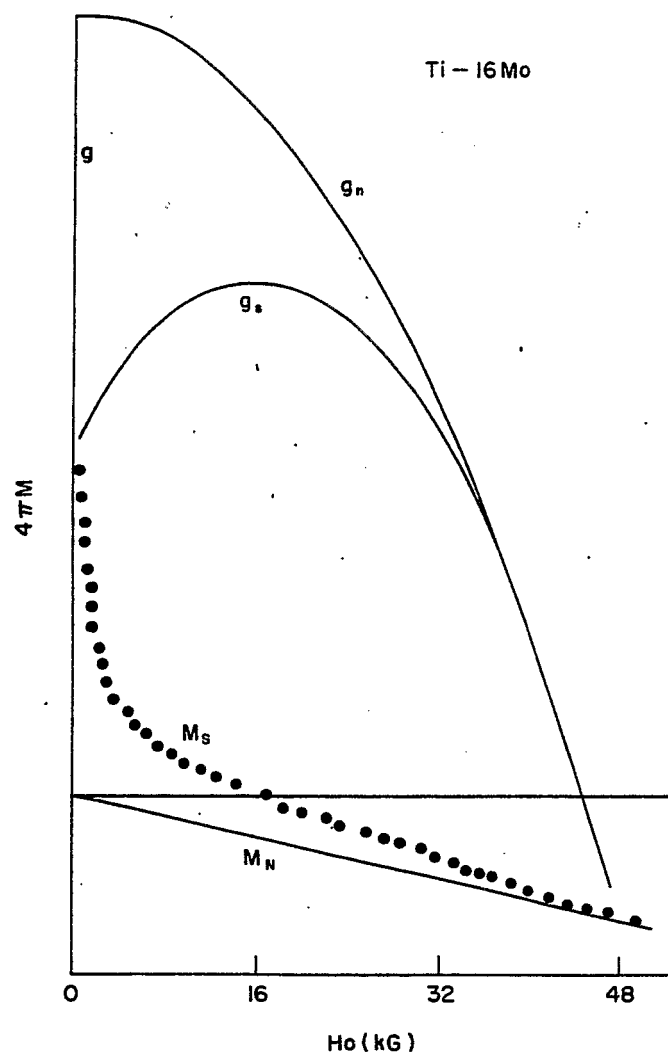


Fig. 20. Magnetization and derived free energy for Ti16%Mo alloy after Ref. 34.



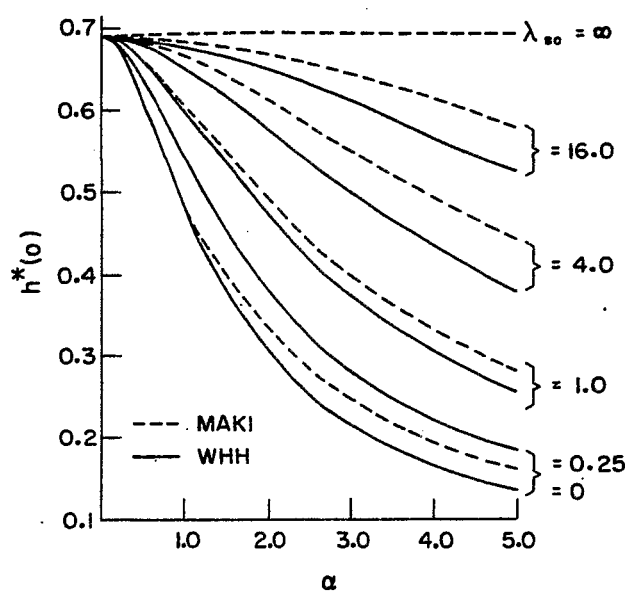


Fig. 21. The reduced field  $h^*(0)$  as a function of  $\alpha$  and  $\lambda_{so}$  from theories of Maki and WHH after Ref. 34.

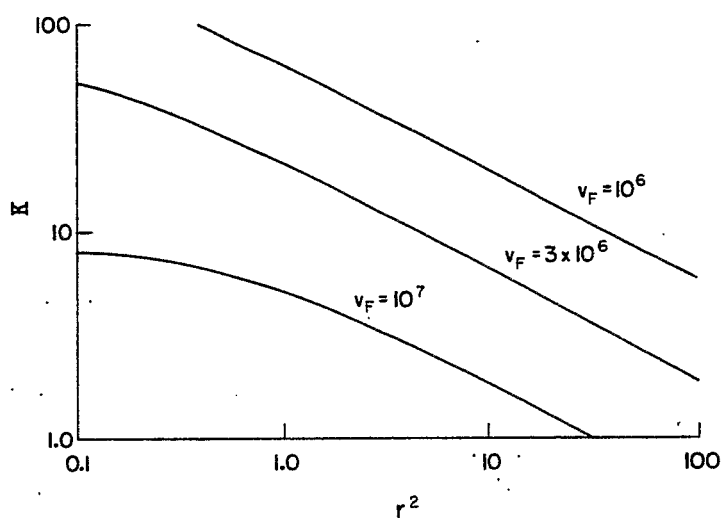


Fig. 22. Dependence of  $\kappa$ , in two-band model for  $\text{Nb}_3\text{Sn}$ , on Fermi velocity and parameter  $r^2$ .

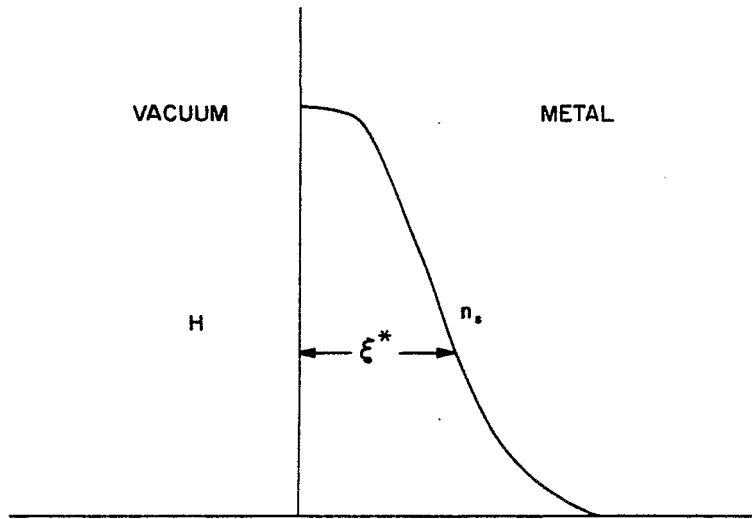


Fig. 23. Spatial variation of order parameter for surface superconductivity ( $H_{c2} < H < H_{c3}$ ).

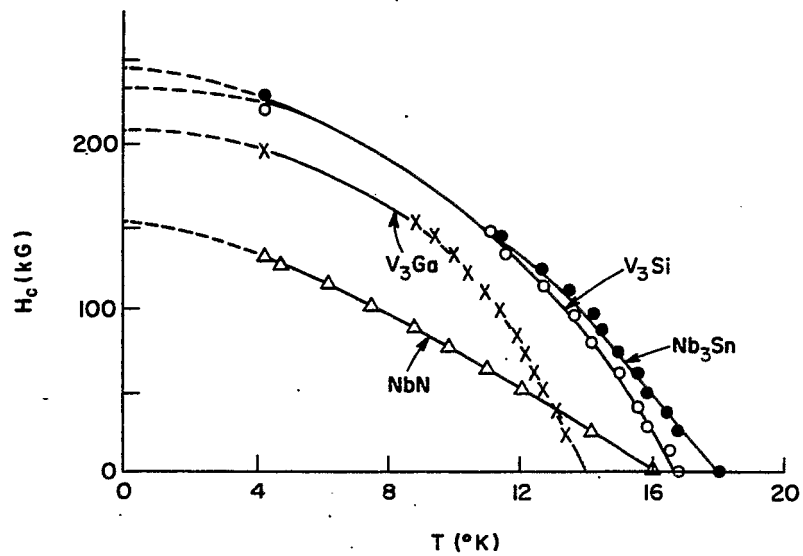


Fig. 24. Critical field curves of  $Nb_3Sn$ ,  $V_3Si$ ,  $V_3Ga$  and  $NbN$  after Ref. 51.

# THE EFFECT OF RADIATION ON THE PROPERTIES OF SUPERCONDUCTING MATERIALS\*

G.W. Cullen  
RCA Laboratories  
Princeton, New Jersey

It has been clearly demonstrated that the physical perfection of superconducting materials has a large influence on the superconducting properties. In general, it has been found that the current carrying capacity is proportional to the defect density, and also to the degree of difference between the defect and the matrix. Physical heterogeneities have been introduced into the materials by mechanical deformation, inclusion of second phases, voids, and impurities, and, finally, by irradiation. The inhomogeneities are viewed as pinning centers which restrict the motion of magnetic flux through the material. On the basis of a Lorentz force model, as the flux motion is pinned, higher transport currents may be supported by the material. An analysis of the kinds of pinning centers which are effective in the various superconducting materials, and the energetics involved, have been given in some detail in the first two presentations of this session of the Summer Study by J. Livingston<sup>1</sup> and W. Webb.<sup>2</sup> The flux pinning model was originally developed in a series of papers over about a two-year period by Anderson,<sup>3</sup> Friedel, de Gennes and Matricon,<sup>4</sup> Silcox and Rollins,<sup>5</sup> Kim, Hempstead and Strnad,<sup>6</sup> and Anderson and Kim.<sup>7</sup>

Introduction of defects by irradiation offers several advantages over the other methods of creating physical heterogeneities, particularly for the brittle beta-tungsten intermetallic compounds. The radiation damage may be introduced quantitatively, and, for certain types of radiation, the defects are introduced uniformly throughout the sample. Although the fine structure within an individual damaged "spot" is complicated and difficult to examine, the size and distribution of the damage spots is uncomplicated as compared to other types of structural heterogeneities. The size and density of the induced damage may be detected quantitatively by transmission electron microscopy, and thus the possibility is offered to relate these factors directly with the electrical properties. To date relatively little direct examination of radiation damage in the superconducting materials has been done. The radiation effects in the soft superconductors anneal out at room temperature, and thus direct observation of the defect structure in these materials is impractical. In the refractory type II superconductors the radiation effects do not anneal out at room temperature, but direct observation of the defect structure has been delayed by the difficulties involved in preparing well-defined single phase material, and in thinning the material for observation by transmission microscopy.

A number of investigations have been carried out since 1960 on the effect of irradiation on the properties of the superconducting materials. General trends may be defined:

- In Pb and Sn, the superconducting properties have been altered by deformation, alloying and irradiation, but the largest effects have been realized by deformation. The irradiation effects generally anneal out below room temperature.

---

\*The research reported in this paper was sponsored by the Air Force Materials Laboratory, Air Force Systems Command, Wright Patterson Air Force Base, Ohio, under contract Number AF33(657)-11208 and RCA Laboratories, Princeton, New Jersey.

- In the NbZr and NbTi alloys, large changes in the superconducting properties have been introduced by deformation and introduction of second phases, but with the exception of a "peak" effect observed in NbZr, irradiation has very little influence on the superconducting properties of both annealed and worked material.
- In Nb, both deformation and irradiation alters the superconducting behavior, but the largest change has been realized by neutron irradiation. The samples were exposed to irradiation at room temperature, and thus the effects observed are stable at room temperature.
- In the beta-tungsten compounds, the superconducting properties have been shifted by introduction of second phases and irradiation. The largest changes in the current density have been realized by irradiation. The irradiation induced properties (at least  $J_c$ ) are stable to temperatures well above room temperature.

It is clear that the most fruitful area for investigations of irradiation effects on superconducting properties lies with the type II superconductors. These materials are of practical importance, the effects observed are large, and are stable at temperatures used for observation of the defects. Single crystal Nb has been available for several years, and single crystal Nb<sub>3</sub>Sn has recently been prepared.

A review of investigations of the effect of irradiation on the properties of superconducting materials is presented in the following sections. The soft superconductors are included for background information, but for the reasons stated above, the emphasis is placed on the beta-tungsten materials.

#### THE EFFECT OF IRRADIATION ON THE PROPERTIES OF THE SOFT SUPERCONDUCTORS

In an effort to compare the effect of alloying and radiation damage on Sn, Rinderer and Schmid<sup>8</sup> irradiated pure tin strips with 5.3 MeV  $\alpha$  particles at 4.2°K. The more massive  $\alpha$  was used to produce a large number of defects. The sample thickness was chosen to be  $\sim 2 \times$  the penetration depth of  $\alpha$  particles in Sn ( $\sim 0.2$  mm) and the samples were exposed on both sides. Large increases in resistance were realized, and the  $T_c$  was decreased by a factor of 50 more than alloyed samples with equivalent resistance changes (Lynton et al.<sup>9</sup>). However, van Itterbeek and coworkers<sup>10</sup> later found the same  $T_c$  as a function of resistivity relationship for  $\alpha$ -irradiated samples as had been observed in the alloyed samples. Thallium and indium samples were also  $\alpha$  irradiated at 4.2°K. The irradiated Tl behaved similarly to Tl wires plastically deformed at 4.2°K, and the In compared, in  $T_c$  vs  $\rho$  behavior, to TeIn alloys. The radiation damage in these soft materials anneals out at low temperatures. More than half of the effect is lost at 16°K for the In (van Itterbeek et al.<sup>10</sup>), and all of the irradiation induced effect is annealed out of the Sn at room temperature in 24 hours (Rinderer and Schmid<sup>8</sup>).

Druyvesteyn and van Ooijen<sup>11</sup> measured the increase in the critical field of Pb after neutron irradiation at 78°K. As with the former two groups, these investigators found that the superconducting property measured, in this case  $H_c$ , may be related to the radiation induced change in resistivity. The  $dH_c/d\rho$  obtained by irradiation and by cold rolling at 78°K are similar. Cold rolling, however, leads to changes in  $H_c$  which are a factor of ten larger than that induced by neutron damage for fluxes of  $\sim 10^{18}$  n/cm<sup>2</sup>.

In two of the three investigations of the influence of irradiation on superconducting properties of the soft metals, the relation between the change in the super-

conducting property measured with the change in resistivity was similar, independent of the means of introducing the lattice defects. Since the defects resulting from irradiation, alloying, and cold rolling introduce quite different types of crystallographic inhomogeneities, the superconducting properties appear to be more directly related to resistivity. Disagreement between the measured effects and those anticipated by theory is explained on the assumption that the sample is heterogeneous and contains microscopic regions with different resistivities.

Blank and coworkers,<sup>12</sup> from magnetization measurements, observed increases in the frozen-in magnetic moment for rhenium and tin which had been neutron irradiated at 77°K. The  $T_c$  of Rh increased, while that of Sn decreased, as has also been seen by the other investigators. The changes in  $T_c$  and the magnetization were not related to  $\rho$ , but it was noted that addition of tungsten also increases the  $T_c$  of Rh, while the introduction of impurities decreases the  $T_c$  of Sn. The comparative temperatures of annealing out of the introduced damage may be related to the comparative melting points of these two materials.

Coffey and coworkers<sup>13</sup> observed changes in the resistivity of pure annealed lead which had been deuteron irradiated at 30°K. A change in the normal resistivity of  $0.5 \times 10^{-8} \Omega \cdot \text{cm}$  was observed at the highest exposure of  $\sim 10^{21}$  deuterons/cm<sup>2</sup>. About 75% of the induced resistivity increase remained after a 77°K anneal, and 1% after a 300°K anneal.

#### THE EFFECT OF IRRADIATION ON THE PROPERTIES OF NbZr

Babcock and Riemersma<sup>14</sup> observed no change in the operation of a Nb75%Zr25% solenoid after exposure, in liquid helium, to a 400 MeV proton flux of  $8 \times 10^{10}$  p/cm<sup>2</sup>.

McEvoy et al.<sup>15</sup> observed no change in the flux shielding properties of 25% cold worked Nb75%Zr25% after an exposure to a fast neutron flux of  $1 \times 10^{18}$  n/cm<sup>2</sup> (at  $\sim 50^\circ\text{C}$ ), and proposed that the lack of change was due to the fact that the material had already been cold worked prior to irradiation. However, Keller et al.<sup>16</sup> observed no change in the current carrying characteristics, with the exception of a peak effect near  $H_{c2}$ , of annealed NbZr exposed to a deuteron flux of  $10^{17}$  d/cm<sup>2</sup> at 30°K. Coffey et al.,<sup>13</sup> at the same laboratory, observed about a 20% decrease in the  $J_c$  of cold worked NbZr and NbTi, deuteron irradiated under the same conditions as stated above.

#### THE EFFECT OF IRRADIATION ON THE PROPERTIES OF Nb

Chaudhuri and coworkers<sup>17</sup> have measured the superconducting and normal state low temperature thermal conductivity of single crystal Nb and V samples irradiated by  $1 \times 10^{18}$  n/cm<sup>2</sup> at 30°C. Both the superconducting and normal (driven normal by a magnetic field) thermal resistivity of the Nb increased after irradiation, but only the superconducting thermal resistivity of the V increased. These investigators proposed that the exposure to the fast neutrons resulted in the formation of vacancy-interstitial pairs which condense into dislocation loops. The strain fields around the dislocations act as phonon scatterers. A possible difference between the Nb and V is that, at the 30°K measurement temperature, both interstitials and vacancies can migrate in the lower melting V, but only vacancies migrate in Nb.

Swartz and coworkers<sup>18</sup> observed no effect of fast neutron irradiation (to levels as high as  $1.5 \times 10^{18}$  n/cm<sup>2</sup>) on the magnetization of arc cast Nb and Nb70%Ta30% alloys. Under the same conditions, however, these investigators did detect changes in the intermetallic superconductors Nb<sub>3</sub>Sn, Nb<sub>3</sub>Al, V<sub>3</sub>Ga and V<sub>3</sub>Si. The differences were attributed to the difference in the degree of order between these two classes of materials.

But later Kernohan and Sekula<sup>19</sup> found that almost ideal irreversible type II behavior in the magnetization of single crystal Nb could be realized by fast neutron irradiation of  $2 \times 10^{19}$  n/cm<sup>2</sup> (at 40°C). Effects were also observed at the lower irradiation levels employed by Swartz and coworkers,<sup>18</sup> so that the differences observed by these two groups must be attributed to the difference in the nature of the arc cast Nb as compared to annealed single crystal Nb. As is observed in the compound superconductors, the irradiation of Nb to the  $2 \times 10^{19}$  n/cm<sup>2</sup> level resulted in relatively little change in the  $T_c$  (~1% decrease). It is interesting to note that the neutron induced flux pinning centers are more effective in Nb than inhomogeneities introduced by mechanical deformation. Essentially irreversible behavior has not been achieved in Nb by cold working.

Tucker and Ohr<sup>20</sup> have observed neutron induced effects in polycrystalline Nb by transmission electron microscopy. These investigators find evidence to show that the neutron induced spots are indeed dislocation loops. The damage spots were found to be near the foil surfaces, even though the sample appears to have been thinned after irradiation.

These investigators do not relate the directly observed defect structure with superconducting properties.

#### THE EFFECT OF IRRADIATION ON THE PROPERTIES OF THE BETA-TUNGSTEN SUPERCONDUCTORS

A number of groups have been active in investigating the influence of irradiation on the superconducting properties of the beta-tungsten compounds. Before summarizing this work, it is important to point out that the microstructure of these hard, brittle materials is very much influenced by the method of preparation. Particularly in investigations such as these, where the physical perfection is an important variable, one expects to see differences in the effect of irradiation for materials prepared by the different methods. For example, in vapor deposited Nb<sub>3</sub>Sn, very small preparative variables yield slightly off stoichiometric material which behaves radically differently than the stoichiometric material after exposure to fast neutron fluxes. The investigators at the General Electric Research Center (Swartz et al.<sup>18</sup>; Bean et al.<sup>21</sup>) have used, for the most part, arc cast material. At the Westinghouse Research Laboratories (Coffey et al.<sup>13</sup>), Nb<sub>3</sub>Sn vapor deposited by RCA on a Hastelloy substrate (Hanak<sup>22</sup>; Hanak et al.<sup>23</sup>) has been employed. The Siemens investigators (Bode and Wohlleben<sup>24</sup>) have prepared Nb<sub>3</sub>Sn by diffusion. At RCA (McEvoy et al.<sup>15</sup>; Cullen and Novak<sup>25,26</sup>; Cody, unpublished) vapor deposited Nb<sub>3</sub>Sn on ceramic substrates (Cullen<sup>27</sup>), and single crystals prepared by a closed tube transport process (Hanak and Berman<sup>28</sup>) have been investigated.

Swartz and coworkers<sup>18</sup> detected changes in the magnetic hysteresis of arc cast Nb<sub>3</sub>Sn, Nb<sub>3</sub>Al, V<sub>3</sub>Ga and V<sub>3</sub>Si after an irradiation of  $1.5 \times 10^{18}$  n/cm<sup>2</sup>. The magnitude of the changes observed is inversely proportional to the average atomic mass of the elements making up the compounds. The largest change in the calculated  $J_c$  was observed in V<sub>3</sub>Si;  $\Delta J_c = 7 \times 10^5$  A/cm<sup>2</sup> for  $10^{18}$  n/cm<sup>2</sup>. The Nb<sub>3</sub>Sn was prepared by both arc casting and diffusion, and considerable differences were observed in the effect of irradiation between these two samples even though the unirradiated transition temperatures were very similar. The transition temperature is relatively insensitive to material changes which have large effects on the  $J_c$ . The largest change in the  $T_c$  observed in this investigation was -0.22°K for the arc cast Nb<sub>3</sub>Al.

At the same laboratory, Bean and coworkers<sup>21</sup> investigated the effect of thermal neutron irradiation on the superconducting properties of Nb<sub>3</sub>Al and V<sub>3</sub>Si doped with fissionable uranium and boron. After exposure to a flux of  $1.7 \times 10^{18}$  n/cm<sup>2</sup> the

material containing 0.321 at % U exhibited current densities as high as  $2 \times 10^6$  A/cm<sup>2</sup> at 30 kOe. This represents an increase in the  $J_c$  by more than a factor of 100 over the preirradiated value, and is higher by a factor of  $\sim \times 10$  than had been previously realized for these materials in the 30 kOe field. Above 10 kOe the  $J_c$  becomes relatively insensitive to the magnitude of the applied field, and thus the current carrying behavior of these samples does not adhere to the Lorentz force model. As in the investigations on the undoped materials, the increase in the  $J_c$  of the irradiated doped V<sub>3</sub>Si is two to three times that of the Nb<sub>3</sub>Al. Similar decreases in the transition temperatures were also observed as for the undoped samples,  $\sim -0.22^\circ\text{K}$  for V<sub>3</sub>Si, and  $\sim -0.45^\circ\text{K}$  (below the preirradiated  $T_c$ ) for the Nb<sub>3</sub>Al.

Coffey and coworkers<sup>13</sup> have examined the effect of low temperature deuteron irradiation on the superconducting properties of vapor deposited Nb<sub>3</sub>Sn on the Hastelloy ribbon substrate. The samples were exposed to a  $1 \times 10^{21}$  d/m<sup>2</sup> flux at 30°K. Critical current measurements were made at temperatures between 5.1 and 12.2°K. Appreciable differences were observed between two samples which exhibited different preirradiation current carrying capacities.

At 5.7°K the  $J_c$  of the initially low  $J_c$  sample increased on irradiation from 6 to  $10 \times 10^8$  A/m<sup>2</sup> in a 20 kOe field and remained at the higher  $J_c$  after annealing at 300°K. At a measurement temperature of 10.7°K, the  $J_c$  of the same sample decreased after irradiation, and exhibited recovery after the 300°K anneal. The  $J_c$  was decreased at all measurement temperatures for a sample with a preirradiation  $J_c$  of  $\sim 4 \times 10^9$  A/m<sup>2</sup> at 20 kOe. As with the low  $J_c$  sample, the deuteron induced behavior was stable to a 300°K anneal for a 5.1°K measuring temperature, but unstable at 12.2°K. The transition temperatures were lowered and broadened by the deuteron irradiation, and 75-80% of the effect remained after a 300°K anneal. A linear increase in the resistivity with increasing deuteron exposure was observed, of which  $\sim 57\%$  remained after annealing at 300°K.

Bode and Wohlleben<sup>24</sup> have observed over 300% enhancement of the  $J_c$  of diffused Nb<sub>3</sub>Sn after proton irradiation of  $8 \times 10^{16}$  p/cm<sup>2</sup> at temperatures between 100 and 200°C. Above this irradiation level the  $J_c$  decreases. The postirradiation  $J_c$  is essentially independent of the applied magnetic field up to 50 kOe, thus the behavior of these samples does not follow the Lorentz force model. By comparing the levels of neutron (Cullen et al.<sup>29</sup>) and proton irradiation which lead to the same  $J_c$  enhancement, a ratio of effective levels of  $N_p/N_n = (3-6) \times 10^{-2}$  was derived. These investigators calculate that at this ratio, for a displacement energy of 20 eV, the same concentration of defect clusters will be produced by either neutrons or protons. The proton induced  $J_c$  is not altered by a 12 hour anneal at 250°C. The original  $J_c$  is restored by annealing at temperatures between 700 and 800°C. A condensation of overlapping clusters is proposed as the mechanism to explain the decrease in the enhanced  $J_c$  at irradiation levels above  $8 \times 10^{16}$  p/cm<sup>2</sup>.

#### THE EFFECT OF NEUTRON-INDUCED DEFECTS ON THE PROPERTIES OF Nb<sub>3</sub>Sn: Investigations Carried Out at the RCA Laboratories

Various investigations have been carried out at the RCA Laboratories on the effect of fast neutron irradiation on the properties of polycrystalline and single crystal Nb<sub>3</sub>Sn. The properties measured are: flux shielding, current carrying capacity, resistivity, transition temperature, and magnetization. The lattice expansion, and recovery of the lattice on annealing, has also been investigated. In an attempt to relate the electrical properties with structural changes, the neutron induced defects are now being directly observed by transmission electron microscopy.

The magnetic flux shielding properties of polycrystalline vapor deposited Nb<sub>3</sub>Sn on ceramic substrate tubes (Cullen<sup>27</sup>) was studied (McEvoy et al.<sup>15</sup>) by placing a field

probe both inside and outside of the tube. Using this method originally suggested by Kim and coworkers,<sup>6</sup> the currents circulating in the tube which result in the flux shielding can be readily derived. The current densities derived from this method are in good agreement with direct current measurements on the strips of the same material (Cullen et al.<sup>30</sup>). The cylinders were exposed to a fast neutron flux of  $10^{18}$  n/cm<sup>2</sup> at  $\sim 50^\circ\text{C}$ . The magnetization curves,  $H$  internal vs  $H$  external, were determined at  $4.2^\circ\text{K}$ . Prior to irradiation, no flux jumps were observed. But after irradiation, flux jumps occurred to such an extent that it was difficult to establish a postirradiation critical state curve. It was evident that the current density of a sample with a preirradiation  $\alpha^* = 6.4 \times 10^6$  kG·A/cm<sup>2</sup> had been enhanced by at least 50%. Because of more extensive flux jumping, no estimate could be made of the increase in the current density after irradiation of a sample with a preirradiation  $\alpha = 1.5 \times 10^6$  kG·A/cm<sup>2</sup>. Although it was difficult to obtain quantitative results from this type of measurement, the increase in the superconducting current carrying capacity as a result of irradiation had been established.

Because of the difficulty in obtaining quantitative results from the flux shielding experiments, the more laborious direct measurement of the critical currents on strip samples were made (Cullen and Novak<sup>25,26</sup>). Current and potential contacts were soldered to nickel-plated lands on thin Nb<sub>3</sub>Sn strips supported by a flat ceramic substrate. The adherence of the current carrying characteristics to the Lorentz force model (Kim et al.<sup>6</sup>) had previously been established on the Nb<sub>3</sub>Sn ceramic supported strips. The critical current, both as a function of the applied field intensity, and the orientation of the current carrying axis in the field, is in excellent agreement with the Lorentz force model to less than 1% for fields as high as 100 kG (Cullen, Cody and McEvoy<sup>30</sup>; Cody, Cullen and McEvoy<sup>31</sup>; Cody and Cullen, to be published). The strip samples were exposed to fast neutron fluxes under the same conditions as had previously been employed for the tabular samples. The critical current densities in a transverse field at  $4.2^\circ\text{K}$  were measured as a function of the exposure to neutron fluxes as high as  $1.4 \times 10^{18}$  n/cm<sup>2</sup>. A variety of samples were measured with various "as deposited"  $\alpha$ 's between  $1.4$  and  $19 \times 10^6$  kG·A/cm<sup>2</sup>. A summary of the results is shown in Table I.

The JH product (measured at 14 kG) of the sample with the lowest preirradiation  $\alpha$  of  $1.49$  kG·A/cm<sup>2</sup> increased by more than an order of magnitude after irradiation of  $14 \times 10^{17}$  n/cm<sup>2</sup>, while the JH of the highest initial  $\alpha$  sample of  $19.4$  kG·A/cm<sup>2</sup> increased slightly after exposure to a flux of  $3.4 \times 10^{17}$  n/cm<sup>2</sup>, and then decreased by more than an order of magnitude after an exposure of  $7.2 \times 10^{17}$  n/cm<sup>2</sup>. The first of these samples is essentially stoichiometric Nb<sub>3</sub>Sn, while the second sample is slightly Nb rich. This emphasizes that small differences in preparative variables can result in large differences in the way the superconducting properties are influenced by irradiation, and implies that the radiation induced defects interact strongly with heterogeneities already present in the sample. If the "as prepared" heterogeneities are larger than the irradiation induced damaged areas, as is undoubtedly the case, these defects may "short out" the irradiation induced damage, or the irradiation induced defects may condense on the larger heterogeneities and form larger and less effective pinning points. It is also possible that the manner in which the neutrons initially transfer energy to the lattice is strongly influenced by the presence of heterogeneities. It is interesting to note in this regard that Brimhall and Mastel<sup>32</sup> have observed a concentration of defect structures in twin boundaries and denuded zones around the boundaries of neutron irradiated Ni.

---

\*The current carrying characteristics of Nb<sub>3</sub>Sn in an applied field are described in terms of  $\alpha$  of the Kim et al.<sup>6</sup> relationship  $J = \alpha / (H + B_0)$ , where  $\alpha$  is a constant dependent on the structure of the material. For low  $\alpha$  specimens,  $B_0 \sim 600$  G.



TABLE I

Initial Sample Characteristics and Current Carrying Behavior  
as a Function of Irradiation

Sample	Composition (wt % Sn)	$T_c$ midpoint (°K)	$\Delta T_c$ (°K)	$(n/cm^2)$ $\times 10^{-17}$	JH ( $kG \cdot A/cm^2$ ) $\times 10^{-6}$		JH ( $kG \cdot A/cm^2$ ) $\times 10^{-6}$		(kG·A/cm <sup>2</sup> ) $\times 10^{-6}$	
					H = 10 kG	H = 14 kG	H = 10 kG	H = 14 kG	$\alpha_1$	$\alpha_2$
FS-20(5)	29.5 ± 0.3	18.3	0.04	0	1.36	1.33	1.49	---	---	---
				3.4	5.30	6.46	6.58	14.3	---	---
				7.2	9.38	11.4	14.3	28.6	---	---
				10.5	13.0	16.8	24.1	90.5	---	---
				14.0	15.0	18.2	35.0	76.0	---	---
75(3)	28.0 ± 0.1	16.1	0.80	0	4.0	4.48	6.5	---	---	---
				3.3	6.6	7.84	12.1	---	---	---
				6.9	8.0	9.66	15.6	---	---	---
				10.1	6.2	7.56	10.1	19.5	---	---
74(4)	29.2 ± 0.1	16.9	0.80	0	11.5	13.3	19.4	27.9	---	---
				3.4	11.7	14.1	19.2	29.7	---	---
				7.2	0.89	1.3	1.18	2.32	---	---
Single Crystal	30.8 ± 0.01	18.0	0.10	0			0.15		---	---
				1.0			0.50		---	---

As the critical current density is enhanced by either neutron irradiation or the introduction of chemical heterogeneities, the current carrying behavior cannot be described by the Lorentz force current field relationship. A change in the  $\alpha$  takes place at  $\sim 10$  kG; above this applied field level the  $J_c$  is less dependent on the applied field. An  $\alpha$  for below 10 kG, and an  $\alpha$  for above 10 kG, are given for these samples in Table I, but the current carrying behavior is better described by the JH products at 10 kG and at 14 kG.

The sample resistivities at 300°K and 77°K were measured as a function of the exposure to the neutron flux. The residual resistivities were derived from the  $R_{300K}/R_{77K}$  ratio by an empirical relationship established by Woodard and Cody.<sup>33</sup>

An average change in the residual resistivity with the neutron flux  $dp_0/d\phi$  is  $\sim 5.7 \times 10^{-24} \Omega \cdot cm^3/n$ . This value is independent of the level of the flux exposure, and is within the range of that measured in other metals.

Very little change in the transition temperature was observed (Cooper<sup>34</sup>) as the result of neutron irradiation of these Nb<sub>3</sub>Sn samples. For a sample with an unirradiated  $T_c$  (start) of 18.33°K, and a  $\Delta T_c$  of 0.05°K, no change in magnitude or width of the transition was observed after exposure to a flux of  $4.7 \times 10^{17}$  n/cm<sup>2</sup>. After an exposure of  $2.7 \times 10^{18}$  n/cm<sup>2</sup> the transition temperature decreased by  $0.18^\circ K \pm 0.02^\circ K$ , with no change in width.

Magnetization studies (Cody, unpublished) have been carried out on cylinders cut from single crystals of Nb<sub>3</sub>Sn (Hanak and Berman<sup>28</sup>). The  $\alpha$ 's for the single crystal material are commonly a factor of 10 less than the lowest  $\alpha$  of the polycrystalline materials. At 4.2°K, the magnetization curves are irreversible, and are appreciably shifted by exposure to a neutron flux of  $1 \times 10^{16}$  n/cm<sup>2</sup>. This radiation level is lower

than the lowest exposure used for the polycrystalline material. A flux exposure of  $1 \times 10^{17}$  n/cm<sup>2</sup> typically increases the  $\alpha$  (measured at 4.2°K from 0.15 to 0.50 kG·A/cm<sup>2</sup>). The  $d\alpha/d\phi$  for the single crystal material is slightly higher than that measured on the lowest  $\alpha$  polycrystalline material ( $\sim 3 \times 10^{-12}$  as compared to  $2.5 \times 10^{-12}$  kG·A/n).

This is consistent with the observations made on the polycrystalline material which show that the effect of the neutron damage on  $J_c$  is inversely proportional to the initial sample  $\alpha$ .

The effect of neutron irradiation on the electrical properties of Nb<sub>3</sub>Sn may be summarized as follows:

- 1) The degree to which neutron irradiation influences the current carrying capacity of Nb<sub>3</sub>Sn is a strong function of the initial sample characteristics. The  $d\alpha/d\phi$  is inversely proportional to the initial  $\alpha$ . On this basis the changes realized on single crystal material are in good agreement with changes observed in polycrystalline material.
- 2) The highest  $\alpha$  measured to date on Nb<sub>3</sub>Sn was obtained by irradiation of an initially low  $\alpha$  sample.
- 3) Above a certain initial  $\alpha$  level, the current carrying capacity of the material is decreased by irradiation. Thus the maximum  $\alpha$  obtainable by irradiation is also a function of the initial sample characteristics.
- 4) The JH product, measured at 14 kG, has been increased by as much as a factor of 15 by neutron irradiation.
- 5) The  $dp/d\phi$  is independent of the level of irradiation to a flux level of  $\sim 10^{18}$  n/cm<sup>2</sup>.
- 6) The transition temperature is decreased very little at irradiation levels that have a large effect on the current carrying properties.

The lattice expansion has been measured of polycrystalline vapor deposited samples which were pulverized and encased in sealed quartz X-ray capillary tubes and exposed to neutron irradiation under the conditions previously described. Lattice expansions typically  $\Delta a/a_0 \sim 3 \times 10^{-4}$  were measured after exposure of the samples to a fast neutron flux of  $1 \times 10^{17}$  n/cm<sup>2</sup>. After the initial exposure the lattice expansion is linear to a value of  $\Delta a/a_0 = 14 \times 10^{-4}$  after an irradiation of  $1.4 \times 10^{19}$  n/cm<sup>2</sup>. Although the expansion showed no indication of leveling off at this irradiation level, further measurements were not carried out because of the periods of exposure needed for higher radiation levels. The samples were annealed at various temperatures, for a period of an hour, until the starting lattice constant of 5.2895 Å was obtained. Between the temperatures of 300 and 650°K, the relaxation in the lattice constant is linear and would extrapolate to a complete anneal at  $\sim 1050^\circ\text{K}$ . However, above 650°K the sample anneals more rapidly, and the original cell constant is achieved at 800°K in one hour. More recent experiments indicate that the samples can be completely annealed at 650°K in two hours. The X-ray diffraction lines sharpen in the back reflection region as the sample is annealed, as is expected if a range of lattice spacings are observed as the result of changes in spacing with distance from a damaged area. The expansion in the lattice is consistent with the formation of an area of decreased density resulting from a thermal spike, as has been proposed (Silcox and Hirsch<sup>35</sup>) for the neutron irradiated copper. It is surprising, however, that measurable lattice changes are observed in this material which has a total damaged volume of  $\sim 0.1\%$  (as seen by electron microscopy). The magnitude of the damage, and annealing behavior, are similar to that observed for neutron irradiated copper. The damage is retained at higher temperatures than would be anticipated by comparing the melting points of Cu and Nb<sub>3</sub>Sn, but this may

qualitatively be accounted for by the highly ordered structure of the intermetallic  $\text{Nb}_3\text{Sn}$ .

#### Direct Observation of Neutron Damage in $\text{Nb}_3\text{Sn}$ by Transmission Electron Microscopy

Three different types of  $\text{Nb}_3\text{Sn}$  samples have been employed for transmission electron microscopy:

- 1) Single crystal  $\text{Nb}_3\text{Sn}$  which was irradiated and subsequently thinned by chemical etching.
- 2) Polycrystalline  $\text{Nb}_3\text{Sn}$  which was irradiated and thinned by low angle ion bombardment.
- 3) Polycrystalline  $\text{Nb}_3\text{Sn}$  which was thinned by low angle ion bombardment and then irradiated.

Initially the  $\text{Nb}_3\text{Sn}$  samples were thinned exclusively by chemical etching. This procedure posed serious problems because the polycrystalline material etches rapidly at high energy grain boundaries and at the interfaces caused by the columnar growth. Therefore it was extremely difficult to obtain thin edges useful for transmission electron microscopy. The physically homogeneous single crystal material may be thinned by chemical etching, but an uncertainty arose when it was noted that the planar density of the dark areas observed by microscopy after irradiation do not appear to be a function of the thickness of the samples. It has been established that the dark spots observed are indeed associated with exposure to fast neutrons, and not preparation surface artifacts, but the lack of change in density with thickness presents the possibility of an interaction with defects near the surface with the chemical thinning procedure. This would be easier to explain if the damage areas were lighter (on positive prints of electron micrographs) than the matrix, which could be associated with pits. Tucker and Ohr<sup>20</sup> have concluded, by observation of neutron irradiated Nb foils in bright-field and dark-field electron microscopy, that the dark spots they have observed result from defects lying close to the surfaces of the sample. Since the samples were irradiated prior to electrochemical thinning, this implies an interaction between the defects and the thinning method.

Both of these problems have been obviated by thinning by low angle ion bombardment. The method was developed recently by Professor Paulus of CNRS, France. Since the removed material is not knocked into the sample, but leaves at a low angle, no observable damage occurs on thinning. Samples that contain high energy areas can be thinned uniformly by this physical technique.\* The polycrystalline  $\text{Nb}_3\text{Sn}$  is now routinely thinned by this method. Wedge shape areas of irradiated material have now been observed in which the planar density of defect spots is a function of the sample thickness.

In the chemically thinned single crystal  $\text{Nb}_3\text{Sn}$  samples,  $100 \text{ \AA}$  diameter defect spots were observed after exposure of the samples to a  $10^{18} \text{ n/cm}^2$  flux.<sup>36</sup> The density of the spots is  $\sim 5 \times 10^{15}/\text{cc}$ . This amounts to a 0.1% volume damage of the material. Considering that the film thickness is little more than double the distance between the spots, the volume density changes very little if the assumption is made that the

---

\*The details of the low angle ion bombardment technique have been discussed only in internal reports of CNRS, Bellevue, France. A thinning apparatus has been marketed by Alba Engineers, Asnières, France. A modification of this apparatus has been employed at the RCA Laboratories to thin the  $\text{Nb}_3\text{Sn}$  samples. A thinning apparatus similar to that modified at the RCA Laboratories will be available in the near future from the Materials Research Corporation, Orangeburg, New York.

observed areas lie close to the two surfaces, rather than uniformly throughout the bulk of the sample. To date attempts to resolve the structure of the spots by the various microscopic techniques have been unsuccessful, and it must be concluded that the damaged areas are amorphous.

The spot size and density observed in ion beam thinned polycrystalline samples after the same level of irradiation have been in excellent agreement with those observed in the single crystal material. Because of the interaction between the "as prepared" defects and the neutron induced defects, as shown by the electrical data, attempts are now being made to thin the sample prior to irradiation, and thus examine specifically identified areas both before and after irradiation, and after annealing. The first attempt was unsuccessful because of the formation of a thin oxide on the surface of the sample during the irradiation which obscured the defect structure. This result is not unexpected since a continuous microscopic oxide film which may serve as the insulator in a tunnel diode structure may be formed by heating  $\text{Nb}_3\text{Sn}$  in air at  $100^\circ\text{C}$ . The samples are now irradiated in an atmosphere of a pure inert gas.

Resolution of the fine structure within the damage spots would contribute to an understanding of the mechanism of the damage formation, but it is the size and spacing of the damage areas that is most important for understanding the effect of these heterogeneities on the current carrying properties. Future studies are directed toward establishing a relationship between the density of the damaged areas and the current carrying characteristics of the material. It is also important to examine the microstructure of material exposed to an irradiation level where further damage effects a decrease in the current carrying capability. If possible, the interaction between the complicated "as deposited" structure of polycrystalline material and the added neutron induced defects will be studied. At present, for one level of neutron exposure, the following summary can be offered:

Polycrystalline vapor deposited  $\text{Nb}_3\text{Sn}$ , as deposited  
 $\alpha = 1.5 \times 10^6 \text{ kG}\cdot\text{A}/\text{cm}^2$  exposed to a fast neutron flux of  
 $1 \times 10^{18} \text{ n}/\text{cm}^2$  at  $\sim 50^\circ\text{C}$ .

Damage spot density observed:  $5 \times 10^{15} \text{ spots}/\text{cm}^3$ .

Spot area:  $\sim 100 \text{ \AA}$ .

$d\alpha/d\phi = 2.5 \times 10^{12} \text{ kG}\cdot\text{A}/\text{n}$ .

$d\rho/d\phi = 5.7 \times 10^{-24} \Omega\cdot\text{cm}/\text{n}$ .

$\Delta T_c = \sim -0.18^\circ\text{K}$ , no change in transition width for  
irradiation level of  $2.7 \times 10^{18} \text{ n}/\text{cm}^2$ .

## CONCLUSIONS

An appreciable amount of work has been carried out during the last eight years on the effect of irradiation on the properties of the various superconducting materials. Both the "soft" and the "hard" superconductors have been studied. It is evident at this time that the greatest opportunity for arriving at a quantitative relationship between structural and electrical properties lies in correlating direct observations of the nature of the irradiation induced defect structure with the superconducting properties of the type II materials. The soft superconductors do not lend themselves to such studies because, for the most part, the irradiation induced properties anneal out at temperatures below room temperature and thus direct examination of the defect structures is impractical. Also, larger effects in these materials are realized by mechanical deformation than by irradiation. The  $\text{NbZr}$  and  $\text{NbTi}$  alloys, both cold worked and annealed, are very little affected by irradiation, while large effects on the current carrying properties of these alloys can be brought about by mechanical

deformation. These deformed alloys have been examined by transmission electron microscopy, but the structure is complicated and difficult to analyze quantitatively. The superconducting properties of the beta-tungsten intermetallic compounds are more sensitive to structural defects introduced by irradiation than by chemical introduction of impurities or second phases. The irradiation induced enhancement of the critical current density in these materials is stable to temperatures well above room temperature and therefore it is feasible to undertake direct observation of the defect structure. Well-defined single phase material may now be prepared, and methods have recently been developed for thinning these refractory compounds. The nature (size, density, and distribution) of the irradiation induced defects is simple as compared to that observed in mechanically deformed materials, and the irradiation induced damage may be introduced at well-controlled levels. Therefore, quantitative correlations between the structure and electrical properties are possible.

The critical current density is more influenced by irradiation induced damage than the other superconducting properties. It has been observed in several beta-tungsten compounds that, at irradiation levels where the  $J_c$  is increased by more than an order of magnitude, the  $T_c$  is decreased by only  $\sim 1\%$ . It has also been observed in several compounds by various investigators that the current carrying behavior may be explained by a Lorentz force model prior to irradiation, but that the  $J_c$  is relatively insensitive to the magnitude of the applied field, above certain levels, after irradiation.

A key point that has been brought out by a number of investigators, and by comparing the results of several groups, is that the magnitude of the irradiation induced effects observed is highly sensitive to the initial structure of the material, and therefore sensitive to material preparative variables. This implies a strong interaction between the grown-in defect structure and the irradiation induced defects. The "as prepared" defects may "short out" the radiation induced defects, or the induced defects may condense on the grown-in heterogeneities to form a network of larger, fewer, and less effective flux pinning centers. A similar interaction may also take place as the density of the irradiation induced defects increases. Several investigators have observed a peak in the enhancement of the critical current density as a function of exposure to the irradiation.

The size and density of the irradiation induced defects observed by transmission electron microscopy at one level of irradiation fits well into the flux pinning model. Additional studies at increased levels of irradiation exposure should contribute further to the understanding of the flux pinning model and to an explanation of the effects of irradiation on the superconducting properties which have already been observed.

#### REFERENCES

1. J. Livingston, these Proceedings, p. 377.
2. W. Webb, these Proceedings, p. 396.
3. P.W. Anderson, Phys. Rev. Letters 9, 309 (1962).
4. J. Friedel, P.G. de Gennes, and J. Matricon, Appl. Phys. Letters 2, 231 (1963).
5. J. Silcox and R.W. Rollins, Appl. Phys. Letters 2, 231 (1963); Rev. Mod. Phys. 36, 52 (1964).
6. Y.B. Kim, C.F. Hempstead, and A.R. Strnad, Phys. Rev. 129, 528 (1963).
7. P.W. Anderson and Y.B. Kim, Rev. Mod. Phys. 36, 39 (1964).
8. L. Rinderer and E. Schmid, in Proc. VII Intern. Conf. Low Temperature Physics, Toronto 1960 (University of Toronto Press, 1961), p. 395.

9. E.A. Lynton, B. Serif, and M. Zucker, J. Phys. Chem. Solids 3, 165 (1957).
10. A. van Itterbeek, L. van Poucke, Y. Bruynseraede, and J. David, Physica 34, 361 (1967).
11. W.F. Druyvesteyn and D.J. van Ooijen, Phys. Letters 4, 170 (1963).
12. J. Blank, B.B. Goodman, G. Kuhn, E.A. Lynton, and L. Weil, in Proc. VII Intern. Conf. Low Temperature Physics, Toronto 1960 (University of Toronto Press, 1961), p. 393.
13. H.T. Coffey, E.L. Keller, A. Patterson, and S.H. Autler, Phys. Rev. 155, 355 (1967).
14. R. Babcock and H. Riemersma, Appl. Phys. Letters 1, 43 (1962).
15. J.P. McEvoy, Jr., R.F. Decell, and R.L. Novak, Appl. Phys. Letters 4, 43 (1964).
16. E.I. Keller, H.T. Coffey, A. Patterson, and S.H. Autler, Appl. Phys. Letters 9, 270 (1966).
17. K.D. Chaudhuri, K. Mendelssohn, and M.W. Thompson, Cryogenics 1, 47 (1960).
18. P.S. Swartz, H.R. Hart, and R.L. Fleischer, Appl. Phys. Letters 4, 71 (1964).
19. R.H. Kernohan and S.T. Sekula, J. Appl. Phys. 38, 4904 (1967).
20. R.P. Tucker and S.M. Ohr, Phil. Mag. 16, 643 (1967).
21. C.P. Bean, R.L. Fleischer, P.S. Swartz, and H.R. Hart, J. Appl. Phys. 37, 2218 (1966).
22. J.J. Hanak, in Metallurgy of Advanced Electronic Materials, edited by G.E. Brock (Interscience Publishers, New York, 1963), p. 161.
23. J.J. Hanak, K. Strater, and G.W. Cullen, RCA Review 25, 342 (1964).
24. H.J. Bode and K. Wohlleben, Phys. Letters 24A, 25 (1967).
25. G.W. Cullen and R.L. Novak, Appl. Phys. Letters 4, 147 (1964).
26. G.W. Cullen and R.L. Novak, J. Appl. Phys. 37, 3348 (1966).
27. G.W. Cullen, Trans. Met. Soc. AIME 230, 1494 (1964).
28. J.J. Hanak and H.S. Berman, J. Phys. Chem. Solids, Supplement on Proc. Intern. Conf. Crystal Growth, p. 249 (1967).
29. G.W. Cullen, R.L. Novak, and J.P. McEvoy, RCA Review 25, 479 (1964).
30. G.W. Cullen, G.D. Cody, and J.P. McEvoy, Jr., Phys. Rev. 132, 577 (1963).
31. G.D. Cody, G.W. Cullen, and J.P. McEvoy, Rev. Mod. Phys. 36, 95 (1964).
32. J.L. Brimhall and B. Mastel, J. Appl. Phys. 38, 3027 (1967).
33. P.W. Woodard and G.D. Cody, RCA Review 25, 393 (1964).
34. J.L. Cooper, RCA Review 25, 405 (1964).
35. J. Silcox and P.B. Hirsch, Phil. Mag. 4, 1356 (1959).
36. M.C. Inman, RCA Internal Report (1966).

# NIOBIUM TIN AND RELATED SUPERCONDUCTORS\*

R.B. Britton  
Brookhaven National Laboratory  
Upton, New York

## I. INTRODUCTION

If we attempt to categorize the useful or promising superconductors, we find that they fit into three distinct groups. These are the brittle intermetallic compounds, the ductile metal alloys, and the pure metals. The pure metals are low critical field superconductors, several of which are important for rf cavities. The best compounds have critical magnetic fields and critical temperatures almost twice as high as the best known alloys. For this reason the superconductivity group at Brookhaven has worked mainly with Nb<sub>3</sub>Sn, the only compound available in useful form, in preference to the alloys. This paper will review our knowledge of the superconducting (hereafter SC) compounds and their properties, and who is developing each type. A review will also be made of our experiences with several conductors and of a technique for testing a complete conductor prior to using it in a device.

To show where the compounds fit into superconductivity, Table I gives comparative data about a few of the compounds, alloys, and elements. The difference in ductility of alloys vs compounds is stressed because it determines the geometry in which a material is useful. The compounds may be imagined to be like a ceramic. If they are strained appreciably, they fracture and the SC path is damaged. Therefore the commercially successful compound, Nb<sub>3</sub>Sn, has been made in ribbon form wherein the thickness of substrate plus SC is no more than 0.004 in. This theoretically allows the conductor to be wound about a diameter of 1 in. without damage. In actual practice, conductors with a 0.003 in. over-all thickness for the substrate and Nb<sub>3</sub>Sn have operated well when wound about a 0.25 in. diam post.

The alloys, by comparison, are ductile, and therefore they are practical and lowest in cost when manufactured as round wires. The cross-sectional shape of the alloy and compound conductors has had considerable effect on the winding design of magnets, particularly the paraxial conductor radial field beam magnets which have been recently constructed.

## II. THE SUPERCONDUCTIVE COMPOUNDS

Looking now at the compounds, the most unusual type of compound conductor is fabricated by the multiwire process, Fig. 1, developed by Professor Saur of the University of Giessen, West Germany. The wire starts as a tube about 0.5 in. in diameter into which fine tin-coated wires of niobium are inserted. Up to 900 wires are used in one conductor. The composite is then drawn to an over-all diameter of around 0.020 in. after which it is heat-treated at 900-1200°K to form Nb<sub>3</sub>Sn by a diffusion process at all interfaces between the Nb wires and the Sn matrix. The small size of the SC strands raises the critical field, H<sub>c</sub>, to about 250 kG and results in an over-all current density of 20 000 A/cm<sup>2</sup> at 210 kG. The current density of this conductor is relatively flat over a wide field range so that at fields below 150 kG it is surpassed by that of the Nb<sub>3</sub>Sn ribbons. With the 0.020 in. diam, this conductor must be used on

---

\* Work performed under the auspices of the U.S. Atomic Energy Commission.

TABLE I

Brittle Intermetallic Compounds	Critical Temperatures at B = 0	Critical Fields at 4°K	Comments
Nb <sub>3</sub> (Al <sub>0.8</sub> Ge <sub>0.2</sub> )	20.7°K		
Nb <sub>3</sub> Sn	18.2	245 kG	Only available compound
Nb <sub>3</sub> Al	17.5		
NbN	15.6	153	
Nb <sub>3</sub> Ga	14.5		
NbC	14.0		
V <sub>3</sub> Si	17.1	235	
V <sub>3</sub> Ga	16.8	210	
MoN	12.0		
MoGa <sub>4</sub>	9.8		
<u>Ductile Alloys</u>			
Nb-42Ti-6Ta	10 - 11	140 kG	Japanese development
Nb-48Ti	9.5	122	Best available alloy
Nb-33Zr	10.7	80	Becoming obsolete
Nb-25Zr	11.0	70	Becoming absolute
Pb-56Bi	8.8	15	
Mo-50Re	~ 10.0	~ 15	Used as fine wire for low fields
Bi50, Pb25, Cd12.5, Sn12.5 = Wood's metal	~ 8.0	12	
<u>Pure Metals</u>			
Nb	9.25	1985 G	Rf cavities
Tc	8.22	-	
La (B)	6.3	1600	
V	5.3	1020	
Ta	4.48	830	
Pb	7.19	803	Rf cavities and suggested for ac cables
Sn	3.72	309	
Re	1.698	198	
Ga	1.09	51	
Zr	0.546	47	
Ti	0.39	100	



a form of at least 2.5 to 3 in. diam or the SC filaments will be fractured. It would appear that flattening this conductor into a ribbon prior to heat treatment would make it more flexible and useful for bending around small diameters. If this material can be developed to withstand a small bending radius, it should find immediate use for the cores of high field solenoids. Since the Nb<sub>3</sub>Sn is formed by diffusion, one could undoubtedly form other SC compounds such as V<sub>3</sub>Ga by the same process.

The most popular type of Nb<sub>3</sub>Sn ribbon is the diffusion-formed material illustrated in Fig. 2. The manufacture begins with a niobium ribbon which is coated with tin, heat-treated at 900-1200°K for several hours, and then either clad or plated with a normal conductor such as copper or silver.

The ribbon in bare and copper-plated form was first available in 1964 as Niostan from the National Research Corporation and later from Supercon,<sup>1</sup> a division of the same company. The copper-plated material 0.25 in. wide by 0.0025 in. thick performed well in the first Panofsky-type quadrupoles at Brookhaven. Current densities of about 30 000 A/cm<sup>2</sup> were obtained at a peak field in the corners of about 20 kG. The copper-plated form of this ribbon 0.5 in. wide x 0.0013 in. thick next became available from CSF<sup>2</sup> in 1965. CSF now offers single and double ribbon substrates with Cu plating or cladding in various total thicknesses from 0.0012 to 0.011 in. Standard widths are 6.4, 10, 12.7, and 20 mm. In the United States, CSF superconductors are now distributed by Kawecki.<sup>3</sup>

A diffusion-type Nb<sub>3</sub>Sn ribbon with copper cladding (Cryotape) was offered next by GE<sup>4</sup> in November of 1965. Their commercial ribbons have typically been 0.5 in. wide by 0.0032 and 0.0037 in. thick with ratings of 150 and 300 A respectively at 100 kG. Ribbons with thicker copper - up to 0.010 in. total thickness - as well as more Nb<sub>3</sub>Sn - up to 600 A rating - are available on special order. Figures 3, 4, and 5 are microphotographs of cross sections of GE 150, 300, and 600 ribbons. GE can also produce several of their ribbons with either a single or double substrate, as is observable by comparing Figs. 3 and 4 with Fig. 5. They also offer stainless steel cladding for use in solenoids where the product of radius times current times field yields a force which exceeds the yield strength of soft or hard copper cladding.

In March of 1968, Plessey<sup>5</sup> introduced a diffusion type Nb<sub>3</sub>Sn ribbon (Super Magloy 1) which is available copper clad on one or both sides with a thickness of 0.002 or 0.003 in. Standard width at present is 0.25 in.

A V<sub>3</sub>Ga ribbon of the diffusion type has been developed by Tachikawa<sup>6</sup> during the past year and was tested to current densities of about 20 000 A/cm<sup>2</sup> at 200 kG. The critical field is above 200 kG. The process includes tinning a V ribbon with Ga,

- 
1. Supercon Division of National Research Corporation, 9 Erie Drive, Natick, Massachusetts 01762.
  2. Compagnie Générale de Télégraphie Sans Fil (CSF), 12 Rue de la République, 92 Puteaux, France.
  3. Kawecki Chemical Company, 220 East 42nd Street, New York, N.Y. 10017.
  4. General Electric Vacuum Products, 1 River Road, Schenectady, New York 12305.
  5. The Plessey Company, Ltd., Preformations Division, Cheney Manor, Swindon, Wiltshire, England.
  6. Kyōji Tachikawa, Satoshi Fukuda, and Yoshiaki Tanada, National Research Institute for Metals, Mogūro-Ku, Tokyo, Japan.

plating the Ga with Cu, and then heat-treating at around 980°K for 10 hours. This ribbon is not available commercially.

The vapor deposition process has been equally successful for forming Nb<sub>3</sub>Sn ribbon as illustrated in Fig. 6. The leader in development and sole commercial producer of this material since the summer of 1963 has been RCA.<sup>7</sup> The process uses a quartz furnace heated to 970°K, which is fed with SnCl<sub>2</sub>, NbCl<sub>4</sub>, HCl, H<sub>2</sub>, and He gases, through which the heated ribbon (1270°K) passes. The high thermal energy of the ribbon is sufficient to cause decomposition of the molecular gases on contact such that Sn and Nb appear at the surface in the proper proportions to form superconductive Nb<sub>3</sub>Sn compounds. The large number of variables in this process as compared with the diffusion process allows a greater degree of optimization to be attained. There apparently are differences in the final products since the vapor-deposited ribbon has a critical temperature around 15°K compared with 18°K for the diffusion process material.

Following the deposition of SC, the ribbon is electroplated with a thin layer of Ni and then it is either plated with 0.0005 to 0.0015 in. of pure Ag or clad with 0.001 to 0.004 in. of pure copper. Variations in thickness which originally occurred in the Ag-plated ribbon have now been reduced by a machining process that should hold the thickness tolerance to  $\pm 0.0001$  in.

RCA's commercial production has mainly been of 0.090 in. wide ribbon in at least three current ratings - 60, 110 and 220 A at 100 kG - with Ag plating or Cu cladding to order. With standard Ag plating the thicknesses are 0.0044 and 0.0052 in. A recent addition to their production has been 0.500 in. wide ribbon, developed under contract from Brookhaven. The wide ribbon is available in 300, 600, 900, and 1200 A ratings at 100 kG with either Ag plating or Cu cladding for electrical stabilization. Figures 7, 8, and 9 illustrate developmental ribbons with current ratings of 800, 1200, and 1100 A. The 800 and 1200 photos show defects that seem to be related to loss in stability of these ribbons - namely, delamination within the SC layer and porosity of the SC layer. Both of these ribbons were limited to around 35 000 A/cm<sup>2</sup> when tested in pie windings of around 200 m length. The 1100 sample, which contains a dense SC layer, is from a ribbon length which carries 72 000 A/cm<sup>2</sup>, the highest current density ever achieved in a solenoid at Brookhaven. The "1100" was obtained by extrapolation from 68 kG at which field this 0.005 in. thick ribbon carried 1600 A.

In making coils for use with pulsed currents or 60 Hz current, it is essential to avoid electrical shorts between turns. To do this without greatly reducing the turn density is easiest when redundancy is used in the insulation. This has been accomplished by using insulated ribbon in combination with 0.0005 to 0.002 in. Mylar interleaving for a total insulation of no more than 0.001 to 0.003 in. per turn. When bare ribbon is used, Mylar of 0.005 to 0.010 in. is usually required to avoid shorting by burrs on the edges.

All of the commercial diffusion-type ribbons are offered either bare or insulated with varnish about 0.0003 in. thick per side. The vapor-deposited ribbon has not yet been offered with insulation.

A comparison between most of these superconductors may be seen in Fig. 10 where useful current density,  $J_c$ , taken from manufacturers' curves has been plotted against B, the magnetic field perpendicular to the length of the conductor and parallel with its surface. "Useful" is used here to indicate that the current densities have been based on the area per turn in a typical winding rather than the area of a bare conductor.

---

7. Marketing Department, RCA Superconductive Products, Building 18-3, Harrison, New Jersey 07029.

It must also be understood that the currents are based on short sample measurements, and in actual use in an inductive coil, instabilities will occur which tend to prevent current densities at low fields from exceeding those usually obtainable at 80 to 100 kG. When coils are used as inserts and operated in high background fields, the instabilities tend to disappear and straight sample performances are more likely to be obtained.

At fields above 140 kG, it may be seen that V<sub>3</sub>Ga ribbon and Nb<sub>3</sub>Sn multiwire promise large current density gains over the present commercial products.

At fields below 140 kG, it is painfully clear that the 20 000 A/cm<sup>2</sup> recommended by RCA as proper design for solenoids is far below the current densities obtainable in noninductive samples.

### III. STABILITY

The question now arises as to why a solenoid or inductive sample of SC has a lower quench current than a noninductive SC. There is no concise answer at the present time, but a few facts are considered to be relevant. First, no SC is at present used alone as a high field magnet conductor, mainly because the spontaneous occurrence of a normal (and therefore highly resistive) region in the conductor can cause a sudden burst of joule heating which exceeds the heat transfer capability to the He bath. The result is a rapid local temperature rise and associated increase in the length of the normal region, with an ensuing radial spread of the normal region throughout the solenoid, more commonly referred to as a "quench." The universally accepted method for reducing this "quench" problem is to combine a normal conductor (NC) in parallel with the SC. Now the NC (high purity Ag or Cu) can have a very low resistance in comparison with the normal SC, in fact perhaps only 1/2000 to 1/10 000 as much for an equal thickness. This low resistance material in parallel with the SC apparently serves to reduce greatly the I<sup>2</sup>R joule heating and also to conduct this heat edgewise so that it may transfer to the He bath. The result is a composite conductor which is capable of much higher current densities before the onset of instability, or inability to recover from a normal spot. The optimum amount of NC for 0.5 in. wide ribbon appears to be about 0.001 in. of copper per 0.00025 in. of Nb<sub>3</sub>Sn SC. In actual fact, the stability of the composite is affected by many parameters, including dB<sub>⊥</sub>/dI and B at the position of the conductor and the exposure of the edges and faces of the conductor to liquid helium. dB<sub>⊥</sub>/dI, in this case, is the change in field perpendicular to the ribbon face per unit change in ribbon transport current. B is the background field surrounding the conductor in which the coil is situated.

### IV. EXPERIMENTAL RESULTS

A few results which have been obtained in Sampson's laboratory with devices made from Nb<sub>3</sub>Sn are shown by the points on Fig. 10. Δ<sub>2</sub> is a 1.25 in. bore solenoid made in 1964 which operates at 43 000 A/cm<sup>2</sup> and 83 kG. Δ<sub>1</sub> is a 1.0 in. solenoid made in 1966 which operates at 39 000 A/cm<sup>2</sup> and 103 kG. Δ<sub>3</sub> is a 0.62 in. i.d. x 1.25 in. o.d. insert which operates at 51 000 A/cm<sup>2</sup> and 119 kG. This same coil, operated by itself in superfluid He, produced 48 kG at a J of 71 000 A/cm<sup>2</sup>. The preceding coils were made of 0.090 in. wide vapor-deposited, silver-plated ribbon wound in layers.

Various coils of 0.500 in. wide ribbon are shown by Δ<sub>4</sub>, a 1.5 in. bore pie which produced 69 kG at 71 000 A/cm<sup>2</sup>, Δ<sub>5</sub>, which is a 5.0 in. bore pie winding that produces 50 kG at 41 000 A/cm<sup>2</sup>, and Δ<sub>6</sub>, a quadrupole of 4.0 in. bore x 24 in. length which carries 26 000 A/cm<sup>2</sup> at 20 kG.

Δ<sub>7</sub> shows, for comparison purposes, a Nb<sub>25</sub>Zr solenoid which operates stably at

26 000 A/cm<sup>2</sup> and 53 kG. Since the coil forms are identical,  $\Delta_2$  and  $\Delta_7$  would lie on the same load line.

One characteristic of Nb<sub>3</sub>Sn ribbon which is closely related to stability is flux jumping in inductive solenoids. Flux jumping is observed as voltage spikes that override the emf seen across a coil when the current level is being swept up or down. The size and frequency of flux jumps are always small in coils which are capable of reaching  $I_c$  (where the load line crosses the B-I curve for the conductor), while jumps are large and numerous in unstable coils that quench prior to reaching  $I_c$ .

When all other conditions are held equal, flux jumping is probably dependent on the ratio of superconductor to normal conductor. In other words, a conductor with a very thick Nb<sub>3</sub>Sn layer (say 0.0005 in. or greater) and an Ag or Cu layer less than 0.001 in. thick would make a jumpy or unstable coil.

Stability in coils has been shown by Morgan and Dahl<sup>8</sup> to be related to inductance and, therefore, presumably to dB/dI, by a test of an inductively wound vs a noninductively wound pie of identical geometry and ribbon length. A current of 1350 A was not sufficient to drive the noninductive coil normal while the inductive coil had an instability limit around 800 A.

## V. TESTING TECHNIQUES

Since work was begun at Brookhaven on Nb<sub>3</sub>Sn ribbon, there has been a search for better methods to test materials prior to actually building a device with them. The first method was to cut a short (~ 1.0 in. long) sample from each end of each ribbon length, clamp it between copper blocks, and measure its critical current as a function of magnetic field perpendicular to the current flow. Then if a solenoid were made from this batch of ribbon, the lengths would be wound such that the highest current densities were on the inside. The problem with short sample tests is that they indicate almost nothing about the stability of a long length of ribbon, as may be seen from the high current densities obtainable at low fields in short samples compared with the low current densities which are actually possible in coils.

Once a solenoid is assembled, an obvious test is to measure the current limit of each length of ribbon in it. This is most informative when tests are performed at various current sweep rates and at several levels of fixed background field produced by the outer sections. Any length which operates poorly in the coil is then replaced.

A third method for testing is to energize a complete solenoid in series and put it into the persistent mode with a shorting switch. After it has stabilized, emf's are read across each section to locate bad joints and poor lengths of ribbon.

A continuous testing method for Nb<sub>3</sub>Sn ribbon has also been developed. The ribbon is passed through a Dewar at a rate up to 0.5 m/sec and, en route, it passes through a magnetic field of 50 kG. At the entrance to and exit from the field, coils encircle or lie close to the face of the ribbon and produce an output which is related to the diamagnetic properties of the SC ribbon and to the nature of the NC bonded to it. With an integrator driven by the coils connected in opposition, the diamagnetic strength of the SC layer has been measured and defects have been detected in the SC and in the SC to NC bond.

---

8. G.H. Morgan and P.F. Dahl, Brookhaven National Laboratory, private communication.

Another test which has been used by Sampson recently is measurement of the conductivity of the normal conductor at close to SC temperatures. It has been found that Cu cladding used by manufacturers has around twice the conductivity of Ag plating. It has also been found that the Ag plating will increase in conductivity by a factor of about two (becoming equal to the Cu) when it is properly annealed. Even after annealing, the Ag plating is poor (resistance ratio  $\sim 60$ ) compared with commercial fine silver foil (resistance ratio  $\sim 200$ ). In tests of solenoids made of 0.090 in. ribbon as well as pies made of 0.500 in. ribbon, there appears to be a positive correlation between conductivity of the plating and stability of the coil. This has been shown with two coils each containing approximately 1000 m of 0.090 in. ribbon which operated unstably and would only carry 60-70 A. After annealing, the current limits were raised to around 95 A, which was still not at the B-I limit.

Another test which we have made on superconductors to understand their performance is to measure their critical temperatures. A coil containing approximately 1 ft of conductor with thermocouples and current leads attached to each end is enclosed in a copper sheet to provide a uniform temperature environment. With 10 A flowing through the coil, it is slowly raised out of the helium bath while thermocouple emf is read from each end of the coil. When the emf across the sample reaches 1 mV, it is assumed to be above  $T_c$  at the high temperature end. The two ends were never more than 0.5°K apart. The only difference found to date is that vapor-deposited ribbon has a  $T_c < 15^\circ\text{K}$  while diffusion ribbon has a  $T_c \approx 17.5^\circ\text{K}$ .

A newly established method<sup>9</sup> by which we can test complete lengths of 0.500 in. ribbon for stability is the 5.0 in. bore pie test. The usual run of lengths is from 180 to 500 m and over this range, the value of  $dB_L/dI$  at the inner turn is a very weak function of the amount of ribbon being tested. These coils are very easy to construct and test compared with useful magnets, so it is advantageous to test lengths of ribbon in this fashion prior to winding them into a more complex design. At present, some 20 pieces of ribbon (approximately 300 m each) have been tested this way and current densities have varied from 22 000 to 54 000 A/cm<sup>2</sup> at fields to 70 kG. The time saving with the pie test is large when you consider that four ribbon lengths for a quadrupole may be wound as pies and tested in two man days compared with eight man days required to perform the same experiments with the quadrupole.

---

9. Specification for Superconductive Ribbon, Brookhaven National Laboratory SPEC. AGS-481, June 18, 1968.

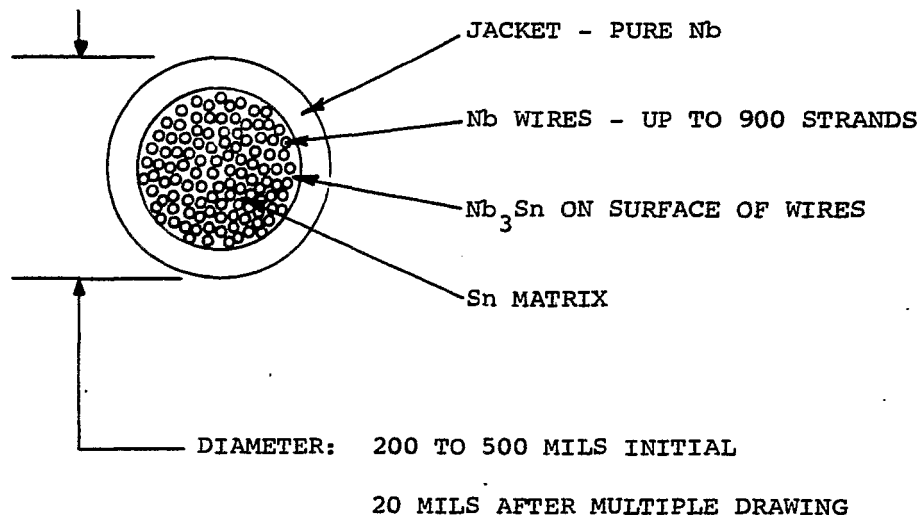


Fig. 1. Multiwire diffusion process.

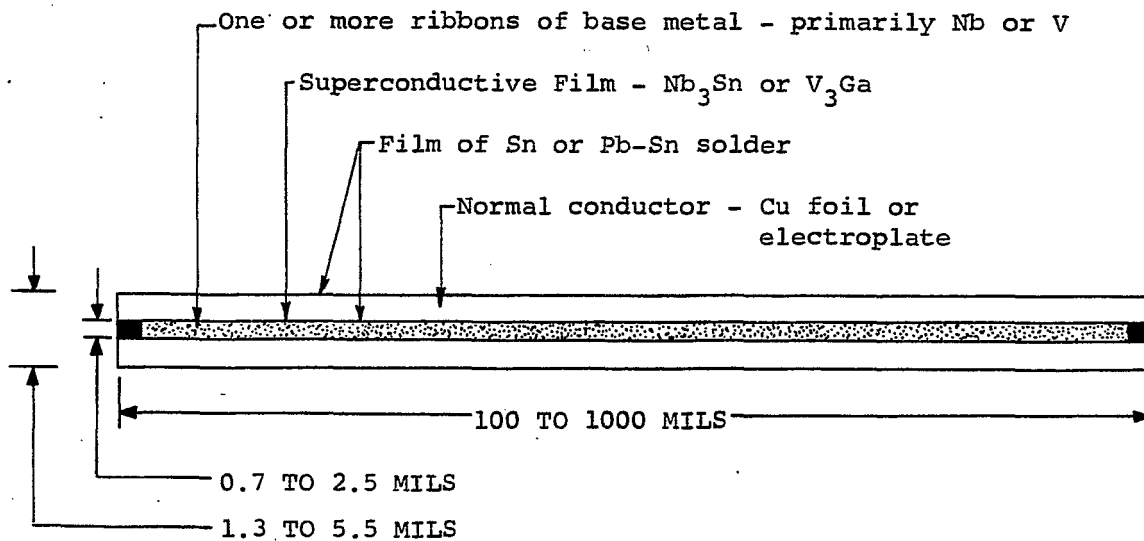


Fig. 2. Diffusion process -  $Nb_3Sn$  or  $V_3Ga$  ribbon.

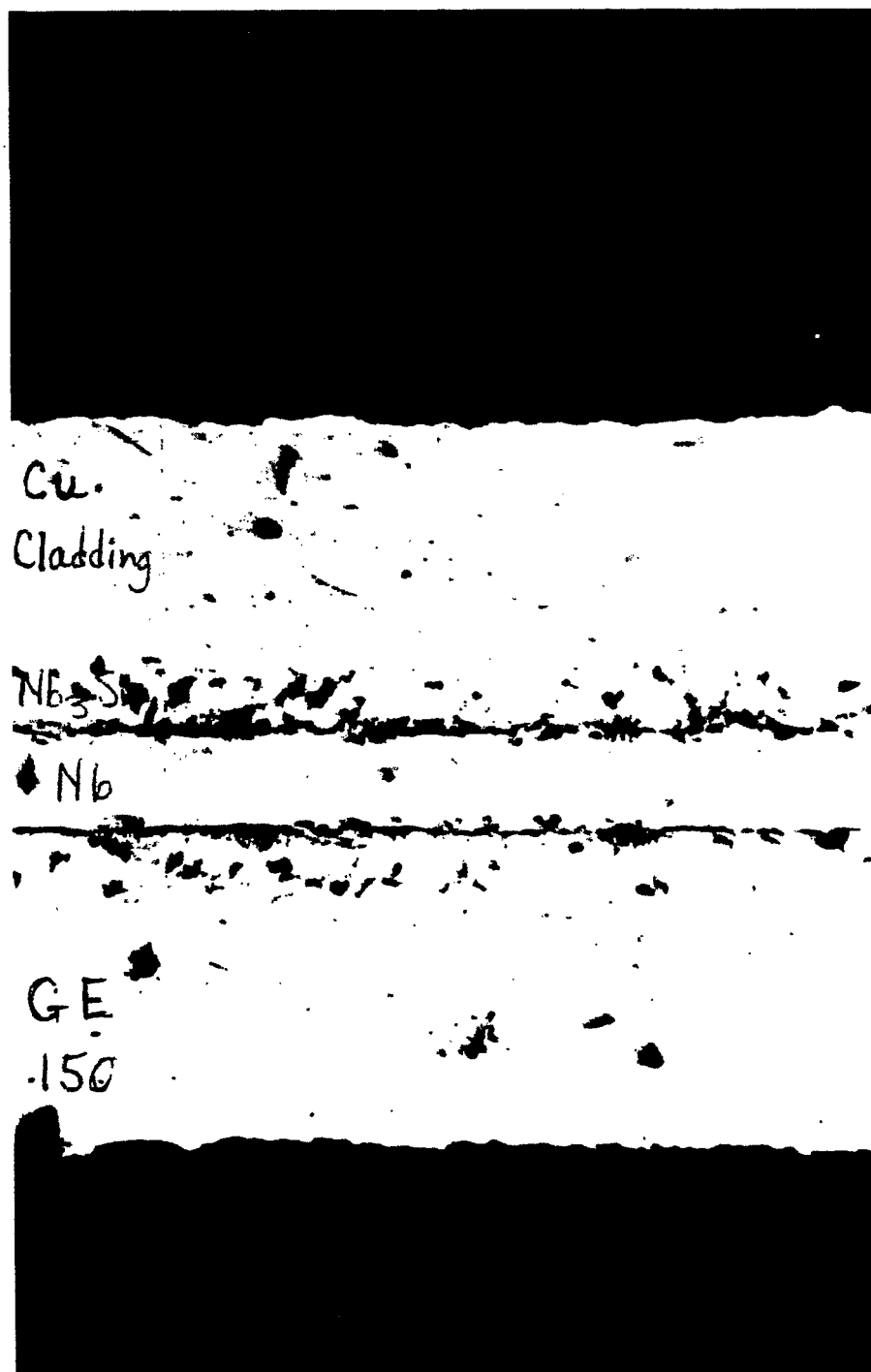


Fig. 3. Microphotograph of cross section - GE 150 ribbon.



GE  
300

The image is a high-contrast, black and white microphotograph showing a cross-section of a material. It features three distinct horizontal layers. The top layer is a solid, dark, rectangular block. Below it is a thin, light-colored layer with a granular or speckled texture. The middle layer is a darker, more irregular band with some internal structure. Below that is another thin, light-colored granular layer. The bottom layer is a dark, irregular band. The overall appearance is that of a layered material, possibly a composite or a coated metal. The text 'GE 300' is handwritten on the left side of the image.

Fig. 4. Microphotograph of cross section — GE 300 ribbon.



Ca

Judding

$Nb_3Sn$

Nb

$Nb_3Sn$

Nb

GE

600

Fig. 5. Microphotograph of cross section - GE 600 ribbon.

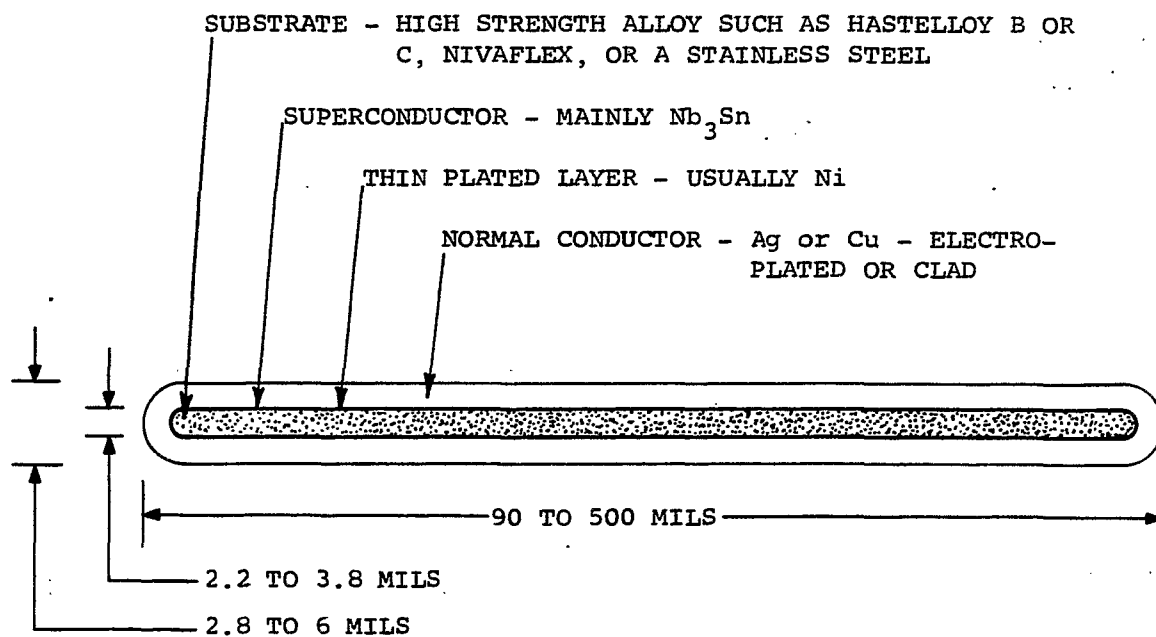


Fig. 6. Vapor-deposition process -  $Nb_3Sn$  ribbon.

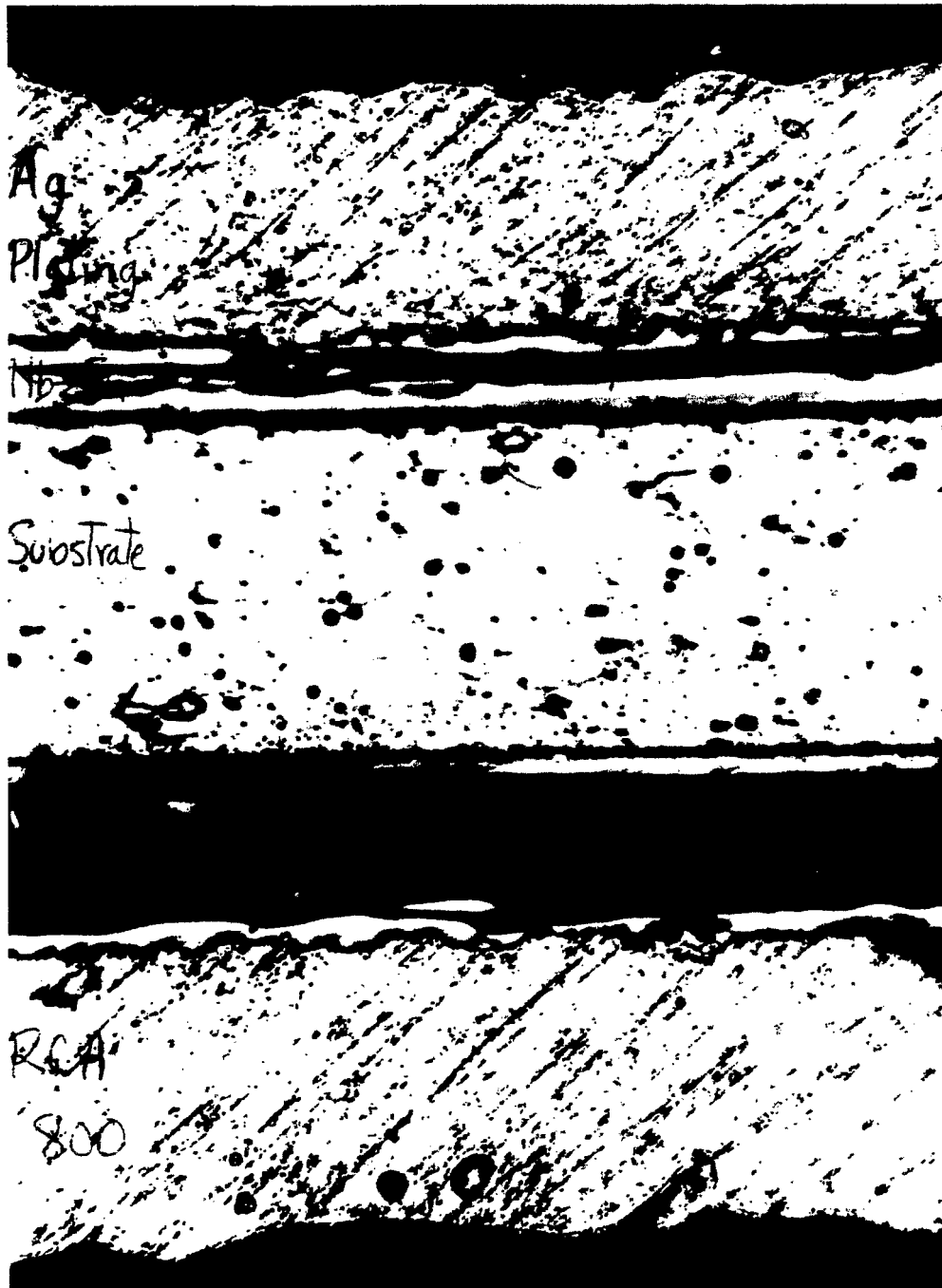


Fig. 7. Microphotograph of cross section — RCA 800 developmental ribbon.

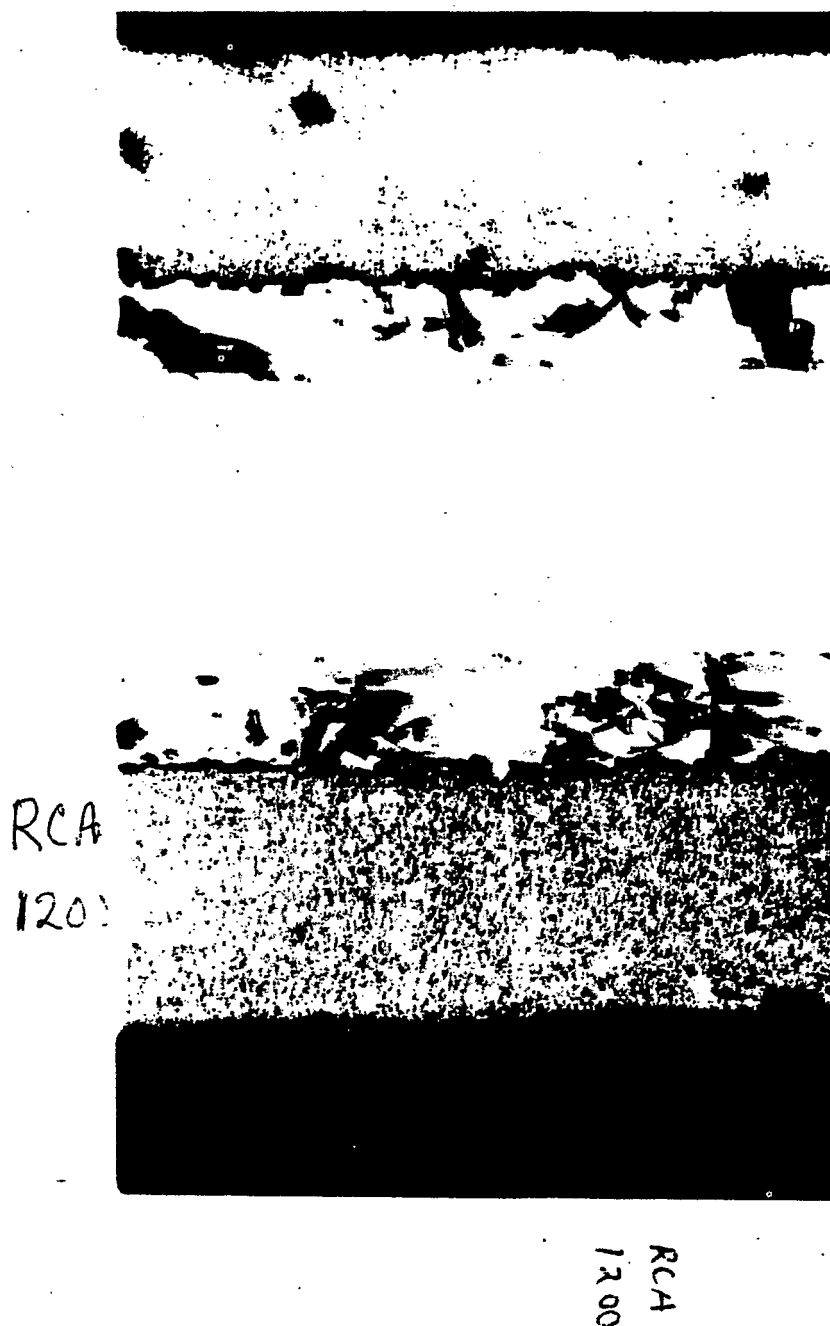


Fig. 8. Microphotograph of cross section - RCA 1200 developmental ribbon.

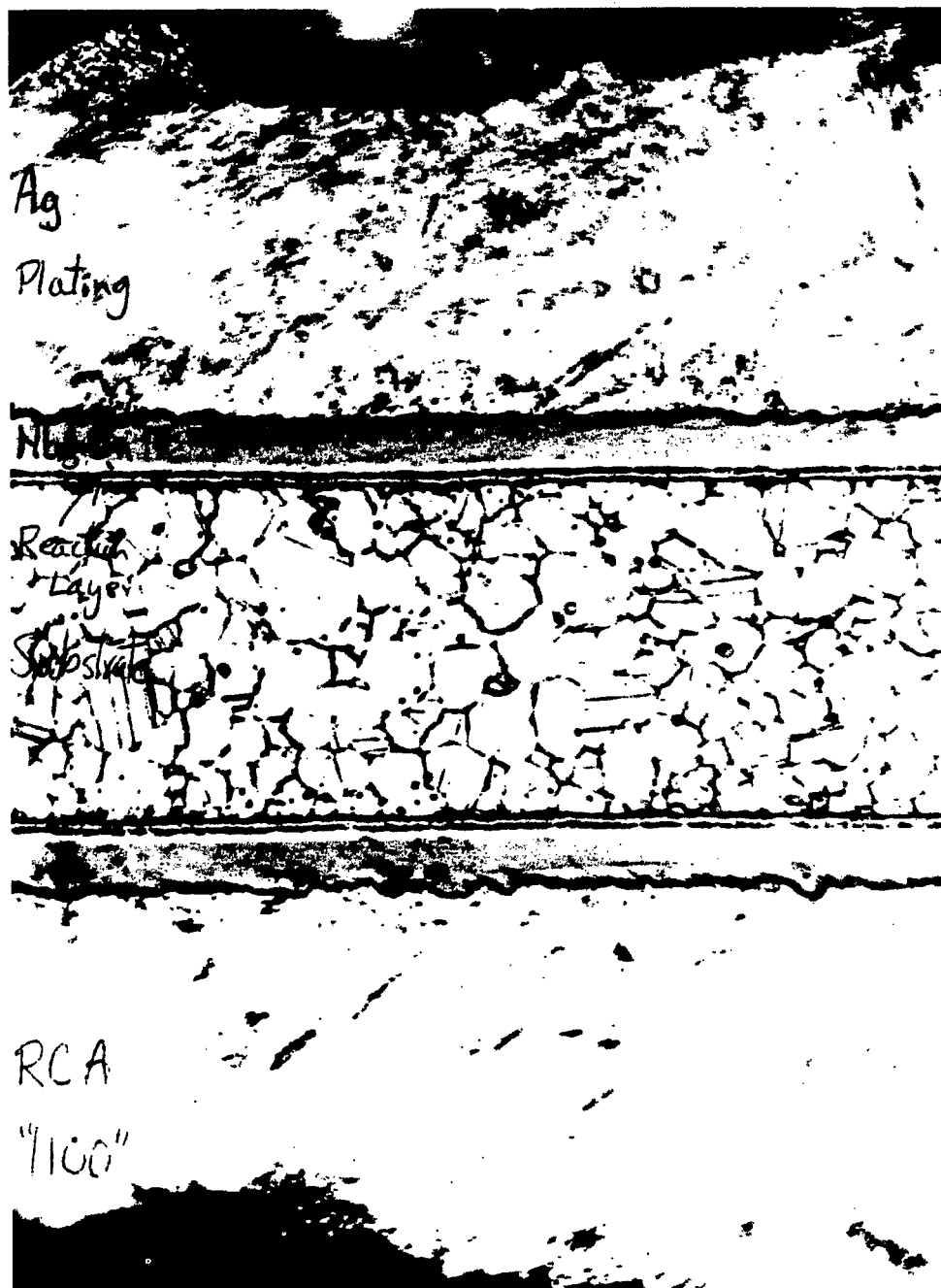


Fig. 9. Microphotograph of cross section - RCA "1100" developmental ribbon.

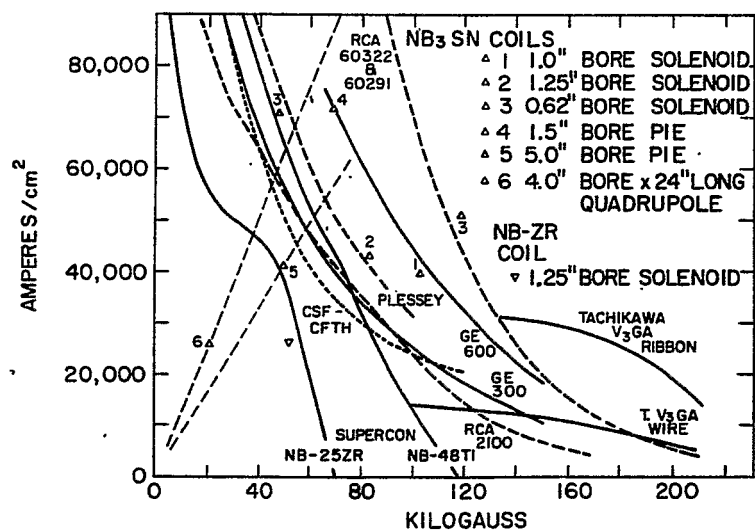


Fig. 10. Useful current density vs field at 4.2°K

## COMPOSITE MATERIALS\*

A.D. McInturff  
Brookhaven National Laboratory  
Upton, New York

This talk will be a briefing on the "state of the art" as it is known by the author. Most of the information acquired with respect to fabrication was obtained while the author was a "Senior Research Physicist" at Atomics International, where metallurgist Gordon Chase and the author worked on alloy development of TiNb as a superconductor. A small fraction of the metallurgical work presented here was performed after the author's arrival at Brookhaven.

There are certain criteria which will be applied to a material to rate its usefulness. (These are by no means all the criteria that are relevant, e.g., upper critical field, critical temperature, etc.) These criteria are:

- 1) The critical current density for the superconductor plus normal material [Cu, Ag, and/or mechanical support material, if needed, etc. (maximum)] vs applied perpendicular magnetic field.
- 2) The magnetization of the materials [this is a function of  $J_c$  ( $H_{\text{applied}}$ ) and geometry, thermal and electrical environment (minimum)].
- 3) Flux jump stability [this parameter is a function of mechanical rigidity and criteria 1) and 2) (maximum)].
- 4) Reproducibility of these properties with a given production process:
  - a) For small quantities and all sizes of conductors.
  - b) For larger quantities and all sizes of conductors.

The materials used in the experiments were in most cases commercially available samples with known metallurgical histories. Some were obtained to test from users, who had them submitted by the producers for a particular contract. Samples tested originated from the following manufacturers: Atomics International, Avco, Cryomagnetics, General Electric, Radio Corporation of America, and Supercon. This paper will not refer to a sample by its producer, because in certain cases a great deal of time was spent to find a piece of the material which displayed a desired characteristic, be it an asset or a detriment. The materials tested were  $Nb_3Sn$  and various alloys of TiNb. Most of the fabrication techniques with respect to composites where applicable to TiNb alloys are usually applicable to NbZr alloys as well.

The composites discussed will be of three different types. There will be some overlap, of course. These types are:

### I. Cable (strands):

- A. Cable composed of a nonstabilized individual superconductor, stranded with and soldered to stabilizing, high-conductivity normal material (e.g., annealed Cu). (See Fig. 1.)

---

\* Work performed under the auspices of the U.S. Atomic Energy Commission.

B. Cable composed of individually stabilized wires, where the normal metal jacket is thick enough to enable the entire superconductor to go into the normal state, and the current to divert through the high-conductivity jacket without sufficient heat being generated to cause the normal region to propagate to the rest of the conductor, stranded and soldered together to produce a high-current cable. Actually, this type can be run under partially stabilized or fully stabilized conditions quite reliably.

II. The filamentary or strand composite [which will include from a few to several hundred filaments ( $\leq 0.01$  cm in diameter) or strands ( $\geq 0.01$  cm in diameter)]:

The superconductor is located as filaments or strands in (a) a metallurgically, or (b) a mechanically-bonded, high-conductivity metal matrix. There may be sufficient high-conductivity metal present to stabilize the total composite current or a fraction thereof. (See Fig. 2.)

III. A multilayered composite, which might be fabricated by the following processes:

A. Vapor deposition (normally a ribbon geometry). (See Fig. 3.)

B. Soldered layers (normally a ribbon geometry).

C. Plating.

D. Diffusion (or reacted). (See Fig. 4.)

E. Casting (normally a ribbon geometry).

F. Any combination of the above.

The actual fabrication of the ductile alloys (e.g., TiNb) that would go into types I, II, III-B, III-C, and III-E of the composites will be evaluated with respect to criteria 1), 2), and 3).

There are various metallurgical processes for a given alloy which can optimize criterion 1), i.e., obtain the maximum critical transport supercurrent for a given perpendicular applied field. The process usually consists of some schedule of heat treatment and cold work (% area reduction). Both of these processes are thought to provide pinning sites in the alloy.<sup>1,2</sup>

The yield point and fracture point start to coincide and the hardness increases as the critical current of these alloys increases in the region where the applied fields are in excess of that required to totally penetrate the superconductor with flux. Therefore, the difficulty of further fabrication or handling of the alloys in this metallurgical state, where they would have a high current density, is greatly increased.

The mechanical parameters and the flux jump stability of the sample are quite different depending on whether the last step in the process is cold work (reduction) or heat treatment.

---

1. J.B. Vetrano and R.W. Boom, J. Appl. Phys. 36, 1179 (1965).

2. A.D. McInturff et al., J. Appl. Phys. 38, 524 (1967).



A superconducting sample, whose critical current density is not maximized with respect to the variation of the last step in the fabrication process (e.g., cold work or heat treatment time) will in general not undergo flux jumps at fields in excess of the penetration field if the bond (metallurgical or mechanical) between the alloy and the high-conductivity material (thermal and/or electrical) is good (low resistance). Even if the sample undergoes flux jumps in that region, the flux jumps will tend to be localized and not occur across the entire conductor.

If samples are being mapped for a maximum in the critical transport current density at a given perpendicular field  $H_a$  [where  $H_a \gg H^*$  (field of complete magnetic flux penetration) as shown in Fig. 5] as a function of various values for the last step in fabrication (e.g., % cold work), certain generalizations may be made about the resulting superconductor. These generalizations, of course, are subject to the bond quality. Assume that it is good (high conductivity, thermal and/or electrical). The samples which lie to the left of the peak will either not undergo flux jumps, or if they do, the jumps will tend to be localized and less numerous. The samples which lie on the right side of the peak (Fig. 5) will have flux jumps which are both numerous and catastrophic.

There are various possibilities that will cause flux jump instability to increase in frequency and/or magnitude:

- 1) A diffusion layer of the superconductor into the high-conductivity surroundings, causing a resistive bond at very low applied fields (either excess heat treat temperature and/or time). (A very thick layer of alloys and/or compounds formed by the superconducting alloy and the interdiffusion and reaction of the high-conductivity matrix.)
- 2) A mechanical breaking of the bond.
- 3) Physical break-up of the superconductor because of brittleness.
- 4) Cold-working of the superconductor to a high degree as the last step.

It should be noted here that although one can usually obtain slightly higher current densities for short samples with cold work as the last step in fabrication, the resulting superconductor is, in general, much more flux-jump unstable, the reason being that  $\partial J_c(H)/\partial H$  has a larger magnitude for cold-worked samples in general. Such samples can be used reliably only in composites I-A, II-B (with a lower conductivity jacket, e.g., cold-worked Cu), and III-B, which tends to negate the higher current density in the windings due to lower over-all current densities of the resulting composite. The reproducibility of the desired characteristic in large quantities (or even the production of long, continuous lengths) is much more difficult. The chances of mechanically breaking the superconductor to high-conductivity metal bond is greater for this type of fabrication.

Heat treatment, as a last step in a process, can result in diffusion layers being formed between the superconductor and the high-conductivity material. This is usually the result of excessive heat treat temperature in an effort to obtain a maximum  $J_c(H)$  in a desirably (from a production cost standpoint) short time.

It should be noted that even with vapor-deposited superconductors ( $Nb_3Sn$  or  $TiNb$ ) that have been plated or vapor-deposited over with a high-conductivity material, a heat treatment which metallurgically bonds the components together will greatly affect the flux-jump stability (see Fig. 6).

It is obvious from the figures that the high-conductivity matrix affects the behavior of the superconductor drastically. This point will be expanded in the Ac Session paper.

Geometry is probably the next most important factor to be considered. In Fig. 7 an extreme example (a thin sheet geometry of Nb<sub>3</sub>Sn) is taken with the upper diagram representing the hysteresis curve for 0.97 cm width, the middle, 0.6 cm width, and the lower, 0.3 cm width. Data for TiNb on a similar geometry displayed the same behavior. No matter how good the mechanical and thermal environment, if the geometry is poor the performance will be likewise.

When size independence experiments<sup>2</sup> were performed and found to be valid, two large conductors were designed and fabricated. It was found that, although they had extremely high critical currents during short sample tests with large cold-welded leads on them, a magnet section that was fabricated with them was very noisy (large number of flux jumps), and great care had to be taken during the charging cycle during which there was a large helium boil-off.<sup>3</sup> This behavior was due to the flux-jump instability in the particular geometry chosen, namely that of a very large superconductor (which of course is a very cheap conductor to fabricate). This problem can be partially remedied by applying a saturation field with the outer sections of the magnet. The effectiveness of the saturation field results from the fact that most of the flux jumps occur at fields less than 10 kG in Ti22a/oNb. There have been samples fabricated as large as 0.170 cm. Although with large leads cold-welded to them and with a low resistance shunt across them, these large samples would carry very high current densities (up to short sample characteristics of smaller samples), they were flux-jump unstable. The effects of this instability can be remedied with massive amounts of high-conductivity material in good electrical contact with the superconductor (e.g., I-B, II, III-A, III-E). The jumps will still occur, but the magnet will not quench, a relatively poor design in light of up-to-date information.

Now to recapitulate the discussion, an outline is presented which uses the various composites as the division basis and the performance standards as subdivisions.

I. Stranded cable - materials normally used are a ductile alloy of TiNb or NbZr potted in a solder.

A. Composed of nonstabilized superconductors.

1. The critical current density vs applied magnetic field of the superconductors can be quite high, but by the time the stabilizing or partially stabilizing high-conductivity material and solder are added, the over-all current density is quite a bit lower,  $\approx 10^4 \rightarrow 10^3$ .
2. Magnetization of the composite is completely a function of the size of the superconductors used for a given cross section of superconductor desired.
3. Flux-jump stability of the composite is a function of the impregnation of the cable and that of the individual conductors (geometry, metallurgical history, etc.).

B. Composed of stabilized superconductors.

1. Critical current density vs applied field is good. After a number of these stabilized wires are stranded together their combined current density is less markedly reduced,  $\approx 10^4$ .
2. The magnetization of the composite is determined by the size of the individual superconductors for a given cross section of superconductor desired (these are normally twisted).

---

3. H. Brechna, private communication.

3. Flux-jump stability is no longer a function of the impregnation of the cable, only that of the individual conductor jacket (geometry, metallurgical history, etc.). I-B is usually much more stable with smaller losses during charging of a coil than I-A. Because of the greater flux-jump stability, the smaller diameter I-B types can more readily be run in a partially stabilized configuration than the smaller diameter I-A types.

II. Filamentary or strand composite — materials normally used are the ductile alloys (e.g., TiNb, NbZr), but if a high-temperature, high-conductivity material were available with slow Sn diffusion rate — slower than Nb — then the intermetallic compounds such as Nb<sub>3</sub>Sn with their higher H<sub>c2</sub> and T<sub>c</sub> could be used. Normally, the last step in fabrication is a heat treatment.

A. Metallurgically bonded (usually an extruded plug in a soft-annealed state and subsequently drawn and then heat treated).

1. The critical current density is at an optimum for any configuration (geometry) that is desired, be it filamentary or strands. It may be totally stabilized or only partially. The ability to reproduce short-sample characteristics is excellent in such a process.
2. The magnetization curves are governed by the individual size of the filaments or strands and their proximity to one another. [Enhancement factors of three have been found by proximities of the order of filament diameters (0.003 cm) in samples 7 cm long.] The ratio of the magnitude of the magnetization of the composite to a given total cross section for the superconductor may be minimized here by variation of the filament size and various properties of the surrounding matrix.
3. The flux-jump stability, where a heat treatment is picked to give optimum conductivity of the matrix, optimum bond of matrix to superconductor, and high J<sub>c</sub>(H<sub>applied</sub>), can be maximized by minimizing the absolute value of  $\partial J_c(H)/\partial H_T$  const. and  $\partial J_c(T)/\partial T_H$  const.

B. Mechanically bonded (same as II-A above).

III. Multilayer composite (usually ribbons). The intermetallic compounds such as Nb<sub>3</sub>Sn are normally commercially made in this form, but the ductile alloys may also be fabricated in this form.

A. Vapor deposition — evaporation process is versatile and allows production of composite conductors that cannot be made otherwise. The process is most efficient for depositions  $\geq 0.003$  cm thick over large areas, for example 0.003 cm of TiNb may be deposited on 5 to 15 cm wide strips at the rate of 120 m/h using 30 kW for evaporation.

1. Critical current densities vs applied field are good although those achieved so far seem to be slightly less than those obtained with other methods of fabrication (this observation is for ductile alloys only).
2. Magnetization curves for normal vapor-deposited composites tend to be high due to their width (perpendicular magnetic field). In some cases the samples are in the form of a flattened-out cylinder. This can be remedied somewhat by subdivision.

3. Flux-jump stability is not optimum here, but this is a function of the normal geometry (ribbon-like), not the process. It is critical in the thin disk configuration.
- B. Soldered layers. Here the individual superconductor is soldered into a stabilizing or partially stabilizing matrix.
1. Critical current density in the superconductor may be quite high, but in the entire composite it is considerably reduced for complete stability. The process is normally difficult for more than a few such layers.
  2. Magnetization of the composite is usually that of the superconductor. Here again the geometry is usually poor (wide one) and the magnetization is quite large.
  3. The flux-jump stability for this type is not optimum due to normal geometry. It also suffers from one more drawback than III-A, namely that of impregnation of the composite with solder, and hence, the possibility of voids.
- C. Plated composite. This is a process normally used to give partial stability to the material (adding on high-conductivity material), and results mainly in aiding criterion 3), "greater flux-jump stability." This process does not lend itself readily to the fabrication of very thick layers.
1. Same as III-A-1.
  2. Same as III-A-2.
  3. Same as III-A-3.
- D. Diffusion composite. The conductors normally fabricated by this process are in the form of a ribbon of one of the constituents of the desired superconductor, which is coated by the other constituent or placed in physical contact with the other and then reacted together in a diffusion process. The resulting material is normally one of the intermetallic compounds, e.g. Nb<sub>3</sub>Sn. A drawback to this procedure is that the resulting composites are generally weak mechanically.
1. Critical current densities of the over-all composite are usually quite high in this process.
  2. The magnetization is the same as III-A-2, except that any of the unreacted Nb ribbon left adds to the low field magnetization of the sample. (Since this is also the mechanical strength member, a compromise in size must be chosen.)
  3. The flux-jump stability seems slightly increased over III-A. This additional stability may be due to the presence of the Nb providing low field shielding of the flux.
- E. "Casting" of a composite is an idea that has been around a long time because it would be a cheap method of fabrication, but to the best of the author's knowledge the major difficulties of temperature vs superconducting bond problems have not been worked out.
1. Critical current densities are very low.
  2. Magnetization is unknown.
  3. Flux-jump stability is unknown.
- F. Combination of the above processes resulting in a composite. The properties would be a combination of the above.

Examples of all of the criteria have been shown previously in the figures except criterion 1). Figure 8 shows typical  $J_c(H_{\text{applied}})$  vs  $H_{\text{perpendicular}}$  curves for various materials now available.

In conclusion allow me to state a personal observation, first of what would be optimum from the standpoint of dc and ac applications based on what is presently known, and second, what probably will be the future course of action.

First, I believe and a lot of other people with me believe it to be obvious that multifilament composites containing only the superconductor in appropriate filament size with sufficient amounts of high-conductivity metal to insure flux-jump stability, and enough high-conductivity metal to allow several stable filament superconductors to undergo normal transitions and return to the superconducting state, are the answer for both ac and dc applications. I do not believe that it is necessary to go to smaller filaments than 30-40  $\mu$ , and indeed maybe not even that small when one takes into account the proximity effects of the magnetization of the composites, unless one is able through the introduction of resistance to decouple the strands or filaments, especially in light of calculations presented by various speakers<sup>4-7</sup> at this Summer Study. If a high-temperature, high-conductivity material with a very slow Sn diffusion rate could be developed, the multifilament composite could employ  $Nb_3Sn$  as well as the ductile TiNb and NbZr alloys. But for the near future probably scribed layers of either vapor-deposited or diffusion-processed  $Nb_3Sn$  will be available.

Upon evaluation of papers presented by Wipf,<sup>4</sup> Hart,<sup>5</sup> Smith,<sup>6</sup> and Stekly<sup>7</sup> during the weeks of the Summer Study, the conclusions of the author were slightly modified in that perhaps a highly resistive diffusion layer, that is, a very small thermal conduction barrier, might greatly reduce the coupling in twisted multifilament composites having filament diameters around 0.003 cm.

#### ACKNOWLEDGEMENTS

The author wishes to thank G.H. Morgan for his helpful comments on this paper, and W.B. Sampson and R.B. Britton for the use of their magnets in these experiments.

---

4. S.L. Wipf, these Proceedings, p. 511.

5. H.R. Hart, *ibid.*, p. 571.

6. P.F. Smith, *ibid.*, p. 913.

7. Z.J.J. Stekly, *ibid.*, p. 748.

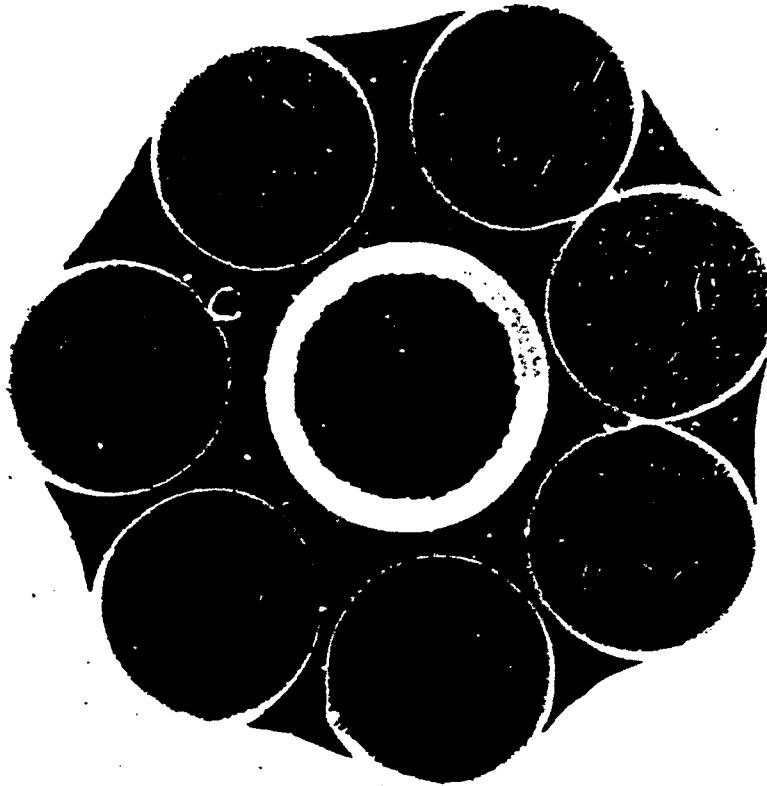


Fig. 1. Micrograph of a stranded cable consisting of a Ti22a/oNb copper-coated center strand (0.0508 cm diameter) with six highly annealed copper strands (0.0508 cm diameter) around it, potted in a SnAg solder.

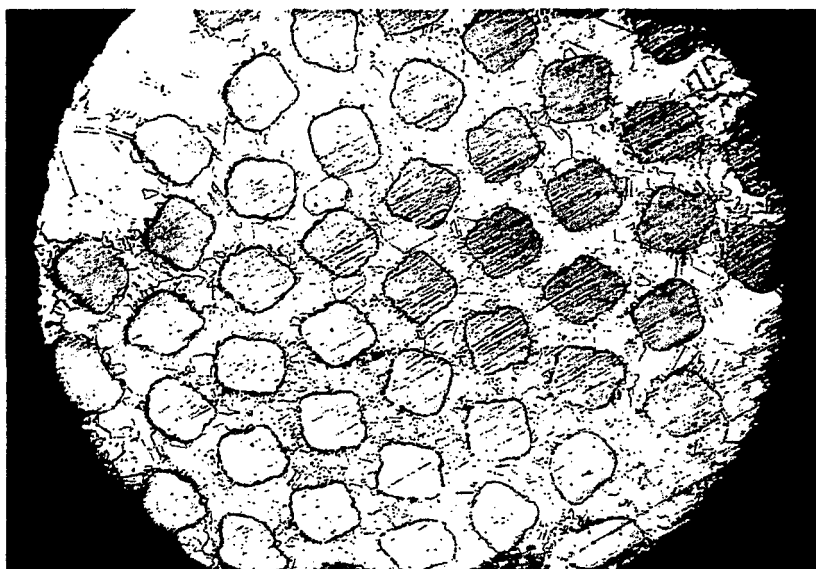


Fig. 2. Micrograph of a multifilament conductor (0.0508 cm diameter) containing 52 TiNb filaments (individually  $\approx 0.0038$  cm in diameter) in a highly annealed copper matrix.

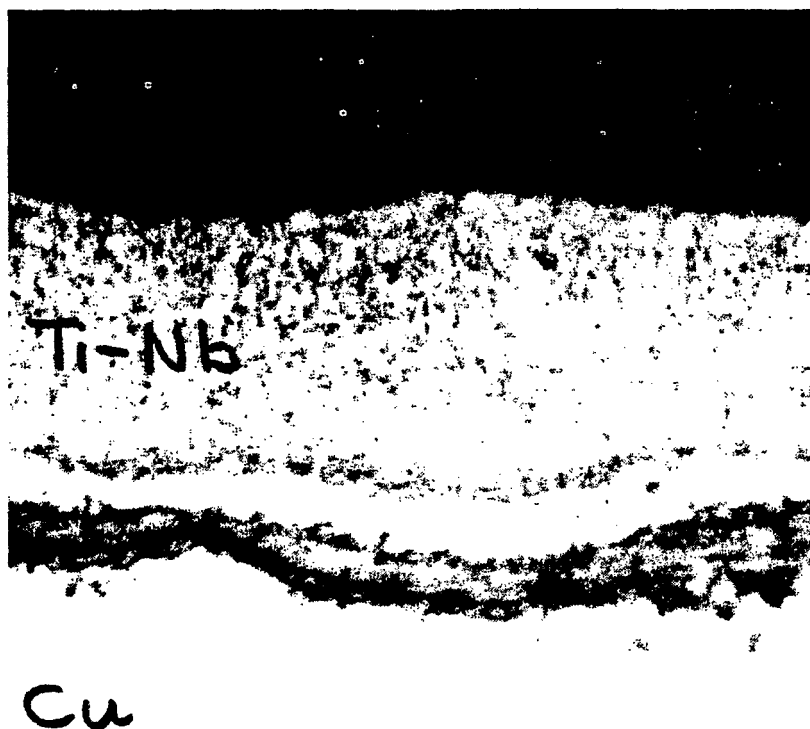


Fig. 3. Micrograph of a multilayer composite in which the superconductor was obtained by vapor deposition on a substrate (Cu).

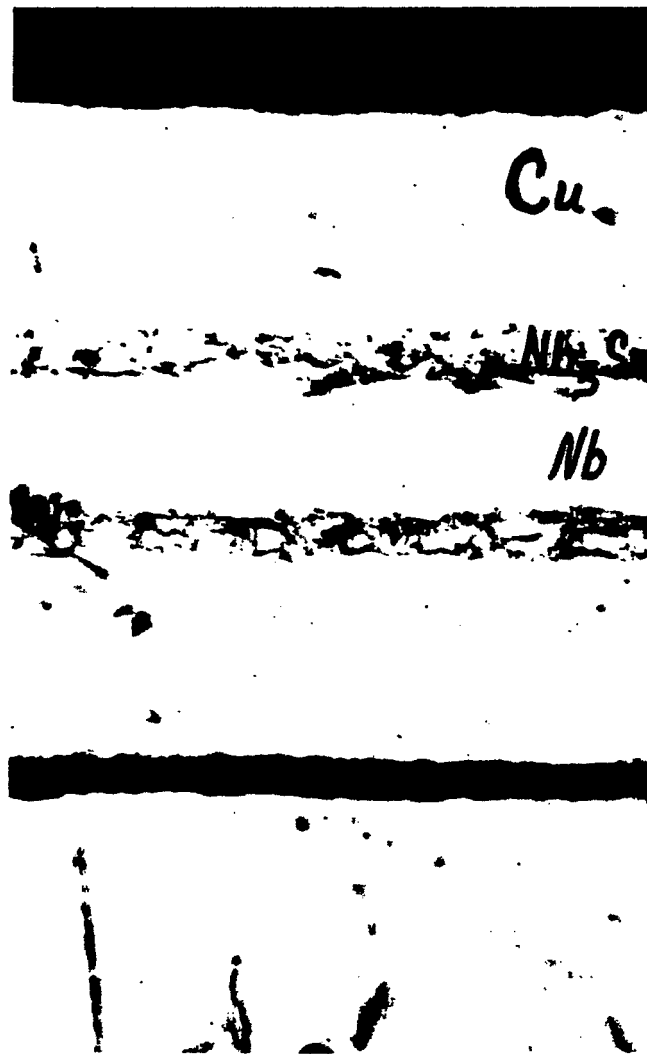


Fig. 4. Micrograph of a multilayer composite in which the superconductor was obtained by diffusing a Sn solder layer into a Nb ribbon and then copper-plating.



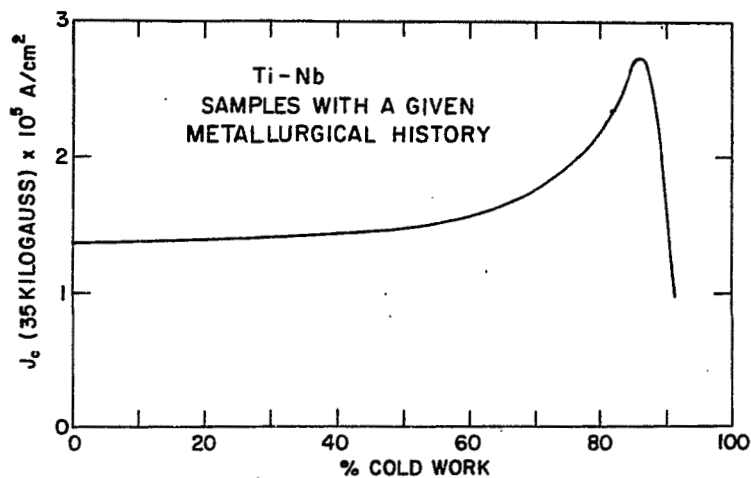


Fig. 5. A map of one of the various metallurgical parameters that are varied to obtain a given superconductor with various desired properties (these are data obtained by the author for a test sample).

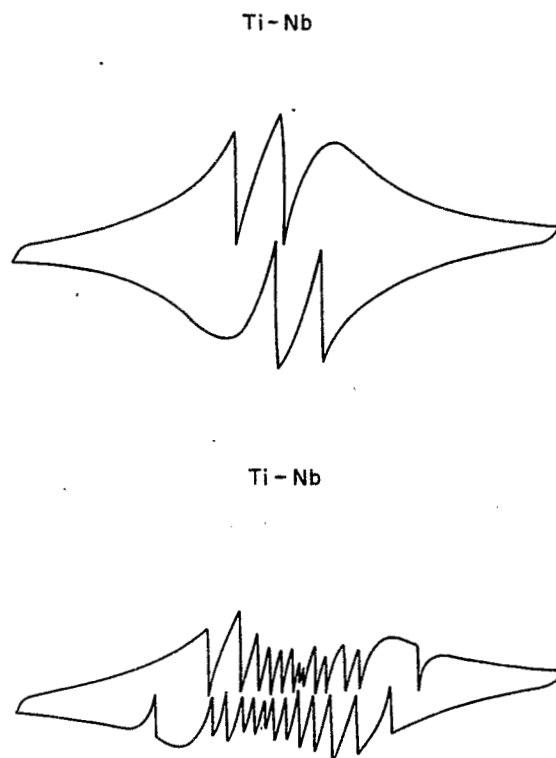


Fig. 6. Tracings of an x-y recorder for  $\bar{M}$  on the y-input and  $\bar{B}$  on the x-input ( $H_{\max} = \pm 40 \text{ kG}$ ). The upper curve is for a sample of Ti48a/oNb with an excellent bond between superconductor and copper. The lower curve represents an identical sample except the bond between superconductor and copper was very resistive and mechanically weak. These samples had the same  $J_c(H_a)$  (perpendicular) curves when the copper was etched off and the samples were sand-blasted and indium-tinned and then soldered to large copper pads for transport current connections.

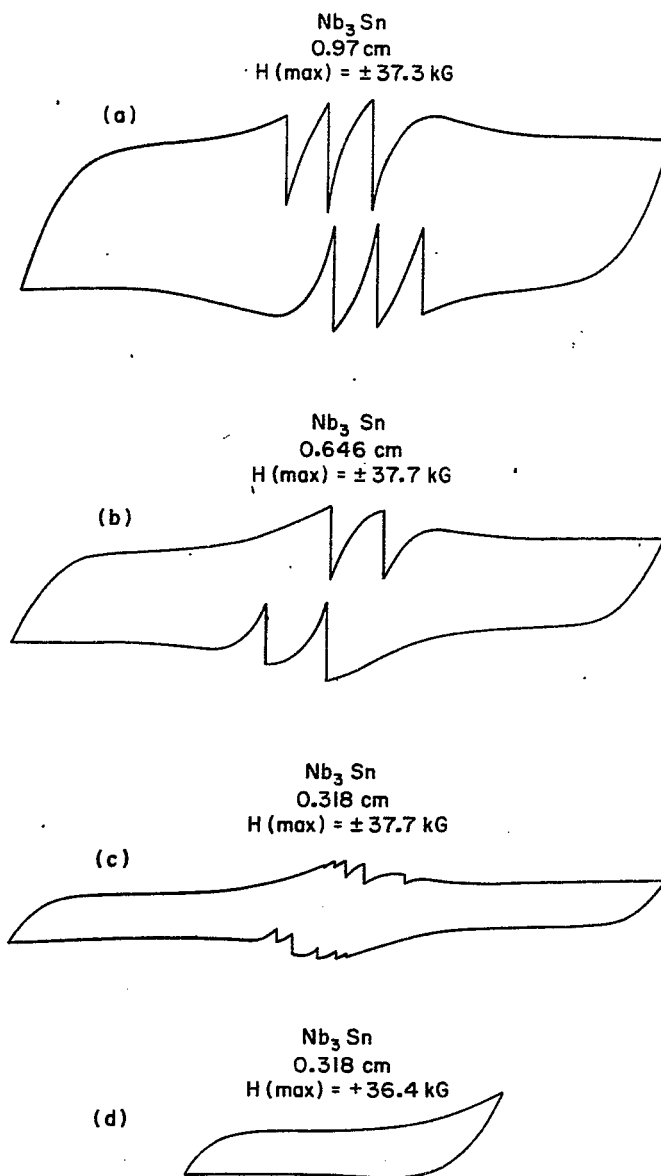


Fig. 7. Tracings of an x-y recorder for  $\bar{M}$  on the y-input and  $\bar{B}$  on the x-input ( $|\bar{H}_{\max}| \cong 40$  kG. In curves (a), (b), and (c) the field  $\bar{H}$  has both positive and negative values. In curve (d),  $\bar{H}$  is only negative. Curves (a), (b), and (c) represent variations of the smallest perpendicular width for a ribbon sample, with the field  $\bar{H}$  perpendicular to the flat side.

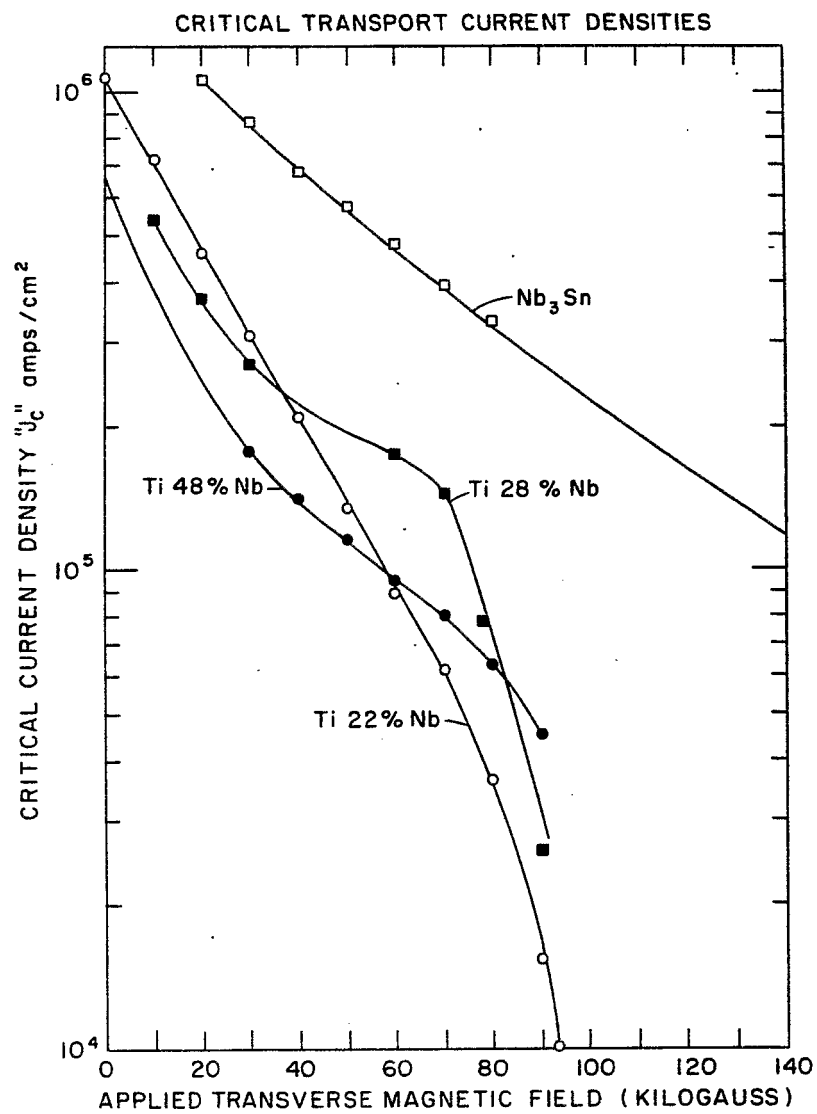


Fig. 8. Critical transport current density vs applied perpendicular field (H) for various type II superconductors.

# MATERIALS AND CONDUCTOR CONFIGURATIONS IN SUPERCONDUCTING MAGNETS\*

H. Brechna  
Stanford Linear Accelerator Center  
Stanford University, Stanford, California

## I. INTRODUCTION

The configuration, form, shape and composition of a superconducting-normal metal matrix for high energy, plasma, or solid state physics, or for other applications are primarily dictated by the performance reliability of the device to be used. Several factors do affect this, such as operational stability; electromagnetic, thermal, and mechanical stresses; manufacturing and technological problems; fatigue and environmental effects. Optimization of a composite conductor is also dictated by economic considerations.

If a superconductor is stabilized by means of adequate normal metal, and operated in the nucleate boiling region of liquid helium, the over-all current density in such a conductor is low. There are, however, possible ways to improve the over-all current density without jeopardizing operational safety in case of transient flux motion, or gross discontinuities in current or coolant supply, or other unforeseen incidents.

Flux instabilities encountered in the operation of superconducting magnets are primarily caused by power dissipation in superconductors. However, quantitative results on the instability phenomena are scarce, merely due to the circumstance that the problem is nonlinear and many material properties are not known properly.

Instability in superconductors, composite cables and conductors, and magnets has been studied by Kim and Anderson,<sup>1</sup> Iwasa and Williams,<sup>2</sup> Wipf,<sup>3</sup> Hart,<sup>4</sup> and Hancox.<sup>5</sup> Their qualitative observations are briefly summarized: Any high field superconductor that conforms to the Kim-Anderson model of flux release from pinning centers under the combined Lorentz force and thermal activation is intrinsically unstable. Resistance is observed in a type II superconductor when the Lorentz force exceeds the field-dependent "pinning force" determined by the defect structure of the superconductor. This "flux jump" or "flux flow" resistance yields power losses in the superconductor, which must be dissipated by the coolant in order to avoid a so-called "runaway" transition from superconductivity to normality over the entire length of the conductor.

A field or temperature disturbance changes both Lorentz ( $F_L$ ) and pinning ( $F_p$ ) forces, the first because of the field gradient between two points of equal magnetic field  $B$ , the second because of temperature changes due to energy dissipation. An increase in temperature reduces the pinning force. A disturbance also causes a reduction in the Lorentz force. As long as the changes  $\Delta F_L > \Delta F_p$ , the equilibrium is stable. On

---

\* Work supported by the U.S. Atomic Energy Commission.

1. Y.B. Kim et al., Phys. Rev. 131, 2486 (1963).
2. Y. Iwasa and J.E.C. Williams, Appl. Phys. Letters 9, 391 (1966).
3. S.L. Wipf, Phys. Rev. 161, 161 (1967).
4. H.R. Hart, Jr., GE Notes (unpublished).
5. R. Hancox, Proc. IEE (London) 113, 1221 (1966).

exceeding the limit  $\Delta F_L \cong \Delta F_p$ , the flux movement is accelerated until a flux jump occurs. In a magnet, instabilities are triggered by flux jumps occurring in some parts of it. When the magnetic field is increased, the field profile within the superconductor,  $B(r)$ , is determined by the shielding current  $I_s$ , which flows in the conductor surface. Inside the superconductor,  $B$  is zero, except in the shielding layer of thickness  $\Delta = B_{ext}/4\pi J_c$ . The shielding layer has everywhere the current density  $J_c$  and is in a "critical state." As  $B_{ext}$  is increased, the front of the critical state region propagates towards the center filament of the superconductor with the velocity

$$v_L = \frac{1}{4\pi J_c} \cdot \frac{dB_{ext}}{dt} \quad (1)$$

Since the flux front is moving, an electric field is induced in the conductor according to

$$\vec{U} = \vec{v}_L \times \vec{B}_{int} \quad (2)$$

which results in a power dissipation per unit volume given by

$$P = U \cdot J_c = \frac{1}{4\pi} \cdot B_{int} \cdot \frac{dB_{ext}}{dt} \quad (3)$$

Ignoring displacement current and assuming that in the superconductor the relative permeability  $\mu_r$  is unity (i.e.  $B_{int} = B_{ext} = B$ ), the field propagation in the superconductor is given by

$$\frac{\partial B}{\partial t} = \frac{\rho}{\mu_0} \cdot \nabla^2 B = D_m \cdot \nabla^2 B \quad (4)$$

which is the magnetic diffusion equation.  $D_m$  is the magnetic diffusivity, and  $\rho$  the resistivity due to a flux disturbance in the superconductor.

For a cylindrical wire one may write Eq. (4) explicitly in the form

$$\frac{\partial^2 B}{\partial z^2} + \frac{\partial^2 B}{\partial r^2} + \frac{1}{r} \frac{\partial B}{\partial r} + \frac{1}{r^2} \frac{\partial^2 B}{\partial \phi^2} = \frac{1}{D_m} \cdot \frac{\partial B}{\partial t} \quad (5)$$

If the magnetic field is parallel to the axis of a semi-infinite conductor, Eq. (5) is simplified to

$$\frac{\partial^2 B}{\partial r^2} + \frac{1}{r} \frac{\partial B}{\partial r} = \frac{1}{D_m} \cdot \frac{\partial B}{\partial t} \quad (6)$$

If the external magnetic field is perpendicular to the conductor axis, surface effects in a single conductor are not of great importance and thus, even in this case, solution of the diffusion Eq. (6) may yield a first order approximation and has been calculated by Wipf.<sup>6</sup>

Wipf<sup>6</sup> gives as a first approximation for the resistivity of a cylindrical superconducting wire of radius  $r_0$  in a creeping magnetic field parallel to the conductor axis the value of

---

6. S.L. Wipf, J. Appl. Phys. 37, 1012 (1966).

$$\rho_c \cong 2.5 \times 10^{-9} \cdot \frac{r_0}{J_c} \cdot \frac{\partial B}{\partial t}, \quad (7)$$

and, for the resistivity in case of a flux jump, the value

$$\rho_{\Delta} = 1.5 \times 10^{-10} \frac{\partial B}{\partial t}. \quad (8)$$

Taking a typical value of  $\partial B / \partial t = 10^3$  G/sec, we get for the case of a flux jump

$$\rho_{\Delta} = 1.5 \times 10^{-7} \Omega \cdot \text{cm},$$

which results in a magnetic diffusivity in the superconductor of

$$D_{\Delta, m} = 12 \text{ cm}^2 \text{ sec}^{-1}.$$

The magnetic diffusivity,  $D_m$ , is counterbalanced by the thermal diffusivity,  $D_{th}$ , of the superconductor, or generally by the thermal diffusivity of the composite conductor.

For a composite conductor consisting of a superconducting core embedded in a normal metal we may write the thermal diffusion equations:

$$\begin{aligned} \frac{\partial^2 \theta}{\partial z^2} - \frac{hf}{k_s \cdot A_s^{\frac{1}{2}}} \cdot \frac{(1 + A_n/A_s)^{\frac{1}{2}}}{1 + A_n k_n / (A_s k_s)} \cdot \theta + J_s^2 \cdot \frac{\rho_s}{k_s} \cdot \frac{1 + \rho_n A_s / (\rho_s A_n)}{1 + k_n A_n / (k_s A_s)} \\ = \frac{1}{D_{th, n}} \cdot \frac{D_{th, n} / D_{th, s} + A_n k_n / (A_s k_s)}{1 + A_n k_n / (A_s k_s)} \cdot \frac{\partial \theta}{\partial t}, \end{aligned} \quad (9)$$

with

$$\theta = T_c - T_b,$$

where the subscript s denotes the superconductor, n the normal shunt metal, and k,  $\rho$ , h and D are thermal conductivity, electrical resistivity, heat transfer coefficient, and thermal diffusivity, respectively. A is the cross-sectional area, and f a factor linking the over-all perimeter of the composite conductor to the cross-sectional area of the normal matrix.

Assuming that the heat flow has a velocity  $v_q$  parallel to the conductor axis and is linear, i.e.

$$\frac{\partial \theta}{\partial t} = -v_q \cdot \frac{\partial \theta}{\partial z},$$

where  $v_q$  is the heat propagation velocity, solutions of the thermal diffusion Eq. (9) have been calculated by Stekly,<sup>7</sup> Whetstone,<sup>8</sup> Gauster et al.,<sup>9</sup> Lontai,<sup>10</sup> and Brechna.<sup>11</sup>

7. Z.J.J. Stekly and J.L. Zar, Avco-Everett Laboratory Report 210 (1965).
8. C.N. Whetstone and C.E. Roos, J. Appl. Phys. 36, 783 (1965).
9. L.M. Lontai, Argonne National Laboratory Engineering Notes (1966).
10. W.F. Gauster et al., Oak Ridge National Laboratory Report ORNL-T-M-2075 (1967).
11. H. Brechna, Bulletin S.E.V. (Swiss) 20, 893 (1967).

The limit of stable current is calculated from  $v_q = 0$  to be:

$$I_s = \left[ \frac{h \cdot \Delta T}{\rho_n} \cdot A_n S_c \right]^{\frac{1}{2}}, \quad (10)$$

where  $S_c$  is the cooled perimeter.

The two differential Eqs. (6) and (9) can be combined in a set of simultaneous nonlinear equations, and we may conclude, for a purely adiabatic representation, that no instability occurs unless

$$\left. \frac{\Delta Q_m}{\Delta T} \right|_{T_1} \cong \left. \frac{\Delta Q_{th}}{\Delta T} \right|_{T_1}$$

or, in simplified form, unless  $D_m \cong D_{th}$ .  $\Delta Q_m$  = magnetic energy difference, and  $\Delta Q_{th}$  = thermal energy difference.

Referring now to Table I, the thermal and magnetic diffusivities of a number of materials are presented at 4.2°K. Data for thermal diffusivities as a function of temperature are given in Fig. 4.

At  $T \leq T_c$  the thermal diffusivities of type II superconductors are small compared to the magnetic diffusivities, and thus we may conclude that during a flux jump, which has a duration of only a few microseconds, the superconductor may be thermally isolated from the substrate. Due to the poor thermal conductivity in the superconductor, the temperature distribution inside the superconductor is anisotropic, and thus the exact evaluation of the diffusion mechanism proves to be difficult and will be treated later.

In a composite conductor we have three regions of flux exclusions:

- a) Field stability: If the field or current perturbation has subsided, the conductor recovers its superconducting state.
- b) Metastability or limited instability: A small perturbation may drive the conductor normal, but the region of normality may subside when the conductor transport current is reduced below its recovery value.
- c) Runaway instability: Region of normality may propagate over the entire length of the conductor.

Field stability ( $d\phi/dt$  and  $dp/dt$  must be limited) is achieved by adding normal metal to the superconductor. In this case the bond between superconductor and normal metal must be appropriate (thermoelectrical bond) in order that the boundary layer shall not decelerate the heat transfer from the superconductor to the normal metal.

The temperature rise due to  $dp/dt$  is limited by utilizing materials of high thermal capacity such as silver, lead, or helium within a composite conductor.

The solution of Eqs. (6) and (9) suggests that the heat capacity ( $c_p \delta$ ) of the system must be improved. Based on one-dimensional models, Hancox<sup>12</sup> gives the upper stable screening field

$$H_s \cong (8\pi c_p \delta \cdot T_0)^{\frac{1}{2}}. \quad (11)$$

---

12. R. Hancox, Phys. Letters 16, 208 (1965).

TABLE I

Properties of Elements and Alloys at 4.2°K

Material	Density (g/cm <sup>3</sup> )	Specific Heat (J/g °K)	Thermal Capacity (J/cm <sup>3</sup> °K)	Therm. Conductivity (W/cm °K)	Therm. Diffusivity (cm <sup>2</sup> /S)	Magnetic <sup>(a)</sup> Diffusivity (cm <sup>2</sup> /S)
Ag (99.999%)	10.6	$1.35 \times 10^{-4}$	$14.3 \times 10^{-4}$	130	$9.0 \times 10^4$	0.08
Al (99.996%)	2.7	$2.8 \times 10^{-4}$	$7.56 \times 10^{-4}$	33	$4.36 \times 10^4$	1.25
Cu (99.95% an)	8.95	$10^{-4}$	$8.95 \times 10^{-4}$	2.5	$0.28 \times 10^4$	0.95
In (99.993%)	7.28	$1.2 \times 10^{-3}$	$8.73 \times 10^{-3}$	8.5	$0.973 \times 10^4$	2.47
Na (99.999%)	1.009	$1.7 \times 10^{-3}$	$1.71 \times 10^{-3}$	48	$28.07 \times 10^4$	0.135
Pb (99.998%)	11.25	$8.0 \times 10^{-4}$	$90.0 \times 10^{-4}$	22	$0.24 \times 10^4$	0.32 <sup>(b)</sup>
He	$15 \times 10^{-3}$	2.1	$31.5 \times 10^{-3}$	$3.14 \times 10^{-4}$	$10^{-2}$	
	@ 15 atm	@ 15 atm	@ 15 atm			
Nb <sub>3</sub> Sn	5.4 <sup>(c)</sup>	$2.1 \times 10^{-4}$	$11.34 \times 10^{-4}$	$4.0 \times 10^{-4}$	0.35	
Nb25%Zr	8.1	$1.8 \times 10^{-4}$	$14.58 \times 10^{-4}$	$0.8 \times 10^{-3}$	5.4	
Nb60%Ti	5.6	$1.8 \times 10^{-4}$	$10.1 \times 10^{-4}$	$1.2 \times 10^{-3}$	1.18	

(a) Data for resistivity without strain.

(b)  $H > H_c$ .

(c) The density of Nb<sub>3</sub>Sn is about 8 g/cm<sup>3</sup>, but the  $c_p$  calculation from Vieland's measurements (Ref. 20) indicate  $\delta = 5.4$  g/cm<sup>3</sup>.



Depending on the diameter ratio of the superconductor to normal metal  $d_s/d_n$ , the average stable current density in the composite conductor is given by

$$J_{av} = \frac{1}{d_n} \left[ \frac{3 \times 10^9}{4\pi} c_p \delta \cdot \frac{d_s}{d_n} \cdot T_0 \right]^{\frac{1}{2}} \quad (12)$$

$T_0$  is a temperature less than the critical temperature of the superconductor;  $[T_0 = -J_c/(dJ_c/dT)]$ .

The diameter of a single superconductor filament must follow the relation:

$$d_f \leq \frac{1}{J_c} \left( \frac{3 \times 10^9}{4\pi} c_p \delta \cdot T_0 \right)^{\frac{1}{2}} \quad (13)$$

to avoid flux jumps.

The balance between the magnetic and thermal diffusivity also suggests improving the ratio between the perimeter and cross-sectional area of individual superconductors, which leads to a conductor with many filamentary superconductors. The minimum size and the distribution of individual superconducting filaments in the normal metal substrate and the quality of the surface bond are presently being investigated by several laboratories. However, it may be pointed out that the heat dissipated by a disturbance in individual filaments must be absorbed and conducted to the coolant bath, before it may heat up the superconductor such that the region of normality can spread over the entire length of the composite conductor.

In a composite conductor the distribution of filaments in the matrix leads to inductive coupling of magnetization currents which can lead, in turn, to heating of the conductor during flux change (charging or discharging rate sensitivity) and may trigger flux jumps. The normal metal substrate must have adequate thermal capacity to absorb this additional heating phenomenon.

Improvement of the heat transfer coefficient by utilizing forced cooling with helium was proposed by Brechna<sup>13</sup> using hollow (internally cooled) composite conductor. Using supercritical helium was suggested by Kolm.<sup>14</sup> With this scheme, using a particular conductor geometry (over-all dimensions  $0.5 \times 0.5$  cm, coolant passage  $0.22 \times 0.22$  cm) and a flow rate of 0.8 liter/min of helium, a stable current density of  $1.6 \times 10^4$  A/cm<sup>2</sup> was measured at an external field of 5 T.

Introducing of liquid or gaseous helium in the composite matrix (porous substrate) by using sintered porous metals of low sintering temperature such as cadmium has been proposed by Brechna and Garwin.<sup>15</sup> The substrate porosity can be 50% or less. Individual, partially stabilized, superconducting filaments are located within the porous substrate, which acts as a support structure and enables the coolant to be in contact with the filaments. Although data of over-all current densities of such conductors are not available at present, calorimetric measurements indicate that an over-all thermal capacity of  $\sim 0.15$  J/cm<sup>3</sup> °K can be achieved with porous copper immersed in liquid helium.

---

13. H. Brechna, in Proc. Intern. Cryogenic Engineering Conf., Kyoto, 1967, p. 119.

14. H.H. Kolm, in Proc. Intern. Symp. Magnet Technology, Stanford, 1965, p. 611.

15. H. Brechna and E. Garwin, SLAC Proposal 1967.

Smith et al.<sup>16</sup> suggests the use of fine filaments embedded in a high resistance matrix (i.e., Cu-Ni alloy), in order to reduce cross magnetization currents between extreme located filaments in the matrix. The diameter of individual superconductor filaments should not exceed  $5 \times 10^{-3}$  cm. They also propose to twist the bundle of filaments in the matrix with a periodicity of about 2-3 cm.

Improvement of over-all current densities in the magnet shall by no means affect the safety of the magnet. High current densities at transverse high flux densities in large magnets will yield Lorentz forces which make the use of conductor reinforcement imperative. Additional stresses are produced by the differential contraction of various materials. Thus in large magnets the stress and strain behavior of the conductor and insulation material will primarily dictate the over-all current densities, not the instability phenomena. Table II illustrates the over-all current densities and conductor stresses in some procured and proposed high energy magnets.

One more factor which dictates the form and composition, as well as coil configuration and reinforcement, is the field reproducibility. Magnets generally are warmed up in periods between experiments. Fatigue behavior is encountered in insulation structures and in highly stressed substrates. Coils may become loose and flux jumps due to wire movements may occur.

It is evident that average current densities in coils are not primarily dictated by the ac behavior of the superconductor alloys, but by the stress-strain properties of the composite. Large magnets ( $E_{field} > 1$  MJ) will be designed with moderate average current densities, up to  $15 \times 10^3$  A/cm<sup>2</sup>, while smaller coils may achieve current densities in excess of  $5 \times 10^4$  A/cm<sup>2</sup> at fields of 4 T.

It is important that the maximum stress on the composite conductor shall not exceed  $\sim 20\%$  of the 4.2°K yield strength in order to avoid early fatigue.

Prior to a discussion of optimization studies, the physical and mechanical properties of composite conductors are presented in quantitative form.

## II. PHYSICAL AND MECHANICAL PROPERTIES OF SUPERCONDUCTORS TYPE II, NORMAL METALS, AND COMPOSITE CONDUCTORS

### 1. Thermal Conductivity

The thermal conductivities of Nb(25%)Zr wires and bars<sup>11</sup> at  $B_{ext} = 0$  and  $B_{ext} = 5$  T are illustrated in Fig. 1 and compared to data for Nb(60%)Ti wires at  $B_{ext} = 0$  measured at MIT-NML,<sup>17</sup> and data for Nb<sub>3</sub>Sn measured by Cody.<sup>18</sup> In Nb(25%)Zr the conductivity values are different for 0.025 cm wires in the longitudinal direction and for bars, which suggests that the superconductor is thermally anisotropic. The effect of magnetic field is also pronounced in all superconducting type II alloys.

It may be pointed out that the major contribution to the thermal conductivity at temperatures below transition values is from phonons rather than electrons, which become less active. Wiedemann-Franz law in the usual form is not applicable to superconductors and to commercially available normal metals used with superconductors.

---

16. P.F. Smith et al., Brit. J. Appl. Phys. 16, 947 (1965).

17. J.R. Hale, MIT Bitter National Magnet Laboratory, private communication (1968).

18. G.D. Cody and R.W. Cohen, Rev. Mod. Phys. 36, 121 (1964).

## 2. Electrical Resistivity

The electrical resistivities of three types of superconductor type II are given in Fig. 2. Measurements have been performed at low external field. Further investigations at various external fields are in progress. The electrical resistivities of some normal materials are compared to the data for superconductors. For OFHC copper the electrical resistivity as a function of external field is shown in Fig. 3. The resistivity follows the correlation<sup>19</sup>:

$$\rho_{4.2^{\circ}\text{K}, B} = \rho_{300^{\circ}\text{K}, B=0} \left[ \frac{0.9}{\rho_{300^{\circ}\text{K}, B=0} / \rho_{4.2^{\circ}\text{K}, B=0}} + 0.25 \times B \times 10^{-2} \right], \quad (14)$$

where B has the dimension of (T).

## 3. Thermal Diffusivity

The thermal diffusivities of several normal metals are illustrated in Fig. 4. Data at 4.2°K for some superconductors type II are given in Table I.

## 4. Specific Heat

Specific heats and thermal capacities of metals and a few superconductors type II are given in Table I. The specific heats for Nb(25%)Zr and Nb<sub>3</sub>Sn are illustrated in Fig. 5 and may be compared to values given for some normal metals.<sup>20</sup> Data for NbTi are presently not available.

## 5. Mechanical Properties

The effect of cold work (tension on the composite conductor) on resistivity was measured by Brookhaven,<sup>21</sup> and RHEL.<sup>22</sup> Extensive data on the effect of stress on elongation of copper and aluminum are obtainable from NBS handbooks. The effect of stress on resistivity and cold work on composite conductors (NbTi thermoelectrically bonded to OFHC copper) is illustrated in Figs. 6a and 6b.

From these measurements one obtains a Poisson ratio at 4.2°K of  $m = 0.32$  and a modulus of elasticity of  $E = (1.7-1.8) \times 10^6 \text{ kg/cm}^2$  according to the type of composite, compared to  $m = 0.33$  and  $E = 1.34 \times 10^6 \text{ kg/cm}^2$  for OFHC copper.

The modulus of elasticity of NbTi alloy depends grossly on the Ti content.

## III. COMPOSITE CONDUCTORS AND CABLES

The size and shape of the composite conductor, the ratio of superconductor to normal metal, the quality of the metallurgical (thermoelectrical) bond between superconductor and normal metal, the thermal capacity of the system, and the heat transfer from superconductor to the coolant are directly related to the stable current density

---

19. C.W. Whetstone et al., in Proc. Intern. Cryogenic Engineering Conference, Kyoto, 1967, Paper B7.

20. L.J. Vieland and A.W. Wicklund, Phys. Letters **23**, 227 (1966).

21. Bubble Chamber Group, Brookhaven National Laboratory Report BNL 10700, p. 78 (1966).

22. P. Clee, Rutherford High Energy Laboratory Report EDN 0001.

limit of the composite conductor. As mentioned, stability against flux motion (jumps) is presently achieved by using relatively large cross sections of normal metals surrounding individual superconducting filaments, providing adequate coolant channels for circulating helium, insuring direct contact of coolant to the normal metal or superconductor, subdividing the superconductor in small filamentary wires adequately spaced in the normal metal matrix, and enhancing the thermal capacity of the conductor.

The conductor is stable up to the critical current of the superconductor and even at currents somewhat higher, with the excess current flowing through the normal metal.

Magnets are generally exposed to thermal and magnetomechanical stresses. In many applications, even if average high current densities with regard to flux instabilities would be permissible, material stress-strain behavior would limit the upper over-all current density limit.

Several design problems must be considered prior to the choice of current density field parameters. Among these are questions relating to:

- a) Over-all field or field-gradient distribution in a usable volume.
- b) Field or gradient reproducibility over the lifetime of the experimental setup.

Generally, field uniformity in the order of  $10^{-4}$  and field reproducibility in the order of  $10^{-5}$  are required in large multimegajoule experimental magnets and in beam transport magnets.

These problems have been one factor limiting the current densities in medium size and large superconducting magnets to less than  $5000 \text{ A/cm}^2$ . With the reinforcement technology and better understanding of the flux instability phenomena, it is now possible to design magnets with over-all current densities of  $1.5 \times 10^4 \text{ A/cm}^2$  at fields of 5 T. Table II illustrates a few examples of tested, procured, and proposed experimental magnets with field energies in excess of 1 MJ.

From an earlier stage of partially or completely stabilized superconducting cables (roped superconducting and copper filaments) impregnated with indium, or for strength purposes with silver-tin alloys (Fig. 7), the technology of producing long conductors has been advanced considerably. Modern composite conductors contain several hundred superconducting filaments, metallurgically bonded to a copper or aluminum matrix (Fig. 8). While in a cable, due to manufacturing difficulties, individual superconductors had seldom a diameter as small as  $10^{-2} \text{ cm}$ , in composite conductors, individual filaments of NbTi may have diameters of  $5 \times 10^{-3} \text{ cm}$  or less.

Flux jump instabilities are present in all superconducting magnet wires, when the diameter of the individual filament is larger than the value calculated from (12). However, larger filament sizes may be usable, if the region of normality can be cooled prior to propagation of heat along the conductor. Partially stable or metastable conductors are interesting for dc applications if adequate cooling is provided. A one-dimensional solution of Eqs. (15) and (9), or systematic measurements of flux jump instabilities in various conductor configurations can result in an adequate lower limit of filament diameter and a ratio of normal metal to superconductor.

Measurements with small size coils ( $a_1 = 2\text{-}4 \text{ cm}$ ;  $a_2 = 10 \text{ cm}$ ;  $2b = 15 \text{ cm}$ , field energies  $\leq 50 \text{ kJ}$ , maximum field 6.5 T) built by partially stabilizing six-stranded Nb(60%)Ti cables of the type shown in Fig. 7 with copper, and insulated according to Fig. 8 show an interesting flux jump pattern. At self-fields smaller or equal to  $H_{c1}$ , no flux jumps were measured (Fig. 9). By increasing the transport current and with it the field at a constant rate ( $dB/dt = \text{const}$ ), flux jumps were made to occur suddenly,

TABLE II

Procured, Designed, and Proposed Large Superconducting Magnets

Laboratory	Type	i.d. (cm)	o.d. (cm)	Length (cm)	$B_{0,0}$ (T)	$B_m$ (T)	$J_c$ $A/cm^2$	$\lambda J_{over-all}$ $A/cm^2$	$\sigma_{hoop}$ $kg/cm^2$	Remarks
<u>1. Procured and tested magnets</u>										
Avco	Saddle	30.5	84	305(a)	3.7	4.25	$1.4 \times 10^5$	$< 10^3$	?	Nb(25%)Zr Cu-Strip. Cond.
CERN	Helmholtz	40	66.5	66	6	6.6	$6 \times 10^4$	$5 \times 10^3$	$1.4 \times 10^3$	Nb, Ti and Cu Cond. Nb, Ti and Al Cond.
NASA	Solenoid	15	48.5	34.5	13.5	13.8	$2.45 \times 10^5$	$1.34 \times 10^4$	$2.16 \times 10^3$	Nb <sub>3</sub> Sn and Hastelloy- Cu Stabilized Cond.
SLAC	Helmholtz	30	90	70	7	8	$3.7 \times 10^4$	$4 \times 10^3$	$10^3$	Nb, Ti and Cu Cable
<u>2. Procured magnets</u>										
Argonne N.L.	Helmholtz (B.B.C.)	488	550	287	2	2	$4.0 \times 10^5$	$10^3$	$7.62 \times 10^2$	Nb, Ti and Cu Composite Strip
Brookhaven N.L.	Helmholtz (B.B.C.)	240	276	224	3	4	$1.8 \times 10^5$	$2.53 \times 10^3$	$6.4 \times 10^2$	Nb, Ti and Cu Comp. Strip, SS Reinforced
<u>3. Proposed magnets</u>										
Brookhaven N.L.	Helmholtz (B.B.C.)	498	589	430	3	4.05	$1.75 \times 10^5$	$1.1 \times 10^3$	$1.13 \times 10^3$	Nb, Ti and Cu Comp. Strip, SS Reinforced, with $\sigma_h = 3 \times 10^3 kg/cm^2$
Rutherford H.E.L.	Helmholtz (B.B.C.)	190	340	230	7	8	$3.7 \times 10^4$	$1.2 \times 10^3$	$10^3$	Nb, Ti and Cu Comp. Strip, SS Reinforced
SLAC	Helmholtz (B.B.C.)	140	236	130	7	8.2	$3.0 \times 10^4$	$2.5 \times 10^3$	$10^3$	Nb, Ti and Cu hollow Composite Cond. with SS reinforcement with $\sigma_h = 3.2 \times 10^3 kg/cm^2$
NAC	Helmholtz	710	880	426.5	3.8	6.0	$8.0 \times 10^4$	$1.4 \times 10^3$	$1.06 \times 10^3$	Nb, Ti and Cu hol- low Composite Cond., SS reinforcement, with $\sigma_h = 3.8 \times 10^3$ $kg/cm^2$

(a) The uniform field length is approximately 80 cm.

and they repeated themselves at regular time intervals. When central fields of  $\sim 1.5$  T were reached, corresponding to about 1.9 - 2 T at the conductor, the intervals between flux jumps became shorter until no more, with the exception of a few sporadic ones, were observed. The number of total flux jumps over a particular field region remained constant regardless of the speed of flux sweep. However, at very low dB/dt values, only a few flux jumps were observed (Fig. 10). This flux jump behavior is observed with increasing and decreasing fields.

The occurrences of the flux jumps can be referred to conductor movements in the coil due to the Lorentz forces. The spiral-wound insulation (Nomex) is gradually compressed. If a few interturn and interlayer short circuits were originally present, the inductance in the conductor region changes in jumps because of the enhancement of the local short circuits, leading to flux jumps. When the coils are compacted due to the magnetic forces, no wire movements are encountered and flux jumps disappear. However, in this region, where flux jumps due to short circuits are generated, flux jumps due to the flux motion may occur also, until the flux has penetrated to the central fibers of the individual filaments. When wire movement and internal short circuits were prevented, no flux jumps due to change in transport current were observed. Flux jumps did occur sporadically when the external field was altered.

Critical current densities were reached in several types of composite conductors (Fig. 11), where the diameters of individual filaments were  $\sim 1.5 \times 10^{-2}$  cm and the copper-to-superconductor ratio exceeded 3:1. For most designs, if appropriate cooling can be provided, a copper-to-superconductor ratio of 3:1 is adequate. Filament diameters of  $10^{-2}$  cm may be the lower limit for most dc magnets, operating at fields up to 8 T.

Single layer coils with an inner diameter of  $2a_1 = 5$  cm were placed inside a 7 T superconducting magnet, and thermal and magnetic pulses, as proposed by Iwasa and Williams,<sup>23</sup> were applied to the conductor to measure the minimum propagating current density ( $J_{mp}$ ), and the quenching ( $J_C$ ) and recovery ( $J_R$ ) current densities.

With conductors up to sizes of  $0.4 \times 0.4$  cm<sup>2</sup>, and numbers of filaments up to 78 with Nb(60%)Ti filament diameters up to  $25 \times 10^{-2}$  cm, the following minimum propagating currents were measured:

$$B = (B_{ex} + B_{self}) = 7 \text{ T} : J_{mp} \cong 10^4 \text{ A/cm}^2$$

$$B = 6.3 \text{ T} : J_{mp} \cong 1.3 \times 10^4 \text{ A/cm}^2 .$$

Approximately 70% of the cooling surface area was exposed to helium. Surface heat flux measured at 7 T and  $J_{mp} = 10^4$  A/cm<sup>2</sup> was  $h\Delta T = 0.76$  W/cm<sup>2</sup>.

For high field magnets, where magnetomechanical stresses on the composite conductor may exceed the elastic limit of the composite conductor, reinforcements based on stainless steel, or Be(2.5%)Cu strips, films, or wires are used for reinforcement. In order to avoid material creep due to repeated thermal contraction and expansion (thermal cycling in repeated operations), the maximum hoop stress on the conductor shall not exceed certain limits below the yield strength of the material. Figure 12 shows a possible type of reinforced composite conductor where stainless steel wires are inserted in the copper matrix.

---

23. Y. Iwasa and J.E.C. Williams, J. Appl. Phys. 39, 2547 (1968).

Stress-strain studies by the H<sub>2</sub> bubble chamber group at RHEL<sup>24</sup> indicate that hard copper, annealed and tempered, yields a higher strength (~ 6%) and a smaller resistivity increase (~ 20%) at 0.1% strain than copper directly work-hardened (1/8 hard) from soft annealed copper.

Similar methods of reinforcing Nb<sub>3</sub>Sn ribbon by means of stainless steel or Hastelloy substrates have been utilized in high current density pancake type wound magnets. In these cases the substrate will carry practically all the thermal and magnetomechanical load.

#### IV. HOLLOW COMPOSITE CONDUCTORS

First tests with hollow composite conductors date back to November 1965.<sup>25</sup> Short-sample tests on square hollow conductors of 0.63 x 0.63 cm<sup>2</sup> over-all dimensions with a coolant hole of 0.3 x 0.3 cm<sup>2</sup> were carried out. Nb<sub>3</sub>Sn strips were indium-soldered in two grooves on the outside surfaces. The ratio of Cu to superconductor was approximately 20:1. Saturated liquid helium passing at a speed of ~ 25 cm/sec was passed through the hole. Although average current densities measured were less than 10<sup>3</sup> A/cm<sup>2</sup> at ~ 4 T, the results were encouraging and justified further studies.

With the same conductor configuration, a one-layer solenoid with an i.d. of 15 cm and 8 turns was built and placed inside the 30 cm coil for evaluation of transport current density vs helium flow rate. Short-sample behavior could be repeated although no supercritical helium was utilized. Figures 13 and 14 illustrate at 4 T external field, the current-voltage characteristics of the coil with flow rates of saturated liquid helium as the parameter. At a helium speed of 87 cm/sec, and an external field of 4 T, an average current density of 2.8 x 10<sup>3</sup> A/cm<sup>2</sup> was measured, which complies with the Nb<sub>3</sub>Sn short-sample critical current.

In the meantime, hollow superconductors using copper shunt metal and Nb(60%)Ti are commercially available. Figures 15 and 16 illustrate two such conductors where, in the case of 0.5 x 0.5 cm<sup>2</sup> conductor with a coolant hole of 0.22 x 0.22 cm<sup>2</sup>, the copper-to-superconductor ratio is 2.8:1. The cross sections of the superconducting filaments were severely deformed during the first trial manufacturing. Sweeping the current at various speeds up to 4000 A, which is the limit of the laboratory capability, did not cause any detectable flux jumps (dI/dt > 4000 A/sec), nor did introduction of heat pulses of 100 J quench the conductor.

To correlate the results obtained from square composite conductors, tests on long hollow superconductors having a copper-to-superconductor ratio of 4:1 - 5:1 and superconductor filament sizes of ~ 0.025 cm diameter are being prepared. The composite hollow conductor will be wound in pancakes or double pancakes and the conductor will be insulated by means of glass fiber tapes impregnated with filled epoxies, to match thermal contraction.

The main advantage of hollow conductors is in reliable performance, the coils are compact, and support problems are easy to solve. The helium reservoir is omitted. The coil is embedded in superinsulation and placed in a vacuum vessel. A possible method of insulating individual hydraulic passages by means of reinforced ceramic tubing is shown in Fig. 17.

---

24. D. Thomas, Rutherford High Energy Laboratory, private communication.

25. H. Brechna, Argonne National Laboratory Report 7192, p. 29 (1966).

A few measured and calculated properties of hollow superconductors follow:

## 1. Anisotropy Effects

For hollow conductors, as well as for other composite conductors, anisotropy effects are of prime importance. The critical current density in strip shaped composite conductors has varied in some cases to about 5:1 when placed parallel and perpendicular to the magnetic field. The anisotropy effect has been measured also in composite conductors where the individual superconducting filaments were not distorted. For hollow composite conductors the anisotropy effect is less pronounced, as seen from Fig. 18. A distortion of the filaments in the copper or aluminum matrix is with the present technologies unavoidable; it is proposed to twist or transpose the superconducting filaments in the matrix, reduce the filament size to  $\sim 1.5 \times 10^{-2}$  cm, and avoid filament distortion by more than an aspect ratio of 2:1.

## 2. Minimum Heat Flux

In large magnets using pool boiling, stable heat flux values have seldom exceeded  $0.4 \text{ W/cm}^2$  (well within nucleate boiling region of saturated liquid helium).

The minimum heat flux value is calculated from the relation<sup>26</sup>

$$h\Delta T_{\min} = 0.5 [T_V \cdot \delta_V] \left[ \frac{10^{-5} \cdot \sigma(\delta_L - \delta_V)}{(\delta_L + \delta_V)^2} \right]^{0.25}, \quad (15)$$

where  $T_V$  = heat of vaporization (J/g),  
 $\delta_V; \delta_L$  = densities of vapor and liquid ( $\text{g/cm}^3$ ),  
 $\sigma$  = liquid surface tension (N/cm).

The main heat flux is not a function of the hydraulic diameter,  $d_h$ , of the coolant flange, when  $d_h \geq 0.04$  cm. However, a pressure drop dependency is observed. At a pressure drop of  $\Delta p = 1 \text{ kg/cm}^2$  we calculate  $h\Delta T_{\min} = 0.18 \text{ W/cm}^2$ , which corresponds to measurements by Wilson.<sup>27</sup>

For forced cooling, utilizing supercritical helium at pressures  $> 2.3 \text{ kg/cm}^2$ , the heat transfer coefficient is given by the well-known correlation:

$$h = C \cdot \frac{k_f}{d_h} \cdot (\text{Re})_f^{0.8} \cdot (\text{Pr})_f^{0.4} \quad (16)$$

with

$$\text{Re} = \frac{d_h \cdot \delta \cdot v}{\eta} = \text{Reynolds number},$$

and

$$\text{Pr} = \frac{C \cdot \eta}{k} = \text{Prandtl number}.$$

26. M.A. Green, University of California, Lawrence Radiation Laboratory Engineering Note UCID 3050 (1967).

27. M.N. Wilson, Rutherford High Energy Laboratory, private communication (1966).



The Nusselt number coefficient  $C$  has values in the range  $2.3 \times 10^{-2}$  to  $4 \times 10^{-2}$ , and in the above expressions

$$\begin{aligned} v &= \text{mean helium velocity} \quad (\text{cm/s}) \\ \eta &= \text{viscosity} \quad (\text{g/cm}\cdot\text{s}) \\ C_p &= \text{specific heat} \quad (\text{J/g } ^\circ\text{K}) \\ k &= \text{thermal conductivity} \quad (\text{W/cm}\cdot^\circ\text{K}) \end{aligned}$$

Unfortunately, quantitative data for  $\eta$  and  $k$  of supercritical helium are available only in limited pressure and temperature intervals. Detailed data are currently being measured by NBS.<sup>28</sup>

For supercritical helium at  $15 \text{ kg/cm}^2$  passing through a channel of  $d_h = 0.5 \text{ cm}$  with a speed of  $v = 5 \text{ m/sec}$ , we obtain for  $T \cong 4.5^\circ\text{K}$ :

$$h = 0.516 \text{ W/cm}^2 \text{ } ^\circ\text{K} ,$$

using the lower limit for  $C = 2.3 \times 10^{-2}$ .

Allowing only a temperature rise of  $2^\circ\text{K}$  in the liquid, a heat flux of

$$h\Delta T = 1.03 \text{ W/cm}^2$$

may be carried by the supercritical helium.

If a certain length of the hollow superconductor is driven normal, the heat propagates along the composite conductor as well as along the coolant, which, in turn, will warm up the downstream portion of the conductor. We define a length of normality as "critical" when the region does not propagate along the total length of the conductor. Any length of normality shorter than the critical length is "self-healing" and the normal region will disappear. If the normal region is longer than the critical length, it may spread along the conductor and lead to a coil quench.

For a hollow (inner cooled) composite conductor, the thermal diffusivity Eq. (9) must be extended by the heat equation in the moving coolant. For one-dimensional heat flow along the conductor we may write:

$$\begin{aligned} \frac{d^2\theta}{dz^2} - \frac{hf}{k_s A_s} \cdot \frac{(1 + A_n/A_s)^{1/2}}{1 + A_n k_n / (A_s k_s)} \cdot (\theta - \theta_f) + J_s^2 \cdot \frac{\rho_s}{k_s} \cdot \frac{1 + \rho_n A_n / (\rho_s A_s)}{1 + k_n A_n / (k_s A_s)} \\ + v_{q_c} \cdot \frac{1}{D_{th,n}} \cdot \frac{D_{th,n}/D_{th,s} + A_n k_n / (A_s k_s)}{1 + A_n k_n / (A_s k_s)} \frac{d\theta}{dz} = 0 \end{aligned} \quad (17)$$

$$k_f A_f \frac{d^2\theta}{dz^2} + c_{p,f} \delta_f v_f \cdot \frac{\partial\theta}{\partial z} + c_{p,f} \delta_f \frac{\partial\theta}{\partial t} + hf A_f (\theta - \theta_f) = 0 \quad (18)$$

---

28. NBS Proposal, 1967.

where  $c_{p,f}$  = specific heat of the fluid,  
 $v_f$  = velocity of the fluid,  
 $v_{qc}$  = propagation velocity of the normal region,

with  $\theta = T_c - T_b$  .

A set of three simultaneous equations, including magnetic diffusivity Eq. (4), must be solved to give conditions for a flux jump or a quasi steady state behavior.

### 3. Pressure Drop

For a single phase flow through a hydraulic passage the pressure drop may be given by

$$\Delta p = \delta \cdot \frac{v^2}{2g} \left[ 2C_f \frac{\ell}{d_h} + (C_e + C_c) \right] ; \quad (19)$$

where  $C_f$  = friction coefficient,  
 $C_c$  = contraction factor at the passage entrance,  
 $C_e$  = expansion factor at the passage exit.

The entropy-enthalpy diagram for supercritical helium indicates that a pressure drop along a hydraulic passage for a constant (J/g) is associated with a temperature rise along the passage. A pressure drop of  $\Delta p = 5 \text{ kg/cm}^2$  will yield a temperature rise in the supercritical helium of  $\sim 0.8^\circ\text{K}$ . This rise in coolant temperature is undesirable in high field magnets ( $B_{0,0} \cong 7 \text{ T}$ ) because of the considerable reduction in  $J_c$ .

A possible scheme is to operate with high pressure drops and consequently high coolant velocities only during magnet charging. In steady-state conditions, the pressure drop can be reduced to operate with helium velocities of  $\sim 1 \text{ m/sec}$ . The refrigerator system will operate during this time at a fraction of its nominal cooling power.

### 4. Frictional Losses

Supercritical helium passing at a certain speed through a hydraulic passage will generate frictional losses at the interface on the passage walls. The losses can be calculated from shearing stresses on the helium boundary layer<sup>29</sup>:

$$\tau_0 = \frac{1}{8} \cdot \lambda \cdot \frac{\delta}{g} \cdot v^2 . \quad (20)$$

$\lambda$  is the frictional resistance coefficient, explicitly written as:

$$\lambda = 0.3164 \left( \frac{v \cdot \delta \cdot d_h}{v} \right)^{-\frac{1}{4}} , \quad (21)$$

where  $v$  is the dynamic viscosity.

---

29. J. Kestin, Boundary Layer Theory (McGraw-Hill, 1960), 4th ed.

Inserting  $\lambda$  in Eq. (20) we get:

$$\tau_0 = 3.955 \times 10^{-2} \frac{\delta_f}{g} \cdot \bar{v}^{7/4} \cdot v^{1/4} \cdot d_h^{-1/4} \quad (22)$$

$\tau_0$  changes with  $\bar{v}^{7/4}$  rather than linearly, as for laminar flows, according to Stokes' law.

The frictional losses per unit surface area are given by:

$$\begin{aligned} P &= \tau_0 \cdot \bar{v} \\ &= 3.955 \times 10^{-2} \cdot \frac{\delta_f}{g} \cdot \bar{v}^{11/4} \cdot v^{1/4} \cdot d_h^{-1/4} \end{aligned} \quad (23)$$

Hydraulic passages in large magnets have generally a length of  $\sim 100$  m and many passages may be connected in parallel, hydraulically but in series electrically. The choice of pressure drop, helium velocity, and obtainable heat flux should be correlated such that frictional losses do not exceed 10% of the total static losses.

### CONCLUSIONS

To optimize size, geometry and type of a composite superconductor, one has to consider the following requirements:

- 1) Field distribution within the useful aperture of a magnet.
- 2) Field reproducibility over the operational lifetime of the equipment.
- 3) Operational reliability.
- 4) Economy of operation.

With the type of magnet to be designed, the basic field and force distributions over the coil are known, which automatically provide a first order estimate for the over-all dimensions of the conductor and the necessity for reinforcements.

Instabilities due to flux motion on the other hand dictate the size of individual films or filaments, their distribution, the choice of substrate, the enthalpy of the system, and cooling methods.

It is evident that small size magnets, where Lorentz forces on the conductor are not of prime importance, can be built on the basis of  $\text{Nb}_3\text{Sn}$  films on a Hastelloy substrate and stabilized by means of copper, silver, or superfluid helium. Over-all metastable current densities achieved in such magnets may exceed  $5 \times 10^4$  A/cm<sup>2</sup> at transverse fields of 5 T.

Although only edge cooling has been widely used, new ways of cooling flat conductor surface are sought.

For large magnets, where Lorentz forces become dominant, moderate over-all current densities in the order of  $1.5 \times 10^4$  A/cm<sup>2</sup> at 5 T may be feasible if the diameter of individual filaments in the substrate is such as to comply with Eq. (13). For ac applications flux jumps must be avoided entirely, which indicates that individual filament size should be  $\sim 3 \times 10^{-3}$  cm. For dc application and efficient cooling, a filament diameter of  $1.5 \times 10^{-2}$  is adequate where the copper-to-superconductor ratio may be 3:1. The diameter of individual superconductors for ac application is typically of a size given by the relation  $d_f \cdot J_c \leq 1500$  A/cm. For most dc applications with

improved matrix heat capacity, this relation is conservative and can be at least doubled. The thermal capacity of the system can be improved considerably if supercritical helium is passed through the coolant passage of a porous matrix supporting individual, partially stabilized superconductors. A conductor in this form is not only useful for dc magnet application, but also for ac magnets and power transmission. The porous matrix may be sintered cadmium with a porosity of 50% or more to allow helium gas to be in direct contact with the superconductor. Its sole purpose is to support individual superconducting filaments and hold them in place along the hollow conductor. For dc applications, composite conductors based on a copper matrix and filamentary NbTi wires are widely used.

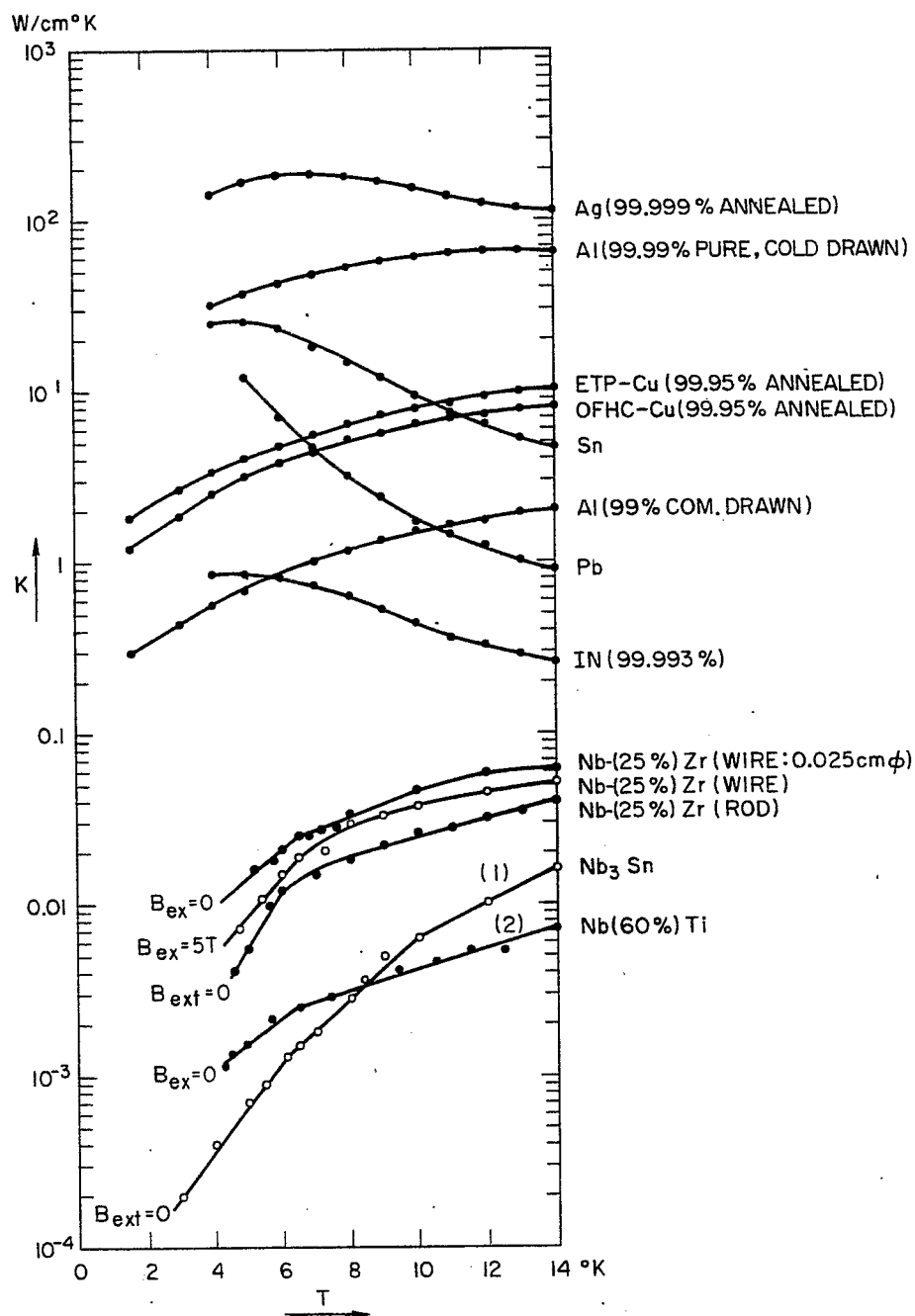


Fig. 1. Thermal conductivities of superconductors type II and normal metals.  
 (1) From Reference 18.  
 (2) From Reference 17.

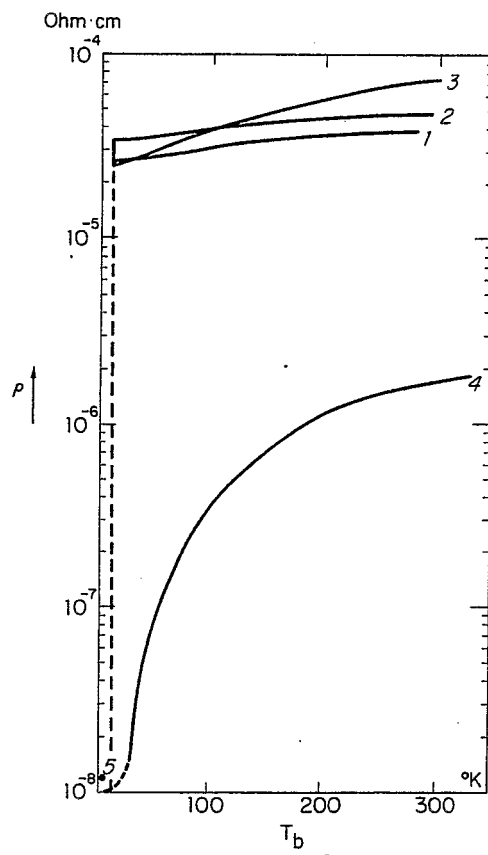


Fig. 2. Electrical resistivities of superconducting type II materials.

1.  $\text{Nb}_3\text{Sn}$ .
2.  $\text{Nb}(25\%)\text{Zr}$ .
3.  $\text{Nb}(60\%)\text{Ti}$ .
4. 99.999% pure annealed copper.
5. 99.995% OFHC copper as received, not annealed,  
 $\rho_{4.2^\circ\text{K}, B=0} = 1.2 \times 10^{-8} \Omega\cdot\text{cm}$ .

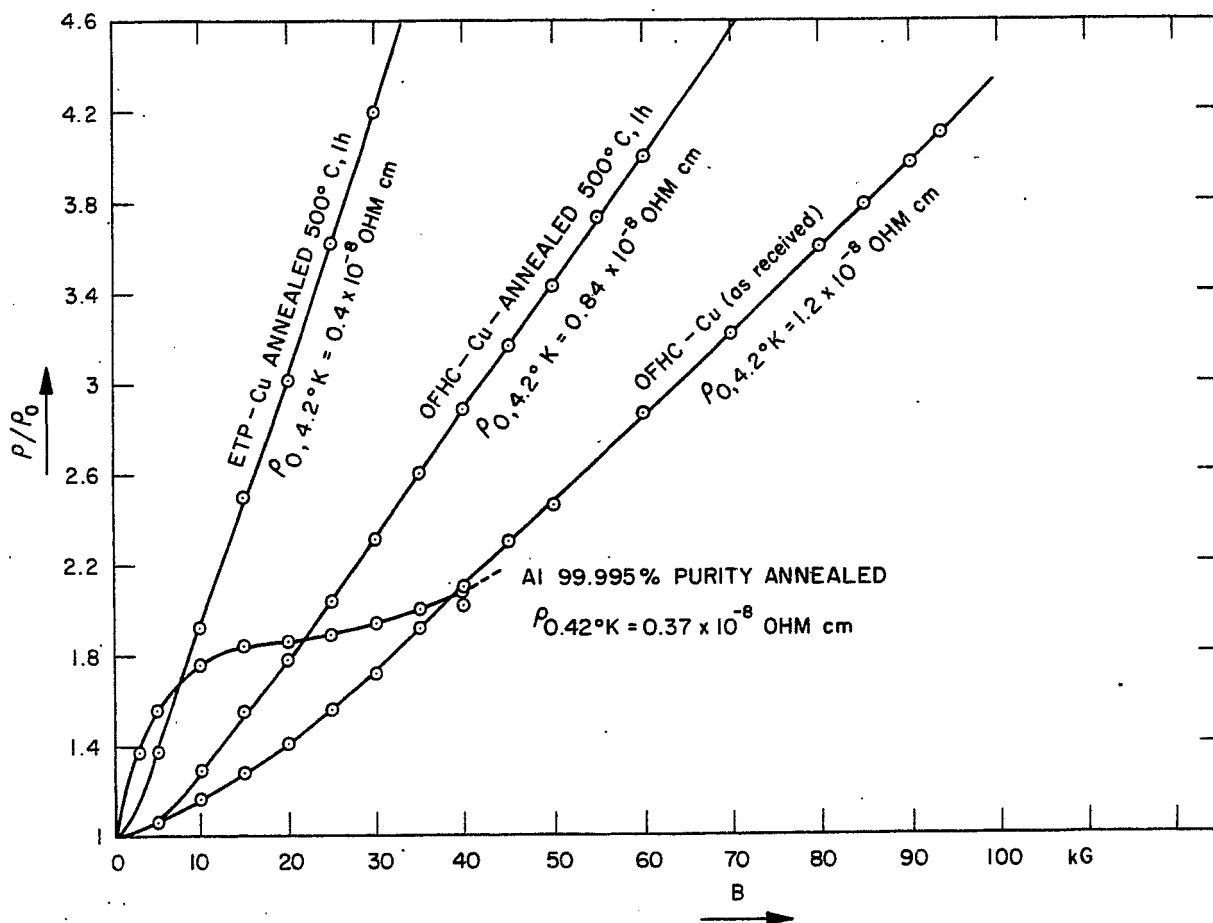


Fig. 3. Magnetoresistivity curves of copper and aluminum.  
(No mechanical stress.)

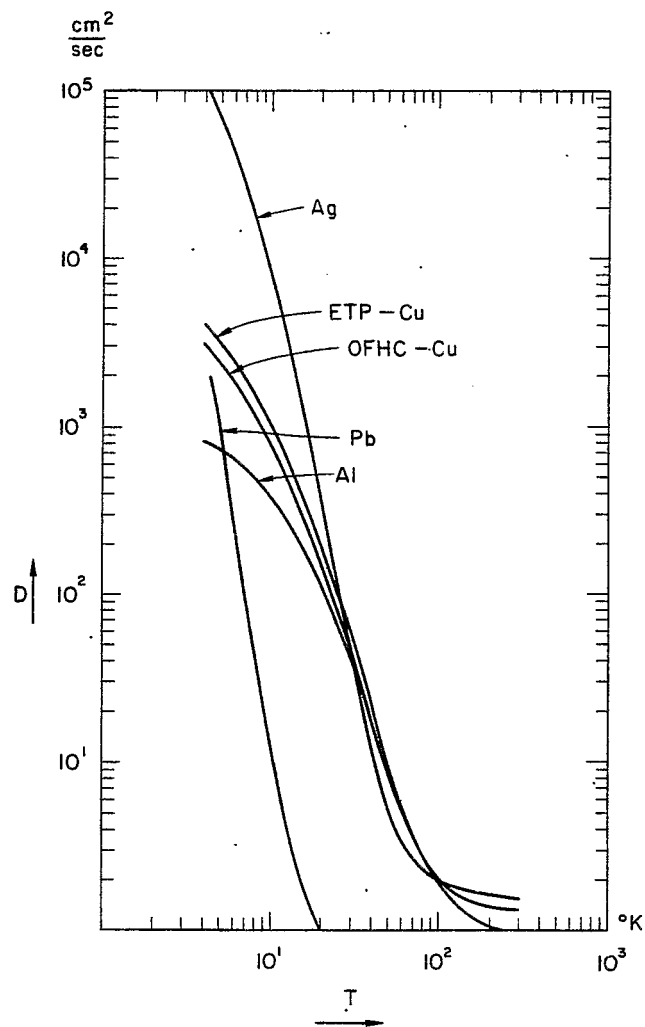


Fig. 4. Thermal diffusivities of a few commercially obtained metals.  
(No mechanical stress.)



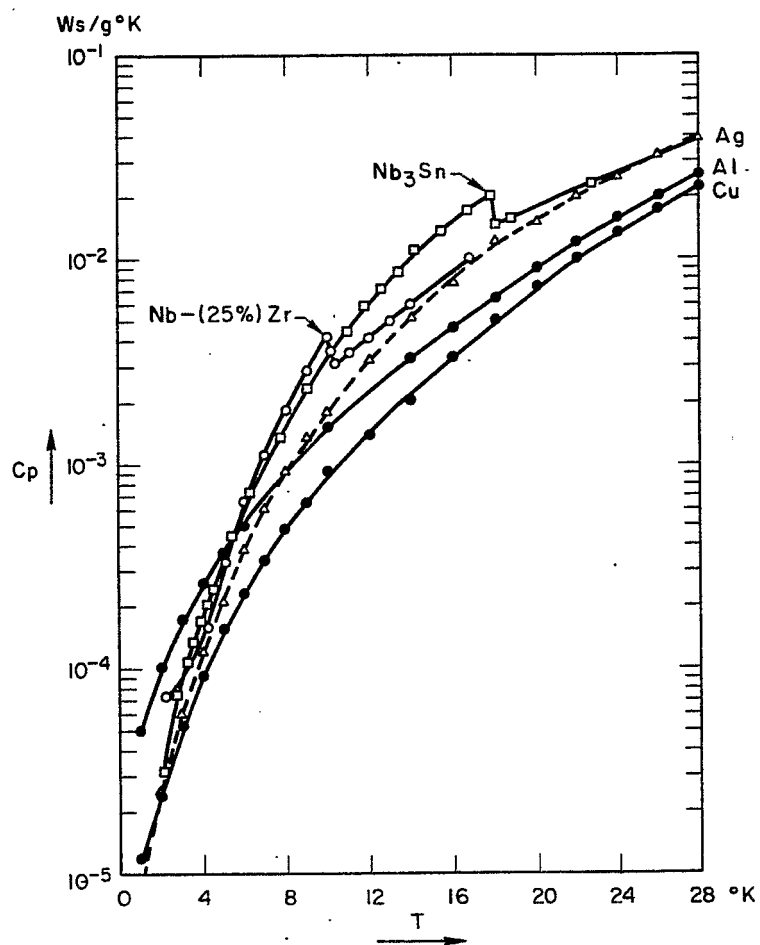


Fig. 5. Specific heat vs temperature for superconducting type II materials and normal metals.

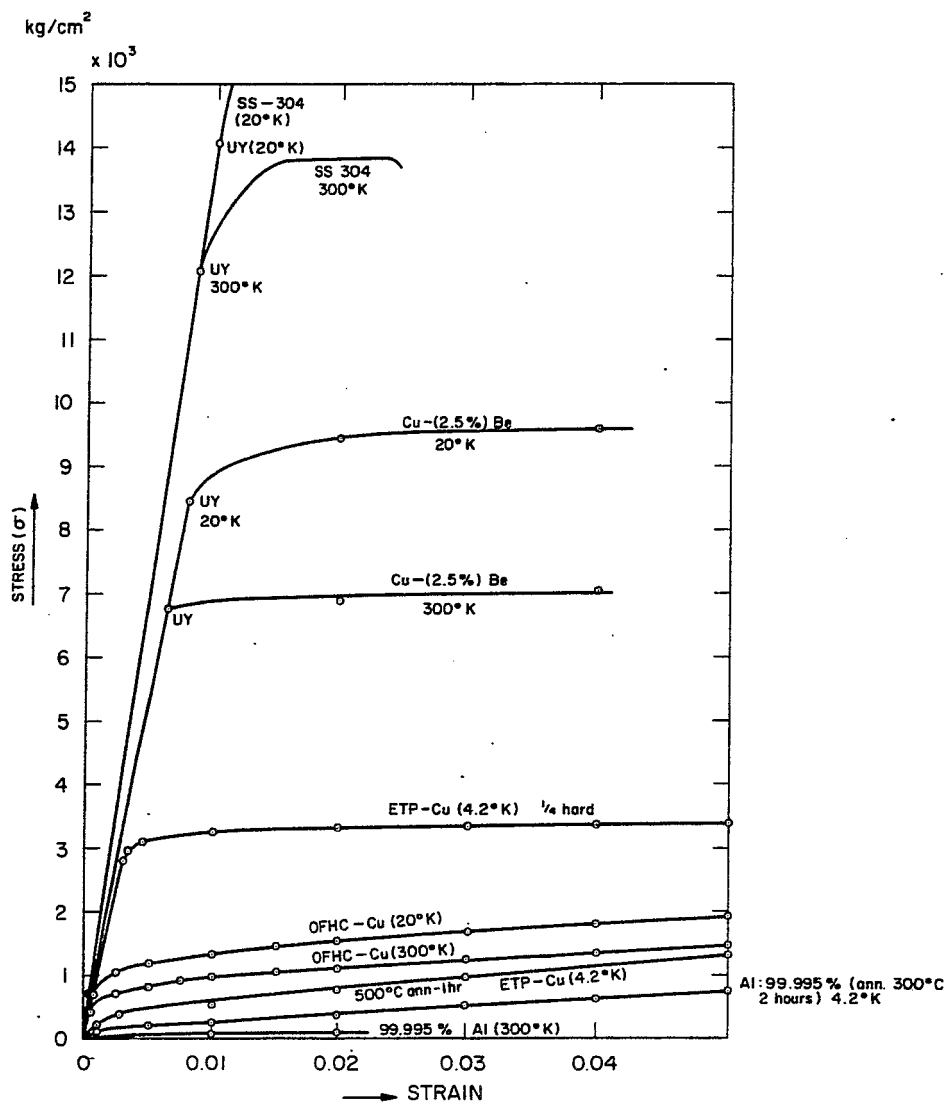


Fig. 6a. Stress-strain diagrams of normal metals.

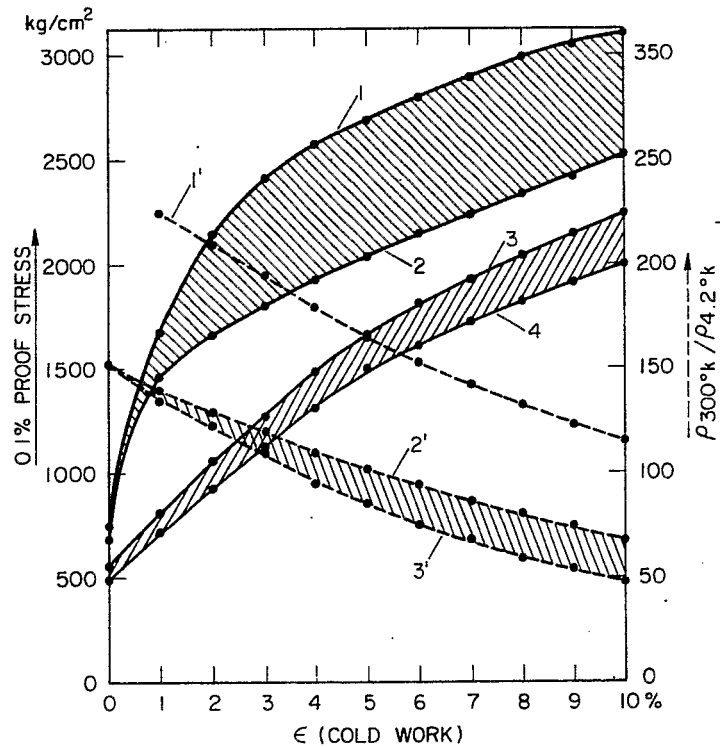


Fig. 6b. Effect of mechanical strain on the performance of copper and composite conductors at 4.2°K:

1. Nb(60%)Ti and Cu, composite conductor: 3 to 1 Cu to SC ratio.
2. Nb(60%)Ti and Cu, composite conductor: 5 to 1 Cu to SC ratio.
3. 99.995% Cu, soft, as received.
4. 99.995% Cu, annealed.
- 1'. 99.995% annealed copper.
- 2'. Nb(60%)Ti and Cu, composite conductor: 5 to 1 Cu to SC ratio.
- 3'. Nb(60%)Ti and Cu, composite conductor: 3 to 1 Cu to SC ratio.

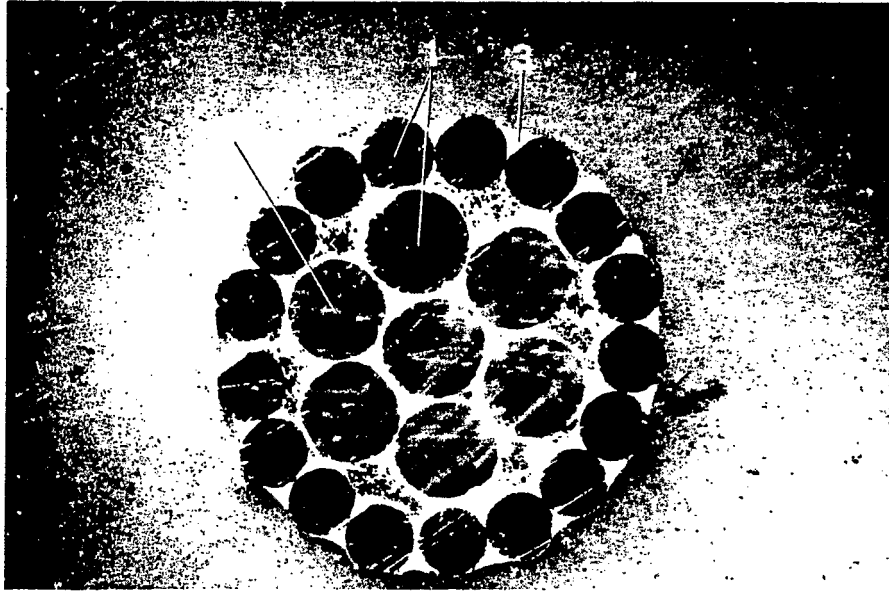


Fig. 7. Nb(22at%)Ti-Cu - cable.  
 1. Cu - strand.  
 2. SC - filament.  
 3. Ag - Sn alloy.

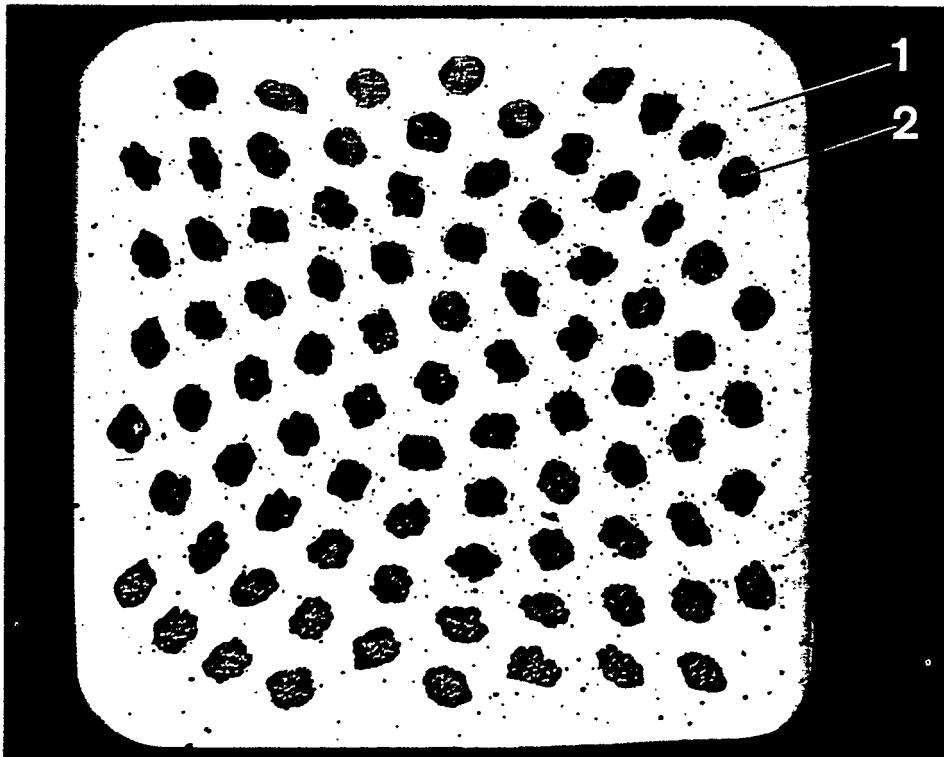


Fig. 8. NbTiCu composite conductor.

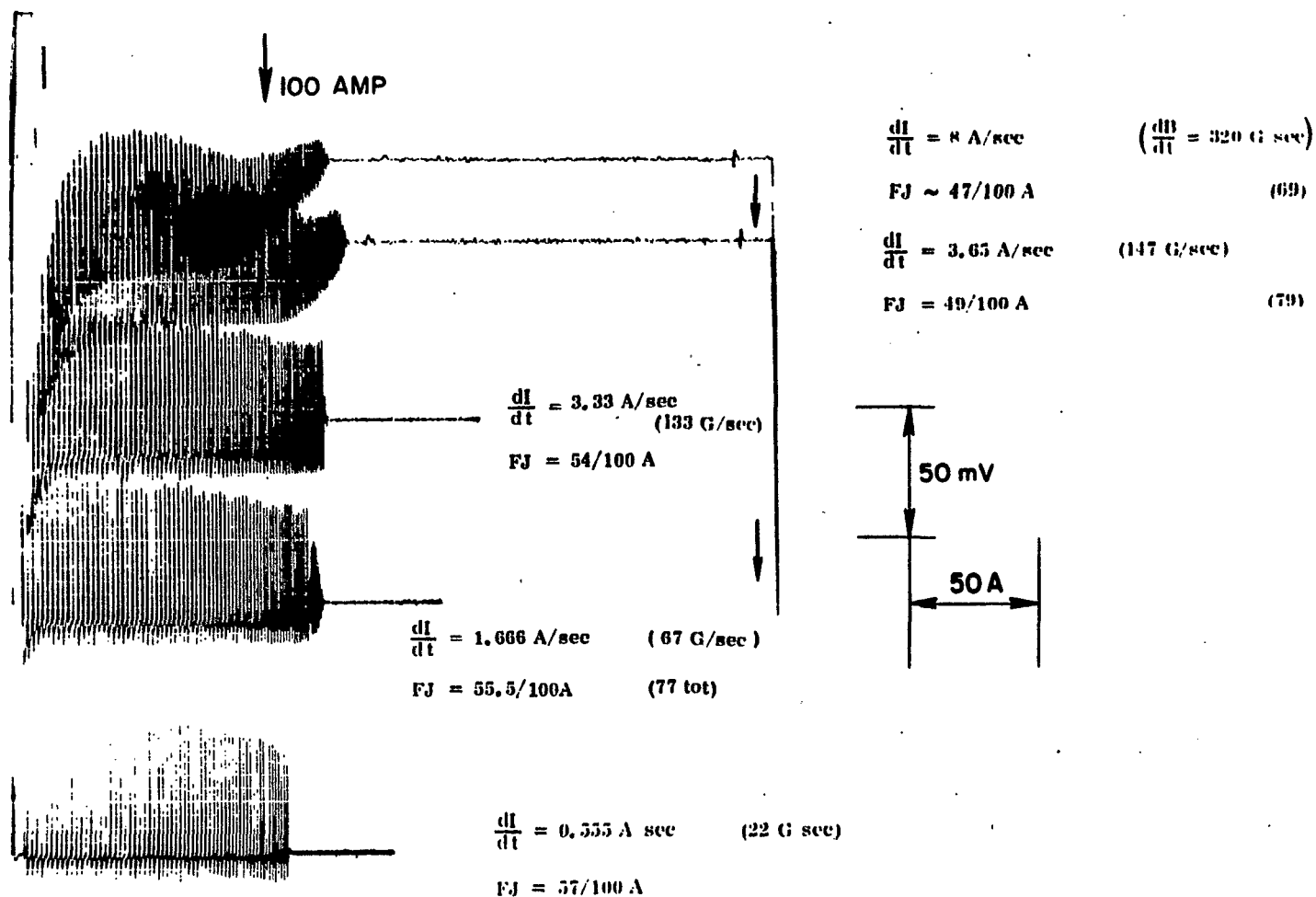
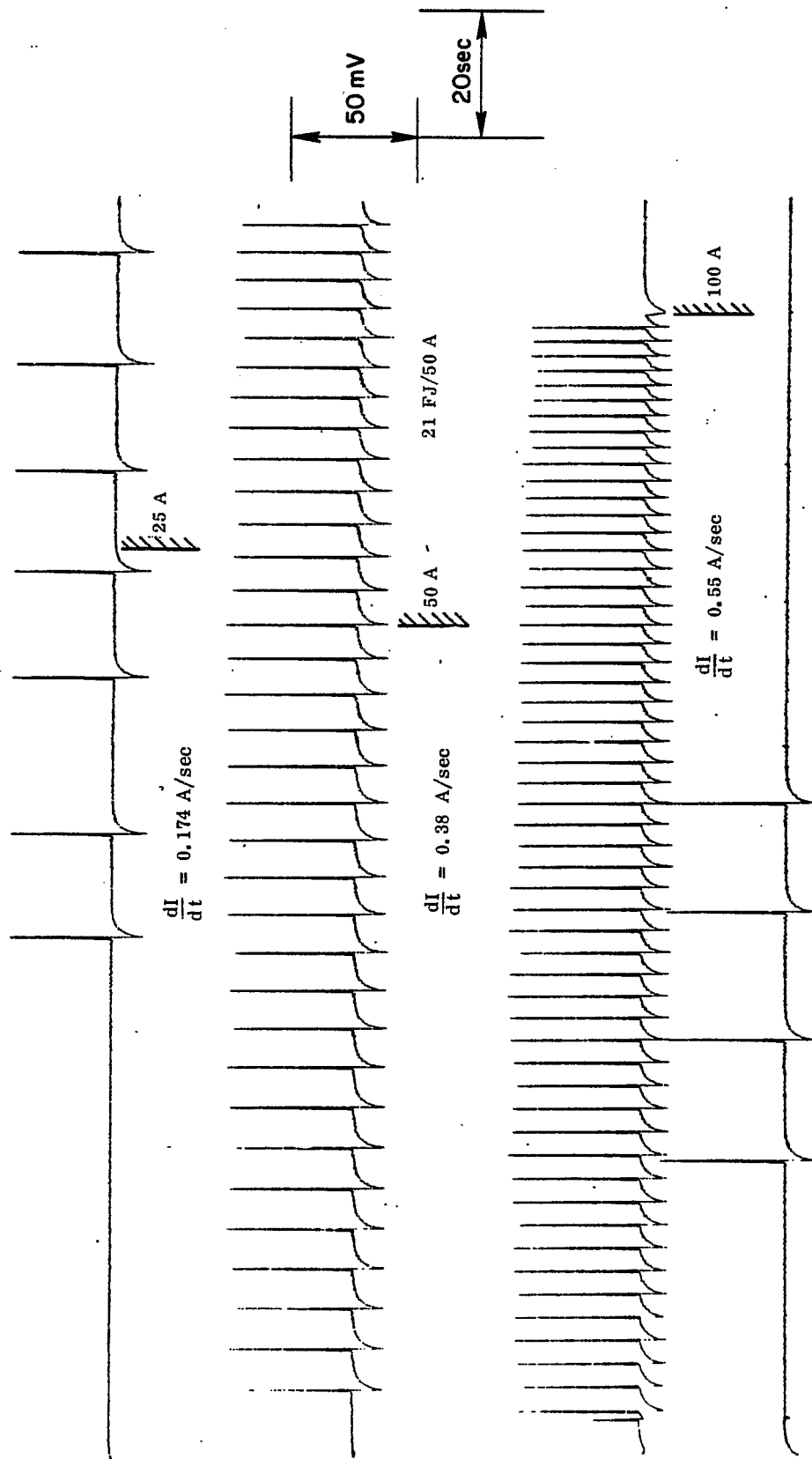


Fig. 9. Voltage current oscillograms of medium size magnets.  
(The individual turns are insulated by means of a multifilamentary nylon ~ Nomex.)



$$\frac{dI}{dt} = 0.125 \text{ A/sec}$$

Fig. 10. Flux jump pattern due to internal short circuits in the magnets.

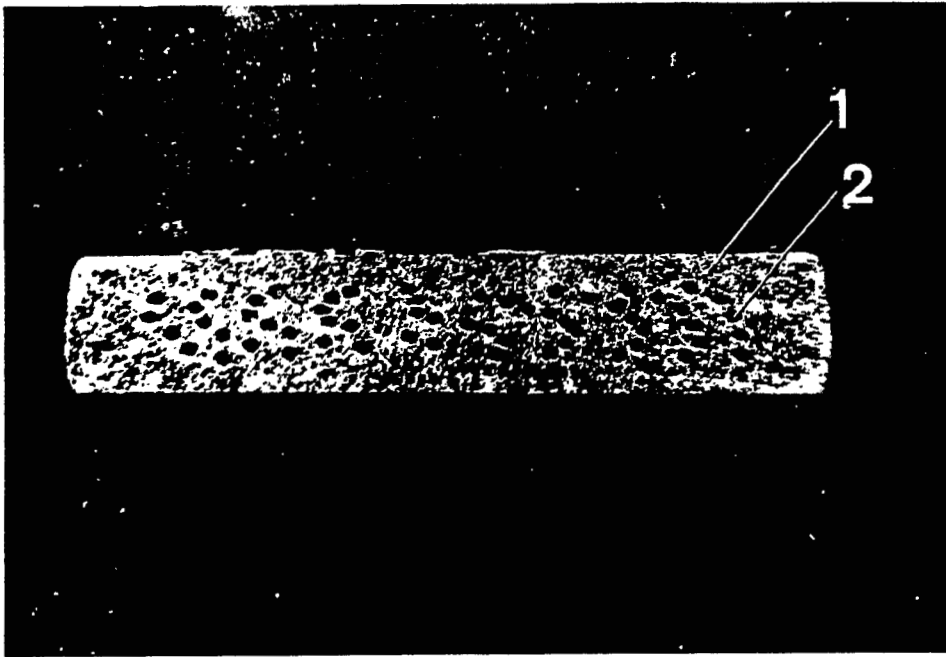


Fig. 11. Nb(60%)Ti-Cu composite strip.



Fig. 12. NbTiCu composite conductor reinforced with stainless-steel wires.

1. Copper substrate.
2. Superconducting filament.
3. Stainless-steel reinforcement.

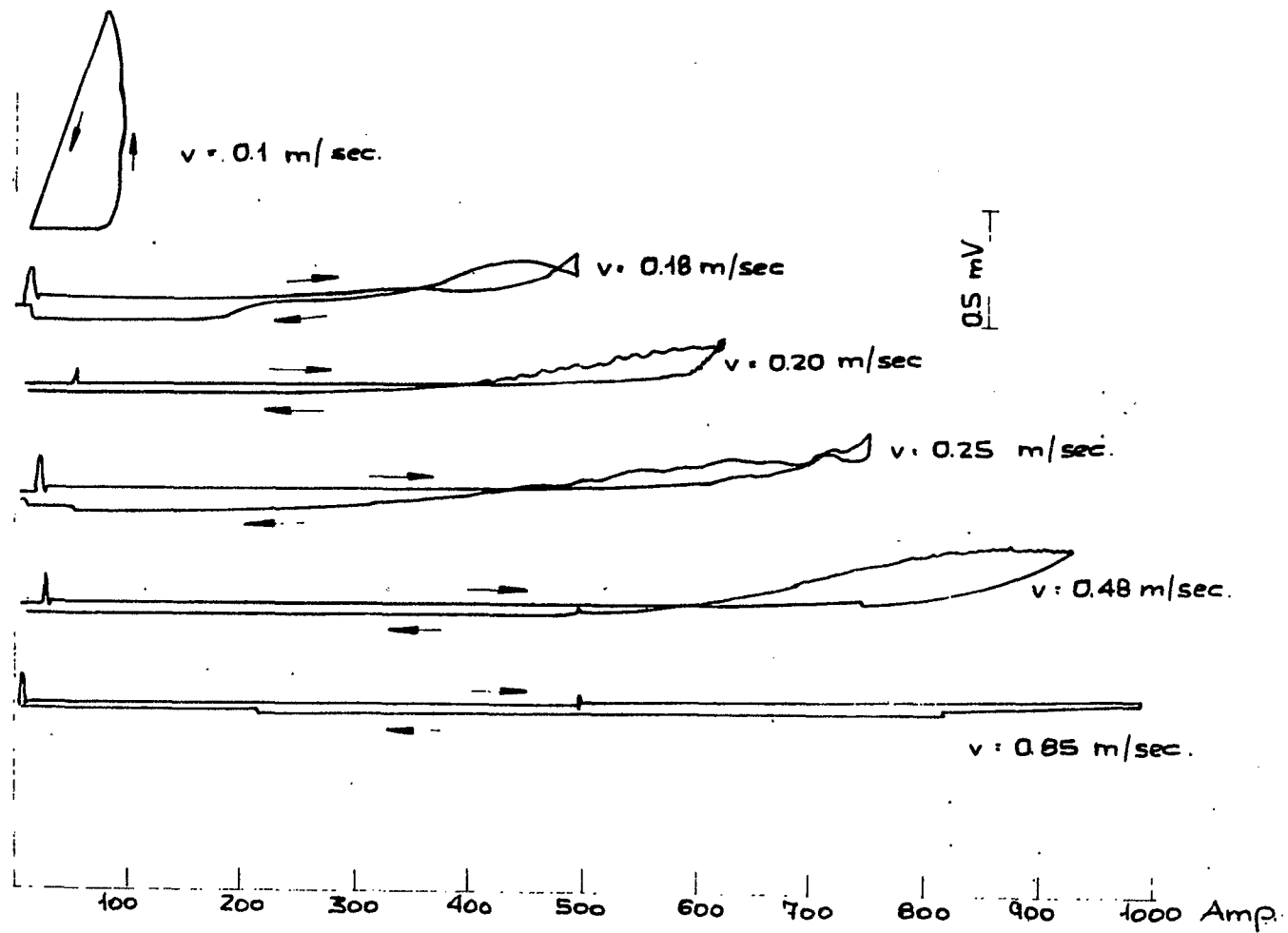


Fig. 13. Current-voltage diagrams measured at various helium flow rates in hollow composite conductor (Nb<sub>3</sub>Sn and Cu).



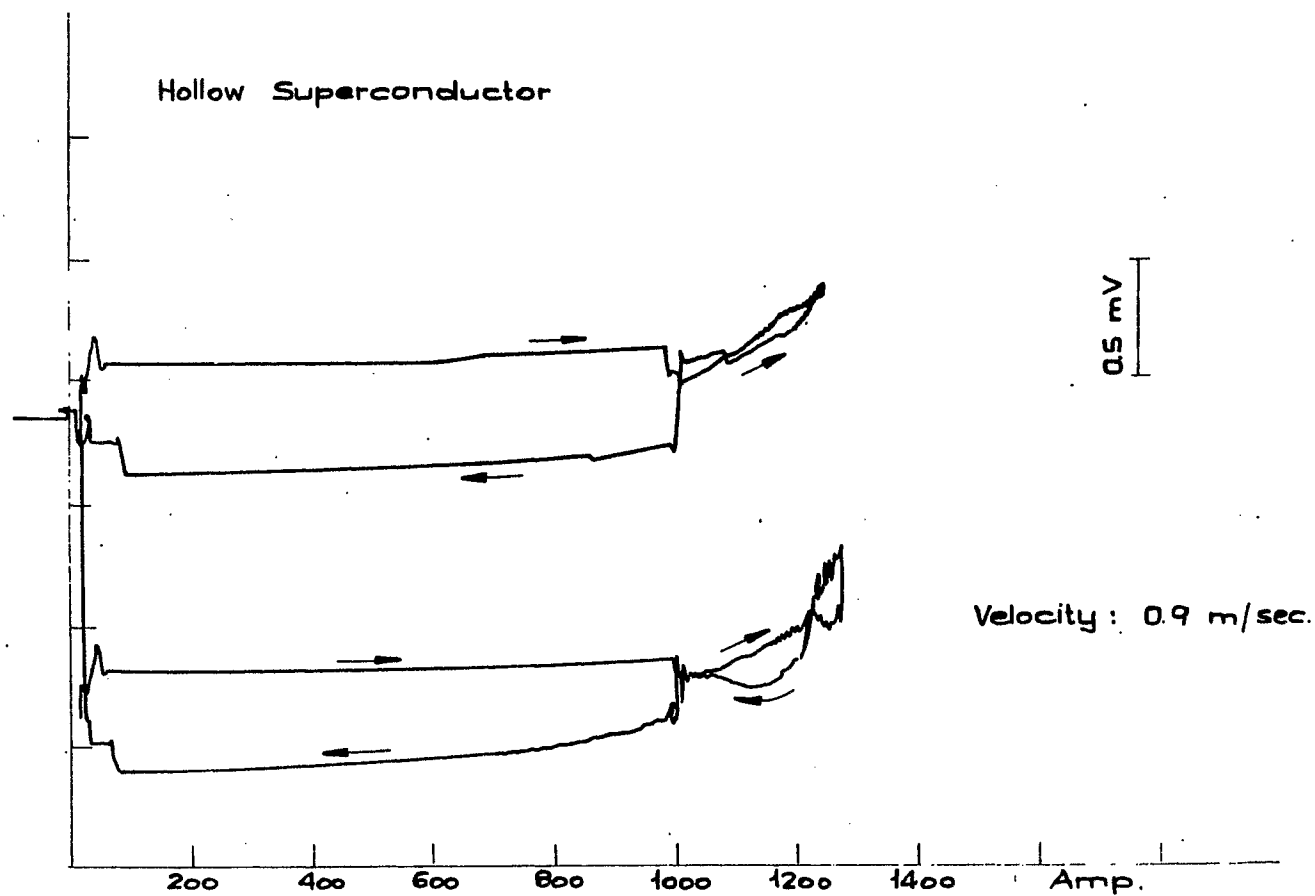


Fig. 14. Voltage-current diagrams in a  $(\text{Nb}_3\text{Sn})$ -Cu hollow conductor wound into a single layer coil. The length of the hydraulic passage is  $\sim 3$  m.

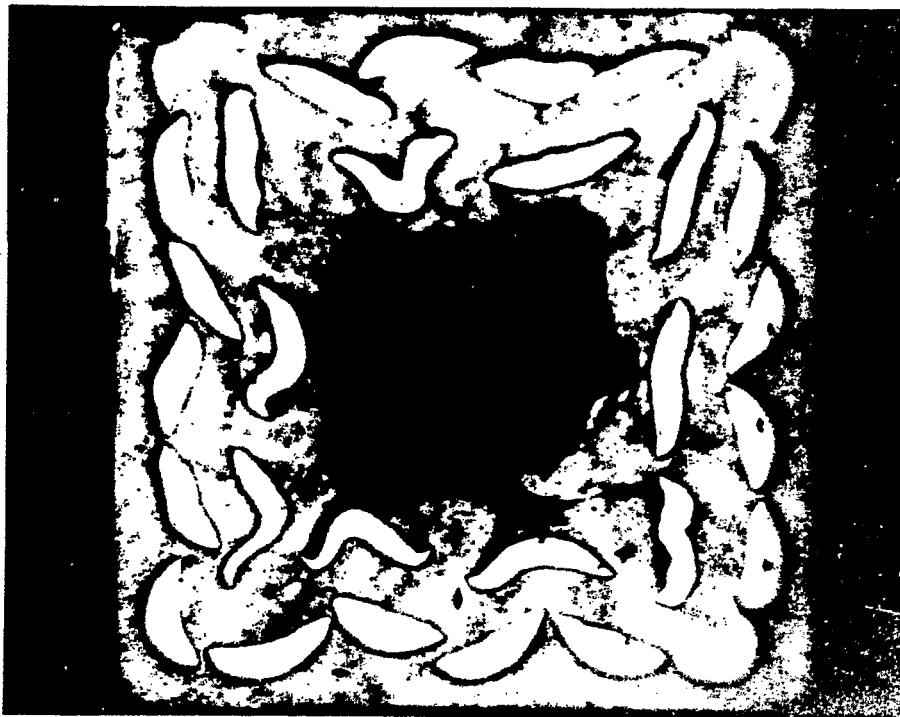


Fig. 15. Nb(60%)Ti-Cu hollow composite conductor,  $0.5 \times 0.5 \text{ cm}^2$  over-all dimensions,  $0.22 \times 0.22 \text{ cm}^2$  coolant hole. Although the individual superconductors are severely distorted, the conductor shows short sample performance (Cu:SC ratio 2.8:1).

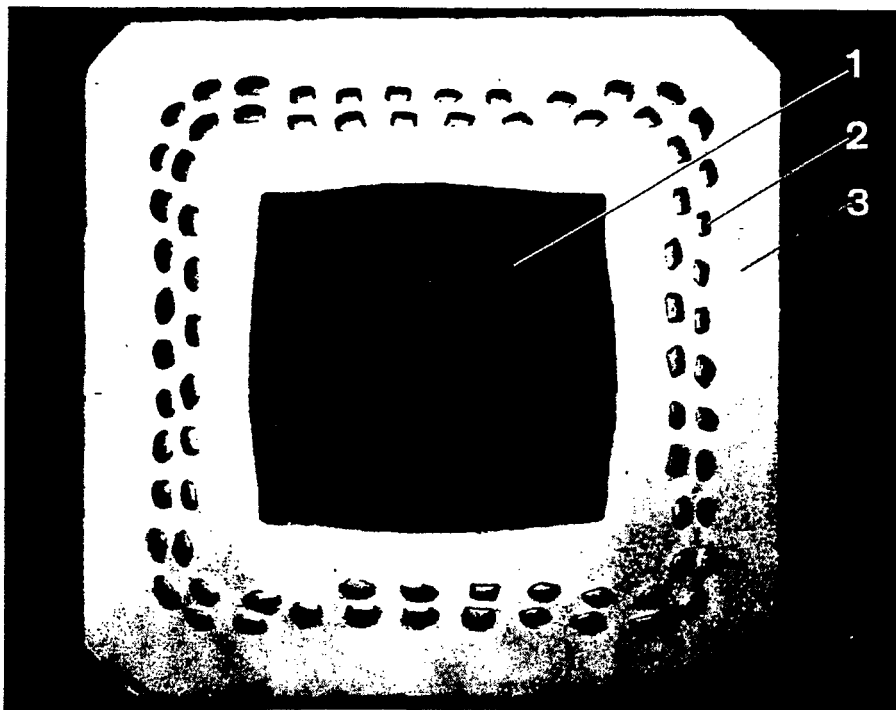


Fig. 16. 5000 A, 60 kG hollow composite conductor. Over-all dimensions  $1.2 \times 1.2 \text{ cm}^2$ .

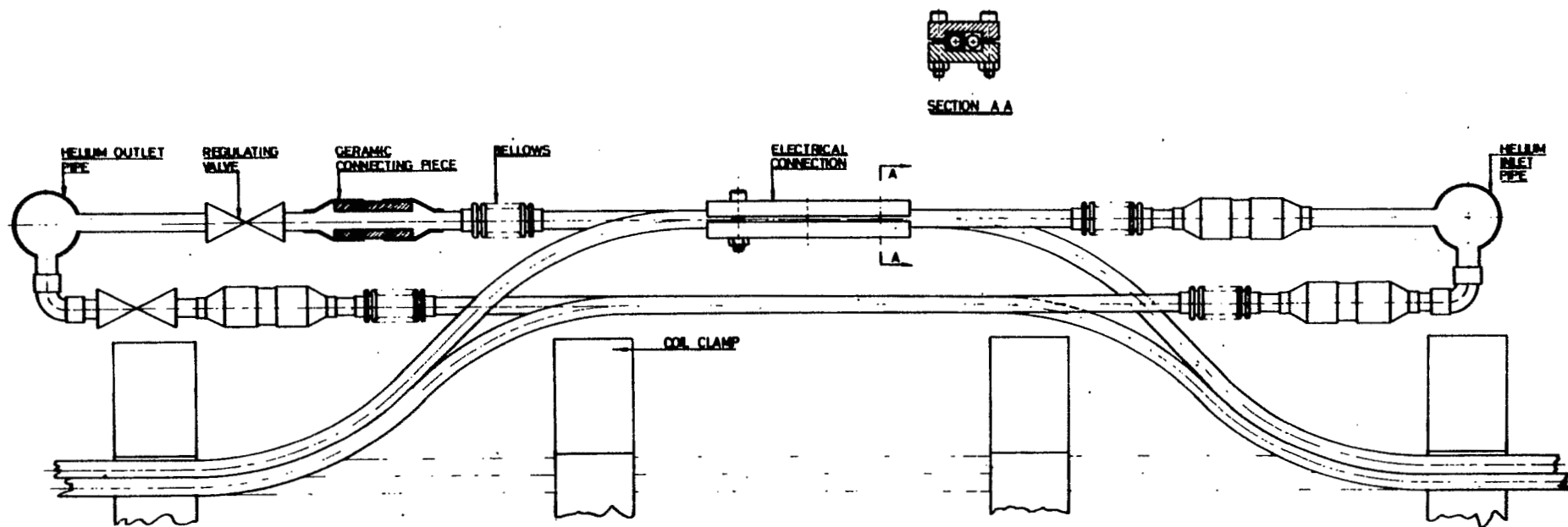


Fig. 17. Proposal to disconnect electrically each hydraulic passage by means of reinforced ceramic tubing.

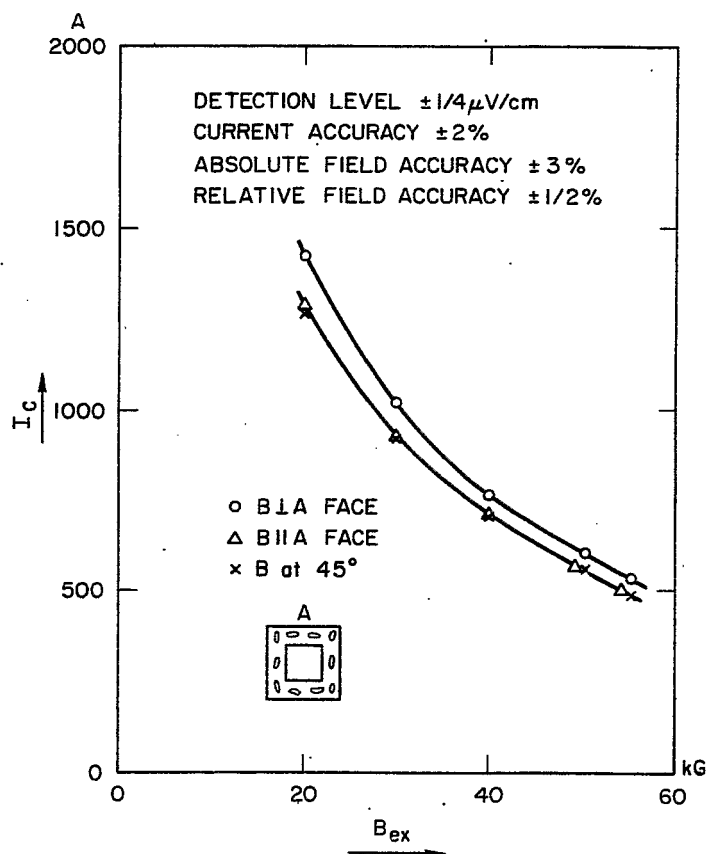


Fig. 18. Anisotropy effect on a hollow composite conductor (courtesy IMI).

## AC LOSSES IN SUPERCONDUCTORS\*

S.L. Wipf  
Atomics International  
A Division of North American Rockwell Corporation  
Canoga Park, California

This is a review of studies of ac losses in superconductors. In a paper<sup>1</sup> published three years ago we read in reference to previous work that "there is frequently considerable disagreement between results obtained with comparable samples in similar experimental conditions (ratios of  $10^2$  or even of  $10^4$ ).". I took this as a challenge.

Looking into this more closely revealed surprising agreement if results are expressed properly. Of course now there are many more results available.

Interest in ac losses is largely a practical one, because:

- 1) Present-day technology, with conventional conductors, uses ac. It is easiest simply to replace the conductor.
- 2) There are special applications, ideal for superconductivity and inherently ac, such as gyroscopes, linear accelerators, etc.
- 3) In a wider sense ac is encountered in any transient, such as charging and discharging of magnet coils, and it is this aspect which interests the accelerator builder most.

The type I superconductor plays an insignificant role in most of these applications. This was decided over a generation ago, because the critical fields and currents are too small (Pb with a critical field of 550 Oe at 4.2°K alone has kept a place).

Type II superconductors almost shared the same fate and it took 30 years before their usefulness was rediscovered, perhaps luckily, for otherwise all of us would probably worry about different problems and there would not have been this Summer Study.

The reason for this is that an ideal type II superconductor becomes resistive at even lower fields and currents, as we see (bottom right-hand graph in Fig. 1) in the critical current vs field diagram. Only a nonideal, or imperfect, type II superconductor carries transport current in high fields as is illustrated at the top right of Fig. 1.

In the mixed state (between  $H_{c1}$  and  $H_{c2}$  in the magnetization curve on the left side of Fig. 1) the bulk superconductor admits magnetic flux (Fig. 2). This flux is bundled into fluxoids by means of a corresponding current pattern, which is shown (top of Fig. 2) together with the internal field.<sup>97</sup> The field maxima are at the normal cores of the fluxoids. This current pattern represents, in a sense, the maximum current density which can be carried in every place of the material. All the currents are flowing in little circles and there is no net current flow. If a transport current is impressed it will have to flow in addition to these currents and therefore create resistance.<sup>98</sup> At the same time, the fluxoids having no preferred places in an ideal material start moving under the influence of Lorentz forces.

---

\*This is an expanded version of a talk given at the Applied Superconductivity Conference in Austin, Texas, 1967 [see J. Appl. Phys. 39, 2538 (1968)].

In an imperfect superconductor the superconducting parameters ( $T_c$ ,  $H_{c1}$ , etc.) have locally different values. We illustrate (bottom of Fig. 2) the local variations of the energy gap  $\Delta$ . If now a transport current is impressed, the flux structure will adjust its position in a way that the current density in the transport current direction is in places where  $\Delta$  is larger whereas the lower  $\Delta$  regions carry current in the opposite direction. Eventually a fluxoid distribution is reached which represents the largest transport current possible. We can also see that as soon as the fluxoids start to move under the influence of Lorentz forces a large dissipation will set in because the transport current will have to flow in regions where it exceeds the critical supercurrent density and therefore creates resistance. This way of looking at what is usually called "flux pinning" is particularly suitable for our ac loss discussion. We are all used to thinking in terms of Ohm's law and the resistance mentioned above is actually measured in certain experiments which we shall discuss.

Our task then is to review ac losses in imperfect type II superconductors.

Of the vast literature covering ac studies in superconductors we have to make a choice in the light of this introduction. Our main interest is in studies which emphasize directly ac losses; it is inevitable that the phase transition under ac conditions is also of great interest in this context. Many ac losses are connected with specific applications, and finally we have to include papers dealing with other special topics which are closely related.

We list the references as follows, vaguely in order of their importance within each group:

1. Ac losses, experimental: references 1 to 32. Of these 1 to 19 provide data which can be compared to each other (see Figs. 14 and 20 and accompanying tables). Other references whose main emphasis puts them into different groups but which also belong here are 34, 36, 59, 60 and 84.
2. Ac losses, theoretical approach and calculations: references 33 to 44; also of interest here are 9, 10, 22 and 23.
3. Ac phase transition (critical ac current): references 45 to 56 and also 6, 8, 19, 27, 57, 58 and 62.
4. Ac studies in coils and incidental to coil performance: references 57 to 62 and also 4, 10, 11 and 33. Reference 63 concerns losses in an adiabatic demagnetization apparatus, and Refs. 64 and 65 deal with superconducting transformers.
5. Studies of cavities and high frequencies: references 66 to 77. Of these only 66 to 73 address themselves specifically to the problem of losses, whereas the others simply report Q's and not further explained differences in Q values. Reference 83 may also be of interest here. Since superconducting cavities have been studied quite extensively prior to the arrival of type II superconductors one should include Ref. 78, which is a review of this earlier work.
6. Special topics: references 79 to 90. This includes resonances,<sup>80</sup> flux jumps,<sup>87</sup> current distribution,<sup>88,89</sup> resistance in increasing field,<sup>81-83</sup> and special experimental methods.<sup>84-86</sup>

Without stating any special claims we hope that this list is reasonably complete in Groups 1-3. It is naturally less so in subsequent groups and in fact quite eclectic in Group 6.

After these introductory remarks we look at the electrodynamic distinction between a normal conductor and a superconductor.

First, we recapitulate the situation in a normal metal: Everybody knows Ohm's law;  $\rho$  is the resistivity,  $j$  the current density (Table I). We have two of the Maxwell

TABLE I  
Normal Conductor

Ohm's law	$E = \rho j$
Maxwell equation	$\text{Curl } B = 4\pi j$ $\text{Curl } E = - \dot{B}$
Diffusion equation	$\nabla^2 B = \frac{4\pi}{\rho} \dot{B}$

equations (units such that  $c = 1$ ). We put Ohm's law into the lower of these equations and substitute the result into the curl of the upper equation to obtain the diffusion equation which we know from heat conduction. The electromagnetic diffusivity is the inverse of the factor  $4\pi/\rho$ .

For an alternating field the solution for the induction inside a conductor is given in Fig. 3, with  $\lambda$  being the penetration depth (Fig. 3). We find that the amplitude falls off into the interior and at the same time the phase shifts (as indicated by the imaginary component). The penetration depth is inversely proportional to  $\sqrt{\omega}$ , a well-known fact.

About type I superconductors we shall not say much (Table II). Ohm's law is valid for the normal electrons, the current being made up of a normal and a supercurrent, and London's equation applies for the superconducting part. There is a kind of  $L di/dt$

TABLE II  
Type I Superconductor

$$\left. \begin{aligned} E &= \rho j_n \\ E &= \frac{\delta}{\delta t} \Lambda j_s \end{aligned} \right\} j = j_n + j_s$$

$$\frac{j_s}{j_n} = \frac{\rho}{\Lambda 2\pi \nu}$$

$$\Lambda \approx 10^{-31}$$

$$\rho \approx 10^{-20}$$

$$j_n \text{ negligible for } \nu < 10^{10} \text{ Hz}$$

term. Only  $\Lambda$  is so very small that  $j_n$  is practically zero even if  $di/dt$  is not. If the process which led to the diffusion equation is followed, a similar equation is obtained and the solution shows  $j_s/j_n$  to be proportional to  $\rho/(\Lambda \text{ times frequency})$ . With order of magnitude values for  $\Lambda$  and  $\rho$  it turns out that  $j_n$  is negligible below  $10^{10}$  Hz. At these frequencies, which reach into the far infrared region, the radiation energy becomes comparable to the energy gap. This means that in the process of the absorption the Cooper pairs are destroyed.

For lower frequencies there are no losses inside the superconductor. A type II superconductor behaves as a type I below  $H_{c1}$ , and therefore this result applies also.

In a type II superconductor Ohm's law (if we can call it that) still looks the same, with the important modification that  $\rho = 0$  if  $j < j_c$  (Fig. 4). This makes all the difference. If  $j$  exceeds the critical value,  $\rho$  will change very rapidly through many orders of magnitude in a very small current interval. Since  $j_c$  is large, it is a good practical assumption that  $j$  in this equation is constant and, therefore,  $\rho$  is proportional to  $E$  and with  $E$  it is proportional to  $dB/dt$ .

The Maxwell equation involving curl  $B$  is given for a plane slab with  $X$  direction into the superconductor. (We can assume a constant  $j_c$  independent of  $B$  which will turn out to be an adequate simplification.)

A field will penetrate into the material with the illustrated slope, inducing the critical current density everywhere in the penetration layer ( $dB/dx = 4\pi j_c$ ). If the field moves in the opposite direction it will induce the critical current density in the opposite direction. The field inside changes in the manner indicated with arrows until the opposite amplitude is reached.

Note that at the same external  $H$ , between the extremes, the internal field is different depending on whether the field goes up or down. This gives the hysteresis in the magnetization curve.

The diffusion equation is obtained as before, but  $\nabla^2 B$  is essentially constant for the  $dB/dt$  values under consideration because of the proportionality between  $\rho$  and  $dB/dt$ .

This proportionality between  $\rho$  and  $dB/dt$  may need some elaboration and also some experimental corroboration (Fig. 5). If we consider a cylinder in a parallel field large enough to penetrate to the center and increasing at the rate  $dH/dt$ , one has inside  $dB/dt = dH/dt$  outside (to a near approximation).

We can work out the electric field at a point  $r$  by the Maxwell equation: circumference times  $E =$  flux change inside. One gets  $E = \frac{1}{2}r dH/dt$ . We know that  $j = j_c =$  constant. It follows that  $\rho \propto dH/dt$ . If now a longitudinal transport current is applied we must get a voltage drop following Ohm's law with an average value of  $\rho \propto (b/j_c) dH/dt$ . We may call this the "dynamic resistivity."

A word about the averaging factor. In our example we deduce that  $\rho = 0$  at the center of the specimen ( $r = 0$ ), and Kirchhoff's law would then require the transport current to flow through the center with infinite density. But with the total current density being limited to a value close to  $j_c$ , the transport current will flow over the whole cross section, with resistance everywhere. Without getting involved in the complicated problems of the details of this current flow<sup>88,89,99</sup> we assume a uniform distribution and obtain the average value given. We can get the same results by using solutions of the diffusion equation, known from the thermal equivalent ( $H$  corresponds to  $T$  and the thermal diffusivity  $\alpha$  to  $\rho/4\pi$ ). The advantage is that many mathematical solutions exist; in this case we need the temperature difference between the center of a specimen (cylindrical, infinitely long) and its surface which has a uniformly increasing (or decreasing) temperature.

Let us look at the experimental results shown in Fig. 6. Rayroux, Itschner and Müller<sup>81</sup> made measurements on a bifilar coil in an increasing external field. The transport current through the coil creates a voltage which we see here. Observe that there is no voltage until the field, which completely penetrates the wire, is reached, because then there is a completely superconducting core which does not see  $dH/dt$  and carries the transport current without loss. Afterwards we encounter the resistivity just calculated. The same is true on reducing the field from 15 kG; there is no



resistance until the penetration field ( $\sim 14$  kG) is reached.

Comparison of these results with other results is made in Table III. In the first column the radius of the cylinder is given, a 10 mil wire measured by Taquet<sup>61</sup> (using the same geometry which was subsequently used by Rayroux<sup>81</sup>) and a 5 mil wire mentioned in Fig. 6. The second column gives the resistivity divided by  $dH/dt$ . The last column shows for comparison the ratio  $\rho j_c / (b dH/dt)$ . The difference in these numbers is partly a factor due to different geometry and partly uncertainty in the applicable  $j_c$  values. The first case (Lubell and Wipf<sup>83</sup>) which is calculated, using the thermal equivalent, gives the same factor as presented in Fig. 5.

TABLE III  
Resistivity in Type II Superconductors

	$b$ (cm)	$\rho / (dH/dt)$ ( $\Omega \cdot \text{cm} \cdot \text{sec} \cdot \text{Oe}^{-1}$ )	$\rho j_c / (b dH/dt)$ ( $\Omega \cdot \text{A} \cdot \text{cm}^{-2} \cdot \text{sec} \cdot \text{Oe}^{-1}$ )
Lubell and Wipf (Ref. 83)	$6.5 \times 10^{-1}$	$10^{-13}$	$2.5 \times 10^{-9}$
Taquet (Ref. 61)	$1.27 \times 10^{-2}$	$4.5 \times 10^{-16}$	$3.6 \times 10^{-9}$
Rayroux et al. (Ref. 81)	$6.35 \times 10^{-3}$	$2.66 \times 10^{-16}$	$2.6 \times 10^{-9}$

What can we use from this for our ac discussion? Realizing that  $\rho$  in the normal state is  $\approx 10^{-6} \Omega \cdot \text{cm}$  or more, we see that up to  $dH/dt$  corresponding to at least several kHz this way of looking at a superconductor will be adequate. Remembering our peculiar diffusion equation this means that the loss per cycle is independent of frequency and to a large extent independent of the wave shape, as is in fact observed.

To complete our background discussion we distinguish four different regions depending on the peak ac field. In each of these regions, I, II, III, IV, we find a different behavior. In the top half of Fig. 7 we see a magnetization curve. An ideal type II superconductor would follow the solid line to the lower critical field  $H_{c1}$  and then the dashed curve to the upper critical field  $H_{c2}$ . Between  $H_{c2}$  and  $H_{c3}$  only a superconducting surface sheath remains with a negligible contribution to the magnetization. On reducing the field this curve would be retraced. The imperfect superconductor follows the magnetization curve shown by the solid line.

For each region is indicated (in the lower half of the figure) how the field penetrates a cylindrical specimen. In region I, below  $H_{c1}$ , no flux penetrates. The shielding is done by a surface current. We do not expect any losses here because the bulk does not see any ac field. Whatever losses appear (in spite of this) should be proportional to the surface exposed to the ac field. In region II, between  $H_{c1}$  and the penetration field, a surface current still remains, but the ac field now penetrates to a certain depth below the surface. This flux is pushed in and out against the pinning forces and this gives the loss. An equivalent way of putting it: the changing field in this layer creates a resistance (which we have discussed) and this resistance in the presence of the critical current density (which does the shielding) causes the loss. We shall later calculate this loss. In the magnetization curve we describe a loop as indicated by shading, and this area constitutes the loss per cycle. The core of the superconductor does not see the changing fields and therefore we again expect the losses to be proportional to the surface exposed to the ac field.

In region III, between  $H_p$ , which depends on the thickness and the critical current density of the specimen, and the upper critical field, the whole specimen sees the field, and the losses become proportional to the volume. The losses usually become

large enough to destroy superconductivity. This has not encouraged much research in this region. (The recent interest in using superconducting magnets in accelerators where cyclic field variations of 50 kG amplitude or more are required has stimulated fresh investigations,<sup>94,95</sup> but at a very low frequency of 1 Hz or less.)

At this point one should mention that there is practically no difference whether the surface field is produced externally or by an ac current flowing parallel to the axis. In the case of a current the field is directed circumferentially parallel to the surface. (The current will flow in the shielding layer.)

Experiments are often made on the effect of having a dc field superimposed on the ac. One might then go through a magnetization hysteresis loop as indicated in Fig. 7. In that case, the ac does not penetrate the whole specimen; the loss behavior is similar to region II. As a rule the losses are higher because the smaller critical currents allow more flux to enter and leave cyclically.

For completeness we mention region IV, between  $H_{c2}$  and  $H_{c3}$ , where only the surface remains superconducting. For most high field superconductors straight ac amplitudes reaching above  $H_{c2}$  are unavailable, and there is little applied interest in this region. The study of this region yields information about the surface current. We shall not further discuss this region.

Preceding a discussion of the results we review the various methods employed to study ac losses. The most popular method is the calorimetric one, shown in Fig. 8. The heat produced is measured by the amount of helium boiled off by the specimen which is immersed in it. The sensitivity is moderate, about 1 mW. This usually requires several meters of wire as a specimen. A bifilar arrangement is preferred, in order to have a uniform relation between current and surface field. Another way to overcome low sensitivity is by the use of higher frequencies. It is well established<sup>5,6,9</sup> that the total loss increases linearly with frequency (up to over 20 kHz) as mentioned before. The loss per cycle is independent of frequency.

Next in popularity is an electrical method. By measuring the current and voltage across the specimen with the true phase relation between the two, one obtains the loss by the integral of the product over one cycle. It has been established,<sup>1</sup> by measuring the same specimens, that the two methods are equivalent.

The independence of frequency of the loss per cycle makes static methods possible. The area under a full cycle of the magnetization curve will give the loss (Fig. 9). Again there are measurements<sup>13</sup> on the same material showing agreement between results obtained by this method or a dynamic one. In the chosen example<sup>20</sup> the shape of the material,  $V_3Ga$  in powder form, makes this an ideal method.

A very high sensitivity is obtained by more sophisticated calorimetric methods<sup>5</sup> (Fig. 10). Here the specimen, a 3 in. to 4 in. long piece of wire, is in a vacuum chamber and both of its ends are in thermal contact with the bath. The three thermometers fixed on the wire give a temperature profile along the wire. From this information and the thermal conductivity, the heat produced in the wire is calculated. A heater fixed near the center serves for calibration, which in this case means a determination of the thermal conductivity.\*

Some more exotic methods should also be mentioned. They may not give quantitative results which can easily be compared with others but they sometimes expose new aspects otherwise unobserved.

---

\* Reference 5 includes values for the thermal conductivity in NbZr at temperatures between 2 and 4.2°K.

One such method is the study of L-C circuits made of superconductors. In Fig. 11 we see two pictures of decaying oscillations (in an L-C circuit of PbBi). One portion indicates ac losses, the other, a very much slower decay, the loss in the dielectric. These losses are due to flux pinned in the surface. There seems to be an indication here that below a certain amplitude the ac losses become zero. As we shall see later, this might be expected, but there are no other reports of similar observations.

Measurements of the Q values of rf cavities also belong here.

Figure 12 shows another static method in which mechanical forces or torques are measured. A rotating field can be represented as two crossed ac fields  $90^\circ$  out of phase. In this way we can use a torque meter to measure the pinning. This method is most useful in region III, for fully penetrating fields. Then the torque is directly proportional to the pinning strength, which can be highly anisotropic as is seen in Fig. 13 for a vanadium single crystal. We see a plot of the torque, which is proportional to the pinning strength, versus angle — one full rotation — and at various fields.

We now come to discussion of the over-all results. It is clear that losses measured in region I and II should be given as loss per unit surface vs the peak field which this surface sees. In Fig. 14 we show the results for Nb alloys. This includes — here undistinguishable — NbZr (20-40% Zr) and NbTi (20-50% Nb). Each of these twenty-odd curves represents a whole set of measurements, usually one curve per publication. So you are looking at the result of a considerable amount of work. The curves are labelled a, b, c, through v, w. The references and explanatory information for each curve are found in Table IV. It is remarkable that this graph covers 10 orders of magnitude in the loss values.  $H_{c1}$  of these materials is around 100 Oe. We are therefore in region I below this value.

TABLE IV  
Ac Losses in Nb Alloys (see Fig. 14)

<u>Curve</u>	<u>Reference</u>	<u>Investigators</u>	<u>Materials</u>	<u>Dimensions</u>	<u>Geometry</u>	<u>Method</u>	<u>External Ac</u>
a	9	Di Salvo	Nb 25% Zr	10 mil wire, 10- 20 in.	Coil open circuit	Boil- off	Ac field
b	9	Di Salvo	Nb 25% Zr } NbTi }	5 mil wire	Coil open circuit	Boil- off	Ac field
c	9	Di Salvo	NbTi	2.5 mil wire	Coil open circuit	Boil- off	Field
d	13	Nakayama and Takano	Nb 25% Zr	5 mil (x 2 lower) 10 mil } 20 mil }	70 mm long bundle 5 mm diam	Boil- off magnet- ization hyster- esis	Field
e	10 (Fig. 5)	Pech and Fournet	Nb 25% Zr	10 mil } 20 mil }	Various coils	Boil- off	Current
f	8	Rhodes et al.	Nb 25% Zr	10 mil	Bifilar wide spacing	Boil- off	Current

TABLE IV (continued)

<u>Curve</u>	<u>Reference</u>	<u>Investigators</u>	<u>Materials</u>	<u>Dimensions</u>	<u>Geometry</u>	<u>Method</u>	<u>External Ac</u>
g	19	Taylor	Nb 25% Zr	10 mil 6 in. long	Straight	Current voltage	Current
h	11	Pech and Fournet	Nb 25% Zr	10 mil 6 m long	Bifilar	Current voltage	Current
i	6	Bogner and Heinzel	Nb 33% Zr	9 mil 3 m	Bifilar	Current voltage	Current
k	1	Pech et al.	Nb 25% Zr	10 mil	Bifilar	Boil- off phase shift	Current
l	9 (Figs. 2,4)	Di Salvo	Nb 25% Zr	10 mil	Bifilar	Current voltage	Current
m	15	Claude and Mailfert	Nb 25% Zr	10 mil	Bifilar widely spaced	Current voltage	Current
n	4 (Fig. 4) (Fig. 7)	Jones and Schenck	Nb 25% Zr	8.5 mil 125ft long 10 mil 680ft long	Coil	Boil- off	Current
o	1	See k	Different sample				
p	14	Damman et al.	NbTi	10 mil 10 m long	Bifilar spaced	Current voltage	Current
q	14	Damman et al.	Nb 25% Zr	10 mil	Bifilar		
r	12 (Sample 2,3)	Takano	Nb 25 % Zr	10 mil 20 mil 10 m long	Bifilar	Boil- off	Current
s	12 (Sample 4,5)	Takano	Nb 48% Zr	5 mil 10 mil			
t	12 (Sample 1)	Takano	Nb 25% Zr	5 mil			
u	7	Heinzel	Nb 25% Zr	0.19 mm 3.6 m long	Bifilar	Magnet- ization	
v	5	Wissemann et al.	Nb 33% Zr	10 mil		Calori- metric (thermal conduc- tivity)	Current
w	5 (Fig. 5)	Wissemann et al.	Nb 25% Zr	10 mil			

The curves v and w represent all of the measurements of Wisseman, Boatner and Low<sup>5</sup> (see Fig. 10). The three single points labelled i may be somewhat suspect; all other points of that work follow curve i.

Region III is roughly above  $\sim 2000$  Oe. The penetration field  $H_p$  depends on the radius and the critical current density. The kink in curve a indicates  $H_p$  for a 10 mil wire, in curve b for a 5 mil wire, and in curve c for a 2.5 mil wire. If we plot these three branches of region III in terms of loss per unit volume they fall close together.

Between 150 and 2000-3000 Oe we have region II which we shall discuss in more detail. We see that towards the top the curves all have roughly the same slope, close to  $H^3$ . Towards smaller fields they bend downwards to a greater degree and meet region I which has very low losses. We shall see that this trend is reasonably well understood, when we follow the calculations (Table V).

TABLE V  
Calculation of Loss per Cycle

Magnetization hysteresis loop	$\frac{1}{4\pi} \oint H dB$
Poynting vector	$\frac{1}{4\pi} \int_{\text{surface}} E \times H df$
Joule loss	$\int_{\text{volume}} E j dv$
Pinning forces	$\int F_p dx dv$

We calculate the losses by using any one of four equivalent methods:

- 1) Area under magnetization curve: Integral over one full cycle of  $H dB$ .
- 2) By considering the Poynting vector: We observe how much energy goes through the surface into the sample and how much comes out, by forming the integral of  $E \times H$  over one cycle and the surface.
- 3) Joule heating: By integrating the product  $Ej$  over the volume.
- 4) By working out the energy lost by the movement of flux lines against the pinning forces,  $F_p dx$  over one cycle and then integrating over the volume.

We find all of these calculations in the literature. Notably London<sup>33</sup> and Bean<sup>34</sup> have presented such calculations (see also Refs. 9, 35).

Let me very quickly review the joule heating method. Illustrated in Fig. 15 is the penetration depth which during each cycle is filled with flux first in one direction and then in the other. The current density always opposes the electric field, therefore there is always loss. The total flux which passes  $r$  during one cycle is here  $B_s (1 - r/d)(D - r)$ ; multiply this by  $j_c$ . The integration gives the answer for loss per cycle: a factor  $\times B_s^2/j_c$  and in technical units the factor becomes  $4.22 \times 10^{-9} \text{ J}\cdot\text{A}/\text{Oe}^3\cdot\text{cm}^4$ . If  $j_c$  is not constant with field we have further smaller terms.<sup>37</sup>  $B_s$  is the induction near the surface.

Now we establish the relation between  $B_s$  and the external field  $H$  (Fig. 16). We

know that the surface can carry a surface current density which is partly due to the ideal equilibrium magnetization and partly due to separate flux pinning qualities of the surface. This means: as we lower the field,  $B_s$  does not immediately change as it would if we only had the ideal surface step. We first have to reverse the surface pinning current and reach a lower field  $H'$  before  $B_s$  starts changing. The total surface step which is operative here is denoted by  $\Delta H$ .

We therefore have the complete loss formula where  $B_s$  is replaced by  $(H - \Delta H)$ . This formula gives the losses in region II (loss in erg,  $H$  in Oe,  $j_c$  in A/cm<sup>2</sup>). If we insert a current density of  $4 \times 10^5$  A/cm<sup>2</sup> which is an average value for most of the Nb alloys represented in Fig. 14 ( $j_c$  varies between  $10^5$  and  $10^6$  A/cm<sup>2</sup>) we have finally the very simple form given in Fig. 16 for the losses.

The values for  $\Delta H$  in Fig. 17 were measured by Ullmaier and Gauster<sup>79</sup> who also pointed out its importance for ac losses.<sup>38</sup> Using these  $\Delta H$  values in conjunction with the formula of Fig. 16 gives curves 2 and 3 of Fig. 18. The shading indicates the majority of the curves in Fig. 14. Also indicated here as curve 1 is  $H^3$ . For comparison the loss in copper (resistivity  $\sim 10^{-8}$   $\Omega \cdot \text{cm}$ ) which goes as  $H^2$  is given. Of course the loss per cycle depends on the frequency, because of the penetration depth.

We see that the superconductor is better by orders of magnitude. Unfortunately the peak fields are not high enough for most of us to get excited about this.

Figure 19 shows a comparison between  $(H - \Delta H)^3$  and  $H^n$  since most authors discuss their losses in terms of  $n$ . Here, then, are unadulterated values as quoted for measurements over the indicated range. The comparison is with curves 2 and 3 of Fig. 18 and also with a constant value of 100 and 200 Oe for  $\Delta H$ . Ullmaier and Gauster's measurements of  $\Delta H$  were for  $\Delta H$  less than 500 Oe; the dashed part is an extrapolation by me. So much for region II.

Many measurements have been made on pure Nb (Table VI, Fig. 20) and some on pure Pb (Fig. 21). Nb has a lower critical field of  $\sim 1100$ -1420 Oe, depending on purity.<sup>100</sup> Therefore most measurements seen here are in region I going over on the right-hand side into region II very steeply.

Figure 14 showed losses per cycle up to  $10^{-3}$  J/cm<sup>2</sup>. The bulk of the curves in Fig. 20 lie below the curves in Fig. 14. The large scatter indicates that the surface treatment of the specimens is of great importance. The loss mechanism is somewhat different and there is no quantitative theory worked out yet.<sup>101,36</sup> Qualitatively we can visualize the origin of these losses in the following way: Whatever flux is trapped in the superconductor will somewhere pierce the surface. Each fluxoid will somewhere enter the specimen and at some other point, leave it. At these entry and exit points the outside field is of course seen. The action of the ac field tries to shift these points around. The surface has a pinning force which then leads to losses.

The experimental evidence that this viewpoint is correct includes the fact that specimens without trapped flux have the lowest losses, as seen in Fig. 22 for Pb and Nb. We see the losses vs the field during cool-down.

As mentioned with the L-C circuit decay (Fig. 11), a cutoff amplitude is expected below which fluxoids are truly pinned without movement. Only tenuous experimental evidence exists as yet.

So far we have talked simply about losses and without exception about losses in materials and under conditions of applied interest. There are, of course, many other ac effects; let me mention just one which easily qualifies for our discussion.

In Fig. 23 is shown what can be interpreted as a cooperative phenomenon in the

TABLE VI  
Losses in Pure Niobium

<u>Curve</u>	<u>Reference</u>	<u>Investigators</u>	<u>Specific Dimensions</u>	<u>Geometry</u>	<u>Method</u>	<u>External Ac</u>
a	17	Easson and Hlawiczka	Hollow cylinder slit (o.d. 3/4 in.)	Mech. polished	Boil-off	Field
b	8 (Sample 1)	Rhodes et al.	10 mil 3 1/2 m	Bifilar	Boil-off	Current
c	17	Easson and Hlawiczka	Same as (a) as machined			
d	8 (Sample 2)	Rhodes et al.	Same as (b)		Different sample	
e	8 (Sample 3)	Rhodes et al.	Same as (b), (d)		Specimen annealed	
f	6 (Figs. 7, 8)	Bogner and Heinzel	0.15 mm 5.1 m	Bifilar	Voltage	Current
g	14	Dammann et al.	0.25 mm 10 m	Bifilar	Current voltage	Current
h	2 (Fig. 2)	Buchhold and Molenda	5 mm x 25 mm	Cylinder	Calorimetric (spec. heat)	Field (parallel)
i	3	Buchhold and Molenda	Same as (h)			
k	12	Takano	10 mil 10 m long	Bifilar	Boil-off	Current
l	12	Takano	6 mil	Bifilar		
m	3	Buchhold and Molenda	Same as (i)		Best specimen	
n	2 (Fig. 3)	Buchhold and Molenda	Same as (h)	Different specimen from same ingot		
o	16 (Fig. 5a)	Rocher	4 mm diam 55 mm long Sample 1 $\Gamma = 1030$	Cylinder	Calorimetric (see Ref. 2)	Field
p	16 (Fig. 4d)	Rocher	#4 $\Gamma = 120$	Cooled in earth field		
q	16 (Fig. 4b)	Rocher	#2 $\Gamma = 850$	Cooled in earth field		
r	16 (Fig. 4d)	Rocher	Same as (p)	Cooled in zero field		
s	16 (Fig. 4b)	Rocher	Same as (q)	Cooled in zero field		

fluxoid structure. In region III of a weak pinner we see loss maxima which look like resonances of the whole flux lattice. This observation is very sensitive also to anisotropy of pinning.

For accelerator applications the interest is clearly in region III and to simplify or complicate matters - according to whether you look at it as an experimentalist or as a theorist - the emphasis lies on the performance of a complete coil.

A good starting point for calculations in these cases is the paper by Hancox,<sup>39</sup> even if the match with experimental results (as we shall hear in subsequent papers<sup>94,95</sup>) is apparently not yet ideal. I feel inclined to think that the dynamic resistance, which will be discussed in more detail by Rayroux, may contribute much to the understanding of region III.

The real limiting factor evidenced in region III is the phase transition or the ac critical current (since we talk almost always about self-fields of ac currents) which is intimately connected with the large losses.

Figure 24 gives the available experimental material and some expected limits. The plot gives frequency vs peak ac critical field. The points represent experiments (see Table VII). The curves, numbered 1-5, are theoretical limits discussed below.

TABLE VII  
Critical Ac Currents

<u>Curve or Point</u>	<u>Reference</u>	<u>Investigators</u>	<u>Material</u>	<u>Dimension and Geometry</u>
a	48 (Fig. 4c)	Finzi and Grasmehr	Nb 25% Zr	10 mil, 6.8 cm, straight (in perpendicular dc field of 7650 Oe)
b	48 (Fig. 4a)	Finzi and Grasmehr		(In perpendicular dc field of 3100 Oe)
X	6 (Fig. 3)	Bogner and Heinzel	Nb 33% Zr	0.23 mm, 3 m, bifilar
Δ	47 (Figs.1,2)	Young and Schenk	Nb 25% Zr	5 mil, 3/8 in., straight
O	47 (Figs.1,2)	Young and Schenk	Nb 25% Zr	10 mil, 3/8 in., straight
□	47 (Figs.1,2)	Young and Schenk	Nb 25% Zr	20 mil, 3/8 in., straight
	45	Rogers	Nb 25% Zr different suppliers	8 cm, straight (50 Hz only) diameters (from low to high field) in mm: 0.191; 0.254; 0.269; 0.403; 0.254; 0.888.
+	19 (Fig. 3)	Taylor	Nb 25% Zr	10 mil, 6 in., straight

We can think of three types of limitations of the critical current:

- 1) There is a superconducting limit, equal to the short sample dc critical current given by maximum flux pinning. The arrows indicate these values (calculated for the samples used) for a 5 mil wire (Δ), a 10 mil wire (O),



and a 20 mil wire ( $\square$ ) of NbZr. It is not surprising that this seems to be an upper limit.

- 2) Runaway heating. With increasing losses the temperature of the specimen rises, this leads to higher losses, to a further temperature rise, etc. If this process is not self-limiting, by reaching an equilibrium with the cooling capacity, the runaway heating will destroy superconductivity (Ref. 48, curves a and b, attempts an explanation of this kind).

As a criterion for runaway heating one might choose the start of film boiling, if, as usual, the specimen surface is in contact with liquid helium. Taking as a rough figure  $1 \text{ W/cm}^2$  as the transition from nucleate to film boiling we obtain curve (1) as the locus for average ac losses of this magnitude. The return from film to nucleate boiling takes place at a much lower value of  $\sim 0.1 \text{ W/cm}^2$  represented by curve (2). Keeping in mind that during the whole ac cycle dissipation only takes place during about half the time but then at twice the value, we reach  $1 \text{ W/cm}^2$  already for curve (3). Curves 1-3 are all calculated with  $j_c = 4 \times 10^5 \text{ A/cm}^2$  and  $\Delta H = 0$ . If values for  $\Delta H$  are taken from Fig. 17, then curve (2) is modified into curve (4).

Although these curves and the experimental points have the same slope, the discrepancy otherwise is large enough to leave some doubt whether this is the whole story. The heat transfer from a surface into liquid helium<sup>102</sup> happens to be far too complicated to be representable in one or two figures. It may be that a direct visual observation through high speed photography will eventually provide a satisfactory answer.

- 3) Instability. Coils often have a lower critical current caused by instabilities (coil degradation). A similar phenomenon is expected in straight wires of sufficient thickness, provided the self-field at the surface reaches a value high enough for instabilities to occur ( $> \sim 4 \text{ kG}$ ). If the frequency is above  $\sim 20 \text{ Hz}$  we may assume adiabatic conditions for the flux penetration process and calculate a flux jump field as curve (5) according to Ref. 103 (assuming  $H < H_p$ ). This same phenomenon should also limit the dc critical current but below  $10 \text{ Hz}$  the process is no longer adiabatic and the limit, therefore, more difficult to calculate. So far this limit has not been experimentally observed because the currents were not high enough, i.e., the sample not thick enough.\*

It is perhaps best to conclude with these experimental suggestions lest somebody thinks that all problems are solved.

In summary we can say that we understand reasonably well the losses in region II.

We have only two material properties  $j_c$  and  $\Delta H$  influencing the losses. (Any other variables such as temperature, applied dc field, etc., influence the losses through these material properties.) On the other hand, we have the amount of surface and the peak field as external variables and they are influenced by the particular geometry.

In conclusion we can safely say that this study shows that there is very little immediate need for more loss measurements in pure Nb or Nb alloys (unless, of course, with specific applications in mind). However, there are very few measurements on the brittle materials Nb<sub>3</sub>Sn, V<sub>3</sub>Ga, etc. But we ought to increase our understanding of  $\Delta H$ . This may open the door towards reducing ac losses.

---

\*For instabilities observed under ac conditions, in a cylindrical tube, see Ref. 87.

## REFERENCES

### Group 1

1. T. Pech, J.P. Duflot, and G. Fournet, Phys. Letters 16, 201 (1965).
2. T.A. Buchhold and P.J. Molenda, Cryogenics 2, 344 (1962).
3. T.A. Buchhold and P.J. Molenda, General Electric Progress Report No. 1; AF-33(657)-11722; BPSN 63-6899-737102 (1963), pp. 47-52.
4. C.H. Jones and H.L. Schenk, in Advances in Cryogenic Engineering (Plenum Press, 1962), Vol. 8, p. 579.
5. W.R. Wisseman, L.A. Boatner, and F.J. Low, J. Appl. Phys. 35, 2649 (1964).
6. G. Bogner and W. Heinzel, Solid-State Electronics 7, 93 (1964).
7. W. Heinzel, Phys. Letters 20, 260 (1966).
8. R.G. Rhodes, E.C. Rogers, and R.J.A. Seebold, Cryogenics 4, 206 (1964).
9. F. DiSalvo, Avco Everett Research Laboratory Report AMP-206 (1966).
10. T. Pech and G. Fournet, Cryogenics 7, 26 (1967).
11. T. Pech and G. Fournet, in Advances in Cryogenic Engineering (Plenum Press, 1968) Vol. 13, p. 60.
12. N. Takano, in Proc. First Intern. Cryogenic Engineering Conference, Kyoto, 1967, (Heywood-Temple, 1968), p. 184.
13. Y. Nakayama and N. Takano, *ibid.*, p. 186.
14. G. Dammann, E. Santamaria, J. Maldy, and L. Donadieu, Phys. Letters 24A, 574 (1967).
15. M.L. Claude and M.A. Mailfert, Phys. Letters 24A, 150 (1967).
16. Y.A. Rocher and J. Septfonds, Cryogenics 7, 96 (1967).
17. R.M. Easson and P. Hlawiczka, Phys. Stat. Sol. 23, K129 (1967).
18. R.M. Easson and P. Hlawiczka, Brit. J. Appl. Phys. 18, 1237 (1967).
19. H.F. Taylor, Appl. Phys. Letters 11, 169 (1967).
20. H.R. Hart and P.S. Swartz, General Electric Progress Report, loc. cit. Ref. 3, pp. 19-25.
21. H.R. Hart and P.S. Swartz, Bull. Am. Phys. Soc. 9, 252 (1964).
22. H.A. Ullmaier, Phys. Stat. Sol. 17, 631 (1966); see also Phys. Letters 21, 507 (1966).
23. T.W. Grasmehr and L.A. Finzi, IEEE Trans. MAG2, 334 (1966).
24. J. Huret, Rev. de Phys. Appl. 2, 133 (1967).
25. J.L. Zar, Rev. Sci. Instr. 34, 801 (1963).
26. J.L. Zar, J. Appl. Phys. 35, 1610 (1964).
27. R.A. Kamper, Phys. Letters 2, 290 (1962).
28. R.A. Kamper and P.F. Chester, in Proc. 8th Intern. Conf. Low Temperature Physics, London, 1962 (Butterworth, 1963), p. 371.
29. R.M. Easson and P. Hlawiczka, Phys. Letters 20, 333 (1966).
30. R.J. Slaughter, E.C. Rogers, and R. Grigsby, Phys. Letters 23, 214 (1966).
31. A.N. Lord, J. of Metals 16, 90 (1964).
32. B.F. Figgins and T.A. Shepherd, Nature 202, 890 (1964).

## Group 2

33. H. London, Phys. Letters 6, 162 (1963).
34. C.P. Bean, Phys. Rev. 36, 31 (1964).
35. H.R. Hart and P.S. Swartz, General Electric Progress Report, loc. cit. Ref. 3, pp. 5-18.
36. T.A. Buchhold, Cryogenics 3, 141 (1963).
37. H. Voigt, Phys. Letters 20, 262 (1966).
38. H.A. Ullmaier, Phys. Letters 21, 507 (1966).
39. R. Hancox, Proc. IEE (London) 113, 1221 (1966).
40. I.M. Green and P. Hlawiczka, Proc. IEE (London) 114, 1329 (1967).
41. H.J. Fink, Phys. Rev. 161, 417 (1967).
42. A. Mailfert, Phys. Letters 25A, 247 (1967).
43. F. Irie and K. Yamafuji, Phys. Letters 24A, 30 (1967).
44. P. Graneau, Phys. Letters 5, 15 (1963).

## Group 3

45. E.C. Rogers, Phys. Letters 5, 317 (1963).
46. E.C. Rogers, Phys. Letters 22, 365 (1966).
47. F.J. Young and H.L. Schenk, J. Appl. Phys. 35, 980 (1964).
48. L.A. Finzi and T.W. Grasmehr, IEEE Trans. MAG 3, 277 (1967).
49. A. Mailfert, G. Fournet, and J. Huret, Phys. Letters 7, 227 (1963).
50. V.V. Sychev, V.B. Zenkevich, V.V. Andrianov, and V.A. Al'tov, Soviet Phys. Doklady 9, 978 (1965).
51. R.M. Easson, P. Hlawiczka, and J.M. Ross, Phys. Letters 20, 465 (1966).
52. R.M. Easson and P. Hlawiczka, Phys. Letters 25A, 53 (1967).
53. R.M.F. Linford, Phys. Letters 17, 18 (1965).
54. M.A.R. LeBlanc and H.G. Mattes, Solid State Commun. 4, 267 (1966).
55. J. Maldy, E. Santamaria, and L. Donadieu, Phys. Letters 25A, 318 (1967).
56. J.E. Mercereau and L.T. Crane, Phys. Rev. Letters 9, 381 (1962).

## Group 4

57. R.C. Wolgast, H.P. Hernandez, P.R. Aron, H.C. Hitchcock, and K.A. Solomon, in Advances in Cryogenic Engineering (Plenum Press, 1968), Vol. 8, p. 601.
58. C. Grenier and B. Elschner, Philips Res. Reports 20, 235 (1965).
59. J. Ruefenacht and A. Steinemann, Z. Angew. Math. Phys. 16, 713 (1965).
60. S. Kurtin, S. Foner, and E.J. McNiff, Jr., Rev. Sci. Instr. 38, 600 (1967).
61. B. Taquet, J. Appl. Phys. 36, 3250 (1965).
62. R.W. Meyerhoff, J. Appl. Phys. 38, 3913 (1967).
63. A.C. Anderson, W.R. Roach, and R.E. Sarwinski, Rev. Sci. Instr. 37, 1024 (1966).

- 64. A. Mailfert and G. Fournet, Compt. Rend. 258, 2271 (1964).
- 65. T. Pech, Rev. Gen. Elec. 76, 271 (1967).

#### Group 5

- 66. L. Rinderer, J. Ruefenacht, and A. Susini, Phys. Letters 2, 119 (1962).
- 67. J. Ruefenacht and L. Rinderer, in Proc. 8th Intern. Conf. Low Temperature Physics, London, 1962 (Butterworth, 1963), p. 326.
- 68. W.M. Fairbank, J.M. Pierce, and P.B. Wilson, *ibid.*, p. 324.
- 69. J.M. Pierce, H.A. Schwettman, W.M. Fairbank, and P.B. Wilson, in Proc. 9th Intern. Conf. Low Temperature Physics, Columbus, Ohio, 1964 (Plenum Press, 1965), Part A, p. 396.
- 70. C.R. Haden and W.H. Hartwig, Phys. Letters 17, 106 (1965).
- 71. J.M. Victor, G.A. Persyn, and W.L. Rollwitz, Cryogenics 7, 119 (1967).
- 72. C.R. Haden, Proc. IEEE 54, 417 (1966).
- 73. C.R. Haden, W.H. Hartwig, and J.M. Victor, IEEE Trans. MAG 2, 331 (1966).
- 74. J.M. Victor, G.A. Persyn, and W.L. Rollwitz, Cryogenics 7, 119 (1967).
- 75. N.I. Krivko, Soviet Phys. 9, 1033 (1965).
- 76. Nguyen Tuong Viet, Compt. Rend. B264, 1227 (1967); *ibid* B258, 4218 (1964).
- 77. F. Biquard, A. Septier, and P. Grivet, Electronics Letters 3, 47 (1967).
- 78. E. Maxwell, in Progress in Cryogenics (Heywood & Co., 1964), Vol. 4, p. 123.

#### Group 6

- 79. H.A. Ullmaier and W.F. Gauster, J. Appl. Phys. 37, 4519 (1966).
- 80. J.C. Renard and Y.A. Rocher, Phys. Letters 24A, 27 (1967).
- 81. J.M. Rayroux, D. Itschner, and P. Müller, Phys. Letters 24A, 351 (1967).
- 82. W.F. Druyvesteyn, Phys. Letters 25A, 31 (1967).
- 83. M.S. Lubell and S.L. Wipf, J. Appl. Phys. 37, 1012 (1966).
- 84. M. Garbuny, M. Gottlieb, and J. Conroy, J. Appl. Phys. 36, 1177 (1965).
- 85. M. Gottlieb and M. Garbuny, Rev. Sci. Instr. 35, 641 (1964).
- 86. S.L. Wipf, Conference Type II Superconductors, Cleveland, Ohio, 1964; Westinghouse Scientific Paper 64-1J0-280-Pl.
- 87. D.A. Gandolfo and C.M. Harper, J. Appl. Phys. 37, 4582 (1966).
- 88. M.A.R. LeBlanc, J. Appl. Phys. 37, 3 (1966).
- 89. P. Martinoli, J.L. Olsen, and P. Zoller, Phys. Letters 20, 12 (1966).
- 90. G.M. Foster, Phys. Rev. Letters 11, 122 (1963).

#### Recent ac references\*

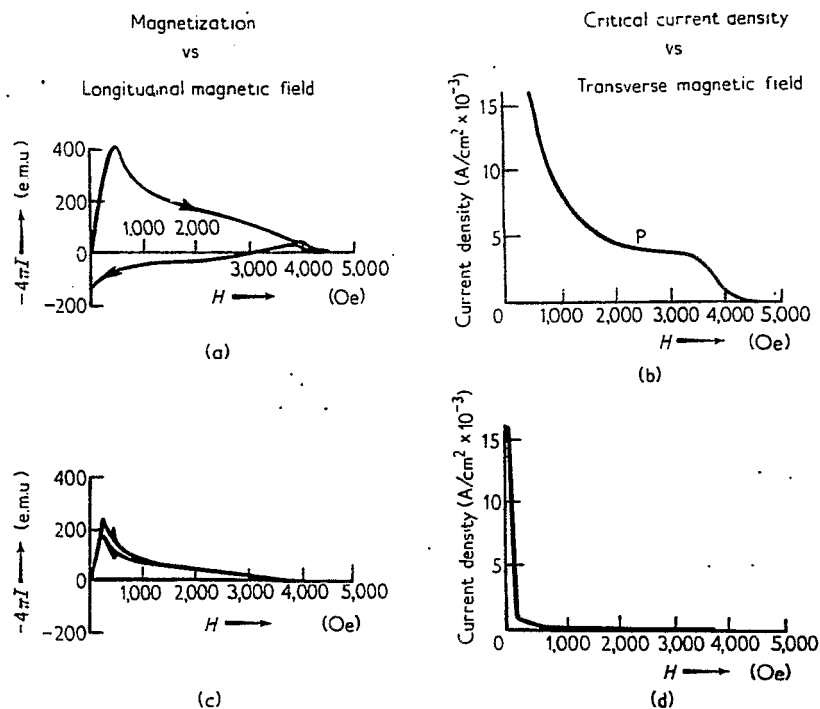
91. H.F. Taylor, Phys. Rev. 165, 517 (1968); see also Ref. 19.
92. S.V. Odenov and V.A. Shukman, Soviet Physics JETP Letters 7, 125 (1968).
93. D.A. McLachlan, Physik Kondensierten Materie 7, 226 (1968).
94. W.B. Sampson, R.B. Britton, G.H. Morgan, and P.F. Dahl, in Proc. 6th Intern. Conf. High Energy Accelerators, Cambridge, Mass., 1967 (CSFTI, Springfield, Va., 1967), p. 393.
95. W.S. Gilbert, R.E. Hintz, and F. Voelker, Lawrence Radiation Laboratory Report UCRL-18176 (1968).

#### Other references

96. J.W. Heaton and A.C. Rose-Innes, Cryogenics 4, 85 (1964).
97. U. Essmann and H. Träuble, Phys. Letters 24A, 526 (1967).
98. W. Klose, Phys. Letters 8, 12 (1964).
99. C.J. Bergeron, Jr., Appl. Phys. Letters 3, 63 (1963).
100. D.K. Finnemore, T.F. Stromberg, and C.A. Swenson, Phys. Rev. 149, 231 (1966).
101. J.I. Gittleman and B. Rosenblum, J. Appl. Phys. 39, 2617 (1968).
102. R.D. Cummings and J.L. Smith, in Pure and Applied Cryogenics (Pergamon Press, 1966), Vol. 6, p. 85.
103. S.L. Wipf and M.S. Lubell, Phys. Letters 16, 103 (1965).

---

\*The list (Refs. 1-90) was completed Dec. 1967.



*Critical currents and magnetizations of Ta<sub>45</sub>-Nb<sub>55</sub> wires at 4.2° K*

Fig. 1. Phenomenological difference between a type II superconductor with pinning (top) and without pinning (bottom) (Ref. 96).

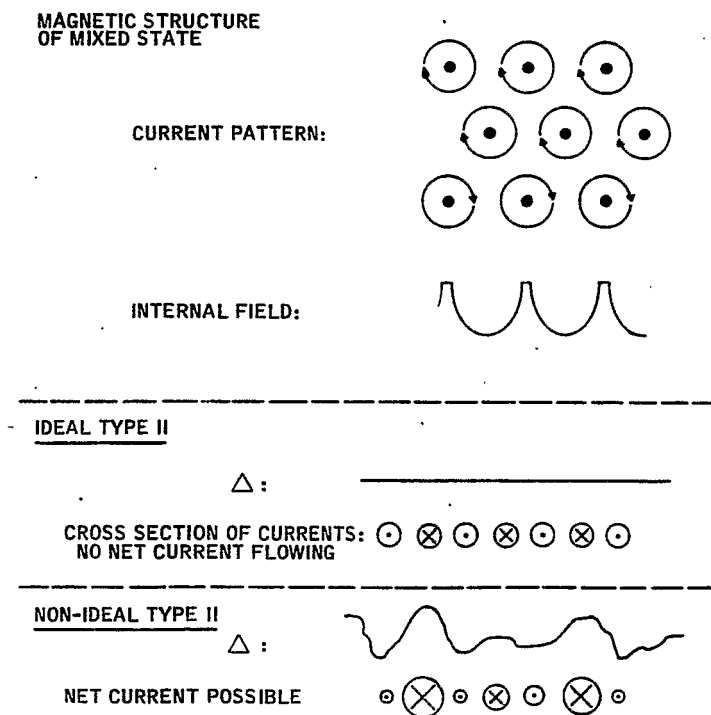


Fig. 2. Microscopic difference between ideal (no pinning) and imperfect (pinning) type II superconductor.

FOR A SURFACE FIELD  $H_0 e^{i\omega t}$

THE SOLUTION OF THE DIFFUSION EQUATION GIVES

$$B = H_0 e^{\lambda x} e^{i\omega t}$$

WITH  $\lambda = -[2\pi\omega/\rho]^{1/2} (1+i)$

PENETRATION DEPTH  $[2\pi\omega/\rho]^{-1/2}$

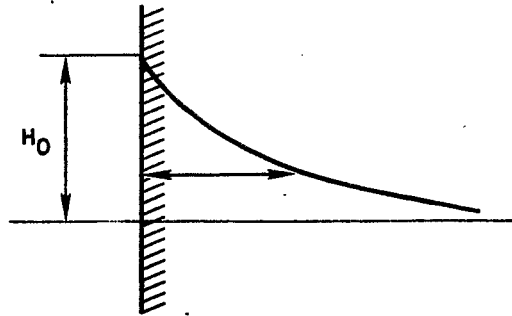


Fig. 3. Illustrating the penetration of an ac field into a normal conductor.

$$E = \rho j \quad \rho = 0 \text{ FOR } j \leq j_c$$

PRACTICALLY:  $j = \text{CONST.} = j_c$ ;  $\rho \propto dB/dt$

$$dB/dx = 4\pi j_c$$

$$\nabla^2 B = \frac{4\pi}{\rho} \dot{B} \quad (\cong \text{CONST})$$

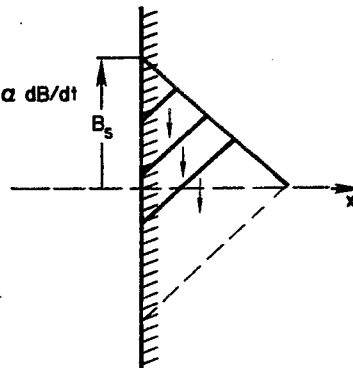


Fig. 4. Illustrating the penetration of an ac field into a type II superconductor with pinning.

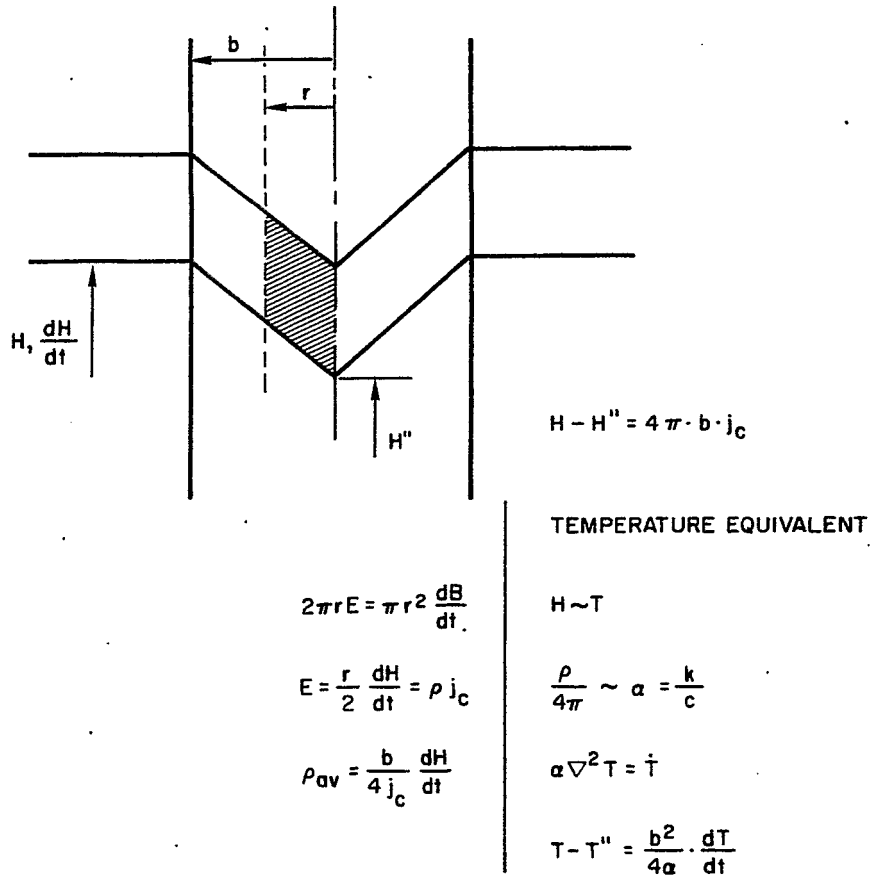


Fig. 5. Dynamic resistivity of a cylindrical superconductor (type II, strong pinning) in parallel, steadily increasing field.

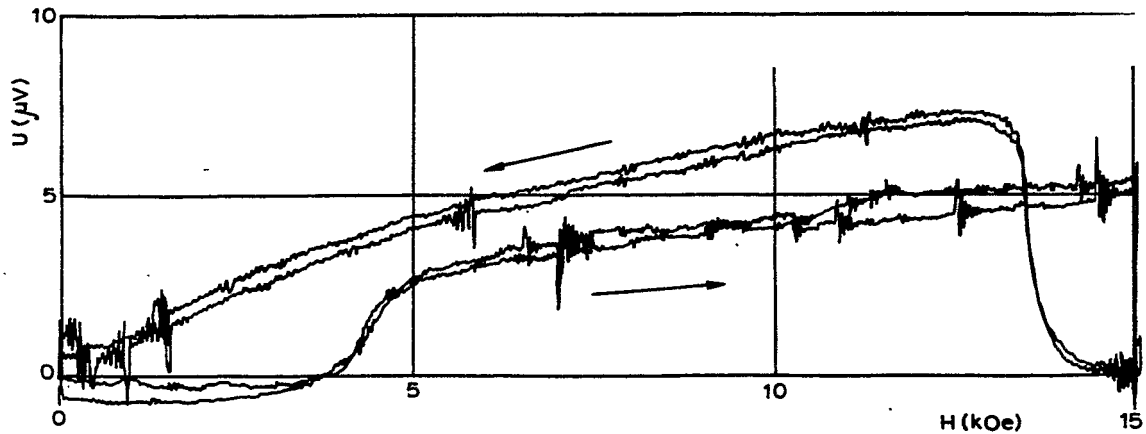


Fig. 6. Measurement of the dynamic resistance of a bifilar coil in coaxial, changing field (Ref. 81).



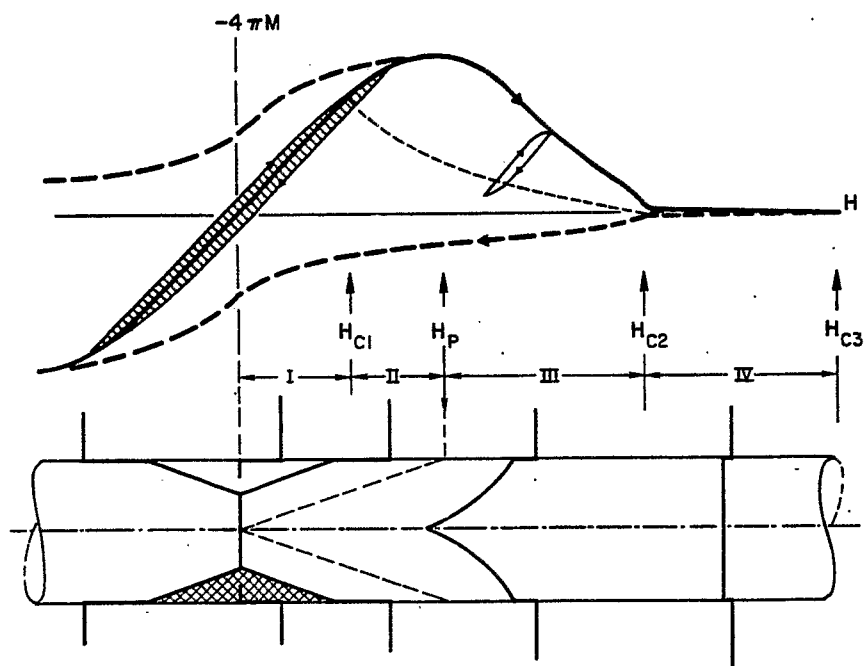


Fig. 7. Four ac loss regions.

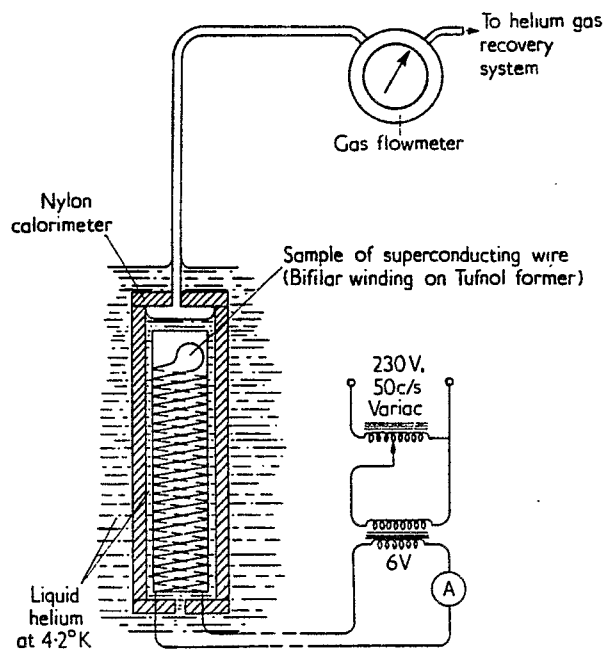


Fig. 8. Experimental method: boil-off calorimeter (Ref. 8).

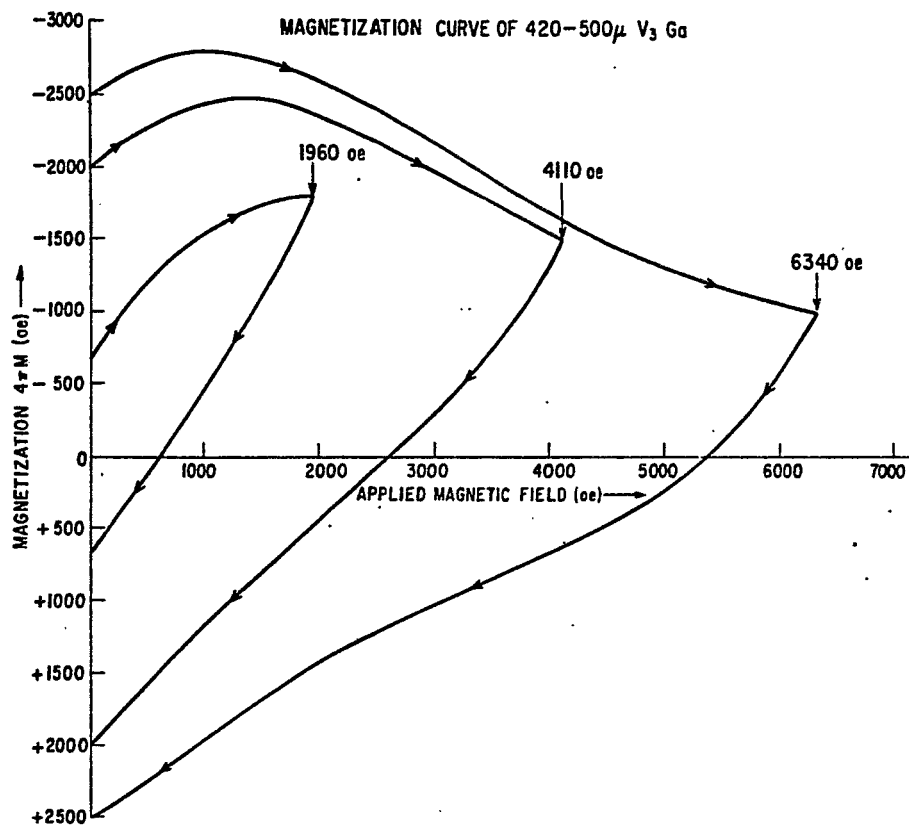


Fig. 9. Experimental method: hysteresis of magnetization loop (Ref. 20).

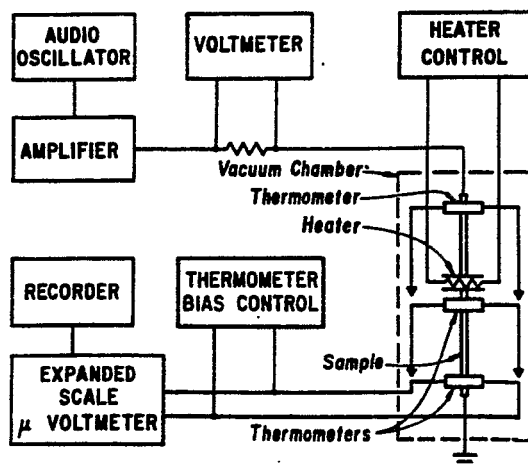
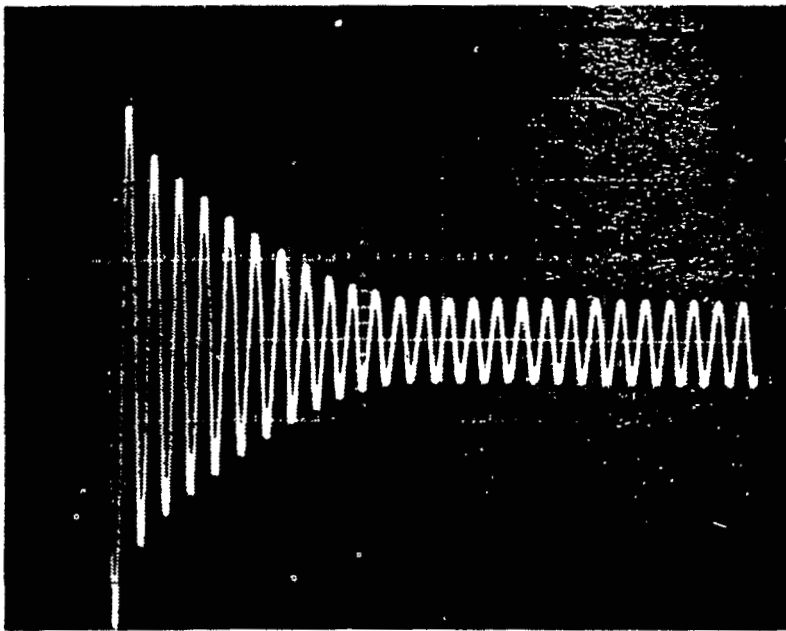
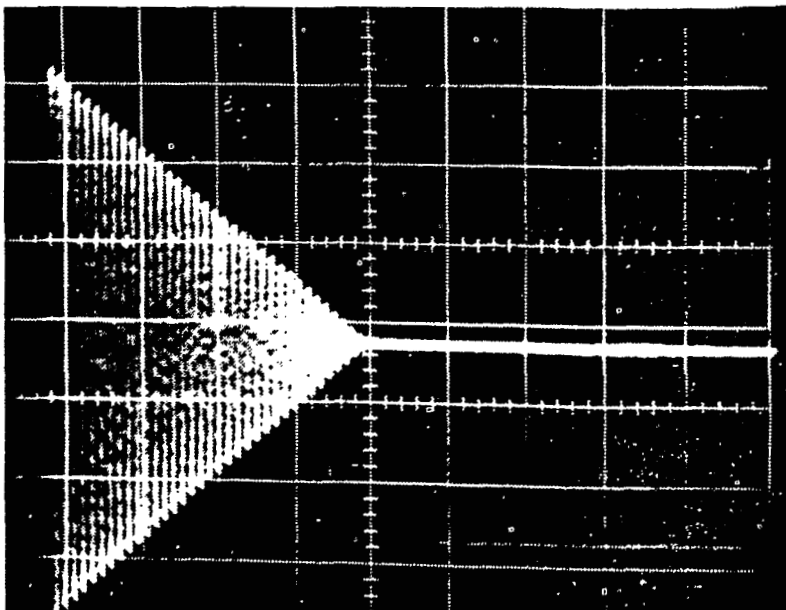


Fig. 10. Experimental method: calorimeter, using thermal conductivity of specimen (Ref. 5).



Two-component decay of voltage oscillations in superconducting L-C circuit. Time scale is 2 msec/div. Initial current was 2 mA.



Linear decay of voltage oscillations in superconducting L-C circuit. Time scale is 2 msec/div. Initial current was 100  $\mu$ A.

Fig. 11. Experimental method: decay of oscillations in superconductive L-C circuit (Ref. 84).

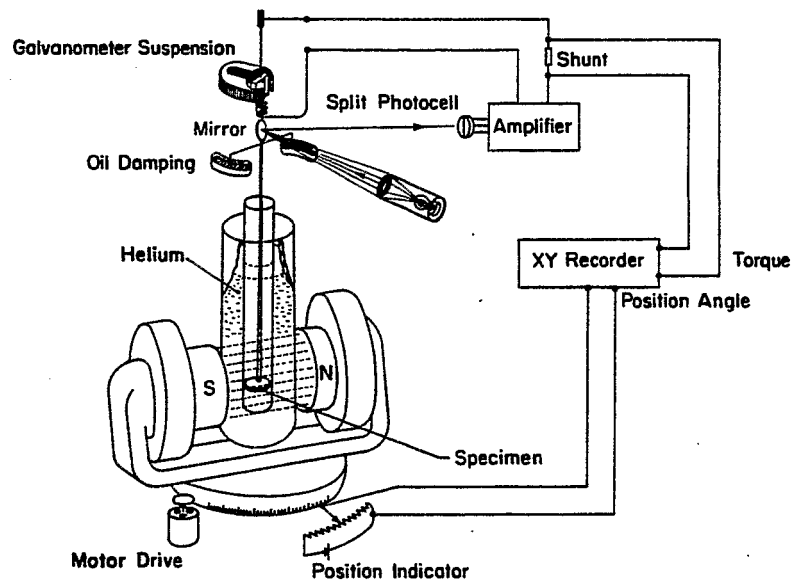


Fig. 12. Experimental method: flux pinning measured as torque which slowly rotating field exerts on specimen (Ref. 86).

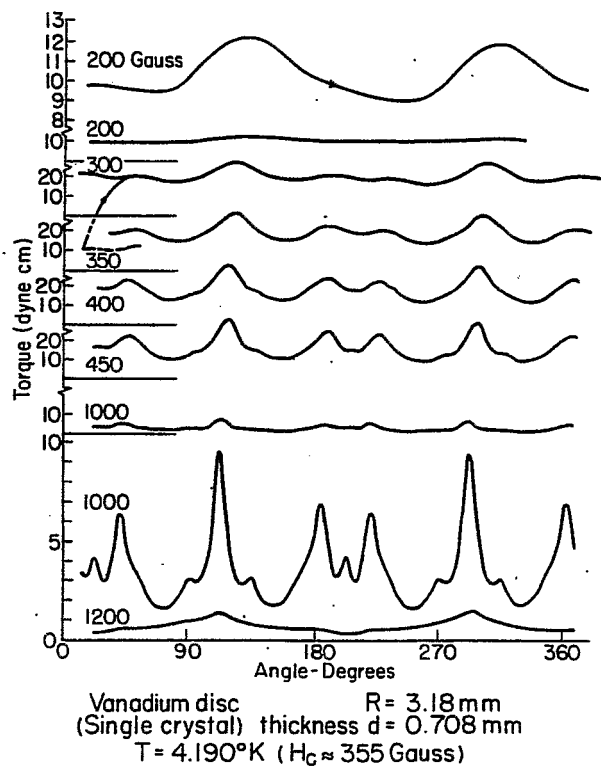


Fig. 13. Anisotropy of flux pinning in vanadium, measured with torque method (Ref. 86).

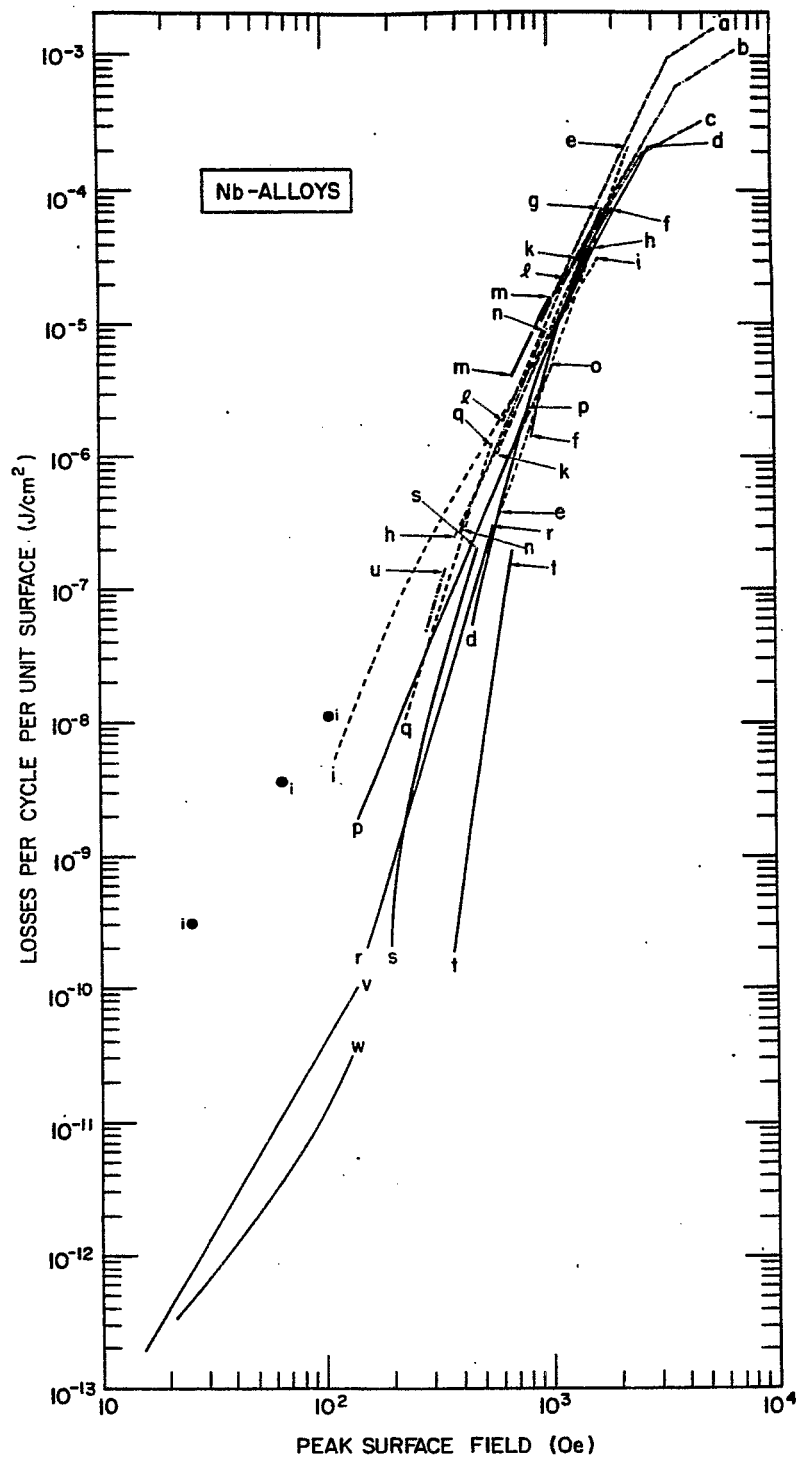
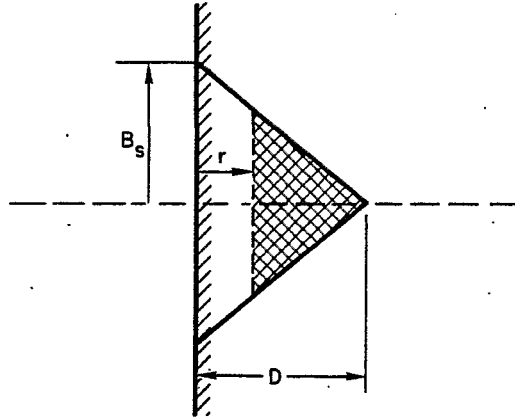


Fig. 14. Reported ac losses in NbZr and NbTi alloys (see Table IV).

Curves: ----- : bifilar coil (corrected for average field at the surface of the wire)  
 ————— : single wire or widely spaced bifilar coil  
 ..... : other geometries (also corrected).

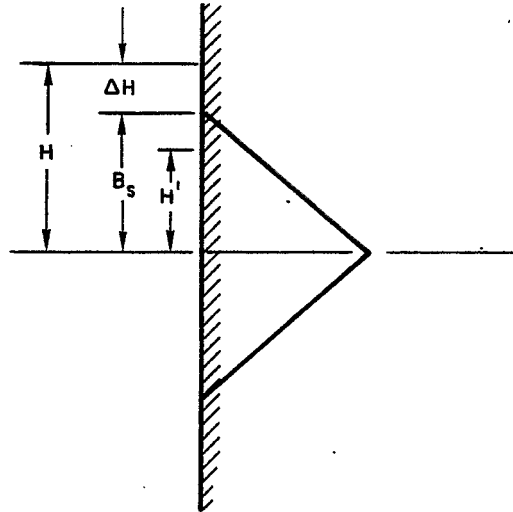
$$\int \oint E j dt dv = \int_0^D \oint \frac{d\phi}{dt} j dt dr$$



$$2 \int_0^D B_s \left(1 - \frac{r}{D}\right) (D - r) j_c dr$$

$$= 2 j_c B_s \left(Dr - r^2 + \frac{r^3}{3D}\right) \Big|_0^D = \frac{B_s^3}{24 \pi^2 j_c}$$

Fig. 15. Loss per cycle by calculating the joule heating.



$$\text{LOSS PER CYCLE} = \frac{(H - \Delta H)^3}{24 \pi^2 j_c}$$

$$\text{FOR } j_c = 4 \times 10^5 \text{ A/cm}^2$$

$$\text{LOSS} = 1.05 \times 10^{-14} (H - \Delta H)^3 \text{ [JOULE/cm}^2\text{]}$$

H in Oe

Fig. 16. Modification of loss by the surface step  $\Delta H$ .

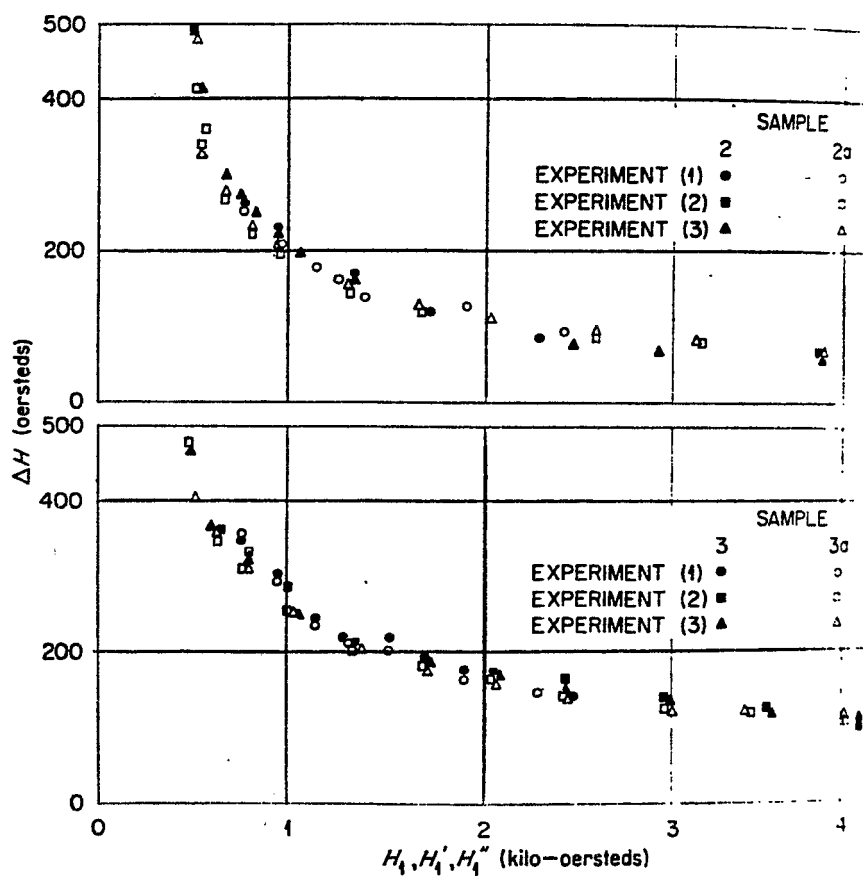


Fig. 17. Measurements of  $\Delta H$  for Nb25%Zr (Ref. 79).  
 Sample 2: diameter 0.68 cm; cold-worked, annealed and machined.  
 Sample 3: diameter 0.63 cm; cold-worked, and mechanically polished.  
 (The open symbols in both cases are for 30  $\mu$  silver-plated surfaces.)

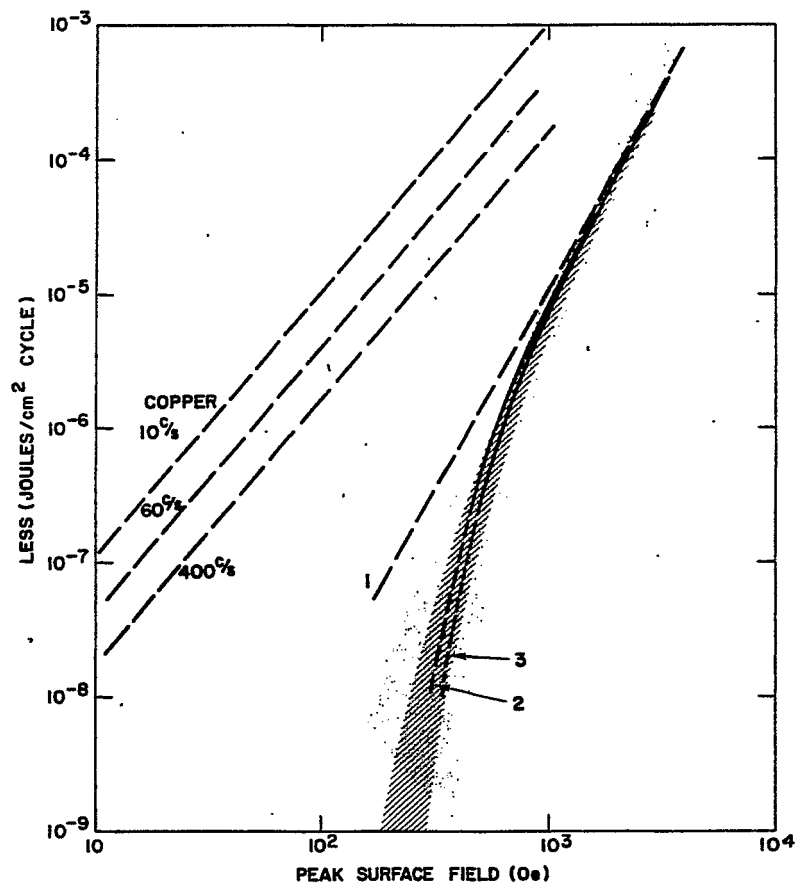


Fig. 18. Comparison of losses in Nb alloys with calculations.  
 Curve 1:  $\Delta H = 0$   
 Curves 2 and 3:  $\Delta H$  corresponding to sample 2 and 3 of Fig. 17.  
 Shading indicates the portion of the curves in Fig. 14.  
 Ac losses for copper ( $10^{-8} \Omega \cdot \text{cm}$ ) are indicated for 10, 60 and 400 c/sec; the sample is assumed to be thicker than twice the penetration depth.



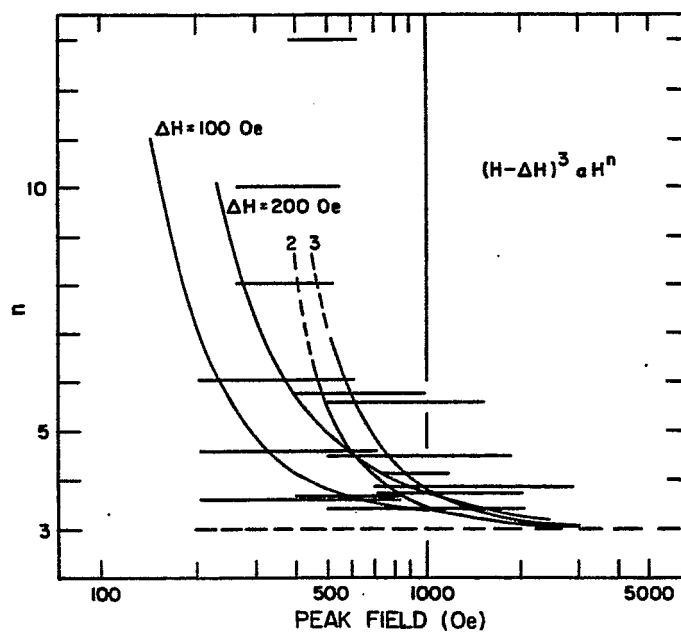


Fig. 19. Comparison between  $H^n$  and  $(H-\Delta H)^3$ . Horizontal bars indicate published values of  $n$ , relating to loss measurements over the indicated range of peak field.

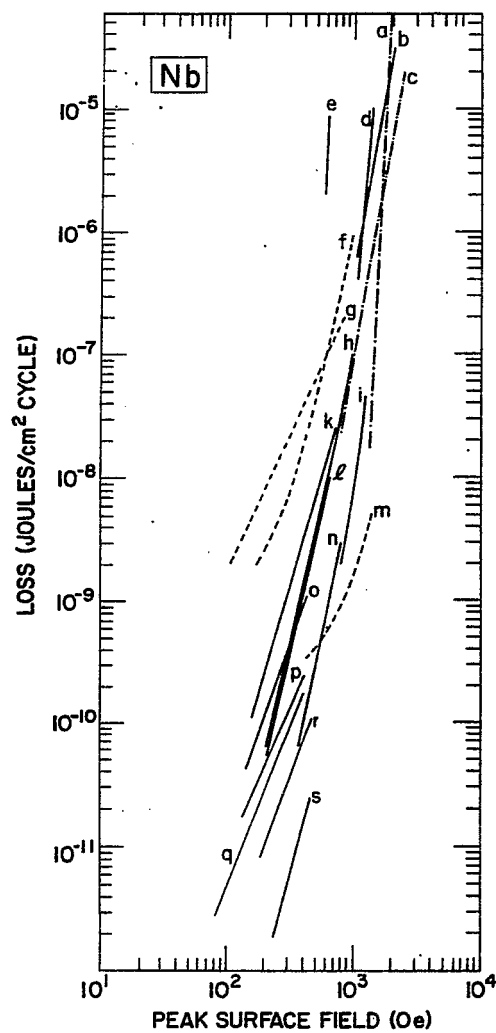


Fig. 20. Reported ac losses in pure Nb (see Table VI). Same curve symbols as Fig. 14.

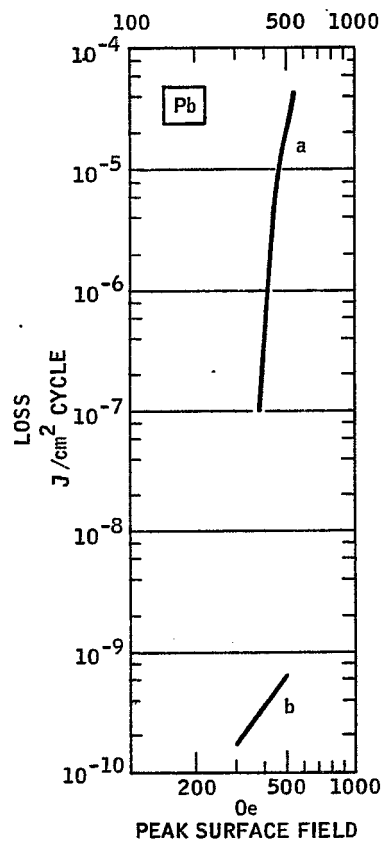


Fig. 21. Reported ac losses in pure Pb.  
Curve a: Ref. 8. Curve b: Ref. 2.

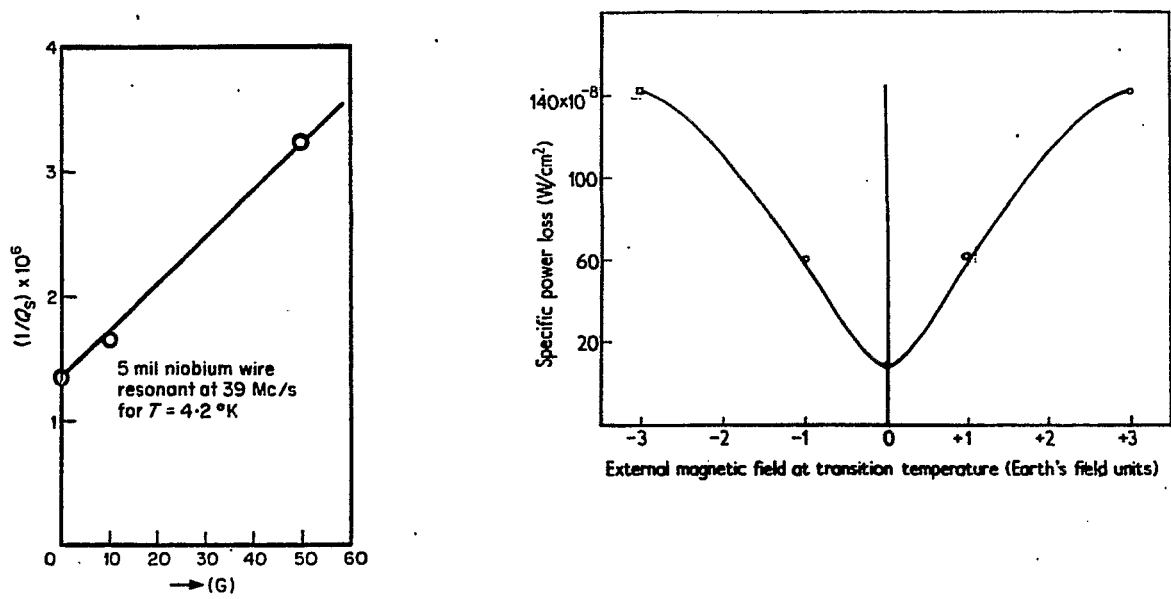


Fig. 22. Loss vs background field during cooldown for Nb (Ref. 71) and for Pb (Ref. 2).

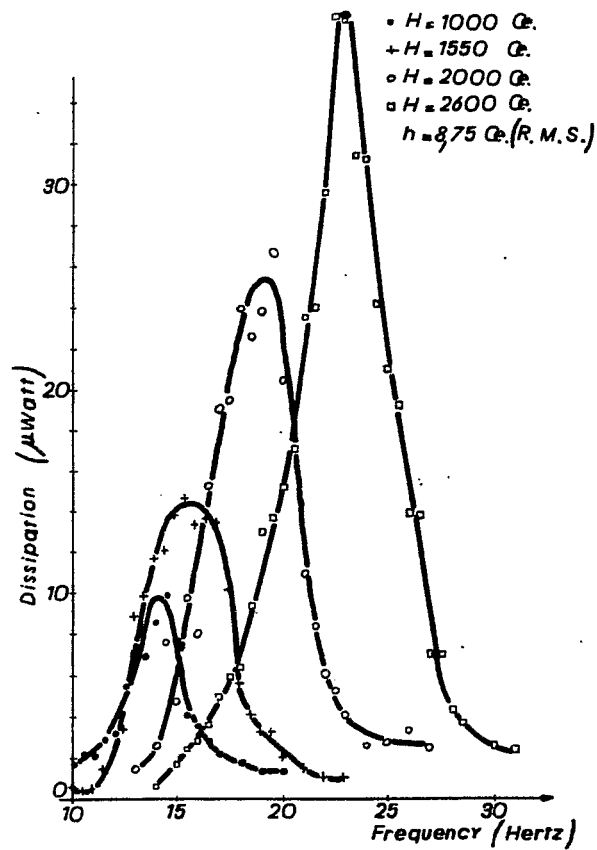


Fig. 23. Resonance of losses in pure Nb (weak pinning) (Ref. 80).

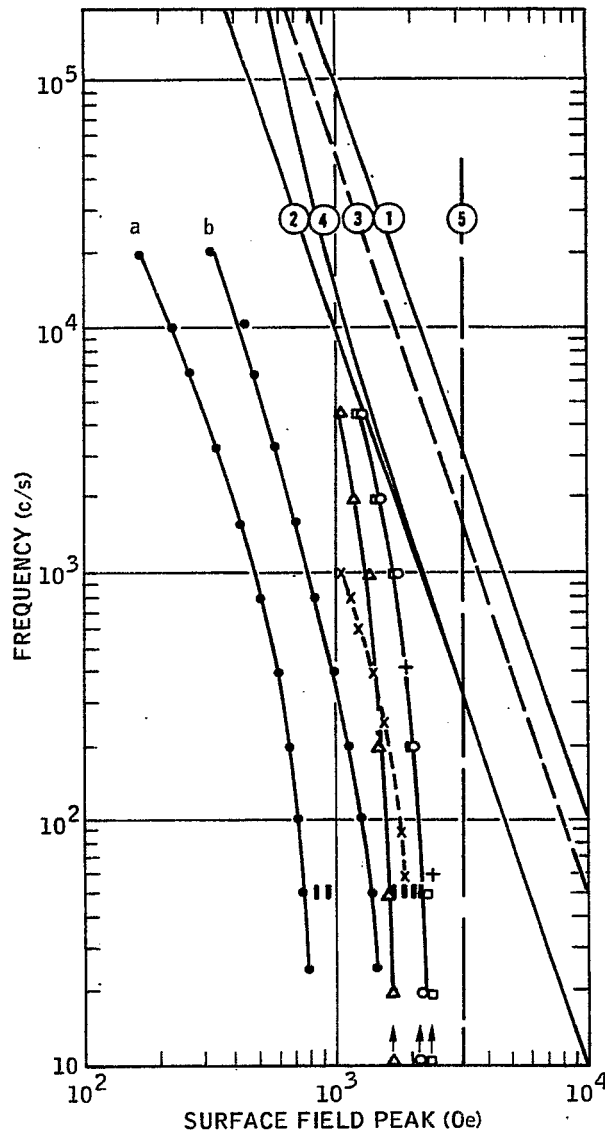


Fig. 24. Experimental ac critical currents plotted as frequency of the ac current vs the surface peak field created by the ac current. The points are referenced in Table VII. The curves numbered 1-5 are theoretical limits explained in the text.

## USE OF SUPERCONDUCTORS IN HIGH ENERGY PHYSICS\*

J.P. Blewett  
Brookhaven National Laboratory  
Upton, New York

### INTRODUCTION

A recent visitor to Brookhaven, after listening to a lecture on our progress in superconductivity, looked at the experimental floor of the AGS and said "If superconducting beam transport is so wonderful why do I still see all of these iron and copper magnets along your high energy beams?" He was told to look again in a few years.

It seems certain that dc superconducting magnets will find many applications in nuclear and high energy physics, in beam transport components, in bubble chamber magnets and in specialized magnets where high fields are required or where fields must be maintained throughout large volumes. This can include cyclotron magnets.

But for accelerators whose magnets are operated under ac or pulsed conditions the story is quite different. Most of the design problems associated with synchrotron magnets have been solved in principle. But the problem remains of reducing the high losses that are met when fields in superconducting magnets must change rapidly with time. Probably this problem will have been solved by the end of next year. The information to be presented this week will, we expect, throw much light on the question.

Although this week's topic is ac effects, I shall speak briefly, for the sake of completeness, about rf cavity applications and dc applications, then turn to possible applications in systems where the field in a magnet must change with time.

### RF APPLICATIONS

Rf applications were covered during the first week of the Summer Study. Most of the work in this field is in the 1000 to 3000 MHz range. The largest group working on rf applications is at Stanford where studies are in progress both in Stanford's Physics Department and at the two-mile linac (SLAC). This work is aimed at an electron linear accelerator with a 100% duty cycle. At Brookhaven we are working toward a 3000 MHz particle separator. At Karlsruhe a large group is experimenting with cavities for both linear accelerators and beam separators.

All of these applications call for high electric fields but do not involve very high magnetic fields (less than 1000 gauss). Lead plated on copper has been rather thoroughly investigated but the present trend is toward niobium cavities either machined or electroformed. To keep losses within tolerable limits it is not possible to operate at the boiling point of liquid helium — the temperature must be reduced to below 2°K into the range where helium becomes a superfluid. Although this calls for more than twice as much power input to the refrigerator, helium at these temperatures is a beautiful coolant. Experience gained at radio frequencies may very well lead magnet designers to call for superfluid helium cooling.

---

\*Work performed under the auspices of the U.S. Atomic Energy Commission.

Some rf work is in progress at lower frequencies for use in circuits requiring high frequency stability. Q's of over  $10^{10}$  have been obtained and higher values are expected. This makes possible oscillators with stability approaching that of the NBS time standards.

#### MAGNETS FOR BUBBLE CHAMBERS, SPARK CHAMBERS AND LARGE SPECTROMETERS

The first superconducting magnet for a bubble chamber was built at Argonne. It has an inner diameter of 10 in. and runs at 42 kG. So far this is the only superconducting magnet that has been used with a bubble chamber as part of an experimental program. But a number of much more ambitious magnets are under construction or design. The 30-kG magnet for Brookhaven's 7-ft chamber and the 20-kG magnet for Argonne's 12-ft chamber will both be running by the end of this year. The Brookhaven magnet has already been cooled down and excited to half field.

At the Lawrence Radiation Laboratory, spectrometer magnets 7 ft in diameter are under design. At CERN model studies are under way for a 3.5-m bubble chamber magnet to run at 35 kG. The most ambitious such project probably is at the Rutherford Laboratory where a magnet for a 1.5-m bubble chamber is to be run at fields over 70 kG. The stresses to be experienced are to be restrained by an interwinding of stainless-steel strip 3 mm thick.

In all of these magnets high current density is not important because of their large size. All will be wound with fully stabilized NbTi superconductor. The magnets listed are typical - I have listed only a few of the large magnets under design or construction for use with bubble chambers, spark chambers or other large detecting devices.

#### BEAM TRANSPORT MAGNETS

At the AGS our annual power bill is about \$1 million. More than two-thirds of this pays for operation of the dipole and quadrupole magnets that guide and focus secondary particle beams for the various experiments on our experimental floor. We have over 200 of these magnets; their total weight is over 3000 tons. About 180 power supplies provide power for these magnets; they range in size from a few to 600 kW. Total experimental power available is 37 000 kVA; to dissipate this power we need 3500 gal/min of cooling water.

Most of these magnets could be replaced by superconducting units. A 300-kW magnet would be replaced by a dipole dissipating perhaps 20 W. The refrigerator for this unit would require about 15-kW input. Thus the power consumption would be cut by a factor of twenty.

The cost of the present magnets is of the order of \$20 thousand apiece. From present experience we estimate that the superconducting replacement would cost no more than this; eventually it should be cheaper.

Similar situations exist at all of the high energy physics installations. At the 200-GeV machine in Weston the total number of magnets will eventually be considerably larger than the figures I have mentioned. I am confident that they will be largely superconducting from the beginning of operation.

## DESIGN OF DIPOLES AND QUADRUPOLES

Superconducting dipoles and quadrupoles will bear little physical resemblance to their room temperature counterparts. The possibility of an economical increase in current density of two or three orders of magnitude has shaken magnet designers and has resulted in considerable debate as to how best to use it.

First let me be clear that the problem to which I address myself is that of dipoles and quadrupoles with small aperture, although their length normal to the field may be great. If the aperture is large, for example in the dipole magnet for a 7-ft bubble chamber, high current density is no longer so essential and cost and power consumption are the considerations that lead to the choice of a superconducting magnet. But if the aperture dimensions are a foot or less, novel designs are called for.

If infinite current density were available, a dipole or a quadrupole with a circular aperture could provide the desired fields if the current density around the coil varied as  $\cos \theta$  for a dipole or  $\cos 2\theta$  for a quadrupole (see Fig. 1). For finite current density and uniform coil thickness, the  $\cos n\theta$  distribution still gives ideal field patterns inside the aperture.

If, however, inadequate current density is available, the coil will become very thick — when the coil thickness begins to be of the order of the aperture dimensions one finds oneself in the absurd position of adding large quantities of current so far from the aperture that they are making virtually no contributions to the useful field.

Of course accurate establishment of a cosine distribution presents major design problems. Fortunately this is not necessary. Beth,<sup>1</sup> at Brookhaven, has shown that an approximation in the form of three or so blocks of constant current density can, if properly arranged, eliminate higher harmonics of the field pattern to such a high order that further compensation is unnecessary.

Other approaches than that of the coil of uniform thickness have been proposed by Beth at Brookhaven, by Septier at Orsay, and elsewhere. I shall say no more about them because they will be discussed in more detail next week.

Peak field strengths to be used in dipoles and quadrupoles will probably be of the order of 60 kG, at least in the initial stages of development. With the geometries that I am describing forces at fields over 60 kG are becoming unreasonable and are rising with the square of the field.

In the geometry that I have described, the peak field in the useful aperture is the highest field anywhere. Nowhere in the system of conductors is the field any higher.

Peak current densities for 60-kG peak generated by a coil 1.5 cm thick are about 60 000 A/cm<sup>2</sup>.

\* \* \* \* \*

Stray fields outside of air core dipoles or quadrupoles can be quite troublesome in many applications. There are two ways for eliminating them. The first is to build another dipole or quadrupole coil of larger radius coaxial with the first. This can reduce the net external field identically to zero with an attendant sacrifice of a

---

1. R.A. Beth, Brookhaven National Laboratory, Accelerator Dept. Report AADD-135 (1967).



fraction of the field in the useful aperture. The second method is to surround the coil with a cylinder of iron. This will result in an increase in the useful field. If, for example, the radius of the iron cylinder is large enough that the maximum flux density at the iron surface is 20 kG, the addition of iron will add 10 kG to the dipole field and somewhat less to the quadrupole field. The inner radius of the iron cylinder will be of the order of twice the coil radius. Whether or not it is appropriate to include the iron in the cooled volume we have not yet decided.

### STORED ENERGIES

For dc dipoles and quadrupoles usable for beam transport, stored energies are relatively unimportant. If these components are to be pulsed for use in an accelerator, however, stored energies become quite important.

For a dipole or quadrupole having a coil thickness that is negligible compared with the aperture dimensions, it can be shown that the energy stored in the useful aperture and the energy stored in external fields are approximately equal so that, so far as stored energy is concerned, the unit may be said to be 50% efficient. This is better than many iron cored magnets; for example, in the magnets used in the AGS less than one-third of the total stored energy resides inside of the vacuum chamber. But if the coil thickness becomes appreciable the comparison rapidly becomes less favorable. For example, in a dipole whose aperture has a radius of 5 cm and whose coil is 1.5 cm thick, there is almost 50% as much energy stored in the coil as is stored in the useful aperture and the over-all efficiency has dropped from 50% to about 40%.

Again this points up the importance of high current density. If we think of 60-kG fields, the stored energy argument also forces us into the range of 60 000 A/cm<sup>2</sup>.

### PULSING OF SUPERCONDUCTING MAGNETS

Measurements and interpretation of losses in superconductors when the current is changed have already been the subject of much discussion during this Summer Study and are the main topic for this week. I shall not anticipate the coming presentations except to say that losses are too high by a factor between three and ten, if we think of pulsing at the rates now used in the AGS where the field is raised from zero to full field in about one second.

Possibly, if we build a 200-GeV accelerator with superconducting magnets and pulse it very slowly, taking ten to fifty seconds to reach full field, present materials are adequate. But we hope to cycle the machine as rapidly as Nature will allow.

Another complication in using pulsed magnets in an accelerator comes from the fact that the field is used during almost the whole cycle of increasing field. A high order of precision is required throughout the cycle and distortions or flux jump discontinuities will cause the beam to be lost. So, while we ask for high current densities and so cannot allow admission of a lot of normal stabilizing metal, at the same time we require a high order of stability. We hope that these requirements are not completely inconsistent.

### SUPERCONDUCTING SYNCHROTRONS

For acceleration of protons to the range of hundreds or thousands of GeV the synchrotron is the only accelerator of demonstrated capability. It is a device, like the AGS, in which during acceleration the protons travel on a circular orbit in which

they are maintained by a rising magnetic field. It consists essentially of an injector of as high energy as is economically feasible, a set of bending magnets which maintain the circular orbit, a set of focusing magnets which prevent large excursions from the orbit, and a set of rf accelerating cavities. There are many additional complications which are described in many books and reviews on the subject.

For over seven years the AGS has produced protons of the world's highest energy — 33 GeV. But last November the Russians brought into operation a machine for almost 90 GeV; this will be the world's largest for some time. The next step will be either the 200-400 GeV synchrotron at Weston, Illinois, or a 300-GeV synchrotron under design in Europe.

As a major application of superconducting magnets we are studying here a 2000-GeV synchrotron. The AGS would serve as its injector and its main magnet ring would be about two miles in diameter. Fortunately there is adequate space for this on the Brookhaven site.

The main ring would have about four and a half miles of its six mile circumference filled with magnets. About seven-eighths of this distance would be occupied by bending magnets — dipoles with 60-kG peak field. The other eighth would be quadrupoles for focusing. Rf accelerating stations would be distributed at intervals around the ring. The stored energy in the magnet system would be about 700 MJ.

The accelerated beam would be extracted and fed through an array of superconducting beam transport dipoles and quadrupoles to a variety of happy experimenters from all over the world.

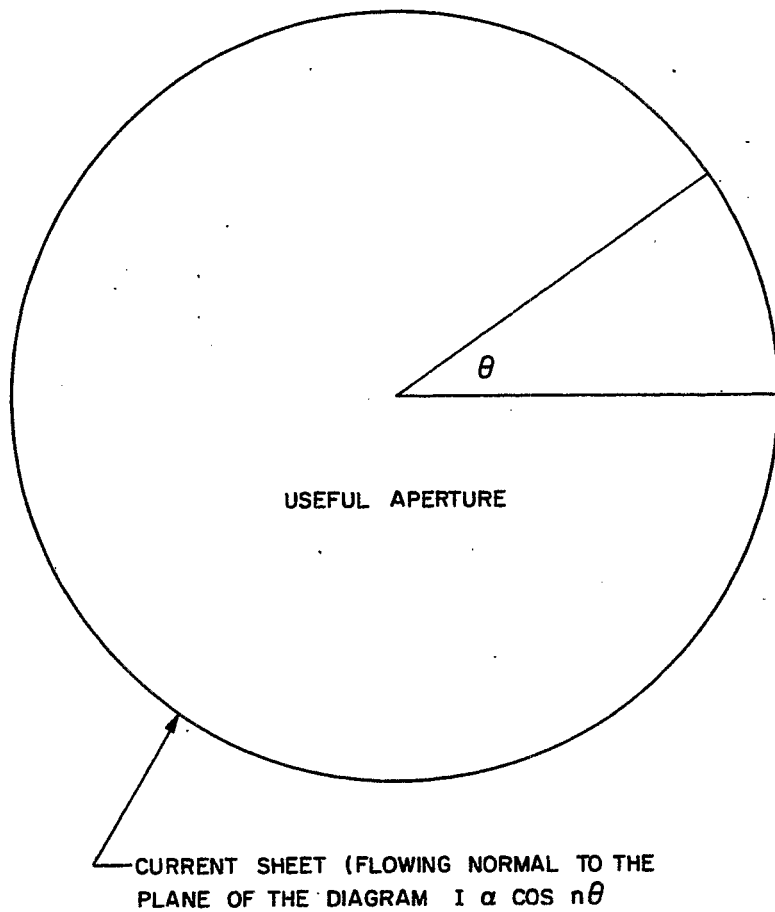


Fig. 1. Geometry for multipole magnet with circular aperture.

# ELECTRICAL LOSS MEASUREMENTS IN A NbTi MAGNET\*

F. Voelker  
Lawrence Radiation Laboratory  
Berkeley, California

## I. INTRODUCTION

Our work on ac losses has been mostly with NbTi wire magnets. These magnets were built for direct current use, but since they were available to us, it was convenient to use them while developing an electrical method of measuring losses.

First, I shall describe this electrical method and then describe some of our results. I shall talk mostly about results obtained since our earlier report.<sup>1</sup>

Most of the results that will be described here were made on a solenoid wound with Supercon NbTi wire which had a 0.015 in. diameter superconducting core in a copper wire of 0.03 in. over-all diameter. The wire was insulated turn-to-turn with a copper-oxide surface, and layer-to-layer with fiberglass cloth. The maximum field on axis was about 70 kG at 120 A. The winding had a 1.5 in. inner diameter, 4.5 in. outer diameter, and was 4.5 in. long.

## II. LOSS MEASUREMENTS

This method of measuring losses depends on measuring the accumulated electrical energy entering the magnet over a period of several cycles. This is accomplished with the circuit shown in Fig. 1. The two key elements are a multiplying circuit to obtain instantaneous power flow between the magnet and power supply, and an integrator to keep track of electrical energy balance into the superconducting magnet.

The multiplier circuit works in the following way. It uses a semiconductor Hall device which develops an output voltage proportional to the product of input current to the Hall device, and magnetic field surrounding the device. A pair of potential leads inserted into the cryostat connects the test magnet to the Hall device through a resistor, so that current input to the Hall device is proportional to the magnet voltage. The Hall device is mounted in the gap of a small magnet which has been designed to give a magnetic field proportional to current in its windings. This magnet is put in series with the superconducting magnet so that the Hall device has a magnetic field input proportional to the current in the superconducting magnet. The inputs to the Hall device then, are proportional to voltage across the superconducting magnet and to current through it, and hence the output of the Hall device is a voltage proportional to instantaneous power into the superconducting magnet. This output voltage changes polarity with the direction of power flow.

The integrator uses a solid-state chopper-input operational amplifier with a feedback capacitor C, and a series resistor R, so that its output voltage is

---

\*Work performed under the auspices of the U.S. Atomic Energy Commission.

1. W.S. Gilbert, R.E. Hintz, and F. Voelker, Lawrence Radiation Laboratory Report UCRL-18176 (1968).

$$e_{\text{out}} = \frac{1}{RC} \int_0^T e_{\text{in}}(t) dt .$$

Drift in the integrator circuit appears on the recorder as an equivalent power loss (except that it can have either sign), and so must be kept small. Typically, we had about 1 mV drift for a period of 1000 sec with a dynamic range of 10 V. For one particular multiplier constant this corresponds to a sensitivity of 1 J in a 1000 sec (or 1 mW) with a dynamic range of 10 000 J (stored in the magnet). We obtained a 1 J sensitivity on a cycle-to-cycle basis by using a digital voltmeter to read the voltage on successive minimum of the integrator output.

A section of the multiple recorder tracing illustrating how the loss information is presented, is shown in Fig. 2. Here the current had a triangular waveform with a peak amplitude of 10 A. The middle trace shows the accumulated energy over a number of cycles as the frequency was increased. The slope of the envelope is directly proportional to the ac losses. (The boil-off gas was almost constant over this run, and change in slope of the right-hand trace is due to changes in chart speed.)

Another kind of data sheet is shown in Fig. 3. In this case, the current waveform is trapezoidal with a constant  $dI/dt$ . Several cycles were run at each current. The constant current intervals were long enough to allow us to read the integrator output with a digital voltmeter. The trace labeled B shows an increasing amount of flux jumping as the current was increased, and more will be said about this later.

### III. EXPERIMENTAL RESULTS

While making cycle-to-cycle loss measurements with a trapezoidal current waveform, we discovered that the first cycle at a new current level had considerably more energy loss than succeeding cycles. On a well stabilized coil we reached an asymptotic value within two or three cycles, while on another coil with less stabilization, it took four or five cycles. When there was a flux jump during a given cycle, the next cycle was extraordinarily lossy. Figure 4 shows several types of information relating to the cycle-to-cycle losses. The loss in joules/cycle is given as a function of the maximum current. Note that there is an envelope of asymptotic values obtained by pulsing a number of times at the same current. The first-cycle envelope was obtained by reversing the direction of current in the magnet at the beginning of each new current value to destroy the "ordering" effect. The energy loss on a cycle after a flux jump, or after increasing current without reversing direction always lay somewhere between the two envelopes. The maximum current of 116 A corresponds to about 67 kG on axis in the solenoid.

In general, the measured losses were within about a factor of two of values calculated by the loss equation in Hancox.<sup>2</sup> We were also able to measure losses over a partial cycle. For example, the current was varied from 0-10 A several times, then from 10-20 A several times, continuing on up to 100 A. The losses for this data are given in Fig. 4 as a partial-cycle envelope. Data for several values of  $\Delta I$  are shown. Since we could record the maximum energy in the coil, as well as the minimum, we were able to measure the stored energy. Figure 5 shows the Q (stored energy/energy loss per cycle) as a function of maximum current during a cycle. The Q had a minimum at around 50 A, which probably corresponds to the current at which the average of the

---

2. R. Hancox, Proc. IEE (London) 113, 1221 (1966).

winding has complete field penetration in the superconductor. We can also calculate the inductance using the relationship: stored energy =  $\frac{1}{2} LI^2$ . The inductance is not constant, and is shown as a function of current in Fig. 5.

We are interested in ac losses at typical synchrotron repetition rates, and we have made several runs on our magnets at cycling rates as high as once a second, although these magnets were not designed to be pulsed, and even though the losses are very high. Figure 6 shows typical results on the magnet previously described. The loss in joules/cycle are shown as a function of frequency. The maximum current was 10 A, 14 A, and 20 A with triangular, sinusoidal, and trapezoidal waveforms. The 20 A data had to be taken a few cycles at a time in order to keep the magnet from going normal, and so only trapezoidal waveforms were used. At 14 A the magnet could only be pulsed for 8-10 cycles at the higher frequencies, and we suspect that the magnet was heating considerably. The different waveforms merely indicate that the losses are related to  $dI/dt$ , as well as maximum current.

All of these curves show a rise in losses at very low cycling rates. This is because of a constant 60 cycle ripple voltage. When the cycling times are very long, the loss due to ripple voltage accumulates over a longer period and makes data below about 0.05 Hz unreliable. Tests made last week with a transistor-regulated (very low ripple) power supply indicate that the losses are linear with frequency at the low end.

If we calculate eddy currents at 0.5 Hz with a 0-14 A triangular waveform in the copper, we obtain a loss of about 0.53 W. The magnet was wound on a thin stainless steel form and had end flanges of the same material. We calculate 0.272 W loss in each flange and 0.002 W loss for the tube. The total eddy current losses, then, should be

$$P_T = 0.53 + 2 \times 0.272 + 0.002 = 1.1 \text{ W} .$$

From Figure 6, we see that the losses for 0-14 A at 0.5 Hz are about 9 J/cycle or 4.5 W. Thus, the measured eddy current losses are about four times larger than we can account for.\*

Data are shown in Fig. 7 for trapezoidal current waveforms in which the losses were measured after each cycle. (Figure 3 is a typical data sheet for this kind of run.) The maximum current was increased while the  $dI/dt$  was held fixed. If one neglects the repetitive data for very low  $dI/dt$  because it contains appreciable losses due to ripple voltage, we see a definite increase in losses due to increasing  $dI/dt$ . There is a large scatter in data, however, because each pulse has a different loss, depending on the previous history of current, and whether a flux jump occurred in the previous cycle. At the higher currents this scatter is more pronounced as there were often several flux jumps in each cycle.

---

\* Note added in proof: It has been suggested by several people subsequent to this talk, that the copper oxide is not insulating well and that the extra losses are  $V^2/R$  losses due to parallel resistance paths from turn to turn. This kind of loss would have the right frequency dependence.

#### IV. CONCLUSIONS

We feel that this electrical method can be very useful for measuring ac losses in superconducting magnets, or in parts of such magnets. Since accumulated energy can be monitored at many currents during a cycle, it is possible to measure losses and stored energy during the parts of a cycle, which may help to separate some of the complicated phenomena taking place during the cycle.

We are building a magnet which will be a duplicate of the magnet that I have been describing, except that it will be wound with Airco multiple strand wire. The new wire has 130 strands of 1 mil NbTi wire in the same cross section of copper. We hope to compare its performance with its solid-wire sister in time to be presented later in this Summer Study.\*

\* Note added in proof: The magnet tests on the Airco magnet were completed and are given by W.S. Gilbert, these Proceedings, p. 1007.

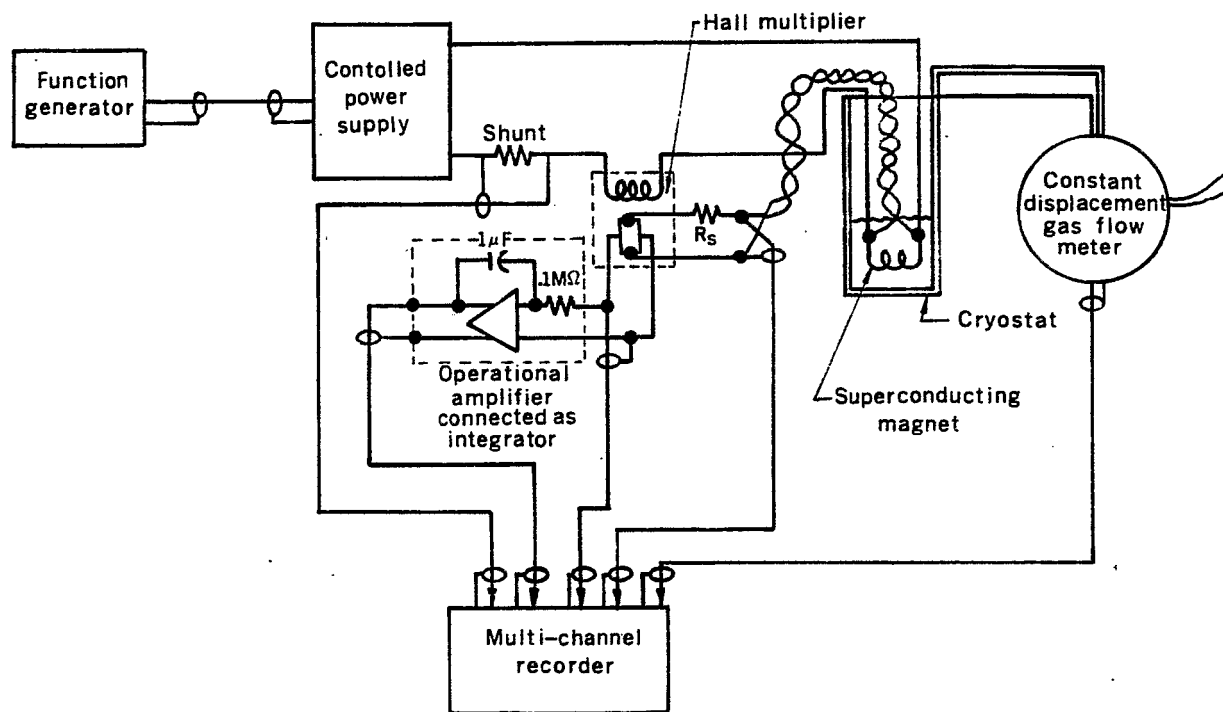


Fig. 1. Schematic representation of pulsed loss experiments.

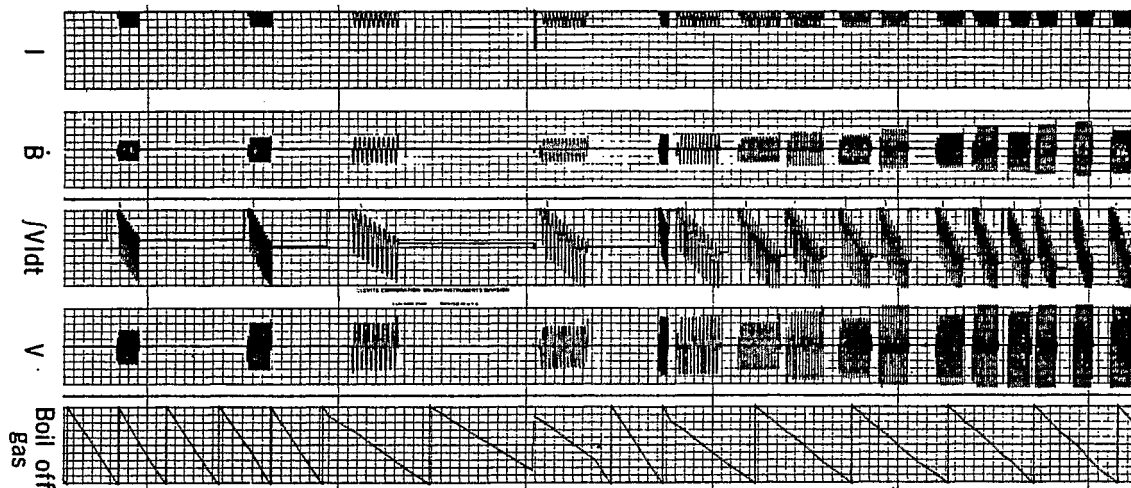


Fig. 2. Data for frequency run.

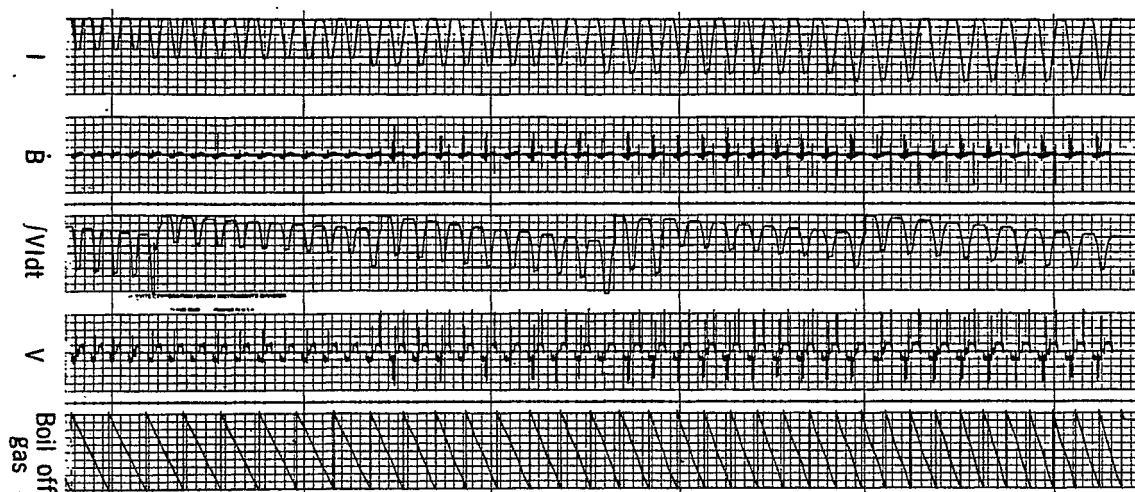


Fig. 3. Data for constant  $di/dt$  run.



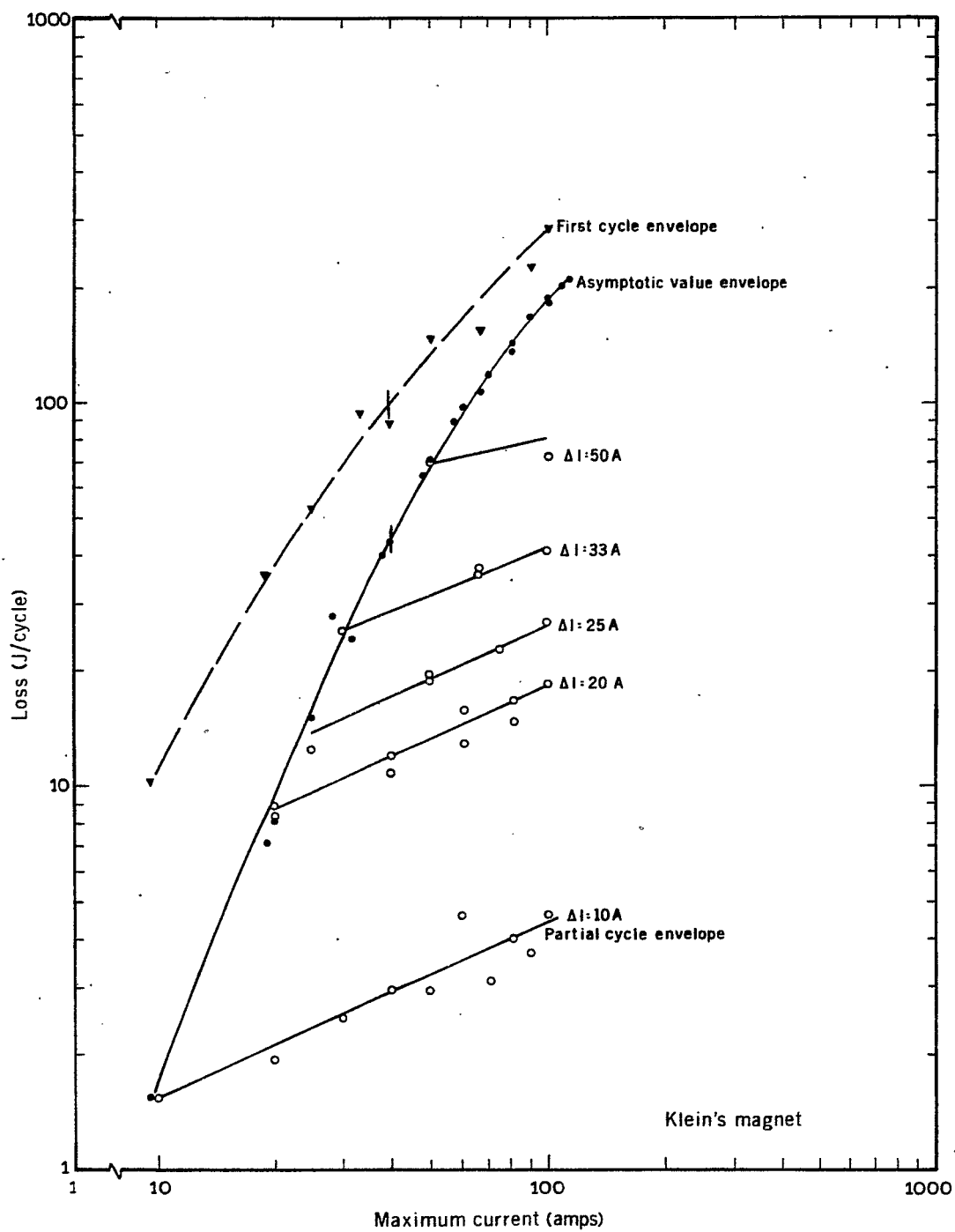


Fig. 4. Hysteresis losses.

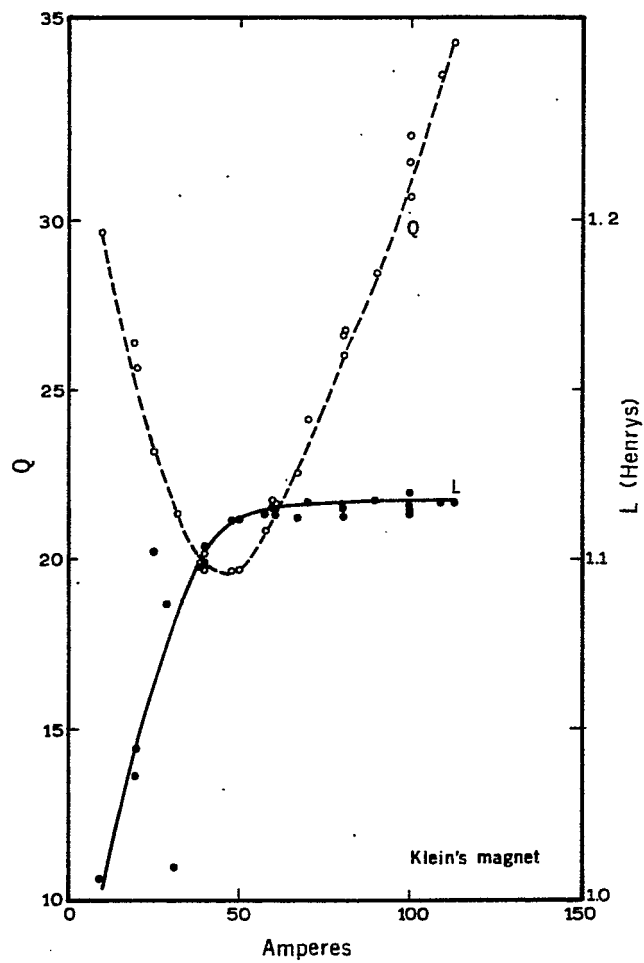


Fig. 5.  $Q$  and  $L$  as a function of maximum current.

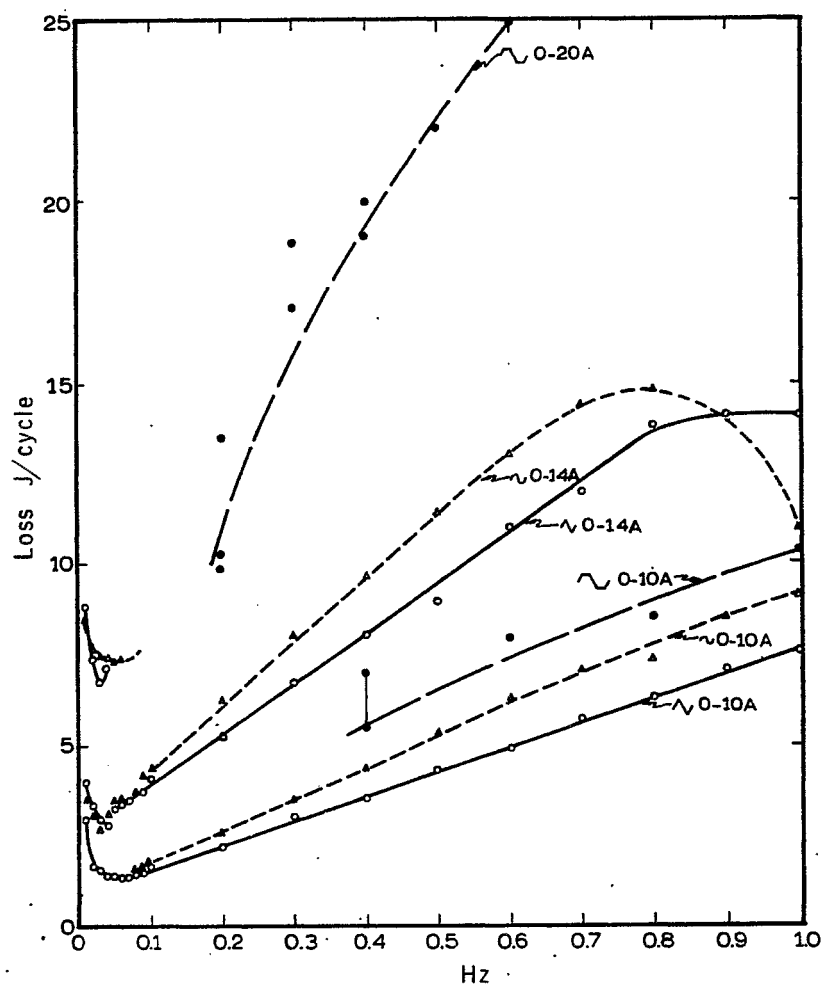


Fig. 6. Eddy current losses

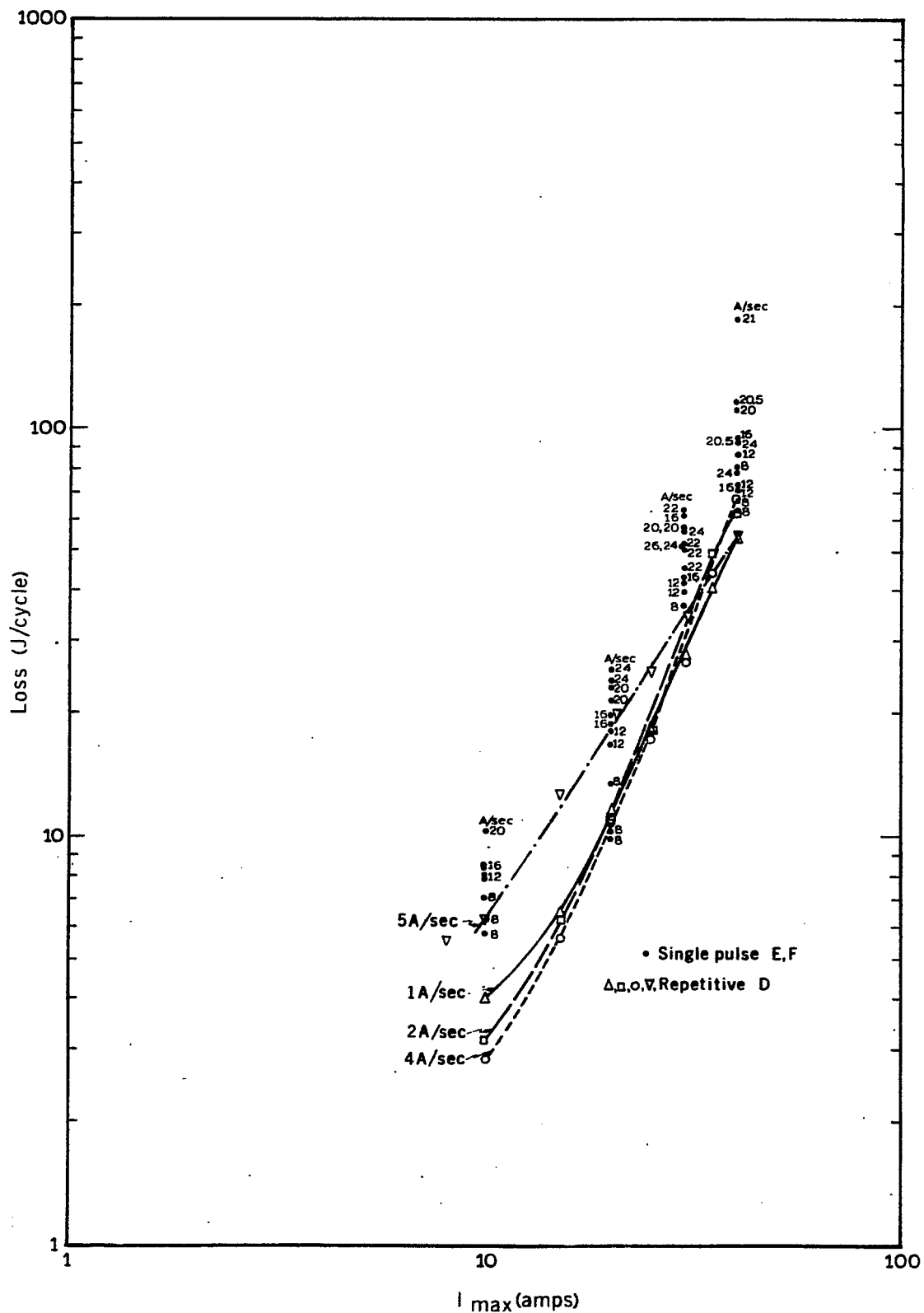


Fig. 7. Losses as a function of  $dI/dt$ .

# AC LOSSES IN MAGNETS MADE OF Nb<sub>3</sub>Sn RIBBON\*

G.H. Morgan and P.F. Dahl  
Brookhaven National Laboratory  
Upton, New York

## I. INTRODUCTION

The possible reduction of size and cost of a proton synchrotron, which can be achieved through the use of high magnetic field strength, has caused much interest in the application to this end of high field superconductors.<sup>1</sup> The success at Brookhaven of magnets wound from  $\frac{1}{2}$  in. Nb<sub>3</sub>Sn ribbon<sup>2</sup> naturally led to interest in the ac loss characteristic of these ribbons. The advantages of Nb<sub>3</sub>Sn ribbon are high current and current density, high winding density, and ease of handling. These characteristics lead to more compact magnets and higher possible field gradients. Furthermore, the superconducting layer in the commercially available ribbons is thin enough that ac losses should be low if the field were parallel to the ribbon. With this justification, the Brookhaven ac loss program began with a study of the losses in three commercially available  $\frac{1}{2}$  in. wide Nb<sub>3</sub>Sn ribbons. Much of the results of this study has been reported elsewhere,<sup>3,4</sup> and will be summarized here.

## II. APPARATUS

Heat produced in the magnet was determined by measuring the volume of helium vaporized. The magnet and a standard heat source consisting of an electrically heated resistor were enclosed in a container submerged in liquid helium. Power for the magnet was provided by either a fast-rise-time dc generator, permitting current pulses to 3000 A at 50 V with frequencies up to 3 Hz, or by the 60 Hz power line through a variable transformer.

## III. MAGNETS AND MATERIALS

The tested magnets were all made of one or more spirally-wound flat coils in which successive turns of the ribbon were separated by  $\frac{1}{2}$  in. wide plastic (Mylar) ribbon of several possible thicknesses. The magnet form most commonly tested was a single "pancake" or circular coil having 2.5 in. i.d. and 6 in. o.d., and from 130 to 370 turns of conductor. Two such coils were combined coaxially to produce either an adjacent or a separated pair. One other magnet consisted of a pair of racetrack-shaped coils with 2 in. spacing having an 8 in. straight section. 2.5 in. i.d., and 6 in. o.d.

---

\*Work performed under the auspices of the U.S. Atomic Energy Commission.

1. P.F. Smith, Nuc. Instr. and Methods 52, 298 (1967).
2. P.G. Kruger, W.B. Sampson, and R.B. Britton, Brookhaven National Laboratory, Accelerator Dept. Report AADD-104-R (1966).
3. W.B. Sampson, R.B. Britton, G.H. Morgan, and P.F. Dahl, in Proc. 6th Intern. Conf. High Energy Accelerators, Cambridge, Mass., 1967, p. 393.
4. G.H. Morgan, P.F. Dahl, W.B. Sampson, and R.B. Britton, submitted to J. Appl. Phys.

The tested materials were all Nb<sub>3</sub>Sn composite ribbons, ½ in. wide. Type A was made by RCA by their vapor-deposition process, and types B and C were made by G.E. by a diffusion process. Some of their characteristics are shown in Table I.

TABLE I

<u>Ribbon Type</u>	<u>A</u>	<u>B</u>	<u>C</u>
Thickness (in.)	0.0051	0.0042	0.0036
I <sub>c</sub> at 40 kG (A)	2160	1040	515
J <sub>eff</sub> (A/cm <sup>2</sup> )	21 000	40 000	35 000
Peak field at J <sub>eff</sub> (kG)	24.6	47.4	39.8

In Table I, I<sub>c</sub> is the short sample critical current, J<sub>eff</sub> is the maximum over-all current density obtained in a single pancake during continuous pulsing, and the field listed is the peak field in the winding at that current density. Part of the lower performance of the A ribbon is due to the lower winding density which was used because of surface roughness.

#### IV. RESULTS

There are nine important results. First, the loss per cycle is independent of frequency. Since frequency variation was possible only with the generator, this was conclusively proved only at higher fields, since the lower frequencies required higher fields to produce measurable losses. The 60 Hz data, however, agree with the low frequency data if one accepts the next result.

The second result is that the losses depend on the change in current or field, and are largely independent of the magnitude of the field or current. Again, this was proved only by relatively high field results obtained with the generator, since the task of constructing a 60 Hz source with dc bias proved formidable. As stated above, however, for given peak-to-peak current, the loss per cycle at 60 Hz agreed with that caused by the unidirectional, triangular current pulses from the generator.

The third finding is that the loss per meter of ribbon depends mainly on the average of the change in component of field normal to the ribbon surface. This was proved by demonstrating that all the loss measurements can be correlated on this basis. Figures 1, 2, and 3 illustrate this point. Here are shown all the data taken using type C ribbon. In each figure, the points "G" are data using the double pancake magnet having 1/8 in. separation of the pancakes. All of the remaining points are data using either of two almost identical single pancakes. The figures show, respectively, loss per meter plotted against mean square parallel component of field B<sub>z</sub>, mean square total field B, and mean square radial or normal component of field B<sub>N</sub>. The field is calculated assuming uniform current distribution in the conductor. By mean is meant the spatial average of the peak field during the cycle. As can be seen, the double pancake data merge with the single pancake data only in the plot against radial field component, Fig. 3, and the correlation is poorest in the plot against parallel component, Fig. 1. It should be noted that plotting against mean square, rather than some other power of the normal component, is not essential to obtain correlation, provided that in the case of odd powers, the absolute value of the normal component is used. Thus |B<sub>N</sub>| gives about as good a correlation as B<sub>N</sub><sup>2</sup>. The correlation of loss with change in average normal field allows one not only to make accurate estimates of loss in proposed magnets, but also to predict in which part of a magnet winding the loss is greatest. Figure 4 is an example of this. Here is plotted loss per

meter vs radial position in a single pancake of type C ribbon, operated at the highest current it was capable of, 500 A ( $35\,000\text{ A/cm}^2$ ) with a peak field in the winding of about 40 kG. The loss is least at the inner and outer turns, and greater by a factor of four or more in the middle. It is worth emphasizing that loss prediction requires calculation of the average normal component of field assuming uniform current distribution in the conductor, not the actual normal field component, a much more difficult task.

The fourth finding is that loss is essentially independent of current. Actually, this is a corollary to the third result, since the double pancake which produced the data of Fig. 3 has 51% greater average field for the same current as has the single pancake.

The fifth finding is that loss is independent of current density. This was demonstrated by splitting  $\frac{1}{2}$  in. ribbon, from which the edge was removed, in two to form  $\frac{1}{4}$  in. ribbon. For equal average normal field component, the loss per meter in a pancake made from the  $\frac{1}{2}$  in. wide ribbon was twice that in a pancake made from the  $\frac{1}{4}$  in. wide ribbon. If loss is presumed proportional to the width of the ribbon or to the amount of Nb<sub>3</sub>Sn, this says that loss is independent of current density, since for given normal field component, the current density in the  $\frac{1}{4}$  in. pancake is almost twice that in the  $\frac{1}{2}$  in. pancake.

The sixth experimental finding is concerned with the effect of winding density on loss. Three pancakes were wound with type B material and different thicknesses of Mylar interleaving to give a total pitch, or thickness per turn, of 0.005, 0.010, and 0.014 in. At low fields, the loss per meter for a given field change was the same for all three magnets. With increasing field, however, the loss curves become increasingly separated, and at the highest field common to the three magnets, the coarsely wound magnet has 4.6 times the loss per meter of the most closely wound magnet, and the medium density magnet has twice the loss per meter that the high density magnet has. This could be a current density effect in contradiction to the fifth finding, and to test this point, a bifilar magnet was wound, essentially the magnet of 0.014 in. pitch already described, with the 0.010 in. thickness of Mylar replaced by a sandwich of 0.004 in. of superconductor (more B ribbon) between two 0.003 in. thicknesses of Mylar. With only one of the windings powered, i.e., with the same current density as the 0.014 in. pitch magnet, the bifilar magnet had a loss per meter corresponding to a pitch of 0.007 in., about one-third that of the 0.014 in. pitch magnet. In fact, the total loss of the bifilar magnet was less than (77% of) the total loss of the 0.014 in. pitch magnet, at the highest field. This effect is attributed to an increasingly great reduction of the normal component of field with increasing winding density, or equivalently, increasingly great field exclusion. The fact that loss per meter is the same in the three magnets at low fields says that at low fields, exclusion is complete, so that the loss is a surface phenomenon. In fact, we find that at sufficiently low fields, the loss in all three ribbon types tends to be the same.

The seventh result is the dependence of loss on superconductor thickness, or equivalently for constant  $J_c$ , on  $I_c$ . According to theory,<sup>5</sup> the loss in ribbons in a field parallel to the ribbon should go as thickness or  $I_c$  squared, so using the critical currents listed in Table I, the corresponding loss ratios should be  $A/B = 4.3$  and  $B/C = 4.0$ . The observed ratio of loss in type A to that in type B ribbon is about 3.0 at intermediate and high fields (with both materials at the same winding density of 0.010 in./turn). The observed ratio of loss in B to that in C ribbon (both at a winding density of 0.005 in./turn) is a function of field: 1.4 at intermediate field to 1.0 at high field. In both cases, increasing the Nb<sub>3</sub>Sn thickness results in lower

---

5. R. Hancox, Proc. IEE (London) 113, 1221 (1966).

loss than is predicted by the theory. Assuming that cladding is not a factor, the discrepancy could be due to the field not being parallel to the ribbon, to the assumption that  $J_c$  is the same in all materials, or it could be that field exclusion effects are a function of superconductor thickness, or amount of superconductor per unit volume of winding.

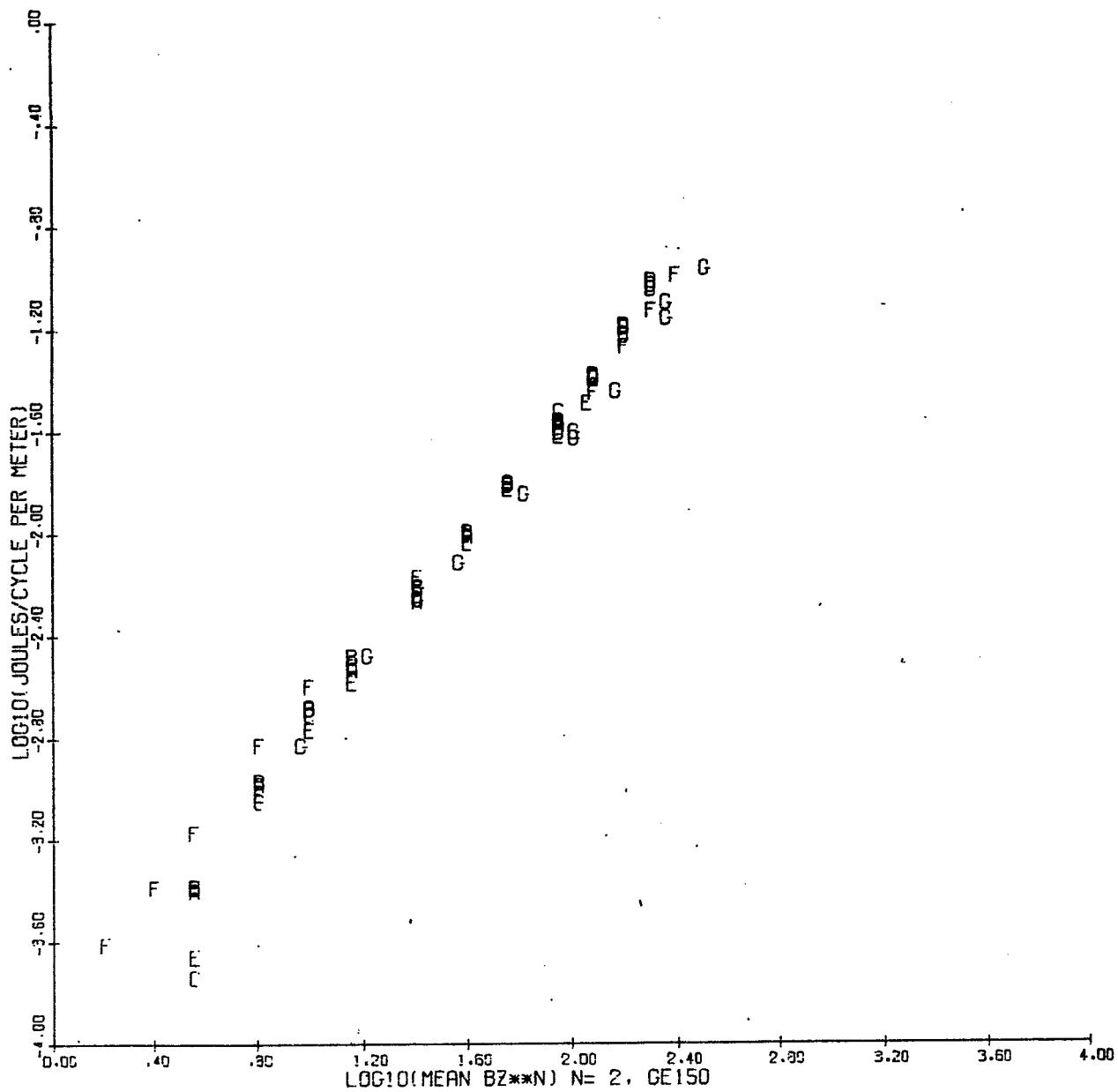
The eighth conclusion one can obtain from the data is that the loss at high field in all materials increases as about the 2.5 power of the normal field. Since the actual normal field, in this field range, increases faster than that calculated on the basis of uniform current distribution, the true field exponent must be less than 2.5. It should be remembered that these observed losses are due to field changes in the material which range from zero (at the kernel of the magnet) up to the maximum at the innermost turn. The observed loss is thus an average over a variety of field changes, and the exponent of the loss curves is accordingly an average.

The ninth result is the finding that in all the tested magnets, the ratio of stored energy to energy loss per cycle,  $E/\Delta E$ , lay within a band ranging from about 100 to 250, with a generally decreasing trend at higher fields. This latter result follows from the 2.5 power dependence of loss on normal field, and the second power dependence of stored energy on field, which together imply a  $1/B$  dependence of  $E/\Delta E$  on field. The constancy of  $E/\Delta E$  from magnet to magnet is possibly a result of the relation between stored energy and length of conductor in compact solenoids.

#### V. COMPARISON WITH THEORY

Comparison of the results with theory is difficult for several reasons. First, some of the ribbon parameters ( $Nb_3Sn$  content) are not known accurately. Second, the contribution of the Nb substrate in the G.E. ribbon is uncertain. Third, the field direction at the ribbon surface is both complex and unknown. Eddy currents in the normal material presumably contribute to the loss, but this contribution is probably small, since we observe no frequency dependence. Using formula (9) of Hancox,<sup>5</sup> we compute the loss for the case of field parallel to the ribbon, which should set a lower limit to the experimental loss. The value obtained is 6.7 or 3.9 J/cycle, depending on whether the Nb substrate is or is not included. The experimental value for G.E. 150 with an average total field change of 19.5 kG was 25.6 J/cycle.





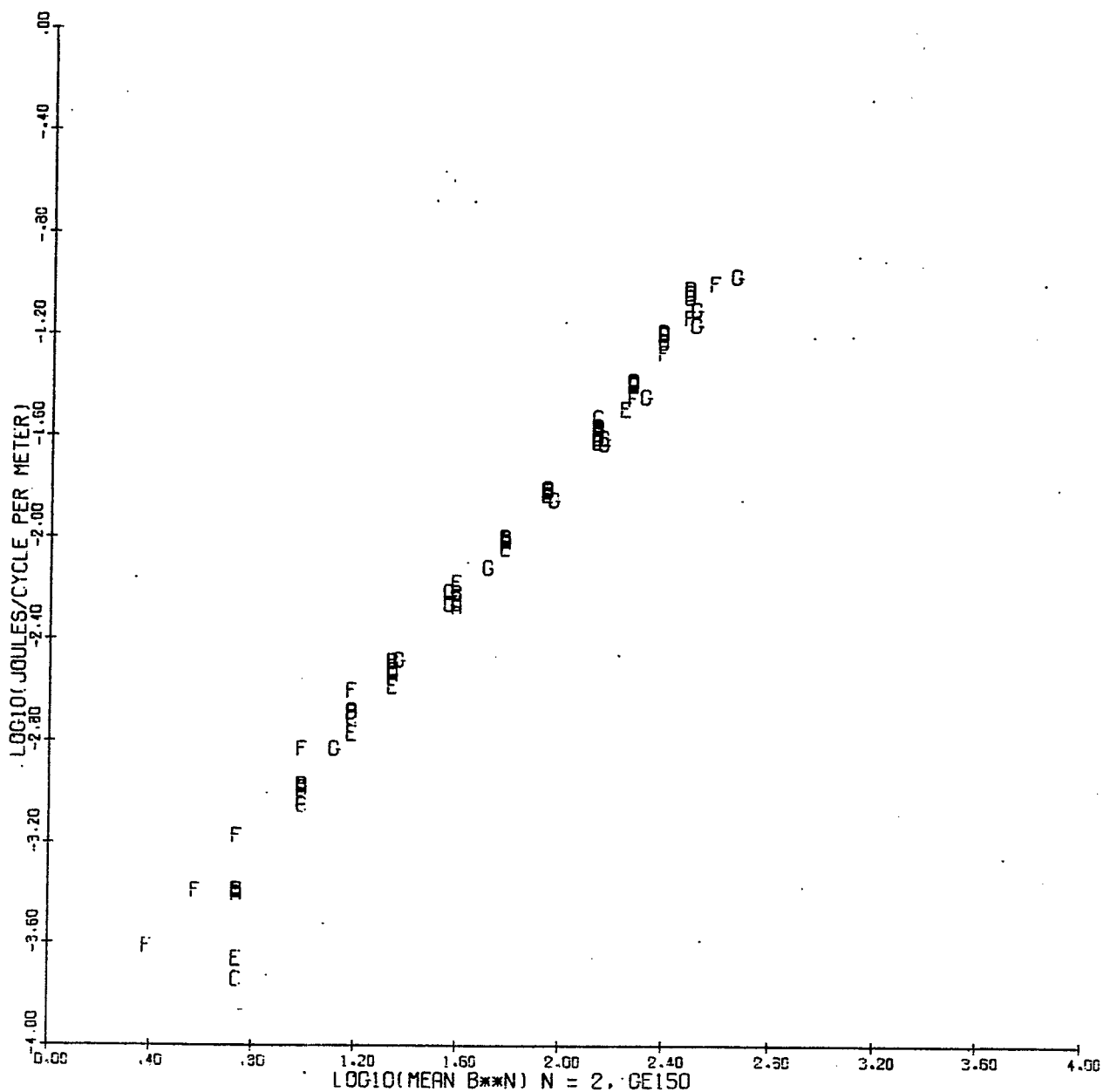


Fig. 2. Energy loss per cycle per meter vs mean square total field..  
The symbols have the same meaning as in Fig. 1.

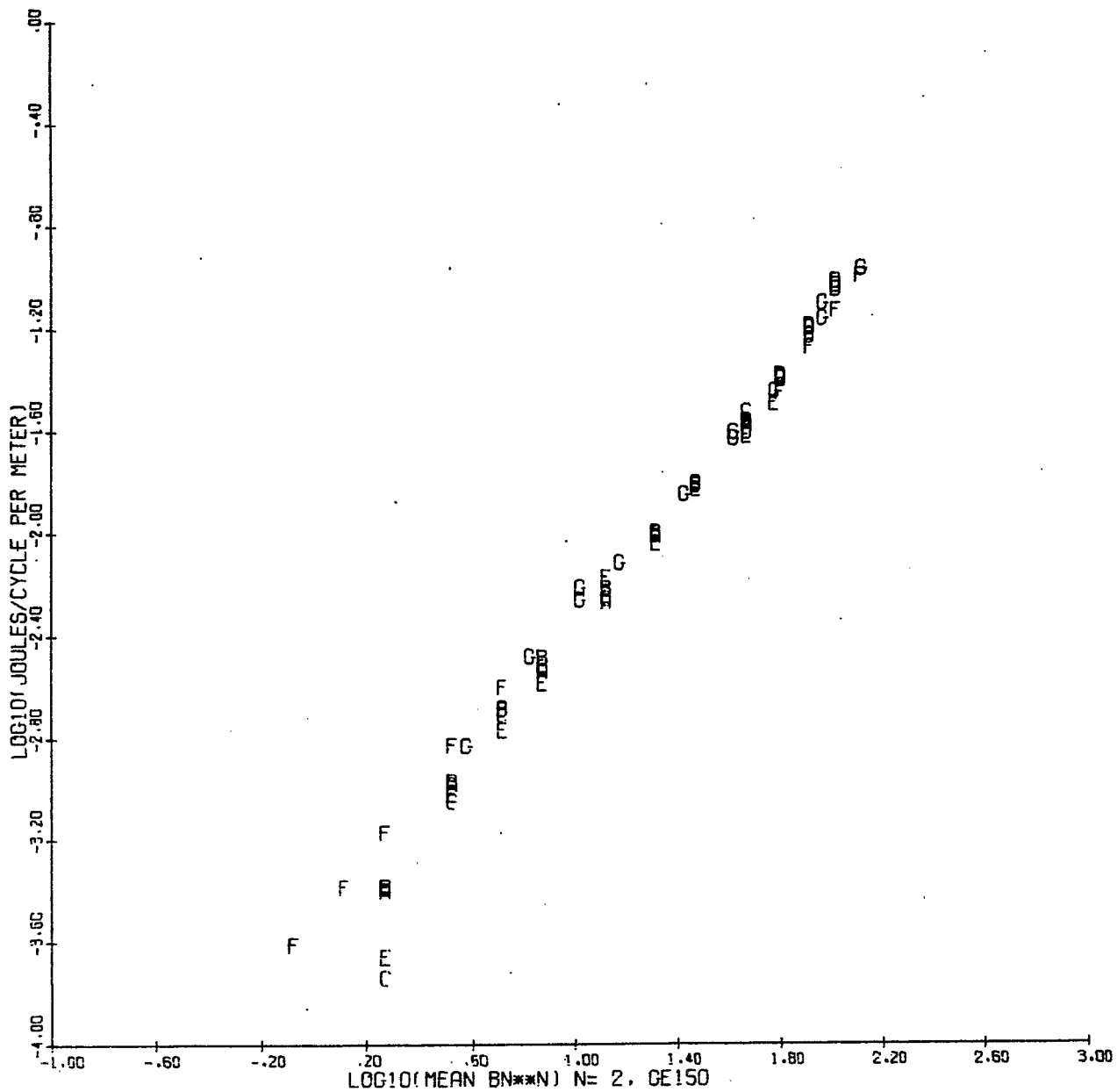


Fig. 3. Energy loss per cycle per meter vs mean square normal component of field. The symbols have the same meaning as in Fig. 1. Note that here, the G's blend in with the remaining points, especially at high field where the data are more accurate.

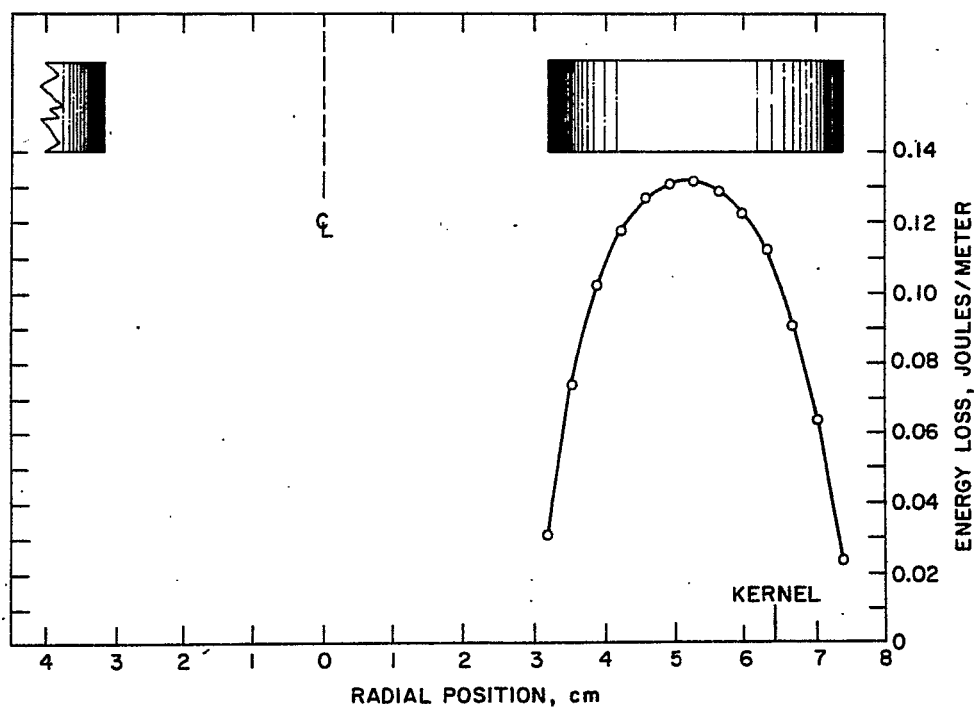


Fig. 4. Energy loss per cycle per meter vs radial position in a pancake magnet. The loss is derived from the data of Fig. 3, which are losses for entire magnets.

# DYNAMIC RESISTIVITY OF HARD SUPERCONDUCTORS IN A PERPENDICULAR TIME VARYING FIELD

R. Altorfer, F. Caimi, and J.M. Rayroux  
Oerlikon Engineering Company  
Zurich, Switzerland

## I. INTRODUCTION

Losses occur in type II superconductors when they are exposed to time varying fields or currents. In this paper we present the results of measurements made on a superconducting wire carrying a constant current while being exposed to a perpendicular field varying linearly with time.

## II. EXPERIMENTAL SET-UP

The experimental arrangement is essentially the same as the one used by Taquet<sup>1</sup> and Rayroux.<sup>2</sup> The sample is wound bifilarly and placed inside a superconducting solenoid so that the magnetic field is perpendicular to the wire to be tested. The potential across the wire is monitored by a microvoltmeter (Keithley type 150) and recorded on a X-Y recorder (Moseley DR-2M). The transport current is first set in the bifilar wire, the field is increased up to some value below  $H_{c2}$  (about 20 kOe for NbZr and NbTi), kept constant for a while, and then set back to zero at about the same rate of change.

## III. RESULTS

The shape of the voltage is identical for any type of hard superconductor. The general characteristics of the signal are the following:

- The magnitude of the voltage is proportional to the transport current and to the sweep rate of the magnetic field,  $dH/dt$ .
- There is a threshold field below which the voltage is essentially zero.
- The voltage vanishes abruptly for  $dH/dt = 0$ .
- The voltage polarity is independent of the sign of  $dH/dt$ .  
The sign of the voltage is the same as in the normal state.

The curves of Fig. 1 show the results obtained with a copper-plated Nb25%Zr wire (diameter of core 0.254 mm) when the field is increased from zero to some 15 kOe.

Instead of plotting the voltage one can express the results in terms of a dynamic resistivity in  $\Omega \cdot \text{cm}$ . The curves of Fig. 2 show that:

- The threshold field is a characteristic of the material itself as well as of its metallurgical treatment.

---

1. B. Taquet, J. Appl. Phys. 36, 3250 (1965).

2. J.M. Rayroux, D.I. Itschner, and P. Müller, Phys. Letters 24A, 351 (1967).

- A possible size effect exists as seen from the 10 mil and 5 mil NbZr data.
- The magnitude of  $\rho/(dH/dt)$  at 10 kOe is of the order of  $10^{-15} (\Omega \cdot \text{cm})/(\text{Oe} \cdot \text{sec}^{-1})$  (compare with the Cu resistivity at  $4^\circ\text{K} \approx 10^{-8} \Omega \cdot \text{cm}$ ).

The characteristics of the threshold voltages indicate clearly a possible relation between the dynamic resistivity and the magnetization. A more careful observation of the signal demonstrates the effect of the magnetic history of the sample. As shown in Fig. 3 the dynamic resistivity of a clean wire starts at zero field while the magnetic hysteresis is the apparent reason for the threshold field. A still more obvious hysteresis effect appears when the field is cycled from zero to H and back to zero (see Fig. 4).

#### IV. EXPLANATION

The first idea that came to our mind looking for an explanation of the hysteretic behavior of the dynamic resistivity<sup>2</sup> was of phenomenological order. We advanced the idea that the dynamic resistivity could be proportional to the product of the induction B by its time derivative  $dB/dt$ :

$$\rho(H) \sim B \frac{dB}{dt} \sim B \frac{dB}{dH} \frac{dH}{dt} \quad (\Omega \cdot \text{m}) \quad (1)$$

Qualitatively at least the graphical product of  $B \cdot dB/dH$  results in a curve similar to Fig. 4. Druyvesteyn<sup>3</sup> used the Bean model and its resulting flux-transport concept across the wire to analyze our first experimental data. He found an equation for the observed electrical field which is in good agreement with the experiments:

$$E = \mu_0 \cdot \frac{dH}{dt} \cdot \frac{J_t}{J_c} \cdot d \quad (\text{V/m}) \quad (2)$$

where  $\mu_0 = 4\pi 10^{-7} \text{ VsA}^{-1} \text{ m}^{-1}$ ,  $d$  = wire thickness,  $J_t$  = density of the transport current, and  $J_c$  = critical current density. Using basically the same approach but introducing the Kim equation for the density of the critical current  $J_c = \alpha/(B_0 + B)$ , we found the following expression for the electrical field of a clean wire below the threshold field:

$$E \approx \frac{(B_0 + B)^2}{2\alpha} \cdot \frac{dH}{dt} \quad (\text{V/m}) \quad (3)$$

where B is the induction at the surface of the wire. Above the threshold field the same treatment gives:

$$E = \frac{\mu_0}{2\alpha} (B_0 + B) \cdot J_t \cdot d \cdot \frac{dH}{dt} \quad (\text{V/m}) \quad (4)$$

which, in accordance with Eq. (2) and with the experiments, also stresses the importance of high critical current density and small conductor size  $d$  for low losses.

It is a pleasure to acknowledge very fruitful discussions with Prof. Dr. J.L. Olsen and Dr. W. Druyvesteyn throughout this work.

---

3. W.F. Druyvesteyn, Phys. Letters 25A, 31 (1967).

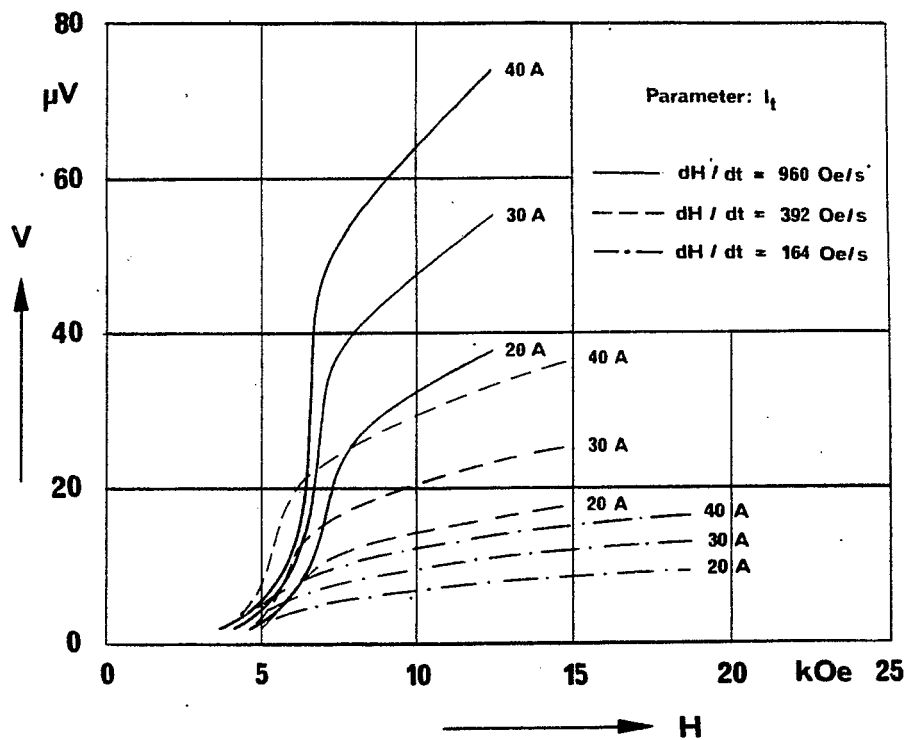


Fig. 1. General behavior of the voltage with transport current and sweep rate of the field as parameters. Sample: Nb25%Zr, diameter = 0.254 mm + 0.025 mm Cu, wire length = 12.8 m.

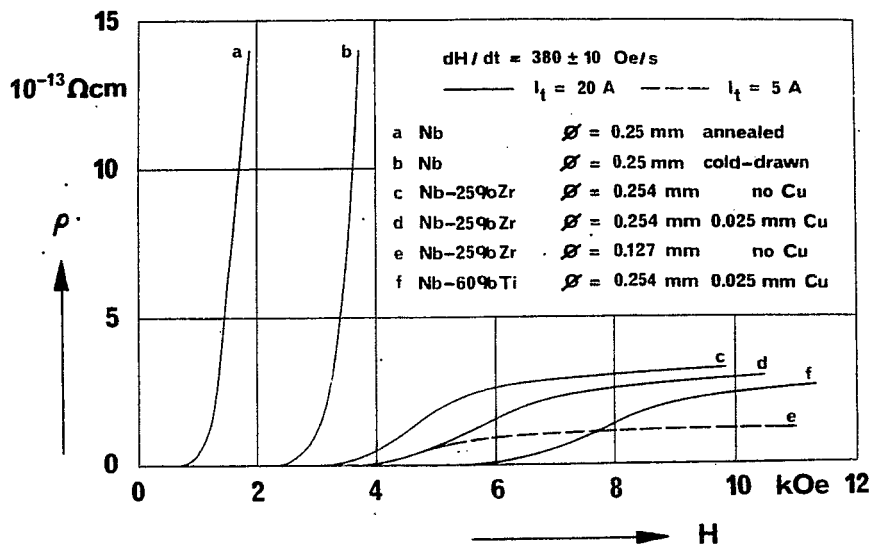


Fig. 2. Threshold field for various hard superconducting wires.

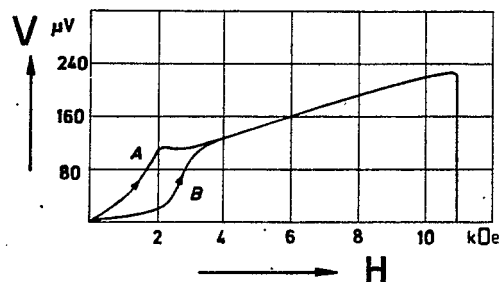


Fig. 3. Effect of magnetic history below the threshold field. Sample: Nb42%Ti cold-worked only, diameter = 0.250 mm + 0.025 mm Cu, length = 20 m; transport current = 10 A. A: magnetically clean wire. B: wire with magnetic hysteresis.

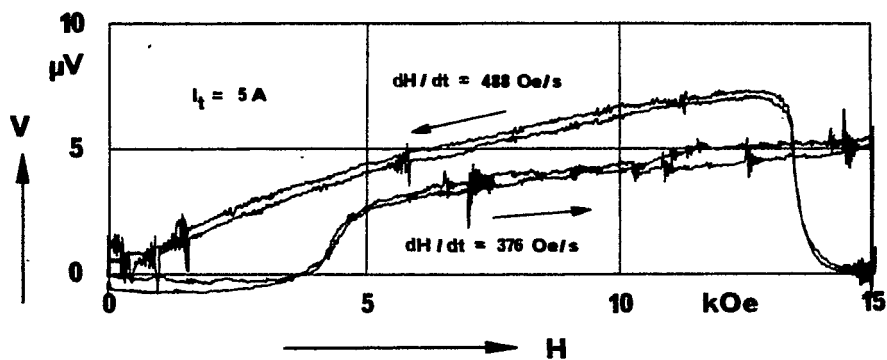


Fig. 4. Voltage on a Nb25%Zr wire (diameter = 0.127 mm, no Cu plating, length = 20 m).



MAGNETIC INSTABILITIES AND SOLENOID PERFORMANCE:  
APPLICATIONS OF THE CRITICAL STATE MODEL

H.R. Hart, Jr.  
General Electric Company  
Research and Development Center  
Schenectady, New York

I. INTRODUCTION

In this informal review I intend to discuss our understanding of the magnetic instabilities which occur in high field superconductors and the implications of our understanding for the design of high field, high current density solenoids. The approach will be mainly tutorial; the bibliography will allow reference to useful review articles and to some of the original sources.

After first mentioning very briefly the stability problems encountered in practical high field superconducting solenoids, we shall review the model which will form the basis of our discussion of magnetic instabilities: the critical state model. After illustrating the use of this model for isothermal situations, we shall consider the much more complicated situation in which the temperature is not constant. We shall find that under some conditions a small disturbance, say a small temperature rise, will grow catastrophically, driving the material into the normal state; the system will be unstable. We shall determine the conditions necessary for stability in certain limits, limits for which we can make simple calculations, limits yielding results useful for solenoid design.

The history and present state of development of solenoids has recently been reviewed very thoroughly by Chester.<sup>1</sup> This material will not be repeated here.

The central problem is the loss of performance of a conductor when it is wound into a solenoid, the degradation effect. As an example, a conductor formed of a high field superconductor may carry 40 A without a measurable voltage drop in a magnetic field of 40 kOe when tested in the form of a short length. The same conductor systematically will carry less than 20 A in a solenoid generating 40 kOe. This kind of performance degradation has been observed in each of the materials used in the construction of high field solenoids; it is a general phenomenon. It has been found experimentally that the superconducting-to-normal transitions leading to this limited performance occur in the lower field regions of the solenoid, not in the high field regions in which the critical current density of the superconductor is generally at its lowest.

The degradation effect can be alleviated to some extent by plating or coating the conductor with a pure normal metal such as copper or silver, or by winding into the solenoid layers of pure normal metal. Further, in some cases, a considerable increase in performance is obtained by running a solenoid in superfluid helium. Fine wire conductors apparently suffer less degradation than larger conductors.

The reader is referred to Chester's review<sup>1</sup> for details and references for the above observations. We shall now turn to a description of the critical state model, the model on which we plan to base our discussion of magnetic instabilities.

## II. THE ISOTHERMAL CRITICAL STATE MODEL

Soon after the demonstration of the high field capabilities of Nb<sub>3</sub>Sn and of alloys such as NbZr, it was found that a rather simple phenomenological model,<sup>2</sup> here called the critical state model, allows one to predict the magnetic behavior of a high field superconductor in terms of a simple empirical parameter. The basic assumption of the critical state model is that a changing flux density in a high field superconductor induces persistent currents up to a limiting or critical current density,  $J_c$ . These persistent currents are induced to flow according to Lenz's law in such a way as to minimize the change in the flux linking the sample. That portion of a superconductor carrying this limiting current density is said to be in the critical state. The parameter  $J_c$  depends on both temperature and magnetic field, though in some cases it is reasonable to assume that  $J_c$  is independent of field. Often  $J_c$  is assumed independent of field merely in order to simplify calculations.

Subsequently this phenomenological critical state model received a more physical basis. For an ideal, defect free, sample of a type II superconductor ( $H_{c1} < H < H_{c2}$ ), the flux filaments threading the sample<sup>3</sup> are free to move about in the sample subject only to their mutual repulsive interactions<sup>3,4</sup> and to a viscous drag<sup>5</sup> which can be characterized by a flux flow resistivity,  $\rho_f$ . Nonuniform distributions of flux filaments, equivalent to field gradients or bulk currents, disappear quickly, with a time constant determined by  $\rho_f$ . However, for nonideal type II superconductors, persistent bulk currents or field gradients can occur when the flux filaments are pinned or trapped by defects in the structure of the material.<sup>6</sup> Such defects can be voids, normal inclusions, grain boundaries, compositional variations, dislocations, etc. A large enough bulk current density or field gradient can free the flux filament from the defect so that it can move; this critical bulk current density is  $J_c$ . The pinning and freeing of the flux filaments may well be a thermally activated process, a process of flux creep.<sup>7</sup> This process, and thus the critical current density itself, is temperature dependent. If the controlling process is flux creep, there is no true persistent critical current density; flux motion and current decay will continue indefinitely, albeit at a very slow and ever decreasing rate. In actual fact, for most purposes the currents can be considered as persistent below a given  $J_c$ . We shall return to this point in a later section.

We have up to this point discussed the critical state model in terms of flux motion or of induced persistent currents. It will be convenient throughout most of this review to think in terms of the relation between the electric field in the material and the current density. We can state the critical state model with some simplifications as follows: The electrical and magnetic properties of the superconductor are characterized by the nonlinear relation between the electric field and the current density indicated in Fig. 1. No current flows in the superconductor unless there has been a change in flux linkage. While the flux linkage is changing, the electric field and current density are related by the above relation and Maxwell's equations; note that local heating occurs,  $P = E \cdot J$ , even though we are dealing with a superconductor. When the steady state has been obtained, we find that a persistent current density  $\pm J_c$  is flowing throughout those regions in which changes in flux linkage or magnetic field are occurred. The sign is given by the sign of the last nonzero electric field. No current is flowing where no changes in flux linkage occurred. The static magnetic properties are determined by Maxwell's equations and the distribution of current density: 0,  $\pm J_c$ . If one restricts himself to isothermal field or current changes, he can easily calculate the final field and current distribution. We call this limit the isothermal critical state model.

In order to illustrate the application of the isothermal critical state model, let us work with the model in its simplest form:  $J_c$  independent of  $H$ , and  $\rho_f$  infinite. Thus the E-J relation is as shown in Fig. 2.

Let us consider a slab of a high field superconductor cooled in a field  $H_0$  parallel to the plane of the slab ( $H_{c1} \ll H_0 < H_{c2}$ ), Fig. 3a. Let us consider the isothermal response of this slab to changes in the applied field. Increasing the applied field causes flux penetration into the sample. For this geometry the Maxwell equation  $\nabla \times \mathbf{H} = 4\pi \mathbf{J}/10$  (practical Gaussian units) reduces to  $\partial_x H_z = -4\pi J_y/10$ , yielding for the isothermal critical state model

$$\frac{\partial H_z}{\partial x} = 0, \mp \frac{4\pi}{10} J_c,$$

where the sign can be chosen by Lenz's law. A change in applied field  $\Delta H_0$  thus yields a triangular penetration of field as indicated in Fig. 3b. The appropriate current distribution is also indicated. The depth of flux penetration,  $\delta$ , is given by

$$\delta = \frac{\Delta H_0}{\frac{4\pi}{10} J_c}.$$

For a sufficiently large change in applied field, the flux penetration from the two sides meet, and the field and current distributions are as indicated in Fig. 3c. Lowering the field from the peak field (Fig. 3d) causes flux to move out of the sample. Starting at the surface of the sample and moving inward, there is a reversal of the local current flow.

It is possible to calculate from this model the field distribution, the local flux penetration or flux linkage, and thus the local heating. For more detailed descriptions of the application of the model and of the results obtained see Bean,<sup>2</sup> London,<sup>2</sup> Kim et al.,<sup>2</sup> Hancox,<sup>8</sup> and Hart and Swartz.<sup>9</sup>

Let us now show similar current and field distributions for a cylindrical wire carrying a transport current. Let us consider the wire to have been cooled in a magnetic field  $H_0$  parallel to the axis ( $H_{c1} \ll H_0 < H_{c2}$ ). Let us apply a transport current parallel to the axis and plot the current distribution and circumferential field or self-field distribution. Before any current is applied there is no self-field (Fig. 4a). Upon the application of a current ( $I < \pi R^2 J_c$ ), a flow of current density, magnitude  $J_c$ , penetrates from the surface (Fig. 4b) to a depth such that  $J_c \cdot \pi(R^2 - R_1^2) = I$ . The self-field is as indicated. The maximum current in the isothermal model is  $\pi R^2 J_c$ , when  $R_1 = 0$ . If, after having reached a peak current  $I_0 < \pi R^2 J_c$ , the current is decreased, a current reversal penetrates from the outside as indicated in Fig. 4c. Again it is possible to calculate local field and current distributions, local flux penetration (including the instantaneous voltage drop down the wire), and local heating. It is possible to carry out the calculations for fields perpendicular to the axis as well. Pertinent references are Refs. 2, 8, and 9, as well as Grasmehr and Finzi.<sup>10</sup>

We have devoted this much space to the critical state model because it will be the basis of our following sections. We have to ask how well does it work in practice. Bean,<sup>2</sup> in static experiments at fields below 10 kOe, has found rather detailed agreement with this model, using  $J_c$  independent of  $H$ . Kim, Hempstead, and Strnad,<sup>2</sup> in static experiments covering a wider range of fields, found agreement with the critical state model predictions (with an important qualification) provided they used a field dependent  $J_c$ . In particular, they used a two-parameter relation:  $J_c(H) = \alpha_c/(H + B_0)$ . Other authors have found in different materials yet other field dependences for  $J_c$ . The field dependence of  $J_c$  is related to the defect structure yielding the flux pinning; this subject is discussed by J.D. Livingston in another paper in this Brookhaven Summer Study series. The important qualification in the work of Kim et al. is that

under some conditions the isothermal critical state collapsed; flux rushed into the sample; a flux jump occurred. Thus we can say that for static experiments and isothermal conditions the isothermal critical state model is a satisfactory description. In this paper we shall try to determine the conditions under which the isothermal conditions cannot be maintained.

Several experiments indicate that the critical state model is useful as well in cases in which smaller, more rapidly varying fields are involved. Grasmehr and Finzi<sup>10</sup> have measured the instantaneous voltage drop along a wire carrying a 0.8 kHz alternating current. In addition they calculated the voltage waveform using the simple form of the critical state model (Fig. 2); the agreement between the model prediction and the experimental results is excellent. Instead of measuring the voltage directly and comparing their results visually, they could have Fourier-analyzed their predicted voltage drop and measured the harmonic content of the experimental voltage. The latter is what Bean<sup>2,11</sup> did for the output of a pickup coil containing samples exposed to alternating fields. Bean calculated for the higher harmonics that

$$V_{n_{\text{odd}}} = \frac{\gamma \cdot h_0^2 f \cdot 5}{J_c (H_{dc}, T) \cdot (n-2)(n+2)} ; \quad V_{n_{\text{even}}} = 0, \quad (n > 1)$$

where  $n$  is the harmonic,  $f$  is the fundamental frequency,  $h_0$  is the alternating field amplitude, and  $\gamma$  is a constant involving the geometry of the sample and the pickup coil. In Ref. 11 the experimentally observed results ( $f = 5$  kHz) are compared with the above predictions. The agreement is excellent through the seventh harmonic; deviations become apparent as one moves towards the seventeenth harmonic.

Agreement was obtained in these dynamic experiments even though the effects of a finite  $\rho_f$  (Fig. 1) were (quite properly) ignored. As we shall see later, there are some situations in which the finite  $\rho_f$  is important. At this point let us simply note that where  $J < J_c$  no flux motion occurs, but where  $J > J_c$  flux moves according to a flux diffusion equation

$$D \frac{\partial^2 B}{\partial x^2} = \frac{\partial B}{\partial t},$$

where

$$D = \frac{10^9 \rho_f}{4\pi}.$$

Thus the time constant for flux redistribution for the slab geometry illustrated in Fig. 3b is roughly  $\tau_m \sim \frac{1}{2} \delta^2 / D$ . Estimates of  $\rho_f$  for useful high field superconductors can be made on the basis of the work of Kim et al.<sup>5</sup>

The critical state model as we have introduced it can be expected to apply best for defect-loaded very high field superconductors such as NbZr, NbTi, or intermetallic compounds such as Nb<sub>3</sub>Sn. If the applied fields are several kOe or more, we are correct in neglecting surface effects<sup>12,13</sup> and the reversible magnetization characteristic of type II superconductors.<sup>3</sup>

### III. ADIABATIC CRITICAL STATE MODEL AND MAGNETIC INSTABILITIES

In Section II we followed the field profile in a slab of material as we increased the applied field isothermally. We predicted a triangular field penetration until the two triangles met. A similar flux penetration is predicted for a cylindrical rod. While in some studies such flux penetration is observed,<sup>2</sup> in many other studies,

especially of superconductors having very large critical current densities, the flux penetration follows the predicted behavior over a limited field change and then a sudden and nearly complete flux penetration occurs.<sup>14</sup> Coffey<sup>15</sup> has probed the field profile in a divided rod of Nb60%Ti upon changing the applied (axial) field. He finds that the initial triangular field penetration ( $H_a < 14$  kOe) is essentially as predicted by the isothermal critical state model. At higher fields there is a marked change in the mode of flux penetration; at some field the isothermal profile collapses and flux rushes in to bring the internal field up to the applied field. A further field increase leads to a new triangular shaped flux penetration profile until another catastrophic flux penetration occurs. These unstable flux penetrations occur rather regularly with a field spacing of between 4 and 8 kOe. These are the flux jumps or magnetic instabilities which we wish to understand; we wish to be able to predict their occurrence in terms of the properties of the high field superconductor.

Let us start out by recognizing the difficulty in maintaining isothermal conditions while changing the field. As pointed out by Swartz and Bean,<sup>16</sup> and by Wipf,<sup>17</sup> the magnetic flux can under some conditions diffuse through the useful high field superconductors much faster than can the heat generated by the moving flux; thus the superconductor can heat appreciably if a sudden field change occurs. The consequence of such a temperature rise can be seen qualitatively by looking at Fig. 3b while recalling that the critical current density of a high field superconductor generally decreases with increasing temperature.<sup>18,19</sup> As we saw in Section II,  $\delta(T) = 10\Delta H_0 / 4\pi J_c(T)$ . Thus a temperature rise leads to a further field penetration, which generates heat leading to a greater temperature rise and, in turn, to a yet greater flux penetration, etc. This thermal-magnetic feedback can under some conditions lead to a thermal runaway, a catastrophic flux jump.

As the field applied to a high field superconductor is increased, flux penetrates the sample. This flux penetration, even in the absence of flux jumps, is not smooth; it is a noisy<sup>20</sup> random process accompanied by local fluctuations of flux density about the critical state profile. Our concern is whether or not these fluctuations grow into gross flux jumps. The general problem is a very complicated one, for we are dealing with two coupled diffusion processes: the diffusion of flux and the diffusion of heat, the coupling arising from the generation of heat upon flux motion and the decrease in flux pinning or critical current density with an increase of temperature. Little progress has been made in this general problem. We shall consider only extreme limits for which simplifications occur.

Let us first consider the instability problem in the limit that no heat flows out of the region of flux penetration, a quasi-adiabatic limit. Let us consider a semi-infinite block cooled in a field  $H_0$  applied parallel to the face of the block ( $H_{c1} \ll H_0 \ll H_{c2}$ ). Let us isothermally increase the applied field by an amount  $\Delta H_0$ . The field profile is now that characteristic of the bath temperature  $T_1$ . We can consider the stability of this profile against small disturbances by calculating the energies involved in going from this profile to others at higher temperatures. In order to simplify the computational details, let us assume that the critical current density is independent of field and that the total heat developed in any flux penetration is spread evenly throughout the region of flux penetration, i.e. the new temperature is uniform across this region. This last rather artificial assumption will later be relaxed. We consider the two uniform temperature critical state profiles illustrated in Fig. 5. We are interested in the amount of heat developed by the motion of flux in going from profile 1 to profile 2,  $Q_m$ , and in the amount of energy absorbed in heating the sample from  $T_1$  to  $T_2$ ,  $Q_T$ . These quantities are illustrated schematically in Fig. 6. In our quasi-adiabatic limit only those profiles are allowed for which  $Q_m = Q_T$ . If the excluded field  $\Delta H_0$  is small (Fig. 7a),  $Q_m$  is always smaller than  $Q_T$  and only one solution is allowed,  $T_2 = T_1$ . The system is stable against small disturbances. For a sufficiently large excluded field  $\Delta H_0$  (Fig. 7b), another higher temperature profile is allowed (and in our simple case is clearly accessible); the system is unstable, for a

small disturbance will start the system towards the higher temperature state. If the initial slope of the  $Q_m$  vs  $T_2 - T_1$  curve is greater than the initial slope of the  $Q_T$  vs  $T_2 - T_1$  curve, instabilities are possible; the extent of the flux jump depends on the nonlinearities of the curves, in particular on the temperature dependences of the heat capacity and the critical current density. In order to determine the important physical parameters, let us calculate  $Q_m$  and  $Q_T$  as functions of  $T_2$  and  $T_1$ . Let us assume the critical current density to be decreasing linearly with temperature<sup>18</sup>:

$$J_c(T) = J_c(T_1) \left( 1 - \frac{T - T_1}{T_u - T_1} \right),$$

where  $T_u \equiv T(J_c = 0)$ , and the heat capacity to be proportional to the cube of the temperature<sup>21</sup>:

$$C(T) = C_1 \cdot (T/T_1)^3 \quad (J/^{\circ}K \text{ cm}^3).$$

We calculate  $Q_m$  by calculating the total energy input to the system using the Poynting vector  $\vec{P} = 10 \frac{E}{c} \times \vec{H}/4\pi$ , and then subtracting that portion of this energy going into the increase in the energy of the magnetic field:

$$\frac{10^{-7}}{8\pi} \int_0^{\infty} [H_2^2(x) - H_1^2(x)] dx.$$

The remainder is the heat generated. We first calculate the various quantities per unit surface area. Using the Poynting vector we find:

$$\begin{aligned} \Delta W_{12} &= \int_{t_1}^{t_2} P dt = \frac{10^{-7}}{4\pi} \int_{t_1}^{t_2} \phi(x=0) \cdot (H_0 + \Delta H_0) dt \\ &= \frac{10^{-7}}{4\pi} (H_0 + \Delta H_0) \Delta \phi_{12}(x=0), \end{aligned}$$

where  $\Delta \phi_{12}(x=0)$  is the total flux crossing the surface in going from profile 1 to profile 2. From the triangular profile (Fig. 5) we find  $\Delta \phi_{12}(x=0) = \Delta H_0(\delta_2 - \delta_1)/2$ . Therefore the total energy input is:

$$\Delta W_{12} = \frac{10^{-7}}{8\pi} (H_0 + \Delta H_0) \Delta H_0 \cdot (\delta_2 - \delta_1),$$

where

$$\delta_2 = \frac{\Delta H_0}{\frac{4\pi}{10} J_c(T_2)},$$

and

$$\delta_1 = \frac{\Delta H_0}{\frac{4\pi}{10} J_c(T_1)}.$$

The total change in field energy is:

$$\begin{aligned}\Delta E_{12} &= \frac{10^{-7}}{8\pi} \left\{ \int_0^{\delta_2} [H_2^2(x) - H_1^2(x)] dx \right\} \\ &= \frac{10^{-7}}{8\pi} \left\{ \int_0^{\delta_2} [H_0 + \Delta H_0(1 - x/\delta_2)]^2 dx - \int_0^{\delta_1} [H_0 + \Delta H_0(1 - x/\delta_1)]^2 dx \right. \\ &\quad \left. - \int_{\delta_1}^{\delta_2} H_0^2 dx \right\},\end{aligned}$$

or

$$\Delta E_{12} = \frac{10^{-7}}{8\pi} \left( H_0 + \frac{\Delta H_0}{3} \right) \cdot \Delta H_0 \cdot (\delta_2 - \delta_1).$$

Therefore the total heat generation (per unit surface area) is:

$$Q_m^I = \Delta W_{12} - \Delta E_{12} = \frac{10^{-7}}{8\pi} \cdot \frac{2}{3} \cdot (\delta_2 - \delta_1) \cdot (\Delta H_0)^2,$$

and the heat generation per unit volume of flux penetration is:

$$Q_m = \frac{Q_m^I}{\delta_2} = \frac{10^{-7}}{8\pi} \cdot \frac{2}{3} \cdot (\Delta H_0)^2 \left( 1 - \frac{\delta_1}{\delta_2} \right) = \frac{10^{-7}}{8\pi} \cdot \frac{2}{3} \cdot (\Delta H_0)^2 \cdot \frac{T_2 - T_1}{T_u - T_1}$$

for  $T_2 \leq T_u$ . The energy absorbed in heating the sample,  $Q_T$ , is simply

$$\int_{T_1}^{T_2} C(T) dT.$$

For our assumed  $C(T)$  we obtain:

$$Q_T = C_1 (T_2^4 - T_1^4) / 4T_1^3.$$

Let us now calculate the excluded field below which no instabilities occur, the excluded field for which the initial slopes of  $Q_m$  and  $Q_T$  are identical. We have:

$$\frac{10^{-7}}{8\pi} \cdot \frac{2}{3} \cdot \frac{(\Delta H_0)^2}{T_u - T_1} = C(T_1) = C_1$$

and thus:

$$\Delta H_0(\text{instability}) = \left\{ 12\pi C_1 \cdot 10^7 \cdot (T_u - T_1) \right\}^{\frac{1}{2}}.$$

Noting that

$$\frac{1}{T_u - T_1} = - \frac{1}{J_c} \frac{\partial J_c}{\partial T},$$

we can write a slightly more general result:

$$\Delta H_0(\text{instability}) = \left\{ 12 \cdot \pi \cdot 10^7 \cdot C_1 \cdot \left( - \frac{1}{J_c} \frac{\partial J_c}{\partial T} \right)^{-1} \right\}^{\frac{1}{2}} .$$

For a given  $C(T)/C_1$  the extent of a flux jump for a given starting  $\Delta H_0$  and an isothermal profile depends on the ratio of  $\Delta H_0$  to  $\Delta H(\text{instability})$  and on the ratio of  $T_u$  to  $T_1$ . For  $C \propto T^3$  and for  $T_1/T_u$  much less than one, flux jumps for  $\Delta H_0/\Delta H(\text{instability})$  just greater than one lead to insignificant flux penetration and heating; for  $T_1$  near  $T_u$  any flux jump leads to complete flux penetration and to a final temperature above  $T_u$ .<sup>16</sup> Even at the lower temperature a sufficiently large  $\Delta H_0$  can lead to a complete or full flux jump. In Fig. 8 we illustrate this dependence of the size of the flux jump on  $\Delta H_0$ ; here  $T_u/T_1 = 5$ . Wipf and Lubell<sup>22</sup> have pointed out that in order to have a full flux jump for the present geometry the following condition must be satisfied in addition to having  $\Delta H_0/\Delta H(\text{instability}) \geq 1$ :

$$10^{-7} \frac{(\Delta H_0)^2}{8\pi} \geq \int_{T_1}^{T_u} C(T) dT .$$

Examining our result for  $\Delta H(\text{instability})$  we see three things: 1) the higher the heat capacity the higher the stable excluded magnetic field; 2) the smaller the decrease in  $J_c$  with increasing temperature, the higher the stable excluded field; in fact if  $\partial J_c/\partial T \geq 0$  the system is inherently stable against small disturbances; and 3) for this semi-infinite geometry the actual magnitude of  $J_c$  cancels out.

Let us now remove the artificial assumption of a uniform final temperature; let us assume no heat flow at all, a locally adiabatic problem. Swartz and Bean<sup>16</sup> have solved this problem exactly. They derive and solve a second order differential equation for the flux crossing a surface  $\Delta\phi(x)$ ; the equation is of the form

$$\frac{\partial^2 \Delta\phi(x)}{\partial x^2} = - \frac{1}{\lambda^2} \Delta\phi(x) + \text{const.} ,$$

where  $\lambda$  is a characteristic distance for flux jumps:

$$\frac{1}{\lambda^2} = \frac{4\pi}{10^9 C} \cdot J_c^2 \left( - \frac{1}{J_c} \frac{\partial J_c}{\partial T} \right) .$$

Their solution indicates that instabilities can occur only if the critical state penetration distance  $\delta$  is greater than  $\frac{1}{2}\pi\lambda$ . This leads to a stable excluded field limit, similar to our  $\Delta H(\text{instability})$ , which they call  $H_{fj}$ :

$$H_{fj} = \left\{ \pi^3 \cdot 10^7 \cdot C \left( - \frac{1}{J_c} \frac{\partial J_c}{\partial T} \right)^{-1} \right\}^{\frac{1}{2}} .$$

This expression differs from our approximate one only by the factor  $(\pi^2/12)^{\frac{1}{2}}$ . Wipf and Lubell,<sup>22</sup> Hancox,<sup>23</sup> and Lange,<sup>24</sup> have derived very similar results. Swartz and Bean have considered in the same limit the size of a flux jump, the effects of different temperature dependences for the heat capacity, and the effect of having a slab of finite thickness. If the thickness of a slab is less than  $\pi\lambda$ , then no flux jumps can occur, for the flux penetration distance can never reach the critical value. Another way of saying the same thing is that if  $H^* < H_{fj}$  the system is stable, where  $H^*$  is the field at which the flux penetrating from the two sides meets at the center. Setting the thickness of the slab,  $w$ , equal to  $\pi\lambda$ , we obtain the first of several stability restrictions on the critical current density and the sample size:



$$J_c^2 w^2 \leq \frac{\pi}{4} \cdot 10^9 \cdot c \left( -\frac{1}{J_c} \frac{\partial J_c}{\partial T} \right)^{-1}.$$

This result implies that stability may be more easily achieved for a finite sample cooled in a large field than for one cooled in a small field, for  $J_c$  usually decreases in increasing fields.

Experimental tests of our results are by no means quantitative; see Swartz and Bean.<sup>16</sup> Though many have observed flux jumps, few have measured the pertinent properties of the samples under study, few have tried to maintain the adiabatic conditions assumed. Neuringer and Shapira<sup>25</sup> have observed a series of incomplete flux jumps in cylinders of NbZr; the spacings of the jumps seem to be about the value predicted by the expression for  $H_{Fj}$ . The present author has found in magnetization studies of a composite superconductor in limited contact with the liquid helium bath that the introduction of a high heat capacity element such as mercury doubled the spacing of the flux jumps, but the studies were not quantitative. One of the better measurements is that of Hancox<sup>26</sup> who studied a sample of porous Nb<sub>3</sub>Sn, again in limited thermal contact with the helium bath. He not only observed flux jumps but also measured the heat capacity and critical current density of the sample. The agreement with the picture presented here was at least semi-quantitative, i.e., within a factor of two. He found, as had Goldsmidt and Corsan,<sup>27</sup> that allowing liquid helium into the porous Nb<sub>3</sub>Sn increased by an order of magnitude the stable excluded field, presumably because of the very large heat capacity of liquid helium.

Livingston<sup>28</sup> showed that in a PbInSn alloy properly heat treated it is possible to obtain  $dJ_c/dT > 0$  over a limited range of field and temperature. He further pointed out that such a material should be stable in that region. The present author and Livingston, in an experiment designed to be especially sensitive to flux jumps, have studied the flux jump behavior of this material.<sup>29</sup> Flux jumps were clearly observed in those regions in which  $dJ_c/dT < 0$ ; flux jumps were absent where  $dJ_c/dT > 0$ .

One can make very similar calculations for nonzero transport currents. Swartz<sup>9</sup> has performed such calculations for isolated round wires and for flat sheets or films. Here we shall simply remark that under some conditions a wire or film will quench at a current well below the isothermal critical current; in fact the quench current can actually decrease as the isothermal critical current is increased. Swartz tested his predictions using deposited NbO films and found agreements somewhat more quantitative than those we mentioned earlier.

Hancox<sup>30</sup> has applied concepts similar to these to wires in the winding of a solenoid. He uses the quasi-adiabatic approximation with which we started. In addition, he approximates a single layer wound from round wire as a thin sheet, thickness  $D$ , for which the field is parallel to the surface; the field is large enough for complete flux penetration. He finds in a calculation analogous to a calculation of  $\Delta H(\text{instability})$  that a winding is stable up to its full critical current provided that

$$J_c^2 D^2 \leq \frac{3}{4\pi} \cdot 10^9 \cdot c \cdot \left( -\frac{1}{J_c} \frac{\partial J_c}{\partial T} \right)^{-1}.$$

Thus stability is improved if the heat capacity is increased, if  $-\partial J_c/\partial T$  is decreased, if  $D$  is decreased (a finer wire), and if  $J_c$  is decreased, e.g., by placing a field on the winding before energizing the winding, as has been discussed by the RCA group.<sup>31</sup>

Hancox also makes a more detailed calculation introducing the temperature dependence of the heat capacity, a calculation in effect of the extent of a flux jump. He considers the field and current density distribution illustrated in Fig. 9. Balancing

the energy dissipated in the flux penetration against the increase in thermal energy he finds the following expression for the current degradation expected in a solenoid:

$$\frac{\pi D^2}{6} \left( J_{c1}^2 - J_{c2}^2 + 6J_{c2}^2 \ln \frac{J_{c1}}{J_{c2}} \right) = 10^9 \cdot \int_{T_1}^{T_2} C(T) dT .$$

Here  $\pi D^2 J_{c1}/4$  is the short sample current for the wire and  $\pi D^2 J_{c2}/4$  is the quench current of the solenoid. Here we are allowing minor or partial flux jumps to occur; small enough flux jumps do not quench the solenoid, they merely give small voltage pulses across the coil<sup>1</sup> and perhaps a noisy field in the solenoid. A sufficiently large flux jump will quench the solenoid. At the Summer Study Hancox presented informally a very complete phase diagram for a wire wound solenoid indicating the conditions under which quenching instabilities are to be expected.

Again the agreement with experience is at best semi-quantitative; the predictions appear optimistic. Iwasa and Williams<sup>32</sup> suggest on the basis of their experiments that we may be optimistic in our predictions because we have always assumed that the flux jump is one-dimensional; we have ignored any variations of the flux penetration in the y or z directions. The importance of their suggestion is not yet clear.

Recalling Hancox's first expression we find essentially the same pertinent parameters determining flux jump stability: the heat capacity of the winding, the loss of  $J_c$  with increasing temperature, the size of the conductor, and the magnitude of  $J_c$ . Let us note that Hancox's stability expression for a slab carrying a transport current is about four times as severe as Swartz and Bean's similar expression for zero transport current (it would be exactly four if the same thermal approximations had been used). This factor of four can easily be reconciled if one recognizes that the field profile for a slab carrying the full isothermal critical current is similar to the profile for one half a slab carrying no transport current but exposed to a field greater than  $H^*$ . The factor is four because the dimension is squared in our expressions.

The stabilization of a solenoid against flux jumps by the use of the heat capacity of the winding is called adiabatic stabilization or enthalpy stabilization. It appears possible to make some conductors fine enough to make them stable<sup>1</sup>; the problem is that these fine conductors are embedded in parallel in a normal metal. In order to obtain the full advantage of the fine conductors there must be an effective transposition of the superconducting wires. Twisting is effective as far as uniform applied fields are concerned, but is not effective for transport currents. The problem is that without transposition there is an effective diamagnetism for times long compared to the period of field increase; this diamagnetism is temperature dependent and can still lead to instabilities. The effectiveness of twisting instead of the much more difficult transposition is yet to be determined.

#### IV. MAGNETIC INSTABILITIES: ATTEMPTS TO INCLUDE THE FINITE THERMAL AND MAGNETIC DIFFUSIVITIES

In the preceding section we have considered magnetic instabilities in the limiting case of the adiabatic critical state model. Though, as pointed out by Swartz and Bean, this is often a rather good approximation for  $Nb_3Sn$  and similar materials, there are some situations in which the nonzero thermal conductivity and the finite flow resistivity are of importance. The treatment of this problem is sufficiently difficult that little progress has been made. The most detailed and general attempt thus far is the work of Wipf.<sup>17</sup> Wipf's discussion is sufficiently complex that I shall refer you to his paper for details. (His introduction is a very good discussion of flux instabilities

in terms of the motion and pinning of fluxoids.) Wipf analyzes the problem of a semi-infinite block excluding a magnetic field, assuming the heat capacity to be independent of temperature. Within this approximation he distinguishes three regions of excluded field:

- 1)  $\Delta H_0 < \Delta H(\text{full stability})$ : No instabilities can occur.
- 2)  $\Delta H(\text{full stability}) \leq \Delta H_0 < \Delta H(\text{limited instability})$ : A flux disturbance can take place but the heat conduction out of the flux penetration region restores  $J_c$  before appreciable flux penetration occurs.
- 3)  $\Delta H(\text{limited instability}) < \Delta H_0$ : If a flux disturbance occurs, the growth of the flux penetration region is too rapid to allow thermal recovery; a near adiabatic runaway instability or full flux jump can occur. (As stated above, this discussion neglects the increase in heat capacity with temperature.)

No simple expressions are given for the boundaries of these regions, except for  $\Delta H(\text{full stability})$ , for which essentially our  $\Delta H(\text{instability})$  or  $H_{fj}$  is obtained. Speaking loosely, if the time constant for flux penetration into the conductor is much longer than the time constant for the diffusion of heat out of the conductor,  $\Delta H(\text{limited instability})$  can be appreciably greater than  $\Delta H(\text{full stability})$ . The time constant for heat flow out of the superconductor depends in a rather simple way on the thermal conductivity and the geometry. The time constant for flux penetration depends on the geometry and on the effective flux flow or flux creep resistivity. Looking back at Fig. 1 we see that the flux motion time constant depends on  $\rho_f$ . For the useful high field superconductors, the thermal conductivities and flow resistivities are such that the thermal time constants are long compared to the magnetic time constants as long as the superconductor experiences an appreciable flux motion or electric field. In this case, i.e., for rapidly varying fields, the adiabatic limit is appropriate and  $\Delta H(\text{limited instability})$  is very close to  $\Delta H(\text{full stability})$ . However, for very slowly varying fields, i.e., very small electric fields, flux creep may be the controlling mechanism; our Fig. 1 is then an oversimplification, there is no sharp corner in the E-J relation near  $J_c$ . In fact, both the flux creep model<sup>7</sup> and the present somewhat limited experimental evidence<sup>7,33</sup> indicate that for small electric fields we should write  $\rho_E = \gamma E$ . Thus for a slow enough rate of change of field the effective resistivity is small enough that the magnetic time constant becomes long compared with the thermal time constant;  $\Delta H(\text{limited instability})$  becomes appreciably greater than  $\Delta H(\text{full stability})$ . This trend is often observed experimentally.

Of more practical interest, the effective magnetic time constant can be greatly increased by introducing pure normal metals in close magnetic coupling with the superconductor, increasing  $\Delta H(\text{limited instability})$  well above  $\Delta H(\text{full stability})$ .

Let us now consider magnetic instabilities in the extreme limit that the magnetic time constant,  $\tau_m$ , is much longer than the thermal time constant, an extreme limit yielding closed form answers of practical importance for certain structures. (It is a limit of interest to the present author.) Let us consider a slab of a high field superconductor of thickness or width  $w$  exposed to a magnetic field parallel to the plane of the slab, a geometry similar to that of Fig. 3. The superconducting or critical state properties of this material are described by Fig. 1 with  $J_c$  assumed independent of  $H$ . The thermal conductivity of the material is denoted by  $K$  ( $\text{W cm}^{-1} \text{ } ^\circ\text{K}^{-1}$ ). There is in addition an interface barrier to the flow of heat out of the superconductor described by the linear relation:  $\dot{Q} = h \cdot \Delta T_s$  ( $\text{W cm}^{-2}$ ). Here  $\Delta T_s$  is the difference between the surface temperature of the superconductor and the temperature of the surrounding medium, perhaps a liquid helium bath, perhaps a normal metal bonded to the superconductor. Initially let us assume that the flux penetration fronts from the two sides have reached a common point, as in Fig. 3c; the critical current density has been induced to flow throughout the entire sample. We shall neglect entirely any stability

resulting from the heat capacity of the superconductor.

We shall apply a sudden small disturbance to the system and calculate whether or not a thermal runaway occurs. For convenience let the initial disturbance be a sudden small temperature rise  $\Delta T$ . Our criterion for stability will now be a dynamic one, in contrast to the static criterion of Section III. The system will be considered dynamically stable if the temperature rise immediately decays back towards the original equilibrium temperature; it will be considered unstable if the temperature increases further yet. We shall neglect any nonlinearities in the problem. This is a rather conservative or pessimistic criterion.

In the extreme limit of a very long magnetic time constant (relative to the thermal time constants) the calculation is greatly simplified because we can then assume that the initial magnetic field profile and the initial current distribution determine the flux motion and heating rate for some time after the initial temperature rise. Upon a sudden increase in temperature there is a sudden decrease in the flux pinning in the superconductor, a sudden decrease in the critical current density, but not in the total current density; flux begins to move through the sample generating heat. Referring to Fig. 10, assuming that  $\rho_f$  is relatively unaffected by the change in temperature, we find that the initial heating rate is:

$$\dot{q}(x) = J \cdot E(x) = J_{c1} \cdot \rho_f \cdot (J_{c1} - J_{c2}) = J_{c1}^2 \rho_f \cdot \left( - \frac{1}{J_c} \frac{\partial J_c}{\partial T} \right) \cdot \Delta T(x)$$

We see that the local heating rate is proportional to the local temperature rise. The dynamic stability of the system is determined by the relative magnitudes of the rates of heat generation and of heat removal. The barriers to heat removal are the internal thermal resistance of the material and the surface interface barrier. We shall solve the problem for the two limiting cases: 1) surface interface barrier predominant, and 2) the internal thermal resistance predominant. We shall quote the result for the intermediate case.

For the first limiting case let us assume that the effective barrier to heat removal is the interface barrier,  $\Delta T = \dot{Q}/h$ . We thus assume that the thermal conductivity of the plate is large enough that we have a uniform temperature across the plate. The stability criterion is obtained by writing an energy balance equation:

$$w \cdot C \cdot \frac{d(\Delta T)}{dt} = w J_{c1}^2 \rho_f \left( - \frac{1}{J_c} \frac{\partial J_c}{\partial T} \right) \cdot \Delta T - 2h \Delta T$$

The solution of this differential equation is an exponential:

$$\Delta T(t) = \Delta T_0 \exp(\alpha t) ; \quad t \ll \tau_m$$

We thus have dynamic stability if  $\alpha < 0$ :

$$\frac{w J_{c1}^2 \rho_f \left( - \frac{1}{J_c} \frac{\partial J_c}{\partial T} \right) - 2h}{w \cdot C} < 0$$

or if:

$$J_c^2 w < \frac{2h}{\rho_f \left( - \frac{1}{J_c} \frac{\partial J_c}{\partial T} \right)}$$

The result just found applies for arbitrary transport current for full flux penetration,  $H > H^*$ . If the flux penetration is incomplete, the width  $w$  is replaced by  $2\Delta H/(4\pi J_c/10)$  and the result is a limiting excluded field:

$$\overline{\Delta H}_s \leq \frac{4\pi h}{10J_c \rho_f \left( -\frac{1}{J_c} \frac{\partial J_c}{\partial T} \right)}$$

Here  $\overline{\Delta H}$  is the average of the excluded fields on the two sides of the slab.

For our second case let us assume that the interface barrier is very small ( $h$  is large) and that the barrier to heat removal is determined by the thermal conductivity  $K$ . Again let us assume complete flux penetration,  $H > H^*$ , an arbitrary transport current, and a field independent  $J_c$ . We must now solve the thermal diffusion equation<sup>34</sup> with a heat generation term:

$$K \frac{\partial^2 \Delta T}{\partial x^2} - C \frac{\partial \Delta T}{\partial t} + \dot{q} = 0 ,$$

where

$$\dot{q} = a\Delta T = J_c^2 \rho_f \left( -\frac{1}{J_c} \frac{\partial J_c}{\partial T} \right) \Delta T .$$

Our boundary conditions are that the surface temperatures ( $x = \pm w/2$ ) are equal to the bath temperature and that the initial temperature, just after the heat pulse, is equal to  $\Delta T_0$ . Our trial solution will be a time-dependent Fourier series. Choosing the origin of the coordinate system in the center of the plate, we can expand the initial temperature disturbance as a cosine series. Our trial solution will thus be the series

$$\Delta T(x,t) = \sum_{n=0}^{\infty} b_n e^{\alpha_n t} \cos \{ (2n+1)\pi x/w \} ; \quad t \ll \tau_m .$$

Introducing the general term into the differential equation we find that we have a solution provided that

$$\alpha = \frac{a - K(2n+1)^2 \left( \frac{\pi^2}{w^2} \right)}{C} .$$

Our requirement for stability is that all terms in the sum decay; none blow up. The most severe requirement is the term  $n = 0$ . Thus the criterion for stability is that:

$$a - K \frac{\pi^2}{w^2} < 0 ,$$

or

$$J_c^2 w^2 < \frac{\pi^2 K}{\left( -\frac{1}{J_c} \frac{\partial J_c}{\partial T} \right) \rho_f} .$$

For incomplete flux penetration and zero transport current we again find a limiting

excluded field:

$$\Delta H_s < \left\{ \frac{\pi^4}{25} \cdot \frac{K}{\rho_f} \cdot \frac{1}{\left( -\frac{1}{J_c} \frac{\partial J_c}{\partial T} \right)} \right\}^{\frac{1}{2}} .$$

It is possible to solve our problem for arbitrary values of  $K$  and  $h$ , as long as the magnetic time constant remains long compared to the thermal time constant. The result for  $H > H^*$  is an inequality:

$$\frac{(Ka)^{\frac{1}{2}}}{h} \cdot \tan \left[ \frac{w}{2} \left( \frac{a}{K} \right)^{\frac{1}{2}} \right] < 1 .$$

Again, for partial penetration and zero transport current, another inequality in which the stable excluded field is determined is:

$$\Delta H_s < \frac{4\pi J_c}{10} \cdot \left( \frac{K}{a} \right)^{\frac{1}{2}} \cdot \arctan \left( \frac{h}{(Ka)^{\frac{1}{2}}} \right) ,$$

where

$$a \equiv J_{cl}^2 \rho_f \left( -\frac{1}{J_c} \frac{\partial J_c}{\partial T} \right) .$$

We have used as our disturbance a uniform heat pulse. The same result would be obtained for a nonuniform heat pulse or for a uniform heating rate. For the latter see Carslaw and Jaeger,<sup>34</sup> p. 404. I must caution you that a disturbance in the form of an instantaneous field rise would not lead to this simple analysis, and might lead to slightly different numerical factors in the resulting expressions. The results we have obtained are pessimistic in that we have neglected any stabilizing influence of the heat capacity of the material.

Before applying these results to a practical system let us note the properties influencing dynamic stability. We see once again that a material having  $\partial J_c / \partial T > 0$  is stable against small disturbances. We see once again that systems presenting small cross sections (small  $w$ ) to the magnetic field tend to be more stable. The new results are that the larger the thermal conductivity, the smaller the boundary resistance, and the lower the effective resistivity, the more stable the system. In composite materials the inclusion of pure normal materials can greatly lower the resistivity and can sometimes increase the pertinent thermal conductivity.

Let us now attempt a simplified application of these dynamic stability concepts to instabilities in structures wound from wide, thin (e.g.,  $\frac{1}{2}$  in.  $\times$  0.005 in.) composite tapes. Such tapes are available commercially and are in use at several laboratories, including AEC laboratories. In those portions of the magnet for which the field is parallel to the plane of the tape, the material is stable by adiabatic stabilization, for

$$J_s^2 d_s^2 < \frac{3 \times 10^9}{4\pi} \cdot c \cdot \left( -\frac{1}{J_c} \frac{\partial J_c}{\partial T} \right)^{-1} ,$$

where  $d_s$  is the thickness of the superconductor, and  $J_s$  is the critical current density of the superconductor. However, for those portions of the magnet where there is an appreciable component of the field perpendicular to the plane of the tape the winding is not adiabatically stable. As described by Graham and Hart,<sup>35</sup> a winding formed

of thin wide tapes is effectively a diamagnetic body for the component of field perpendicular to the tapes; its properties can be described by a critical state model in which the properties are averaged over the cross section. It is thus very similar to the slabs we have just been considering; the thickness of the slab,  $w$ , is the width of the tape. (See Fig. 11.) This composite diamagnetic body is both theoretically and experimentally adiabatically unstable (see Fig. 12); we must depend on dynamic stabilization, the transfer of heat ultimately to helium, to avoid flux jumps (see Fig. 13).

In a simple solenoid the less stable regions occur at the ends of the solenoid where the radial field component (perpendicular to the plane of the tape, parallel to the face of our equivalent slab) is the largest. In quadrupoles the largest perpendicular field can be at the most critical point in the winding, the region of highest winding current density. We shall not attempt an analysis of a real structure; we shall simply discuss the dynamic stability of a slab formed by stacking the tapes. There are several ways in which instabilities can occur; we shall take them in turn.

First, any heat generated because of a temperature rise must be removed from the superconductor itself to the neighboring normal metal. There are two barriers to the removal of this heat, a bond resistance and, more important, the very poor thermal conductivity of the superconductor itself. The following calculation applies to those regions into which the perpendicular (to the plane of the tape) field has penetrated. Assuming perfect magnetic coupling between the superconducting and the normal layers of the tapes, we can write for the local rate of heat generation in the superconducting material (see Fig. 11):

$$\dot{q}_s(y) = J \cdot E = J_s \left\{ \frac{J_s d_s \left( -\frac{1}{J_c} \frac{\partial J_c}{\partial T} \right) \Delta T}{\frac{d_s}{\rho_s} + \frac{d_n}{\rho_n}} \right\} \equiv a \Delta T .$$

Usually we can assume

$$\frac{d_n}{\rho_n} \gg \frac{d_s}{\rho_s} .$$

Applying the same dynamic stability criterion as we did in our earlier calculations, we find the following restrictions on the properties of the superconducting layer in the tape:

$$\begin{aligned} 1) \quad J_s^2 d_s^2 &< 2h \frac{d_n}{\rho_n} \frac{1}{\left( -\frac{1}{J_c} \frac{\partial J_c}{\partial T} \right)} , \\ 2) \quad J_s^2 d_s^3 &< \pi^2 K_s \frac{d_n}{\rho_n} \frac{1}{\left( -\frac{1}{J_c} \frac{\partial J_c}{\partial T} \right)} . \end{aligned}$$

As I have mentioned before, these expressions are somewhat pessimistic. Chester<sup>1</sup> has presented an expression essentially the same as the second of these; his expression is more pessimistic than mine by a factor of  $\pi^2/4$ . This second equation, involving the very poor thermal conductivity of the superconductor, is very important because some of the commercial high current Nb<sub>3</sub>Sn composite tapes presently used are just barely

stable; some others are almost certainly unstable. Notice that for all other properties held fixed, the thicker the superconductor the greater the chance of instability. Notice also that the short sample or isothermal critical current of the tape is proportional to the product of  $J_s$  and  $d_s$ . Thus for constant width of tape there will be a tendency for tapes of higher critical currents to be less stable. The tape user cannot ask the manufacturer to deliver ever higher critical current tapes (of constant width) without running into instabilities at some point. These statements are not meant to stop all progress; they are just a warning. (Again, if  $\partial J_c / \partial T > 0$ , the system is stable.) We save our discussion of the factor  $d_n / \rho_n$  until later.

Now, assuming we have a tape which passes the above stability requirements, we can consider the dynamic stability of our composite slab. If we have a typical disk winding, one in which useful helium does not exist between the tapes, we must have a sufficient transverse thermal conductivity to assure that the heat reaches the tape edge

$$H_1 < \left\{ \frac{\pi^4}{25} \frac{\bar{K}}{\bar{\rho}_f} \left( - \frac{1}{J_c} \frac{\partial J_c}{\partial T} \right)^{-1} \right\}^{\frac{1}{2}},$$

and a sufficient heat transfer to the helium bath to assure stability

$$H_1 < \frac{4\pi\bar{h}}{10J_c \bar{\rho}_f} \left( - \frac{1}{J_c} \frac{\partial J_c}{\partial T} \right)^{-1}.$$

Again, these requirements are not met trivially.

If one takes the care necessary to insure useful liquid helium between the tapes, he greatly increases the interface area and also removes the need for a good transverse thermal conductivity. The use of superfluid helium immediately suggests itself.<sup>36</sup> One still must get the heat out of the superconductor and across any barrier such as stainless-steel strengtheners, insulation, etc., into the liquid helium, as we calculated above.

In each of these expressions there appears a factor such as  $d_n / \rho_n$ , or  $1 / \bar{\rho}_n$ . The magnet builder can influence this factor in two very useful ways. For those regions having large field components perpendicular to the tape he can either order his tape with enough pure enough normal metal bonded to the superconductor to insure stability, or he can co-wind into his disk, along with the composite conductor, a tape of pure normal metal. This extra tape need not be electrically or thermally bonded to the composite superconductor in order to influence  $d_n / \rho_n$  or  $1 / \bar{\rho}_n$ . In our laboratory both techniques have been found quite successful; at this time, however, the amount of normal metal needed must be found empirically.

## V. CONCLUSION

In considering magnetic instabilities and solenoids we have concentrated on understanding two extreme limiting cases, both of which are important in practice. In both limits we find that stable performance would be assured if we could find useful materials for which  $\partial J_c / \partial T \geq 0$ ; I have hopes that such materials will someday be found.

In one limit, the adiabatic limit, we found that small enough conductors ( $\leq 0.002$  cm diam) can be stabilized against flux jumps with their own heat capacity. There is a major qualification: if the fine conductors are connected electrically



at more than one point, some form of transposition will be required to gain the full advantage of the small dimensions. There is some promise that such conductors will be forthcoming (see P.F. Smith's contribution to this Summer Study).

In the other limit, in which the winding is well cooled and the flux motion is slowed by a normal metal, we find that we can attain a useful dynamic stability<sup>1</sup> by the proper use of a very pure normal metal in close magnetic coupling with the superconductor. Again, fine dimensions offer advantages.<sup>1</sup> The positive permeation of a winding with liquid helium, particularly superfluid helium, should aid the attainment of stability.

R. Hancox has prepared, but not yet published, an excellent summary of the effects of instabilities on the performance of wire wound solenoids. P.F. Chester's review of superconducting solenoids<sup>1</sup> deserves careful reading for it has as one of its main themes the importance of magnetic stability for solenoids. Finally, S.L. Wipf's concise review of instabilities printed elsewhere in these Proceedings is recommended to the reader.

I would like to thank my many colleagues in the General Electric superconductivity effort for helping, and forcing me to learn about magnetic instabilities in high field superconductors.

#### REFERENCES

1. P.F. Chester, Reports on Progress in Physics (The Institute of Physics and The Physical Society, London, 1967), Vol. XXX, Part II, p. 561.
2. C.P. Bean, Phys. Rev. Letters 8, 250 (1962); C.P. Bean, Rev. Mod. Phys. 36, 31 (1964); H. London, Phys. Letters 6, 162 (1963); Y.B. Kim, C.F. Hempstead, and A.R. Strnad, Phys. Rev. 129, 528 (1963).
3. A.A. Abrikosov, J. Phys. Chem. Solids 2, 199 (1957).
4. P.G. deGennes, Superconductivity of Metals and Alloys (W.A. Benjamin, Inc., New York, 1966), p. 65; H.T. Coffey, Phys. Rev. 166, 447 (1968).
5. Y.B. Kim, C.F. Hempstead, and A.R. Strnad, Phys. Rev. 139, A1163 (1965).
6. J.D. Livingston and H.W. Schadler, Progr. Mat. Sci. 12, 183 (1964); D. Dew-Hughes, Mater. Sci. Eng. 1, 2 (1966).
7. P.W. Anderson and Y.B. Kim, Rev. Mod. Phys. 36, 39 (1964).
8. R. Hancox, Proc. IEE (London) 113, 1221 (1966).
9. C.P. Bean et al., Technical Report No. AFML-TR-65-431 (1966).
10. T.W. Grasmehr and L.A. Finzi, IEEE Trans. Magnetics MAG-2, 334 (1966).
11. C.P. Bean, R.L. Fleischer, P.S. Swartz, and H.R. Hart, Jr., J. Appl. Phys. 37, 2218 (1966).
12. H.A. Ullmaier, Phys. Stat. Sol. 17, 631 (1966).
13. H.R. Hart, Jr. and P.S. Swartz, Phys. Rev. 156, 403 (1967); P.S. Swartz and H.R. Hart, Jr., Phys. Rev. 156, 412 (1967); W.C.H. Joiner and G.E. Kuhl, Phys. Rev. 163, 362 (1967).
14. P.O. Carden, Aust. J. Phys. 18, 257 (1965); P.S. Swartz and C.H. Rosner, J. Appl. Phys. 33, 2292 (1962); J.H.P. Watson, J. Appl. Phys. 38, 3813 (1967).
15. H.T. Coffey, Cryogenics 7, 73 (1967).
16. P.S. Swartz and C.P. Bean, J. Appl. Phys. (Oct. 1968, to be published), also in Ref. 9.

17. S.L. Wipf, Phys. Rev. 161, 404 (1967).
18. P.R. Aron and G.W. Ahlgren, in Proc. Cryogenic Engineering Conference, Palo Alto, 1967, p. 21.
19. R.D. Cummings and W.N. Latham, J. Appl. Phys. 36, 2971 (1965).
20. Y.B. Kim, C.F. Hempstead, and A.R. Strnad, Phys. Rev. 131, 2486 (1963); C.R. Wischmeyer, Phys. Letters 19, 543 (1965); D.J. van Ooijen and W.F. Druyvesteyn, Phys. Letters 6, 30 (1963); D.J. van Ooijen and G.J. van Gurp, Phys. Letters 17, 230 (1965); G.J. van Gurp, Phys. Rev. 166, 436 (1968).
21. F.J. Morin, J.P. Maita, H.J. Williams, R.C. Sherwood, J.H. Wernick, and J.E. Kunzler, Phys. Rev. Letters 8, 275 (1962).
22. S.L. Wipf and M.S. Lubell, Phys. Letters 16, 103 (1965).
23. R. Hancox, Phys. Letters 16, 208 (1965).
24. F. Lange, Cryogenics 6, 176 (1966).
25. L.J. Neuringer and Y. Shapira, Phys. Rev. 148, 231 (1966).
26. R. Hancox, Appl. Phys. Letters 7, 138 (1965).
27. H.J. Goldsmid and J.M. Corsan, Phys. Letters 10, 39 (1964).
28. J.D. Livingston, Appl. Phys. Letters 8, 319 (1966).
29. H.R. Hart, Jr. and J.D. Livingston, to be published in the Proc. 11th Intern. Conf. Low Temperature Physics.
30. R. Hancox, in Proc. 10th Intern. Conf. Low Temperature Physics, Moscow, 1966, Vol. IIB, p. 43.
31. RCA Review XXV, No. 3, Sept. 1964.
32. Y. Iwasa and J.E.C. Williams, J. Appl. Phys. 39, 2547 (1968).
33. M.S. Lubell and S.L. Wipf, J. Appl. Phys. 37, 1012 (1966).
34. H.S. Carslaw and J.C. Jaeger, Conduction of Heat in Solids (Oxford University Press, London, 1959).
35. C.D. Graham and H.R. Hart, Jr., in Proc. 1st Intern. Cryogenic Engineering Conf., Tokyo and Kyoto, 1967, published as Cryogenic Engineering, Present Status and Future Development (Heywood-Temple Industrial Publications, Ltd., London, 1968), p. 101.
36. W.B. Sampson, M. Strongin, A. Paskin, and G.M. Thompson, Appl. Phys. Letters 8, 191 (1966).

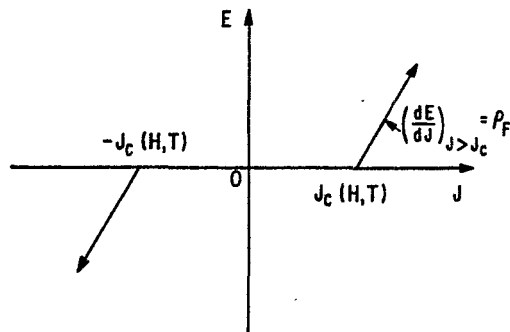


Fig. 1. The nonlinear relation between the electric field  $E$  (V/cm) and the current density  $J$  (A/cm<sup>2</sup>). Here  $\rho_f$  ( $\Omega \cdot \text{cm}$ ) represents the effective flux flow resistivity for the superconductor; in some cases  $\rho_f$  includes the effects of normal metals, i.e., in composite structures. This  $E$ - $J$  relation may be considered one formulation of the critical state model.

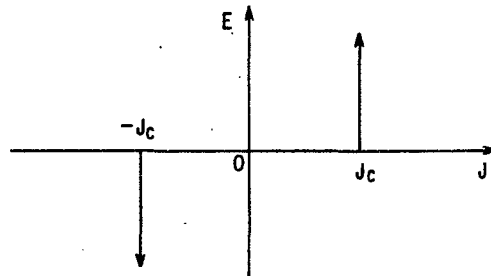


Fig. 2. A simplified relation between  $E$  and  $J$  which is often used in critical state model discussions. In this version the response of a superconductor to a field change is instantaneous.

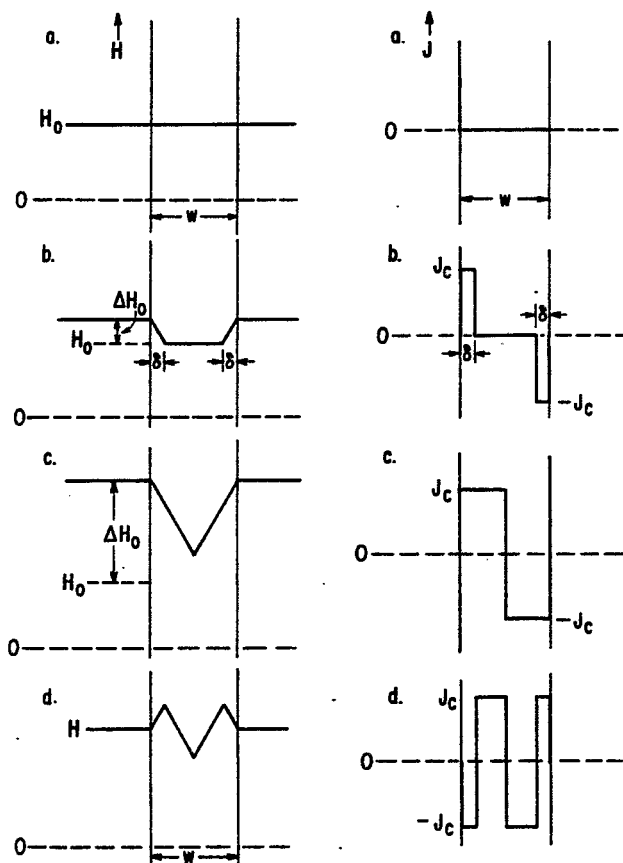


Fig. 3. The history dependent distributions of field and current in a high field superconducting slab with a magnetic field applied parallel to the plane of the slab. The detailed history is described in the text. The excluded field at which the flux fronts from the two sides meet ( $\delta = w/2$ ) is called  $H^*$ . Thus in Fig. 3c,  $\Delta H_0 > H^*$ .

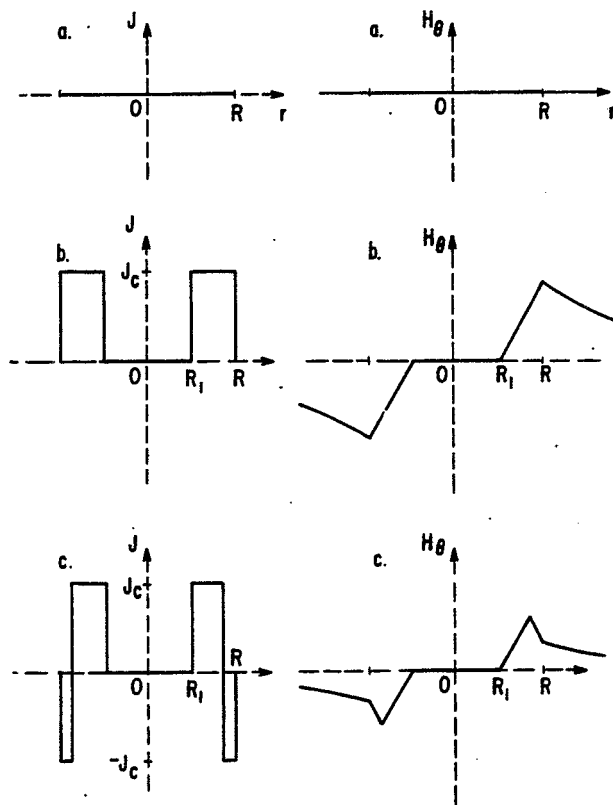


Fig. 4. The history dependent distributions of field and current for a round wire carrying a current. See the text for details.

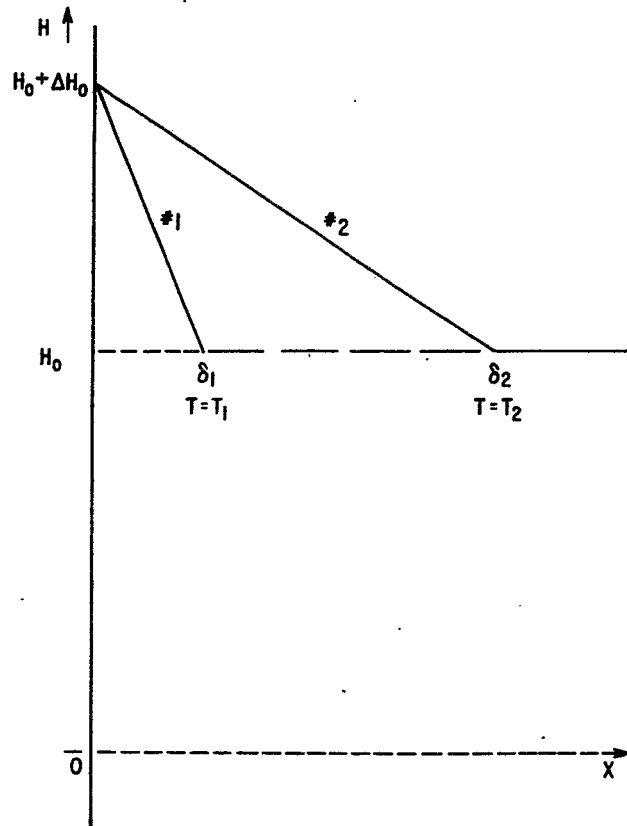


Fig. 5. Uniform temperature flux penetration profiles for a semi-infinite slab for two different temperatures.

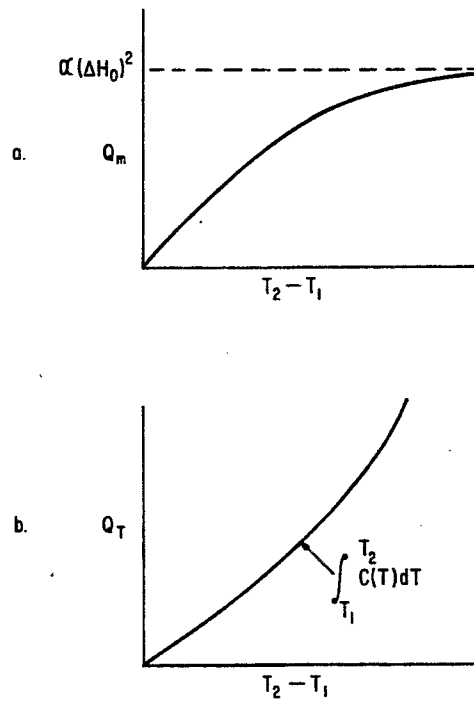


Fig. 6. Schematic illustrations of the heat generated,  $Q_m$ , and absorbed,  $Q_T$ , in going from one field profile, temperature  $T_1$ , to a new field profile, temperature  $T_2$ . The units of  $Q$  in this calculation are  $\text{J}/\text{cm}^3$ .

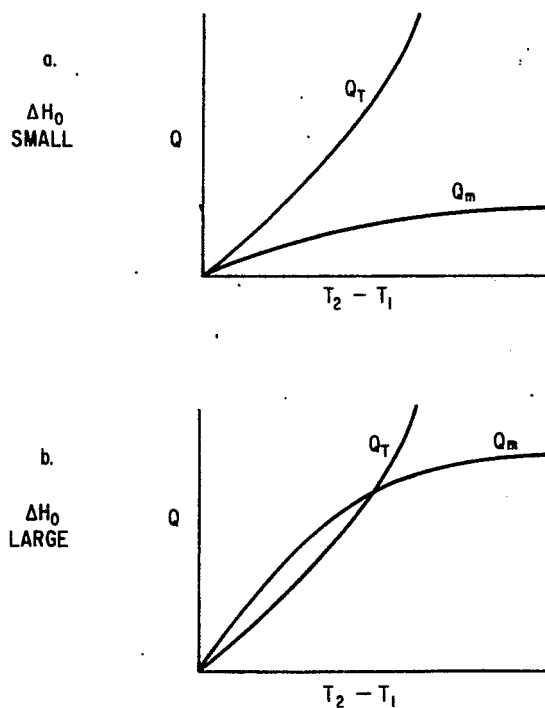


Fig. 7. Schematic illustrations of  $Q_m$  and  $Q_T$  vs  $T_2 - T_1$  for two cases:  
a) Small excluded field; stable against small disturbances.  
b) Large excluded field; unstable.



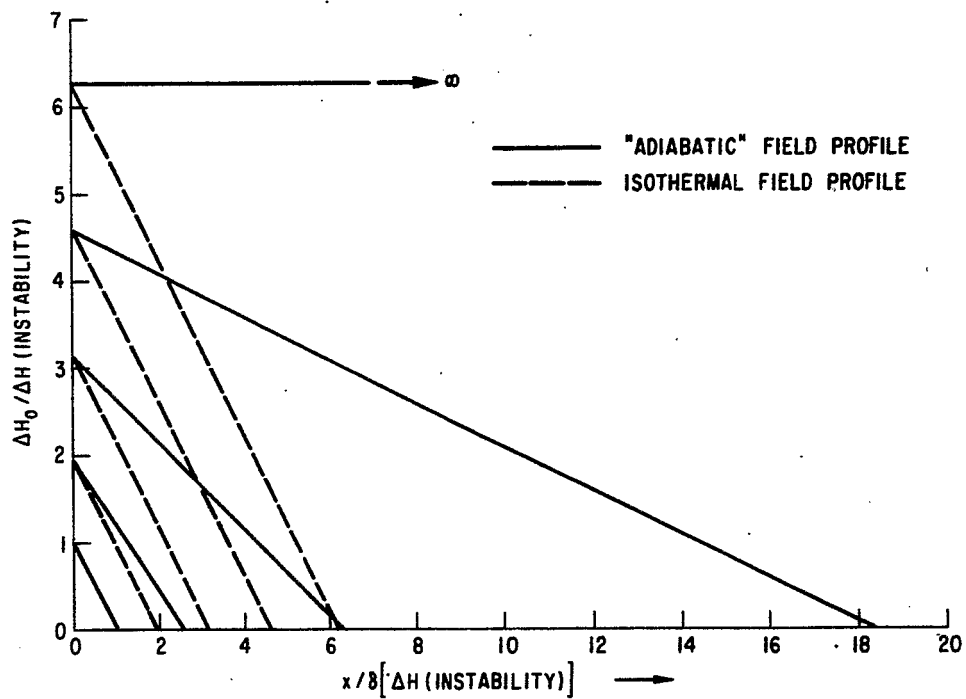


Fig. 8. Isothermal and quasi-adiabatic field profiles (following small disturbances) for a semi-infinite slab of a high field superconductor. The profiles were obtained as described in the text assuming  $T_1/T_u = 0.2$ .

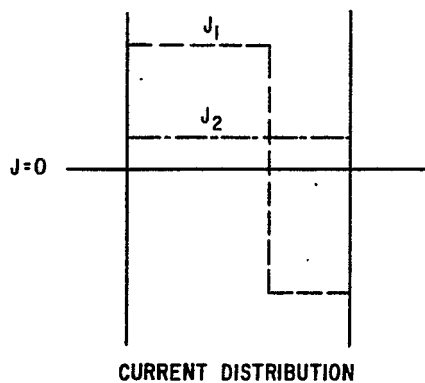
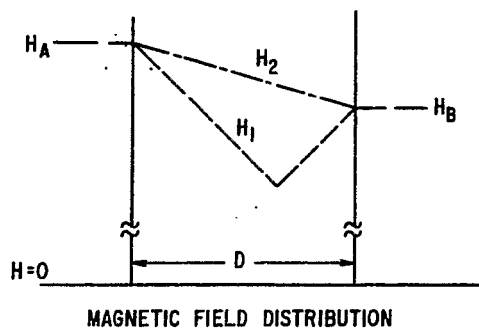


Fig. 9. The distribution of field and current density in a slab exposed to a field parallel to the plane of the slab ( $H > H^*$ ) for a nonzero transport current. The two distributions shown are for the starting temperature,  $T_1$ , and for the highest temperature,  $T_2$ , for which the transport current can be carried as a supercurrent, i.e., the quench temperature. This is the current distribution used by Hancox<sup>30</sup> in his approximate treatment of a winding layer in a round wire solenoid.

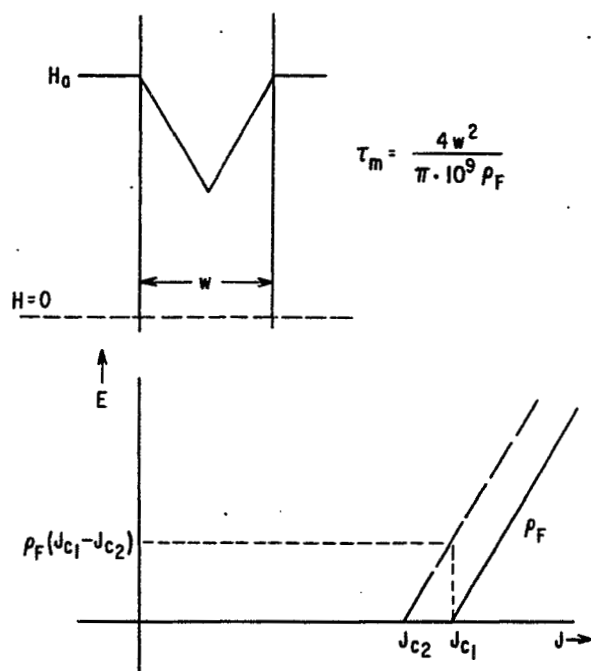
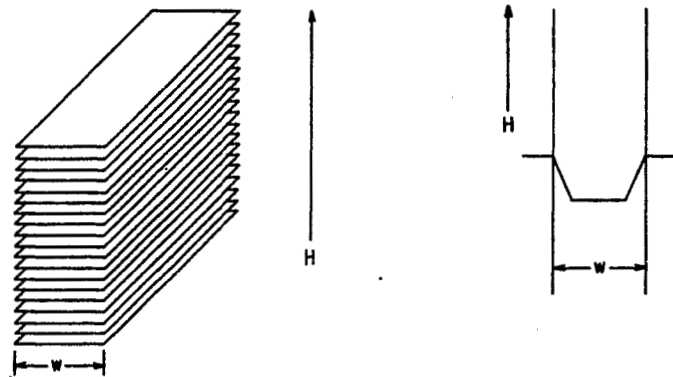


Fig. 10. For  $H > H^*$ , as illustrated, the magnetic time constant  $\tau_m$  is given in terms of the slab thickness and the effective flux flow resistivity. In the lower portion the  $E$ - $J$  relation is given for two temperatures;  $T_2 > T_1$ . The dashed lines illustrate the electric field and current density applicable for  $t \ll \tau_m$  if the temperature is suddenly changed from  $T_1$  to  $T_2$ . The local rate of heat generation is  $E \cdot J$ .



$$\frac{\partial H}{\partial X} = \mp \frac{4\pi}{10} \bar{J}_c$$

$$\bar{J}_c = \frac{d_s}{d_{tape}} \cdot J_s$$

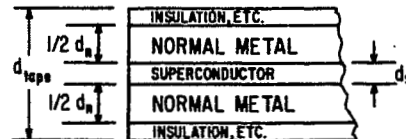


Fig. 11. In our analysis we replace a magnet winding wound from a wide thin composite tape with a stack of such tapes. When there is a component of magnetic field perpendicular to the plane of the tape the stack excludes field as would a critical state superconductor with a critical current density equal to  $\bar{J}_c$ . A simplified cross section of a tape is shown.

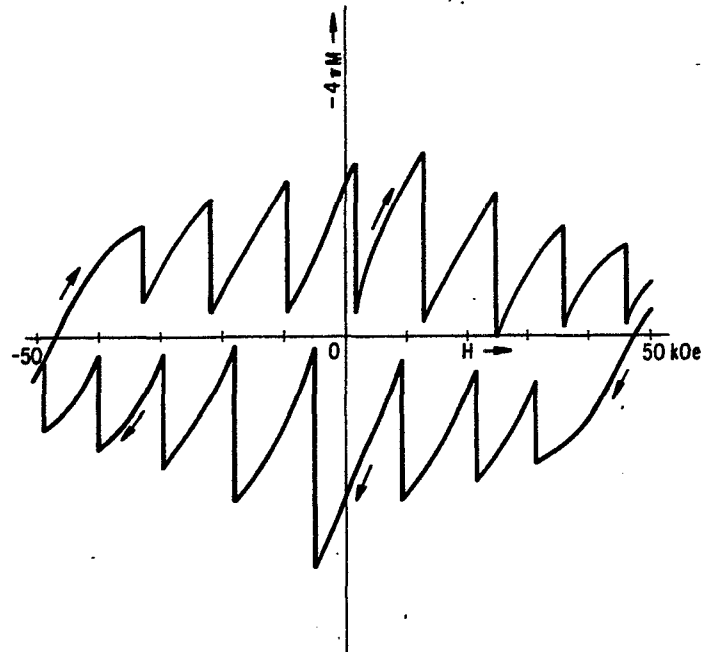


Fig. 12. A stack of disks punched from a thin  $\text{Nb}_3\text{Sn}$ -copper composite tape was exposed to a magnetic field perpendicular to the plane of the tape. The stack (1 in. high,  $\frac{1}{2}$  in. diam) was relatively isolated from the liquid helium bath. The major flux jumps observed in the magnetization curve indicate that the system is not adiabatically stable.

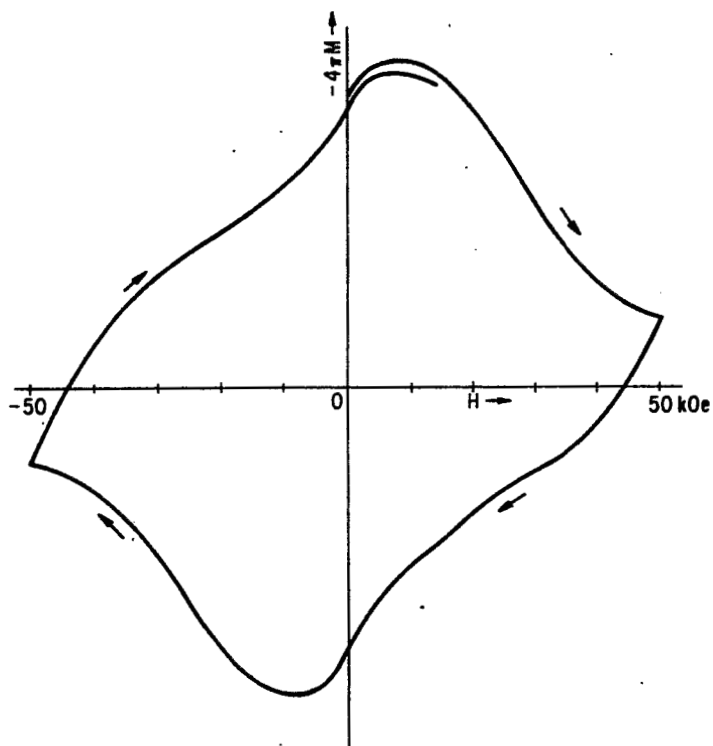


Fig. 13. A magnetization curve for a stack of disks similar to that of Fig. 12 except that very good thermal contact was made with a 4.2°K liquid helium bath. The absence of flux jumps indicates that we have achieved dynamic stability.

MAGNETIC AND THERMAL INSTABILITIES OBSERVED  
IN COMMERCIAL Nb<sub>3</sub>Sn SUPERCONDUCTORS\*

G. del Castillo and L.O. Oswald  
Argonne National Laboratory  
Argonne, Illinois

INTRODUCTION

Instabilities of both magnetic and thermal type have been reported in the literature mostly in connection with fundamental studies of pure type II superconductors. In this paper we are presenting the results of experiments made using commercially available Nb<sub>3</sub>Sn fabricated by the Radio Corporation of America and the General Electric Company. Samples of their products were made available to us<sup>1</sup> in the form of ribbon 0.5 in. wide; each sample was characterized by a given substrate material and different thicknesses depending on the type and quantity of the so-called "stabilizing" and mechanical reinforcing materials used in their fabrication. The following products were studied: General Electric 65A900000, 22CY030, and 65A900001; RCA 60304 and RCA 60299. Their compositions are available in the commercial literature; also a brief description appears in Table I.

This paper is divided into two parts. Part I is an isothermal study. This represents the most common operation of a superconductor, i.e., in a liquid helium bath. The second part is oriented towards the understanding of some fundamental questions related to flux jumps. It is a study of the behavior of these samples in semiadiabatic conditions. One cannot rule out, however, the possibility of operating a coil in such conditions.

I. ISOTHERMAL STUDY

All samples were cut one inch long and matched pairs of each material were attached to a perforated phenolic plate, thus making a one square inch split plate. Two such plates of the same material were used in each test as shown in Fig. 1A. The plates were located between the pole pieces of a magnet in such a manner that the external field was normal to the plates. The magnetic induction in the gap was measured by five magnetoresistance microprobes<sup>2</sup> located halfway along the plates and at the center of the gap. The separation between the plates was 0.1875 in.

Each run consisted of increasing the external magnetic field at a constant rate of about 6 G/sec, from zero up to 5.2 kG and back to zero. In some occasions runs were taken reversing the external field to further develop the instabilities. The magnetic induction between the plates was measured at five spots and recorded in a five-channel recorder. Tests were made on virgin (no magnetic history) and nonvirgin samples. Finally, the external field was increased by hand to 9 kG and suddenly decreased at an average rate of about 1 kG/sec. This part of the test was labeled as "power failure."

---

\* Work performed under the auspices of the U.S. Atomic Energy Commission.

1. Thanks are due to Dr. C.H. Rosner of the General Electric Company and Mr. J.H. Crowe of RCA for supplying the samples used in this work.
2. G. del Castillo and R.W. Fast, J. Appl. Phys. 36, 1973 (1965).

A typical example of the five-probe recording is shown in Fig. 2. The vertical scale represents the magnetic induction between plates, and the horizontal is the external magnetic field. The top traces (A) correspond to the case when the magnetic flux penetrates smoothly into the superconductor. The recording is consistent with what is expected from the magnetic properties of the superconductor. Magnetic probes 2 and 4 which are located at the center of the strips see little change in field as maximum shielding is provided by the samples, whereas probes 1, 3, and 5 follow the changes of the external field. This is especially clear for probe 3 which is located at the joint of the strips; its trace, as one can see in the picture, shows a fast increase in field, which may be interpreted as due to the superposition of macroscopic currents running in opposite directions at the four edges of the strips. These currents do not provide shielding against the external field; in fact, they may even add to it. The possible relation between smooth flux penetration and macroscopic currents was suggested by the authors.<sup>3</sup>

Traces (B) illustrate the case of flux jumps observed in a sample when the external field decreased. The mixing of the traces is clear and becomes evident in case (C) which represents the magnetic behavior after reversing the external field. One can see a large flux jump that reverses the magnetization of the sample, then the smooth penetration in all five probes. Probes 4 and 5, which did not register the initial flux jump, show a smooth cancellation of the local magnetization. Probe 3, however, follows the external field as before, in spite of the strong perturbation caused by the flux jump.

The magnetic field sensitivity of our probes varied, depending on the external field, but an average value of about 1 V/A-kG can be considered as representative of all of them. No particular effort was made to preorient the bismuth crystals to maximize the sensitivity.

The results obtained from these samples at three different temperatures are summarized in Table I. The figures that appear under the temperature columns represent the number of flux jumps observed within the external field interval mentioned above, either increasing (up) or decreasing (down) the field. These figures are the results of only a few runs; they do not represent statistical averages. They are, however, consistent with the results of our previous statistical study.<sup>3</sup>

The first sample GE 65A900000 showed no flux jumps except one at 2.5°K when the external field was changing rapidly. The field penetrated smoothly into this material.

In the second sample we see a very peculiar behavior at 4.2°K and 2.5°K, where the field penetrated smoothly but was expelled by flux jumps (see also Fig. 2). At 1.9°K no jumps were observed in the regular run. The origin of this behavior is puzzling, as in the past our experiments indicated that under the same conditions the mode of penetration remained the same for increasing or decreasing external fields. We had observed, however, a distinct difference in the frequency-extension distribution of flux jumps originated presumably by the sign reversal of  $(dH/dt)_{\text{ext}}$ .

One is tempted to speculate about the origin of these observations. If one assumes that vortex filaments of positive vorticity populate the superconductor when it enters into the mixed state, a change of the sign of  $dH/dt$  could create vortex motion of opposite vorticity.<sup>4</sup> A turbulent mixing of fluids may result with the possible annihilation of vortex motion which will, as a consequence, decrease the magnetic induction in the sample.

---

3. G. del Castillo and R.W. Fast, unpublished.

4. G. del Castillo, Bull. Am. Phys. Soc. 11, 709 (1966).



Annihilation of flux quanta is a concept that was introduced before<sup>5</sup> but always related to the reversal of the sign of  $H_{ext}$ . Our results seem to fit better to the idea that the reversal of the sign of the time derivative is sufficient to cause the instability leading to flux annihilation.

The third sample was RCA vapor deposited  $Nb_3Sn$  which showed flux jumps at 4.2 and 2.5°K for field either increasing or decreasing, but no jumps were observed at 1.9°K.

Next, GE 65A900001 showed somewhat similar behavior as the previous sample, and finally RCA 60299 showed flux jumps in large numbers all the time.

We can see that, except for the last sample, the number of flux jumps after reversal of the sign of  $dH/dt$  is always greater than for field going up.

The power failure test was omitted in many cases where during the normal run flux jumps were observed. Experience demonstrated that a larger  $dH/dt$  will produce more jumps.

As the purpose of this study is to see if this method can be used for selecting a given material for a particular application, one may draw some tentative conclusions from the results shown in the table. Knowing that high critical currents are related to strong pinning<sup>6</sup> and that materials showing flux jumps are strong pinners,<sup>3</sup> one should select RCA 60299 as the best, as far as critical current is concerned. Next should come RCA 60304 followed by GE 65A900001, GE 22CY030, and GE 65A900000.

These findings are consistent with the current rating of the RCA materials, i.e., 1200 A and 600 A at 100 kG, respectively. There is also consistency between the critical currents of the RCA and GE superconductors; the latter group is rated at 300 A at 100 kG. However, the commercial literature does not establish any difference between the three GE materials, and according to our results GE 65A900001 should have a higher critical current than the other two.

On the other hand, let us look into the stability question. If flux jumps are responsible for producing premature normal transitions (quenches) in a coil, one should select as the more stable material GE 65A900000 following the others in vertical order to the most unstable - the RCA 60299.

There are indications<sup>7</sup> that coils wound with GE 22CY030 can be energized without any indications of instability, but premature quenches appear when the current is decreased; this supports the stability argument as mentioned above. For pulsed field application GE 65A900000 should be the best at 4.2°K. All the first four should be good at 1.9°K.

Whether this criterion is valid to select a given material remains to be seen; further comparison of our results with observations made by other investigators that have used such materials is needed.

There is still a fundamental question that has to do with the physical reasons for the different behavior of these samples. Outside the well-known differences that result from the GE and RCA production processes, the influence of the additional materials

---

5. J. Silcox and R.W. Rollins, Rev. Mod. Phys. 36, 52 (1964).

6. R.W. Meyerhoff and B.H. Heise, J. Appl. Phys. 36, 137 (1965).

7. J. Purcell, private communication.

in modifying the magnetic behavior is not clear. An indication that the thermal conductivity of the composite (superconductor plus extra materials) is playing a role can be concluded from data obtained at 2.5°K; nevertheless, more work is needed in this direction.

## II. SEMIADIABATIC STUDY

The same samples were used for studying their magnetic and thermal behavior in nearly adiabatic conditions. A calorimeter built for this purpose was first used to calibrate three carbon thermometers (1/8 W, 560  $\Omega$  at 300°K) against a germanium cryoresistor.<sup>8</sup> The temperature values were translated into galvanometer deflections of a multichannel recorder; in this manner the temperature measurements were made directly from the graph. The calibration curves for two temperature ranges are shown in Figs. 3 and 4. These curves remained the same during the time taken by the experiment (two months). Although the resistors went through many cooling cycles and handling, it was found that readings, reproducible within a few hundredths of a degree, could be obtained by adjusting the current through the carbon resistors to the same potential difference obtained at 4.2°K during their initial calibration. After calibration the three resistors were cemented using GE 7031 to the various samples of superconductor and assembled in the calorimeter as shown schematically in Fig. 1B.

For these tests two matched samples of superconductor were used. Each was 0.5 in. wide and 1.0 in. long. The same parallel plate arrangement normal to the external field was used. Besides the three carbon resistors that were attached to one of the plates, a manganin wire heater was used to select the operating temperature and to produce the superconducting to normal transition whenever a virgin sample run was desired. A single bismuth microprobe was used for measuring the field, and a small coil of fine wire was used as an induction probe. Except for some special cases that will be mentioned in what follows, the external field was increased (or decreased) at the same constant rate of 6 G/sec. All five signals (three temperature and two field) were fed into the five-channel recorder.

The samples were initially mounted in such a manner as to make a good thermal contact with their support; however, it was found that when the inner pressure in the calorimeter was only a few microns, the samples never reached the transition temperature except at the ends where the thermal contact was made. It was then decided to thermally insulate the samples from the support and to allow some helium gas to remain in the calorimeter for better heat exchange. Thus, all runs were made at 30 mm Hg helium pressure measured at room temperature.

In these samples we observed four types of magnetic and thermal activity. These are shown in Fig. 5. The ordinate represents either temperature for the upper trace or magnetic induction for the lower one. The abscissa is the external magnetic field, which as mentioned before is a function of time.

Type ( $C^2$ ) behavior was perhaps the simplest and most commonly expected from theoretical grounds.<sup>9</sup> It consisted in a heat pulse that occurred at the same time of the flux jump. Experimentally, we found in Part I that thermal energy was released during the jump, as indicated by small increases of the inner pressure in the helium Dewar. But entropy considerations show that, under adiabatic conditions, the temperature of the material should decrease during the superconducting to normal transition. We have,

---

8. CryoCal Inc., 1371 Avenue E, Riviera Beach, Florida.

9. P.W. Anderson and Y.B. Kim, Rev. Mod. Phys. 36, 39 (1964).

however, observed what might have been cooling pulses only in a very few cases — mostly at low temperature (below 4.2°K) where the sensitivity of the carbon thermometer was high. It is probable that any cooling that occurred in these materials was overshadowed by a heating pulse that presumably resulted from losses due to inductive currents originated during the flux rearrangement. Cooling has been reported to occur in pure samples of niobium in the mixed state.<sup>10</sup>

Type (C<sup>1</sup>) activity looked like (C<sup>2</sup>) with no magnetic jump. It may not necessarily represent a different type from the physics point of view, as it could always be attributed to a low sensitivity of the magnetic probe and the recording apparatus, which, in our experiment was about 0.5 G at 2 kG. We will come back to discuss this point further.

Type (A) is unique. It was observed first in NbZr<sup>11,12</sup> and now in Nb<sub>3</sub>Sn. It consisted in a thermal oscillation of low frequency (period  $\approx$  1 sec) and 40 to 100 millidegrees amplitude that always appeared before a temperature jump with magnetic signature (flux jump). A copy of the actual record is shown in Fig. 6. An effect not reported before in the literature was observed here, namely, the coherence of the thermal oscillations. Although the amplitude of the oscillation is very small, one can see in this figure that even small details are reproduced in all three traces. This represents temperature changes of the same phase that cover an area of at least 2 cm<sup>2</sup>. The origin and coherent nature of the thermal oscillation is not yet understood. It could be interpreted as collective oscillation of the type already described in the literature.<sup>13</sup> The Type (A) activity terminated in a large temperature (6°-9°K) jump accompanied by a flux jump. This was followed by a quiet period where temperature dropped a few millidegrees, remaining the same until a new cycle was completed.

Type (B) consisted in heat spikes of increasing amplitude showing no magnetic signature until the last one that had a large amplitude and a longer decay time (1 sec).

Type (D) consisted of groupings of several incomplete Type (B); they were terminated by a heat and flux jump.

In all types, cessation of all thermal activity was observed after a flux jump, which was always registered by the magnetic probe. It is probable that the absence of magnetic signature observed in many heat jumps was not due to poor sensitivity of our probe, but it really indicated that no flux rearrangement took place as concluded from the still present thermal activity. Work is under way to further clarify this point.

The results of this study are summarized in Table II. They covered the temperature range from 10°K to 1.9°K. In each column the number of flux jumps appear together with the observed type of activity. For simplicity no distinction was made between the two types of C activity which only appeared in a few cases always above 5°K. Type A, on the other hand, was observed almost in all runs; we should point out that in many cases it consisted only of a thermal oscillation without flux or temperature jumps. This observation was made at temperatures above 4.2°K. At temperatures below 4.2°K a transition from thermal oscillation to thermal spikes was observed in some samples. This is listed in the table as AB and AD activity.

---

10. S.M. Wasim, C.G. Grenier, and N.H. Zebouni, Phys. Letters 19, 165 (1965).

11. N.H. Zebouni, A. Venkataram, G.N. Rao, C.G. Grenier, and J.M. Reynolds, Phys. Rev. Letters 13, 606 (1964).

12. L.J. Neuringer and Y. Shapira, Phys. Rev. 148, 231 (1966).

13. P.G. deGennes and J. Matricon, Rev. Mod. Phys. 36, 45 (1964).

Sample GE 22CY030 again presented an interesting example of activity change from 5.5°K down to 1.9°K. It started with Type A that gradually was transformed into Type D. The other samples did not go through such clear evolution.

Outside of presenting the results of this experiment, we are not in a position to offer a consistent physical picture to account for these observations.

Thanks are due to Mr. Howard Hart and Mr. Vincent Patrizi for their help in taking data and construction of parts of the equipment used in this work.

#### ISOTHERMAL

COMPOSITION OF MATERIAL	LEGEND P. F. = Power Failure	4.2°		2.5°		1.9°	
		JUMPS		JUMPS		JUMPS	
		UP	DOWN	UP	DOWN	UP	DOWN
S. S. + CU + Nb <sub>3</sub> Sn + CU + S. S.	G. E. 65A900000	SLOW	0	0	0	0	0
	P. F.	0	0	0	1	0	0
CU + Nb <sub>3</sub> Sn + CU	G. E. 22CY030	SLOW	0	4	0	8	0
	P. F.					0	1
Ag + Nb <sub>3</sub> Sn + Ag	R. C. A. 60304	SLOW	2	5	2	9	0
	P. F.						
CU + Nb <sub>3</sub> Sn + S. S.	G. E. 65A900001	SLOW	7	16	0	1	0
	P. F.						
CU + Nb <sub>3</sub> Sn + CU	R. C. A. 60299	SLOW	14	20	45	14	24
	P. F.						12

#### ADIABATIC

LEGEND: P. F. = Power Failure T. A. = Thermal Activity		10°		7°		5.5°		5.0°		4.2°		3.5°		2.5°		1.9°	
		JUMPS		JUMPS		JUMPS		JUMPS		JUMPS		JUMPS		JUMPS		JUMPS	
		UP	DOWN	UP	DOWN	UP	DOWN	UP	DOWN	UP	DOWN	UP	DOWN	UP	DOWN	UP	DOWN
G. E. 65A900000	SLOW	0	0	0	0	0	0	-	-	0	2	0	2	1	1	1	1
	P. F.	0	0	3	2	-	3										
	T. A.		0		C	A	C			A	AB	A	B	AB	AB	AB	AB
G. E. 22CY030	SLOW	0	0	0	1	0	1	0	2	2	5	3	5	4	5	4	3
	P. F.	0	2														
	T. A.	0	0		0		A	A	A	A	A	A	AD	AD	AD	D	D
R. C. A. 60304	SLOW	0	0	0	0	0	0	0	0	3	6	4	10	8	9	8	7
	P. F.	-	0	-	8												
	T. A.		0		C		0		0	A	A	AB	AB	AB	AB	AB	AB
G. E. 65A900001	SLOW	0	0	1	1	-	-	0	1	2	2	3	2	3	2	3	3
	P. F.																
	T. A.		0	A	A		-		A	AB	AB	AD	AD	AD	AD	AD	AD
R. C. A. 60299	SLOW	0	0	0	0	3	2	-	-	4	2	4	2	3	2	2	1
	P. F.	0	0	-	4												
	T. A.		0		C		B		-	AD	AD	D	D	AD	AD	AD	AD

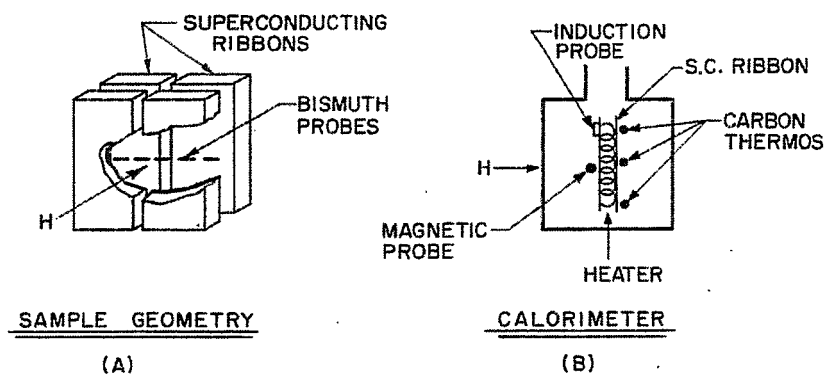


Fig. 1. (A): Split plate arrangement. For clarity the separation between strips and their thickness have been exaggerated. Five magnetoresistance microprobes measured the magnetic induction in the gap.  
 (B): Schematic view of the calorimeter and samples.

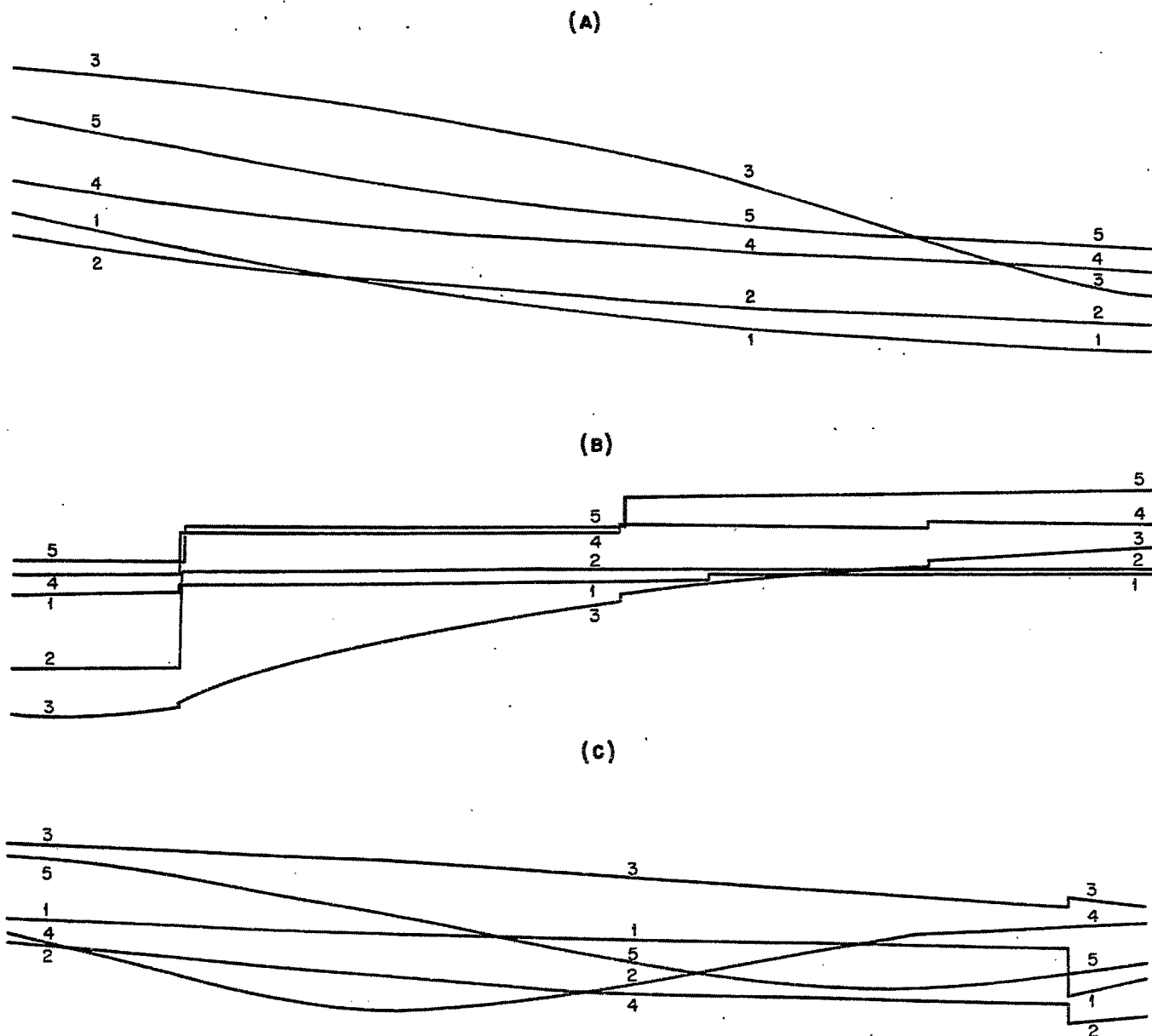


Fig. 2. Observations made on sample GE 22CY030.

- (A): Smooth flux penetration for positive  $dH/dt$ . In all traces the vertical scale represents the magnetic induction between the plates. The external magnetic field  $H(t)$  was measured in the horizontal scale. In A and C it increased from right to left, whereas it decreased in traces B.
- (B): Flux jumps observed for negative  $dH/dt$ . These traces were obtained after (A) above.
- (C): Smooth penetration is observed again after reversal of the external field. Partial cancellation of the positive magnetization, remaining from the cycle (A)(B) above, occurred through the flux jump seen at the beginning of the record.

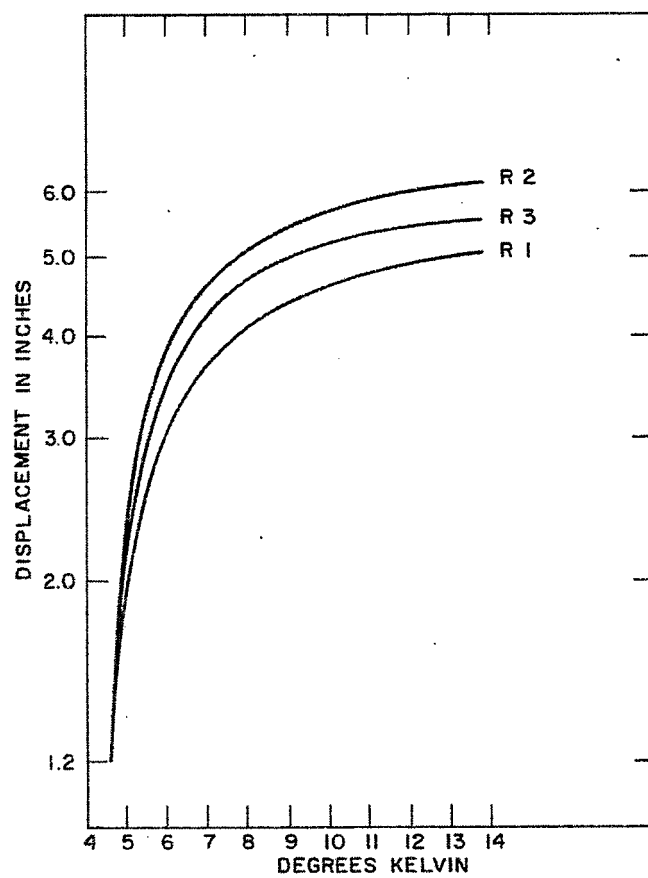


Fig. 3. Typical calibration curves for the temperature range between 4.2°K to 14°K.

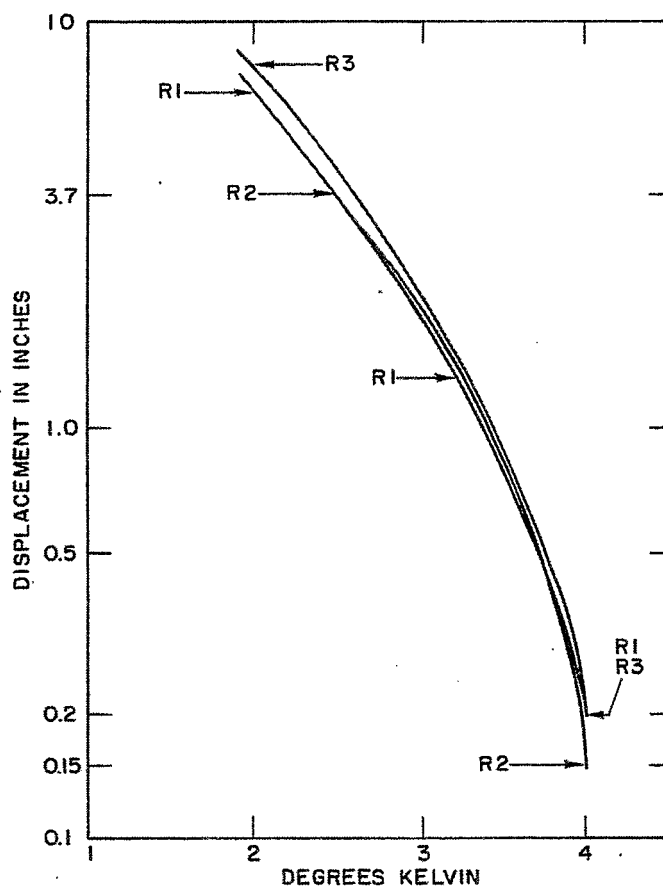


Fig. 4. Calibration curves below  $4.2^{\circ}\text{K}$ . The apparent discrepancy in the slope resulted from the definition of the zero displacement point.



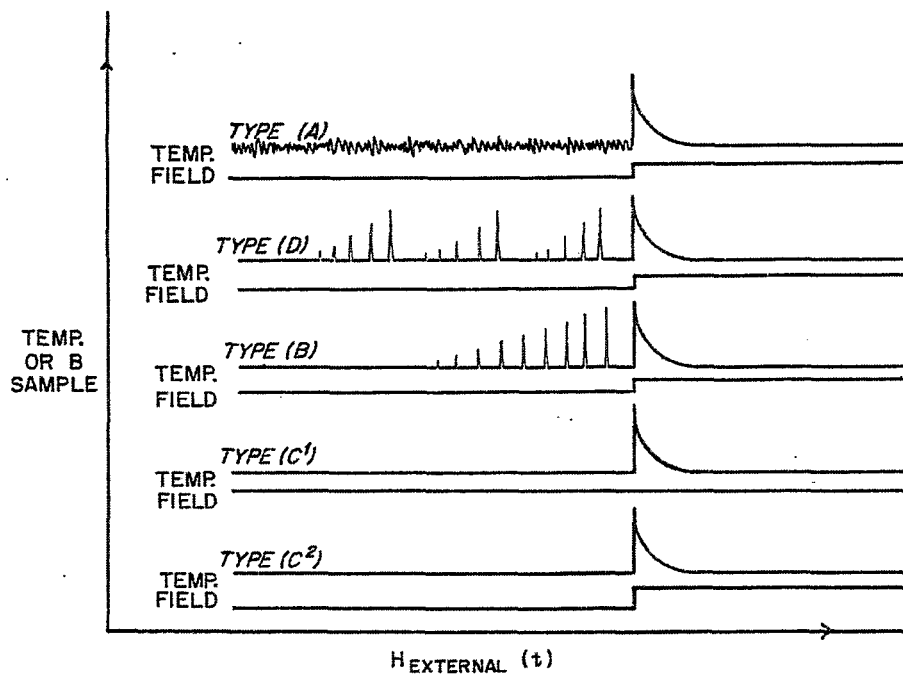


Fig. 5. Different types of thermal activity observed under semiadiabatic conditions.

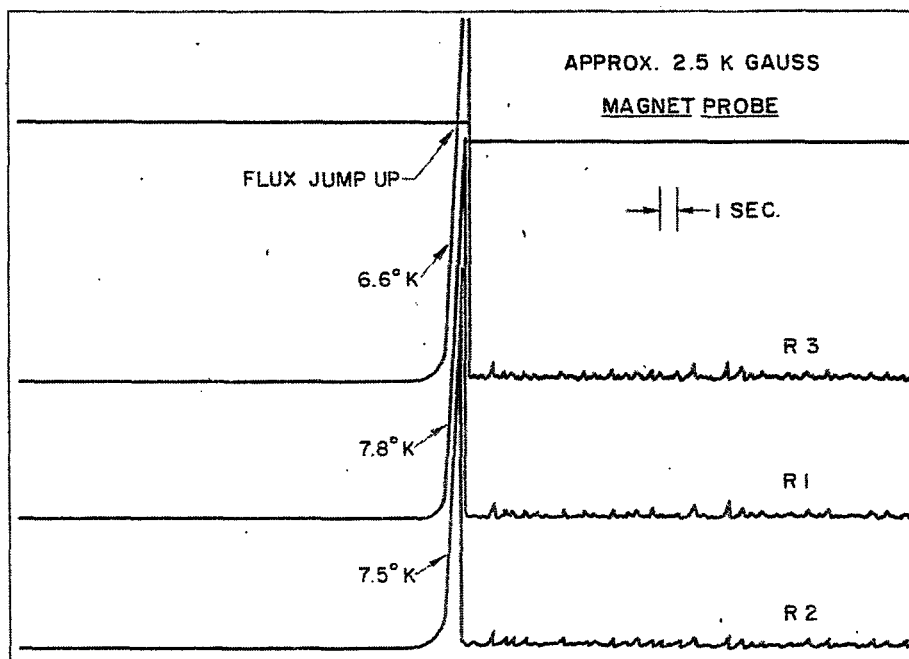


Fig. 6. A copy of an actual record showing Type A activity.

OBSERVATIONS OF FLUX JUMP BEHAVIOR RELATED TO VARIOUS CHANGES  
OF GEOMETRY, AND THERMAL AND ELECTRICAL ENVIRONMENT\*

A.D. McInturff  
Brookhaven National Laboratory  
Upton, New York

These observations were made in the process of measuring hysteresis curves for Nb<sub>3</sub>Sn ribbons, and TiNb ribbons, wires, and composites. The term flux jump stability for the duration of this paper will be in reference to the frequency or number, and the magnitude [percentage of  $\bar{M}(H_a)$  changed during a flux jump only] of the flux jumps as they occur in the magnetization curves. The term thermal environment will refer to the helium bath or vapor temperature and also whether the sample is thermally insulated from or is well ventilated with that bath or vapor. The term electrical environment refers to the effects of  $\partial H/\partial t$ , the probability of flux jumping at a given (H) field, external transport current effects on the flux jump behavior, field reversal effects on the flux jump behavior, and the conductivity (electrical and/or thermal) of the normal metal matrix surrounding the superconductor. The geometry changes, which were made in the study of flux jump behavior, were changes in sample dimensions, in the angle of the sample with respect to the magnetic field, and in the magnetic field-transport current geometry.

The experimental setup (similar to that of Fietz<sup>1</sup>) consisted of various carefully matched ( $\leq 1$  turn in  $10^4$ ) coil pairs, one pair for each geometry to be investigated. Several variations from infinite sheet to thin disk were investigated, with or without transport current (see Fig. 1). One coil was used to measure  $\partial \bar{H}(\text{helium} + \text{sample})/\partial t$ , the other to measure  $\partial \bar{H}(\text{helium})/\partial t$ . The difference signal from these coils was integrated, employing a chopper-stabilized operational amplifier, and was displayed on the y-axis of an x-y recorder. The signal from the  $\partial \bar{H}(\text{helium})/\partial t$  coil was integrated similarly and displayed on the x-axis of the recorder. The time constant for the magnetization  $\bar{M}$  integrator (difference signal) was 0.01 to 0.05 sec.

The sample was placed in the specimen coil and the magnetic field was cycled either from  $H = 0 \rightarrow H_{\max} \rightarrow H = 0$ , or  $\rightarrow - H_{\max}$ . The resulting hysteresis curve was simultaneously plotted on the x-y recorder. When transport current was employed only two of the sequences mentioned by LeBlanc<sup>2</sup> were used. First the transport current was raised to some predetermined value and then the field was cycled, or alternatively the field (H) was cycled to a given magnitude and then the transport current was applied until the superconducting sample became resistive. The latter sequence was performed on both the diamagnetic and paramagnetic portions of the magnetization curves  $\bar{M}$ .

The thermal dependence of the flux jumps can most dramatically be seen in Fig. 2. The dramatic increase in flux jumps at lower temperatures had previously been reported by several investigators.<sup>3-8</sup> This thermal effect can be generalized by the following statement: a decrease in temperature will increase the frequency, but reduce the magnitude of the individual flux jumps. The reduction in magnitude shown in Fig. 2b can probably be attributed to the fact that these results are obtained below the  $\lambda$  point of helium, where the tremendous increase in thermal conductivity of the bath made possible a more efficient transfer of heat away from the sample. This more efficient transfer of heat would restrict the amount of sample that would be heated during the flux jump.

---

\* Work performed under the auspices of the U.S. Atomic Energy Commission.

The frequency of the flux jumps seems to increase as  $\partial \bar{H} / \partial t$  is increased from a few gauss/minute to several hundred gauss/minute. Once the rate has reached several kilogauss/minute, the flux jumps seem (given all other parameters the same) to have almost identical characteristics. The flux jumps observed seem to be more frequent at fields less than or equal to  $\bar{H}^*$  ( $\bar{H}^*$  = the magnetic field necessary for complete penetration) and in some cases slightly greater than  $\bar{H}^*$ . The exceptions to this observation were in those cases where a transport current equal to a significant percentage of the critical transport current was present. Then the flux jumps would occur even at fields several times greater than  $\bar{H}^*$ . These flux jumps would almost always result in the samples becoming resistive. This might be explained if one notes that in these experiments the current and magnetic field were perpendicular. Therefore, due to this geometry, a large Lorentz force could have caused physical motion.

The effect of magnetic field reversal greatly increased the flux jump instability, as is illustrated in Fig. 3c vs Fig. 3d. This phenomenon can be understood from arguments presented by Schweitzer and the author<sup>9</sup> in a paper on flux mobility recently submitted for publication.

The configuration of a thin plate [e.g., 1 cm wide ribbon (Nb<sub>3</sub>Sn or TiNb) with  $\bar{H}$  perpendicular to the large flat surface] is, usually for the commercially available type II superconductors, flux jump unstable. Figures 3 and 4 show a typical geometry dependence of the magnetization of a thin plate as a function of the minimum width dimension of the superconductor. Figures 5 and 6 show the effect of high conductivity metal bonded to the type II superconductors Nb<sub>3</sub>Sn and TiNb. This effect can probably be attributed to the thermal conductivity in that these samples were edge-cooled stacks. Future experiments will be necessary to validate the above remark.

Some early results seem to indicate that scribing the normal metal reduces the flux jump instability. But the corresponding reduction in magnetization and flux jump instability that was reported for the Nb<sub>3</sub>Sn sample did not seem to be valid for the TiNb samples. It should be noted that these data are very crude measurements and future experimentation will be necessary to validate them.

There was a coupling effect on the magnetization and flux jump stability observed in the process of these measurements. If a sample stack is prepared with no electrical insulators between layer or ribbon samples, the magnetization rises to much greater values and the severity of the flux jumps greatly increases as well. (This is easily understood by the flux jump stability criteria put forth by various workers in the field.<sup>10-14</sup>) If the samples were electrically (and thermally) insulated the frequency of the flux jumps was greatly increased.

In conclusion it would seem to the author that the aforementioned data present a favorable case for multifilament conductor contained in a high conductivity (thermal) matrix. From arguments presented by P.F. Smith<sup>15</sup> one would also conclude that a low electrical conductivity interface between the superconductor and the matrix to prevent possible coupling is required.

These data were taken to compare with pulsed coil data<sup>16</sup> for loss rate determination. The values used for comparison were taken to be those that would have been present if the flux jumps had not occurred. These results seem to check fairly consistently if one takes into account the diamagnetic effects of the superconductors on the field as calculated for copper windings.

The author expresses his sincere thanks to P.F. Dahl for his corrections to and suggestions for this paper and to W.B. Sampson and R.B. Britton for the use of their magnets in these experiments.

#### REFERENCES

1. W.A. Fietz, Rev. Sci. Instr. 36, 1621 (1965).
2. M.A.R. LeBlanc, Phys. Rev. Letters 11, 149 (1963); M.A.R. LeBlanc, Phys. Rev. Letters 6, 140 (1963); M.A.R. LeBlanc et al., Phys. Rev. Letters 14, 704 (1965).
3. Y.B. Kim et al., Phys. Rev. 131, 2486 (1963).
4. G. Kuhn et al., Compt. Rend. Paris 255, 2923 (1962).
5. R.D. Blangher et al., Cleveland Conference on Superconductivity, 4, p. 121 (1968).
6. L.J. Neuringer et al., Phys. Rev. 148, 231 (1966).
7. J.M.P. Watson, J. Appl. Phys. 37, 516 (1966).
8. M.R. Wertheimer et al., J. Phys. Chem. Solids 28, 2509 (1967).
9. D.G. Schweitzer and A.D. McInturff, to be published.
10. R. Hancox, private communication.
11. S.L. Wipf, these Proceedings, p. 511.
12. H.R. Hart, Jr., ibid., p. 571.
13. P.F. Smith, ibid., p. 839.
14. Z.J.J. Stekly, ibid., p. 748.
15. P.F. Smith, ibid., p. 913.
16. G.H. Morgan, P.F. Dahl, W.B. Sampson, and R.B. Britton, to be published.

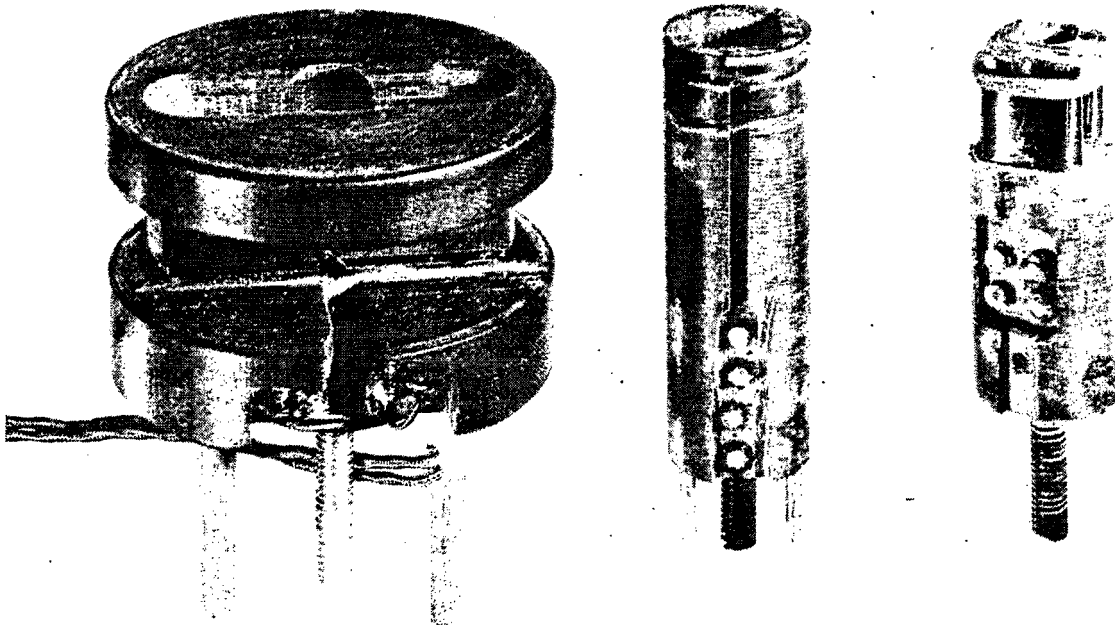


Fig. 1. Three of the coil pairs used in the experiments. The coils on the left are for thin disk and perpendicular transport current ( $5 \times 10^3$  turns each of No. 50 wire). The middle coils are thin disk coils (for stacks) ( $10^4$  turns each of No. 50 wire). The coil pair on the right are for the infinite sheet geometry ( $2 \times 10^4$  turns each of No. 50 wire).

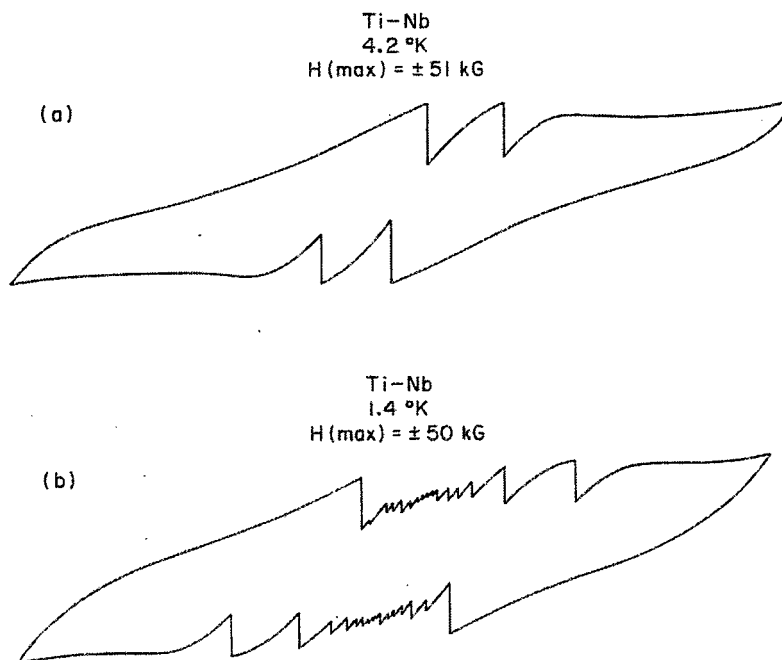


Fig. 2. Tracings of an x-y recorder of  $\bar{M}$  vs  $H$  for Ti48a/oNb at 4.2°K. and below the  $\lambda$  point 1.4°K. These tracings are for the same sample.

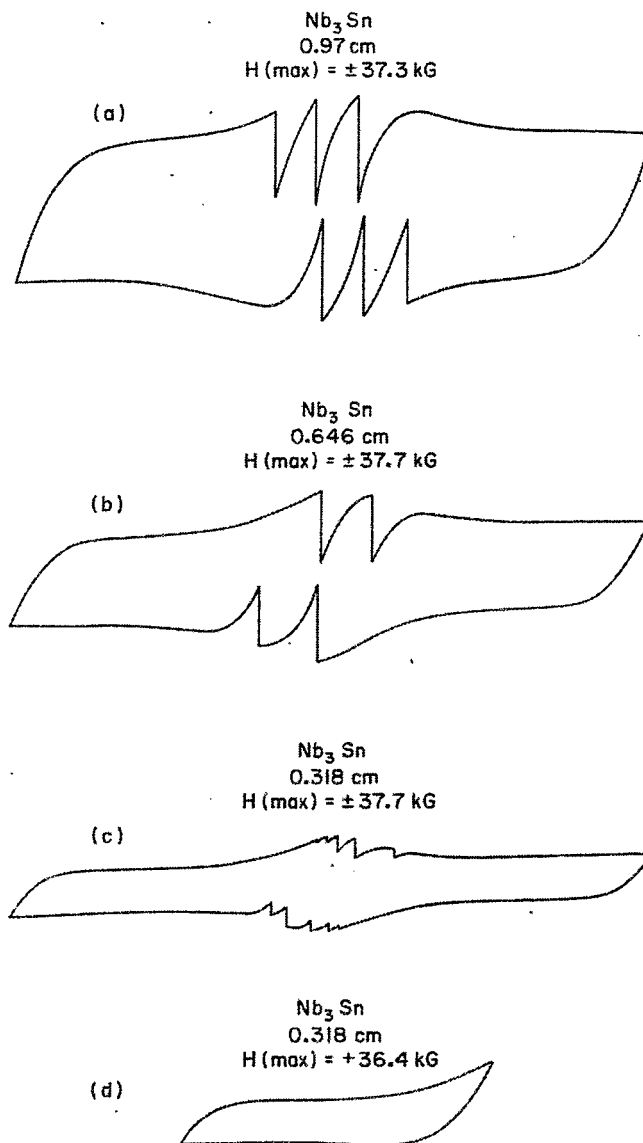


Fig. 3. Tracings (a sample of vapor-deposited Nb<sub>3</sub>Sn) of an x-y recorder with  $\bar{M}$  as the y-input and H as the x-input. Curves 3a, b, and c are for both senses of  $\bar{M}$  (plus  $H_{\max}$  and minus  $H_{\max}$ ). Curve 3d is for the plus  $H_{\max}$  only.

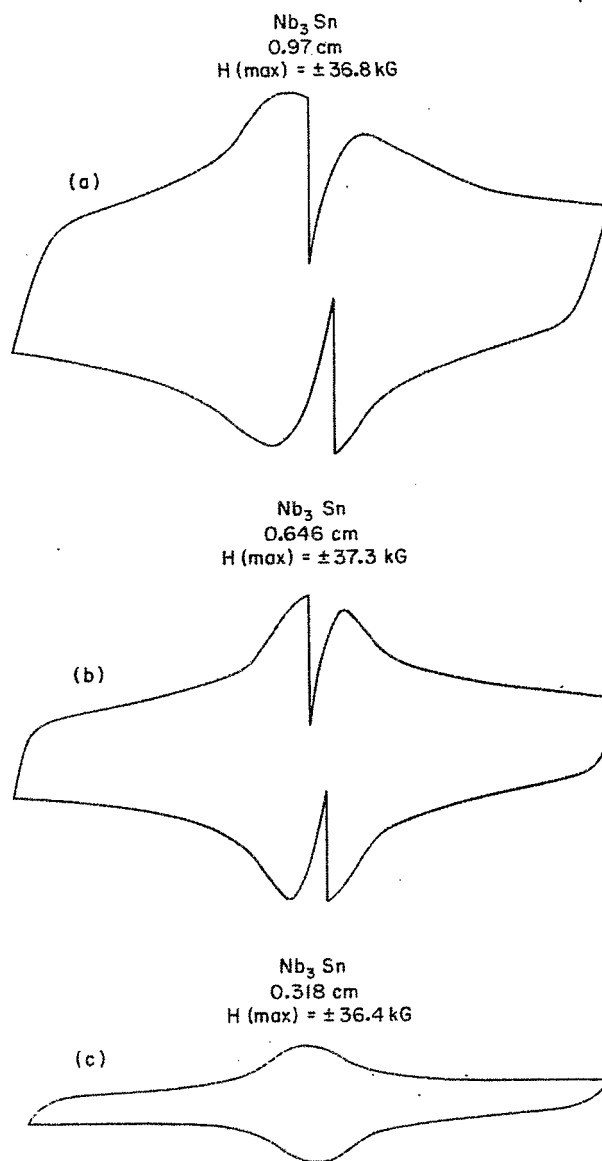
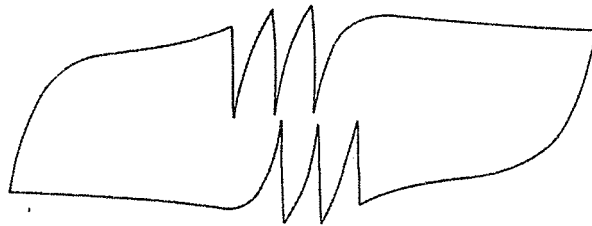


Fig. 4. Tracings of an x-y recorder (a sample of diffusion processed Nb<sub>3</sub>Sn); y-axis is  $\bar{M}$  and x-axis is  $\bar{H}$ . These curves are for the same sample, only varying the width of the ribbon (but not the amount).

Nb<sub>3</sub>Sn



Nb<sub>3</sub>Sn

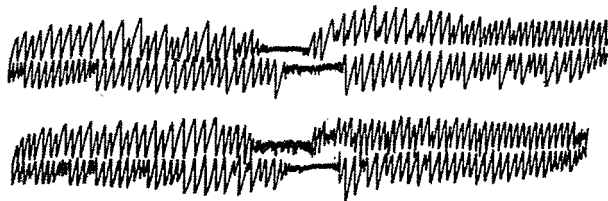
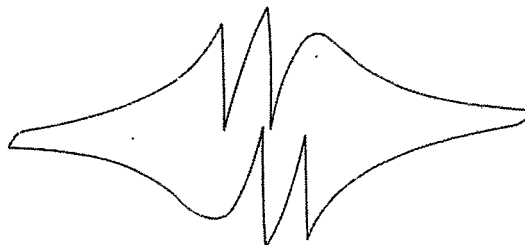


Fig. 5. Tracings of an x-y recorder (Nb<sub>3</sub>Sn); y-axis is  $\bar{M}$  and x-axis is  $\bar{H}$ . The upper curve is taken with the Ag plating in good contact; in the lower curve that contact is broken.  $H_{\max} = \pm 50$  kG. This is a thin disk configuration (1 cm x 1 cm).

Ti-Nb



Ti-Nb

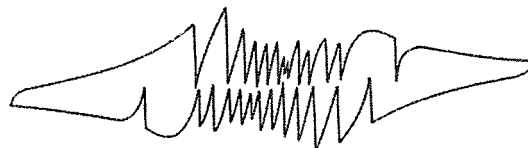


Fig. 6. Tracings of an x-y recorder for  $\bar{M}$  as the y-axis and  $\bar{H}$  on the x-axis ( $H_{\max} = \pm 40$  kG). The upper curve is for a Ti48a/oNb sample with an excellent Cu to TiNb bond; in the lower curve the bond was highly resistive. This is for a thin disk configuration (1 cm x 1 cm).



## INSTABILITIES AND FLUX ANNIHILATION

S.L. Wipf  
Atomics International  
A Division of North American Rockwell Corporation  
Canoga Park, California

I would like to present a small argument to show why I think that flux annihilation is not as important in creating instabilities as is sometimes implied<sup>1</sup> and was mentioned this morning.

We look at a region inside the superconductor where flux lines in one direction (positive) are replacing flux lines in the opposite direction (negative), i.e., annihilate each other (such a situation is illustrated in Fig. 1a for a plane slab geometry). We must remember the following: From our basic knowledge of type II superconductors we have to conclude that a Meissner region will separate the regions between positive and negative flux. The Meissner region, of course, is bounded by London penetration surfaces which shield the interior completely from the adjacent magnetic field which has a value of  $H_{c1}$  at the boundary. We want to answer two questions: What is the mechanism by which this Meissner region travels inwards as the external field increases? How far apart are the boundaries or how thick ( $= 2\rho$ ) is the region?

The superconductors under consideration here always show flux pinning, otherwise a field profile of the type given in Fig. 1 cannot arise. Pinning, being a defect-connected property is probably not very uniform and consequently we have to imagine that the boundary of the Meissner region may be quite rough and full of bumps and protrusions, etc.; this will not affect the basic ideas of the argument.

A fitting way of looking at forces connected with flux lines is in terms of the Maxwell tensor. It consists of a lateral pressure of  $B^2/8\pi = n^2 \phi_0^2/8\pi$  (if we express  $B$  in terms of density  $n$  of flux lines) and a longitudinal tension also of  $B^2/8\pi$ . We experience these forces as repulsion between two equal magnet poles or as attraction between two opposite poles, and if we consider the forces transmitted through the median plane between the two poles we find the pressure between parallel flux lines in one case and the tension along flux lines in the other. The fluxoids then repel each other with a force inversely proportional to their distance and the resulting net force due to the gradient in fluxoid density (equivalent to  $dB/dx$ ) is just large enough to overcome pinning and keep the fluxoids moving while the outside  $H$  increases with  $dH/dt$ . At the Meissner region boundary exists a pressure of  $H_{c1}^2/8\pi$  which is countered by what has been called the London pressure; but of special interest here is the longitudinal tension of  $n \phi_0^2/8\pi$  in a fluxoid,<sup>2</sup> which allows us to think of it as if it were a stretched rubber band. If such a band is bent around a radius of curvature  $\rho$ , a lateral pressure ( $n \phi_0^2/8\pi\rho$ ) is created which also can overcome pinning.

- 
1. See C.R. Wischmeyer, Phys. Rev. 154, 323 (1967); the present argument was a private reply to a discussion of the Meissner region ("Interface") in this paper and in defense of a statement in the last paragraph of a paper by the author [Phys. Rev. 161, 404 (1967)] then in the process of publication.
  2. The total fluxoid line energy is given as  $(\phi_0/4\pi\lambda)^2 \ln \lambda/\xi$  in P.G. deGennes and J. Matricon, Rev. Mod. Phys. 36, 45 (1964).

A whole sequence of two fluxoids annihilating each other is illustrated in Fig. 2, the various stages numbered 1-5:

1. The two opposing fluxoids are separated by the Meissner region which shields their mutual attraction.
2. With the outer fluxoid moving closer (because of  $dH/dt$  on the outside) the mutual attraction starts deforming the fluxoid pair in places where pinning has minima.
- 3 & 4. Further deformation leads to coalescence of the fluxoids under the formation of sections with radius of curvature  $\rho$ .
5. With  $\rho$  being small enough for the line tension to overcome pinning the curved sections move away from each other, thus annihilating two flux lines. The stage is set for a repeat of the same sequence.

The Meissner region moves deeper into the specimen by gradual redistribution of flux as indicated in Fig. 1b-d. Figure 1b shows the situation immediately after the annihilation process leaving the Meissner boundary at a slightly higher field than  $H_{c1}$ . Figure 1c shows what kind of flux movement corrects this situation. The left side admits flux through the surface, leaving  $H$  outside unchanged; the right side redistributes the flux, leaving the total flux inside the specimen constant. The result is a somewhat larger thickness ( $> 2\rho$ ) of the Meissner region (corresponding to stage 1 of Fig. 2). Figure 1d: further rise in the outside field by  $\Delta H$  will reduce the thickness to  $2\rho$ , and by comparison with Fig. 1a the Meissner region has moved a small distance. The next annihilation takes place.

In this whole mechanism there are never more than one fluxoid pair involved. The energy dissipation due to annihilation will of course be released as heat in the Meissner region. This heat per unit volume may be somewhat different from the corresponding value in other parts of the shielding region where it comes from the ordinary pinning dissipation and this may constitute more or less of a disturbance of the pinning equilibrium. But on the whole the process is not so different in character from the ordinary growth of a shielding layer (without negative flux present) and the criterion for instability, i.e., the question whether the whole shielding region is in a stable or unstable equilibrium, may be marginally modified but remains unchanged in principle.

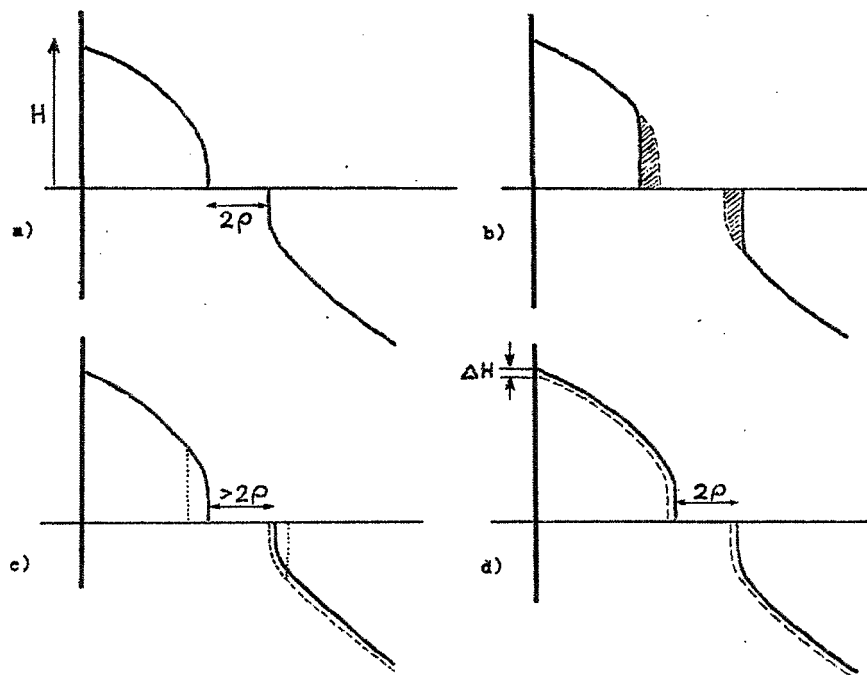


Fig. 1. Motion of the boundary of the Meissner region during flux annihilation.

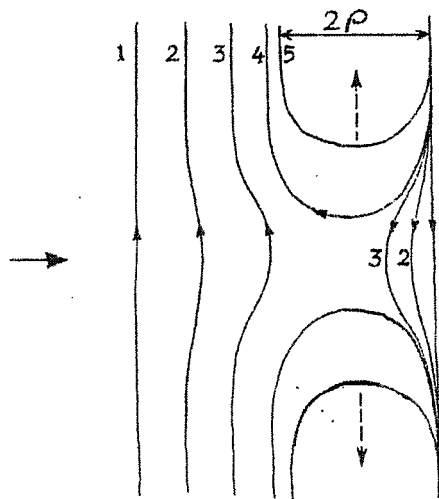


Fig. 2. The process of flux annihilation.

# SUPERCONDUCTING TRANSMISSION LINES - COMMUNICATION AND POWER\*

N.S. Nahman  
Radio Standards Engineering Division  
National Bureau of Standards  
Boulder, Colorado

## INTRODUCTION

During the past few years interest has grown in the application of superconductors to electrical power transmission lines and other power apparatus.<sup>1-11</sup> The probability of doing so seems very remote to the majority of the industrial and scientific community. However, there are those of us who believe that such large scale superconductive systems are practical and, when realized, will provide technical and economic advantages.<sup>12-17</sup> Make no mistake about the motive for utilizing superconductors; simply put, the economic payoff would be very great.

The purpose of this paper is to strongly declare that a superconductive power transmission system would (and should) be much more than a power transmission line. Considering the capital investment required to build such a system it is then imperative that the maximum economic benefit be derived from the system. Accordingly it is my contention that the subject under discussion is not a superconductive power line, but a much more encompassing system, a "Superconductive Transmission System" (SCTS).

As seen through my mind's eye, the SCTS would consist of four subsystems:

1. Data Processing Subsystem.
2. Cryogenic Liquid Transport Subsystem.
3. Electrical Power Transmission Subsystem.
4. Electrical Communication Subsystem.

Consequently, it is apparent that my vision is actually concerned with four systems and not just one system. The four subsystems have a common characteristic within the perspective of our technologically based society: each subsystem may span great distances. Furthermore, operation of such a multifaceted utility complex would require very effective interaction between the constituent utilities. There may be some raised eyebrows as a result of my calling a data processing system "a utility," but if everybody in the cities of tomorrow is going to have access to a computer, then an extensive time share system of the magnitude of a utility will be necessary.

With the preceding comments serving as an introduction, my remarks will now center upon some aspects of the four subsystems. It is my intention to discuss in greater detail that which I know something about. Accordingly, I will not say much about the data processing subsystem or the cryogenic fluid transport subsystem. Also I will deal in somewhat of a broader sense with the power transmission subsystem in order to clearly establish in your minds that dc power transmission is presently a reality and that superconductive dc power transmission is only an extension to superconductivity and not to dc. Finally, I will discuss in greater detail the superconductive communication transmission subsystem as I know more about such systems by virtue of experience and training.

---

\*The mention in this paper of trade names or proprietary products is not to be construed as an endorsement of these items by the National Bureau of Standards.

## DATA PROCESSING SUBSYSTEM

The data processing subsystem would have two functions: an internal one and an external one. Internally, the data processing subsystem would provide data processing services to the other three subsystems in order to execute the required instrumentation and control for each subsystem. Externally, the data processing subsystem could provide time share computer facilities for subscribers along the length of the SCTS.

The data processing subsystem could be implemented by using cryogenic digital and analog electronic components which possess inherently large packing densities.<sup>18</sup> These brief remarks comprise my discussion of the data processing subsystem. I will now briefly discuss the cryogenic liquid transfer subsystem.

## CRYOGENIC LIQUID TRANSPORT SUBSYSTEM

Many industrial and research centers require cryogenic fluids for their operations. Accordingly, a SCTS connecting such centers could provide a means of transporting cryogenic fluids to the individual centers. For example, if a SCTS passed through the helium producing fields in Kansas, liquid helium could be introduced into the SCTS at the helium production source and then be distributed by transmission through the SCTS network. The cryogenic and gas transport industries could no doubt think of many ingenious ways to utilize the SCTS. In any event my brief remarks may serve as stimuli to their thoughts. Next, I will discuss the status of superconductive power transmission.

## POWER TRANSMISSION SUBSYSTEM

A superconducting wire can transmit a dc current without losses or an ac current with an extremely small loss. At first glance, the complete absence of losses in the dc case engenders some attractive possibilities for dc power transmission, while the existence of ac losses (due to electrical and mechanical forces) apparently decreases the practicality of ac power transmission. That such is the case, stems from consideration of refrigeration costs. Personally, I do not believe that ac power transmission systems are to be ruled out. However, in terms of our present-day lack of experience with really large-scale superconductive systems, it is probably prudent to concentrate our present speculation on dc power systems. Present-day developments and future experience will no doubt engender ac systems.<sup>5</sup>

Dc transmission of large amounts of electrical power is a reality.<sup>19</sup> Today, there exist roughly six systems in operation ranging over distances of 72 to 750 miles, operating in the voltage range of 100 kV to 800 kV, and transmitting powers in the range of 30 MW to 750 MW. Also, there is a similar number of systems under design and construction which will cover distances of 25 to 875 miles, operate in the voltage range of 130 kV to 800 kV, and transmit powers ranging from 78 MW to 1440 MW. The input and output terminals of these dc systems are mercury-arc grid controlled rectifiers which convert and invert ac to dc and dc to ac, respectively. Consequently, the idea of using superconductive dc power transmission is clearly an extension of technology only to superconductive systems, not to dc systems.

As I mentioned earlier, considerable analytical work has been done on the possibilities for superconducting power transmission. In many of the papers cited, economic data were presented which indicated when superconducting power transmission would be economically favorable. I will not go into any specific cases; but I should point out that some of the papers developed economic data on transmission systems having capacities which could be fully utilized today or in the next few years. For example,

Norris and Swift<sup>15</sup> discussed transmitting 750 MW at 100 kV dc and 750 MVA at 33 kV ac. On the other hand, Garwin and Matisoff<sup>14</sup> envisioned economically transmitting very large amounts of power, 100 GW at 200 kV dc over distances of 1000 km.

Superconductive power transmission studies have entered the experimental phase. In England, an experimental line has been constructed and operated.<sup>20</sup> Also, a 3000 hp superconductive motor is being built.<sup>21</sup> In the U.S.A., Meyerhoff, Beall and Long<sup>22</sup> have designed and are to construct a 20 ft section of niobium coaxial power line. A 60 ft section of a superconductive power line is being built in West Germany.<sup>23</sup> In France, and in the U.S.A., liquid hydrogen cooled (20°K) cryogenic power apparatus is being designed and constructed.<sup>8,24</sup> Also, power apparatus manufacturers are recruiting engineers and scientists to work on the development of superconductive power apparatus.<sup>25</sup> Consequently, it is evident that superconductive power systems are already with us in a limited sense. The remainder of my comments will be concerned with superconductive electrical communication transmission.

### ELECTRICAL COMMUNICATION SUBSYSTEM

First of all, I would like to briefly describe a fairly general model of a communication system.<sup>26</sup> By my doing so, you will have some idea of how communication electrical engineers view a communication system. The model is general enough to characterize all forms of wired or radio communications. The system consists of a serial chain of elements beginning with a data source and ending with a data processing and storage element. Information flows unidirectionally through the system in serial order starting from element No. 1 and ending at element No. 7; the elements are as follows:

1. Data Source. A system which produces the information to be transmitted.
2. Encoder. A system which transforms the data into a favorable form which insures successful transmission through the noisy transmission channel.
3. Modulator and Transmitter. A system which converts the encoded information into a signal form capable of passing through the transmission channel.
4. Transmission Channel. A noisy system or physical medium through which the signal flows. Noise is inherent in any transmission channel and arises from natural physical causes or unnatural (man-made) causes.
5. Receiver and Demodulator. A system which extracts the signal information from the noisy output of the transmission channel and converts the extracted information into a form suitable for the decoding operation.
6. Decoder. A system which converts the encoded information into some form for data storage and processing.
7. Data Storage and Processing. The recipient system requiring the information generated by the Data Source (element No. 1).

Upon considering the various elements comprising a communication system, it is evident that a superconductive one could employ a large amount of integrated circuit cryoelectronics. Of particular interest to me is the utilization of the superconductive coaxial line as the physical transmission channel. Other electrical waveguides such as hollow metal pipes for microwaves or light pipes for laser wavelengths could also be employed with improved characteristics compared to their room temperature counterparts. However, the coaxial line can be miniaturized and transmit a baseband signal whose frequency components extend upward from dc.

The baseband signal propagates in the TEM electromagnetic mode which is the ordinary two-conductor transmission line mode (as contrasted to single conductor modes).

The TEM mode can exist in any two-conductor transmission line and extremely great baseband bandwidths may be realized with the coaxial geometry. In a lossless coaxial line waves of any frequency are propagated without loss. Above a certain frequency undesirable higher order modes (single conductor modes) can propagate.<sup>27</sup> Consequently, for a given coaxial line the upper operating frequency is usually chosen to be less than that of the lowest frequency higher order mode. As the diameter of the coaxial line is decreased, the higher order mode cutoff frequency is increased; for example in a 50  $\Omega$  coaxial line having a relative dielectric constant of approximately 2.0 and a 0.03 in. o.d., the higher order mode cutoff frequency is approximately 100 GHz.

Before summarizing the results achieved to date with miniature superconductive coaxial lines, I am going to make a few remarks about cryogenic normally conducting coaxial lines. Depending upon the metal purity and structural order (electronic mean free path length) the classical or anomalous skin effect may occur. The anomalous skin effect strongly occurs when the electronic mean free path is greater than the electromagnetic field penetration (skin) depth. For short (impure metal) or long (pure metal) electronic mean free paths the high frequency complex attenuation of the coaxial line will follow an  $s^{1/2}$  or an  $s^{2/3}$  variation, respectively, where  $s$  is the complex frequency variable.<sup>28</sup> Furthermore, the anomalous skin effect produces a greater attenuation than would be expected (classical theory) from the increased dc metal conductivity produced by the low temperature environment. Typically, for copper having a 4.2°K to 293°K conductivity ratio of 400, one would expect a 10 GHz classical attenuation reduction of 20 while in practice the anomalous skin effect may yield an attenuation reduction of 5.

Because the high frequency losses in a superconductor are dependent upon the normal state of electronic mean free path and decrease with increasing mean free path, the superconductor purity and structural regularity strongly affect the surface impedance frequency dependence. Experimental data from superconductive coaxial transmission lines have been compared with the two-fluid superconductivity theory.<sup>29</sup> The results suggest that the particular superconductor samples employed possessed relatively short normal state electronic mean free paths. Typical transmission line parameters were as follows: 50  $\Omega$  characteristic impedance, polytetrafluoroethylene dielectric, Nb 0.015 in. diam center conductor, Pb 0.045 in. i.d. outer conductor, and 1360 ft length. In terms of the two-fluid model, at 8 GHz, the metal losses would produce a transmission attenuation of 35 dB or 0.7 dB for a purely classical normal component or a purely anomalous normal component, respectively. The observed attenuation was 10 dB. Consequently, improvements in the superconductor metallurgy should provide an attenuation approaching that of the anomalous limit. The effect of the normal state electronic mean free path was strikingly seen in the time domain response curves. For a long mean free path the step response rose abruptly with a 10-90% rise time of about 5 psec. For a short mean free path, the step response rose relatively slowly reaching the 80% level in about 30 psec.

Using the two-fluid model curves,<sup>29</sup> the transmission characteristics of a miniature superconductive line can be compared against that of a room temperature 2 in. i.d. corrugated circular waveguide. Using a circular waveguide operating frequency of 56 GHz in the TE<sub>01</sub> mode, one obtains an attenuation of 1.5 dB/mile,<sup>30</sup> with perhaps a bandwidth of 20% of the operating frequency, 11.2 GHz. A 50  $\Omega$  superconductive coaxial line made of the same materials mentioned above and having an 0.061 in. i.d. outer conductor would have a higher order mode cutoff frequency of 56 GHz. The lowest temperature listed in the two-fluid model curves is 2.3°K. Upon using the anomalous limit at 2.3°K, the superconductive line attenuation would be 3.5 dB/mile at 56 GHz. Consequently, it is seen that the superconductive line provides a baseband bandwidth of greater than 50 GHz while the circular waveguide yields a bandpass bandwidth of greater than 10 GHz centered at 56 GHz; the attenuation values are comparable. Also, because of its baseband characteristic, the miniature superconductive coaxial line is

capable of transmitting baseband digital information at very rapid rates. Therefore, it is evident that such miniature lines could provide large bandwidth transmission channels for use in a SCTS.

#### SUMMARY

It has been declared that a superconductive power transmission line system could be much more than just a power transmission line, but rather a composite of four subsystems: (1) data processing, (2) cryogenic liquid transport, (3) electrical power transmission, and (4) electrical communication.

At present, dc power transmission in superconducting cables appears to be economically feasible. However, ac transmission with its associated joule heating losses is not to be discounted. Improvements in cryogenic refrigeration, operating experience, and technical convenience will no doubt engender ac systems.

Cryoelectronics has a great potential for implementing the various subsystem electronic systems. The cryoelectronics components developed to date have demonstrated that the electronic functions necessary for the various subsystems can be implemented with such components. The spectrum of components includes active analog elements, digital elements, transmission lines, waveguides and large-scale digital systems.

Finally, the idea of transporting cryogenic liquids through a SCTS network offers some intriguing possibilities for the transportation of gases. Not only does this suggest transporting the usual cryogenic liquids, but also other liquefied gases.

#### REFERENCES

1. R. McFee, *Electrical Engineering* 81, No. 2, 122 (1962).
2. M. Carruthers, *Engineering* 196, No. 5085, 420 (1963).
3. D. Atherton, *Elec. News and Eng.*, 74, No. 11, 52 (1965).
4. K.J.R. Wilkinson, *Proc. IEE (London)* 113, 1509 (1966).
5. D.A. Swift, paper presented at the 12th Intern. Congress of Refrigeration, Madrid, Spain, 1967, Sec. 1.46, 1-11.
6. D.R. Edwards and R.J. Slaughter, *Electrical Times* (Aug. 3, 1967), p. 166.
7. E.C. Rogers and D.R. Edwards, *Electrical Review* (Sept. 8, 1967), p. 348.
8. S. Neal, paper presented at the American Power Conference, 30th Annual Meeting, Chicago, Ill., 1968.
9. N. Kurti, *New Scientist* 36, No. 574, 604 (1967).
10. M. Styrikovitch, *Nauka i Zhizn*, No. 11 (1967).
11. V.L. Gani, M.Sc. Thesis, *Electrical Engineering Dept.*, University of Colorado, Boulder, Colo. (1968).
12. W.F. Gauster, D.C. Freeman, and H.M. Long, Paper No. 56 in Proc. World Power Conference (1964).
13. V.S. Okolotin, *Energetika*, No. 10, 35 (1965).
14. R.L. Garwin and J. Matisoo, *Proc. IEEE* 55, 538 (1967).
15. W.T. Norris and D.A. Swift, *Elec. World* 168, No. 4 (July 1967).
16. N. Kurti, paper presented at the 12th Intern. Congress of Refrigeration, Madrid, Spain, 1967, Pl.a, 1-24.



17. A. Kusko, IEEE Spectrum 5, No. 4, 75 (1968).
18. Special Issue on Cryogenic Electronics, R.W. Schmitt, Ed., Proc. IEEE 52, No. 10 (1964).
19. Editorial Summary in International Conversion Equipment Journal 12, No. 1 (1967).
20. N. Kurti refers in Ref. 16 to work done by the Central Research and Engineering Division of the British Insulated Callender's Cables, Ltd.
21. A.D. Appleton, IEE Electronics and Power 14, 114 (1968).
22. W.T. Beall and R.W. Meyerhoff, Union Carbide, Linde Division, Indianapolis, Ind., and H.M. Long, Tonawanda, New York.
23. Linde Aktiengesellschaft, München, West Germany.
24. P. Burnier, Rev. Gen. Elect. 74, 623 (1965).
25. Advertisement by Allis-Chalmers, Physics Today 21, No. 5, 137 (1968).
26. M.V. Mahoney, A.M. Sutton, and C.F. Panati, in Digital Communications Lecture Notes, 2nd Ed. (RCA Institutes, New York, 1967).
27. S. Ramo, J.R. Whinnery, and T. Van Duzer, in Fields and Waves in Communication Electronics (John Wiley & Sons, Inc., New York, 1965).
28. N.S. Nahman, IRE Trans. on Circuit Theory CT-9, 144 (1962).
29. W.D. McGaa, Jr. and N.S. Nahman, J. Appl. Phys. 39, 2592 (1968).
30. S.P. Morgan and J.A. Young, Bell Syst. Tech. Journal 35, 1347 (1956).

# · SUPERCONDUCTING TRANSMISSION LINES - COMMUNICATION AND POWER\*

N.S. Nahman  
Radio Standards Engineering Division  
National Bureau of Standards  
Boulder, Colorado

## INTRODUCTION

During the past few years interest has grown in the application of superconductors to electrical power transmission lines and other power apparatus.<sup>1-11</sup> The probability of doing so seems very remote to the majority of the industrial and scientific community. However, there are those of us who believe that such large scale superconductive systems are practical and, when realized, will provide technical and economic advantages.<sup>12-17</sup> Make no mistake about the motive for utilizing superconductors; simply put, the economic payoff would be very great.

The purpose of this paper is to strongly declare that a superconductive power transmission system would (and should) be much more than a power transmission line. Considering the capital investment required to build such a system it is then imperative that the maximum economic benefit be derived from the system. Accordingly it is my contention that the subject under discussion is not a superconductive power line, but a much more encompassing system, a "Superconductive Transmission System" (SCTS).

As seen through my mind's eye, the SCTS would consist of four subsystems:

1. Data Processing Subsystem.
2. Cryogenic Liquid Transport Subsystem.
3. Electrical Power Transmission Subsystem.
4. Electrical Communication Subsystem.

Consequently, it is apparent that my vision is actually concerned with four systems and not just one system. The four subsystems have a common characteristic within the perspective of our technologically based society: each subsystem may span great distances. Furthermore, operation of such a multifaceted utility complex would require very effective interaction between the constituent utilities. There may be some raised eyebrows as a result of my calling a data processing system "a utility," but if everybody in the cities of tomorrow is going to have access to a computer, then an extensive time share system of the magnitude of a utility will be necessary.

With the preceding comments serving as an introduction, my remarks will now center upon some aspects of the four subsystems. It is my intention to discuss in greater detail that which I know something about. Accordingly, I will not say much about the data processing subsystem or the cryogenic fluid transport subsystem. Also I will deal in somewhat of a broader sense with the power transmission subsystem in order to clearly establish in your minds that dc power transmission is presently a reality and that superconductive dc power transmission is only an extension to superconductivity and not to dc. Finally, I will discuss in greater detail the superconductive communication transmission subsystem as I know more about such systems by virtue of experience and training.

---

\* The mention in this paper of trade names or proprietary products is not to be construed as an endorsement of these items by the National Bureau of Standards.

## DATA PROCESSING SUBSYSTEM

The data processing subsystem would have two functions: an internal one and an external one. Internally, the data processing subsystem would provide data processing services to the other three subsystems in order to execute the required instrumentation and control for each subsystem. Externally, the data processing subsystem could provide time share computer facilities for subscribers along the length of the SCTS.

The data processing subsystem could be implemented by using cryogenic digital and analog electronic components which possess inherently large packing densities.<sup>18</sup> These brief remarks comprise my discussion of the data processing subsystem. I will now briefly discuss the cryogenic liquid transfer subsystem.

## CRYOGENIC LIQUID TRANSPORT SUBSYSTEM

Many industrial and research centers require cryogenic fluids for their operations. Accordingly, a SCTS connecting such centers could provide a means of transporting cryogenic fluids to the individual centers. For example, if a SCTS passed through the helium producing fields in Kansas, liquid helium could be introduced into the SCTS at the helium production source and then be distributed by transmission through the SCTS network. The cryogenic and gas transport industries could no doubt think of many ingenious ways to utilize the SCTS. In any event my brief remarks may serve as stimuli to their thoughts. Next, I will discuss the status of superconductive power transmission.

## POWER TRANSMISSION SUBSYSTEM

A superconducting wire can transmit a dc current without losses or an ac current with an extremely small loss. At first glance, the complete absence of losses in the dc case engenders some attractive possibilities for dc power transmission, while the existence of ac losses (due to electrical and mechanical forces) apparently decreases the practicality of ac power transmission. That such is the case, stems from consideration of refrigeration costs. Personally, I do not believe that ac power transmission systems are to be ruled out. However, in terms of our present-day lack of experience with really large-scale superconductive systems, it is probably prudent to concentrate our present speculation on dc power systems. Present-day developments and future experience will no doubt engender ac systems.<sup>5</sup>

Dc transmission of large amounts of electrical power is a reality.<sup>19</sup> Today, there exist roughly six systems in operation ranging over distances of 72 to 750 miles, operating in the voltage range of 100 kV to 800 kV, and transmitting powers in the range of 30 MW to 750 MW. Also, there is a similar number of systems under design and construction which will cover distances of 25 to 875 miles, operate in the voltage range of 130 kV to 800 kV, and transmit powers ranging from 78 MW to 1440 MW. The input and output terminals of these dc systems are mercury-arc grid controlled rectifiers which convert and invert ac to dc and dc to ac, respectively. Consequently, the idea of using superconductive dc power transmission is clearly an extension of technology only to superconductive systems, not to dc systems.

As I mentioned earlier, considerable analytical work has been done on the possibilities for superconducting power transmission. In many of the papers cited, economic data were presented which indicated when superconducting power transmission would be economically favorable. I will not go into any specific cases; but I should point out that some of the papers developed economic data on transmission systems having capacities which could be fully utilized today or in the next few years. For example,

Norris and Swift<sup>15</sup> discussed transmitting 750 MW at 100 kV dc and 750 MVA at 33 kV ac. On the other hand, Garwin and Matisoff<sup>14</sup> envisioned economically transmitting very large amounts of power, 100 GW at 200 kV dc over distances of 1000 km.

Superconductive power transmission studies have entered the experimental phase. In England, an experimental line has been constructed and operated.<sup>20</sup> Also, a 3000 hp superconductive motor is being built.<sup>21</sup> In the U.S.A., Meyerhoff, Beall and Long<sup>22</sup> have designed and are to construct a 20 ft section of niobium coaxial power line. A 60 ft section of a superconductive power line is being built in West Germany.<sup>23</sup> In France, and in the U.S.A., liquid hydrogen cooled (20°K) cryogenic power apparatus is being designed and constructed.<sup>8,24</sup> Also, power apparatus manufacturers are recruiting engineers and scientists to work on the development of superconductive power apparatus.<sup>25</sup> Consequently, it is evident that superconductive power systems are already with us in a limited sense. The remainder of my comments will be concerned with superconductive electrical communication transmission.

### ELECTRICAL COMMUNICATION SUBSYSTEM

First of all, I would like to briefly describe a fairly general model of a communication system.<sup>26</sup> By my doing so, you will have some idea of how communication electrical engineers view a communication system. The model is general enough to characterize all forms of wired or radio communications. The system consists of a serial chain of elements beginning with a data source and ending with a data processing and storage element. Information flows unidirectionally through the system in serial order starting from element No. 1 and ending at element No. 7; the elements are as follows:

1. Data Source. A system which produces the information to be transmitted.
2. Encoder. A system which transforms the data into a favorable form which insures successful transmission through the noisy transmission channel.
3. Modulator and Transmitter. A system which converts the encoded information into a signal form capable of passing through the transmission channel.
4. Transmission Channel. A noisy system or physical medium through which the signal flows. Noise is inherent in any transmission channel and arises from natural physical causes or unnatural (man-made) causes.
5. Receiver and Demodulator. A system which extracts the signal information from the noisy output of the transmission channel and converts the extracted information into a form suitable for the decoding operation.
6. Decoder. A system which converts the encoded information into some form for data storage and processing.
7. Data Storage and Processing. The recipient system requiring the information generated by the Data Source (element No. 1).

Upon considering the various elements comprising a communication system, it is evident that a superconductive one could employ a large amount of integrated circuit cryoelectronics. Of particular interest to me is the utilization of the superconductive coaxial line as the physical transmission channel. Other electrical waveguides such as hollow metal pipes for microwaves or light pipes for laser wavelengths could also be employed with improved characteristics compared to their room temperature counterparts. However, the coaxial line can be miniaturized and transmit a baseband signal whose frequency components extend upward from dc.

The baseband signal propagates in the TEM electromagnetic mode which is the ordinary two-conductor transmission line mode (as contrasted to single conductor modes).

The TEM mode can exist in any two-conductor transmission line and extremely great baseband bandwidths may be realized with the coaxial geometry. In a lossless coaxial line waves of any frequency are propagated without loss. Above a certain frequency undesirable higher order modes (single conductor modes) can propagate.<sup>27</sup> Consequently, for a given coaxial line the upper operating frequency is usually chosen to be less than that of the lowest frequency higher order mode. As the diameter of the coaxial line is decreased, the higher order mode cutoff frequency is increased; for example in a 50  $\Omega$  coaxial line having a relative dielectric constant of approximately 2.0 and a 0.03 in. o.d., the higher order mode cutoff frequency is approximately 100 GHz.

Before summarizing the results achieved to date with miniature superconductive coaxial lines, I am going to make a few remarks about cryogenic normally conducting coaxial lines. Depending upon the metal purity and structural order (electronic mean free path length) the classical or anomalous skin effect may occur. The anomalous skin effect strongly occurs when the electronic mean free path is greater than the electromagnetic field penetration (skin) depth. For short (impure metal) or long (pure metal) electronic mean free paths the high frequency complex attenuation of the coaxial line will follow an  $s^{1/2}$  or an  $s^{2/3}$  variation, respectively, where  $s$  is the complex frequency variable.<sup>28</sup> Furthermore, the anomalous skin effect produces a greater attenuation than would be expected (classical theory) from the increased dc metal conductivity produced by the low temperature environment. Typically, for copper having a 4.2°K to 293°K conductivity ratio of 400, one would expect a 10 GHz classical attenuation reduction of 20 while in practice the anomalous skin effect may yield an attenuation reduction of 5.

Because the high frequency losses in a superconductor are dependent upon the normal state of electronic mean free path and decrease with increasing mean free path, the superconductor purity and structural regularity strongly affect the surface impedance frequency dependence. Experimental data from superconductive coaxial transmission lines have been compared with the two-fluid superconductivity theory.<sup>29</sup> The results suggest that the particular superconductor samples employed possessed relatively short normal state electronic mean free paths. Typical transmission line parameters were as follows: 50  $\Omega$  characteristic impedance, polytetrafluoroethylene dielectric, Nb 0.015 in. diam center conductor, Pb 0.045 in. i.d. outer conductor, and 1360 ft length. In terms of the two-fluid model, at 8 GHz, the metal losses would produce a transmission attenuation of 35 dB or 0.7 dB for a purely classical normal component or a purely anomalous normal component, respectively. The observed attenuation was 10 dB. Consequently, improvements in the superconductor metallurgy should provide an attenuation approaching that of the anomalous limit. The effect of the normal state electronic mean free path was strikingly seen in the time domain response curves. For a long mean free path the step response rose abruptly with a 10-90% rise time of about 5 psec. For a short mean free path, the step response rose relatively slowly reaching the 80% level in about 30 psec.

Using the two-fluid model curves,<sup>29</sup> the transmission characteristics of a miniature superconductive line can be compared against that of a room temperature 2 in. i.d. corrugated circular waveguide. Using a circular waveguide operating frequency of 56 GHz in the TE<sub>01</sub> mode, one obtains an attenuation of 1.5 dB/mile,<sup>30</sup> with perhaps a bandwidth of 20% of the operating frequency, 11.2 GHz. A 50  $\Omega$  superconductive coaxial line made of the same materials mentioned above and having an 0.061 in. i.d. outer conductor would have a higher order mode cutoff frequency of 56 GHz. The lowest temperature listed in the two-fluid model curves is 2.3°K. Upon using the anomalous limit at 2.3°K, the superconductive line attenuation would be 3.5 dB/mile at 56 GHz. Consequently, it is seen that the superconductive line provides a baseband bandwidth of greater than 50 GHz while the circular waveguide yields a bandpass bandwidth of greater than 10 GHz centered at 56 GHz; the attenuation values are comparable. Also, because of its baseband characteristic, the miniature superconductive coaxial line is

capable of transmitting baseband digital information at very rapid rates. Therefore, it is evident that such miniature lines could provide large bandwidth transmission channels for use in a SCTS.

#### SUMMARY

It has been declared that a superconductive power transmission line system could be much more than just a power transmission line, but rather a composite of four subsystems: (1) data processing, (2) cryogenic liquid transport, (3) electrical power transmission, and (4) electrical communication.

At present, dc power transmission in superconducting cables appears to be economically feasible. However, ac transmission with its associated joule heating losses is not to be discounted. Improvements in cryogenic refrigeration, operating experience, and technical convenience will no doubt engender ac systems.

Cryoelectronics has a great potential for implementing the various subsystem electronic systems. The cryoelectronics components developed to date have demonstrated that the electronic functions necessary for the various subsystems can be implemented with such components. The spectrum of components includes active analog elements, digital elements, transmission lines, waveguides and large-scale digital systems.

Finally, the idea of transporting cryogenic liquids through a SCTS network offers some intriguing possibilities for the transportation of gases. Not only does this suggest transporting the usual cryogenic liquids, but also other liquefied gases.

#### REFERENCES

1. R. McFee, *Electrical Engineering* 81, No. 2, 122 (1962).
2. M. Carruthers, *Engineering* 196, No. 5085, 420 (1963).
3. D. Atherton, *Elec. News and Eng.*, 74, No. 11, 52 (1965).
4. K.J.R. Wilkinson, *Proc. IEE (London)* 113, 1509 (1966).
5. D.A. Swift, paper presented at the 12th Intern. Congress of Refrigeration, Madrid, Spain, 1967, Sec. 1.46, 1-11.
6. D.R. Edwards and R.J. Slaughter, *Electrical Times* (Aug. 3, 1967), p. 166.
7. E.C. Rogers and D.R. Edwards, *Electrical Review* (Sept. 8, 1967), p. 348.
8. S. Neal, paper presented at the American Power Conference, 30th Annual Meeting, Chicago, Ill., 1968.
9. N. Kurti, *New Scientist* 36, No. 574, 604 (1967).
10. M. Styrikovitch, *Nauka i Zhizn*, No. 11 (1967).
11. V.L. Gani, M.Sc. Thesis, *Electrical Engineering Dept.*, University of Colorado, Boulder, Colo. (1968).
12. W.F. Gauster, D.C. Freeman, and H.M. Long, Paper No. 56 in Proc. World Power Conference (1964).
13. V.S. Okolotin, *Energetika*, No. 10, 35 (1965).
14. R.L. Garwin and J. Matisoo, *Proc. IEEE* 55, 538 (1967).
15. W.T. Norris and D.A. Swift, *Elec. World* 168, No. 4 (July 1967).
16. N. Kurti, paper presented at the 12th Intern. Congress of Refrigeration, Madrid, Spain, 1967, Pl.a, 1-24.

17. A. Kusko, IEEE Spectrum 5, No. 4, 75 (1968).
18. Special Issue on Cryogenic Electronics, R.W. Schmitt, Ed., Proc. IEEE 52, No. 10 (1964).
19. Editorial Summary in International Conversion Equipment Journal 12, No. 1 (1967).
20. N. Kurti refers in Ref. 16 to work done by the Central Research and Engineering Division of the British Insulated Callender's Cables, Ltd.
21. A.D. Appleton, IEE Electronics and Power 14, 114 (1968).
22. W.T. Beall and R.W. Meyerhoff, Union Carbide, Linde Division, Indianapolis, Ind., and H.M. Long, Tonawanda, New York.
23. Linde Aktiengesellschaft, München, West Germany.
24. P. Burnier, Rev. Gen. Elect. 74, 623 (1965).
25. Advertisement by Allis-Chalmers, Physics Today 21, No. 5, 137 (1968).
26. M.V. Mahoney, A.M. Sutton, and C.F. Panati, in Digital Communications Lecture Notes, 2nd Ed. (RCA Institutes, New York, 1967).
27. S. Ramo, J.R. Whinnery, and T. Van Duzer, in Fields and Waves in Communication Electronics (John Wiley & Sons, Inc., New York, 1965).
28. N.S. Nahman, IRE Trans. on Circuit Theory CT-9, 144 (1962).
29. W.D. McGaa, Jr. and N.S. Nahman, J. Appl. Phys. 39, 2592 (1968).
30. S.P. Morgan and J.A. Young, Bell Syst. Tech. Journal 35, 1347 (1956).

## RECENT DEVELOPMENTS IN SUPERCONDUCTIVITY IN JAPAN

The Committee of Superconducting Magnets  
of the Institute of Electrical Engineers of Japan

Presented by

N. Takano  
Tokyo Shibaura Electric Co., Ltd.  
Komukai, Kawasaki, Japan

Recent developments in Japan of the study on 1) superconducting wires, 2) magnets, 3) other devices, 4) cool down techniques for the magnets, and 5) some aspects of future projects, are described in this paper.

### I. SUPERCONDUCTING WIRES

In Japan the study on superconducting wires was started in 1962, and since 1966 several kinds of superconducting wires have been developed in many research laboratories.

#### Alloys

The superconducting wires developed in Japan have the interesting feature that most of them are ternary alloys with niobium base material. Some typical ternary alloys are NbZrTi, NbTiHf, and TiNbTa. Each of these have better  $H_c$ ,  $I_c$  characteristics than the usual binary alloys such as NbTi or NbZr.

Binary alloys have also been investigated. Several of these are NbTa, NbZr, NbTi, NbMo, TaRe, V-Cr, V-Ti, InPb, SnIn, ZnMn and ZnCd. These alloys are not all necessarily being developed to achieve good characteristics for wire for superconducting magnets. Some are for the study of basic phenomena and some are to develop materials which have higher critical temperatures.

#### Compounds

Many basic studies on the superconducting compound wires have been carried out but no practical wires have yet been developed. To get basic data, Nb<sub>3</sub>Sn, NbB<sub>2</sub>, NbMoB<sub>2</sub>, NbS<sub>2</sub>, NbN, Nb<sub>3</sub>V, V<sub>3</sub>Ga, etc. are being studied. The last compound, especially, V<sub>3</sub>Ga, is being examined with keen interest as a possible practical material that can be produced on an industrial scale. The V<sub>3</sub>Ga is made into a tape with the continuous diffusion method and has a critical field of about 200 kG at the current density of  $10^5$  A/cm<sup>2</sup>. This is a value higher than that obtained with other materials such as Nb<sub>3</sub>Sn.

#### Composite Conductors

Large current conductors for the MHD saddle-type magnets and high energy physics magnets have been studied. Techniques of embedding a number of superconductors into normal metals such as copper or aluminum are being studied.

The ratio of the cross section of superconductors to that of normal metal and the contact resistance between these two are studied as part of the development of the optimum stabilized superconductors.



Some results of these studies are being made use of in the National R&D Program for the MHD generator and at the present time the construction of a saddle-type magnet is in progress.

## II. MAGNETS

In Japan the development of superconducting magnets is being carried out for MHD generators, for high energy physics, and for other applications. The first type of magnets have saddle shape configurations, so that they can be used as the field windings of electrical machines such as dc motors or alternating machines.

### Saddle-Type Magnets

The saddle-type superconducting magnets are being developed as part of the National R&D Program for MHD generators planned by the Agency of Industrial Sciences and Technology. The parameters of one of these magnets which has already been constructed and tested are given in Table I. This magnet is only a prototype for the MHD generators, but another magnet which is to be combined with an experimental generator is now under construction. This second magnet is to be set in a Dewar which has a room temperature bore at the center. The magnet has an inner diameter of 38 cm and is to produce the field strength of 45 kG at the center of the bore. This magnet system is to be completed by early 1969. The details of this magnet are listed in Table II.

TABLE I  
Details of a Model of Saddle-Type Magnet

	<u>Tested</u>	<u>Under Test</u>
Inner diameter	33 cm	33 cm
Outer diameter	43.5 cm	57 cm
Coil length	91.3 cm	91.3 cm
Weight	600 kg	1200 kg
Stored energy	110 kJ	-
Field strength at the center of bore	13.8 kG	16 kG
Current	695 A	-

TABLE II  
Details of Saddle-Type Magnet for MHD Generator

Inner diameter	38 cm
Room temperature bore	25 cm
Coil length	190 cm
Field strength at the center of bore	45 kG
Stored energy	6 MJ
Current	585 + 540 A
Weight	6 ton

## High Energy Physics Magnets

For preliminary studies for high energy physics magnets such as bubble chamber or beam focusing magnets, many small magnets wound using the stabilized strip conductors are being tested in many research laboratories. For instance, one magnet consists of a Helmholtz pair which have an inner diameter of 5 cm, an outer diameter of 20 cm, and a length per coil of about 20 cm. The gap between two coils can be changed to adjust the field distribution. The field strength at the center of the bore of one coil is about 40 kG. Another example is a pancake coil that has an inner diameter of 8 cm, a length of about 63 cm, and a field strength of 56 kG at the center.

A cusp magnet, which can confine the high temperature plasma produced by laser rays, is also being tested. This magnet has an inner diameter of 1.5 cm, an outer diameter of 9 cm, a length of 5 cm, and can produce a field strength of 40 kG at the center of one coil.

## Various Magnets for Experiments

A number of magnets have been constructed and used for the study of solid state physics. In general, superconducting alloy wires are used up to about 60 kG or so and higher magnetic fields are generated by Nb<sub>3</sub>Sn tape-wound magnets. The highest magnetic field produced by superconductors in Japan so far is about 100 kG.

### III. OTHER DEVICES

To reduce the heat input through large current power leads from room temperature to low temperature devices, flux pumps are also being studied. At present no practical flux pumps have been constructed, but to get useful data for the construction of more effective flux pumps, a number of basic data have been taken as part of the National R&D Program for the previously mentioned MHD generator.

Two types of flux pumps have been studied. One is a moving magnet type and the other is a rectifier type like that developed by Dr. Buchhold. One of the first type was used to supply a current of about 200 A to a small magnet, but the output voltage of this type of flux pump is very small. Therefore, efforts are now focused on how to increase the output voltage as well as to increase the current capacity. The second type of rectifier has not generated a current, but the dynamic performance needed for a complete pump has been tested successfully with a half wave rectifier circuit. This flux pump will have an output voltage of about 10 mV and the current of about 500 A.

### IV. MAGNET COOL DOWN TECHNIQUES

Liquid helium is so expensive in Japan that the techniques used to cool the large superconducting magnets from room temperature to 4.2°K are very important from an economic point of view.

For small superconducting magnets, precooled by liquid nitrogen before using liquid helium is widely practiced. But this method is not appropriate for the cool down of larger magnets because it causes contamination of helium gas. Therefore, cool down from room temperature to slightly above liquid helium temperature is generally accomplished with a refrigerator.

The previously-mentioned saddle-type magnet tested at the Electrotechnical Laboratory of the Agency of Industrial Sciences and Technology was cooled to 47°K by a refrigerator and then liquid helium was transferred.

The cool down process combined with the refrigeration system in one research laboratory has been analyzed. The process is as follows: First, the magnet is cooled down to about 90°K by helium gas which is cooled by liquid nitrogen. The magnet is then cooled down by a helium refrigerator from 90°K to about 20°K, after which liquid helium is transferred from a liquid helium storage Dewar. In the analysis, the cool down time is calculated using several parameters which include the weight of the magnet, the heat input to the magnet, the efficiency of heat transfer between the magnet and the cooling fluid, and the power of the refrigeration system. The results of this calculation are represented in graphical charts to estimate the cool down time immediately.

## V. FUTURE PLANS

It is difficult to discuss what fields have opened for the applications of superconductivity.

Considering, however, the extremely rapid advances in superconducting technologies since the discovery of practical superconducting wires in 1957, many devices may be improved by making use of new knowledge of various superconducting phenomena to be obtained in the near future. As seen in the development of V<sub>3</sub>Ga wire, for example, efforts are still being continued to develop new materials which are able to produce still higher magnetic fields. If it is to be easy to generate high magnetic fields over 200 kG by a superconducting magnet, a number of developments must come in the field of engineering as well as in basic science.

Applications for the ac devices are considered to be just at the starting point as compared with dc devices, although the basic research has long been done.

If superconducting materials applicable for ac devices are developed, electrical machines will occupy an important position in future superconducting applications.

Thus, the superconducting technology which has advanced from small superconducting magnets to the present large size magnets is now gradually changing into the technology that is useful in applications for industrial equipment such as generators, motors, transmission lines, and so on.

## THE CASE FOR FLUX PUMPS AND SOME OF THEIR PROBLEMS

S.L. Wipf  
Atomics International  
A Division of North American Rockwell Corporation  
Canoga Park, California

### I. INTRODUCTION

As an introduction to this morning's session let me recapitulate the principle of flux pumping.

Complete lack of resistance in a closed circuit leads to conservation of magnetic flux linked with it. We see this by writing Faraday's induction law for a closed circuit with inductance  $L_c$ :

$$\frac{d\Phi}{dt} = -V = -RI - d(L_c I)/dt \quad (1)$$

With resistance  $R = 0$ , this integrates to:

$$\Phi + L_c I = \text{const.} \quad (2)$$

The superconducting circuit meets any change in external flux  $\Phi$  with a corresponding change in current to fulfill Eq. (2). A flux pump is a device which can change the constant in Eq. (2). Figure 1 shows the flux pump principle. Flux from a small permanent magnet does not enter a superconducting circuit (Fig. 1a) until a switch is opened and closed again (Fig. 1b). On removal of the magnet the current  $\Delta I$  will then preserve the flux (Fig. 1c). To accumulate more current by repetition of this process, care is taken that the previously induced current is not lost during switching. One provides a bypass which itself has a switch (Fig. 1d). To make a pump practical one has to avoid mechanical switches (although for small currents they are feasible and have certain advantages<sup>1</sup>). It is sufficient, instead, to introduce some resistance by locally destroying superconductivity. This can be done by exceeding the critical temperature of the superconductor, using a heater as in some of the earliest pumps,<sup>2,3</sup> or else by exceeding the critical field. This last approach, magnetic switching, is the most widely used. In its simplest version the same magnet which is used for pumping (the exciting or energizing magnet) is also used for switching because close to the poles the field strength easily exceeds the critical field of superconductors such as lead or niobium (with critical fields of 550 G or  $\sim 3000$  G at  $4.2^\circ\text{K}$ ). The magnetic switching method also allows the replacement of the loop in Fig. 1d by a plate in Fig. 1e. The high field right in front of the magnet pole will form a normal zone containing the flux and by moving this zone across the sheet — it follows the magnet —

- 
1. I.D. McFarlane, *Cryogenics* 7, 297 (1967); see also: *Product Engineering*, Feb. 27, 1968, p. 27.
  2. A.F. Hildebrandt, D.D. Elleman, F.C. Whitmore, and R. Simpkins, *J. Appl. Phys.* 33 2376 (1962); D.D. Elleman and A.F. Hildebrandt, in *Proc. 8th Intern. Conf. Low Temperature Physics*, London, 1962 (Butterworth, London, 1963), p. 332.
  3. H.L. Laquer, *Cryogenics* 3, 27 (1963).

the same function as in Fig. 1d is performed.<sup>4</sup> The arrangement is, of course, such that the removal of the magnet from the circuit occurs without interrupting the superconductivity; the circuit (other than the loop or the plate) may be located far away from the pole so that the critical field of the circuit superconductor is nowhere reached and usually it is made out of high field material anyway.

Flux pumps can be operated mechanically (Fig. 1e) or without moving parts as in Fig. 2 where a "loop" and a "plate" arrangement is shown. It is practical to distinguish between "moving magnetic field" type pumps of which this plate pump is an example, as well as that of Fig. 1, and "rectifier" type pumps, illustrated by the upper example of Fig. 2. The next paper (Rhodenizer) will detail the rectifier pump which has been developed by GE<sup>5</sup> to a high perfection. The present paper will emphasize the moving magnetic field type.

## II. THE CASE FOR FLUX PUMPS

Once the idea is presented it seems to be obvious that one should use flux pumps as soon as a current source, or power, is needed in liquid helium. The only viable alternative is current leads from room temperature into the cryogenic environment. Lubell will compare the two.

One might think that the dc transformer suggested by Giaever<sup>6</sup> could provide another alternative. This device is akin to the flux pump illustrated in Fig. 1e. We imagine the plate seen there, which is the secondary, to be very thin and to be sandwiched together with another very thin plate or film, which is the primary, with an insulating oxide layer in between. All thicknesses have to be small compared to the spacing of fluxoids which will thread both films at right angle and which may be produced by a stationary field which is smaller than the critical field. The fluxoids are set into motion by the Lorentz force of a current (parallel to the secondary current to be induced) passed through the primary film. Due to the closeness of the two films the identical fluxoids which move through the primary are dragged through the secondary and thus perform the same function as the mechanically moved exciting magnets of the flux pump. To date this device has not replaced the flux pump, however, because the fluxoids are "sheared off" and remain stationary in the secondary under the influence of both the pinning forces and the Lorentz force of a rather small secondary current.

Why do we have to plead a case for flux pumps? Why does one who favors them find himself in the role of a salesman or on the defensive? It can hardly be ignorance for there have been good reviews by the groups at Philips<sup>7</sup> and Leiden.<sup>8</sup> It may be fear of disadvantages which have perhaps not been spelled out too clearly. If in this morning's session we manage to dispel some of these fears we may be successful in our plea.

---

4. J. Volger and P.S. Admiraal, Phys. Letters 2, 257 (1962); also in Philips Techn. Rev. 25, 16 (1963).

5. T.A. Buchhold, Cryogenics 4, 212 (1964); T.A. Buchhold, in Pure and Applied Cryogenics (Pergamon Press, 1966), Vol. 6, p. 529.

6. I. Giaever, Phys. Rev. Letters 15, 825 (1965), and 16, 460 (1966).

7. J. Van Suchtelen, J. Volger, and D. Van Houwelingen, Cryogenics 5, 256 (1965).

8. H. Van Beelen, Miss A.J.P.T. Arnold, H.A. Sypkens, J.P. Van Braam Houckgeest, R. De Bruyn Ouboter, J.J.M. Beenakker, and K.W. Taconis, Physica 31, 413 (1965).

The following table lists what I consider the advantages and disadvantages of flux pumps (if applicable, the comparison is with conventional power supplies at room temperature and current leads).

<u>Advantages</u>	<u>Disadvantages</u>
Large currents ( $10^4$ - $10^5$ A)	Shielding from ambient fields necessary
Persistent mode when idle	
Forward or backward operation	Protection required
Ideally suited to compensate for small resistive losses in circuit	Losses in liquid helium while operating
Over-all space requirement small (same as with superconducting magnets)	Volume inside cryostat required ( $\sim 50 \text{ cm}^3/\text{W}$ ) therefore small power
Flexible (can operate at several times rated optimum output power at the price of increased losses)	

### III. SOME PROBLEMS

The remainder of this talk will be devoted to the problems as they are encountered in moving magnetic field pumps if one strives to develop a theory or to increase either the efficiency or the ultimate current.

#### Theory

One of the simplest examples of a pump which is in practical use is illustrated in Fig. 3. Its main feature is a normal zone which is moved through a superconducting sheet without ever entering or leaving it. Mathematical treatments of similar arrangements<sup>9-11</sup> do exist and have been tested experimentally<sup>9,10,12</sup> with what one could term semiquantitative success. They produce formulae for the output voltage and for the loss,

$$\text{emf} = n \cdot \omega (P - L_p I_{\text{load}}) \quad (3)$$

$$\text{Loss} = n \cdot \omega L_p I(0)^2 \quad (4)$$

The rotation speed,  $\omega$ , is assumed to be small enough to neglect terms with  $\omega^2$ .  $n$  is the number of poles of the rotor,  $I$  the load current, and  $P$  the flux per normal spot due to the rotor poles.  $L_p$  is an effective inductance, and  $I(0)$  an effective current. In practice these effective quantities are adjustable parameters which cannot be calculated. This considerably spoils the success of the mathematical approach. In fact,

- 
9. S.L. Wipf, in Proc. Intern. Symp. Magnet Technology, Stanford, 1965, p. 615.
  10. D. Van Houwelingen and J. Volger, Philips Res. Rep. 23, 249 (1968).
  11. H. Voigt, Z. Naturforsch. 21a, 510 (1966).
  12. R. Weber, Z. Angew. Phys. 22, 449 (1967).

to be quite honest, this lack of a good theory reflects our poor understanding of what seems to be such a simple process as moving a normal spot across a superconducting sheet.

Let us discuss this process in some more detail. Illustrated in Fig. 4 is a normal zone containing flux  $\Phi$  and moving through a superconducting sheet which carries a load current density. We separate two processes which are indicated by their current patterns. One is the induction of eddy currents within the normal spot. They flow along closed paths, partly within the spot and partly without. Because the size of the eddy currents is proportional to the speed of the spot ( $v = 2\pi r\omega$ ), their over-all contribution to the total voltage and losses of the pump are proportional to  $v^2$  (and higher terms) and have been neglected in the given formulae (3) and (4); eddy currents are reasonably understood and in what follows we shall only consider very low speeds. The other process, which we may call the switching process, takes place in the leading edge of the normal spot (indicated by narrow crosshatching in the figure) where the superconductor is made normal in the presence of a current density  $j$ . The ohmic voltage thus generated will drive the current into an alternate distribution while some of it is dissipated. The corrections to the output voltage and the loss are reflected in Eqs. (3) and (4) and will be discussed a little further. Without the switching process the current increase per pump cycle, as seen in Fig. 1, is  $\Delta I = \Phi/L_c$ . The output voltage, therefore, is given by  $L_c dI/dt = L_c \Delta I \omega = \Phi\omega$ .

The width  $\Delta s$  of the leading edge depends on the time constant of the switching process and it is therefore inversely proportional to the rotation speed. For simplicity we assume that the normal spot is moved in small steps by a distance equal to the width  $\Delta s$  of the leading edge. Also it is assumed that the initial total current in the leading edge is  $I_{e0} = \Delta s \cdot j$ , and further that there is current flow only across the narrow ends of the edge (top and bottom in Fig. 4) and that the resistance of the edge is  $R$ . Unfortunately,  $R$  is not constant and depends on the current as we will discuss later.

The voltage across the leading edge is then,  $RI_e = L_e dI_e/dt$ , where  $L_e$  is the inductance of the alternate current path (which is the short circuit of the edge through the rest of the sheet). We can assume a linear decay of  $I_e$  to zero during each step, which gives an average voltage of  $L_e I_{e0} 2\pi\omega / \Delta s = L_e j 2\pi\omega$ . We can assume that  $j$  is not zero when no load current is flowing and that it has a component which is proportional to the load current; thus,  $j 2\pi = I_0 + k I_{load}$ . The voltage correction becomes  $\omega L_e (I_0 + k I_{load})$  and it is negative (i.e., decreasing  $I_{load}$ ). Comparison with Eq. (3) gives:  $P = \Phi - L_e I_0$ , and  $L_p = k L_e$ .

The loss is obtained similarly. If there are  $N$  steps per cycle ( $N = 2\pi / \Delta s$ ), the loss per cycle becomes  $\frac{1}{2} N L_e I_{e0} dI_e/dt = \frac{1}{2} L_e \omega j^2 (2\pi)^2$ . The total loss is  $\frac{1}{2} \omega L_e \cdot (I_0 + k I_{load})^2$ , and comparison with Eq. (4) gives  $L_p = k L_e$ , and  $I(0) = (I_0 + k I_{load}) / \sqrt{2k}$ . The factor  $1/\sqrt{2k}$  is only a means to keep  $L_p$  in both Eqs. (3) and (4) formally unchanged; this is convenient because one usually obtains the quantities  $P$  and  $L_p$  according to Eq. (3) from measurements of the voltage, and then  $I(0)$  from loss measurements.

A word about the various quantities: we now have  $k$ ,  $L_e$ , and  $I_0$  which we can neither measure directly nor calculate. The accuracy of measuring  $\Phi$  directly is also insufficient to notice the difference between  $P$  and  $\Phi$ . It is useful, however, to have an idea about the formal validity of Eqs. (3) and (4), and we shall see that they can serve as guidelines through the experimental results.

It has already been mentioned that  $R$  depends on current. This becomes clear when the leading edge region is described in more detail. At its outer boundary it adjoins the fully superconducting phase with a resistance of zero; at its inner boundary it may be fully normal with the resistivity at the normal constant value. We have, therefore,

to distinguish two parts in this resistive current carrying region which we have called the leading edge: one is fully normal, the resistivity is constant (magnetoresistance and temperature effects are insignificant), and the currents decay exponentially; the other is in the critical state, the external field is below the upper critical value, but the current density is critical making it resistive. This part we call the critical region. The resistivity in the critical region is rather similar to the dynamical resistivity introduced in the discussion of ac losses.\* It has to be proportional to  $dH/dt$  because of the magnetic diffusion equation; other than that its value is too difficult to calculate.

Critical regions can also be described as regions where magnetic flux moves under the influence of pinning forces. Many problems are easier to visualize by using this concept.

Critical regions are not confined to the leading edge alone, they occur also at the trailing edge of the spot and even in other parts of the pumping sheet. In fact, they do occur wherever the perpendicular field component through the sheet changes with time ( $dH_{\perp}/dt \neq 0$ ) and the total field is less than critical. The leading edge is only different from these other regions in that it also may have a fully normal section which carries current (other than eddy currents).

The situation would be similar if the normal spot were created by exceeding the critical temperature instead of the critical field.<sup>13</sup> Temperature gradients around the edges would then create the critical regions.<sup>14</sup>

Critical regions are always shorted out by alternate current distributions through the fully superconducting parts of the sheet. These distributions, i.e., their inductances, are determined by the flux conservation principle because the sheet with pinning behaves just like a superconducting wire mesh screen trying to conserve the flux through each mesh. To obtain information about critical regions and current distributions one makes field measurements.

In Fig. 5 there is an xy plot of the tangential and radial fields close to the outer surface and at the center of the sheet vs the angular position of the very slowly turning rotor. The sheet consists of a threefold thickness of Nb foil, 0.001 in. thick. This type of pump is illustrated in Fig. 3; the rotor has three wings as illustrated in the insert to Fig. 5. The measured field is a combination of the field due to the rotor, which is given by the zero current line (dashed), and that due to the load current which increases by 450 A per revolution.

A uniform current distribution in the cylindrical sheet would produce zero radial field and a uniform tangential field, somewhat smaller than the increase reflected in the plot (there is a small contribution from the current leads of the circuit). The tangential plot then is not very sensitive to nonuniform distributions, but any contribution to the radial field distribution is entirely due to nonuniformity. The increasing current creates a dip in front of the pole and depresses the front edge while enhancing the back edge of the pole field. An accurate calculation of the current distribution from such field measurements would require still more field profiles near the edges of the sheet, since it is a three-dimensional problem because the rotor is not thick enough to allow a two-dimensional solution. We can guess the current distribution

---

\* See, for example, S.L. Wipf, these Proceedings, p. 511 and p. 683.

13. J.F. Marchand and J. Volger, Phys. Letters 2, 118 (1962).

14. F.A. Otter and P.R. Solomon, Phys. Rev. Letters 16, 681 (1966);  
A.T. Fiory and B. Serin, Phys. Rev. Letters 16, 308 (1966).



vs the angle to be roughly triangular between the poles with the maximum current density (the apex of the triangle) closer to the front edge of the pole and shifting towards the middle with increasing current. On the other hand the critical current density, limited by the field of the poles, would have a flat maximum in the middle between the poles and would be otherwise almost symmetrical. It might then be expected that the triangular current distribution could reach the critical current near its apex, but not near the back edge and not even near the front edge of the poles. That this is indeed so can be read from the radial field plot. We see that the radial component undergoes a change between the poles; this indicates a critical region. This region becomes large and moves towards the middle with increasing current.

Another important effect can be observed in Fig. 5. This effect corresponds to a sudden rearrangement of the current distribution as seen at  $185^\circ$  in the curve relating to the radial distribution for 6000 A; the same and similar effects are seen near  $210^\circ$  in the tangential curves (the difference of  $25^\circ$  in position is the distance of the two Hall probes). We call this an instability and it corresponds to a sudden breakdown of the pinning forces which in many other situations is observed and described as flux jump.

### Efficiency

A typical setup used to measure the losses is illustrated in Fig. 6. The torque transmitted to the shaft is measured at room temperature. Instead of loops as in Fig. 6, we use a sheet of 0.08 mm thick niobium, in triple thickness. The circuit has four turns of 7.4 cm diameter at the center of which a Hall probe measures the current. A simple potentiometer converts the distortion angle of the torsion spring (approximately  $15^\circ/\text{lb in.}$ ) into a voltage which is calibrated and recorded along with the output current vs the rotation angle. (The device shown in Fig. 6 employs visual torque observation.) Such a record is shown in Fig. 7.

We recognize two new features. One is the relaxation angle between zero and full torque, the other the irregular small jumps as the rotation proceeds under full torque while the current increases steadily. These can easily be interpreted as consequences of flux pinning as is illustrated in the accompanying qualitative picture, which shows a pole at rest, and a pole before reaching full torque. Flux pinning occurs between a lower critical field ( $H_{c1}$ ) and an upper critical field ( $H_{c2}$ ), this region being shaded in the picture. It can be seen how the distortion of the flux lines increases the extent of this region, before the flux pattern, which will move with the pole, reaches an equilibrium. Even this equilibrium movement will occur in small jumps due to instabilities caused by the inhomogeneities in the flux pinning strength. The shaded regions adjacent to the moving spot can be identified with the critical regions discussed above.

In Fig. 8 are shown input equilibrium torques measured and plotted in this manner vs  $P$ , in units of joules/rotation ( $1 \text{ J/rot} = 1.59 \times 10^6 \text{ dyn}\cdot\text{cm} = 1.41 \text{ lb}\cdot\text{in.}$ ). Also given is the output  $I\Delta L_{\text{load}}$ , shown as a dashed line, which is obtained from the measured current increase  $\Delta I$  per rotation. This is equivalent to  $\text{emf} \times I \times \Delta t$ , but, in order that eddy current effects can be completely neglected, the experiments are done at a very low speed which is not necessarily constant. This prohibits good emf measurements. The zero current line represents pure loss since there is no output.

There is a marked maximum of the losses between  $1$  and  $2 \times 10^{-4} \text{ V}\cdot\text{sec}$ , followed by a minimum and a gradual increase towards higher values of  $P$ . The average field in front of the poles is also given in Fig. 8 and by comparison it is seen that the maximum occurs between  $1$  and  $3 \text{ kG}$ , i.e., below the upper critical field. This means that there is no properly normal zone developed at the center of the pumping spot; the entire spot pins the flux, hence the big loss. Above  $3 \text{ kG}$  there is a normal zone, the

pinning area is only at the edges of the spot and the losses are smaller. Another way of saying the same thing is: below  $H_{c2}$  the resistance in the spot has to be created entirely by exceeding the critical current locally which is done by induction from the moving pole pieces, i.e., by the distortion of the flux pattern.

The input increases with the load current but now there is an output which according to Eq. (3) is proportional to  $IP$  (given as thin line in Fig. 8a) minus  $L_p I^2$ , with  $L_p$  being the effective inductance of the current path around the spot. From both the 1600 A and 3200 A results one obtains  $L_p = (3.75 \pm 0.02) \times 10^{-8}$  H. We further notice the current limit for low  $P$  values, when  $P = L_p I$  and the emf becomes zero. The current limit for high values of  $P$  can have various origins as seen later. This pump reached a maximum current of 5000 A at about 0.2 mV·sec for  $P$ .

The results for the power efficiency, which is the ratio of output to input, is given in Fig. 8b. One is usually interested in the total energy efficiency (total energy input/total energy stored in the circuit), and with the efficiency being zero for zero current, this value is considerably lower. In the best case, it is between 20 and 30% for this pump.

By subtracting the output from the input one obtains the losses. In discussing these we try using Eq. (4) and obtain first the effective  $I(0)$  for the zero current losses which has values between 4500 A for the maximum loss and 3100 A for the minimum. Adding to these values the actual transport current, 1600 A or 3200 A respectively, and using again Eq. (4) gives calculated values which are higher than the measured ones. The differences are plotted in Fig. 8c. The result is not surprising and indicates that the current density around the spot represents now part of the load current, while under zero current conditions it was purely induced without being much different as such. It is also interesting to note that the relaxation angle, given in Fig. 8e together with an outline of the rotor, has its maximum where the measured loss is largest relative to the calculated loss (maximum in the loss difference curves Fig. 8c). If one presumes that with the rotor relaxed, the transport current is more or less uniformly distributed, then the movement over the relaxation angle produces the nonuniformity discussed earlier and with it the enlarged extended critical regions.

Here another observation may be made relating to the torque. After unwinding through the full relaxation angle, the rotor will either come to rest at zero torque and will need a smaller torque in the opposite direction to drive the pump backwards, or, if the current is high enough, the rotor will continue unwinding with a small steady torque remaining until at a lower current this torque becomes zero. If, in this latter case, the unwinding torque is made zero,  $\omega$  will be limited by eddy current losses. This spontaneous unwinding, or operation of the pump as a motor, is observed for  $0.2 < P < 0.5$  mV·sec and for currents above 900 A.

Another way of discussing the losses would be to take the zero current loss as a pinning loss in addition to any current switching losses calculated as  $L_p I^2$ . After subtracting both the zero current loss and the switching loss there is still a fairly large loss left which would be interpreted as coming from increased critical regions (see Fig. 8d). The large relaxation angles would correspond to this increase in critical regions.

Neither of the two ways of looking at the losses is very satisfactory and this illustrates very well the shortcomings of the simple theory using only two parameters  $L_p$  and  $I(0)$ . This is, perhaps, even better seen when one tries to locate the regions where the losses actually occur. Such information can be extracted from field plots as given in Fig. 5. Figure 9 gives a complete field plot constructed from radial and tangential components and further indicates the places where the flux density changes in fields below 3 kG and, consequently, where there are losses. These are the places where the critical current is exceeded or, equivalently, where the flux moves against pinning forces.

This discussion suggests the principles for designing pumps of higher efficiency. To reduce the losses one has to reduce the area of critical regions surrounding a spot, and to increase the output one has to increase  $P$ . A rotor with a minimum number of large poles (usually two) and a good flux return path are suggested.

Such pumps have been built. Lubell will mention an example with a measured total energy efficiency of 60%.<sup>15</sup>

There is no reason why, with some development effort directed towards improving the rotating field pattern by shaping the rotor poles and the flux return path, an optimal efficiency could not be reached which is close to its theoretical limit. The term optimal is used to indicate that the efficiency would probably depend on current level, power output, and sense of rotation. The question is only whether the increased complexity and sophistication are a fair exchange for a saving in liquid helium, and the answer may depend on economic decisions.

### Ultimate Current

The pumps of higher efficiency generally use iron as a good flux return path mainly to increase  $P$ . This also increases  $L_p$  in Eq. (3) and therefore reduces the maximum current reached:  $I_{\max} = P/L_p$ . The pump mentioned in the last paragraph has a current limit of about 2500 A. Van Houwelingen and Volger<sup>10</sup> used six similarly designed pumps in parallel to produce a record of 12 800 A. The problem we want to discuss is how do we design a single pump to give a large current?

The pump used for the experiments described below is illustrated in Fig. 10. It has a corrugated sheet of 0.001 in. thick Nb foil. The corrugations which provide a large contact area with liquid helium are about 1.5 mm deep and number an average of 20 per centimeter.

At first we focus on the effective  $L_p$ . From Eq. (4) it can be seen that  $L_p$  is associated with the energy lost in switching the transport current from the front of the spot to the back, but, from Eq. (3), it can be interpreted as describing the flux due to the transport current and linked with the spot in opposition to the active pumping flux  $P$ . If this flux,  $L_p I$ , becomes equal to  $P$ , the pumping stops because the net flux linked with the moving spot is zero. That this second view is more adequate for the present problem is demonstrated in a comparison of the measured effective  $L_p$  with the calculated  $L_p$  of the path with the smallest inductance around the spot. Such values are found in Fig. 11 which also illustrates the dependence of  $L_p$  on the geometry of the rotor. The scale of the rotors and pole faces is indicated in the figure, the thickness of the poles being 1.2 cm. The smallest inductance is calculated for a loop of wire about 2 mm thick (roughly the thickness of the corrugated sheet) which surrounds the pole face area. Taking a thinner wire would increase the inductance because of the higher field at the surface of the wire and taking a thicker wire increases it also because the loop becomes bigger if the central hole stays the same. For similar reasons a wider portion of the sheet surrounding the spot also has a larger inductance.<sup>16</sup> It is seen that the measured effective  $L_p$  values are an order of magnitude smaller than the calculated minimum inductances while the ratios between the three are comparable in both groups and also similar to the ratios of the pole face areas (0.44, 0.64; 1.24 cm<sup>2</sup> for the 8, 4, and 3 pole rotor).

---

15. M.S. Lubell and S.L. Wipf, in Advances in Cryogenic Engineering (Plenum Press, 1968), Vol. 13, p. 150.

16. F.W. Grover, Inductance Calculations (Van Nostrand, 1946; Dover, 1962).

These results imply good pump performances up to limiting currents of the order of  $10^5$  A, taking  $P$  of the order of  $10^{-4}$  V.sec, if the pumping sheet and the circuit are capable of carrying such currents. If Nb is taken as a pump sheet then generally a current density of approximately  $8 \times 10^4$  A/cm<sup>2</sup> can be expected in a field of 1 kG perpendicular to the sheet, and about half this value if the field is 2 kG. Above 3 kG the performance drops rapidly. This experience agrees very well with the average published current densities of cold-worked Nb.<sup>17</sup> Circuits from commercial high field superconductors, stabilized by copper, can easily be dimensioned to take any required current. Connections to the sheet are made by spot welding between the superconducting materials, and superconducting joint currents in excess of 100 A per spotweld are quite common.

Using the three rotors of Fig. 11 (and other rotors) in the pump of Fig. 10, whose sheet and circuit are capable of currents exceeding 20 000 A, a new performance limiting phenomenon is experienced as was already observed as shown in Fig. 5 and has been described as an instability. It is a sudden breakdown and rearrangement of the current distribution in the sheet and usually happens at a current density which would correspond to a surface power density of 2 W/cm<sup>2</sup> if the sheet were normal. It is tempting to associate this current density level with the criterion for what has been described as enthalpy stabilization<sup>18</sup>; the evidence so far is too tenuous to construct a definite connection. For the corrugated Nb sheet used here and described above, this current level is at about 6000 A. In Fig. 12 are seen examples of current and voltage traces vs time for each of the three rotors at a constant low rotation speed (the 8-pole trace and the beginning of the 3-pole trace include a number of rotations in the opposite direction at the same speed). The instabilities are seen as voltage spikes but these spikes can have either direction, positive in the 8-pole case, negative in the 3-pole case. The net effect of the instability caused current redistribution in terms of shift of flux is not at all obvious; it may reduce the pumping process as in the 3-pole case or, seemingly, aid it.

The size and the direction of the current redistribution depend considerably on the shape of the rotor and, if the direction is different for the 3- and 8-pole rotors, there should be a case in between for which it is zero. The 4-pole rotor has indeed a much smaller instability activity but the over-all current limit is still given by an instability somewhere above 10 000 A. In this kind of process the current then falls back to around 5000 A. This current limit may be more characteristic of the sheet itself rather than the number and shape of the poles since at this current density all criteria for current stability in superconductors are greatly exceeded. The question of instabilities is complicated by the dependence on speed of rotation. Increasing the speed results in stronger and more frequent (per number of rotations) instabilities and also in a lowering of the final, instability governed, current limit. This dynamic dependence of flux jumping is generally connected<sup>19</sup> with the viscous motion of flux, also named flux creep,<sup>20</sup> which is equivalent to a finite resistance of the superconduc-

- 
17. C.S. Tedmon, R.M. Rose, and J. Wulff, in Metallurgy of Advanced Electronic Materials (Interscience, Philadelphia, 1962), Vol. 19, p. 89;  
D. Kramer and C.G. Rhodes, Trans. Met. Soc. AIME **233**, 192 (1965);  
W. DeSorbo, Phys. Rev. **134**, A1119 (1964);  
M.A.R. LeBlanc and W.A. Little, in Proc. 9th Intern. Conf. Low Temperature Physics, Toronto, 1960, p. 362.
  18. R. Carruthers, D.N. Cornish, and R. Hancox, in Proc. 1st Intern. Cryogenic Conference, Kyoto, 1967 (Heywood Temple), p. 107.
  19. S.L. Wipf, Phys. Rev. **161**, 404 (1967).
  20. Y.B. Kim, C.F. Hempstead, and A.R. Strnad, Phys. Rev. **131**, 2486 (1963).

ting material. For a closed superconducting circuit flux creep is experienced as a slow decay of the current. It has been suggested<sup>21</sup> that such a decay be logarithmic in time.

However, the decay observed in the present case is different from any simple model. Figure 13 shows current traces vs time on a greatly enlarged current scale (see bar representing 10 A). They are obtained by pumping at various constant rates to the current stated and then stopping the rotation of the pump. The decay, always fairly rapid immediately at the beginning, is practically finished after about 20 min and the total current reduction is of the order of 10 A. The decay curves for a higher current never reach the ones for a lower current nor are the lower ones similar in shape to a portion of the higher ones after a certain time interval. This is borne out by the example of the 10 000 A case where, after a decay of 50 min and 25 A, the original current level is regained by three full rotations (which included several instabilities, one of which reduced the current by about 15 A as shown in the tracing in Fig. 13) and the ensuing decay curve is quite different. Also a very long decay run made at 11 000 A showed no decay bigger than  $\sim 1\%$  (equivalent to the drift of the recording equipment) over 40 hours. These decays have to be attributed to a relaxation of the current distribution in the sheet which, as we concluded earlier, has after all a resistive region (current induced) when the spots are moving. At the end of the decay the current distribution must have reached an equilibrium distribution in a then fully superconducting sheet.

These observations will also have importance when pumps are used to measure very high critical currents; in general, it will be necessary to make the load inductance sufficiently large.

#### IV. CONCLUSION

We have shown the inadequacy of the mathematical treatment which does not account for the existence of critical regions in the sheet of a moving magnetic field flux pump. The losses in the critical regions are of the same nature as the ac losses discussed earlier and they contribute heavily to the over-all losses in the pump. The instability of the critical regions limits the ultimate output current. A good pump design is one which minimizes the extent of critical regions and avoids instabilities. To fulfill both conditions in the same pump design may not be possible. The analytical difficulties leave many design problems to intuitive solutions. This is characteristic of the present-day art of flux pump making, and scientists, of course, are always a little suspicious of artists.

- 
21. Y.B. Kim, C.F. Hempstead, and A.R. Strnad, Phys. Rev. Letters 9, 306 (1962);  
P.W. Anderson and Y.B. Kim, Rev. Mod. Phys. 36, 39 (1964);  
J. File and R.G. Mills, Phys. Rev. Letters 10, 93 (1963);  
J. File, J. Appl. Phys. 39, 2335 (1968).

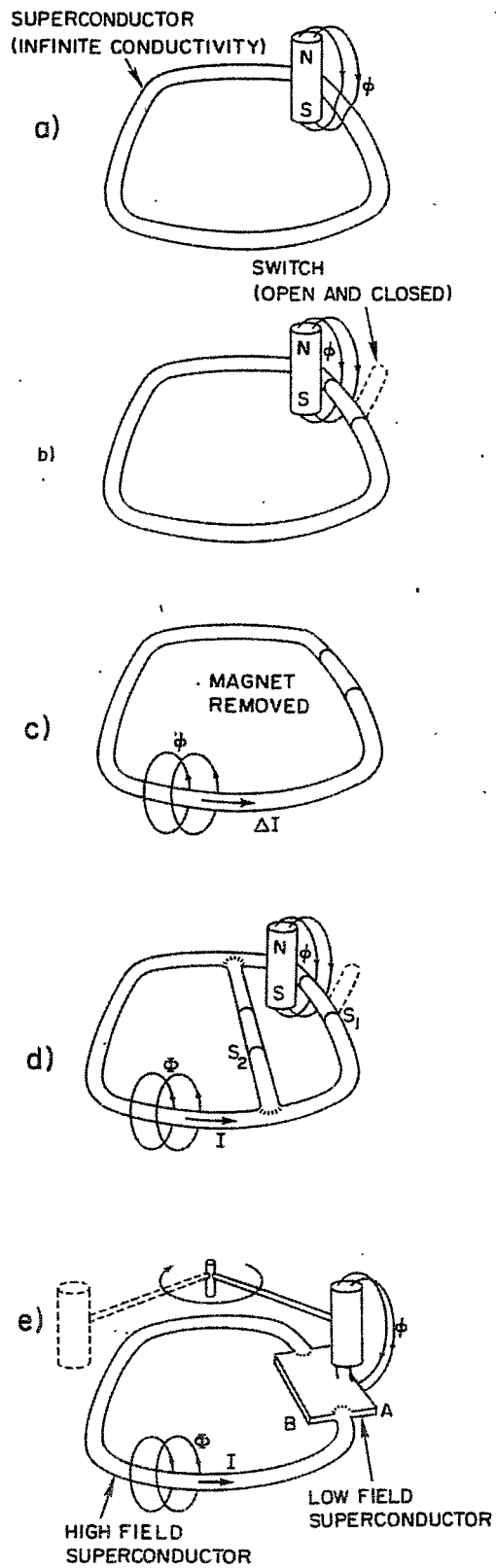


Fig. 1. Principle of flux pumping.

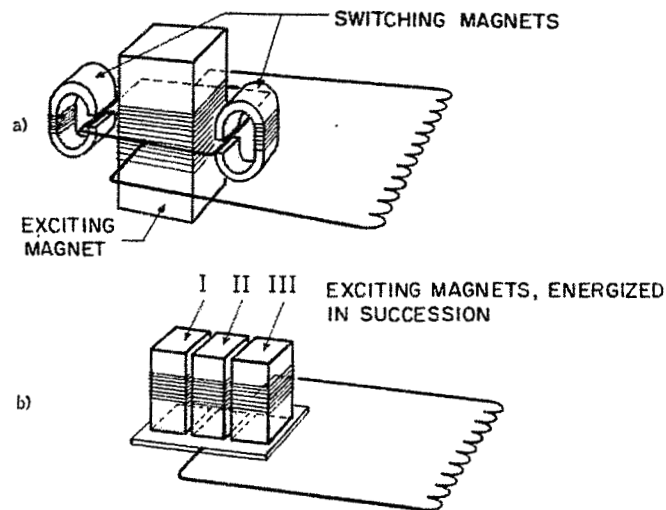


Fig. 2. Two arrangements of flux pumps without moving parts (from Ref. 9). The upper example is a rectifier type [see Ref. 5 and J.L. Olsen, J. Appl. Phys. 29, 537 (1958); R. Fasel and J.L. Olsen, in Proc. 11th Intern. Congress on Refrigeration, Madrid, 1967; also in Z. Kältetech. Klimat. 19, 274 (1967)]. The lower example uses a moving magnetic field. This version is feasible but ineffective because of the poor shape of the normal spot (large critical regions, high  $L_p$ ) [see S.L. Wipf, in Advances in Cryogenic Engineering (Plenum Press, 1964), Vol. 9, p. 342; D. Van Houwelingen et al., Phys. Letters 8, 310 (1964); B.S. Blaisse et al., Phys. Letters 14, 5 (1965)].

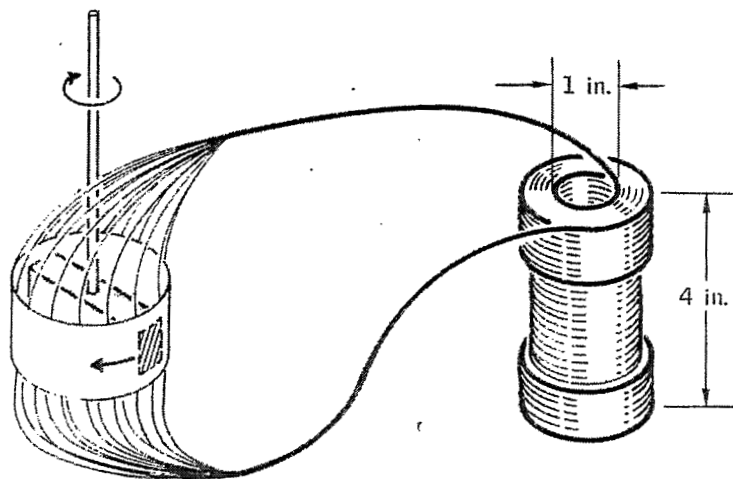


Fig. 3. Typical example of moving magnetic field flux pump. Not shown here are coils to magnetize the iron rotor so that the poles all have the same magnetic polarity, see Fig. 6 (from Ref. 15).

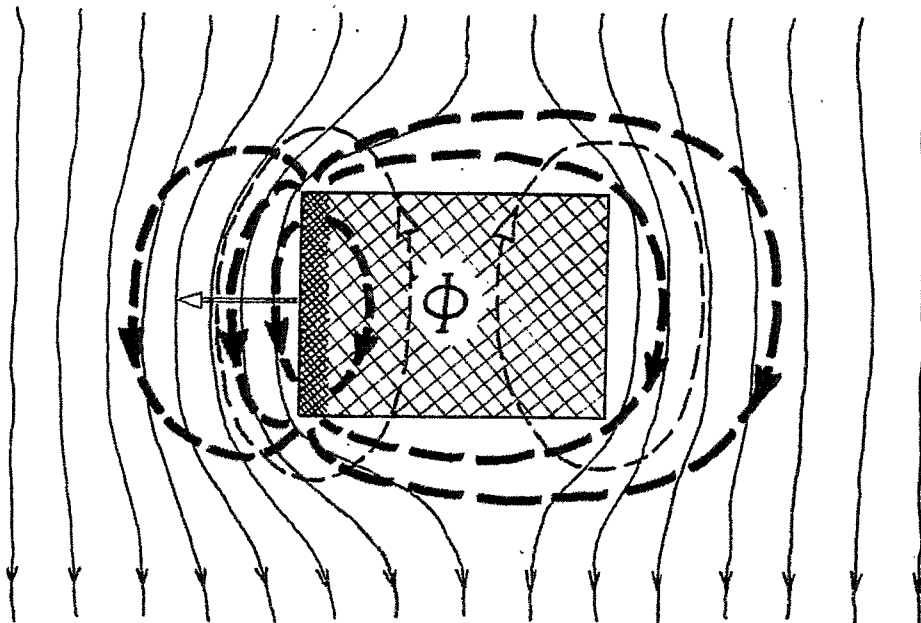


Fig. 4. Schematic current distribution around moving normal spot containing flux  $\Phi$  :

- |                    |   |                                                                                                   |
|--------------------|---|---------------------------------------------------------------------------------------------------|
| Horizontal arrow   | : | Direction of movement                                                                             |
| Crosshatch         | : | Resistive (normal) region                                                                         |
| Narrow crosshatch  | : | Leading edge                                                                                      |
| Thin solid lines   | : | Load current distribution                                                                         |
| Thin broken lines  | : | Eddy current distribution                                                                         |
| Thick broken lines | : | Alternative current distribution for current which is driven resistively out of the leading edge. |



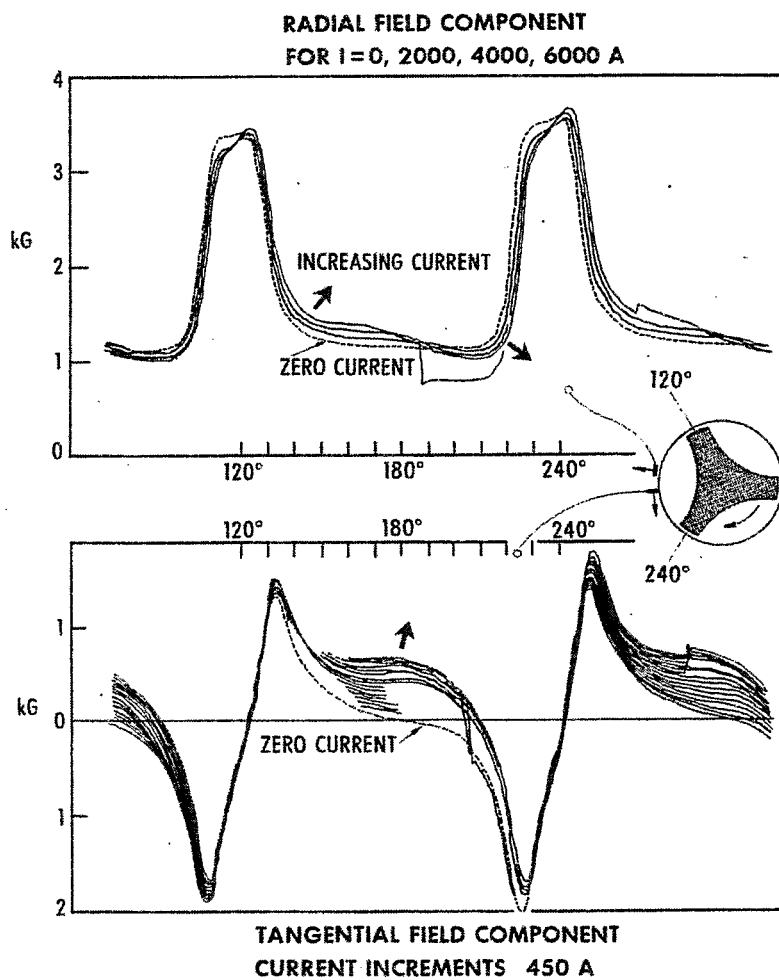


Fig. 5. Radial and tangential field components vs angle (relative to rotor). Measured by stationary Hall probes at the outer surface of the pumping sheet and at the center of the path of the pumping spot. The diameter of the sheet is 7.9 cm, the rotor diameter 7.6 cm, width of pole face 1.35 cm, thickness of rotor 1.22 cm. The distance of the center of the Hall probe from the surface of the sheet is 0.3 cm. (The pump is shown in Fig. 10 with a different sheet.)

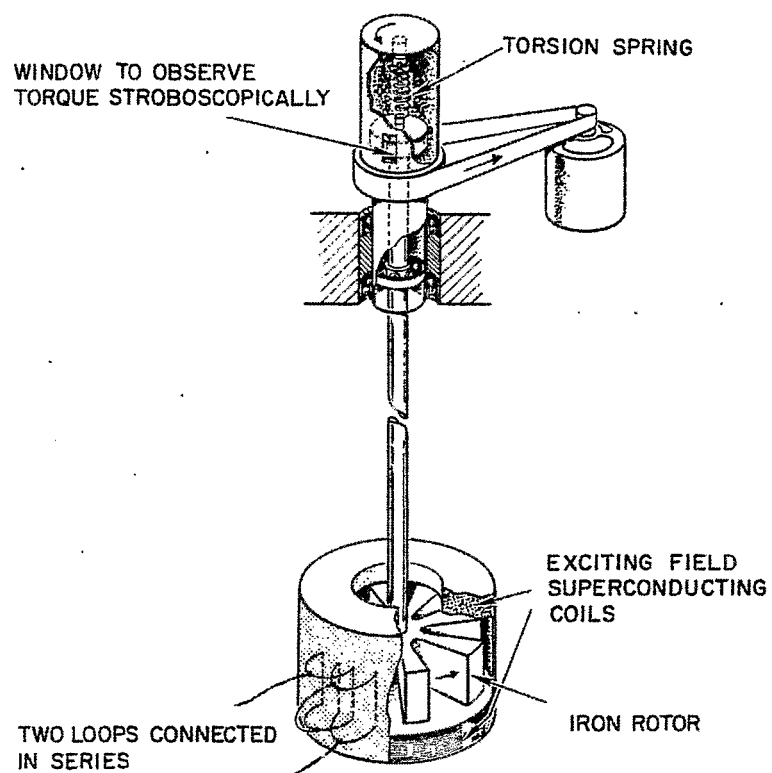


Fig. 6. Example of pump used to measure losses (from Ref. 9). The exciting coils are energized in series opposition to give all poles the same polarity.

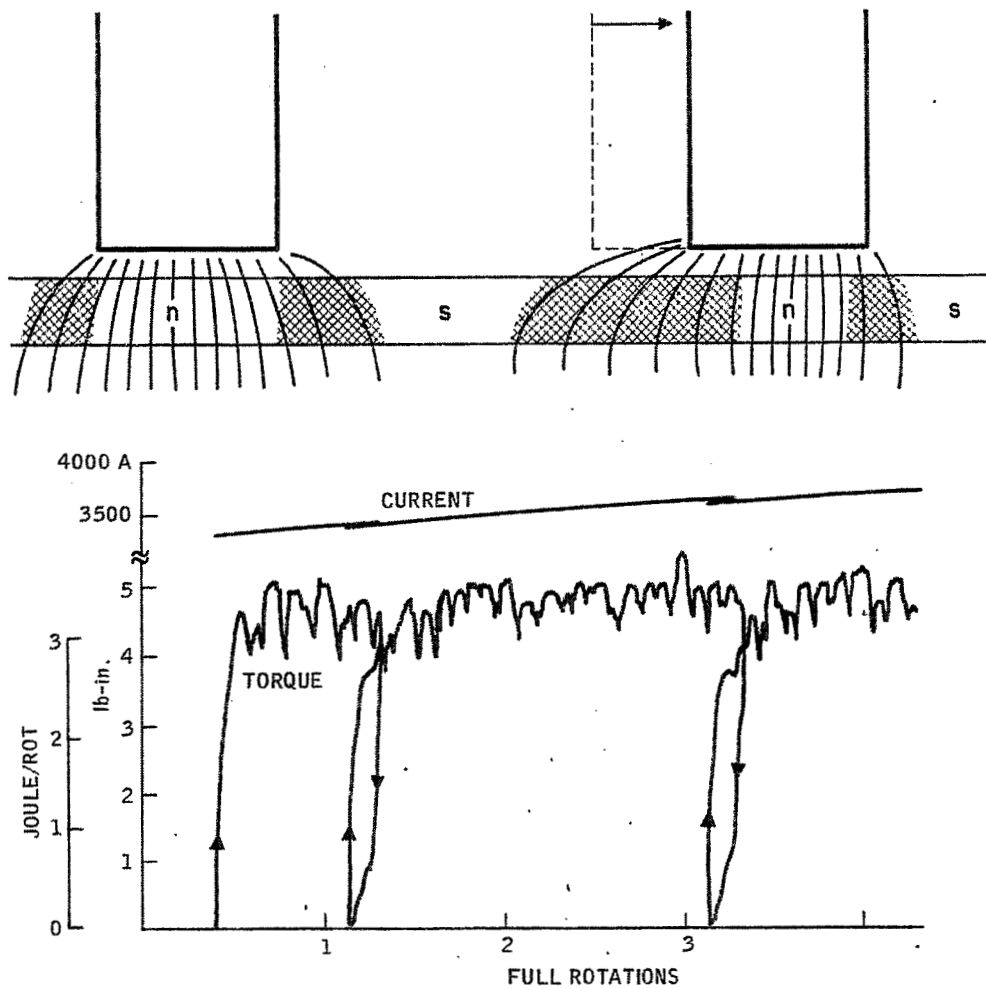


Fig. 7. XY traces of input torque and output current vs rotation angle for pump with a sheet of 7.0 cm diameter and a rotor illustrated in Fig. 8e. Above: illustration of relaxation angle in terms of flux pinning (see text).

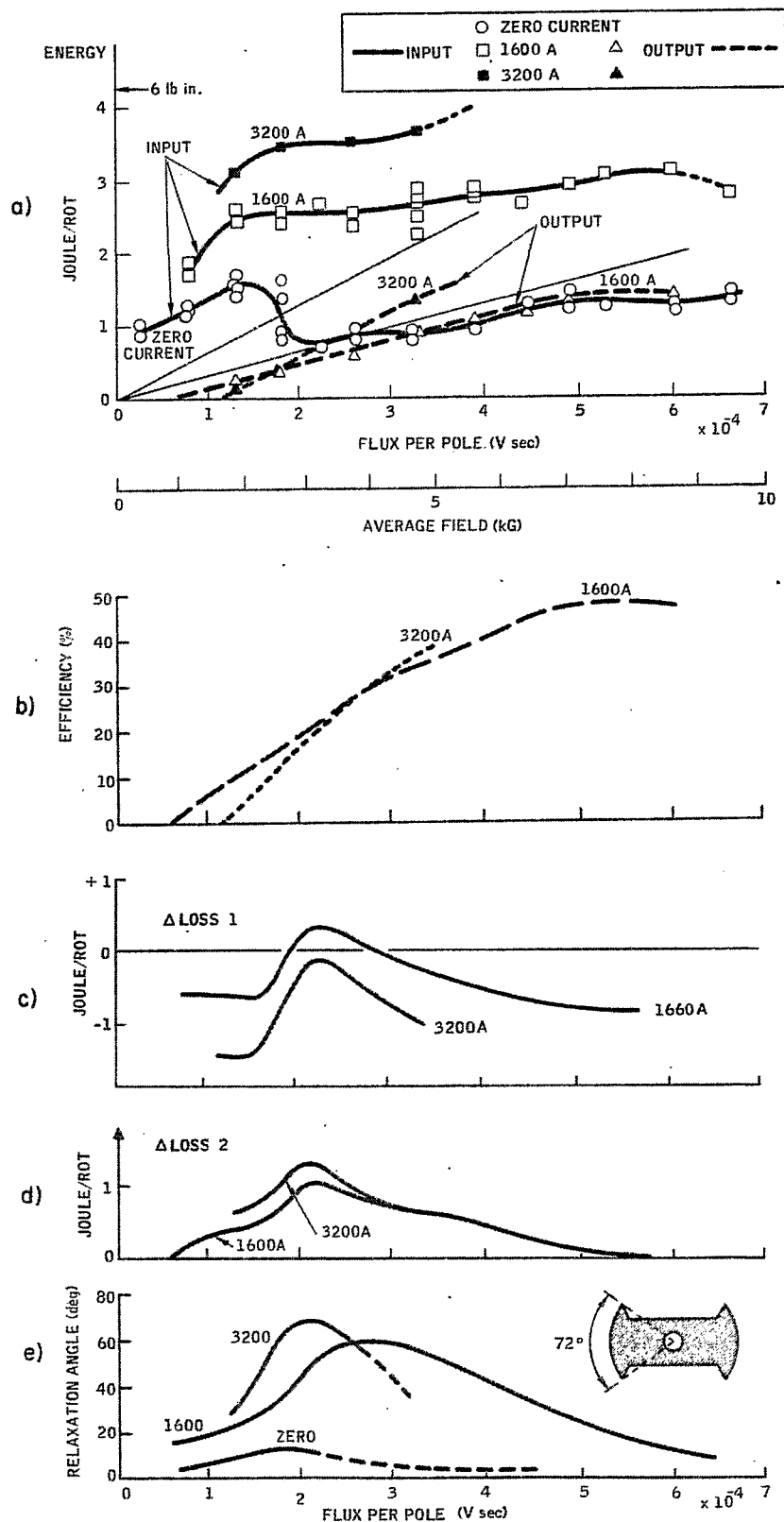


Fig. 8. a) Input and output power vs flux per pole (P) and vs average field in front of poles. For 0, 1600, 3200 A output current.   
 b) Power efficiency (output/input power) vs P.   
 c) and d) Difference between Eq. (4) and measured losses with two different interpretations of  $I(0)$  (see text).   
 e) Relaxation angle vs P. Insert: outline of rotor, diameter 6.72 cm, thickness 1.78 cm.

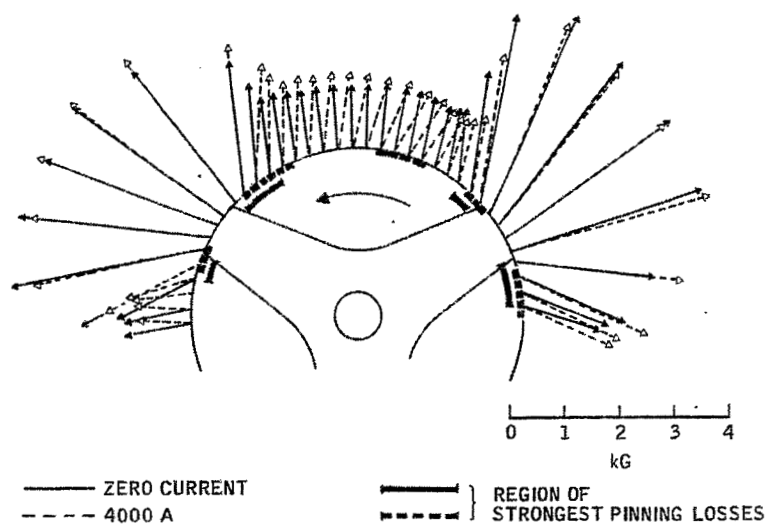


Fig. 9. Field distribution constructed from Fig. 5 for zero and 4000 A currents, with indication of extent of critical regions.

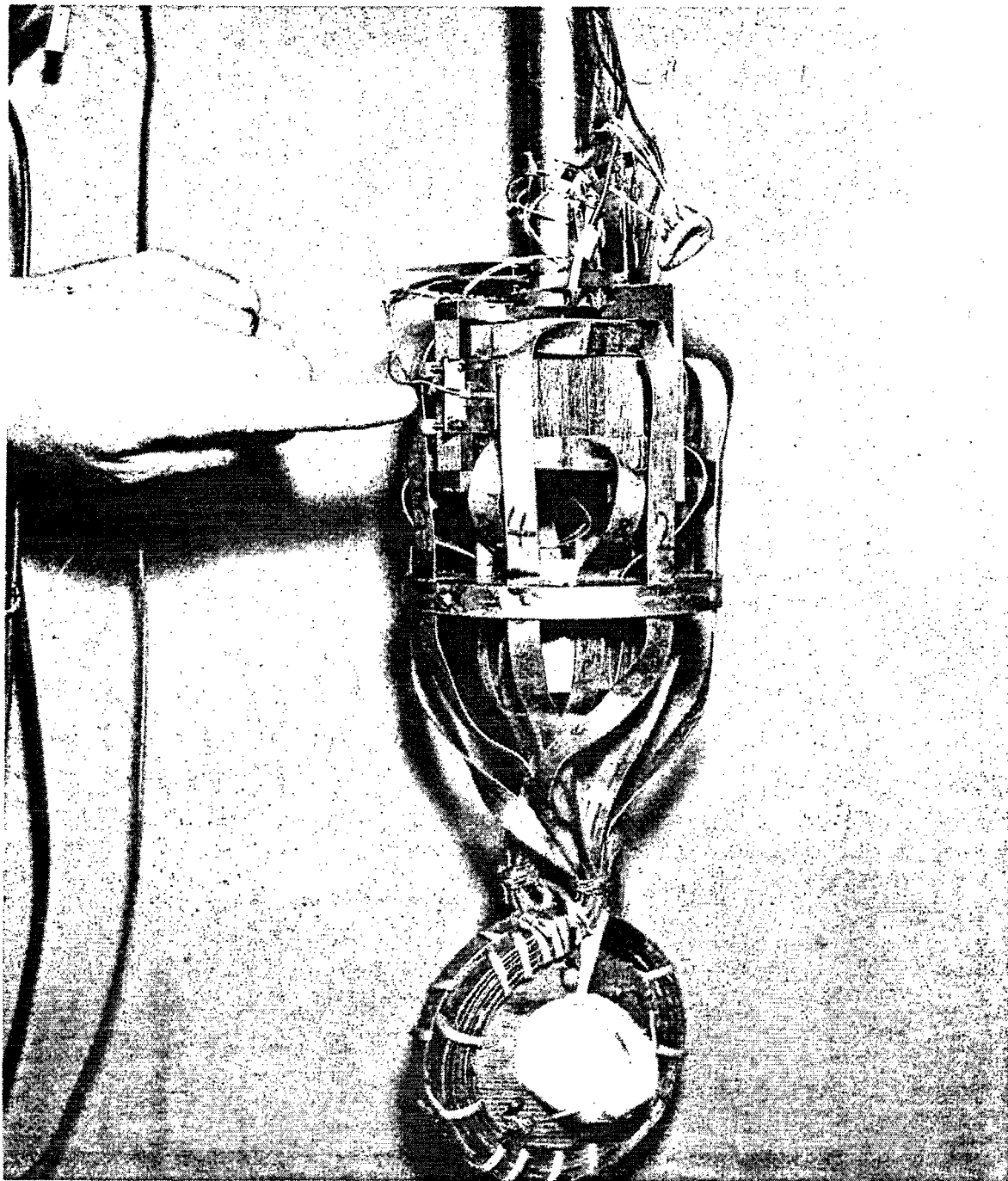
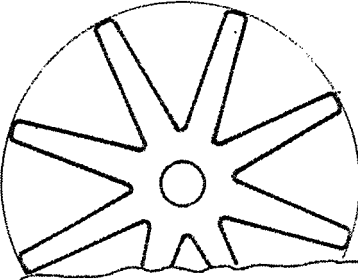

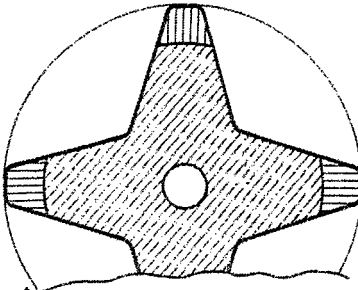

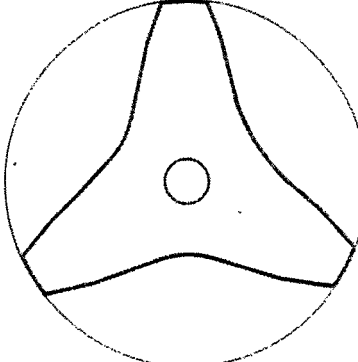



Fig. 10. Example of flux pump for high currents. Circuit consists of 8 tapes of NbTi strip sandwiched between copper strips. The current produces 0.230 G/A at the center of two turns of 9.0 cm i.d. where it is measured by calibrated Hall probes. The finger points to Hall probes which are used to measure field profiles as in Fig. 5.

$$\text{emf} = n\omega (P - L_p I)$$

ONE POLE ↗

↘ TOTAL CURRENT

ROTOR	POLE FACE	$L_p$ MEASURED (H)	$L$ (LOOP) CALCULATED (H)
a) 		$4.5 \times 10^{-10}$	$(5.7 \times 10^{-9})$
b) 		$1.15 \times 10^{-9}$	$(8.1 \times 10^{-9})$
c) 		$1.93 \times 10^{-9}$	$(1.42 \times 10^{-8})$

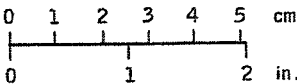


Fig. 11. Three different rotors used in pump of Fig. 10. Comparison of measured  $L_p$  with minimum inductance of loop around pole face. Rotors and pole faces are drawn to scale.

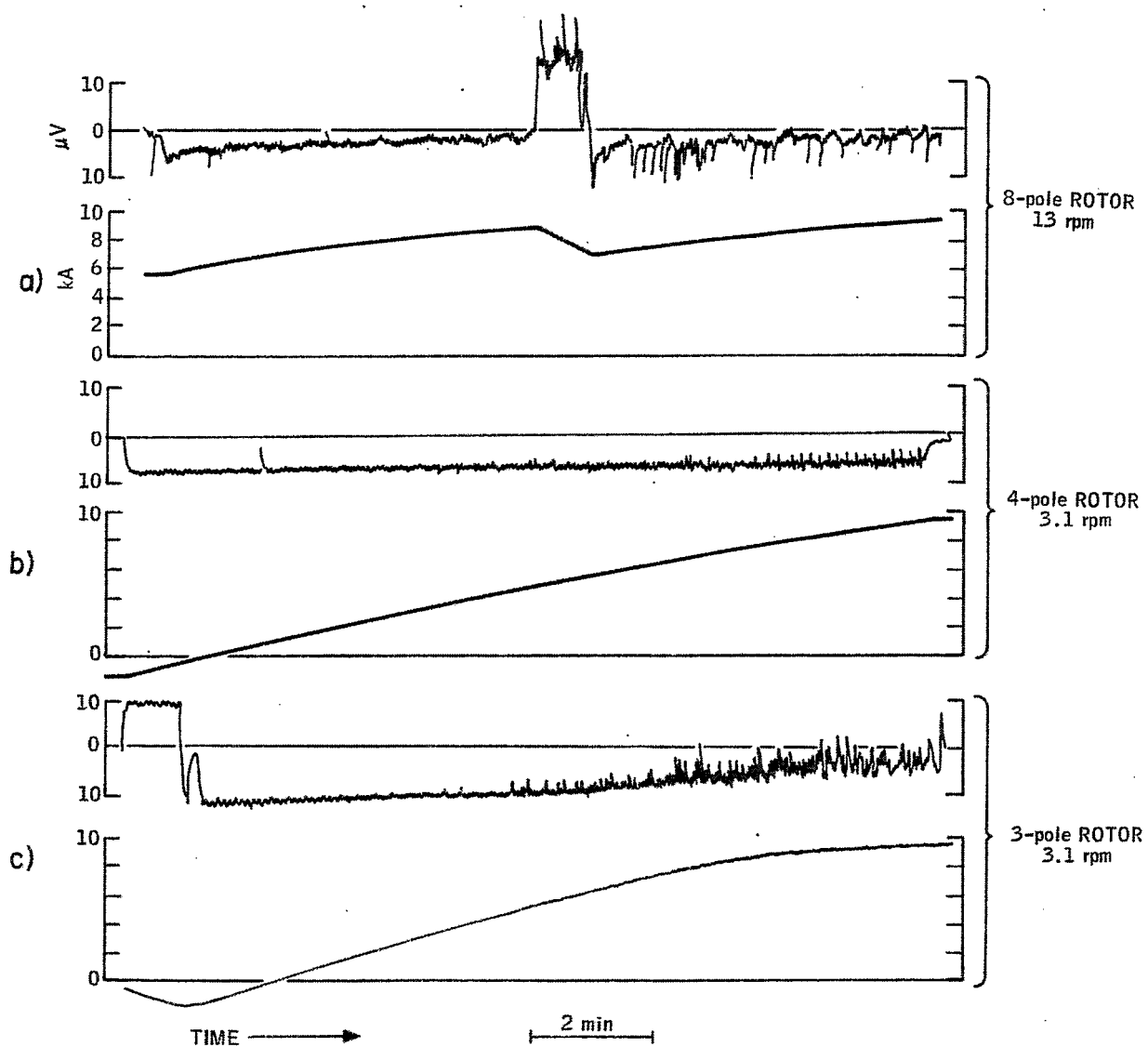


Fig. 12. Traces of emf (in  $\mu\text{V}$ ) and output current (in  $\text{kA}$ ) vs time for the three different rotors of Fig. 11 used in the pump of Fig. 10.



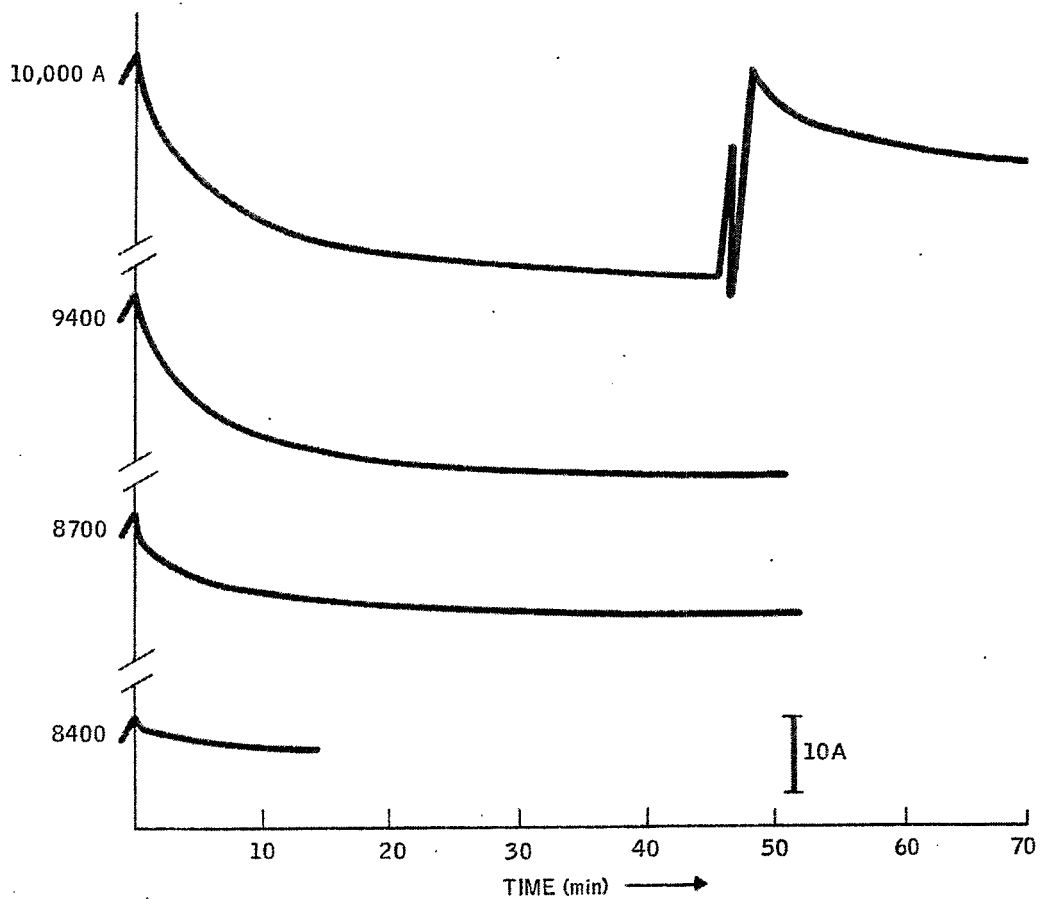


Fig. 13. Decay of current on expanded current scale (see scale for 10 A) vs time after pump has been stopped. Initial current indicated in amperes, 8-pole rotor, 10 rpm before stopping. Pump and rotor as in Figs. 10, 11.

## DESIGN PRINCIPLE AND CHARACTERISTICS OF THE G.E. FLUX PUMP

R.L. Rhodenizer  
General Electric Company  
Research & Development Center  
Schenectady, New York

### INTRODUCTION

There have been several methods proposed for generating or otherwise creating a large direct current in a low temperature environment to avoid the losses associated with conducting high current to a low temperature region from a room temperature source. If such a device is operated in conjunction with a superconducting magnet system, it is desirable that the current source also be superconducting, and be constructed so that flux is introduced within a closed superconducting circuit. These devices can then be considered as flux pumps.

One of the methods for accomplishing this is to use a transformer-rectifier circuit, made from superconductive components, to transform a small alternating current input into the high level current required, which can then be rectified to obtain a large direct current. The transformer can be fabricated in a conventional manner using superconductive windings, but novel methods are required to achieve the rectification function with superconductive components. The situation is further complicated in that, in the case of energy storage systems such as superconducting magnets, phase-controlled rectification is desired so that energy can be removed from as well as added to the load.

The flux pump to be discussed here was invented and developed by T.A. Buchhold and uses a transformer-controlled rectifier configuration to convert a small alternating current input to the output characteristics needed for energizing superconductive magnet systems. This device operates with very high efficiency and is capable of producing sufficient output power for practical use in many magnet applications. As this concept has undergone considerable improvement and refinement over the past several years, an up-to-date summary of the characteristics of this type of flux pump and its capabilities will be given.

### FLUX PUMP OPERATION

The key concept introduced by Buchhold is a unique combination of magnetically-controlled, cryotron-like switches used in conjunction with saturable core reactors to achieve phase-controlled rectification. Figure 1 shows the low temperature portion of his flux pump circuit and the arrangement of the various components.

The input transformer has superconductive windings on an iron core and is excited by a square wave, room temperature voltage source. As the transformer has a high primary to secondary turns ratio, the input current requirement is low and, therefore, small cross-section input leads may be used to connect to the room temperature source.

The secondary circuit is connected in a two-phase arrangement which requires two sets of the cryotron-reactor "rectifiers." The load is connected between the cryotrons and the center tap of the transformer secondary winding. The primary winding of the saturable reactor, the gate of the cryotron switch and all interconnecting leads are made from superconductive material, usually niobium. Thus, in the absence of cryotron excitation, the entire secondary circuit is superconducting.

Ideally, of course, the cryotron switches would have zero resistance in the "on" state and infinite resistance in the "off" state. The former condition is met by the use of a superconductive cryotron gate material, but the finite resistance of the gate in the off state is one of the primary factors limiting the efficiency of the flux pump. This will be discussed more fully later. The cryotron is switched between the on, or superconducting state, and the off, or normal state, by means of a superconducting magnetic control winding. This is excited by an external, room temperature, source.

The saturable core reactors consist of three windings on a torroidal core of Deltamax. The primary winding is connected in series with the gate of the cryotron switch, the retarding winding is connected in series with the cryotron control, and the signal winding is wound from a normal metal and extends to the room temperature control circuit. The functions performed by these windings are best shown by a description of the circuit operation, but it is pointed out that the reactor core is normally in saturation except during short periods in the switching cycle. Thus the impedance of the reactors is usually negligible except for short periods when the core leaves saturation. It will be shown that this characteristic is a key factor in the high efficiencies obtained with this concept.

Figure 2a shows some of the wave forms which illustrate the circuit operation in a simple rectification cycle, that is, rectification without phase control. For this operation the retarding windings on the saturable core and the phase shifting circuit may be ignored. To follow the action of the circuit throughout a basic rectification cycle, first assume that the upper cryotron in Fig. 1 is superconducting or on, while the lower cryotron is off. At this point, both saturable reactor cores are in saturation and the load sees the voltage across one half of the transformer secondary,  $e_1$ , and the load current increases according to the relation:

$$\frac{dI_L}{dt} = \frac{e_1}{L}$$

where  $L$  is the load inductance.

At the end of the positive cycle, the transformer voltage reverses polarity and it becomes necessary to switch both cryotrons in order to achieve rectification. To do this, an external circuit detects the change in polarity of the primary voltage and produces a signal which interrupts the control current flow in the lower cryotron. Thus the control field goes to zero. The cryotron gate tries to revert to the superconducting state, but, as the gate resistance decreases, the current tends to increase. This would cause large losses and inhibit the switching process if it were not for the reactor in series with the gate. The rectangular hysteresis loop characteristics of the saturable reactor core prevents a rapid build-up of the gate current as is shown in Fig. 2b.

Point A in Fig. 2b shows the position on the hysteresis loop of the core before the change in polarity of the input voltage. The core is in saturation with a current,  $I_b$ , flowing through the primary winding. The current,  $I_b$ , is determined by the voltage across the full transformer secondary and the resistance of the lower cryotron in the off state. When the voltage reverses polarity and the cryotron switches to the on state, the current through the core primary tends to build up toward the value it will conduct when on. However, as the current goes through zero, the core leaves saturation and the current is limited to a low value,  $i_0$ , determined by the width of the hysteresis loop. The time for which the current is limited depends on the design of the circuit and is set to give the gate of the cryotron sufficient time to complete its normal to superconducting transition at the low current level.

The upper saturable core reactor also performs an important function at this time. As the lower cryotron is switched to the on state and the lower reactor goes into saturation, the entire secondary circuit is of very low impedance. Thus, the current in the secondary is commutated very quickly from the upper half of the circuit to the lower half by the transformer voltage. As the current in the upper half is driven through zero, the core of the upper reactor comes out of saturation and the changing flux in the core induces a voltage in the signal winding. This signal is then used to trigger current flow in the upper cryotron control from the room temperature circuit which switches the upper cryotron gate to the normal state. By repeating this process with the polarity changes in the input voltage, it is seen that rectification is achieved and energy can be fed into an inductive load.

In order to change the rate at which energy is fed into the load or to remove energy from the load, a means for phase shifting the rectification cycle with respect to the input voltage is required. This is accomplished with two modifications to the circuit.

The first is the addition of a means for delaying the signal derived from the input voltage reversals which is used to switch the appropriate cryotron to the on state. This is easily accomplished in the room temperature electronic circuit by conventional circuit techniques. The second change is the addition of the retarding winding to the cores of the saturable reactors. As stated before, this winding is connected in series with the cryotron control coils so that the cryotron control signal also passes through the retarding winding.

The wave forms of Fig. 3 show the operation of the circuit with phase shift  $\alpha$ . Again assume a point in the positive half cycle where both cores are in saturation, the upper cryotron is on, and the lower is off. When the voltage reverses polarity, there is now no switching action because of the signal delay,  $\alpha$ . There are two changes, however.

First the current through the off lower cryotron reverses due to the input voltage polarity change. With no retarding winding, this would cause the lower core to come out of saturation. However, as the core action is needed only when the cryotron is to be switched on, a means must be provided to hold the core in saturation until the proper time. This is accomplished by connecting the retarding winding in series with the cryotron control so that the control current creates sufficient mmf to overcome that of the primary winding and keep the core in saturation.

The second effect is that, because neither cryotron has been switched, the load current decreases due to the reversed input voltage polarity.

After the delay,  $\alpha$ , a signal is produced to turn the lower cryotron on. This signal now interrupts the cryotron control current and removes the retarding winding mmf from the core. The cryotron gate then returns to the superconducting state and the bottom core leaves saturation at the proper time to allow the gate to switch on at a low current. When this is completed, the secondary current commutates and the upper cryotron is switched off by the means described previously. The output voltage is thus again positive up to the next reversal in the input square wave.

It is seen that the phase delay,  $\alpha$ , provides a means for controlling the fraction of a period for which the load is exposed to a positive or a negative voltage. The load charging rate can then be easily adjusted in the room temperature circuit for adding or removing energy. It is also clear that the electronic circuit can be de-energized at any time to leave a persistent current in the magnet circuit.

## FLUX PUMP CHARACTERISTICS AND APPLICATION

If one considers the application of this flux pump concept in conjunction with a superconductive magnet system, the performance of the system can be summarized by a few simple equations.

First, the load current is given as:

$$I_L = \int_0^t \frac{V}{L} dt ,$$

where  $V$  is the effective output voltage of the flux pump, and  $L$  is the inductance of the load.

As the inductance of a superconducting coil is normally a function of the field, it has been included under the integral sign, but in a simplified analysis it will be assumed that  $L$  is constant.

The maximum output voltage is shown as a function of current for a typical flux pump in Fig. 4. It is seen that the voltage decreases somewhat with current, the decrease depending mainly on the output impedance of the square wave source exciting the transformer primary. If this decrease is also neglected, the load current can be approximately expressed as:

$$I_L = \frac{V}{L} t .$$

With these conditions, the total load charging time is then:

$$t = \frac{2 W_s}{P_M} ,$$

where  $W_s$  is the energy stored in the magnet system, and  $P_M = V I_{\max}$ , the flux pump output power at the maximum current.

In turn one can define a maximum efficiency factor as:

$$\eta_m = \frac{P_M}{P_M + P_L} ,$$

where  $P_L$  is the loss in the low temperature section of the flux pump.

Because the efficiency of the flux pump determines to a main extent whether or not the device can provide an economic savings in a given application, this definition deserves further clarification. It is found that the predominant flux pump losses are nearly independent of the output current. Thus if one plots the efficiency as a function of output current, the curve in Fig. 5 results. This shows that the efficiency is zero, by this definition, at zero current, but rises rapidly with the current to approach its maximum value at the full output. It should also be pointed out that the losses are nearly independent of the phase shift in the rectification cycle, so that the definition assumes the maximum output voltage with no phase delay.

Further rearrangement of these equations shows that the instantaneous power loss is related to the efficiency and maximum power output as:

$$P_L = \left( \frac{1 - \eta_m}{\eta_m} \right) P_M \approx (1 - \eta_m) P_M .$$

The energy lost in charging a coil system to its final energy at the maximum charging rate is:

$$Q_L = 2 \left( \frac{1 - \eta_m}{\eta_m} \right) W_s \approx 2 (1 - \eta_m) W_s .$$

That is, the inefficiency on an energy basis is twice that found from the power equation.

These equations show that the energy lost in energizing a magnet system is related only to the efficiency of the flux pump, while the charging time is a function of the power capability of the pump. The instantaneous power loss, on the other hand, is affected both by the efficiency and power capability of the device.

If some typical flux pump parameters are assumed, the following values can be found for a representative application. Consider a 50 W, 98% efficient flux pump designed to energize a magnet system storing 50 000 J of energy. The time required to energize the magnet at the maximum pumping rate will be about 33 minutes, and approximately 2000 J will be dissipated in the liquid helium. The instantaneous power dissipation will be about 1 W, which is equivalent to a liquid helium boil-off rate of 1.4 l per hour, and total helium consumption is about 0.75 l. This example illustrates that very high flux pump efficiencies are desirable to achieve low system losses, and the power range which must be considered to achieve practical charging rates is also indicated.

#### FLUX PUMP DESIGN AND CAPABILITIES

As with many engineering devices, careful optimization procedures must be followed to maximize the efficiency of a flux pump unit for a specific application. This optimization process generally defines the maximum efficiency that can be attained in practice while the power capabilities are defined by the physical size of the unit or by practical fabrication constraints. Usually it is possible to design for given power levels with any combination of current and voltage so that a design can be matched to the load with little effect on the efficiency characteristics of the device.

The limit on flux pump efficiency is set by the properties of the cryotron switches. Table I shows the various components of flux pump loss and gives the percentage of the total loss attributed to each component in a typical design. This clearly shows the dominant effect of the cryotron loss in present flux pumps.

TABLE I. Distribution of Flux Pump Losses

1. Input Transformer	- 15%
a. Winding loss	
b. Core loss	
2. Saturable Reactor	- 5%
a. Winding loss	
b. Core loss	
3. Cryotron	- 80%
a. Gate ohmic loss	
b. Gate hysteresis loss	
c. Control winding loss	
d. Iron loss	

An analysis of the losses occurring in the cryotrons shows that the total loss and, thus, the ultimate efficiency of a flux pump depends mainly on the superconductive properties of the gate material. This is due to the fact that the ohmic cryotron loss is inversely proportional to the length of the gate in the cryotron, or to the volume of the cryotron, while hysteresis loss increases directly with the volume. Thus, there is an optimum design which makes the two loss components equal, the optimized loss then depending on the properties of the gate material.

Recent development programs have devoted a significant effort toward the development of new cryotron gate materials so that the device efficiency can be improved. This has resulted in the use of certain niobium alloys which display characteristics particularly suited for use in construction of the cryotron gates.

The design of the remaining flux pump components follows from rather conventional considerations to attain the desired operational characteristics. Every component must, however, be carefully designed and constructed to avoid needless loss and to maximize the output characteristics for a given size.

Over the past several years improvements in the design and fabrication procedures has resulted in continually improved flux pump models for practical use. Several flux pump units have been built and used with superconductive magnets. These have ranged from an original 3 W feasibility model having a maximum efficiency of about 90%, to more recent models in the 50-60 W range, having maximum efficiencies of almost 98%. The current ratings of these units has ranged from about 300 A to more than 1700 A at approximately constant power output. However, there appears to be no serious technological barrier to further increases in flux pump power levels if the need should arise. There is always, however, a need to improve efficiency which could result from further improvements related to high current cryotrons.

In applying flux pumps to systems, several problems had to be solved which were not directly related to the flux pump itself. One of these was the need to shield the flux pump when used in close proximity to a high field magnet. Use of static superconductive shields was found to be only partially effective but active shield concepts have been used successfully in several cases. For a simple solenoid an active shield can consist of a superconductive winding placed between the magnet and the flux pump and connected in series with the main coil, but with the opposite field sense.

Another problem was the possibility that the flux pump could be driven normal during a coil quench with the energy of the load being dumped into the flux pump components. This, of course, overheats and damages the flux pump components. This problem was overcome with the development of special semiconductive "avalanche breakdown" devices which operate reliably at liquid helium temperatures. These units can be custom fabricated to breakdown at low voltage and pass high currents and are connected directly across the flux pump output to limit the energy which can be dumped back into the flux pump from the load.

Figure 6 shows a typical flux pump-magnet system which includes these features. This figure shows a shield winding between a 100 kG Nb<sub>3</sub>Sn magnet and the flux pump, which is enclosed in a niobium housing. The copper heat sink in which the protective semiconductor is mounted is also visible.

Figure 7 shows a typical 300 A, 50 W flux pump. The efficiency of this unit is close to 98% and is similar to that in Fig. 6. For comparison another 50 W flux pump designed for 1700 A is shown in Fig. 8.

The flux pump control unit shown in Fig. 9 is relatively compact and has several features useful in system applications. These include automatic selection of field level, protective discharge in case of low helium levels, two pumping voltages to

minimize losses at low pumping rates, and continuous rate control between maximum charge and discharge. In addition, of course, persistent current operation is possible by simply de-energizing the control unit.

In summary it can be said that this flux pump concept has been developed to a point where flux pumps are considered as a commercial item rather than a research device. Present applications have been in association with research type, superconductive magnet systems where only modest power requirements exist. It is still true that flux pumps only become competitive with conventional systems for loads requiring relatively high currents, and low inductance loads are desirable to achieve rapid charging rates. As for magnet systems storing many megajoules of energy, where a conventional power system is used, the use of a flux pump can still be considered to supply the energy dissipated in the resistive joints of the load, or to attain fine field adjustment.

#### ACKNOWLEDGEMENTS

The flux pump concepts described here were originally conceived and developed by Dr. T.A. Buchhold of the General Electric Research & Development Center. R.K. Terbush has also made many significant contributions throughout the development program.

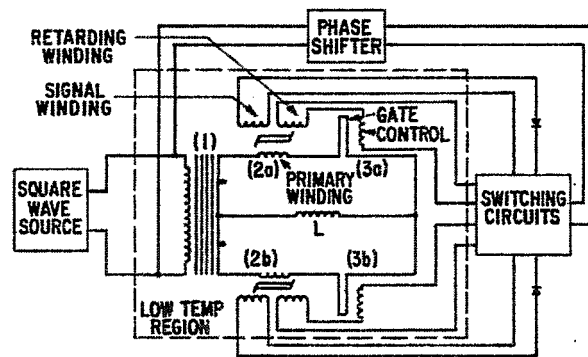
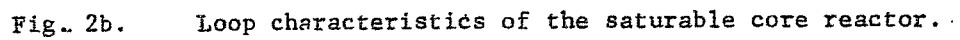
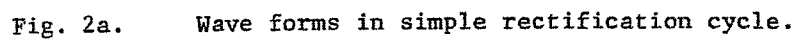


Fig. 1. Schematic of the flux pump with phase shifting.





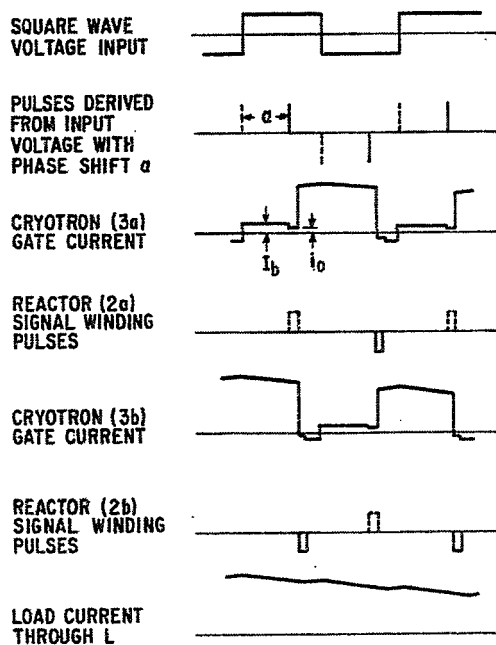


Fig. 3. Wave forms for rectification with phase shift.

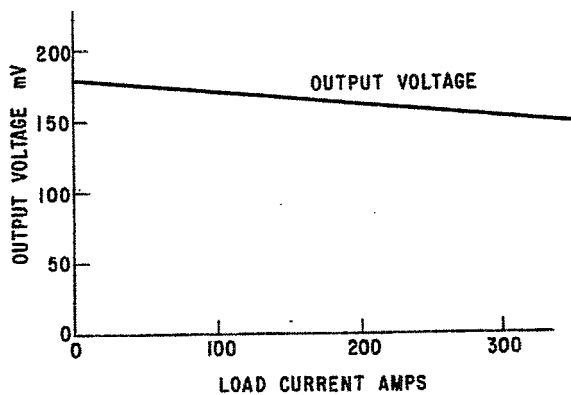


Fig. 4. G.E. superconductive flux pump characteristics.

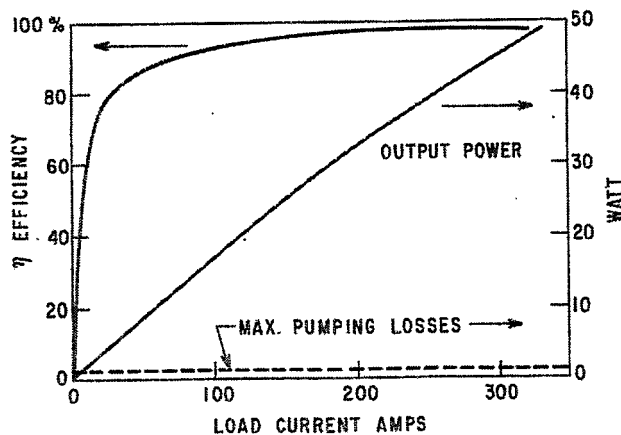


Fig. 5. G.E. superconductive flux pump characteristics.

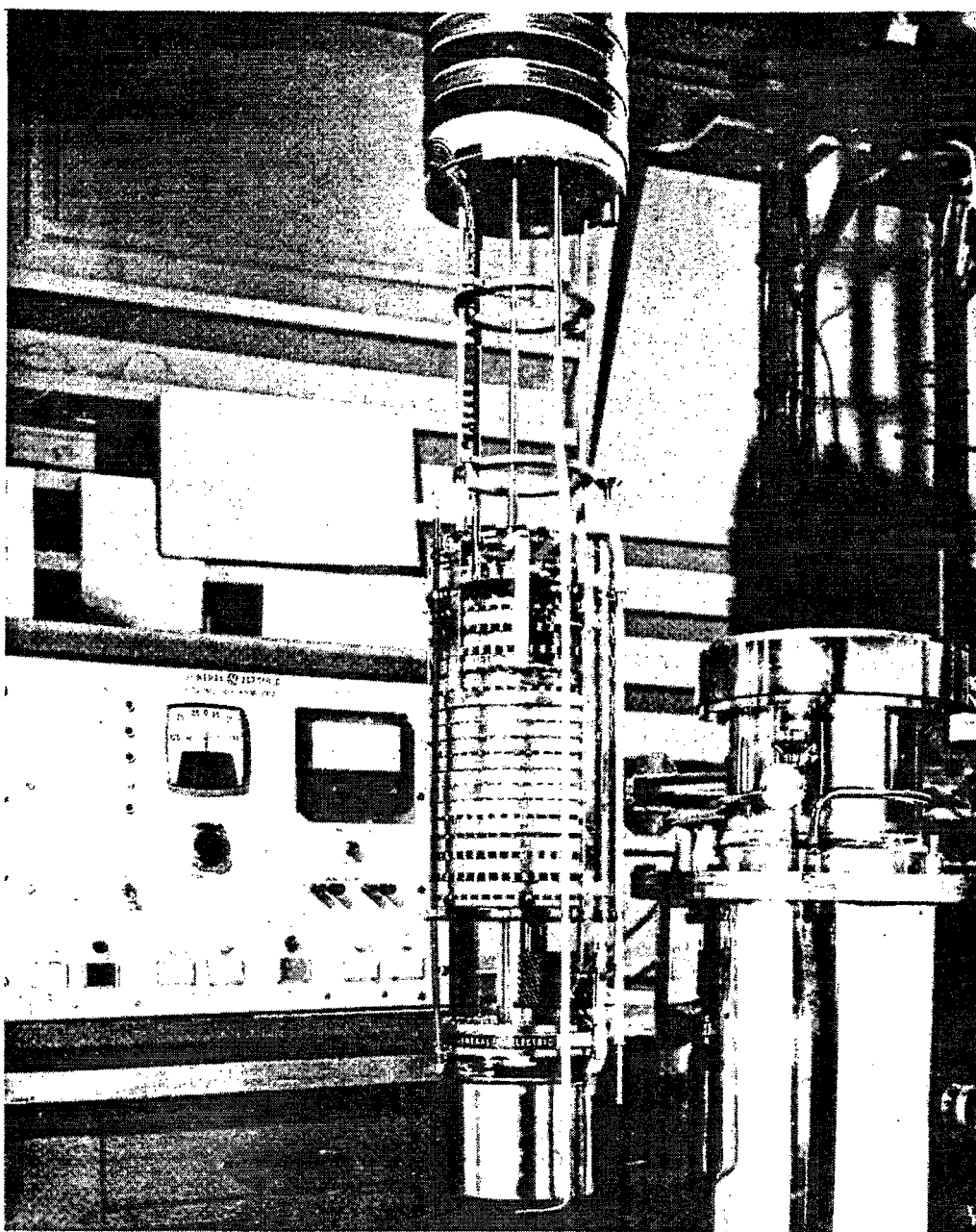


Fig. 6. 100 kg magnet system with flux pump.

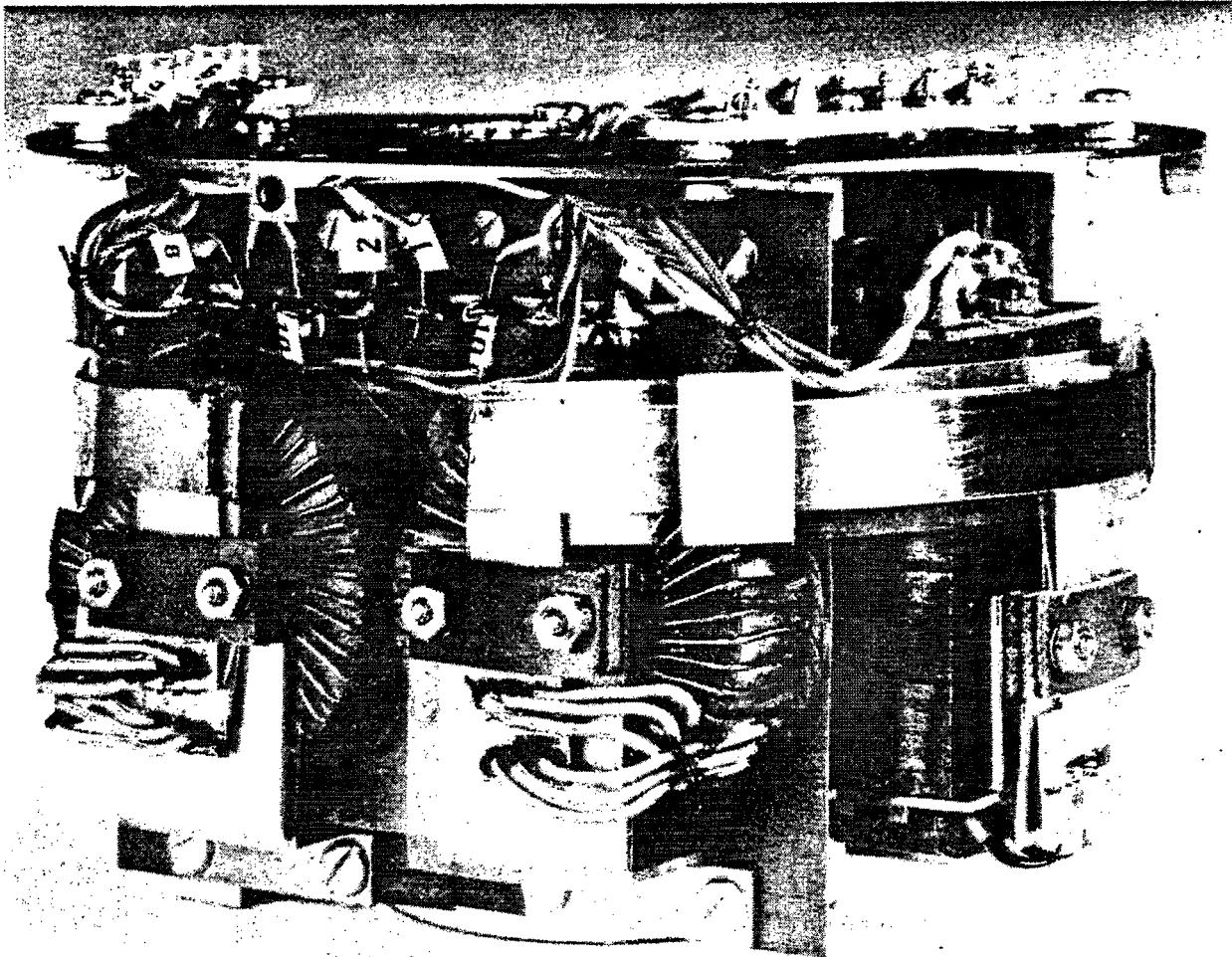


Fig. 7. 300 A, 50 W flux pump.

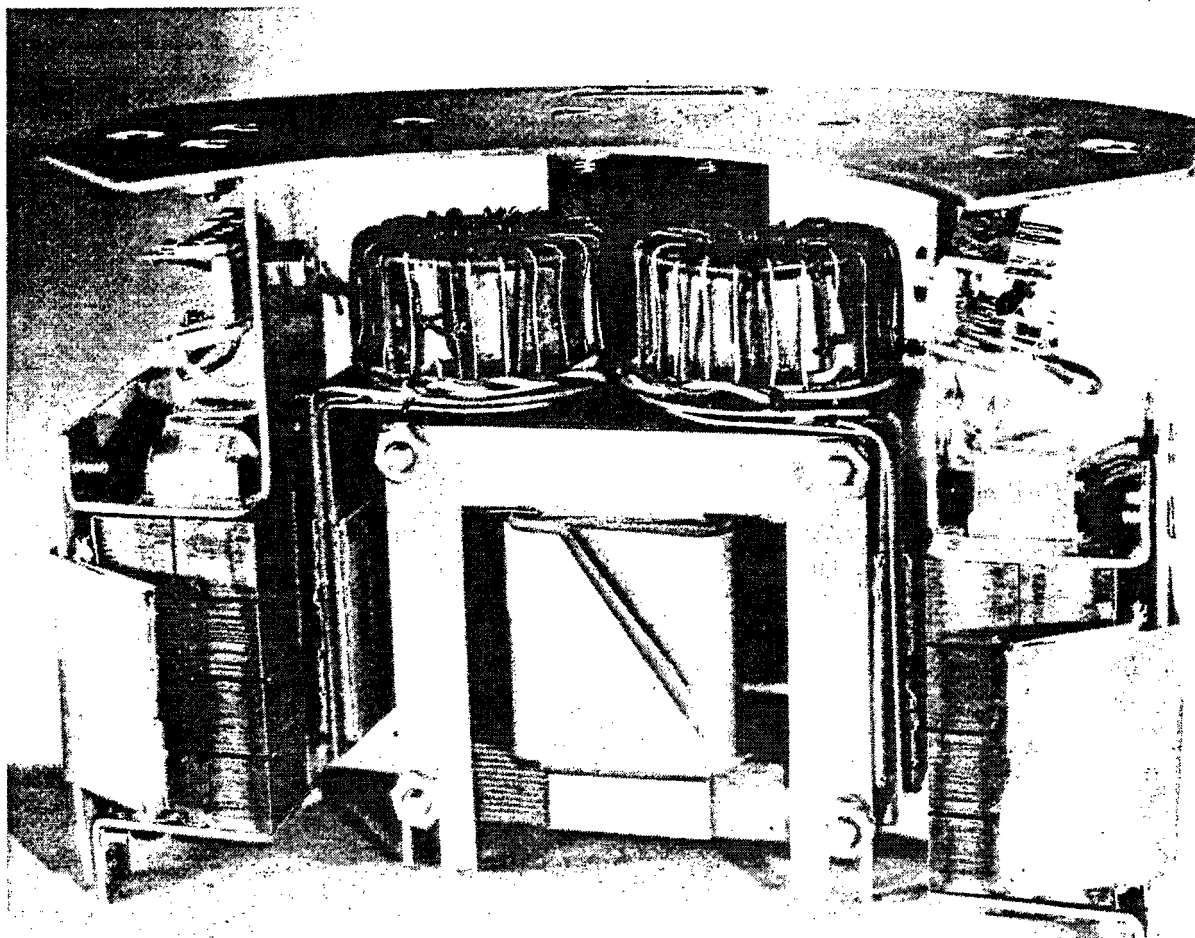


Fig. 8. 1700 A, 50 W flux pump.

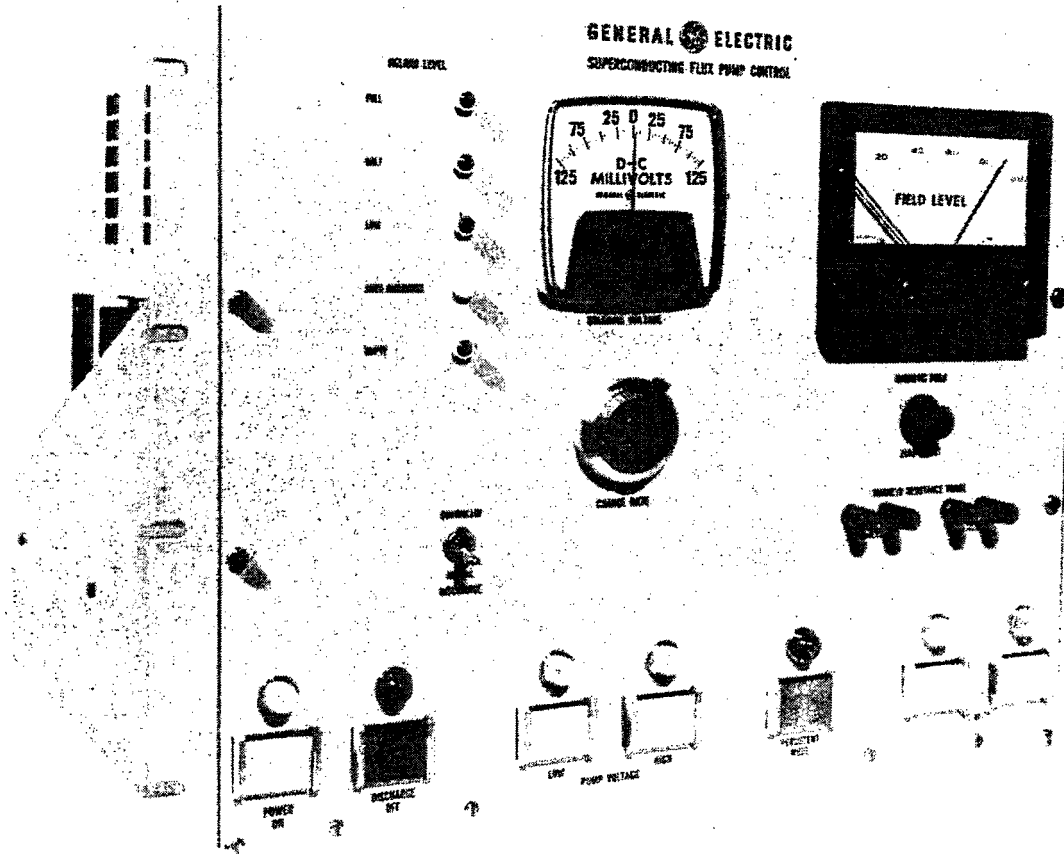


Fig. 9. Flux pump room temperature control unit.

# FLUX PUMPS AS POWER SUPPLIES IN COMPARISON WITH ALTERNATIVES\*

M.S. Lubell and K.R. Efferson  
Oak Ridge National Laboratory  
Oak Ridge, Tennessee

## INTRODUCTION

For a better understanding of the losses associated with energizing a superconducting magnet, a comparison of the relative performance between a flux pump and vapor-cooled input leads supplied by a conventional power source will prove illuminating. Thus, for the same magnet, the flux pump losses for various modes of operation and the losses for vapor-cooled leads optimized for the same operating current will be calculated. Since both calculations are based closely on experimental results, the comparison that is presented for a particular magnet is quite realistic. The inferences and conclusions, however, may not be applicable to all magnet systems since only one type of flux pump is discussed. The loss problem becomes more important with the size of the magnet, and so a scheme for powering large magnets with minimum loss will be proposed. Only partial experimental observation is available on this latter point.

## LOSS CALCULATIONS

Flux Pump. The general theory of the losses associated with flux pumps has been presented by various authors.<sup>1-3</sup> It has also been shown how these theories - along with some experimentally determined parameters - can be applied to a particular system to obtain the losses associated with pump switching as a function of the rotation frequency<sup>4</sup> for a rotating magnet, Nb-foil flux pump. In addition to the switching losses, one must also consider the ac losses of the current carrying pump material and the joule losses in the normal shunt. For the small magnet system, which has been previously described<sup>4</sup> ( $H_{\max} = 39$  kG at  $I_{\text{total}} = 1480$  A), the loss rate (in watts) takes the form

$$\text{Switch loss} = 9 \times 10^{-3} \omega + 4.7 \times 10^{-2} \omega^2, \quad (1)$$

$$\text{Ac loss} = 2 \times 10^{-2} \omega, \quad (2)$$

$$\text{Shunt loss} = 3.5 \times 10^{-4} (dH/dt)^2. \quad (3)$$

The relationship between  $dH/dt$  (G/sec), the rate of increase of the field, and  $\omega$  (rev/sec), the pump rotation frequency, was experimentally determined. For the mode of operation consistent with the above equations,  $\omega = 0.105$  dH/dt rev/sec as shown in

---

\* Research sponsored by the U.S. Atomic Energy Commission under contract with the Union Carbide Carbide Corporation.

1. S.L. Wipf, in Proc. Intern. Symposium on Magnet Technology, Stanford, Calif., 1965, p. 615.
2. D. van Houwelingen and J. Volger, in Proc. Intern. Cryogenic Engineering Conference, Tokyo and Kyoto, Japan, 1967, p. 135.
3. H. Voigt, Z. Naturforsch. **219**, 510 (1966).
4. M.S. Lubell and S.L. Wipf, in Advances in Cryogenic Engineering (Plenum Press, New York, 1968), Vol. 13, p. 150.

Fig. 1. The total losses in watts [Eqs. (1), (2), and (3)] for different rates of energizing are shown in Fig. 2. As is readily evident, the loss increases rapidly with rotation or  $dH/dt$ . This particular pump was operated at a maximum speed of 4 rev/sec, but rotating pumps have been operated at much higher rates<sup>1,5</sup> so larger rates will be considered in the analysis. For the magnet being discussed, a  $dH/dt = 26.3$  G/sec was equivalent to a  $dI/dt = 1$  A/sec.

Vapor-Cooled Leads. A description has recently been given for the design of current leads which are cooled by the helium boil-off gas.<sup>6</sup> The size of the leads and number of woven silver-plated copper conductor tubes (also serving as gas passages) are chosen to minimize the losses at the anticipated maximum operating current.

For a comparison with the system discussed above, a set of vapor-cooled leads which are optimized for 1480 A are needed. Since data for this are not available, a close approximation (described in Fig. 2 of Ref. 6) will be used. The loss rate as a function of current is given for a set of leads (3/4 in. o.d., 80 conductor strands, optimized for 1320 A) up to a maximum current of 1400 A. The loss as a function of current can be obtained in analytic form by fitting the experimental loss data with a quadratic dependence on current. For the leads optimized for high currents, this approximation is quite good. The loss rate in watts for a pair of 1400 A leads is

$$\dot{m} = 1.55 + 6.7 \times 10^{-7} I^2 \quad (4)$$

For the magnet system being considered, the current can be expressed in terms of the rate of energization as

$$I = 137 (dH/dt) t_h \quad (5)$$

where  $dH/dt$  is given in G/sec and  $t_h$  is the time in hours necessary to reach the maximum current. Since the flux pump losses depend only on the rate of excitation while the vapor-cooled leads depend on the current level in addition to an appreciable zero current heat leak, the only way to compare them is to calculate the total loss in liters of helium for various energizing rates and times. For the vapor-cooled leads, the total loss in liters of helium is obtained by substituting Eq. (5) into Eq. (4) and integrating. The loss in liters of helium is

$$\text{Loss} = (2.07 + b t_h^2) t_h \quad (6)$$

where  $b = 5.6 \times 10^{-3} (dH/dt)^2$  and the latent heat of helium is  $2.7 \times 10^3$  J/liter (hence 3/4 W dissipates 1 liter/h).

Comparison of Losses. In comparing the losses between a flux pump and vapor-cooled leads on the same system, we are assuming that the Dewar losses are the same and that the losses introduced by the magnet support structure are identical, and not significantly dependent on the helium level. We are also assuming that the flux pump can be attached to the existing structure without introducing any significant heat leak and also that the vapor-cooled leads do not require any additional supports.

---

5. K.R. Efferson, Rev. Sci. Instr. 38, 1776 (1967).

6. For an up-to-date discussion of the Buchhold flux pump, see R.L. Rhodenizer, these Proceedings, p. 654.



Figure 3 shows the losses as a function of time for various rates of energizing for a flux pump and a set of vapor-cooled leads. The losses due to the flux pump cease as soon as the maximum operating current is reached — thus, with the system in persistent mode, there are no operating losses at maximum field. On the other hand, while the losses for the vapor-cooled leads are small if the system is energized rapidly, the operating losses at maximum field are large and continue, of course, until the magnet is de-energized. We are comparing here only the energizing and operating losses, but in practice one must also consider the losses on decreasing the field. Even in the special case considered here, the essential features are evident; the mode of operation (steady state or ramp) and the rate of energizing determine which system of powering a magnet leads to minimum loss. Except for the fastest rates, the vapor-cooled leads have much larger losses. Even for the fastest rate considered,  $10^3$  G/sec, however, the total losses of the vapor-cooled leads surpass the flux pump losses after four hours of operation.

In common practice most magnet systems are operated at a preset field for a long interval. In these cases, the flux pumps available at present are much more efficient than the vapor-cooled leads for small magnet systems. The flux pump considered in this discussion has an efficiency of approximately 50%, so that the comparison would be even more striking had we used the Buchhold-type of flux pumps,<sup>6</sup> which have efficiencies approaching 95%.

#### POWERING LARGE MAGNETS

The rotating magnet flux pumps are unsuitable for powering large magnets because of their low efficiencies. Buchhold-type pumps have been built with output powers of 50 W, but even these would only be adequate for magnets with stored energies below, say, about 0.5 MJ. It seems most likely, therefore, that in the near future only vapor-cooled leads will be used for energizing large magnet systems. To reduce the over-all losses, we suggest the following operating scheme as being possible for large magnets: (1) Use vapor-cooled leads to energize the magnet. (2) After maximum current is reached, the system can be placed in persistent mode with a superconducting short. The normal state resistance of the switch should be hundreds of ohms so as not to interfere with the charging. (3) At this point to further reduce the heat leak into the system, the current contact at the top of the vapor-cooled leads (after the current is reduced to zero) can be opened. In this manner the system's only thermal contact to room temperature is through thin-walled stainless steel. The thin-walled stainless-steel tubes of ohms or tens of ohms resistance connected in parallel provide both an exit vent for the helium vapor and also serve the important function of an external short for protection should it be necessary to discharge the magnet rapidly because of a quench, loss of coolant, failure of switch, etc. (4) For very large systems operated in persistent mode, it may be necessary to also employ a flux coil detection system which can be used to remotely control a relay activated motor to quickly reconnect the vapor-cooled leads. With this refinement the stainless-steel tubes only have to carry the load current during discharge for the short time necessary to reactivate the main current leads.

The ideal persistent switch,<sup>2,7</sup> of course, is a small flux pump to overcome any decay due to resistive contacts and joints, etc. Although this over-all scheme has not to our knowledge been employed, we have used vapor-cooled leads on a test system and

---

7. Private communication with S.L. Wipf; H. Brechna at SLAC and P.F. Smith at Rutherford are both contemplating use of a flux pump as a persistent switch and field trimmer.

the anticipated saving in refrigeration requirements was realized when the external electrical and thermal contact was broken (Fig. 4). Figure 4 shows a schematic of this system and the measured losses are also indicated. With the contacts in the open position, the helium vapor exits through thin-walled stainless-steel tubes. Note that the leads are switched in a vacuum chamber and thus, no frosting occurs to prevent a low resistance contact from being re-established. Even without the use of a persistent switch, detachable contacts to vapor-cooled leads aid in keeping the heat input to the system at a minimum between use and save in over-all refrigeration requirements.

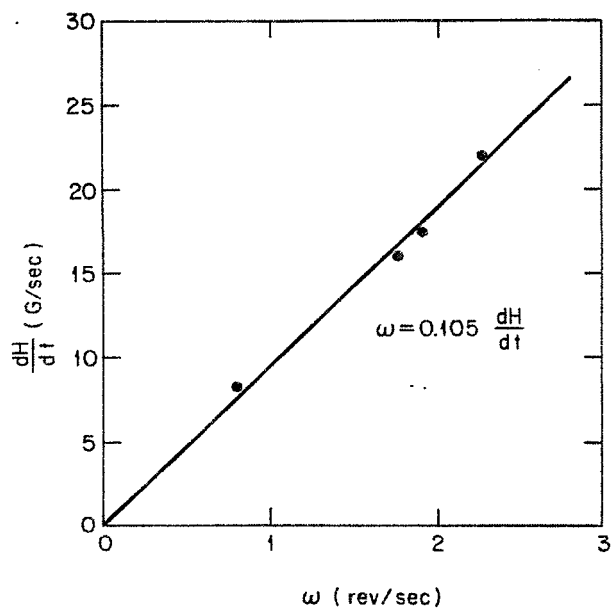


Fig. 1. Rate of field increase vs flux pump rotation from data of Ref. 4.

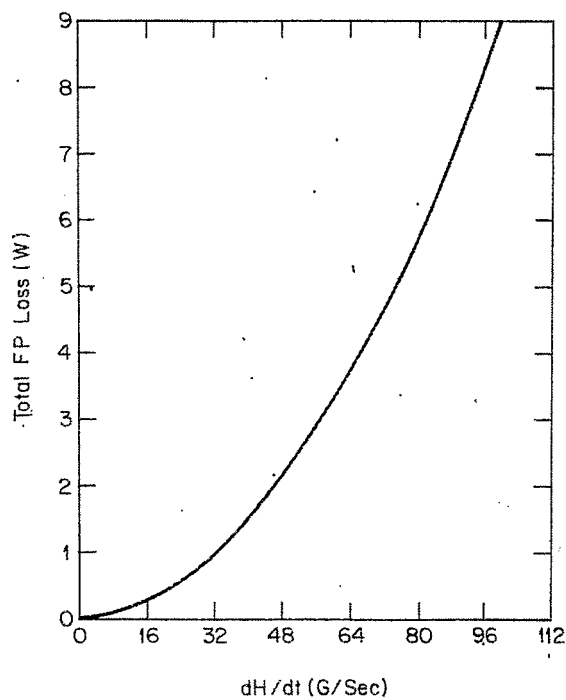


Fig. 2. Flux pump loss rate [Eqs. (1)-(3)] vs rate of field increase.

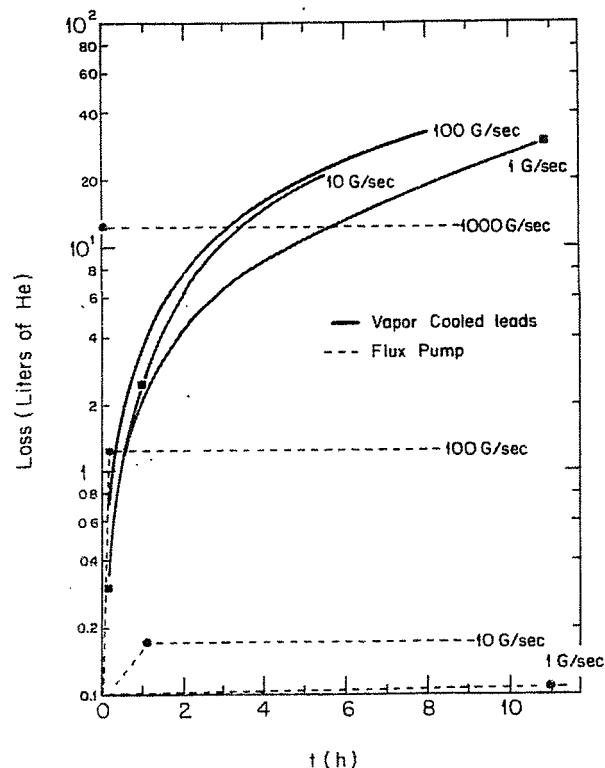
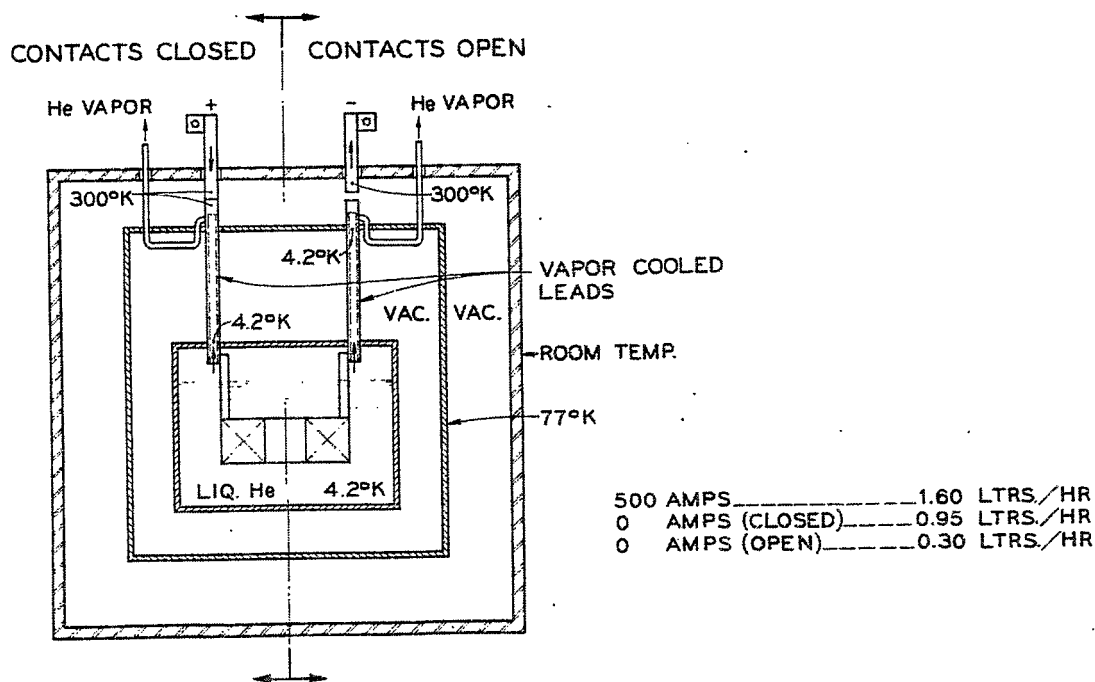


Fig. 3. Comparison between flux pump and vapor-cooled leads of loss vs time for different rates of energizing. The symbols indicate the time at which the maximum operating current was reached. For the vapor-cooled leads, faster rates ( $dH/dt \geq 10^3$  G/sec) are undistinguishable from the 100 G/sec curve after approximately 3 hours.



### CRYOGENIC CONTACTS

Fig. 4. Measured heat leak through vapor-cooled leads compared with the leads being opened. With the contacts in the open position, the helium vapor passes out through thin-walled stainless-steel tubes.

## FLUX PUMP WORK AT LOS ALAMOS\*

H. Laquer  
Los Alamos Scientific Laboratory  
Los Alamos, New Mexico

Flux pump work at Los Alamos has a long but somewhat sporadic history. I started thinking about what we now call flux pumps in October, 1961, when for both mechanical and electrical reasons, I had some coils made from large cross-section Kunzler wire and ribbon, and somehow could not get the courage to push 1000 A into a liquid helium cryostat. I think we all feel differently now and an additional heat load of 2 to 4 W is of small consequence in the big engineered coils to be used in most high or medium energy physics experiments.

However, there is a regime of medium sized coils with field energies below 50 or 100 kJ where relatively high flux pump inefficiencies may be tolerated. Specifically, these are situations where a pumping loss of 10 to 30 liters of liquid helium can be of the same magnitude as the cool-down losses. This then has to be weighted against a steady loss of 2 to 4 liters/hour for the duration of the experiment. Unfortunately, even this comparison is not necessarily clear-cut because you also have to consider disconnectable or extendable leads, i.e., variable loss leads in conjunction with a thermally, magnetically, or automatically operated persistent switch. So what I am really saying is that we have a complex systems analysis problem involving questions of operational stability, simplicity, and reliability that are hard to evaluate. Hence there is still need for new concepts and for novel implementations of the old ideas to suggest alternatives for the systems designer. That is essentially the objective of our present, part-time flux pump effort. We are trying a number of approaches, but cannot as yet quote definite numbers for flux pump efficiencies or for power levels.

As I mentioned, some of our first flux pumps (Fig. 1) were built with rigid, heat treated, large diameter Kunzler Nb<sub>3</sub>Sn wire.<sup>1</sup> We minimized joints and made persistent contacts through NbSn powder-filled capsules. In 1963 we actually pumped one of these coils, which was potted in indium, well into the Kim-Anderson flux creep region (at 10 kG and 800 A). Our switches (Fig. 2) were just copper capsules with gas inlet and outlet tubes covering a previously flattened section of the conductor. There were several things wrong with this approach:

- 1) The switches were short. Hence, their "off" or "resistive" state resistances were small. This lengthened the time for flux transfer and, hence, limited the repetition rate of the pumps.
- 2) Our switching process was highly irreversible. We really just had triggered instabilities, as indicated by the fact that the switches worked best at 1000 A.
- 3) We had to use a fairly complicated electronic timer to synchronize power supply reversal, the programming of the primary current, and the timing of the switches.

---

\*Work performed under the auspices of the U.S. Atomic Energy Commission.

1. H.L. Laquer, Cryogenics 3, 27 (1963).

Our second flux pump<sup>2</sup> tried to avoid these shortcomings by making the switches automatic. It arose out of some discussions about the nature of persistent currents in superfluid helium and the magnitude of the critical superfluid velocities, a phenomenon which is quite analogous to the onset of electrical resistance in a superconductor. Hammel<sup>3</sup> was interested in determining critical velocities from the persistent circulation possible in a parallel superfluid circuit (Fig. 3). Since soldering is quicker than glass-blowing, and since field or flux measurements are easier than the observation of superfluid circulation, Hammel asked me to assemble the equivalent superconducting circuit which consists of a small and large inductance in parallel, either in a ring circuit (Fig. 4) or as separate entities (Fig. 5).

The performance of this superconducting equivalent turned out completely as one might predict. At a fixed applied voltage, current will divide inversely as the inductances, until the smaller ( $L_2$ ) reaches its critical or limiting value and it takes the entire applied voltage ( $E$ ) just to maintain a constant limiting current through  $L_2$ ; hence the power dissipated in  $L_2$  and in the liquid helium bath is  $E I_2$ . The field in the larger coil will continue to build up and, as long as the voltage is maintained, all the additional current will flow into  $L_1$ . Reduction of the applied voltage will make  $L_2$  immediately superconductive again, trapping all flux. When the external current reaches zero, a field will have been trapped in  $L_1$  and the current in  $L_2$  will have been reversed. The process can be repeated with external current leads or with a low temperature condenser until  $L_1$  reaches its critical current. We can reduce fields by simply reversing polarities and we have a hysteresis loop (Fig. 6). The hysteresis figure suggests an optimum critical current in the switching inductance just equal to the desired maximum current in  $L_1$ .

One also wants these slightly contradictory properties in  $L_2$ : minimal inductance, maximum "normal" or perhaps "flux flow" resistance, and stable (non flux jump) switching. Also, it is evident that there may be some advantages in varying or controlling the critical current in  $L_2$  by magnetic or thermal biasing.

A device of the type just described is clearly not a flux pump since it requires the introduction of at least  $2I_{1 \text{ max}}$  into the cryostat. A flux pump needs a changing or moving magnetic field at a low temperature, such as a step-down transformer. I always felt that an iron core was desirable for energetic reasons. However, Dick Britton last week showed me a very cleverly designed pump without any iron in it. There are some real advantages in not having to worry about fringe fields saturating the iron.

Now the problem of putting a transformer on the circuit of Fig. 5 lies in (a) avoiding losing on the back swing what was gained on the forward swing, and (b) getting the flux into the (single turn) secondary if it is a superconducting circuit. The solution which we originally applied to these problems was (1) putting a small resistance  $R_0$  into the secondary circuit, and (2) applying an asymmetric primary current so that  $R_0$  can limit the secondary current during the back swing to a value insufficient to switch  $L_2$  (Fig. 7).<sup>\*</sup> It is also apparent that a dc field bias

\* The equipment necessary for these experiments is now readily available commercially. We use a Hewlett-Packard 3300 A Function Generator with a 3304 A Sweep-Offset plug-in. Presently, the transformer primary is driven from an HP 6824 A  $\pm 50 \text{ V} \pm 1 \text{ A}$  Power Supply/Amplifier, but the new Kepco BOP 36-5M  $\pm 36 \text{ V} \pm 5 \text{ A}$  Bipolar Operational Power Supply should allow higher primary currents.

2. H.L. Laquer, K.J. Carroll, and E.F. Hammel, Phys. Letters 21, 397 (1966); in Pure and Applied Cryogenics (Pergamon Press, 1966), Vol. 6, p. 539.
3. P. Sikora, E.F. Hammel, and W.E. Keller, Physica 32, 1693 (1966); see also Proc. 10th Intern. Conf. Low Temperature Physics, Moscow, 1966, Vol. 2B, p. 347.

on  $L_2$  should make it switch more easily for one current direction than for the other direction. This, of course, would eliminate the need for an asymmetric primary current and we have done some preliminary experiments along this line. These experiments quickly pointed out the obvious fact that one needs a rather carefully calculated winding profile in order to make the bias field most effective in producing the maximum "normal state" resistance.

Our main effort in the last few months, however, has been on the switch proper. There are again conflicting requirements in that one wants a steep and stable rise in the E-I curves to minimize switch losses. We have reported on solder switches that could be used up to 200 A and niobium switches stable at 600 A.<sup>4</sup> However, what one really would like is a 1000 A switch which can be readily soldered into the circuit. It may be possible to obtain copper-clad niobium wire or ribbon, but lacking this kind of material we did what should make the wire manufacturers shudder. We took some 750 A at 20 kG, 0.050 in. diameter multistrand NbTi conductor and heat treated it for two hours at 700°C. The resulting material had a critical current of about 400 A at 2.6 kG so that it would switch itself in a coil with 5.2 turns/cm. Hence, we obviously need a less severe heat treatment.

Once the bias switches are working, we can consider replacing  $R_0$  with another biased automatic switch. At this point, then, we have probably six wires leading to the flux pump so that it is no longer a simple device and we will have to ask ourselves again:

- 1) Are the resistances of our inductive switches on one hand and their losses on the other still competitive with externally controlled noninductive switches?
- 2) Are flux pumps themselves competitive with high current leads?

The answer to the first question lies, I believe, in a more complete understanding of partial stability, and the answer to the second question may well limit flux pumps to field energies below 100 kJ.

There is, of course, still another unexplored possibility, namely the use of truly automatic, passive, semiconductor rectifiers at liquid helium temperatures. This is again a materials problem. Commercial 5 A silicon rectifiers can be operated at 50 A in liquid nitrogen, but 4°K operation will require III-V or IV-VI semiconductors such as gallium-arsenide and lead-telluride. As a further speculation one might even consider a niobium-niobium oxide structure which would avoid one of the normal to superconducting metal contacts.

---

4. H.L. Laquer, J. Appl. Phys. 39, 2639 (1968).

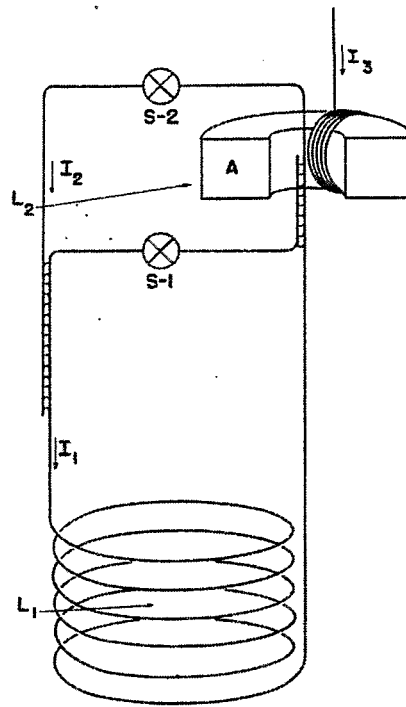


Fig. 1. Electrical flux pump with externally timed switches.

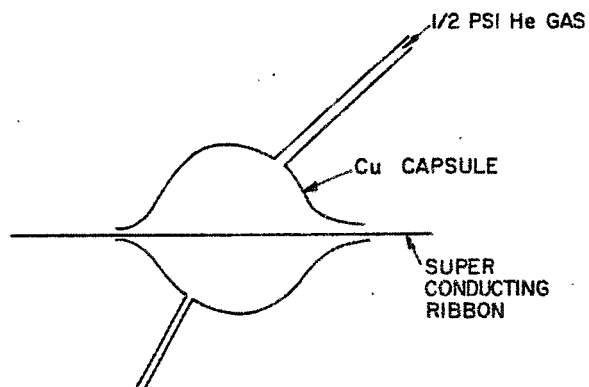


Fig. 2. Switch using warm helium gas.



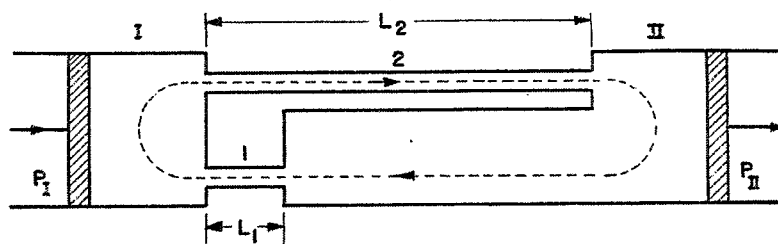


Fig. 3. Superfluid circuit with persistent circulation of He II.

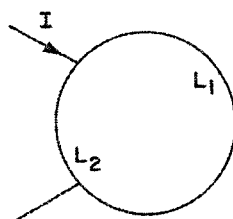


Fig. 4. Simple ring circuit with self-switching properties.

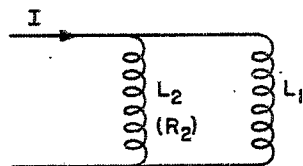


Fig. 5. Parallel inductance circuit, with  $L_2$  acting as an automatic switch.

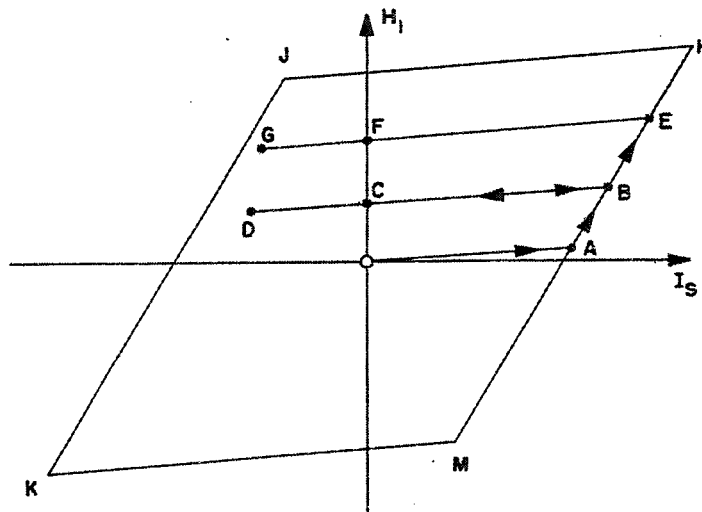


Fig. 6. Complete hysteresis pattern of circuit in Fig. 5. Field  $H_1$  in coil  $L_1$  as a function of externally applied current  $I_S$ .

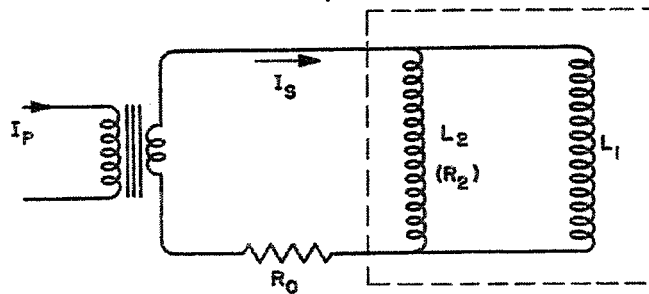


Fig. 7. Automatic flux pump with limiting resistor  $R_0$ .

## 60 Hz FLUX PUMPS\*

R.B. Britton  
Brookhaven National Laboratory  
Upton, New York

Interest in flux pumps at Brookhaven arose almost simultaneously with the receipt in late 1965 of 1.27 cm wide Nb<sub>3</sub>Sn ribbon that was capable of working at 500 to 700 A. Since we desired to run tests for periods of an hour or more at these currents, the problem of lead inefficiency with the associated helium loss was great. Now, the design of efficient leads for use up to 3000 A has become straightforward, but for steady dc operation of beam magnets above about 500 A, we are still interested in flux pumps.

From the start, we have concentrated on a pump design that could operate from 60 Hz, at first from a three-phase line, but in the latest pumps, from single phase. The cold part of the pump contains three parts: an air-core step-down transformer of ratio 120:1, and two identical switches that operate magnetically with no moving parts. These are wired as shown in Fig. 1.

Operation is as follows: An autotransformer (Variac) is used to control ac which is applied through a capacitor to the transformer. The capacitor provides 70-80° of phase shift in the current flow in the transformer primary. The secondary of the transformer has the two switch elements connected in series across it. The superconducting device or magnet is placed in parallel with one switch element. Each switch element is a length of fine, multistranded, soft superconductor (such as Pb30%Sn solder). The element can carry the full magnet current with no field around it, but is fully switched when immersed in a field of 600 to 2000 G. Each switching field is produced by a 1 in. bore air-core solenoid made of Nb48%Ti wire with extra spacing for helium flow. The solenoids are capable of cycling 0 to 10 kG to 0 at a 60 Hz rate (operating biased), but in switching use, 0 to 1.5 kG is about optimum. The switch magnets are driven in parallel from a second autotransformer. Each coil, however, has a diode in its circuit to bias it in one direction. A damping resistor is used across each coil to smooth out the diode action. The diodes are bucking so that the coils operate 180° out of phase. The total phasing is such that as one switch is energized and resistive, the transformer is drawing flux from space across the resistive element and into the SC circuit. On the next half-cycle, the first switch becomes SC and the second switch resistive. The transformer is now on the opposite swing so that it forces the flux through the second switch element and into the magnet.

In normal operation, the switch drive is adjusted with an oscilloscope to the point where the elements return completely to SC between cycles. The pumping rate is then fully adjustable with the transformer input control. To put the load, or magnet, into a persistent mode, the switches and transformer drive are turned to zero.

Two pumps of this type have been made. The first produced 1.5 W and was able to drive a 103 kG, 1 in. bore magnet normal, with a final current of 119 A. The second pump has larger switches and pumps at a 5 W maximum rate. The efficiency at present is not good — mainly because of losses in the switch elements. At maximum rate the efficiency is about 50%, while at one-half rate it appears to be somewhat better.

---

\*Work performed under the auspices of the U.S. Atomic Energy Commission.

Since a very small (approximately 0.5 W) pump will be used with each beam magnet, and only to counteract resistive joint losses, this efficiency is quite satisfactory.

A novel modification to the pump was suggested by K.E. Robins, namely, to add a second load magnet across the vacant switch. This has been tried and works as Robins predicted, both magnets being energized simultaneously at the same voltage.

A great deal of credit is due here to W.B. Sampson and K.E. Robins, who performed many of the preliminary experiments that led to this design.

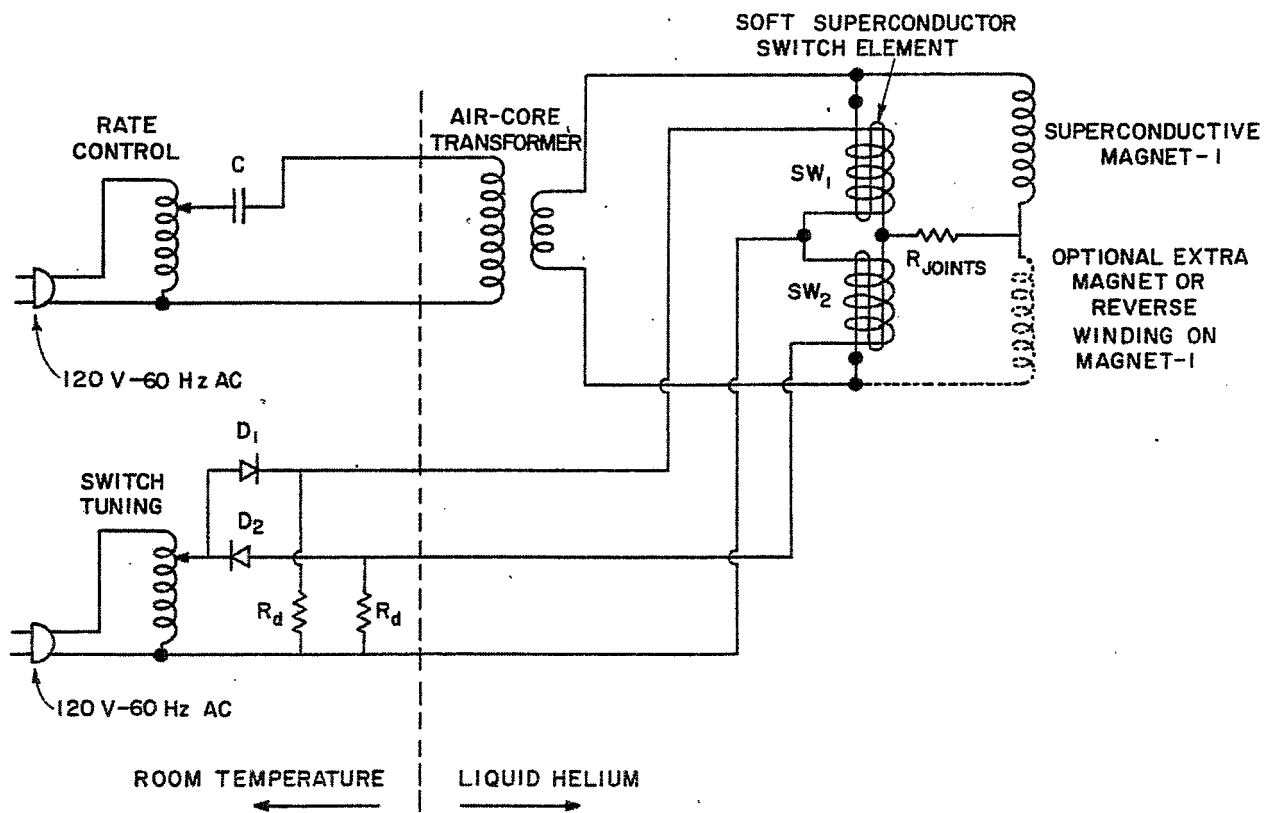


Fig. 1. Flux pump to make up resistive losses in dc beam magnet.

PROPOSAL FOR A FLUX PUMP UTILIZING THE INVERSE ETTINGSHAUSEN  
EFFECT IN HARD TYPE II SUPERCONDUCTORS IN THE MIXED STATE\*

W.H. Bergmann  
Argonne National Laboratory  
Argonne, Illinois

Most of today's superconducting magnets require large dc currents. Usually these currents are produced at room temperature and are transferred through leads into the low temperature environment of the magnet. The resulting heat losses are often a major component of the total losses. Therefore the attempt was made to equip the first superconducting magnets with thermally-operated superconductive switches. Such a device permits - in principle - operation of the magnet in a persistent mode, disconnecting the input leads. Unfortunately, it is nearly impossible to construct a superconducting magnet without normal resistive joints between the different superconductors. Therefore, most of the magnets operating in the persistent mode show a decrease of field with time. Thus devices with small heat losses which can charge the superconducting magnets and operate at liquid helium temperature are of interest. To these ends three different approaches have been made up to now. Giaever<sup>1</sup> demonstrated the principle of a superconducting dc transformer. Buchhold<sup>2</sup> introduces a small primary ac current, transforms and rectifies it with controlled power cryotrons at liquid helium temperatures. Volger<sup>3</sup> proposed the first superconductive generator by which a "macroscopic fluxoid" by appropriate motion was threaded literally into the magnet circuit.

Especially the latter class of devices invites speculation as to whether the dynamic properties of the Abrikosov vortices in type II superconductors could not be utilized for charging a superconducting magnet. Otter and Solomon<sup>4</sup> recently observed in type II superconductors two thermomagnetic effects analogous to the Ettingshausen and Nernst effects, which are associated with the motion of vortices. In particular, they measured the temperature gradient produced by the transport of entropy when vortices flow across a type II superconducting sample. They also established the existence of the inverse effect - the motion of vortices along an imposed temperature gradient. By this they demonstrated that thermal gradients are a driving force for moving vortices away from the warmer part of the sample.

We would like to propose, therefore, to connect the terminals of the superconducting magnet with a type II superconducting ribbon in the mixed state, much in the same fashion as it is done with superconductive switches for operation in the persistent mode. Under constant current operating conditions, this strip would act as a persistent mode switch. If we wish to change the field in the magnet, then we would have to apply a transverse temperature gradient across this strip. This would result in the vortices flowing either to the "inside" or to the "outside" of the strip and, since the vortices carry flux, it would transport flux either into the magnet circuit or out of it.

---

\*Work performed under the auspices of the U.S. Atomic Energy Commission.

1. I. Giaever, Phys. Rev. Letters 15, 825 (1965).
2. T.A. Buchhold, Cryogenics 4, 212 (1964).
3. J. Volger and P.S. Admiraal, Phys. Letters 2, 257 (1962).
4. F.A. Otter, Jr. and P.R. Solomon, Phys. Rev. Letters 16, 681 (1966).

It is very difficult at present to estimate the efficiency of such a flux pump. Otter and Solomon made their experiments with a very "weak" type II superconductor, an alloy of In with 40 atomic percent of Pb. They give the critical current density at 600 G as 40 A/cm<sup>2</sup>. But they demonstrated that the thermal driving forces are of the same order as the Lorentz forces.

Thus experiments with superconductors of high current-carrying capacity and variable pinning forces, as, for instance, niobium-titanium alloys, and niobium tin are indicated. But the important advantage of this flux pump would be that it could lead to an "autocharging" of superconducting magnets. The whole magnet could be constructed of one short-circuited superconductor of which only one short region has to be equipped with an appropriate temperature control. This region should preferably be situated in the low field region of the magnet winding where Lorentz forces do not compete with the thermal driving forces for the vortices. The Meissner-Ochsenfeld effect could possibly be utilized to initiate the charging process.

## SUMMARY OF THE FOURTH WEEK - AC LOSSES, INSTABILITY AND FLUX PUMPS

S.L. Wipf  
Atomics International  
A Division of North American Rockwell Corporation  
Canoga Park, California

### I. INTRODUCTION

The fourth week, reduced to three working days by the Fourth of July weekend, was the shortest of the six week-long sessions. (It is nice to have started with a definitely true statement; the remainder of this summary I dare not present with the same amount of conviction - at best it will be scientific truth, as I understood and remember it from the presentation of my colleagues, at worst it will be my own opinion.)

The shortness of our week was probably justified by it being the least hardware-oriented among the whole set of weekly studies, and we all know the economic difference between brain efforts and big plumbing projects - it is the difference between kilo- and mega-bucks. This, incidentally, may also explain why we never particularly discussed any economics during the three days, to the regret of but few participants.

The titled daily topics were: Ac Losses, Magnetic Instabilities, and Flux Pumps. These three topics all have to do with some aspect of the same phenomenon, namely, "dynamics of flux motion," and are therefore not as disconnected as one might think at first. In this summary I want to talk about each of the three topics in turn, giving you a quick survey of the individual contributions, followed by a somewhat longer resume of the present state of the art as it emerged and came into focus during the meeting. After this there should be some time left to discuss the fourth topic which was also included in the formal sessions and which concerned the present assessment and the outlook for the whole field. This fourth part is easily of most general interest and may serve as dessert after the first three courses of a more bread-and-butter-like character.

### II. AC LOSSES

Table I lists the presentations dealing with ac losses, each characterized by a few key words.

The coil studies (Voelker, Morgan) were similar in nature. Losses of a complete coil (designed to be useful for accelerator applications) were measured. The losses per cycle are proportional to  $H^n$ , with  $H$  the peak-to-peak amplitude in field and  $2 < n < 3$ . The frequencies are typically of the order of 1 Hz or less for the highest fields ( $\sim 30$  kG).

The resistance of a superconductor in a changing field has been measured in detail for various alloys and wire diameters by Rayroux (see Figs. 8 and 9). It is inversely proportional to the wire diameter which suggests the use of the smallest possible wire for ac applications. If many such filaments are paralleled in a pure copper matrix one has to twist the assembly to avoid breakdown of the outer filaments due to shielding of transverse flux. These ideas were put forward independently both by R. Hancox, reporting on behalf of P.F. Smith,\* and by M. Foss. The importance of this will no doubt soon be substantiated by experiments.

\* P.F. Smith presented his views in detail in the fifth and sixth week which he attended (these Proceedings, p. 913 and p. 967).

## TABLE I\* - AC LOSSES

REVIEW: S.L. Wipf, AI.

### EXPERIMENTS - Reports on coil studies:

- F. Voelker (W.S. Gilbert, R.E. Hintz), LRL: Coils wound with round wire, NbTi.
- G.H. Morgan (W.B. Sampson, R.B. Britton, P.F. Dahl), BNL: Coils wound with ribbon, Nb<sub>3</sub>Sn.
- J.M. Rayroux (D. Itschner, P. Müller), BBC: Dynamic resistivity, NbZr, NbTi.

### SHORT COMMENTS:

- W.T. Beall (R.W. Meyerhoff), UCC: Short samples of ultra-pure Nb and Nb alloys.
- R. Hancox (P.F. Smith), RHEL: Very thin multifilaments, twisted.
- M. Foss, Carnegie-Mellon U.: Twisted filaments.

---

\* The names of the authors making the presentation are given with the other authors in parentheses. The affiliation is abbreviated; see list of participants for details.

---

### State of the Art (Resume):

For practical applications one is concerned with ac losses in type II superconductors exhibiting flux pinning, i.e., superconductors with high critical currents in high fields. Energy is lost when magnetic flux has to move inside such a superconductor; pinning is very similar to friction, but we can also look at it in terms of resistivity, as we shall see.

Figure 1 shows the three regions we have to distinguish, demonstrated with the help of a magnetization curve (vs H) of a cylinder in a parallel field H. We remember that a changing field will induce currents at and below the surface of the superconductor which try to shield the field change from the interior. The current density in this shielding layer is always critical ( $j_c$ ), either positive or negative, and it corresponds to a gradient in magnetic induction B which is given by one of the Maxwell equations (in this case  $dB/dx = 4\pi j$ ). The lower portion of Fig. 1 illustrates the gradient of B in the shielding layer of the cylinder for which the magnetization is shown. In this case the shielding currents are solenoidal but the same illustration is also good for a transport current along the cylinder which then would flow in the shielding layer and produce a circular external field.<sup>†</sup> The losses are always determined by the ac field

---

<sup>†</sup> A discussion of the "critical state" is found in Hart's review of instabilities (these Proceedings, p. 571).



at the surface no matter whether this field is externally applied or due to an applied current. According to the peak of the ac field,  $H_a$ , one distinguishes:

$$\text{Region I : } H_a < H_{c1} .$$

Below  $H_{c1}$  all the shielding is done by a surface current (in the London penetration depth). There is no flux movement inside and there should be no loss.

$$\text{Region II : } H_{c1} < H_a < H_p .$$

The crosshatched area represents the flux being pushed in and out during a cycle. There is still a step at the surface,  $\Delta H$ . The loss is represented by the shaded hysteresis loops. The magnetization has a different value for increasing and decreasing fields because the shielding layer during each half cycle consists of two parts, one close to the surface with the direction of  $j_c$  given by the present field change, and the remainder with the opposite direction of  $j_c$  established by the preceding half cycle. The bulk of the available experiments (50 to 10 000 Hz) belong to region II.

$$\text{Region III : } H_p < H_a < H_{c2} .$$

$H_p$  is the value of the external field for complete penetration of the superconductor. While in region II there is always a core which does not see the ac field, in region III the thickness of the penetration layer  $[(H_a - \Delta H)/4\pi j_c \geq r]$  would become greater than the radius of the specimen and then ac losses will occur throughout the volume of the superconductor. For the losses in coils this region is of most interest.

$$\text{Region IV : } H_{c2} < H_a < H_{c3}$$

is of more theoretical than practical interest and is only mentioned for the sake of completeness.

Let us discuss the results for region I, II, and III in turn.

Figure 2 shows experimental loss results for Nb where  $H_{c1}$  has a value of roughly 1000-1500 Oe (according to purity). It is clear that in region I and II the losses have to be given per unit surface exposed to the ac field and vs  $H_a$ . Most of these results represent losses in region I and we notice that they are all over the place. The surface polish and the amount of frozen-in flux seem to be crucial for the differences. We have said that there should be no losses, because there is no flux moving in and out of the superconductor. However, each fluxoid frozen into the specimen has to pierce the surface in two points, one of entry and one of exit. Under the influence of the external ac the position of these points will oscillate with a corresponding loss due to the fluxoid movement at and immediately below the surface. Such a qualitative explanation is substantiated by measurement of losses vs the background field during cooldown (which is a measure of the amount of frozen-in flux) given in Fig. 3.

The transition from region I to region II, which in Fig. 2 does not appear very clearly, is very well demonstrated in Fig. 4 which was presented by Beall (see Table I) who made measurements on Nb of very high purities (up to a resistance ratio of 20 000!).

In Fig. 5 we see the results of most published loss measurements on Nb alloys. With the exception of curves v and w, which belong to region I ( $H_{c1} \approx 100-400$  Oe), and the upper parts of curves a, b, c, which belong to region III (and fall much closer together if plotted as loss per unit volume), all others are in region II and show a trend which is close to  $H^3$  at the upper end. The calculation (with the simplifying assumption of  $j_c = \text{const}$ ) gives:

$$\text{Loss/cycle/cm}^2 = 4.22 \times 10^{-9} (H - \Delta H)^3 / j_c \quad (1)$$

with the dimensions for the constant  $[J \cdot A \cdot Oe^{-3} \cdot cm^{-4}]$ . There are only two material properties,  $j_c$  and  $\Delta H$ , which determine the losses. Of these  $\Delta H$ , which depends largely on surface qualities, is not very well investigated. Figure 6 shows measurements\* of  $\Delta H$  vs  $H$  for NbZr; it is equal to  $H_{c1}$  ( $\approx 500$  Oe) at  $H_{c1}$  and reduces to less than 100 Oe in higher fields. These data are used in Fig. 7 together with a value of  $j_c = 4 \times 10^5$  A/cm<sup>2</sup> to obtain curves 2 and 3 (corresponding to samples 2 and 3 in Fig. 6); the shading indicates the majority of curves in Fig. 5, and curve 1 corresponds to  $\Delta H = 0$ . Also indicated in this figure are the losses one would have in copper at 4.2°K ( $\rho = 10^{-8}$   $\Omega \cdot cm$ ) provided the conductor is thick in comparison to the skin depth. The loss per cycle depends on frequency as does the skin depth. The superconductor is better only by one or two orders of magnitude for  $H_a > 1$  kOe.

In region III the losses become so high that a normal transition due to thermal runaway may already occur at a peak field which is very small compared to  $H_{c2}$ , unless, of course, the frequency is drastically reduced. This is the reason why one expects to run coils with high peak fields only at very low repetition rates. In this region, where the whole volume of the superconductor is lossy, it is useful and convenient to talk about the dynamic resistance of the superconductor. A simple case is treated in Fig. 8. A cylinder of diameter  $2b$  is in an external parallel field  $H$  ( $> H_p$ ) which increases at a steady rate  $dH/dt$ , and the field profile through the cylinder is given at two different times ( $j_c$  independent of  $H$  is assumed). Faraday's induction law gives the electric field  $E$  at a radius  $r$ .  $E$  is parallel to  $j_c$  (which is constant everywhere) and the ratio  $E/j_c$  gives the local resistivity which is proportional to  $r$ . Should we now send a transport current (small compared to  $\pi b^2 j_c$ ) through the cylinder it would encounter an average resistivity:

$$\rho_{\text{dyn}} = A \cdot \frac{b}{j_c} \frac{dH}{dt} \quad (2)$$

The distribution of the transport current is a nontrivial problem, but if a uniform distribution is assumed the proportionality constant  $A$  becomes  $\frac{1}{4}$ .†

Because this is a magnetic diffusion problem, a comparison with the more familiar thermal diffusion problem with its many existing mathematical solutions is helpful.  $H$  is equivalent to temperature  $T$  and  $\rho/4\pi$  to the diffusion constant  $\alpha$ . The diffusion equation for a steadily increasing temperature gives the stated solution for the temperature difference between the surface and the center. This also corresponds to an  $A$  of  $\frac{1}{4}$ . The heuristically valuable comparison, however, has its limitation in the fact that  $\rho$  is by no means a constant.

We see a measurement of this resistivity in Fig. 9 which shows the voltage due to a transport current across a bifilar coil in a steadily increasing or decreasing field whose value is given in the abscissa.  $H_p$  is about 4.5 kG and below this value the voltage is zero because the transport current flows through the completely superconducting core. The same is true on reversing the field sweep at 15 kG where a shrinking

\*  $\Delta H$  in Eq. (1) has at least four distinct components, corresponding in origin to: the reversible magnetization, the surface pinning, the surface barrier, and the surface sheath (the last three are not necessarily different mechanisms); thus  $\Delta H = \Delta H_{\text{rev}} + \Delta H_{\text{s.p.}} + \Delta H_{\text{s.b.}} + \Delta H_{\text{s.s.}}$ . The results presented in Fig. 6 do seemingly not include the reversible part except very near  $H_{c1}$ , but the irreversible components are included twice. Strictly speaking,  $\Delta H$  of Fig. 6 and  $\Delta H$  of Eq. (1) are two different quantities, though very similar in magnitude.

† In practical units:  $A = 2.5 \times 10^{-9} \Omega \cdot A \cdot \text{sec} \cdot \text{cm}^{-2} \text{ Oe}^{-1}$ .

dc field core remains until 13 kG is reached. Rayroux presented results showing the agreement with the given formula for  $\rho_{\text{dyn}}$  with regard to  $b$  and  $dH/dt$ .

Although in a complete coil there are always the losses of region I and region II sections, they disappear in comparison to region III losses. Calculation of these losses — even only approximate — is quite complicated; possibly the concept of the dynamic resistivity will prove useful.

### III. MAGNETIC INSTABILITIES

Magnetic instabilities manifest themselves as sudden redistributions of the field profile inside a superconductor, commonly called flux jumps (this term is often avoided when less than the whole cross section of the superconductor is affected). The importance, or the nuisance value, of instabilities is the possibility of a quench or normal transition due to the accompanying large heat dissipation.

Table II lists the presentations related to this topic.

TABLE II — INSTABILITIES

REVIEW: H. Hart, GE.

EXPERIMENTS — Flux jumping in commercial tape conductor ( $\text{Nb}_3\text{Sn}$ ):

L.O. Oswald (G. del Castillo), ANL.

A.D. McInturff, BNL.

SHORT COMMENTS:

Y. Iwasa, MIT: Upper field limit of instability (experiments).

R. Hancox, CLA: Survey of instability regions in coils.

S.L. Wipf, AI: Flux annihilation and instabilities.

---

#### State of the Art (Resume):

The instability problem is very complex and one is still at the stage of trying to find all the important variables to be fed into the theory. The superconductor under consideration is in general in a stable state of thermodynamic nonequilibrium (e.g., the critical state). Under certain conditions this state becomes unstable, i.e., an excursion caused by a small disturbance will grow and result in a transition to a new (nonequilibrium) state. We restrict ourselves to illustrating why instabilities occur (we follow Hart's review). Consider the field profile inside a superconductor which is always defined by the critical current ( $j_c$ ) and previous magnetic history. We keep the external field constant, and consider a uniform rise in temperature,  $\Delta T$ , which will reduce the critical current and require a new field profile. This establishes itself by diffusion of flux coming from the outside. The heat released in this process,  $\Delta Q_m$ , can be calculated; locally it is of the same order as the change in potential magnetic energy,  $(\Delta B)^2/8\pi$ ; over-all it is a function of temperature and external field. A qualitative picture is given in Fig. 10a. Assuming adiabatic conditions, the heat absorbed by the temperature rise,  $\Delta Q_T$ , can also be given (Fig. 10b). If  $\Delta Q_m$  is always less than  $\Delta Q_T$ , the initial state is stable (Fig. 10c), but if the tangent of

$\Delta Q_m$  is above the tangent of  $\Delta Q_T$  at the origin then it is unstable (Fig. 10d). We observe that in the unstable case the two curves cross again, thus determining another stable field profile. If the temperature of this crossover point is not too high (compared to the critical temperature) one has a limited instability that does not result in a temporary normal transition. Otherwise a runaway instability, a catastrophic flux jump, is the result. One can easily calculate the limit of full stability, but not the experimentally important event, the onset of runaway instability. There are two main complications. At the beginning, the magnetic excursion may be very slow allowing heat conduction out of the superconductor. This reduces the temperature rise and helps to limit the instability, as is seen in Fig. 10e where  $\Delta Q_T$  is modified to include thermal diffusion. On the other hand, if a superconducting coil is considered, the transport current produces an additional dissipation, raising the effective  $\Delta Q_m$  and thus the danger of instabilities. Hart presented a few calculations for suitably restricted situations, but he includes some very real coil cases (wound with GE tape, of course).

Although the agreement between experiment and calculations is so far rather poor, our qualitative understanding progresses. Hancox presented a way of looking at instabilities which I think has great appeal and will help to reduce some of the existing confusion. This is illustrated in Fig. 11 where in an I vs H diagram the various stability regions (for a coil) are entered. Both fully stable regions correspond to situations given in Fig. 10c; in the high field region  $\Delta Q_m$  becomes small because the superconducting wire is fully penetrated and  $j_c$  is small. Little flux is required to change the field profile and the dissipation is small. Iwasa presented experimental data for the upper field limit of instability,  $H_{st}$ , in 0.010 in. Nb25%Zr wire; it is between 25 and 30 kG.  $H_{fi}$  which terminates the lower stability region is around 3 kG. Hancox also gives calculations for  $L_*$  and the boundary between limited and catastrophic instabilities (which lead to breakdown in coil performance). He further pointed out that coils have to be designed so that no region of the coil falls into the catastrophic instability area.

One can extend the diagram to include temperature as a third dimension and one may indicate how a low  $dH/dt$  (or a high thermal diffusivity) may reduce the catastrophic instability region.

Through coil degradation experiments<sup>1</sup> one has been aware for some time of the shape and position of the catastrophic instability region. The constructors of coils, knowing that instabilities do occur, have always tried to keep them limited to prevent catastrophic jumps. These "stabilization" efforts can be seen as either affecting (a)  $\Delta Q_T$ , or (b)  $\Delta Q_m$  by:

- (a) avoiding a large temperature rise by increasing the effective specific heat (liquid helium in porous conductor, proximity of other metals such as Pb or Cd); improving the cooling (spaced windings for circulating helium); slowing down flux motion (by providing shorts and copper sheets between layers);
- (b) providing a low resistivity bypass to avoid heating by transport current (paralleling the superconductor by copper, silver, etc.), using very thin wire to reduce  $H_{st}$ .

Most commercial conductors as well as large coils use a combination of these stabilization techniques. The conservative character of some of these approaches indicates how little one trusts our present understanding of the instability problem.

Having talked about the occurrence and the effect on coils of instabilities, we might ask what is the experimental appearance of an instability? Oswald presented results which show a variety of limited instabilities distinctly different in character.

Plotted against the increasing field in Fig. 12, some look like noise while others represent larger flux movements, seen as temperature spikes; these spikes may form repeating groups with the spikes increasing in size in each group, etc. Such a variety of manifestations shows the complexity of the problem most directly.

The mathematical difficulty seems to me to lie in the fact that two diffusion equations have to be solved simultaneously, one for the temperature and one for the magnetic field, whereby the magnetic diffusion coefficient is not constant but a non-linear function of both T and curl H. From the notorious scattering of experimental results (under equal conditions the catastrophic flux jump field scatter is 5-20%), one might say that nature itself seems to have trouble with this problem.

#### IV. FLUX PUMPS

The idea of using superconducting coils is not much older than the idea of using superconducting power supplies to feed them. The possibility of very large currents in combination with coils of few turns is a major advantage. What has hampered progress?

Achievements and problems were highlighted in presentations by most flux pump builders in this country, as summarized in Table III.

TABLE III - FLUX PUMPS

##### PROGRESS REPORTS:

- S.L. Wipf, AI: Moving magnetic field pumps.
- R. Rhodenizer, GE: Rectifier type flux pump (Buchhold).
- M.S. Lubell, ORNL: Comparison between flux pumps and vapor-cooled leads.
- H.L. Laquer, LASL: Automatic switching flux pump (rectifier for asymmetric ac); flux pump equivalent in superfluid helium.
- R.B. Britton, BNL: Flux pump program at Brookhaven.

##### SHORT COMMENTS:

- W.H. Bergmann, ANL: Possibility of flux pumping by using Nernst-Ettinghausen effect equivalent.

---

##### State of the Art (Resume):

The flux pump principle is illustrated in Fig. 13. (a) A closed loop is shown which because of its zero resistance conserves any flux linked with it. (b) Only if its zero resistance is interrupted can flux from a small magnet be admitted. (c) Removal of the magnet induces a current increment to keep the flux constant. (d) On repeating the process, previously accumulated current is preserved by providing a zero resistance bypass. "Switching" is preferably done by creating a resistive region by exceeding the critical field; this allows the same magnet to be used for both switching and pumping if its field strength close to the pole exceeds the critical field. (e) In a popular arrangement the bypass loop is replaced by a sheet,

allowing the creation of a normal, flux containing zone opposite the magnet pole, which it will follow, being swept across the sheet into the closed circuit. The same process can be realized without moving parts as in Fig. 14, which shows a "loop" and a "plate" arrangement. It has become convenient to distinguish between "rectifier type" flux pumps of which the upper is an example, and "moving magnetic field" flux pumps of which the lower is an (albeit impractical) example. In its useful versions the second type employs rotating shafts as a typical example demonstrates in Fig. 15.

To dwell on the achievements we discuss the rectifier type pump (Rhodenizer) which, in the very thoroughly developed version (by Buchhold) of GE, is to date the only commercially available flux pump. Its salient features are best explained by means of the diagram in Fig. 16 where we see an ordinary full wave rectifier arrangement with a primary, a transformer core, a secondary, and a load L. Both primary and secondary are superconducting; we see the parts of the flux pump which are in liquid helium. Instead of the usual one-way-valve rectifying elements, we have switches X and Y (see Fig. 13d and Fig. 14-top) consisting of superconducting tape which can be made resistive by magnets ("power cryotrons"). These elements do not rectify automatically, they have to be driven by programmed current from outside the cryostat. In order to keep the losses to a minimum it is imperative to operate a cryotron only when the current flowing through it is exactly zero. Otherwise there is a resistive loss until the initial current is driven into the other branch by the ohmic voltage. Next to each cryotron, in the GE device there are sensors of the form of saturable reactances, which not only indicate when the current through the cryotrons is zero but also lengthen the time interval of this zero flow, giving the cryotrons time to switch. Sophisticated electronic gear (at room temperature) allows the regulation of the output at a fixed primary frequency ( $\sim 10$  Hz). The losses are quite small and come from the back current through the resistive cryotrons, the ac losses in the superconductive windings (including the s-n transition in the cryotron), and the hysteresis losses in the ferromagnetic cores.

The moving magnetic field type pump is well suited to illustrate a few problems. Figure 17 shows a normal zone in a superconducting sheet and the type of current distribution which is set up during its movement. We see the eddy current distribution induced in the normal spot, which corresponds to the back current through the cryotrons of the rectifier type; the ensuing loss is in principle unavoidable. A more serious loss comes from the current distribution which is encountered by the leading edge as it becomes normal. The resulting ohmic voltage drives this current out of this region, partly in front of, partly behind, and partly into the normal zone, accompanied by considerable dissipation. The difficulty of treating this process analytically makes an (ill-patronized) art out of improving this type of pump. In principle, it is possible to arrange inductively for zero current at the leading edge and to avoid this type of loss which is avoided in the GE pump by the use of Buchhold's saturable reactors.

The moving magnet field pump is attractive in its simplicity and its suitability for producing large currents. Currents in excess of 10 000 A have been reached and maintained, although not in coils of any size. The upper current limit is generally reduced by the occurrence of catastrophic instabilities in the sheet. These seem to be caused by the imbalance of the current distribution when the leading edge (see Fig. 17) switches too much current, either ahead of or behind the spot, to maintain equilibrium during one full rotation (see Fig. 15). Simple remedies for increasing efficiency or increasing the limiting current seem to be divergent, at least in my own limited experience.

Figure 18 shows the reported efficiencies of various pumps.  $E$  is the energy stored in the coil and  $\Delta E$  the energy lost in the pump while the coil is pumped up. The solid curve gives the possible efficiency of a given pump vs the inverse ratio of power output to volume of the periodically switched superconducting material in the flux pump. The shape of this curve is determined by the unavoidable loss (back current, eddy current);

its position with regard to the abscissa is less strictly fixed and reflects considerations of instabilities (degradation) and protection against burnouts of the pump.<sup>2</sup> The superior efficiency of the GE pump (newest results 4-6% higher) which is the only rectifier pump in this graph is evident.

Table IV summarizes a comparison of the two types of pump. We imply that the moving magnet type has not been in the fortunate position — notwithstanding a considerable amount of publicity<sup>3</sup> — of receiving the determined and successful development effort which GE gave to the rectifier pump.

TABLE IV — COMPARISON BETWEEN THE TWO FLUX PUMP TYPES

<u>Moving Magnetic Field</u>	<u>Rectifier</u>
Simple to build ( $\sim 10^3$ \$)	Complicated ( $\sim 10^4$ \$)
Not well understood	Well understood
Difficult to develop	Well developed
Good for high current	High efficiency
Two problems:	
Shielding ( $< 100$ Oe)	
Protection	

Shielding and protection are the two problems which need consideration when pumps are to be used in conjunction with large coils. Proper operation is only achieved in low background fields because of ferromagnetic components and, to a lesser degree, because of low field superconductors (such as Nb) in the switches. Pumps without these components, employing thermal switching, tend to be very ineffective (Laquer). The protection problem seems to be solved by a diode, developed by GE, which operates in liquid helium and has a symmetric V-I characteristic. If the voltage exceeds  $\pm V_c$ , its resistance drops to practically zero.

There is a general consensus that power leads from room temperature will be used for charging or discharging large coils. Any permanent operation will give preference to flux pumps, even at their presently available low efficiency, over the best vapor-cooled leads (Lubell). Flux pumps will function in lieu of persistent switches, able to compensate for small resistive losses in the system.

Other ways of producing currents<sup>4</sup> in superconducting circuits, e.g., by means of the Nernst-Ettinghausen effect as suggested by Bergmann, even if they are shown to be feasible, are unlikely to be of great practical interest for some time to come.

## V. ASSESSMENT AND OUTLOOK

The spreading and gathering of opinions and prophecies are parts of the business which are relegated to corridor discussions of bigger and shorter conferences and which many people feel are among the most useful functions which any meeting fulfills. We decided to bring these activities into the lecture hall as much as possible, the audience being comfortably small.

Table V summarizes the contributions under this heading.

# TABLE V - ASSESSMENT OF PRESENT AND OUTLOOK

J.P. Blewett, BNL: Actual and potential uses of superconductors in experimental nuclear physics.

N.S. Nahman, NBSB: Superconducting transmission lines for power and communications.

## REPORTS FROM ABROAD:

JAPAN: N. Takano, Toshiba.

EUROPE: J.M. Rayroux (Switzerland, France, Holland).  
G. Bogner, Siemens (Germany).  
R. Hancox (England).

OPINION: Questionnaire.

---

Of the two major talks, Blewett's was for the benefit of the majority of the participants whose main field is solid state physics and who were largely ignorant about the requirements in high energy physics. If I gave details in this gathering I would be carrying coals to Newcastle.

Undoubtedly one of the highlights of the week was Nahman's talk about transmission lines. He interprets this term in its widest sense and points out the possible uses which a trench filled with a Dewar pipeline may have. Not only could the obvious power be transmitted but also - and this in a superior way to most alternatives - information. One might as well use the same hardware to pipe liquid cryogenics around the country and, as a fourth possibility, join small but powerful cryogenic computers and memories into the system with the transmission line facilitating the access. As an expert for many years in superconducting delay lines, he detailed the communication transmission line aspect, extolling the advantages in bandwidth over existing alternatives. If this sounds Utopian to some of you, you should remember that political boundary conditions will most likely prevent the full use of these possibilities long after the technological problems are solved.

The reports from abroad did not sustain any excess optimism generated by Nahman's talk.

Japan has been very successful in producing practical superconducting wires using Nb-based alloys or  $V_3Ga$ ; it is also engaged in a number of larger magnet projects for MHD and for high energy physics. Maybe progress does not seem to be so rapid as one might have hoped.

The European scenery has similarities to the scenery here, yet bubble chamber projects at CERN and at the Rutherford Laboratory as well as the British homopolar motor, existing in a 50 hp and projected in a 3000 hp version, show great promise.

This brings us to the last item on the agenda, namely an opinion poll. You understand that the results from this poll should be considered as being a good deal less formal than Mr. Harris' and Mr. Gallup's reports in the dailies. There remains the entertainment value.

The questionnaire (see Table VI) had three sections. The first section should reflect the present status of the topics dealt with by comparing their importance with



regard to present and future problems, and by indicating the necessity for research. The second section considered the importance of various superconductivity applications in the future and also distributed the responsibility for their research. Of course everybody is aware that the funding source for this research is largely the same in all three cases (namely, 100% for Federal Government, 80-90% for universities, and perhaps 70% for private industries). The third part asked for the background of the respondent, who otherwise remained anonymous. Fifteen returned questionnaires could be evaluated and the results are presented in Table VI. For better visual impact it is the diameter of the black dots which corresponds to the percentage. For "comparative importance," only partial agreement was found and given in words.

Since an equal number of government and industrial representatives answered the "responsibility for research" question, it is interesting to compare the two groups and the percentages are given in each box, top right for industry and bottom left for government. We notice that such a comparison reflects the popularity of a subject. When we find that each group feels that the other ought to carry the ball we are not surprised that the field in question already has a somewhat tarnished history such as MHD and Computers, or has not an immediately strong appeal, like transmission or transportation. Such fields have been marked by a B for beggars.

It is fitting for this Summer Study that the only field showing an enthusiastic reception is the one of accelerators. It has been marked with a P for prima donna.

#### REFERENCES

References to papers presented during this Summer Study (see Tables I-III, V) are given by name.

1. E.R. Schrader and F. Kolondra, RCA Review 25, 582 (1964);  
M.S. Lubell, J. Appl. Phys. 37, 258 (1966);  
M.S. Lubell, in Advances in Cryogenic Engineering (Plenum Press, 1966), Vol. 11, p. 652;  
W.B. Sampson, M. Strongin, A. Paskin, and G.M. Thompson, Appl. Phys. Letters 8, 191 (1966);  
K. Yasukochi, T. Ogasawara, N. Usui, H. Tobayashi, and T. Ando, in Cryogenic Engineering, Proc. 1st Intern. Cryogenic Engineering Conference, Kyoto, 1967 (Heywood-Temple, London), p. 175.
2. S.L. Wipf, in Cryogenic Engineering, op. cit. p. 137.
3. D. van Houwelingen and J. Volger, Philips Res. Rep. 23, 249 (1968).
4. T.A. Buchhold, in Cryogenic Engineering, op. cit. p. 133.
5. Detailed references to Figs. 2 and 5 are found in Table IV and VI of Wipf's review of ac losses (these Proceedings, p. 511).
6. J.M. Victor, G.A. Persyn, and W.L. Rollwitz, Cryogenics 7, 119 (1967).
7. T.A. Buchhold and P.J. Molenda, Cryogenics 2, 344 (1962).
8. H.A. Ullmaier and W.F. Gauster, J. Appl. Phys. 37, 4519 (1966).
9. J.M. Rayroux, D. Itschner and P. Müller, Phys. Letters 24A, 351 (1967).
10. S.L. Wipf, in Intern. Symp. Magnet Technology, Stanford University, Palo Alto, Calif., 1965, p. 615.
11. M.S. Lubell and S.L. Wipf, in Advances in Cryogenic Engineering (Plenum Press, 1968), Vol. 13, p. 150.

12. T.A. Buchhold, in Pure and Applied Cryogenics (Pergamon Press, 1966), Vol. 6, p. 529.
13. H. Van Beelèn, Miss A.J.P.T. Arnold, H.A. Sypkens, J.P. Van Braam Houckgeest, R. De Bruyn Ouboter, J.J.M. Beenakker, and K.W. Taconis, Physica 31, 413 (1965).
14. S.L. Wipf, Westinghouse Res. Lab. Report, 1966 (unpublished).

TABLE VI

## QUESTIONNAIRE

BROOKHAVEN SUMMER STUDY, WEEK OF JULY 1-3, 1968

Please reflect your opinions as to the present and future status of topics related to this week's discussions:

1. Present Status

	Present Problems or Emphasis of Necessary Research (make up to 100% ←→)				Comparative Importance (rank as: 1,2... ↓)		Remarks
	Basic	Applied	Develop- ment	Engineer- ing	Present	Future	
Ac losses	●	●	●	●	fairly	most	
Ac critical currents and fields	●	●	●	●			
Instabilities	●	●	●	●	most		
Flux pumps	●	●	●	●	least	least	
Other							(fatigue properties)

2. Future, with respect to applications:

		When will it become important? (make up to 100% ←→)			Who should sponsor research? (make up to 100% ←→)			Remarks
		1-3 yrs	3-10	> 10 yrs	Fed. Govt.	University	Private Ind.	
Accelerators	P	●	●	●	73 ● 55	19 ● 33	8 ● 12	← Industry ← Government
Transmission	B	●	●	●	31 ● 46	2 ● 4	67 ● 50	
Transportation (levitation)	B			●	40 ● 50	5 ● 10	55 ● 40	
Small devices (weak link, etc.)		●	●	●	15 ● 17.5	52.5 ● 37.5	32.5 ● 45	
Computers	B		●	●	8 ● 26.5	20 ● 26.5	71.5 ● 47	
MHD	B			●	28 ● 55	5 ● 7	67 ● 33	
Other								Machinery (Ind.) Fusion (Govt.) Room temp. S.C. (Govt.)

3. I describe myself as:  
(answer each column)

(make up to 100% ↑↓)

Experimentalist	●	Basic	●	Government	●
Theoretician	●	Applied	●	University	●
Commercial	●	Development	●	Industry	●
		Engineering	●		

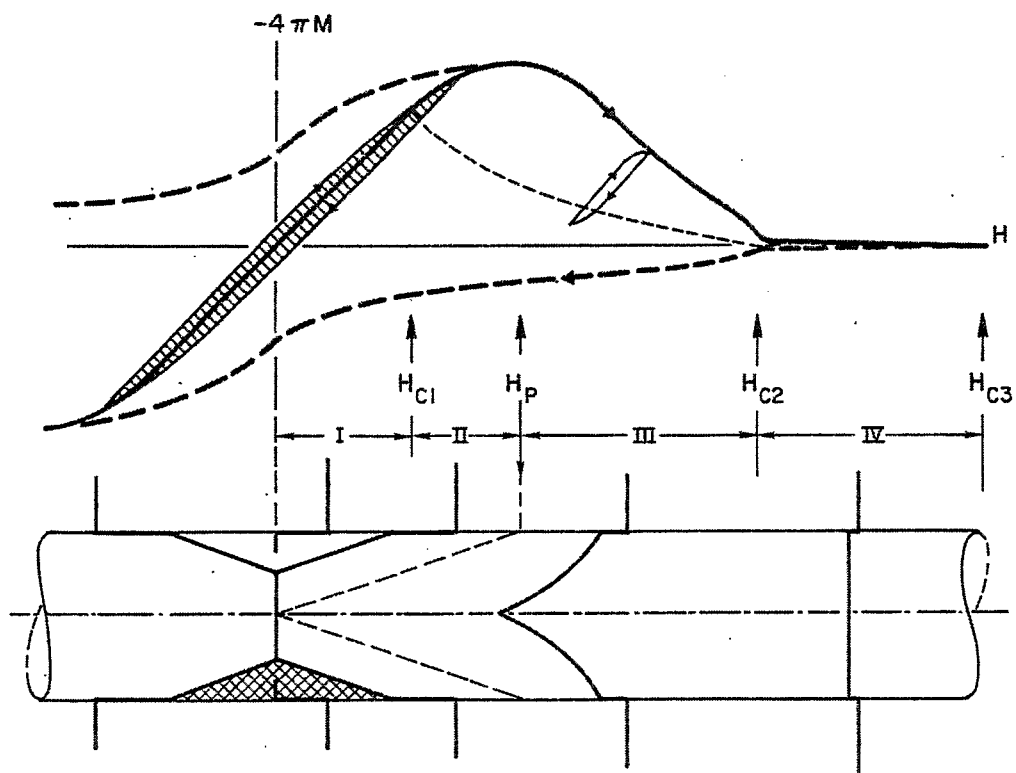


Fig. 1. Ac loss regions.

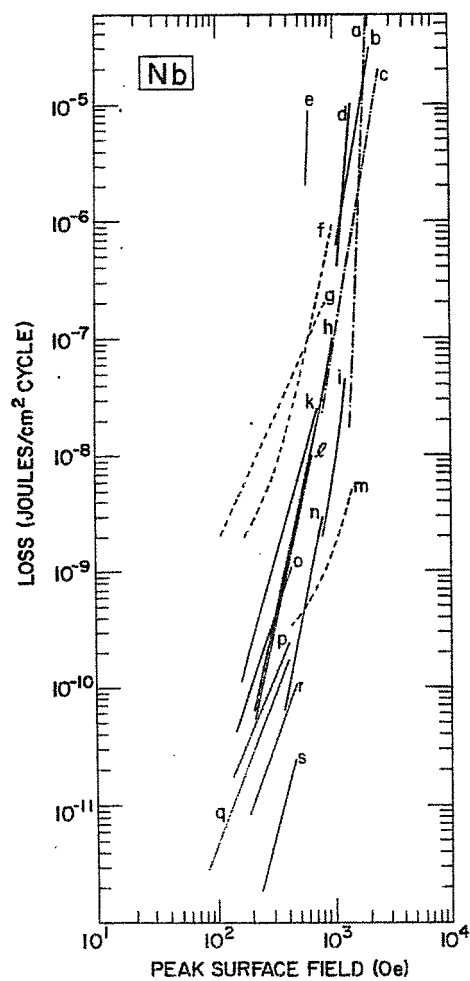


Fig. 2. Reported ac losses of pure Nb (Ref. 5).

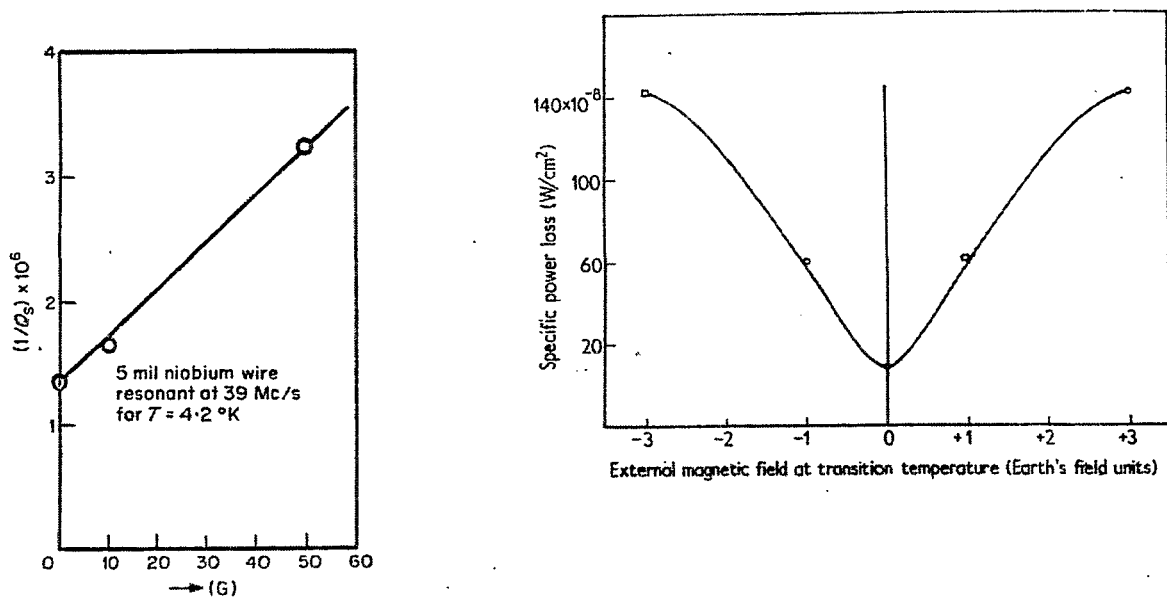


Fig. 3. Illustrating the dependence of ac losses in region I on frozen-in flux (Refs. 6 and 7).

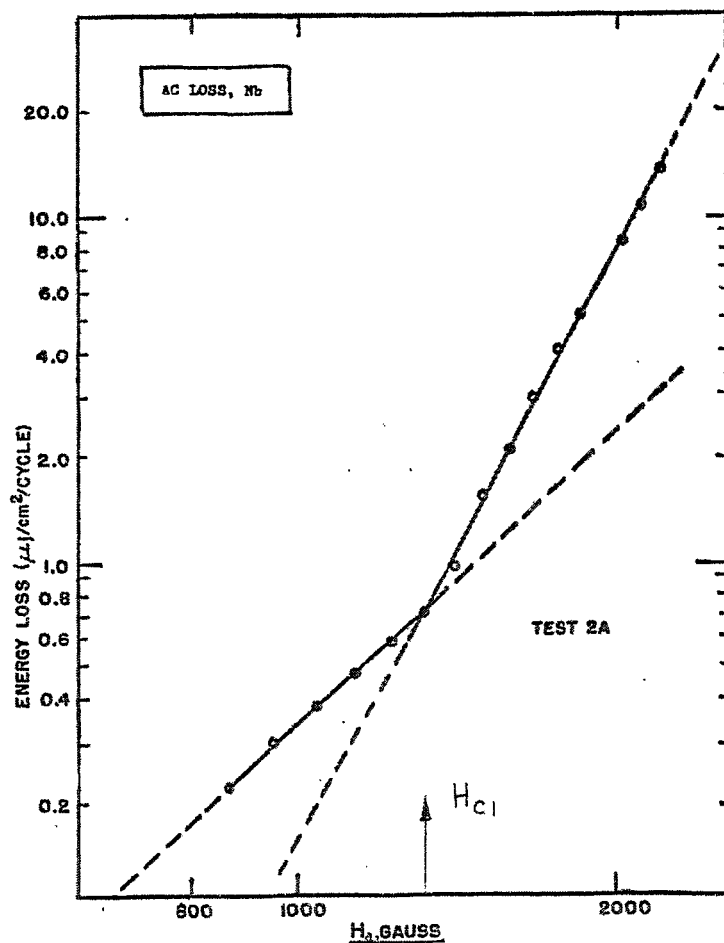


Fig. 4. Ac loss in Nb; transition from region I to region II (Beall and Meyerhoff).

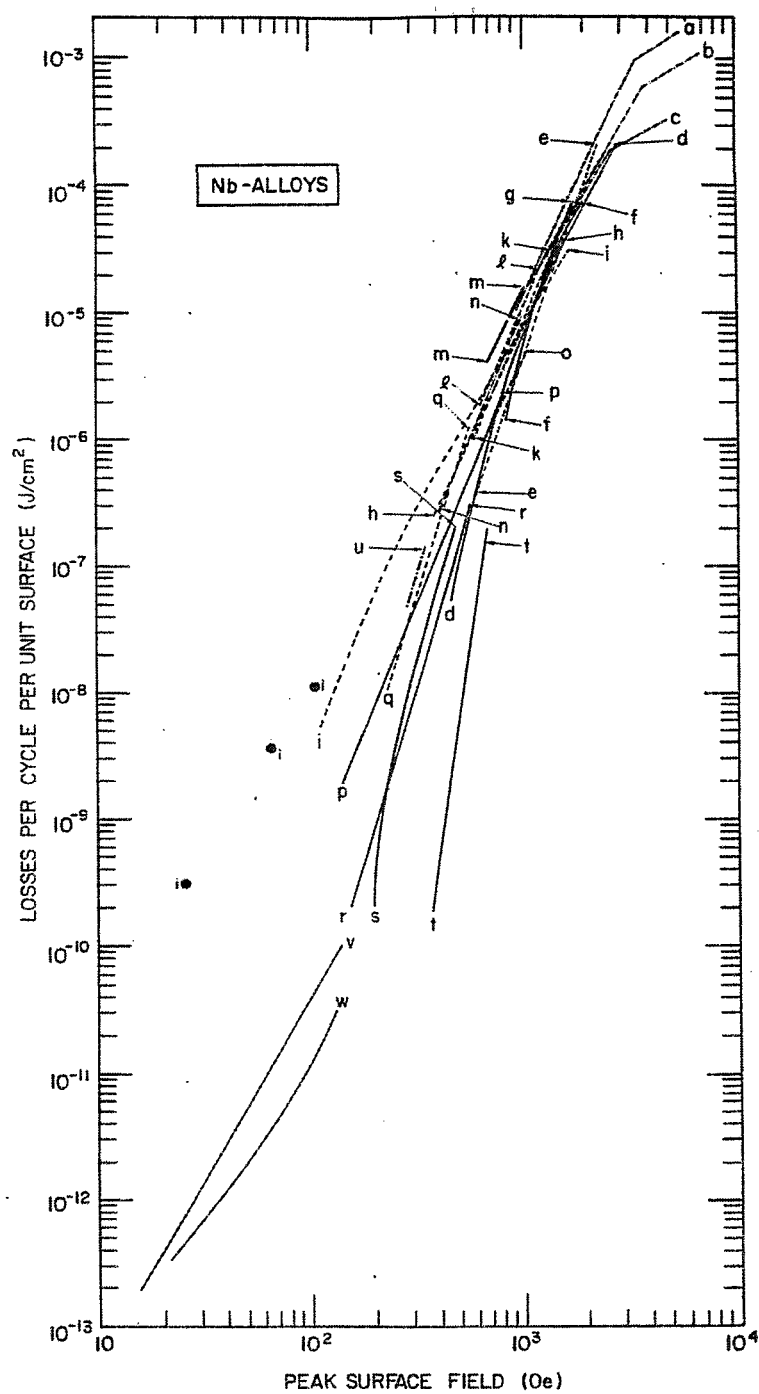


Fig. 5. Reported ac losses of Nb alloys (includes Nb20%-40%Zr, and Nb50%-80%Ti) (Ref. 5).

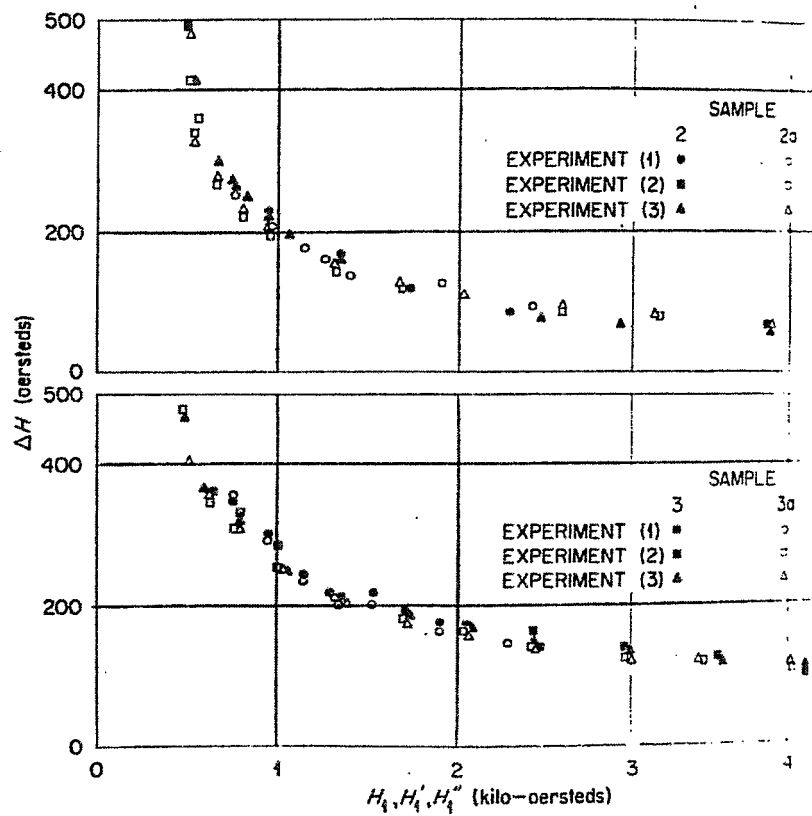


Fig. 6. Measurements of  $\Delta H$  in Nb25%Zr (Ref. 8).



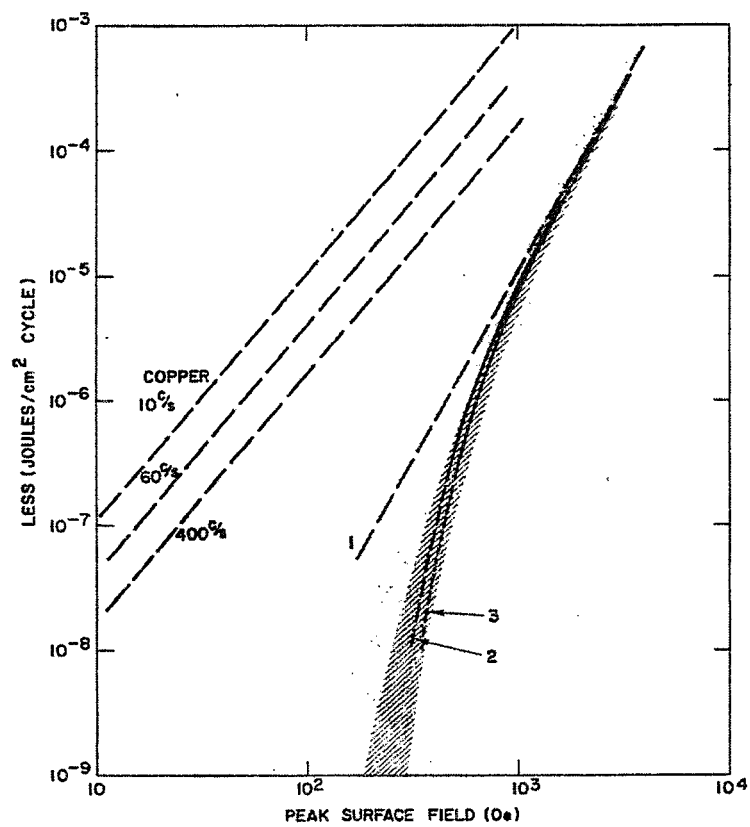
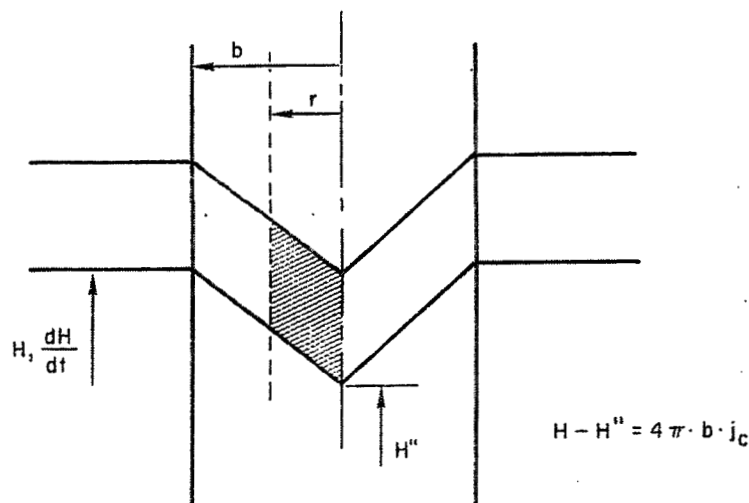


Fig. 7. Comparison of calculations of ac losses in Nb alloys and copper.



$$H - H'' = 4\pi \cdot b \cdot j_c$$

TEMPERATURE EQUIVALENT

$$H \sim T$$

$$\frac{\rho}{4\pi} \sim \alpha = \frac{k}{c}$$

$$\alpha \nabla^2 T = \dot{T}$$

$$T - T'' = \frac{b^2}{4\alpha} \cdot \frac{dT}{dt}$$

$$2\pi r E = \pi r^2 \frac{dB}{dt}$$

$$E = \frac{r}{2} \frac{dH}{dt} = \rho j_c$$

$$\rho_{av} = \frac{b}{4j_c} \frac{dH}{dt}$$

Fig. 8. To illustrate the dynamic resistivity of a cylinder in a parallel, changing field.

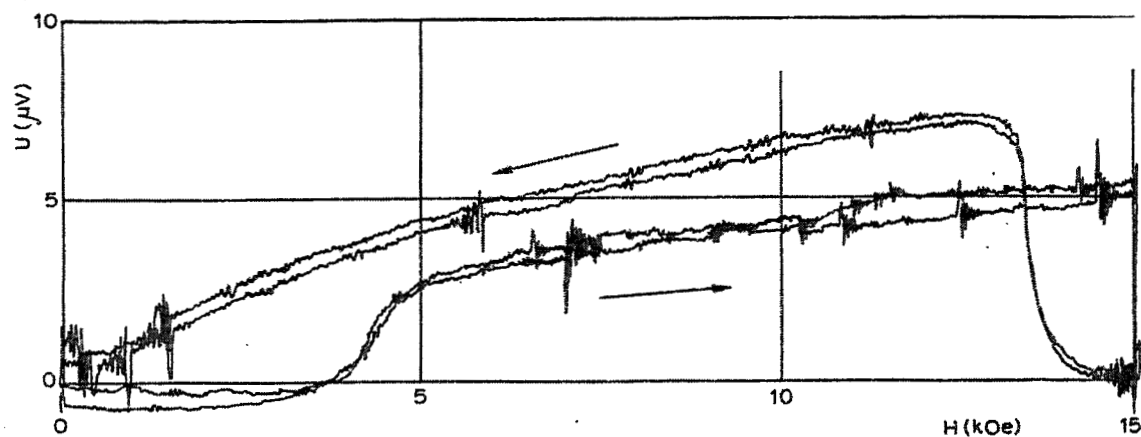


Fig. 9. Measurement of dynamic resistance of bifilar coil in coaxial changing field (Ref. 9).

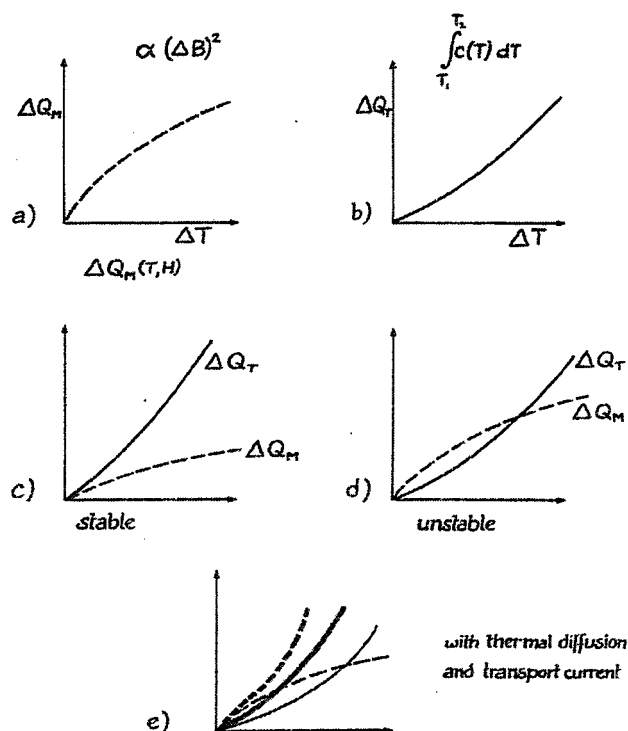


Fig. 10. Illustration explaining the occurrence of magnetic instabilities (after Hart).

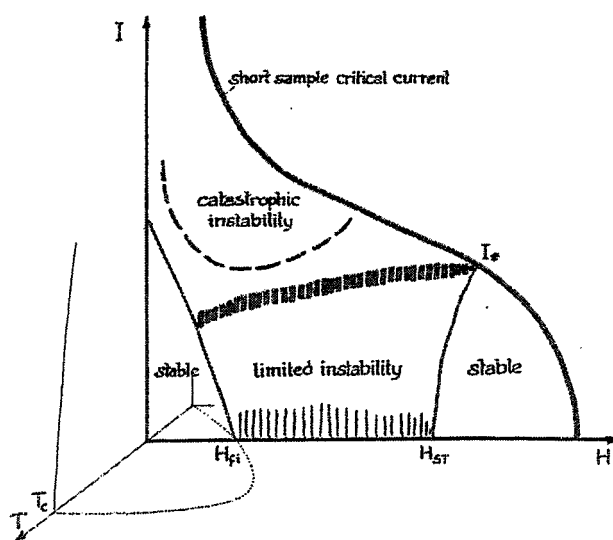


Fig. 11. Sketch of stability regions (for wire wound into a coil) in a  $I$ - $H$  ( $-T$ ) diagram (after Hancox). Heavy black lines indicate boundary between regions of catastrophic and limited instability. Dashed line indicates the effect of very slow  $dH/dt$  on this boundary.

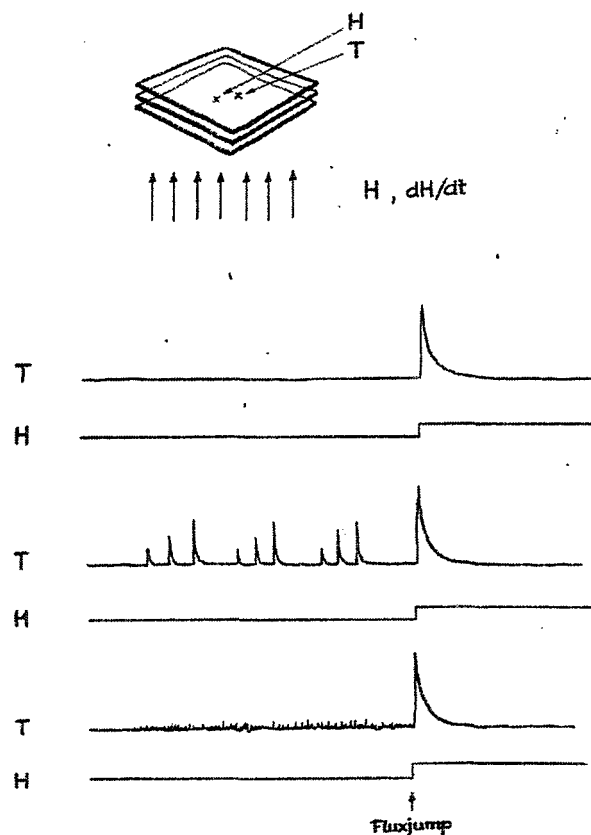


Fig. 12. Measurement of instabilities on specimens of  $Nb_3Sn$  tape in perpendicular, changing field. Records of H and T (measured near center of specimen) vs time indicate limited and complete flux jumps (after Oswald).

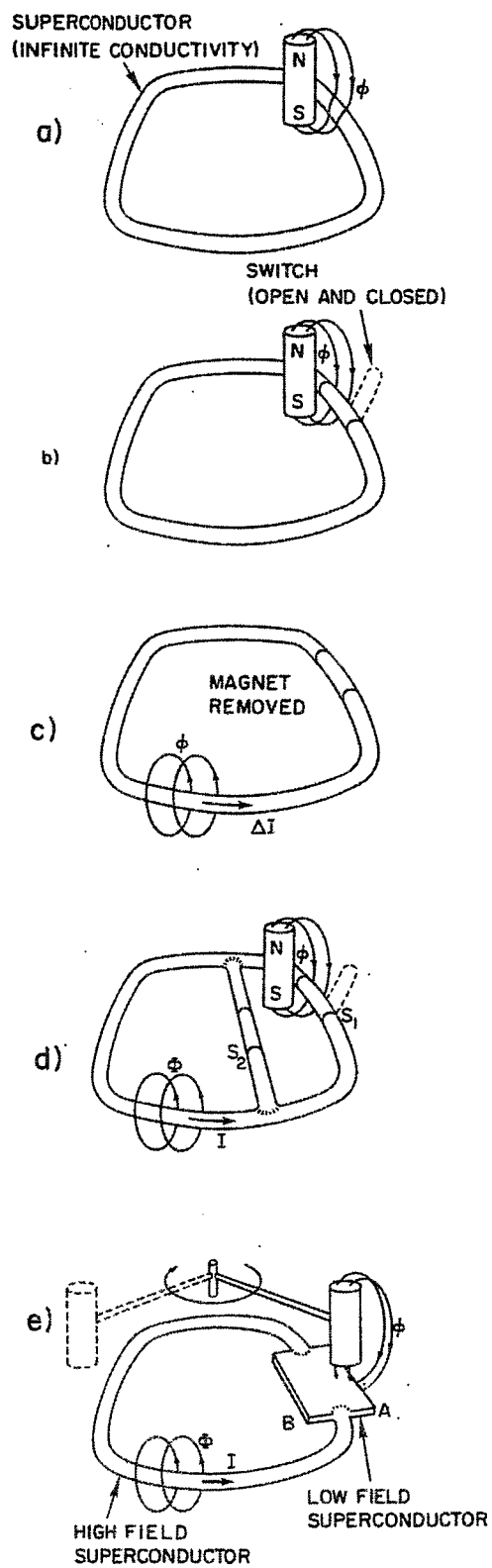


Fig. 13. Illustrating the principle of flux pumping.

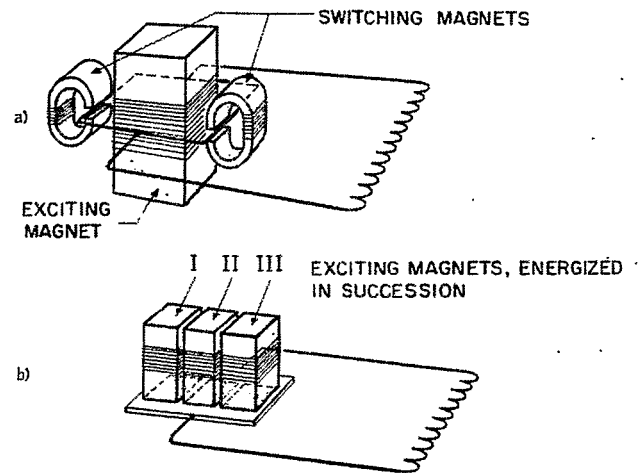


Fig. 14. Two arrangements of flux pumps without moving parts (Ref. 10).

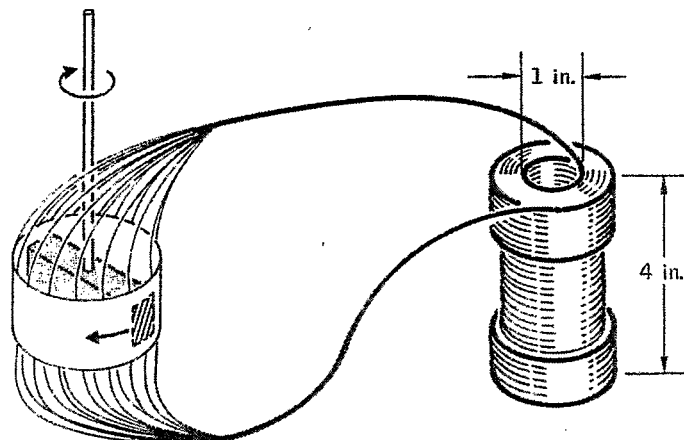


Fig. 15. Typical example of moving magnetic field pump. (Not shown are coils to magnetize the rotor so that the poles all have the same magnetic polarity.) (Ref. 11)

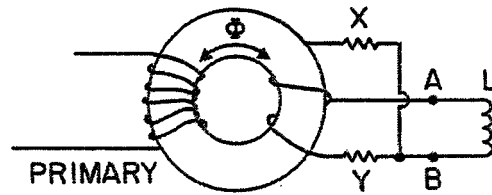


Fig. 16. Diagram of rectifier pump.

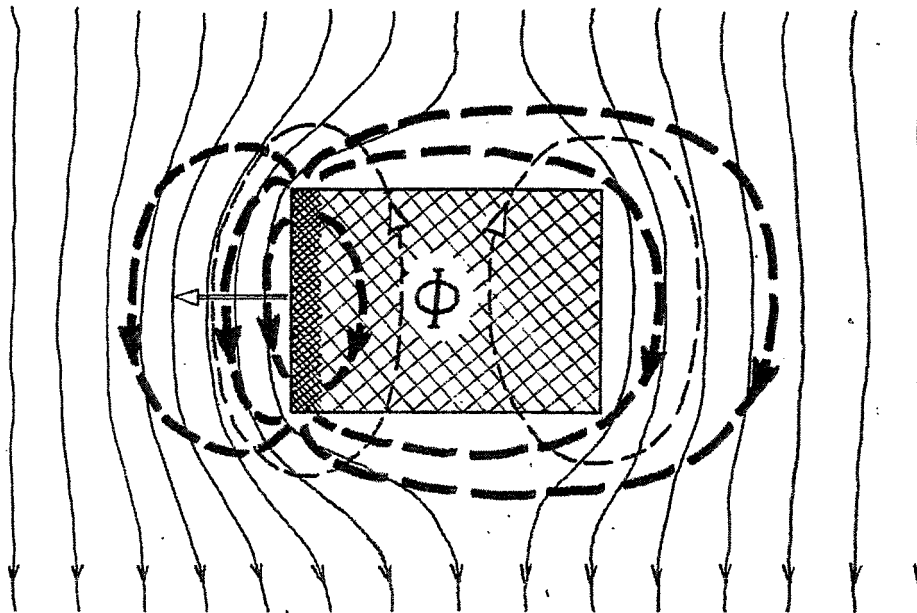


Fig. 17. Schematic current distribution around moving normal spot containing flux  $\Phi$ .

Horizontal arrow:	Direction of movement
Crosshatch:	Resistive region
Thin solid lines:	Load current distribution
Thin broken lines:	Eddy current distribution
Thick broken lines:	Alternative current distribution for current which is driven resistively out of the leading edge (narrow crosshatch)..

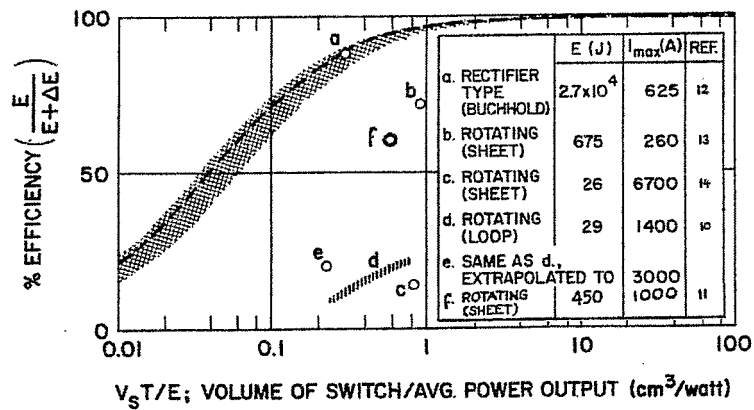


Fig. 18. Energy efficiency as reported for various pumps (Ref. 2).



# STRESS PROBLEMS ASSOCIATED WITH SUPERCONDUCTING AND CRYOGENIC MAGNETS

P.G. Marston  
Magnetic Engineering Associates  
Cambridge, Massachusetts

## INTRODUCTION

The following will be a general discussion of a broad variety of stress problems encountered in the design of superconducting and cryogenic magnets of various types. Details of specific problems will not be discussed. This should be considered merely a design problem check-off list with some comments on approach.

The three fundamental forces are magnetic, thermal, and mechanical. A system design must properly consider their relative interaction.

## MAGNETIC FORCES

Magnetic forces arise from four basic interactions. These are:

1. Torque on a magnetic dipole in a uniform (or gradient) field.
2. Forces on a dipole in a gradient field.\* To calculate this force one must first know the magnetic properties of the material (i.e., permeability or susceptibility), the geometry of the body, and also, of course, the field gradient. The induced dipole moment will be a function of magnetic properties, geometry (demagnetization factor), and applied field. The force will be proportional to the dipole moment and also to the field gradient.
3. Lorentz interaction. This is, of course, the fundamental load on windings and any current-carrying element, i.e., leads, buswork, etc. It is simply the cross product of current and field.
4. Induction. A time changing field will induce currents in any conducting medium within the field. The resulting Lorentz interaction (and possible heating) is often overlooked.

## THERMAL FORCES

Any system in which the operating temperature distribution is different from the initial temperature distribution or is composed of materials having different thermal coefficients (and undergoes a change in temperature) will be subject to thermal stresses. It is important to understand how the system gets from its initial to its operating state since the worst case stresses may occur during this transient. For low temperature systems it is obvious that the system orientation can have an extremely important effect on the transient temperature distribution.

---

\* I hope it is unnecessary to note that there is no net force on a dipole in a uniform field!

## MECHANICAL FORCES

In addition to the magnetic and thermal loads there are usually various other loads imposed by vacuum, pressure, dynamic experimental equipment, emergency, failure, start-up conditions, and other requirements which may be part of a total performance specification.

In any system analysis it is important to determine what combination of operating, test, or emergency conditions will give the worse case loads.

## STRESSES

In order to calculate stresses one must first know the field and force distribution in the magnetic structure. There exist a number of very powerful computer codes to solve these problems. It is fatuous not to use them for systems of any consequence. There also exist a number of rather elegant general solutions for stress problems of this type. I cannot, however, overemphasize the danger of using general analyses or rules of thumb which have been developed by other people for other types of devices. One must be intimately aware of the assumptions used in order to evaluate realistically whether or not they can be applied to the problem under consideration.

## AIR CORE SOLENOID

Here the force distribution gives rise to two principal stresses, the hoop stress or tangential stress in the conductor, and an axial compressive stress on the winding structure. To analyze and design any system one should have an intimate understanding of the elemental forces in the structure and how they are distributed. With this information cumulative loads can be calculated. Models assuming a body force distribution in a homogeneous material having predictable mechanical properties will not give realistic results! In general it is possible to mechanically (and electrically) regionalize any system so that the cumulative loads are within safe limits for all materials in the composite structure. These would include conductors, conductor supports, insulations, spacers, and over-all system support structures.

The dominant stress problem in a solenoid system is the hoop stress which can be easily calculated for an elemental conductor by multiplying the conductor radius in meters by the current in amperes by the axial field in teslas. This will give the hoop force on that elemental conductor in newtons.\* This can easily be converted to stress over any arbitrary cross section of conductor and/or conductor support. It is interesting to note that in a solenoid system having an "alpha" (o.d. over i.d. ratio) greater than 2, the peak hoop stress does not occur at the winding i.d. This further tells us that if such a winding structure is a solid monolithic form then peak stresses in the body of the windings will couple to the i.d. and increase that stress level. This emphasizes the practicality of regionalization techniques. It is generally desirable to break up the winding into a number of self-supporting mechanical regions and further to operate these at different current densities.

A simple approach to a stress-limited solenoid design is to start with an inside region of small radial dimension operating in the peak field strength it is desired to produce and having some average radius. With this and the mechanical characteristics of the conductor and support used, one can calculate the current this inner region can carry within safe stress limits. Having thus designed the inner winding region and

---

\* I very cleverly call this the RIB force.

having calculated the central field contribution of this region, one then moves to a next outer radial region and repeats the process with the new radius of curvature and new (lower) field in which the conductors must operate, etc. Concentric windings are not self-centering and must be rigidly supported against relative radial motion.

In cases where stresses are a problem, one is generally dealing with composite conductors and supports and must, of course, take great care to properly consider all of the relative mechanical characteristics of the materials in use.

#### THERMAL PROBLEMS WITH COMPOSITE CONDUCTOR/SUPPORTS

This is perhaps most emphatically demonstrated in the design of cryogenic magnets where one is generally trying to support a very high purity, very weak, and very low modulus aluminum conductor in a high field. In order to realize the full potential of their high resistivity ratio, one must operate these conductors in an essentially strain-free condition. It is, however, impossible to find a high modulus support material which does not have a thermal coefficient substantially less than that of aluminum. Thus during cooldown the aluminum conductor either shrinks away from the support material (and must later yield into it), or if it is bonded to its support has a large thermal strain induced.\*

#### SPLITS

When a solenoid is split into a coil pair or multicoil system the problems are complicated somewhat. The major new considerations are the large force between windings and the fact that people do not make splits unless they want lots of free access in a region that ought to be mainly support structure.

#### USE OF IRON

In many instances it is sensible to use iron with superconducting and cryogenic systems.

The use of iron in a system changes the field distribution significantly and, therefore, the force and stress distribution. The relative stress problems depend largely on the ultimate field strength it is necessary to produce.<sup>†</sup> A very large fraction of the total field can be from the magnetized iron contribution. This means that the current in the windings can be reduced, and therefore the forces and winding stresses are also reduced. This is particularly true with systems having a large diameter-to-length ratio (small beta).

The axial loads in low field iron-bound systems are dramatically reduced and, in fact, in most cases can be made arbitrarily low.

---

\* I am confident that support structures can be designed to accommodate this, and that dynamic resistivity ratios of greater than 1000 can be realized in fields of hundreds of kilogauss, although to my knowledge this has not yet been achieved.

<sup>†</sup> I would like to note that it is very reasonable to consider the use of iron with these systems up to field strengths of at least 50 kG and perhaps even higher.

With split coils the intercoil forces can be made such that the coils either attract or repel.

The interaction of the windings with the surrounding iron creates some problems but also allows additional design flexibility. In a simple system magnetically centered windings are in a state of unstable equilibrium within the iron structure. Thus if they move away from their magnetic center, they will pull into the iron structure more strongly in that direction.

It is possible to design an over-all geometry in which the windings are stable in at least two directions within the system, and therefore require support in the third direction only. This has obvious implications to the design of low heat leak structures in iron-bound superconducting and cryogenic systems. An interesting possibility is that of a winding which, with a simple feedback system, could be completely magnetically supported within the surrounding iron, and therefore would require no mechanical structure at all between the low temperature bath and the outside world.

#### TRANSVERSE FIELD SYSTEMS

The next category of systems of general interest might be those that do not have cylindrical symmetry. This would include the various "saddle" and rectangular coil systems for transverse field generation.

Here the basic Lorentz interaction cannot be supported by the conductor and therefore requires some external structure. This relieves the strain on the conductor but is apt to suffer from nonuniform load and stress distribution and high local stresses on conductors and insulations. There is also a general lack of mechanical rigidity likely with this system. Resulting motion could give problems in marginally stable superconducting systems.

Of major consideration with these more complicated support structures are the cryostat and refrigeration costs which may be associated with necessarily higher heat leaks. It is often desirable to operate systems which are traditionally horizontal in a vertical orientation in order to improve thermal design.

#### FORCE CALCULATION

Here again the most useful method of estimating forces and stresses is simply to look at the elemental and then cumulative Lorentz interaction forces. One must be careful at the ends of the system and must make realistic assumptions of manufacturing tolerances and relative load distributions.

#### DANGER

The various analogies of magnetic pressure, thick walled cylinders, etc., can be useful but in my estimation only rarely! They suffer from dangerous limitations which tend to get one into a great deal of trouble. If assumed forces do not correlate with a simple  $I \times B$  or  $J \times B$  calculation something is wrong!

#### SPECIAL PROBLEMS

There are always certain special problems associated with the design analysis of a magnetic system. One must be careful that he is working to a complete performance requirement specification. Important basic considerations are the following:

1. The effects of time changing fields during field increase or decay should be considered. Under emergency or "quench" conditions the latter might be quite rapid, and additional forces and/or redistribution of forces resulting from conducting loops coupled to the magnetic system, or possible short circuits in the winding structure should be considered.

2. Nonuniform cooldown and localized hot spots during a quench can often create serious thermal stress conditions. Judicious use of materials to take advantage of differential thermal coefficients and prestressing to increase spring constants and/or optimize final operating force distributions should be considered. Thermal walking and loosening must not be allowed.

3. External interactions must be thoroughly evaluated. These might be with magnetic bodies, current leads, buswork, etc.

4. If system operation is dynamic due to constantly changing or pulsed fields or perhaps dynamic external equipment, one must be sure that fatigue characteristics are properly considered. It is important to note that the field, force, and stress solutions associated with fast pulse systems are significantly different from those of steady state or slowly time changing systems.

5. One must consider all possible emergency and failure conditions of the magnet and associated equipment.

6. One must also be sure that he has adequate and accurate information regarding the properties of materials in use and how these properties may change as a function of temperature and field. In general, these are well understood and should present no surprises. One possible exception is the martensitic (nonmagnetic to magnetic) transformation of stainless which can occur if it is cooled in a severely coldworked condition. This could obviously create unexpected stress and, possibly, experimental problems.

Unfortunately there are no good general texts on these problems but a great deal of information can be gleaned from the following. Again one must be extremely careful to select that information which is applicable and correct.

H. Kolm et al., ed., Proc. Intern. Conf. High Magnetic Fields, Cambridge, Mass., 1961, (M.I.T. Press and J. Wiley, 1962).

R. Pauthenet, ed., Actes du Colloque International sur les Champs Magnétiques Intenses, Grenoble, 1966 (No. 166, Editions du Centre National de la Recherche Scientifique, Paris, 1967).

H. Brechna and H.S. Gordon, ed., Proc. Intern. Symposium on Magnet Technology, Stanford, California, 1965 (available from the Clearinghouse for Federal Scientific and Technical Information, Springfield, Va., USA).

H. Hadley, ed., Proc. 2nd Intern. Conf. Magnet Technology, Oxford, 1967 (available from R.C. Pepperell, Rutherford Laboratory, Chilton, Didcot, Berks., England).

One should not overlook the many useful suggestions for stress analysis given by S. Timoshenko, W. Flügge, J.P. Den Hartog, R.J. Roark, and the like!

## STRESSES IN MAGNETIC FIELD COILS

W.F. Westendorp and R.W. Kilb  
General Electric Company  
Research & Development Center  
Schenectady, New York

### I. INTRODUCTION

The computation of the mechanical stresses in cylindrical magnetic field coils requires a knowledge of the distribution of forces acting upon the conductor, and a theory whereby this force pattern may be converted into a stress pattern.

The methods found in the literature are either accurate and cumbersome<sup>1</sup> or simplifications<sup>2,3</sup> that may lead to serious errors.

### II. THEORY OF A SIMPLE COIL

For thick-walled pressure vessels, to which a cylindrical coil may be compared, there exists a stress theory<sup>4</sup> in which it is pointed out that the problem is two-dimensional if pressures are applied inside and outside. In this case the  $z$  component of the stress tensor is zero everywhere. If, however,  $\vec{J} \times \vec{B}$  body forces are introduced, this will, in general, not be the case for an isotropic material. However, a coil consisting of layers of rectangular wire or of pancakes of metal ribbon is not isotropic, and since the wire or the metal ribbons is provided with a thin coating of plastic insulation, the shear stress between wires or ribbons is negligibly small, and the compressive stress in the  $z$  direction will depend only on the boundary conditions. If we assume that the axial forces will be taken up by suitable coil forms repeated at distances small compared to the diameter, we may neglect the entire  $z$  component of the stress tensor, and the problem reverts to the simpler two-dimensional case. A differential equation may be derived in a manner analogous to Lamé's original method. We will here follow the standard textbook<sup>5</sup> treatment except for the introduction of  $J\theta B_z$  body forces and the new boundary conditions with zero inside and outside pressures.

Figure 1 shows a view of the coil, with details at "a" and "b". Under the influence of the electromagnetic forces, the circle of radius  $r$  in the unstressed state between inner radius  $r_i$  and outer radius  $r_o$ , becomes a circle of radius  $r + u$ , where  $u$  is the outward displacement of any point,  $r$ . Thus  $u$  is a function of  $r$ , although

- 
1. J.D. Cockcroft, *Trans. Roy. Soc. London* 227, 317 (1928); also W.F. Giauque, *Rev. Sci. Instr.* 31, 374 (1960).
  2. H.P. Furth, M.A. Levine, and R.W. Waniek, *Rev. Sci. Instr.* 28, 949 (1957).
  3. D.B. Montgomery, *The Generation of High Magnetic Fields*, pp. 70-104 (see p. 80).
  4. G. Lamé and B.P.E. Clapeyron, *Mémoire sur l'équilibre intérieur des corps solides homogènes*, *Mémoires présentés par divers savants*, Vol. 4 (Académie des Sciences, Paris, 1833).
  5. J.P. Den Hartog, *Strength of Materials* (McGraw-Hill, 1949, and Dover Publ., 1961), pp. 140-145.

numerically very small in comparison to  $r$ . All lengths of the circle with original radius  $r$  are increased in the ratio  $(r + u)/r$  or  $1 + (u/r)$ . A piece  $ds$  of the circle becomes  $ds + u ds/r$ , which means that the tangential strain is  $u/r$ .

To find the strain in the radial direction, we look at the detail "b" in Fig. 1 showing an element in the undistorted state in full lines, which, after loading, goes to the dotted-line picture. The location of the inner point is  $r$ , and it goes to  $r + u$ , because of the magnetic pressure. The location of the outer point was  $r + dr$  and it goes to  $r + dr + u + du$  because  $u$  varies with  $r$ . Thus the original radial length of the piece was  $dr$ , and its distorted radial length is  $dr + du = dr(1 + du/dr)$ . Hence the radial strain is  $du/dr$ .

We will assume that there are no axial forces acting upon the coil and no shear forces between layers of the winding. The two strains can then be expressed in terms of the radial and tangential stresses  $S_r$  and  $S_t$  as follows<sup>6</sup>:

$$\frac{u}{r} = \frac{1}{E} (S_t - \mu S_r) \quad , \quad (1)$$

$$\frac{du}{dr} = \frac{1}{E} (S_r - \mu S_t) \quad . \quad (2)$$

$E$  is the Young's modulus and  $\mu$  the Poisson's ratio. These are two equations in the three unknowns  $u$ ,  $S_t$ , and  $S_r$ . A third equation is found from the equilibrium of an element  $dr \cdot rd\theta$  shown at "a" in Fig. 1 and enlarged in Fig. 2. The radial force 1 is  $S_r \cdot rd\theta$  per unit length perpendicular to the paper. The force 2 on top is similar but both  $S_r$  and  $r$  are slightly different; thus force 2 is  $S_r \cdot rd\theta + d(S_r \cdot rd\theta)$  and the resultant of 1 and 2 outward is

$$d(S_r \cdot rd\theta) = \frac{d(rS_r)}{dr} drd\theta \quad .$$

The forces 3 and 4 are numerically equal but not quite opposite since the faces they act upon make an angle  $d\theta$ . Hence their resultant is directed inward and has the magnitude

$$F_3 d\theta = S_t drd\theta \quad .$$

The fifth force that keeps the element in equilibrium is the electromagnetic body force  $J_\theta B_z rd\theta dr$  acting outward upon the volume element with unit length in the  $z$  direction.

Equating forces in the radial direction, we find

$$F_2 - F_1 + J_\theta B_z rd\theta dr = F_3 d\theta \quad .$$

After substituting the appropriate values and dividing by  $drd\theta$  we get

$$\frac{d(rS_r)}{dr} + rJ_\theta B_z = S_t \quad . \quad (3)$$

---

6. J.P. Den Hartog, Ref. 5, Eq. (8), p. 75.

Solving Eqs. (1) and (2) for  $S_r$  and  $S_t$ , we find:

$$S_r = \frac{E}{1 - \mu^2} \left( \frac{du}{dr} + \mu \frac{u}{r} \right) , \quad (4)$$

$$S_t = \frac{E}{1 - \mu^2} \left( \frac{u}{r} + \frac{du}{dr} \right) . \quad (5)$$

Substitution of Eqs. (4) and (5) into Eq. (3) then yields the differential equation:

$$\frac{d^2 u}{dr^2} + \frac{1}{r} \frac{du}{dr} - \frac{u}{r^2} = - \frac{1 - \mu^2}{E} J_\theta B_z . \quad (6)$$

The homogeneous solutions of Eq. (6) are  $r$  and  $1/r$ . The general solution of Eq. (6) may therefore be written as<sup>7</sup>

$$u = Ar + \frac{B}{r} , \quad (7)$$

where  $A$  and  $B$  are functions of  $r$  that satisfy the first order differential equations:

$$\frac{dA}{dr} = - \frac{1 - \mu^2}{2E} J_\theta B_z , \quad (8)$$

$$\frac{dB}{dr} = - r^2 \frac{dA}{dr} . \quad (9)$$

Integration of Eqs. (8) and (9) gives two integration constants, which are to be determined by the boundary condition that the radial stress  $S_r$  is zero at the inside and outside coil radii.

For a uniform current density  $J_\theta$ , it is usually sufficient to assume that  $B_z$  varies linearly with radius from  $B_i$  at the inside radius  $r_i$ , to a small negative value  $B_o$  at the outside radius  $r_o$ . The radial force may then be written:

$$J_\theta B_z = \alpha - \beta r , \quad (10)$$

where  $\alpha$  and  $\beta$  are constants.

$$\alpha = \frac{J_\theta (B_i r_o - B_o r_i)}{r_o - r_i} , \quad (11)$$

$$\beta = \frac{J_\theta (B_i - B_o)}{r_o - r_i} . \quad (12)$$

---

7. D.H. Menzel, Fundamental Formulas of Physics (Dover Publ., 1960), p. 35.



Using Eq (10), we may easily integrate Eqs. (8) and (9) to find the solutions:

$$A = \frac{1 - \mu^2}{E} \left( \frac{C_1}{1 + \mu} - \frac{1}{2} \alpha r + \frac{1}{4} \beta r^2 \right) \quad (13)$$

$$B = \frac{1 - \mu^2}{E} \left( \frac{C_2}{1 - \mu} + \frac{1}{6} \alpha r^3 - \frac{1}{8} \beta r^4 \right) \quad (14)$$

$$u = \frac{1 - \mu^2}{E} \left( \frac{C_1 r}{1 + \mu} + \frac{C_2}{(1 - \mu)r} - \frac{\alpha r^2}{3} + \frac{\beta r^3}{8} \right) \quad (15)$$

$$S_r = C_1 - \frac{C_2}{r^2} - \frac{\alpha(2 + \mu)r}{3} + \frac{\beta(3 + \mu)r^2}{8} \quad (16)$$

$$S_t = C_1 + \frac{C_2}{r^2} - \frac{\alpha(1 + 2\mu)r}{3} + \frac{\beta(1 + 3\mu)r^2}{8} \quad (17)$$

The constants  $\alpha$  and  $\beta$  are found from Eqs. (11) and (12),  $\mu$  is Poisson's ratio, and  $E$  is Young's modulus. Note that the radial and tangential stresses,  $S_r$  and  $S_t$ , do not depend on Young's modulus. The radial displacement  $u$  is, however, a function of Young's modulus.

As mentioned above, the constants  $C_1$  and  $C_2$  are found by setting  $S_r = 0$  at the inside and outside coil radii. This yields:

$$C_1 = \frac{\alpha(2 + \mu)(r_o^2 + r_o r_i + r_i^2)}{3(r_o + r_i)} - \frac{\beta(3 + \mu)(r_o^2 + r_i^2)}{8} \quad (18)$$

$$C_2 = r_i^2 r_o^2 \left( \frac{\alpha(2 + \mu)}{3(r_o + r_i)} - \frac{\beta(3 + \mu)}{8} \right) \quad (19)$$

### III. APPLICATION TO SIMPLE COIL

The computation derived above has been applied to the case of a "superconducting coil." In this coil the copper is employed primarily for purposes of thermal stability, and it has a cross section large compared to that of the actual superconductor, a niobium-tin alloy. The ribbon<sup>8</sup> of which the coil is wound consists of two strips of copper a few thousandths of an inch thick with the niobium-tin of only a few ten-thousandths of an inch sandwiched between. Therefore, in the computation the stress contribution of the niobium-tin may be entirely ignored even though both its Young's modulus and its ultimate strength are higher than those of copper. For this reason we shall refer to this type of superconducting coil as the "copper" coil. The coil is supported by a metal spool 20-in. i.d. so that the copper has an i.d. equal to 21 in. ( $r_i = 26.67$  cm). The outside diameter of this particular coil was dictated by the size of a Dewar vessel, 38-in. i.d., and was consequently assumed to be 36-in. o.d. ( $r_o = 45.72$  cm). The axial dimension of the coil was 4 in., but it formed part of a coaxial system of coils, and the field values and stresses computed here are all

---

8. M.G. Benz, G.E. Research & Development Center Report No. 66-C-044 (1966).

for this coil as part of the coaxial fully-energized system. The coil was known as a large size "end" coil, there being one smaller "end" coil beyond it. In all cases considered here, the central field at the center of the assembly and on the axis was 75 kG. Digital computer field determinations under these conditions gave for the "copper" coil:  $B_i = 91$  kG,  $B_o = -18$  kG, and  $J = 9.88$  kA/cm<sup>2</sup>. Taking the Young's modulus of copper as  $1.03 \times 10^{12}$  dyn/cm<sup>2</sup> ( $14.93 \times 10^6$  psi) and the Poisson's ratio of copper as  $\mu = 0.33$ , we found for the "copper" coil the tangential tensile stress curve, so marked in Fig. 3, going from  $17.2 \times 10^8$  dyn/cm<sup>2</sup> (24 000 psi) on the inside of the coil to  $8.04 \times 10^8$  dyn/cm<sup>2</sup> (11 600 psi) on the outside. The radial compressive stresses are plotted as a negative stress on the left in Fig. 3 and the radial motion on the right in Fig. 3. The maximum compressive stress ( $1.6 \times 10^8$  dyn/cm<sup>2</sup> or 2320 psi) although low for copper, should be considered with regard to the insulation used on the metal ribbon. The radial motion is greatest on the inside (0.0445 cm or 0.0175 in.) and also the largest of the three systems considered.

#### IV. APPLICATION TO REINFORCED COIL

Because of the high tangential stress on the inside (24 900 psi) it was decided to consider other configurations than the "copper" coil.

The second design considered is referred to as the "two band" coil. It has an inner "band", consisting of the "copper" winding, of 21-in. i.d. and 31-in. o.d. ( $r_o = 39.37$  cm), which carries the current, and a stainless-steel band of 31-in. i.d. and 36-in. o.d. ( $r_x = 45.72$  cm), which carries no current but serves strictly as reinforcement. Because of the different location of the magnetizing ampere turns, the digital computer was again used to determine the field, and the result was  $B_i = 99$  kG and  $B_o = -20$  kG and  $J = 14.7$  kA/cm<sup>2</sup>. In the mathematical stress-strain treatment of this combination, the "copper" is handled as before with the exception that at the outside boundary of the copper the radial stress must equal the radial stress of the stainless steel. For the stainless steel, Eqs. (11) through (17) may be used provided we set  $J_0 = 0$  so  $\alpha = 0$  and  $\beta = 0$ . The ratio  $E_{ss}/E_{cu}$  was taken as 2 and  $\mu_{ss} = 0.30$ . Another condition is that the external radial displacement  $u_{cu}$  of the copper must equal the internal radial motion  $u_{ss}$  of the stainless-steel band. The four unknowns  $C_{1cu}$ ,  $C_{2cu}$ ,  $C_{1ss}$  and  $C_{2ss}$  may therefore be found from the four boundary conditions:  $S_r = 0$  at  $r_i$  and  $r_x$ ;  $u_{cu} = u_{ss}$  and  $S_{rcu} = S_{rss}$  at  $r_o$ .

Carrying through this procedure leads to the curves marked "two band coil" in Figs. 3a and 3b. The main surprise is that the improvement is so small, the new maximum tensile stress in the copper being  $14.9 \times 10^8$  dyn/cm<sup>2</sup> or 21 600 psi. The maximum compressive stress has more than doubled,  $3.6 \times 10^8$  dyn/cm<sup>2</sup> or 5210 psi, and the radial motion has been reduced to a maximum at the inside of the coil of 0.0385 cm or 0.0151 in.

#### V. COPPER-STEEL RIBBON COIL

A third attempt was made to reduce the maximum tensile stress in the copper, while keeping the over-all dimensions the same. This time the coil was considered to be wound of a combination of copper and stainless-steel ribbons so that in the compound ribbon the area of the copper was twice that of the steel.

Consider this compound or sandwich coil as consisting of a "new" material with a mean Young's modulus expressed as follows:

$$E_m = f_c E_c + f_s E_s$$

and a Poisson's ratio

$$\mu_m = f_c \mu_c + f_s \mu_s$$

where  $f_c$  is the fraction of the total cross section that is copper,  $f_s$  is the fractional area for the stainless steel, and  $E_c$  and  $E_s$  the corresponding moduli, etc. This value of the mean Young's modulus may be rigorously derived for the case where the compound ribbon hangs vertically and is loaded by a weight causing a strain,  $\delta$ , in both copper and stainless steel and tensile stresses, respectively  $S_c$  and  $S_s$ . The material may even be subjected to a stress,  $S_r$ , perpendicular to the ribbon.

According to Eq. (1) with some rearranging:

$$S_c = \delta E_c + \mu_c S_r \quad \text{and} \quad S_s = \delta E_s + \mu_s S_r$$

The mean stress may be written as

$$S_m = f_c S_c + f_s S_s$$

or by substitution

$$S_m = \delta f_c E_c + f_c \mu_c S_r + \delta f_s E_s + f_s \mu_s S_r$$

or rearranged

$$S_m = \delta (f_c E_c + f_s E_s) + (f_c \mu_c + f_s \mu_s) S_r$$

and since for the "new" material we must have

$$S_m = \delta E_m + \mu_m S_r$$

we conclude

$$E_m = f_c E_c + f_s E_s \quad \text{and} \quad \mu_m = f_c \mu_c + f_s \mu_s$$

The results are shown in the curves marked "sandwich coil". The mean Young's modulus became  $1.37 \times 10^{12}$  dyn/cm<sup>2</sup> and the mean Poisson's ratio 0.32, when  $f_c = 2/3$  and  $f_s = 1/3$ . It can be seen in Fig. 3 that the maximum tangential stress in the copper for the sandwich coil has dropped to  $13 \times 10^8$  dyn/cm<sup>2</sup>, which is 3/4 of the  $17.2 \times 10^8$  dyn/cm<sup>2</sup> for the simple copper coil.

Note that the maximum tangential stress in the steel of  $26 \times 10^8$  dyn/cm<sup>2</sup> is twice as great as the  $13 \times 10^8$  dyn/cm<sup>2</sup> value for the copper, which is the same ratio of two as for their Young's moduli. This ratio follows from Eq. (1) if we recall that the maximum stress point occurs at the inside surface of the coil where  $S_r = 0$ . Since the radial motion  $u$  is essentially the same for the copper and steel in the ribbon, we then have from Eq. (1) that  $S_{tcu}/E_c = S_{tss}/E_s$ , which shows that the ratio of the maximum tangential stresses in the two materials is in the ratio of their Young's moduli.

A further point is that the total tangential stress  $S_t$  at a given radius is essentially the same whether the coil is a "simple copper" coil or a "sandwich coil". For the sandwich coil we have

$$S_t = f_c S_{tcu} + f_s S_{tss}$$

where  $S_{tcu}$  and  $S_{tss}$  are the tangential stresses in the copper and steel, respectively, and  $f_c$  and  $f_s$  are the fractional area cross sections of the copper and steel in the sandwich ribbon. At the inside coil surface we may substitute  $S_{tss} = E_s S_{tcu} / E_c$  in the above equation, and solve it for  $S_{tcu}$ :

$$S_{tcu} = \frac{1}{f_c + f_s E_s / E_c} S_t$$

Since  $S_t$  is the same for the "simple copper" and "sandwich coil", the factor  $1/(f_c + f_s E_s / E_c)$  gives the reduction in maximum stress in the copper of the "sandwich coil" as compared to the "simple copper" coil. For  $f_c = 2/3$ ,  $f_s = 1/3$  and  $E_s / E_c = 2$ , this reduction factor is  $3/4$ , just as the numerical values in Fig. 3 show. Also note that the maximum reduction occurs in the limit of very little copper ( $f_c \rightarrow 0$ ) and nearly all steel ( $f_s \rightarrow 1$ ), in which case the reduction factor becomes  $E_c / E_s$ . Thus the greatest possible reduction in the copper tangential stress is 50%, which occurs when the ribbon is nearly all steel. Note that one-third copper and two-thirds steel would give a reduction factor of 60%.

## VI. CHARTS AND GRAPHS

For the simple coil we have set up a computer program that determines the field in the center, in the center plane on the inside wall and on the outside, and in various places inside the winding at the mean radius. From these values the tangential tensile and the radial compressive stresses are computed. The radial components at the mean radius allow us to compute the maximum axial compressive stress in the center. We are not considering the increased strain caused by the superposition of tangential tension and axial compression nor what theory of strength to use. Figure 4 in the original report was a "fold out and fold up" chart in which the central field may be found from length/i.d. and o.d./i.d. on the left and to the right by means of nomograms from current density and i.d. and by a final reading on the extreme right. Figure 5 shows other field values expressed in the one read from Fig. 4.

Figure 6 is a chart similar to Fig. 4 showing at the extreme right the maximum tangential tensile stress based on, from left to right, length/i.d., o.d./i.d., current density, and i.d..

Figure 7 shows other stresses expressed in the tensile stress read from the chart.

If coils are loosely wound or have very compressible insulation the tensile stress becomes higher than read in the chart. Figure 8 shows the maximum factor of increase for the "loose" coil.

In all cases the space factor has been assumed to be unity. Actual current densities, tensile and compressive stresses are higher and may be found by dividing by the appropriate space factors.

For certain coil shapes of o.d./i.d. ratio larger than two the maximum tensile stress may occur at a radius larger than the inside and the compressive stress at smaller radii disappears. The computer program and the charts take this into account.

## VII. CONCLUSION<sup>9,10</sup>

We have derived an accurate theory for the tangential and radial stresses in simple cylindrical coils. To apply this theory, the maximum and minimum values of  $B_z$  should be found by means of a computer program. From there on the computation involves only the determination of two integration constants in the expressions for the two stresses and the tangential strain.

The theory may also be applied to a coil surrounded by a reinforcing band, but in this case four constants have to be determined from the boundary conditions.

For a third situation, where the coil is wound of a compound ribbon made up of two different materials, our theory is adequate provided we use specified mean values of Young's modulus and Poisson's ratio.

By means of a computer program charts and graphs were plotted of magnetic fields in various places and of the three maximum stresses for a large range of shapes and sizes of coils of the simplest type.

- 
9. Since the original publication date of this report (August 1966, Report No. 68-C-255), the following paper was presented on this subject, which contains further references to recent literature: A.J. Middleton and C.W. Trowbridge, Proc. 2nd Intern. Conf. Magnet Technology, Oxford, 1967, p. 140.
  10. R.W. Kilb and W.F. Westendorp, G.E. Research & Development Center Report No. 67-C-440 (1967).

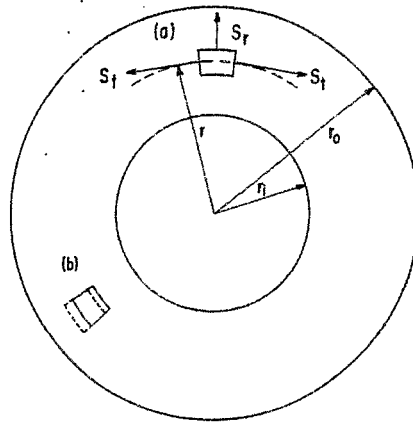


Fig. 1. Cross section of coil considered as a thick-walled pressure vessel showing stresses (a) and deformation (b).

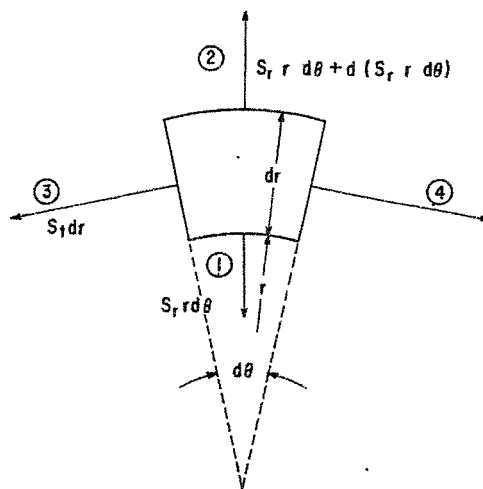


Fig. 2. Forces acting on an element. Not shown is the electromagnetic force  $J_\theta B_z r d\theta dr$ , directed radially outward.

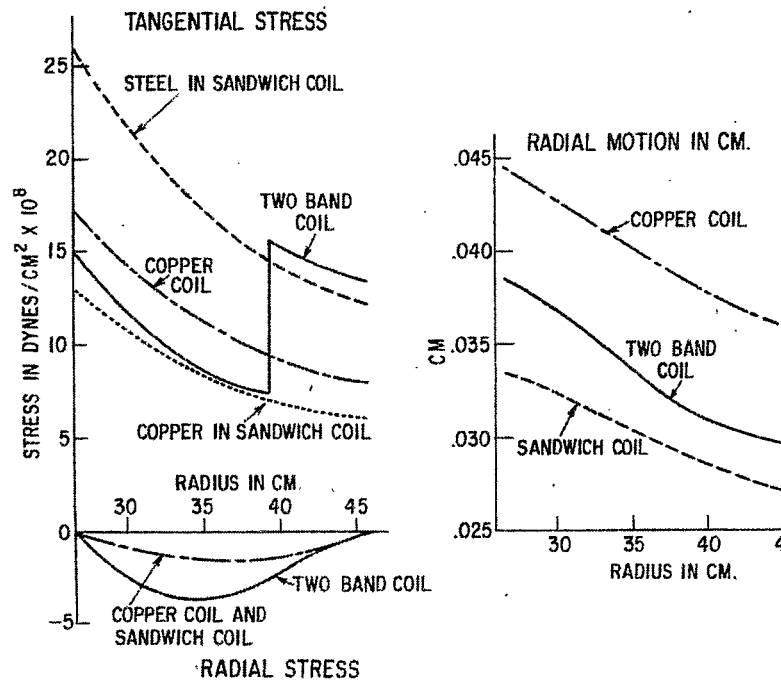


Fig. 3. Stresses and radial motion shown as a function of radius. For the "copper coil"  $r_i = 26.67$  cm,  $r_o = 45.72$  cm,  $B_i = 91$  kG,  $B_o = -18$  kG,  $J = 9.88$  kA/cm<sup>2</sup>; "sandwich coil" same as copper coil; "two-band coil"  $r_i = 26.67$  cm,  $r_o = 39.37$  cm,  $r_x = 45.72$  cm,  $B_i = 99$  kG,  $B_o = -20$  kG,  $J = 14.7$  kA/cm<sup>2</sup>,  $E_{ss}/E_{cu} = 0.33$ ,  $\mu_s = 0.3$ .

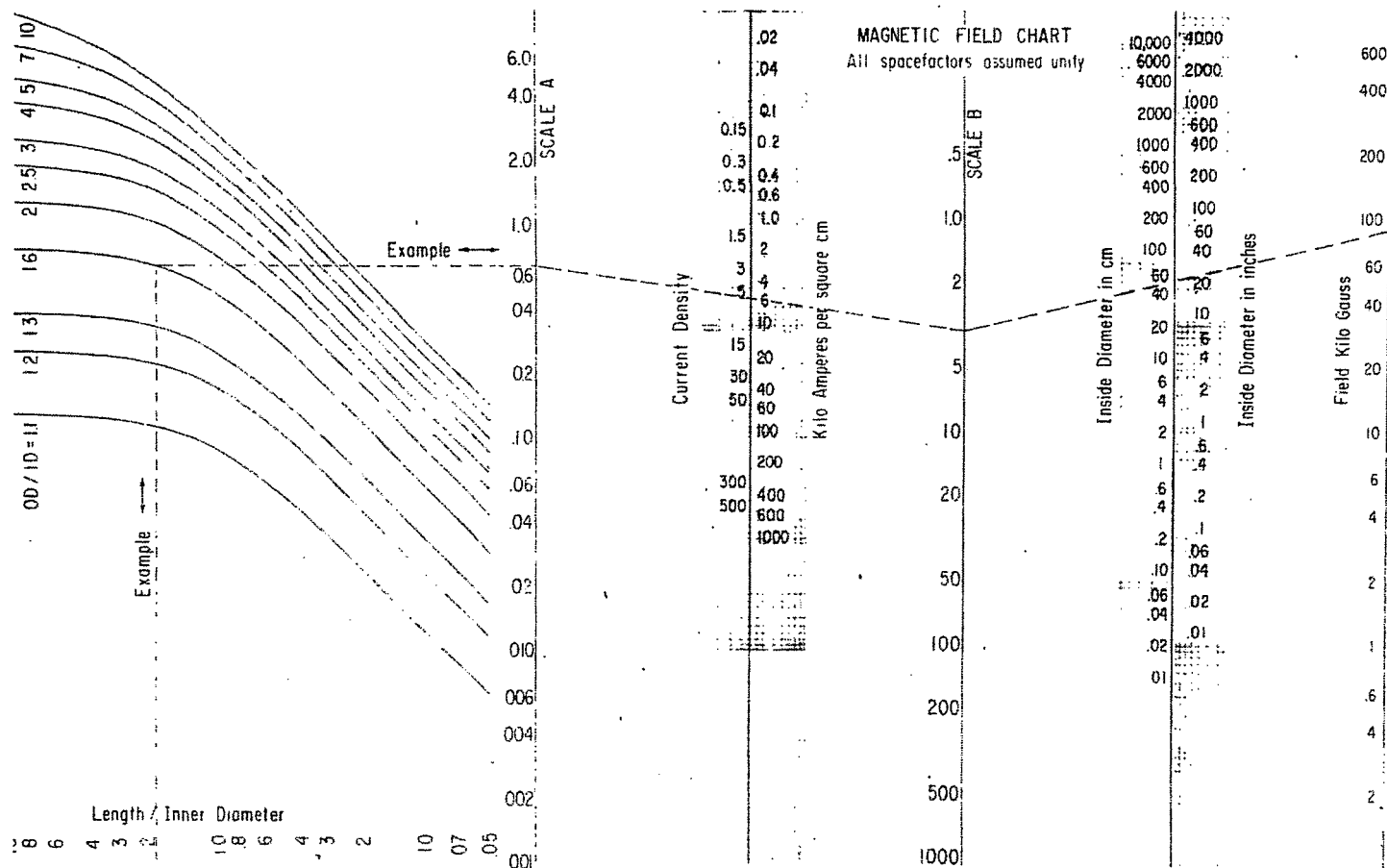


Fig. 4. Magnetic field chart.

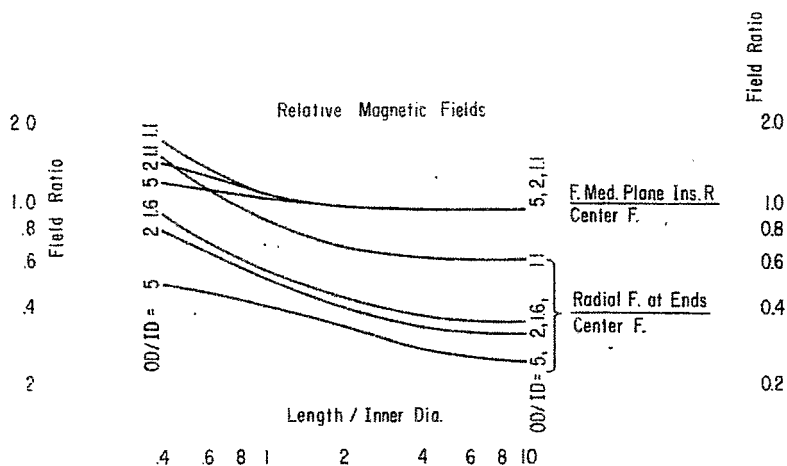


Fig. 5. Ratios of magnetic fields in conductors to field in center.



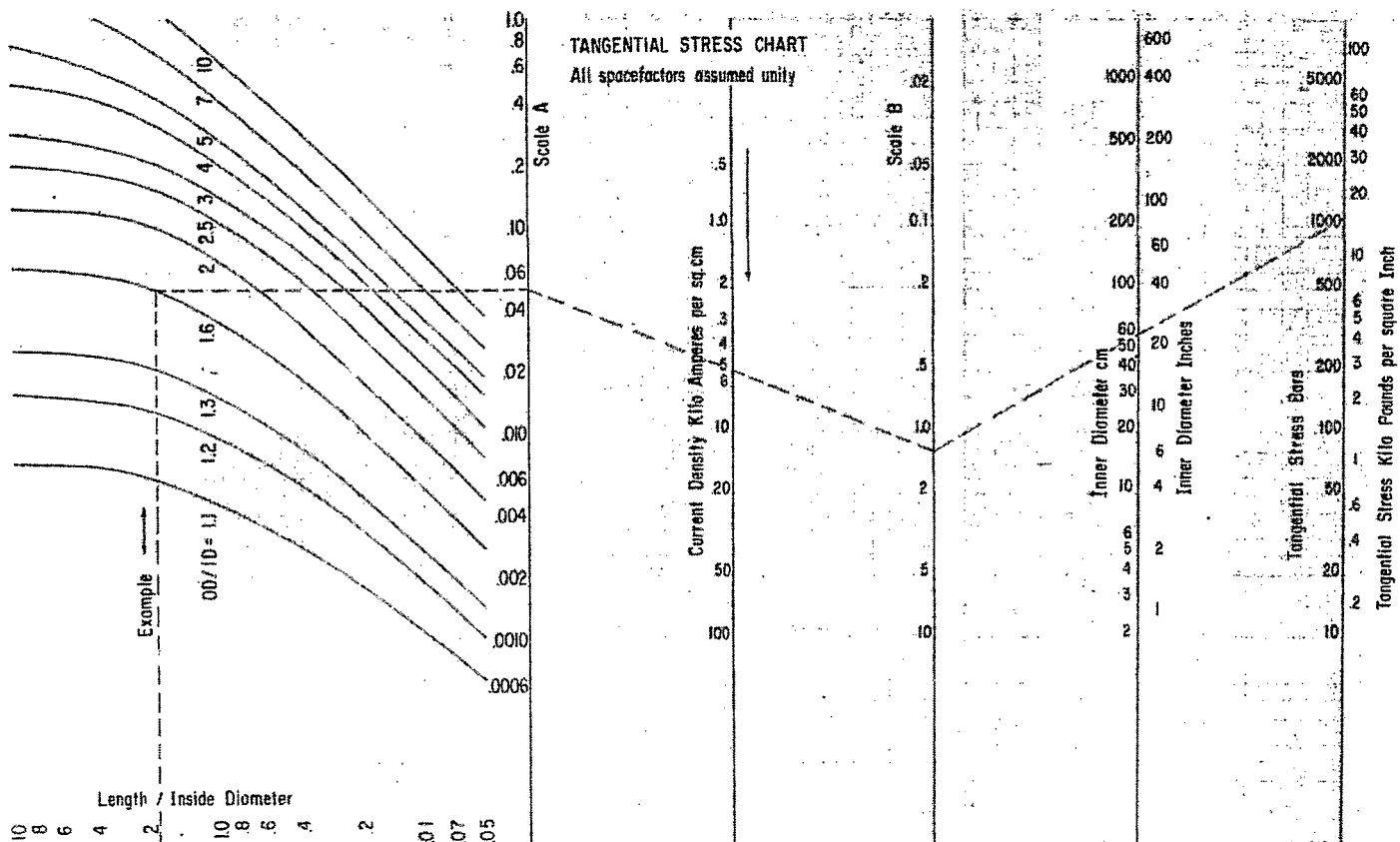


Fig. 6. Tangential, tensile stress chart.

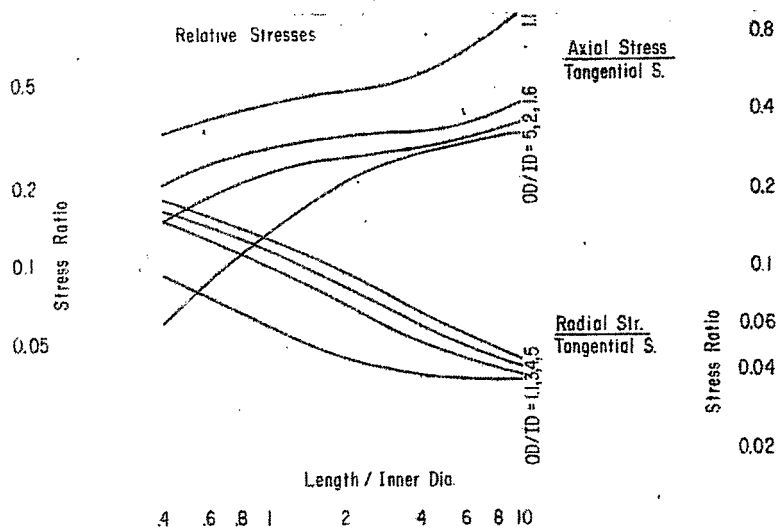


Fig. 7. Ratios of axial and radial compression stresses to maximum tensile stress.

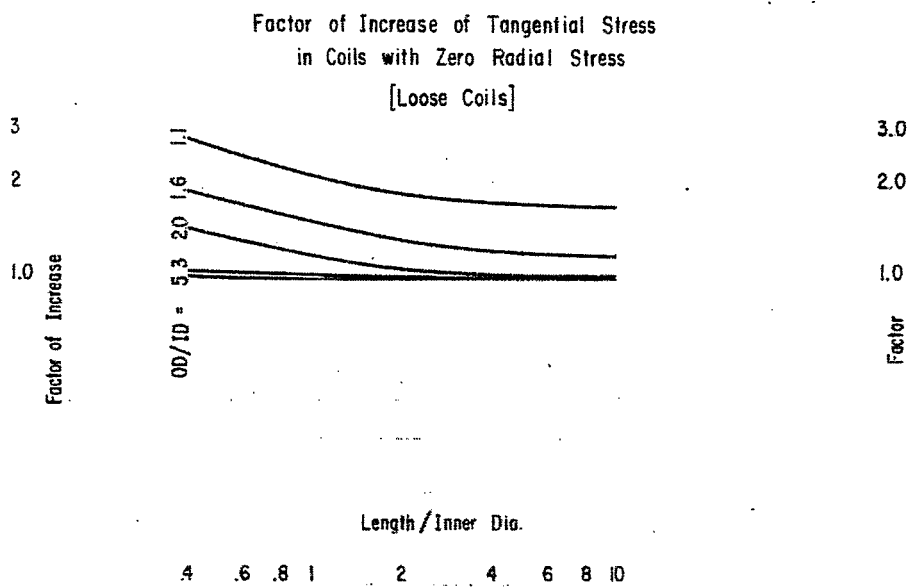


Fig. 8. Factor of increase of tangential stress for a "loose" coil.

## VERY HIGH FIELD HYBRID MAGNET SYSTEMS

D. Bruce Montgomery, J.E.C. Williams,\* N.T. Pierce,  
R. Weggel, and M.J. Leupold

Francis Bitter National Magnet Laboratory<sup>†</sup>  
Massachusetts Institute of Technology  
Cambridge, Massachusetts

### I. GENERAL CONSIDERATIONS

The term "hybrid" magnet has been coined to describe coils in which only part of the field is generated by superconductors and part by nonsuperconductors. Such systems have the advantage that they can produce higher fields than can be produced by either of their parts alone. In addition, they can represent a rather economical approach to very high fields for laboratories who already possess either power supplies or refrigerators of reasonable capacity.

The most compelling reason to consider hybrid systems is that superconductors by themselves are limited by their upper critical field. If one wants to produce a field above this level, it is clear that the superconductor cannot do it alone. If, on the other hand, we replace those sections of the winding which are exposed to a field too high for the superconductor by nonsuperconducting materials, we can go on increasing the field limited only by our ability to power or cool the now dissipative inner regions. Needless to say, one must separate the two sections by a suitable cryostat. This cryostat must not only provide low loss temperature isolation, but must support very large magnetic interaction forces as well.

When one designs an actual hybrid system it is necessary to take a more subtle approach than simply replacing only those windings which would be above the upper critical field of the superconductor. One needs to take into account the power (or cryogenic cooling) available, the space required for the nonsuperconducting insert, and the cost of the superconducting magnet as a function of field and bore.

Let us first consider the relative cost of superconducting magnets as a function of field. This will give us an indication both of how high field a superconducting coil we will be willing to invest in for the hybrid, and at the same time indicate what practical upper limits of field we might expect from an all superconducting system.

It is well known that the current carrying capacity of superconductors drops rapidly as the critical field is approached. Figure 1 shows the critical current for a widely used commercial Nb<sub>3</sub>Sn material nominalized to that at 100 kG for 4.2°K<sup>1</sup> and for 1.5°K.<sup>2</sup> If we wish our conductor to carry a fixed current, the amount of Nb<sub>3</sub>Sn which must be used in the conductor must increase as the inverse of Fig. 1. As the conductor price is related almost directly to the amount of Nb<sub>3</sub>Sn, we can construct a relative cost curve as in Fig. 2. We have added as well the relative cost of NbTi in the low field region as it becomes less costly than Nb<sub>3</sub>Sn.

---

\* Present address, Oxford Instrument Co. Ltd., Oxford, England.

<sup>†</sup> Supported by the U.S. Air Force Office of Scientific Research.

1. RCA Nb<sub>3</sub>Sn ribbon R60291 0 < H < 140 kG; above 140 kG data from D.B. Montgomery and W.B. Sampson, Appl. Phys. Letters 6, 108 (1965).
2. W.B. Sampson, private communication.

To compute the relative cost of magnets from Fig. 2 we must make assumptions about the amount of material per unit volume of the magnet which requires that we settle on the number of subdivisions, current density, and on the number of turns/cm<sup>2</sup>. For small bore, high field coils reasonable current density and turns/cm<sup>2</sup> to assume are given in Fig. 3 and are based on adding Nb<sub>3</sub>Sn to maintain constant current and adding copper in proportion to the linearly increasing magnetoresistance.

Figure 4 plots the relative cost of 1.5 inch bore, all superconducting magnets under the assumptions discussed for various numbers of subdivisions of the coil. It is clear that costs rise extremely rapidly at high fields, even at reduced temperatures. We might expect from such a figure to see hybrid systems considered for any fields above 175 kG, and certainly for all fields at 200 kG or higher. While future materials may alter these dividing points somewhat, the fact remains that there will always be a dividing point at which it is advantageous or necessary to consider hybrids.

As an indication of materials to come, Fig. 1 also gives the critical current density of some V<sub>3</sub>Ga material<sup>3</sup> in its absolute relation to that of Nb<sub>3</sub>Sn at 4.2°K. Its probable performance at 1.5°K should make it the best available material for this very high field range.

Superconducting coils for use in hybrid systems must, of course, have much larger bores than those in Fig. 4, but will be subject to the same steep rises in costs as fields increase. Figure 5, for example, indicates the relative cost of a 10 in. room-temperature bore superconducting system relative to the cost at 50 kG. Cryostat and power supply costs have been included in this case, and the relative cost of material is based on Fig. 2 and an assumed current density of  $5 \times 10^3$  A/cm<sup>2</sup>. We note that the system costs at 120 kG is nearly twice what it is at 100 kG.

It is of interest to examine the magnitude of the absolute costs of this 10 in. system. If we tie Fig. 2 to a typical figure for cost per ampere per meter at today's prices we can calculate the material costs. If we take \$16.50 per kA/m at 100 kG we obtain a material cost for the 12 in. 50 kG superconducting coil (10 in. room-temperature bore) of \$30 000 and with the \$20 000 additional system cost get a normalizing nonsalary cost for Fig. 5 of \$50 000 at 50 kG. In addition, one would need to add engineering and labor costs which can easily be equal to material costs in prototype systems. Taking the nonsalary figure of \$50 000 at 50 kG we thus note that a 100 kG system is worth \$150 000 in material costs alone and a 120 kG system, \$265 000. We are therefore talking about major investments and we see that we are unlikely to wish to exceed 100 kG by very much in the superconducting part of the hybrid.

Let us now shift our attention to the nonsuperconducting insert. This can be a water-cooled coil or a cryogenic coil and which one to choose depends on a number of variables. Probably the most important factor is what is already available to the designer. Most of the larger high energy physics laboratories, for example, can make at least several megawatts of power available as can any of the laboratories already engaged in high field water-cooled magnet work. Some facilities, on the other hand, have large cryogenic capacity and a shortage of power. If one is starting from the beginning with nothing available, the problem is more complex and the decision is often most heavily influenced by what else might be done with the facility were it available.<sup>4</sup> In this paper we will restrict our attention to water-cooled inserts as we already have considerable dc power and the need for many hours of continuous fields.

- 
3. Ribbons made by K. Tashikawa, National Research Institute for Metals, Tokyo, and tested at the Francis Bitter National Magnet Laboratory by Y. Iwasa.
  4. R. Stevenson and P. Marston, Colloque international sur les champs magnétiques intenses, Grenoble, 1966 (CRNS, Paris, 1967), p. 169.

We will start our discussion by considering what fields one might expect to achieve given a 100 kG superconducting coil of sufficient size to accommodate water-cooled coils at various power levels. This is shown in Fig. 6. With 2 MW we can achieve 200 kG in a 1.5 in. bore coil (1.25 in. working bore) and with 4 MW, 250 kG. Above a field of 250 kG the insert itself begins to suffer from some of the same limitations of critical current that affect superconductors, namely that the magnetic stresses are becoming so high that performance begins to suffer. The coil must either use increasingly strong conductors or give up increasing space to support structure. The power required per gauss therefore goes up. We have therefore shown the curve in Fig. 6 dividing above 250 kG; the upper curve represents an ideal situation of no limitation, and the lower one, the more practical case. Nonetheless, we note that with 10 MW one can achieve a field of over 300 kG.

We next examine how large a superconducting coil we need to build for a given hybrid system. The minimum size is dictated by the smallest bore large enough to contain a coil able to dissipate the power we wish to use. This is generally not the optimum size, however, as we shall discuss. Let us assume that we wish to generate 200 kG in a 1.25 in. bore and we have 2.5 MW of power available. We would first proceed to calculate the field that an insert of 1.5 in. inside diameter would produce as a function of its outer diameter. As the insert coil is enlarged, the gauss per watt goes up due to the increase in the coil's Fabry factor and the decrease in operating temperature. The increase in insert field with outer diameter means that less field need be generated by the superconducting coil to reach 200 kG, but also requires that the superconducting coil have a progressively larger bore to accommodate the larger insert. It is thus necessary to examine the balance between the cost of increasing the bore against that of producing a higher field at a smaller bore. Figure 7 shows the results for this case and for a 5 MW, 250 kG case. We note that there is an insert coil outer diameter which yields a minimum cost system at the given power and required field. Where the minimum will lie depends upon the type of insert, the power level, the field range and the cost of the superconductor. The minimum can thus be expected to shift with changing economics of the superconducting material. Figure 7 is given only to indicate that there will be an optimum size to pick and that within plus or minus one to two inches, it is not particularly critical.

Having found the optimum, it is necessary to go back and be sure that it is feasible to build a coil within that optimum space which can be supported and cooled. This is a more complex question as there is seldom an absolute limit on performance. A pair of typical insert coils are shown in Fig. 8 to give an indication of what is possible. The insert coil has an i.d. of 1.5 in. and an o.d. of 4.375 in. and absorbs 1.1 MW to generate 75 kG. It could easily absorb 1.5 MW. The second coil of 4.6 in. i.d. and 13 in. o.d. absorbs 5 MW and generates 100 kG. The over-all diameter outside the retaining structure is 14 in. A proposed future coil system has been designed to absorb 16 MW within the same envelope although with a different coil arrangement. Based on our experience with coils like these we feel that the minimum allowable size will generally fall below the optimum size, particularly if multiple coil arrangements are used.<sup>5</sup>

A 10 in. room temperature bore superconducting coil as discussed in connection with Fig. 5 would be close to the optimum size for a 2.5 MW insert, and if it generates 90 kG would give a 200 kG central field. This coil would represent an investment of about \$120 000 exclusive of salary costs and would be considerably less costly than the all-superconducting coils indicated in Fig. 4. As the field required increases further, hybrids must be used and the question is no longer one of economics.

---

5. D.B. Montgomery, Colloque international sur les champs magnétiques intenses, Grenoble, 1966 (CRNS, Paris, 1967), p. 51.

## II. PROTOTYPE HYBRID MAGNET

### 1. Over-all System

We are constructing a prototype hybrid system which will use various water-cooled insert coils in a 14 in. room temperature bore 60 kG superconducting coil. Total fields of 225 kG in a 1.25 in. bore or 200 kG in a 2.125 in. bore can be produced for 5 MW of power input. Later inserts at 10 and 16 MW can be expected to produce fields close to 300 kG. While it appears technically and economically feasible to construct outer coils up to 120 kG, the lower field prototype was selected to remain within the convenient range of NbTi and to minimize coil development problems. As we shall discuss, there are a number of severe problems which must be met in connection with the cryostat design, as well as an immediate need for the system in the magnet facility; we therefore considered it expedient to choose a superconducting coil of modest performance. Before discussing the design details of the superconducting coil, we shall examine the over-all system and the cryostat design.

Figure 9 shows the over-all system, which consists of the superconducting magnet cryostat, external 250 liter storage vessel, 8 kW power supply, and a typical water-cooled insert. The storage cryostat is considered a permanent part of the system and is connected to the magnet cryostat by a permanently installed, shielded, low loss transfer tube. Helium can be transferred into the magnet cryostat for operation and the excess out again after the run. Between runs the coil will be held at 20°K by a small regenerative refrigerator.<sup>6</sup>

The power supply can charge the 2 MJ superconducting magnet in 15 minutes and sweeping operation will then be accomplished by the insert. An energy removal protective system parallels the coil by a permanently installed 0.1  $\Omega$  resistor and disconnects the protected power supply by means of a two-pole breaker.

When additional hybrid systems become operational in the laboratory, it is proposed to connect them all together with a 500 W helium refrigerator.

### 2. Magnet Cryostat

The superconducting magnet cryostat and the two-coil water-cooled insert are schematically shown in Fig. 10. The insert is similar to that pictured in Fig. 8. All water and power connections are located at the bottom and the 14. in. o.d. retaining structure and coils can be easily removed as a unit up through the open bore of the magnet cryostat without disturbing the cryostat. Any other standardized insert can then be reintroduced, all without any necessity of warming up the superconducting coil.

The magnet cryostat can be very short as it needs to contain no reservoir of helium, the helium being supplied from the external storage vessel. The helium cryostat is welded shut to avoid seal problems and is suspended from supports at 77°K by 1/8 in. diameter stainless-steel cables running from the bottom of the helium cryostat to the top of the nitrogen cryostat and vice versa. A nitrogen shield cryostat is used rather than a gas cooled shield because of the desire to hold the coil at 20°K when no helium is present; the nitrogen reduces the load that the 20°K refrigerator must supply. The nitrogen cryostat and vacuum vessel are aluminum, the radiation shields copper, and the helium cryostat stainless steel. Cooldown weight of the coil and helium cryostat is 2000 lb.

---

6. W. Hogan and R.W. Stuart, Cryodyne Refrigerator, ASME 63-WA (1963)  
by A.D. Little, Inc.

Access to the helium cryostat is provided through a 40 in. long 3 in. diameter stack tube. This allows the use of long counter flow leads<sup>7</sup> and minimizes the neck tube loss. The leads may be remotely disconnected near the top of this stack and the low temperature side of the disconnect is shielded from heat input by a separate vacuum space. The leads will remain connected during operation as no persistent operation is possible (due to coupling with the changing field of the copper coil), but will be disconnected between runs to minimize heat input which must be removed by the 20°K refrigerator.

The principal design problem which must be met in the magnet cryostat is the support of the magnetic interaction forces between the insert and superconducting coil. The interaction forces, calculated on an inductance basis, result in an axial spring constant of 40 000 lb/in. and a radial spring constant of 6000 lb/in. of radial displacement. Under ordinary conditions the axial force is a restoring force and, by proper alignment and the allowance of some relative axial motion, would not be troublesome. However, during assymmetric failure of the copper coil, the magnetic centers would be displaced and a large accelerating force would be introduced. While these conditions will only exist during the 300 msec period required to fully open the breakers, the peak accelerating force can reach 24 g. The axial support cables running from the helium cryostat to the nitrogen cryostat, and from the nitrogen cryostat to the vacuum vessel, contribute an effective spring constant of 10 000 lb/in. and under higher off-center loads, stretch elastically to allow the inner cryostat to come up against stops (not shown in the figure) carried by the upper and lower radiation shield covers. They thus transfer the loads directly to the vacuum vessel covers. The vacuum vessel (and the insert magnet assembly) are both mounted on stiff spring systems and can then move to reduce the off-center loads. The coil is held inside the helium cryostat by long bolts passing through a cover plate above the coil and threaded into the cryostat base plate.

The radial forces are unstable and it is therefore necessary to have a restoring radial spring constant in the cables greater than the upsetting magnetic spring constant. A restoring spring constant of 15 000 lb/in. is provided. Radial cables running from the helium to the nitrogen cryostat are fixed in place, while those running from the nitrogen cryostat to the vacuum vessel are externally adjustable to minimize forces by proper initial alignment. Experience with the first system will indicate if this adjustment feature is necessary.

The estimated helium losses for the cryostat under various conditions, as well as cooldown requirements, are given in Table I.

### 3. The Superconducting Coil

A. Coil construction. The design parameters for the superconducting coil to be used with the prototype hybrid system are given in Table II. The coil is to be constructed from 24 double pancakes, with each double pancake wound from a single 620 ft piece of 0.079 in. x 0.397 in. copper NbTi composite material.<sup>8</sup> The specified conductor parameters are given in Table III.

The turns of the pancakes are separated by 0.1 in. long by 0.015 in. high polyester-glass spacers which are cemented in place by a silicone adhesive coating on both

---

7. K.R. Efferson, Rev. Sci. Instr. 38, 1776 (1967).

8. The composite material was manufactured by Cryomagnetics, Inc. Denver, Colorado.

TABLE I  
Estimated Cryostat and Cooldown Losses

1. Input to helium cryostat (4.2 - 77°K)	
Axial cables	0.04 W
Centering cables	0.17 W
Neck tube	0.10 W
Radiation (emissivity = 0.05)	<u>0.21 W</u>
	0.52 W $\cong 750 \times 10^{-3}$ liter/h
Lead losses at 1500 A	3.0 W $\cong 4.2$ liter/hr
2. Input to nitrogen cryostat	
Axial cables	0.6 W
Centering cables	2.4 W
Radiation (0.25 in. superinsulation)	<u>9.3 W</u>
	12.3 W $\cong 0.27$ liter/h
3. Helium cooldown requirements (perfect exchange conditions)	
To cool from 77°K	140 liter
To cool from 70°K	115 liter
To cool from 20°K	5 liter

TABLE II  
Coil Parameters

Inside diameter	16 in.
Outside diameter	26 in.
Length	23 in.
Number of double pancakes	24
Number of turns per pancake	52
Length of individual conductors (single length per double pancake)	610 ft
Total conductor length	14 700 ft
Coil weight	1500 lb
Internal cooling passages	0.017 in. $\times$ 0.3 in. (75% of internal surface)
Edge cooling	80% of each pancake face
Central field	60 kG
Maximum winding field	65 kG
Design current	1500 A
Maximum fault current	1650 A
Energy storage	$2 \times 10^6$ J

TABLE III  
Conductor Parameters

Cross section	0.397 in. $\times$ 0.079 in. (10 mm $\times$ 2 mm)
Ratio of copper to superconductor	8:1
Number of superconducting strands	60
Diameter of superconducting strands	$\approx 0.0091$ in.
Exposed surface/cm length	$2.25 \text{ cm}^2$
Anticipated resistivity at 65 kG	$3.75 \times 10^{-8} \Omega \cdot \text{cm}$
Stability parameters (Fig. 16)	$\alpha_n = 0.25, \beta_n (4.2^\circ\text{K}) = 0.3$
Maximum heat flux (1650 A)	$0.25 \text{ W/cm}^2$



sides of 0.001 in. Mylar tape.<sup>9</sup> The bond will resist a modest force of 100 lb at 77°K applied parallel to the tape surface per square inch of bond surface. The faces of each pancake are fully exposed for cooling with the exception of 64 0.2 in. wide radial Micarta spacer strips which separate the pancakes and support the axial forces. They cover 15% of the face cooling surface. The integrated axial compression force at the mid-plane is 300 000 lb, giving a compressive force on the insulator strip of 5500 psi.

The pancakes are banded at the outer diameter by a yellow brass tension band 0.187 in. thick, closed by a half inch bolt. The yellow brass has a yield strength of 45 000 psi at 300°K and an integrated contraction<sup>10</sup> higher than that of copper ( $\Delta L/L = 397 \times 10^{-5}$  from 300°K to 0°K).

The peak conductor stress is 10 800 psi distributed across the conductor and the resultant strain is so small that no adverse effect on resistivity is anticipated. The thermally induced stress resulting from the differential contraction of copper and NbTi for the 8:1 copper-to-superconductor ratio composite adds an additional 2500 psi (see Fig. 15).

All connections are at the outside of the coil and are overlapped, soldered, and bolted to a support structure. The pancakes are wound on a removable mandrel and are thus not wound on a core tube. The cross-over turn from one half of the pancake to the other is supported by appropriately placed insulated pieces.

B. Choice of conductor and anticipated coil performance. In view of the potential problems associated with the cryostat and operation of the prototype system it was decided to build as conservative a coil as possible. The coil is expected to be fully stable (that is, have a recovery current higher than the operating current) and to operate at a relatively modest current density of  $5 \times 10^3$  A/cm<sup>2</sup>. To specify and select an appropriate conductor, a number of tests on magneto- and stress-induced resistivity, thermal stresses, heat transfer, thermal conductivity, and finally voltage-current characteristics of short samples were undertaken.

i) Heat flux measurements. A test was made to determine the take-off and recovery heat fluxes for the conductor and passage geometry to be used in the coil. A 0.25 W carbon resistor was embedded in a 1 cm wide copper conductor backed with a stainless-steel heater strip. The conductor was then spaced off a vertical plate by the 0.017 in. insulator strips to be used in the coil, and the heater strip side blocked off from effective contact with the helium. The results are shown in Fig. 11. The recovery heat flux of 0.31 W/cm<sup>2</sup> can be further reduced to 0.25 W/cm<sup>2</sup> if sufficient additional heat is put into a heater below the test section, choking the passages with bubbles. It is clear that the most conservative approach would limit the heat flux with all the current in the copper to 0.25 W/cm<sup>2</sup>, and this we have done.

We have selected a passage height of 0.017 in. as a reasonable compromise between overly restricting heat flux and reducing the packing fraction. The influence of changing the passage height on the total conductor required is shown in Fig. 12 insofar as the passage height changes the turns/cm<sup>2</sup> and hence the over-all current density at fixed current. We note that the coil size and conductor thickness make the influence of passage size on conductor length rather small.

ii) Stress and resistivity. In order to anticipate what reasonable value of resistivity to expect for the conductor a series of tests was undertaken. Magnetoresistance data taken on magnet wire and five NbTi copper composites are summarized in Fig. 13.

---

9. Mylar double coated "Scotchpar," 3M Company Tape No. Y930.

10. R.B. Scott, Cryogenic Engineering (Van Nostrand, Princeton, N.J., 1959).

We note that the slopes of all the curves are very similar and that only the materials of a resistivity less than the 100:1 deviate appreciably from a linear relationship. Once knowing the initial resistivity and the slope one can estimate rather well the operating resistivity.

Also shown in Fig. 13 is the relationship between stress-induced resistivity and magnetoresistance. Curves 1 and 2 and curves 7 and 8 represent two samples before and after strain. The curves simply move up and consequently can also be constructed from zero field strain-resistivity measurements and zero strain magnetoresistance measurements. The magnetoresistance measurements in Fig. 13 were taken at 12°K so that resistivity of the copper could be measured in the presence of superconductors in the composite.

The effect of strain on zero field resistivity for annealed magnet wire is shown in Fig. 14. It is interesting to note that most of the strain-induced resistivity introduced at low temperature in copper anneals out upon returning to room temperature.

Stress can be introduced both by magnetic forces and by thermal contraction. The thermally induced stress in a NbTi copper composite (assuming zero stress at 300°K) is shown in Fig. 15 as a function of the ratio of copper to superconductor. The figure is based on a measured<sup>11</sup> modulus at 4.2°K of  $E = 12.2 \times 10^6$  for NbTi and  $E = 20 \times 10^6$  for copper, and a measured<sup>11</sup> 300°K to 77°K integrated contraction of  $\Delta L/L = 131 \times 10^{-5}$  for NbTi and  $\Delta L/L = 310 \times 10^{-5}$  for copper. For large copper-to-superconductor ratios, the stress is small, and little effect on resistivity from thermal contraction alone would be expected above a ratio of 2 to 1.

iii) Stability. Having explored allowable heat fluxes and expected resistivities, it is possible to specify the desired characteristics of the composite in regard to the ratio of copper to superconductor and the number of strands of superconductor. The parameters of the composite chosen for our 60 kG coil are given in Table III.

The stability parameters are defined in Fig. 16. It will be noted that the usual stability parameter,<sup>12</sup>  $\alpha$ , has to be redefined as  $\alpha_n$  to allow the use of a nonlinear heat transfer coefficient. We have also introduced a second parameter,  $\beta_n$ , relating to the temperature rise associated with thermal gradients within the superconductor. The simple model used assumes a uniform distribution of current within the superconductor and a mean temperature rise given by Eq. (4), Fig. 16. The influence of  $\alpha_n$  and  $\beta_n$  can be combined into a single stabilization equation<sup>13</sup> as given in Fig. 16.

We can demonstrate the effect of  $\alpha_n$  and  $\beta_n$  on stability by the use of Fig. 17 and Fig. 18. Figure 17 assumes  $\beta_n = 0$  and shows only the effect of the nonlinear heat transfer which is assumed to be of the sample form of Eq. (1), Fig. 16, with  $h_0 = 4$ ,  $n = 2$ . One notices discontinuities at  $I = I_c$ , an occurrence which has been reported previously.<sup>14</sup> Figure 18 assumes a fixed value of  $\alpha_n = 0.25$  and shows the effect of gradients in the superconductor. These gradients can also introduce discontinuities at  $I = I_c$ . One must therefore know something about the thermal conductivity of the superconductor, and should then choose  $N$  to limit the discontinuity of the critical

---

11. Measured at the Francis Bitter National Magnet Laboratory by N.T. Pierce and C. Park.

12. Z.J.J. Stekly and J.L. Zar, IEEE Trans. Nucl. Sci. NS-12, No. 3, 367 (1965).

13. D.B. Montgomery, Magnet Design (John Wiley & Sons, New York, 1969), Chap. 6.

14. W.F. Gauster and J.B. Hendricks, in Proc. IEEE Intermag Conference, Washington, 1968 (to be published).

current chosen. (For a fixed current, if  $N$  gets larger, the strand diameter must get smaller.)

The thermal conductivity of NbTi at  $H = 0$  is given<sup>15</sup> in Fig. 19 and is a rapidly changing function of temperature. (In Fig. 18, the conductivity is assumed fixed and if taken at the 4.2°K value, for example, will obviously overemphasize the effect.) To assure no discontinuity we chose a large number of individual conductors,  $N$  being 60 for our composite.

15. These measurements were made by A. Milner and R. Hale at the Francis Bitter Magnet Laboratory. The material was supplied by Cryomagnetics, Inc., Denver, Colorado.

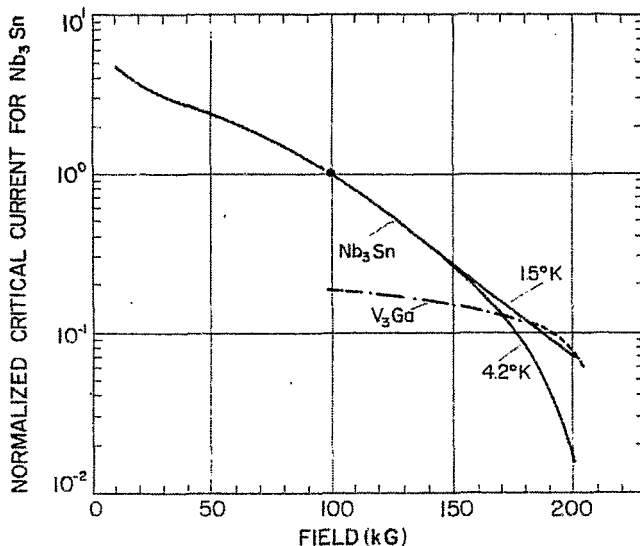


Fig. 1. Critical currents for Nb<sub>3</sub>Sn ribbons at 4.2°K (Ref. 1) and 1.5°K (Ref. 2) as a function of field, normalized to their values at 100 kG. Also shown is a sample of V<sub>3</sub>Ga (Ref. 3) at 4.2°K in its absolute relation to Nb<sub>3</sub>Sn at 4.2°K on the basis of equivalent over-all cross section.

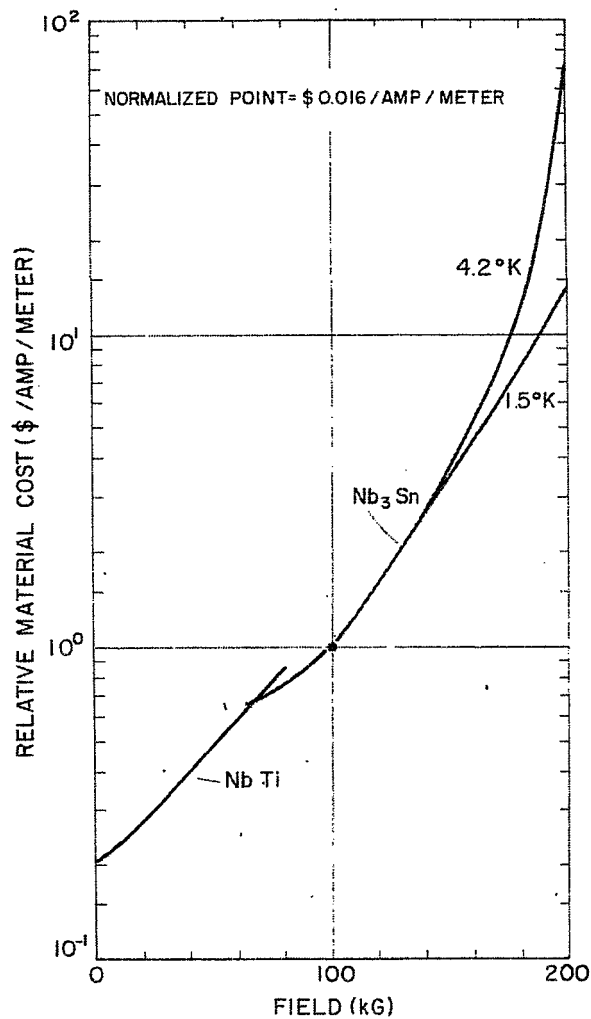


Fig. 2. Relative cost of NbTi and Nb<sub>3</sub>Sn at 4.2°K and 1.5°K based on Fig. 1 and the assumption that cost is inversely related to current at fixed field. The curves have been normalized to 1 at 100 kG where current prices indicate an average approximate cost of \$16.50 per kA/m.

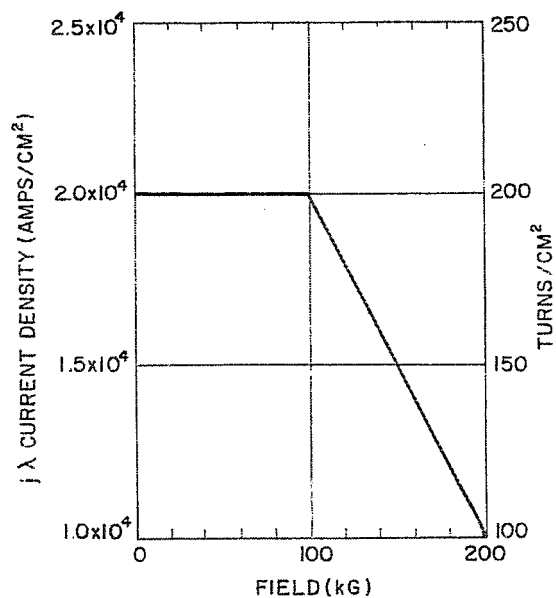


Fig. 3. Assumed over-all current density and turns/cm<sup>2</sup> used with Fig. 4.

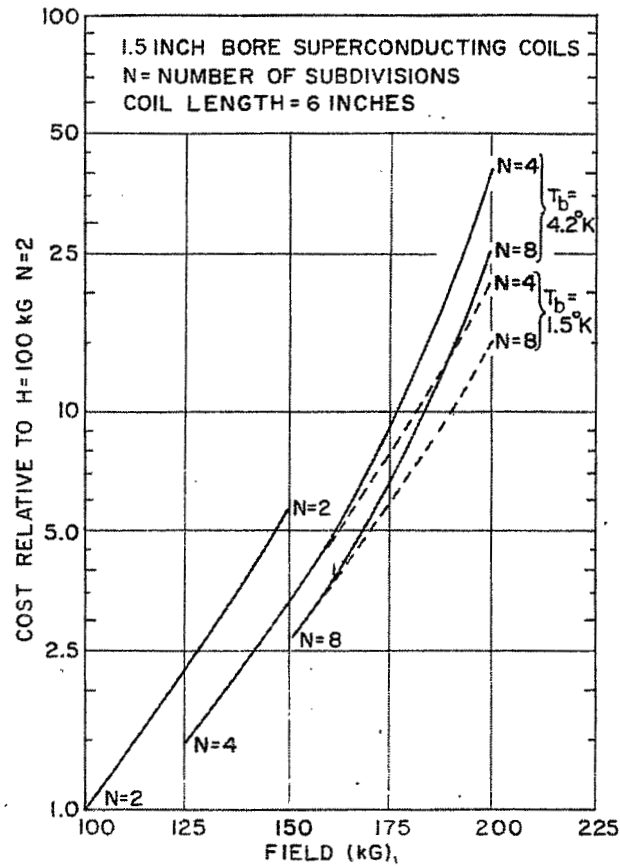


Fig. 4. Cost of 1.5 in. bore superconducting coils in relation to costs at 100 kG. The number N is the number of subdivisions of the coil. Each subdivision, starting at the inside, is assumed to produce a field  $h_1 = 1$  unit,  $h_2 = 2$  units ... ,  $h_n = n$  units, thus generating progressively more field with the lower field coils. Curves are shown for  $4.2^\circ K$  and  $1.5^\circ K$ . We note that the cost of 200 kG coils ranges from 15 to 40 times costs at 100 kG.

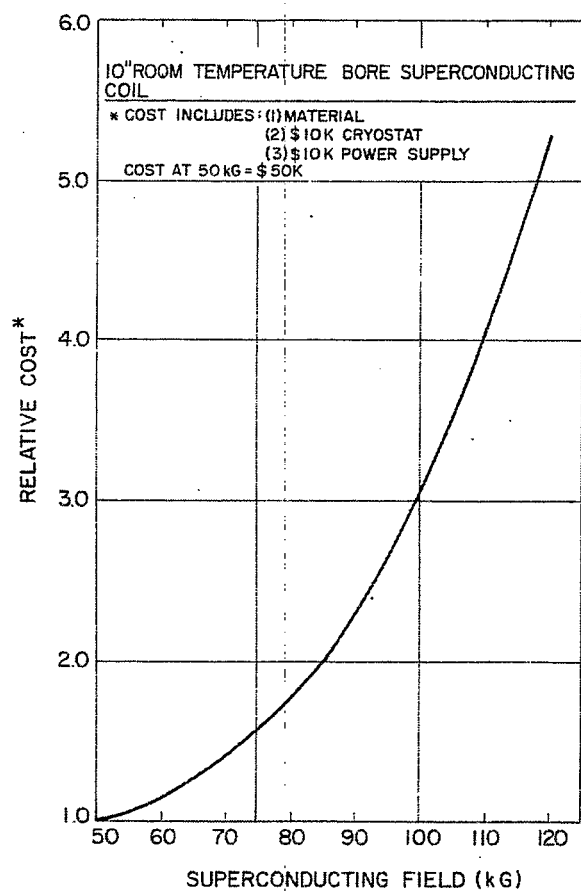


Fig. 5. Relative cost of a 10 in. room temperature bore (12 in. i.d.) superconducting coil as a function of field. The normalized cost at 50 kG includes \$10 000 for a cryostat and \$10 000 for a power supply and \$30 000 for materials. No construction costs are included.

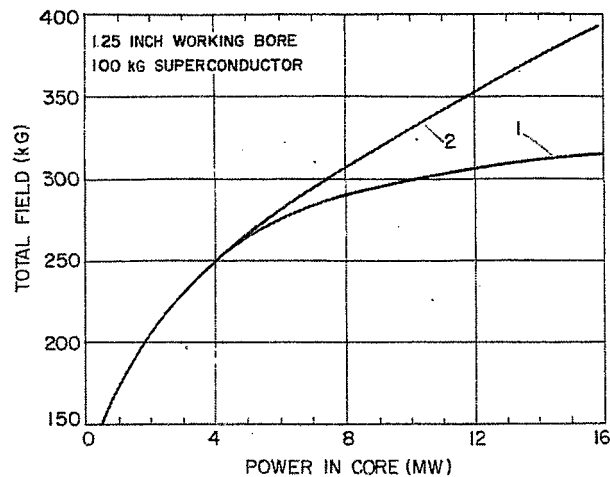


Fig. 6. Total field in a 1.25 in. bore resulting from a 100 kg superconducting coil surrounding a water-cooled insert absorbing various amounts of power. Curve 2 assumes no limitation of stress, and curve 1 shows the effect of stress limiting in the water-cooled insert.

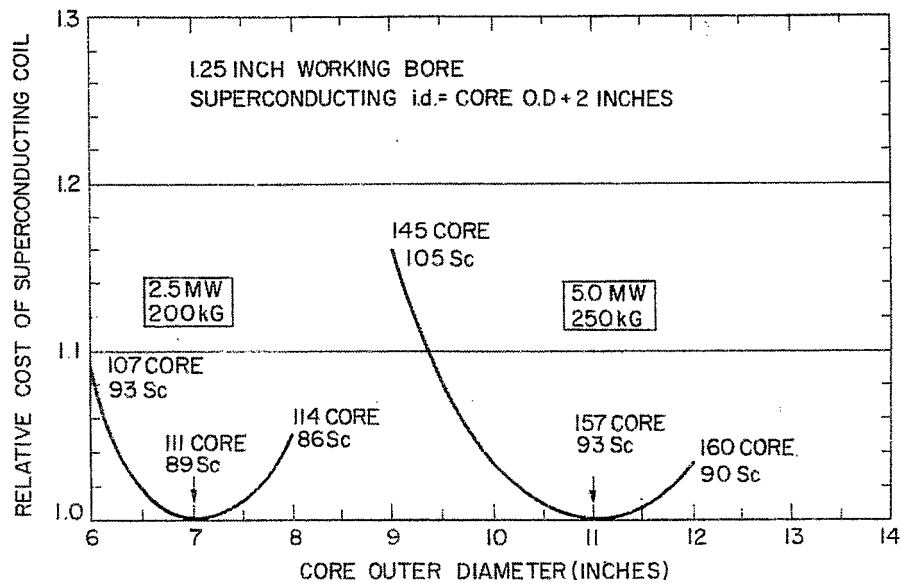


Fig. 7. Relative cost of superconducting outer coils as a function of the outer diameter of the insert core. The superconducting coils are assumed to be 2 in. larger than the core o.d. (see text).



Fig. 8. A typical 5 MW water-cooled insert (Ref. 5) consisting of two coils, the inner producing 75 kG and the outer 100 kG. The clearance dimension outside the containing barrel is 14 in.



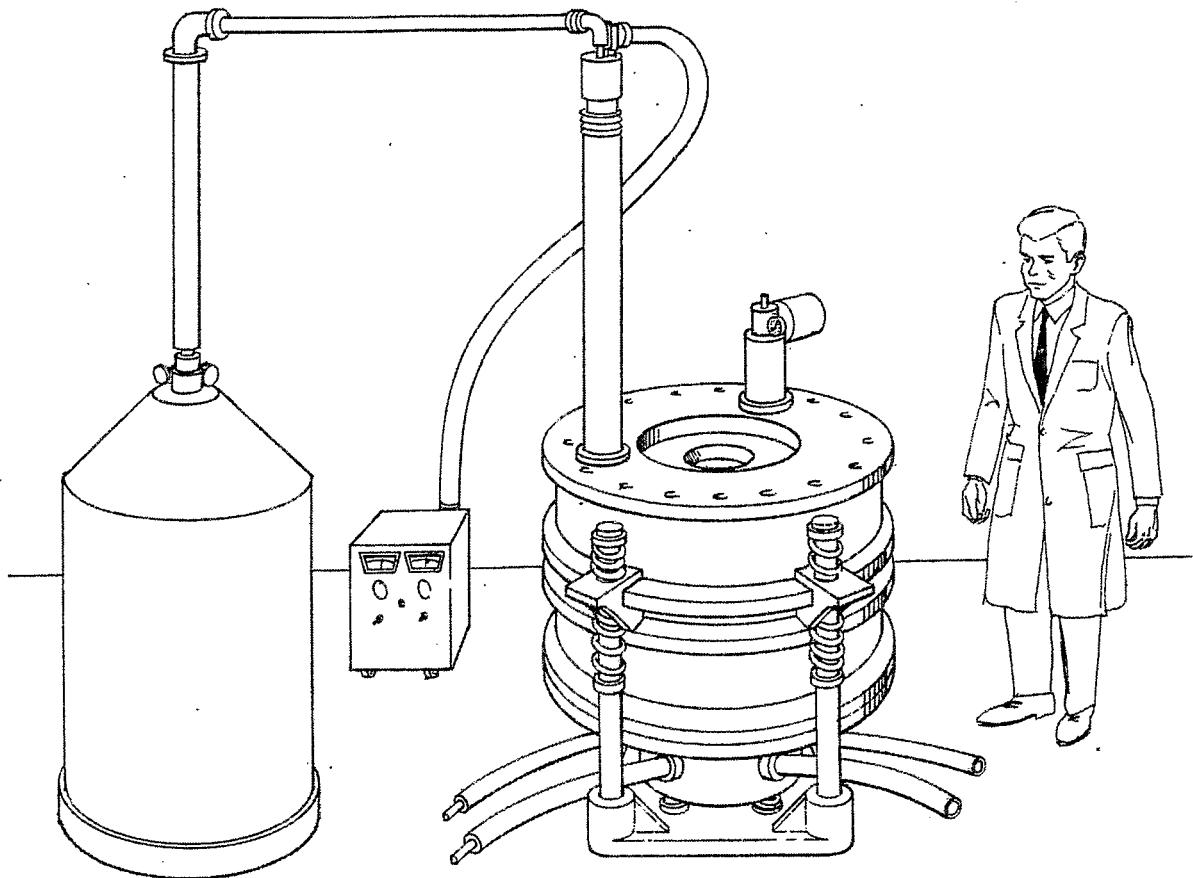


Fig. 9. Over-all view of the 225 kG hybrid water-cooled and superconducting magnet system being developed at the Francis Bitter National Magnet Laboratory. The external helium storage vessel is at the left and supplies helium to the magnet cryostat. The 8 kW power supply is shown between the cryostats. A small refrigerator is shown mounted on top of the magnet cryostat and is used to hold the magnet at  $20^{\circ}\text{K}$  between scheduled operations. The magnet cryostat is mounted on heavy springs to allow relative motion between the two coil systems under fault conditions.

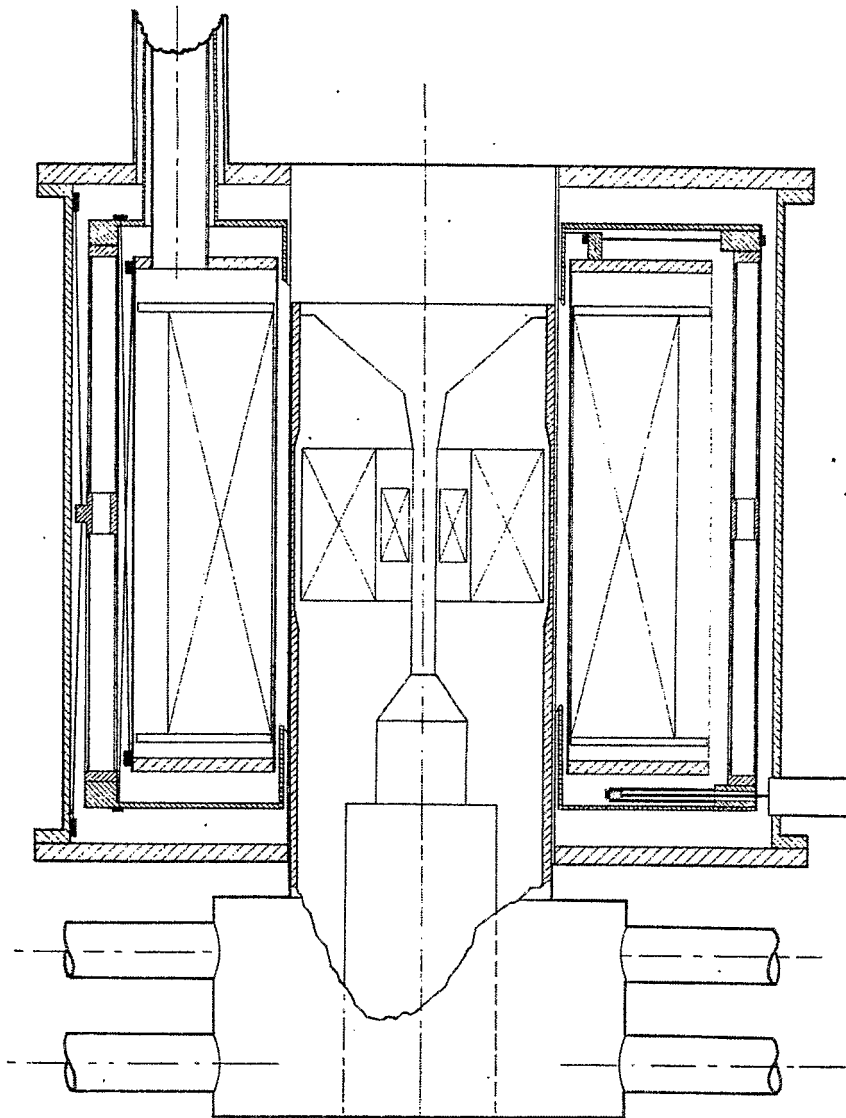


Fig. 10. Schematic of the 225 kG hybrid magnet. A pair of water-cooled coils consuming 5 MW of dc power are to be operated inside a 14 in. room temperature bore 60 kG superconducting coil. The superconducting coil will weigh 1600 lb and store 2 MJ of energy. The helium Dewar containing the coil as well as the nitrogen shield Dewar are suspended against the very large magnetic interaction forces by the spokes indicated schematically in the left-hand section. Access for electrical leads and cryogenic fluids is provided through the 3 in. neck tube shown at the top left of the cryostat. The water-cooled insert can be exchanged easily for alternate cores without disturbing the superconducting coil. All water and power connections for the water-cooled section are located below the insert.

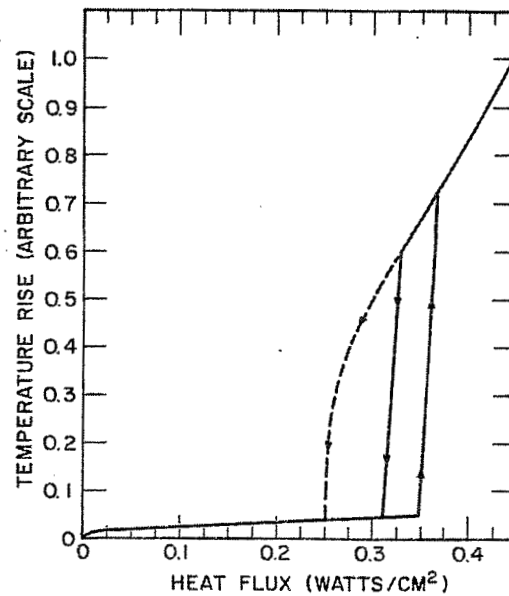


Fig. 11. Critical heat flux measurements in passages simulating those in the magnet, 0.017 in. high by 0.3 in. wide by 0.397 in. long. The dotted curve results when a large input of bubbles is produced with a heater below the test section, simulating a normal zone in a lower pancake.

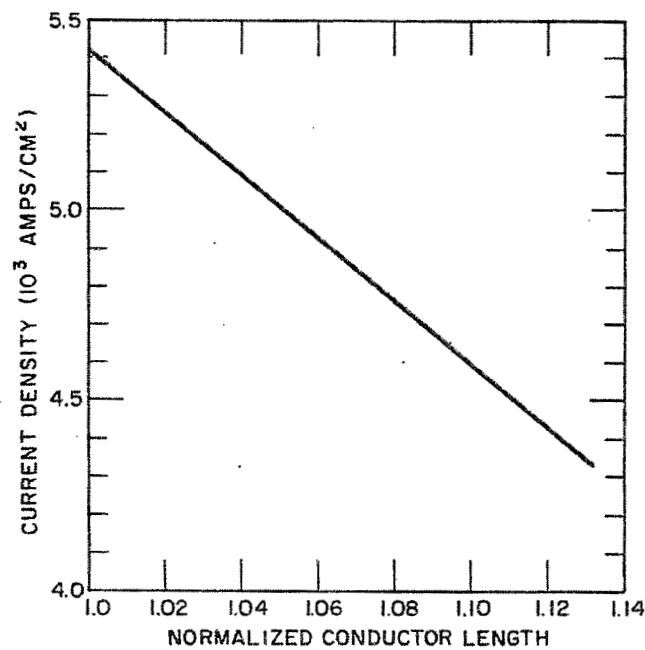


Fig. 12. Effect on conductor length of changing passage height and consequently the turns/cm² and the over-all current density at fixed current.

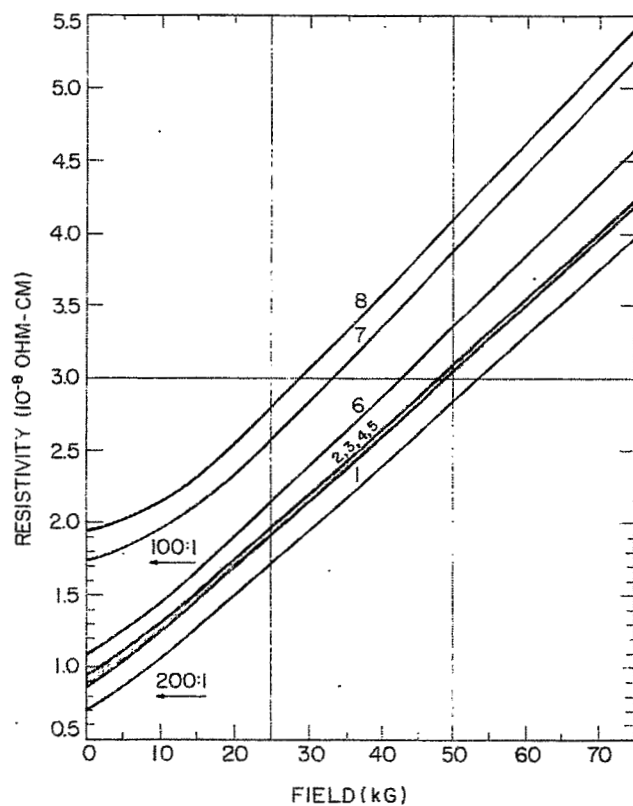


Fig. 13. Effect of magnetoresistance on a variety of composite samples of different initial resistivities. Curves 1 and 2 and 7 and 8 before and after strain, illustrating the simple additive nature of the two resistivity contributions.

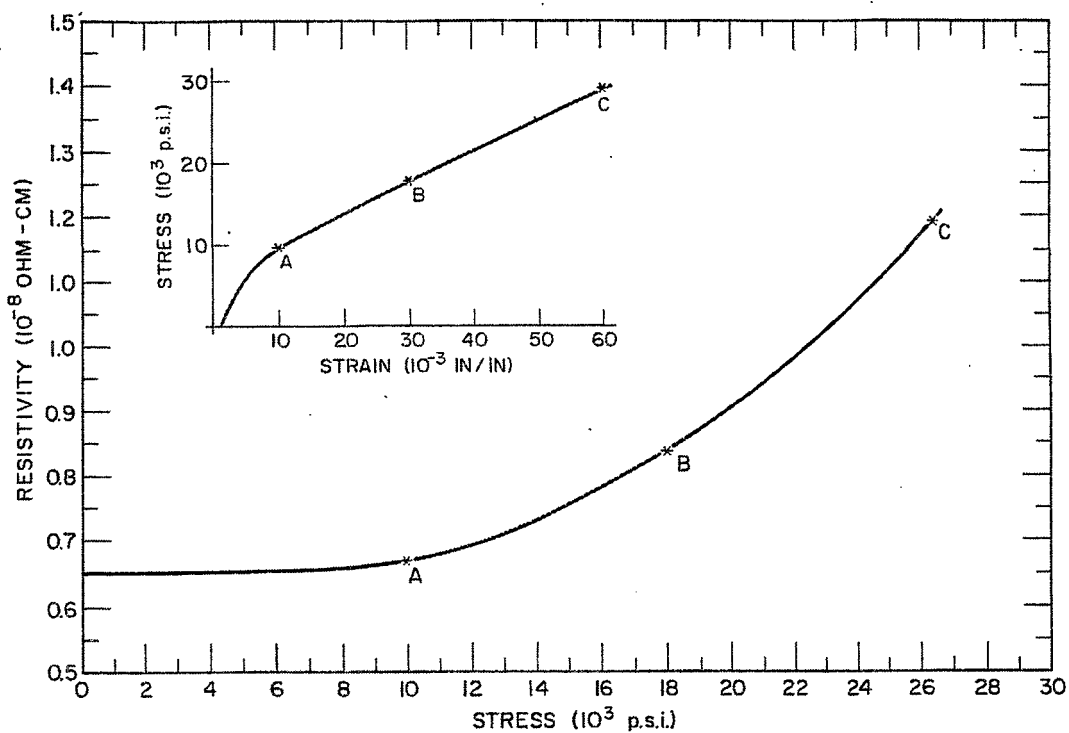


Fig. 14. Effect of stress and strain on the resistivity of copper magnet wire. A 1% strain is required before any effect on resistivity is noted.

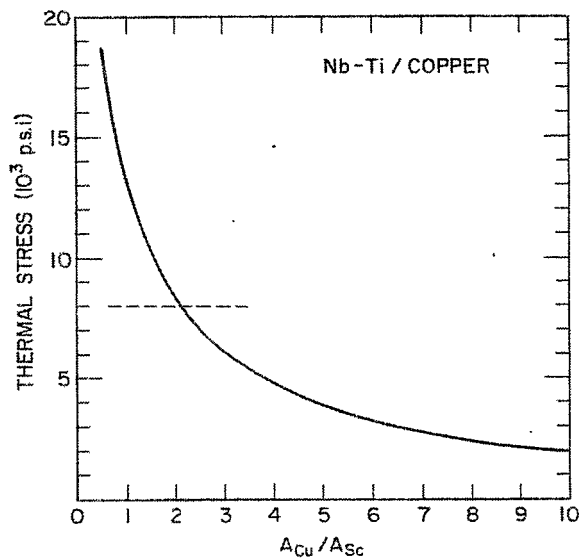


Fig. 15. Thermal stress induced in the copper portion of a copper-NbTi composite conductor as a function of the area ratio of copper to superconductor (see text).

$$(1) \quad \omega_s = h_0 \Delta T^n$$

$$(2) \quad \Delta T = \left( \frac{I_R}{I_c} \cdot \frac{I}{I_c} \cdot \frac{\rho}{A \Phi h} I_c^2 \right)^{1/n} = i_R \cdot i \cdot \alpha_n$$

$$(3) \quad \alpha_n = \frac{I_c^2 \frac{\rho}{A}}{\Phi h_0 (T_c - T_b)^n}$$

$$(4) \quad \Delta T g_s = \frac{\left( \frac{I_R}{I_c} \cdot \frac{\rho}{A} \right) \frac{I_s}{I_c} \cdot I_c^2}{8 \pi k N} = i_R \cdot i_s \cdot \beta_n$$

$$(5) \quad \beta_n = \frac{I_c^2 \frac{\rho}{A}}{8 \pi k N (T_c - T_b)}$$

$$(6) \quad \beta_n i_R^2 + i_R (1 - \beta_n i) - \alpha_n i_R^{1/n} \cdot i^{1/n} + 1 - i = 0$$

Fig. 16. Formulation used to describe the stability of copper-superconductor compounds (see text).

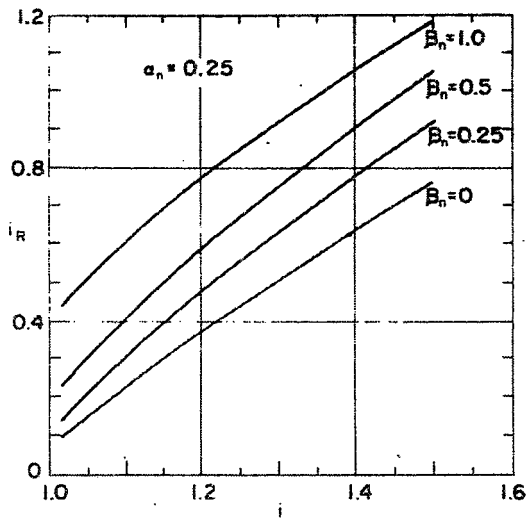


Fig. 17. Plot of Eq. (6) with  $\beta_n = 0$ , thus illustrating the effect of a nonlinear heat transfer in producing a discontinuity at the critical current. The normalized current,  $i$ , is the total current normalized to the critical current,  $I_c(H)$ , and  $i_R$  is the current in the normal path normalized to  $I_c(H)$ .

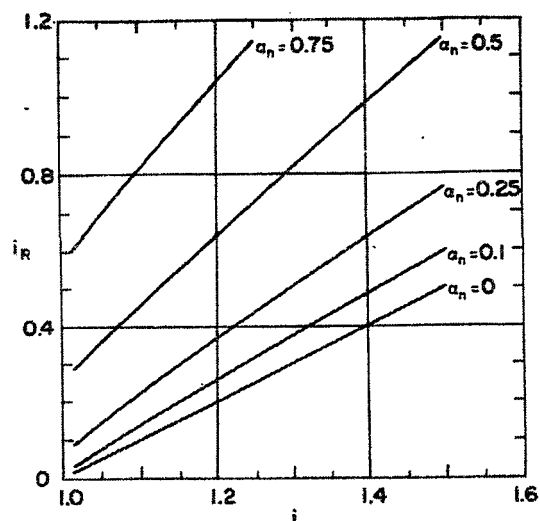


Fig. 18. Plot of Eq. (6) with  $\alpha_n = 0.25$ , thus illustrating the effect of a gradient within the superconducting core on discontinuities at the critical current. The normalized currents,  $i$  and  $i_R$ , are defined in Fig. 17.

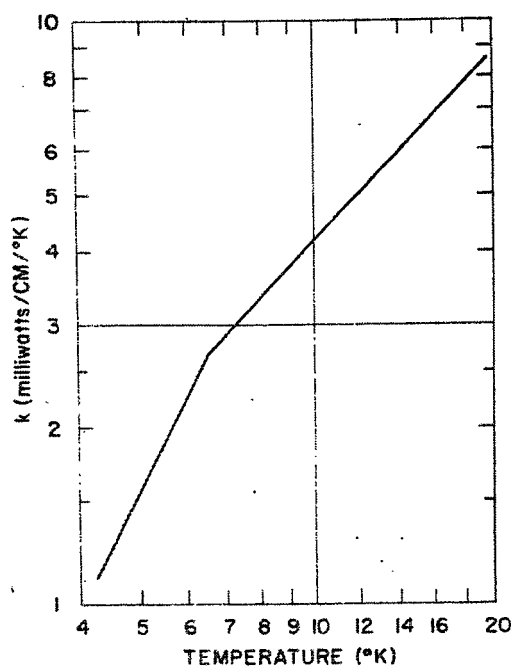


Fig. 19. Thermal conductivity of NbTi (Ref. 15) as a function of temperature at zero field. The sample consists of 19 parallel strands of 0.020 in. diameter NbTi. The measurements were made along the wire in a high vacuum cryostat.

# PRINCIPLES OF STABILITY IN COOLED SUPERCONDUCTING MAGNETS\*

Z.J.J. Stekly, R. Thome, and B. Strauss  
Avco Everett Research Laboratory  
A Division of Avco Corporation  
Everett, Massachusetts

## INTRODUCTION

The behavior of a composite conductor is determined by the characteristics of the superconductor, the substrate which surrounds it and the characteristics of the cooling medium used to carry away the heat.

This paper considers the general case of a composite conductor taking into account the temperature drop within the superconductor itself, a thermal interface resistance between the superconductor and the substrate, and the cooling of the conductor by a coolant.

The approach taken consists of analyzing the steady state characteristics. Since the purpose of studying the stability of a conductor is to achieve steady state stability, the problem should be tractable by understanding the steady state behavior, with onset of instability being derived from the response of the coil in a quasi-steady manner to a transient triggering phenomenon.

In the following treatment the emphasis is on the physics of the phenomenon rather than the derivation of a set of equations that can accurately predict the terminal characteristics of a particular composite conductor.

## FORMULATION OF EQUATIONS

Consider the general case of a conductor composed of superconductor (in many strands) and a cooled stabilizing substrate which completely surrounds each strand of superconductor.

The following assumptions will be made:

- 1) All the superconducting strands have equal properties and have the same shape and size.
- 2) There are no thermal gradients in the stabilizing substrate.
- 3) The heat generated within a superconducting strand is transferred to the substrate through a surface thermal contact resistance which is assumed to be uniform throughout.
- 4) There are no thermal gradients along the conductor so that we can deal with heat flow transverse to the conductor length.
- 5) The current density at any point within each superconducting strand is assumed to depend only on the local temperature. Also the current density is assumed to decrease to zero linearly with increasing temperature:

---

\* Prepared under Contract NAS8-21037 for the National Aeronautics and Space Administration, George C. Marshall Space Flight Center, Huntsville, Alabama.



$$j_s = j_{ch} \left[ 1 - \frac{T_s - T_b}{T_{ch} - T_b} \right] , \quad (1)$$

where  $j_s$  = local superconductor current density,

$j_{ch}$  = local superconductor current density at bath temperature,

$T_s$  = local superconductor temperature,

$T_b$  = bath or coolant temperature,

$T_{ch}$  = temperature at which the current density goes to zero.

(In the presence of whatever magnetic field exists.)

The temperature distribution within each superconducting strand is determined by heat conduction toward the superconductor-substrate interface and by the heat generation within the superconductor when a voltage exists across it. Without specifying the detail shape of the superconducting strands, we can write down the equation for their temperature distribution:

$$k \nabla^2 T_s = v \cdot j_s , \quad (2)$$

where  $k$  = thermal conductivity (assumed constant),

$v$  = voltage per unit length of conductor.

The right-hand side of Eq. (2) represents the heat generated per unit volume within the superconductor itself.

At the surface of the superconducting strand the temperature is assumed to be uniform and equal to  $T_w$ .

The total current carried by all the superconducting strands is:

$$I_s = n \int j_s dA_s , \quad (3)$$

where  $n$  is the number of superconducting strands.

All the heat generated within a superconducting strand flows through the thermal contact resistance at the superconductor-substrate interface into the substrate:

$$v \cdot \left( \frac{I_s}{n} \right) = h_i P_i (T_w - T_{sub}) , \quad (4)$$

where  $h_i$  = superconductor-substrate interface heat transfer coefficient,

$P_i$  = perimeter of one strand of superconductor in contact with the substrate,

$T_{sub}$  = temperature of the substrate.

All the heat generated within the conductor passes from the substrate to the coolant:

$$v \cdot I = hP(T_{sub} - T_b) , \quad (5)$$

where  $I$  = total current in the conductor,

$h$  = heat transfer coefficient at the substrate-coolant interface,

$P$  = perimeter exposed to the coolant.

The voltage per unit length of conductor is determined by the current that flows in the normal substrate:

$$v = \frac{\rho}{A} (I - I_s) \quad , \quad (6)$$

where  $\rho$  = resistivity of the substrate,

$A$  = cross-sectional area of the substrate.

It is very informative to put the equations into dimensionless form:

$$\frac{j_s}{j_{ch}} = 1 - \frac{T_s - T_b}{T_{ch} - T_b} \quad (7)$$

$$\frac{kA (T_{ch} - T_b)}{\rho I_{ch} j_{ch} r_w^2} \nabla'^2 \left( \frac{T_s - T_b}{T_{ch} - T_b} \right) = \left( \frac{vA}{\rho I_{ch}} \right) \left( \frac{j_s}{j_{ch}} \right) \quad (8)$$

where  $\nabla'$  has been nondimensionalized with respect to the half width or half thickness of a superconducting strand  $r_w$ :

$$\frac{I_s}{I_{ch}} = \int \left( \frac{j_s}{j_{ch}} \right) \frac{dA_s}{A_s} \quad (9)$$

$$\left( \frac{vA}{\rho I_{ch}} \right) \left( \frac{I_s}{I_{ch}} \right) = \left( \frac{nh_i P_i A (T_{ch} - T_b)}{\rho I_{ch}^2} \right) \left( \frac{T_w - T_{sub}}{T_{ch} - T_b} \right) \quad (10)$$

$$\left( \frac{vA}{\rho I_{ch}} \right) \left( \frac{I}{I_{ch}} \right) = \frac{hPA(T_{ch} - T_b)}{\rho I_{ch}^2} \left( \frac{T_{sub} - T_w}{T_{ch} - T_b} \right) \quad (11)$$

$$\left( \frac{vA}{\rho I_{ch}} \right) = \frac{I}{I_{ch}} - \frac{I_s}{I_{ch}} \quad (12)$$

In the above equations

$I_{ch}$  = critical current =  $j_{ch}A_s$ ,

$A_s$  = total superconductor cross section,

$r_w$  = half thickness or radius of superconducting strand.

Let us now define the following variables:

$$J = j_s/j_{ch} \quad (13)$$

$$\theta = \frac{T - T_b}{T_{ch} - T_b} \quad (\text{with appropriate subscript } s, \text{ sub, } w) \quad (14)$$

$$V = \frac{vA}{\rho I_{ch}} \quad (15)$$

$$\tau = I/I_{ch} \quad (16)$$

$$\alpha = \frac{\rho I_{ch}^2}{hPA(T_{ch} - T_b)} \quad (17)$$

$$\alpha_i = \frac{\rho I_{ch}^2}{nh_i P_i A(T_{ch} - T_b)} \quad (18)$$

$$r_{cs} = \sqrt{\frac{k(T_{ch} - T_b)A}{\rho j_{ch} I_{ch}}} = \frac{A}{I_{ch}} \sqrt{\frac{k(T_{ch} - T_b)}{\rho} \frac{A_s}{A}} \quad (19)$$

With these variables the equations reduce to:

$$J = 1 - \theta_s \quad (20)$$

$$\left(\frac{r_{cs}}{r_w}\right)^2 \nabla'^2 \theta_s = VJ \quad (21)$$

$$\left(\frac{I_s}{I_{ch}}\right) = \int J \frac{dA_s}{A_s} \quad (22)$$

$$V \left(\frac{I_s}{I_{ch}}\right) = \frac{\theta_w - \theta_{sub}}{\alpha_i} \quad (23)$$

$$V\tau = \frac{\theta_{sub}}{\alpha} \quad (24)$$

$$V = \tau - \left(\frac{I_s}{I_{ch}}\right) \quad (25)$$

Eliminating and rearranging the above equations we arrive at:

$$V = \tau - 1 + \alpha V\tau + \alpha_i V(\tau - V) + \int (\theta_s - \theta_w) \frac{dA_s}{A_s} \quad (26)$$

The quantity  $\theta_s - \theta_w$  is the dimensionless temperature rise in the superconducting strands.

Making use of Eqs. (20) and (21) it can readily be shown that:

$$\nabla'^2 [(\theta_s - \theta_w) - (1 - \theta_w)] + V \left(\frac{r_w}{r_{cs}}\right)^2 [\theta_s - \theta_w - (1 - \theta_w)] = 0, \quad (27)$$

which has a solution of the form:

$$\theta_s - \theta_w = (1 - \theta_w) + F \left[ \left(\frac{r}{r_{cs}}\right) \sqrt{V} \right], \quad (28)$$

where  $F[ ]$  denotes a functional relationship. At  $r = r_w$ ,  $\theta_s = \theta_w$  and the quantity  $1 - \theta_w$  can be eliminated:

$$\theta_s - \theta_w = F \left[ \left( \frac{r}{r_{cs}} \right) \sqrt{V} \right] - F \left[ \left( \frac{r_w}{r_{cs}} \right) \sqrt{V} \right] . \quad (29)$$

The quantity under the integral sign in Eq. (26) is simply the average value of  $\theta_s - \theta_w$  over the superconductor area, which means integration over  $r$ , so:

$$\int (\theta_s - \theta_w) \frac{dA_s}{A_s} = G \left[ \left( \frac{r_w}{r_{cs}} \right) \sqrt{V} \right] , \quad (30)$$

where  $G[ ]$  represents a functional relationship. Substitution into Eq. (26) yields the final relationship:

$$V = \tau - 1 + \alpha V\tau + \alpha_i V(\tau - V) + G \left[ \left( \frac{r_w}{r_{cs}} \right) \sqrt{V} \right] \quad (31)$$

given the quantities  $\alpha$ ,  $\alpha_i$ , and  $r_w/r_{cs}$  and the geometry of the strands so that the functional relationship  $G$  is defined, the curve of  $V$  vs  $\tau$  is completely determined.

#### DISCUSSION

Equation (31) above shows very graphically the effects of heat transfer to the coolant, the interface thermal resistance, and the conductor size. Very simply the equation

$$V = \tau - 1 \quad (\tau > 1) \quad (32)$$

is the dimensionless voltage per unit length for a superconductor and a substrate, all current above the critical current ( $\tau = 1$ ) flows in the normal substrate and produces a voltage proportional to the excess current over the critical value. As yet no account has been taken of the heating of the conductor as a whole, which is the product of the voltage times the current.

If the next term is added to Eq. (32):

$$V = \tau - 1 + \alpha V\tau \quad (\tau > 1) \quad (33)$$

The additional term is indeed proportional to the dimensionless voltage times the dimensionless current  $V\tau$ , and the proportionality constant:

$$\alpha = \frac{\rho I_{ch}^2}{hPA(T_{ch} - T_b)}$$

is simply the temperature rise with all the current in the substrate divided by the temperature rise for the current density to go to zero in the superconductor.

The term  $\alpha V\tau$  can be thought of as an additional voltage which appears across the superconductor due to imperfect cooling by the coolant. The quantity  $\alpha$  is a measure of the cooling effectiveness.

The next term to be added is  $\alpha_i V(\tau - V)$ . Referring to Eq. (25) this term can be written as  $\alpha_i V(I_s/I_{ch})$ . In this form it is analogous to the  $\alpha V\tau$  term, with the

difference that the interface perimeter and heat transfer coefficient are used, and that since the temperature drop across the interface is proportional to the voltage times the superconductor current rather than the total current, the quantity  $\tau$  is replaced by  $I_s/I_{ch}$ .

The constant of proportionality  $\alpha_i$  is analogous to the quantity  $\alpha$  except that the interface heat transfer coefficient  $h_i$  and total perimeter of contact  $nP_i$  are used.

The last term in Eq. (31) contains the quantity  $(r_w/r_{cs})\sqrt{V}$ . It is evident that if  $V = 0$  there is no heating in the superconductor, and therefore  $G(0) = 0$ .

The effect of superconductor size and its interaction with other quantities is best revealed by examining the slope of the voltage-current characteristic at the critical current ( $\tau = 1$ ) when voltage first begins to appear ( $V = 0+$ ).

Taking the derivative of Eq. (31) with respect to  $V$ :

$$1 = \frac{d\tau}{dV} + \alpha \left[ \tau + V \frac{d\tau}{dV} \right] + \alpha_i \left[ (\tau - V) + V \left( \frac{d\tau}{dV} - 1 \right) \right] + \frac{dG}{dV} \quad (34)$$

at  $\tau = 1$  and  $V = 0$  we can solve for  $d\tau/dV$ :

$$\frac{d\tau}{dV} = 1 - \alpha - \alpha_i - \frac{dG}{dV} \quad (35)$$

The derivative  $dG/dV$  is evaluated as follows:

$$\frac{dG[u]}{dV} = \frac{dG}{du} \cdot \frac{du}{dV} = \frac{1}{2} \frac{du^2}{dV} \cdot \frac{dG}{u du} = \frac{1}{2} \left( \frac{r_w}{r_{cs}} \right)^2 \frac{dG}{u du} \quad (36)$$

where

$$u = \frac{r_w}{r_{cs}} \sqrt{V}$$

$$\left. \frac{d\tau}{dV} \right|_{\tau=1} = 1 - \alpha - \alpha_i - \frac{1}{2} \left( \frac{r_w}{r_{cs}} \right)^2 \left[ \frac{dG}{u du} \right]_{u=0} \quad (37)$$

The quantity  $dG/u du$  is a function of  $u$  only, and as  $u \rightarrow 0$  it takes on a numerical value (determined by the shape of the superconductor).

Taking the inverse of Eq. (37) we have:

$$\left. \frac{dV}{d\tau} \right|_{\tau=1} = \frac{1}{1 - \alpha - \alpha_i - \frac{1}{2} \left( \frac{r_w}{r_{cs}} \right)^2 \left[ \frac{dG}{u du} \right]_{u=0}} \quad (38)$$

The general condition for stability against small voltage excursions is to have  $dV/d\tau$  finite, which requires the denominator to be non-zero.

This leads to the general stability requirement that

$$\alpha + \alpha_i + \frac{1}{2} \left( \frac{r_w}{r_{cs}} \right)^2 \left[ \frac{dG}{u du} \right]_{u=0} < 1$$

for stability against small disturbances at the critical current. Stability against large disturbances requires detailed knowledge of the complete  $V-\tau$  curve.

Several illustrative curves will now be examined.

#### CONSTANT $\alpha$ ( $\alpha_i, r_w \rightarrow 0$ )

The case for constant heat transfer coefficient  $h$  leads to the situation where  $\alpha$  can be considered to be a constant for a particular geometry of conductor. Figure 1 (from Ref. 1) shows the curve of dimensionless voltage vs dimensionless current for various values of  $\alpha$ .

Two distinct types of operation are possible, depending on the value of  $\alpha$ . For  $\alpha < 1.0$  no voltage appears until  $\tau = I/I_{ch} = 1$  (the superconductor critical current). For  $I > I_{ch}$  the voltage increases gradually with current. The characteristic is everywhere single-valued.

For  $\alpha > 1.0$  the operation is more complicated:

$$\begin{aligned} 0 < \tau \leq \frac{1}{\alpha} & \quad V = 0 \text{ all current in superconductor} \\ \frac{1}{\alpha} \leq \tau \leq 1 & \quad \text{double-valued operation} \begin{cases} V = 0^* \\ \text{or} \\ V = \tau \end{cases} \\ \tau > 1 & \quad \text{all current in substrate (} V = \tau \text{)} \end{aligned}$$

For this case of constant  $\alpha$ , stable operation occurs for  $\alpha \leq 1.0$ . For  $\alpha > 1.0$  stable operation is limited to currents up to  $I_{ch}/\alpha$ . In the region of current above  $I_{ch}/\alpha$ , metastable operation with all the current in the superconductor is still possible up to  $I_{ch}$ , however the current can switch from the superconductor to the substrate should a large enough disturbance occur.

#### NONLINEAR HEAT TRANSFER CHARACTERISTIC

The nonlinear characteristic of the boiling curve of liquid helium can, to a first approximation, be represented by a region of constant heat transfer coefficient up to a surface temperature,  $T_m$ , which is the maximum temperature at which nucleate boiling can occur.<sup>2</sup> Above this temperature a transition to film boiling will occur, and to a first approximation we can assume a constant heat flux per unit area.

Under these assumptions the conductor terminal characteristics can be calculated. Figure 2 (from Refs. 3 and 4) shows the case where

\* Operation on the negative resistance part of the curve is unstable for constant current.

1. Z.J.J. Stekly and J.L. Zar, Avco Research Report AMP 210 (1965); IEEE Trans. Nucl. Sci. NS-12, No. 3, 367 (1965).
2. C.N. Whetstone and R.W. Boom, in Advances in Cryogenic Engineering (Plenum Press, New York, 1968), Vol. 13, p. 68.
3. Z.J.J. Stekly, Avco Research Report AMP 231 (1967); paper presented at the Intern. Cryogenic Engineering Conference, Kyoto, Japan, 1967.
4. Z.J.J. Stekly, R. Thome, E. Lucas, B.P. Strauss, and F. DiSalvo, Final Report NAS8-21037 (1968).

$$\theta_m = (T_m - T_b)/(T_{ch} - T_b) = 0.25 .$$

For  $\alpha < 1$  no voltage appears until the current reaches the critical value ( $\tau = I/I_{ch} = 1$ ), the voltage then rises gradually until the limit of nucleate boiling is reached. At this point all the current is expelled suddenly from the superconductor and transferred to the substrate. If the current is then reduced, a recovery occurs in which all or most of the current transfers back into the superconductor. (This cycle is shown in Fig. 2 for  $\alpha = 0.5$ .) For  $\alpha > 1$  no voltage appears until the current reaches the critical value, then the current transfers abruptly out of the superconductor. Lowering of the current to a recovery value will again result in a return of all the current into the superconductor.

As can be seen in Fig. 2 there are three points which characterize the behavior of a particular conductor exposed to a magnetic field.

- 1) The critical current.
- 2) The transition from nucleate to film boiling from a condition where current is shared between the superconductor and the substrate. (This occurs above the critical current.)
- 3) The recovery from film boiling to nucleate boiling starting from a condition of all the current in the substrate.

A behavior map can be drawn of the different regions of operation for a particular behavior. This type of map is shown schematically in Fig. 3. In general, the map must take into account the variation of the critical temperature, the critical current, and the resistivity of the substrate with magnetic field.

The behavior of a typical superconductor has the following regions and curves:

- a) I-H curve - represents the critical current of the superconductor.
- b) Recovery curve - defined by the condition for the transition from film to nucleate boiling with all the current in the substrate.
- c) Take-off curve - defined by the transition from nucleate to film boiling with current sharing between superconductor and substrate.
- d) Stable zero resistance region - below the recovery curve and I-H curve.
- e) Stable resistive region - above the I-H curve and below the recovery curve.
- f) Metastable region - between the take-off and recovery curves: either above or below the I-H curve in which the conductor can be triggered into fully normal state from either a fully superconducting or current sharing condition.
- g) Unstable region - operation is possible only with all the current in the normal conductor.

Figure 4 shows a portion of a stability map generated experimentally for a NbTi conductor.<sup>5</sup>

---

5. Z.J.J. Stekly, E.J. Lucas, T.A. deWinter, B.P. Strauss, and F. DiSalvo, J. Appl. Phys. 39, 2641 (1968).

## EFFECT OF THERMAL CONTACT RESISTANCE BETWEEN SUPERCONDUCTOR AND SUBSTRATE

Figure 5 shows the terminal characteristics for  $\alpha = 0.5$  and for various values of  $\alpha_i$ . As expected from Eq. (38), the slope at the onset of resistance becomes infinite at  $\alpha + \alpha_i = 1$ , or  $\alpha_i = 0.5$  in the case shown.

For  $\alpha_i > 0.5$  the voltage-current curves are double-valued below  $I/I_{ch} = 1$ . For this case below a certain value of current only the fully superconducting condition is possible, above this value of current the curve becomes double-valued.\* Above the critical current, operation occurs with a significant fraction of the current in the substrate.

Specifically, for  $\alpha_i = 5$  up to currents approximately 0.7 of the critical value the operation is single-valued. Between 0.7 and 1.0 of the critical current there is a metastable region where the voltage can remain zero or be triggered to the upper portion of the curve. At the critical current the voltage increases abruptly until about 95% of the current switches into the substrate. If the current is now lowered the current begins to transfer back into the superconductor and at about 0.7 of the critical current the voltage drops abruptly to zero.

Figure 6 summarizes the effect of interface thermal contact resistance. It shows on a logarithmic plot of  $\alpha$  vs  $\alpha_i$  the stable region (defined by  $\alpha + \alpha_i \leq 1$ ) and the dimensionless voltage  $V_R$  and the dimensionless current  $I_R$  at recovery to the superconducting state.

The region in the upper left of Fig. 6 ( $\alpha$  large,  $\alpha_i$  small) exhibits a behavior which is independent of  $\alpha_i$ . Physically this region is poorly cooled to begin with and recovery occurs from the condition of all the current in the substrate, consequently at the beginning of the recovery there is no current in the superconductor and, therefore, no heat need be conducted across the superconductor-substrate interface.

It should be emphasized at this point that for the model of the conductor considered, which has the same current and temperature distribution along the conductor length, the current does not transfer from substrate to superconductor or vice versa along the conductor. Therefore, the electrical contact resistance is immaterial as long as the voltage drop per unit length is essentially the same in both the substrate and superconductor. It is the thermal contact resistance which plays a major role.

In practice, electrical contact is easier to make than thermal contact, and in conductors such as cables, wires embedded in strips, and soldered assemblies it is important to verify that good thermal contact has been achieved. This is best done by measuring the slope of the voltage-current curve at the critical current for a well-cooled ( $\alpha \rightarrow 0$ ) sample.

## EFFECT OF SUPERCONDUCTOR SIZE

The question of what effect the size of the superconducting strands has on the performance of a particular conductor is a very important one.

It is not the purpose of this paper to fully answer this question, but merely to point out that from a steady state stability point of view there are two mechanisms which have size dependence - the surface contact resistance, the temperature rise in the superconductor itself.

---

\* Operation on the negative resistance portion of the curve is unstable for a constant current source.



The total interface perimeter between the superconductor and substrate for round wires of diameter  $d$  is:

$$n P_i = n \pi d$$

If we desire a constant current in the over-all conductor then

$$I_{ch} = j_{ch} \frac{\pi d^2}{4} n \quad (40)$$

combining Eqs. (40) and (39) results in:

$$n P_i = \frac{4 I_{ch}}{j_{ch} d} \quad (41)$$

For a superconductor with current density independent of size  $d$ , the perimeter increases inversely with  $d$ , which results in  $\alpha_i$  proportional to  $d$ . However, in most superconductors the current density increases inversely as the square root of the size, so that the gain in perimeter is then only inversely as the square root of the diameter.

In a conductor with poor interface characteristics it would be expected that an improvement would result from going to smaller diameter strands if it could be assured that the same interface heat transfer coefficient would exist.

The temperature drop in the superconductor itself is more sensitive to size variations than the interface thermal contact resistance parameter  $\alpha_i$ .

Figure 7 shows the results<sup>4</sup> of the dimensionless voltage-current calculations for a well-cooled ( $\alpha = 0$ ) round wire. For  $r_w/r_{cs} > \sqrt{8}$  the onset of resistance at the origin is abrupt and a double-valued region exists below the critical current.

As an example, let us consider a 0.020 in. (0.0508 cm) outer diameter wire with a single 0.010 in. (0.0254 cm) diameter NbTi strand at 50 kG which carries 60 A. We then have the following conditions:

$$\begin{aligned} 2 r_w &= 0.0254 \text{ cm} \\ A &= 1.52 \times 10^{-3} \text{ cm}^2 \\ I_{ch} &= 60 \text{ A} \\ P &= 0.16 \text{ cm} \\ j_{ch} &= 1.3 \times 10^5 \text{ A/cm}^2 && (\text{NbTi at 50 kG}) \\ k &= 2 \times 10^{-3} \text{ W/cm}^\circ\text{K} && (\text{NbTi}) \\ \rho &= 2.5 \times 10^{-8} \Omega \cdot \text{cm} && (\text{Cu at 50 kG}) \\ T_{ch} - T_b &= 2.6^\circ\text{K} && (\text{NbTi at 50 kG}) \\ h &= 1 \text{ W/cm}^\circ\text{K} \end{aligned}$$

The value of  $r_{cs}$  is:

$$r_{cs} = 0.00635$$

and

$$\frac{r_w}{r_{cs}} = 2$$

According to the plot in Fig. 7 this is a significant effect on the terminal characteristics even if the conductor is well cooled ( $\alpha \rightarrow 0$ ).

For round wires it has been shown<sup>4,6</sup> that the initial slope at the first appearance of resistance is (neglecting  $\alpha_i$ );

$$\frac{dV}{d\tau} = \frac{1}{1 - \alpha - \frac{1}{8} \left( \frac{r_w}{r_{cs}} \right)^2} \quad (42)$$

Using the values given:

$$\alpha = 0.142$$

If we take the ratio of  $dV/d\tau$  taking into account the wire size to the value assuming  $r_w \rightarrow 0$  then:

$$\frac{dV/d\tau}{[dV/d\tau]_{r_w \rightarrow 0}} = \frac{1 - \alpha}{1 - \alpha - \frac{1}{8} \left( \frac{r_w}{r_{cs}} \right)^2} = 2.4$$

This is a very significant effect and points to the fact that in this particular conductor the strand size cannot be neglected as far as its effect on the terminal characteristics is concerned.

The characteristic conductor size can be written as:

$$r_{cs} = \sqrt{\frac{k(T_{ch} - T_b)}{\rho j_{ch} j_{sub}}} \quad (43)$$

where  $j_{sub}$  is the substrate current density  $I_{ch}/A$ .

This relationship is shown plotted for round wires in Fig. 8 for a composite NbTi conductor at 50 kG. The quantity  $d_w = 2r_{cs}$  is the wire diameter at which the strand begins to affect the terminal characteristic. If  $d_w = 2/\sqrt{8} r_{cs}$  then the wire size is large enough to result in a jump in voltage at the critical current. Also shown on the plot are values for the ratio of copper area to superconductor area. Most commonly available high current density multistrand composites have ratios of copper to superconductor areas ranging from 3 to 1. The curve shows that depending on  $j_{sub}$ , wire diameters between 5 and 2.5 mils respectively would result in practically no effect on the terminal characteristics. On the other hand, strand diameters between 14 and 8 mils respectively would result in instabilities due to the strands themselves.

The actual numerical values used may be in error, especially the thermal conductivity, which has been assumed to be  $2 \times 10^{-3}$  W/cm °K, so that the actual numerical results must be interpreted very loosely.

---

6. Z.J.J. Stekly, to be published.

## CONCLUDING REMARKS

The steady state stability of composite superconductors has been reviewed taking into account cooling of the substrate, interface thermal contact resistance and temperature rise within the superconductor itself. Gradients along the conductor itself were not considered.

The general equations were derived and the effects of substrate cooling, interface thermal contact resistance and temperature rise in the superconductor were shown to affect the slope of the voltage-current curve at onset of resistance.

It should be re-emphasized at this point that the treatment in this paper is aimed at presenting relatively simple results so as to provide a maximum of physical insight into the behavior of composite superconductors rather than a detailed prediction of the terminal characteristics.

The assumption of constant heat transfer coefficient, and the assumption of very steep resistance rise at the critical current for the superconductor alone are both relatively crude approximations.

The effects of varying heat transfer coefficient can easily be taken account of in any single instance by estimating a voltage-current curve with constant heat transfer coefficient (constant  $\alpha$ ), computing the heat flux and then recomputing a new curve with the correct heat transfer coefficient at each value of heat flux. This procedure can be performed numerically or graphically until the results converge.

The approximation of the superconductor characteristic by a more complex model can also be done relatively easily; this, however, introduces more parameters, and it was felt that little additional physics would result from a more complex model.

The results derived are based on a steady state analysis of the terminal characteristics. Regions defined as fully stable, with all the current in the superconductor, are expected to be fully superconducting in reality.

However, in all metastable regions there exists the possibility of a triggering disturbance that will force the current out of the superconductor into the substrate.

For instance, in all cases considered one branch of the voltage-current curve is the  $V = 0$  line extending up to the critical current. There is nothing in the analyses presented that indicates anything more than that in certain current ranges there are other operating points (usually with all or large fractions of the current in the normal substrate).

It can be concluded that if only one stable operating point exists then the conductor will operate there. If there is more than one operating point then it is necessary to study the triggering process.

It should be borne in mind that the aim of studying stability of superconductors is to achieve magnets that can operate reliably at a given current, and do not quench at the slightest mechanical or electrical disturbance. Since the desire is to achieve steady state stability, the conditions for achieving this stability as well as its limits should be obtainable from a study of steady or quasi-steady characteristics of the conductor.

Finally, one of the important results in this paper is that below a certain strand size, the temperature rise in the superconductor is very small ( $r_w < r_{cs}$ ). For these conditions the temperature of the superconductor is essentially equal to that of the substrate. In order for superconductor generated instabilities to occur

it is necessary to have a temperature rise in the superconductor. It can, therefore, be concluded that for  $r_w < r_{cs}$  no superconductor generated instabilities or flux jumps can occur. If  $r_w > \sqrt{8} r_{cs}$  the individual strands are unstable at their critical currents. In the region  $r_{cs} < r_w < \sqrt{8} r_{cs}$  the possibility of collective interaction exists where strands may interact with each other.

The analysis presented in this paper is intended to explain in a quasi-quantitative way some of the experimental behavior of composite conductors. In doing so it points out the important variables which influence stability or the lack of it. Experimental work is necessary to verify (or contradict) the predicted characteristics of composites. It is hoped that the theory presented here can provide a framework for these experiments.

#### ACKNOWLEDGEMENTS

The work described herein is a summary of the results derived in work performed under Contract No. NAS8-21037 for the NASA Marshall Space Flight Center in Huntsville, Alabama.

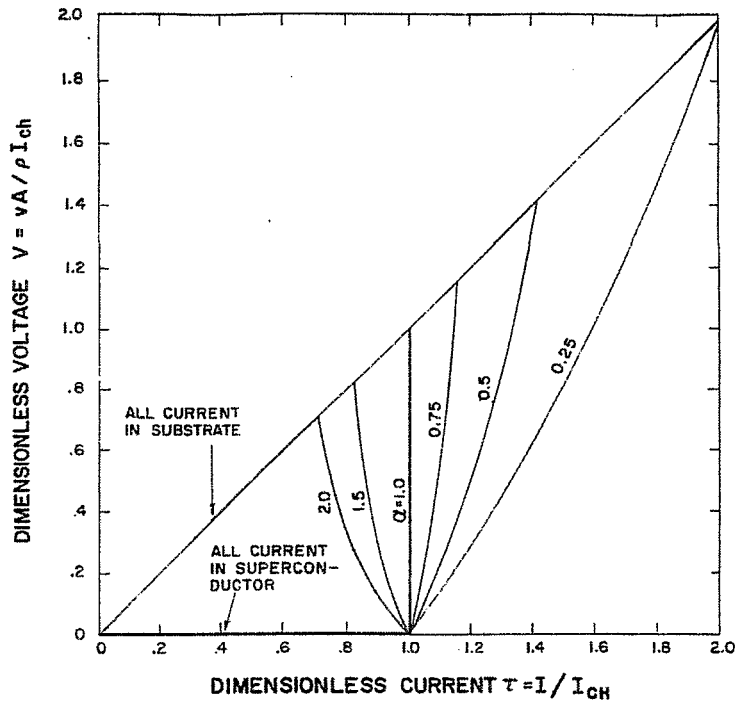


Fig. 1. Voltage-current characteristics for a stabilized superconductor-substrate combination.

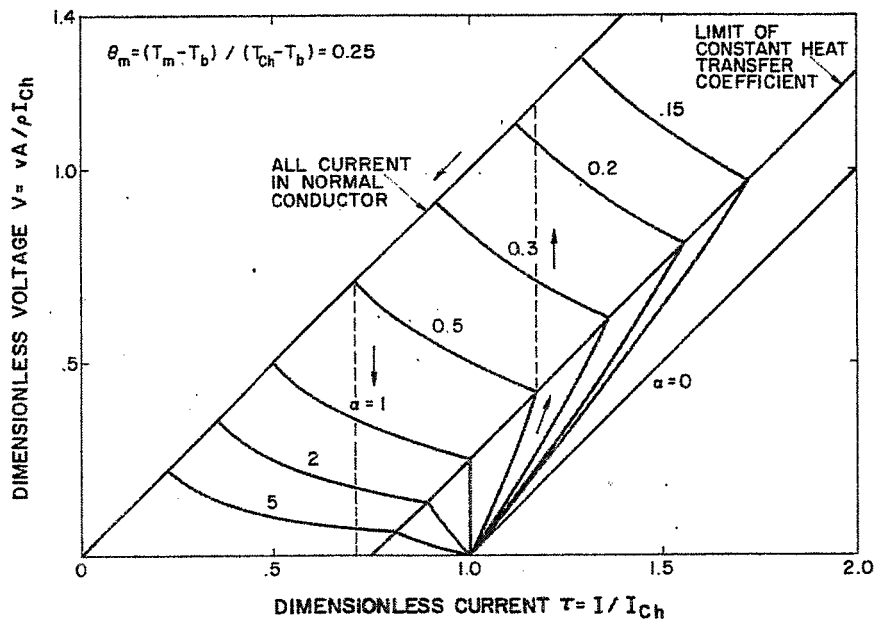


Fig. 2. Dimensionless terminal characteristics of a conductor taking into account through a simplified model the change in heat transfer characteristics resulting from a transition from nucleate to film boiling.

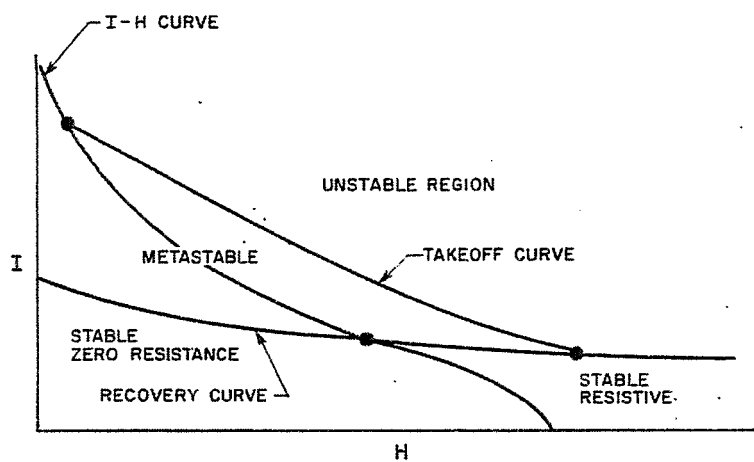


Fig. 3. Map indicating modes of behavior taking into account the nonlinear heat transfer characteristics of liquid helium.

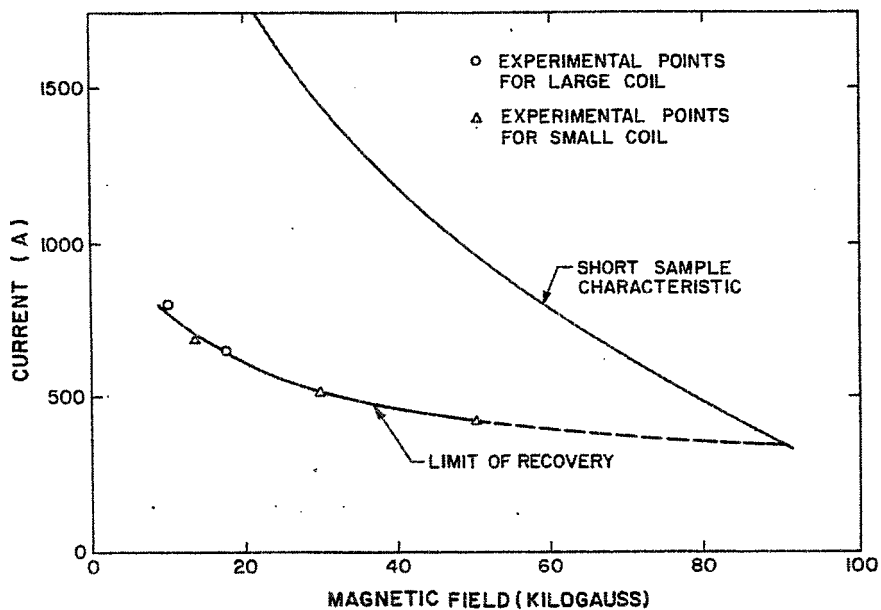


Fig. 4. Short sample and operating characteristics for the NbTi coil.

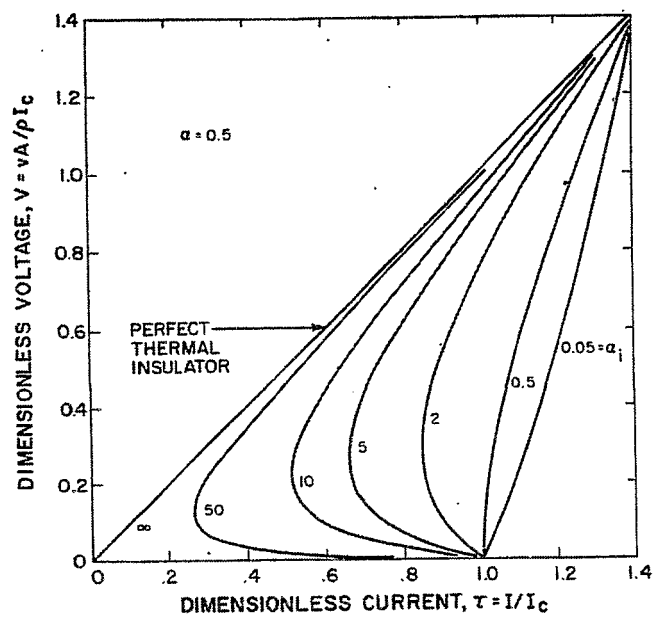


Fig. 5. Dimensionless terminal characteristics showing the effect of thermal contact resistance between the superconductor and substrate.

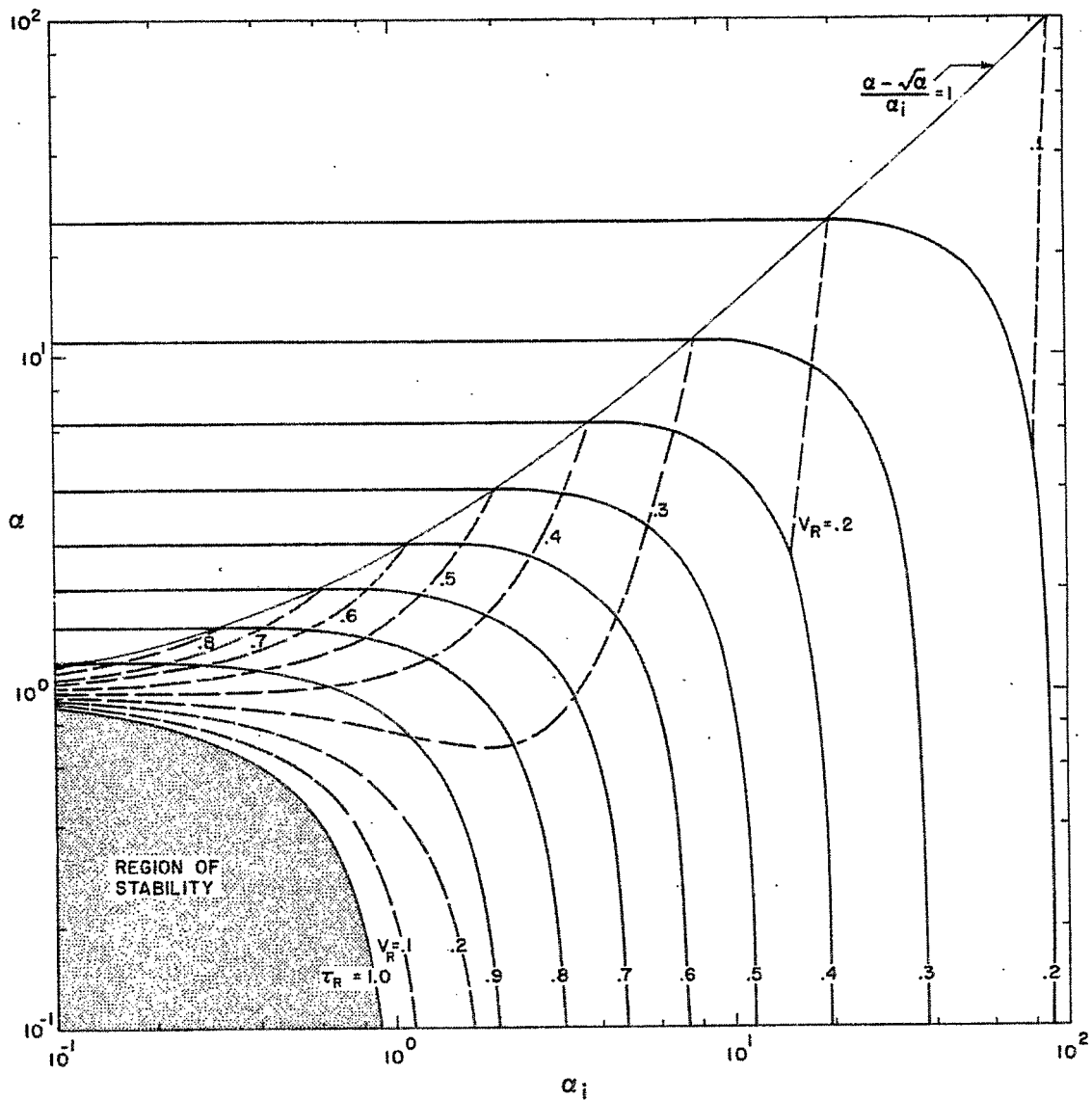


Fig. 6. Dimensionless recovery current  $\tau_R$  and dimensionless recovery voltage  $V_R$  as a function of  $\alpha$  and  $\alpha_i$ .

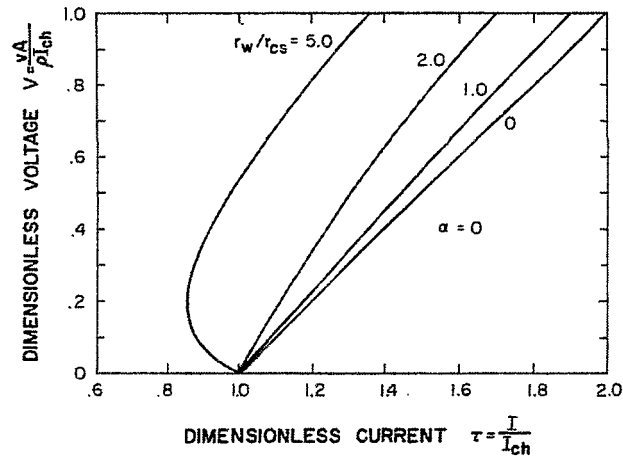


Fig. 7. Dimensionless terminal characteristics for a well cooled conductor ( $\alpha \rightarrow 0$ ) as a function of the superconducting strands.

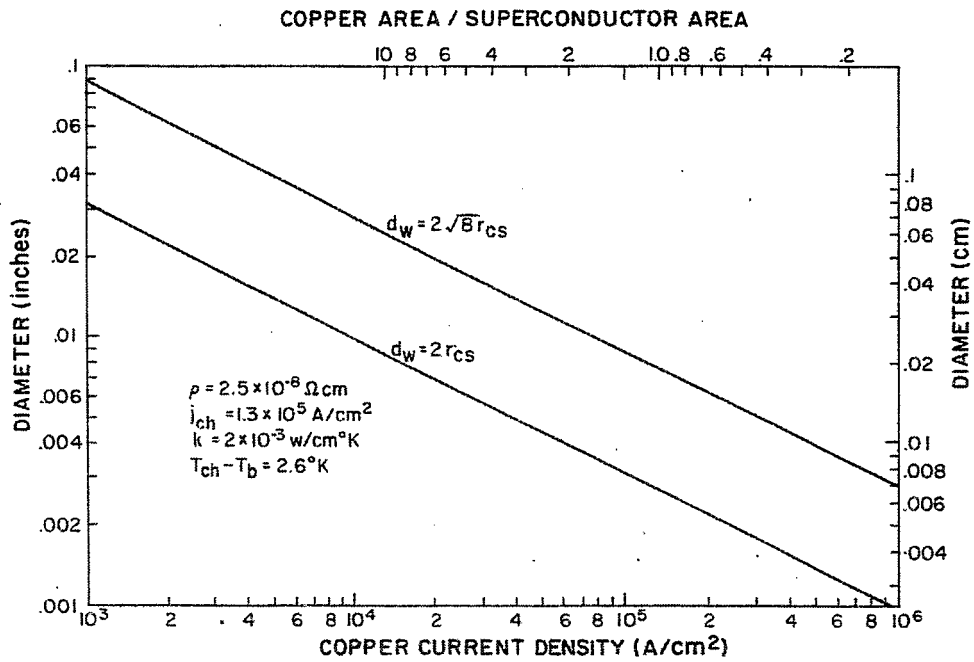


Fig. 8. Plot of  $r_{cs} = \sqrt{\frac{k(T_{ch} - T_b)}{\rho j_{ch} j_{sub}}}$  NbTi conductors at 50 kG.



# THE 1.8 TESLA, 4.8 M I.D. BUBBLE CHAMBER MAGNET\*

J.R. Purcell  
Argonne National Laboratory  
Argonne, Illinois

## INTRODUCTION

The 1.8 T\*\* magnetic field for the ANL 3.7 m chamber (Fig. 1) is provided by energizing coils (Fig. 2) wound from copper-clad, Nb48%Ti strip (Fig. 4) and immersed in liquid helium at 4.5°K (1.2 bar†) contained in a toroidal stainless-steel reservoir. The 4.8 m i.d. coils are located in a carbon steel yoke which forms a low reluctance return path for the magnetic flux. The use of iron reduces the ampere-turns needed to produce the required magnetic field. The carbon steel yoke and heavily copper-clad superconductor were chosen to give a reliable conservative magnet. The coil and cryostat are cooled by a separate closed cycle liquid helium refrigeration plant. A conventional power supply is used to energize the coil which is protected by low resistance, room temperature resistors. These can be switched across the coil terminals when required. The 3000 A, 10 V dc power supply is adequate to charge the magnet to design current in 2.5 hours.

The operating cost of the coil should be \$400 000/year less than an equivalent copper coil because of the saving in electrical power. A conventional electromagnet of this performance with copper coils would have the same capital cost as the supermagnet (\$3 000 000). It may be possible to replace the present coil with a 4.0 T coil which has the same winding space at some future date. The principal characteristics of the magnet are given in Table I.

The arrangement of the superconducting coils within the iron yoke and bubble chamber system is shown in Fig. 3. The inner and outer vacuum cans, and intermediate radiation shield can be seen in more detail in Fig. 4, where their position with respect to the windings is shown. The use of iron with a simple rectangular coil section results in a high field uniformity over the chamber volume (15%). Stray magnetic fields are reduced by the iron which also provides a sturdy mechanical foundation for the whole structure. The major portion of the frame is made up of castings weighing up to about 100 t.‡ Eddy current heating in the moving parts of the bubble chamber system is low because the field uniformity is high. This reduces the production of heat in the moving parts of the expander system and consequently the heat load on the hydrogen refrigeration system.

## ENERGIZING COIL SYSTEM

The coil structure is split into two sections (Figs. 1, 3, and 4) to permit the beam of high energy particles to enter the chamber in a plane perpendicular to the line

---

\* Reprinted from Argonne National Laboratory Report ANL/HEP 6811 (1968), edited by C. Laverick.

\*\* 1 T = 10 kG.

† 1 bar = 0.99 atm = 100 000 N/m<sup>2</sup>.

‡ 1 t = 1000 kg.

# THE 1.8 TESLA, 4.8 M I.D. BUBBLE CHAMBER MAGNET\*

J.R. Purcell  
Argonne National Laboratory  
Argonne, Illinois

## INTRODUCTION

The 1.8 T\*\* magnetic field for the ANL 3.7 m chamber (Fig. 1) is provided by energizing coils (Fig. 2) wound from copper-clad, Nb48%Ti strip (Fig. 4) and immersed in liquid helium at 4.5°K (1.2 bar†) contained in a toroidal stainless-steel reservoir. The 4.8 m i.d. coils are located in a carbon steel yoke which forms a low reluctance return path for the magnetic flux. The use of iron reduces the ampere-turns needed to produce the required magnetic field. The carbon steel yoke and heavily copper-clad superconductor were chosen to give a reliable conservative magnet. The coil and cryostat are cooled by a separate closed cycle liquid helium refrigeration plant. A conventional power supply is used to energize the coil which is protected by low resistance, room temperature resistors. These can be switched across the coil terminals when required. The 3000 A, 10 V dc power supply is adequate to charge the magnet to design current in 2.5 hours.

The operating cost of the coil should be \$400 000/year less than an equivalent copper coil because of the saving in electrical power. A conventional electromagnet of this performance with copper coils would have the same capital cost as the supermagnet (\$3 000 000). It may be possible to replace the present coil with a 4.0 T coil which has the same winding space at some future date. The principal characteristics of the magnet are given in Table I.

The arrangement of the superconducting coils within the iron yoke and bubble chamber system is shown in Fig. 3. The inner and outer vacuum cans, and intermediate radiation shield can be seen in more detail in Fig. 4, where their position with respect to the windings is shown. The use of iron with a simple rectangular coil section results in a high field uniformity over the chamber volume (15%). Stray magnetic fields are reduced by the iron which also provides a sturdy mechanical foundation for the whole structure. The major portion of the frame is made up of castings weighing up to about 100 t.‡ Eddy current heating in the moving parts of the bubble chamber system is low because the field uniformity is high. This reduces the production of heat in the moving parts of the expander system and consequently the heat load on the hydrogen refrigeration system.

## ENERGIZING COIL SYSTEM

The coil structure is split into two sections (Figs. 1, 3, and 4) to permit the beam of high energy particles to enter the chamber in a plane perpendicular to the line

---

\* Reprinted from Argonne National Laboratory Report ANL/HEP 6811 (1968), edited by C. Laverick.

\*\* 1 T = 10 kG.

† 1 bar = 0.99 atm = 100 000 N/m<sup>2</sup>.

‡ 1 t = 1000 kg.

TABLE I  
Superconducting Magnet Characteristics

Operating current at 1.8 T central field	2200 A
Ampere turns (30 pancakes of 84 turns each)	$5.5 \times 10^6$
Inductance at windings	40 H
Field uniformity over working volume	$\pm 2.5\%$
Current density in conductor	$1700 \text{ A/cm}^2$
Average current density in windings	$775 \text{ A/cm}^2$
Energy stored in field	$80 \times 10^6 \text{ J}$
Weight of copper in windings	45 000 kg
Weight of superconductor	300 to 400 kg
Coil axial compressive force	$6.8 \times 10^5 \text{ kg}$
Compressive stress on coil separators	$140 \text{ kg/cm}^2$
Outward force between coil halves	450 000 kg
Weight of iron	$1.45 \times 10^6 \text{ kg}$
Inside diameter of coil	478 cm
Outside diameter of coil	528 cm
Length of coil	304 cm
Power supply voltage	10 V
Charging time	2.25 h
Heat transfer rate required for 100% stability	$0.13 \text{ W/cm}^2$
Resistance/cm of conductor copper at 2.0 T field and 4.2°K	$1.32 \times 10^{-8} \text{ } \Omega/\text{cm}$
Total winding resistance at 4.2°K and 2.0 T assuming superconductor completely normal	0.031 $\Omega$
Total power dissipation at 2200 A (no superconductor)	150 kW

of sight of the cameras which are located on top of the system. The coil system and cryostat weigh 45 t each. They are hung from the magnet yoke by pairs of stainless-steel pipes of total cross-sectional area  $690 \text{ cm}^2$  spaced at  $90^\circ$  to each other. The complete support system can accommodate a vertical load of 450 t. The tension in the central connector ring during operation is 450 t since each coil half is attracted to its adjacent pole piece when the coil is energized. The coil system is centered magnetically with respect to the iron. If displaced it could experience a force of 20 t/cm of vertical displacement which increases in direct proportion to its distance from the equilibrium position.

Similarly the constant for lateral displacement is 14 t/cm. The maximum lateral force is 45 t and the lateral support structure is designed to withstand 225 t. This lateral support structure consists of two sets of four 7.95 cm diameter, 1.5 m long titanium rods spaced at  $90^\circ$  to each other which connect the top and bottom 10 cm thick stainless-steel girder rings in the winding structure to the iron return frame. The

heat leak to the helium bath from the magnet iron through the lateral support rods is limited to 50 W by wrapping each rod with gas cooling tubes and flowing 50°K helium gas through the tubes to intercept the incoming heat.

The enclosing vacuum vessel of the cryostat is fabricated from 2.5 cm thick type 503 aluminum and is designed in accordance with Section VIII of the ASME Unfired Pressure Vessel Code for an external pressure of 1.01 bar and an internal pressure of 1.38 bar. It has a 25 cm diameter emergency vent which is activated at 1.38 bar. This vessel acts as a short-circuited turn around the magnet with an 8 sec time constant. This is considerably longer than the 0.25 sec time constant for the helium' can so that most of the coil energy on fast discharge will be absorbed by the external coil circuit and this can. The two beam access windows in the cryostat are spaced 90° to each other with an aperture of 18 cm x 68°. Aluminized Mylar multilaminar insulation is used in conjunction with an aluminum radiation shield.

Each coil half comprising 15 pancake units is divided into two coil sections each of which has its own liquid helium container (Figs. 2 and 4). This is accomplished by fitting annular stainless-steel vessels over each coil section and welding them to the central support rings (see Fig. 5). These rings serve as the primary support and alignment reference for the complete coil structure and contain suitable interconnections for the liquid helium chambers so as to form a single helium reservoir for the coil structure. The diameter of the helium can structure will shrink 1.5 cm during cooldown from 300°K to 4.2°K so the vertical and radial support systems are arranged to accommodate this contraction. Each of the four liquid helium containers is provided with an inlet and outlet gas manifold and interconnecting holes permit access for current leads, instrumentation leads and emergency helium ejection if necessary. The venting system and helium vessel pressure ratings (4.5 bar) are adequate to support a 200 kW power dissipation inside the helium reservoirs if necessary although it is difficult to see how this can occur. The wall thickness of the helium vessels at the inner diameter is 2.5 cm and at the outer diameter is 1.5 cm while the normal internal operating pressure will be 1.2 bar.

Eight spirally wound pancake units are assembled in the lower section and seven in the upper section to comprise the 15 pancake 2.8 m high stack of each coil half. The spacing between each coil half is 51 cm. The pancakes of each coil stack are assembled with spacer blocks between them covering only a small fraction of the total cooling surface area. These pancake stacks are then tied together by rods welded to the stainless-steel rings on either side of the stack. The assembly is shown in Fig. 5 where the arrangement of the pancakes with respect to the containing vessels is shown. The top ring of the top coil half and the bottom ring of the bottom coil half are actually the top and bottom, respectively, of the helium Dewar vessel. The interpancake electrical connections consisting of double sections of the stabilized conductor are attached to the i.d. and o.d. turns of the pancakes to form a series circuit. The winding ends and the jumper leads are anchored mechanically to prevent any motion and stressing of these electrical joints. The coil terminal leads are treated in the same manner. These details are obvious from Fig. 6 in which the mode of clamping of the coil stacks to the girder ring with stainless-steel tie rods is shown as are the spacer blocks, thermal clamps, pancake interconnections and conductor clamps.

The 60 spacers located between adjacent pancakes at 6° intervals are epoxy-coated aluminum having a cross section of 5 cm x 1.25 cm thick. They extend beyond the i.d. and o.d. when installed. Each section is capped with a set of spacers and a clamp plate. The clamp plates are connected to the central girder rings via 2.2 cm diameter threaded aluminum rods. There are 60 rods on the i.d. and 60 rods on the o.d. The aluminum rods are screwed to the clamp plate, but pass through holes in the girder ring. They are prestressed to approximately 276 bar via nuts which bear against the

girder ring. The 0.45 cm differential contraction between the pancake structure and girder ring diameters on cooldown is taken up by incorporating a sliding interface at the junction between the two.

A section through the copper-clad six-strand Nb48%Ti conductor is shown in Fig. 7 and its principal characteristics are tabulated below. In operation the conductor is edge-cooled in static liquid helium at 4.5°K.

TABLE II  
Conductor Specification 4.8 m i.d. Argonne  
Bubble Chamber Magnet

Width	5.0 cm
Thickness	0.25 cm
Individual piece length	220 m
Individual piece weight	240 kg
Critical characteristics, field parallel to strip cross section	a) 3000 A at 2.5 T - specified b) 4000 A at 2.5 T - measured
Critical characteristics, field normal to strip cross section	3000 A at 1.35 T - specified
Calculated stable current	4300 A at 2.5 T
Calculated recovery current	3300 A at 2.5 T
Resistance ratio of copper cladding $\rho(273^{\circ}\text{K})/\rho(4.2^{\circ}\text{K})$	200
Design stress	840 kg/cm <sup>2</sup>
Percentages of copper and superconductor in strip	96% Cu, 4% Nb48%Ti in six separate strands
Resistance/cm of conductor at 4.2°K and 2 T	$1.32 \times 10^{-8} \Omega$
Area of strip/cm length of conductor exposed to helium bath	0.5 cm <sup>2</sup>
Estimated heat transfer rate from exposed conductor surface for 0.1°K temperature rise in conductor	0.13 W/cm <sup>2</sup>
Operating current at 1.8 T central field	2200 A

The measured performance of the conductor exceeded its specified performance by more than 30% (Table II). The edge-cooled pancakes will operate in the stable mode if necessary with a heat dissipation of 0.13 W/cm<sup>2</sup> of exposed conductor surface for a 0.1°K temperature rise in the conductor. The cryogenic system is adequate for such a heat load. The strip contains sufficient copper to support the hoop stresses generated during magnet operation. The design characteristics for the strip were further checked by cutting each of the first three lengths delivered in half and winding them to form a six pancake coil of 60 cm i.d., 85 cm o.d., and 38 cm height. The total winding length was 690 m and the coil weight was 800 kg. Teflon tape and epoxy formed the

interturn insulation and bond. When tested the coil carried 4600 A while developing maximum fields of 3 T parallel and 1.9 T normal to the strip cross section and it was the 1.9 T condition which caused the transition in the superconductor. Current sharing between the copper and superconductor began at 4650 A which exceeds the minimum acceptable specifications of Table II by a large margin, thus providing an ample reservoir of performance stability. This test coil is shown in Fig. 8.

#### THERMAL PROBLEMS ON COOLDOWN

One of the major design problems in using such large structures at low temperatures is that of minimizing thermal stress. The large diameter of the magnet makes it very sensitive to thermal stress. Vertical thermal gradients produce a shear load on the bond between turns within the coils. Keeping the total vertical temperature differential,  $\Delta T$  to less than  $10^\circ\text{K}$  will limit this shear stress to less than 140 bar. Laboratory tests have shown that this type of bond has a shear strength of from 210 to 700 bar. Temperature gradients are no problem during operation of the magnet because it is at a uniform temperature of  $4.5^\circ\text{K}$ . The thermal gradient problem occurs only during cooldown or on accidental discharge of the magnet and must be considered over the range from  $300^\circ\text{K}$  down to about  $50^\circ\text{K}$ . Below this temperature, thermal expansion coefficients are so small that thermal stress is not a problem. In order to limit the  $\Delta T$  to  $10^\circ\text{K}$ , the cold gas used for cooling is introduced into each coil compartment through a manifold that extends completely around the circumference of the coils. This manifold has small holes spaced about every 6 in. to spray the cold gas downward and mix it with the warm gas within the container. Initially, liquid nitrogen will be used to cool this incoming gas so the inlet temperature will be about  $80^\circ\text{K}$ . The helium refrigerator compressor will be used to circulate this gas during cooldown. The gas is returned to the compressor through another  $360^\circ$  manifold at the bottom of each coil package. Introducing the cooling gas in this manner sets up convection currents within each coil compartment resulting in a very large mass flow of gas. The average temperature of this large gas flow is only slightly below that of the coils resulting in a uniform coil temperature. A second method of improving temperature uniformity is thermally shorting the ends of the aluminum spacer blocks together. This is done with a heavy copper braid and is shown in Figs. 2, 6, and 9.

The design philosophy was checked by constructing a model similar to the test coil using only copper strip. The thermal clamps chosen to equalize temperatures throughout the larger structure were used in this model which is shown in Fig. 9. The technique chosen for bonding the turns together was also used in this model. The mechanical integrity of the structure when subjected to several successive thermal shocks by cycling its temperature from  $77^\circ\text{K}$  to room temperature was found to be adequate.

#### COIL FABRICATION

A single pancake is shown in Fig. 10 in position on its winding jig in ANL after completion of the winding process. The coils were wound in a horizontal plane to permit easy access to the pancake during winding. The winding line consisted of an initial splicing and inspection station followed by cleaning and tensioning equipment and then the 6 m diameter winding fixture. The Teflon insulation was fed through an epoxy roll coater and guided onto the winding fixture about  $30^\circ$  ahead of the point where the conductor was fed in. Six lengths of the 210 m long pieces supplied were connected together by using 30 cm long, lead tin soldered, copper rivetted lap joints between successive lengths to form the continuous single lengths required for each pancake. Abrasive brushes were used to remove burrs from the conductor which was sand-blasted and then washed with alcohol to provide a good keying surface for the interturn epoxy bonding material.

The combination of the thin layer of brittle epoxy adhesive with a comparatively thick layer of flexible insulating sheet as interturn insulation was chosen to permit some shearing to take place without breaking the brittle bond. The flexible fluorinated ethylene-propylene insulation was etched prior to application of the epoxy to provide a better bonding surface.

The degree of flatness and accuracy of winding thickness for the pancakes was assured by hand grinding using an appropriate fixture. This was necessary for accurate and rigid assembly of the final coil stack. All pancakes were tested for turn-to-turn electrical short circuits to ensure their freedom from such defects before installation in the final stacks. When one section of a 15 pancake half coil assembly had been stacked and clamped to the girder rings, the entire structure was turned over and the other portion was stacked and clamped to form the complete package shown in Fig. 2. The assembly with all its leads, connectors, and instrumentation was then fully inspected and tested before the helium cans were welded into place on the girder ring.

#### COIL STACK TEST PROCEDURES

The following tests were made to ensure correct assembly of the magnet and to provide information for future maintenance.

The actual location of the windings with reference to the girder ring was determined at  $90^\circ$  intervals to  $\pm 0.075$  cm. The entire assembly was carefully cleaned and inspected. All parts were checked for mechanical integrity. All log books, drawings, and records were reviewed to ascertain that every component had been installed according to design.

The coil stack was energized at room temperature to 15 A at 39 V and turn-to-turn voltage drop measurements were carried out and recorded. The voltages at all potential taps were recorded to check their potential tap location. All instrumentation leads were checked for continuity, resistance, isolation, etc. (as applicable). The resistances between the coils and support structures were measured. A check was made to ensure that there were no shorts or possible shorts which could arise from magnetic forces on unsupported current-carrying elements.

A field profile at the i.d. of the windings was made at the approximate location of the i.d. of the helium can, and the vacuum can. All internal structures were inspected to determine the existence of closed electrical loops which could interact with a time changing field. The winding sense of the coil structure was noted and the external leads were marked appropriately.

#### MAGNET YOKE AND SUPPORT STRUCTURE

Constraints on the yoke design included its large size, the means of absorbing the pulsating expander forces, accommodating the coil and cryostat structure, and integrating the complete system. Cyclic operation of the expander system generates inertial forces equivalent to the weight of the magnet iron (1360 t). Restrictions on the basic design and fabrication techniques with such a large structure are imposed by available manufacturing facilities. Shipping and material handling capacities limit the size of individual pieces.

Lateral forces on the windings are minimized by making the iron structure symmetrical about its central axis. There are no forces on the windings when they are magnetically centered. The requirement for two beam access windows of 2.4 m azimuthal width located at  $90^\circ$  with respect to one another, coupled with the need for cylindrical

symmetry in the iron structure, dictated that there be four 2.4 m windows equally spaced (90°) in the median plane. Low reluctance return paths and high field uniformity are achieved with the geometry used for this yoke. The magnet poles form the top and bottom of the hydrogen chamber vacuum can. Accidental liquid hydrogen leakage can be contained by the aluminum cryostat vacuum can around the hydrogen chamber and vacuum wall.

The magnet iron consists of top plate and bottom plate assemblies, each 7.6 m<sup>2</sup> by 1.27 m separated by four corner posts at a distance of 3 m. The top and bottom plate assemblies each contain 500 t of steel in eight pieces ranging in weight from 15 to 100 t. The return legs contain 600 t of steel in eight identical pieces (two 75 t pieces in each of the four corners). The principal estimated loads on the top and bottom magnet blocks are given in Table III.

TABLE III  
Estimated Magnet Block Loads

Induced vacuum loading on top and bottom core blocks	154 t
Outward loading on top and bottom core blocks due to 11 bar vacuum can test pressure	1540 t
Bottom core loading due to chamber operation	
a) At 12 bar maximum operating pressure	1260 t
b) At 15.8 bar maximum test pressure	1530 t
Due to limitation of pressure differential across the omega bellows to 4 bar	
a) At 8.3 bar operating pressure on piston bottom	1090 t
b) At 11.7 bar test pressure on piston bottom	1540 t
Due to 4 bar cyclic pressure	220 (constant) ± 220 (cyclic) t downwards
Maximum circular deflections at the vacuum can sealing surfaces on the more highly stressed bottom core blocks	0.06 cm
Weight of each bottom core block piece	100 t

The maximum allowable impurities for the magnet iron as shown by a ladle analysis are: carbon - 0.20, silicon - 0.05, manganese - 0.80, sulphur - 0.05, phosphorous - 0.05, and aluminum - 0.05. The minimum allowable yield and tensile strengths for the highly stressed core blocks are 2000 and 4000 bar, respectively. The remaining parts of the yoke have minimum yield and tensile strengths of 1300 and 2600 bar, respectively. Minor surface and internal imperfections are tolerated in most portions of the yoke so long as they do not impair the gross mechanical integrity of the piece.

Tolerances on individual pieces were chosen to give a mechanically sound structure. Shimming was allowed provided that the shim at any joint covers the entire



mating surface area and is of uniform thickness over that area. Localized imperfections were tolerated along mating surfaces if they did not degrade the structural integrity. Repair welding was allowed anywhere. Tolerances on unmachined and external surfaces were chosen to minimize cost. Small imperfections were tolerated on all machined surfaces except the pole piece vacuum seals. Alignment pins, dowels, handling holes, bosses, and lifting eyes were permitted in the iron wherever they did not interfere with system assembly. These simplify repeated construction and breakdown. The complete iron structure was assembled at the vendor's plant prior to breakdown into separate pieces for shipment.

#### POWER SUPPLY AND ENERGIZING COIL SYSTEM

The power supply is a three-phase, full wave, thyristor controlled unit whose time average output voltage can be varied by adjusting the firing angle of the thyristors. It is equipped with the usual safety interlocks and fault indicating lamps. These circuits include a holding circuit so that the appropriate lamp has to be reset manually to energize the power supply when a fault has been cleared. Provisions have been made for a remote permissive interlock to operate in conjunction with the relay contacts of the fault indicator. This contact interlock in the bubble chamber control room should be closed before the power supply can be energized.

The magnet windings are protected against a sudden release of the stored magnetic energy if for some reason the coil begins to discharge quickly. A possibility would be a sudden increase in coil resistance due to the liquid helium level dropping below the top of the coil and the subsequent loss of cooling. Two means of protection are provided. The first method consists of a "dump resistor" (Fig. 11) which is always in the electrical circuit, connected in parallel with the coil. Should a resistive region develop in the coil, both the power supply and the stabilizer resistors will be disconnected from the circuit and the coil current will flow through the dump resistor. The energy stored in the magnetic field will then be dissipated in the dump resistor at an initial rate of approximately 0.4 MW (2000 A at 200 V for designed operating conditions). Even in the worst case, with the whole coil being resistive, at least 60% of the energy will be dissipated in the dump resistor. The second protective measure guards against pressure buildup in the helium vessel and high local temperature rise in a resistive coil region. At a preset pressure rise in the Dewar (caused by helium vaporization in the proximity of the power dissipating region), the bulk of the liquid helium can be rapidly transferred from the Dewar to a dump tank. With the helium removed, the whole coil will become normal and power will be uniformly dissipated throughout the windings. If the full stored magnetic energy of 80 MJ and 1.8 T is absorbed by the total thermal mass of the windings, the coil temperature will rise only to about 90°K. Since the liquid helium has been removed from the tank, the temperature rise of the coil will not result in any serious pressure rise of the system.

The emergency dump resistor is a 0.1  $\Omega$ , grounded center tap, large thermal mass resistor. A heavy duty, double pole switch is located close to and on the power supply side of this resistor. When this switch is opened, the magnet current (and field) will decay with a time constant of approximately 6.6 min. Under normal conditions, the dump resistor will absorb very nearly the total energy stored in the system. If the magnet windings were to become completely resistive, the dump resistor would absorb approximately 60% of the total stored energy. It contains approximately 942.5 kg of No. 1008 carbon steel strip wound in 10 pancakes connected in series parallel to give the correct resistance. Its temperature rise with 100 MJ input and no cooling would be 250°C. The dump resistor value was selected to limit the peak voltage across the system to approximately 300 V dc. The energy dump switch interrupts both power leads to the magnet (double pole, single throw). The switch is designed to interrupt a maximum magnet current of 3000 A dc.

The dump system will be tested at incrementally increasing current levels during initial system checkout. A  $0.2\ \Omega$  (grounded center tap) resistor and an automatically operated power supply output shorting switch are connected across the power supply bus on the power supply side of the dump switch. The former will protect the power supply from high voltage transients during dump switching and the latter will protect the water-cooled free-wheeling diode in the event of loss of cooling.

A schematic diagram of the power supply circuit is given in Fig. 12. The frequency response from the input of the thyristor control unit to the output of the power supply should be 7 Hz minimum. The power supply, free-wheeling diode, and fast discharge resistor are all water-cooled. Protection against flow failure and component overheating is provided. The shunt resistors across the magnet limit the peak voltage to less than 600 V during all discharge conditions. Manual reversing links are provided so that the current flow in the magnet may be reversed if required.

The voltage regulated supply has its reference derived from the error signal between the magnet current and a reference. The purpose of the voltage loop is to remove any power line induced voltage variations and also to linearize the voltage control. The voltage loop, which consists of the differential amplifier  $A_2$ , a ripple filter, and the amplifier  $A_1$ , has an open loop gain of 100. The operator may select either the voltage or current regulation mode by a switch on the front panel of the power supply. When operated in the voltage regulate mode, the supply voltage is set by a front panel control. When the power supply is operated in the current regulate mode, the operator may set the charge rate of the power supply by a front panel control.

Current control is provided by a circuit which compares the current read by the precision current transducer to the reference voltage. When the error voltage into the temperature stabilized amplifier  $A_3$  exceeds approximately 80  $\mu\text{V}$  (0.004% at 2000 A) the relay  $K_1$  will operate which switches the input to  $A_1$  to either the charge rate reference or to ground (0 volts). The reference voltage for  $A_3$  is derived from a temperature regulated zener diode and a stabilized buffer amplifier. Control of the reference voltage is by a four-position thumbwheel switch which permits a resolution of  $10^{-4}$  in setting the magnet current. The variation of the supply current and coil voltage with current during operation is shown in Fig. 13. The necessary degree of field stability is maintained with this on-off control because of the large inductance and high stored energy of the magnet. The basic accuracy of the current readout transducer is 0.1% at 2000 A. The accuracy will degrade to about 2% at currents below 500 A. The output from the transducer is used as the feedback voltage for the regulator and for external use.

The normal current decay of the power supply is set by the forward voltage drop across the free-wheeling diodes and the voltage drop in the dc bus which connects the magnet to the power supply. For a 0.5 V drop in the diodes, the decay rate is  $13.2 \times 10^{-3}$  A/sec. The fast discharge resistor has been provided to increase the current decay to 0.250 A/sec. This is a manually triggered operation. The return to the normal current decay rate is automatic when the magnet current reaches the value preset on the current reference. The anticipated long-term current deviations are as tabulated below:

- 1) Current reference -  $24.8 \times 10^{-6}$  V/ $^{\circ}\text{C}$ .
- 2) Current sensing amplifier -  $0.1 \times 10^{-6}$  V/ $^{\circ}\text{C}$ .
- 3) Current transducer -  $34 \times 10^{-6}$  V/ $^{\circ}\text{C}$ , based on a  $10^{-3}$  V/A.

Based on a temperature variation of  $\pm 5^{\circ}\text{C}$ , a total error of  $\pm 29.4 \times 10^{-6}$  V is predicted. This is equivalent to  $\pm 0.015\%$  at 2000 A.

The safety circuits are designed to protect the magnet in the event of a power failure. If the cooling system fails or the power supply overheats the primary voltage is removed from the rectifier transformer, and the output shorting switch is closed. The shorting switch around the fast discharge resistor will be closed if it overheats and the power supply will continue to operate normally. The magnet is protected by meter relays against overvoltage (either polarity) and overcurrent. The meters, which are located on the control panel of the power supply, have a visible trip point which is manually adjustable from the front of the meter.

#### HELIUM REFRIGERATOR

The performance characteristics and main load for the helium refrigerator are given in Table IV. The refrigerator is also used to cool the superconducting coils and containers from ambient temperature to liquid helium temperature. When used in this fashion the full compressor flow is taken through the exchangers and then to the cooldown distribution header of the magnet. Warm helium vapor is removed from the magnet can and returned to the compressor section after this gas has passed through a heater. The helium refrigerator has to maintain the superconducting magnet of the 3.7 m bubble chamber at a temperature of 4.5°K for continuous and indefinite periods of time. High reliability with periods of downtime kept to short duration is the primary requirement for the refrigerator.

TABLE IV

#### Load Characteristics for the Helium Refrigerator

Performance characteristics under:

- a) Normal operation with liquid hydrogen precooling.
- b) Modified operation with liquid nitrogen and a second expansion engine in place of the hydrogen stage.

Cooling for insulation shield around the magnet reservoir	500 W at 50°K - normal 500 W at 80°K - modified
Maintenance of liquid in storage and magnet Dewar	400 W at 4.45°K - normal 320 W at 4.45°K - modified
Counterflow cooling of power supply leads and supports	25 liquid liter/h of helium - normal and modified

Liquid hydrogen is available in large quantities in this bubble chamber complex and is also generated by a hydrogen refrigerator of large capacity so liquid hydrogen precooling is used. An expansion engine in parallel with the J-T (Joule-Thomson) expansion valve is used to lower the capital investment in the plant and to give high reliability. The expansion engine can be removed and installed without interruption of refrigerator operation. The helium refrigeration system can be used to cool the magnet and its container from ambient to operating temperature. Liquid nitrogen and liquid hydrogen can be used for cooling the magnet to decrease the time required for cooldown.

A second expansion engine can be used instead of liquid hydrogen precooling to provide refrigeration at times when liquid hydrogen is not desired in the bubble chamber building. A substantial storage capability for liquid helium is provided. Vacuum-jacketed transfer lines which can be replaced in a short period of time without need

For purging or evacuation are incorporated. The cold box of the refrigerator is divided into two parts so that equipment containing hydrogen liquid and vapor can be placed in a separate enclosure containing an inert atmosphere. This ensures greater safety. The system uses components of proven capability.

The helium refrigerator together with the liquid storage Dewar (11 000 liter capacity, including 1000 liters of ullage volume), and the superconducting magnet can (6500 liter volume) constitute a closed system. Ignoring leakage, gas and liquid is kept in the system for an indefinite period of time. Gas can be stored in a vessel, which has a capacity of  $2100 \text{ m}^3$ .

The rate of liquid vaporization may temporarily exceed the capacity of the refrigerator. During this time, excess gas is compressed by the compressor and put in the gas storage vessel. When excess gas is present, the suction pressure of the compressor will increase and the compressor will automatically handle more gas. Gas will be drawn from the vessel when the rate of liquefaction exceeds the rate of liquid vaporization. This occurs automatically since the suction pressure of the compressor is then reduced. The helium refrigerator system will operate automatically without attendance. The compressor requires occasional blowdown of oil knockout drums. The helium purification system requires occasional reactivation (once every 24-48 hours, depending on level of contamination). Except for these two operations, the system will operate and adjust itself to upsets in the form of more or less demand for refrigeration. The automatic operation is achieved by means of pressure and liquid level sensors. Pressure sensors will automatically monitor and maintain the suction pressure of the compressor. It may happen that the compressor discharge pressure will decay, but this will only be a result of excess refrigeration capacity and a depleted gas storage vessel.

The instrumentation necessary for checkout and operation of the helium refrigerator is concentrated in two areas. Compressor operation with its pressure and temperature indicators, controllers and alarms is located in the compressor room. Cold box instrumentation is divided between the compressor room and a panel located near the helium-helium cold box. The refrigerator system is operated from the compressor room so that information required during normal operation of the system is available in the compressor room. This information is supplemented with information available at the helium-helium cold box. The local information is useful during the initial checkout of the refrigeration system. As an example, all temperature and some pressure data are needed to assess the heat exchanger performance, but once these have been checked out, abnormal conditions will be indicated by the pressure readouts in the compressor room.

#### PRINCIPAL PERFORMANCE PARAMETERS - HELIUM REFRIGERATOR

The three main parameters which determine the performance of the refrigerator are, the heat transfer, insulation, and expander efficiencies, assuming the compressor operation to be satisfactory.

The heat exchangers have been designed to perform with a predetermined temperature difference between the high and low pressure helium streams. When the low pressure gas does not reach its design temperature at the warm end of the heat exchangers, the high pressure gas becomes too warm at the cold end of the exchanger. This causes a large deterioration in heat exchanger performance, e.g. a  $1^\circ\text{K}$  increase in high pressure gas temperature at the cold end of Exchanger III represents a loss of 200 W of refrigeration. Temperature sensors are provided for both low and high pressure gas streams at both ends of the exchangers to allow an assessment of heat exchanger performance to be made at any time.

Loss of insulation of the high vacuum from 0.013 to 13 or 130 ubar will represent a loss of several hundred watts of refrigeration. All vacua except those in the

transfer lines are monitored by vacuum gauges, but it is easy to detect poor vacua by sensing outside vacuum wall temperatures of the equipment. Heat is supplied from the air to the wall at an approximate rate of  $5000 \text{ J/h}\cdot\text{m}^2$  for each  $1^\circ\text{C}$  of temperature difference.

The total amount of refrigeration provided at the  $4.5^\circ\text{K}$  temperature level is divided between J-T effect and expander work. Under normal operating conditions, the J-T effect accounts for one-third and the expander for two-thirds of the total refrigeration. The contribution of the J-T effect is easily determined from a measurement of the temperatures of the gas at the warm end of Exchanger III. The contributions of the expander inlet and outlet temperatures are approximately the same. The expander is equipped with the means to observe P-V diagrams which permit evaluation of the machine performance. This evaluation should always begin with a check of the thermal, insulation, and expander efficiencies and the compressor performance.

### SAFETY CONSIDERATIONS

The sealing surface at the lower magnet pole is subject to cyclic deflection as a result of expander loading. Although the core blocks are rectangular, the deflection contours at this radius are approximately circular. All deflections are small and there will be no degradation of the "O" ring seals. These seals are protected against rupture due to a hydrogen spill by suitable heaters, flow deflectors, and superinsulation. The system is designed to permit an overpressure due to a hydrogen spill into the vacuum space of 11.376 bar, above which it will be automatically vented to the atmosphere. It will also withstand a pressure of 1.01 bar in the vacuum space and in vacuum between the chamber bottom plate and the piston which could occur due to operator error. The vacuum vessel and its beam window are protected from external damage by the cryostat vacuum can which forms a capsule around that entire system.

This yoke is designed to withstand all the magnetic, pressure and vacuum, and expander system loads. The bolting procedures for the upper and lower core blocks have been clearly specified by prevent failure due to improper bolting. The iron structure can withstand any reasonably anticipated hydrogen spill without cracking. The bottom plate assembly components are subject to fatigue. They will be inspected carefully during initial repeated cooldowns to  $77^\circ\text{K}$  and routinely inspected during normal operation.

The most critical hazards are those which could change the over-all force distribution on the winding structure. Interlocks are provided to prevent the magnet from being energized without the top and bottom poles and core blocks in place. Forces on all coil support members are routinely monitored and checked. Coil hoop stresses and clamping tie bar stresses are monitored using strain gauges. The design stress values can be exceeded by a large margin without hazard.

Connectors and leads will withstand all anticipated magnetic forces and thermal motions. Voltage taps are located across each joint and connection so that possible failures can be detected. Coil temperatures are monitored to limit thermal stresses during cooldown. The major effects of thermal stresses would be loss of the turn-to-turn bond in the winding pancakes and pancake-to-spacer bonds which should not affect operation. An alarm will indicate a low helium level condition. Such a condition should not damage the winding structure. All windings have been carefully tested to ascertain that there are no shorts at installation. Strainers have been installed at the helium systems to keep short-causing chips and debris to a minimum. Any shorts in the windings during a field transient could redistribute the currents and hence the magnetic forces. The energy will be dumped at a low field level each time the magnet is turned on to determine the vertical forces on the winding support structure and assess if any significant change has taken place.

If the field decay rate is dominated by the vacuum can, the stresses induced in the can may cause the aluminum to yield but not break. The can is securely locked into place in the iron so that it cannot move during such a field transient. It also serves as a protective capsule around the hydrogen chamber and its vacuum wall and can withstand and vent hydrogen spills due to simultaneous failure of the beam windows in both the hydrogen chamber and the hydrogen chamber vacuum wall. The vacuum can is adequately vented to accept helium vessel failure. Low vacuum in the can will actuate an alarm but the vacuum space also has a radiation shield and superinsulation so that in the event of vacuum failure, both the heat leak and resulting pressure rise in the helium bath will be relatively slow.

The helium refrigeration system provides adequate liquid helium storage to permit eight hours of magnet system operation without the refrigerator. This should allow adequate time for normal maintenance and emergency repair of the refrigeration system if necessary.

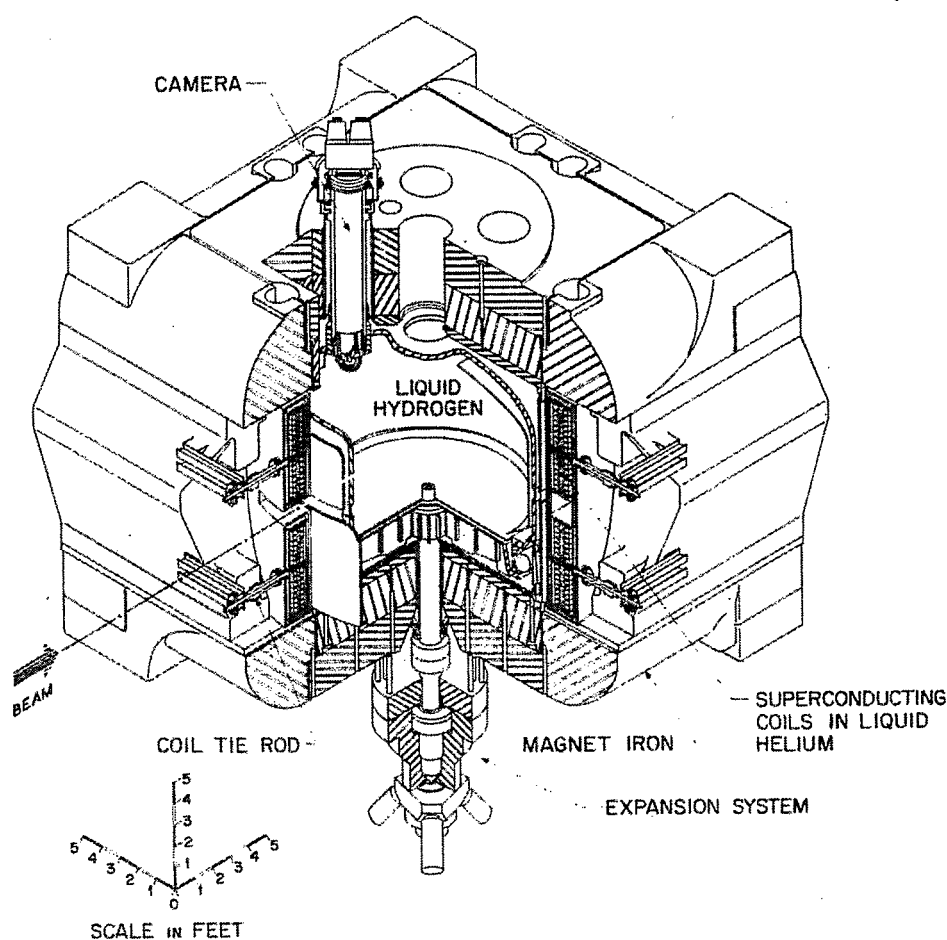


Fig. 1. Over-all view of the ANL 3.7 m hydrogen bubble chamber showing the location of the chamber, expansion system, coil assembly and cryostat with respect to the iron yoke and particle beam access window.

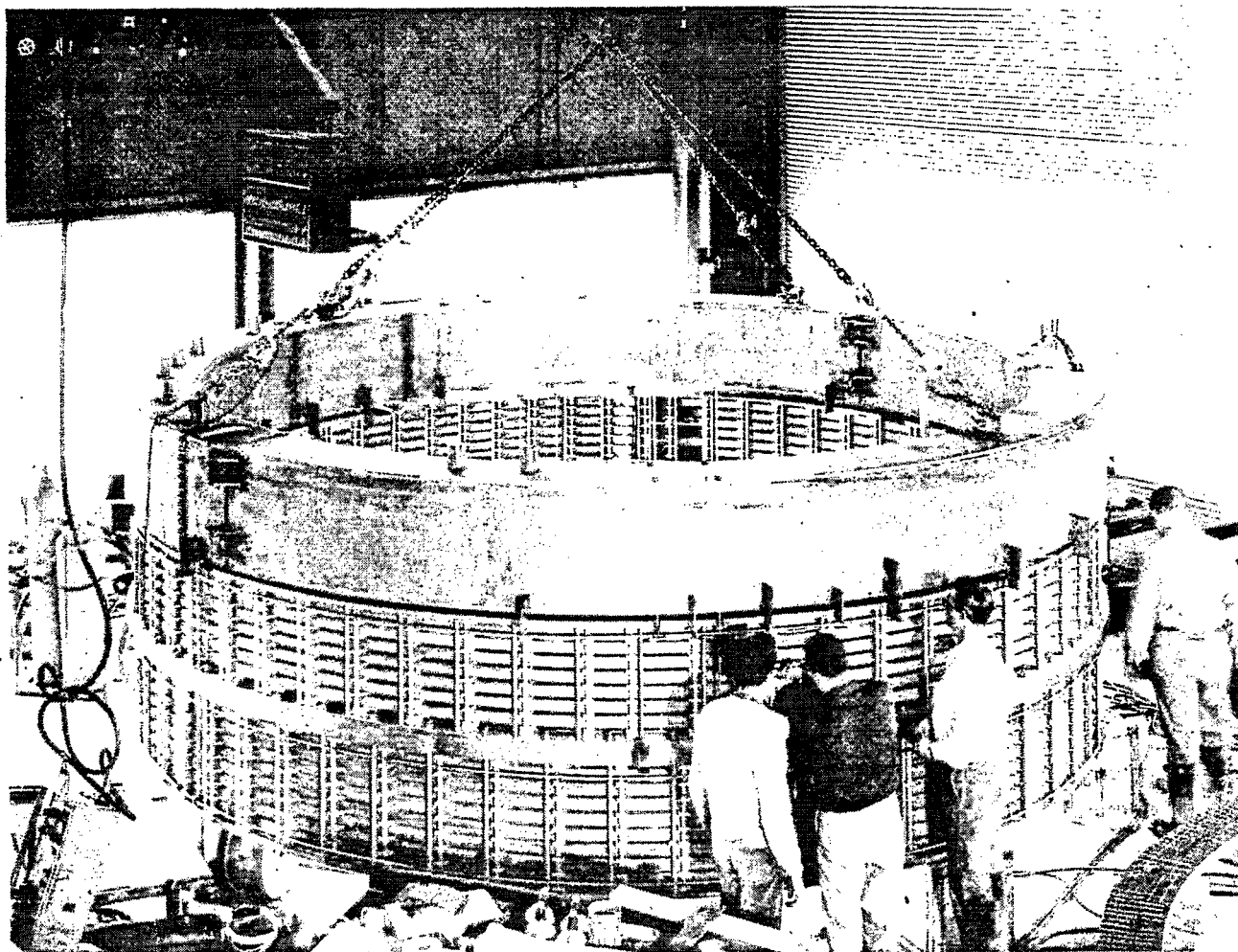


Fig. 2. One of the two 4.8 m i.d. coil halves of the 1.8 T hydrogen bubble chamber magnet showing details of the 15 pancake assembly. The vertical braided copper thermal interconnections between separate pancake units minimize temperature differentials and hence thermal stresses during cooldown. A section of the stainless-steel helium can is shown suspended above the assembly. This can forms the vacuum tank for the magnet.

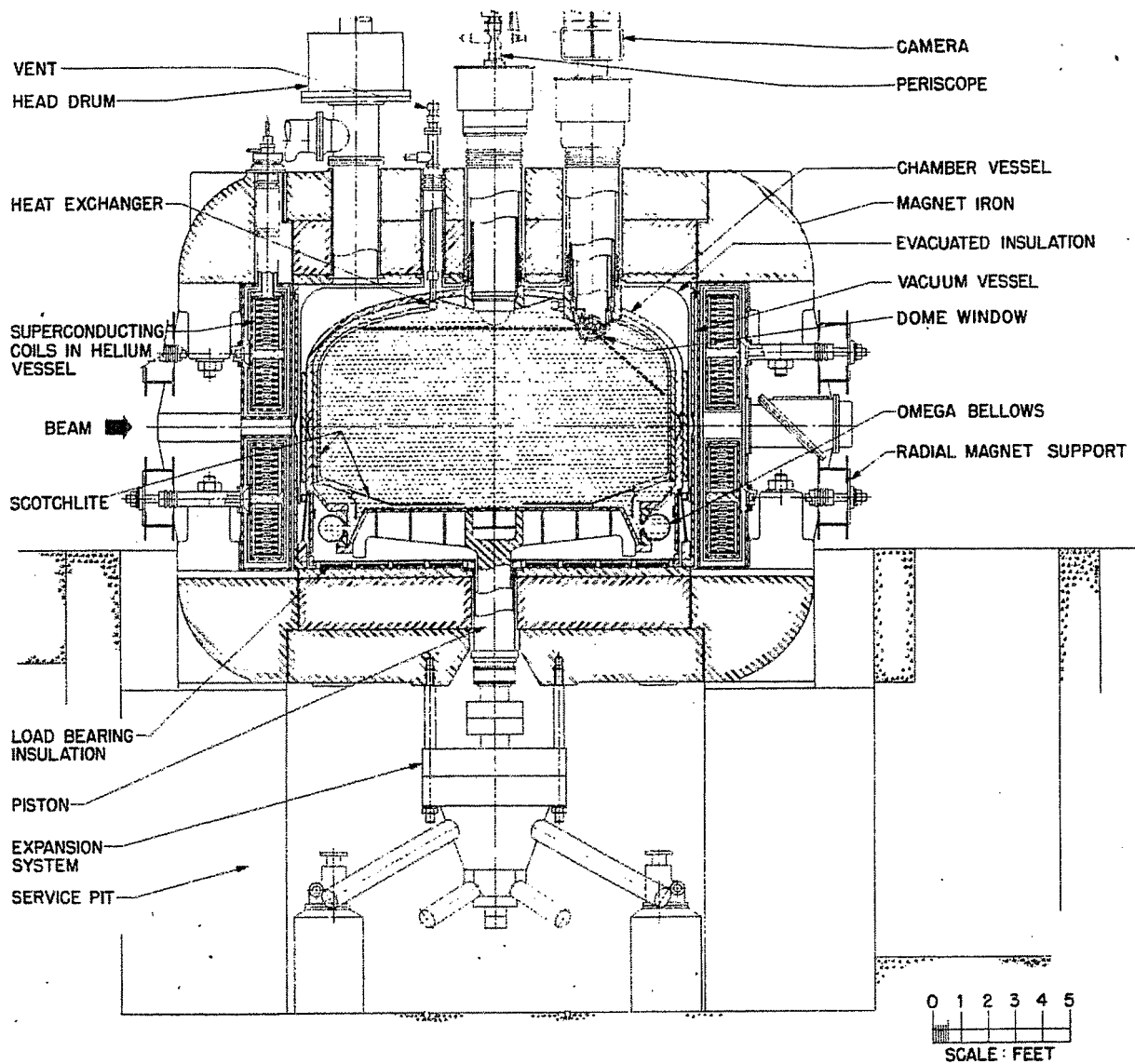


Fig. 3. A cross section through the ANL 3.7 m hydrogen bubble chamber system.



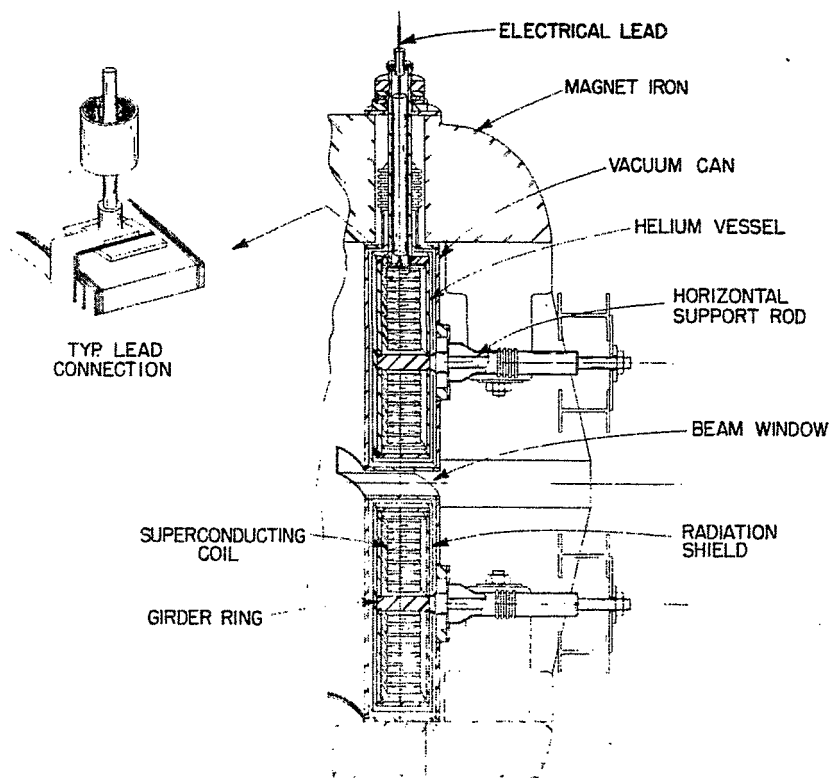


Fig. 4. Schematic of a portion of the magnet cross section showing the location of the coil assemblies in the helium vessel and vacuum enclosure, their respective locations and the support structure.

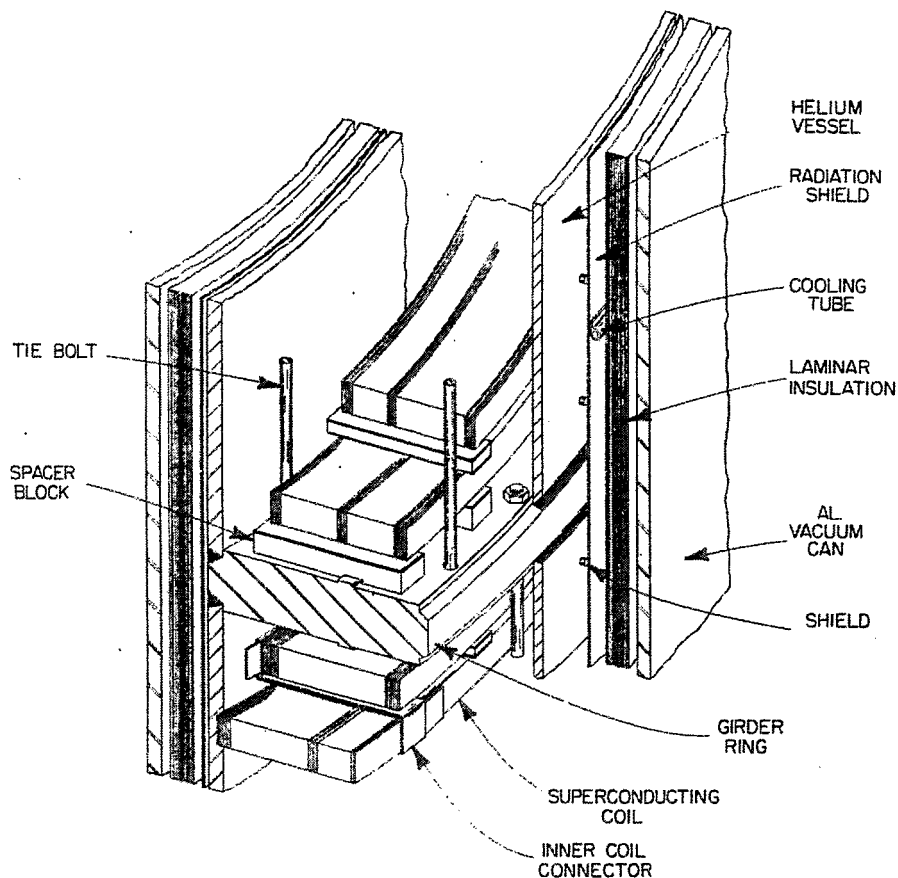


Fig. 5. Detail showing the arrangement of the individual pancakes with respect to the containing vessels, the mode of connection of the internal girder rings to the helium vessel, the type of electrical interconnections between pancakes and the spacer block arrangement between pancakes.

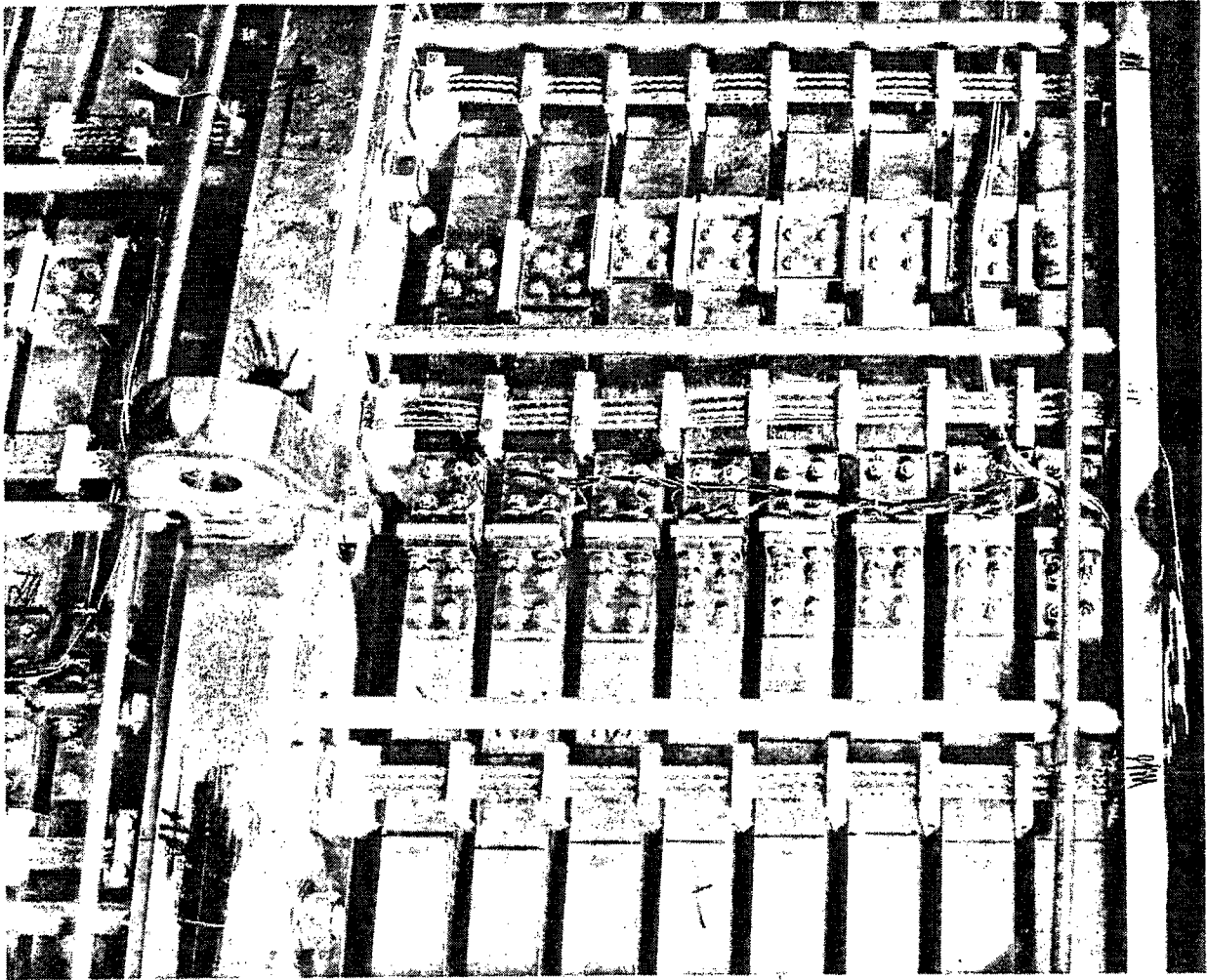


Fig. 6. Photograph of a portion of a coil assembly showing the mode of clamping of a coil stack to the girder ring with stainless-steel tie bolts, the thermal clamps, the electrical interconnections between pancakes and the mechanical clamping arrangement for the ends of the conductor.



Fig. 7. A cross section of the copper-clad six-strand Nb48%Ti conductor for the 1.8 T, 4.8 m i.d. hydrogen bubble chamber magnet.

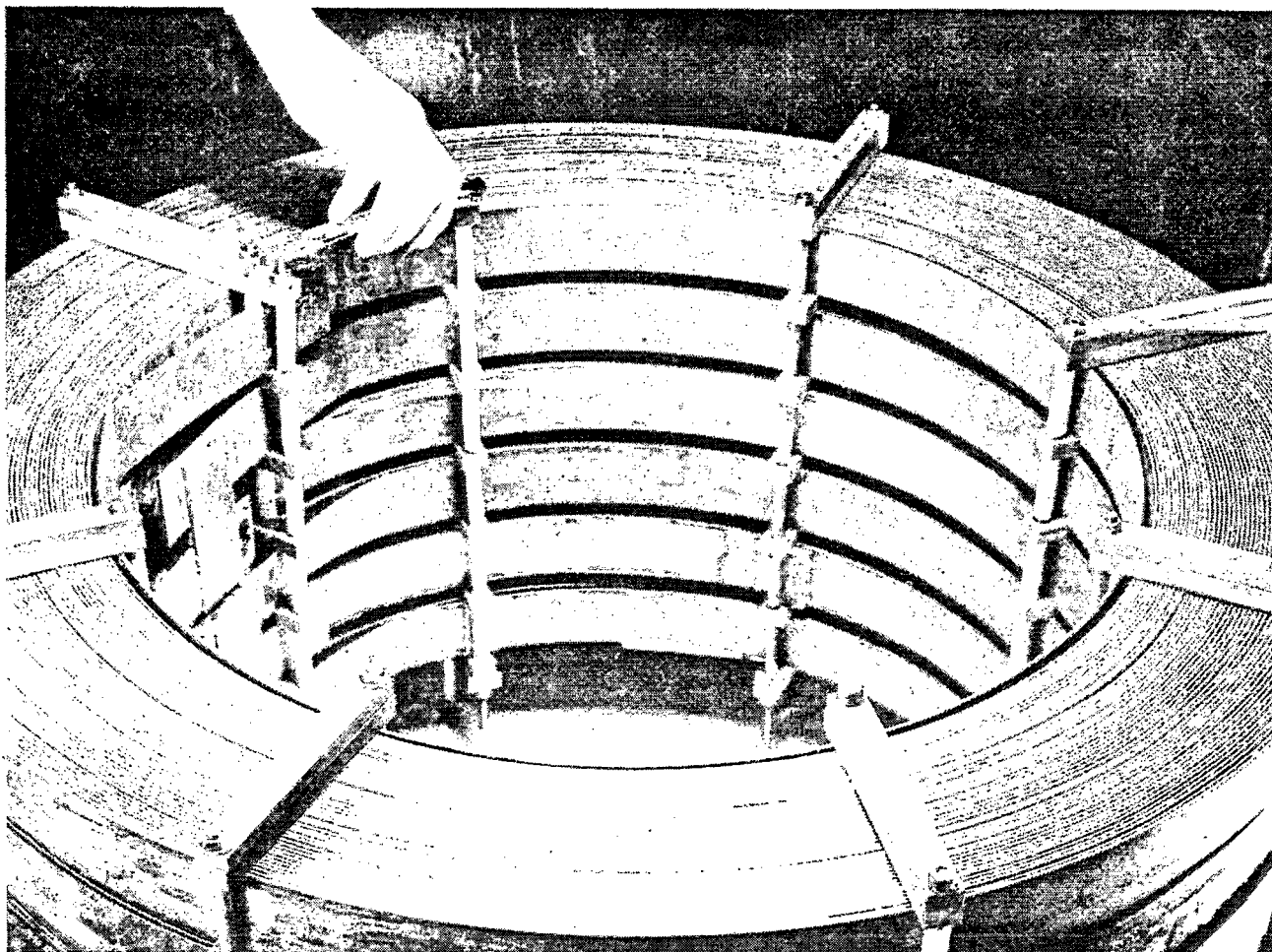


Fig. 8. A six pancake, 4600 A, 2.5 T test coil using the first three lengths of composite strip supplied for the large hydrogen bubble chamber magnet project.

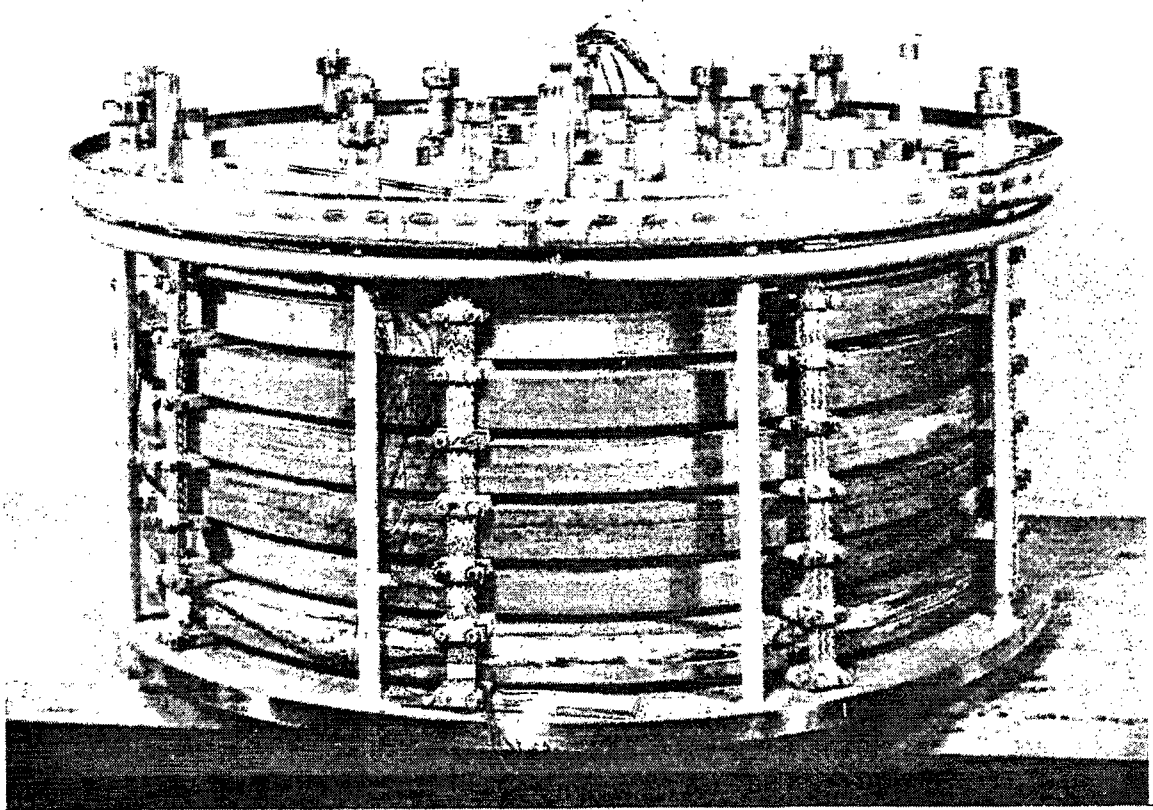


Fig. 9. Cooldown test model to check the efficiency of the design from the point of view of minimizing thermal stresses.

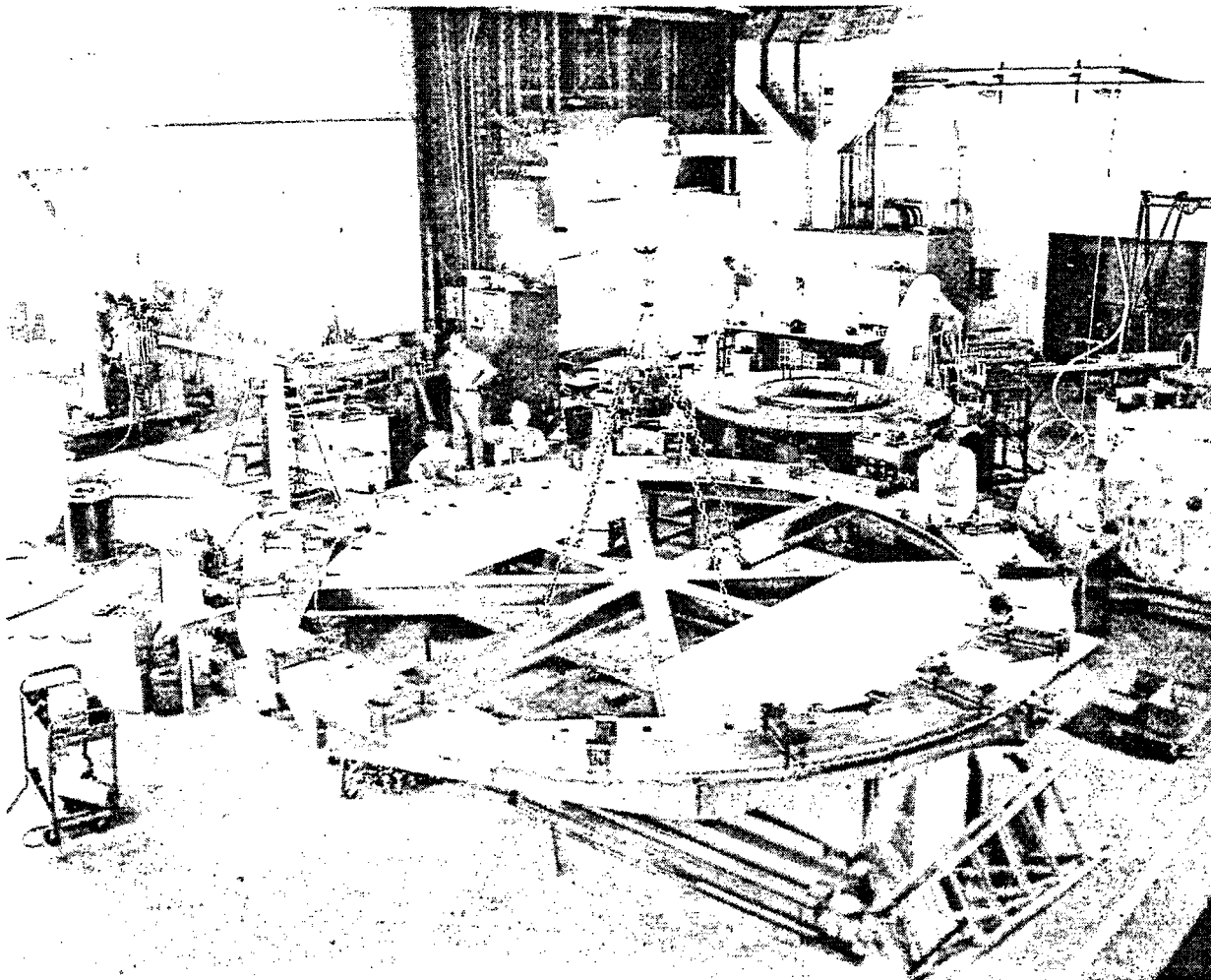


Fig. 10. A general view of the magnet winding facility showing a single pancake of the 1.8 T, 4.8 m i.d. bubble chamber coil in position on its winding jig.

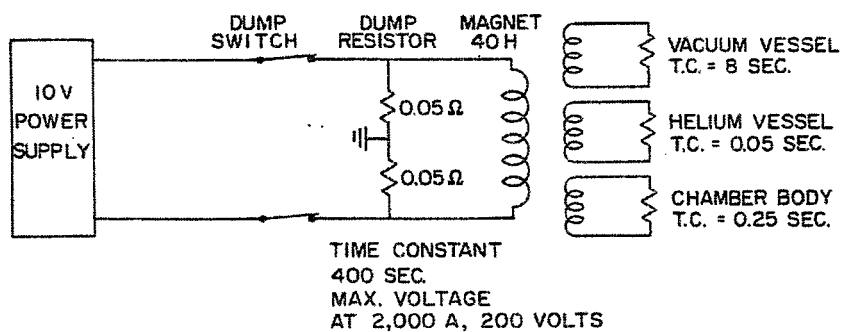


Fig. 11. Simplified diagram of the energizing and protective system for the large magnet system.

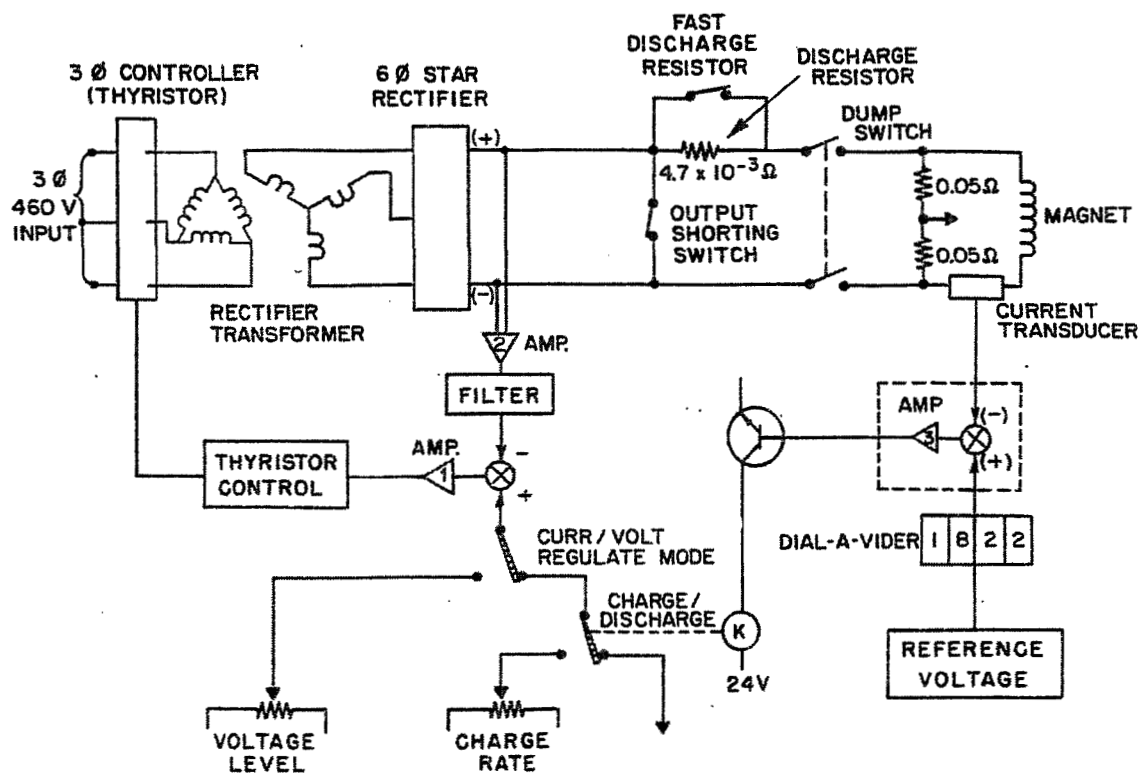


Fig. 12. Schematic circuit diagram of power supply.

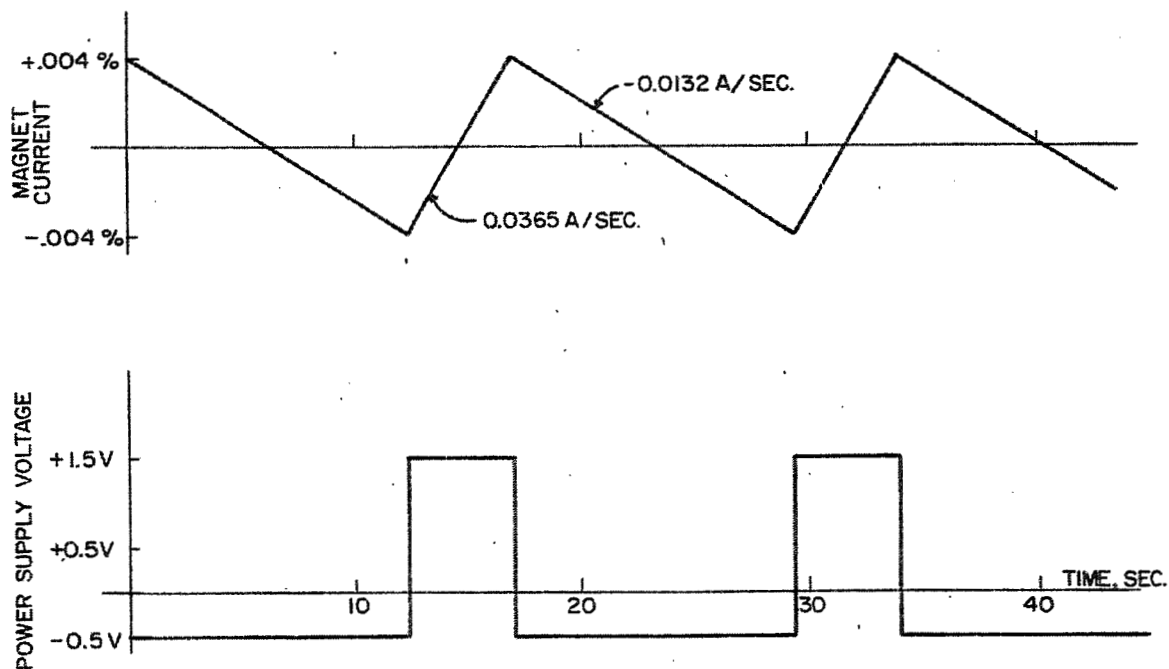


Fig. 13. Variation of coil current and on-off power supply voltage with time for normal magnet operation.

# THE SUPERCONDUCTING MAGNET FOR THE PROPOSED 25-FOOT CRYOGENIC BUBBLE CHAMBER\*

A.G. Prodel  
Brookhaven National Laboratory  
Upton, New York

A preliminary proposal has been made for the construction of a 25-ft cryogenic bubble chamber for use at the 200 GeV accelerator at the National Accelerator Laboratory. This chamber, which is to be designed by Brookhaven National Laboratory, is to have an air-core superconducting split-pair magnet capable of generating an average magnetic field intensity of 40 kG over the bubble chamber volume. The superconducting air-core design makes more accessible the component parts of the bubble chamber assembly and gives large savings in magnet costs and power for operation.

To eliminate the need for a magnet helium Dewar and to achieve a magnet coil configuration that is compact and mechanically strong, it is proposed that the 25-ft chamber magnet conductor be a hollow stabilized superconducting conductor cooled by an internal flow of helium.

Hollow stabilized superconducting conductors have recently been fabricated which consist of a number of superconducting filaments embedded in the wall of a tube of copper of square, or rectangular cross section. These conductors may be cooled by an internal flow of helium which is maintained at a temperature of 4.5°K and at pressures above its critical pressure of 2.23 atm. By maintaining the pressure of the helium fluid above 2.23 atm, the formation of two phases within the conductor is prevented. The one-phase positive fluid flow through the conductor insures that cooling is continually brought to all parts of the magnet conductor. The total volume of helium in contact with the conductor is less than that required to cool the magnet by pool boiling. Thus liquid and gas storage requirements are minimized with the hollow superconducting design.

The normal conductor material in which the superconducting filaments are bonded not only stabilizes the superconductors but also aids in supporting the electromagnetic forces to which the magnet is subjected. The amount of normal conductor to be bonded to the superconductor for stabilization for a given magnet current depends on the rate of heat transfer from the conductor to the helium coolant and on the resistivity of the normal conductor. The resistivity of the normal conductor is a function of its purity, of the stress in the conductor, and of the magnetic field intensity at the conductor.

The 25-ft bubble chamber magnet is designed for  $3 \times 10^7$  ampere-turns to generate a central field of 38 kG with an average magnetic field intensity of 40 kG over the chamber volume. At this value of average field, the maximum field at the magnet windings will be 65 kG and the magnet coil will be subjected to total radial pressures of the order of 2800 psi. To aid in supporting the stresses in the magnet windings, to limit deformation of the conductor material, and to reduce the amount of normal conductor required, a reinforcing or stiffener strip of a high strength material such as stainless steel is wound in the magnet coil windings with the hollow conductor. A thin strip of fiberglass epoxy or Mylar tape is also wound in the magnet coil between the

---

\*Work performed under the auspices of the U.S. Atomic Energy Commission.

surfaces of the hollow conductor strip and the stiffener strip to provide turn-to-turn electrical insulation. A schematic of the proposed magnet coil configuration is shown in Fig. 1. A hollow copper-multifilament superconductor composite of the type shown in the schematic, 0.75 in. square with an 0.375 in. diameter hole, may be designed to carry 8500 A in a magnetic field of 65 kG. Sufficient reinforcement is also wound in with the conductor to limit the stress in the copper to 15 000 psi.

The 25-ft bubble chamber magnet is a split-pair of coils, each coil-half consisting of a number of single layer pancakes as shown in Fig. 2. The pancakes are insulated from each other by thin sheets of fiberglass epoxy. Each pancake is made self-supporting against radial forces by clamping the external free end of the conductor at the periphery of the coil. The pancakes are connected electrically in series with stabilized superconducting connectors soldered and clamped at the inner and outer diameters of the magnet coils. The pancakes are connected in parallel to the helium supply manifold at the inner diameter of the magnet and to the helium return manifold at the outer diameter of the magnet coil.

The single layer pancakes are stacked vertically for each of the two magnet-half coils. Each magnet-half coil is 4 ft 6 in. high and has an inner diameter of 23 ft 6 in. and an outer diameter of 29 ft 2 in. The two half-coil assemblies are separated by 5 ft to allow for particle beam entry to the bubble chamber. This large coil separation permits the winding of magnet coils of a smaller diameter, reduces the axial forces on the coils, and improves the uniformity of the magnetic field over the bubble chamber volume. It also permits the large curved beam window section of the bubble chamber to extend 2 ft into the gap between the coils, as shown in Fig. 3, for easy entry of particle beams with a large range of momentum. The magnetic field intensity transverse to the beam axis has an average value of about 22 kG in the volume in the beam window between the coils. An elevation view of the magnetic field intensity plot is shown in Figs. 4 and 5. With a total of  $3 \times 10^7$  ampere-turns in the magnet and an average field over the chamber volume of 40 kG, the two coil-half assemblies are attracted to one another with a force of the order of 30 000 tons. This force between the coils is supported by a coil spacer which is reinforced around the chamber beam window so that a large aperture is available in the spacer for beam entry.

The pancakes of each magnet-half coil assembly are tied together by vertical rods at the inside and outside diameters of the magnet which are threaded into or bolted to stainless-steel washers at the top and bottom of each coil-half. These rods serve to align the coils. The bottom washer of the top coil and the top washer of the bottom coil are bolted to the coil spacer, while the bottom washer of the bottom coil is bolted to the three support legs. These legs support the magnet and bridge assembly in the bubble chamber vacuum tank and are designed to carry the total weight of approximately 400 tons. Thermal insulating pads are placed between the coil-halves and the coil bridge, and between the bottom coil and the support legs to minimize the heat leak from these structures to the coil. The magnet is thermally insulated from the bubble chamber and the vacuum tank by multilayer insulation.

The final figure, Fig. 6, shows an isometric view of the main assembly of the bubble chamber.

This brief description represents a summary of some of the preliminary general design concepts being developed by the Bubble Chamber Group at Brookhaven National Laboratory for the superconducting magnet for the 25-ft cryogenic bubble chamber.



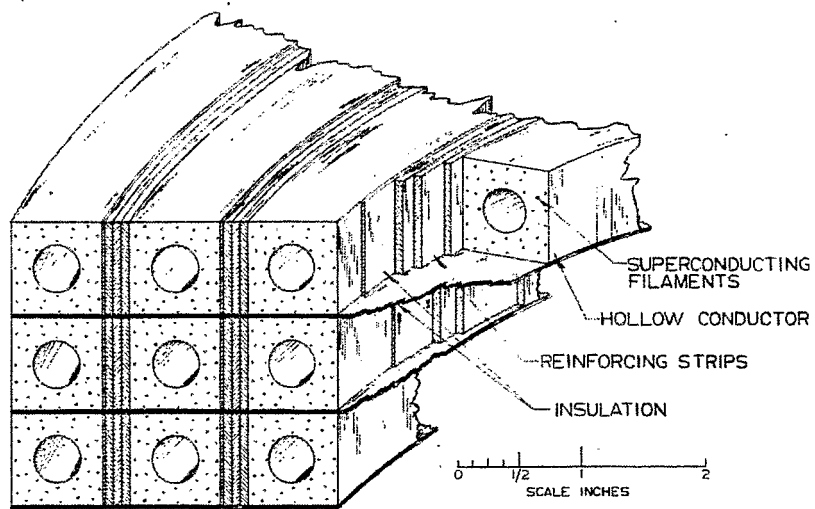


Fig. 1. Magnet coil components.

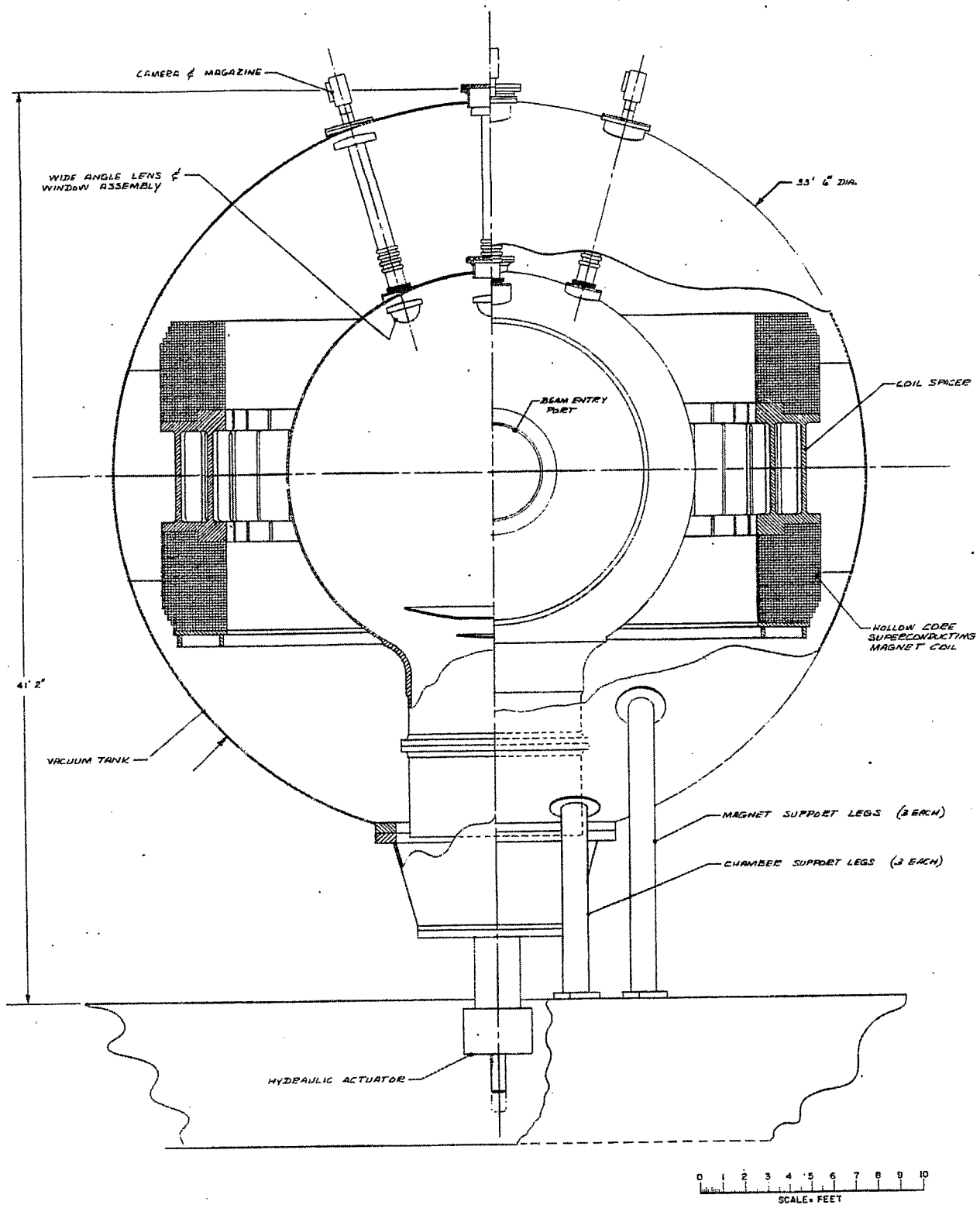


Fig. 2. 25-ft bubble chamber main assembly - front elevation sectioned view.

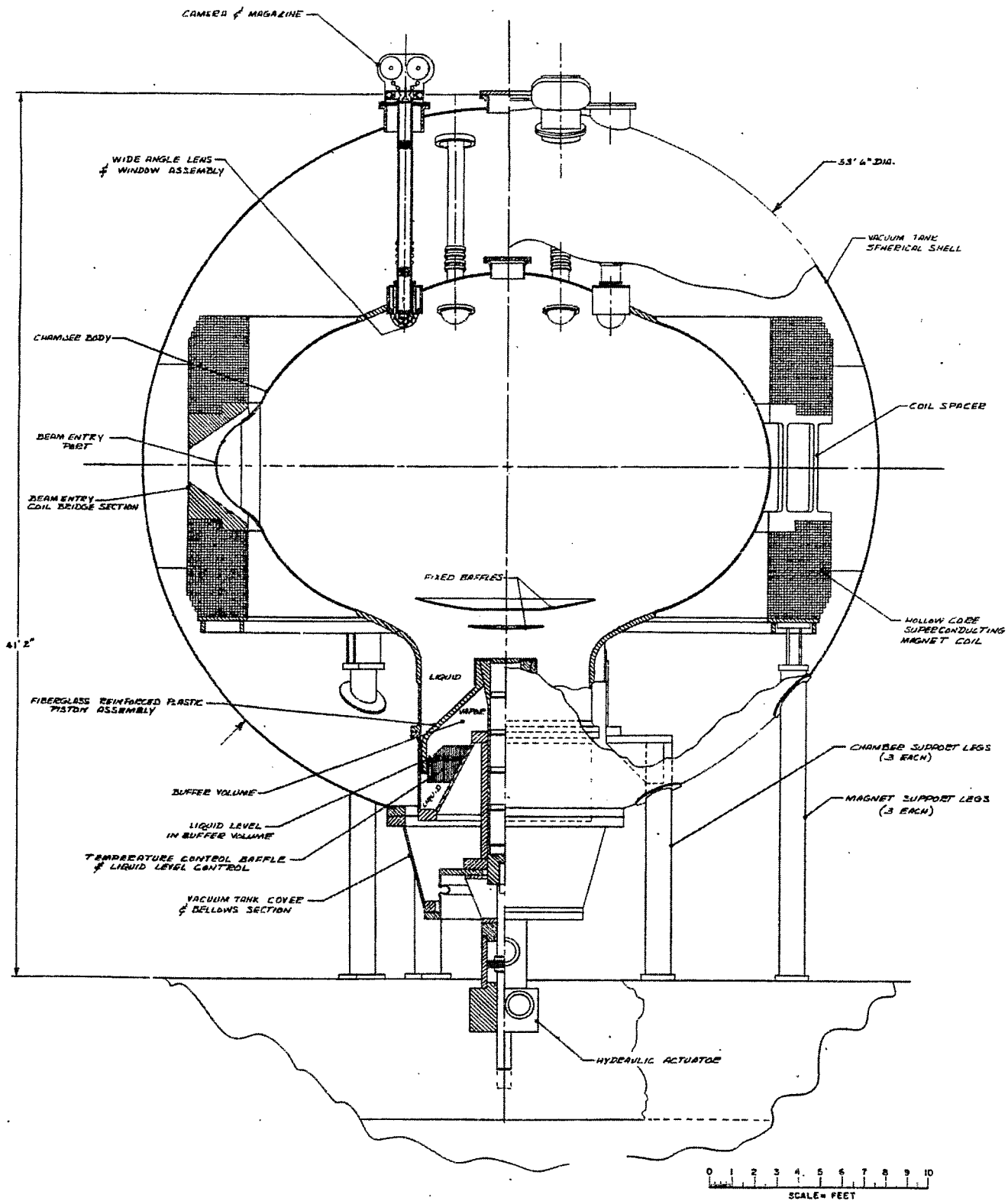
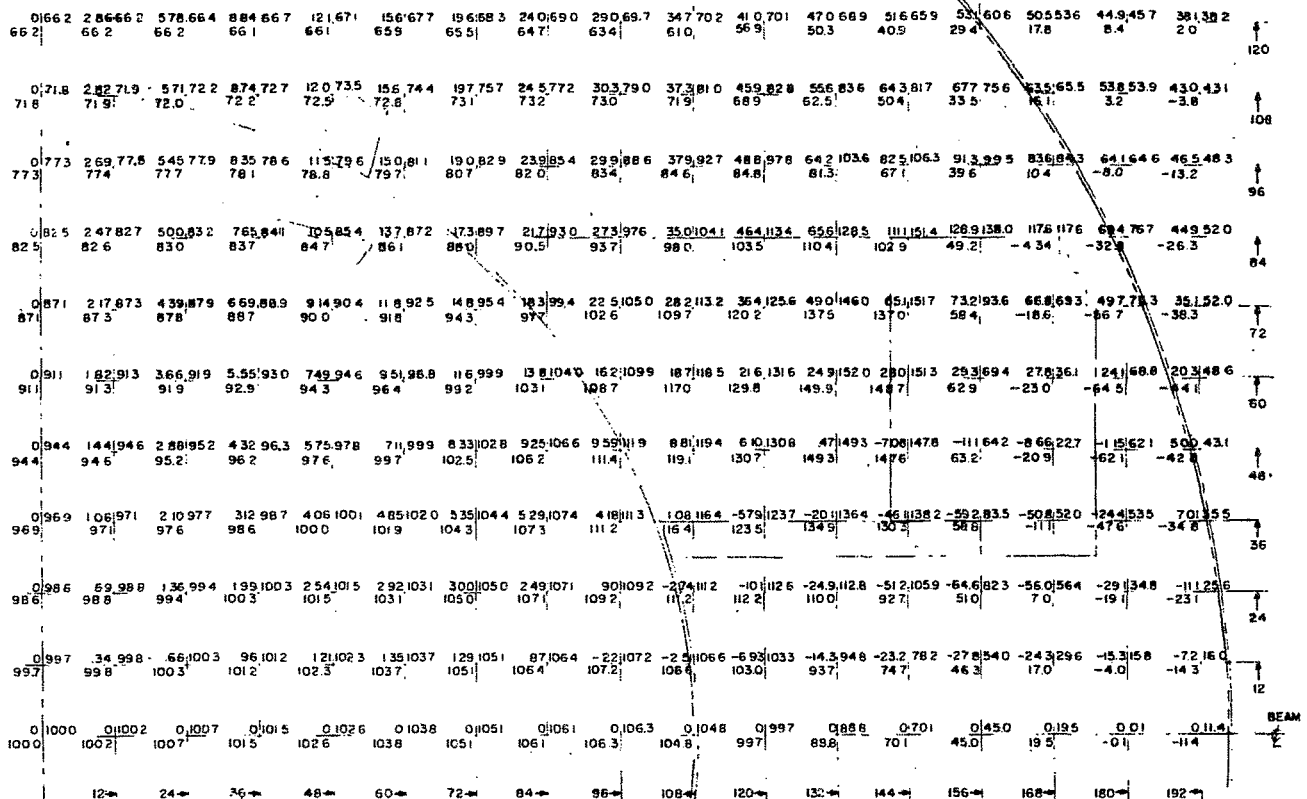
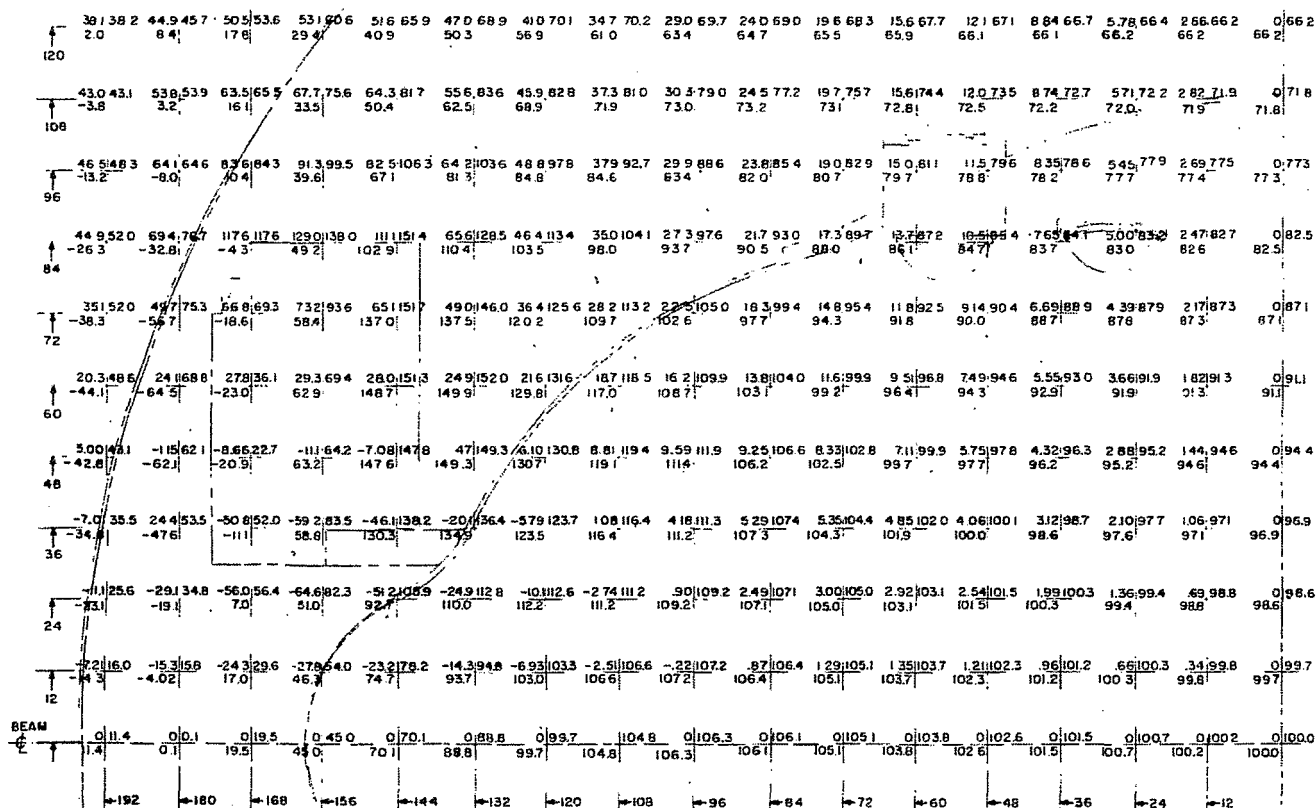


Fig. 3. 25-ft bubble chamber main assembly - side elevation sectioned view.



RADIAL FIELD STRENGTH TOTAL FIELD STRENGTH  
VERTICAL FIELD STRENGTH

Fig. 4. Field strengths expressed in percent of field strength at intersection of vertical center line and beam center line.



SIDE ELEVATION  
QUARTER SECTION

RADIAL FIELD STRENGTH / TOTAL FIELD STRENGTH  
VERTICAL FIELD STRENGTH

Fig. 5. Field strengths expressed in percent of field strength at intersection of vertical center line and beam center line.

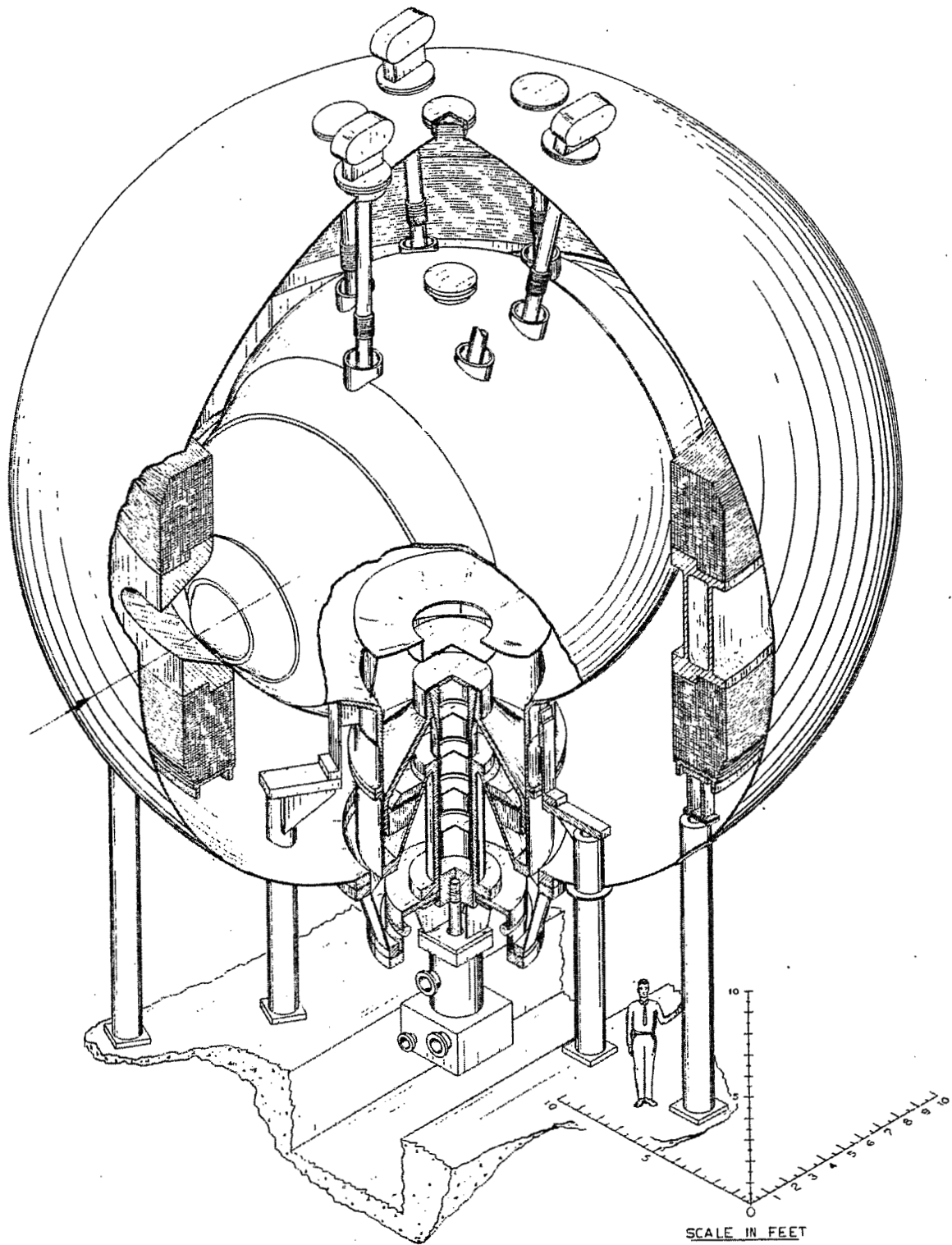


Fig. 6. 25-ft bubble chamber main assembly - isometric view.

THE SUPERCONDUCTING MAGNET FOR THE  
BROOKHAVEN NATIONAL LABORATORY 7-FOOT BUBBLE CHAMBER\*

D.P. Brown, R.W. Burgess, and G.T. Mulholland  
Brookhaven National Laboratory  
Upton, New York

INTRODUCTION

An air core, fully stabilized superconducting magnet has been constructed for the Brookhaven National Laboratory 7-Foot Bubble Chamber. The magnet incorporates conductor face cooling and stainless-steel reinforcement in an effort to maximize the performance-cost ratio. The design approach is integral with that of the Bubble Chamber. The conductor selection, the magnet design, construction considerations, cryogenic support facilities, and preliminary test results are described.

THE MAGNET

The magnet<sup>1</sup> has 16 double layers, or pancakes, wound with a conductor consisting of six NbTi (48% Ti by volume) cores metallurgically bonded to, and evenly distributed within a 2 in.  $\times$  0.078 in. OFHC<sup>†</sup> copper substrate. Each turn contains four strips: the stabilized superconductor, a Mylar insulator, a stainless-steel strength member, and a copper cooling channel spacer, in that order radially outward (Fig. 1). The double wound layers are arranged in two stacks in an annular helium Dewar concentric with the chamber's vertical axis. The two stacks are separated from each other by a bridge structure to allow the entry of particle beams into the chamber (Fig. 2).

The layers are connected in series electrically and externally powered through gas-cooled leads by a conventional power supply. The central field expected is 30 kG at 6000 A (see Table I).

CONDUCTOR SELECTION AND TEST RESULTS

Preliminary investigations indicated that the minimum superconductor current density expected in the processed composite conductor (actual  $4.3 \times 10^4$  A/cm<sup>2</sup>) was an order of magnitude higher than the composite conductor current density (actual  $6 \times 10^3$  A/cm<sup>2</sup>) required, allowing thermal and stress considerations to proceed without detailed consideration of the superconductor but assuming a reasonable distribution of superconductor in the copper and good thermal and mechanical contact.

If the copper, by virtue of its own strength or in combination with the strength of a reinforcing strip, can support the forces involved without significant resistivity change, the full stability criterion can be written as:

---

\* Work performed under the auspices of the U.S. Atomic Energy Commission.

† Oxygen free high conductivity, American Metals Climax trademark.

1. D.A. Kassner, in International Colloquium on Bubble Chambers, Heidelberg, 1967, (Yellow Report CERN 67-26), p. 435.

TABLE I  
7-Foot Bubble Chamber Magnet Parameters

Number of double pancakes	16
Total number of layers	32
Turns per layer	44
Total number of turns	1408
Coil current (A)	6000
Central field (kG)	30
Maximum vertical field (kG)	40.5
Maximum radial field (kG)	27.9
Coil inside diameter (in.)	94.6
Coil outside diameter (in.)	108.4
Conductor length per layer (ft)	1160
Total conductor length (ft)	37 200
Weight per pancake (lb)	2000
Total coil weight (lb)	41 000
Inductance (H)	4
Energy (MJ)	72

$$I = \left( \frac{\eta k t_c t_s h^{3/2}}{\rho(H_{\max})} \right)^{1/2}, \quad (1a)$$

$$J \cong \frac{h^{-1/2}}{(t_c + t_s)} \left( \frac{\eta k t_c t_s}{\rho(H_{\max})} \right)^{1/2}, \quad (1b)$$

where  $I$  is the fully stable current (A),  $\eta$  is the normalized surface exposure and flow efficiency parameter (0.5, here),  $k$  is the critical heat flux proportionality constant<sup>2</sup> ( $6 \text{ W/cm}^{5/2}$ , in the region of interest),  $t_c$  is the thickness of copper (cm),  $t_s$  is the thickness of cooling channel (cm),  $h$  is the channel and conductor height (cm),  $\rho(H_{\max})$  is the resistivity at the highest field within the coil ( $\Omega \cdot \text{cm}$ ) [resistance ratio at  $H = 0$ ,  $\rho(300^\circ\text{K})/\rho(4^\circ\text{K}) = 200$ ], and  $J$  is the average current density ( $\text{A/cm}^2$ ).

The product term  $\sqrt{t_c t_s}$  causes a rather flat current density maximum at  $t_s = t_c$ , allowing  $t_c$  to be increased (decreased) as  $t_s$  is decreased (increased) for reasons of strength (economics) with little effect on  $J$ .\*

---

\*  $J_{\text{actual}} = 2.5 \times 10^3 \text{ A/cm}^2$ .

2. M.N. Wilson, in Pure and Applied Cryogenics (Pergamon Press, 1966), Vol. 6, p. 109.



The maximum heat flux with all the current in the copper is  $0.34 \text{ W/cm}^2$ . This number is in good agreement with the demonstrated stability of the Maddox and Taylor magnet<sup>3</sup> at  $0.4 \text{ W/cm}^2$  with similar cooling provisions.

A stress analysis<sup>4</sup> taking into account (1) the nonlinear stress-strain relationship for copper, (2) the addition of an elastic reinforcing material, (3) the details of radial and axial support, and (4) the thermal contraction differences, was used as the basis for a computer study<sup>5</sup> of the stress distribution within the coil. The results of the study indicated that a stainless-steel strip 0.012 in. thick was sufficient to reinforce the 0.078 in. copper at the maximum (full field) load.

The important features of the reinforcement approach (the layers are tightly wound) taken here are: (1) the copper, required by the stability considerations, is used to its yield strength, (2) each turn transfers the stress in excess of that consistent with the mean layer strain to the next outer turn, until (3) the strength required of each turn is very nearly equal, resulting in minimum composite conductor and stainless steel material requirements. Note that here the stainless steel does not support the major portion of the (hoop) forces but guards against what at room (or higher) temperatures would be called "creep" in the copper.

The maximum stresses in the copper and stainless steel at 30 kG are 16.0 and 38.5 kpsi, respectively. The thermal stresses, which account for 1.25 kpsi in the copper and 6.7 kpsi in the stainless steel (Fig. 3),\* are given by:

$$\sigma_1 = \frac{\left[ \int (\pm \Delta T) dT \right] E_1 t_2}{(E_1/E_2) t_1 + t_2}, \quad (2)$$

where  $E$  = elastic modulus,  $t$  = radial thickness,  $\Delta T$  = differential thermal expansion coefficient,  $T$  = temperature, and subscripts 1 and 2 refer to copper and stainless steel, or vice versa. Using the fact that most of the stress is hoop stress and that the calculation takes the circumferential conductor and reinforcement strains equal, the "effective" elastic modulus of the copper is less than

$$\bar{E}_c < \frac{(16.0 - 1.25) 28 \times 10^3 \text{ kpsi}}{(38.5 + 6.7)} = 9.2 \times 10^3 \text{ kpsi}.$$

It is interesting to note that the superconductor, with a modulus of  $\sim 13 \times 10^3$  kpsi, and 115 kpsi ultimate tensile strength, can lend some of its strength to the mechanical composite. The superconductor strength and a conservative approximation to the copper stress-strain relationship serve as the design margin.

The selection of stainless steel as the reinforcement material in this application is not to imply that it is the best material as the thickness of reinforcement approaches that of the composite conductor in larger diameter magnets of equal field (at the coil) and current density. In fact, Eq. (2) suggests that a copper alloy

---

\* The differences between the quoted stresses and those implied by Fig. 3 are radial and axial copper bending stresses.

3. B.J. Maddock et al., in Proc. 2nd Intern. Conf. Magnet Technology, Oxford, 1967, p. 533.

4. R.P. Shutt, Brookhaven National Laboratory Internal Notes (1966).

5. S. Kern, Brookhaven National Laboratory Program MAGIC (1966).

(e.g. BeCu, or phosphor bronze) may be a better choice with the nonlinear stress-strain relationship of the copper affording the stress transfer mechanism.

The test results obtained in the Brookhaven 8-in. bore 60-kG superconducting magnet test facility<sup>6</sup> on the composite conductor, which was manufactured<sup>7</sup> to a conservative 4000 A - 20 kG central field specification (the original design), indicated that the conductor would actually perform to critical currents consistent with central fields of 24 to 28 kG. The composite conductor exhibited a 5:1 critical current anisotropy favoring the vertical field component, so that the region of highest radial field, and not that of the highest total field, within the coil determined the limiting condition. In an effort to maximize the ratio of central field to maximum radial field by redistribution of the conductors at the extremes of the magnet coil, various coil configurations were studied. Construction details and helium Dewar constraints limited the possibilities to the 9% increase of Fig. 4b. The ratio change increased the predicted central field value to between 25.4 and 29.7 kG. By selecting conductor lengths with the higher critical current values for magnet pancakes in the higher field regions, the upper magnetic field limit may be achieved.

#### CONDUCTOR MECHANICAL CONSIDERATIONS

The composite superconductor material contains six niobium-titanium cores, each with a cross-sectional area of approximately 0.00375 sq.in., arranged in the copper conductor as shown in Fig. 1. Polished and etched sections examined under  $\times 500$  magnification (see Fig. 5) demonstrated that the bonding was sound and free of voids. Short pieces were acid etched on one side to expose three NbTi cores. The cores were gripped at one end and peeled away from the copper. The break occurred in the copper and not at the Cu-NbTi interface.

When copper and NbTi are metallurgically bonded, the composite material exhibits a higher tensile strength than copper alone, and a higher ultimate elongation than NbTi alone, as illustrated in Figs. 6 and 7. The copper supports the NbTi cores to the extent that the NbTi has an increase of approximately 25% in its elastic limit. This can be seen from the difference in strain to the apparent yield points in the curves in Figs. 6 and 7. X-ray photographs of a fractured specimen of the composite material showed that each NbTi core had yielded and fractured in succession at a number of places.

#### MAGNET CONSTRUCTION

A top and a bottom layer, each of 44 turns, are wound to make a double "pancake" assembly. The inside ends of the conductor are electrically connected and mechanically clamped to a curved plate at the inside diameter (Fig. 9). This allows the inter-pancake electrical connections to be made on the (exposed) outside diameter of the assembly. Open phenolic insulating spacers of 0.125 and 0.625 in. thicknesses separate the layers and pancakes, respectively, to allow the radial and axial flow of liquid helium (Fig. 8). The 0.625 in. spacers are assemblies of 0.75 in. wide blocks, spaced 1.5 in. on center by tubular spacers mounted on 0.125 in. phosphor bronze connecting rods.

---

6. J.A. Bamberger et al., in Advances in Cryogenic Engineering (Plenum Press, 1968), Vol. 13, p. 132.

7. J. Wong et al., J. Appl. Phys. 39, 2518 (1968).

In the double-layer winding procedure the inside ends of the composite superconductor strips are soldered to the crossover plate and clamped along with the Mylar-backed stainless-steel strip. The strips are formed around the ends of the crossover plate with a cuff made from a short length of composite superconductor soldered at the inner diameter to compensate for the reduction in critical current caused by the sharp bend. The plate is then mounted to a mandrel on the winding table. The table is rotated by a geared, constant torque, variable speed air motor.

The lower layer is wound with the upper coil supply reels of superconductor and Mylar-backed stainless-steel strip riding at the center of the table. The copper cooling spacer strip is fed in so that all three strips are wound simultaneously. After 44 turns are wound the ends of the strips are clamped to the table and the excess cut off. The upper layer supply reels that were riding at the center of the winding table are now placed on the supply tables (adjusted to the new level), the 0.125 in. insulating spacers are positioned on the lower layer, and the upper layer is wound in counter rotation. Two aluminum bronze electrical connector backing plates (Fig. 10) are sandwiched in the last turn of each layer in positions that vary from one double pancake to the next to offset alternately the radial clamps, and to comply with the arrangement of electrical connections (Fig. 14).

A fiberglass end clamp is then fixed in position between the upper and lower conductor ends, and the ends are formed around it and secured with bolted clamping plates (Fig. 11). The end clamp restrains the hoop forces transferred to the outer turns of the coil, causing each conductor end to pull against the other.

When the twelve radial clamps (Fig. 12) are secured to the coil, the double layer assembly is complete (Fig. 13). Eight double layers are stacked, with interleaved 0.625 in. spacers, on a stainless-steel bottom washer, and the whole assembly is tied together by 0.625 in. diameter 7075-T6 aluminum rods to a stainless-steel top washer. The top washer of the lower magnet half has upward protruding threaded studs to form, together with a T-section, an I-section stainless-steel "bridge" structure which separates the lower and upper magnet halves. The upper coils are similarly stacked on the T-section structure, and tied with aluminum rods to a top washer.

The bolts that fasten the magnet to the Dewar base and the aluminum tie rods must withstand the 2g dynamic loading (82 klb) associated with the bubble chamber expansion. The tie rods are pre-tensioned, because of this dynamic loading, with Preload Indicating Washers to assure that the stack is held tightly. Aluminum, rather than stainless steel, was chosen as the tie rod material as it has a higher thermal contraction than the copper-phenolic combination and acts as a thermal compensator on cooldown, reducing the necessary room temperature pre-tension to 48 kpsi. The maximum vertical loads due to the magnetic forces occur at approximately 1/3 the magnet half height, measured above and below the beam bridge, and are directed toward the center. At 30 kG this corresponds to a compressive stress of 10.3 kpsi in the copper of the conductor at the 0.75 in. wide phenolic spacers. The pitch of the phenolic insulating spacers is a compromise between the open space necessary for free liquid helium flow and a reasonable stress level.

When both halves of the magnet are placed in the Dewar and secured, parallel composite superconductor electrical inter-pancake jumper strips are temperature control soldered and clamped in place. The arrangement (Fig. 14) was designed to give the jumper strips sufficient length so they could be bowed to allow the flexibility required by the sum of the copper and phenolic spacer thermal contractions.

## DESCRIPTION OF DEWAR, REFRIGERATOR AND PLUMBING

The magnet Dewar is an annular vessel of type 316L stainless steel that fits closely around the magnet and shares a common vacuum tank with the bubble chamber. Approximately 3000 liters of liquid helium are required to fill the vessel with the magnet in place.

The Dewar is supported by three legs which rest on pads cooled with liquid hydrogen. The legs are designed on the basis of a vibrational analysis of deflections and forces on the magnet during the bubble chamber expansion cycle, and leg deflection due to contraction of the Dewar relative to its room temperature supports. These considerations have made it necessary to use a leg cross section which is heavier than that required to support the weight of the magnet and Dewar in the static situation. The hydrogen cooling of the legs, however, provides a means of reducing conduction losses to the helium Dewar to a low value.

Each of the cylinders which form the walls of this vessel have cooling loops on the vacuum side. The coolant passes through 0.75 in. o.d. tubing that has been tack-welded and soft-soldered to the walls. The loops are provided for precooling the magnet with liquid nitrogen and liquid hydrogen while pressurizing the magnet Dewar with helium gas, thus eliminating the necessity of purging the main Dewar volume at low temperatures.

Originally the magnet current leads were helium gas cooled. Each lead was constructed of 76 parallel 0.125 in. o.d. copper tubes soldered into terminal blocks at both ends. The gas flow was inside of the tubes. Each lead was about 0.75 in.<sup>2</sup> in cross section and 36 in. in length. The leads were extrapolated from leads used to supply the current for the short sample test program described earlier. The test leads had an optimum at 2900 A, but were used for short periods of time at 6000 A.

The Dewar was insulated only with NRC-2 aluminized Mylar insulation applied at a density of 100 layers per inch. Four inches of insulation are used in the vacuum space between room temperature and helium temperature. One inch of insulation is used in the vacuum space between hydrogen (bubble chamber) temperature and helium temperature.

The cooldown weight of the magnet and Dewar is about 53 klb. There are 14 tons of copper, 12 tons of stainless steel and 0.5 tons of plastics.

The helium refrigerator-liquefier used with the magnet is an ADL Model 2000 machine. It has a capacity of 60 liter/h as a liquefier, and 240 W at 4.5°K as a refrigerator. The machine uses liquid nitrogen precooling and has two 3 in. bore expansion engines. A non-lube three-stage Norwalk compressor supplies gas for the system.

The flow from the refrigerator goes to an intermediate supply Dewar and then to the magnet Dewar. A simplified schematic is shown in Fig. 15. The intermediate supply Dewar is used to insure a liquid helium supply for the magnet in the event of a refrigerator failure.

A schematic of the helium cooldown and fill system is shown in Fig. 16. During cooldown, liquid helium or cold gas is introduced at the bottom of the Dewar, directly under the magnet coils. The gas flows upward, enters the gas return piping, and can either be returned to the refrigerator or directly to compressor suction through a warm-up coil. When the Dewar has been filled, flow into the Dewar is directed to the top, instead of the bottom. The boil-off gas is returned to the refrigerator.

In addition to the vent and relief valves on the gas phase lines, two 1.5 in. liquid vent valves and a 6 in. rupture disk at the bottom of the Dewar provide protection against overpressure of the vessel.

#### TRIAL COOLDOWN

A trial cooldown of the magnet without the hydrogen bubble chamber was conducted from May 9 to June 2, 1968. Attempts to fill the Dewar with liquid helium were unsuccessful, but it was possible to run the magnet at 3300 A and 16.5 kG, in cold gas.

The magnet Dewar and refrigeration system were purged and liquid nitrogen pre-cooling started on May 9. The magnet had reached a temperature of less than 100°K in about four days. It had not been planned to use a liquid hydrogen precool for this test, but because of the slow rate of cooling obtained with the helium liquefier, some plumbing changes were made and liquid hydrogen was circulated in the cooling loops on May 21. This cooled the magnet to about 30°K. A series of attempts were made to cool the magnet further with the refrigerator. It soon became apparent that the heat load exceeded the capacity of the refrigerator and that additional refrigeration in the form of purchased liquid would have to be used. A number of attempts were made to supply liquid from the refrigerator while at the same time maintaining flow from an outside Dewar. Because of plumbing limitations, the procedure was finally abandoned and an intermittent transfer operation was employed. This allowed the use of liquid at a rate in excess of liquefier capacity.

On May 25, the magnet was cooled to a temperature of 5 to 6°K when an interruption of the nitrogen flow due to a plugged supply Dewar caused a loss of refrigeration and leg cooling. The magnet warmed up and it was decided to interrupt the helium cooling flow in order to reliquefy all the helium gas in storage. The magnet was maintained at a temperature of 25°K with liquid hydrogen during this operation.

On June 1, the magnet was cooled to less than 5°K. Repeated attempts were made to fill the Dewar with liquid, using "bottom fill" mode, "top fill" mode and a combined "top-bottom fill" mode. No detectable amount of liquid was collected in the Dewar. By the morning of June 2, there was not enough liquid in storage to fill the Dewar. It was decided to attempt to run the magnet in cold gas. As the current was increased through 3300 A, the coil went normal causing the Dewar pressure to rise about 5 psi to 8 psig. The excess pressure was vented through the liquid dump valves. The magnet current had slowly decreased to 1500 A when the rest of the field energy was dumped into an external resistor. Strain gauges installed on the magnet showed no significant movement during the entire test.

A number of system modifications were indicated by these tests. Modifications which are to be included prior to the next cooldown are:

- 1) A hydrogen-cooled radiation shield using the effluent gas from the bubble chamber cooling loops as the coolant will be added.
- 2) The transfer lines will be liquid nitrogen shielded.
- 3) Hydrogen, instead of helium, gas will be used for power lead cooling. Because the helium refrigeration is supplied by a closed system, the gas used to cool the leads reduced the refrigeration available for other purposes by about 80 W.
- 4) A better system for utilization of purchased liquid in parallel with the refrigerator will be installed.

- 5) A bypass around the J-T heat exchanger of the refrigerator will be added.

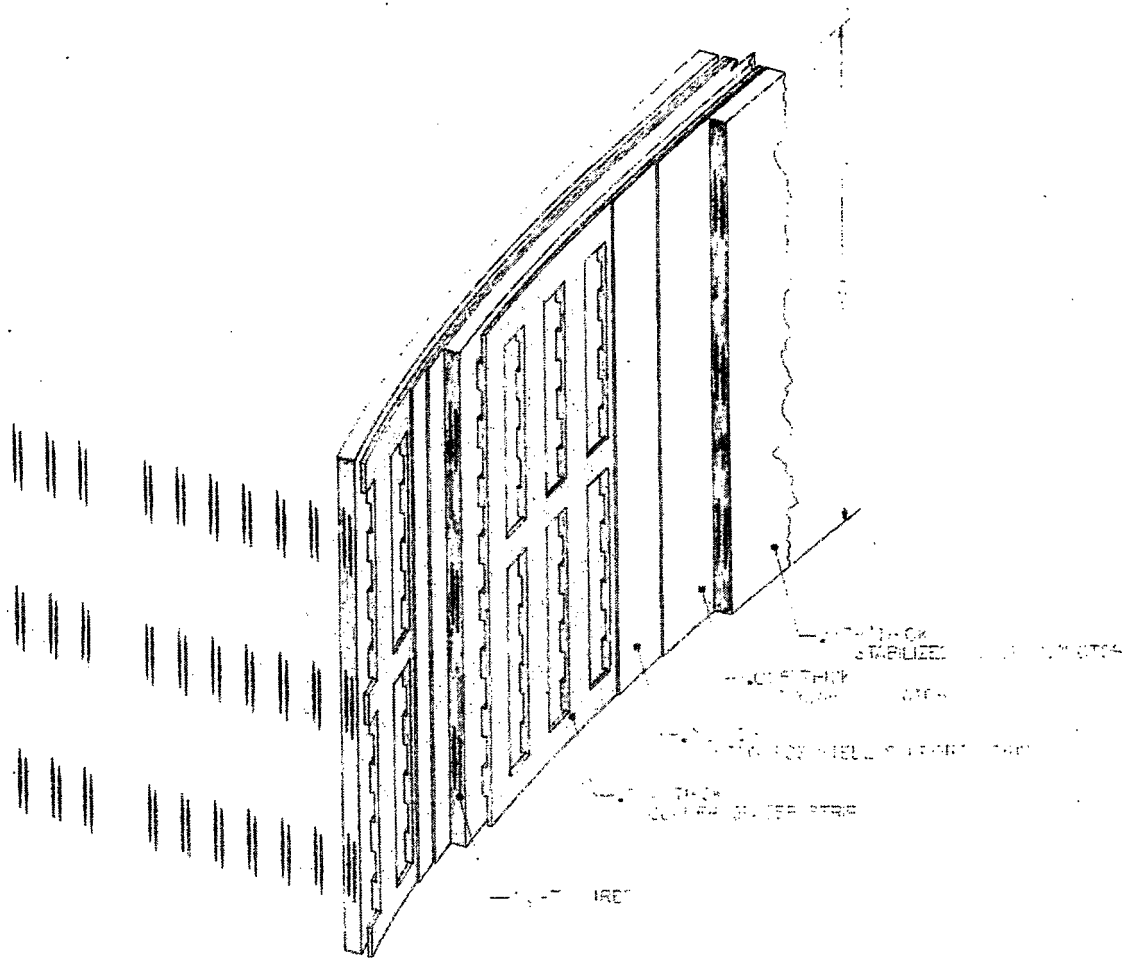
These modifications are expected to result in a reduction of refrigeration required by over 100 W.

We are studying and plan to run some tests, as required, on the feasibility of changes to the fill system.

#### ACKNOWLEDGEMENTS

The authors have reported on the work of the Bubble Chamber Magnet Group under the chairmanship of Dr. A.G. Prodell. The group members are: J.A. Bamberger, D.P. Brown, R.W. Burgess, B.B. Culwick, C. DiLullo, W.B. Fowler, D.A. Kassner, J.T. Koehler, G.T. Mulholland, R.P. Shutt, and W.A. Tuttle.

The authors and the group wish to thank the Brookhaven technicians for their extra special efforts in this project.



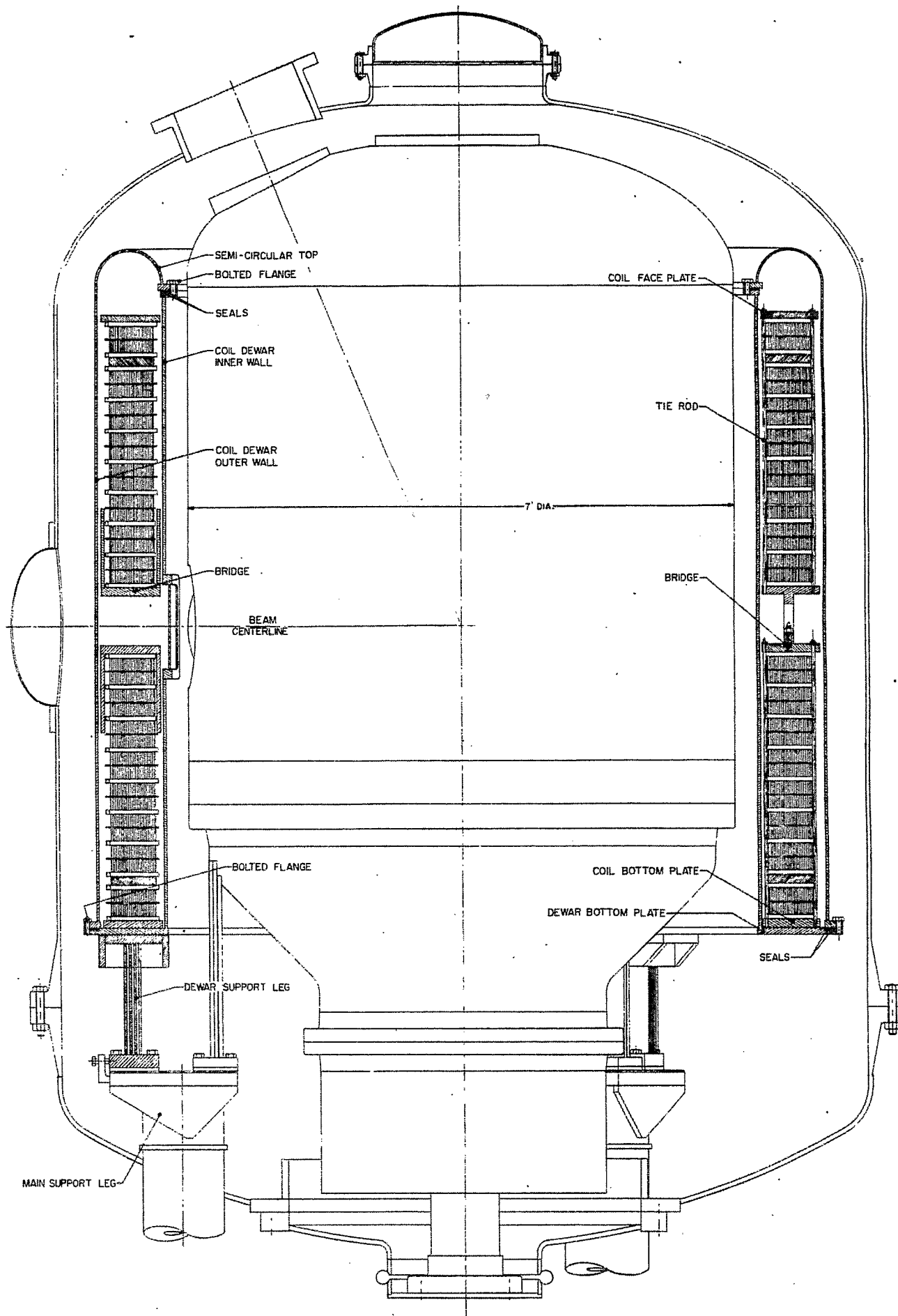


Fig. 2. Chamber over-all.



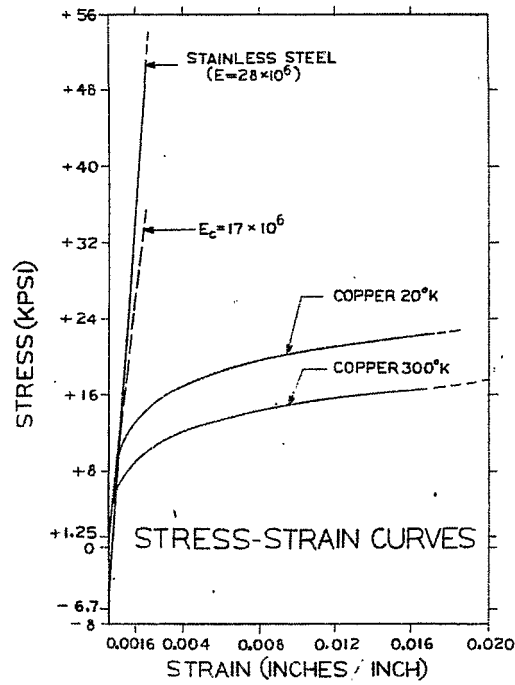


Fig. 3. Stress-strain, stainless steel-copper.

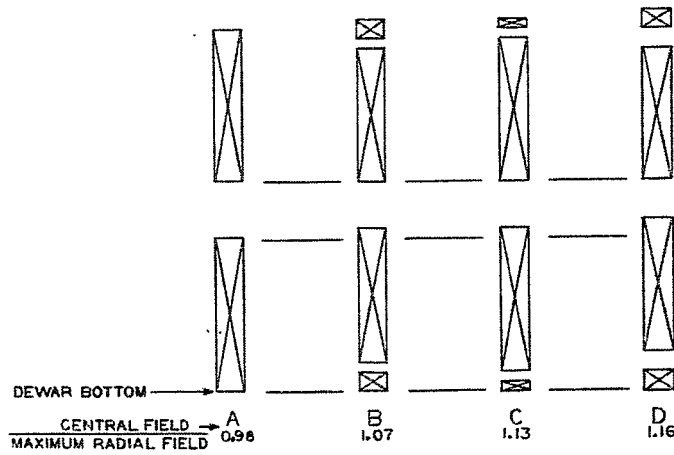


Fig. 4. Configurations considered, 7 ft magnet.



Fig. 5. Photomicrograph of NbTi core in Cu.

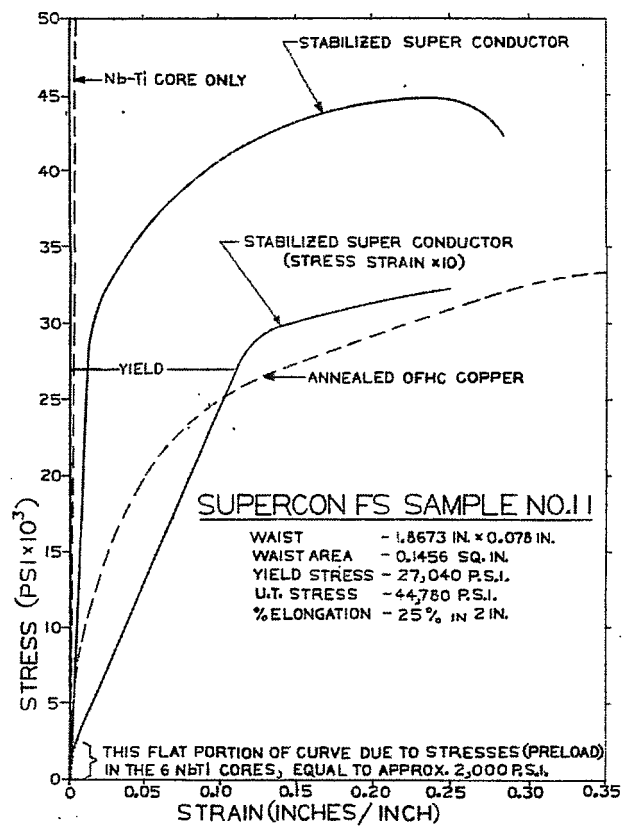


Fig. 6. Stress-strain curve of composite superconductor.

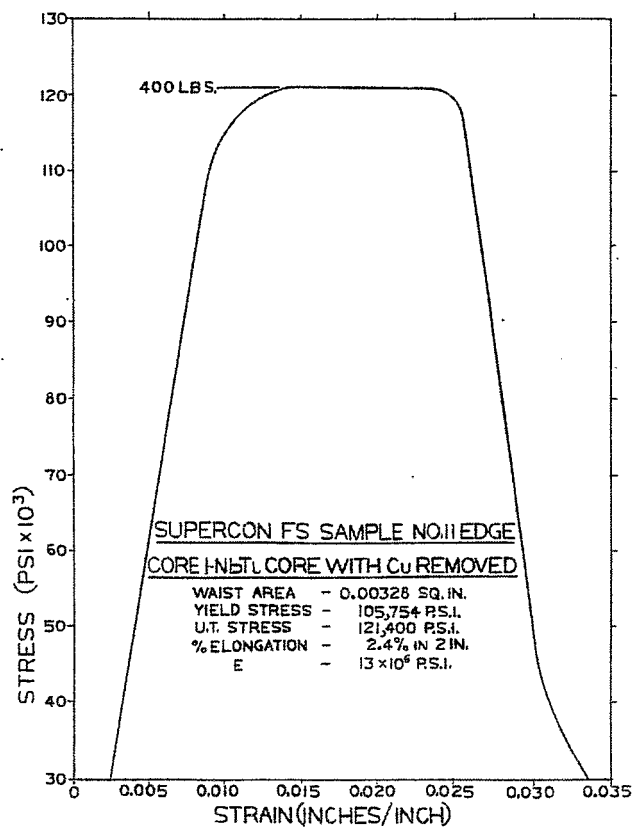


Fig. 7. Stress-strain curve of NbTi superconductor core.

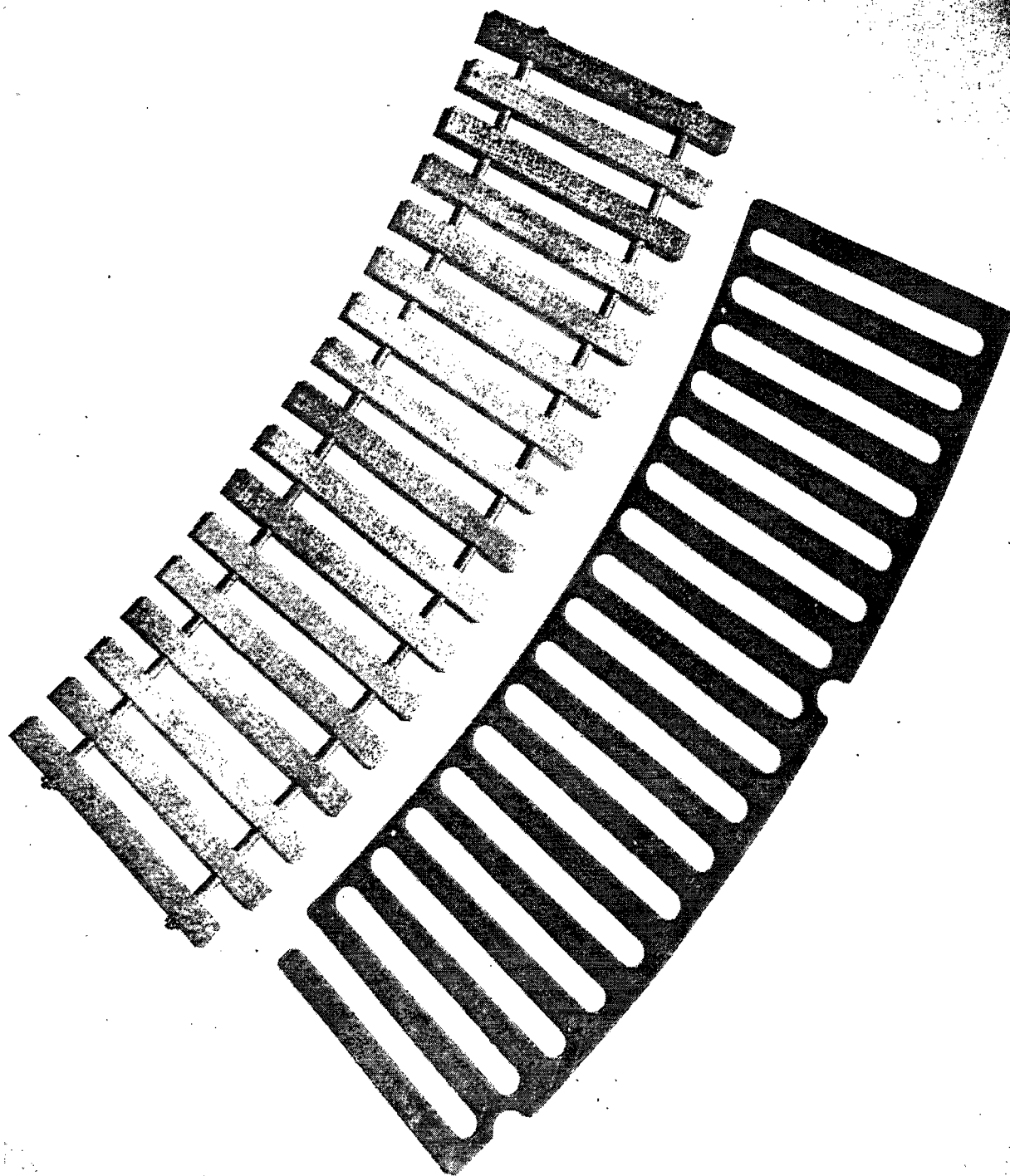


Fig. 8. 1/8 in. and 5/8 in. phenolic cooling spacers.

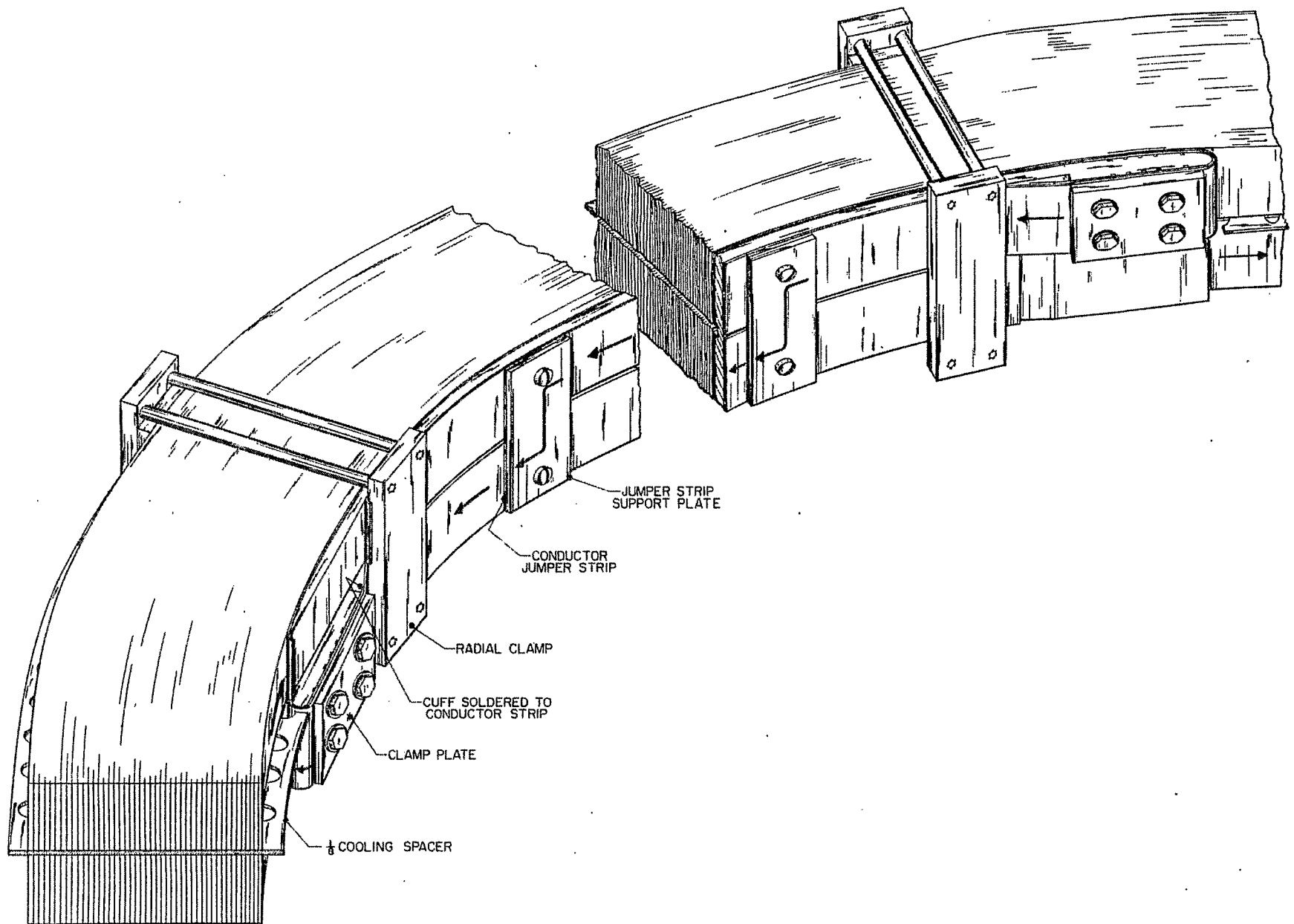


Fig. 9. Internal crossover plate assembly.

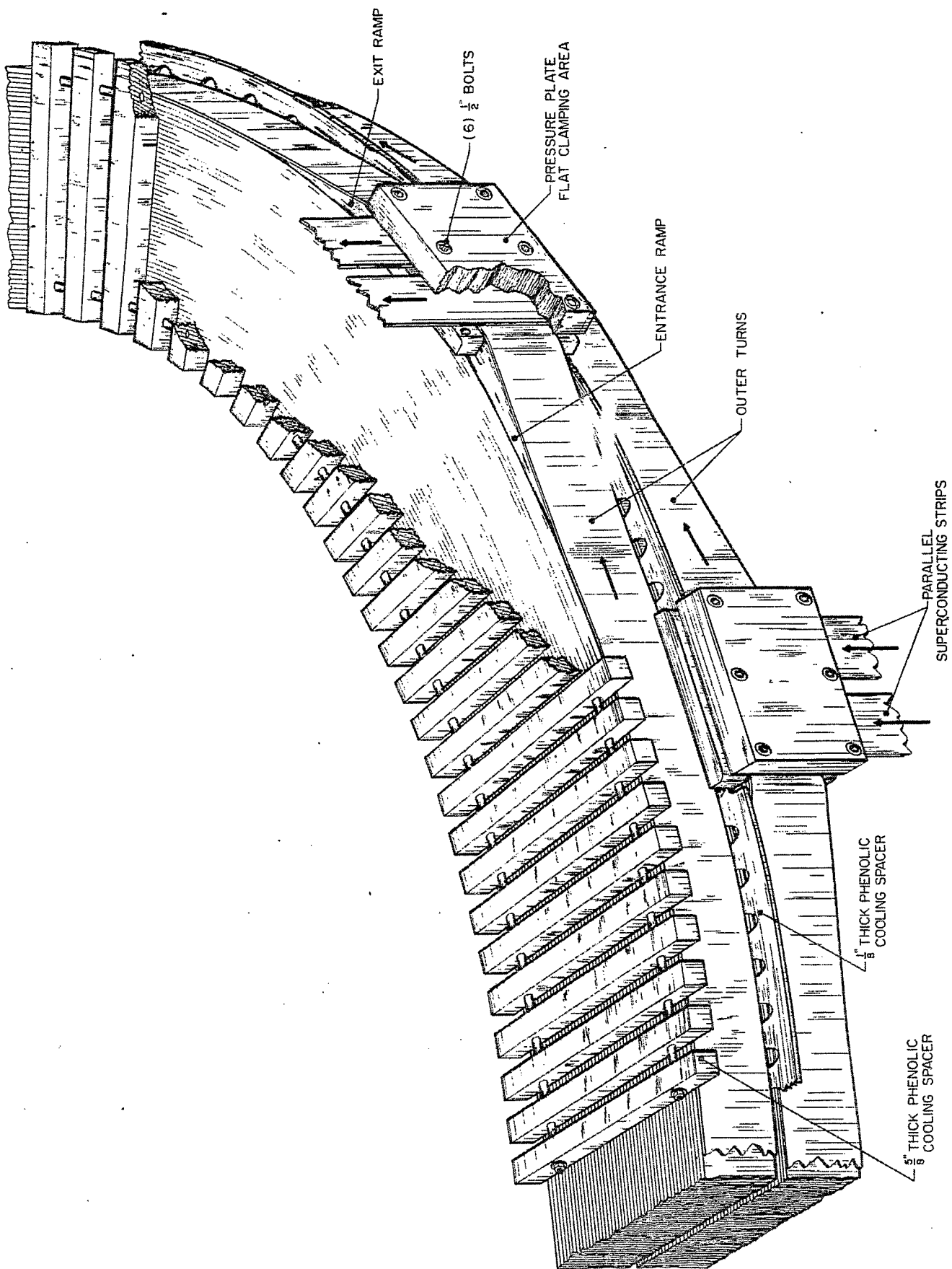


Fig. 10. Inter-pancake electrical connectors.

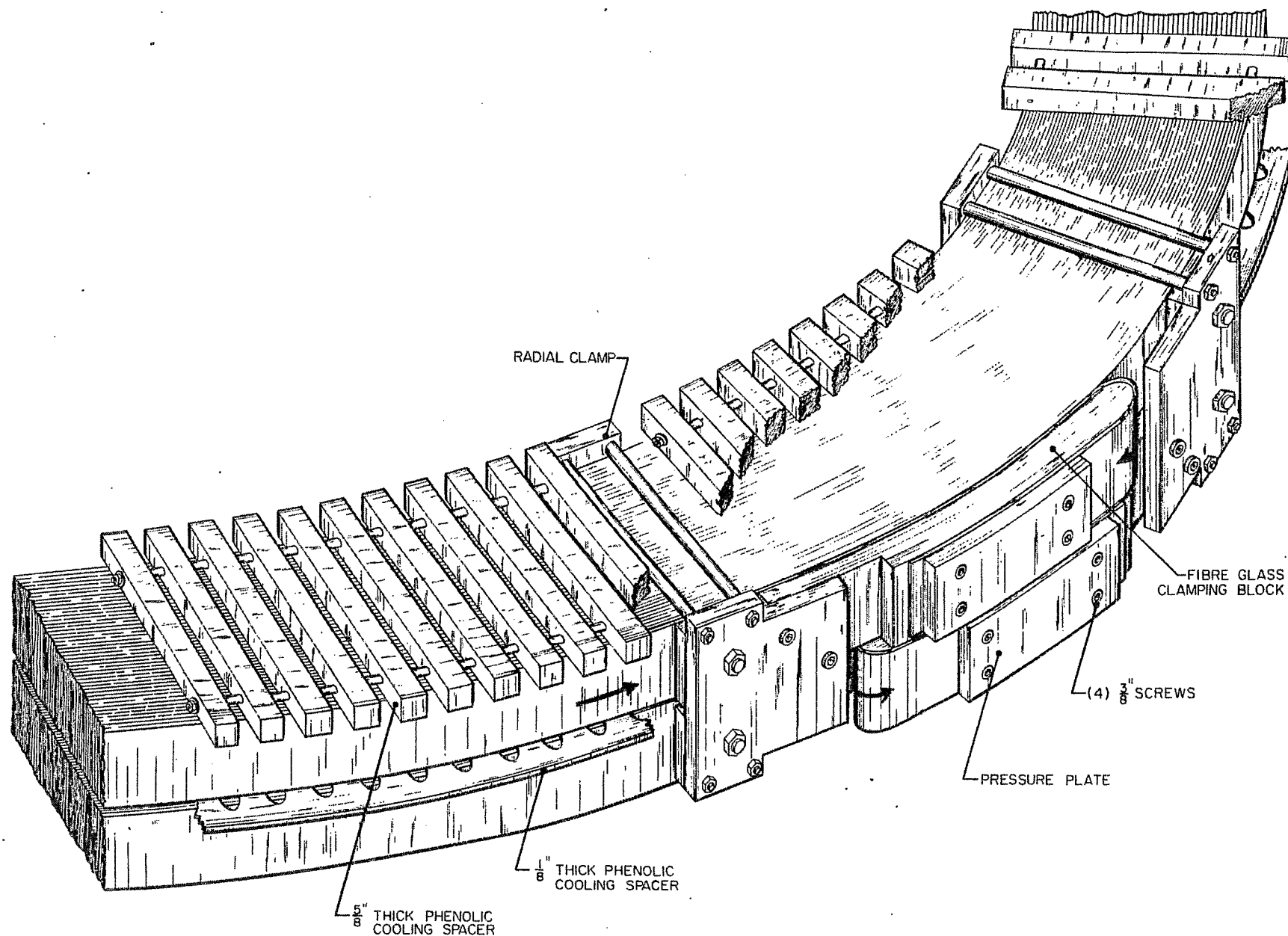


Fig. 11. End clamp assembly.

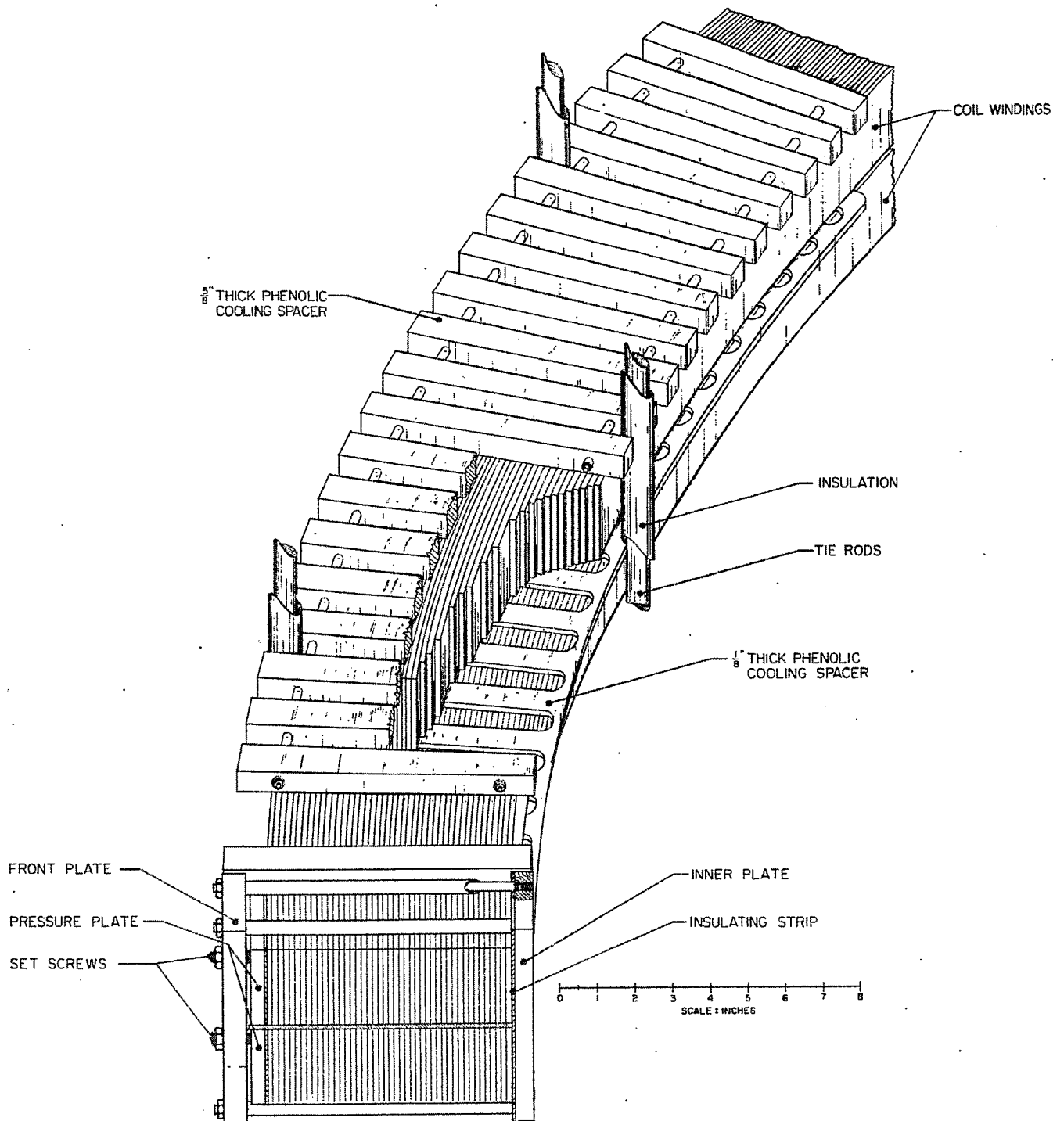


Fig. 12. Radial clamp and cooling spacer details.



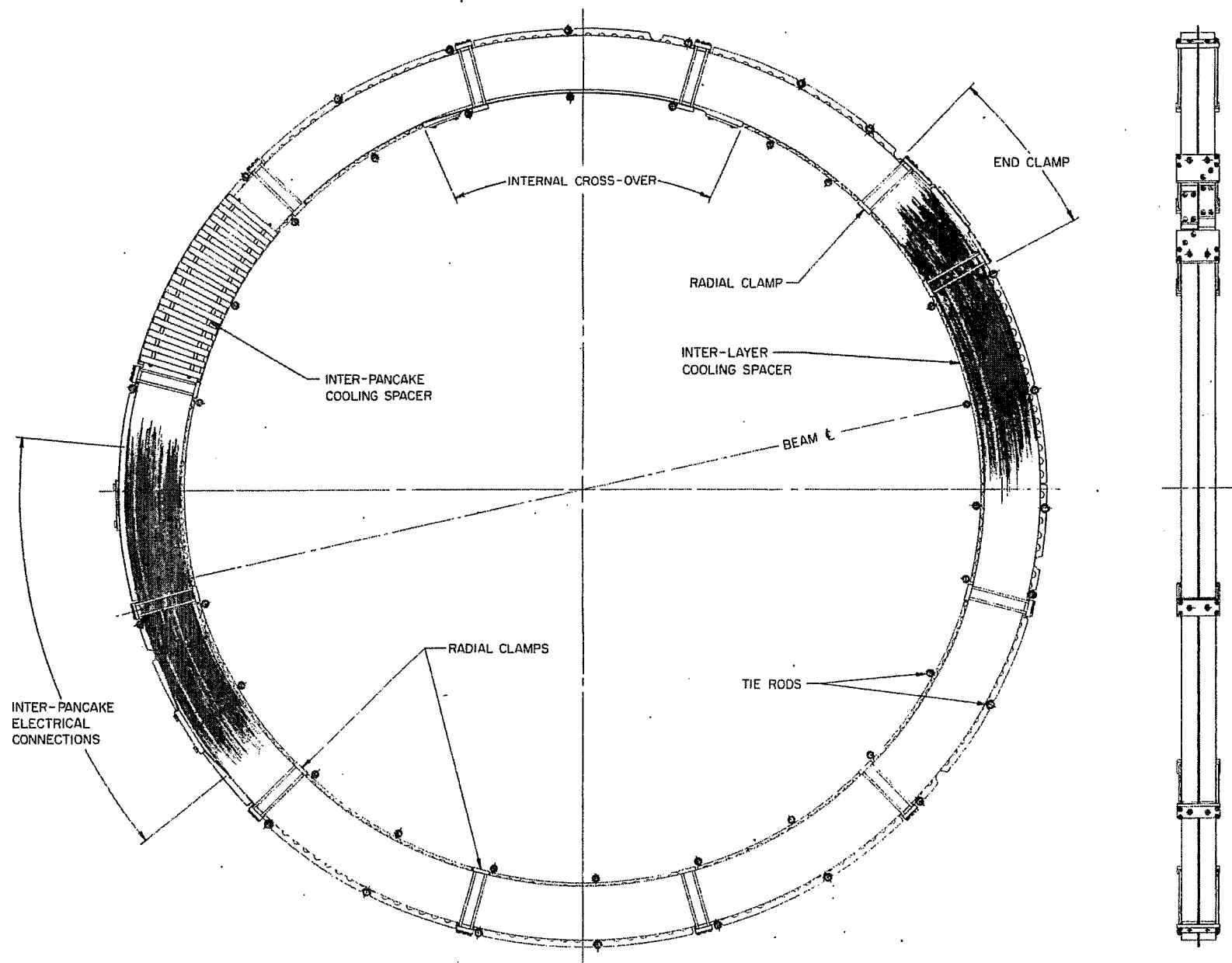


Fig. 13. Plan view of completed pancake.

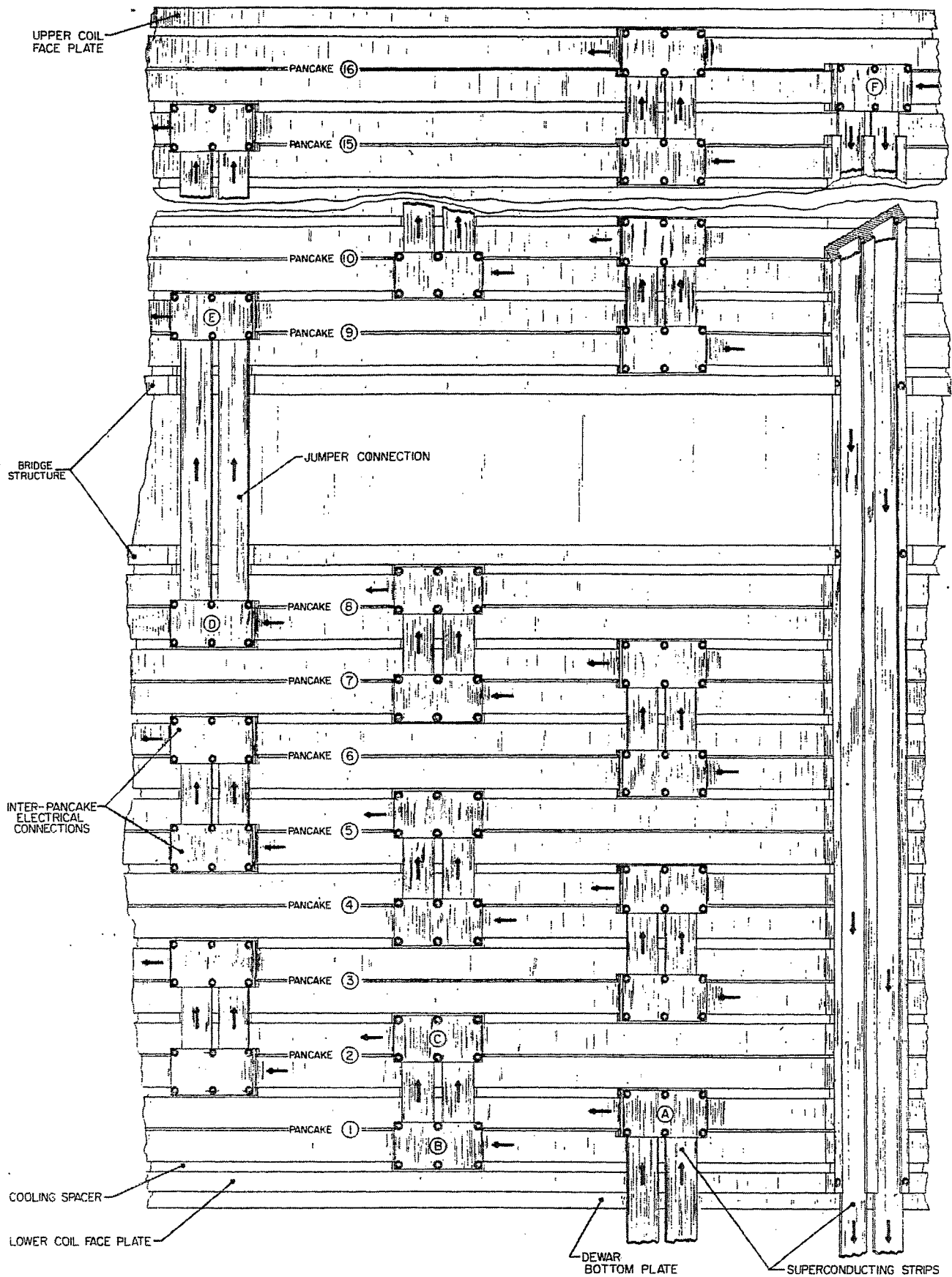


Fig. 14. Inter-pancake electrical assembly.

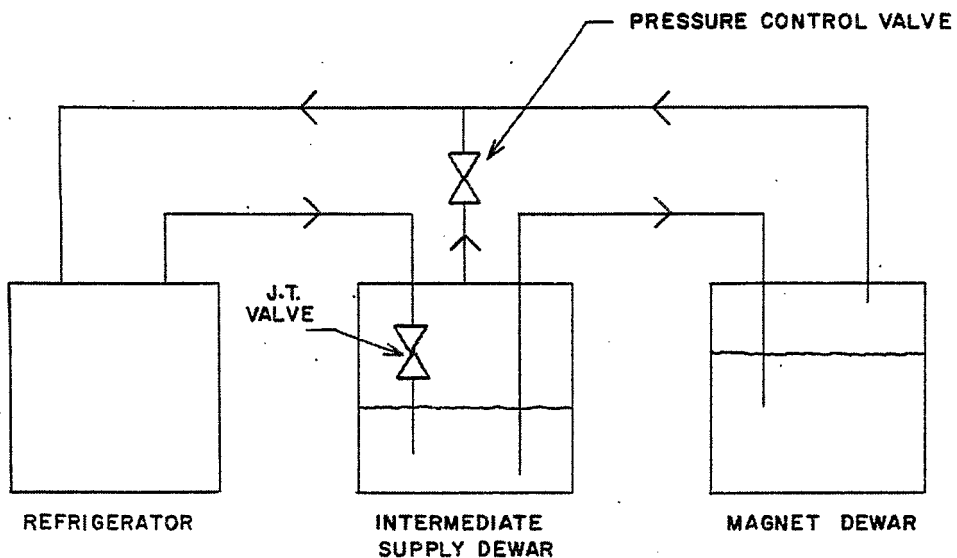


Fig. 15. Simplified refrigerator flow schematic.

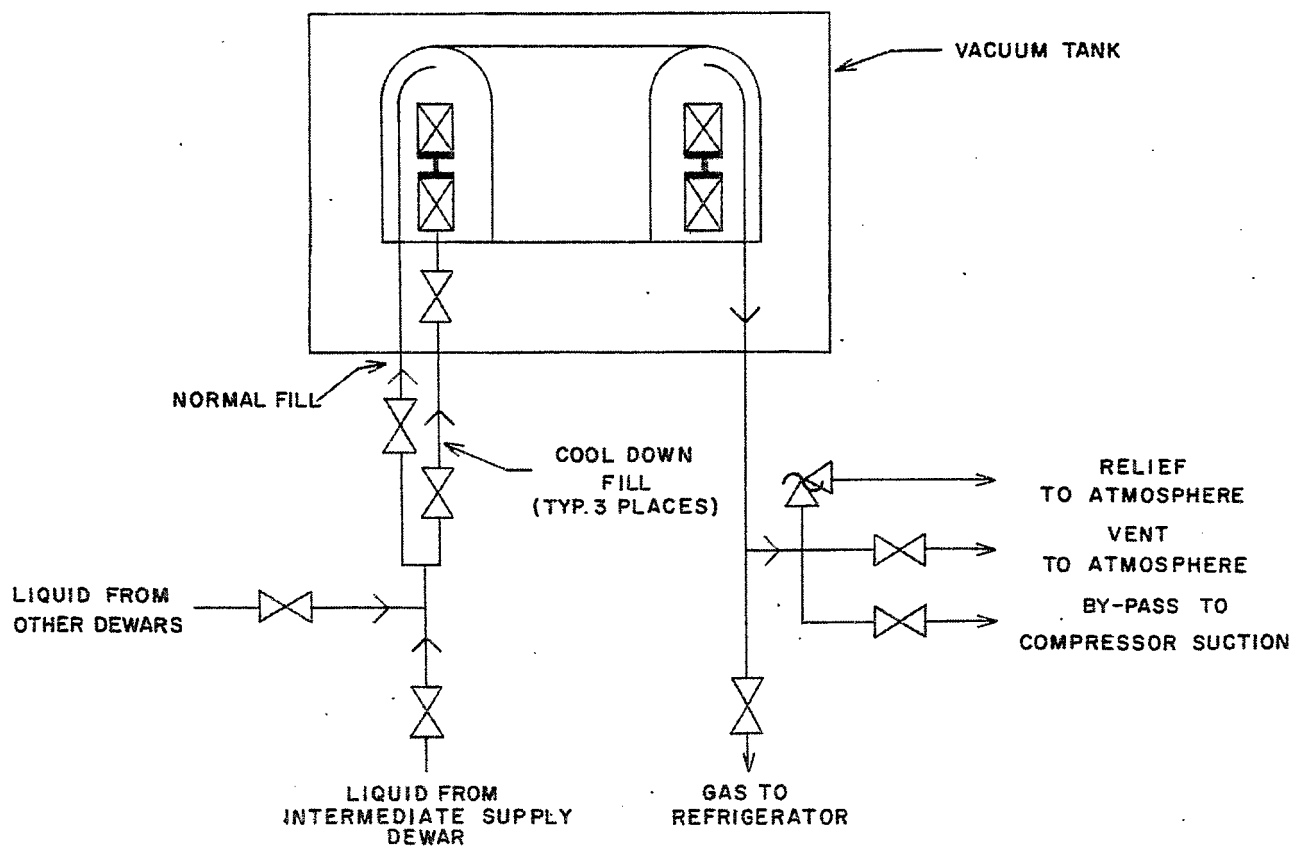


Fig. 16. Magnet cooldown and fill system.

A 70 KILOGAUSS MAGNET FOR THE PROPOSED RUTHERFORD LABORATORY  
1.5 METER DIAMETER HYDROGEN BUBBLE CHAMBER

P.T.M. Clee, D.B. Thomas, and C.W. Trowbridge  
Rutherford Laboratory  
Chilton, Berks., England

I. INTRODUCTION

In January 1967 a design study report<sup>1</sup> was produced on a new hydrogen chamber for the Rutherford Laboratory. Since that date R&D funds have been made available to investigate aspects of the design which are essentially novel. The superconducting magnet is, of course, a major item in the development program, and a considerable proportion of the available effort has been concentrated upon it. Some of the results obtained have recently been reported in print.<sup>2</sup>

Work now being performed or already completed in connection with the superconducting magnet can best be described under four headings: selection of geometry of magnet and surrounding iron shield including proposed winding configuration; selection of stabilized superconductor; full-scale winding trials; and construction of a test magnet from full-size stabilized superconductor.

II. SELECTION OF PARAMETERS FOR THE SUPERCONDUCTOR MAGNET

The physics specification for the High Field Chamber (HFC) calls for a reasonably uniform magnetic field of 70 kG over the fiducial volume of the chamber, this being a cylindrical region 1.5 m diameter by 1 m deep. Particle beam entry across the median plane of the fiducial volume requires the field to be provided by a pair of coils separated sufficiently to allow entry channels of at least 10 cm height and 50 cm width.<sup>3</sup>

A general idea of the magnet-bubble chamber system can be obtained from Fig. 1. The latest dimensions of the evolving design of magnet coils are given in schematic form in Fig. 2 and the principal parameters are listed in Table I. The proposed winding configuration is shown in Fig. 3. Copper-stabilized niobium-titanium superconducting strip of dimension 50 mm by 4 or 5 mm is interwound with a cooling strip, interturn insulation and stainless steel reinforcing strips.

The cooling strip, as conceived at present, allows cooling of about 75% of one face of the conductor and is to be manufactured by spot-welding a regular pattern of stainless steel buttons of about 6 mm diameter and 1 or 2 mm thickness to a stainless steel backing strip 50 mm wide by 1 mm thick. This backing strip serves as part of the necessary reinforcement to carry hoop stresses. A sample length of cooling strip of this type is shown in Fig. 4. The economics of producing such a strip in quantity

- 
1. Design Study for a High Magnetic Field Hydrogen Bubble Chamber for Use on Nimrod. Rutherford Laboratory Report RHEL/S/101 (1967).
  2. Progress Report for 1967 on the Research and Development Program for the High Field Bubble Chamber, Rutherford Laboratory Report AP/DS/HFC/10 (1968).
  3. Proceedings of the Study Week on Optics and Beam Entry and Exit Problems for the High Field Bubble Chamber, Rutherford Laboratory Report AP/DS/HFC/9 (1967).

TABLE I  
Main Parameters of Magnet Coils

Nominal central field	70 kG
Computed central field with chosen parameters (excluding contribution of surrounding iron shield)	71.4 kG
Computed peak field	80.6 kG
Total ampere turns	$2.16 \times 10^7$
Inductance	11.9 H
Stored energy	$3.4 \times 10^8$ J
Over-all current density	1400 A/cm <sup>2</sup>
Operating current	7500 A
Number of single pancakes per coil	18
Number of turns per pancake	80
Thickness of pancake	50 mm
Thickness of interpancake insulation	10 mm
Thickness of each turn (including conductor, cooling strip, insulation and reinforcement strip)	9 mm

(which would involve the use of a custom-built machine) have not yet been fully investigated. Initial studies are sufficiently promising for the selection of this type of cooling strip for a test magnet now under construction.

In the HFC coils, with 75% of one face and 75% of both edges of the conductor exposed to liquid helium, full stabilization requires a heat transfer coefficient of about 0.25 W/cm<sup>2</sup>/°K. This figure is calculated on the basis of a conductor of cross section 50 mm by 5 mm, a resistivity at 80 kG of  $5 \times 10^{-8}$  Ω·cm and an operating current of 7500 A.

Additional interwound stainless steel strips have also been included to carry the hoop stresses generated in the coil. The total thickness of strip required (including cooling strip backing) has been determined to be 3 mm after a stress analysis of the most highly stressed pancake in the coil. A computer program which solves the differential equations for stresses in a nonhomogeneous cylindrical pancake has been devised. Since each pancake employs a multiple element winding with several strips of different material interwound (including cooling channels) the problem is treated numerically. A finite element method is used which ensures a balance of forces at each station. Nonlinear stress-strain curves can be handled allowing elastic-plastic deformation to be included. The principal stresses are tabulated as output together with the strain and displacements.

The HFC coil geometry is such that the radial stress is compressive, ensuring the validity of the above method. The dependence of radial stress on coil geometry has been discussed elsewhere.<sup>4</sup>

---

4. A.J. Middleton and C.W. Trowbridge, Proc. 2nd Intern. Conf. Magnet Technology, Oxford, 1967, p. 140.

The results of these and other force calculations for the proposed coils are shown in Table II.

TABLE II  
Stresses and Forces in HFC Coils

Maximum hoop stress in stainless steel reinforcement	21.5 kg/mm <sup>2</sup>
Maximum hoop stress in conductor	2.93 kg/mm <sup>2</sup>
Maximum radial (compressive) stress	0.93 kg/mm <sup>2</sup>
Maximum axial (compressive) stress	1.80 kg/mm <sup>2</sup>
Maximum hoop strain	0.11%
Total attractive force between pair of coils	8680 tons

Additional hoop forces which arise from differential contraction between the conductor and the stainless steel reinforcing strip on cooling from 300°K to 4°K must also be considered. Assuming that the conductor is pure copper rather than superconducting composite, the differential contraction produces a tensile stress of 2.5 kg/mm<sup>2</sup> in the copper (4 mm thickness) and a compressive stress of 3.3 kg/mm<sup>2</sup> in the stainless steel (3 mm thickness). Stresses due to differential contraction are thus much smaller than those due to current-field interaction.

The variation of hoop stress with radius in the most highly stressed pancakes in each coil is shown in Fig. 5. Only stresses due to the electromagnetic forces are included. The stress levels in both the stainless steel reinforcing strip and the conductor are a maximum at the inside edge of the coil where the peak field of 80 kG occurs and fall off as the radius increases.

It should prove possible by pre-tensioning both the copper and the stainless steel at the coil winding stage to produce a locked-in distribution of hoop stress in the windings, which, when added to that due to electromagnetic forces, results in a somewhat more uniform stress distribution across a particular pancake. The proposed coils are rather suitable for this type of treatment for the ratio of external to internal diameter is almost 2.

Surrounding the superconducting magnet, an iron shield is positioned to protect ancillary equipment from the effects of stray magnetic fields. (The shield also serves as part of the support structure for the bubble chamber itself.) An optimization of the geometry of the iron shield has been carried out so as to provide adequate shielding using a minimum weight of iron. A computer program TRIM, which originated at the Lawrence Radiation Laboratory in Berkeley, has been modified to solve this type of problem. Numerous different shapes of iron configuration have been investigated. One example is shown in Fig. 6. As might be expected with a 70 kG coil, the presence of an iron shield somewhat distant from the coils makes very little difference to the magnitude of the central magnetic field — only a few percent.

### III. SELECTION OF STABILIZED SUPERCONDUCTOR

A research contract was placed in October 1967 by the Rutherford Laboratory with the one British manufacturer of co-processed niobium-titanium in copper, Imperial Metal Industries (Kynoch), Ltd. One of the objects of this contract was the development of a conductor suitable for the HFC. Numerous samples have been produced and

measurements of their electrical and mechanical properties carried out. No test facility is available in the U.K. which is capable of measuring the critical current of conductors of the size required for the HFC coils. Tests have therefore been confined to samples of much smaller section and current rating, or to single filaments cut from larger samples. Fields up to 45 kG are available at the Rutherford Laboratory at present. An 80 kG 3 cm bore split pair of niobium-tin coils should become operational later this year. This new magnet will be mounted with its axis horizontal in its cryostat. Each sample under test will be aligned vertically in the 2 cm gap between the coils. With this arrangement single filaments or groups of filaments cut from full-sized conductor samples can have their critical currents measured at all fields up to 80 kG. Furthermore, the chosen arrangement permits rotation of the sample about its longitudinal axis with respect to the applied transverse magnetic field without removal of the sample from the cryostat or de-energization of the magnet. (The sample will form one straight leg of a hairpin with the return current flowing through a length of superconductor of much higher critical current, this being the other permanent leg of the hairpin.)

Anisotropy in critical current in rectangular samples of composite superconductor rolled from the round has been noted, and the extent to which this occurs in the selected samples can be speedily determined for any angle between the applied magnetic field and the wide dimension of the conductor. The evidence already existing that the relationship connecting critical current and this angle is elliptical in form will be extended or modified. The variation of anisotropy with absolute magnetic field value at fixed angular orientations will also be determined. The variation of anisotropy with field for one of the samples measured in the existing 45 kG magnet is shown in Fig. 7. An 80 kG test facility of the modest size described should allow large numbers of samples to be evaluated quickly, and could indeed be used for quality control of conductor for the bubble chamber itself.

Resistivity tests on numerous copper samples have also been carried out at 4°K (without magnetic field) and these indicate that better resistance ratios can be obtained from Electrical Tough Pitch copper (ETP) than with Oxygen Free High Conductivity copper (OFHC). Consistent resistance ratios of greater than 250:1 can be obtained with ETP copper and figures as high as 600:1 have been achieved on occasion.

Facilities also exist at the Rutherford Laboratory for measuring stress-strain curves, ultimate strengths, etc. at 4°K for superconducting composites, structural materials, welds and joints of various types with applied loads up to 3500 kg. An investigation of the strength of various solders has recently been completed.

It is proposed to join individual lengths of conductor to form a continuous length sufficient for the fabrication of one double pancake of the HFC coils by an explosive welding technique. This has been shown to produce joints of low resistance ( $10^{-9} \Omega$  or less for conductor cross sections of  $0.25 \text{ cm}^2$ ) with good mechanical strength, even after machining the joint down to exactly the same cross section as the conductor itself.

#### IV. COIL WINDING TRIALS

Stress calculations have shown that stainless steel reinforcement of thickness 3 mm is required to support each turn in the highly stressed regions of the coils. A number of thinner strips of the same total thickness may be preferable to a single 3 mm strip to minimize the bending stresses induced in this thick member at the coil winding stage. Furthermore, thinner strips would certainly be easier to wind into a coil.

To establish the relative difficulty of interwinding reinforcing tapes of different thicknesses, either singly or with several in parallel, into a coil of the required

dimensions, full-scale winding trials have been carried out. A further object of these trials was to evaluate the practical engineering problem which would arise in coil winding, and to determine winding tensions, etc.

A standard motorized turntable, 8 ft square, from an Asquith Boring Machine, was temporarily converted to a coil winding machine. A general view of the winding jigs and fixtures around the winding table is shown in Fig. 8. Three 50 mm by 1 mm stainless tapes are shown being interwound with 50 mm by 5 mm annealed copper. In this final winding test 18 composite turns were added, free ends were then secured, and the resulting coil was removed from the machine. Figure 9 shows the completed coil of 18 turns.

In earlier winding operations 0.5 mm, 1 mm and 3 mm thick steel tapes were tried in various formations. No cooling strip was available and no interturn insulation was incorporated. For simplicity, winding tensions were applied by squeezing the conductor or reinforcement strip between "Tufnol" blocks with a known force and reliance placed on friction to produce a constant tension. More sophisticated tensioning systems will probably be required for the final coils.

The minimum tension required to produce a tightly wound coil was determined for the different strips, and this varied between about 20 kg for the 0.5 mm thick steel tape ( $0.8 \text{ kg/mm}^2$ ) to 150 kg for both the 3 mm thick steel and 5 mm thick copper ( $1 \text{ kg/mm}^2$  and  $0.6 \text{ kg/mm}^2$ ). In some tests tensions were increased to the equivalent of  $4 \text{ kg/mm}^2$  without noticeable change in the tightness of wind. The final thickness of each coil was compared with the value calculated from the known individual strip thicknesses. The difference in corresponding figures never exceeded 3%. As it was not possible to slide a fine feeler gauge between turns, it is concluded that this 3% additional build-up was due to known factors such as edge burrs on the stainless steel tapes, etc.

The general conclusion from the winding trials is that little difficulty should be experienced in winding conductors and steel support strips of the required thickness at the required diameters. Indeed, the whole winding operation proved much easier than had been anticipated.

## V. RACoon TEST COIL

A test magnet made from full-size bubble chamber conductor is at present under construction. Coil winding should be completed in September of this year. This magnet, code named RACoon, uses approximately the same winding configuration as the HFC magnet, and will thus be used to check the performance of the selected stabilized superconductor in a thermal and magnetic environment similar to that which will prevail in the large coils. This test coil, being for experimental use only, need not be built with such a high safety margin on stability. Indeed the prime purpose in building such a coil is to determine quantitatively the stability margin of the proposed design of the large coils.

The conductor specified for RACoon is to carry 7500 A at 80 kG — the same as the HFC coils. Conductor dimensions have been chosen at 50 mm by 3 mm to be less conservative than the HFC coils (50 mm by 4 or 5 mm). A cooling channel thickness of 1.5 mm has been adopted (cf. HFC coils 1 to 2 mm thickness). Because of the small diameter of the test magnet, no stainless steel reinforcement of the coils other than that provided by the cooling strip itself is required. The over-all current density for RACoon is  $2600 \text{ A/cm}^2$ , almost twice that of the HFC magnet ( $1400 \text{ A/cm}^2$ ).

The principal dimensions of RACoon are given in Fig. 10. The magnet comprises six double pancake coils. Initially all these double pancakes will be identical in



construction, but it is envisaged that additional double pancakes will be manufactured and substituted at a later stage. These special pancakes will test different conductors or winding configurations or perhaps have many explosively welded conductor joints, etc.

At the specified operation current the RACOON coil alone will provide a central field at 26 kG and a peak field of 27 kG. Since the conductor is rated at 7500 A at 80 kG, it should also be capable of carrying more than 15 000 A at 50 kG. It is thus proposed to provide a 15 000 A power supply to energize RACOON to fields up to 52 kG. At this upper limit, the magnet will be only partially stabilized (about 1 W/cm<sup>2</sup>) so that it should prove possible to study the effect of flux jumps in wide conductors under somewhat extreme conditions. The main parameters of RACOON are given in Table III.

The dimensions of the RACOON coil have been carefully selected so that it can operate as an insert coil to the CERN test facility BRARACOURCIX. Under these conditions, with normal operating currents in both BRARACOURCIX and RACOON, peak fields of over 80 kG should be achieved. It is hoped to arrange such a joint test late this year or in early 1969. (In Fig. 10, the outer chain-dotted regions represent the BRARACOURCIX coils.)

If all this proves possible, the RACOON coil will have duplicated the thermal and magnetic environment to be expected in all regions of the proposed HFC coils.

TABLE III  
Main Parameters of RACOON Coil

Internal diameter of windings	135 mm
External diameter of windings	304 mm
Length of coil	655 mm
Number of double pancakes	6
Number of turns per pancake	16
Total number of turns	192
Specified conductor current at 80 kG	7500 A
Magnetic field produced by coil	
1. With 7500 A excitation	
Central field	26 kG
Peak field	27 kG
Over-all current density in windings	2640 A/cm <sup>2</sup>
2. With 15 000 A excitation	
Central field	52 kG
Peak field	54 kG
Over-all current density in windings	5280 A/cm <sup>2</sup>
3. With 7500 A excitation as an insert in BRARACOURCIX (1000 A)	
Central field	~ 84 kG
Peak field	~ 85 kG

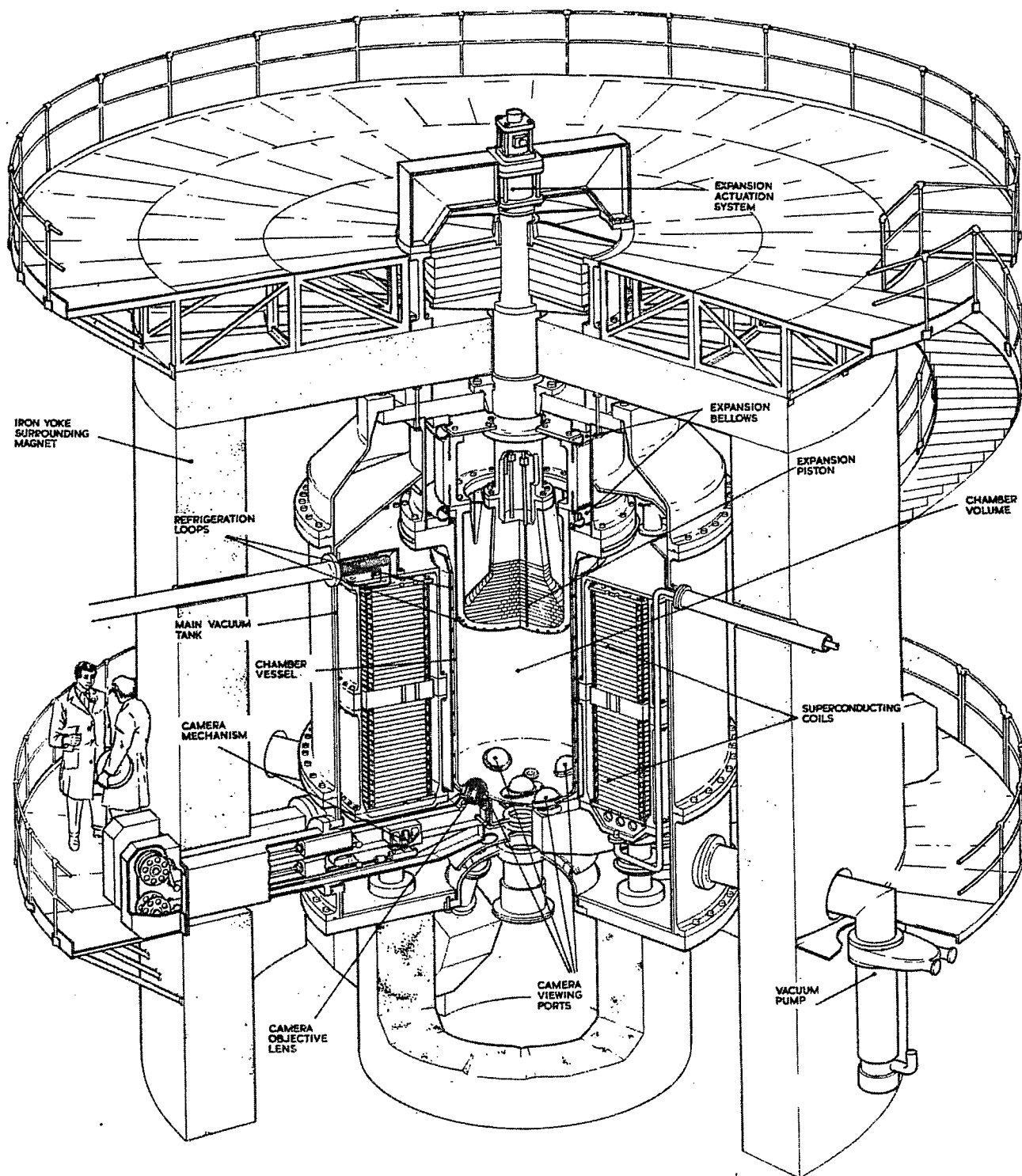


Fig. 1. Artist's impression of proposed High Field Chamber.

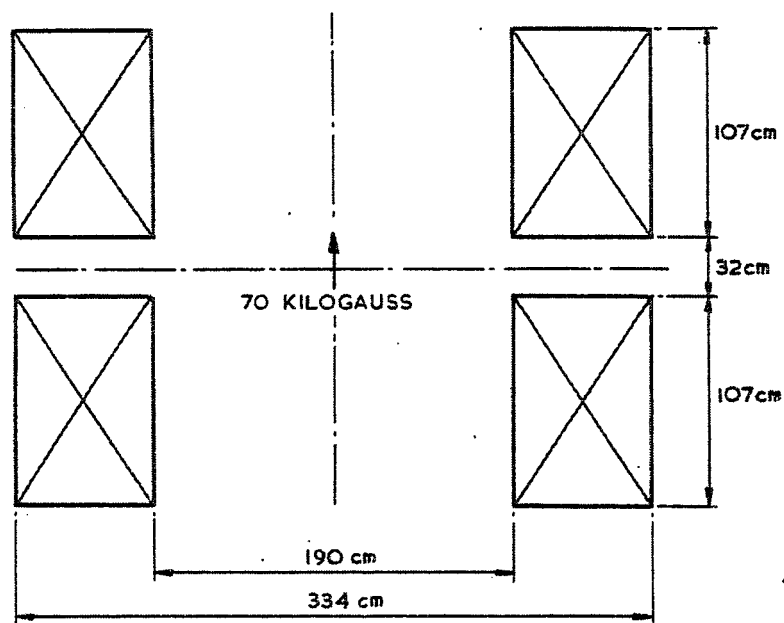


Fig. 2. Principal dimensions of High Field Bubble Chamber magnet coils.

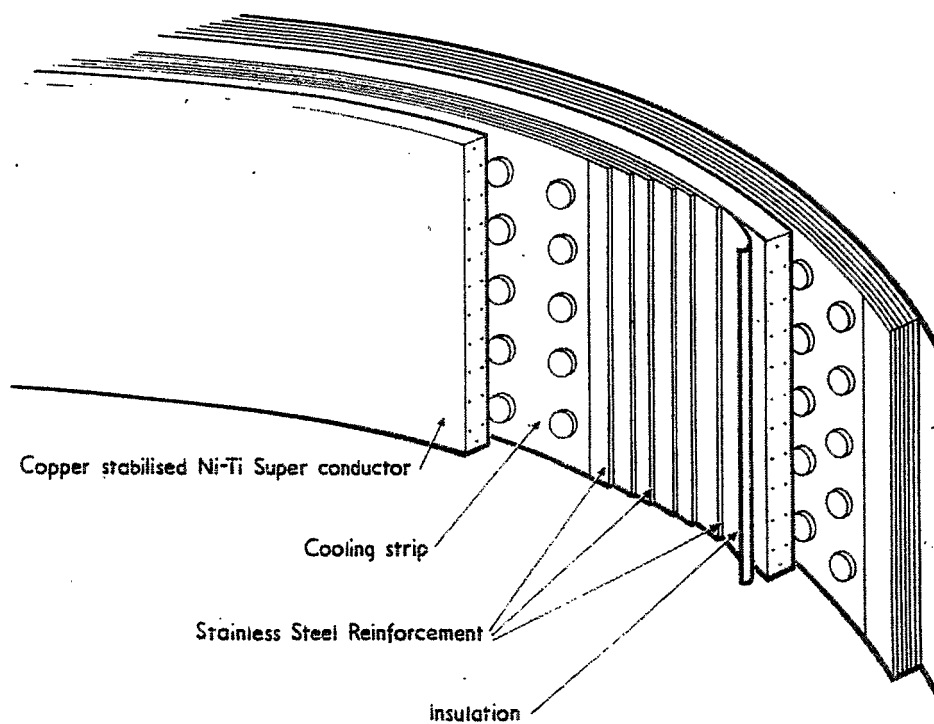


Fig. 3. Proposed winding configurations for superconducting coils of High Field Bubble Chamber.

Conductor	50 mm x 4 or 5 mm
Cooling channels	50 mm x 2 or 1 mm (75% of one conductor face exposed)
Stainless-steel reinforcement	50 mm x 3 mm total thickness
Insulation	50 mm x 0.2 mm

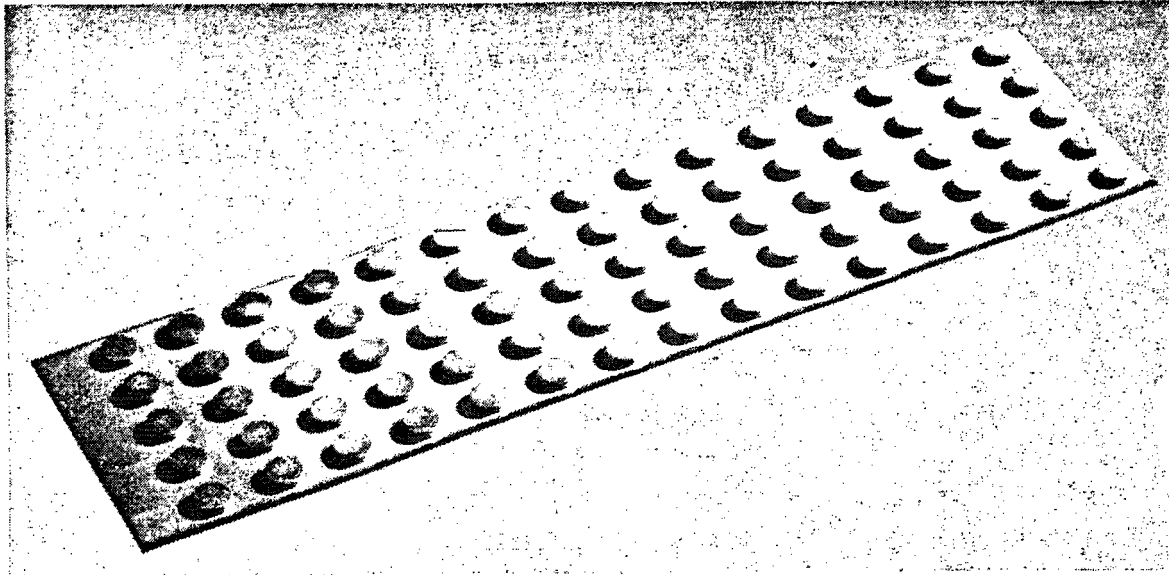


Fig. 4. Stainless-steel cooling strip.

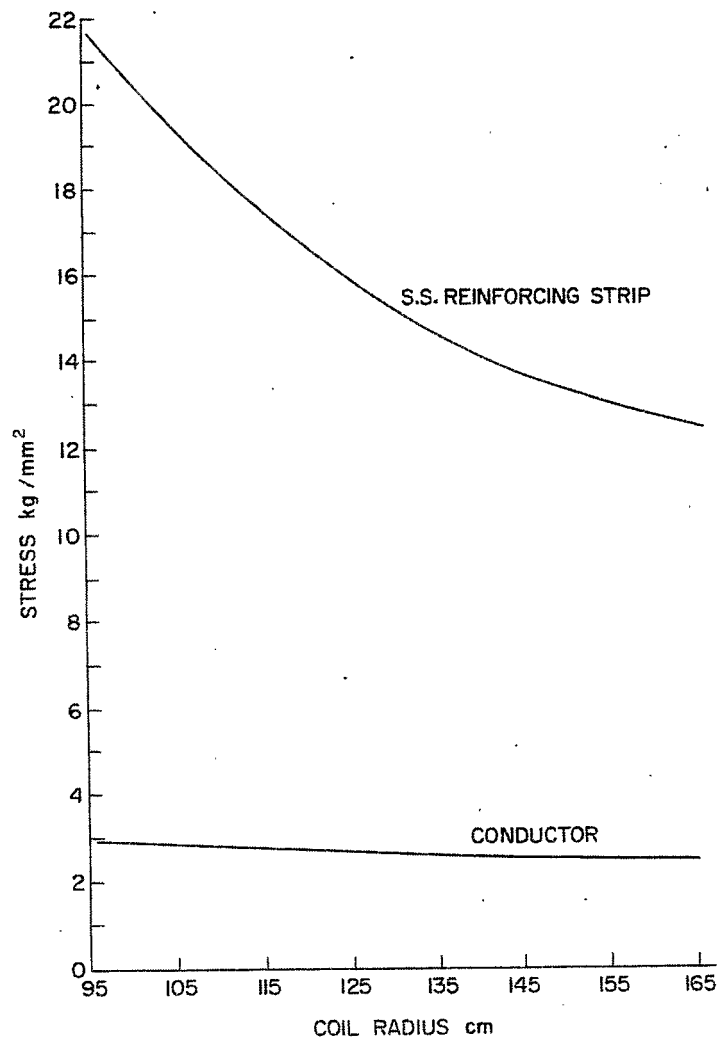


Fig. 5. Hoop stresses vs coil radius for most highly stressed pancake in HFC coil.

WEIGHT OF SCREEN=926.5 TONS

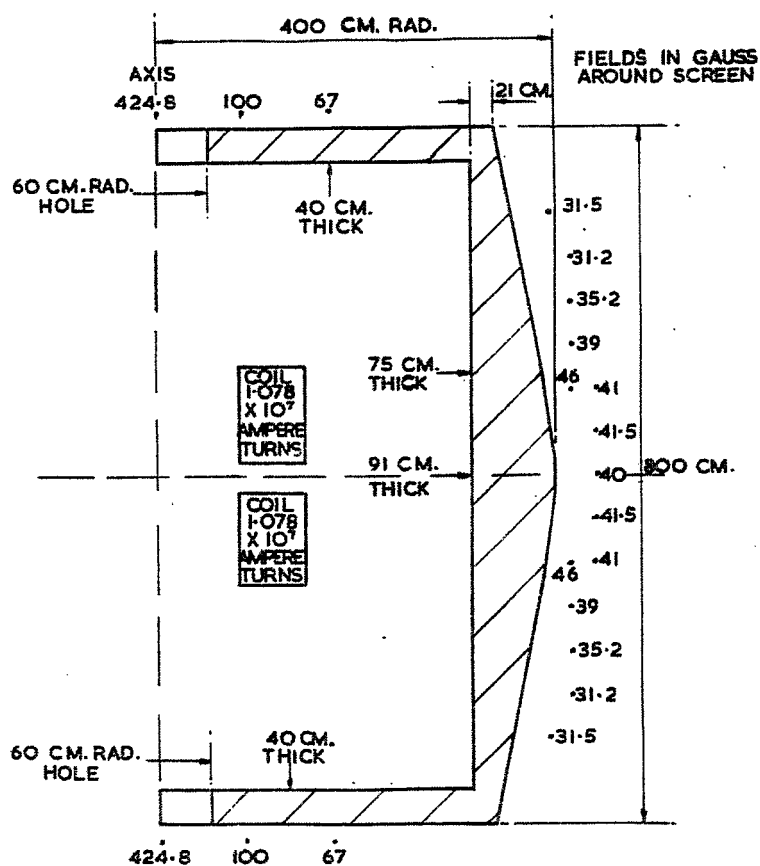


Fig. 6. High Field Bubble Chamber screen No. 5A.

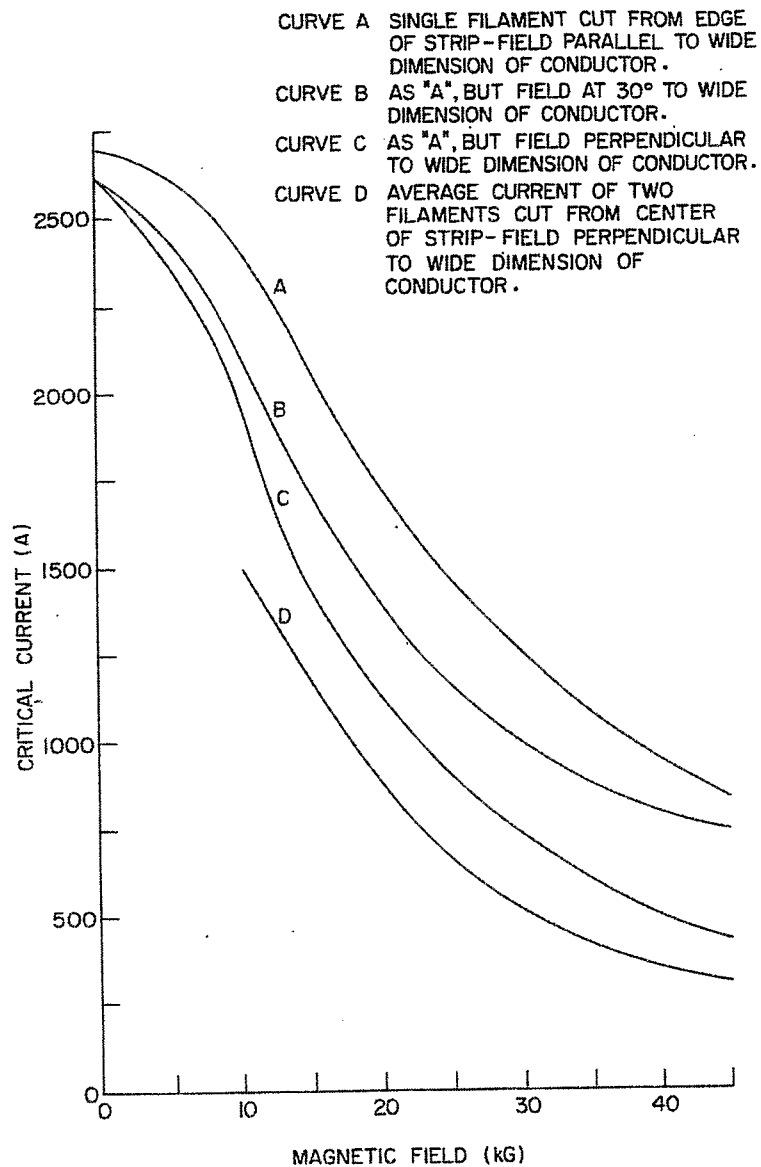


Fig. 7. Anisotropy test of I.M.I. Niomax-M sample BC4/1D.

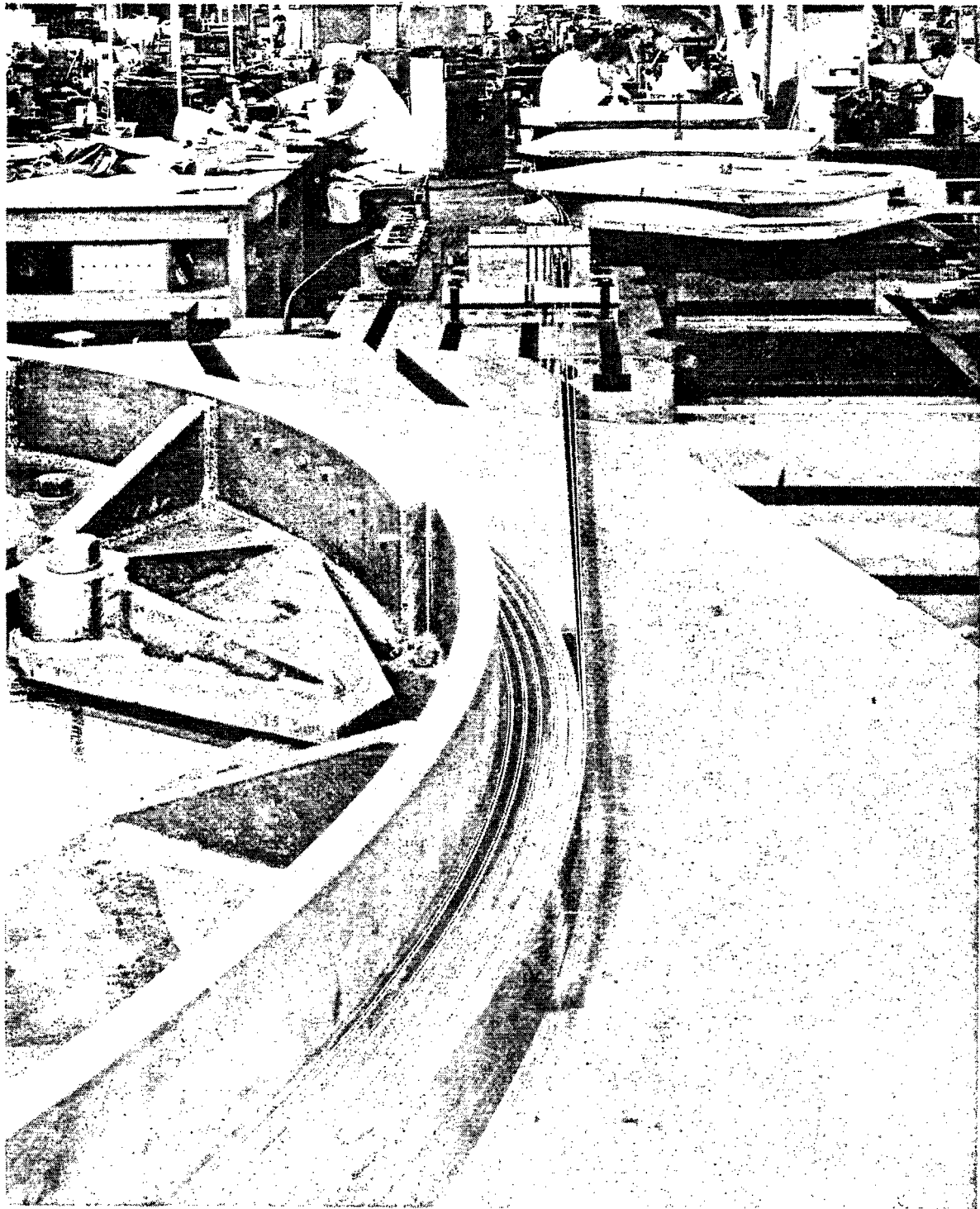


Fig. 8. Testing winding of full-scale single pancake.

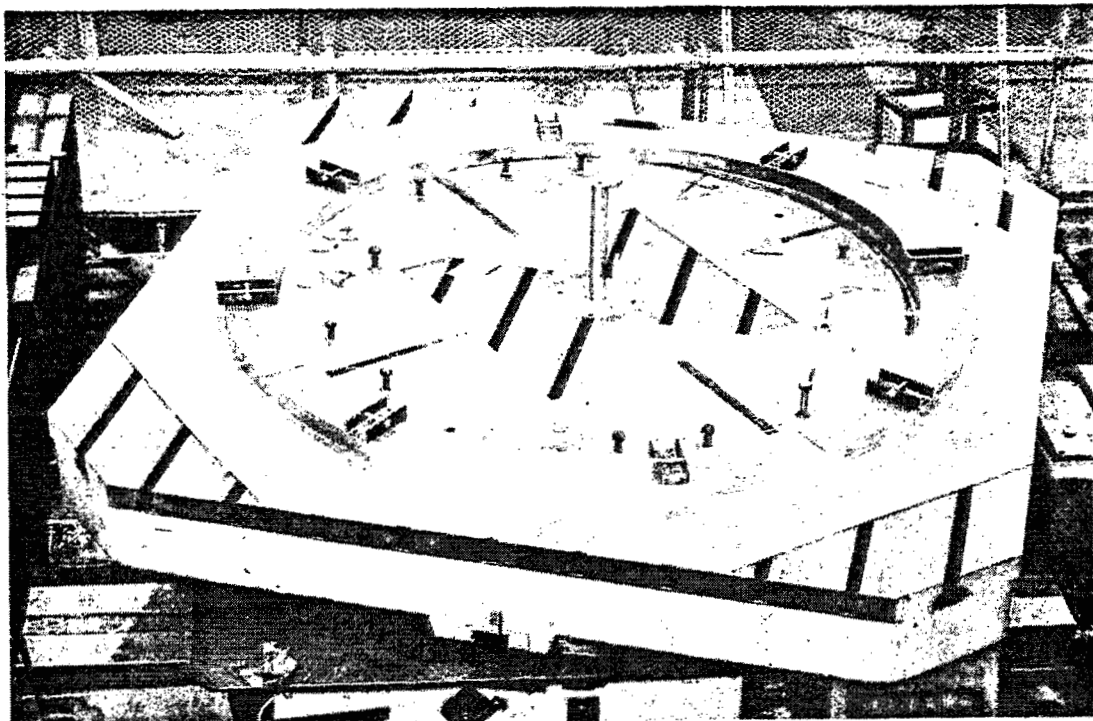


Fig. 9. Completed test pancake.

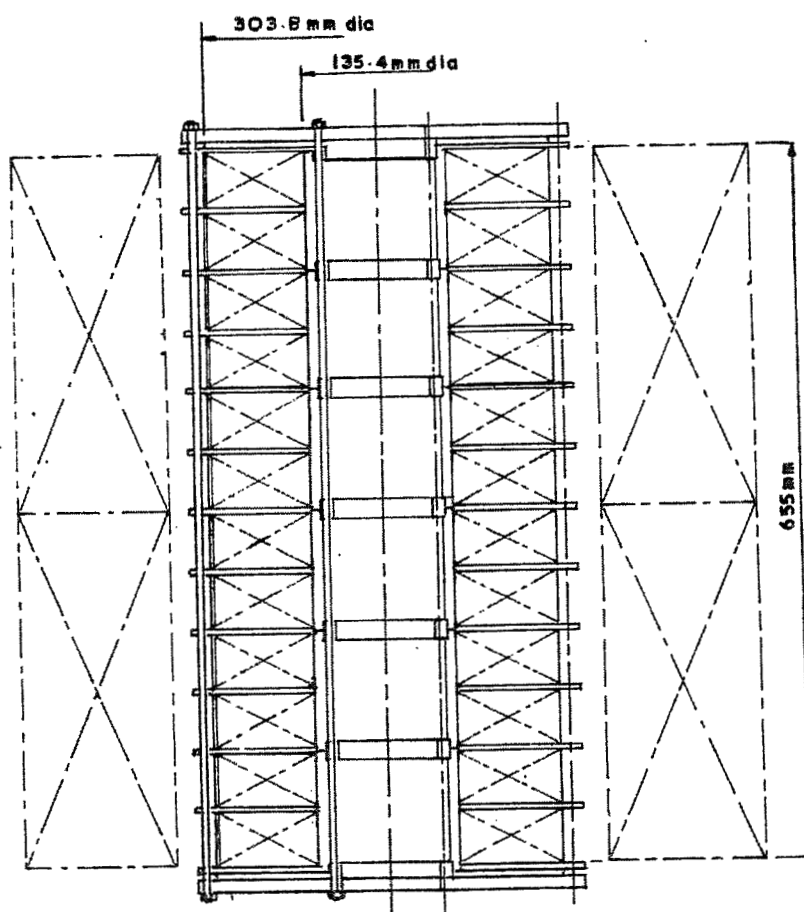


Fig. 10. Cross section of RACON coil.



# DEVELOPMENT PROGRAM FOR THE MAGNET OF THE EUROPEAN 3.7 METER BUBBLE CHAMBER (BEBC)

CERN Study Group for the Large European Bubble Chamber

Presented by

F. Wittgenstein  
CERN, Geneva, Switzerland

## I. INTRODUCTION

In order to define major parameters and to gain some operational experience with superconducting magnets, a magnet development program has been established. This program should lead to the final design of the BEBC magnet.

Figures 1 and 2 give some general view of the entire project.

The magnet has been designed to produce a magnetic field of 3.5 T in the center of the chamber. Consisting of two coils separated by a gap and surrounded by an iron stray field shield, it has at the present time the following characteristics:

Total number of ampere turns	$2.05 \times 10^7$
Rated current (copper stabilization)	8 kA
(aluminum stabilization)	10 kA
Axial peak field on the conductor	5.1 T
Radial peak field on the conductor	3.8 T
Stored magnetic energy	750 MJ

## II. MODEL MAGNET

The first experimental device which has been put into operation was a 1:20 model of the BEBC magnet which has been used to determine the stray field around the chamber and the various forces acting on the coils for different shield geometries.

With an iron shield of about 1800 tons, composed of two pole pieces of 500 mm thickness and a cylinder of 12 m diameter and 340 mm thickness, the stray field will be reduced by a factor of 6 above and below the pole pieces and by a factor of 1.25 around the shielding cylinder. The stray field distribution is presented in Fig. 3.

The lateral force caused by the presence of an iron neutrino filter will amount to about 18 tons and the attraction between the coils and the pole plates will amount to about 800 tons.

## III. SHORT SAMPLE TEST FACILITY

To test the conductors proposed by different manufacturers for the winding of the BEBC magnet, a test facility named BRARACOURCIX was developed. The general lay-out is shown in Fig. 4. This facility consists of a split coil magnet housed in a ring-shaped cryostat, and a short sample stretching device suitably arranged in a central separate Dewar. The stretching device is shown in Fig. 5. It is made of a stainless-steel

bellows which can be pressurized by helium. The maximum force developed by the pneumatic-hydraulic system is 9000 kg, with a maximum stroke of 1.5 mm.

The magnet has the following general characteristics:

Inner diameter of the first layer	400 mm
Free bore of central Dewar	363 mm
Total height of the assembled coils	699 mm
Total ampere turns	$4.14 \times 10^6$
Rated current	1000 A
Total inductance	4.1 H
Central field	6 T
Stored energy	2.05 MJ
Current density of the top coil (Al-stabilized conductor)	4900 A/cm <sup>2</sup>
Current density of the bottom coil (Cu-stabilized conductor)	4420-5180 A/cm <sup>2</sup>

On short samples of the coil conductors the following results have been obtained at 6.6 T:

<u>Copper-stabilized conductor</u> (cross section $10 \times 1.5 \text{ mm}^2$ )	
Resistivity	$3.3 \times 10^{-8} \Omega \cdot \text{cm}$ at 4.2°K
Recovery current	1200 A
<u>Aluminum-stabilized conductor</u> (cross section $5 \times 3 \text{ mm}^2$ )	
Resistivity	$1.12 \times 10^{-8} \Omega \cdot \text{cm}$ at 4.2°K
Recovery current	1350 A

The resistances of all joints on either type of conductor are better than  $3 \times 10^{-8} \Omega$ .

The measuring arrangement is represented in Fig. 6. It also shows the 2000 A, 5 V power supply and the dumping resistors.

Some typical recordings of the differential voltage signals are given in Fig. 7. These signals have been measured with outside dumping resistors of  $2 \times 0.250 \Omega$ .

When exposed to the magnetic field and stretched by the above-mentioned system, the short samples are fed by a power source delivering a maximum current of 16 000 A at 4 V.

Figure 8 illustrates the lay-out of the above-described test system.

Figure 9 shows short samples from different suppliers in their final test form.

#### IV. GEOMETRY OF BEBC MAGNET

For the time being the coil parameters are envisaged as follows:

Number of coils	2
Number of pancakes per coil	14
Number of turns per pancake	
a) with copper stabilization	91
b) with aluminum stabilization	72
Inner diameter of the first turn	4720 mm
Over-all current density with copper stabilization	1030 A/cm <sup>2</sup>

The configuration of the pancake winding inspired by the development at Brookhaven for the 7-ft Bubble Chamber is shown in Fig. 10.

Models of the chosen arrangement are at present prepared in order to check the thermal behavior of the system. Results will be reported later.

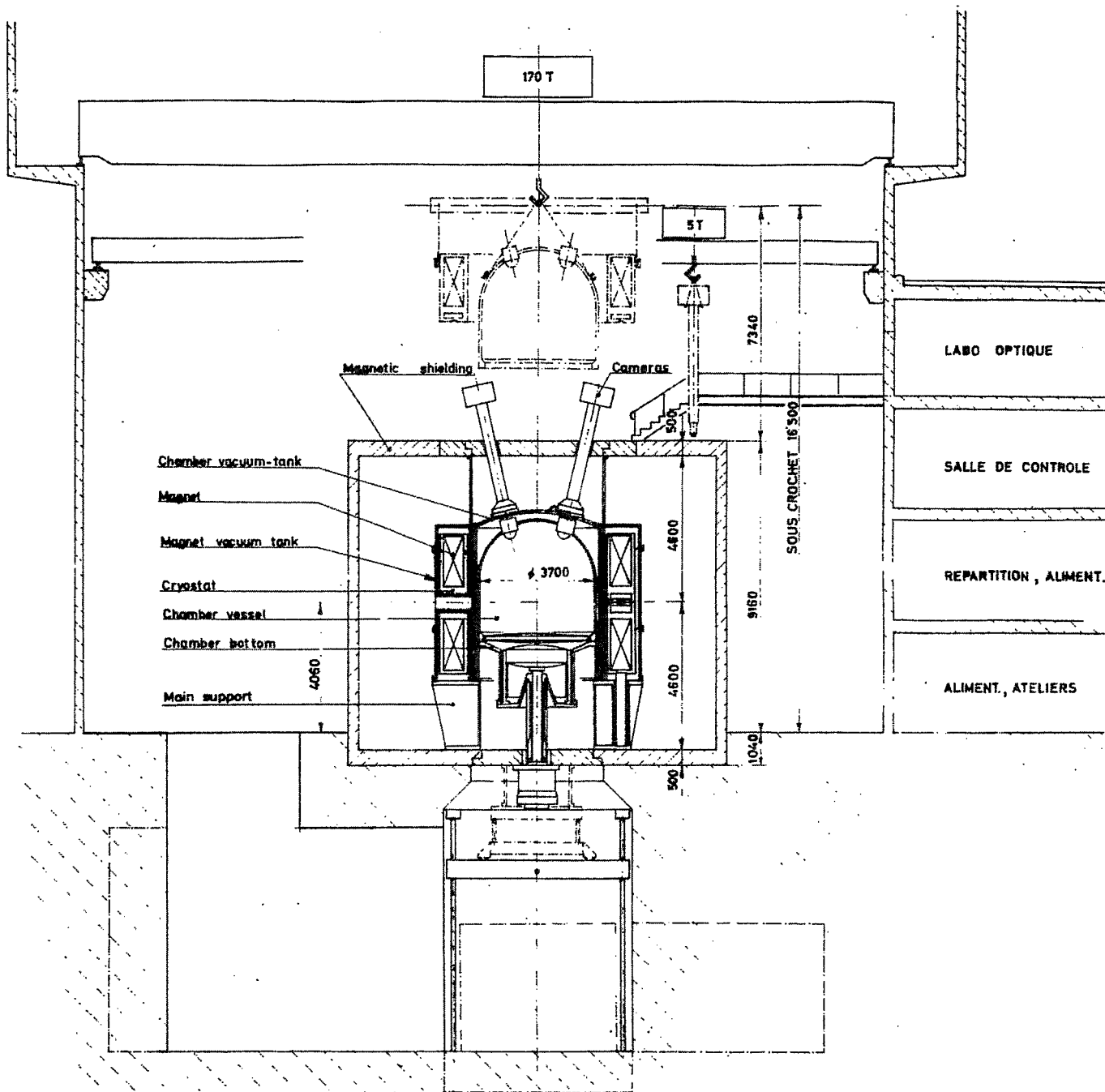


Fig. 1. General assembly of the Bubble Chamber.



# STRAY FIELD (in Gauss)

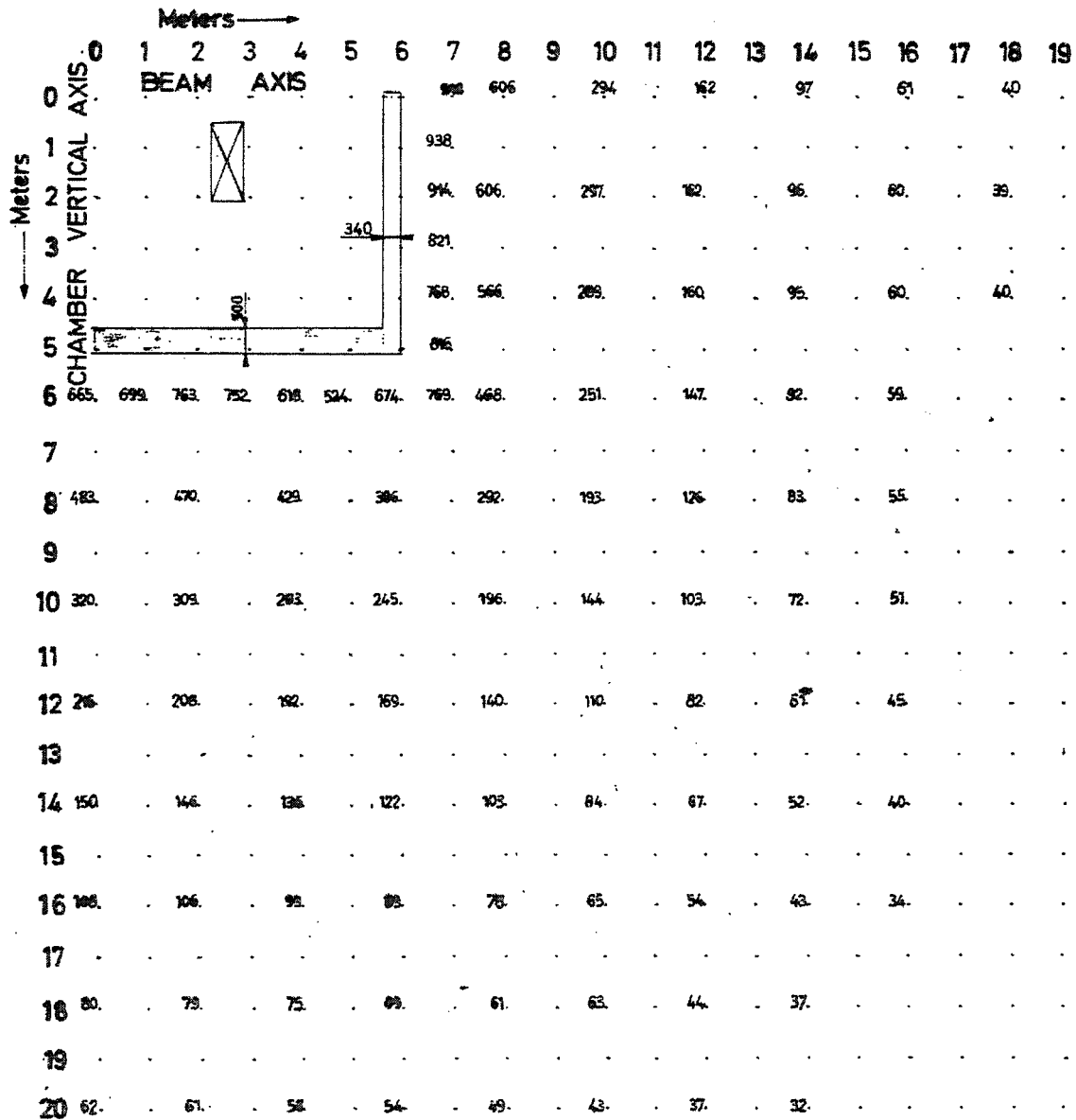


Fig. 3. Stray field around the rion shield.

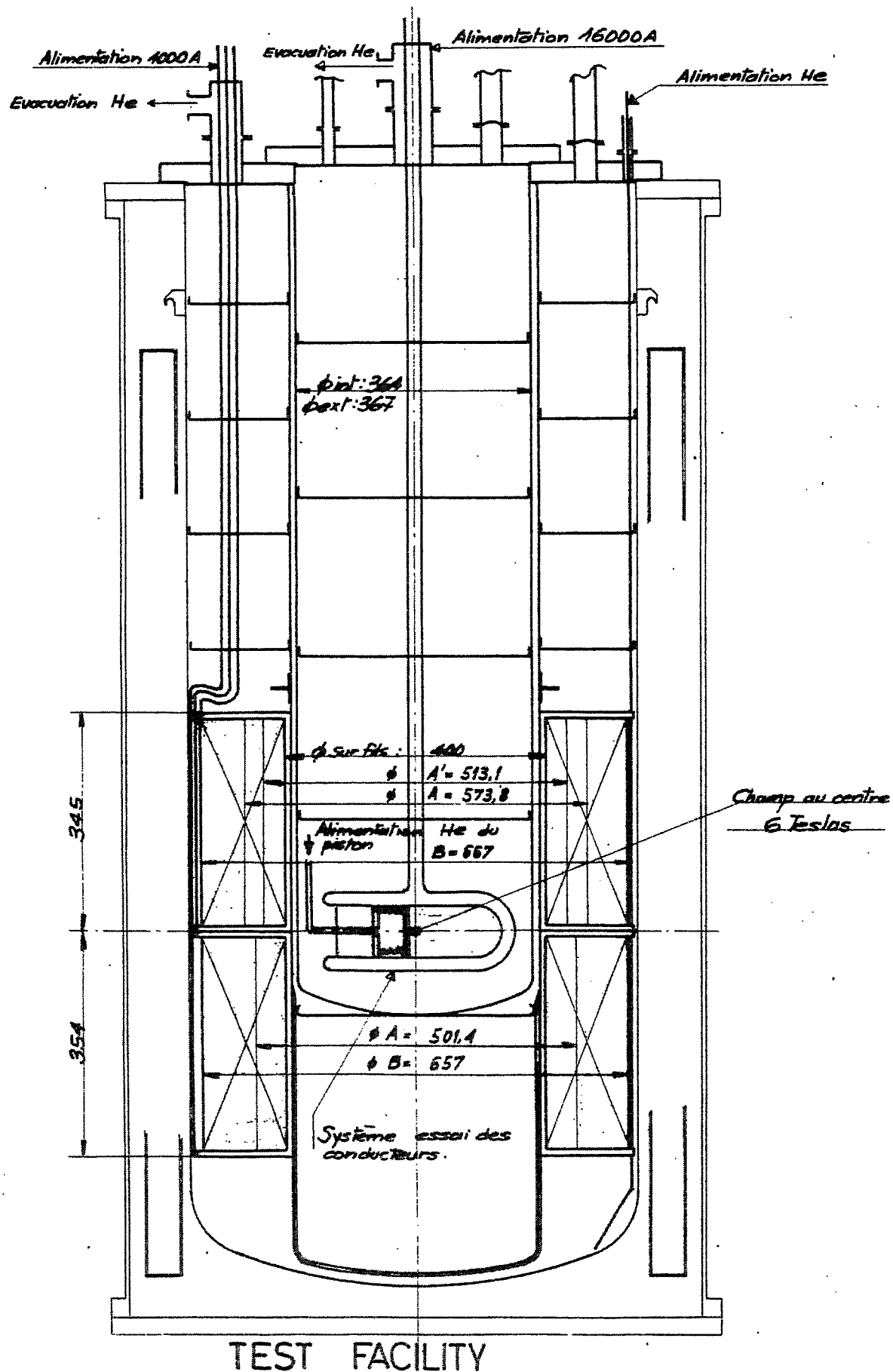


Fig. 4. Lay-out of the BRARACOURCIX test facility.

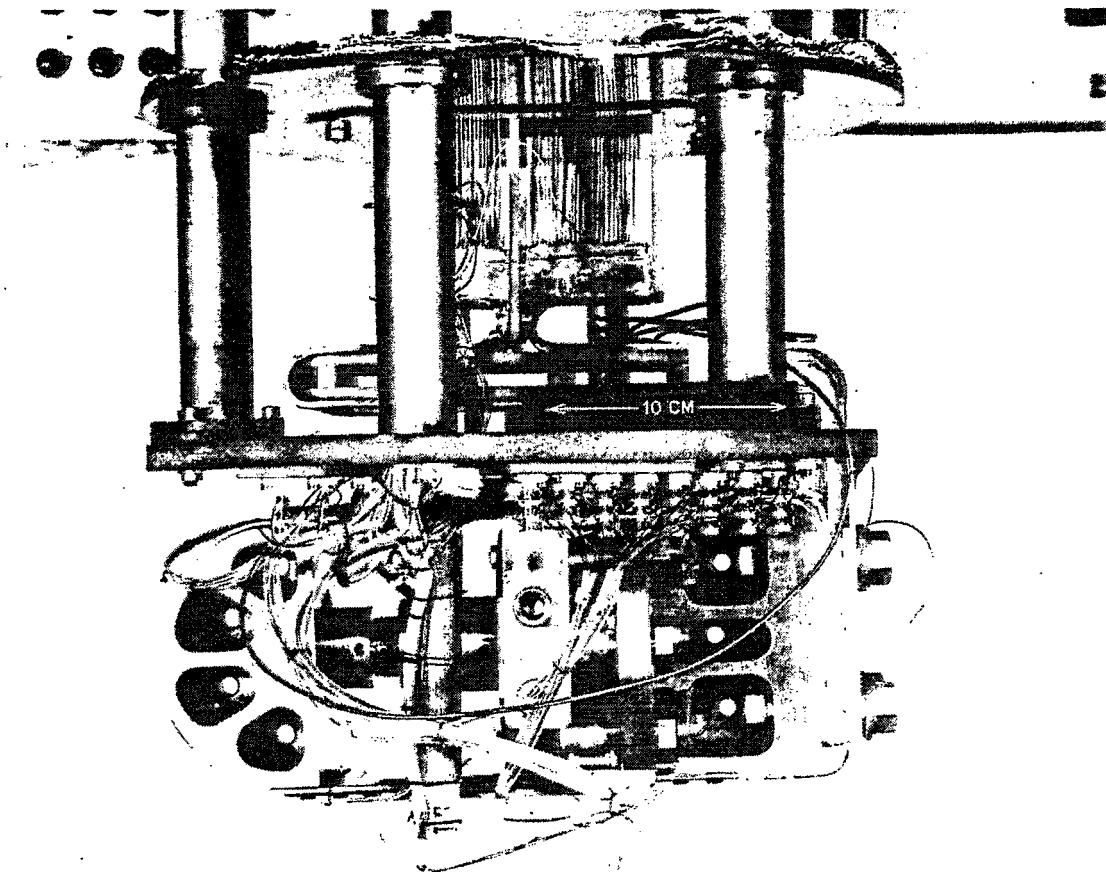


Fig. 5. Stretching device.

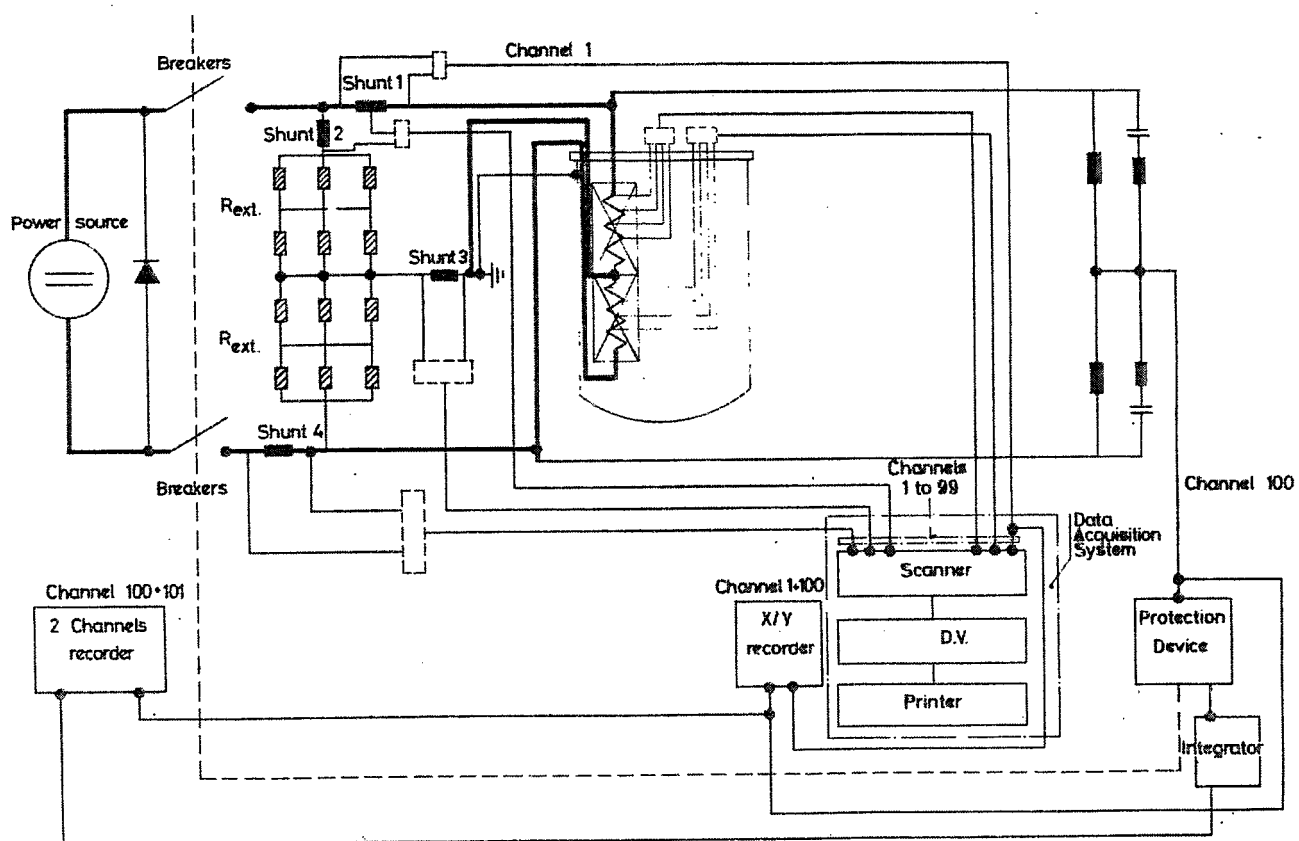


Fig. 6. BRARACOURCIX measuring system.



CURRENT INCREASE WITH 2 V - CHANNELS 1 AND 100

TEST OF "BRARACOURCIX"

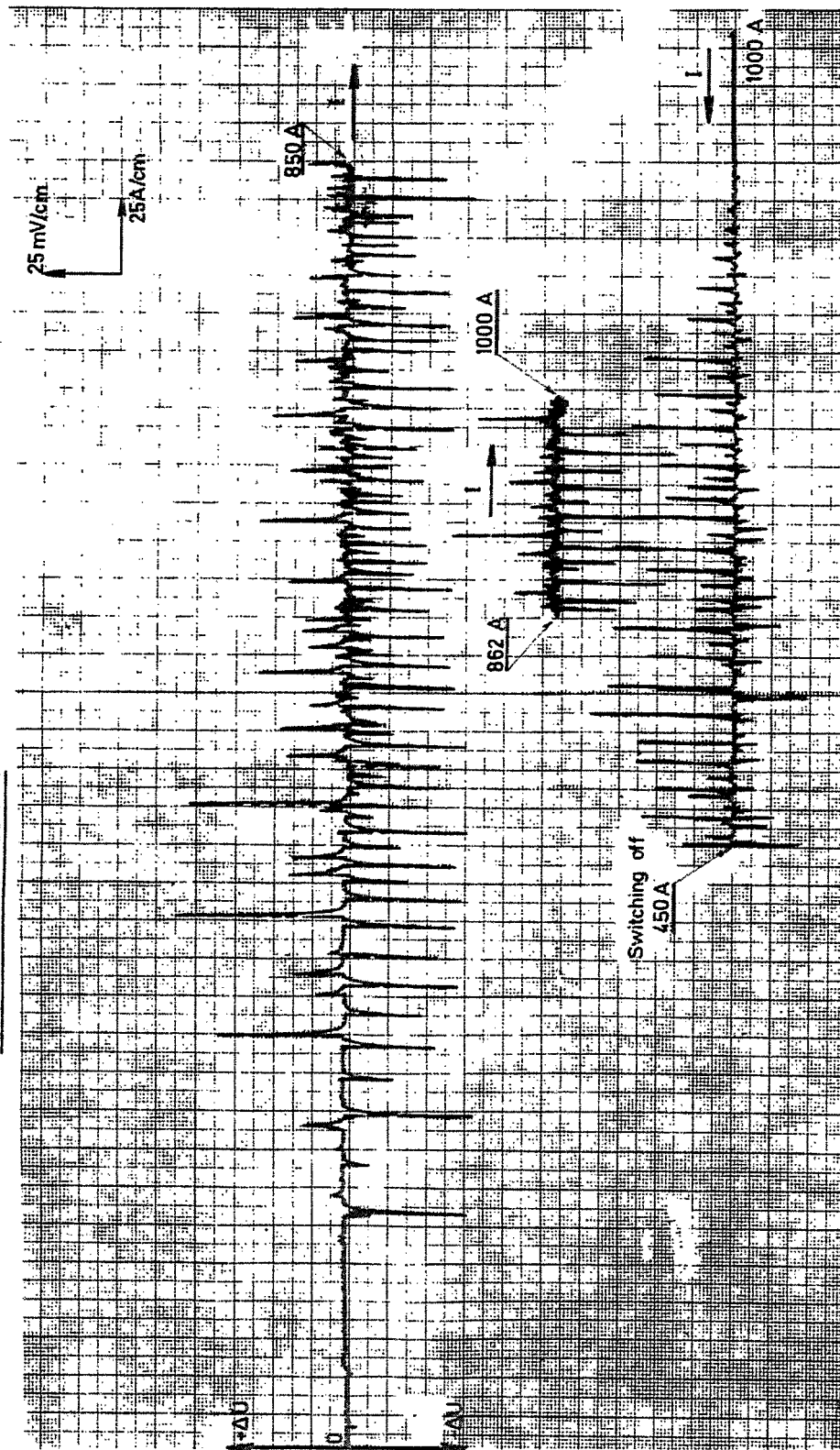


Fig. 7. Recording of voltage signals during energizing of BRARACOURCIX.

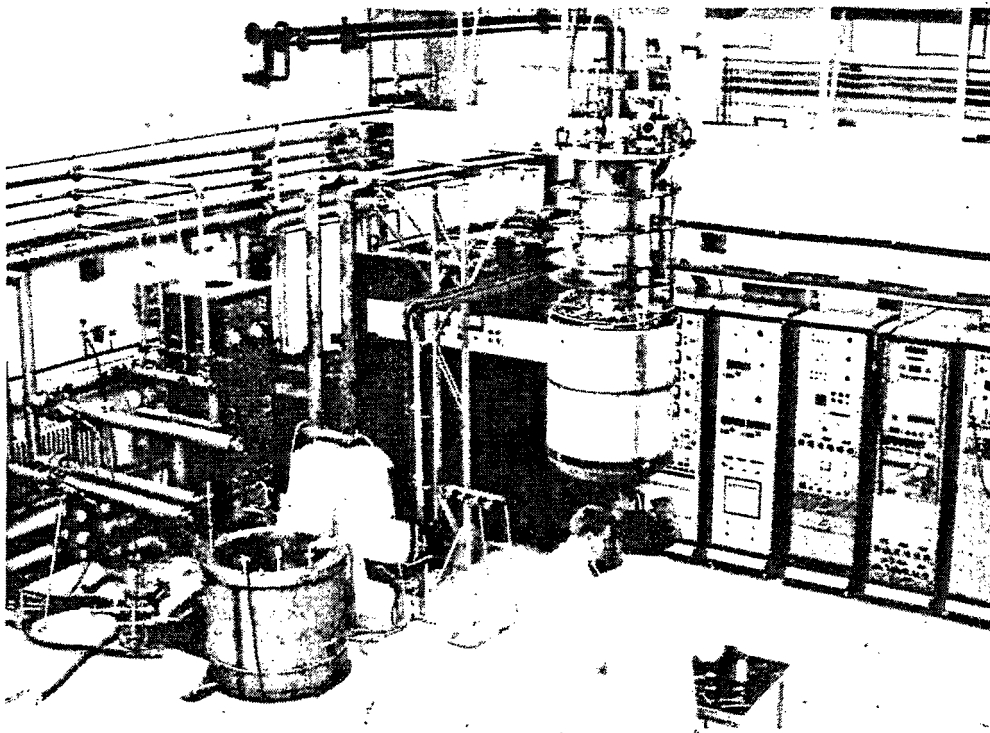


Fig. 8. General view of the BRARACOURCIX test facility.

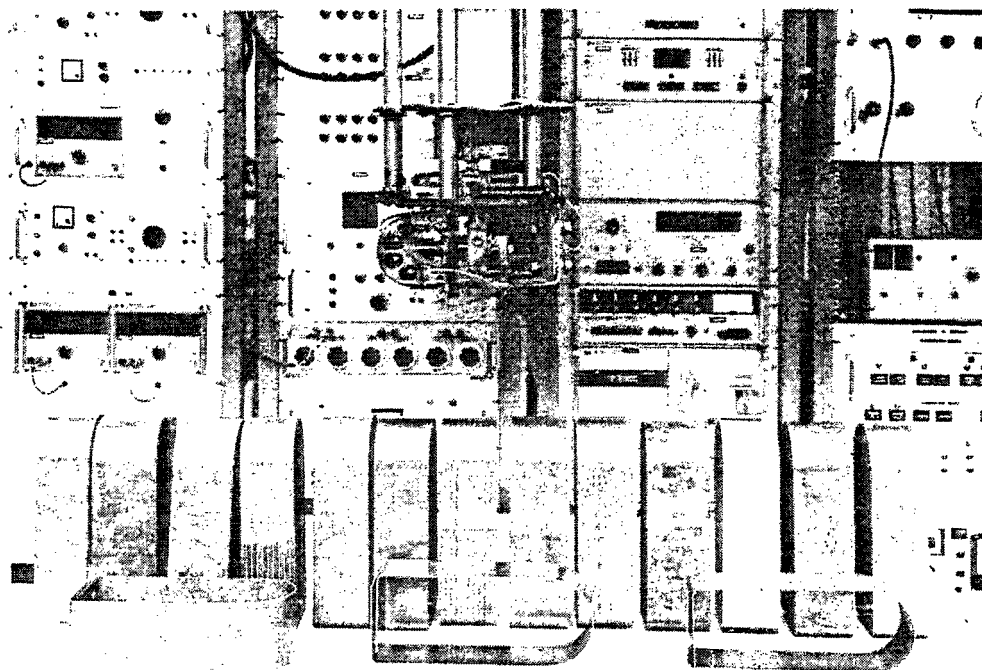


Fig. 9. Short samples of potential conductors for the BEBC magnet.

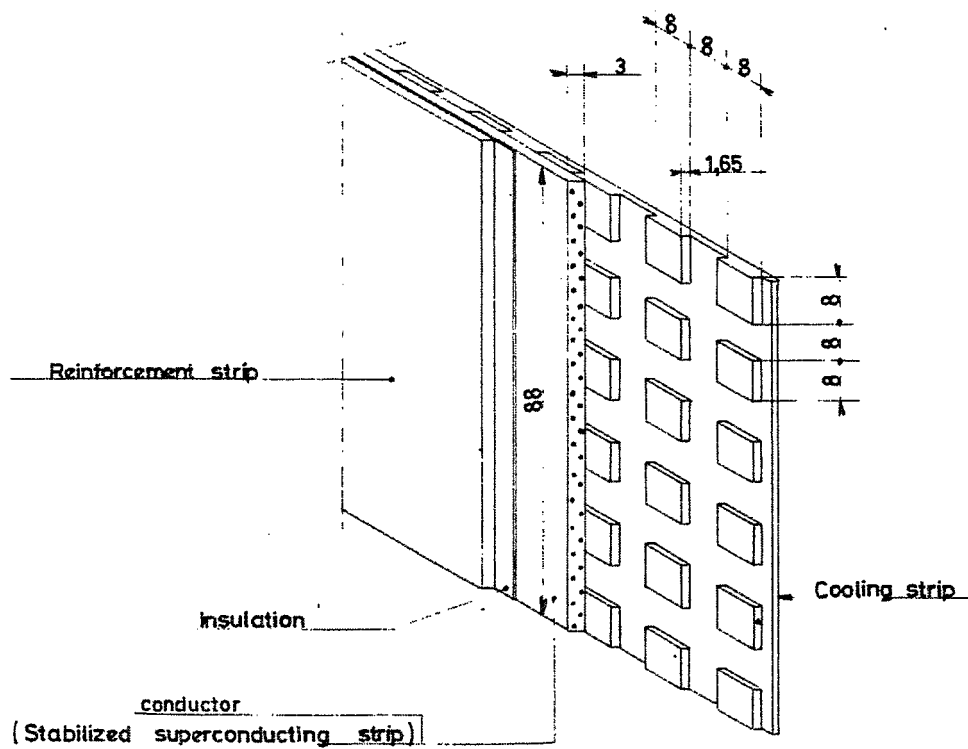


Fig. 10. Configuration of the pancake winding for the BEBC magnet.

# A POSSIBLE SOURCE OF INSTABILITY IN "FULLY STABILIZED" MAGNETS

P.F. Smith, M.N. Wilson, and J.D. Lewin  
Rutherford Laboratory  
Chilton, Berks., England

The purpose of this brief note is to draw attention to a problem which could affect the performance of fully stabilized magnets made from wide strip conductor.

The fully stabilized conductor is designed by assuming that the full transport current may flow in the normal metal and equating the power dissipation to the surface heat transfer with, typically, a safety factor of 2.

This safety factor may, however, be insufficient to cope with the power dissipation during a flux jump, since in the lower field regions of the coil the superconductor can support a magnetization current density which is much higher than the peak transport current density.

An approximate quantitative estimate of this effect may be obtained as follows:

1) In addition to the transport current, the conductor throughout most of the coil is filled with magnetization currents. When the superconducting filaments are connected by low resistance metal, the finite rate of rise of field will in general be sufficient to cause these currents to flow around the entire composite, instead of being confined within the individual filaments (Fig. 1). The magnetic energy associated with this current distribution is

$$Q = \frac{2\pi}{3} \frac{J^2 \ell^2}{10^9} \quad (\text{J/cm}^3) \quad , \quad (1)$$

where  $J$  is the over-all current density.

2) Since  $J$  increases as  $H$  decreases, the maximum value of  $J\ell$  will occur approximately at the field which just achieves complete penetration of the strip. Let this occur at  $J_1\ell = H_1$ , say. Let the over-all current density be  $J_p$  at the peak field  $H_p$ , and assume  $J \propto 1/H$ , so that  $J_1 \sim H_p J_p / H_1$ . Then

$$H_1^2 \sim (J_1 \ell)^2 \sim H_p J_p \ell \quad (2)$$

which is the value to be inserted in (1), and also

$$J_1^2 \sim J_p^2 \times (H_p / J_p \ell) \quad (3)$$

3) To see what these equations could mean in practice, consider a specific example of a large coil with  $H_p = 60\,000$  G, and suppose a superconductor-copper composite with  $J_p = 1500$  A/cm<sup>2</sup>, and  $2\ell = 8$  cm. Then  $J_1^2 \sim 10 J_p^2$  at  $H_1 \sim 19\,000$  G. If, during a flux jump in this part of the coil, all the superconductor in the cross section became resistive, the magnetization currents would transfer to the normal metal, and decay with an initial power dissipation about 10 times as great as the design value (neglecting the reduction in magnetoresistance).

The time constant for the decay of these currents is approximately  $(16/10^9\pi)(\ell^2/\rho)$ , which in this case is about 2 sec. The thermal time constant,  $S\ell^2/2k$  ( $S$  in  $\text{J}/\text{cm}^3$ ,  $k$  in  $\text{W}/\text{cm}\cdot^\circ\text{K}$ ) is about  $10^{-3}$  to  $10^{-2}$  sec, so that uniform heating can be assumed; the total energy released, given by (1), is about  $0.7 \text{ J}/\text{cm}^3$ .

4) Since only part of this energy can be transferred immediately to the liquid helium there will be a rise in temperature, which in this case could amount to  $15\text{-}25^\circ\text{K}$ . Thus, the example we have considered would appear to be reasonably safe, since a temperature rise of this order would cause very little increase in the resistivity of the copper, the transport current would still be stabilized, and the conductor would recover. There remains, however, the possibility that the increased heat transfer rate associated with the higher temperature might be sufficient to vaporize the liquid helium in the (narrow) cooling channel, after which the transport current would no longer be stabilized. This appears difficult to assess with any certainty.

These effects could, of course, become more serious with wider conductors, higher peak fields and lower-enthalpy materials such as aluminum. They are, however, unlikely to be observed in lower field coils such as those for the Argonne bubble chamber.

The preceding calculations are based on some apparently rather pessimistic assumptions: firstly that the length of conductor involved in the flux jump is sufficiently great for longitudinal and radial heat conduction to be negligible, and secondly that a complete flux jump occurs, whereas in practice it may well be partially or completely extinguished by the electromagnetic and thermal damping provided by the copper.

An approximate estimate of the conditions under which normal metal may prevent flux jumping has been made by Chester<sup>1</sup> for the case of thin sheets of superconductor embedded in a good thermal conductor. Using the same approach we obtain the following criterion for absence of flux jumping in a composite containing circular filaments of diameter  $d$  (cm):

$$d^2 \leq (T_0 k/\rho) (1/J_m J_c) \quad (4)$$

where  $T_0 = J_c/(-dJ_c/dT) \approx 3^\circ\text{K}$ ,

$k$  = thermal conductivity of superconductor,  $\sim 10^{-3} \text{ (W}/\text{cm}\cdot^\circ\text{K})$ ,

$\rho$  = resistivity of normal metal,  $\approx 2 \times 10^{-8} \text{ (}\Omega\cdot\text{cm)}$ ,

$J_c$  = current density in superconductor (at appropriate field value),

$J_m$  = mean current density in composite (at appropriate field value).

Putting  $J_c = 2 \times 10^5 \text{ A}/\text{cm}^2$ , and  $J_m = 5 \times 10^3 \text{ A}/\text{cm}^2$ , (4) gives  $d \leq 1.2 \times 10^{-2} \text{ cm}$  (0.005 in.).<sup>2</sup> The approximate derivation we have used is uncertain by various factors of order 2, and also assumes the copper to be a perfect heat sink, which assumption may not be valid if the perturbation initiating the flux jump is large. There is at present no experimental confirmation of this theory, and the predictions which it makes for copper-clad  $\text{Nb}_3\text{Sn}$  tapes, typically that superconducting layers less than  $\sim 10 \mu$  thick should be stable, are in evident disagreement with observation.

1. P.F. Chester, Rep. Progr. Phys. 30, Pt. 2, 361 (1967).

2. Note that this criterion refers only to flux motion across the entire composite, and not to flux jumping in the individual filaments. These criteria are considered in more detail in a separate paper in these Proceedings (p. 913).

In the present state of knowledge, therefore, one cannot be at all confident of specifying a fully stabilized composite in which low field flux jumping is absent, but the preceding calculations suggest that even in extreme cases the heating effects only just begin to reach a dangerous level.

On balance, there seems to be a reasonable chance that no instabilities of this kind will be encountered in any of the large magnets now being planned. Nevertheless, in view of the importance and high cost of such projects, some experimental reassurance appears desirable before finalizing their design.

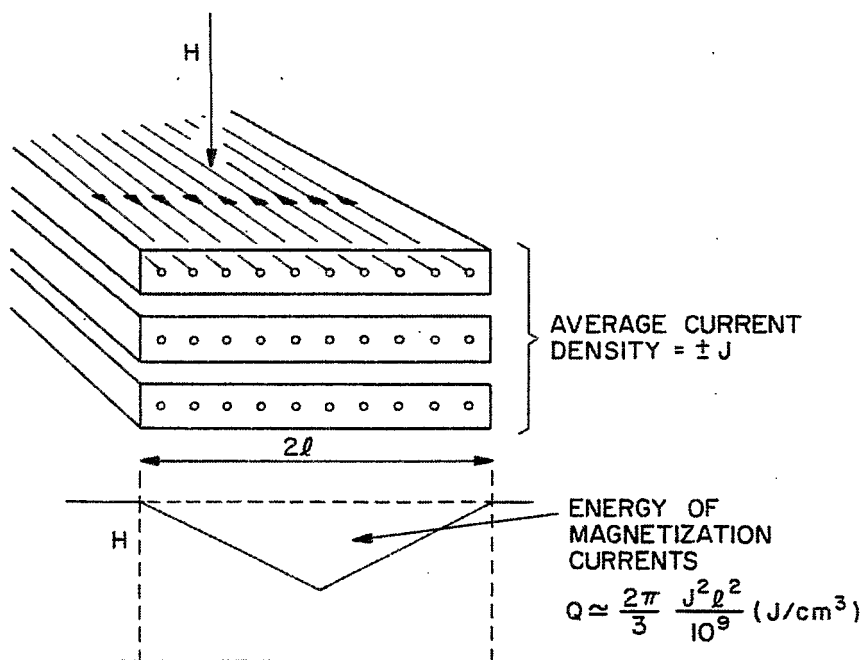


Fig. 1. Energy of magnetization currents.

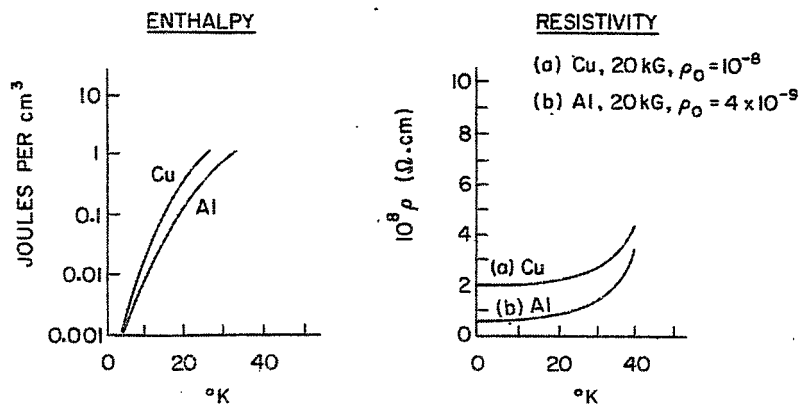


Fig. 2. Typical temperature variation of enthalpy and resistivity for copper and aluminum.

# ANALYTICAL DESIGN OF SUPERCONDUCTING MULTIPOLAR MAGNETS\*

Richard A. Beth  
Brookhaven National Laboratory  
Upton, New York

## INTRODUCTION

The analysis of magnetic fields produced by currents is an essential part of the design and construction of superconducting magnets. Beyond this, of course, a broad range of engineering judgements is involved, such as those concerning cost, materials, mechanical design, machining, production, assembly, testing, etc. These are not taken up in this summary, nor is the use of iron in the magnetic field.

A static magnetic field is always a three-dimensional configuration in space. While the basic physical principles are well understood their detailed analytical application to a whole three-dimensional magnet can rapidly become unmanageable, even with computers, unless appropriate simplifications and idealizations are introduced.

For accelerator and many other applications transverse magnetic fields are used to guide and focus beams of charged particles. When the beam cross section dimensions are small compared to the radius of curvature of the beam it is often an appropriate simplification to use a two-dimensional analysis to make the initial design of a magnet. Three-dimensional features, such as end effects, can later be taken into account as necessary along with engineering modifications once an idealized two-dimensional design has been chosen.

It should be clearly recognized, however, that certain, possibly very useful, three-dimensional patterns, such as spiral or alternating spiral fields, are expressly left out of consideration when we restrict ourselves to an idealized two-dimensional design.

The main purpose of the present paper is to describe and illustrate some of the methods now available for the analysis of two-dimensional fields.

## I. TWO-DIMENSIONAL FIELDS PRODUCED BY CURRENTS

### Required Field and Aperture

The components,  $H_x$  and  $H_y$ , of the transverse field required in a beam handling magnet will lie in an  $X,Y$  plane normal to the beam and the beam cross section will lie within a specified "aperture" region in this  $X,Y$  plane. The primary problem is to find an arrangement of longitudinal currents, assumed infinitely long, straight and perpendicular to the  $X,Y$  plane (current filaments, current sheets, or solid current "blocks") lying outside the aperture which will produce the required two-dimensional field within the aperture. Usually this primary problem is solved in an inverse way - i.e., by assuming a distribution of current magnitudes and locations and calculating the field that would be produced, then modifying the assumed currents and/or their locations until the calculations give the required field with sufficient

---

\*Work performed under the auspices of the U.S. Atomic Energy Commission.



Obviously the efficiency of this procedure will be greatly enhanced if the assumed current distributions can be guided by idealized but mathematically precise analytic solutions such as those which can be obtained by the methods described here.

These methods also enable us to obtain analytical solutions to a wide range of secondary problems in the idealized case - for example, finding the external field, the field within conductors, the field forces acting on conductors, and the energy stored in the magnetic field.

### Complex Representation

Maxwell's equations for a static two-dimensional magnetic field parallel to the X,Y plane may be written in the form

$$\begin{aligned}\frac{\partial H_Y}{\partial X} - \frac{\partial H_X}{\partial Y} &= 4\pi\sigma(X,Y) \\ \frac{\partial H_X}{\partial X} + \frac{\partial H_Y}{\partial Y} &= 0\end{aligned}\tag{1}$$

where  $\sigma(X,Y)$  is the density of current normal to the X,Y plane and  $B = H$ . When  $\sigma = \text{constant}$  (including 0), these two Maxwell equations may be identified<sup>1</sup> with the two Cauchy-Riemann equations

$$\begin{aligned}\frac{\partial U}{\partial X} &= \frac{\partial V}{\partial Y} \\ \frac{\partial V}{\partial X} &= -\frac{\partial U}{\partial Y}\end{aligned}\tag{2}$$

which are necessary and sufficient for

$$F \equiv U + iV$$

to be an analytic function,  $F(Z)$ , in any region of the  $Z = X + iY$  plane. It is easily seen that the identification may be made by setting

$$\begin{aligned}U &= H_Y - 2\pi\sigma X \\ V &= H_X + 2\pi\sigma Y\end{aligned},$$

or

$$F = H - 2\pi\sigma Z^*\tag{3}$$

where  $Z^* = X - iY$  and

$$H \equiv H_Y + iH_X = i(H_X - iH_Y)\tag{4}$$

is taken, by definition, as the complex field.

---

1. R.A. Beth, J. Appl. Phys. 38, 4689 (1967).

### Field as a Complex Power Series

In any region without currents (e.g., in a magnet aperture),  $\sigma = 0$  and  $H(Z)$  is itself an analytic function without singularities. Hence any two-dimensional field that satisfies Maxwell's equations can be written as a complex power series

$$H(Z) = H_1 + H_2 Z + H_3 Z^2 + \dots = \sum_{n=1}^{\infty} H_n Z^{n-1} \quad (5)$$

about any point within the regular region as origin. The complex coefficients,  $H_n$ , completely specify  $H(Z)$ ; thus  $H_1$  specifies the dipole component,  $H_2$  the quadrupole,  $H_3$  the sextupole, and, in general,  $H_n$  the  $2n$ -pole component.

For many applications the desired field will be antisymmetric above and below some "median plane" through the origin. When the X-axis represents the median plane all of the  $H_n$  coefficients are real.

### Current Filaments

The magnetic field at  $Z$  due to a filament current  $I$  at  $z$  is<sup>2</sup>

$$H(Z) = \frac{2I}{Z - z} = H_Y + iH_X \quad (6)$$

Thus an isolated filament current  $I$  constitutes a simple pole with residue  $2I$  for the two-dimensional magnetic field defined by Eq. (4).

Since the integral of  $H(Z)$  around any closed contour  $C$  in the  $Z$ -plane is  $2\pi i$  times the sum of the residues within  $C$ , it follows that

$$\oint_C H dZ = 4\pi i I_C \quad (7)$$

where  $I_C$  is the total current within  $C$ .

### Current Sheets

If  $dI$  is the filament current flowing along the elements of a cylinder perpendicular to the  $Z$ -plane in the interval  $dz$  then the field discontinuity between the right and left sides of  $dz$  can be shown from (6) to be<sup>3</sup>

$$H_R(z) - H_L(z) = 4\pi i \frac{dI}{dz} \quad (8)$$

where  $H_R(z)$  and  $H_L(z)$  are the limit values at the cylinder where  $Z = z$  of the fields  $H_R(Z)$  and  $H_L(Z)$  in the regions to the right and left of the cylindrical current sheet.

---

2. R.A. Beth, J. Appl. Phys. 37, 2568 (1966).

3. R.A. Beth, Brookhaven National Laboratory, Accelerator Dept. Report AADD-102 (1966).

## Current Blocks

When the current density is uniform ( $\sigma = \text{constant}$ ), a straight conductor, represented by its cross section in the  $Z$ -plane, may be called a current block. For such a current block the function  $F(Z)$  in Eq. (3) can be shown to be<sup>1</sup>

$$F(Z) = i\sigma \oint_C \frac{z^* dz}{z - Z} \quad (9)$$

where  $z = x + iy$  represents the points of the cross-section boundary, and  $z^* = x - iy$ . Then the fields inside and outside the conductor are

$$\begin{aligned} H_{in} &= F(Z_{in}) + 2\pi\sigma Z_{in}^* \\ H_{out} &= F(Z_{out}) \end{aligned} \quad (10)$$

These are both given by the single formula

$$H = i\sigma \oint_C \left( \frac{z^* - Z^*}{z - Z} \right) dz \quad (11)$$

since the residue of  $Z^*/(z - Z)$  is  $Z^*$  for  $Z = Z_{in}$  and is zero for  $Z = Z_{out}$ .

## Field Forces

The resultant field force acting on a unit length of all the currents within an arbitrary contour  $C$  in the  $Z$ -plane can be shown<sup>4,5</sup> to have  $X$  and  $Y$  components which are given by the contour integral

$$f \equiv f_Y + if_X = -\frac{1}{8\pi} \oint_C H^2 dz \quad (12)$$

Similarly the force  $df$  acting on unit length of a current sheet in the interval  $dz$  is given by<sup>6</sup>

$$\frac{df}{dz} = \frac{1}{8\pi} \left[ H_L^2(z) - H_R^2(z) \right] \quad (13)$$

which, using (8), can be written in the form

$$\frac{df}{dz} = -i\bar{H}(z) \frac{dI}{dz} \quad (14)$$

---

4. R.A. Beth, Brookhaven National Laboratory, Accelerator Dept. Report AADD-107 (1966).

5. R.A. Beth, in Proc. 2nd Intern. Conf. Magnet Technology, Oxford, 1967, p. 135.

6. R.A. Beth, in Proc. 6th Intern. Conf. High Energy Accelerators, Cambridge, Mass., 1967, p. 387.

where

$$\bar{H}(z) = \frac{1}{2} \left[ H_L(z) + H_R(z) \right] \quad (15)$$

is the mean of the limits of the left and right fields at the current sheet.

### Potentials

In any simply connected region without currents the integral of the analytic function  $H(Z)$  between two points is independent of the path of integration. The vector and scalar potentials,  $A(X,Y)$  and  $\Omega(X,Y)$ , are then given by

$$-A - i\Omega = W(Z) = \int_0^Z H dZ = \sum_{n=1}^{\infty} \frac{1}{n} H_n Z^n, \quad (16)$$

where  $H$  is defined as in (4) and  $Z = 0$  lies in the regular region. Conversely, the field is given by

$$H = \frac{dW}{dZ} \quad (17)$$

The curves  $A = \text{constant}$  give the lines of force of the magnetic field and are everywhere orthogonal to the scalar equipotentials,  $\Omega = \text{constant}$ .

It will be seen that the vector potential  $A(X,Y)$  in this two-dimensional case is really only the component of the three-dimensional vector potential normal to the field plane; the other two components lie in the field plane and are constant.

### Field Energy

The vector and scalar potentials

$$A = A(X,Y) \quad \text{and} \quad \Omega = \Omega(X,Y) \quad (18)$$

specify a transformation from the  $X,Y$  plane to an  $A,\Omega$  plane whose Jacobian is

$$J = \frac{\partial(A,\Omega)}{\partial(X,Y)} = \begin{vmatrix} \frac{\partial A}{\partial X} & \frac{\partial A}{\partial Y} \\ \frac{\partial \Omega}{\partial X} & \frac{\partial \Omega}{\partial Y} \end{vmatrix} = \begin{vmatrix} -H_Y & H_X \\ -H_X & -H_Y \end{vmatrix} = H_Y^2 + H_X^2 = HH^*, \quad (19)$$

i.e.,  $J$  is proportional to the field energy density. Hence the field energy per unit thickness in any region  $R$  of the  $X,Y$  plane is proportional to the area of the transformed region  $R'$  in the  $A,\Omega$  plane,<sup>5,7</sup> i.e.,

$$E_R = \frac{1}{8\pi} \iint_R J dXdY = \frac{1}{8\pi} \iint_{R'} dAd\Omega \quad (20)$$

---

7. R.A. Beth, Brookhaven National Laboratory, Accelerator Dept. Report AADD-106 (1966).

When the potential function  $W(Z)$ , defined in (15), is known in complex form it is often convenient to calculate the area of the region  $R'$  in the  $W$  plane as a contour integral around its boundary  $C'$ :

$$\iint_{R'} d\text{Ad}\Omega = \frac{1}{2i} \oint_{C'} W^* dW = \frac{i}{2} \int_{C'} W dW^* , \quad (21)$$

where  $W^*$  is the complex conjugate of  $W$ .<sup>7</sup>

## II. ILLUSTRATIVE EXAMPLES

### Multipole Field in a Circular Aperture

The most general nonsingular Maxwell field in two dimensions may be represented as a superposition of multiple fields as in (5).

Suppose we wish to produce the  $2n$ -pole component

$$H_{in}(Z) = H_n Z^{n-1} \quad (22)$$

within a circular aperture of radius  $a$  by an array of current filaments.

The array of minimum lateral size and minimum field energy storage will be obtained with a cylindrical current sheet tightly surrounding the required circular aperture. Let the points  $z$  of the cylinder cross section, and the arc length  $s$  measured around the circumference be

$$\begin{aligned} z &= ae^{i\theta} & 0 \leq \theta < 2\pi \\ s &= a\theta \end{aligned} \quad (23)$$

Then  $z^* = ae^{-i\theta} = a^2/z$  and  $dz = izd\theta = i(z/a)ds$ .

By means of the current sheet theorem (8) we can see that the required current distribution is

$$\frac{dI}{ds} = -\frac{1}{4\pi a} \left( H_n z^n + H_n^* z^{*n} \right) = -\frac{|H_n|}{2\pi} a^{n-1} \cos(n\theta + \theta_n) , \quad (24)$$

where  $H_n = |H_n| e^{i\theta_n}$ , and the external field is

$$H_{out}(Z) = -H_n^* \frac{a^{2n}}{Z^{n+1}} . \quad (25)$$

Thus the required linear current density in the cylinder is proportional to  $a^{n-1}$  and varies sinusoidally as an  $n$ th harmonic of the central angle  $\theta$  around the circumference of the cylinder. Note that the phase angle  $\theta_n$  merely specifies the orientation of the multipole field with respect to the direction chosen for  $\theta = 0$ .

The field force acting on unit area of the current sheet,  $df/ds$ , can be evaluated by using the force theorem (14). It turns out that the radial component is everywhere zero and the tangential component is

$$\frac{df_\theta}{ds} = \frac{dI}{ds} \cdot |H_n| a^{n-1} \sin(n\theta + \theta_n) \quad (26)$$

Thus the tangential force density (26) is zero where the current density (24) is zero or has maximum magnitude. The tangential force is directed toward the nearest absolute maximum of (24) at intermediate points.

It can be shown from the energy theorem (20) that the internal and external field energies are equal for a circular multipole current sheet and that

$$E_{in} = E_{out} = \frac{|H_n|^2 a^{2n}}{8n} \quad (27)$$

For an elliptic aperture and current sheet the formulas are somewhat more complicated; they have been worked out together with the case of two confocal elliptic (or concentric circular) cylinders required to produce a prescribed field within the inner cylinder while cancelling the field external to the outer cylinder.<sup>8</sup>

#### Step-Function Approximation for $\cos \varphi$

We may wish to approximate the smoothly varying current density (24) by a step function made up of intervals of constant current density. We set

$$\varphi = n\theta + \theta_n \quad (28)$$

and seek to approximate  $\cos \varphi$  by a function of  $N$  steps per quadrant. With cosine symmetry as shown in Fig. 1, the Fourier composition of the step function is

$$S(\varphi) = \sum_{m=1}^{\infty} C_m \cos(2m-1)\varphi \quad ,$$

where the coefficients  $C_m$  will depend on  $N$  values of  $g_v$  and  $N$  values of  $\varphi_v$ . These  $2N$  values can be chosen to make  $C_1 \neq 0$  and  $C_m = 0$  for  $m = 2, 3, \dots, 2N$ . The solution<sup>9</sup> is

$$\begin{aligned} g_v &= \frac{\cos(v - \frac{1}{2})\alpha}{\cos \frac{1}{2}\alpha} \quad , \quad v = 1, 2, \dots, N \\ \varphi_v &= v\alpha \quad , \quad v = 1, 2, \dots, N \quad , \end{aligned} \quad (29)$$

where

$$\begin{aligned} \alpha &= \frac{\pi}{2N+1} = \frac{2\pi}{M} \\ M &= 4N+2 \quad . \end{aligned} \quad (30)$$

8. R.A. Beth, IEEE Trans. Nucl. Sci. NS-14, No. 3, 386 (1967).

9. R.A. Beth, Brookhaven National Laboratory, Accelerator Dept. Report AADD-135 (1967).

With these values of  $g_v$  and  $\varphi_v$  the Fourier expansion of the step function is

$$S_N(\varphi) = \frac{M}{\pi} \tan \frac{\pi}{M} \left[ \sum_{k=0}^{\infty} \frac{\cos (kM+1) \varphi}{kM+1} - \sum_{k=1}^{\infty} \frac{\cos (kM-1) \varphi}{kM-1} \right] \quad (31)$$

so that, after the fundamental, all harmonics are eliminated up to the  $\cos (4N+1) \varphi$  term — which, in view of (28), means sinusoidal functions of  $n(4N+1)\theta$  and a deviation of the order of

$$\frac{1}{4N+1} \left( \frac{Z}{a} \right)^{4Nn} \quad \text{times the fundamental} \quad (32)$$

from the ideal field (22).<sup>9</sup> Figures 2 through 6 show the general form of  $S_N(\varphi)$  and the first few cases  $N = 1, 2, 3$ , and 4.

It will be seen that the approximation is so good that practical construction inaccuracies will soon outweigh the deviation of  $S_N$  from a pure  $\cos \varphi$  field even for  $N = 3$  or 4. The construction of step-function dipoles and quadrupoles was described by Britton during this Summer Study.<sup>10</sup>

#### Constant Gradient Field in an Elliptic Aperture

Any desired field (5) can be produced within an elliptic aperture by providing the proper current distribution on the elliptic cylinder determined by the specified aperture; the resulting external field and field energy can be calculated.<sup>8</sup>

The relations for a constant gradient field in an elliptical aperture may be summarized as follows<sup>5</sup>:

To produce the field

$$H_{in} = B_o (1 + KZ) \quad (\text{dipole} + \text{quadrupole}) \quad (33)$$

within the elliptical cylinder whose normal section is

$$z = a \cos \theta + ib \sin \theta = re^{i\theta} + \delta e^{-i\theta} \quad (0 \leq \theta < 2\pi) \quad (34)$$

where

$$r = \frac{1}{2}(a + b) \quad \delta = \frac{1}{2}(a - b) \quad (35)$$

requires the current distribution in the cylinder elements

$$\frac{dI}{d\theta} = - \frac{B_o}{2\pi} (r \cos \theta + r^2 K \cos 2\theta) \quad (36)$$

with

$$\begin{aligned} c^2 &= a^2 - b^2 = 4r\delta & W_1 &= 2r(r + \delta) \\ \xi &= z + \sqrt{z^2 - c^2} & W_2 &= 2r^2(r^2 + \delta^2)K \end{aligned}$$

---

10. R.B. Britton, these Proceedings, p. 893.

The external field is

$$H_{\text{out}} = -B_0 \left[ W_1 \xi^{-1} + 2W_2 \xi^{-2} \right] / \sqrt{Z^2 - c^2} . \quad (37)$$

The complex potentials are  $W = - (A + i\Omega)$  such that  $H = dW/dZ$

$$W_{\text{in}} = B_0 \left[ Z + \frac{1}{2} KZ^2 \right] \quad W_{\text{out}} = B_0 \left[ W_0 + W_1 \xi^{-1} + W_2 \xi^{-2} \right] . \quad (38)$$

Vector potential  $A$  is continuous across the ellipse when  $W_0 = r\delta = c^2/4$ .

Circular cylinder case:  $r = a = b$ ,  $\delta = 0$ ,  $c = 0$ .

The field energies per unit length are:

$$\begin{aligned} E_{\text{in}} &= \frac{1}{8} B_0^2 \left[ ab + \frac{1}{4} K^2 ab(a^2 + b^2) \right] \\ E_{\text{out}} &= \frac{1}{8} B_0^2 \left[ a^2 + \frac{1}{8} K^2 (a^2 + b^2)^2 \right] \\ E_{\text{total}} &= \frac{1}{8} B_0^2 (a + b) \left[ a + \frac{1}{8} K^2 (a + b)(a^2 + b^2) \right] . \end{aligned} \quad (39)$$

The ring magnets of the Brookhaven Alternating-Gradient Synchrotron provide a constant gradient field with  $K = 0.0425 \text{ cm}^{-1}$  within a roughly elliptical aperture for which  $a = 8.8 \text{ cm}$ ,  $b = 4.0 \text{ cm}$ .

Such a field can be produced by an elliptic cylinder current sheet chosen to fit the aperture. The equipotential curves  $U = -A(X,Y) = \text{const}$  and  $V = -\Omega(X,Y) = \text{const}$  are plotted in the left side of Fig. 7 and the corresponding  $A, \Omega$  plot with areas proportional to field energy is shown in the right side of the same figure.<sup>5</sup>

The  $U = \text{const}$  curves show lines of force of the magnetic field in the space plot. Since the total field energy is always finite, the potential plot will always cover only finite regions of the  $U, V$  (or  $A, \Omega$ ) plane. Areas can be calculated by the area theorem (21). Selected corresponding regions have been crosshatched similarly to elucidate the interrelations of the two plots.

#### Superposition of Elliptical Current Blocks

By means of the integral formula (9) the fields (10) inside as well as outside an elliptical conductor bounded by

$$z = a \cos \theta + ib \sin \theta$$

and carrying a uniform current density,  $\sigma = \text{const}$ , can be evaluated<sup>1</sup>:

$$\begin{aligned} H_{\text{in}} &= \frac{4\pi\sigma}{a+b} (bX - iaY) \\ H_{\text{out}} &= \frac{4\pi\sigma ab}{Z + \sqrt{Z^2 - c^2}} , \end{aligned} \quad (40)$$

where

$$c^2 = a^2 - b^2 .$$



If we superpose two equal area elliptical conductors with  $\sigma' = -\sigma$ ,  $ab = a'b'$ , and centers at  $Z_0 = -X_0$ ,  $Z'_0 = X_0$ , as shown in Fig. 8(a), then the overlap region forms an empty aperture (since  $\sigma + \sigma' = 0$ ) with the resultant interior constant gradient field:

$$H_{in} = \frac{4\pi\sigma}{(a+b)(a'+b')} \left[ (ab' + a'b + 2bb') X_0 + (a'b - ab') Z \right] \quad (41)$$

where

$$ab = a'b'.$$

We obtain a pure dipole field

$$H_{in} = \frac{8\pi\sigma b X_0}{a+b} = \text{const} \quad (42)$$

for equal ellipses,  $a' = a$  and  $b' = b$ , as in Fig. 8(b).

We obtain a pure quadrupole field

$$H_{in} = \frac{4\pi\sigma (a'b - ab')}{(a+b)(a'+b')} \bar{Z} \quad (43)$$

when both ellipses are centered at the origin,  $X_0 = 0$ , as in Fig. 8(c).

\* \* \* \* \*

#### Remarks on Complex Methods

The complex variable methods for two-dimensional fields described and illustrated in this paper go beyond the older methods which focus on setting up a potential that satisfies Laplace's equation in a region without currents. Here the natural emphasis is on the pair of field components which have direct physical significance everywhere — even within current bearing regions where both potentials cannot be defined. Currents are systematically taken into the theory as singularities and all three aspects of analytic functions — Cauchy-Riemann equations, Cauchy integrals, and power series representations — turn out to have useful physical applications. Field forces and field energy storage can be calculated. In these and other ways the methods described form useful extensions of the usual complex treatment of two-dimensional fields.

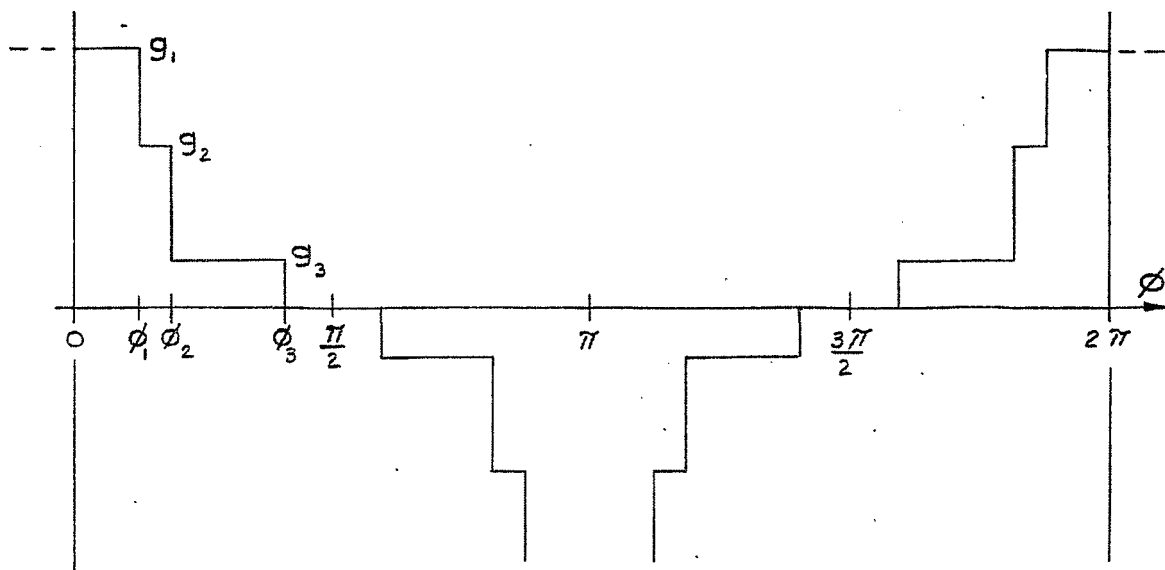


Fig. 1. General form of step function.

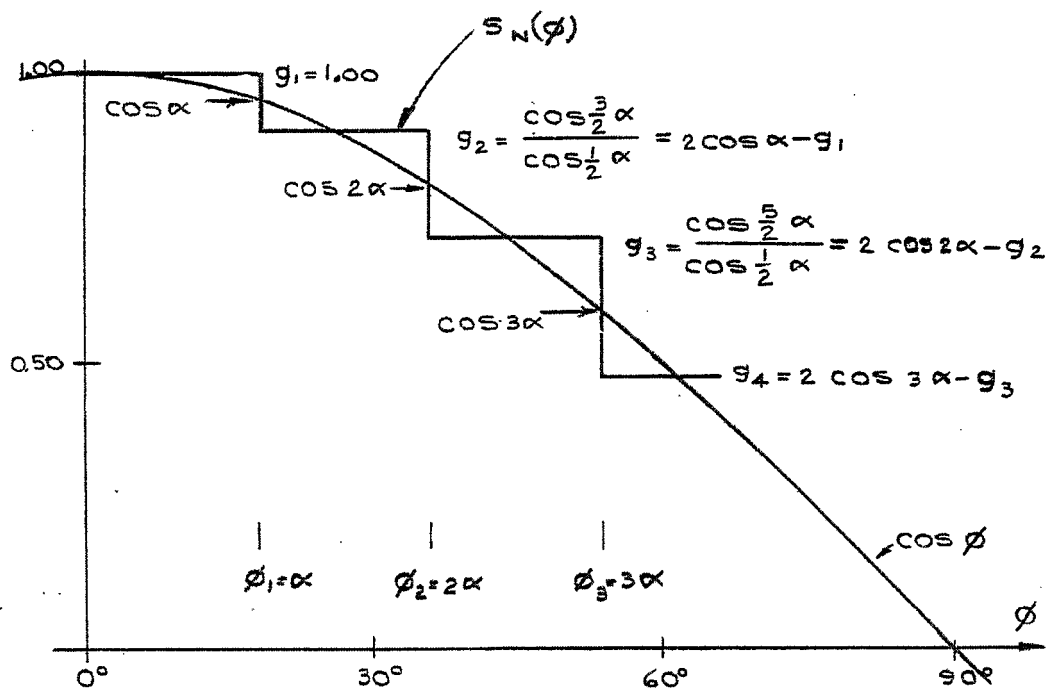


Fig. 2. Form of  $S_N(\varphi)$  for arbitrary  $N$ .

$$N \text{ steps} \quad \alpha = \frac{\pi}{2N+1} \quad M = 4N+2$$

$$\frac{2}{\alpha} \tan \frac{\alpha}{2} = \frac{M}{\pi} \tan \frac{\pi}{M}$$

$$S_N(\varphi) = \frac{M}{\pi} \tan \frac{\pi}{M} \left[ \cos \varphi - \frac{\cos (M-1) \varphi}{M-1} + \frac{\cos (M+1) \varphi}{M+1} - \frac{\cos (2M-1) \varphi}{2M-1} + \frac{\cos (2M+1) \varphi}{2M+1} - \frac{\cos (3M-1) \varphi}{3M-1} + \frac{\cos (3M+1) \varphi}{3M+1} - \dots + \dots \right]$$

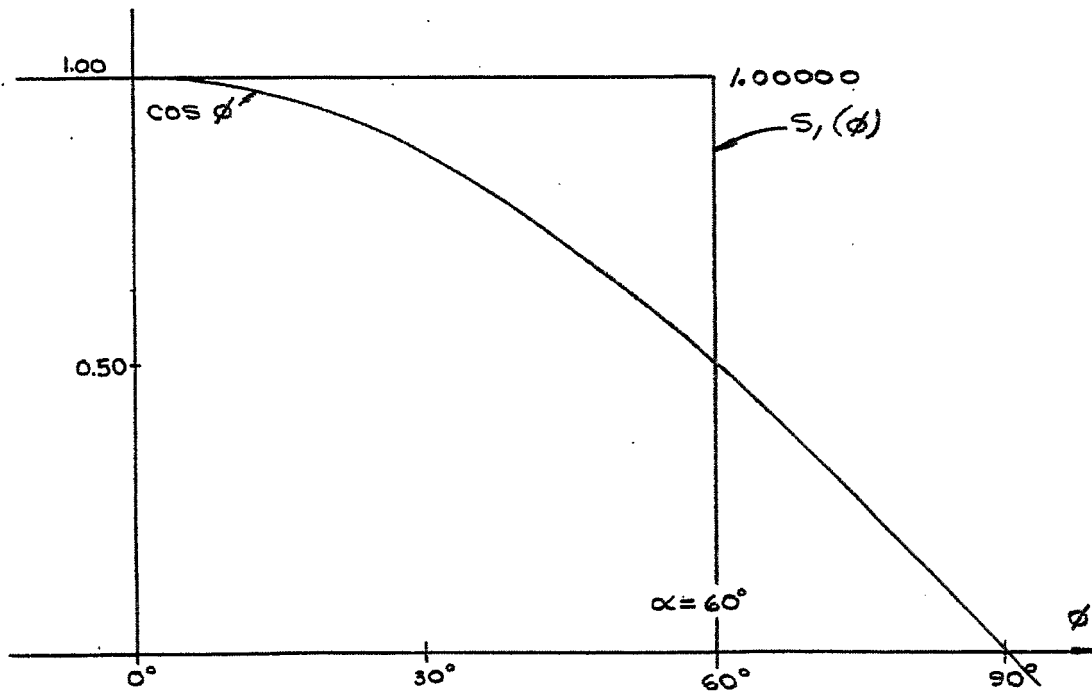


Fig. 3.  $S_1(\varphi)$ .

$$N = 1 \text{ step} \quad \alpha = \frac{\pi}{3} \rightarrow 60^\circ \quad M = 6$$

$$\frac{2}{\alpha} \tan \frac{\alpha}{2} = \frac{6}{\pi} \tan 30^\circ = 1.10266$$

$$S_1(\varphi) = 1.10266 \left[ \cos \varphi - \frac{1}{5} \cos 5\varphi + \frac{1}{7} \cos 7\varphi \right. \\ \left. - \frac{1}{11} \cos 11\varphi + \frac{1}{13} \cos 13\varphi \right. \\ \left. - \frac{1}{17} \cos 17\varphi + \frac{1}{19} \cos 19\varphi \right. \\ \left. - \dots + \dots \right]$$

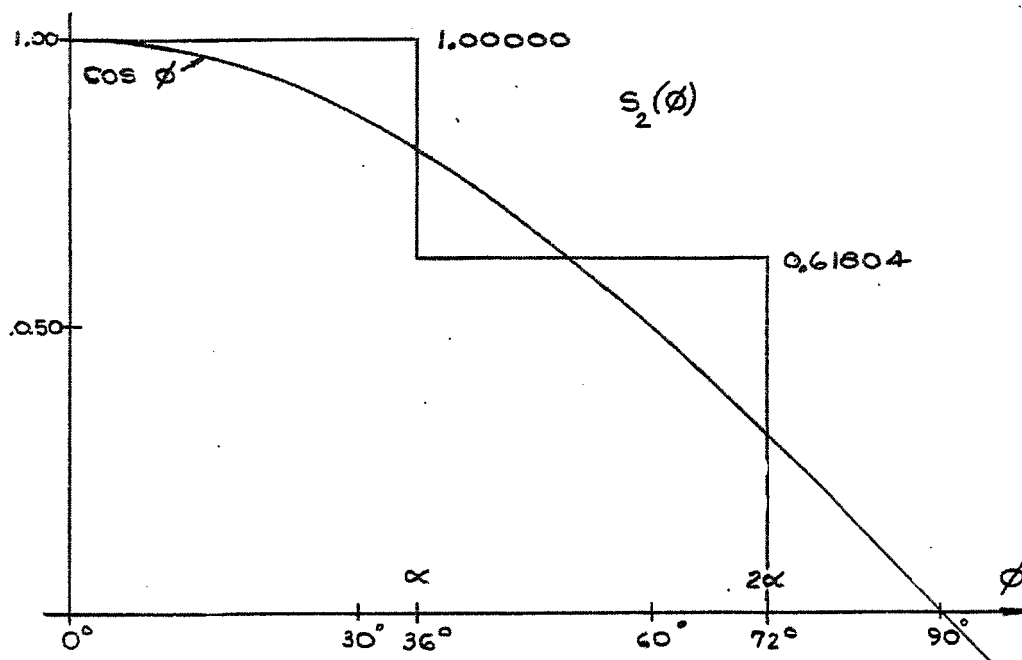


Fig. 4.  $S_2(\varphi)$

$$N = 2 \text{ steps} \quad \alpha = \frac{\pi}{5} \rightarrow 36^\circ \quad M = 10$$

$$\frac{2}{\alpha} \tan \frac{\alpha}{2} = \frac{10}{\pi} \tan 18^\circ = 1.03425$$

$$S_2(\varphi) = 1.03425 \left[ \cos \varphi - \frac{1}{9} \cos 9\varphi + \frac{1}{11} \cos 11\varphi - \frac{1}{19} \cos 19\varphi + \frac{1}{21} \cos 21\varphi - \frac{1}{29} \cos 29\varphi + \frac{1}{31} \cos 31\varphi - \dots + \dots \right]$$

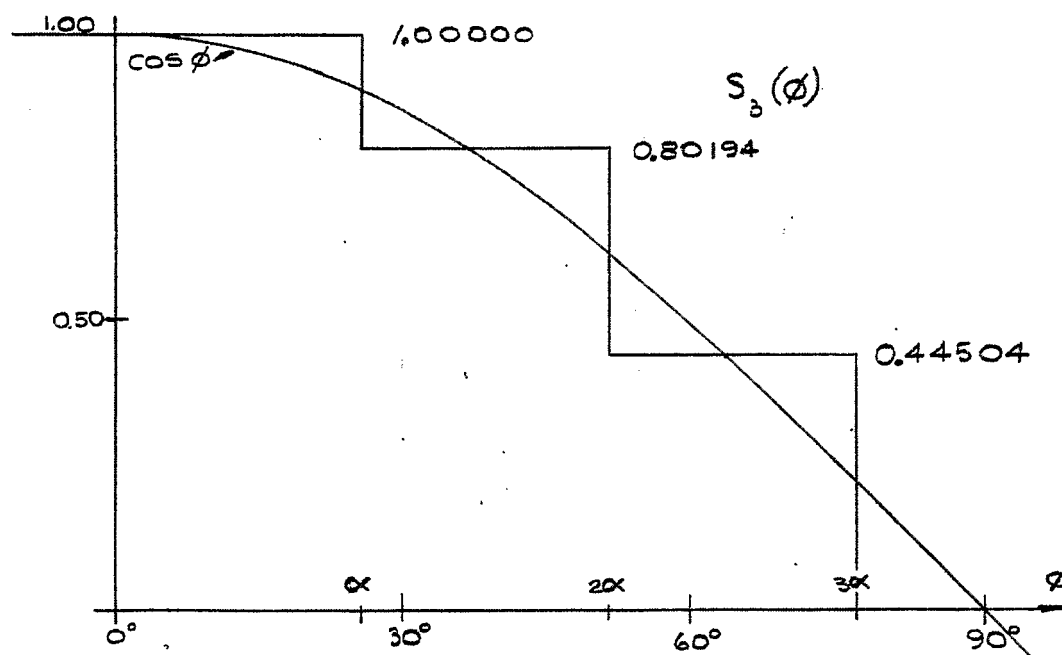


Fig. 5.  $S_3(\varphi)$

$$N = 3 \text{ steps} \quad \alpha = \frac{\pi}{7} \rightarrow 25 \frac{5}{7}^\circ \quad M = 14$$

$$\frac{2}{\alpha} \tan \frac{\alpha}{2} = \frac{14}{\pi} \tan 12 \frac{6}{7}^\circ = 1.01712$$

$$S_3(\varphi) = 1.01712 \left[ \cos \varphi - \frac{1}{13} \cos 13\varphi + \frac{1}{15} \cos 15\varphi - \frac{1}{27} \cos 27\varphi + \frac{1}{29} \cos 29\varphi - \frac{1}{41} \cos 41\varphi + \frac{1}{43} \cos 43\varphi - \dots + \dots \right]$$

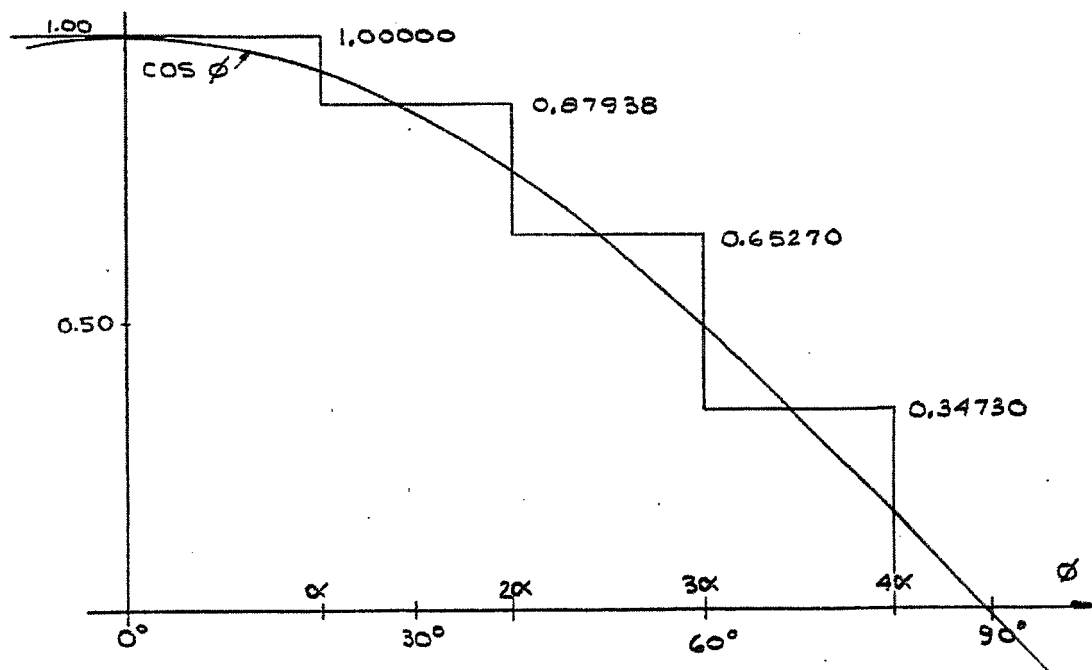


Fig. 6.  $S_4(\varphi)$

$$N = 4 \text{ steps} \quad \alpha = \frac{\pi}{9} \rightarrow 20^\circ \quad M = 18$$

$$\frac{2}{\alpha} \tan \frac{\alpha}{2} = \frac{18}{\pi} \tan 10^\circ = 1.01030$$

$$S_4(\varphi) = 1.01030 \left[ \cos \varphi - \frac{1}{17} \cos 17\varphi + \frac{1}{19} \cos 19\varphi \right. \\ \left. - \frac{1}{35} \cos 35\varphi + \frac{1}{37} \cos 37\varphi \right. \\ \left. - \frac{1}{53} \cos 53\varphi + \frac{1}{55} \cos 55\varphi \right. \\ \left. - \dots + \dots \right]$$

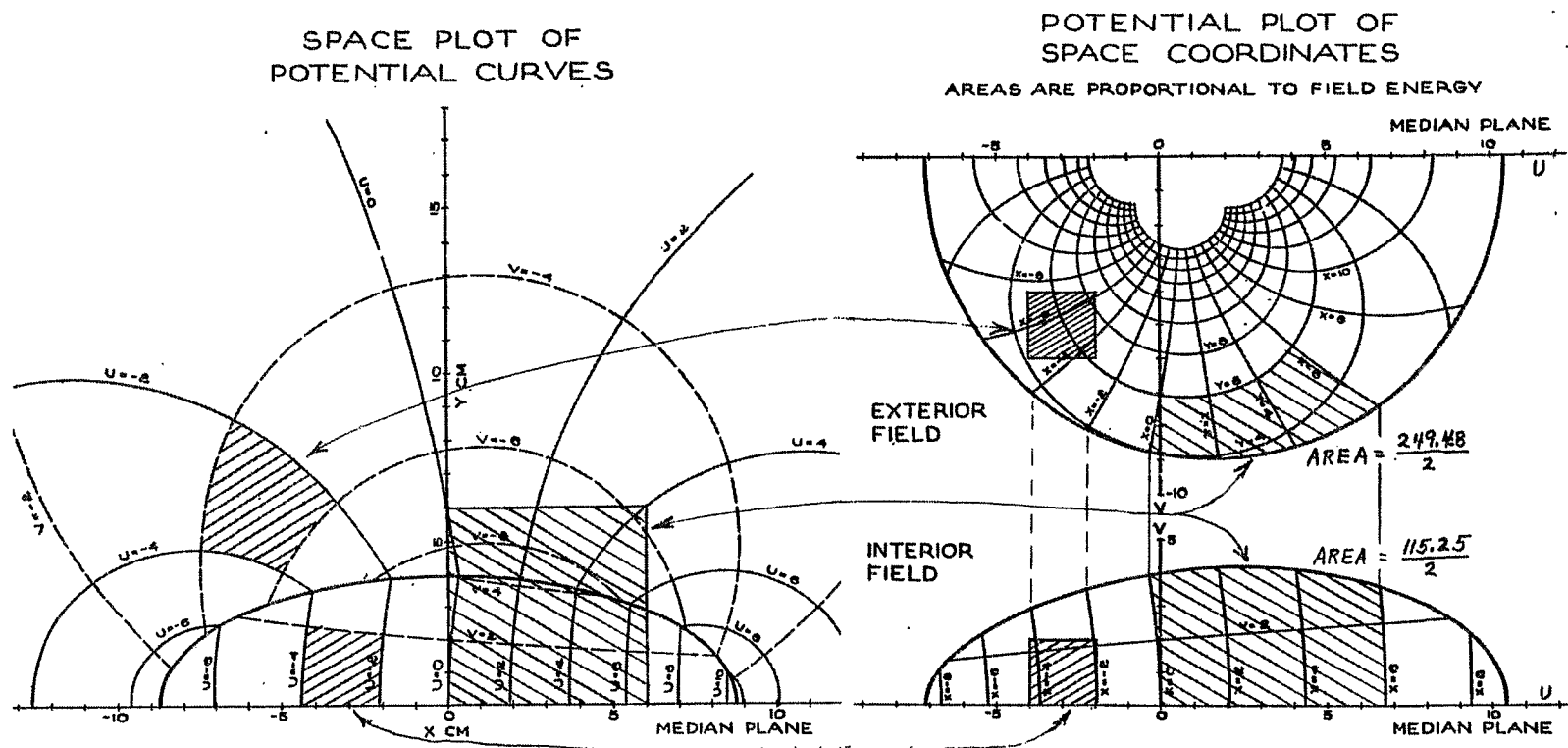


Fig. 7. Constant gradient field within an elliptical current sheet.

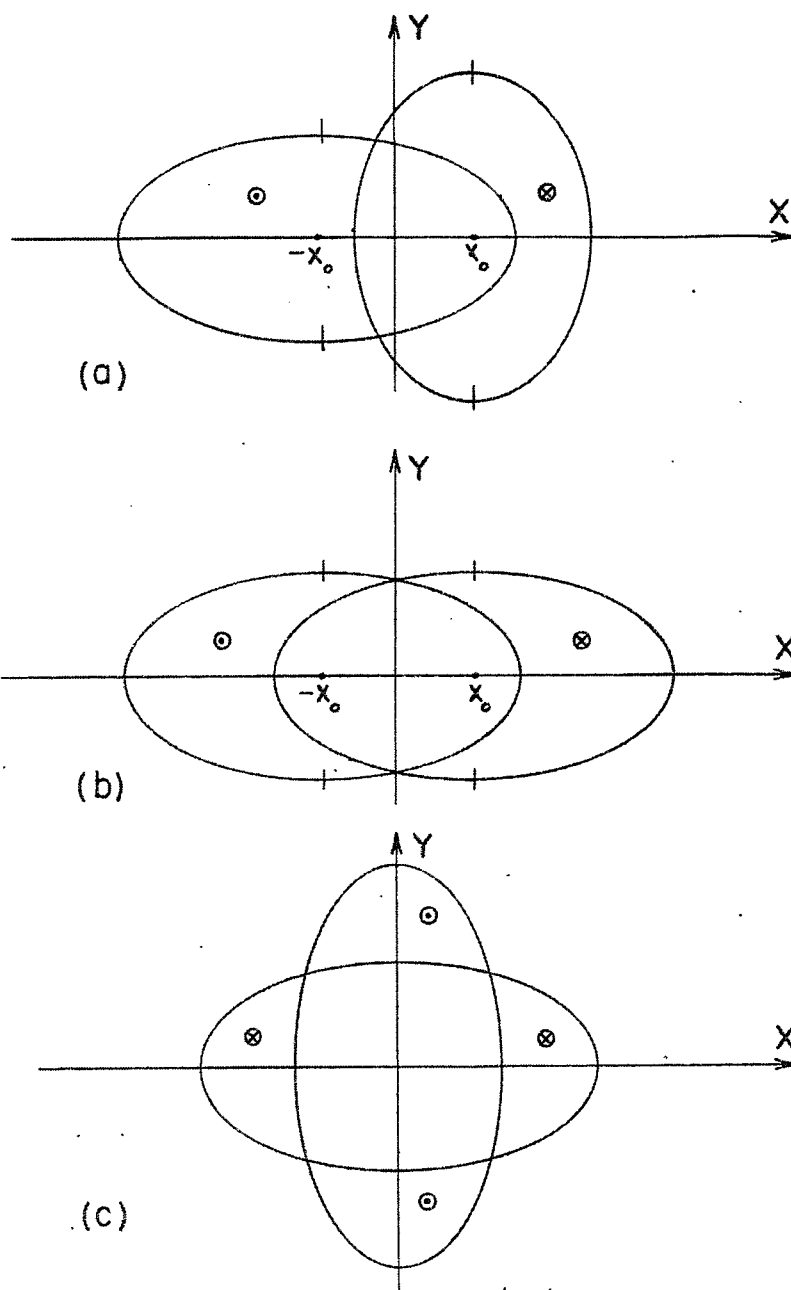


Fig. 8. Apertures formed by overlapping elliptical conductors.  
 (a) Constant gradient field.  
 (b) Dipole field.  
 (c) Quadrupole field.



# SUPERCONDUCTING MAGNETIC DIPOLES\*

G. Parzen  
Brookhaven National Laboratory  
Upton, New York

## I. INTRODUCTION

This paper describes an approach to the design of superconducting magnetic dipoles. Numerical results are given for dipoles having several different geometrical arrangements of the conductors. The procedure applied here to the design of dipoles should be applicable to any magnet shape.

One of the few analytical solutions available in the design of superconducting magnetic dipoles is the  $\cos \theta$  distribution of the current density around a circle, or the corresponding distribution around an ellipse. However, the usefulness of the  $\cos \theta$  solution is limited by a number of other requirements. The magnetic field needs to be uniform to a high accuracy, approximately one part in a thousand. The conductors have considerable thickness and it becomes difficult to place them so that the  $\cos \theta$  distribution is achieved at all radii. For reasons of support and ease of winding, a surface made out of a series of planes may be more desirable than the elliptical surface required by the  $\cos \theta$  distribution.

It seems likely that some other more general approach to calculating the current distribution to obtain the dipole field is desirable which will permit considerable freedom in the geometrical arrangement of the current-carrying conductors. One such approach is investigated in this paper. In this approach, the field is specified at a certain number of discrete points on the median plane. Then for a given geometrical arrangement of rectangular conductors, the current is found in each conductor to give the desired field by solving a set of linear equations relating the currents and the field. The details of this procedure are given in Section V.

## II. TWO-PLANE RECTANGULAR DIPOLE

Magnetic dipoles were investigated having three different geometries. Each dipole had a good field aperture of  $9 \times 18 \text{ cm}^2$ . The geometrical arrangement of the conductors in each dipole is shown in Figs. 1 and 2, where one quadrant of the dipole is shown.

One dipole, shown in Fig. 1a, has a rectangular arrangement of conductors. The inner surface of the rectangle is at  $\pm 10.5 \text{ cm}$  and  $\pm 6 \text{ cm}$ , which allows  $1.5 \text{ cm}$  between the conductors and the good field region that can be used for the vacuum tank and supports for the conductors. There are ten conductors in each quadrant, each conductor being a region of constant current density, and each conductor has a thickness of  $2.54 \text{ cm}$ , which would correspond to two layers of a  $0.5 \text{ in.}$  ribbon.

The currents in the ten conductors for a  $50\,000 \text{ G}$  field are given in Table I. The field variation in the median plane over  $\pm 9 \text{ cm}$  is  $\Delta H/H = 1.6 \times 10^{-6}$ . If we define the good horizontal aperture as a region where the field variation  $\Delta H/H$  is less

---

\*Work performed under the auspices of the U.S. Atomic Energy Commission.

TABLE I. The current distribution for three magnetic dipoles having different geometries.  $\Delta H/H$  is the fractional variation of the magnetic field in the median plane.  $\Delta x$  is the horizontal good aperture in centimeters.

Current in $10^5$ A			
Conductor Number	2-plane Rectangular	3-plane Elliptical	1-plane Planar
1	1.00025	1.16559	2.76034
2	1.01546	1.89295	2.99422
3	1.06907	2.27930	3.19995
4	2.26290	0.24313	3.21642
5	1.99581	1.05001	2.43819
6	0.46032	0.41540	0.84723
7	0.39499	0.65559	0.71688
8	0.25653	0.07148	0.25205
9	0.14740	0.14594	0.19254
10	0.04673	0.01953	0.05337
Total current, kA	865	794	1667
Maximum current density, kA/cm <sup>2</sup>	59	59	42
$\Delta H/H$ , $y = 0$	$1.6 \times 10^{-6}$	$1.6 \times 10^{-5}$	$6.0 \times 10^{-6}$
$\Delta x$ , $y = 0$	18	18	19
$\Delta x$ , $y = 2.5$	18	15	21
$\Delta x$ , $y = 4.5$	16	9	17
$H_{\max}$ , kG	56	57	82.5

than  $2 \times 10^{-3}$ , then the good aperture at  $y = 0$  is  $x = \pm 9$  cm, at  $y = 2.5$  cm,  $x = \pm 9$  cm, at  $y = 4.5$  cm,  $x = \pm 8$  cm. Thus almost the entire region contained by the two-plane array has a satisfactory field. The maximum field at the conductors is 56 000 G or 12% higher than the field on the median plane. The largest current density is 59 000 A/cm<sup>2</sup> and the total current required in one quadrant is 865 000 A.

### III. THREE-PLANE ELLIPTICAL DIPOLE

The second dipole is shown in Fig. 1b, and represents an attempt to approximate an ellipse more closely. The ellipse is shown by a dotted line. This dipole also allowed 1.5 cm for the vacuum tank and support and also had ten conductors in each quadrant with a thickness of 2.54 cm.

The currents in the ten conductors for a 50 000 G field are given in Table I. The field variation in the median plane over  $\pm 9$  cm is  $\Delta H/H = 1.6 \times 10^{-5}$ . The good horizontal aperture at  $y = 0$  is  $x = \pm 9$  cm, at  $y = 2.5$  cm,  $x = \pm 7.5$  cm, and at  $y = 4.5$  cm,  $x = \pm 4.5$  cm. The good field region is close to that indicated by the ellipse with axis  $4.5 \times 9$  cm shown in Fig. 1b. The total current required in one quadrant is 794 000 A. This is about 9% less than the current required for the two-plane array. However, one has to balance this against the smaller good field aperture that is obtained by the three-plane array. The maximum field at the conductors is 56 900 G, and the largest current density is  $59\,000\text{ A/cm}^2$ .

One can detect no important advantage for either the two-plane rectangular array or the more elliptical three-plane array. The choice between the two would be determined by the shape of the good field aperture required, and by consideration of the construction difficulties.

### IV. PLANAR DIPOLE

The third dipole is shown in Fig. 2. This dipole has all the conductors in a single plane. Although clearly less efficient than the other two geometries, it may be worth considering because of the ease of winding this dipole. In particular, this type of dipole may be considered if the requirements on the uniformity of the field can be relaxed.

This dipole also allowed 1.5 cm for the vacuum tank, and the lower surface of the plane is 6 cm above the median plane. The required good field aperture is again  $9 \times 18\text{ cm}^2$ . There are ten conductors in each quadrant, with a thickness of 2.54 cm. The plane is 60 cm wide, or about 3.5 times as wide as the 18 cm of good horizontal aperture.

The currents in the ten conductors for a 50 000 G field are given in Table I. The field variation in the median plane over  $\pm 9$  cm is  $\Delta H/H = 6 \times 10^{-6}$ . The good horizontal aperture at  $y = 0$  is  $x = \pm 9.5$  cm, at  $y = 2.5$  cm,  $x = \pm 10.5$  cm, and at  $y = 4.5$  cm,  $x = \pm 8.5$  cm. Thus almost the full rectangle of  $9 \times 18\text{ cm}^2$  is a region of good field. The total current required in one quadrant is 1 667 000 A, which is about twice the current required in the rectangular geometry. The maximum field at the conductors is 82 500 G, or about 60% higher than the median plane field. The largest current density is 42 000 A.

The efficiency of this dipole could be improved if a less uniform magnetic field were acceptable.

### V. THEORY

The problem to be solved is: given a geometrical arrangement of  $N$  conductors, find the current in each conductor,  $C_n$ , in order to obtain a desired magnetic field in the median plane. Let us suppose that the magnetic field is specified at  $L$  points in the median plane, the points are designated by  $x_i$ , and the magnetic field at these points by  $H_i$ .

The equations for the  $C_n$  can be written in terms of  $G_{i,n}$ , which is the magnetic field at point  $x_i$  due to a unit current flowing in conductor  $n$ . The  $G_{i,n}$  can be calculated from the geometry of the conductor arrangement. One can then write down the  $L$  equations

$$\sum_{n=1}^N G_{i,n} C_n = H_i \quad (1)$$

In principle one might solve Eq. (1) by making  $L$  and  $N$  equal. This, however, leads to mathematical difficulties in solving the equations. Solution of the equations requires a high degree of numerical precision, and the solution often gives currents too high to be acceptable. It is preferable to make  $L$  larger than  $N$ , and to solve the equations by a least squares procedure. One chooses the currents  $C_n$  by minimizing the expression

$$E = R^2 + q C^2 \quad (2a)$$

$$R^2 = \sum_{i=1}^L \sum_{n=1}^N (G_{i,n} C_n - H_i)^2 \quad (2b)$$

$$C^2 = \sum_{n=1}^N C_n^2 \quad (2c)$$

The term  $q C^2$  is added in order to help rule out solutions with large oscillating currents. The parameter  $q$  is determined by trial, and a  $q = 10^{-11}$  was used in the results listed in this paper.

Minimizing  $E$  in Eq. (2a) yields the equations for  $C_n$ ,

$$(G' G + q I) C = G' H \quad (3)$$

Equation (3) is a matrix equation.  $G$  is the matrix  $G_{i,n}$ ,  $G'$  is the transpose of  $G$ ,  $C$  has the elements  $C_n$ ,  $H$  has the elements  $H_i$ , and  $I$  is the identity matrix.

The solutions for  $C_n$  found from Eq. (3) were still not satisfactory, as so far only the field on the median plane has been specified. It was found that although the field on the median plane was equal to the specified field to a high degree of accuracy, the field off the median plane departed considerably from the desired field. Thus it was found desirable to specify the magnetic field at  $L_x$  points on the median plane and at  $L_y$  points along the  $y$ -axis off the median plane.

In order to specify the magnetic field along the  $y$ -axis, the following relations for the field along the  $y$ -axis may be used. Let us assume that the field in the median plane is given by the power series

$$H_y(x,0) = \sum_m b_m x^m \quad (4)$$

It follows from Maxwell's equations that the field along the  $y$ -axis is then given by

$$H_y(0,y) = b_0 - b_2 y^2 + b_4 y^4 - b_6 y^6 + \dots \quad (5a)$$

$$H_x(0,y) = b_1 y - b_3 y^3 + b_5 y^5 - b_7 y^7 + \dots \quad (5b)$$

In computing magnetic dipoles,  $H_y$  was specified along the y-axis. In computing quadrupoles, it would be more desirable to specify  $H_x$  along the y-axis as  $H_y = 0$ .

#### ACKNOWLEDGEMENT

This paper is considerably indebted to K. Jellett for aid with the programming and the computer calculations.

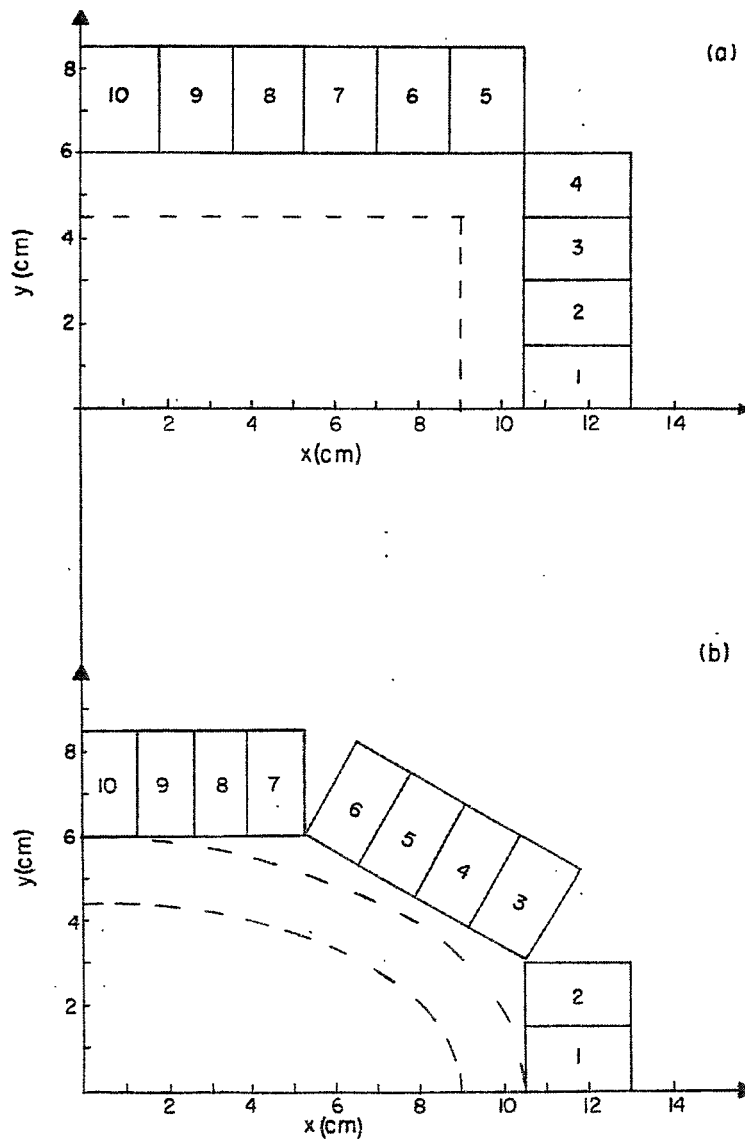


Fig. 1. The arrangement of the conductors in two magnetic dipoles, the two-plane rectangular dipole and the three-plane elliptical dipole.

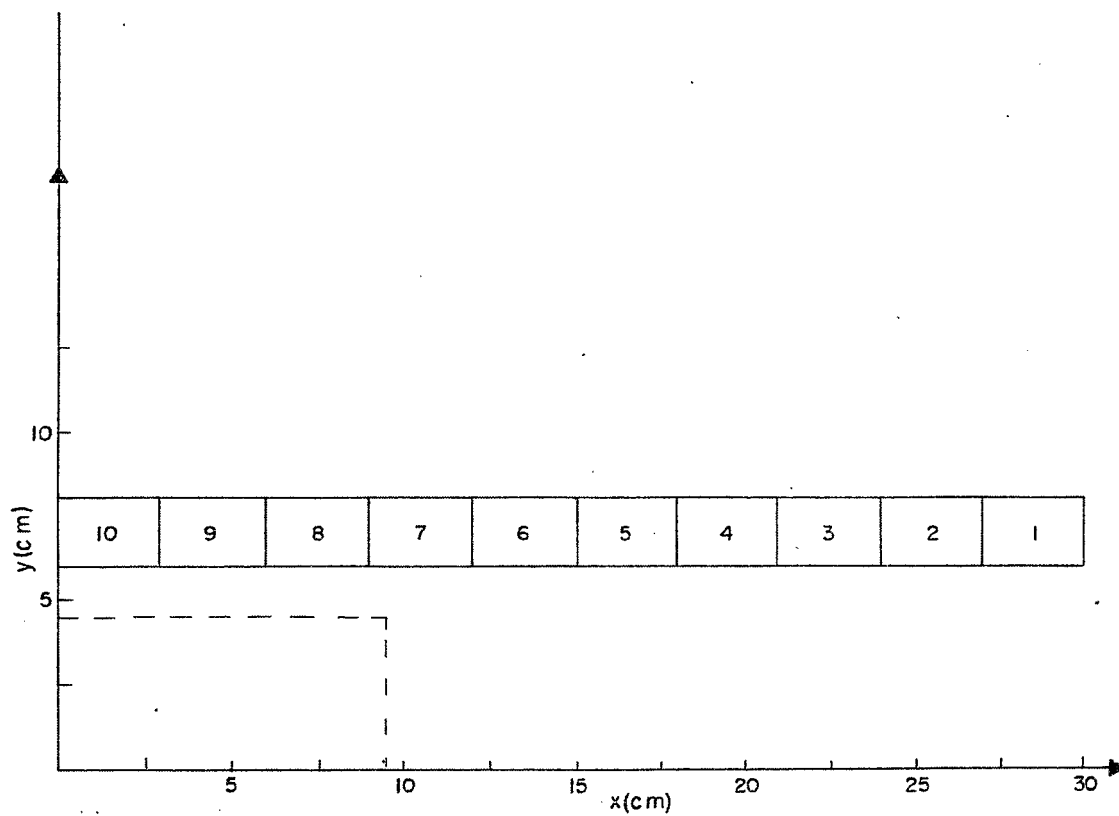


Fig. 2. The arrangement of the conductors in a planar magnetic dipole.

# SUPERCONDUCTING QUADRUPOLE FOCUSING LENS

## Part I: Analytical Design and Full-Scale Copper-Wound Pole

A. Asner  
CERN  
Geneva, Switzerland

### I. INTRODUCTION

In 1966 CERN decided to design a first superconducting beam transport element, a quadrupole lens, with the aim of gaining operational experience with such magnets in external beams of the Proton Synchrotron and of sponsoring European superconductor technology.

A collaboration between CERN, the Culham Laboratory and the Oxford Instrument Company (both of the latter being in Great Britain) has since been established, the project being partially financed by the British Ministry of Technology.

This paper gives a theoretical analysis of the quadrupole lens and describes a full-scale, copper-wound pole model made at CERN with the aim of performing magnetic measurements and of establishing the winding procedure and the mechanical construction in view of the four poles to be wound with superconductors.

### II. THE ANALYTICAL DESIGN OF THE QUADRUPOLE LENS

Several authors have considered the problem of obtaining accurate two-dimensional dipole, quadrupole -  $2n$  pole fields in general - within a certain aperture by computing the required current density distribution around it. Grivet<sup>1</sup> has examined rectangular, uniform current density configurations; Beth<sup>2</sup> has developed a method of best approximation for an ideal sine-like line-current distribution around a circular aperture, since in any real case the current density and the coil height will be finite. The sine-like distribution is approximated by a number of uniform current density steps, yielding the required magnetic field, field gradient, etc. uniformity within the aperture.

The theory of the quadrupole lens under consideration is based on an independent though similar approach.<sup>3-5</sup> A finite current density and coil height around a circular aperture had been assumed and the appropriate configuration for uniform current density, yielding the (dipole) quadrupole field, etc., with required precision computed.

We start with the vector potential  $A$  at point  $P(\rho, \psi)$  of a line current  $+I$  placed at  $r, \varphi$ , according to Fig. 1. Cylindrical coordinates are used.

- 
1. A. Septier, European Organization for Nuclear Research Report CERN 60-6 (1960).
  2. R.A. Beth, Brookhaven National Laboratory, Accelerator Dept. Report AADD-135 (1967).
  3. A. Asner, F. Deutsch, and Ch. Iselin, CERN Report MPS/Int. MA 65-12, TN 75 (1965).
  4. A. Asner and Ch. Iselin, in Proc. 2nd Intern. Conf. Magnet Technology, Oxford, 1967, p. 32.
  5. F. Deutsch, CERN Report MPS/Int. MA 67-9, TN 90 (1967).

The vector potential at P is given by:

$$A = \frac{1}{2} \lambda \ln [r^2 + \rho^2 - 2r\rho \cos (\varphi - \psi)] \quad (1)$$

with

$$\lambda = \frac{I\mu_0}{2\pi} \quad (2)$$

The expression for the vector potential can be expressed as the following trigonometric power series<sup>6</sup>:

$$\begin{aligned} \frac{A}{\lambda} &= -\frac{1}{2} \ln [r^2 + \rho^2 - 2r\rho \cos (\varphi - \psi)] \\ &= -\ln r + \sum_{k=1}^{\infty} \frac{a^k \cos k (\varphi - \psi)}{k} \end{aligned} \quad (3)$$

for  $a = \rho/r < 1$ , and as:

$$\frac{A}{\lambda} = -\ln \rho + \sum_{k=1}^{\infty} \frac{\cos k (\varphi - \psi)}{k \cdot a^k} \quad (4)$$

for  $a = \rho/r > 1$ .

For a symmetric arrangement of four line currents according to Fig. 2, the vector potential at  $P(\rho, \psi)$  is:

$$\frac{A}{\lambda} = 4 \sum_{k=1}^{\infty} \frac{a^{2k-1}}{2k-1} \sin [(2k-1)\varphi] \sin [(2k-1)\psi] \quad (5)$$

for  $a = \rho/r < 1$ .

If, according to Fig. 3, four symmetric sector coils with uniform current density  $j$  are assumed so that  $dI = j r dr d\varphi$ , and if the sectors cover the angular region between  $\alpha$  and  $(\pi/2) - \alpha$ , etc., and between the radii  $R_1$  and  $R_2$  the vector potential  $A$  is given by:

$$\begin{aligned} A &= 2\lambda (\sin 2\psi) (\cos 2\alpha) \rho^2 \ln \frac{R_2}{R_1} + \\ &+ \sum_{k=1}^{\infty} \frac{\sin [(4k+2)\psi] \cos [(4k+2)\alpha]}{2k(4k+2)^2} \rho^{4k+2} \left( \frac{1}{R_1^{4k}} - \frac{1}{R_2^{4k}} \right) \end{aligned} \quad (6)$$

From the vector potential the magnetic field components  $B_\rho$  and  $B_\psi$  can be obtained as follows:

---

6. H.B. Dwight, Tables of Integrals and Other Mathematical Data (MacMillan, New York, 1955), Formula 418, p. 85.



$$B_{\rho} = [\nabla A]_{\rho} = \frac{1}{\rho} \frac{\partial A}{\partial \psi} = 4\lambda (\cos 2\psi) (\cos 2\alpha) \rho \ln \frac{R_2}{R_1} + \sum_{k=1}^{\infty} \frac{\cos [(4k+2)\psi] \cos [(4k+2)\alpha]}{2k(4k+2)} \rho^{4k+1} \left( \frac{1}{R_1^{4k}} - \frac{1}{R_2^{4k}} \right) \quad (7)$$

$$B_{\psi} = [\nabla A]_{\psi} = - \frac{\partial A}{\partial \rho} = - 4\lambda (\sin 2\psi) (\cos 2\alpha) \rho \ln \frac{R_2}{R_1} - \sum_{k=1}^{\infty} \frac{\sin [(4k+2)\psi] \cos [(4k+2)\alpha]}{2k(4k+2)} \rho^{4k+1} \left( \frac{1}{R_1^{4k}} - \frac{1}{R_2^{4k}} \right) \quad (8)$$

For  $\psi = 0$ , Eq. (7) yields the field  $B_{\rho}$  in the horizontal  $\rho$ -axis, and for  $\psi = \pi/4$ , Eq. (8) yields the field  $B_y$  or  $B_x$ , respectively. Differentiating Eqs. (7) and (8) under these conditions one obtains for the field gradient:

$$g_{\rho} = \left( \frac{\partial B_{\rho}}{\partial \rho} \right)_{\psi=0} = 4\lambda (\cos 2\alpha) \ln \frac{R_2}{R_1} + \sum_{k=1}^{\infty} 2\lambda \frac{(4k+1)}{k(4k+2)} \cos [(4k+2)\alpha] \rho^{4k} \left( \frac{1}{R_1^{4k}} - \frac{1}{R_2^{4k}} \right) \quad (9)$$

$$g_x = \left( \frac{\partial B_y}{\partial x} \right)_{\substack{\psi=45^\circ \\ x=\rho}} = 4\lambda (\cos 2\alpha) \ln \frac{R_2}{R_1} - 2\lambda \sum_{k=1}^{\infty} \frac{(-1)^k \cos [(4k+2)\alpha]}{k(4k+2)} (4k+1) \rho^{4k} \left( \frac{1}{R_1^{4k}} - \frac{1}{R_2^{4k}} \right) \quad (10)$$

Equations (9) and (10) are very convenient for the design of a quadrupole lens: the first constant term corresponds to the wanted constant gradient, the sum to the error terms. By putting  $\alpha = 15^\circ$ , which in accordance with Fig. 3 corresponds to  $30^\circ$  sector coils, the first dodecapolar error term vanishes, and the gradient error is mainly determined by the 20th harmonic. A simple calculation shows that the same reasoning is valid for sector coils between the angles  $\alpha_2$  and  $(\pi/4)(\alpha_2 - \alpha_1)$ , respectively, between  $(\pi/2) - \alpha_2$  and  $(\pi/4) + (\alpha_2 - \alpha_1)$  (see Fig. 4).

Two ways of eliminating both the 12th and 20th harmonic and of obtaining an even more uniform gradient within the aperture are shown in Figs. 5 and 6. By introducing an intermediate sector radius  $R_1$  — as shown in Fig. 5 — and by introducing the angles  $\alpha_1$  and  $\alpha_2$  the  $g_{\rho}$  gradient (for example) becomes:

$$\begin{aligned}
(g_p)_{\text{Fig. 6}} &= 4\lambda \left( \cos 2\alpha_1 \ln \frac{R_2}{R_i} + \cos 2\alpha_2 \ln \frac{R_i}{R_1} \right) + \\
&+ \sum_{k=1}^{\infty} 2\lambda \frac{(4k+1)}{k(4k+2)} \rho^{4k} \times \\
&\times \left\{ \cos [(4k+2)\alpha_1] \left( \frac{1}{R_i^{4k}} - \frac{1}{R_2^{4k}} \right) + \cos [(4k+2)\alpha_2] \left( \frac{1}{R_1^{4k}} - \frac{1}{R_i^{4k}} \right) \right\}.
\end{aligned} \tag{11}$$

Choosing  $\alpha_1 = 9^\circ$  and  $\alpha_2 = 27^\circ$  the 20th harmonic is eliminated. The 12th harmonic is eliminated by choosing  $R_i$  such that

$$\cos 54^\circ \left( \frac{1}{R_i^4} - \frac{1}{R_2^4} \right) + \cos 162^\circ \left( \frac{1}{R_1^4} - \frac{1}{R_i^4} \right) = 0 \tag{12}$$

or

$$\begin{aligned}
1.318 \frac{1}{R_i^4} &= 0.88 \frac{1}{R_1^4} + 0.432 \frac{1}{R_2^4} = M; \\
R_i &= \sqrt[4]{\frac{1.318}{M}}.
\end{aligned} \tag{13}$$

If according to Fig. 6 two constant current density sectors with  $j_1$  and  $j_2$  are chosen, and again  $\alpha_1 = 9^\circ$ ,  $\alpha_2 = 27^\circ$ , Eq. (9) changes into:

$$\begin{aligned}
(g_p)_{\text{Fig. 7}} &= 4\lambda_1 \cos 2\alpha_1 \ln \frac{R_2}{R_1} + 4(\lambda_2 - \lambda_1) \cos 2\alpha_2 \ln \frac{R_2}{R_1} + \\
&+ \sum_{k=1}^{\infty} \frac{(4k+1) \rho^{4k}}{k(4k+2)} \left( \frac{1}{R_1^{4k}} - \frac{1}{R_2^{4k}} \right) \times \\
&\times \left\{ 4\lambda_1 \cos [(4k+2)\alpha_1] + 4(\lambda_2 - \lambda_1) \cos [(4k+2)\alpha_2] \right\}.
\end{aligned} \tag{14}$$

The 20th harmonic is again eliminated with  $\alpha_1 = 9^\circ$  and  $\alpha_2 = 27^\circ$ ; the 12th harmonic by making:

$$4\lambda_1 \cos 54^\circ + 4(\lambda_2 - \lambda_1) \cos 162^\circ = 0 \tag{15}$$

$$j_2 = j_1 \frac{1.318}{0.88} = 1.5 j_1. \tag{16}$$

When designing superconducting quadrupoles it is important to know the field inside the winding in order to determine the mechanical forces and stresses as well as the magnetic field outside the winding.

By a similar computation as before one finds for the magnetic field components  $B_\rho$  and  $B_\psi$  inside the winding, i.e., for  $R_1 < \rho < R_2$ :

$$\begin{aligned}
B_\rho &= 4\lambda \rho (\cos 2\psi) (\cos 2\alpha) \ln \frac{R_2}{\rho} + \\
&+ \sum_{k=1}^{\infty} \frac{\cos [(4k+2)\psi] \cos [(4k+2)\alpha]}{2k(4k+2)} \rho \left[ 1 - \left( \frac{\rho}{R_2} \right)^{4k} \right] + \\
&+ \sum_{k=1}^{\infty} \frac{\cos [(4k-2)\psi] \cos [(4k-2)\alpha]}{2k(4k-2)} \rho \left[ 1 - \left( \frac{R_1}{\rho} \right)^{4k} \right] \quad (17)
\end{aligned}$$

$$\begin{aligned}
B_\psi &= -4\lambda (\sin 2\psi) (\cos 2\alpha) \rho \ln \frac{R_2}{\rho} - \\
&- \sum_{k=1}^{\infty} \frac{\sin [(4k+2)\psi] \cos [(4k+2)\alpha]}{2k(4k+2)} \rho \left[ 1 - \left( \frac{\rho}{R_2} \right)^{4k} \right] + \\
&+ \sum_{k=1}^{\infty} \frac{\sin [(4k-2)\psi] \cos [(4k-2)\alpha]}{2k(4k-2)} \rho \left[ 1 - \left( \frac{R_1}{\rho} \right)^{4k} \right] \quad (18)
\end{aligned}$$

For the field outside the quadrupole ( $R_2 < \rho < \infty$ ) one finds:

$$B_\rho = 4\lambda \sum_{k=1}^{\infty} \frac{\cos [(4k-2)\psi] \cos [(4k-2)\alpha]}{2k(4k-2)} \frac{1}{\rho^{4k-1}} \left( R_2^{4k} - R_1^{4k} \right) \quad (19)$$

$$B_\psi = 4\lambda \sum_{k=1}^{\infty} \frac{\sin [(4k-2)\psi] \cos [(4k-2)\alpha]}{2k(4k-2)} \frac{1}{\rho^{4k-1}} \left( R_2^{4k} - R_1^{4k} \right) \quad (20)$$

Similar expressions can be derived for dipole fields.<sup>3-5</sup> In order to obtain a field uniformity required for high energy physics beam transport and accelerator magnets, the elimination of a larger number of harmonics than in the quadrupole case will be necessary. When doing so, the method demonstrated approaches the analysis of Beth.

The CERN-Culham Laboratory quadrupole will be shielded by a magnetic steel cylinder, concentric with the longitudinal axis of the lens. It is useful to compute the minimum radius  $r_s$  of this cylinder as well as the effect of the imaged currents on the field and the field gradient within the useful aperture.

Normally one would choose  $\rho = r_s$  such that the field components outside the quadrupole winding  $B_\rho$  and  $B_\psi$  [see Eqs. (19) and (20)] are  $B_\rho, B_\psi \leq B_{\text{sat}} \approx 2 \text{ T}$ .

The minimum cylinder thickness is found from Eq. (21):

$$\begin{aligned}
\Delta_{\min} &= \frac{\Phi}{B_{\text{sat}}} \approx \frac{1}{B_{\text{sat}}} \int_{r_s}^{\infty} \lambda \cos 2\alpha \left( R_2^4 - R_1^4 \right) \frac{d\rho}{\rho^3} \\
&\approx \frac{1}{B_{\text{sat}}} \frac{\lambda \cos 2\alpha (R_2^4 - R_1^4)}{2 r_s^2} \quad (21)
\end{aligned}$$

In order to find the additional magnetic field  $(B)_s$  or gradient  $(g)_s$  due to the magnetic screen for a single sector, uniform current density quadrupole, the coordinate system shown in Fig. 7 will be used.

By imaging the winding radii on  $r_s$  one obtains:

$$R'_1 = \frac{r_s^2}{R_1}, \quad R'_2 = \frac{r_s^2}{R_2} \quad (22)$$

and for the imaged current density from:

$$j r dr d\varphi = j' r' dr' d\varphi' \quad (23)$$

$$j' = j \left( \frac{r_s}{r} \right)^4. \quad (24)$$

By a similar analysis as applied to the main winding field and gradient computation, one finds for:

$$\begin{aligned} (B_y)_{\text{screen}} = & - \frac{\mu_o j r_s^4}{\pi} \sum_{n=0}^{\infty} \frac{4}{(4n+2)(4n+4)} \times \\ & \times x^{(4n+1)} \sin [(4n+2)\varphi_o] \left( \frac{1}{R_1^{(4n+4)}} - \frac{1}{R_2^{(4n+4)}} \right) \end{aligned} \quad (25)$$

and

$$\begin{aligned} \left( g = \frac{\partial B_y}{\partial x} \right)_{\text{screen}} = & - \frac{\mu_o j r_s^4}{\pi} \sum_{n=0}^{\infty} \frac{4(4n+1)}{(4n+2)(4n+4)} \times \\ & \times x^{4n} \sin [(4n+2)\varphi_o] \left( \frac{1}{R_1^{(4n+4)}} - \frac{1}{R_2^{(4n+4)}} \right). \end{aligned} \quad (26)$$

The gradient  $g$  according to Eqs. (9) and (10) is increased by

$$(\Delta g)_{\text{screen}} \approx \frac{\mu_o j}{2\pi} \sin 2\varphi_o \left[ \left( \frac{R_2}{r_s} \right)^4 - \left( \frac{R_1}{r_s} \right)^4 \right]. \quad (27)$$

### III. THE QUADRUPOLE PARAMETERS

Based on the expressions derived so far and taking into account the performance obtained with the NbTi composite superconductor wound test coil, as stated in paragraph 3 of the second part of this paper, written by D. Cornish, the nominal superconducting quadrupole parameters - without screening effect - have been chosen as follows (see Fig. 8):

Quadrupole length	l	70.0 cm
Winding inner radius	$R_1$	6.5 cm
Winding outer radius	$R_2$	14.8 cm
Useful aperture radius	$R_0$	5.0 cm
Screen radius	$r_s$	33.5 cm
Angles of sector coil	$\varphi_1 ; \varphi_2$	$2^\circ ; (30-2)^\circ$
Over-all current density	j	$1.15 \times 10^4$ A/cm
Nominal current	I	820.0 A
Nominal field gradient	g	57.0 Vs/m <sup>3</sup> (5.7 kG/cm)
Maximum field in winding straight part	$B_{o \text{ lin}}$	4.5 T (45 kG)
Maximum end field	$B_{\text{max}}$	4.9 T
Maximum tangential and compressive winding stress	$\sigma_t, \sigma_c$	$< 4.0 \text{ kg/mm}^2$
Quadrupole inductance	L	0.6 H
Stored energy	A	200 kJ

Figure 9 shows the quadrupole gradient errors on the main axes.

#### IV. WINDING OF A FULL-SCALE UPPER POLE

In order to gain experience in winding the four poles with a rather unusual geometry, a full-scale pole had been wound at CERN with a copper conductor of the final  $1.52 \times 4.05 \text{ mm}^2$  (0.06 in.  $\times$  0.16 in.) composite Cu-superconductor cross section.

Figure 10 shows the four pole cores and two of the  $2^\circ$  side plates. Before winding, the core is clad with slotted, 1 mm thick vetronite (glass reinforced epoxy resin), providing electrical insulation and efficient helium flow into the winding.

Since the conductors are wound in layers parallel to the  $28^\circ$  faces of the pole cores, the layers start to depart from the inner cylinder at point P (Fig. 8). As shown in Fig. 11 radial segments have been foreseen to guide the layers and determine the  $90^\circ$  angle of a completely wound pole. In a similar way the upper circumferential segments determine the winding outer radius.

The model pole proved to be very useful in studying and determining many details of the winding technique such as twisting the conductor in order to obtain smooth layers in the coil straight parts, casting of the end helmet inner epoxy layers to fit closely the coil end geometry and machining of the  $2^\circ$  side plates in strict accordance with the staircase-shaped straight coil parts.

The four coils will be slightly overwound so that when assembled with their side plates and pressed with the outer cylinder — one half of which is shown in Fig. 12 with helium passages and grooved vetronite insulation at the inside — a compact arrangement is obtained preventing relative displacements of individual conductors due to thermal and electromagnetic stresses.

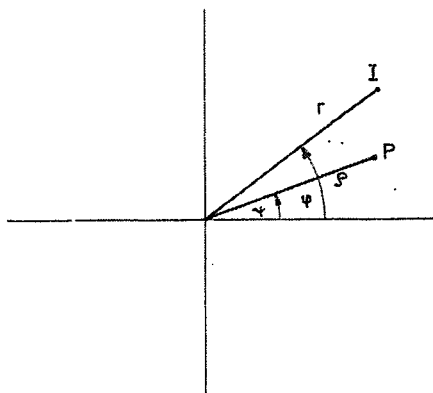


Fig. 1. Vector potential of line current  $I(r, \varphi)$  in  $P(\rho, \psi)$ .

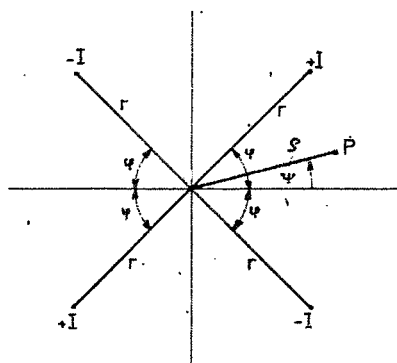


Fig. 2. Vector potential of four symmetric line currents  $\pm I$  in  $P(\rho, \psi)$ .

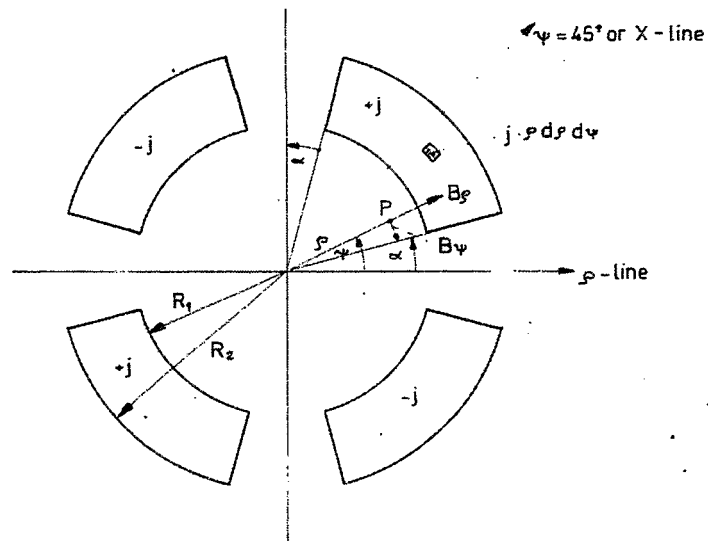


Fig. 3. Computation of field components  $B_\rho$  and  $B_\psi$  for constant current density  $-j$  ( $\text{A}/\text{cm}^2$ ) - sector coils between the radii  $R_1$  and  $R_2$  and angles  $\alpha$  and  $(\pi/2) - \alpha$ .

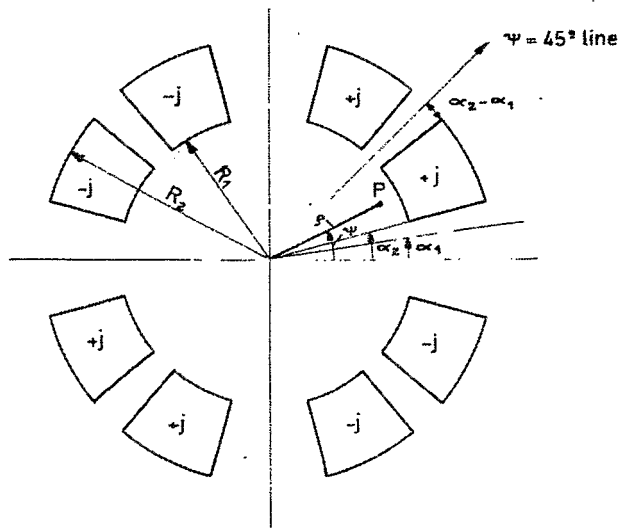


Fig. 4. Same, but for sector coils between  $\alpha_2 - \alpha_1$  and  $(\pi/4) - (\alpha_2 - \alpha_1)$ .

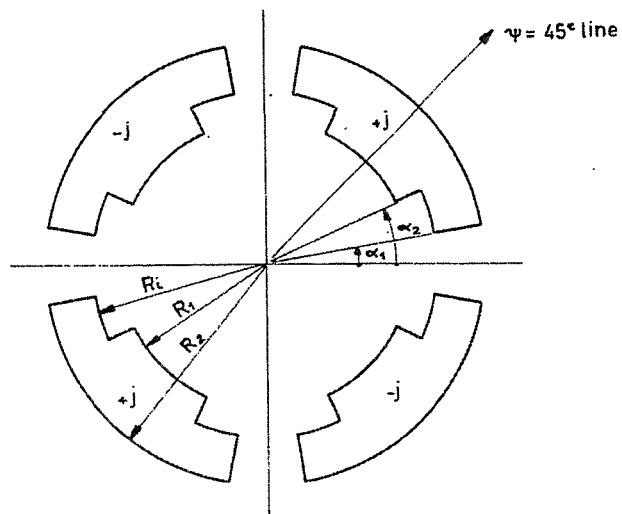


Fig. 5. Uniform current density sector coil quadrupole winding with intermediate radius  $R_1$ .

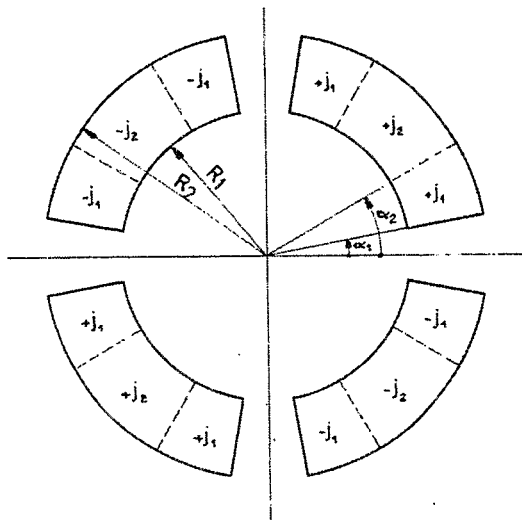


Fig. 6. Sector coil quadrupole winding with two current densities  $j_1$  and  $j_2$ .



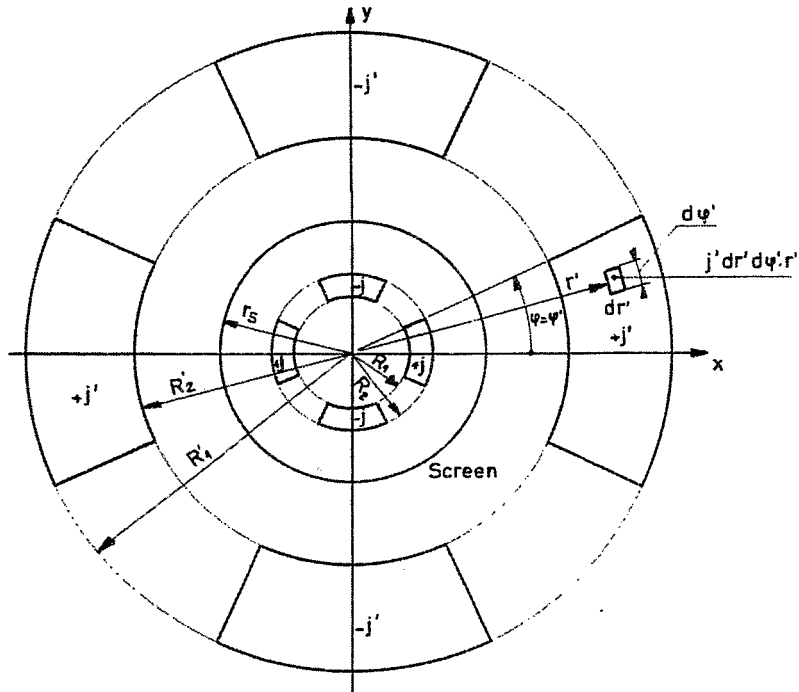


Fig. 7. Influence of concentric screen on uniform current density sector coil quadrupole winding.

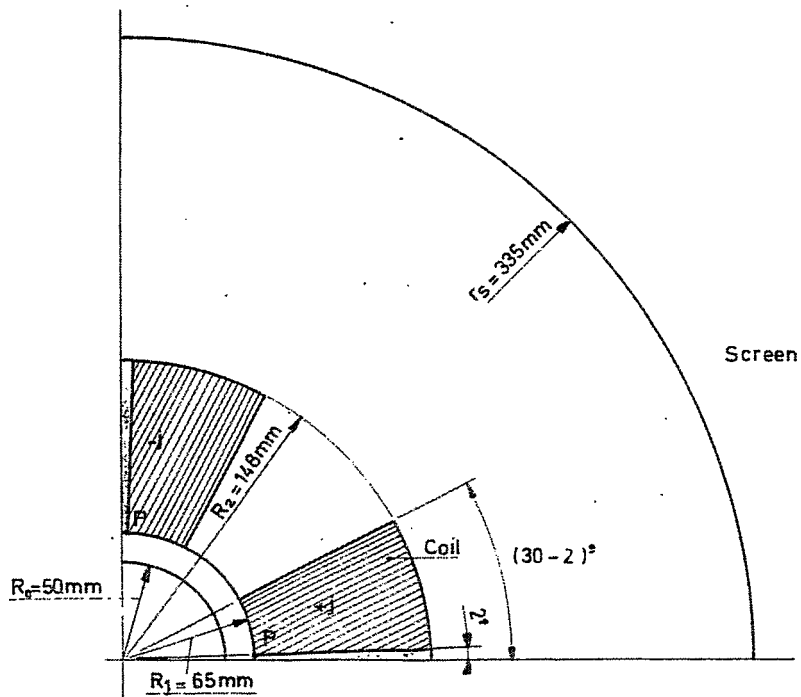


Fig. 8. Main geometrical parameters of the CERN superconducting quadrupole lens.

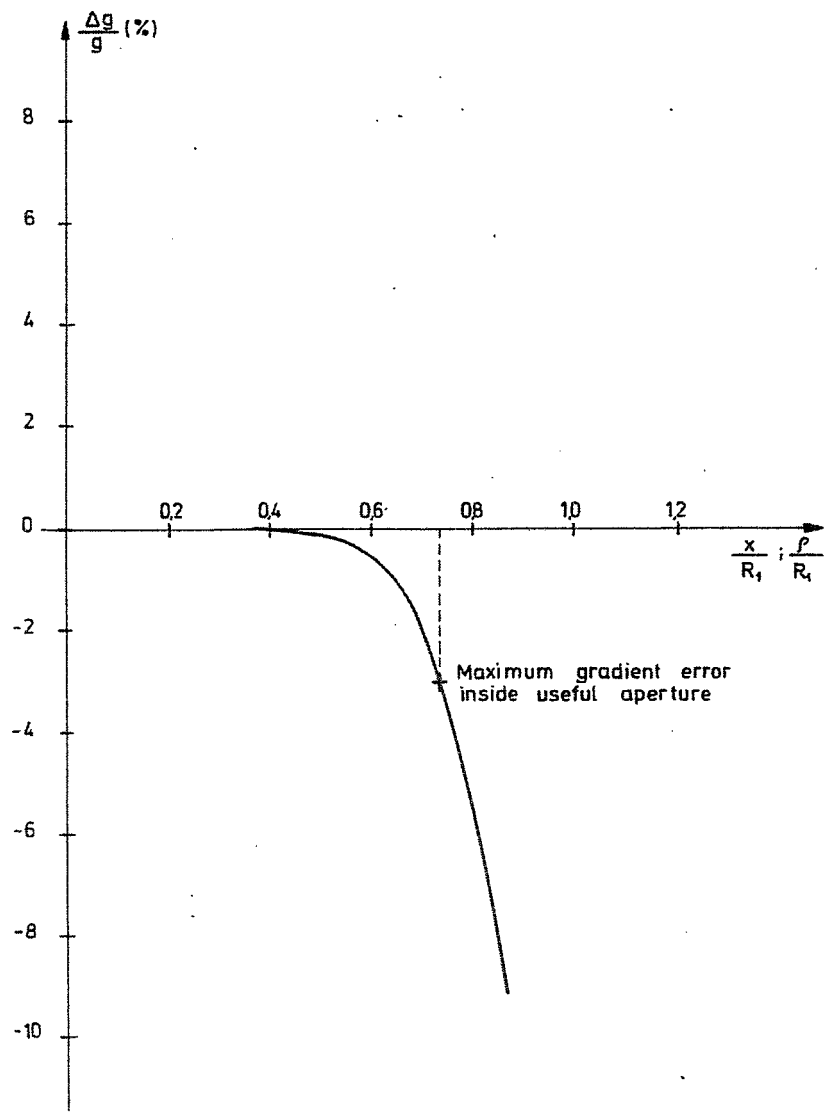


Fig. 9. Relative gradient error of the CERN SC quadrupole lens.

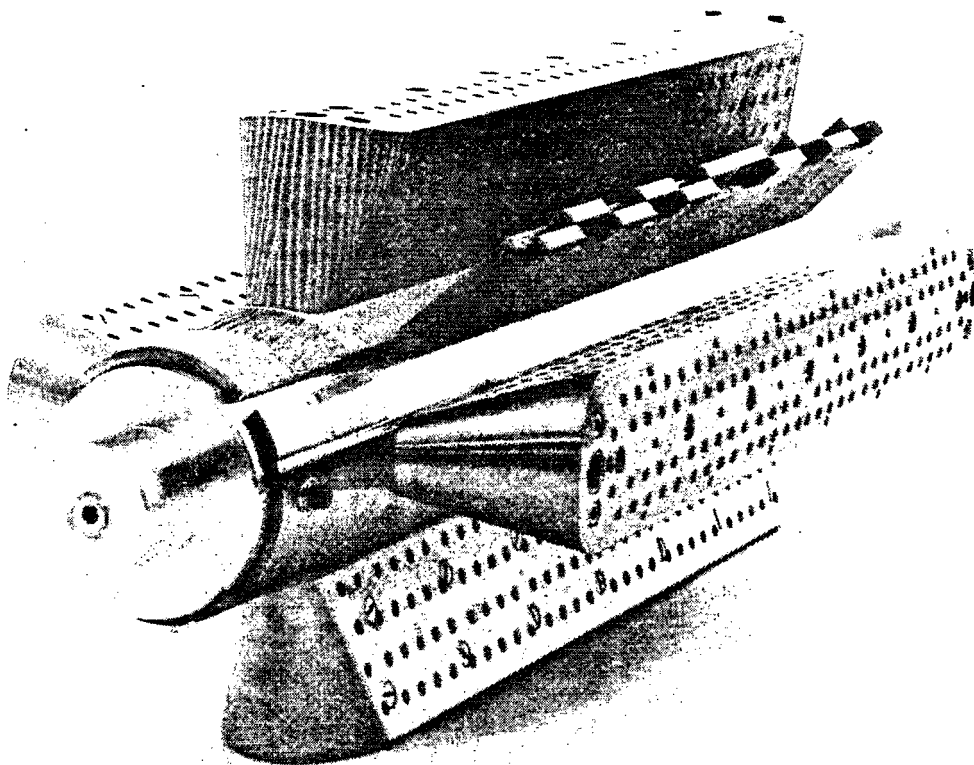


Fig. 10. The four pole cores, top one clad with vetronite, and two 2° side plates.

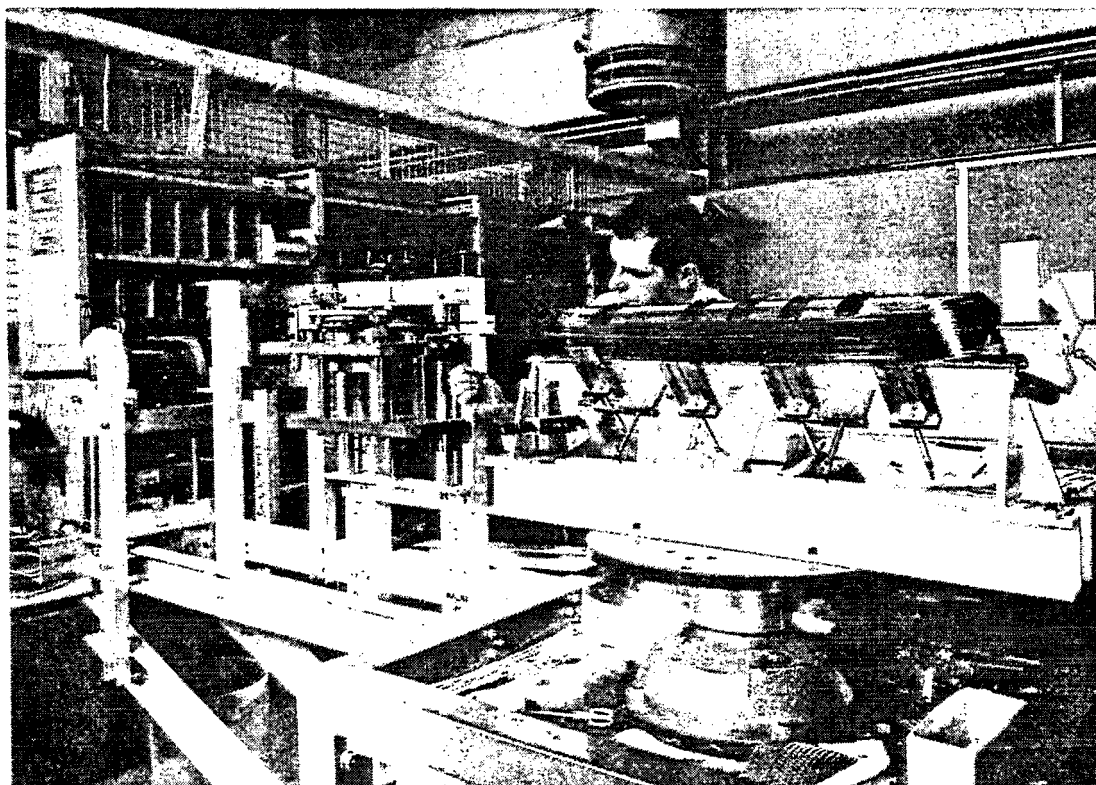


Fig. 11. Winding of the full-scale model pole with copper.

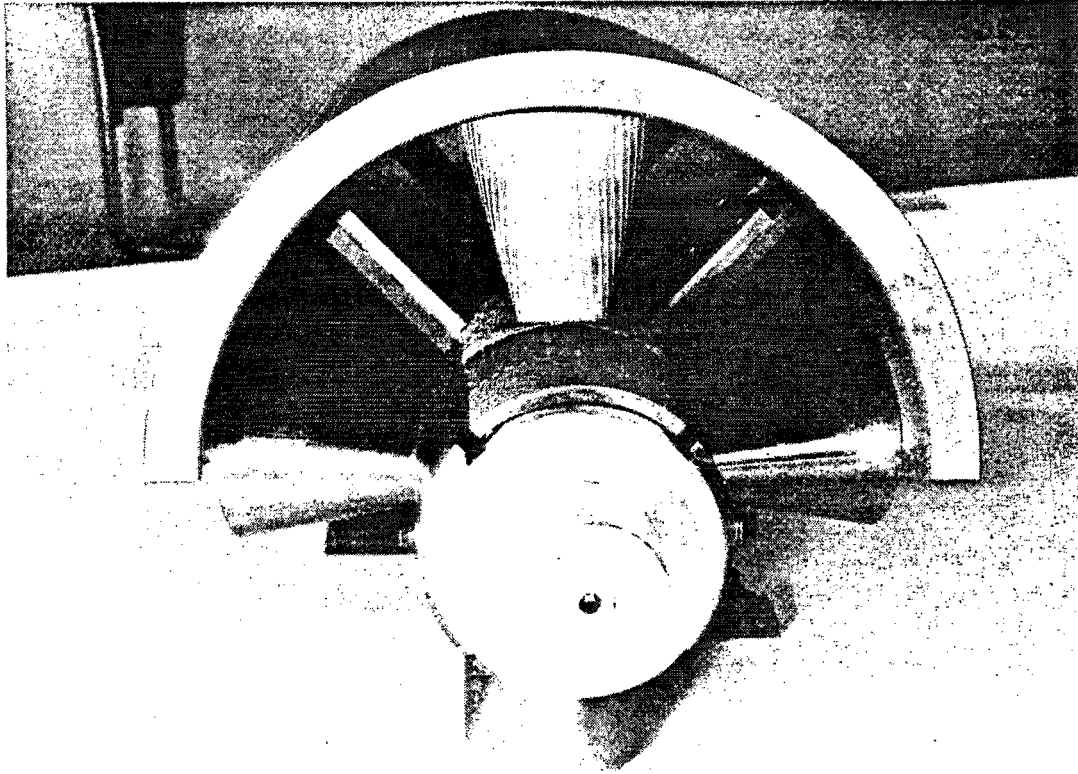


Fig. 12. Pole cores, 2<sup>o</sup> side plates and one-half of outside clamping cylinder.

# SUPERCONDUCTING QUADRUPOLE FOCUSING LENS

## Part II: Construction and Preliminary Tests

D.N. Cornish  
U.K.A.E.A. Research Group, Culham Laboratory  
Abingdon, Berks., England

### I. INTRODUCTION

A quadrupole focusing lens is being developed using NbTi/copper composite superconductor. CERN, the Culham Laboratory and the Oxford Instrument Company are cooperating to carry out the work, which is also being partially financed by the Ministry of Technology. This paper discusses the problems associated with the superconductor, the general construction of the quadrupole, and preliminary tests on a test solenoid. The analytical design of the lens is described in the paper by Dr. A. Asner.

### II. WINDING DETAILS

#### 1. Selection of Superconductor

Since a high over-all current density is required in the winding if a worthwhile performance of the quadrupole is to be obtained, a fully copper stabilized winding is unsuitable for this application. The coil has been designed, therefore, to operate in the partially stabilized mode such that transient normalities, associated with short lengths of the conductor, will not result in a quench of the coil. To obtain this the heat transfer at the surface of the conductor has been limited to  $0.4 \text{ W/cm}^2$  and cooling channels 0.01 in. wide have been provided between all layers.

From current density considerations, the optimum size of conductor would be a copper-clad 0.01 in. diameter NbTi wire, but the problems of winding a coil of this shape with such a small wire and preventing subsequent wire movements are very severe. A larger, rectangular conductor incorporating a number of superconducting filaments has therefore been used.

Details of the conductor, manufactured by I.M.I., are as follows:

Over-all dimensions	0.06 in. $\times$ 0.16 in.
NbTi superconductor	16 strands 0.01 in. diam
Operating current	820 A (at approx. 46 kG)
Copper resistance ratio	$\geq 200:1$ ( $H = 0$ )
Critical current	900 A at 50 kG
Conductor insulation	0.00075 in. thick Formvar

#### 2. Interlayer Insulation

A specially manufactured nylon net is inserted between all layers to ensure that the two wide surfaces of the conductor are in contact with liquid helium. The net consists of 0.012 in. diam nylon monofilaments, spaced 16 to the inch, in a direction perpendicular to the direction of the winding, held in position by interwoven 0.0001 in.

diameter filaments. The woven net is calendered to an over-all thickness of 0.01 in. to increase the surface area in contact with the conductor. The over-all current density in the winding is  $1.1 \times 10^4$  A/cm<sup>2</sup> with a conductor current of 820 A.

### 3. General Winding Details

Figure 1 is an illustration prepared from preliminary drawings to show the general arrangement of the quadrupole. The windings are wound on hollow formers fabricated from nonmagnetic stainless steel. Winding surfaces are insulated with resin-bonded glass fiber sheets with machined channels for liquid helium access. Part way through the winding the length of the layers is gradually decreased. These layers are supported by progressively inserting a thin steel plate, backed with stepped and channelled insulation, along the straight faces of the pole as the winding proceeds.

When the winding is completed a metal helmet is placed around the curved ends, with a small thickness of epoxy cast between it and the outside of the winding. To reduce the maximum field strength at the ends of the poles, the current density is reduced by inserting half-moon-shaped pieces of insulation between the layers at a number of points in the winding (not shown on illustration). Steel bands surround the four poles to restrain the windings against the outward radial electromagnetic forces.

### III. TEST COIL

Before commencing manufacture of the first pole, a small test solenoid was wound to check the operation of the conductor in a thermal environment similar to that in the quadrupole. The coil parameters were as follows:

Inside diameter	1.0 in.
Outside diameter	4.37 in.
Length	3.94 in.

The anticipated load line of the quadrupole and that of the test solenoid are shown on Fig. 2. The solid (H-I) curve was obtained by multiplying the manufacturer's typical curve for a 0.01 in. diam wire by 16. The dotted curve has been drawn parallel to this through a single spot check point measured on a sample of the conductor used in the coil.

#### 1. Tests on Solenoid

For the first series of tests the coil was mounted with its axis vertical. In all instances the coil was cooled to 77°K by heat transfer through helium gas to nitrogen outside the helium cryostat. The pressure in the vacuum chamber of this cryostat was raised to allow heat transfer to take place and it was repumped when cooling below 77°K was commenced.

When fully immersed in liquid helium the coil was energized and the current increased until it quenched. This procedure was repeated a number of times - the quenching value being 930 A on all occasions except the first which was 850 A. The coil was then remounted with its axis horizontal and the test repeated; the results of this series are shown on Fig. 3.

Since the minimum angle between the plane of the layer and the horizontal plane will be 26° on the quadrupole, the coil was then tested with its axis tilted at this angle. The coil was quenched many times, reaching the critical current on each occasion. The current through the coil was also reversed without affecting the quench value.

The final run in this series of tests was carried out with the coil horizontally-mounted exactly as on the previous occasion. The critical current was now reached every time.

## 2. Flux Jumping

A copper search coil had been wound on the outside of the test solenoid and its output signal was continuously recorded on a multichannel recorder during all the above tests. It is interesting to note the current at which signals were observed on this trace immediately prior to a quench during the second series of tests when the coil behaved erratically with the axis horizontal. The positions of the last few "flux jumps" have been shown for this series on Fig. 3. This trace also indicated that all quenches at 930 A, with the exception of run number 12, started with a smooth runaway whereas all the other quenches were initiated by a "flux jump."

## 3. Tests with Added Axial Pressure

The forces caused by the axial component of the magnetic field tend to expand the central turns of a layer more than the end turns where this component is weaker. The radial component of field produces axial compressive forces along the layers. It was thought possible that the signals observed on the pickup coil might have been triggered by interturn movement resulting from the radial pressure being released in jumps as the frictional force between turns was overcome. The coil was rewound after the weld holding one of the end checks to the form had been machined off and was now held to the form by three axial tie bolts. With the coil mounted vertically, its performance was checked by running it up to 915 A a number of times without a quench occurring. The tie bolts were then tightened such that the coil length was reduced by 0.025 in. There was no change in the signals on the pickup coil and the coil performance was unaltered. After tightening two bolts to their full extent, compressing the coil by a further 0.012 in., the brazing on the third bolt broke. The coil performance was again unaltered.

After repairing the tie bolt, further tests were carried out and, while the flux jump signals were unaltered, the coil behavior was erratic and quenched at currents between 500 and 810 A. Potential taps had been added to a number of the layers when the coil had been rewound and signals from these indicated that the quenches were being triggered by flux jumps and that the quench was propagating from varying points in the vicinity of the central layers. When the coil quenched at full current, it started in the inner, high field, region.

Subsequent examination of the coil showed that the PTFE packing at the ends of the layers had been axially compressed by the force of the tie bolts and this had resulted in a corresponding expansion in the radial direction between the interlayer nylon strands, thus partially blocking many of the cooling passages.

## 4. Conclusions from Solenoid Tests

The following conclusions are drawn from the results so far obtained on the test coil:

- a) The coil produces transient signals which appear to be caused by flux jumps and not by mechanical movement of the wiring or heating due to frictional forces.
- b) If the cooling passages are not blocked, the performance is unaffected by these disturbances and the critical current of the conductor is reached before the coil quenches.

- c) If the cooling passages are partially blocked, the energy associated with the flux jumps is sufficient to cause the coil to quench prematurely. In these cases normality is initiated in a low field region.

The behavior of the coil when tested horizontally suggests that the cooling ducts were partially blocked the first time but that the blockage was cleared for subsequent tests.

- d) The current interval between flux jumps appears to be related to the probability of quenching at a flux jump. Above about 700 A, in most cases, if the current interval between jumps is not greater than 60 A then the coil will not quench until the critical current is reached. If, however, the current is increased by more than this amount without a flux jump occurring, it is probable that the next flux jump will initiate a quench.

#### IV. PRESENT POSITION OF QUADRUPOLE

The first pole has now been wound and it will be tested in the near future.

##### Note added by the Editor

We have received from Mr. Cornish a letter dated August 30, 1968 which includes the following information:

"The design current for the whole magnet is 820 A giving a field gradient of 5.5 kG/cm. The first pole has now been tested and the current was raised to 1000 A without quenching. The maximum value of field at this current was approximately 50 kG.

"We are very satisfied with this performance and thought you might be interested in the result."



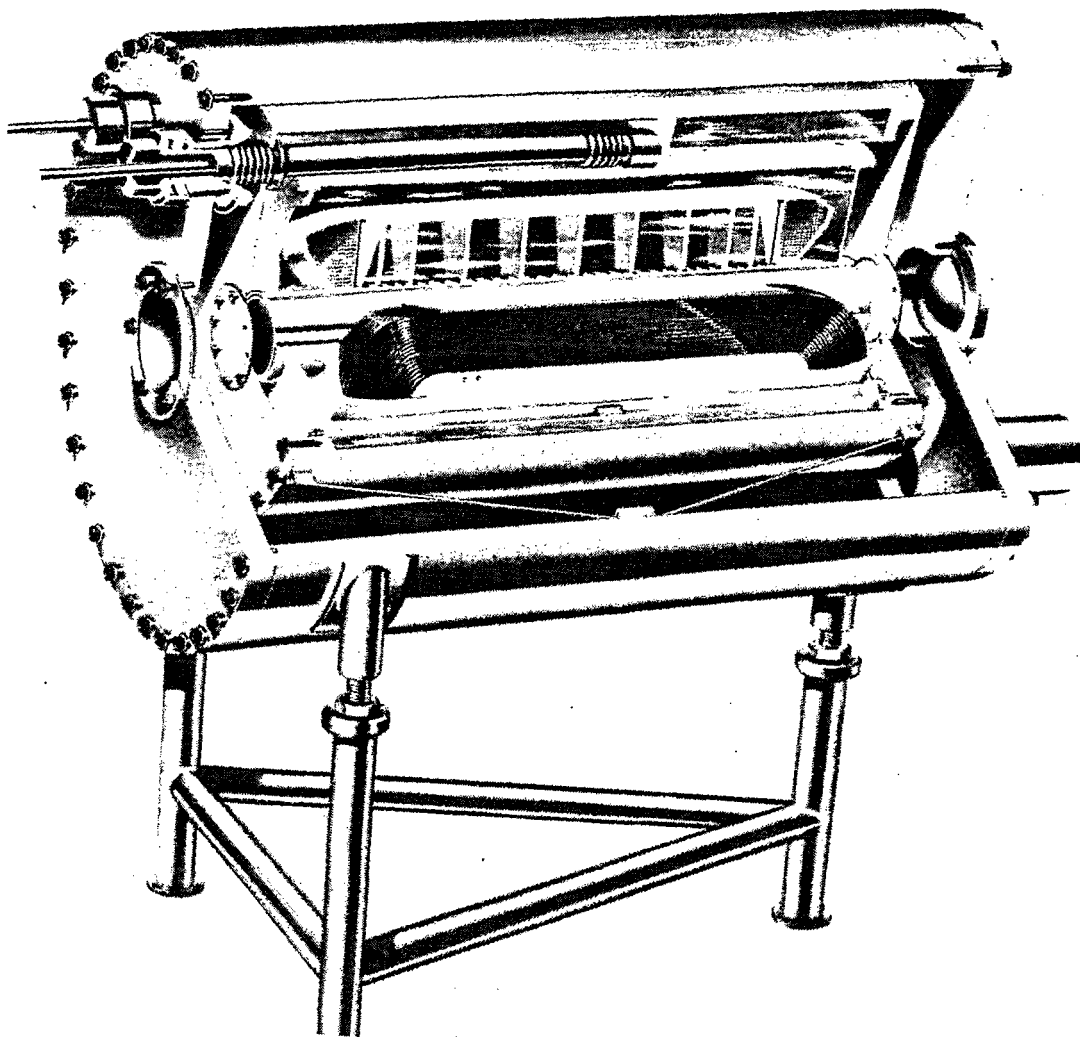


Fig. 1. Superconducting quadrupole focusing lens.

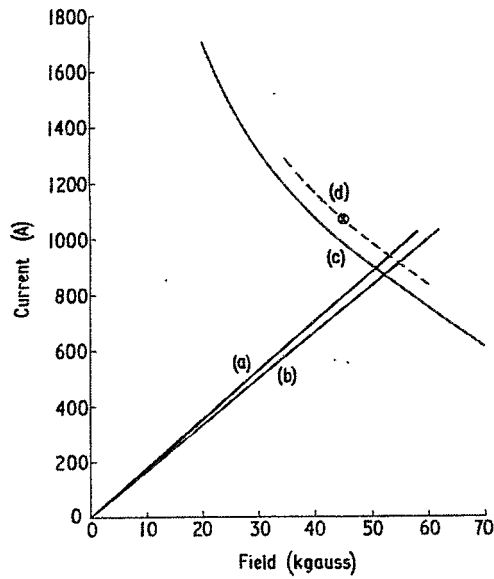


Fig. 2. (a) Load line of maximum B in quadrupole.  
 (b) Load line of maximum B in test coil.  
 (c) Typical critical current.  
 (d) Curve through measured point on critical curve.

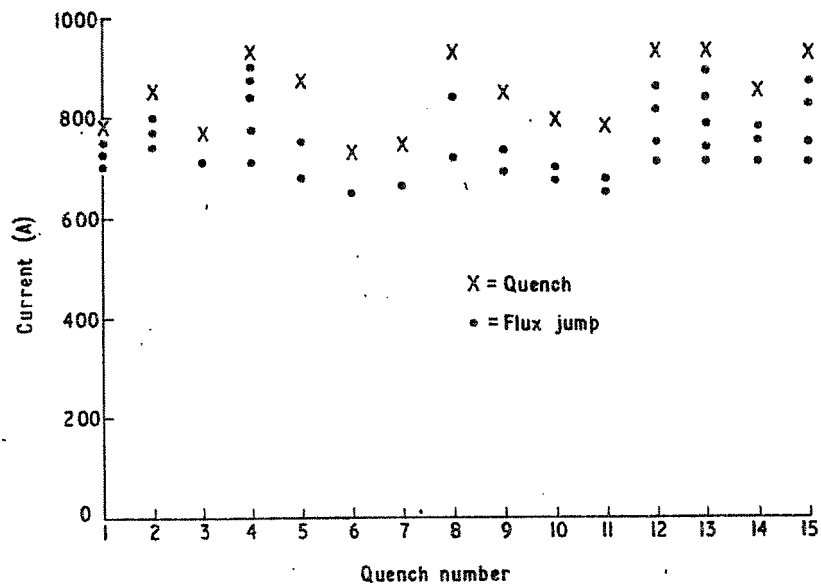


Fig. 3. Quench and flux jump currents with test coil mounted horizontally.

## QUADRUPOLE FOCUSING MAGNET\*

J.D. Rogers, W.V. Hassenzahl, H.L. Laquer, and J.K. Novak  
Los Alamos Scientific Laboratory  
Los Alamos, New Mexico

Particle accelerators consume enormous amounts of electrical energy. A very large fraction of this power is dissipated in the windings of the magnets used to guide and focus the primary beam during acceleration and in the primary and secondary beam lines which transport protons, electrons, muons,  $\pi$  mesons, and K mesons after acceleration. The magnets in beam lines are usually dc devices and their capital cost is a large percentage of the installation cost. Because these magnets operate at essentially fixed fields they are ideal candidates for superconducting materials. Such magnets provide the means for obtaining high fields and field gradients in small volumes with low power demands. Operating costs for superconducting magnets may be as much as a factor of ten less than for conventional, copper conductor, iron yoke magnets. The associated equipment includes Dewars, power supplies, and helium refrigerators. These are of such a nature and size that their physical space requirements and connecting utilities are modest and can be moved with ease compared to the bulky conventional magnets.

Because of the possible savings and convenience some portions of the LAMPF experimental area beam transport systems could use superconducting systems. A superconducting quadrupole doublet has been designed at LASL and is now being constructed. The parameters are listed below. The field gradient, 3 kG/cm, is somewhat higher than will be required for the LAMPF experimental area.

Beam aperture (room temperature)	15 cm diam
Field gradient	3 kG/cm
Effective length	> 30 cm
Doublet focal length for 800 MeV protons	~ 60 cm
Optical alignment capability	$\pm 0.010$ in.
Dipole correction	$\pm 0.020$ in.

Each quadrupole is to be made of four aluminum bobbin forms which bolt together and are then close to 30 cm o.d. and 20 cm i.d. The forms are of two types and approximate the necessary current-turns density in six graded steps. One of the doublets is stepped with varying radial thickness of windings about a median cylindrical surface whereas the other has windings of uniform radial thickness but varying circumferential dimension with aluminum spacers of different widths. The room temperature duct of the containing Dewar is 15 cm.

Two different types of commercially available superconducting wire will be used. The first is a single, large strand of superconductor in a copper sheath; the second is a recently developed multiple-strand wire consisting of a matrix of 49 small strands of superconductor in copper. The former material has a copper to superconducting ratio of three, the latter four. Both wires are 0.050 in. o.d. with Nomex braid insulation

---

\* Work performed under the auspices of the U.S. Atomic Energy Commission.

with 50% coverage. The multiple-strand wire is expected to have superior performance characteristics, but it is more expensive.

In addition to the quadrupole doublet, superconducting double dipoles will be placed around each quadrupole to make fine adjustments in the beam trajectory. The dipole magnets will be capable of shifting the quadrupole field centerline by about  $\pm 0.020$  in. with a maximum field of 600 G.

#### SUMMARY

Two superconducting quadrupole magnets with correcting dipoles enclosed in a single Dewar to form a focusing doublet, iron magnetic shielding, and liquid helium refrigerator are being designed and constructed for use in the LAMPF facility.

#### ACKNOWLEDGMENT

The authors are indebted to James H. Fretwell, Donald H. Lester, Robert W. Stokes, and John C. Bronson who have assisted with some of the work.

# THE RUTHERFORD LABORATORY BENDING MAGNET

M.N. Wilson, R.V. Stovold, and J.D. Lawson  
Rutherford Laboratory  
Chilton, Berks., England

## I. INTRODUCTION

In May 1967 we decided to build a fully stabilized bending magnet to provide a field of 40 kG over a length of 140 cm with a room temperature aperture of 17 cm. Not only will this be a useful item for the new Nimrod experimental area, but we hope to learn some of the engineering difficulties encountered in constructing and operating a large magnet, and to gain experience in running it under operational conditions in the experimental area. In the design, the principle of full stabilization has been deliberately pushed to its limit, the peak nucleate boiling heat flux having been assumed. Although any magnets ultimately produced in quantity will no doubt differ substantially from this one, we are also keeping careful account of the cost and labor involved in making it.

## II. BASIC DESIGN FEATURES

A drawing of the magnet (omitting some features which have not yet been finalized) is shown in Fig. 1. The uniform field is produced by intersecting current distributions of approximately elliptical shape, as suggested by Beth.<sup>1</sup> The conductor is a fully stabilized I.M.I. composite consisting of NbTi strands in copper, and held in position by slotted strips of nylon, loaded with 40% glass to minimize the mismatch on contraction. At the ends of the magnet the windings are bent into a circular shape, in a plane perpendicular to the axis, and held by radial slotted nylon strips. End thrusts are taken by a series of flanges mounted on the central stainless-steel spool and by longitudinal tie bolts, and lateral thrust is taken by stainless-steel clamps held with transverse bolts. Details of the winding procedure, including the correct locating of the bends and the special spacers at the corners is complicated; this has been studied with the aid of a model, but tests with dummy conductor on the final spool are now being made prior to finalizing the details.

## III. TABLE OF PARAMETERS

In this section the quantitative features of the design are listed under various headings:

### 1. Performance

Angle of bend of 7 GeV beam =  $12^\circ$   
Sagitta (including end region) = 5 cm

---

1. R.A. Beth, in Proc. 6th Intern. Conf. High Energy Accelerators, Cambridge, 1967, p. 387.

## 2. Dimensions

Effective length = 140 cm  
Over-all length (including cryostat) = 200 cm  
Central tube diameter = 22 cm  
Room temperature aperture = 17 cm  
Outer diameter of winding = 41 cm

## 3. Conductor and Winding

Material: I.M.I. copper composite, containing 32 strands of NbTi  
Diameter = 0.15 in.  
Length = 12 300 ft (370 m)  
Number of joints = 8  
Spacing between conductors = 1 mm  
Number of layers = 20  
Number of turns = 1036

## 4. Magnetic and Electrical Parameters

Magnetic field = 40 kG  
Uniformity: 0.4% across the cross section at the center of magnet  
and  $\Delta \int B \, dl < 3\%$  within 8 cm of the axis  
Peak field at winding = 44 kG  
Current = 1690 A  
Current density = 7260 A/cm<sup>2</sup>  
Heat transfer to helium, assuming all current in copper at  
4.2°K = 0.8 W/cm<sup>2</sup>  
Inductance = 0.75 H  
Stored energy = 1.1 MJ

## 5. Forces and Weights, etc.

Weight of conductor = 770 lb  
Weight of coil assembly = 2.4 tons  
Weight of cryostat = 2 tons  
Weight of shielding (see Section V) = 6 tons  
Total lateral force on winding = 340 tons  
Maximum lateral force on conductor = 7.2 kg/cm  
Helium capacity of cryostat = 350 liters  
Expected helium boil-off when running (with current leads  
removed) = 2-4 liters/hour

## 6. Cost

Estimated cost, excluding internal labor costs = £45 000

## IV. SPECIAL FEATURES

In order to conserve helium, detachable current leads and a persistent current switch (not shown in the figure) will be used. A flux pump, controlled by a field monitor in the magnet, will replace flux which leaks away because of the finite resistance of the joints in the winding. The details of these items are not yet worked out. Early tests on contact resistance suggested that this would be too high to permit the use of mechanical switches for the persistent current switch or

the flux pump, though this is being reconsidered in the light of measurements by Zar.<sup>2</sup> The alternatives are a thermal switch, which might tend to be unstable, and a flux pump of the type developed by van Suchtelen et al.<sup>3</sup> in which a normal region is made to move across a superconducting niobium sheet. Present plans are for such a pump, which is kindly being supplied by Dr. Volger. A disadvantage of this device is that good shielding is required; a NbSn cylinder designed to provide such shielding has been ordered from the Fulmer Research Institute.

## V. CRYOSTAT

In the design of the cryostat every effort has been made to reduce the heat flow into the magnet vessel. To this end, in addition to the detachable current leads, a helium vapor-cooled shield is to be interposed between the helium vessel and the annular nitrogen vessel and around the down tube assembly. The concentric vessels are supported by rods attached to thick rings at the ends and located axially by rods relative to the mid-length to minimize the effect of the differential contraction on cool-down. To avoid the effect of eddy currents when the magnet is shut down, the end radiation shields attached to the annular nitrogen vessel are constructed from thin stainless-steel sheets, rolled to form channels with an interspace of 0.125 in. depth. Through these channels liquid nitrogen passes into a sleeve, consisting of thin concentric cylinders, through the central bore of the magnet.

On assembly the vessels will be dimensionally centered within each other. Strain gauges mounted on the jacks supporting the cryostat within the magnetic shielding will then enable the magnet to be centered in the shielding.

## VI. MAGNETIC SHIELDING

In order to reduce the external field in the beam line where the magnet will be used to tolerable proportions, an iron shield is being designed. This will be 20 cm thick in a horizontal plane, reducing to zero in a vertical direction. The inner edge of the shield will be 45 cm from the axis. Care is needed to prevent large forces arising from misalignments in a direction perpendicular to the axis.

## VII. PROTECTION

Voltage taps will be taken for monitoring and protection purposes from every layer of the winding. If a normal region develops, an external 0.25  $\Omega$  protection resistor will be placed across the magnet within a few tens of milliseconds by reconnecting the current leads and opening the persistent current switch. With this value of resistance the discharge voltage will be about 200 V, the current will decay in about 2 sec, depositing some 5% of the energy in the helium. These estimates were made using a computer program<sup>4</sup> which calculates the rate of spread of a normal region assuming the reduced rate of heat transfer appropriate to film boiling. To minimize the danger of breakdown in the magnet the central tube and flanges have been covered with a thin tough plastic coating (PTFCE). The conductor itself will not be insulated. Despite initial hopes it has not proved possible to provide an effective insulating coating without seriously impairing the heat transfer.

---

2. J.L. Zar, Avco Everett Research Laboratory Report AMP 234 (1967).

3. J. van Suchtelen, J. Volger, and D. van Houwelingen, Cryogenics 5, 256 (1965).

4. M.N. Wilson, to be published as Rutherford Laboratory Memorandum.

#### VIII. ACKNOWLEDGEMENTS

Many people have contributed to the design of the magnet. P.F. Smith contributed to the early formulation of the design; B. Colyer has been responsible for the cryogenic and mechanical aspects; J. Dawson and N. Cunliffe have contributed to the special winding problems, and electrical control monitoring and protection respectively; G.J. Homer and J. Brown have carried out much of the laboratory design work and testing of special items; and R.Q. Apsey has been responsible for much of the detailed mechanical design.



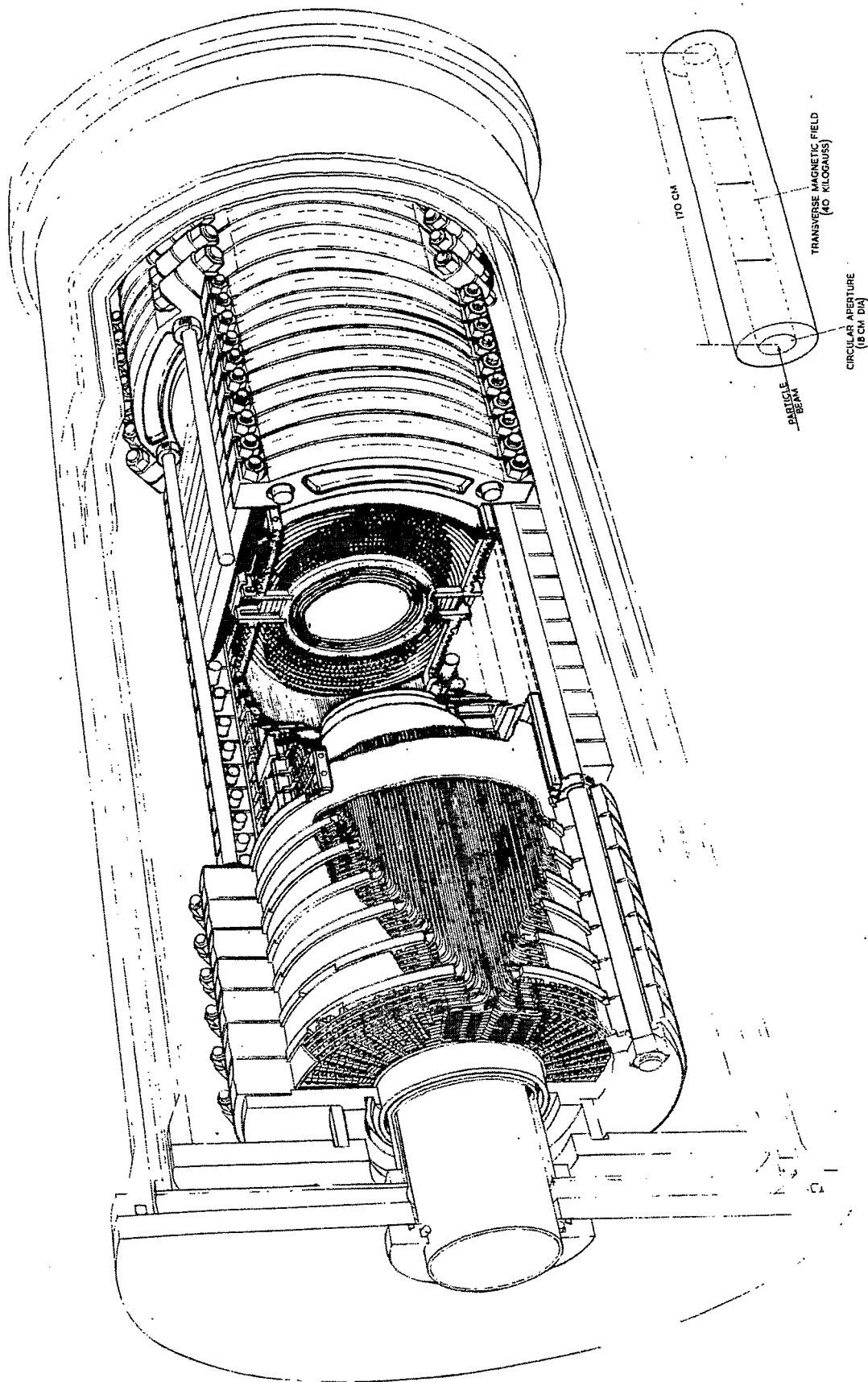


Fig. 1. Superconducting bending magnet.

## BROOKHAVEN SUPERCONDUCTING DC BEAM MAGNETS\*

R.B. Britton  
Brookhaven National Laboratory  
Upton, New York

Superconducting (SC) beam magnet development was started in the Accelerator Department at Brookhaven in the spring of 1965. Work has since progressed to the point where dc quadrupoles are considered (by the author at least) to be ready for application to experimental beam lines. Dipole development, however, is just beginning and is running about two years behind. For both types of magnets, the field strengths obtained to date (15 to 35 kG peak) have been limited by instabilities to about one-half of the potential for niobium-tin superconductors when used in a single layer of 1.27 cm wide ribbon. By potential is meant the field at which the current in the magnet would reach the level obtainable in a short sample of the same material. This level is attainable in small solenoids.

The beam magnet work was initiated by Sampson and Kruger with ideas for a Panofsky-type quadrupole,<sup>1,2</sup> as shown in cross section in Fig. 1. This magnet consisted of four slabs of uniform current density arranged to form a square parallelepiped. Gradients up to 10 kG/cm were produced in a 3 cm diam bore, but despite the good performance, this winding method was abandoned because of the following deficiencies: the windings are not convertible to any multipole magnets other than quadrupoles; the magnetic field is highest in a small region at the corners which causes the entire superconductive block to be limited by the corner turns; the end loops introduce field errors and are exceedingly bulky; and the windings are tedious to construct. Nevertheless, several of the quadrupoles were developed, as shown in Fig. 2.

A more desirable topology for a radial field magnet winding, shown by the cross sections in Fig. 3, was arrived at in November of 1965. With this method of laying coils first against an octagon and then flat against a circular or elliptical beam space, one can readily develop multipole fields having two, four, six, eight, or more poles. The first quadrupole using coils wound on a cylindrical form, shown in Fig. 4, was tested in January 1966, and developed 8.5 kG/cm in a 7.6 cm bore. The ideal current and winding distribution, shown in Fig. 5, for such magnets was not obvious, however, and it remained for Beth to solve this and all other problems<sup>3</sup> related to optimizing the position of current blocks for minimum field errors within multipole magnets of various cross sections. The electrical theory which is required for the design of these radial field magnets has thus been available and has remained unchanged since the summer of 1966.

A solution to the field purity at the center of a long magnet does not, of course, guarantee a workable field at the ends of the coils. To determine these errors in our quadrupoles, Sampson, Robins, and Kruger have made measurements both by a short

---

\* Work performed under the auspices of the U.S. Atomic Energy Commission.

1. L.N. Hand and W.K.H. Panofsky, Rev. Sci. Instr. 30, 927 (1959).
2. P.G. Kruger, W.B. Sampson, and R.B. Britton, Brookhaven National Laboratory, Accelerator Dept. Report AADD-104-R (1966).
3. R.A. Beth, Brookhaven National Laboratory, Accelerator Dept. Reports AADD-102 (1966), AADD-112 (1966), AADD-135 (1967), AADD-103 (1966).

filamentary bismuth probe<sup>2</sup> which could be revolved at various radii in planes perpendicular to the axis, and by a long (78 cm) integrating coil which summed the field completely at a radius of 3.5 cm through a 60 cm length element. The conclusions from the two methods of measurement are that the fields fall off smoothly as one leaves the end of this type of magnet (see Fig. 6). The experimental measurements appear to be in good agreement with calculations made by Kruger et al.<sup>4</sup> It is therefore assumed that the present shape of the winding end loops is close to optimum and that any changes found necessary to produce perfect field fall-off at the ends will be small and topologically possible with brittle ribbon conductors.

Mechanical design of frames to contain the windings was the next problem. The first design for this was an externally supported, bolted, composite structure of high efficiency but also high cost because of the requirement for excessive machining time. This structure is used in our 10 cm bore x 60 cm length quadrupole element, shown in Fig. 7.

To reduce fabrication time for the magnet frame, an internally supported, monolithic frame was designed. The machining time for this solid frame was only about one-tenth of the time required for the composite. However, it can only hold 70-80% of the theoretical maximum number of turns per coil section, and the turns must work at a 5-20% greater diameter than the theoretical minimum. This penalty is small for large metal frame dipoles with few sections, but can be severe for small bore, non-metal frame quadrupoles or higher order magnets which require many coil sections. A solid frame for an elliptical bore dipole is shown in Fig. 8.

The insulation for ribbon superconductors as used in all beam magnets at Brookhaven has been either a thin ribbon of stainless steel or a varnish coating put on the ribbon by the manufacturer. For small magnets (less than 25 mH), at currents up to 700 A, the varnish insulation has been satisfactory. When the stored energy exceeds about 10 000 J, however, it becomes advisable from a protection point of view to use metal interleaving. The function of the metal is to provide uniform electrical shorting between turns throughout the winding. It also has better heat transfer properties than organic insulation. The shorting is highly resistive compared with the superconductor and does not affect the normal, slow energizing of the device. If the magnet quenches, however, the relaxation time constant for the shorted winding in the normal state is long enough to allow the magnetic energy to dissipate uniformly through the winding in the form of heat. When large coils of Nb<sub>3</sub>Sn ribbon are operated without shorting, a quench at high current will frequently precipitate an arc that then destroys a portion of the winding.

Insulation has also been found necessary for the frames of beam magnets, though less than one might expect. The problem is not one of avoiding long time constants due to shorting through the frame, but rather that of avoiding any great asymmetry in time constants between, say, the four coils of a quadrupole. The insulation which is presently being used for stainless-steel frames is a spray paint applied by a technique developed by F. Abbatiello of our laboratory. The same method works for aluminum. Two other methods used to insulate aluminum are to have it anodized, or to treat it in Alrok solution after all machining is done.

The development of a superconductor for beam magnets is a long story — one which the author believes will continue for many decades. The part which has made the Brookhaven beam magnets practical, however, has been the competitive development of Nb<sub>3</sub>Sn in a ribbon of appropriate width, length, uniformity of thickness, strength,

---

4. P.G. Kruger, J.N. Snyder, and W.B. Sampson, Brookhaven National Laboratory, Accelerator Dept. Report AADD-113-R (1966).

and stable current density,  $J_s$ . The  $J_s$  referred to here is that obtainable in the magnet winding. An appropriate width for a beam magnet conductor is about one-eighth of the bore diameter (with greater widths, the wedges consume too much winding space), and for strength a thickness of at least 75  $\mu$  assuming the material to be primarily copper on a niobium or nickel alloy substrate. The minimum length is about 100 m if one wishes to avoid having joints in the high current density sections. Ideally, each coil or section would contain a single length. At the moment, ribbon is most readily available in either 0.23 or 1.27 cm width, but some companies offer any width up to 5.0 cm. Lengths of 300 to 950 m are available without a joint. Yield strengths are typically 7 lb or more for ribbon 1.27  $\times$  100  $\mu$  thick.

The requirement of uniform thickness has been difficult for the manufacturer to meet. We presently are trying to get  $\pm 2.5\%$  thickness tolerance on ribbon of 75 to 200  $\mu$  total thickness. Thickness variations affect winding density which directly determines current density, and the latter, of course, affects the shape and precision of the magnetic field. The thickness variations existing in much of the ribbon obtained to date have made it difficult to produce a quadrupole of 10 cm bore precise to better than  $\pm \frac{1}{2}\%$  at 80% aperture.

The most difficult conductor requirement to obtain is a high  $J_s$ . If one fixes the conductor width and for the sake of minimizing complexity uses only a single layer of winding, then the maximum field obtainable in a dipole, or at the wall of a quadrupole is as follows:

$$B = \frac{2\pi}{10} J \times 1.27 \approx 0.798 J \quad ,$$

where B is in gauss, J is in A/cm<sup>2</sup>, and 1.27 is the width of the current sheet in cm. Similarly, the field gradient, G, in gauss/cm is given by

$$G = \frac{2\pi}{10} \frac{J}{r} \times 1.27 \approx 0.798 \frac{J}{r} \quad ,$$

where r is the mean radius of the current sheet in cm.

In windings which contain a large volume of Nb<sub>3</sub>Sn ribbon, the limiting factor in their performance is stability.<sup>5</sup> In other words, they are not limited by critical field and critical current but by a statistical probability of a sudden quench at a  $J_c \times B$  product far below the straight sample performance of the material. This limit appears to be on current density alone, and for single layer windings which are exposed to helium on one or both sides, the limit is always above 25 000 A/cm<sup>2</sup> and usually below 55 000 A/cm<sup>2</sup> for a winding containing between 200 and 800 m of ribbon.

The only fact which is known about the current density problem is that some pieces of supposedly identical ribbon are over twice as good as others. For this reason, our present technique is to test every piece of ribbon in a simple pie winding prior to putting it into a device. In addition to yielding data on  $J_s$ , this test also gives winding thickness and provides an opportunity to search for flaws.

---

5. W.B. Sampson, Brookhaven National Laboratory, Accelerator Dept. Report AADD-111 (1966).

There are at present two SC beam magnets under construction at Brookhaven. One is a quadrupole<sup>6</sup> designed by Sampson and the author. The frame of this magnet is shown in Fig. 7, and a finished winding for it in Fig. 9. The winding distribution is essentially the same as that shown in Fig. 5. Two of these elements have been wound and tested to gradients of about 3.5 kG/cm. A horizontal Dewar has been obtained for one element and is being tested without a magnet at present.

The other magnet is a dipole designed by D. Jacobus and the author. The bore is an ellipse, 17 cm x 7 cm, and the effective length is 60 cm. Four current sections are used per coil, as shown in the lower part of Fig. 10, with different current densities in each so that the current blocks essentially cover the circumference. Various views of the aluminum frame containing a single dummy winding are shown in Figs. 8, 11, and 12. A field of 25 to 30 kG is expected in this magnet with a uniformity of  $\pm \frac{1}{2}\%$  over the full cross section at the center. Diamagnetic effects similar to those seen in solenoids are expected to affect the field uniformity more than winding errors. A Dewar for this dipole is being fabricated at Brookhaven.

An estimate of the cost for duplicating these magnets is given in the following table. The cost of refrigerators, which can easily exceed the cost of a single magnet, has not been included.

TABLE I  
Estimated Duplication Costs for Brookhaven Beam Magnets

	Quadrupole Doublet 10 x 60 cm each <u>3.5 to 7 kG/cm Gradient</u>		Elliptical Bore Dipole 7 x 17 x 60 cm <u>25 to 50 kG Field</u>	
Frames	2 Composite		1 Monolithic	
	1100 shop hours	\$11 000	100 shop hours	\$1 000
Superconductor				
1.27 cm wide x 125 $\mu$ thick	1600 m @ \$6/m	\$9 600	1200 m	\$7 200
Dewars	Outside shop	<u>\$8 000</u>	Brookhaven shop	<u>\$16 000</u>
		\$28 600		\$24 200
Winding and assembly time for magnets		12 man-days		6 man-days

6. R.B. Britton and W.B. Sampson, IEEE Trans. Nucl. Sci. NS-14, No. 3, 389 (1967).

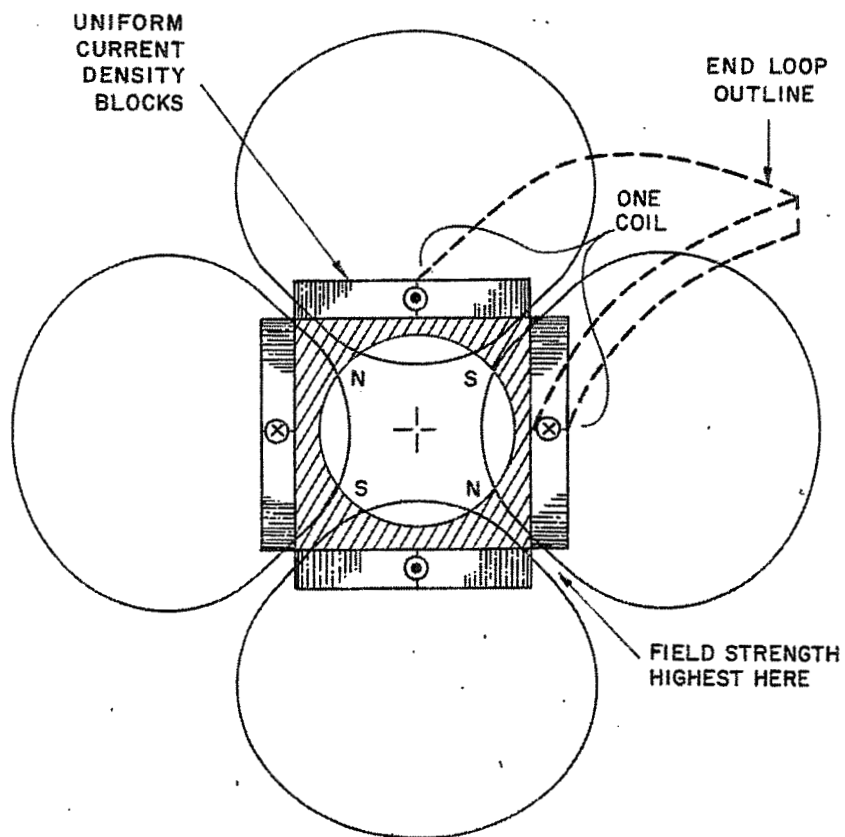
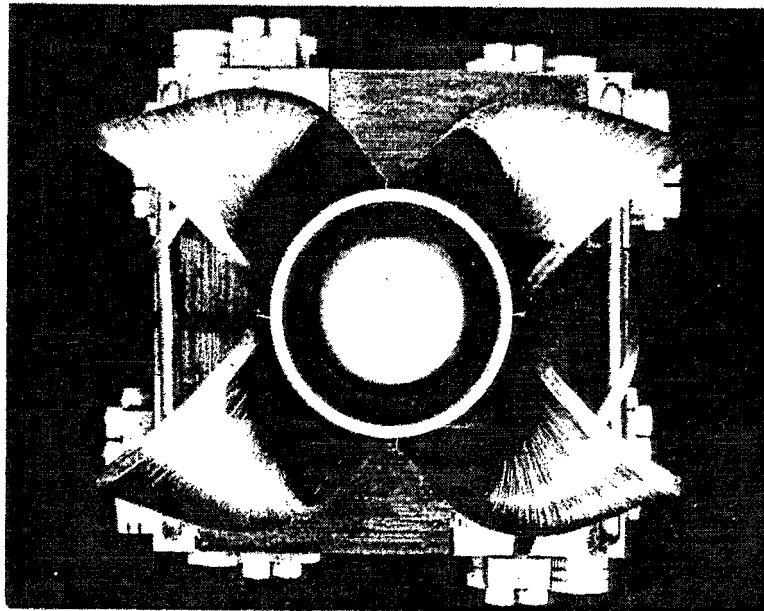
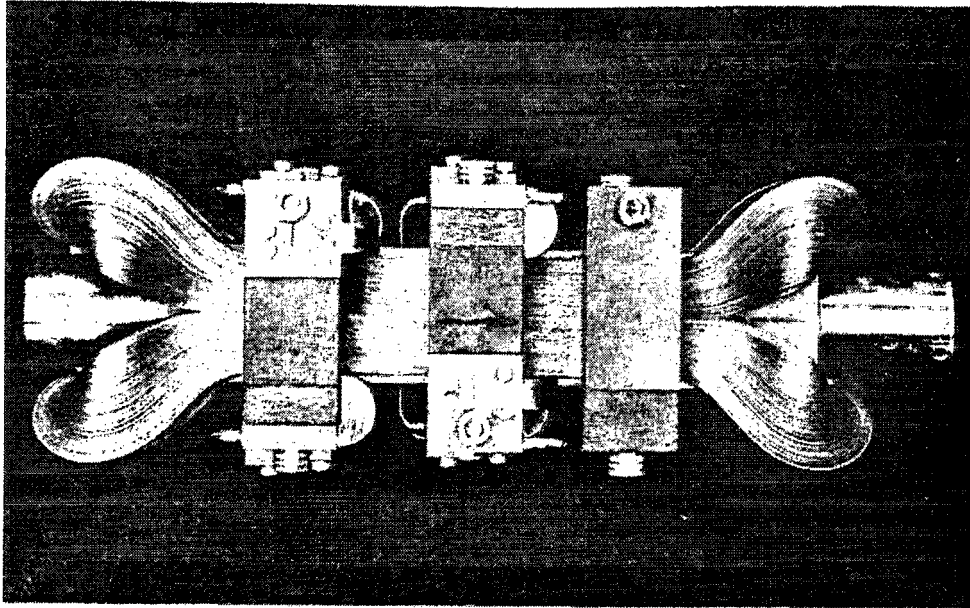


Fig. 1. Panofsky-type quadrupole - cross section.

Fig. 2. Superconductive Panofsky quadrupole.



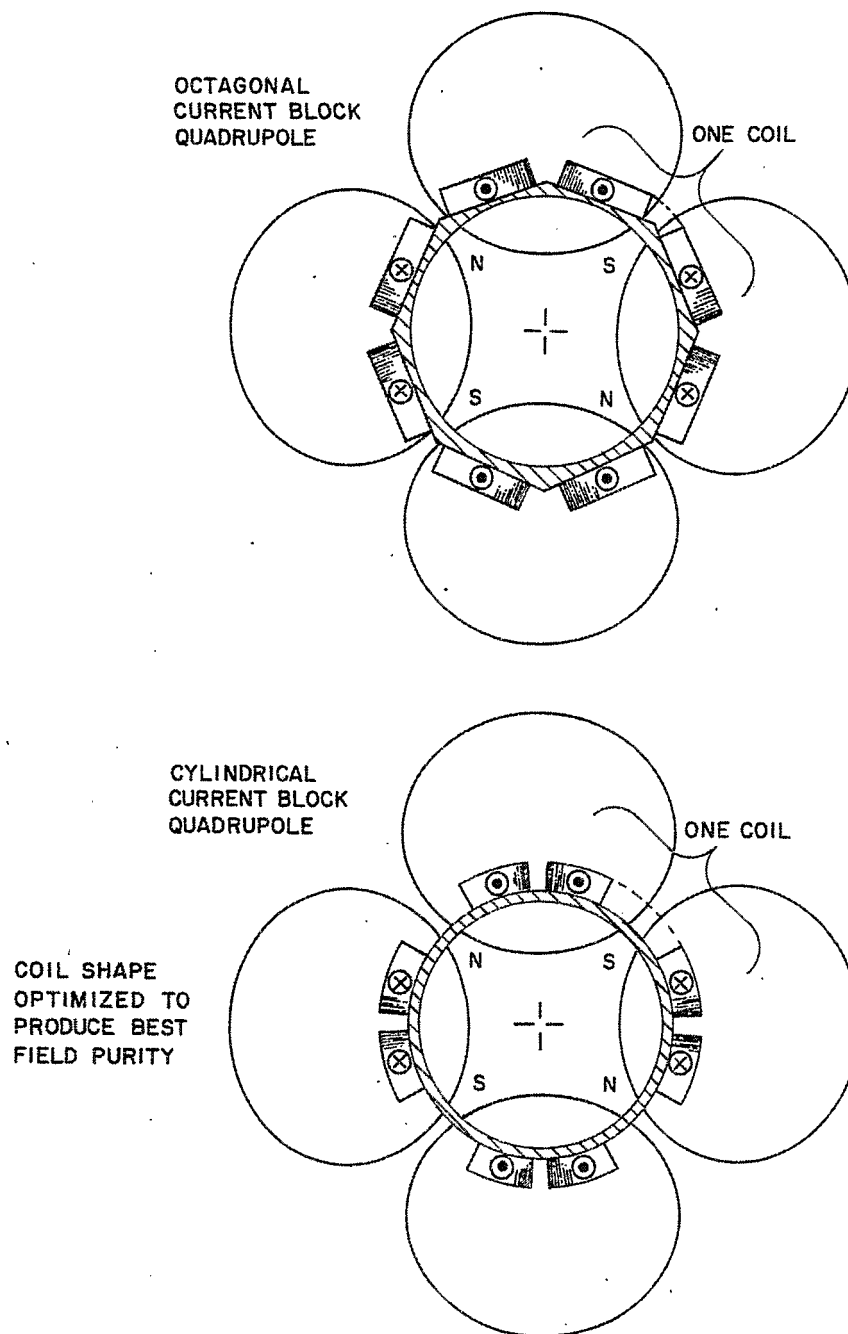


Fig. 3. Octagonal and cylindrical current block quadrupole cross sections.



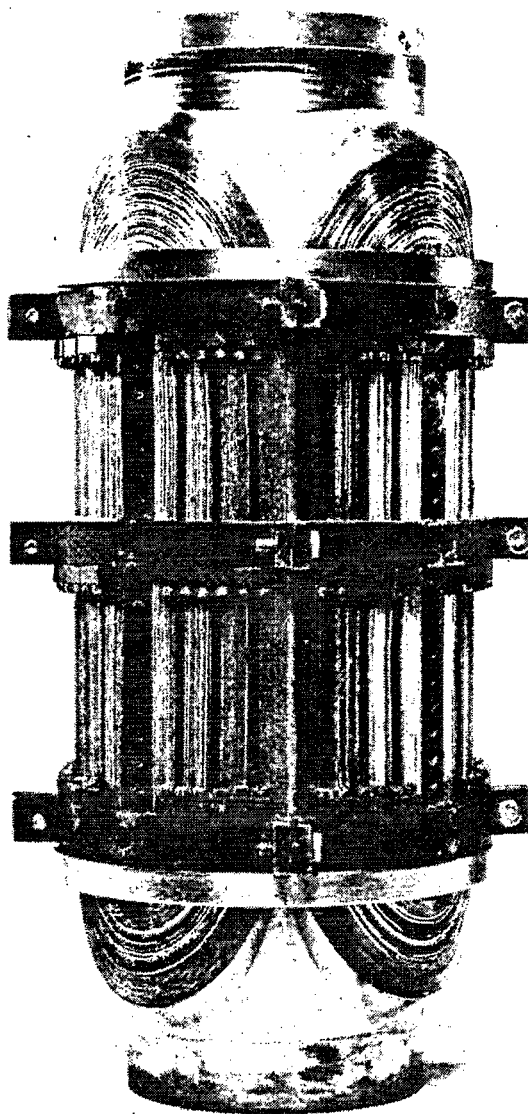


Fig. 4. Cylindrical current block superconducting quadrupole.

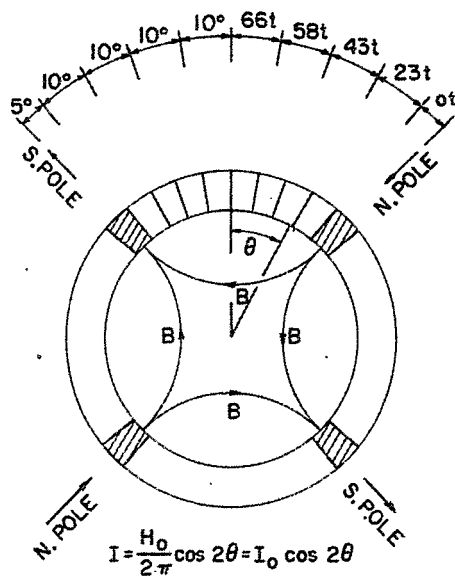


Fig. 5. Turns distribution for cylindrical quadrupole.

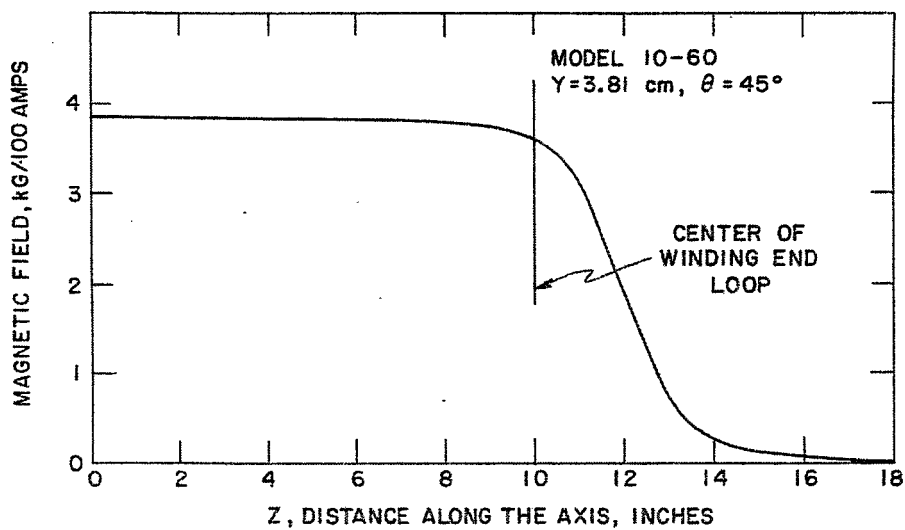


Fig. 6. Field strength vs axial position in quadrupole.

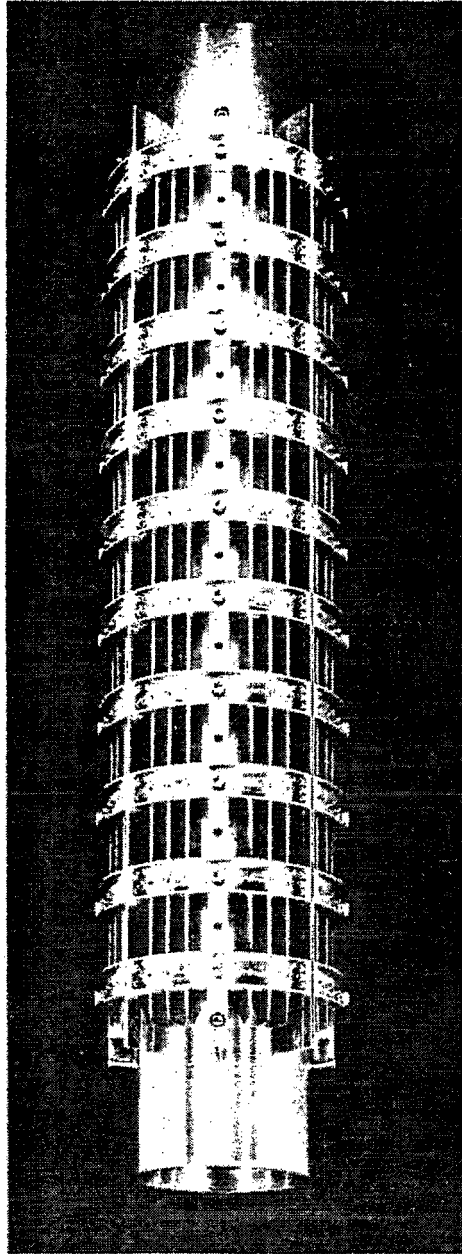


Fig. 7. Externally supported frame construction for quadrupole.

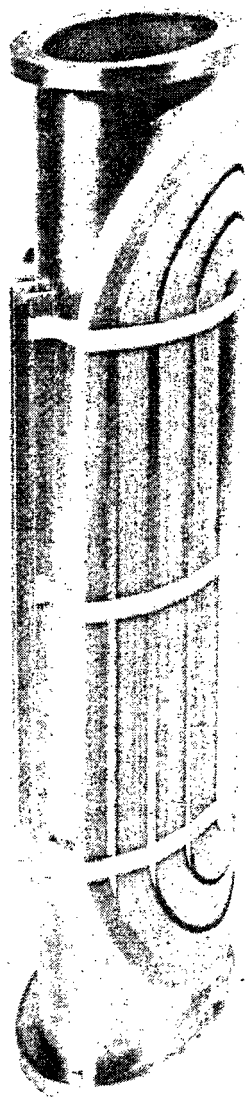


Fig. 8. Internally supported frame construction for dipole.

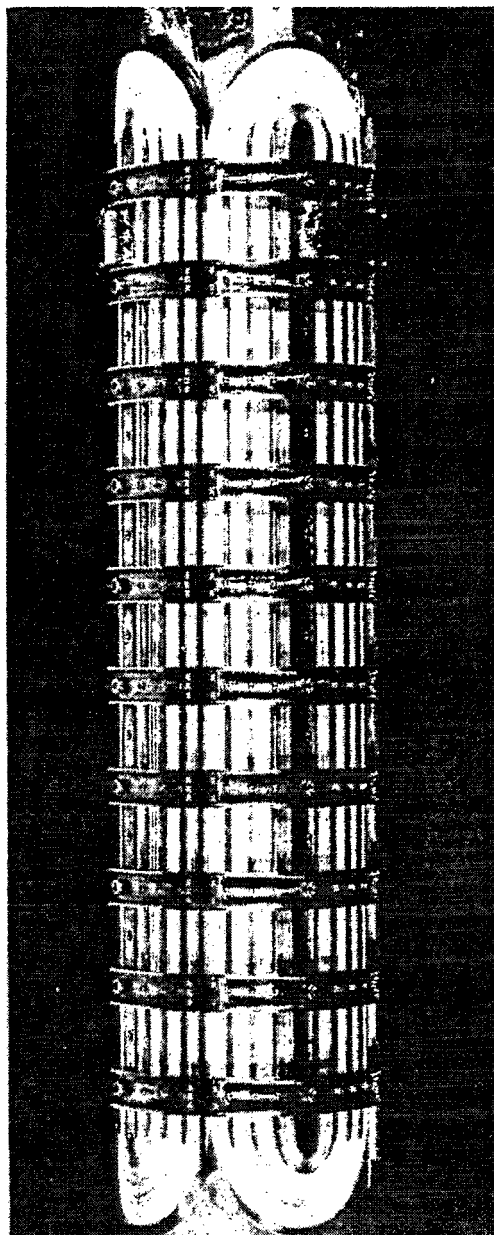


Fig. 9. Quadrupole element - 10 cm bore x 60 cm length.

SUPERCONDUCTING DIPOLES

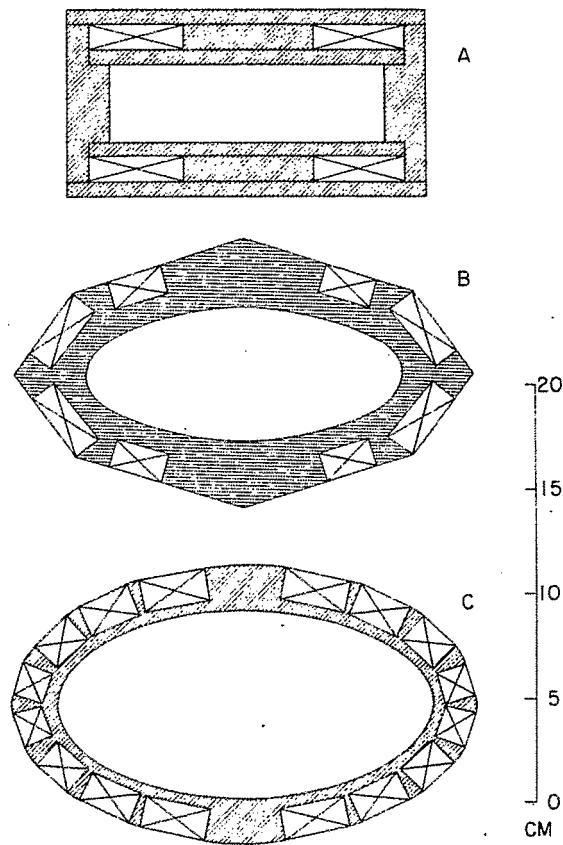


Fig. 10. Winding cross sections of superconducting dipoles.

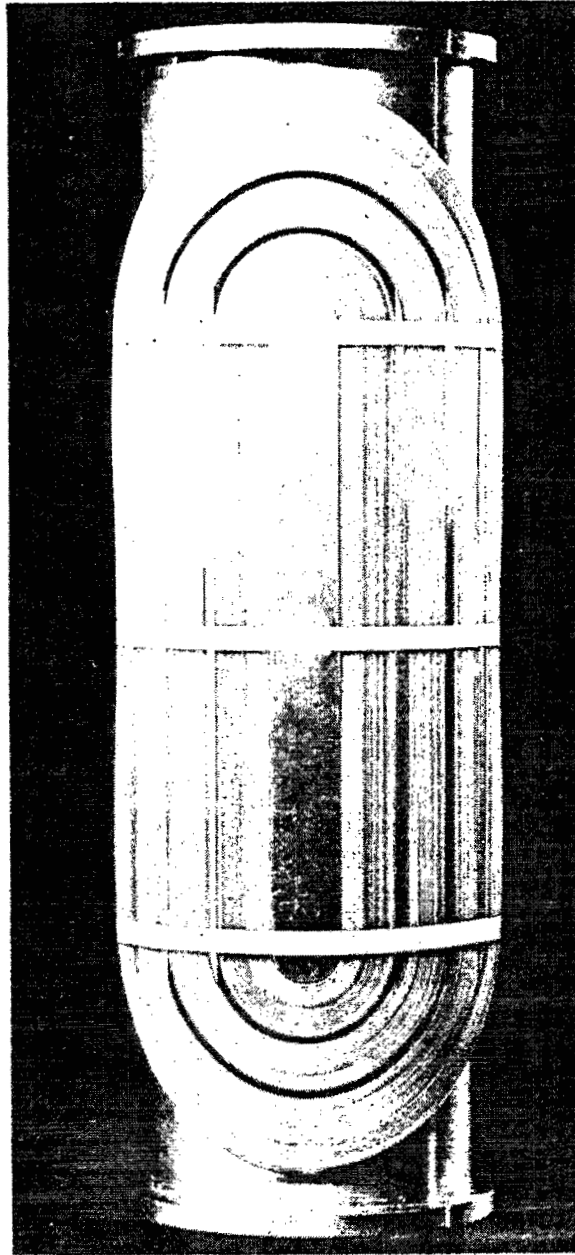


Fig. 11. Top view of elliptical dipole with dummy winding.

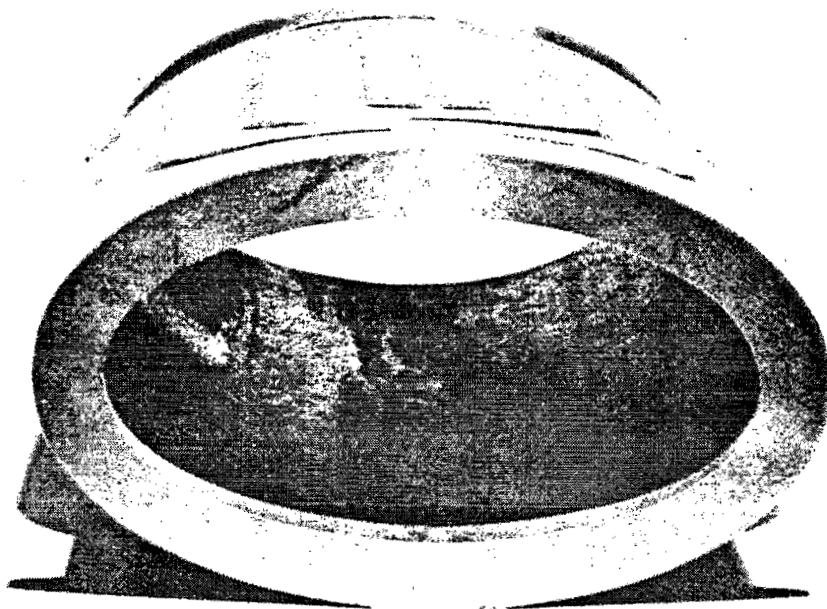


Fig. 12. End view of elliptical dipole.



## PULSED SUPERCONDUCTING MAGNETS\*

W.B. Sampson  
Brookhaven National Laboratory  
Upton, New York

### INTRODUCTION

The possibility of achieving substantial economic gains by using superconducting magnets in large proton synchrotrons has inspired an experimental program at Brookhaven aimed at investigating the properties of pulsed superconducting magnets. Some of the measurements resulting from this program have been described during this Summer Study<sup>1</sup> and elsewhere.<sup>2,3</sup>

There are two main aspects to the use of such magnets in accelerators: the first being that the losses incurred during pulsed operation must be low enough to make their use economically desirable, and the second that the magnets must operate in a reliable and predictable manner. I shall concentrate on the latter aspect, that is, how the devices we have been testing perform as magnets and how much they must be improved before they will become serious candidates for use in future high energy machines.

### EXPERIMENTAL DETAILS

With the exception of one coil all the magnets tested were made using  $\frac{1}{2}$  in. wide Nb<sub>3</sub>Sn conductor clad with a small amount of copper or silver. This material was chosen because of its very high current density potential. High current density is required in synchrotron magnets in order to minimize the energy stored in the windings and thus the size and cost of the power supply.

The coils are of identical geometry with an i.d. of 2.5 in., an o.d. of 6 in., and a length of 0.5 in. (i.e., single spiral windings of  $\frac{1}{2}$  in. wide conductor). Figure 1 shows a typical ribbon magnet and plastic former. The slots in the end plates allow liquid helium access to approximately 60% of the ribbon edges. Electrical insulation is provided by  $\frac{1}{2}$  in. wide Mylar ribbons of various thicknesses. A commercial inductance bridge was used to measure the coils during winding to ensure that there were no shorted turns.

A programmable 100 kW motor generator was used to pulse the magnets with a triangular current waveform similar to that used in synchrotrons. The losses were determined by measuring the boil-off gas produced during pulsing. This method is described elsewhere in the Proceedings.<sup>1</sup>

---

\* Work performed under the auspices of the U.S. Atomic Energy Commission.

1. G.H. Morgan and P.F. Dahl, these Proceedings, p. 559.
2. W.B. Sampson et al., in Proc. 6th Intern. Conf. High Energy Accelerators, Cambridge, Mass., 1967, p. 393.
3. G.H. Morgan et al., J. Appl. Phys., in press.

## EXPERIMENTAL RESULTS

The results are summarized in Table I. The numbers appearing in quotation marks after GE refer to the nominal critical current of these ribbons at 100 kG. Coils 2, 3 and 4 are made of the same material but with fewer turns, the reduction in winding density being achieved by using thicker Mylar insulation. Those currents marked with an asterisk represent the critical currents for the values of the field listed in the table and indicate that these magnets are not limited by instabilities. The figures in brackets in the maximum power column are the cycle times used in seconds which represent approximately twice the rise times. The current densities are for the total magnet cross section and include the insulation. The maximum energy flux was calculated from the peak power assuming that 60% of both edges of the ribbon was exposed to helium and includes a factor which takes into account the nonuniform production of energy in the coil.<sup>1</sup>

The dependence of the loss on magnetic field is shown in Figs. 2 and 3 where the "Q", or energy loss per cycle divided into the stored energy, is plotted against field.

TABLE I

	Magnet	No. of Turns	Maximum Current (A)	Current Density (kA/cm <sup>2</sup> )	Maximum Field (kG)	Maximum Power (W)	Energy Flux (W/cm <sup>2</sup> )
1	GE "150"	371	515*	35	41	6.6(2)	0.09
2	GE "300"	350	680*	42	50	10.5(2)	0.12
3	GE "300"	175	960*	30	36	9.8(1)	0.22
4	GE "300"	122	1280*	28	33	12.0(1)	0.38
5	RCA	168	600	20	22	5.5(1)	0.16
6	GE "600"	175	800	25	30	5.0(1)	0.14
7	CSF	553	276	30	33	11.0(2)	0.30
8	T48B	1195	50	11	13	2.7(2)	-

## DISCUSSION

As the results show, simple magnets can be pulsed to high current densities and, in fact, in some cases to critical currents in times of the order of one second. The poorest performing magnet was constructed from NbTi wire of 0.019 in. diam which was copper clad and insulated to a total diameter of 0.025 in. This poor performance is probably due in part to the fact that this coil did not have helium in contact with all the turns, but the low "Q" indicates that this material has considerably higher losses than Nb<sub>3</sub>Sn, at least in wire form.

All the Nb<sub>3</sub>Sn coils behave in essentially the same way but with a number of interesting differences. The "Q" of the CSF coil does not go to very high values at low fields despite the fact that this material is similar to the GE ribbon. Another notable difference is in the performance of the two magnets made from materials capable of very high "short sample" critical currents. These coils, 5 and 6, of RCA and GE "600" ribbon respectively, do not reach critical current and in fact quench at energy dissipation rates considerably lower than some of the other magnets. This suggests that the early quenches are not due to difficulties in transferring the heat produced during the field change from the edges of the normal material to the helium bath but rather

in getting the thermal energy from the superconductor into the normal metal cladding. The reason for this effect may be due to the poor conductivity of Nb<sub>3</sub>Sn which would lead to larger temperature gradients across the thicker high current samples. A similar effect would result, of course, from a poor bond between the superconductor and the normal metal.

#### CONCLUSIONS

The results are summarized in the following statements (see also Ref. 1):

- 1) The loss per cycle is independent of frequency (at least in the range investigated, 0.1 to 60 Hz). This means that "Q" is independent of frequency in marked contrast to conventional magnets whose "Q's" decrease with frequency approaching zero for dc operation.
- 2) The loss is approximately proportional to the square of the average of the component of field perpendicular to the surface of the ribbon. This means that, for a considerable range of field, the "Q" is independent of field.
- 3) Fields as high as 50 kG and current densities up to 42 kA/cm<sup>2</sup> have been achieved in simple magnets using pulses with rise times of the order of one second.
- 4) The current density in a pulsed superconducting magnet cannot be increased by simply increasing the thickness of superconductor since there appears to be a limit set by the thermal conductivity of the superconductor itself. A reduction in loss would presumably lead to improved current density.

The results indicate that the goal<sup>4</sup> of 60 kG pulsable dipoles operating at 60 kA/cm<sup>2</sup> with "Q's" in excess of 1000 may be obtained in the near future, particularly in view of the promise of the subdivided conductors now under investigation.<sup>5</sup>

---

4. W.B. Sampson, these Proceedings, p. 998.

5. P.F. Smith, these Proceedings, p. 913.

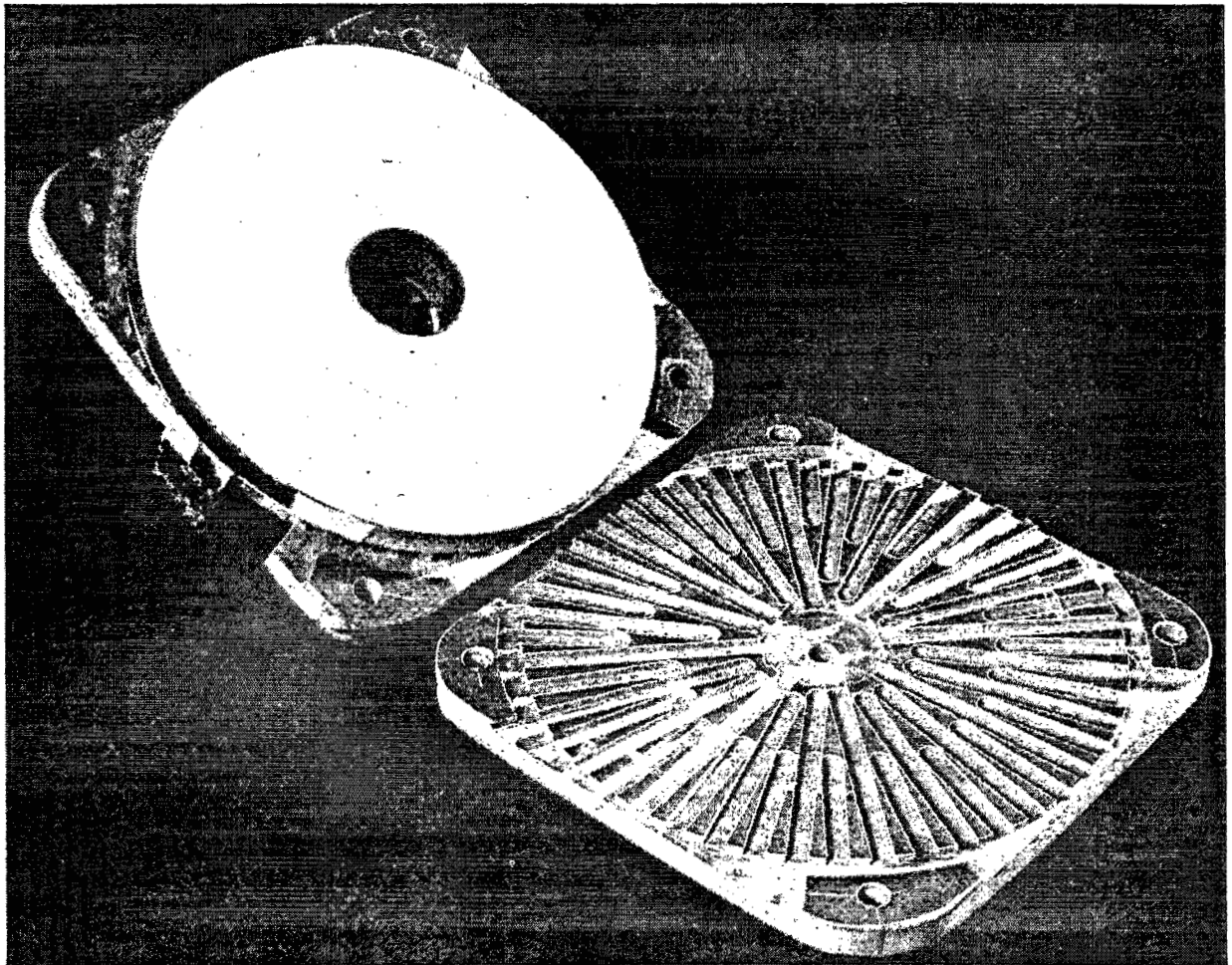


Fig. 1. Pulsed magnet and plastic former.

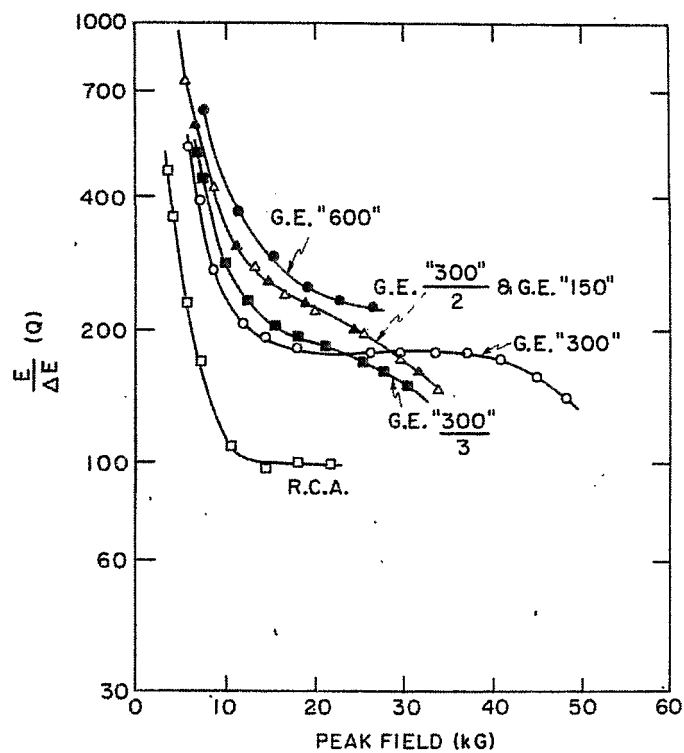


Fig. 2. "Q" plotted against field for pulsed magnets.

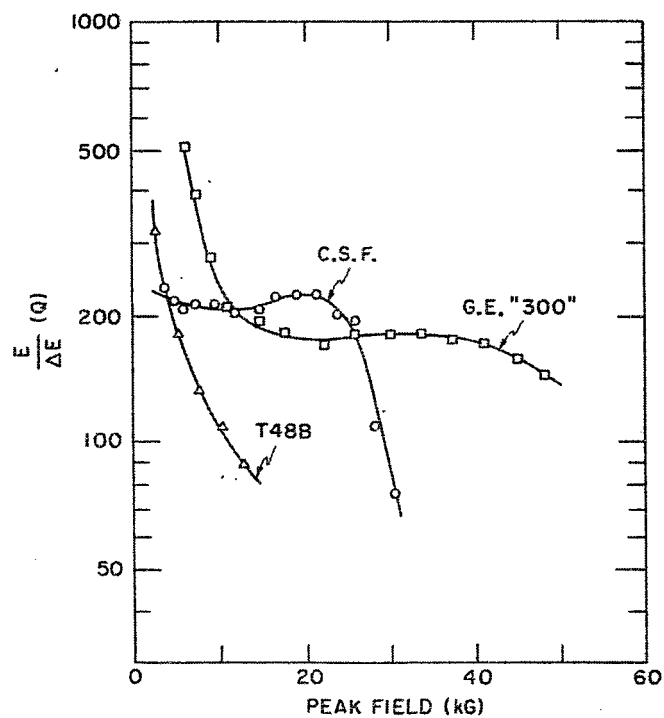


Fig. 3. "Q" plotted against field for pulsed magnets.

## INTRINSICALLY STABLE CONDUCTORS

P.F. Smith, M.N. Wilson, C.R. Walters, and J.D. Lewin  
Rutherford Laboratory  
Chilton, Berks., England

It is generally believed that flux jumps are the only real obstacle to obtaining reliable short sample performance in superconducting coils. The sudden local release of energy results in a premature transition to the resistive state and prevents the reliable attainment of high current densities. Even in large, fully-stabilized coils, the flux jumps which could occur in wide conductors might in some cases release sufficient energy to cause an undesirably large temperature rise, perhaps of the order of 15-25°. This is discussed in a separate paper.

During the last few years, the development of realistic theoretical models for the electrical and thermal processes which occur during a flux jump has led to some remarkably simple criteria which indicate that flux jumping should be absent in superconducting wires typically less than about 0.002 in. in diameter, and in certain arrangements of superconducting filaments and normal metal.

There is, therefore, an obvious incentive to try to develop conductors using these criteria. With this objective, theoretical and experimental work has been in progress at the Rutherford Laboratory since early 1967, and was reported briefly last year.<sup>1</sup> Closely related to this is the possibility of developing a conductor with an ac loss small enough for use in pulsed synchrotron magnets, which could also be achieved by the use of finer filaments.

Since the beginning of 1968 the scale of this work has increased, and experiments are being carried out on samples and small coils of a wide variety of filamentary composites developed in collaboration with Imperial Metal Industries, Ltd. (U.K.). Although the initial tests are encouraging in many respects, much still remains to be done and we would not normally publish any results at this stage. However, in view of the growing interest in this possibility, we have agreed to set down the essential features and principal conclusions of the theory, and to summarize the experimental results obtained so far, as a guide to those planning similar programs, but with the reservation that some of our statements may turn out to require modification in the light of further experimental data.

We discuss the subject under the following headings:

- Theory of single filaments of superconductor.
- Theory of composites of superconductor and normal metal.
- Conductor configurations being tested.
- Description of the four types of test being used.
- Main results so far.

More detailed accounts of both theoretical and experimental work will be published at a later date.

---

1. P.F. Smith, in Proc. 2nd Magnet Technology Conference, Oxford, 1967, p. 543.

## INTRINSICALLY STABLE CONDUCTORS

P.F. Smith, M.N. Wilson, C.R. Walters, and J.D. Lewin  
Rutherford Laboratory  
Chilton, Berks., England

It is generally believed that flux jumps are the only real obstacle to obtaining reliable short sample performance in superconducting coils. The sudden local release of energy results in a premature transition to the resistive state and prevents the reliable attainment of high current densities. Even in large, fully-stabilized coils, the flux jumps which could occur in wide conductors might in some cases release sufficient energy to cause an undesirably large temperature rise, perhaps of the order of 15-25°. This is discussed in a separate paper.

During the last few years, the development of realistic theoretical models for the electrical and thermal processes which occur during a flux jump has led to some remarkably simple criteria which indicate that flux jumping should be absent in superconducting wires typically less than about 0.002 in. in diameter, and in certain arrangements of superconducting filaments and normal metal.

There is, therefore, an obvious incentive to try to develop conductors using these criteria. With this objective, theoretical and experimental work has been in progress at the Rutherford Laboratory since early 1967, and was reported briefly last year.<sup>1</sup> Closely related to this is the possibility of developing a conductor with an ac loss small enough for use in pulsed synchrotron magnets, which could also be achieved by the use of finer filaments.

Since the beginning of 1968 the scale of this work has increased, and experiments are being carried out on samples and small coils of a wide variety of filamentary composites developed in collaboration with Imperial Metal Industries, Ltd. (U.K.). Although the initial tests are encouraging in many respects, much still remains to be done and we would not normally publish any results at this stage. However, in view of the growing interest in this possibility, we have agreed to set down the essential features and principal conclusions of the theory, and to summarize the experimental results obtained so far, as a guide to those planning similar programs, but with the reservation that some of our statements may turn out to require modification in the light of further experimental data.

We discuss the subject under the following headings:

- Theory of single filaments of superconductor.
- Theory of composites of superconductor and normal metal.
- Conductor configurations being tested.
- Description of the four types of test being used.
- Main results so far.

More detailed accounts of both theoretical and experimental work will be published at a later date.

---

1. P.F. Smith, in Proc. 2nd Magnet Technology Conference, Oxford, 1967, p. 543.

## I. THEORY OF SINGLE FILAMENTS

An external field applied to a piece of superconductor induces loops of current at the critical current density  $\pm J_c$  (A/cm<sup>2</sup>). These are known as magnetization currents and, in typical 0.010 in. diameter wires, are observed to be unstable and may suddenly decay rapidly with release of energy. A simple integration of  $H^2 dV$  for the field associated with these currents [for the case, say, of an infinite slab of thickness  $d$  (cm)] shows that the energy released is about  $(2\pi/3)(J_c^2 d^2)/10^9$  joules/cm<sup>3</sup>. This is enough to cause, for example, a temperature rise of 10°K in 0.010 in. wire, but only 0.1°K in 0.002 in. wire; this calculation by itself indicates the use of finer wires.

Several authors have analyzed this instability in more detail and have shown that the flux jump should not occur provided that

$$d \leq (10^9 S T_o f)^{1/2} / J_c, \quad (1)$$

where  $S$  is the heat capacity (joules/cm<sup>3</sup> °K),  $T_o$  (°K  $\equiv J_c / (-dJ_c/dT)$ ) and is usually of order  $T_c/2$ , and  $f$  is a numerical factor in the region 0.6 to 0.9, depending on detailed assumptions.

The right-hand side of (1) is typically of order  $1500/J_c$ , so if, for example, the maximum (low field) value of  $J_c$  is 300 000 A/cm<sup>2</sup>, flux jumping should not occur provided that  $d < 5 \times 10^{-3}$  cm (0.002 in.).

Among the authors who have derived and discussed this result are Hancox, Carden, Swartz and Bean, Neuringer and Shapira, Wipf, Kim, Lange, etc. It is probably most well known from the papers by Hancox,<sup>2-4</sup> who has also extended the theory to include the effect of the temperature rise on the transport current,<sup>3</sup> and has shown that undegraded performance should in general be possible under somewhat less stringent conditions than suggested by Eq. (1) (see Fig. 1).

This was all done in 1965 and 1966, but at that time reliable ways of manufacturing filaments below 0.005 in. diameter were not available. By 1967, however, it became possible to make finer superconducting filaments provided they were embedded in a matrix of normal metal.

## II. THEORY OF COMPOSITES

We thus want to know what happens when a number of parallel superconducting filaments are joined together by normal metal.

Consider the simplest (two-dimensional) case of two parallel sheets of superconductor (Fig. 2). If they are separated by an insulator, then obviously the magnetization current loops flow separately in each (Fig. 2a). But if they are connected by a low resistance metal, then in general the voltage associated with the finite rate of rise of field  $\dot{H}$  (G/sec) is sufficient to drive the current from one strand to the other

---

2. R. Hancox, Phys. Letters 16, 208 (1965).

3. R. Hancox, Culham Laboratory Report CLM-P121 (1966).

4. R. Hancox, in Proc. 10th Intern. Conf. Low Temperature Physics, Moscow 1966, Vol. 2B, p. 45.



through the normal metal, forming one large loop occupying the full width of the composite (Fig. 2b). It can then be shown that phenomena such as stability and ac losses are governed by the full width and not the strand width.

We find, theoretically, that the transverse currents occupy a finite length of conductor  $\ell_c$  (cm), given by

$$\ell_c^2 \approx 10^8 \lambda J_c d \rho / \dot{H} \quad , \quad (2)$$

where  $d$  (cm) is the superconductor thickness,  $J_c$  (A/cm<sup>2</sup>) its current density,  $\rho$  ( $\Omega \cdot \text{cm}$ ) is the matrix resistivity, and  $\lambda$  is a space factor, discussed later. (Note that transient and steady-state derivations of this formula only differ by a factor of 2 in the right-hand side.)

Therefore, if the conductor length is less than  $\ell_c$ , only part of the magnetization current will cross the matrix and the rest will be confined to the separate filaments. (Fig. 2c). As an example, taking  $J_c$  (at low field) = 300 000,  $d = 0.003$ ,  $\rho \sim 2 \times 10^{-8}$ ,  $\dot{H} \sim \text{G/sec}$  (and ignoring  $\lambda$  for the moment), we find  $\ell_c \sim 14$  cm. So for a length  $> 28$  cm the sample behaves as a conductor of width  $w$ , but for a length  $\ll 28$  cm it behaves as two strands of width  $d$ .

Considering now the three-dimensional situation, we can in fact achieve the latter condition in an arbitrarily long length of wire, simply by twisting with a pitch  $\leq \ell_c$ . The local emf's cancel in adjacent segments of wire, each loop acts independently, and the system is effectively cut into lengths equal to one-half the twist pitch. How much less than  $\ell_c$  the twist must be is not known. By simple arguments, it need only be typically in the region  $0.3 \ell_c$ , but we have some theoretical and experimental evidence that, owing to an additional heating effect resulting from the localized penetration of flux at the cross-over points, the twist pitch may possibly have to be as small as  $0.01 \ell_c$  for stability. However, in dc coils this should usually present no problem since one can increase  $\ell_c$  by lowering  $\dot{H}$ .

We have also examined the theory for more complicated systems containing many filaments. Some useful features to note are the following:

- 1)  $\ell_c$  is independent of  $w$ , the strand separation.
- 2)  $\ell_c$  is unaffected by intervening superconducting filaments.
- 3) In a composite containing several values of  $\rho$  in a path connecting two filaments, it is, to a good approximation, the highest value of  $\rho$  which governs  $\ell_c$ , and not the average value.
- 4) In a three-dimensional system, only some fraction  $\lambda$  of the direction parallel to the field is occupied by superconducting filaments, so that in any particular case some guess must be made at an effective value of  $\lambda$  for insertion into Eq. (2).
- 5) When the radial or axial field gradients become appreciable, one must transpose rather than simply twist the filaments. Approximate criteria are:

$$\frac{\Delta \dot{H} \text{ across composite}}{\text{Mean (mod } \dot{H}) \text{ across composite}} > \frac{d}{w}$$

and

$$\frac{\Delta \dot{H} \text{ along one twist}}{\text{Mean (mod } \dot{H}) \text{ along twist}} > \frac{d}{w}$$

This usually seems to suggest that it is sufficient to twist a basic 0.010 in. composite, but multistrand cables formed from this may have to be transposed. Even with mutually insulated filaments, of course, some degree of transposition or twist is necessary, in view of the fact that all the filaments are connected together at the end of the conductor.

In the case of pulsed synchrotron magnets, where  $\dot{H}$  may be as high as 60 000 G/sec,  $\ell_c$  in the preceding calculation reduces to  $\sim 0.2$  cm, presumably making it difficult to achieve the necessary rate of twist. However, by using a higher resistance alloy, with  $\rho \sim 2 \times 10^{-5} \Omega \cdot \text{cm}$ ,  $\ell_c$  increases to the more manageable value of 5 cm. Alternately, it has been suggested that it may be possible to create a high resistivity layer around each filament.

Recently, it has been found that there is a second, independent, criterion for absence of flux jumping in a composite. This requires the assistance of the normal metal itself to slow down the flux motion, and has been discussed by Chester.<sup>5</sup> Using this approach for the case of filaments of thermal conductivity  $k$  (W/cm  $^{\circ}\text{K}$ ) embedded in a matrix of resistivity  $\rho$  ( $\Omega \cdot \text{cm}$ ), we obtain the approximate criterion:

$$d^2 < (T_0 k / \rho) (1 / J_m J_c) \quad , \quad (3)$$

where  $T_0$  is the same as in (1),  $J_c$  is the critical current density in the filament, and  $J_m$  is the mean current density in the composite;  $J_m$  and  $J_c$  apply to the magnetization currents, so that values appropriate at low fields must be used.  $k$  is of order  $10^{-3}$  for NbTi. Note that (3) is identical to the criterion given in the paper by Stekly at this Summer Study,<sup>6</sup> which was derived independently using a different approach. Note also that the derivation assumes the normal metal to be a perfect heat sink, so that it may not be valid for perturbations above a certain level.

At the time of writing, the numerical factors in the derivation are somewhat uncertain and the right-hand side of (3) could, for example, be greater by a factor of four. This new criterion tends to lead to similar values of  $d$  ( $\sim 2$  mil), but in this case a low resistance matrix is essential, and a twist is no longer necessary except to reduce ac heating effects during charging.

To summarize, the theory in its present stage suggests two distinct ways of achieving an intrinsically stable conductor:

Method 1:	$d < 1500 / J_c$ Twist $\ll \ell_c$	Low $\rho$ suitable for dc coils, but high $\rho$ necessary for pulsed magnets
Method 2:	$d < (T_0 k / \rho J_m J_c)^{1/2}$ No twist necessary	Low $\rho$ essential; not suitable for pulsed magnets

5. P.F. Chester, Rep. Prog. Phys. 30, Part 2, 361 (1967).

6. Z.J.J. Stekly, these Proceedings, p. 748.

A conductor satisfying both criteria, for example composed of 0.002 in. filaments in copper with a twist pitch of a few centimeters, looks particularly attractive, and initial coil tests with conductors of this type are giving encouraging results. Whether it is actually necessary, in Method 2, to also satisfy criterion (1), is not clear at the present time.

### III. RANGE OF SAMPLES

For the initial stages of this work, quantities of the order of 2 lb of each configuration (e.g., 8000 ft of 0.010 in. diameter composite) are being produced. The range of parameters being covered is as follows:

Filament diameter	- 0.0005 in. to 0.004 in.
Composite diameter	- 0.005 in. to 0.020 in.
Number of filaments	- in range 10 to 100
Ratio NbTi/normal metal	- approximately 1/1.3
Resistivity	- $2 \times 10^{-8}$ (copper) or $2 \times 10^{-5}$ (cupronickel)
Twist	- 0 or 1/in.

Three-component composites, containing both Cu and CuNi, are also being designed (mainly for protection reasons).

### IV. EXPERIMENTAL PROGRAM

Four types of test are being used, summarized in Fig. 3:

- 1) Swept field. Using a small single-layer coil, the external field is increased with a fixed transport current, enabling the intrinsic stability to be determined as a function of sweep rate and current density.
- 2) Magnetization. Using the same coil as in the swept field test, the M-H curve for the material is determined as a function of sweep rate, showing the relative contribution of matrix and filament.
- 3) Ac losses. Loss measurements as a function of frequency provide confirmation of the results of the magnetization tests.
- 4) Coil degradation. The transport current in small coils wound from about  $\frac{1}{2}$  lb material is determined for various values of an externally applied field.

### V. INITIAL RESULTS

Results so far on short samples are in very good agreement with theory. The onset of instability has been determined as a function of filament diameter, and is consistent with the relation  $J_c d = \text{const}$ , the constant being in the region  $10^3$  as predicted by (1).

The effect of twisting is also clearly shown in these tests, the samples without a twist being highly unstable down to much lower values of  $J_c$ . An experiment was also carried out in which a single sample, initially without a twist and unstable, was subsequently twisted and found to be stable below a certain value of  $\dot{H}$ .

A few magnetization and ac loss results are available which approximately confirm the formula for  $\ell_c$ . Further experiments to determine  $\ell_c$  and its effect on stability are in progress.

Coil tests using cupronickel composites with no twist show considerable degradation, as expected, the currents obtained being similar to those obtained from coils of unstabilized 10 and 20 mil wire.

Coils of the twisted cupronickel composites reached much higher currents, often approaching short sample, but still show some degradation and variability of performance at all field levels. This effect is independent of filament diameter, and is at present believed to be caused by internal heating due to wire movement; the effect of impregnation of the coil with, for example, grease or oil, is being investigated.\*

Initial coil tests using copper composites are giving short sample performance. For example, a small ( $\frac{1}{2}$  lb) coil of 0.020 in. composite containing 0.002 in. filaments reached its short sample current of about 120 A at 50 kG, corresponding to a current density in the region 40 000 A/cm<sup>2</sup>. Larger coils wound from the filamentary copper composites will be tested in the near future.

---

\*Note added in proof: We have now confirmed this; a coil of cupronickel composite, previously showing some residual degradation, reliably went to short sample current after impregnation with oil.

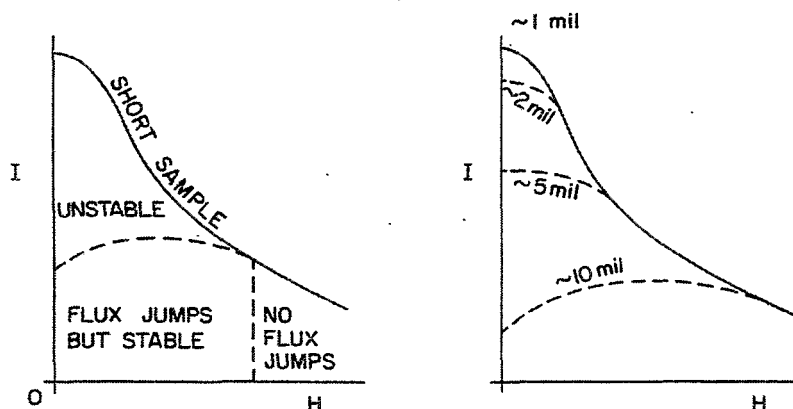


Fig. 1. Stability of transport current predicted by Hancox' theory.

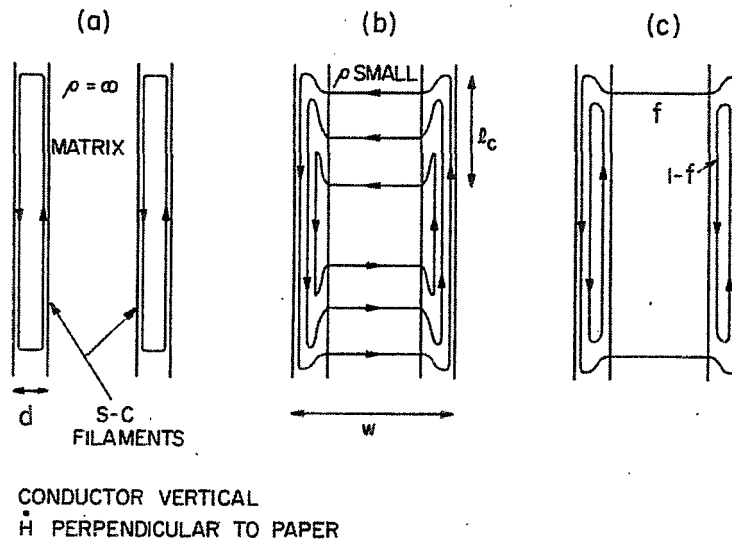


Fig. 2. Current distribution in composite conductors.

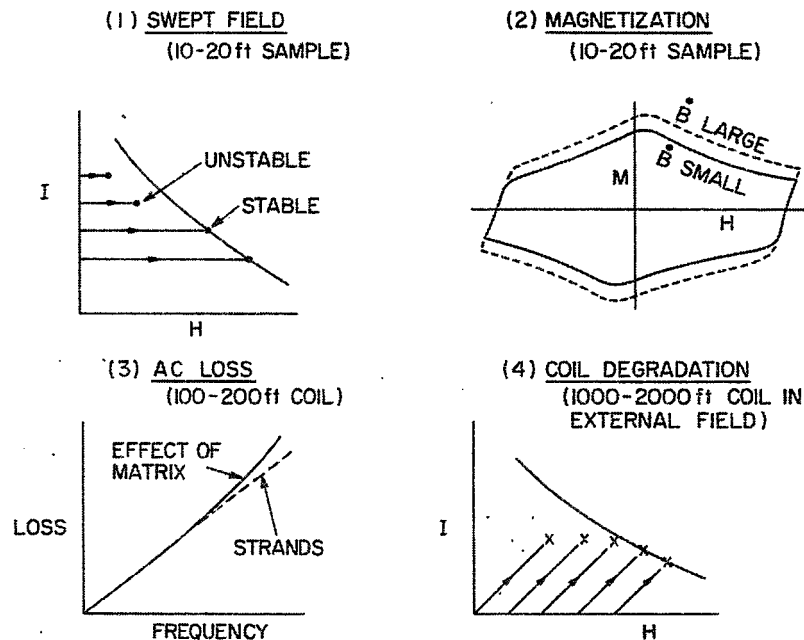


Fig. 3. Experimental program on filamentary composites.

# SUPERCONDUCTING MAGNETS FOR CONTROLLED THERMONUCLEAR RESEARCH\*

C.E. Taylor  
Lawrence Radiation Laboratory  
Livermore, California

Some of the general considerations for magnetic fields used in controlled thermonuclear research (CTR) are outlined in this paper, along with a list of a few of the early superconducting coils which have been built for this purpose and a list of coil systems now planned or under construction. These comments are intended as a general orientation for persons unfamiliar with CTR but with some understanding of superconducting magnets.

Basic to this discussion are some fundamental requirements for a fusion reactor. Most plasma confinement schemes receiving serious consideration today require a magnetic field which, if strong enough, confines moving charged particles to a helical motion about magnetic field lines and limits plasma escape across field lines to that net motion produced by classical scattering effects or by small-scale turbulence. In an "open-ended machine," escape of plasma along field lines is limited by the "magnetic mirror"<sup>1,2</sup> effect to particular components of the plasma which, by scattering, acquire enough momentum along field lines. In a "closed-ended" machine,<sup>3</sup> particles remain on magnetic "surfaces" contained within the vacuum chamber and are lost by diffusion and instabilities, but are not subject to the severe end losses of open systems.

Some basic general requirements for a fusion reactor are:

- 1) Plasma pressure must be less than "pressure" of the confining magnetic field:  $2nkT < B^2/8\pi$ .
- 2) A simplified power balance<sup>4</sup> for an ideal deuterium-tritium (D-T) system - assuming a reactor which produces heat by fusion reactions and by radiation only, which recovers this heat with an efficiency of 1/3, and which consumes only enough additional energy to heat the fuel to reaction temperature - leads to the criterion that  $n\tau > 10^{14}$  sec/cm<sup>3</sup> for a positive power balance. This neglects all other loss mechanisms and power requirements, and therefore to this extent represents an optimistic limit.

For an optimum temperature of 15 keV, the above two criteria can be combined<sup>5</sup> to give

---

\*Work performed under the auspices of the U.S. Atomic Energy Commission.

1. R.F. Post, Rev. Mod. Phys. 28, 338 (1956).
2. R.F. Post, in Progress in Nuclear Energy, Series XI, Plasma Physics and Thermonuclear Research (Pergamon Press, 1959), Vol. 1, p. 154.
3. W.P. Allis, Nuclear Fusion (D. Van Nostrand, 1960), Ch. IX, "Stellarators."
4. J.D. Lawson, Proc. Phys. Soc. (London) B70, 6 (1957).
5. L.A. Artsimovich, Controlled Thermonuclear Reactions (Gordon and Breach, 1965).

$$B^2 \tau > 6 \times 10^7 \text{ G}^2 \cdot \text{sec} ,$$

which relates B to average confinement time.

It can be seen that for  $\tau \approx 1$  sec,  $B > 8$  kG, and at first glance it would seem that relatively weak fields might suffice for a dc system or that a pulsed system operating at, say, 60 cps might require only 60 kG. (There are some schemes for pulsed reactors involving very high densities for much shorter pulses which will not be discussed here, since superconducting coils do not appear appropriate for very fast field pulses.) At the optimum temperature,  $P = 7 \times 10^{-17} B^4 \text{ W/cm}^3$  for the ideal D-T reactor<sup>5</sup> and, therefore, at say 10 kG,  $P \approx 0.07 \text{ W/cm}^3$ , which requires very large apparatus for reasonable central-station-scale power levels. Cost considerations may require P to be much higher; for example, if  $P = 10 \text{ W/cm}^3$ ,  $B \approx 20$  kG. Also, because of various stability limits<sup>6</sup> the ratio

$$\beta = \frac{2n kT}{B^2/8\pi}$$

may be required to be much smaller than one, and therefore stronger fields would be required. It can be concluded that for fusion reactors there may be an ultimate lower limit to B of about 8 kG, but because of various plasma loss mechanisms, and required economical minimum power density, this limit is more likely to be at least about 20 kG. Since  $P \propto B^4$ , it is unlikely that fields much above the minimum will be required. Therefore, fusion reactors will probably be operated at fields only slightly larger than the minimum required for positive power output, and will probably require very large plasma volumes, perhaps several meters in radius. Since the ratio of the confining field at the plasma to the maximum field at the conductor may be as high as 3:1 for complex coil shapes (such as baseball coils), the field at the conductors may be about 60 kG which is well within the limit for practical NbTi materials using today's technology.

The above comments apply only to a theoretical fusion reactor. Present CTR experiments are not miniature fusion reactors but are designed to explore confinement and stability. Therefore, the above power reactor conditions and scaling laws do not, in general, apply. Usually, the experimental apparatus must have dimensions larger than a minimum number of particle orbit radii so that true plasma conditions can be achieved. For protons this radius is about 1 cm for 5 keV at 10 kG (typical for Alice<sup>6</sup>). For a minimum of 20 orbit diameters within the plasma, a coil size of at least 1 m is necessary. Required field strength can usually be reduced by increasing apparatus size, the deciding factor becoming cost. Plasma generation techniques must also be scaled to larger plasma volumes and this requirement makes small-volume, high-field apparatus desirable for most research. Plasma energies much lower than required for a reactor are sufficient for studying confinement in open-ended systems. This allows consideration of weaker magnetic fields and/or smaller apparatus size. However, present technology for building neutral beam sources (a currently popular method for creating a plasma) limits energies to a minimum of a few keV. At lower energies practical beams may become so weak that the losses may become competitive with plasma generation rates. The point to be emphasized here is that the size and strength of any open-ended CTR magnet system is strongly dependent on the state of the art in plasma source and vacuum technology, and parameters such as size and field can be varied over a wide range. Therefore, the next "generation" of open-ended coil systems may not necessarily involve larger size coils or higher field strengths if plasma production techniques can be significantly improved.

---

6. R.F. Post, Lawrence Radiation Laboratory, Livermore, UCRL-70681 (1967). (Presented at Intern. Conf. on Plasma Confined in Open-Ended Geometry, Gatlinburg, Tenn., 1967).

Three examples of open-ended coil systems are illustrated in Fig. 1. Figure 1a is the simple mirror system used in many early experiments. Note that two of these systems, Figs. 1b and 1c, are not simple axially symmetric solenoid systems but involve three-dimensional current patterns. Figure 1b shows the superposition of a multipole field and a pair of mirror coils. This class of open-ended system has been used in many laboratories with pulsed or dc copper coils, originally without the multipole component; more recently, most such systems have a multipole component, which was demonstrated by Ioffe<sup>7</sup> to result in much more stable confinement. The plasma, being diamagnetic, tends to move toward the minimum-B region which these coils produce. Another current distribution which produces a similar field - using a single coil - is the baseball (or tennis ball) coil shown in Fig. 1c.

Some early superconducting solenoids were designed<sup>8,9</sup> and built for plasma studies and single-particle containment studies. The first superconducting minimum-B system used in a plasma experiment was a baseball coil,<sup>10</sup> although it was too small and weak for really useful results. A similar coil was built by Bronca et al.<sup>11</sup> but was not used for plasma studies. The first large superconducting minimum-B systems are now under construction: the IMP machine at ORNL,<sup>12</sup> a high-field mirror/Ioffe-bar system at NASA-Lewis, and a superconducting version of the Alice experiment in Livermore.<sup>13</sup> Some parameters of these coils are described in Table I. A major complexity of these coils is due to the noncircular shape which requires a support structure capable of withstanding bending stresses as well as hoop stresses.

Another class of CTR experiments which have been more recently proposed involves closed-ended systems with floating or levitated superconducting rings. Toroidal experiments with external coils have been made for many years<sup>3</sup> and have usually required only pulsed fields of a few milliseconds duration; therefore, superconductors have not been considered. However, to satisfy present requirements for good confinement, external coil systems such as stellarators must have high shear fields which, in a practical sense, require complex windings placed around a toroidal vacuum tank with exacting mechanical tolerances. A simpler way to provide a strongly stabilizing toroidal container is to have one or more current-carrying conductors buried within the plasma; i.e., the flux surfaces on which plasma is distributed completely surround the conductors. This is a simpler way to provide high shear and/or "minimum average B," although more investigation is required to determine the relative importance of these two parameters.

- 
7. M.S. Ioffe and E.E. Yushmanov, Nucl. Fusion Suppl. 1, 177 (1962).
  8. L.J. Donadieu and D.J. Rose, in High Magnetic Fields (M.I.T. Press/John Wiley & Sons, Inc., 1962). (Proc. Intern. Conf. High Magnetic Fields, Cambridge, Mass., 1961.)
  9. J.C. Lawrence and W.D. Coles, in Advances in Cryogenic Engineering (Plenum Press, 1965), Vol. 11, p. 643.
  10. C.E. Taylor and C. Laverick, in Proc. Intern. Symposium on Magnet Technology, Stanford, California, 1965, p. 594.
  11. G. Bronca, J. Krikorian, J.P. Pouillange, and D. Rappanello, in Proc. 2nd Intern. Conf. Magnet Technology, Oxford, 1967, p. 547.
  14. D.L. Coffey and W.F. Gauster, these Proceedings, p. 929.
  13. C.D. Henning, R.L. Nelson, M.O. Calderon, A.K. Cargin, and A.R. Harvey, to be published in Advances in Cryogenic Engineering (Plenum Press, 1968), Vol. 14.



TABLE I  
Superconducting Coils now Under Construction for Controlled Fusion Research

<u>Open-Ended Systems</u>				
Laboratory	Type	Characteristic dimensions, cm	Central field, kG	Max. field at conductor, kG
Oak Ridge Natl. Lab.	Mirror and quadrupole	35 diam, 70 long	20	75
NASA-Lewis	Mirror and multipole	51 diam	75	90
LRL-Livermore	Baseball	120 diam	20	75
<u>Closed Systems - Levitated Rings</u>				
Laboratory	Type	Ring diameter, cm	Ring current, kA	
Princeton Plasma Physics Lab.	1 ring "Spherator"	152 (major diam)	375	
Princeton Plasma Physics Lab.	2 ring	101	460	
	FM	202	325	
LRL-Livermore	1 ring "Levitron"	80	500	
Culham, UK <sup>a</sup>	1 ring	50	500	

<sup>a</sup>Tentative.

Several such devices have been built utilizing a temporarily levitated, inductively energized central conductor,<sup>14</sup> or conductors suspended on support rods.<sup>15</sup> In the inductively energized case, the time-varying ring currents are accompanied by large toroidal plasma currents because of close inductive coupling; these plasma currents lead to undesirable instabilities. In the rod-supported cases, collisions between supports and plasma cause rapid losses. A group of experiments is now under construction utilizing superconducting, magnetically levitated conductors. Princeton plans a two-ring "quadrupole" device, called FM (floating multipole). LRL-Livermore is building a single-ring machine of somewhat smaller size.

Similar experiments have been proposed at the University of Wisconsin, the Culham Laboratory in England, and the Institute for Plasma Physics at Garching in West Germany. The technological problems imposed by levitated coils are unique; for example,

14. H.P. Furth, in Plasma Physics (Intern. Atomic Energy Agency, Vienna, 1965), p. 411.

15. T. Okawa and D. Kast. Phys. Rev. Letters 1, 41 (1961).

such coils must be periodically recooled to remain below their transition temperature; therefore, there is reason to use Nb<sub>3</sub>Sn because of its higher critical temperature rather than because of its high field capability. Practically all present design experience has been with coils immersed in saturated liquid helium at 1 atm or lower, whereas these floating coils will be subject to periodic temperature cycling and may be immersed in a gaseous rather than liquid environment when energized. The Princeton coils will be Nb<sub>3</sub>Sn, will be energized through removable leads, and will be immersed in saturated liquid when energized; the LRL coil will have no external leads, will be inductively energized, and will be contained in a sealed toroidal container which is permanently pressurized with helium gas to provide heat capacity. The heat transfer and general cryogenic design problems of periodically recoiling these rings are, of course, unique. The ring position must be magnetically controlled by a system which maintains stability, because all such systems of current interest are inherently unstable.<sup>16</sup> Stability can be accomplished in a straightforward manner by a system of position-correcting coils and position sensors connected in an appropriate servo system. However, another possible way to stabilize such rings is to use superconducting surfaces located outside the plasma. If these surfaces were cooled below their critical temperature while the ring was mechanically held in its equilibrium position, then subsequent ring motion would be resisted by inductively generated eddy currents in the superconducting surfaces. Design of such surfaces is theoretically possible; this would represent a novel application for superconducting materials.

#### CONCLUSIONS

Because of many parameters which can be varied in fusion experiments, it is difficult to generalize about specific requirements for magnets. Most research requirements can be satisfied by a range of coil shapes, sizes, and field strengths. The deciding factor usually is cost.

Superconducting magnets will be used for many nonpulsed controlled fusion experiments in the near future, mainly because of their lower cost compared to conventional systems for these inherently large size experiments.

The dc levitated coils for closed systems must be superconducting. Here the determining factor is not cost but rather the fact that no other practical method appears to be available.

---

16. J. File, G.D. Martin, R.G. Mills, and J.L. Upham, J. Appl. Phys. 39, 2623 (1968).

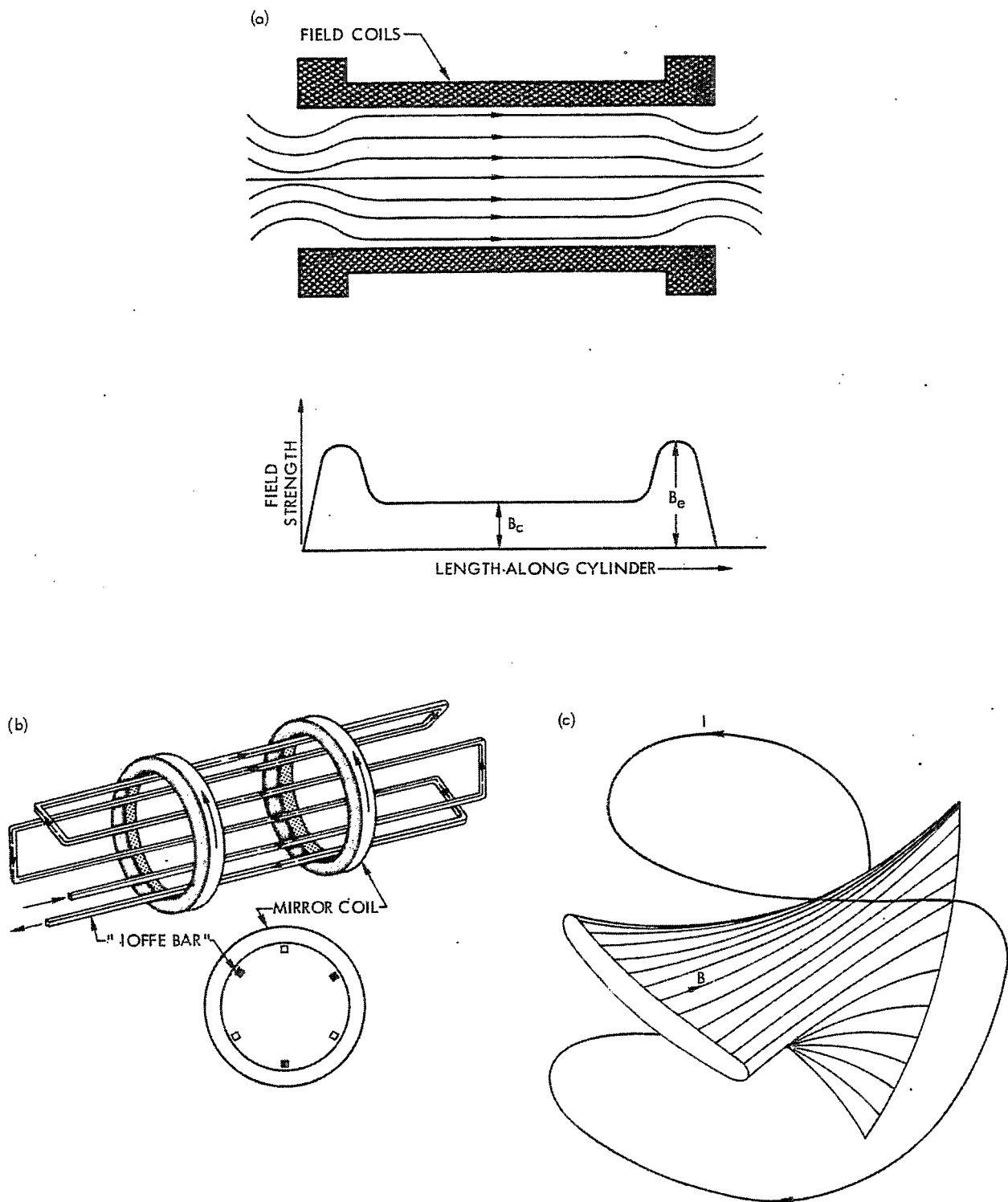


Fig. 1. Some open-ended coil systems.

## ON He II MICROSTABILIZATION OF Nb<sub>3</sub>Sn\*

W.H. Bergmann  
Argonne National Laboratory  
Argonne, Illinois

The Abrikosov-Mendelssohn<sup>1</sup> theory describes the hard superconductor of the second kind in the mixed state as a multiply connected structure of supercurrent filaments orthogonally penetrated by an array of flux vortices of diameter of the coherence length. The coexistence of the normal and superconducting phase has become possible through the "hardening process," which made the surface energy for boundaries between the two phases negative. On the one hand, this has improved the current-carrying capacity in these materials to such a degree that superconducting magnets became feasible. But, on the other hand, it also enhanced their instability since no positive boundary energy inhibits the propagation and growth of the normal phase zones propagating as "flux jumps" in the superconductor.

With changing field and/or current density, the density of fluxoids changes and the vortices move through the superconductor in or against the direction of the Lorentz force. This flow is not a continuous movement but an erratic one, since the vortices display an affinity to crystal defects and lattice imperfections. Within the course of this discontinuous, rapid movement, joule heat is being dissipated, heating the superconductor locally. If this heat is allowed to accumulate, it can form macroscopic normal zones - macroscopic in terms of the coherence lengths - which propagate as "flux jumps" through the superconductor until their propagation is impeded by the rapidly rising specific heat, or until they have driven the total superconductor normal.

The condition limiting the formation of macroscopic normal zones is that the electromagnetic diffusivity has to be smaller than the thermal diffusivity. The importance of these two quantities was first discussed by Furth<sup>2</sup> in connection with pulsed magnets. Kim<sup>3</sup> discusses their relationship macroscopically for superconducting magnets. It is also essential to secure this condition on a microscopic scale compatible with the coherence length.

One approach in this direction is to divide the superconductor into very fine filaments embedded in a metal matrix of high thermal capacity and thermal and electric conductivity. This approach finds its limitations in the Wiedemann-Franz law, which governs the ratio of thermal to electrical conductivity in metals; the low strength of ultrapure metals used as stabilizers on superconductors, which introduce severe mechanical support problems in high field magnets; and fabrication technology, since a metallurgical bond of high electrical and thermal conductivity is required between the

---

\*Work performed under the auspices of the U.S. Atomic Energy Commission.

1. A.A. Abrikosov, J. Exp. Theor. Phys. 32, 1442 (1957);  
R.A. French, J. Lowell, and K. Mendelssohn, in Proc. 9th Intern. Conf. Low Temperature Physics (Plenum, New York, 1965), Part A. p. 540;  
R.A. French, J. Lowell, and K. Mendelssohn, Cryogenics 7, 83 (1967).
2. H.P. Furth, M.A. Levine, and R.W. Waniek, Rev. Sci. Instr. 28, 949 (1957).
3. Y.B. Kim, Phys. Today 17, No. 9, 21 (1964).

superconductor and its stabilizing metal. This approach usually leads to average current densities within the coil-winding body, which do not exceed 10% of the current densities within the superconductor itself, at the same field and temperature conditions. Voluminous coil windings with their inherent mechanical and thermal problems are the consequence.

There appears to be a second intriguing possibility. We have seen above that the basic problem of stability is the heat of dissipation associated with the discontinuous movement of the fluxoids. Stabilizing a superconductor means to remove this heat before it can accumulate into macroscopic normal regions. The principal question, therefore, is how to extract this heat most expediently. It has been pointed out — for instance, by Hancox<sup>4</sup> — that the thermal capacity of liquid helium is more than one hundred times greater than that of Nb<sub>3</sub>Sn. Several experimenters<sup>4,5</sup> have demonstrated that porous sintered cylinders of Nb<sub>3</sub>Sn could be stable against flux jumping for field changes up to 50 kG if liquid helium is admitted freely to the pores. Within the sintered material, Claude achieved 150 kA/cm<sup>2</sup> current density at 50 kG in such a sintered cylinder by circulating liquid helium through the material, without any flux jumps occurring. These results should encourage one to attempt stabilization of Nb<sub>3</sub>Sn by supercritical helium, but we believe that before one should proceed in this direction, one should first investigate the unique possibility nature has provided us for this very problem. One should attempt to exploit the unique heat transport mechanism of superfluid helium, which can set up heat flows of several W/cm<sup>2</sup> over temperature gradients of only millidegrees with very small losses, and possibly even no losses at all.

One has to separate carefully the above effects from those which are due to the increase in current-carrying capacity with decreasing temperature.

We have started experiments aiming at the observation of He II microstabilization of Nb<sub>3</sub>Sn. As a first step, we have constructed two identical solenoids, consisting of two counterwound spirals of 100 turns each. The over-all dimensions are 2 in. i.d., 3½ in. o.d., and 1-1/32 in. axial length. The first solenoid was wound with RCA-R-60322 silver-plated 1200 A at 100 kG niobium-tin vapor-deposited superconductor. This ribbon was wound interleaved with a stainless-steel ribbon of 0.001 in. x 0.4 in.<sup>6</sup> In the second coil, we removed the silver-plating completely — by chemical means — laying bare the niobium tin. The space vacated by the silver and stainless-steel ribbon was filled by fiberglass cloth. The first coil was initially operated at 4.2°K in boiling He I. The coil could be charged up to about 50 kG at a current density of 40 kA/cm<sup>2</sup>. During the charging process, "flux jumps" could be observed with a magnitude of up to 50 mV. In the second experiment, the coil was again charged, but at a temperature of 1.85°K in superfluid helium. The most pronounced difference between these two experiments was the noise reduction during the charging process.<sup>7</sup> Only small "flux jumps" with an amplitude of about 1 mV could be observed. This noise level experienced further reduction below the limit of detectability of our system, which was about 10 µV, during the charging of the second coil at 1.85°K in superfluid helium. We have not yet attained with the second coil any higher current densities or fields than with the first one, since we had to leave the silver on the very ends of the superconductor ribbons in

- 
4. R. Hancox, Phys. Letters 13, 208 (1965).
  5. M.L. Claude and M. Williams, in Proc. 2nd Intern. Conf. Magnet Technology, Oxford, 1967, p. 497.
  6. Kindly supplied to us by W.B. Sampson of Brookhaven National Laboratory.
  7. W.B. Sampson, M. Strongin, A. Paskin, and G.M. Thompson, Appl. Phys. Letters 8, 191 (1966).

order to solder the joints and possibly because the superfluid had access only to the surface of the vapor-deposited layer. We have evidence that the second coil was quenched from "flux jumps" propagating from these joints into the spirals, but we feel that the most significant observation of this experiment is the complete elimination of "flux jumps" propagating partially through the coil during charging operations, which suggests to us that we may have been successful in preventing the development of macroscopic normal zones. Further investigations are in progress to clarify whether this interpretation is justified.

The author is greatly indebted to J.J. Davids and R.J. Diaz for their skilled experimental assistance.

## PROGRESS ON THE IMP FACILITY\*

D.L. Coffey and W.F. Gauster  
Oak Ridge National Laboratory  
Oak Ridge, Tennessee

The conceptual magnet design of the "IMP" ("Injection into Microwave Plasma") facility of the Oak Ridge National Laboratory has been briefly described as an example of a nonaxisymmetrical superconducting magnet system in a paper which discusses general problems in designing such systems.<sup>1</sup> In the following additional detail will be presented.

The IMP facility consists of two mirror coils surrounded by a quadrupole magnet system ("Ioffe bars") as shown in principle in Fig. 1. The inside diameter of the mirror coils is 18 cm. The field strength in the centers of the mirror coils is 40 kG and that in the center of the entire system is 20 kG. The quadrupole produces an additional magnet field such that the total field increases from the minimum value of 20 kG in the system center to at least 26 kG when one proceeds from the center in any direction ("B-minimum field"). The maximum field strength in the mirror coils is 68 kG, that in the quadrupole is 75 kG.

Figure 2 shows the midplane cross section of the magnet system. The current density in the quadrupole was assumed to be  $11\,300\text{ A/cm}^2$ , that in the mirror coils to be  $10\,600\text{ A/cm}^2$ . In order to provide a free cylindrical opening for the mirror coils, the quadrupole coils were supposed to have saddle shape. Applying the computation methods described at another place,<sup>1</sup> it became obvious that, for a symmetrical quadrupole design as shown in Fig. 2, the space between Ioffe coils (positions  $S_1$  to  $S_4$  in Fig. 2) is especially important for providing ampere turns, i.e., ampere turns at these places of the quadrupole are most effective. When using stainless-steel-reinforced  $\text{Nb}_3\text{Sn}$  ribbons for the quadrupoles, it would be possible to fill out almost entirely the spaces  $S_1$  to  $S_4$  and to make the windings in saddle shape. Such a design of a  $\text{Nb}_3\text{Sn}$  quadrupole has been described by Sampson et al.<sup>2</sup> In the case of the IMP project, the electromagnetic forces on the windings are so high that very strong stainless-steel reinforcement would be necessary, and it would not be possible to reach the desired average current density.

Windings made of NbTi can carry certain hoop stresses and for axisymmetrical magnet systems simple reinforcements, say, in the form of stainless-steel bands, can be conveniently provided if necessary. For nonaxisymmetrical magnet systems, the only practical solution is to encase the magnet windings by strong mechanical structures. In order not to lose precious winding spaces  $S_1$  to  $S_4$  by the walls of the supporting winding cases, it is preferable to provide a nonsymmetrical design as shown in Fig. 3. The computation method used for volume optimization of quadrupole windings is described elsewhere.<sup>1</sup> To build such a quadrupole with saddle-shaped coils would be difficult, and it was decided to provide the simpler "race track" shape (see Fig. 1 of Ref. 1).

---

\*Research sponsored by the U.S. Atomic Energy Commission operated by the Union Carbide Corporation.

1. W.F. Gauster and D.L. Coffey, J. Appl. Phys. 39, 2647 (1968).

2. P.G. Kruger, J.N. Snyder, and W.B. Sampson, J. Appl. Phys. 39, 2633 (1968).

A disadvantage of the race track shape is that the "turn arounds" of the larger quadrupole windings (Coils A and A' and B and B' in Fig. 3) would interfere with the mirror coils if the quadrupole coils did not have sufficient axial length. However, this disadvantage seemed to be not decisive, and the project assumes that the larger quadrupole coils are sufficiently long.

As discussed in Ref. 1, the electromagnetic forces acting on the mirror and the Ioffe coils of the IMP facility are very high. Here, we will not describe in detail the force and stress analysis of the IMP magnet system, but we restrict ourselves to making a few general remarks about problems of this kind.

First, if we assume the use of NbTi for winding the coils, we have to consider the performance of compound conductors made up of two different materials with different Young's (and strictly speaking also Poisson's) moduli and different thermal expansion coefficients. At 77°K, the Young's moduli are<sup>3</sup>

$$E_1 = E_{\text{copper}} = 20 \times 10^6 \text{ psi}$$

$$E_2 = E_{\text{NbTi}} = 12.2 \times 10^6 \text{ psi}.$$

These values are not very different from those at 4.2°K.

When cooling down from room temperature to 4.2°K, the contraction is<sup>4</sup>

$$\frac{\Delta l}{l}_{\text{copper}} = - 326 \times 10^{-5} = \bar{\alpha}_1 \times (4.2 - 300)$$

$$\frac{\Delta l}{l}_{\text{NbTi}} = - 131 \times 10^{-5} = \bar{\alpha}_2 \times (4.2 - 300).$$

By applying the well-known stress-strain relations, we obtain an equivalent Young's modulus  $E$ , and an equivalent average expansion coefficient  $\bar{\alpha}$  as follows:

$$E = \frac{1 + a(e - 1)}{e} E_1 \quad (1)$$

$$\bar{\alpha} = \frac{\bar{\alpha}_1 ea + \bar{\alpha}_2 (1 - a)}{1 + a(e - 1)} \quad (2)$$

Here, the quantities  $a$  and  $e$  are the ratios

$$a = \frac{\text{cross section area of copper}}{\text{total cross section area}}$$

and

$$e = \frac{E_1}{E_2}.$$

---

3. D.B. Montgomery, private communication.

4. National Bureau of Standards Nomograph 29.



Using Eqs. (1) and (2), stress and strain of the two components of a compound conductor (which has been prestressed at room temperature and then cooled down) can be calculated as if it were a uniform body.

Unfortunately, at this time insufficient research has been done to enable one to calculate reliable values of the stresses in nonaxisymmetrical coil systems, i.e., in coils of nonaxisymmetrical shape or in axisymmetrical coils exposed to nonaxisymmetrical electromagnetic forces. For instance, the mirror coils of the IMP device are axisymmetric; however, the total electromagnetic forces, considering the fields generated by the Ioffe coils, are not axisymmetric. At the Oak Ridge National Laboratory, approximation methods for treating cases of this kind have been worked out and have been used for designing the mechanical structure of IMP. Here, we will not discuss this rather complicated matter, but we will present only a few related simple problems of a general nature.

The first problem concerns the forces in a wire and on the spool when a coil is wound with stressed wire. No electromagnetic forces are considered. If the spool radius is  $r$  and if friction is not taken into account, the hoop stress  $\sigma$  and the tension  $S$  are

$$S = \sigma A = pr, \quad (3)$$

where  $A$  is the wire cross section and  $p$  the force exerted on the spool per unit length of the wire. If the wire is wound with the tension  $S$  in one layer of  $n$  turns on a spool with the length  $l$ , it could be expected that the pressure  $\sigma_r$  on the spool is

$$\sigma_r = \frac{n}{l} \frac{S}{r}. \quad (4)$$

The assumption of no friction is, however, unrealistic. After Euler's formula, the forces  $S$  and  $S_0$ , acting on the cross sections of a rope which is wound around an angle  $\varphi$  over a spool (Fig. 4), are correlated by

$$S = S_0 e^{f\varphi}, \quad (5)$$

if  $f$  is the coefficient of static friction between rope and spool surface. Practically, it is very difficult to estimate with sufficient accuracy the friction coefficient,  $f$  [which should be known very exactly since  $f$  appears in Eq.(5) in the exponent of an  $e$ -power].

The difficulty becomes worse if we try to determine the pressure  $\sigma_r^*$  on the spool surface for the case of a winding with a certain number of layers instead of a single layer. We assume that in the wire the tension  $S$  decreases in some way with increasing distance from the point where the wire leaves the spool during the winding process. We will use a simple model which considers only a relatively small number of layers,  $\gamma$ , stressed, however, with the full wire force  $S$ , and we write

$$\sigma_r^* = \frac{n}{l} \frac{S}{r_{av}} \gamma. \quad (6)$$

$r_{av}$  is the average radius corresponding to  $\gamma$  layers. In this model, the pressure  $\sigma_r^*$  acts on the first of the remaining unstressed layers. The next step is to find the pressure on the spool. If we assume that the unstressed part of the winding reacts against the pressure  $\sigma_r^*$  like an elastic body, it can be shown that the pressure on the spool surface is

$$\sigma_r^* \leq 1.54 \sigma_r^*. \quad (7)$$

$\sigma_r^*$  increases with increasing total thickness of the winding; however, the limit  $1.54 \sigma^*$  is reached soon.

We made experiments with a "race track" shaped coil similar to those which we intended to be used for the IMP quadrupole winding. The coil spool was divided in two parts (Fig. 5), and a load cell was provided in order to measure the force exerted by the winding. A tension of 52 lb was used during the winding process. The compound conductor consisted of multistrand NbTi in a copper matrix with  $0.057 \times 0.114$  in. cross section. A spiral wrap of  $0.080$  in.  $\times$   $0.005$  in. "Nomex paper" has been applied to the conductor for insulation. Approximately 50% of the conductor surface was exposed. Figure 6 shows the load cell force vs number of layers. After an approximately linear increase the force becomes almost constant, i.e., additional layers do not increase the force on the spool. The decreases in the magnitude of force as indicated at several places in Fig. 6 are due to interruptions of the winding process for making splices and repairing spots of damaged insulation.

Other measurements of the mechanical winding performance were made with a test apparatus called "coil expander" which is described in Ref. 1. These tests showed that appreciable differences can be expected between the actual performance of the coil winding volume under stress and the performance of an elastic body of identical shape which is exposed to the same volume forces. However, the elastic body model for a winding is at least a very important guideline for the stress analysis in coil winding.<sup>5</sup>

A much simpler approach for approximate stress calculations of axisymmetrical coils considering the electromagnetic forces due to the self-field can be achieved by assuming that the displacement vector  $\vec{u}$  has one constant magnitude for the entire coil volume. Furthermore, end effects have been neglected. A similar method has been described by Appleton, Cowhig, and Caldwell.<sup>6</sup> We made such calculations for several typical cases, and we found reasonable agreement with the stricter elastic model computations. However, none of these methods were sufficient to the stress analysis of the windings and structures of the IMP quadrupole system and, as it has been mentioned before, it was necessary to use additional special approximation methods.

Another major effort in the design of IMP has been toward the selection of an adequate superconductor. We have very carefully studied the use of multifilament NbTi in copper with current densities of about  $10\,000$  A/cm<sup>2</sup>. However, encouraged by the work of Sampson,<sup>2</sup> we have undertaken a parallel study program to determine if a higher current density ( $\sim 15\,000$  A/cm<sup>2</sup>) Nb<sub>3</sub>Sn design would provide a more reliable quadrupole coil system. Since the data are not yet complete for the Nb<sub>3</sub>Sn alternative, the following discussion will be limited to the NbTi coil system.

The central question in the design of an appropriate superconductor is that of the electrical stability of the conductor in the magnet system. Early attempts to use superconductors in mirror-quadrupole systems indicated the presence of electrical instabilities which are more severe than in axisymmetrical magnet systems. We have purchased a variety of superconducting samples from several manufacturers and subjected each sample to both short sample and coil tests to evaluate the stability of the various conductor designs. In general, we have found that the conductor performance seems to depend principally upon the conductor design rather than the special

---

5. R.W. Kilb and W.F. Westendorp, General Electric Co., Report No. 67-C-440 (1967).

6. A.D. Appleton, T.P. Cowhig, and J. Caldwell, in Proc. 2nd Intern. Conf. Magnet Technology, Oxford, 1967, p. 553.

manufacturing process. In testing the conductors, we have attempted to answer the following questions:

- 1) What influence has the copper/superconductor ratio?
- 2) What effect is found with smaller superconductor filaments?
- 3) Does the shape of the short sample curve, in the current sharing region (determined with constant field and variable current), relate to the performance of the conductor in a coil?
- 4) What conductor configurations show flux jumps in short sample tests (determined with constant current and variable field), and what effects do they have on coil performance?
- 5) Is the normal state surface cooling rate ( $W/cm^2$ ) a reasonable coil design parameter?

These questions have been examined primarily through the analysis of the results obtained with two standardized test methods which we have developed for short sample and coil performance. It has not been possible to find final answers to the questions listed, but the results of our tests show some influence of these effects and serve as a guide in selecting conductor.

The basic conductor shown in Fig. 7 was selected for our study. It is rectangular rather than square or round to facilitate good winding and to withstand most effectively the high electromagnetic forces in mirror quadrupole systems. The figure indicates 15 superconducting filaments; actually, our test samples contained as many as 252 filaments in this size conductor. Insulation is provided by a 50% coverage of Dupont Nomex paper 0.005 in. thick x 0.080 in. wide. The Nomex paper was selected after compressive displacement tests showed that under electromagnetic forces it allows less motion of the magnet windings than Mylar. However, the Nomex paper has a much lower shear strength than Mylar which must be provided for by the coil construction. The compressive displacement test also establishes the maximum winding section dimension which can be used without the danger that certain conductor loops become dislocated into void winding spaces resulting from electromagnetic forces.

The standard short sample test developed at ORNL uses the sample holder shown in Fig. 8. With this apparatus the conductor is suspended in free flowing liquid helium and is subjected only to hoop stresses due to the sample current and applied field. The test employs a very low impedance power supply so complete test cycles can be safely performed. The critical current, the region of current sharing, the normal state transition, and the recovery to the superconducting state can be measured. Our facility allows the test to be run in fields up to 75 kG and at sample currents up to 3000 A.

The standard coil test utilizes approximately 1000 ft of conductor wound into two identical coils which are operated in series-cusp mode as shown in Fig. 9. They are tested with a horizontal axis in the vertical field of a large 6 MW copper magnet which produces a homogeneous background field of up to 60 kG. As indicated, the peak forces are axially outward at the bottom of the coil, and axially inward at the top. The maximum field is found in the winding section near the midplane. The cusp coil test has been selected as that which best reproduces the extreme forces and field gradients of the mirror-quadrupole system. It also allows measurements over a wide range of magnetic fields and in a thermal environment which closely simulates that of the final IMP coils. Figure 10 shows an actual cusp coil after testing. Note the heavy series 310 stainless-steel structure required to restrain the forces generated by the cusp coil. Preliminary tests showed that perforated interlayer insulation sheet did not influence

the critical current or the charge rate sensitivity and therefore all tests were conducted with this additional insulation to avoid interlayer shear.

The results of these short sample and cusp coil tests are shown in Fig. 11. The data shown include the manufacturer of the conductor and the number of filaments (e.g., Supercon 18), the average filament diameter, the copper-to-superconductor ratio, test coil performance, and short sample performance.

Those parts of Fig. 11 which show test coil performance include the short sample  $I_c(H)$  for comparison (marked SS). As indicated by the parallel load lines, an externally applied background magnetic field of 0-60 kG is used to study the performance of the coil over a wide range of fields. Critical currents vary with the rate of current rise,  $dI/dt$ , in the test coil (e.g., the Supercon 18 coil reached  $I_c$  values from 550 A to 680 A, over the maximum field range 17 to 80 kG, when charged at 0.2 A/sec). At high charging rates (10 A/sec) the critical current was found to be relatively insensitive to the magnetic field.

Short sample tests of the conductors used in the coils are also shown in Fig. 11. In these tests, with a fixed background field of 0-75 kG, the sample current was increased beyond  $I_c$  into the current sharing region and then past the take-off current so that essentially all current was carried by the copper. Then, lowering the current, a copper resistance curve (marked 70, 60 and 50 kG) was determined. Finally, the recovery current was established as the temperature became low enough that the current returned to the superconductor.

The results of the short sample and coil tests lead to some tentative answers to the five conductor design questions which were listed above.

1) What influence has the copper/superconductor ratio?

Generally the samples with greater proportions of copper were more stable. However, exceptions are noted for those conductors with smaller filament diameters.

2) What effect is found with smaller superconductor filaments?

The coil with the smallest filament diameter (0.0030 in.) was found to be the most stable of those tested. It was possible to charge it at a rate of 1 A/sec (34 G/sec, maximum) to values very near short sample. With zero applied field, critical currents within 10% of short sample were measured at charging rates up to 10 A/sec. These results are in contrast to those obtained with the other test coils at zero applied field, all of which measured far below the short sample curve with fast charging rates. At slower charging rates, only the two cusp coils with conductors containing 0.0030 and 0.0111 in. filaments reached short sample performance over the full range of applied fields. The reason for the unusually good performance of the Supercon 15 coil is not clear, since a very similar Supercon 18 coil performed very differently.

3) Does the shape of the short sample curve, in the current sharing region (determined with constant field and variable current), relate to the performance of the conductor in a coil?

There seems to be a definite correlation on this point. Those conductors which exhibited smooth transitions into the current sharing region also behaved well in cusp coil tests. It is very likely that a smooth transition is necessary to allow continuous and steady dissipation of the trapped currents which are generated between filaments within a conductor by the increasing magnetic field. If the transition is not

smooth and reversible, the energy associated with the trapped current can be momentarily released causing  $T > T_c$  and the initiation of normal state propagation. Below the minimum propagation current (approximately given by the 10 A/sec performance line), temperature excursions above  $T_c$  are of little consequence since they do not initiate propagation.

- 4) What conductor configurations show flux jumps in short sample tests (determined with constant current and variable field), and what effects do they have on coil performance?

Short sample tests with fixed current and swept field operation show large flux jumps at low fields (5-10 kG) followed by a series of smaller flux jumps in the field range 10-45 kG in the Supercon 18, Cryomag 37 and Airco 85 conductors. The Supercon 15 conductor did not exhibit the large flux jumps at low fields but had the smaller flux jumps at higher fields. The Avco 252 sample did not show any flux jumps, suggesting that the filament diameter 0.0030 in. is sufficiently small to be stable in the manner suggested by a number of authors.<sup>7</sup> Those samples which showed large low field flux jumps performed poorly in coils. The smaller flux jumps at higher fields seem to have no detectable influence on coil performance.

- 5) Is the normal state surface cooling rate ( $W/cm^2$ ) a reasonable coil design parameter?

In our coil tests normal state transitions have been recorded over a range of currents which would correspond to 0.6 to 12  $W/cm^2$  surface dissipation if the current were completely in the copper. In partially stabilized coils, i.e., beyond 0.2 to 0.4  $W/cm^2$ , the surface cooling rate does not seem to be a sensible design parameter.

The test cusp coils have been operated up to short sample performance of 20 000 A/cm<sup>2</sup> at 60 kG. They have yielded complementary data to aid in the evaluation of short sample tests. In addition, using the information from these tests, we have wound and tested two 7 in. bore, 1 H mirror coils (Fig. 12) which employ 6000 ft of Supercon 15 conductor each. The performance of the mirror coils was predictable by the cusp coil tests. Each mirror coil reached short sample performance at 67 kG, 600 A (10<sup>4</sup> A/cm<sup>2</sup>) with 0.2 A/sec charging rate. With faster charging rates the critical current was degraded in quantitative agreement with cusp coil tests.

Figure 13 shows the entire IMP facility. The two mirror coils will be installed in the fall of 1968. It is expected that the complete magnet system (including the four quadrupole coils which surround the mirror coils) will be operational in 1969.

---

7. P.F. Chester, in Reports on Progress in Physics (The Institute of Physics and the Physical Society, London, 1967), Vol. 30, Part II, p. 561.

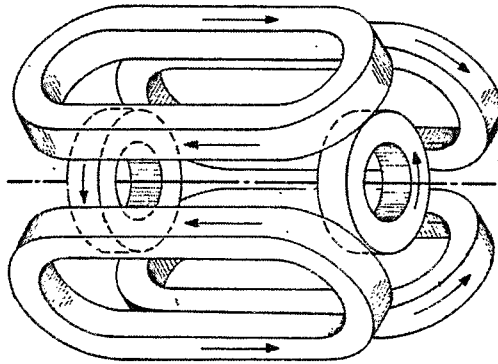


Fig. 1. Schematic of a B-minimum magnet system

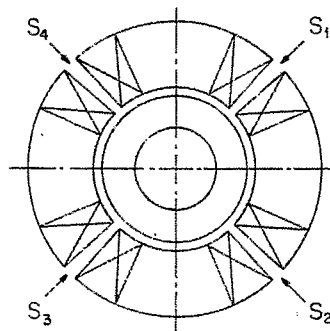


Fig. 2. Conceptual design of the IMP magnet system with wedge-shaped saddle coils forming symmetrical quadrupoles.

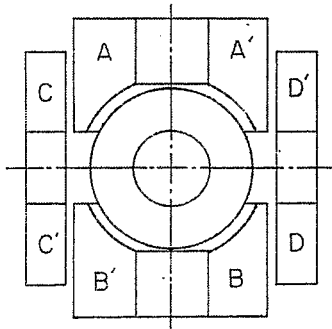


Fig. 3. Nonsymmetrical magnet system for IMP.

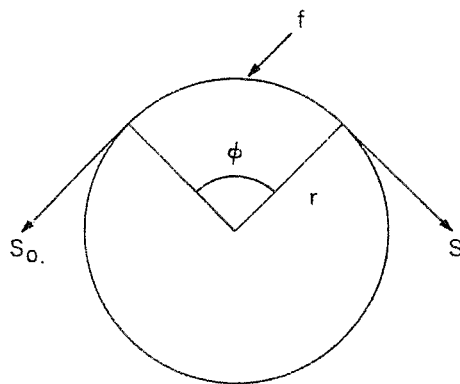


Fig. 4. Forces in a rope wound around a spool.

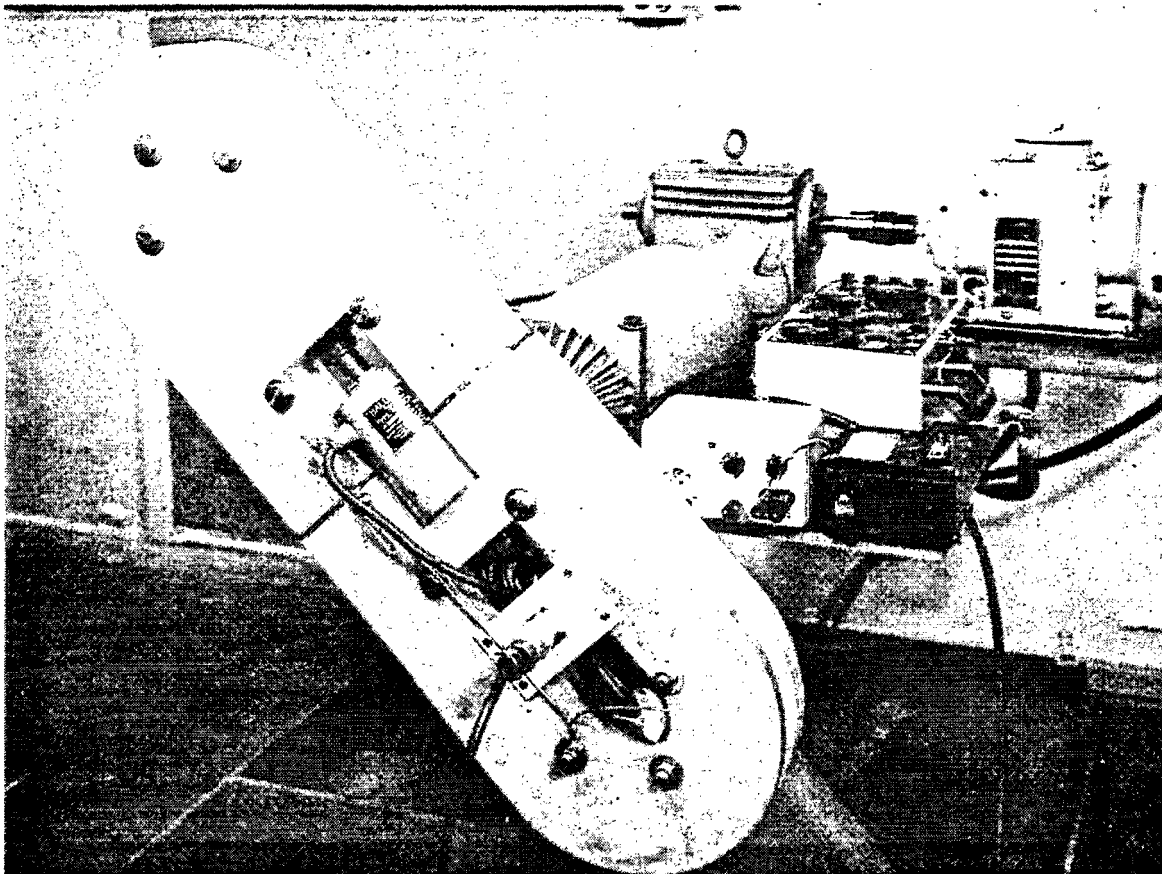


Fig. 5. Race track coil winding experiment.

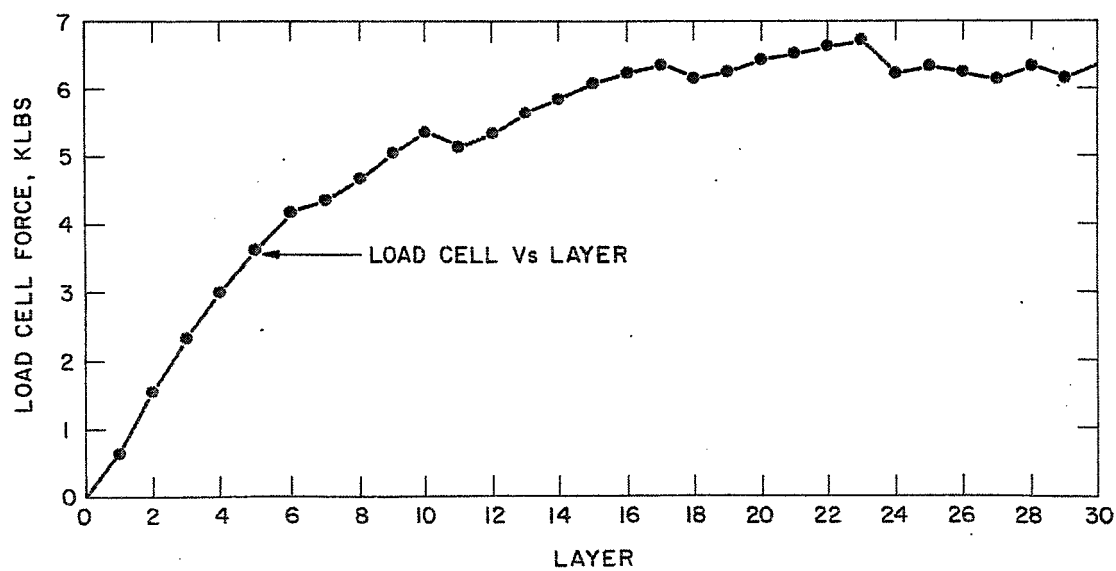


Fig. 6. Results of race track coil winding experiment.



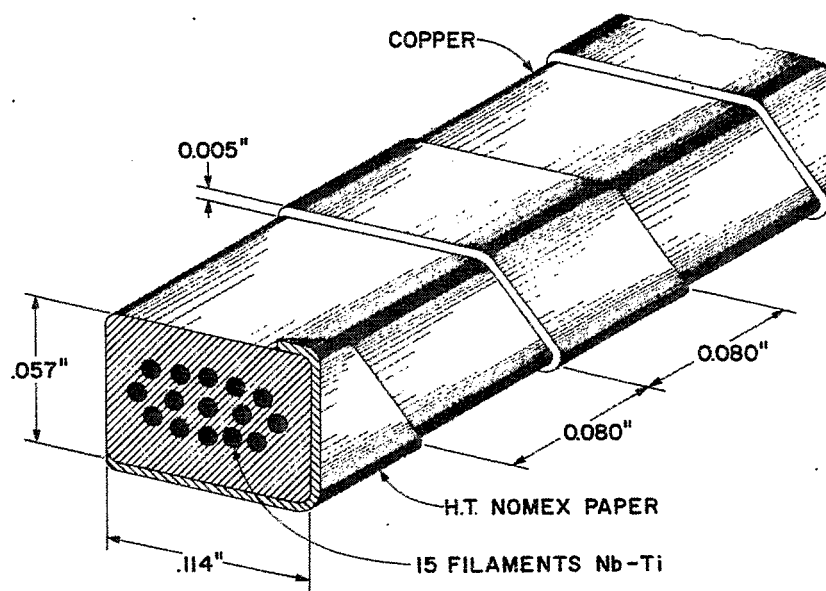


Fig. 7. IMP superconductor.

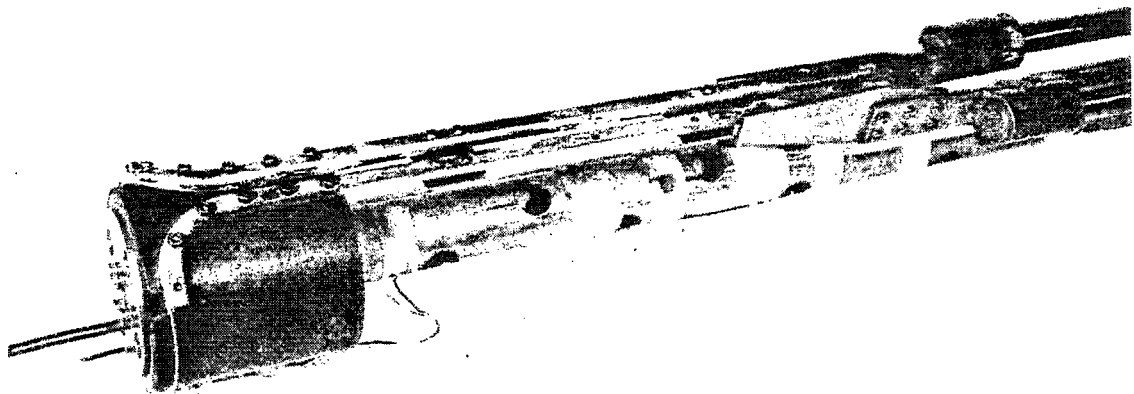


Fig. 8. Short sample test holder.

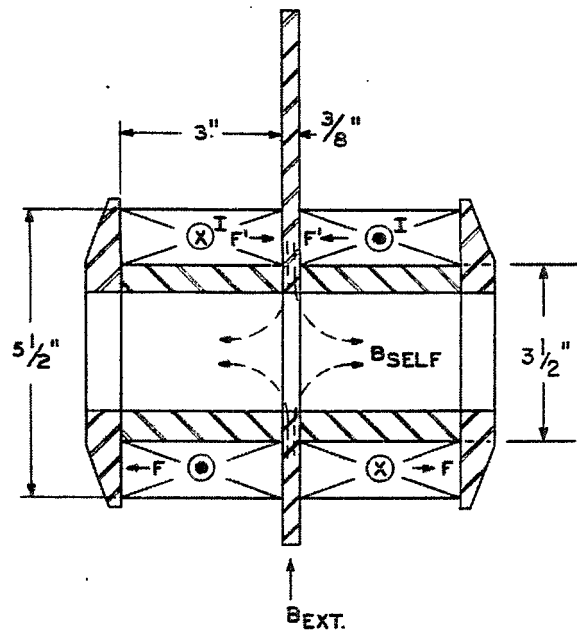


Fig. 9. Large cusp test coil.

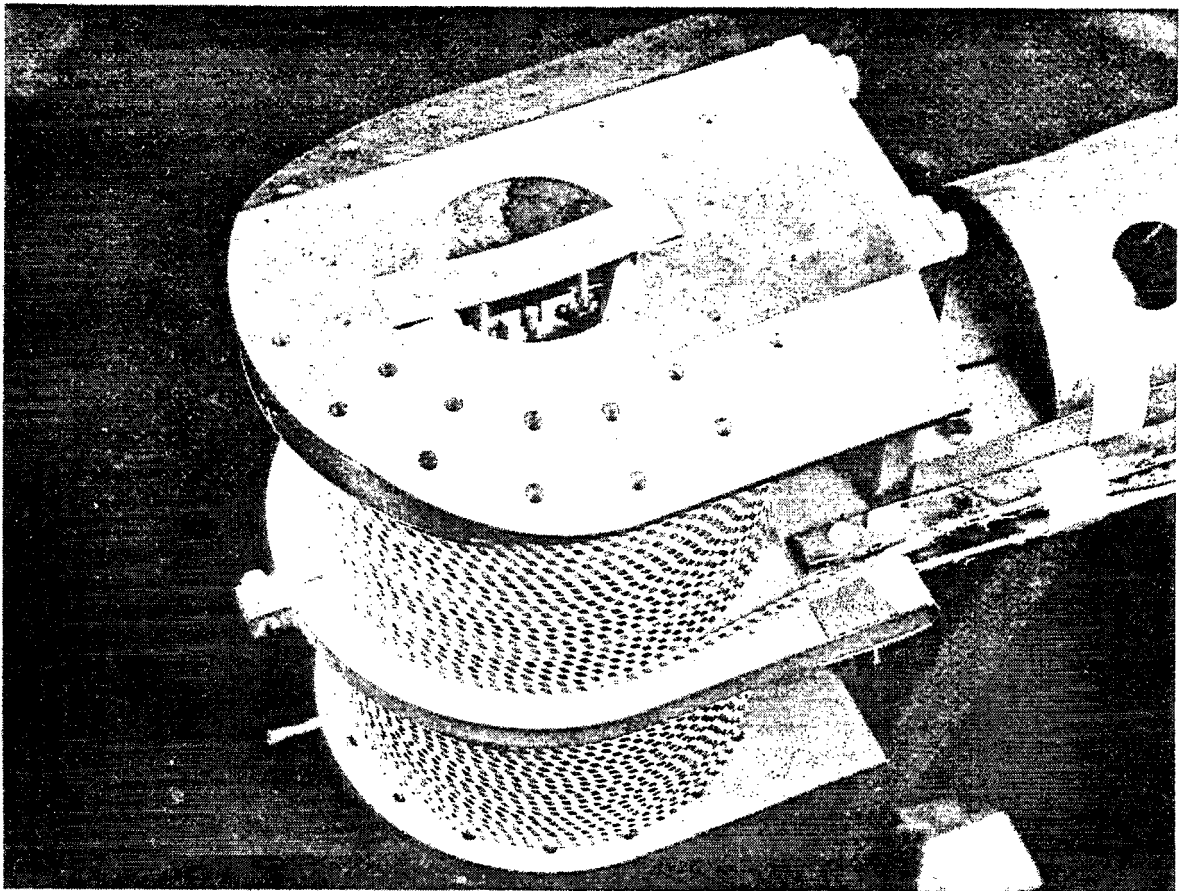


Fig. 10. Completed cusp test coil.

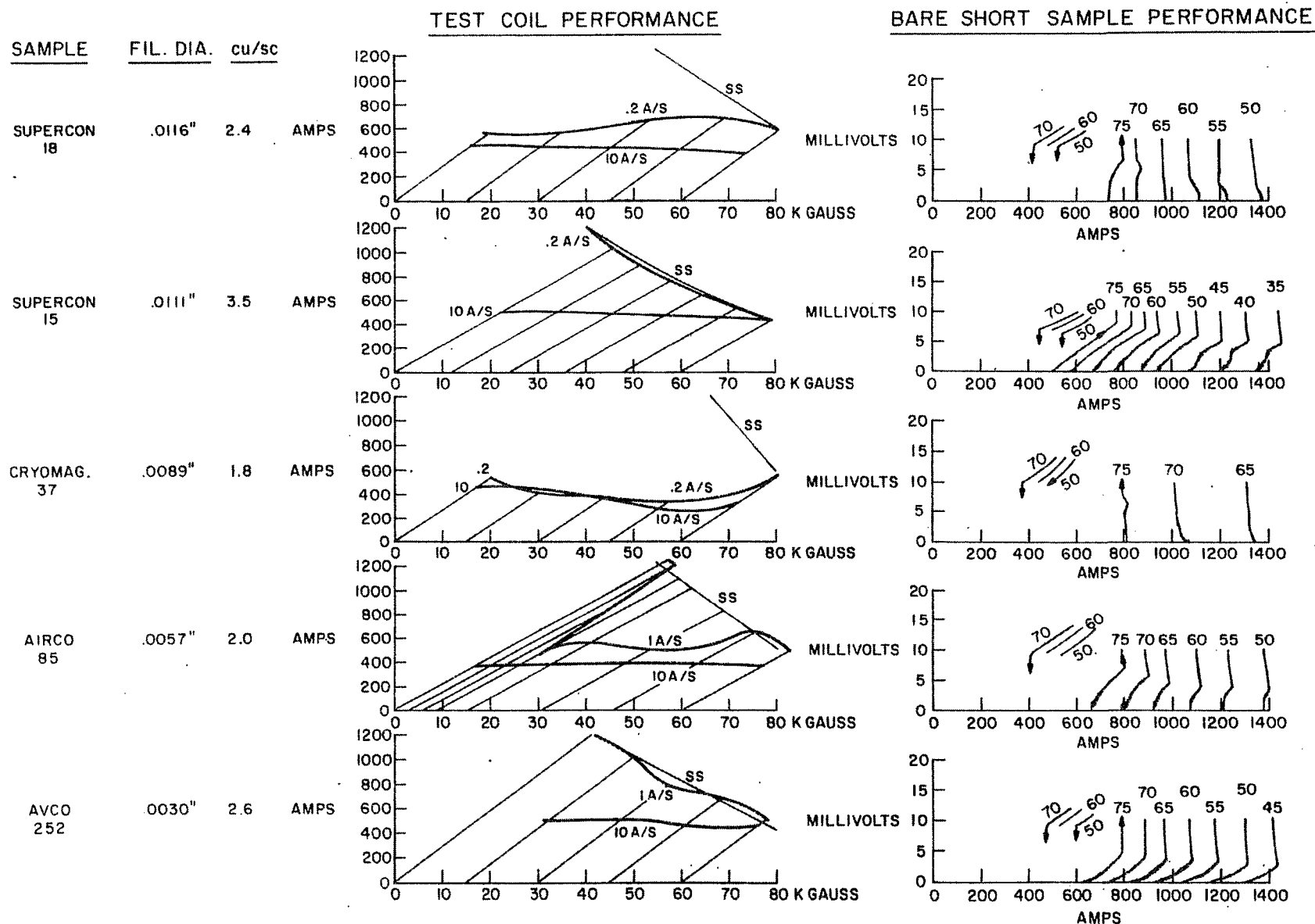


Fig. 11. Coil and short sample tests of 0.057 in. x 0.114 in. NbTi conductor.

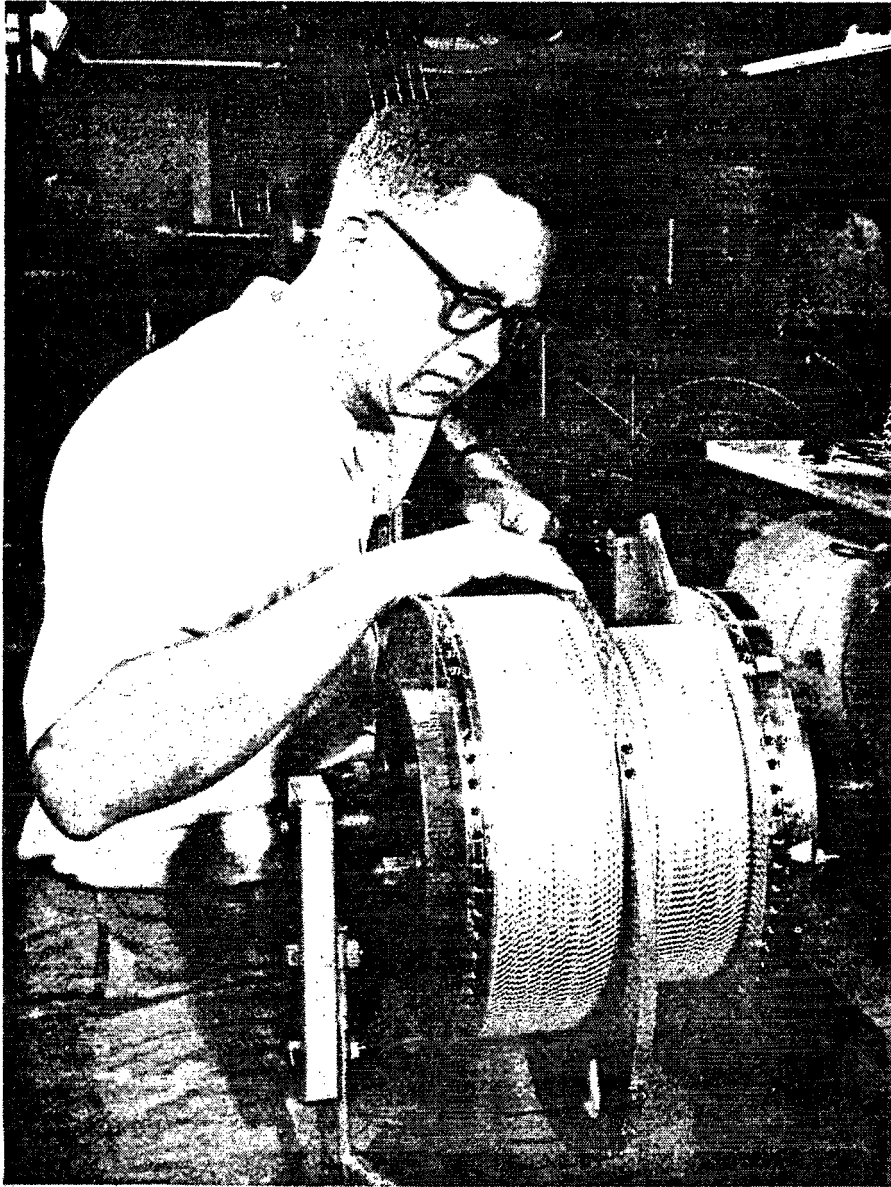


Fig. 12. IMP mirror coil A during winding.

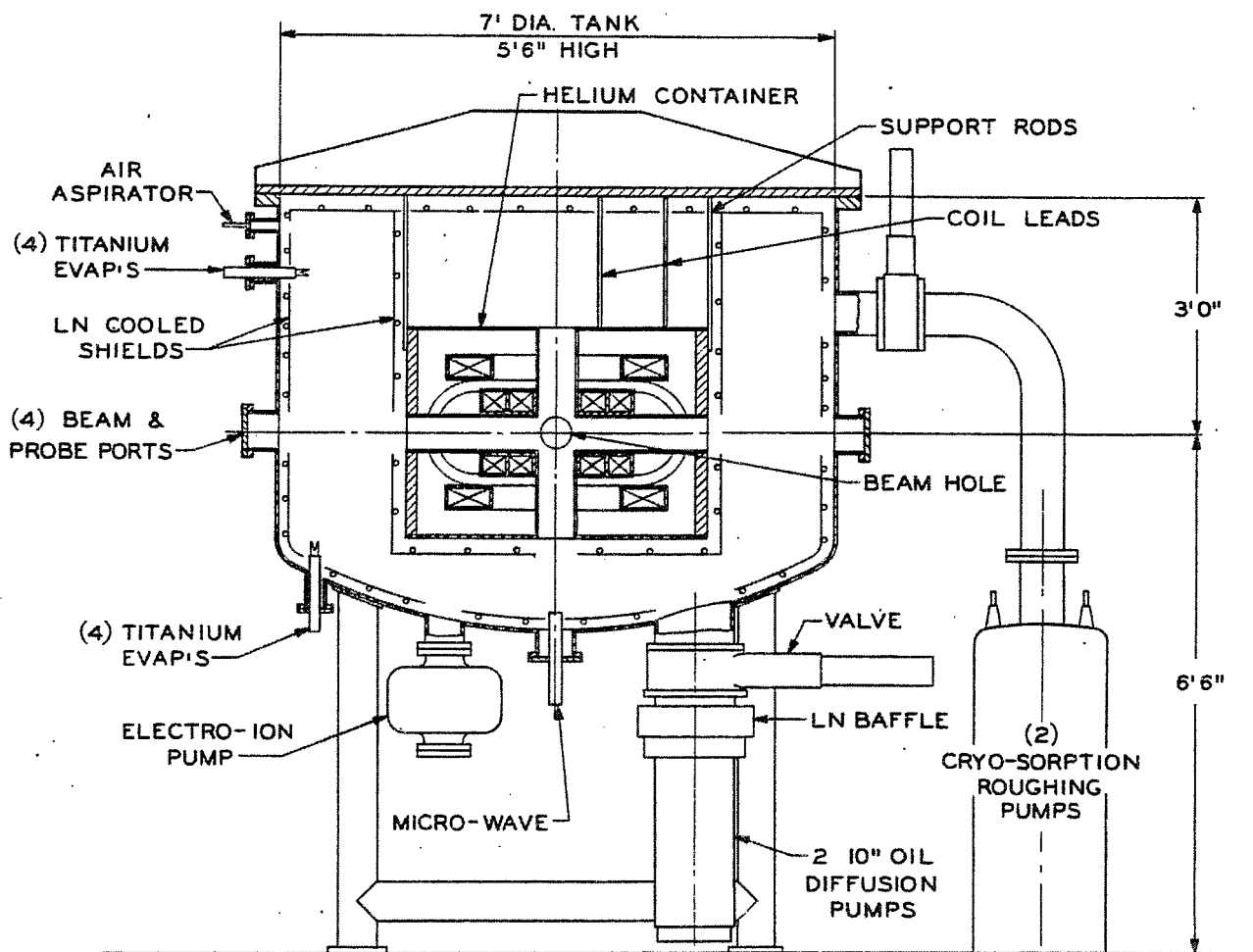


Fig. 13. IMP facility.

## STANDARDIZED TESTS FOR SUPERCONDUCTING MATERIALS\*

W.F. Gauster  
Oak Ridge National Laboratory†  
Oak Ridge, Tennessee

It has become necessary to define more clearly the properties of commercial winding materials for superconducting magnet coils and to standardize appropriate test methods. Basic physical constants (e.g., critical temperature of the superconductor, or the resistance of the substrate of a compound conductor) are important data which can be determined by means of well-known experimental procedures. However, they are not sufficient to describe fully all of the relevant properties of commercial superconductive materials. More complex performance data are of interest which call for special test methods.

First of all, I shall discuss the concepts of the critical current  $I_c$ , the take-off current  $I_t$ , and the recovery current  $I_r$ . The dependence of these three quantities on the external field  $H$  should be determined by short sample tests in unrestricted liquid helium flow. Furthermore, the current source should have such a characteristic that complete test cycles involving  $I_c$ ,  $I_t$ , and  $I_r$  can be run without damaging the sample.<sup>1</sup> Besides these three numerical values, complete flux flow diagrams are desirable for describing fully the stability performance of short samples, because different forms of the flux flow characteristics can be observed. "Stability Case A" means a smooth transition from resistanceless superconducting state to a stable flux flow state which is terminated by "take-off" to the normal state. "Stability Case B" designates discontinuous transition from the resistanceless state to a stable flux flow state, and finally, "Stability Case C" stands for abrupt transition from superconducting to normal state without attaining a stable flux flow state.<sup>2</sup>

In addition to these tests with noninductive short samples, tests with inductive samples (conductor lengths from a few hundred to a thousand feet) are of interest. At ORNL such a special test, called "Cusp Coil Test," has been developed.<sup>3</sup> The superconducting material is wound in a split coil with horizontal axis. In the two halves the current flows in opposite directions so that a "cusp field" is produced. This split coil is exposed to a vertical external field of up to 60 kG which is generated by a "conventional" magnet coil with an inside diameter of 32 cm. Critical currents of the test cusp coil are most conveniently measured by raising the cusp coil current with constant external field. The windings of the cusp coil are exposed to a nonaxisymmetrical field which results from the superposition of the external and the self fields. Thus, the magnitude of the resulting field in the various volume elements of the windings varies between the sum and difference of self and external fields. The cusp coil characteristics deviate appreciably from the short sample characteristics of the same winding materials. Furthermore, significant influence of the rate of rise of the external field can be observed. The cusp coil test, which can be done with a not too

---

\*Work sponsored by the U.S. Atomic Energy Commission and NASA.

†Operated by the Union Carbide Corporation.

1. W.F. Gauster and J.B. Hendricks, J. Appl. Phys. 39, 2572 (1968).
2. W.F. Gauster and J.B. Hendricks, in Proc. Intermag Conf. 1968 (to be published).
3. W.F. Gauster and D.L. Coffey, J. Appl. Phys. 39, 2647 (1968).

large quantity of superconducting winding material, seems at present to be the most realistic test for the material performance in the actual magnet coil. However, the cusp coil test needs a coil of large working diameter for providing the external field, and this restricts this test method to larger laboratories.

After this discussion of test procedures, we arrive at the following conclusions: In the interest of both manufacturers and users, it is highly desirable to work out clear concepts and definitions concerning the performance of winding materials of superconducting magnet coils. In order to achieve well reproducible test data, standardized test methods should be used. There have been undisputed benefits of the various standardized test procedures now generally employed in almost all fields of engineering. I would suggest the formation of a working group (most fittingly in the frame of the IEEE) with the goal of working out clear definitions of the nomenclature used in connection with the performance of commercial superconducting winding materials and to standardize methods for determining the relevant numerical test data.

SUPERCONDUCTING MAGNETS FOR THE  
200 GEV ACCELERATOR EXPERIMENTAL AREAS\*

R.B. Meuser  
Lawrence Radiation Laboratory  
Berkeley, California

INTRODUCTION

The experimental areas of the 200 GeV accelerator provide an opportunity to realize a really large payoff from the use of superconducting magnets. Costs might be reduced because of the virtual elimination of the electric power and the systems necessary for delivering and dissipating that power. Further savings, and perhaps better physics, may result from the shortening of beam lines made possible by the higher magnetic fields.

A major part of the cost of an experimental area is associated with the dc magnets used for transporting secondary particle beams, and it is these magnets which are under consideration in this paper. If it is decided to make them superconducting, that decision must be made before large sums of money are committed for furnishing the electrical and cooling systems and other features of the experimental areas associated with conventional magnets. For the first of the three experimental areas planned, the decision must be reached by the fall of 1969. An early decision will furnish an impetus to the development of magnets suitable for that application.

The multitude of problems associated with superconducting magnets can be divided into two groups. The "priority program" comprises those items necessary for reaching a decision at an early date on whether to adopt conventional or superconducting magnets. The "nonpriority program" comprises the remaining items aimed at deriving the maximum benefit from superconducting magnets by continued improvement of the technology.

The priority program must include not merely the magnets but also the entire system associated with large numbers of magnets, and the interaction between that system and the performance of physics experiments.

To be acceptable, the superconducting magnet system must be economical. But, the economics will probably be rather different from a system of conventional magnets. At present it seems that the total capital cost of the superconducting magnet system will be higher than a system of conventional magnets. If initial equipment money is limited, this may mean that the superconducting system must be acquired at a slower rate. But a strong argument could be made for enhanced equipment funds to be traded off against lowered operating costs.

To be acceptable, superconducting magnets must be predictable, reliable, and easy to operate. If each of the 20 to 40 magnets on a beam had the characteristics of a temperamental laboratory device the physicists would find it intolerable. The optical properties must be at least as good as conventional magnets, and this requires careful design, precise conductor placement, and freedom from hysteresis effects. Short focal lengths and large acceptance angles may cause additional problems.

---

\* Work performed under the auspices of the U.S. Atomic Energy Commission.



SUPERCONDUCTING MAGNETS FOR THE  
200 GEV ACCELERATOR EXPERIMENTAL AREAS\*

R.B. Meuser  
Lawrence Radiation Laboratory  
Berkeley, California

INTRODUCTION

The experimental areas of the 200 GeV accelerator provide an opportunity to realize a really large payoff from the use of superconducting magnets. Costs might be reduced because of the virtual elimination of the electric power and the systems necessary for delivering and dissipating that power. Further savings, and perhaps better physics, may result from the shortening of beam lines made possible by the higher magnetic fields.

A major part of the cost of an experimental area is associated with the dc magnets used for transporting secondary particle beams, and it is these magnets which are under consideration in this paper. If it is decided to make them superconducting, that decision must be made before large sums of money are committed for furnishing the electrical and cooling systems and other features of the experimental areas associated with conventional magnets. For the first of the three experimental areas planned, the decision must be reached by the fall of 1969. An early decision will furnish an impetus to the development of magnets suitable for that application.

The multitude of problems associated with superconducting magnets can be divided into two groups. The "priority program" comprises those items necessary for reaching a decision at an early date on whether to adopt conventional or superconducting magnets. The "nonpriority program" comprises the remaining items aimed at deriving the maximum benefit from superconducting magnets by continued improvement of the technology.

The priority program must include not merely the magnets but also the entire system associated with large numbers of magnets, and the interaction between that system and the performance of physics experiments.

To be acceptable, the superconducting magnet system must be economical. But, the economics will probably be rather different from a system of conventional magnets. At present it seems that the total capital cost of the superconducting magnet system will be higher than a system of conventional magnets. If initial equipment money is limited, this may mean that the superconducting system must be acquired at a slower rate. But a strong argument could be made for enhanced equipment funds to be traded off against lowered operating costs.

To be acceptable, superconducting magnets must be predictable, reliable, and easy to operate. If each of the 20 to 40 magnets on a beam had the characteristics of a temperamental laboratory device the physicists would find it intolerable. The optical properties must be at least as good as conventional magnets, and this requires careful design, precise conductor placement, and freedom from hysteresis effects. Short focal lengths and large acceptance angles may cause additional problems.

---

\* Work performed under the auspices of the U.S. Atomic Energy Commission.

Various conductor materials and forms and various winding configurations and methods should be investigated with emphasis on those which lend themselves to producing lots of, say, ten to twenty magnets. Cryostats must be designed to be compatible with magnetic shielding, to hold the windings and shields rigidly, and to minimize dead space at the ends. It is not clear that one has gained anything if to double the field available with conventional magnets one must use a cryostat having a length twice the effective length of the winding.

Cutting across all facets of the problem, and highest on the priority program, is the construction and operation of a beam line having as many beam transport elements as practicable. In addition to demonstrating feasibility of a system and providing both the opportunity and the necessity for solving some of the known problems it might provide answers to questions we do not yet know how to ask.

#### MAGNET REQUIREMENTS

As a part of a study of the refrigeration requirements a model of the experimental areas was developed, using as a basis the NAL Design Report, the various studies on experimental use, and discussions with various LRL and NAL personnel.<sup>1</sup> In order to determine the numbers of the various kinds of magnets required it was assumed that the bending and focusing power required for the various beams was supplied by modular superconducting magnets having the following characteristics:

Bending magnets:	35 to 40 kG in aperture
Quadrupoles:	30 to 35 kG at edge of aperture
Effective length:	1.75 m

These assumptions lead to a requirement for 254 magnets which may be grouped as follows:

Type:	
Quadrupoles	77%
Dipoles	23%
Radiation shielding:	
Probably required	53%
Probably not required	34%
Possibly required	13%
High fields useful for shortening beams:	
High fields useful	39%
High fields not useful	61%
(rf separated and	
neutrino beams)	
Sizes:	
Most quadrupoles have 4 in. diameter apertures	
A few 8 in. and 12 in.	
Most bending magnets require aperture widths of 8 in.	
Magnetic shielding:	
Required for most magnets	

---

1. M.A. Green, G.P. Coombs, and J.L. Perry, 500 Incorporated Report (1968).

Excluded from the list are a number of large spectrometer magnets, and the bubble chamber magnets. Also excluded are the hyperon beam magnets packed within the shielding near the targets.

For the latter the high fields attainable with superconducting magnets will probably result in shorter beam lines, and greater admittance solid angles. The shorter beam lines will result in greater particle fluxes and savings in shielding and real estate. The use of superconducting magnets for these applications has not been investigated in detail, and we are not yet in a position to list quantities, sizes, and kinds.

#### MAGNET DESIGN AND THE CURRENT DENSITY GAME

Most magnets will require magnetic shielding to minimize interaction between beam lines. The use of iron shielding enhances the field of a bending magnet by 5 to 10 kG and of a quadrupole by 2 to 5 kG. Iron shielding is the subject of a recent LRL study,<sup>2</sup> and Beth of Brookhaven has investigated the use of counterwindings to cancel the stray field.<sup>3</sup> Magnets with counterwindings can sometimes be made more compact than iron-shielded magnets, but the total amount of superconductor required is much greater. Nevertheless, they may find application where space is dear — close to targets, for example. Even a low-field iron-shielded superconducting magnet can be made more compact than the equivalent conventional magnet (unless one is willing to expend astronomical quantities of electric power on the latter).

Figures 1 and 2 illustrate the effect of current density, size, and field strength upon ampere-turn requirements for iron-shielded dipoles and quadrupoles, respectively. The ordinate is normalized to the current required for a thin winding having infinite current density. The necessity for high current densities for small high-field magnets, particularly quadrupoles, is apparent.

Current densities of more than  $15 \text{ kA/cm}^2$  at fields of more than 60 kG have been obtained with NbTi in solenoids of the size of the beam transport magnets under consideration. In fact, however, no beam transport elements using NbTi have been completed. It is probable that twice the current density can be obtained by using fine-filament conductors, but it remains to be proved. Current densities of 40 to  $60 \text{ kA/cm}^2$  at around 50 kG have been obtained in Nb<sub>3</sub>Sn quadrupoles, somewhat too small for use at the 200 GeV accelerator, by Sampson and Britton at Brookhaven, and by others (G.E., British Oxygen) using substantially the Brookhaven configuration. No bending magnets using Nb<sub>3</sub>Sn have been built of a size useful for the 200 GeV accelerator, but a small one at Brookhaven is well along.

If we adopt as a working hypothesis that Nb<sub>3</sub>Sn costs twice as much as NbTi per ampere foot and that current densities of 15 and  $40 \text{ kA/cm}^2$  are applicable to NbTi and Nb<sub>3</sub>Sn, respectively, we find, using Figs. 1 and 2, the following cross-over points.

- 
2. R.B. Meuser, Lawrence Radiation Laboratory Report UCRL-18318 (1968).
  3. R.A. Beth, Brookhaven National Laboratory, Accelerator Department Reports AADD-103 and AADD-110 (1966).

<u>Field strength</u>	<u>Inside radius of winding (in.)</u>	
	<u>Bending magnets</u>	<u>Quadrupole magnets</u>
40 kG	< 1	1.9
55 kG	< 1	2.5

On this basis, Nb<sub>3</sub>Sn wins the game for the smaller sizes and higher fields. However, many of the magnets for the 200 GeV accelerator application are larger than that for crossover at 55 kG, and for most of the magnets it is doubtful if there is any technical or economic reason to demand fields even as high as 55 kG. For many applications, however, the field strength, and therefore the current density, should be pushed as high as the state of the art will permit.

Clearly such numbers games as this are subject to many factors which cannot be accurately evaluated at present. We do not know how accurately present prices reflect actual production costs, or how the costs and production technology will be affected by time, quantity, or subsidization. Manufacturers are popping into and out of the field at frequent intervals, and prices sometimes vary by a factor of two between successive orders placed a few months apart. The cost of the conductor does not tell the whole story; it appears to this author that the costs of constructing a large number of Sampson-type Nb<sub>3</sub>Sn magnets would be substantially less than for any of the magnets using NbTi now under construction, but if any of several alternative ways of building NbTi magnets worked out satisfactorily the picture could be reversed. It appears, therefore, that both Nb<sub>3</sub>Sn and NbTi beam transport magnets should be pursued, and that in the end there will probably be some applications for which one is superior to the other.

#### THE LRL PROGRAM

##### Refrigeration

In the fall of 1966 the National Bureau of Standards undertook for us a study of the refrigeration problems.<sup>4</sup> The practicability and relative costs of a number of systems for supplying refrigeration were investigated.

In the fall of 1967, 500 Incorporated, a subsidiary of Arthur D. Little, Inc., was induced to undertake, at their own expense, a further study of the refrigeration system, and the results of that study have been recently published.<sup>1</sup> A summary was presented at this Summer Study by M.A. Green.<sup>5</sup>

It is convenient to treat the cryostat design and the refrigeration systems as separate problems, but in fact they interact quite strongly. For some systems the cost of the refrigeration system is insensitive to the heat load of the magnet cryostat, whereas other systems — for example, where many magnets are serviced from one

4. T.R. Strobridge, D.B. Mann, and D.B. Chelton, National Bureau of Standards, Boulder, Colorado, NBS Report 9259 (1966).

5. M.A. Green, these Proceedings, p. 293.

refrigerator or storage Dewar — are quite sensitive to the heat load of the cryostat. Although large transfer-line systems for liquid hydrogen are now commonplace, no such systems for helium have been built, and hence there has been little incentive to develop cheap and efficient ones. It would seem that a modest effort might result in such systems' becoming a reality, and this might change the complexion of the refrigeration system economics and the cryostat design.

#### Over-all Systems Studied

A preliminary study of the relative costs of conventional and superconducting magnets was presented at the Particle Accelerator Conference in March 1967.<sup>6</sup> The NBS study of the refrigeration problems, plus feedback from the industry, was used as the basis for estimating the cost of the refrigeration.

Over the next year we intend to continue developing a coherent picture of the superconducting magnet system. Operation of a superconducting beam line will be important to the development of that picture.

#### Magnets and Beam Lines

Early in 1967 we decided to attempt to build a beam transport magnet and install it on the beam line of an actual physics experiment as quickly as possible. There came to our attention the need for a solenoid capable of producing a  $\int B_z dz$  of 140 kG·ft for an experiment at the 184-inch Cyclotron. The axis was to be horizontal and a 4 in. diameter clear warm bore was required. The construction of such a magnet would give us experience in all the aspects of the problems of a beam transport element except that the winding configuration would be different. It was agreed that we should build it, and design started in mid-year. The magnet has since been completed and is installed and operating. Its characteristics are, briefly, as follows<sup>7</sup>:

Conductor: Nb48%Ti, round wire, 0.015 in. diam core, 0.030 in. diam copper sheath.	
Clear inside diam of warm bore	4.25 in.
Winding length	35.75 in.
Maximum field on axis	65.5 kG
Stored energy	200 kJ
Current density based on coil envelope	16.6 kA/cm <sup>2</sup>

We started early in 1968 on a bending magnet model using 0.080 in. square NbTi conductor that was on hand. The procedure adopted was to wind flat double pancakes, race-track shaped, and then bend them over a cylinder. No potting or adhesive is used. Nine such double layers assembled on each side of a cylinder comprise the winding. A nonsuperconducting mock-up has been built to work out the fabrication techniques, and the winding of the superconductor has started. The winding has a 5 in. inside diameter, an over-all length of 15 in. A solenoid using the same conductor has operated at a current density of 14 kA/cm<sup>2</sup>. With that current density the bending magnet model should produce a field of 30 kG without an iron return path. This is too small a magnet to be useful on a beam line, but it is intended to serve as a model for future magnets of a more useful size.

- 
6. R.B. Meuser, IEEE Trans. Nucl. Sci. NS-14, No. 3, 372 (1967).
  7. R.B. Meuser, W.H. Chamberlain, and R.E. Hintz, Lawrence Radiation Laboratory Report UCRL-18179 (1968). (To be published in Proc. 2nd Intern. Cryogenic Engineering Conference, Brighton, England, 1968.)

It is planned that a 6 in. aperture bending magnet be built by early 1969, to be followed by additional elements, and installed on a beam line at the Bevatron. A refrigerator for cooling these magnets has been purchased.

Fast and inexpensive winding techniques are made possible by the use of random-wound round wire. Complicated windings for motor and generator armatures and field coils and television deflection yokes, which are actually small bending magnets, can be wound in seconds. The space factor is poor - 50 to 70% - but by using small cores and a minimum of copper the over-all current density may still be acceptable. A small effort - one summer student - is being expended toward the utilization of this technique. Preliminary tests using inexpensive plaster and plastic winding forms have been promising, and somewhat better tooling is now being built.

Methods of winding round wire in a more orderly fashion are being contemplated by LASL and the British Oxygen Co. We have given some thought to the matter but have not yet devised a scheme that we feel will be satisfactory.

#### Pulsed Magnet Operation

To help gain an understanding of the effects produced during the turn-on of a superconducting magnet, some experimental work has been done with pulsed operation of solenoids. This was reported on at this Summer Study by Voelker<sup>8</sup> and Gilbert.<sup>9</sup>

---

8. F. Voelker, these Proceedings, p. 550.

9. W.S. Gilbert, these Proceedings, p. 1007.

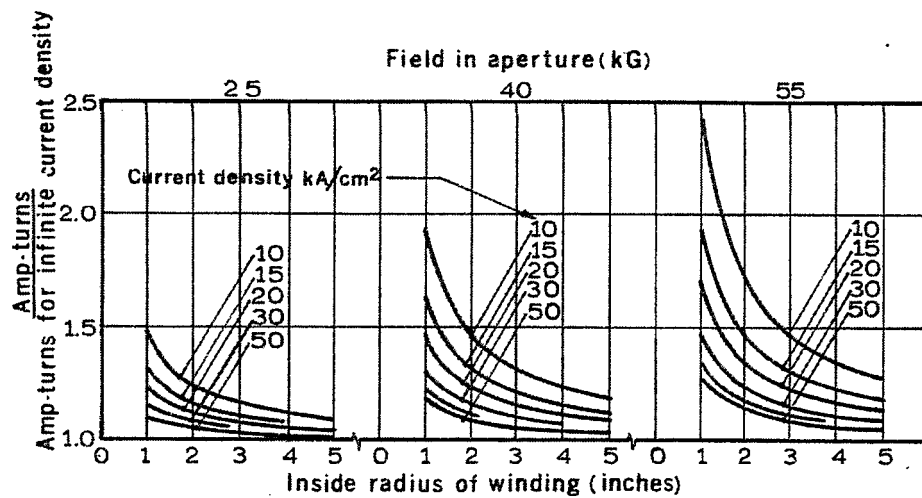


Fig. 1. Ampere turns required; bending magnets.

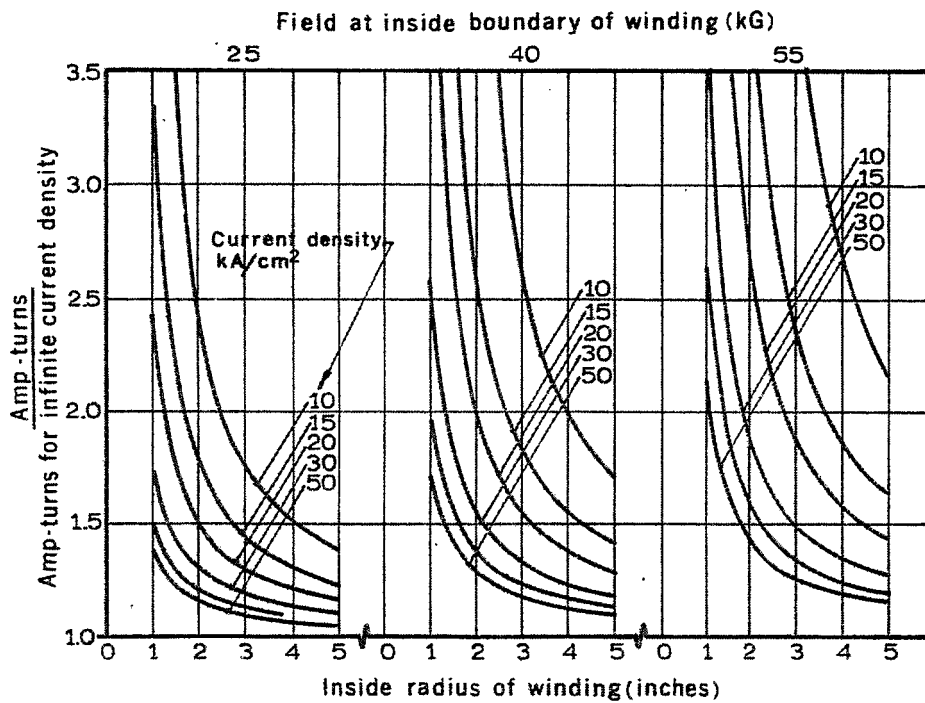


Fig. 2. Ampere turns required; quadrupole magnets.

# CONSTRUCTION OF A SUPERCONDUCTING TEST COIL COOLED BY HELIUM FORCED CIRCULATION\*

M. Morpurgo  
CERN  
Geneva, Switzerland

## I. GENERAL

Superconducting coils are normally operated immersed in a liquid-helium bath. Alternatively, it seems possible to wind the coils with a hollow conductor and to cool them with a forced circulation of helium.

We think that this method of cooling will show the following advantages:

- 1) Each point of the conductor will be correctly cooled, and thus a good coil stability will be guaranteed.
- 2) The absence of flow channels and of empty spaces between conductors will allow an improved mechanical design and construction of the coil. For the same reason, a better electrical coil insulation will be possible.
- 3) The cryostat construction will be simplified. In fact, the cryostat will reduce to a vacuum tank and, if necessary, a cold shield.
- 4) The amount of helium contained in the hollow conductor will, in general, be smaller than the corresponding amount of helium required to fill the cryostat of a conventional superconducting coil.

We think that these advantages will be particularly evident for coils of large dimensions. In the case of small coils, they might be counterbalanced by the difficulty of having (with forced cooling) at the same time a relatively small feeding current and a high over-all current density in the coil cross section. Large values of feeding current will cause power losses in the input leads which would normally be unacceptable for small coils.

For the purpose of studying experimentally the technical problems related to forced cooling of superconducting coils, we have constructed an apparatus to circulate the helium, and a test coil.

Details of this work are reported in the following sections.

## II. FORCED CIRCULATION SYSTEM

Liquid helium at normal pressure is a poor cooling medium in the case of forced circulation. The small helium latent heat of evaporation permits easy formation of vapor and liquid mixture.

---

\* Reprinted from NP Division Report CERN 68-17 (1968).



It has been demonstrated<sup>1</sup> that, on the contrary, supercritical helium at 4.2°K and at a pressure above the critical pressure of 2.26 atm is an excellent cooling medium. As a matter of fact, in these conditions, only one phase can exist, and hence the inconveniences originating from the mixture of liquid and vapor are eliminated.

We have constructed a system to circulate supercritical helium, very similar to the one described in Ref. 1. It should be noted that, while this system is excellent for testing purposes, it is somewhat doubtful whether it would also be convenient for cooling an operational coil. In this case, unless the coil is very small, it will probably be preferable to build the circulating system as an integral part of the helium liquefier.

The forced cooling system and the principle of operation are illustrated in Fig. 1. The vessel (6) is filled with liquid helium. Helium gas is introduced through the line (7) and the valve (8) to the closed loop (1), (2), (3), and (4). The helium is circulated in the closed loop by the pump (3). The helium is brought to a temperature of 4.2°K in the first heat exchanger (1), and subsequently cools down the coil (4). The second heat exchanger (2) of the circuit is used to recuperate, partly, the enthalpy of the helium vapors which are exhausted through (5). The helium in the closed loop is maintained at high pressure, while the pump (3) has only to produce the small pressure drop required for circulation. At the beginning of the operation, before equilibrium conditions are reached, helium must be introduced continuously into the closed loop through (7) and (8). When equilibrium is reached, the valve (8) can be closed.

Figures 2 and 3 give construction details and a general view of the forced cooling system.

The pump (3), which is illustrated in Fig. 4, is a double action piston pump. The piston has a plastic gasket. The valves have no gaskets, but good tightness is ensured by the fine machining of the surfaces. The pump is motor-driven through a long thin rod and crank mechanism, and can be operated at a speed varying between 5 and 200 turns per minute. The maximum speed corresponds to a nominal helium flow of approximately 420 liters/hour.

### III. HOLLOW CONDUCTOR AND TEST COIL

The compound conductor used to wind the test coil is an aluminum pipe in the wall of which six, 0.25 mm, superconducting wires are embedded. The conductor cross section is shown in Fig. 5. The reason for this geometry of the conductor cross section is that, with all the superconducting wires being on one neutral axis, the conductor can be easily bent to a small radius in one plane. In fact, a bending radius of less than 1 cm is possible without damaging the wires, which are of Supercon heat-treated copper-plated NbZr alloy. The aluminum pipe is of high purity (better than 0.9999) metal.

The aluminum resistivity, measured on a heavily cold worked sample at 4.2°K in a transverse magnetic field of 40 kG, is approximately  $1.4 \times 10^{-8} \Omega \cdot \text{cm}$ .

The conductor has been produced, by an extrusion process, by the firm "Atelier électromécanique de Gascogne - R. Creuzet," Marmande, France. The test coil wound with this conductor is shown in Figs. 6 and 7. It consists of 16 double pancakes (each having 36 turns) electrically connected in series. Approximately 300 m of conductor were used to wind the coil. For cooling, the 16 pancakes are fed in parallel

---

1. H.H. Kolm, in Proc. Intern. Symposium Magnet Technology, Stanford 1965, p. 611.

by a common manifold to which they are connected through special insulating joints. The coil has been operated at a pressure between 3 and 4 atm and at a pumping speed of  $\approx 80$  turns/min. The pressure drop in the coil was approximately 0.1-0.15 atm. The coil temperature was measured by means of carbon resistors immersed in the helium flow at the coil input and output. The temperature was  $\approx 4.7^\circ\text{K}$ . In these conditions the current in the coil could be raised up to  $\approx 900$  A corresponding to a field in the center of  $\approx 28$  kG without detecting any dc voltage at the coil terminals. During the current rise time ( $\approx 2$  min from 0 to 900 A) the usual flux jumps could be observed. The maximum value of current was in very good agreement with the value which could be predicted by knowing the short sample characteristic curve of the superconducting wire.

When the current was raised slightly above 900 A, a dc voltage could be detected at the coil terminals. If the current was kept constant, this voltage and the average coil temperature slowly and steadily increased with time. The coil temperature rise was shown by a pressure variation in the circulating helium.

To re-establish the equilibrium conditions it was sufficient to reduce the current to  $\approx 600$  A. The coil current could also be cut rapidly without any inconvenience. In this case the largest fraction of the magnetic energy stored in the coil (approximately 10 000 J at 28 kG) was discharged into an external resistor of  $0.2\ \Omega$  connected in parallel with the coil. After a fast current cut-off the helium pressure in the coil increased by 1 to 2 atm.

The coil was fed by an external power supply through current leads which were cooled by helium vapor. Figure 8 shows the cross section of a lead.

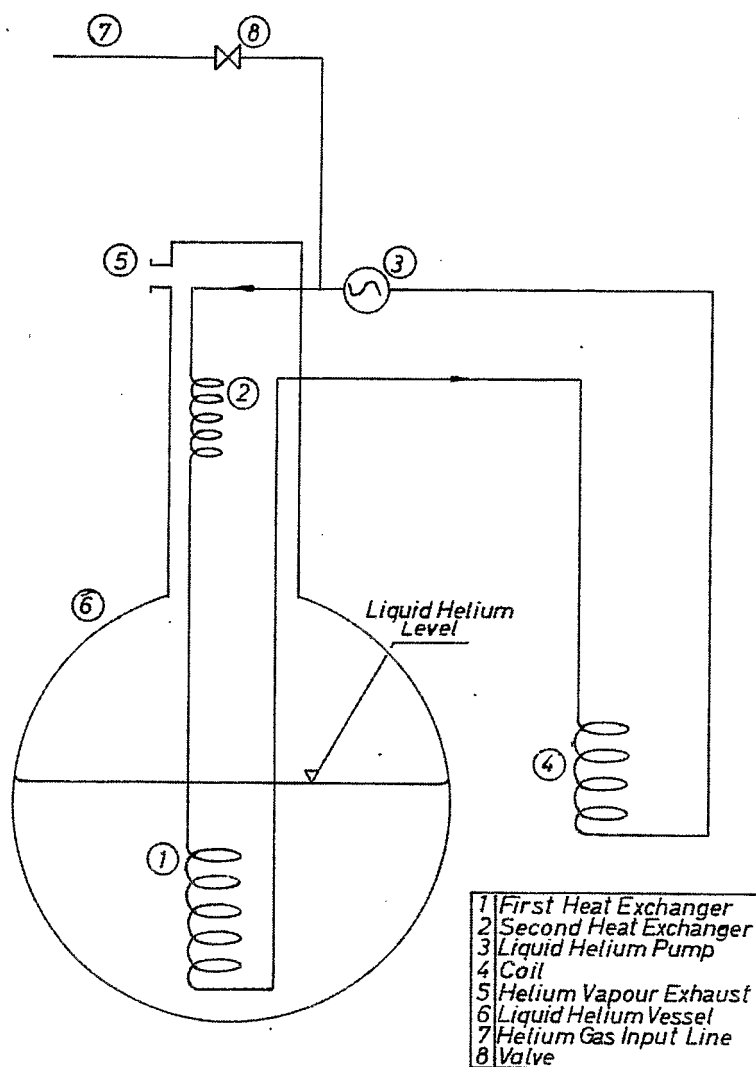
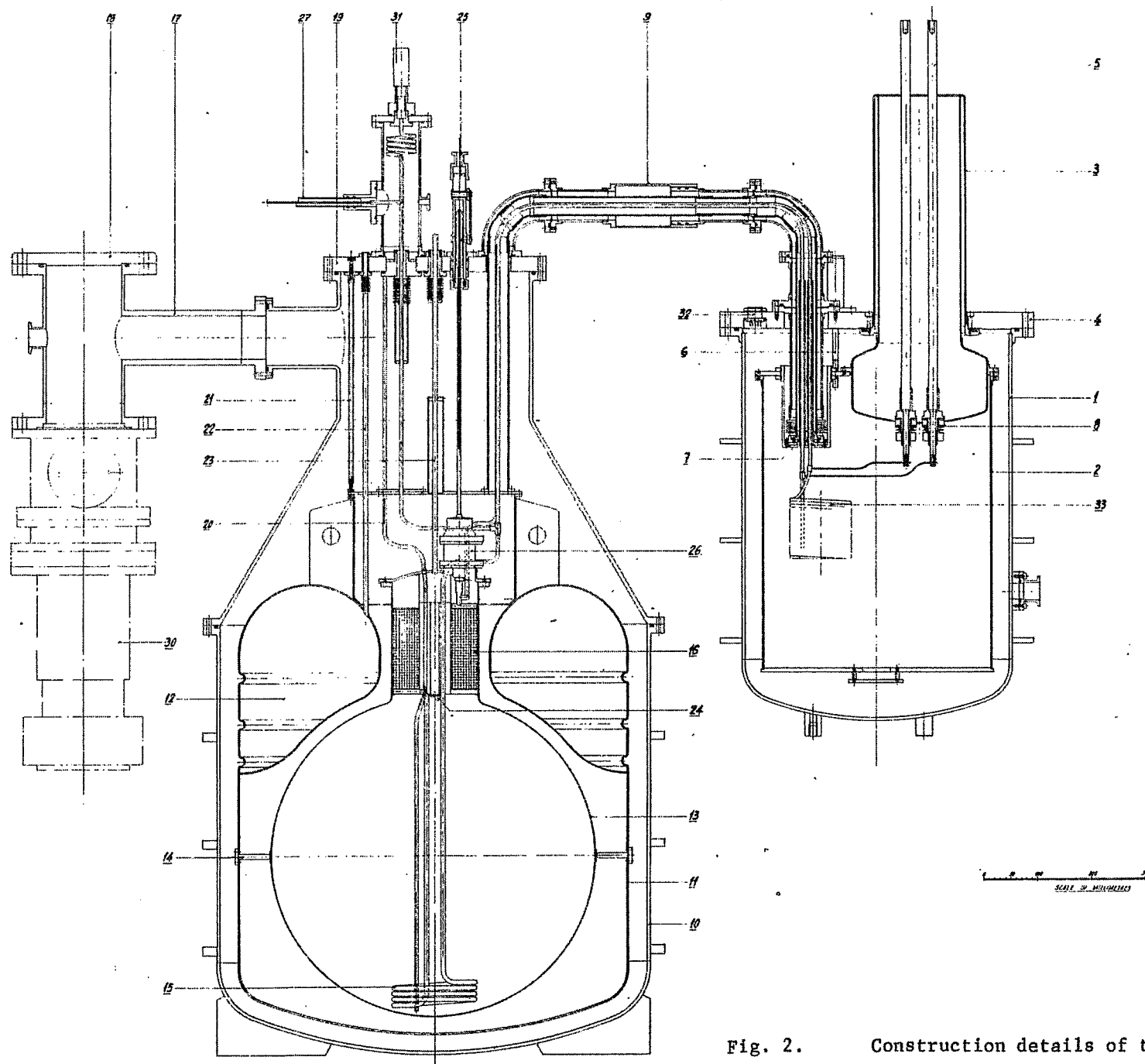


Fig. 1. Schematic diagram of the forced cooling system.



NO.	DESCRIPTION	MATERIAL	QUANTITY
1	TEST CHAMBER, SUPERCONDUCTING HEATING ELEMENTS AND VACUUM INSULATION	STAINLESS STEEL	1
2	SAFETY VALVE 1/2" DIA.	BRASS	1
3	SAFETY VALVE 1/2" DIA.	BRASS	1
4	SAFETY VALVE 1/2" DIA.	BRASS	1
5	SAFETY VALVE 1/2" DIA.	BRASS	1
6	SAFETY VALVE 1/2" DIA.	BRASS	1
7	SAFETY VALVE 1/2" DIA.	BRASS	1
8	SAFETY VALVE 1/2" DIA.	BRASS	1
9	SAFETY VALVE 1/2" DIA.	BRASS	1
10	SAFETY VALVE 1/2" DIA.	BRASS	1
11	SAFETY VALVE 1/2" DIA.	BRASS	1
12	SAFETY VALVE 1/2" DIA.	BRASS	1
13	SAFETY VALVE 1/2" DIA.	BRASS	1
14	SAFETY VALVE 1/2" DIA.	BRASS	1
15	SAFETY VALVE 1/2" DIA.	BRASS	1
16	SAFETY VALVE 1/2" DIA.	BRASS	1
17	SAFETY VALVE 1/2" DIA.	BRASS	1
18	SAFETY VALVE 1/2" DIA.	BRASS	1
19	SAFETY VALVE 1/2" DIA.	BRASS	1
20	SAFETY VALVE 1/2" DIA.	BRASS	1
21	SAFETY VALVE 1/2" DIA.	BRASS	1
22	SAFETY VALVE 1/2" DIA.	BRASS	1
23	SAFETY VALVE 1/2" DIA.	BRASS	1
24	SAFETY VALVE 1/2" DIA.	BRASS	1
25	SAFETY VALVE 1/2" DIA.	BRASS	1
26	SAFETY VALVE 1/2" DIA.	BRASS	1
27	SAFETY VALVE 1/2" DIA.	BRASS	1
28	SAFETY VALVE 1/2" DIA.	BRASS	1
29	SAFETY VALVE 1/2" DIA.	BRASS	1
30	SAFETY VALVE 1/2" DIA.	BRASS	1
31	SAFETY VALVE 1/2" DIA.	BRASS	1
32	SAFETY VALVE 1/2" DIA.	BRASS	1
33	SAFETY VALVE 1/2" DIA.	BRASS	1

Fig. 2. Construction details of the apparatus.

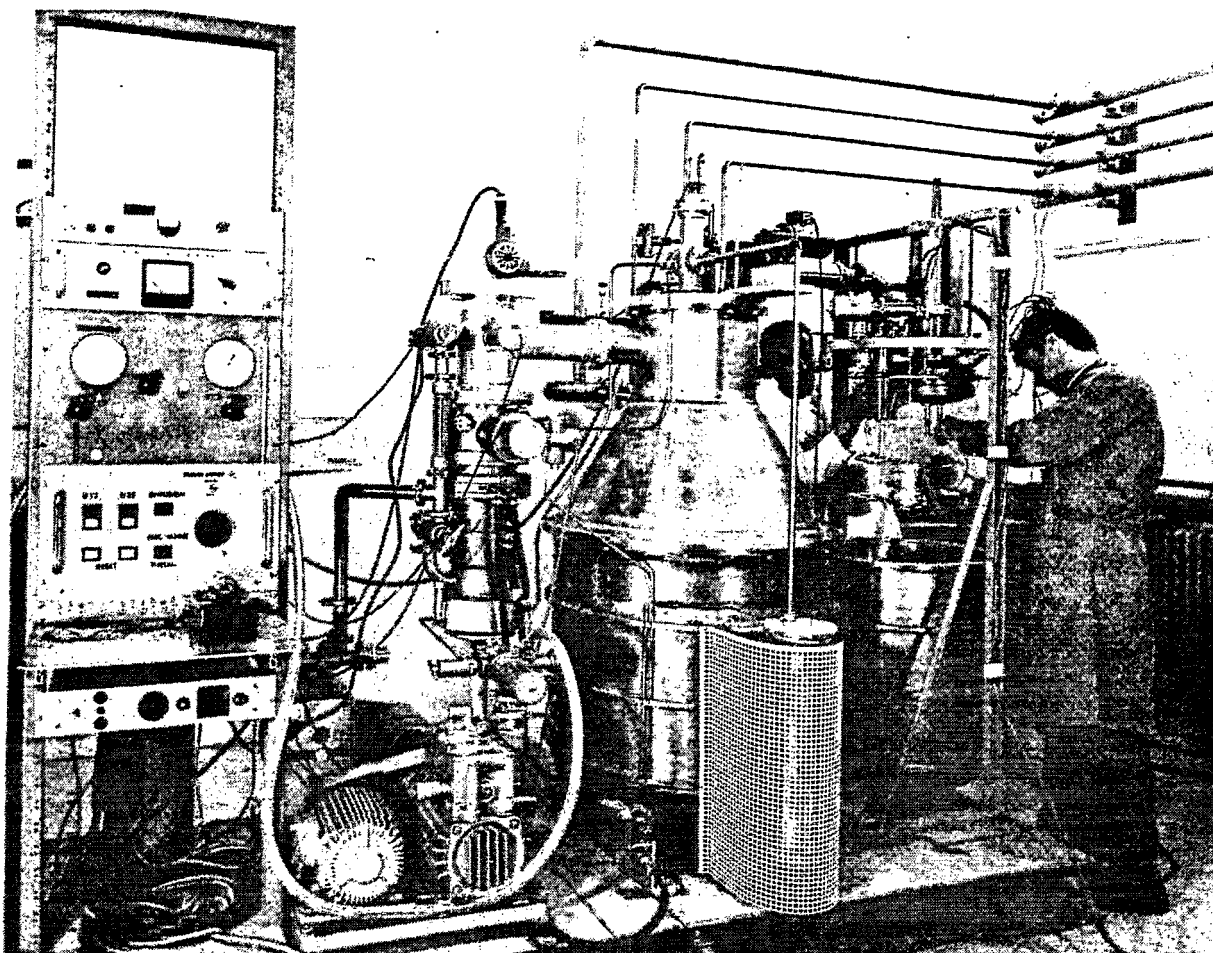
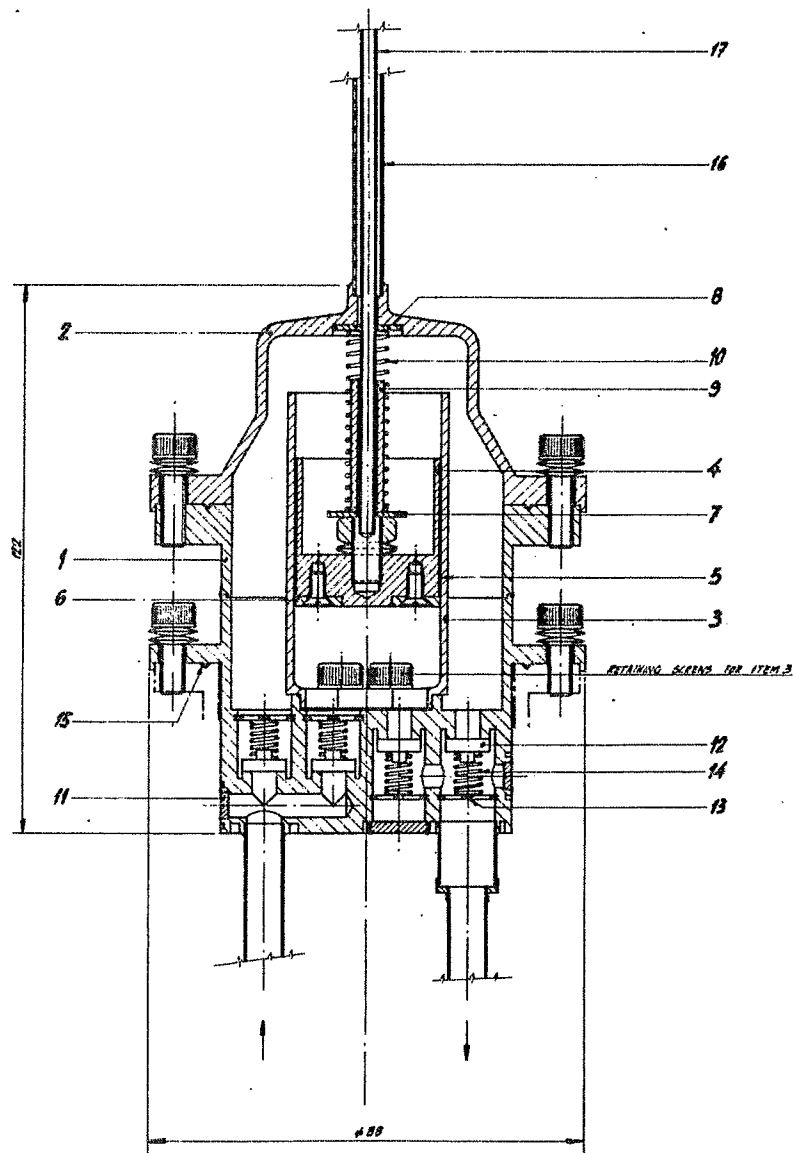
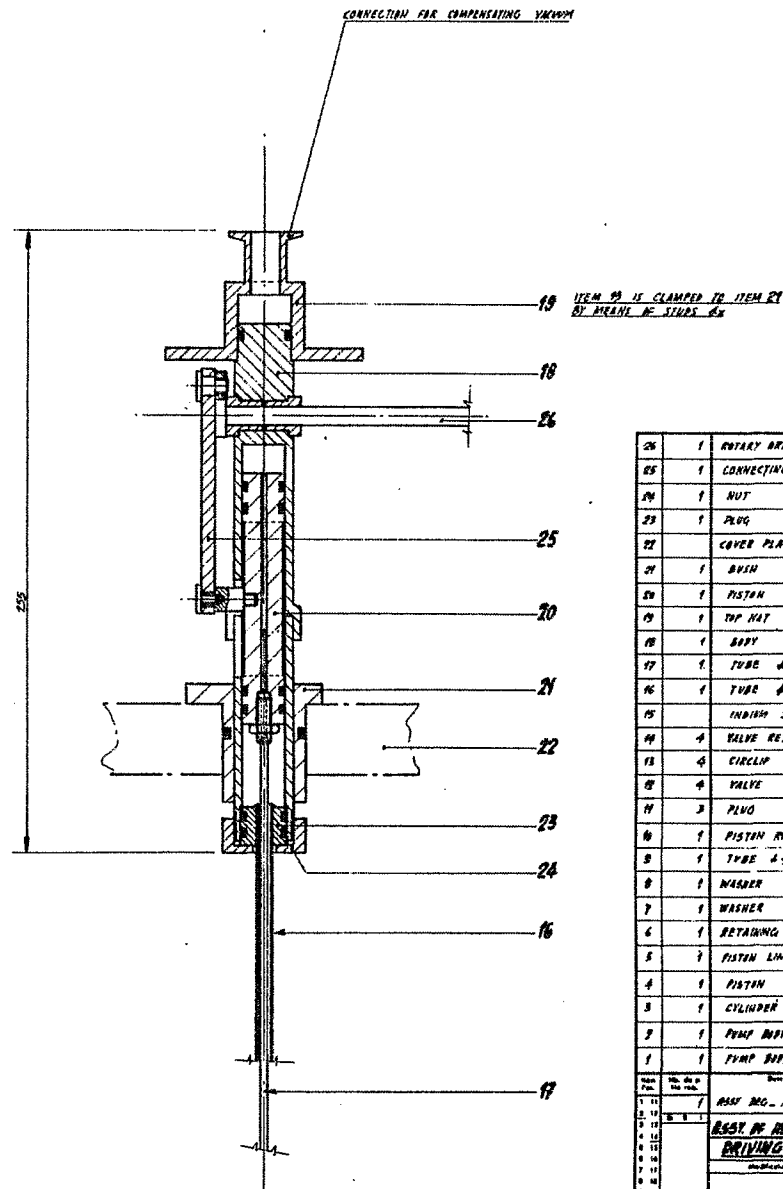


Fig. 3. General view of the system.



FIGS 1-17 ROSE OF HELIUM PUMP  
SCALE 2:1



FIGS 16-26  
ROSE OF PUMP OPERATING MECHANISM  
SCALE 1:1

26	1	ROTARY DRIVE FROM MATIN	ST. STEEL		
25	1	CONNECTING ROD	ST. STEEL		
24	1	NUT	ST. STEEL		
23	1	PLUG	ST. STEEL		
22	1	COVER PLATE	ALUMINUM		
21	1	ROD	ST. STEEL		
20	1	PISTON	BRASS		
19	1	TOP NUT	ST. STEEL		
18	1	BODY	ST. STEEL		
17	1	TUBE 4.5 x 6	ST. STEEL		
16	1	TUBE 4.5 x 3	ST. STEEL		
15	1	INDIAN SEAL			
14	4	VALVE RETURN SPRING	PHOS. BRASS		
13	4	CIRCLIP	ST. STEEL		
12	4	VALVE	ST. STEEL		
11	3	PLUG	ST. STEEL		
10	1	PISTON RETURN SPRING	STEEL		
9	1	TUBE 4.5 x 7	BRASS		
8	1	WASHER	BRASS		
7	1	WASHER	BRASS		
6	1	RETAINING PLATE	ST. STEEL		
5	2	PISTON LINER 4.5 THICK	BRASS		
4	1	PISTON	ST. STEEL		
3	1	CYLINDER	ST. STEEL		
2	1	PUMP BODY - UPPER	ST. STEEL		
1	1	PUMP BODY - LOWER	ST. STEEL		
1	1	ROSE OF PUMP OPERATING MECHANISM			
2	1	ROSE OF HELIUM PUMP			
3	1	ROSE OF HELIUM PUMP			
4	1	ROSE OF HELIUM PUMP			
5	1	ROSE OF HELIUM PUMP			
6	1	ROSE OF HELIUM PUMP			
7	1	ROSE OF HELIUM PUMP			
8	1	ROSE OF HELIUM PUMP			
9	1	ROSE OF HELIUM PUMP			
10	1	ROSE OF HELIUM PUMP			
11	1	ROSE OF HELIUM PUMP			
12	1	ROSE OF HELIUM PUMP			
13	1	ROSE OF HELIUM PUMP			
14	1	ROSE OF HELIUM PUMP			
15	1	ROSE OF HELIUM PUMP			
16	1	ROSE OF HELIUM PUMP			
17	1	ROSE OF HELIUM PUMP			
18	1	ROSE OF HELIUM PUMP			
19	1	ROSE OF HELIUM PUMP			
20	1	ROSE OF HELIUM PUMP			
21	1	ROSE OF HELIUM PUMP			
22	1	ROSE OF HELIUM PUMP			
23	1	ROSE OF HELIUM PUMP			
24	1	ROSE OF HELIUM PUMP			
25	1	ROSE OF HELIUM PUMP			
26	1	ROSE OF HELIUM PUMP			
27	1	ROSE OF HELIUM PUMP			
28	1	ROSE OF HELIUM PUMP			
29	1	ROSE OF HELIUM PUMP			
30	1	ROSE OF HELIUM PUMP			
31	1	ROSE OF HELIUM PUMP			
32	1	ROSE OF HELIUM PUMP			
33	1	ROSE OF HELIUM PUMP			
34	1	ROSE OF HELIUM PUMP			
35	1	ROSE OF HELIUM PUMP			
36	1	ROSE OF HELIUM PUMP			
37	1	ROSE OF HELIUM PUMP			
38	1	ROSE OF HELIUM PUMP			
39	1	ROSE OF HELIUM PUMP			
40	1	ROSE OF HELIUM PUMP			
41	1	ROSE OF HELIUM PUMP			
42	1	ROSE OF HELIUM PUMP			
43	1	ROSE OF HELIUM PUMP			
44	1	ROSE OF HELIUM PUMP			
45	1	ROSE OF HELIUM PUMP			
46	1	ROSE OF HELIUM PUMP			
47	1	ROSE OF HELIUM PUMP			
48	1	ROSE OF HELIUM PUMP			
49	1	ROSE OF HELIUM PUMP			
50	1	ROSE OF HELIUM PUMP			
51	1	ROSE OF HELIUM PUMP			
52	1	ROSE OF HELIUM PUMP			
53	1	ROSE OF HELIUM PUMP			
54	1	ROSE OF HELIUM PUMP			
55	1	ROSE OF HELIUM PUMP			
56	1	ROSE OF HELIUM PUMP			
57	1	ROSE OF HELIUM PUMP			
58	1	ROSE OF HELIUM PUMP			
59	1	ROSE OF HELIUM PUMP			
60	1	ROSE OF HELIUM PUMP			
61	1	ROSE OF HELIUM PUMP			
62	1	ROSE OF HELIUM PUMP			
63	1	ROSE OF HELIUM PUMP			
64	1	ROSE OF HELIUM PUMP			
65	1	ROSE OF HELIUM PUMP			
66	1	ROSE OF HELIUM PUMP			
67	1	ROSE OF HELIUM PUMP			
68	1	ROSE OF HELIUM PUMP			
69	1	ROSE OF HELIUM PUMP			
70	1	ROSE OF HELIUM PUMP			
71	1	ROSE OF HELIUM PUMP			
72	1	ROSE OF HELIUM PUMP			
73	1	ROSE OF HELIUM PUMP			
74	1	ROSE OF HELIUM PUMP			
75	1	ROSE OF HELIUM PUMP			
76	1	ROSE OF HELIUM PUMP			
77	1	ROSE OF HELIUM PUMP			
78	1	ROSE OF HELIUM PUMP			
79	1	ROSE OF HELIUM PUMP			
80	1	ROSE OF HELIUM PUMP			
81	1	ROSE OF HELIUM PUMP			
82	1	ROSE OF HELIUM PUMP			
83	1	ROSE OF HELIUM PUMP			
84	1	ROSE OF HELIUM PUMP			
85	1	ROSE OF HELIUM PUMP			
86	1	ROSE OF HELIUM PUMP			
87	1	ROSE OF HELIUM PUMP			
88	1	ROSE OF HELIUM PUMP			
89	1	ROSE OF HELIUM PUMP			
90	1	ROSE OF HELIUM PUMP			
91	1	ROSE OF HELIUM PUMP			
92	1	ROSE OF HELIUM PUMP			
93	1	ROSE OF HELIUM PUMP			
94	1	ROSE OF HELIUM PUMP			
95	1	ROSE OF HELIUM PUMP			
96	1	ROSE OF HELIUM PUMP			
97	1	ROSE OF HELIUM PUMP			
98	1	ROSE OF HELIUM PUMP			
99	1	ROSE OF HELIUM PUMP			
100	1	ROSE OF HELIUM PUMP			

Fig. 4. Cross section of the helium pump.

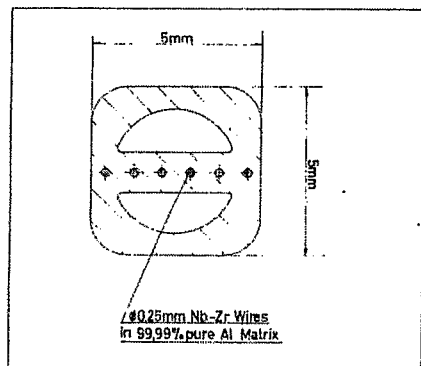


Fig. 5. Cross section of the hollow conductor.

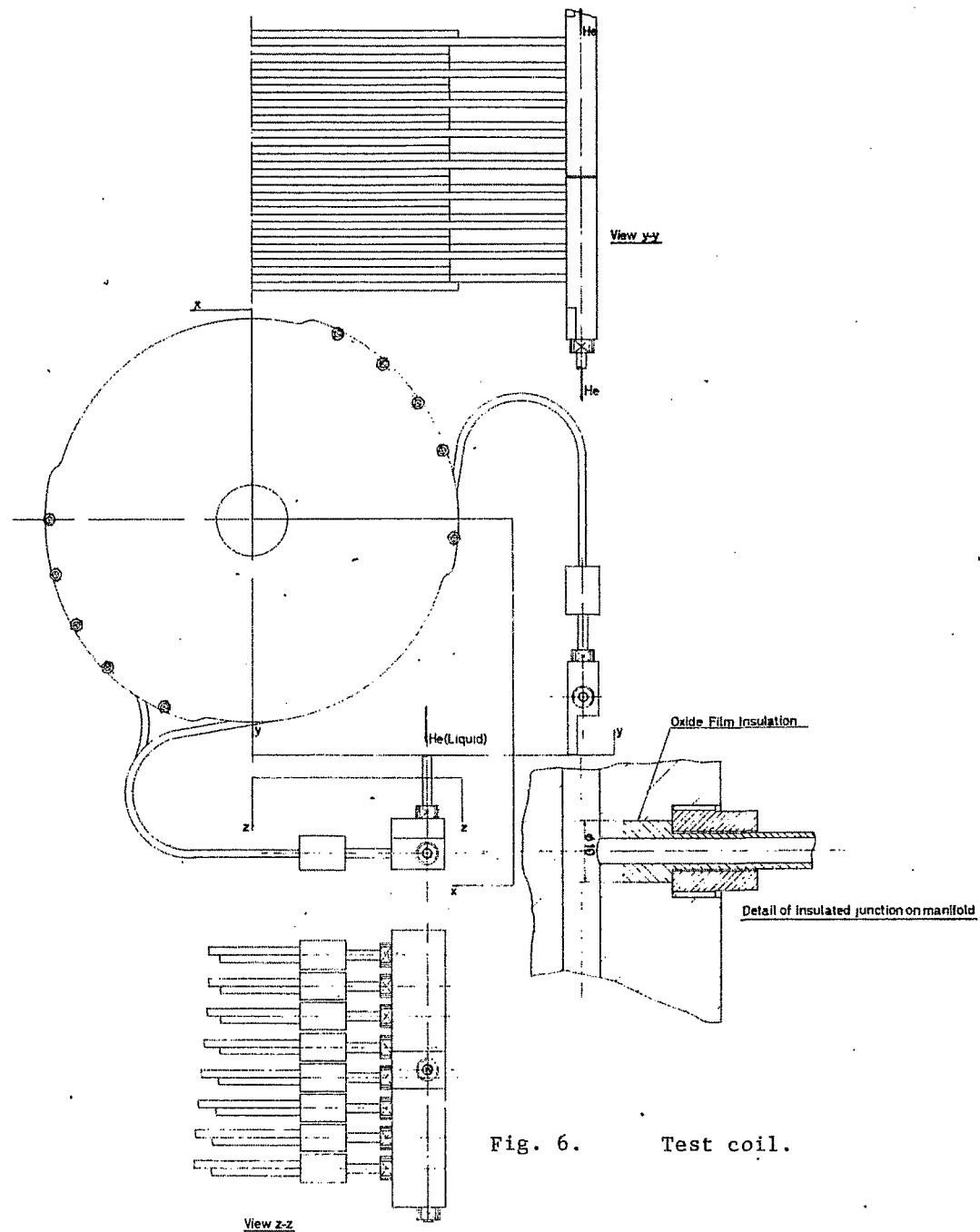
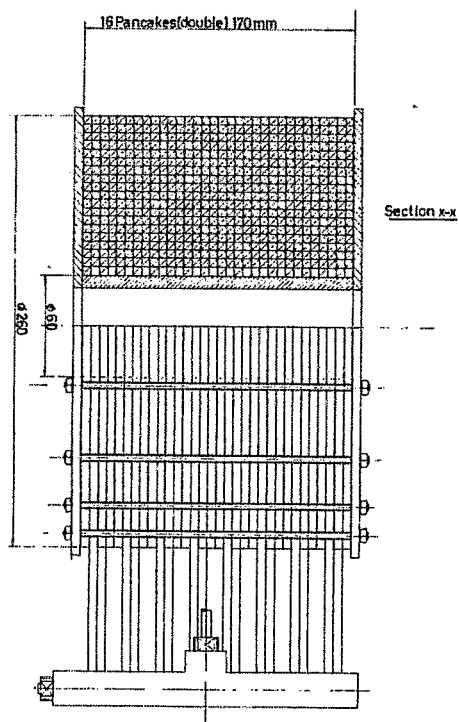


Fig. 6. Test coil.

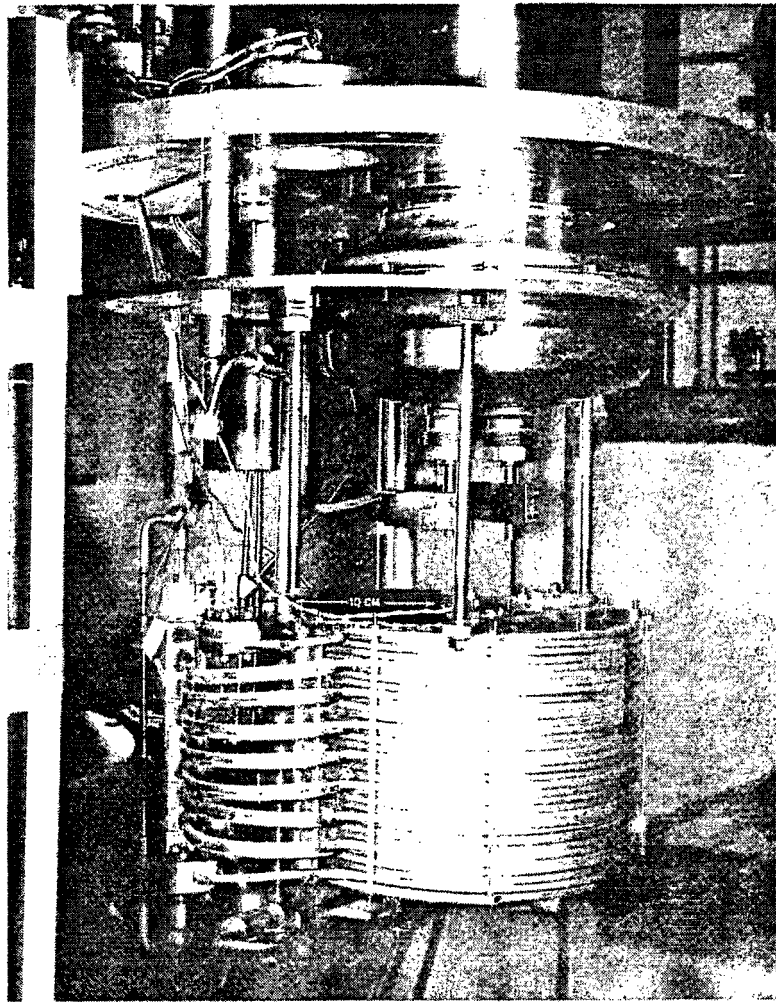


Fig. 7. Test coil with helium manifold and current leads.

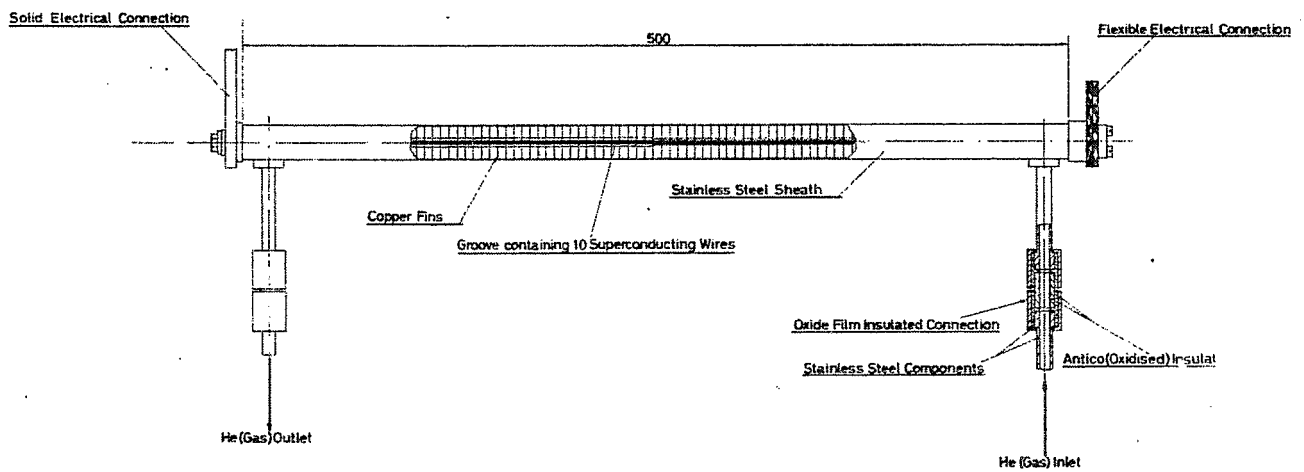


Fig. 8. Detail of electrical connection cooled by helium boil-off gas.



## SUMMARY OF FIFTH WEEK OF 1968 SUMMER STUDY

W.B. Sampson  
Brookhaven National Laboratory  
Upton, New York

The fifth week of the 1968 Summer Study was devoted to superconducting magnets. The program for the first day was composed of papers concerned with general aspects of magnet design such as force calculations and questions of stability. Bubble chamber magnets were the subject for the second day and reports were presented on all the large magnet systems being constructed or designed for this purpose. The third day was devoted to beam handling magnets with progress reports from the major laboratories designing or building such devices. Thermonuclear applications for superconducting magnets occupied a large part of the discussion on the fourth day along with the most interesting ideas of P.F. Smith on the ac losses and stability of twisted multicore conductors. The fifth day included discussions of the use of superconducting magnets at the 200 GeV accelerator as well as a description of the CERN supercritical helium cooled magnet.

### STRESSES

The first paper of the session was by P.G. Marston of Magnetic Engineering Associates and was concerned with the stresses produced in superconducting magnets by thermal, mechanical and magnetic forces. Marston did not cite specific magnets as examples but confined himself to general aspects of magnet design, pointing out sources of stress which are often overlooked such as the interaction between the magnet and induced current in nearby conducting materials during rapid field changes. He emphasized that caution must be used in employing general solutions to specific problems since such solutions can often give misleading results. The use of iron was discussed since it can result in a considerable reduction in the stress and lead to a useful reduction in ampere-turns even at relatively high fields.

The second paper by W.F. Westendorp of the General Electric Company was also about stress calculation. He described a method of calculating the axial and tangential stresses in cylindrical coils with and without reinforcing bands. The results were applied to coils wound from ribbon conductors. Computer calculations were used to prepare monographs which allow the easy determination of the maximum stress and field in simple solenoids if the bore and current density are specified.

### HYBRID MAGNETS

The term "hybrid magnet" has been coined to describe magnets only part of which are superconducting. The design aspects of such magnets were outlined by D.B. Montgomery of the National Magnet Laboratory at MIT. Such a magnet can be an economical approach to high fields for laboratories which have on hand large dc generators or helium refrigerators. For fields above about 175 kG hybrid systems must be used since there are no superconductors currently available which will sustain useful current density above this field. Montgomery emphasized this by pointing out that a 120 kG superconducting magnet costs twice as much as a 100 kG magnet and the cost rises even more steeply at higher fields. The choice between water-cooled and cryogenic inner coils depends on what is available at a particular laboratory, and since the Magnet Laboratory is well supplied with dc power Montgomery confined himself to the use of water-cooled inner solenoids. He calculates that if a background field of 100 kG is available

from the superconducting section it should be possible to reach 200 kG in a 1.5 in. bore with 2 MW of power while 300 kG would require 10 MW. In conclusion he described a hybrid magnet now being built at MIT where the outer section of an existing 225 kG water-cooled magnet will be replaced by a 60 kG superconducting coil reducing the total power required from 10 to 5 MW.

### STABILITY

A review of the steady-state stability of composite superconductors was presented by Z.J.J. Stekly of Avco Everett Laboratories. He derived a set of normalized equations which take into account the cooling of the substrate, the thermal contact resistance between the substrate and superconductor, and the temperature rise in the superconductor itself. These parameters were shown to influence the shape of the voltage current curve at the onset of resistance. Stekly pointed out that for a superconductor strand size smaller than a certain value, the temperature rise in the superconductor is very small and its temperature is essentially the same as that of the substrate. Since it is necessary to have a temperature rise in the superconductor to cause instabilities or "flux jumps," material made from such fine strands should be inherently stable. The question of the inherent stability of finely divided superconductors was the subject of considerable discussion later in the week.

### BUBBLE CHAMBER MAGNETS

The second day of the magnet week was devoted to bubble chamber magnets and the first magnet to be described was the one for the 12 ft diameter ANL chamber which was described by J.R. Purcell. This magnet uses a massive iron yoke and has an inner bore of almost 16 ft. Purcell related some of the problems that occurred during construction and pointed out how all very large magnets tend to become somewhat dated even before they are completed due to rapid progress in superconducting technology. The magnet is designed to use fully stabilized conductor and operate at low current density ( $1000 \text{ A/cm}^2$ ) with modest heat flux requirements ( $0.1 \text{ W/cm}^2$ ) which require only edge cooling of the strip conductor. Some of the details of this and the other bubble chamber magnets are summarized in Table I. The magnet is scheduled for initial cool-down in October 1968.

TABLE I  
Bubble Chamber Magnets

Bubble Chamber	Bore (ft)	Central Field (kG)	Conductor	Iron	Stored Energy (MJ)	Status
ANL 12 ft	15.7	18	Nb48%Ti, 6 conductors in copper 2 in. x 0.10 in.	Yes	80	First test scheduled for Oct. 1968
BNL 7 ft	8	30	Nb48%Ti, 6 conductors in copper 2 in. x 0.08 in.	No	72	Tested in gas, Spring 1968
RHEL	5	70	NbTi in copper 5 cm x 5 cm	Shielding only	340	Design stage
CERN	15.5	35	NbTi in copper or aluminum	Shielding only	750	Design stage

The Brookhaven 7 ft diameter magnet was described by A.G. Prodell. This magnet uses a conductor similar to the Argonne coil but operates at higher current density and has partial face cooling of the conductor due to a novel spacer strip which is wound into the coils. A movie was shown of the coils being wound and assembled. The magnet is designed to produce approximately 30 kG in the chamber volume and does not use iron. A partial test of the magnet was made in the Spring of 1968 but due to refrigeration problems the Dewar could not be filled with liquid helium. It was possible, however, to power the magnet to half field in cold gas. Further tests are scheduled when the complete chamber has been assembled.

A design study for a high field chamber magnet was presented by D.B. Thomas of the Rutherford High Energy Laboratory. The design field of 70 kG poses considerably more difficult stress problems than the lower field magnets. Stainless-steel strip wound in parallel with the conductor is expected to give the required strength while "buttons" welded to the strip would provide face cooling of the conductor in a manner similar to the Brookhaven magnet. An iron shield is planned to reduce the stray field and it is incorporated in the support structure. Thomas also described a facility for testing conductor samples and a method of making joints in the conductor using shaped explosive charges. A small coil is being constructed using the conductor intended for the chamber magnet and this coil which produces 50 kG itself is expected to produce 80 kG when used as an insert in the CERN magnet "Braracourcix."

The CERN design study for a very large bore 35 kG chamber magnet was described by F. Wittgenstein. This magnet also used an iron flux shield. A scale model (1:20) of the magnet called "Braracourcix" has been built to study the fringe field. It consists of two coils of 40 cm bore set up to form a split pair. The upper coil is aluminum-stabilized while the lower half has the more conventional copper stabilizing material.

The final paper of the day was given by P.F. Smith of the Rutherford Laboratory and was concerned with possible instabilities in the wide composite conductors being used in the large bubble chamber magnets. Smith pointed out that while a conductor may be designed to carry the full transport current at field without undue temperature rise this may not be true during a flux jump since the magnetization current density is much higher than the transport current density. This effect is most pronounced for wide conductors and for conductors stabilized with low enthalpy materials such as aluminum. While he did not think that any of the coils previously described would be seriously affected, Smith cautioned that the stakes were very high and some experiments were in order.

#### BEAM HANDLING MAGNETS

The session on beam handling magnets began with an analytical paper by R.A. Beth of Brookhaven. Using a very elegant method of representing magnetic fields by complex quantities he derived ideal solutions for the current density distribution required around the periphery of an elliptical aperture to produce a magnetic field with the desired multipolarity in that aperture. Step function approximations to the ideal distributions were analyzed and coefficients calculated for distributions of up to four separate current density steps. Beth suggested that mechanical inaccuracies and the necessity of placing integral numbers of turns in each step would tend to outweigh the imperfections of the approximation even for three or four steps.

G. Parzen of Brookhaven presented calculations on superconducting dipoles formed from arrays of flat coils with currents chosen to produce a 50 kG central field. He indicated that good field regions could be made with two-plane rectangular arrays and even with single plane coils, although the latter case would lead to a field at the conductor which was 60% higher than the central field.

The first actual beam handling magnet to be described was the CERN quadrupole. The analytical design of this device was presented by A. Asner of CERN while the test procedures and results were given by D.N. Cornish of the Culham Laboratory. The magnet has an effective length of 70 cm and an inner radius of 65 cm of which 5 cm will be at room temperature. The conductor used is rectangular in cross section and has been designed to run at the minimum propagating current at an over-all current density of 15 000 A/cm<sup>2</sup>. A small test coil made from this conductor and designed to produce the same field/ampere as the quadrupole has been operated successfully.

A superconducting bending magnet was described by J.D. Lawson of the Rutherford Laboratory. In cross section the windings of this magnet are in the form of two intersecting ellipses which form a circular aperture of 22 cm diameter. The effective length of the magnet is 140 cm and it is constructed from 0.15 in. round multicore conductor. The use of detachable current leads is planned and a flux pump will be used to maintain the field at a constant value.

R.B. Britton outlined the Brookhaven program on beam handling magnets. To date two quadrupoles have been built and a dipole is under construction. The design of these magnets uses the stepped current density approach outlined earlier by Beth. The magnets are made from  $\frac{1}{2}$  in. wide Nb<sub>3</sub>Sn tape wound with stainless-steel ribbon. The stainless tape serves as an insulation and also to effect the changes in current density. These coils are designed to operate at a very high current density (50 000 A/cm<sup>2</sup>) and are consequently very compact.

A quadrupole doublet of 20 cm i.d. and 30 cm effective length was described by J.D. Rogers of LASL. The quadrupole field is produced by changing the radial thickness of winding in one quadrupole while the other uses aluminum spacers to vary the effective current density.

#### PULSED MAGNETS

The author described some recent experiments on pulsed superconducting magnets made from Nb<sub>3</sub>Sn ribbons. The results indicate that reliable magnets capable of being pulsed to 50 kG in one second can be constructed and made to operate at very high current densities. The losses incurred during pulsed operation are too large to permit the use of such magnets in synchrotrons at least with presently available conductors but it is expected that more suitable materials will be available in the near future.

#### INTRINSICALLY STABLE CONDUCTORS

One of the highlights of the week was a paper by P.F. Smith of the Rutherford Laboratory outlining his work on filamentary superconductors. Smith began his discussion by pointing out that very fine wires should be subject to very small temperature rises during a flux jump and should thus be inherently stable when smaller than a certain diameter. He then extended this to include fine strands of superconductor in a conducting matrix and showed that a conductor formed in this way would act the same as a solid superconductor if its length exceeded a certain value which is always short relative to the lengths used in magnets. He then suggested that by twisting the wire with a pitch shorter than this characteristic length this coupling between the filaments could be removed with a corresponding increase in stability and reduction in ac losses. Smith then described an extensive experimental program designed to test his conclusions. He indicated that preliminary results were in good qualitative agreement with the theory.

## THERMONUCLEAR DEVICES

A survey of the uses of superconducting magnets in controlled thermonuclear experiments was presented by C.E. Taylor of the Lawrence Radiation Laboratory. In almost all experiments of this type magnetic fields are used to confine the charged particles of a plasma. In general such plasma containment devices can be divided into two classifications, "open ended" and "closed ended" machines. The fields required do not usually exceed 60 kG and are thus within the range of present NbTi technology. While superconducting magnets are used in most applications because they are more economical than conventional devices there are some applications where the unique properties of superconductors make them indispensable. An example of this is the floating ring type of experiment in which a ring containing persistent supercurrents is levitated in a magnetic field forming part of the plasma containment vessel. Taylor listed the principal CTR experiments now being planned which utilize superconducting magnets.

The next speaker, W.F. Gauster of the Oak Ridge National Laboratory, described in more detail the superconducting magnet system designed for the IMP project which was mentioned by Taylor. This system consists of two mirror coils and a quadrupole whose fields combine to produce a configuration which has a central field of 20 kG and which increases to at least 26 kG in any direction from the center. The peak field in the system is 75 kG. Gauster pointed out the difficulties in calculating the forces in such a nonaxisymmetrical system. The experimental program associated with the design and construction of these magnets was described by D.L. Coffey. To test the conductors a series of solenoids were constructed with their windings in series opposition to approximate the forces and gradients experienced in large systems. To date the mirror coils have been built and tested and will be installed in the Fall of 1968. The complete system is expected to be operating by 1969.

## SUPERCONDUCTING MAGNETS AT THE 200 GeV ACCELERATOR

R. Meuser of LRL discussed the possible uses of superconducting beam handling magnets at the new 200-400 GeV accelerator being constructed at Weston, Illinois. His survey indicated that about 250 magnets would be required, with 77% of them being quadrupoles and the rest bending magnets. It was estimated that approximately half of these magnets would require radiation shielding and about 40% would be used in beams which would become shorter due to the higher fields and gradients available. Meuser pointed out that current density becomes increasingly important for magnets of small aperture and higher multipolarity and suggested that due to the uncertainties in costs both Nb<sub>3</sub>Sn and NbTi based design should be investigated. He finished by describing the test program at LRL, which includes operating a long solenoid with a closed loop refrigerator.

## FORCED HELIUM COOLING

A magnet constructed from hollow superconductor was described by M. Morpurgo of CERN. The conductor was formed by embedding superconductors of 0.01 in. diameter in an aluminum pipe. The magnet was then cooled by forcing helium through the hollow conductor. The solenoid appeared to operate in a completely stable fashion and could be operated slightly into the resistive region without quenching.

## SUPERCONDUCTING SYNCHROTRONS

P.F. Smith  
Rutherford Laboratory  
Chilton, Berks., England

The subject will be discussed under the following headings:

- I. Costs. Superconductor, engineering, refrigeration, power supply, and radius-dependent costs. Dependence on field, aperture, cycle time and ac loss. Separated function and combined function.
- II. Ac losses. Basic theory; theory of losses in composite conductors; development of low-loss conductors.
- III. Other design problems.
  1. Basic features; coil configurations; typical parameters.
  2. Eddy current heating; particle heating; stabilization and cooling; coil and cryostat materials; radiation damage.
  3. Coil structure; forces; movement; winding accuracy; alignment.
  4. Stray fields; shielding; remanent fields.
  5. Operating current and voltage; protection; power supply; alternative power supply concepts.
- IV. Specific designs. Results of exploratory studies of:
  1. Conversion of Nimrod (7 GeV) to  $\sim 40$  GeV.
  2. Single stage 180 GeV ring, with 50 MeV injection.
  3. Conversion of Nimrod to booster (5-25 GeV) for 100-200 GeV ring.

Most of the topics under Sections I, II, and III, were surveyed in a previous paper.<sup>1</sup> In the present review, attention will be concentrated on any progress made during the past year, and on plans and prospects for the immediate future.

In general, there has been little change in the over-all picture. Although there is widespread interest in this application, its long-term prospects are still rather uncertain compared with dc superconducting magnet applications, and the amount of effort devoted to it is correspondingly small. Paper studies, such as those described in Section IV, are instructive but lack realism until a suitable low-loss conductor is available for model magnet studies.

Development of a suitable conductor is, therefore, the overwhelming priority, and in this direction progress is fairly encouraging. It should not, as was originally feared, require the development of completely new fabrication techniques; theoretical studies of ac losses in composites composed of superconducting filaments in a metallic

---

1. P.F. Smith and J.D. Lewin, Nucl. Instr. Methods 52, 298 (1967).

matrix indicate that a low-loss conductor may be possible with only a moderate extension of existing manufacturing capability. We can anticipate, therefore, that within the next 12 months it should be possible to begin construction of realistic model magnets for tests under conditions of continuous pulsed operation.

## I. CAPITAL COSTS

Accurate forecasts of costs are, of course, impossible at this early stage. It is, however, useful to have some simple approximate cost formulae as a basis for comparing exploratory designs, to indicate which cost components are dominant, and to set an economic limit to the ac loss.

For this purpose we are concerned only with those parts of the cost which are dependent on magnetic field, machine radius, and magnet aperture. To these must be added various fixed costs depending on the nature of the project (new accelerator, conversion of existing accelerator, new injector or booster required, etc.).

In each case the cost is estimated as a function of field  $H$ , radius  $R$ , and aperture, and divided by  $3HR/10^7$  to obtain the cost in £/(GeV/c). It is simplest to consider initially only the bending field and discuss separately the additional cost of providing focusing. These estimates differ only slightly from those in Ref. 1, but dependence on aperture is now included. Based on experience of typical designs, the aperture is now assumed to be circular rather than elliptical (see Section IV).

### 1. Superconductor

Assume a distribution of current  $I_1 \sin \theta$  (A/cm) around a circular aperture, giving a field  $H = 0.2 \pi I_1$  (G). Let  $r$  be the mean radius of the winding given by

$$\begin{aligned} r = & \text{beam aperture radius } a \\ & + \text{thickness of cryostat and coil former} \\ & + \text{half of coil thickness.} \end{aligned}$$

(Typically, for example, we might expect that  $r \approx a + 2$  cm.)

Then the amount of superconductor required, allowing an additional 15% for magnet ends, is  $40 HRr$  (A.cm) or  $1.5 \times 10^8 r$  (A.cm/GeV). Present cost of NbTi conductors is  $4 \times 10^{-10} H$  (£/A.cm) up to  $H \sim 80$  kG; more optimistically we might guess that this could eventually be halved for large quantities. The cost range is therefore:

$$\text{Superconductor cost} = 0.06 rH \text{ to } 0.03 rH \quad (\text{£/GeV}) \quad (1)$$

### 2. Engineering

Cryostat costs are at present usually in the region  $\text{£}0.3 S$ , where  $S$  (cm<sup>2</sup>) is the coil surface area. The coil construction costs are difficult to estimate and are here arbitrarily assumed to be proportional to the quantity of superconductor. Using costs experienced in recent dc magnet projects, and bearing in mind that design and drawing costs should be negligible for a large number of identical units, we guess the following cost range:

$$\begin{aligned} \text{Magnet engineering cost} = & 1000 r + 8 \times 10^7 r/H \quad (\text{£/GeV}) \quad (2) \\ & \text{to } 500 r + 4 \times 10^7 r/H \end{aligned}$$

For example, for a 200 cm long, 60 kG magnet with a 5 cm beam aperture radius, this formula gives an engineering cost of £6000 to £12 000.

### 3. Refrigeration

Consider first the requirements other than the ac loss. There are contributions from conduction and radiation losses, current leads, joints, eddy currents, and particle heating, as estimated in Ref. 1. Assume that with care these can be limited typically to  $\sim 3$  W/m of circumference for  $r \sim 6$  cm, and that they are proportional to  $r$ . Costs of a variety of multimagnet refrigeration schemes have been estimated by Strobbridge et al.<sup>2</sup> and it has subsequently been suggested that costs a factor  $\sim 2$  lower might be achieved.

We arbitrarily assume subdivision into 1200 W units, allowing a factor 2 for transfer losses, at a cost, including distribution, of  $\pounds 3 \times 10^5$  to  $\pounds 6 \times 10^5$  per unit. This gives a basic refrigeration cost of  $0.5$  to  $1 \times 10^8$  r/H (£/GeV).

Now assume an ac loss of  $P$  (W/m) and increase the size of each unit accordingly. At an incremental cost of  $\pounds 100$  to  $\pounds 200$ /W the additional cost is  $2P$  to  $4P \times 10^7$ /H (£/GeV). The total estimated cost range is thus

$$\begin{aligned} \text{Refrigeration capital cost} &= (r + 0.4 P) 10^8 / H & (\pounds/\text{GeV}) \\ &\text{to } (0.5 r + 0.2 P) 10^8 / H \end{aligned} \quad (3)$$

Thus for  $r \sim 8$  cm,  $P$  can be  $\sim 20$  W/m before the cost of refrigeration equipment is doubled.

### 4. Power Supply

Assuming a uniform field up to radius  $r$ , and equal stored energies inside and outside the coil, the total is approximately  $r^2 H / 2$  J/GeV. Cost of conventional power supplies is proportional to the peak rate of energy transfer, and is usually about  $0.04$  £/J for the typical 1 sec rise time. Costs may be proportionately lower at very high stored energies, and because no dc power is required for "flat-top" conditions; on the other hand higher costs may be necessary to improve reliability. This suggests the cost range:

$$\begin{aligned} \text{Power supply cost} &= 0.024 r^2 H & (\pounds/\text{GeV}) \\ &\text{to } 0.012 r^2 H \end{aligned} \quad (4)$$

for a 1 sec rise time  $T$ , and proportional to  $1/T$  in other cases.

### 5. Radius-Dependent Cost

In addition to the magnet tunnel cost, this includes such items as site preparation, magnet installation, vacuum system, site power, etc. In Ref. 1 it was suggested that about  $\pounds 30$  million of the 300 GeV estimate would decrease linearly with radius, which is equivalent to  $12 \times 10^8$ /H (£/GeV). This may, however, be too optimistic, particularly if substantial reductions in magnet tunnel cost are possible. We allow for this by assuming:

$$\begin{aligned} \text{Radius-dependent cost} &= 12 \times 10^8 / H & (\pounds/\text{GeV}) \\ &\text{to } 6 \times 10^8 / H \end{aligned} \quad (5)$$

---

2. T.R. Strobbridge et al., National Bureau of Standards Report 9259 (1966).



There is also the further complication that the tunnel radius will not usually reduce in proportion to the bending radius, since the straight section length is fixed by other considerations. In comparing specific designs, therefore, it is more realistic to take the radius-dependent cost to be £2000-£4000 per meter of circumference.

## 6. Optimum Values

The occurrence of terms proportional to  $H$  and  $1/H$  leads to a cost-optimum field. The optimum costs are shown in Table I, using the means of the preceding cost ranges, for three typical values of  $r$ . The optimum is rather flat, and subject to the uncertainties in costs, so that the figures cannot be taken very seriously. Nevertheless, the general trends are of interest; firstly that the typical optimum fields 40-60 kG conveniently coincide with the field range desirable from practical viewpoints; secondly that all five items tend to be of the same order of cost; and thirdly that for larger apertures the power supply requirements begin to be unreasonably large.

TABLE I  
"Optimum Costs, Without Focusing"

Item	Mean of Cost Range (£/GeV)	Optimum costs in units £1000/GeV (for 3 sec cycle)		
		$r = 10$ cm $H = 37\ 000$ G	$r = 7$ cm $H = 45\ 000$ G	$r = 4$ cm $H = 60\ 000$ G
Superconductor	$0.045\ rH$	17	14	11
Power Supply	$0.018\ r^2H$	67	40	18
Engineering	$750\ r + 6 \times 10^7\ r/H$	24	15	7
Refrigeration	$1.5 \times 10^8\ r/H$	40	23	10
Radius-dependent items	$9 \times 10^8/H$	24	20	15
Total of above items (N.B. Constant cost items <u>not</u> included)		172	112	61

## 7. Cost of Focusing

Quadrupoles have approximately the same costs per unit length as bending magnets for the same field and aperture, with the exception that the power supply cost, proportional to stored energy, is only half as great. Thus, if the ratio of quadrupole length to bending magnet length in a separated function lattice is  $q$ , the above power supply cost is multiplied by  $(1 + q/2)$ , and the other costs are multiplied by  $(1 + q)$ . To a good approximation, therefore, we can assume the optimum to be unaffected, and all costs simply increased by  $\sim (1 + 0.9\ q)$ . In Section IV it will be found that typical values of  $q$  are between 0.15 and 0.3.

For a combined function machine the cost changes are more complicated, and not

uniformly distributed. Simple approximations suggest that, in an equivalent combined function lattice, the over-all cost is multiplied by  $\sim (1 + 0.4 q)$ . It thus follows that a separated function machine is theoretically dearer than a combined function machine by a factor  $\sim (1 + 0.5 q)$ , i.e.  $\sim 10$ -15%. This cost difference, however, makes no allowances for the greater engineering complexity of the asymmetric separated function magnets.

## 8. Comparison with Conventional Magnets

Assuming  $r = a + 2$  cm, the  $r = 7$  figures in Table I (increased by 20% to allow for focusing), may be compared with the corresponding costs for a conventional synchrotron of 5 cm aperture radius, which amount to about \$150 000/GeV. Specific designs, such as those in Section IV, suggest that, for a given energy and number of particles, the required aperture would in fact be smaller than in a conventional machine, resulting in a further cost gain. The economics of the superconducting system would be even more convincing if reductions in the power supply and refrigeration costs become possible. The possible cost gains are, of course, much greater in the case of conversions of existing accelerators, since many of the fixed cost items (site, experimental areas, injector, etc.) are absent.

Comparative running costs have not yet been estimated, and no further thought has been given to combined superconducting + conventional systems.

## II. AC LOSSES

### 1. Objectives

High field superconductors have an irreversible magnetization curve. Changes in field must therefore generate heat, and the heat released per unit volume is proportional to the superconductor width perpendicular to the field. Using 0.025 cm wire, the dissipation in a typical 60 kG, 10 cm aperture diameter synchrotron magnet, with a 3 sec cycle time, would be about 500 W/m length of magnet. A similar or higher loss would be expected using Nb<sub>3</sub>Sn tapes. This is obviously too high, both from economic and magnet design viewpoints, and although it is still not clear exactly how much reduction will be necessary, it appears that for most purposes a limit of 10-20 W/m would be a desirable objective. We are, therefore, faced with the problem of reducing the loss by a factor 25 to 50.

Three ways of doing this have been considered.

- a) Reduction of average strand diameter to 5-10  $\mu$  ( $\sim \frac{1}{4}$  to  $\frac{1}{2}$  mil).
- b) Thin layers of superconductor shaped to follow the field lines.
- c) Increase current density by several orders of magnitude, so that the current is confined to thin surface layers (see below).

Methods b) and c) do not look feasible at present, but a) should be possible using existing manufacturing techniques in which a number of parallel strands are drawn down in a supporting matrix. Ideally the matrix should be an insulator, but a conducting matrix may also be suitable provided the strands are sufficiently twisted or transposed. Some aspects of the theory of this will now be discussed.

### 2. Theory

Consider first the usual calculation of the ac loss for a slab of superconductor (Fig. 1). Magnetization current  $J_c$  (A/cm<sup>2</sup>) is induced by a changing external field,

and completely fills the material when  $H \approx J_c d/2$  (which will be for most of the cycle in the case of thin wires and high fields).

The loss/unit volume at any point is simply the current density times the local electric field (proportional to the magnetic flux crossing the element per unit time). Integrating this over the whole slab one obtains for the total energy released:

$$Q(J) = H(G) \times J_c \times V(\text{volume, cm}^3) \times d(\text{cm}) / 4 \times 10^8 \quad (6)$$

$$= H \times \left[ \begin{array}{c} \text{A-cm of} \\ \text{superconductor} \end{array} \right] \times d \left[ \begin{array}{c} \text{wire} \\ \text{diameter} \end{array} \right] / 4 \times 10^8 \quad (7)$$

More exact estimates for a complete coil must take into account the spatial variation of  $H$ , the variation of  $J_c$  with  $H$ , the transport current, and the shape of the conductor cross section, as discussed in Ref. 1. For small test coils, allowance must also be made for the zero ac loss below  $H_{c1}$  (which may be in the region  $\frac{1}{2}$  to 1 kG).

For coils wound from wide tape, particularly single layer windings, a further correction is necessary for field distortion, and for incomplete penetration of the flux during most of the cycle. Typically these two effects can multiply formula (6) by a factor 0.05 to 0.1, but the loss is usually still higher than in corresponding coils of 0.010 in. wire.

When the penetration depth is  $p$ , the above formula is multiplied by  $(p/d)^2$ , and since  $p \propto H/J_c$ , it follows that  $Q \propto 1/J_c$ , showing the possibility of decreasing  $Q$  by increasing  $J_c$ , as mentioned above.

Now consider the loss in a multifilament conductor. Fig. 2(a) shows two strands of superconductor embedded in an insulator. The two strands are independent (ignoring for the moment the problem of the eventual end corrections), and separate magnetization currents flow in each strand as shown. The ac loss is given by  $J_c \times$  the local electric field, which is approximately proportional to the diameter of the strand.

In Fig. 2(b) the insulator is replaced by a normal conductor. If the resistance of the available path between the strands is sufficiently low, or if the rate of change of field is sufficiently high, the magnetization currents will be driven round the entire composite as shown. The ac loss will still be given by  $J_c \times$  the local electric field, but the latter is now proportional to the distance between the strands.

For a lower rate of change of field, or a higher resistance path between strands, an intermediate state may exist in which some of the magnetization current is confined to the strands and the rest crosses the matrix [Fig. 2(c)].

In general, by providing sufficient twisting or transposition of the strands, a state of this type can be produced in which the majority of the magnetization current is confined to the strands, and the ac loss is then closely proportional to the filament diameter, as required. The criterion is that the twist pitch must be substantially less than a critical length  $\ell_c$  given by

$$\ell_c \sim 10^8 \lambda J_c d \rho / \dot{H} \quad ,$$

where  $\dot{H}$  is the rate of change of field in G/sec,  $\rho$  the matrix resistivity in  $\Omega \cdot \text{cm}$ ,  $d$  the filament diameter in cm,  $J_c$  the filament current density in  $\text{A/cm}^2$ , and  $\lambda$  is a space factor. This is discussed in more detail in the paper on intrinsically stable conductors in these Proceedings.<sup>3</sup>

3. P.F. Smith, these Proceedings, p. 913.

With high resistance alloys, and  $\dot{H} \sim 60$  kG/sec, it may be possible to achieve the required twist pitch. With copper as the matrix material the twist pitch appears to be impracticably low; if required, however, copper may be incorporated in the composite provided it does not directly link two superconducting filaments.

Initial composite diameters in the region 0.010 in. are envisaged, which could then be insulated and formed into multistrand cables to carry higher currents. These will probably have to be transposed rather than twisted cables, because of the magnitude of the field gradient across the conductor. An approximate theory of this effect indicates that twisting should nevertheless be adequate in the basic 0.010 in. composite.

Even if composites with an insulating matrix can be developed, a certain (at present uncalculated) amount of transposition or twist will be necessary because of the end connections. This is one of the difficulties in using a subdivided Nb<sub>3</sub>Sn tape, since only one twist/turn would appear to be possible.

### 3. Experiments

The basic theory of losses in hard superconductors is well established, and amply verified experimentally to better than a factor of 2. Small coils of NbZr wire and Nb<sub>3</sub>Sn tape tested at the Rutherford Laboratory at frequencies between 4 Hz and  $\frac{1}{2}$  Hz have shown losses consistent with theory, and we regard further confirmation as unnecessary.

Our interest is therefore concentrated on the behavior of composites. A variety of samples containing NbTi filaments in a resistive matrix are being tested. Magnetization measurements have been made on small coils as a function of  $dH/dt$ , and the proportion of magnetization current in the strand and in the matrix are essentially in accordance with theory. The effects of twisting are also in accordance with theory. Some ac loss measurements are also being made using these composites.

It is proposed to extend this work to the required  $\frac{1}{2}$  or  $\frac{1}{4}$  mil filament sizes. If large quantities can be produced satisfactorily and economically, such a material should be suitable for synchrotron magnets, and a more thorough and larger scale program of tests may be attempted.

## III. OTHER DESIGN PROBLEMS

It is clearly not possible to make a realistic study of the majority of magnet design problems until the dominant problem of the ac loss is solved, and a clearer picture is obtained of the electrical and mechanical characteristics of the conductor likely to be used. Accordingly, although there has been some crystallization of ideas during the past year, there is relatively little to add to the remarks in Ref. 1.

### 1. Basic Parameters

It is now generally felt that separated function magnets will almost certainly be preferred to combined function magnets. Although the latter theoretically provide the most compact and economical system, the difference is usually fairly small (typically 10-20%, as explained above), and is offset by the greater simplicity and flexibility of the design, engineering, and commissioning of separate bending and focusing units.

The coil cross section could either consist of some convenient approximation to the overlapping ellipses configuration, or current blocks spaced to approximate the

$\sin \theta$  or  $\sin 2\theta$  circumferential distribution. The aim, of course, is to achieve uniformity of field or field gradient, and to minimize the peak field on the windings, with a shape which is reasonably straightforward from an engineering viewpoint. A high current density is essential for a compact and economic design, and a value in the region 30 000 to 50 000 A/cm<sup>2</sup> is usually assumed, giving a coil thickness of about 2 cm.

Typical optimum lattice designs require an aperture radius in the range 3 cm to 6 cm, and the aperture tends to be more nearly circular than in conventional machines. An important question, particularly for small apertures, is how much should be allowed for the difference between aperture radius and inner radius of winding. A figure of  $\sim 1$  cm is usually taken, on the assumption that the beam pipe need not be at room temperature.

Table II shows a revised list of typical parameters for bending magnets of 3 cm and 6 cm usable aperture radius.

TABLE II  
Typical Parameters for Bending Magnets

Beam aperture radius	6 cm	3 cm
Coil internal radius	7 cm	4 cm
Maximum winding thickness	2 cm	2 cm
Coil current density	48 000 A/cm <sup>2</sup>	48 000 A/cm <sup>2</sup>
Magnetic field (uniform)	60 kG	60 kG
Magnetic bending radius	55 cm/GeV	55 cm/GeV
Total magnet length	3.4 m/GeV	3.4 m/GeV
A·cm of superconductor	$3.5 \times 10^8$ /m	$2.2 \times 10^8$ /m
Stored energy/meter	0.57 MJ	0.22 MJ
Stored energy/GeV	1.9 MJ	0.75 MJ
Rise time	1 sec	1 sec
Cycle time	3 sec	3 sec
Refrigeration requirements at 4°K:		
a) Cryostat losses, current leads, eddy currents, particle heating	4 W/m	2.5 W/m
b) Ac losses (filaments $6 \times 10^{-4}$ cm diameter)	20 W/m	12 W/m

## 2. Other Heating Effects

It was shown in Ref. 1 that eddy current heating in any normal metal in a composite conductor will be small provided that the diameter of the strands of composite is in the region 1 mm or less. To prevent excessive heating by high energy particles, the dose must be kept below 10<sup>4</sup> rad/h, and this means that particular care must be

taken to ensure that the extraction loss is sufficiently low and not concentrated in a small region of the circumference.

It is hoped that stabilization will be unnecessary in a filamentary composite, so that the coil can be fully insulated, and impregnated for strength and rigidity, and cooled on the surface only. For an average thermal conductivity of  $\sim 10^{-3}$  W/cm °K, the ac loss and other heating effects would cause a temperature rise of order 1°K. This would presumably be only just tolerable, and some assessment is needed of the possibilities of insulators with a high thermal conductivity.

Eddy current heating appears also to necessitate the use of insulating materials for the cryostat and coil former. A preliminary assessment of this problem would also be of interest. With all these materials (and, to a lesser extent, the superconductor itself) the complication of long-term radiation damage must be taken into account.

### 3. Forces

For a thin winding, the total outward force on the coil is  $aH^2/3\pi$  dyn/cm/length, where  $a$  is the radius of the coil (this is misprinted in Ref. 1). For the magnet dimensions envisaged, this force is smaller than that encountered in many existing or proposed dc magnet projects. Nevertheless there is obviously some anxiety about the rigidity and long-term reliability of the coil under continuous pulsed operation. Stresses arising from differential thermal contraction could present an even greater problem, with the mixed use of metallic and nonmetallic materials.

A related problem is that of defining and maintaining the coil position within the cryostat, to enable the required accuracy of magnet alignment to be achieved.

These problems are unlikely to be studied seriously until the first model magnets are designed.

### 4. Stray Fields

The field at a distance  $d$  (cm) from an unshielded bending magnet (central field  $H$ , mean winding radius  $r$ ) is approximately  $H(r/d)^2$ . This is, of course, much higher than the stray field usually encountered in an accelerator magnet tunnel, and there is at present some disagreement as to whether magnetic shielding will be necessary or not. However, the use of concentric superconducting windings appears to be an expensive luxury, while the alternative of using steel, in addition to increasing the magnet cost by about 5-10%, makes the system much more bulky and less accessible. It might be preferable, therefore, not to have to provide shielding except for special purposes (e.g. rf cavities); a more detailed survey of this problem is needed.

Also under this heading the question of remanent fields can be mentioned. Although large in present superconducting coils, these are automatically reduced, along with the ac loss, by the use of finer superconducting filaments, and are expected eventually to be lower than in iron-cored magnets. This would mean that an accurate field distribution might be retained at lower fields than in conventional magnets, allowing the use of a lower energy (and cheaper) injector; in practice, however, it will not usually be possible to take advantage of this, since space charge limitations necessitate a high injection energy to achieve adequate beam intensity.

### 5. Power Supply

The usual assumption is that conventional power supply systems will be used, with the operating current similar to that of conventional synchrotron magnets, i.e. a few

thousand amperes, and with the magnet ring subdivided as usual to reduce the excitation voltage to a few kilovolts. Lower currents would result in higher voltages or an unreasonable amount of subdivision of the circuit; higher currents would increase the complexity of the superconducting cable, but values in the 10 000 to 20 000 A region might well be considered. To reduce heat leak into the system, current leads need only be brought out to room temperature for connection to the supply, interconnections between magnets being kept at 4°K.

With the high current density coils envisaged, any shorts or normal regions formed within the coil would result in local damage by overheating or voltage breakdown within a few milliseconds. Protection against this appears almost impossible, the usual methods available for dc magnets being unsuitable for pulsed operation. It will undoubtedly be possible, however, to confine the damage to a single magnet unit, so the best solution appears to be to design the coils with an adequate safety margin, and replace individual units in the event of an occasional failure.

Since, in contrast to conventional magnets, no provision has to be made for dc power requirements under "flat-top" conditions, and since there is negligible energy loss per cycle, the possibility can be envisaged of alternative power supply schemes utilizing energy storage in superconducting magnets. This is discussed in a separate paper.<sup>4</sup>

#### IV. SPECIFIC DESIGNS

Some exploratory studies have been made of possible schemes for the conversion or extension of the existing accelerators at the Rutherford Laboratory. Although of somewhat limited general interest, they nevertheless provide a useful guide to the typical parameters of superconducting magnet lattices.

It should be emphasized that no proposal of this nature is being considered at present; the calculations have been carried out simply to obtain a preliminary impression of what might be possible in the future.

Separated function lattices are used throughout, designed with the aid of a computer program and optimized for approximate minimum aperture.

##### 1. Original Nimrod Conversion

Nimrod is a constant gradient proton synchrotron with a 15 MeV injector and an energy of 7 GeV (7.9 GeV/c momentum) at the normal 14 kG peak magnetic field.

The original suggestion was simply to replace the large aperture constant gradient magnet with a small aperture superconducting alternating gradient magnet which, at ~ 70 kG, would have about the same stored energy, ~ 40 MJ. This might allow the energy to be increased to ~ 40 GeV using all the existing facilities except the magnet and rf system. Alternatively, with a separate (larger radius) magnet tunnel and a mean field of 50-60 kG, an energy of 50 GeV might be achieved with the existing power supply.

Closer examination showed that this scheme would not satisfy the future necessity for a higher beam intensity, since, with the assumed aperture radius ~ 5 cm, the space charge limit would be  $\leq 3 \times 10^{12}$  protons/pulse. Nearby, however, there is an operational 50 MeV linear accelerator, which could be used to replace the existing injector

---

4. P.F. Smith, these Proceedings, p. 1002.

and increase the space charge limit to  $\sim 10^{13}$  protons/pulse. Better still, of course, a completely new injector could be provided.

A typical computed lattice is shown in Fig. 3, assuming 60 kG in the bending magnets and peak fields of 60-70 kG in the quadrupoles. With an emittance of  $150 \mu\text{m}\cdot\text{R}$  (corresponding to  $\sim 10^{13}$  protons at 50 MeV) the beam radius for this optimum lattice is about 4.1 cm, to which must be added perhaps 0.5 cm for closed orbit distortions. One long bending magnet is provided per period, which can be omitted to provide a straight section about 4 m long. Assuming only four straight sections and a maximum mean radius of 26 m, one obtains a particle energy of 30 GeV, which represents a more realistic upper limit of what might actually be achieved in the existing magnet hall.

## 2. Single Stage 180 GeV Machine

As a second exercise, the possibility of a larger magnet ring was considered, again using the 50 MeV injector. Guessing a lower limit of 100 G for the injection field, a peak field of 60 kG gives an energy of 180 GeV. Preliminary trials showed that of various quadruplet, triplet, and FODO lattices, the latter gave the smallest apertures for a given peak quadrupole field.

The parameters of one of the best lattices are summarized in Fig. 4. This time a more realistic allowance is made for the ratio of peak field/usable field in the quadrupoles, and the ratio mean radius/bending radius was fixed at 1.35 (or  $\sim 1.6$  with insertions). With these assumptions the beam radius is about 5 cm for an emittance of  $75 \mu\text{m}\cdot\text{R}$ , corresponding to only  $5 \times 10^{12}$  protons.

In this machine the required straight section length would probably be  $\sim 15$  m for extraction purposes, and so would have to be provided by matched insertions rather than by the omission of bending magnets.

## 3. Conversion of Nimrod to Booster

The beam intensity in the previous machine could be increased simply by increasing the beam aperture radius  $a$  ( $a \propto \sqrt{N}$ ), but the figures in Section II show that the cost begins to increase rapidly for  $a > 7$  cm. A less expensive solution is to provide a booster synchrotron at an intermediate energy.

The third exercise, therefore, was to consider the conversion of Nimrod into a 5-25 GeV booster, followed by a high energy machine of very small aperture. In the 180 GeV ring, for example, the space charge limit would allow containment of  $4 \times 10^{13}$  protons in a beam radius of only  $\sim 1$  cm at 5 GeV injection, and  $\sim 0.5$  cm at 25 GeV injection. Since these numbers are now becoming smaller than the allowance necessary for coil former and thickness, the advantage in injecting at 25 GeV rather than 5 GeV is not very great. This immediately suggests the possibility of schemes in which there is an initial conversion to, say, 20-25 GeV, and the same magnet is subsequently used at  $\sim 5$  GeV as a conventional fast cycling booster for a higher energy machine. At 180 GeV, the radius ratio would be  $\sim 6$ , so that  $> 7 \times 10^{12}$  protons/pulse in the booster would be necessary to give  $4 \times 10^{13}$  protons in the main ring. Because of the reduced field, fast cycling at 3-4/sec should not result in any significant power supply or ac loss problems.

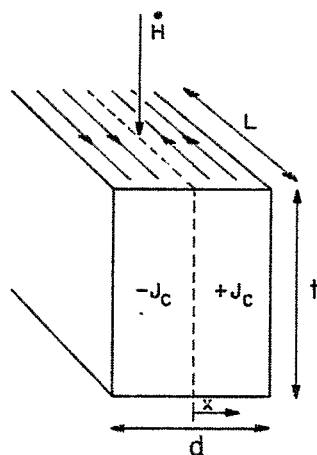
A variety of calculations along these lines are in progress. A typical 25 GeV lattice is shown in Fig. 5, requiring a beam radius of  $\sim 3.8$  cm for  $10^{13}$  particles. In general, for a fixed machine radius of  $\sim 20$  m, the computed beam radii fit the expression  $a = 3.3 \times 10^{-7} p^{0.4} N^{0.5}$ , where  $N$  is the number of particles, for values of the momentum  $p$  between 5 and 30 (GeV/c).



For the main ring, if the lattice of Fig. 4 is used, the beam radius is now reduced to  $\sim 1.1$  cm for  $4 \times 10^{13}$  particles. The smaller aperture, however, allows the use of a higher field gradient so the lattice must be reoptimized; the result is shown in Fig. 5 and the new beam radius is  $\sim 0.9$  cm. Only a small gain results, therefore, from the increase in quadrupole strength (principally because the quadrupoles occupy only about 15% of the circumference) and the optima are, in any case, fairly flat. Much larger changes in beam radius can result, however, from a change in the type of lattice; triplet lattices, for example, appear to require apertures typically twice as great as FODO lattices.

Cost estimates have not yet been made for the above schemes, nor has any detailed consideration been given to rf requirements, injection and extraction efficiencies, etc..

Since the computed lattices cover a fairly wide range of energy and intensity, the magnet parameters are likely to be fairly typical of future requirements. It appears, therefore, that for a 60 kG peak field we can expect bending magnet lengths in the range 1 to 6 m, quadrupole lengths of 0.3 to 1.2 m, and aperture radii between 2 and 6 cm.



$$\begin{aligned}
 \text{POWER} &= \int J E \, dV = \int_{-d/2}^{+d/2} J_c \times (\dot{H} x / 10^8) \times L t \, \delta x \\
 &= \dot{H} J_c \times L t d \times d / 4 \times 10^8 \\
 \dot{Q} &= \dot{H} J_c V d / 4 \times 10^8
 \end{aligned}$$

Fig. 1. Basic ac loss calculation.

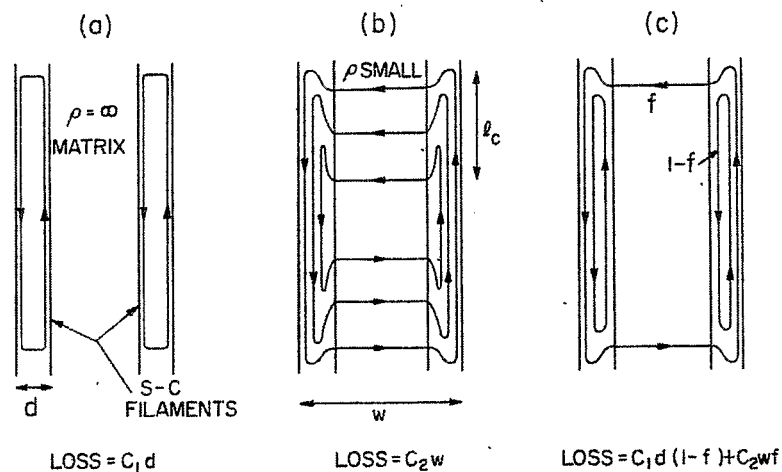


Fig. 2. Distribution of magnetization currents in a composite conductor.

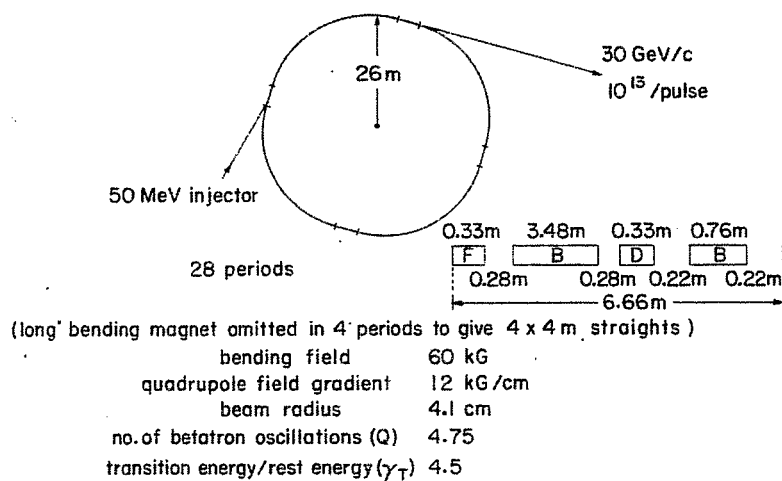


Fig. 3. Typical lattice for Nimrod conversion.

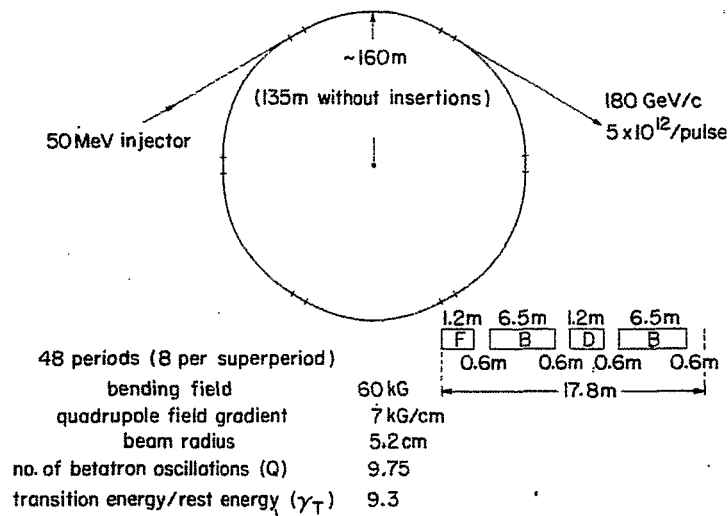


Fig. 4. Typical 180 GeV lattice with 50 MeV injection.

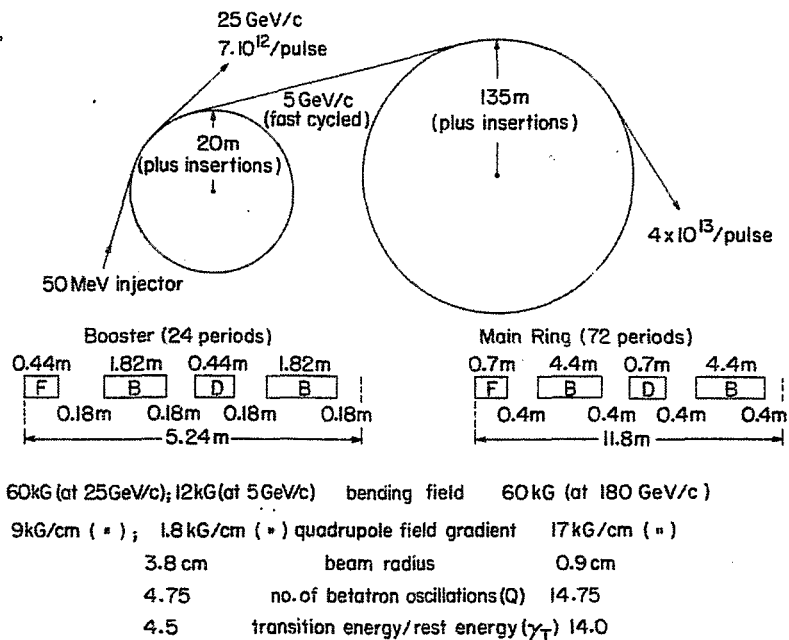


Fig. 5. Typical lattices for 180 GeV with 5 GeV booster.

ECONOMIC FACTORS INVOLVED IN THE DESIGN OF A  
PROTON SYNCHROTRON OR STORAGE RING WITH A  
SUPERCONDUCTING GUIDE FIELD\*

M.A. Green  
Lawrence Radiation Laboratory  
Berkeley, California

INTRODUCTION

A synchrotron with a superconducting guide field will be justified if the synchrotron can be built and operated in such a way that it ultimately saves money. Although it may be argued that a superconducting facility of high cost is justified because it will speed development of the art, the arguments in favor of a superconducting facility must ultimately be economic ones.

I believe that one must take a careful look at the over-all properties of superconducting accelerators. This paper discusses a number of the important economic considerations that are involved in the design of a superconducting synchrotron or storage ring. This paper shows that a superconducting synchrotron is competitive with a conventional machine even when today's high costs and equipment are used.

A cost estimate of energy expansion of the 200 GeV machine using a superconducting ring was made in 1967.<sup>1</sup> That report showed that it might be feasible to expand the energy of the 200 GeV accelerator at a cost lower than was proposed by some schemes. The most important advantage was that one did not have to commit himself to energy expansion at an early date. The cost figures are comparable with ones that were suggested by Smith<sup>2</sup> and by Smith and Lewin.<sup>3</sup>

This paper discusses the unique properties of a superconducting magnet ring and how they should be utilized. The machine parameters that strongly influence cost are also discussed. The interaction of the various machine components strongly influence cost of a superconducting ring, hence the whole system must be looked at in detail.

UNIQUE SUPERCONDUCTING SYNCHROTRON PROPERTIES

The strong focusing synchrotron with a superconducting guide field is quite different from the conventional AGS machine. These differences affect the design of a superconducting machine. The important differences are:

1. Superconductors are capable of operating at high fields and current densities, which permits high-field air-core magnets to be built.

---

\* Work performed under the auspices of the U.S. Atomic Energy Commission.

1. M.A. Green, University of California, Lawrence Radiation Laboratory Report UCRL-17862 (1967).
2. P.F. Smith, in Proc. 2nd Intern. Conf. Magnet Technology, Oxford, 1967, p. 594.
3. P.F. Smith and J.D. Lewin, Nucl. Instr. and Methods 52, 248 (1967).

2. Superconductors have zero resistance except during charging, hence superconducting storage rings appear to be feasible.
3. The energy lost per cycle in the superconductor is independent of frequency, hence the power consumed goes down as the cycle time increases. (It should be noted that superconducting systems with large eddy-current losses behave in the same general way.) Conventional machines require the same amount of power regardless of the cycle time. Long cycle times and storage rings have much lower power consumption and their costs are not power-dependent.
4. Horizontal and vertical aperture cost nearly the same in superconducting dipoles and quadrupoles. As a result magnets with a round aperture are of interest from both an economic and an engineering standpoint.

It should be noted that superconducting devices have a unique set of problems as well as advantages. The superconducting currents must be carefully placed. The high stress levels in a high-field superconducting magnet make it difficult to insure proper magnet performance. A number of problems are associated with the cryogenic environment needed to produce superconductivity. Control of the magnet stored energy during a quench is also needed. A large number of these problems can be solved only by building a number of model magnets and testing them.

#### BASIC MACHINE PARAMETERS

A 100 GeV machine is used as an example. It is a "bare-bones" machine with no external beam lines, target areas, or injector. The machine is assumed to be a separated-function machine with a  $\nu$  value of between 10 and 11. The machine is assumed to have fourfold symmetry with four straight sections that are each one betatron wavelength long. (See Fig. 1.) The straight sections are assumed to have the same quadrupole structure as the bending sections. They are one betatron wavelength long to minimize the radiation dumped into the superconductor during injection and extraction.

The machine parameters are divided into two basic categories, fixed parameters and variable parameters. The primary fixed parameters are final energy, injection energy, and intensity in protons per second. The variable parameters are those determined by economics rather than by fiat. The most important variable parameters are repetition rate or cycle time, aperture, and magnetic field.

The injection energy is assumed to be 5 GeV, the peak or final energy 100 GeV. The study used intensities of  $5 \times 10^{12}$  protons per second. The 100 GeV machine was assumed to have a rather large  $R/\rho$  ratio of two because of the low  $\nu$  value and the one-betatron-wavelength long straight sections. The 1000 GeV examples have a much more reasonable  $R/\rho$  ratio of 1.5.

The repetition rate of the machine is directly related to its aperture if the intensity in protons per second is kept constant. There are compelling arguments both from a power standpoint and from a capital cost standpoint to go to long cycle times. Longer cycle times result in larger apertures if a constant average beam current is maintained. The aperture is assumed to be nearly independent of peak magnetic field. This assumption holds if the beam aperture is emittance-limited. Arguments can be made for or against the preceding assumption; as a result, one has to look at a particular machine in order to find out whether the aperture is dependent on the magnetic field. The magnetic field is strongly dependent on economic factors for the machine of lowest cost per GeV. The optimum magnetic field is also dependent on aperture and repetition rate. (It should be noted that one might want to use a nonoptimum field for other reasons, such as physical site limitations.)

A computer program was written to calculate the costs of a large number of superconducting machines.<sup>4</sup> The program calculates the size of and the cost of the following machine components: (1) the superconducting magnet ring, (2) the ring magnet power supply, (3) the magnet cryostats, (4) the 4.2°K helium refrigeration system for the magnets, (5) the rf system, (6) the machine injection and extraction system, (7) the vacuum system, (8) the machine control system, and (9) the conventional plant facilities (including tunnel, earthwork, foundation, and utilities).

#### THE METHOD OF COST ANALYSIS OF MACHINE COMPONENTS

The detailed equations and assumptions are omitted from this section. One may find these equations and a listing of the program in Ref. 4. The main cost relationships are presented for each of the components.

This paper is relatively conservative in its presentation of costs. Today's costs are used as much as possible. Neither the upward nor downward trend in costs for some products is considered. This paper shows that even at today's costs the superconducting synchrotron can be built more cheaply than the conventional machine.

The superconducting magnet cost can be estimated by knowing the cost of the superconductor, because 70 to 80% of the magnet cost is the superconductor itself. One may calculate the cost of superconductor by calculating the number of ampere meters of superconductor in the system and multiplying it by the cost of the superconductor in dollars per ampere meter. The cost of a typical niobium-titanium and niobium-tin superconducting material is shown in Fig. 2. The cost per ampere meter is a function of winding peak field. It is assumed there is no gradation of the superconductor in the magnet. The number of ampere meters of superconductor is a function of magnet length and ampere turns required. The ampere turns is a function of coil current density, peak central field, and aperture. The coil current density is a function of the peak field in the coil, as shown in Fig. 3.

A 2/3-rule dipole and quadrupole were used as models to calculate the cost of material (see Figs. 4 and 5). Detailed analyses of such a dipole or quadrupole are given by Asner,<sup>5</sup> Bronca,<sup>6</sup> and Halbach.<sup>7</sup> Ampere-turn requirements and stored energy, calculated by using the 2/3-rule model, compare within 10% with those that would be calculated by using a varying current density or intersecting-ellipse models. The use of iron was not considered in the cost estimate.

The magnet cost is one of the largest items in a superconducting synchrotron. Several conclusions can be made that relate magnet cost to machine parameters: (1) The cost of the magnet goes up as the peak central field goes up despite the reduction in magnetic radius; (2) low-current-density magnets require more ampere meters of material than high-current-density magnets; (3) quadrupoles require more material than dipoles of the same peak field and current density.

- 
4. M.A. Green, University of California, Lawrence Radiation Laboratory Report UCID 3204 (1968).
  5. A. Asner and G. Iselin, in Proc. 2nd Intern. Conf. Magnet Technology, Oxford, 1967, p. 32.
  6. G. Bronca and J.P. Pouillange, CERN Report CERN/ECFA 67/W62/US-SG1/JPP2 (1967); and ECFA Utilization Studies for a 300 GeV Proton Synchrotron (CERN, 1967), Vol. 2, p.203.
  7. K. Halbach, Lawrence Radiation Laboratory, private communication.

The power supply is assumed to be a conventional motor generator set such as the ones used on today's synchrotrons. The cost of the power supply is proportional to the magnet stored energy and inversely proportional to the machine rise time. The magnet stored energy goes up as the peak central field to the N power, where N is greater than unity. The power supply costs also go up with aperture to the m power, where m is somewhat less than 2.

There appear to be several schemes which may result in large decreases in power supply cost; one such scheme has been advanced by Smith of the Rutherford Laboratory.<sup>8</sup> This scheme may be particularly promising for short-cycle-time machines. Long flat-tops will require an extremely low ripple factor. Today's power supplies have too high a ripple factor to permit long beam spills. However, superconducting magnets can be made to run in the persistent mode, which is essentially ripple-free.

The magnet cryostat cost is a function of its length, hence is inversely proportional to the peak central field. The cryostat is assumed to be as simple as possible, because the high heat leak found in the simplified Dewar is dominated by other loads in the system. The cryostat is estimated to cost about \$3000 per meter.

The liquid helium refrigeration system would consist of one or more large refrigerators and the appropriate transfer lines. The large system is applicable for an accelerator<sup>9,10</sup> because: (1) the loads are relatively concentrated, (2) the load in the accelerator system greatly exceeds the transfer line losses, (3) the system position is fixed. The system is assumed to consist of a group of central refrigerators with cold gas transport. The J-T (Joule-Thomson) valves and final J-T heat exchangers are located at the Dewar. (see Fig. 6).

There are three primary sources of heating in the 4.2°K region: (1) heat leaks from the outside through the Dewar and power supply leads, (2) heating due to energy loss from the beam, (3) various kinds of ac losses.

Heat leaks into the system are roughly proportional to the cryostat length. It is assumed that 10% of the beam is lost at extraction and 5% of the beam is lost during injection. It is further assumed that 20% of the lost beam energy is dumped into the 4°K region. There could also be a severe local heating problem; it can be reduced by the long straight sections and the use of special quadrupoles in these sections. It is desirable to have as high an extraction and injection efficiency as possible to reduce the beam heating.

The ac losses are divided into two basic terms, a hysteresis-like loss and an eddy-current-type loss. I use Smith's<sup>2</sup> ac loss equation, which is being experimentally confirmed by work at LRL,<sup>11</sup> Brookhaven,<sup>12</sup> Rutherford,<sup>13</sup> and other places. I have assumed that the basic wire dimensions are 0.0025 cm (0.001 in.). There is strong

---

8. P.F. Smith, in Proc. 2nd Intern. Conf. Magnet Technology, Oxford, 1967, p. 589.

9. M.A. Green, G.P. Coombs, and J.L. Perry, report by 500 Incorporated, a subsidiary of Arthur D. Little, Inc., Cambridge, Mass. (1968).

10. M.A. Green, G.P. Coombs, and J.L. Perry, these Proceedings, p. 293.

11. W.S. Gilbert, R.E. Hintz, and F. Voelker, University of California, Lawrence Radiation Laboratory Report UCRL-18176 (1968).

12. W.B. Sampson, R.B. Britton, G.H. Morgan, and P.F. Dahl, in Proc. Sixth Intern. Conf. High Energy Accelerators, Cambridge, Mass., 1967, p. 393.

13. P.F. Smith, these Proceedings, p. 913.

evidence that such a material can be made in a high-resistance substrate. Work is proceeding on such an NbTi material. The same dimensions are used for both the NbTi and Nb<sub>3</sub>Sn cases. An eddy-current term is included in the program. Prevention of eddy-current losses will require extensive use of high-resistivity metals and non-metallic materials in the 4°K region.

The refrigeration cost is based on the Strobridge, Chelton, and Mann<sup>14</sup> estimate. It is assumed that there is one refrigerator at each point where leads leave the enclosure. The cost of each refrigerator can be calculated by using the relationship

$$\text{Refrigerator cost} = \$3720 (\text{Power @ } 4.2^{\circ}\text{K})^{2/3},$$

where the 4.2°K power required is greater than 100 W. The above relationship fits the Strobridge, Chelton, and Mann curve very well. The actual cost of large units is tending to be somewhat lower than the cost predicted by the above relationship.<sup>15</sup>

The rf system cost is primarily a function of rf power, which is a function of the beam power. The injection extraction system consists of fast kickers, thin septums, deflectors, and magnet to get the beam into and out of the machine. The cost of injection and extraction elements is a function of the injection and extraction energies respectively.

The vacuum system consists of vacuum piping in regions where there are no magnet cryostats, vacuum joints, a roughing pump system, and high-vacuum cryogenic pumps using liquid helium. The cost of the vacuum system is roughly proportional to the ring radius. The accelerator control system is assumed to be 5% of the sum of the accelerator cost.

The cost of tunnel, earthwork, and plant facilities is an extremely important part of the cost analysis. The computer program is capable of calculating the conventional facilities cost for three types of sites: hard sites with cut-and-fill methods used, soft sites with cut-and-fill methods used, and a hard-rock bored tunnel site. The soft site was used for the 100 GeV example. The cost of enclosure, shielding, foundation, and earthwork is estimated to be about \$7400 per meter. The tunnel is much like the LRL 200 GeV design study tunnel<sup>16</sup> (see Fig. 7), which may be larger and more expensive than needed. The utilities or plant facilities cost consists of an electric power distribution net and a cooling water system (cooling water is required for the rf system and refrigerators). The cost of the utilities is about \$100 per kilowatt fed into the power consuming systems. The machine subtotal cost is the sum of all the systems. An additional 50% was added for engineering development, civil engineering, architecture, and contingency. The latter was added to make the estimate comparable to today's actual conventional machine costs.

---

14. T.R. Strobridge, D.B. Mann, and D.B. Chelton, National Bureau of Standards Report 9229 (1966).

15. G.P. Coombs (500 Incorporated, a subsidiary of Arthur D. Little, Inc.), private communication.

16. 200 BeV Accelerator Design Study, Vol. II, University of California, Lawrence Radiation Laboratory Report UCRL-16000 (1965).



## THE EFFECT OF MAGNETIC FIELD, APERTURE, AND CYCLE TIME ON TOTAL MACHINE COST

A number of interesting things can be seen from looking at the whole system cost. The variable parameters have a strong effect on machine cost, therefore it is possible to minimize machine cost by varying the variable parameters.

Figure 8 shows clearly that there is a field for which the machine cost is minimum. Also shown in Fig. 8 is the effect of cycle time on both the optimum field and the optimum machine cost. The machine aperture affects the machine cost at all cycle times (see Fig. 9). The difference in cost between NbTi and Nb<sub>3</sub>Sn machines is greater for larger apertures.

The optimum field increases as the cycle time increases (see Fig. 10). The Nb<sub>3</sub>Sn systems at long cycle time have a higher optimum field than the NbTi systems. The optimum field at long cycle times is strongly affected by the current density in the magnet coils. Today Nb<sub>3</sub>Sn coils have a larger coil current density than NbTi except at very low fields. A factor of two increase in current density for NbTi, which will be achieved within a year, will result in higher optimum fields and somewhat lower costs than shown in Figs. 9 and 10.

There is also an aperture and repetition rate which will result in a minimum-cost machine for a given average beam current and duty factor. Table I illustrates that the slow-cycle large-aperture machine may be very attractive from a cost standpoint. A 100 GeV storage ring was included for comparison with the accelerators. A more detailed cost breakdown of the machines shown in Table I is given in the Appendix.

A 1000 GeV accelerator and storage ring are shown in Table II. The 1000 GeV machines have a ratio of average radius to magnetic radius of 1.5 instead of 2.0. The  $v$  value for the 1000 GeV machine is approximately 100, hence the long straight sections do not take up a large part of the machine circumference. It should be noted that the 1000 GeV accelerator has an injection energy of 25 GeV and an aperture diameter of 8 cm. A storage ring is also shown in Table II for comparison with the synchrotron.

## GENERAL CONCLUSIONS AND THE EFFECT OF FUTURE DEVELOPMENTS

A number of conclusions can be drawn from the studies that have been made on the economics of superconducting synchrotrons. These conclusions will be greatly affected by changes in cost and technology of superconductors and other equipment.

This paper shows that niobium-titanium alloys are promising from a cost standpoint. If high fields are required (greater than 50 kG), Nb<sub>3</sub>Sn appears to be the cheapest material, particularly if the aperture of the magnet is small. It is not inconceivable that the quadrupoles may use Nb<sub>3</sub>Sn while the dipoles are made of NbTi. Ductility and the ability to form NbTi into a large variety of shapes are very advantageous. There are NbTi materials that could be used in storage rings today. It is quite evident, however, that more work is required on magnet design so that reliable, uniform magnets are built. Current densities achievable in NbTi materials can be expected to double in the next year or two (to 40 000 A/cm<sup>2</sup> or more in 60 kG coils). As a result NbTi will become increasingly attractive at 50 or 60 kG. There has been a downward trend in material cost, due primarily to improvement in manufacturing techniques, and the possibility of running these materials at their critical current. No definite material choice can be made at this time.

TABLE I. Cost breakdown for two 100 GeV synchrotrons and a storage ring.

	Short-cycle machine	Long-cycle machine	Storage ring
MACHINE PARAMETERS			
Final energy	100 GeV	100 GeV	100 GeV
Injection energy	5 GeV	5 GeV	---
Beam intensity	$5 \times 10^{12}$ p/sec	$5 \times 10^{12}$ p/sec	---
Magnetic field	30 kG	40 kG	45 kG
Cycle time	2.0 sec	20 sec	---
Aperture	5.0 cm	12.5 cm	12.5 cm
Material	NbTi	NbTi	NbTi
MACHINE COMPONENT COST			
Magnets	1.9 M\$	6.6 M\$	8.3 M\$
Magnet power supply	7.9 M\$	6.3 M\$	0.2 M\$
Magnet cryostat	2.5 M\$	2.1 M\$	1.9 M\$
Helium refrigeration	7.1 M\$	3.2 M\$	1.5 M\$
Rf system	2.9 M\$	2.9 M\$	0.2 M\$
Injection-extraction system	1.0 M\$	1.0 M\$	1.0 M\$
Vacuum system	0.8 M\$	0.6 M\$	0.5 M\$
Control system	1.2 M\$	1.1 M\$	0.7 M\$
Enclosure and plant facilities	12.3 M\$	8.7 M\$	7.1 M\$
SUBTOTAL COST	37.6 M\$	32.5 M\$	21.4 M\$
TOTAL COST with EDIA and contingency	56.4 M\$	48.7 M\$	32.1 M\$
YEARLY POWER COST	1.55 M\$	0.65 M\$	0.11 M\$

TABLE II. Cost estimate for a 1000 GeV synchrotron and a storage ring.

	Synchrotron	Storage ring
<b>MACHINE PARAMETERS</b>		
Final energy	1000 GeV	1000 GeV
Injection energy	25 GeV	----
Beam intensity	$3.3 \times 10^{12}$ p/sec	----
Magnetic field	40 kG	45 kG
Cycle time	30 sec	----
Aperture	8.0 cm	8.0 cm
Material	NbTi	NbTi
<b>MACHINE COMPONENT COST</b>		
Magnets	44.3 M\$	56.9 M\$
Magnet power supply	29.6 M\$	1.0 M\$
Magnet cryostat	19.2 M\$	17.9 M\$
Helium refrigerator	14.8 M\$	7.3 M\$
Rf system	28.7 M\$	0.4 M\$
Injection-extraction system	4.6 M\$	4.6 M\$
Vacuum system	3.8 M\$	3.4 M\$
Control system	7.2 M\$	4.6 M\$
Enclosure and plant facilities	63.4 M\$	52.7 M\$
<b>SUBTOTAL COST</b>	215.6 M\$	147.9 M\$
<b>TOTAL COST with EDIA and contingency</b>	323.4 M\$	216.6 M\$
<b>YEARLY POWER COST</b>	3.95 M\$	0.82 M\$

This study indicates that the magnetic field for a minimum-cost machine is lower than what is talked about by Smith<sup>2,3</sup> and Sampson.<sup>17</sup> Fields of 60 kG are high for today's technology. However, changes in material cost, superconductor current density, and the power supply may make the 60 kG field level practical (particularly for long-cycle-time machines) from an economic standpoint. It should be noted, however, that if tunnel cost and cryostat cost can be reduced below the numbers given in this paper, the optimum magnetic field will also be reduced.

This paper indicates that long cycle times are attractive even when the aperture is increased to accommodate a larger beam current. A long flat-top adds very little to the cost, but the ability to produce long beam spill has to be perfected. Superconducting magnets can be made ripple-free if they are run in the persistent mode; which may help solve long spill problems. Short cycle times are desirable for some kinds of experiments. Changes in power supply technology may make shorter cycle times more attractive. It is clear that some thought is required to find a solution that is best with respect to both physics and economics.

In conclusion the following statements can be made. (1) Superconducting technology has advanced far enough that storage rings are possible to build. (2) It appears that costs for a 50 to 100 GeV superconducting synchrotron are competitive with today's conventional machines. (A conventional bare-bones machine would cost 0.7 to 0.8 million dollars per GeV.) (3) A large economic advantage is likely to be gained when machines in the TeV (trillion electron volt) range are built. (Machine costs should be reduced by a factor of 2 or more.) (4) Changes in superconducting technology, cryogenics, and power supply technology should have a favorable effect on the projected cost of a superconducting synchrotron.

Superconductivity has a bright future, but a great deal of realistic thinking and hardware development is required before superconductivity becomes a tool of high energy physics instead of a plaything. The full utilization of superconductivity in high energy physics will require both money and manpower. We must commit ourselves to superconductivity if we are going to realize its promise.

---

17. W.B. Sampson, these Proceedings, p. 998.

# APPENDIX

## A DETAILED COST BREAKDOWN OF THE 100 GEV MACHINE SHOWN IN TABLE I

Table A. 100 GeV machine parameters

Parameter	2-second cycle accelerator	20-second cycle accelerator	Storage ring
General parameters			
Peak final energy	100 GeV	100 GeV	100 GeV
Injection energy	5 GeV	5 GeV	---
Average proton intensity	$5 \times 10^{12}$ P/sec	$5 \times 10^{12}$ P/sec	---
Peak dipole field	30 kG	40 kG	45 kG
Aperture diameter	5 cm	12.5 cm	12.5 cm
Cycle time	2 sec	20 sec	---
Detailed parameters			
Machine average radius	224.2 m	168.2 m	149.6 m
Dipole magnetic radius	112.1 m	84.1 m	74.8 m
Superconducting material	NbTi	NbTi	NbTi
Superconductor cost	$\$2.55 \times 10^{-3}/\text{Am}$	$\$3.48 \times 10^{-3}/\text{Am}$	$\$4.07 \times 10^{-3}/\text{Am}$
Coil current density	31 400 A/cm <sup>2</sup>	23 000 A/cm <sup>2</sup>	19 600 A/cm <sup>2</sup>
Dipole ampere turns	$3.57 \times 10^5$	$1.04 \times 10^6$	$1.23 \times 10^6$
Peak magnet stored energy	25.5 MJ	170.5 MJ	210.2 MJ
Peak MG set power	84.7 MVA	68.0 MVA	---
Magnet rise time	0.6 sec	5 sec	500 sec
Magnet flat-top time	0.7 sec	7 sec	---
Injection time (front porch)	0.1 sec	3 sec	---
Number of refrigerators	4	4	4
Refrigeration required	27 300 W	7600 W	2000 W
Rf power required	504 kW	605 kW	~ 20 kW
Accelerating voltage	$1.49 \times 10^6$ V/turn	$1.34 \times 10^5$ V/turn	---
Injection efficiency	95%	95%	95%
Extraction efficiency	90%	90%	90%
Total power required	19.0 MW	8.5 MW	1.5 MW
Type of site	Soil	Soil	Soil

Table B. The cost of various machine components for the  
100 GeV machine shown in Table I  
(costs in thousands of dollars)

Component	2-second cycle accelerator	20-second cycle accelerator	Storage ring
1. Magnet system			
Dipole cost	1634	5301	6608
Quadrupole cost	104	713	958
Correction magnet cost	<u>174</u>	<u>601</u>	<u>757</u>
Total magnet cost	1912	6615	8323
2. MG set power supply			
Generator cost	1012	788	18
Motor cost	131	1103	7
Rectifier cost	4113	3232	60
Flywheel cost	9	60	74
Leads and bus bar cost	1314	1031	21
Installation cost	<u>1316</u>	<u>1045</u>	<u>40</u>
Total power supply cost	7895	6259	220
3. Magnet cryostat cost	2549	2113	1885
4. Refrigeration system			
Refrigerator cost	6553	2806	1157
Transfer line cost	<u>549</u>	<u>426</u>	<u>385</u>
Total refrigeration system cost	7102	3232	1542
5. Rf system cost	2861	2906	183
6. Injection-extraction system			
Injection system cost	270	270	270
Extraction system cost	<u>725</u>	<u>725</u>	<u>725</u>
Injection-extraction system cost	995	995	995
7. Vacuum system			
Vacuum piping	235	166	147
Vacuum joints	151	122	109
Cryopumps	180	129	114
Roughing pumps	<u>211</u>	<u>159</u>	<u>141</u>
Total vacuum cost	777	576	511
8. Control system cost	1205	1135	683
9. Tunnel earthwork and plant facilities			
Tunnel cost	4651	3488	3100
Earthwork cost	3946	2960	2631
Foundation cost	1832	1374	1221
Utilities cost	<u>1903</u>	<u>846</u>	<u>132</u>
Total plant cost	12 332	8668	7084
Machine subtotal cost	37 628	32 499	21 426
50% EDIA and contingency	18 815	16 250	10 716
Total machine capital cost	56 443	48 749	32 140

Table C. Operating power and annual power cost  
for the 100 GeV machine shown in Table I

	2-second cycle accelerator	20-second cycle accelerator	Storage ring
Power required by the accelerator			
MG set power	3776 kW	2936 kW	50 kW
Refrigerator power	13 643 kW	3783 kW	975 kW
Rf station power	1890 kW	1428 kW	160 kW
Tunnel power (includes air conditioning, lights, etc.)	423 kW	317 kW	282 kW
Total power required	19 032 kW	8464 kW	1477 kW
Annual power cost @ \$0.01/kWh delivered to the equipment (cost in thousands of dollars per year)	1553	645	106

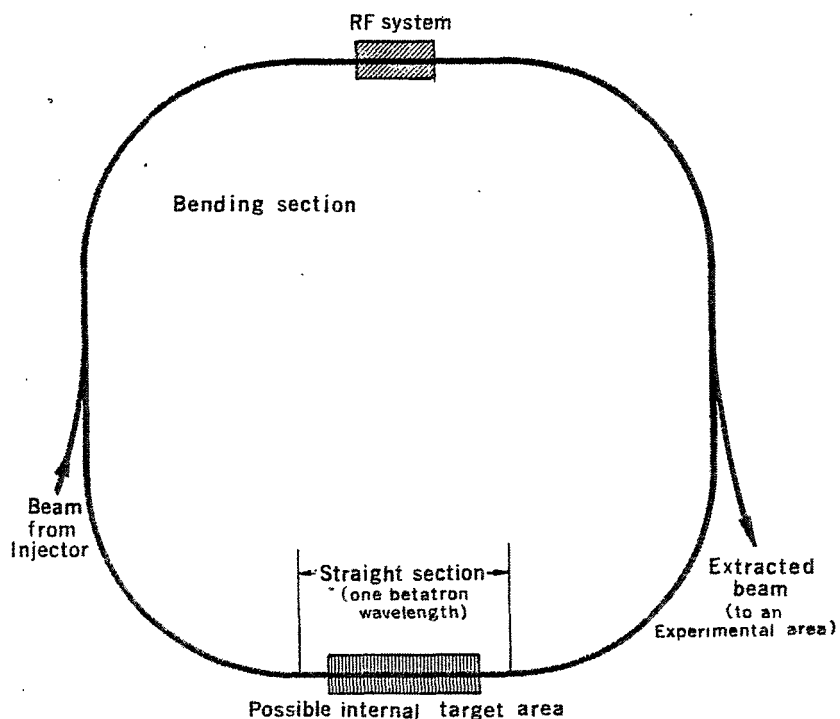


Fig. 1. A superconducting synchrotron with fourfold symmetry.

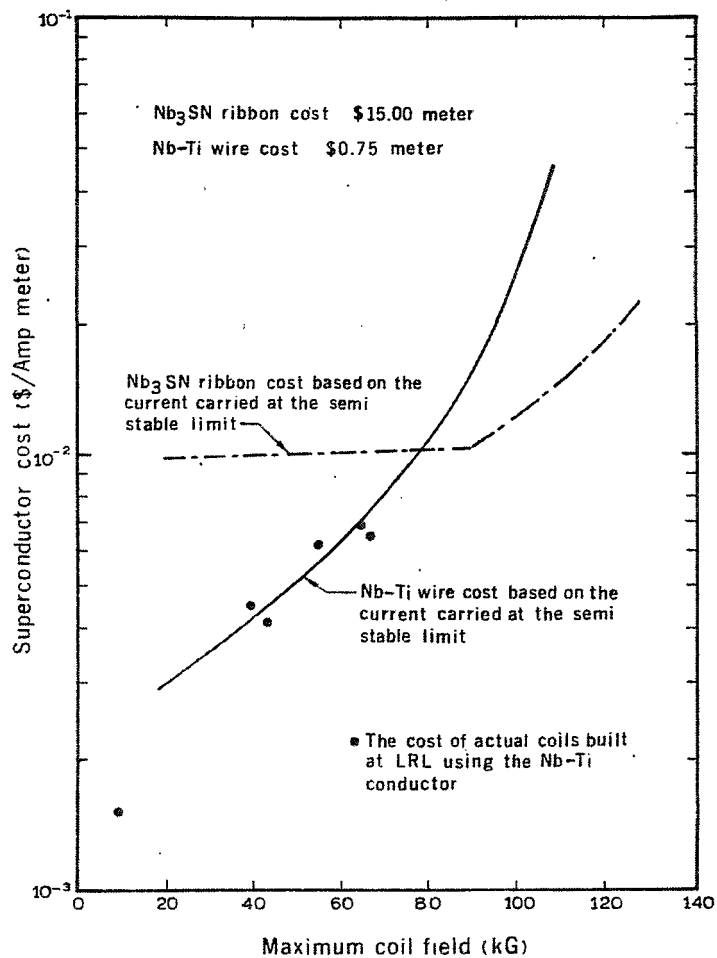


Fig. 2. The cost of a superconductor vs the maximum field in a coil winding.

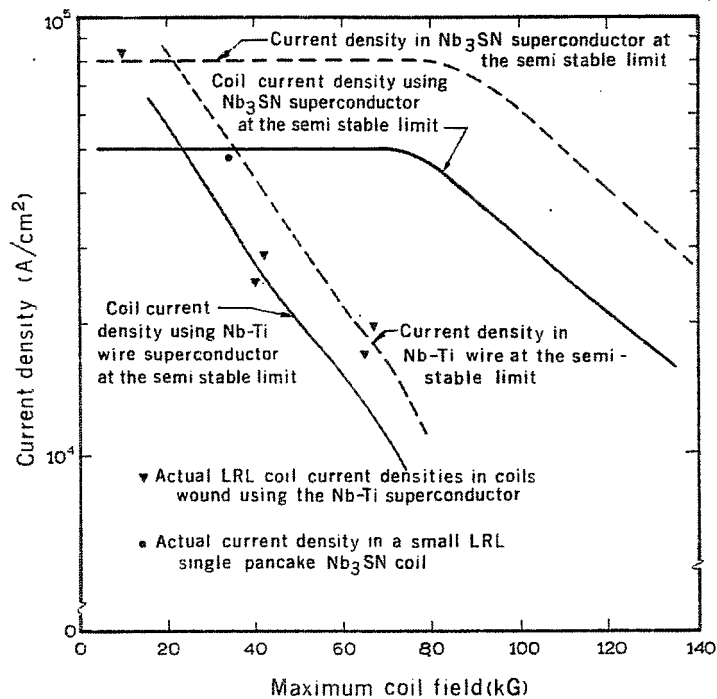
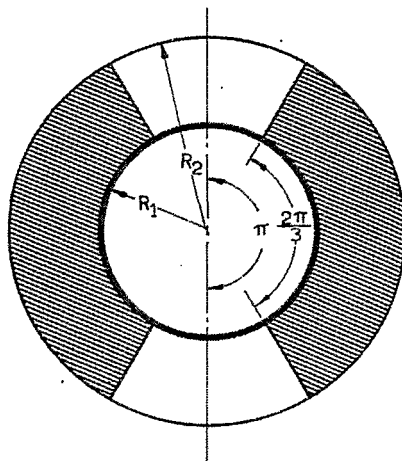


Fig. 3. Coil and superconductor current densities using NbTi and Nb<sub>3</sub>Sn high-current-density superconductors.



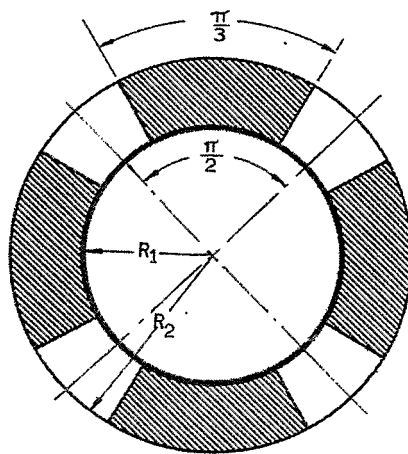


$$B_0 = \frac{\sqrt{3}}{\pi} \mu_0 J_0 (R_2 - R_1)$$

$$N_i = \frac{\pi}{3} (R_2^2 - R_1^2) J_0$$

$$A_m = 2 \left[ L_D + \frac{\pi^2}{6} (R_1 + R_2) \right] N_i$$

Fig. 4. A dipole cross section based on the 2/3 rule.



$$G = \frac{B_1}{R_1}$$

$$G = \frac{\sqrt{3}}{\pi} \mu_0 J_0 \ln \left( \frac{R_2}{R_1} \right)$$

$$N_i = \frac{\pi}{3} (R_2^2 - R_1^2) J_0$$

$$A_m = 2 \left[ L_Q + \frac{\pi^2}{12} (R_1 + R_2) \right] N_i$$

Fig. 5. A quadrupole cross section based on the 2/3 rule.

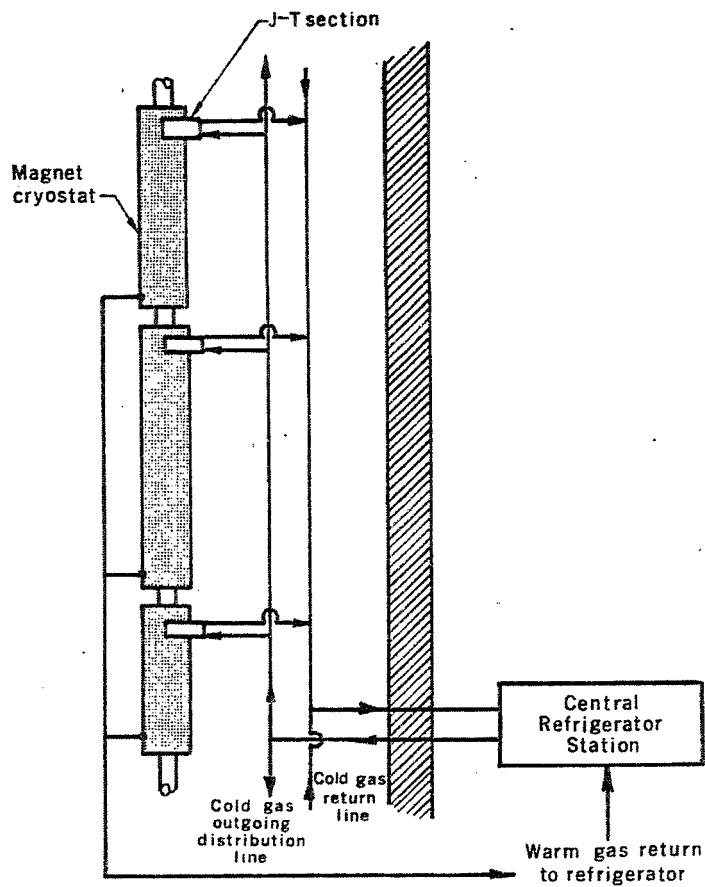


Fig. 6. A superconducting synchrotron refrigeration distribution system.

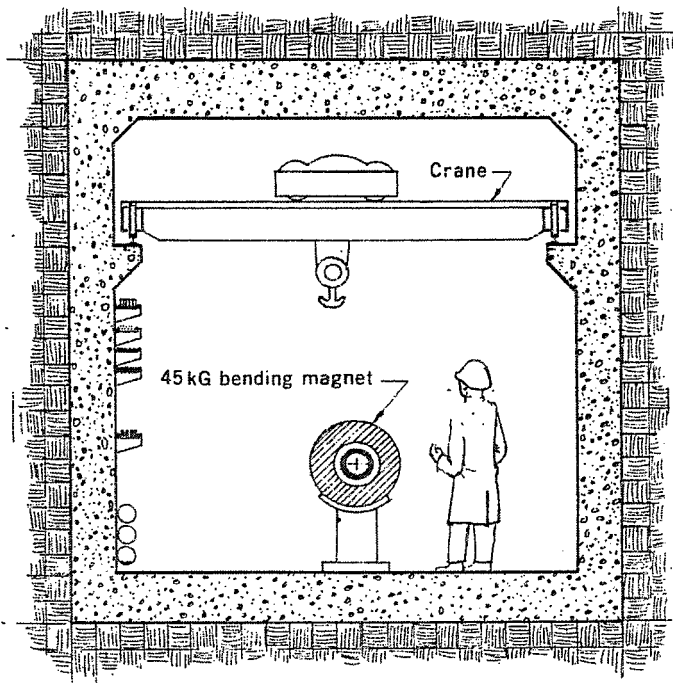


Fig. 7. A typical tunnel cross section showing a 45 kG magnet installed in the tunnel.

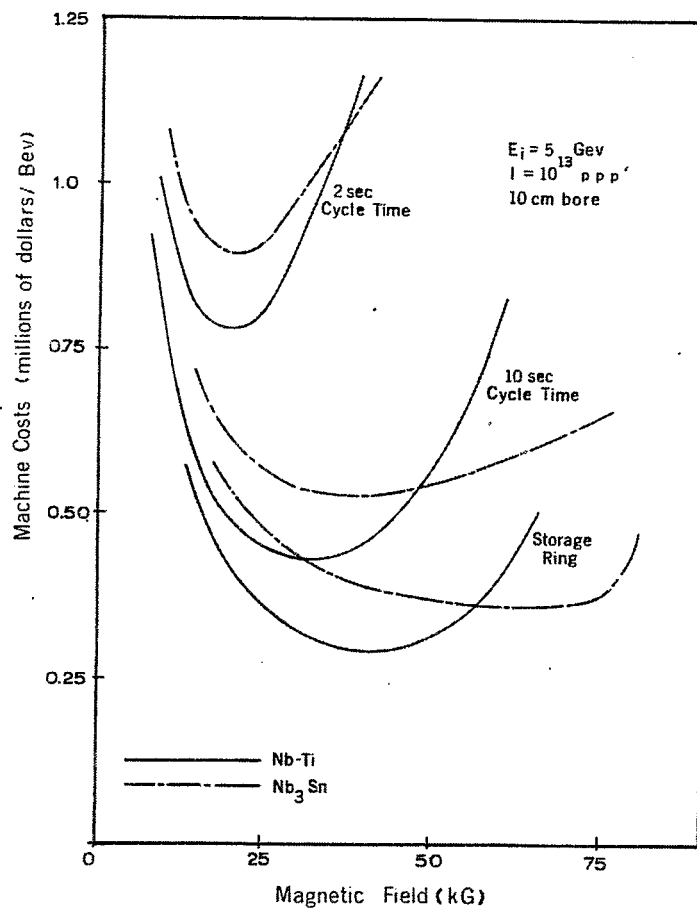


Fig. 8. The cost of a 100 GeV synchrotron vs the bending magnet field.

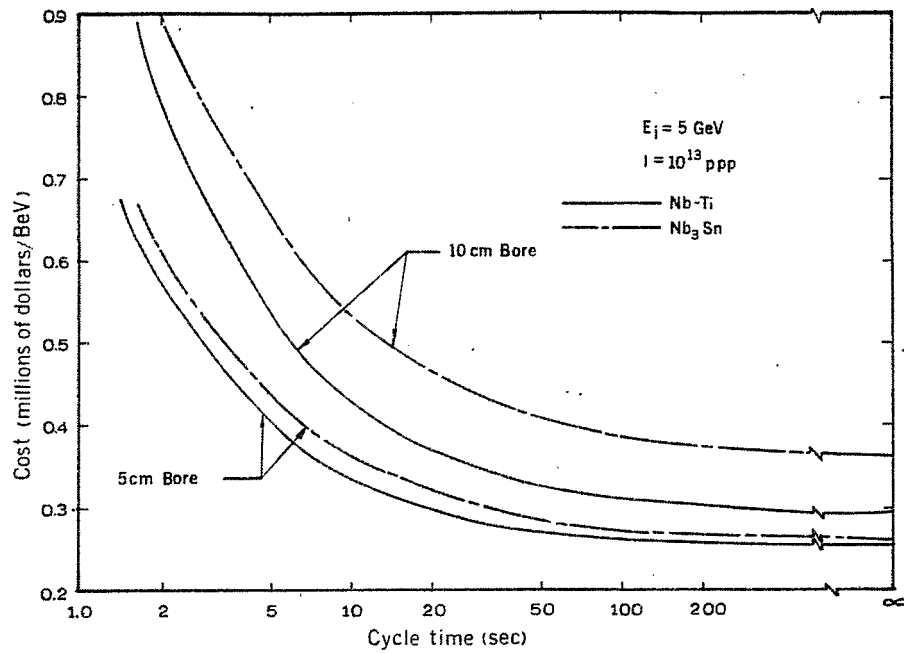


Fig. 9. The cost of a 100 GeV superconducting synchrotron at optimum magnetic field vs cycle time.

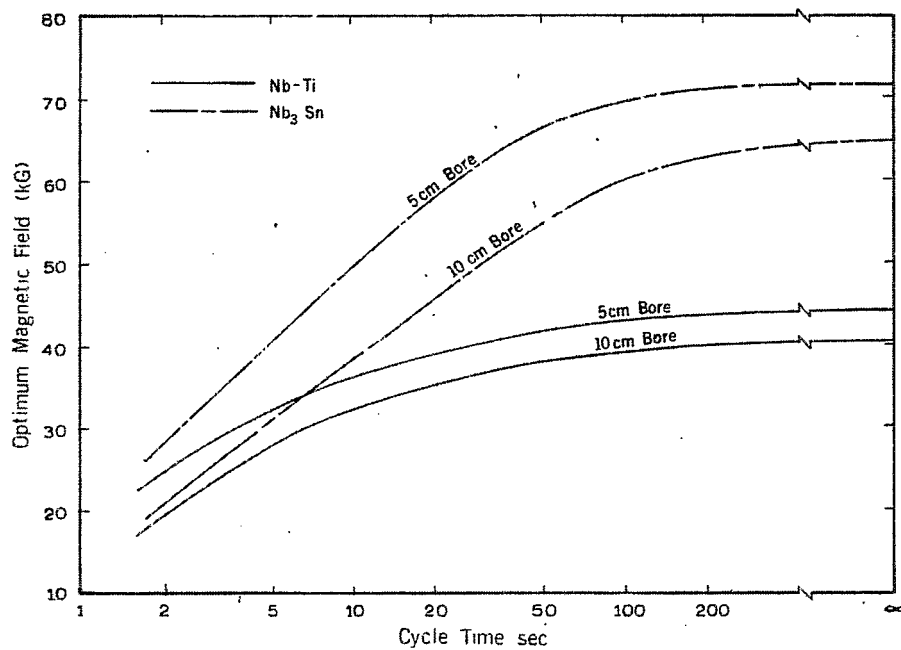


Fig. 10. Optimum magnetic field vs cycle time.

# A 2000 GEV SUPERCONDUCTING SYNCHROTRON\*

W.B. Sampson  
Brookhaven National Laboratory  
Upton, New York

## INTRODUCTION

There are so many unknowns involved in estimating the cost of a superconducting synchrotron that it is largely an academic exercise at the present time. The feasibility of such a machine is strongly dependent on the magnitude of the ac losses produced by the changing guide field, since such losses must be removed at very low temperatures, a notoriously inefficient process. There is relatively little known about how small these ac losses could be made in a practical accelerator magnet, although the subject is being studied extensively. Even if the losses are reduced to a suitable level, the reliability of both the magnets and associated cryogenic equipment has yet to be demonstrated. Despite these deficiencies in knowledge it is possible to make crude estimates of the cost of a 2000 GeV machine based on present experience and reasonable expectations for the future.

## MACHINE PARAMETERS

The machine under discussion is assumed to have the following parameters:

Energy	2000 GeV
Injection energy	30 GeV (AGS)
Radius	1.5 km
Aperture	30 cm <sup>2</sup>
Peak field	60 kG

The energy was chosen as a suitable next step after the 200 to 400 GeV machine being built at Weston. The injector is assumed to be the AGS, which might conceivably be available for such duties by the time the large machine was built. The radius and field were chosen so that the machine would fit on the present Brookhaven site and the assumption was made that 80% of the ring would be filled with bending magnets. Since the cost of both the magnets and power supply are strongly increasing functions of the aperture size, a circular aperture of approximately 3 cm radius has been chosen as the smallest reasonable size. It is possible that a saving could be made by using an intermediate ring between the injector and final ring so that the aperture could be reduced further in the main ring magnets by injecting at approximately 150 GeV.

## MAGNET DESIGN

It is assumed that the accelerator would be of the separated function type consisting of dipoles and quadrupoles arranged in a suitable array.<sup>1</sup>

---

\*Work performed under the auspices of the U.S. Atomic Energy Commission.

1. G.T. Danby et al., IEEE Trans. Nucl. Sci. NS-14, No. 3, 431 (1967).

The magnets would resemble to a considerable degree the high current density dc beam handling magnets being developed at Brookhaven,<sup>2</sup> but would be made with the low loss type of conductor which will be described in the next section. For ease of construction a circular aperture has been chosen, but an elliptical aperture could be used if orbit dynamics require more horizontal than vertical aperture. The required field configuration is obtained by arranging ribbons of conductor around the perimeter of the aperture to form a number of discrete current blocks according to the methods developed by Beth.<sup>3</sup> Shielding of the stray magnetic field is achieved by the use of a laminated iron shield which could also serve as the vacuum jacket of the Dewar. Alternatively, a set of similar windings of lower current density at a larger radius could be used to cancel the external field. The use of iron shielding, sufficiently far from the magnet to prevent saturation, leads to an increase of about 10 kG in the dipole field,<sup>4</sup> while the superconducting shield would lead to a similar reduction in field.

For a dipole field of 60 kG (50 kG without iron), a current of about  $8 \times 10^4$  A/cm of circumference is required in the high density portion of the windings. This corresponds to a current density of approximately  $6 \times 10^4$  A/cm<sup>2</sup> for a conductor width of 0.5 in. The quadrupoles would produce a gradient of about 20 kG/cm for the same current density. Figure 1 is a schematic diagram of the magnet cross section.

#### AC CONDUCTOR

While the losses produced in pulsed magnets using presently available material are rather high,<sup>5,6</sup> it seems possible to reduce such losses by a suitable subdivision of the superconductor.<sup>7</sup> A conductor configuration expected to produce low power dissipation and high current density under pulsed conditions is shown in Fig. 2. This conductor is formed by weaving alternate strands of fine stainless-steel and niobium-tin filaments to form a flat strap. The superconducting filaments are electrically separated by the stainless steel and a ceramic insulator such as boron nitride, and are transposed by the weaving process. The use of such a conductor is expected to lead to a reduction in losses of approximately an order of magnitude over presently available materials. Similar conductors could be made from insulated filaments of NbTi alloy, but they would probably be capable of somewhat lower current densities and would not be as desirable if the magnets were to operate at elevated temperatures in supercritical helium.

#### COMPONENTS

Magnets. The main ring which consists of 80% dipoles will require about  $7.5 \times 10^6$  m of superconducting ribbon capable of carrying about 1000 A.

About  $2 \times 10^6$  m of superconductor would be required for quadrupoles.

- 
2. R.B. Britton, these Proceedings, p. 893.
  3. R.A. Beth, Brookhaven National Laboratory, Accelerator Dept. Report AADD-135 (1967).
  4. J.P. Blewett, these Proceedings, p. 1042.
  5. W.B. Sampson, *ibid.*, p. 908.
  6. G.H. Morgan and P.F. Dahl, *ibid.*, p. 559.
  7. P.F. Smith, *ibid.*, p. 913.

Power Supply. The stored energy of the synchrotron is equal to about 100 kJ/m which represents a total stored energy in the ring of some 750 MJ. Since the power supply must be capable of supplying this much energy in a time equal to the rise time, or approximately one half of the cycle time, the power supply must have a rating of:

$$\text{Power supply} = \frac{750 \times 10^6}{t/2} = 300 \text{ MVA for } t = 5 \text{ sec.}$$

It should be noted here that a superconducting synchrotron is especially suited to low repetition rate operation since the energy loss per cycle is independent of frequency (Refs. 5, 6). It is also possible in principle to have very long flat-tops since little or no energy is required to maintain peak field.

It is possible that the cost of the power supply could be reduced by using superconducting technology<sup>8</sup> especially in view of the fact that the additional refrigeration will be relatively inexpensive due to the large installation required for the synchrotron magnets themselves.

#### REFRIGERATOR

The size of the refrigerator required is determined almost entirely by the ac losses in the magnets since other sources of heat production such as lead loss and beam radiation can probably be made comparatively low by careful design. It is convenient to express the losses produced in the magnets by an effective "Q" defined here as the energy loss per cycle divided into the total stored energy. The losses are then given by

$$\text{ac loss} = \frac{750}{Q} \text{ MJ/cycle}$$

The "Q" of presently available superconducting coils is approximately 200, and if we assume a factor of ten improvement using special conductor, this should give a "Q" close to 2000. The loss then is 375 kJ per pulse which for a repetition rate of once in 5 sec equals 150 kW of refrigeration.

Assuming the most optimum refrigerator efficiency of 30% Carnot,<sup>8</sup> this machine would require 40 MVA for operation.

#### CONCLUSIONS

The feasibility of such a machine depends on the possibility of producing a conductor capable of being wound into magnets of very high "Q". If, in addition, such material could be produced at a price lower than \$5/m, important savings would be possible.

A point of considerable importance concerning pulsed superconducting magnets is that the loss/cycle is independent of repetition rate. Thus a very high energy machine designed for slow cycling could be used at lower energies with a reasonable cycling time and at very high energies with a few pulses/minute. When it became apparent what sort of physics would be done at very high energies and when the required experimental equipment was more fully developed, the power supply and refrigerator of the machine could be upgraded to improve the repetition rate. The superconducting machine is ideally suited for this type of operation since its power requirements vary linearly with repetition rate.

---

8. S.C. Collins, these Proceedings, p. 59.

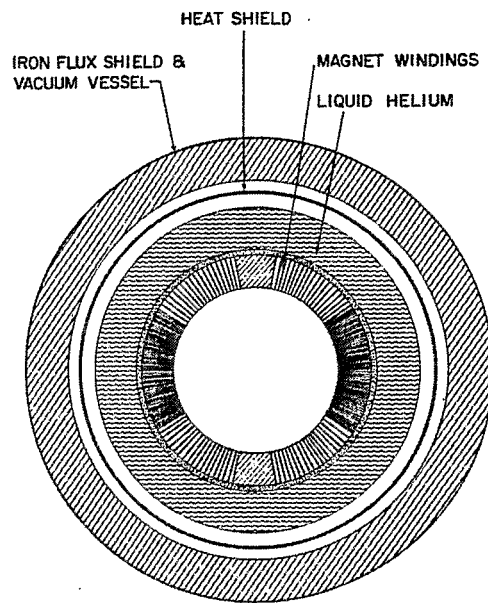


Fig. 1. Schematic drawing of cross section of superconducting accelerator.

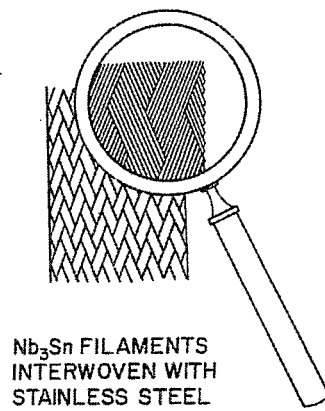


Fig. 2. Low loss ac superconductor.



# SYNCHROTRON POWER SUPPLIES USING SUPERCONDUCTING ENERGY STORAGE

P.F. Smith  
Rutherford Laboratory  
Chilton, Berks., England

## I. INTRODUCTION

The possibility of using energy storage in superconducting coils as the basis of a synchrotron power supply was discussed in a previous paper.<sup>1</sup> The present report re-introduces the idea for comment and discussion, with comments on one or two relatively minor additions to the theory. No significant improvements on the original version of the idea have been achieved, and no assessment has yet been made of its practical feasibility.

This line of thought arises immediately from work on superconducting synchrotron magnets. The energy stored in the latter would be typically at least four times that of conventional magnets (i.e., probably  $\sim 1$  MJ/GeV or more). This not only leads to an undesirably high power supply cost, but also, for very high energy accelerators requiring  $10^8$ - $10^9$  joules, may pose basic problems of feasibility and reliability. (Some authoritative comments on the feasibility of conventional supplies in this energy range would be of value.)

On the other hand, the problem is simplified by the fact that the energy lost per cycle will be very small, and there will be no dc power requirements for "flat top" operation. Under these circumstances there arises the obvious concept of using a superconducting coil storing the same energy as the synchrotron magnet, with some means of transferring the energy from one to the other. Favorable economics results basically from the fact that a single large coil can store energy much more efficiently and cheaply than the large number of small magnets which constitute the synchrotron magnet ring. Nevertheless, over-all economics will obviously depend very much on the efficiency and cost of the energy transfer scheme. In the conventional motor-alternator-rectifier schemes, for example, only about 10% of the flywheel energy is utilized, and the rectifier conversion equipment represents typically half the total cost. The cost of the conventional system is indicated by curve (d) of Fig. 1, as a function of energy transferred. Curve (a) shows the present cost of superconducting coils, which, at the optimum field  $\sim 50$  kG, is about  $\pounds 1$  to  $\pounds 1.5 \times$  (stored energy in joules)<sup>2/3</sup>. Comparison of the two curves in the  $10^8$ - $10^9$  joule region, suggests that we have at least a factor of 10 available to turn the basic superconducting coil into a synchrotron power supply.

## II. ENERGY TRANSFER

Several elementary ways of transferring energy between inductances were discussed in Ref. 1. Most of these involved either appreciable losses or a second energy storage system of a different type (capacitor bank, mechanical system, etc.). The exception was the system of coupled coils shown in Fig. 2. All coils are assumed superconducting, and by appropriate variation of the two coupling coefficients  $k_a$  and  $k_b$ , not only can energy be transferred to and from  $L_g$  (which represents the synchrotron magnet), but in addition the total energy of the system can be kept constant. The process is then completely reversible, and no external work is necessary during any part of the cycle.

---

1. P.F. Smith, in Proc. 2nd Magnet Technology Conference, Oxford, 1967, p. 589.

The simplest solution is when  $L_2 = L_3$ ,  $L_4 = L_5$ , and  $I_1$  is constant. The condition for constant total energy is then

$$k_a^2 + k_b^2 = \text{constant} \quad , \quad (1)$$

where the coupling coefficients are defined in the usual way by  $M_{xy} = k_{xy} (L_x L_y)^{\frac{1}{2}}$ . Zero coupling between  $L_2$  and  $L_3$  is assumed.

For this solution,  $I_2 \propto k_a$  and  $I_3 \propto k_b$ , so that the net effect is simply a reversible interchange of energy between  $L_4$  and  $L_5$ . But although  $L_1$  appears to have a completely passive role in the circuit, it is in fact the largest coil; its stored energy is minimized when  $L_2 = L_3 = L_4 = L_5$ , and is given by

$$\frac{L_1 I_1^2}{L_5 I_2^2 (\text{max})} = \frac{4}{k_m^2} \quad , \quad (2)$$

where  $k_m$  is the maximum value of  $k_a$  or  $k_b$ , and, of course,  $k_m$  must be  $< 1$ .

The stored energy in all the coils can, in principle, be halved by using a synchrotron magnet with a dc bias, and allowing both positive and negative currents in the ac coils. However, the use of separate dc and ac magnets, Fig. 3a, is probably ruled out by the particle dynamics, and the use of superimposed dc and ac windings, with a scheme such as that shown in Fig. 3b, alters Eq. (1) to  $(k_a - k_0)^2 + k_b^2 = \text{const.}$ , which seems to be more difficult to achieve in practice. Nevertheless something along these lines might well be devised.

### III. PRACTICAL SYSTEMS

From Eq. (1), by analogy with the geometric relationship  $\cos^2 \theta + \sin^2 \theta = 1$ , one is led immediately to a simple practical representation of the above circuit, shown in Fig. 4.  $L_2$  and  $L_3$  are mutually perpendicular, rigidly connected, and rotate on a common shaft in the field produced by  $L_1$ . They constitute a mechanically coupled motor and dynamo; provided  $k_a$  and  $k_b$  remain exactly proportional to  $\sin \theta$  and  $\cos \theta$  the forces on  $L_2$  and  $L_3$  are always equal and opposite, and no force is necessary to rotate the system except that required to overcome inertia and friction. Alternatively, of course,  $L_2$  and  $L_3$  may remain fixed while  $L_1$  rotates.

Notice that in the absence of resistance the equations do not contain the time variable. If the rotation is stopped the currents simply remain constant. By programmed rotation or oscillation of the shaft, therefore, any desired current waveform can be fed into  $L_5$ . The initial currents in  $L_1$ ,  $L_3$ , and  $L_4$ , are established by means of dc supplies and superconducting switches.

In the previous paper it was pessimistically assumed that the maximum value of  $k^2$  likely to be achieved was  $\sim 0.5$ . This is true for a configuration of the shape indicated in Fig. 3, but further work has shown that much better coupling could be achieved by using approximations to ideal spherical coils, i.e., with a  $\sin \theta$  distribution of current producing a uniform internal field. For two such concentric windings, of mean radii  $R_1$  and  $R_2$ , the maximum coupling is  $(R_2/R_1)^{3/2}$ , so that for very large coils values of  $k^2$  in the region 0.7 to 0.8 can be envisaged.

As an example, consider a power supply for a 200 GeV superconducting synchrotron magnet storing  $2 \times 10^8$  joules. Assuming a maximum  $k^2$  of 0.7, and no dc bias scheme, the stored energy of  $L_1$  would be  $\sim 1.2 \times 10^9$  joules. At 50 kG, this would be a coil

of radius 240 cm (for a spherical coil  $E = H^2 a^3/3 \times 10^7$ ) costing perhaps  $\pounds 1.5 \times 10^6$ .  $L_2$ ,  $L_3$  and  $L_4$  are  $2 \times 10^8$  joule coils and would bring the total cost up to about  $\pounds 3 \times 10^6$ , plus control and ancillary equipment. It is, however, not clear whether required topological arrangement of  $L_2$  and  $L_3$  can be achieved without significantly decreasing the coupling to  $L_1$ . It may also prove desirable to split the system into several smaller units, which would further increase the cost. Nevertheless these figures suggest that the system may still be competitive with a conventional power supply, which, for  $2 \times 10^8$  joules, might cost about  $\pounds 8 \times 10^6$ .

The ac loss in the superconductor presents much less of a problem than in the synchrotron itself; since it is relatively small in the largest coil  $L_1$ , through which the total flux and current remain constant and only local field variations occur. The loss is sufficient to rule out the use of existing conductors in  $L_2$ ,  $L_3$ , and  $L_4$ , but reduction of the filament size to  $\sim 1$  mil should be sufficient, compared with the 0.2 to 0.4 mil needed for the synchrotron magnet.

Apart from this, very few of the practical aspects of the system have been considered. One major problem, for example, is likely to be the internal stresses, since the forces on  $L_2$  and  $L_3$ , although equal and opposite, are extremely large. Other problems arise from the small losses present in any real system, and from the usual need to subdivide the magnet ring and ensure equality of the parallel currents.

It was originally hoped that a substantial reduction in the size of the  $L_1$   $L_2$   $L_3$  energy transfer system would be possible by devising a multiply-cycled arrangement in which the energy was transferred in smaller increments. So far, no such system has been discovered. The basic reason for this is that the circuit equations require that certain sums of flux terms (of the form  $L_x I_y$ ,  $M_{xy} I_y$ ) remain constant; at the same time we require that the total energy (i.e., the sum of terms of the form  $L_x I_x^2$ ,  $M_{xy} I_x I_y$ ) also remains constant. It is clearly impossible to satisfy these two requirements if the circuit contains only  $L_4$ ,  $L_5$ , and an arbitrarily small energy transfer device, but a rigorous proof of the minimum size of the latter has not been obtained.

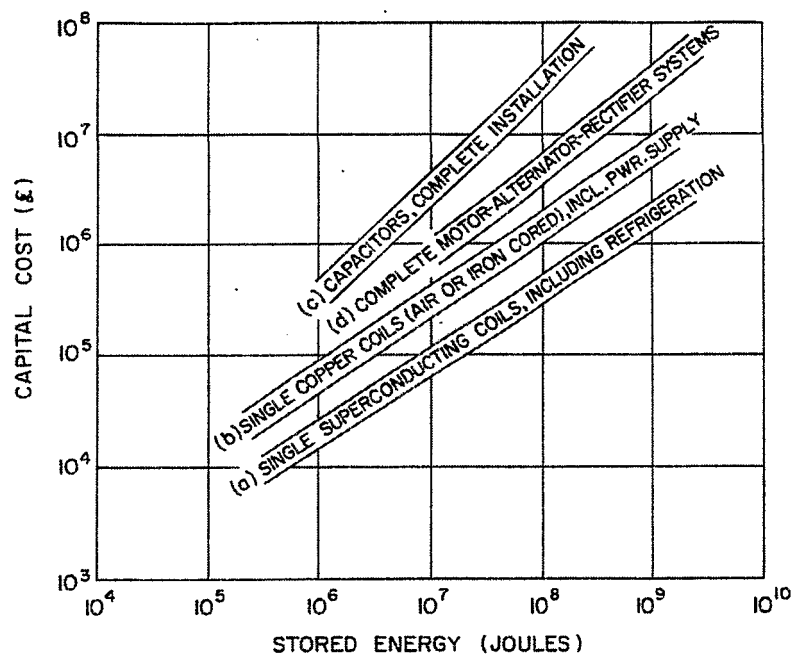


Fig. 1. (a), (b) and (c). Approximate cost of energy storage systems. (d). Cost of conventional synchrotron power supplies as a function of energy transferred.

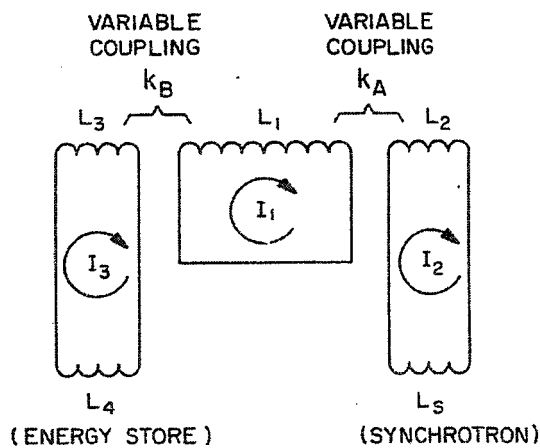


Fig. 2. Constant energy system.

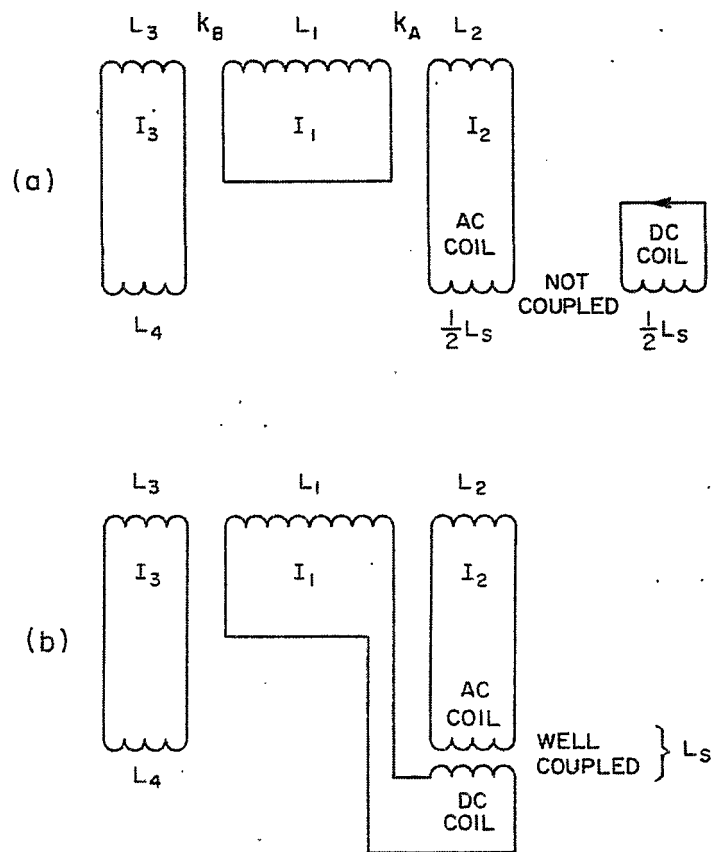


Fig. 3. Dc-biased systems.

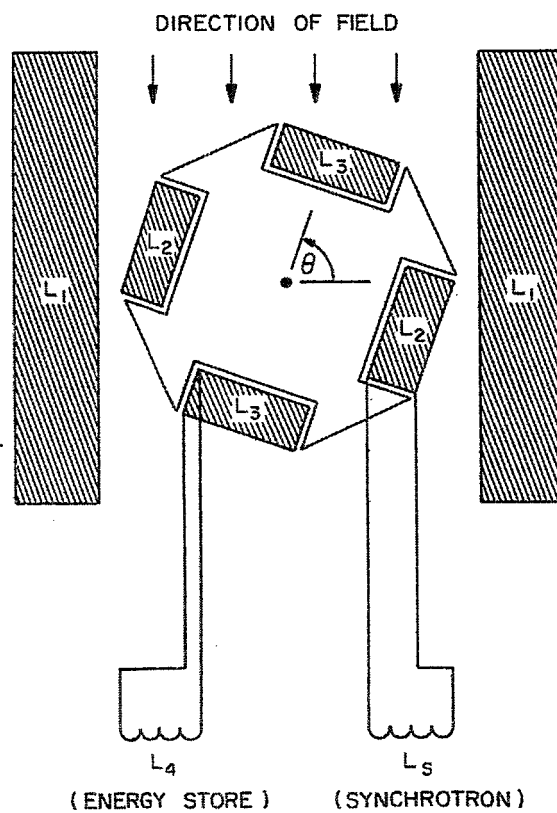


Fig. 4. Motor-dynamo representation.

## SOME AC LOSS DETERMINATIONS BY AN ELECTRICAL MULTIPLIER METHOD\*

W.S. Gilbert  
Lawrence Radiation Laboratory  
Berkeley, California

At the Lawrence Radiation Laboratory in Berkeley we have been measuring cyclic losses in various superconducting magnets with an electrical multiplier method, currently employing Hall effect multipliers. In the range of 1-5 W power dissipation, the evolved helium gas has been monitored to provide a check on the electrical method. The method and test results on several solenoids were presented by Voelker at this Summer Study<sup>1</sup> and pertinent details will be found in his report.

The particular magnet of interest for this talk is a solenoid 4.5 in. long, with a 1.5 in. bore and a 4.5 in. o.d., wound with single core NbTi Supercon wire. The wire core size is 15 mils and the conductor is 30 mils over-all, giving a copper-to-superconductor ratio of 3:1. The wire is insulated by forming a copper oxide coating and fiberglass cloth is used for interlayer insulation. The coil, operated at short sample characteristics, was definitely understabilized. The field was 67 kG on the axis and a few percent higher at the conductor. The average current density is  $\bar{J} = 18\,000\text{ A/cm}^2$  and the gross filling factor is  $\lambda = 0.18$ . Therefore, it seems quite reasonable that if one can increase the amount of superconductor per unit volume,  $\lambda = 0.5$  has been mentioned,  $\bar{J} = 50\,000\text{ A/cm}^2$  seems achievable. Other coils with less copper and NbTi cores have yielded  $\bar{J} > 30\,000\text{ A/cm}^2$  and a single layer solenoid for which the field was only about 6 kG gave  $\bar{J} \approx 85\,000\text{ A/cm}^2$ .

Figure 1 shows the loss/cycle vs frequency for this coil at  $I_{\max} = 10\text{ A}$  and  $15\text{ A}$ . The loss at low frequency is about what one would expect for loss in the 15 mil diameter superconductor. The dependence of loss on frequency has been something of a mystery to us. Eddy current losses in the copper would give the same frequency dependence but are some 50 times smaller than the measured frequency-dependent term. We were unable to find any low resistance shorts, which would yield the same type of data. Smith and Sampson have both pointed out that a number of high resistance shorts could give the same type of results and that our insulating technique might be subject to this condition.

An identical magnet using a multicore conductor made by Airco was tested to give a measure of the effect of core filament size. There were 131 approximately 1.3 mil cores uniformly distributed in the copper matrix. These measurements were made last week before I heard Peter Smith talk, and so perhaps I may be forgiven for thinking, at that time, that his theories on multicore conductor behavior might not be correct. The direct comparison of the Airco and Supercon magnets might then yield the following possible results:

- 1) If Smith were wrong and the loss simply depended on filament size,  $L_{\text{Airco}}/L_{\text{Supercon}} \approx 1/10$ .
- 2) If the normal material tied the superconductor together so that it acted as one core,  $L_A/L_S \approx 1$ .
- 3) If Smith were correct,  $L_A/L_S \approx 2$ .

---

\*Work performed under the auspices of the U.S. Atomic Energy Commission.

1. F. Voelker, these Proceedings, p. 550.

Examination of Fig. 1 shows less frequency dependence in the Airco magnet case than in the Supercon magnet case. If one makes the assumption that in both cases the frequency dependence is due to high resistance shorts, then the relevant loss data is found at the low frequency end of the curves. Then the Airco magnet losses are approximately twice those of the Supercon magnet. For single cycle measurements up to  $I_{\max} = 100$  A (some 57 kG) this same factor of two persists. Therefore, alternative 3) above is the proper one and Smith's suggested solutions to the ac loss problem are the most reasonable to pursue at this time.

A most striking advantage of the Airco magnet as compared with the Supercon magnet was the absence of flux jumps in the small filament Airco case. In both magnets  $\dot{B}$  coils were used to monitor field changes and flux jumps could easily be observed in the Supercon material when the field was changed at a rate greater than a few kilogauss per second. This is a relatively fast charge rate and this magnet is considered reliable, stable, only slightly charge rate sensitive, and generally quite satisfactory. In the Airco case we could not induce measurable flux jumps at even greater rates of field change and so the material seems to be intrinsically stable, as Smith also predicts.

We have also tested an Nb<sub>3</sub>Sn ribbon pancake wound with RCA 600 tape. We used a fiberglass tape for insulation and achieved  $I_c = 1284$  A, or  $48\,000$  A/cm<sup>2</sup> at 52 kG, which is on the short sample curve. The pulse loss data are shown in Fig. 2. The low frequency data are incorrect due to power supply ripple and the curve is dotted in this region. We get agreement with Sampson in the low, 300 A range. Our magnet went normal in the 0.5-1.5 W range while he was able to dissipate 5.5 W. Our Q's at high current were quite low as compared with Sampson's. The most probable reason for the difference is our having high resistance shorts in our pancake.

#### CONCLUSIONS

- 1) High average current density in NbTi systems, above  $50\,000$  A/cm<sup>2</sup>, seem readily achievable if the fraction of stabilizing material can be reduced.
- 2) Losses small enough to make pulsed accelerators attractive have not yet been demonstrated but might well be within a year if experimental programs under way continue to confirm Smith's theory.
- 3) Multicore conductor with large (15 mil) cores is degraded when wound into magnets, not because of heat added through cyclic loss (which we measured) but because of flux jumps.

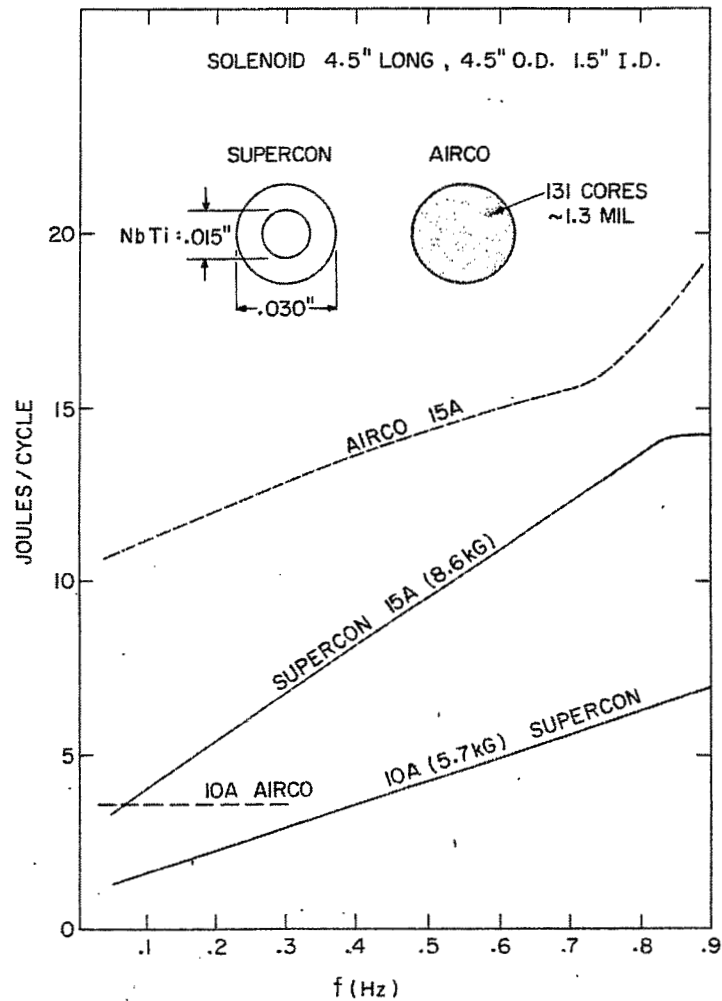


Fig. 1. Loss/cycle vs frequency for 2 solenoids.



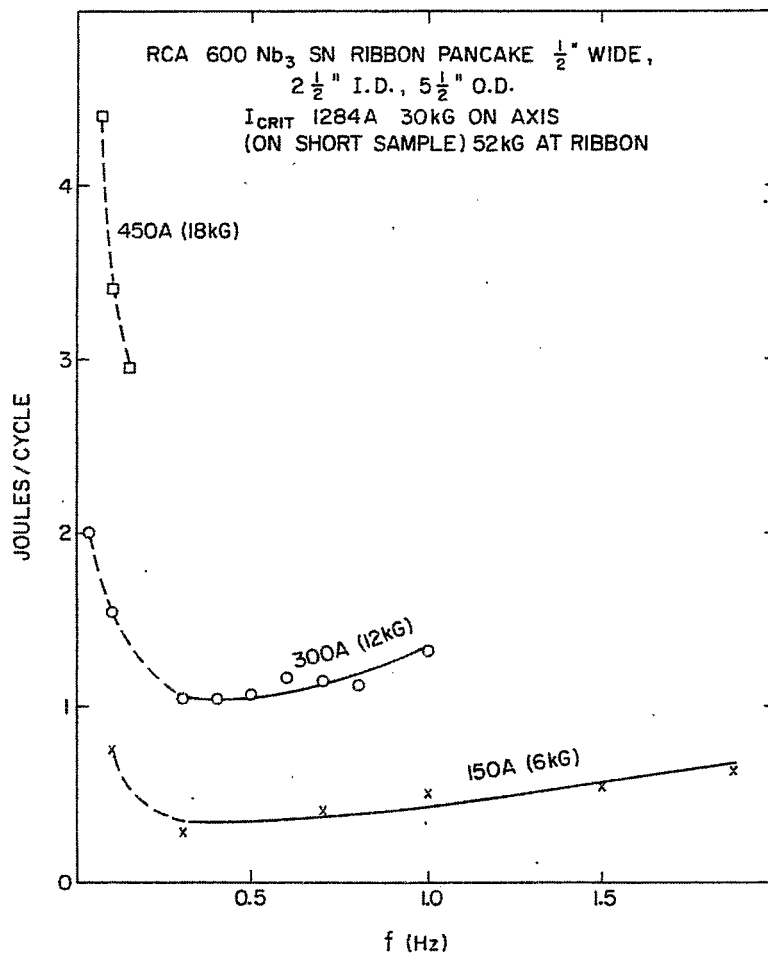


Fig. 2. Loss/cycle vs frequency in an Nb<sub>3</sub>Sn ribbon pancake.

# RADIATION EFFECTS ON SUPERCONDUCTING MAGNETS\*

H. Brechna

Stanford Linear Accelerator Center  
Stanford University, Stanford, California

## I. INTRODUCTION

When subjected to nuclear radiation, superconducting materials, normal metals, structural materials, insulation and the cooling media — in short, the superconducting magnet system — exhibit changes where physical and mechanical properties are altered, modified or degraded. The changes depend on the type of particles, the intensity, spread and distribution of the beam, the irradiation pattern, and the type of material being irradiated.

In order to study radiation effects on a superconducting magnet in a systematic way, the following areas where obvious modifications are encountered are summarized.

- 1) Physical and metallurgical properties of superconducting type II materials are changed.
- 2) Mechanical, electrical and thermal properties of normal shunt materials, thermoelectrically bonded to the superconductor, are altered.
- 3) Structural and coil supporting materials are affected.
- 4) Organic insulation used between turns and between coils and ground is degraded.
- 5) The coolant, such as helium, is contaminated, and isotopes are produced.
- 6) Coolant is evaporated at an accelerated rate, and mass transfer between liquid and gas is enhanced.

The mechanisms responsible for large transport currents in type II superconductors are attributed mainly to cold-working and introduction of defect structures, and through enhancement of the pinning force. Controlled introduction of impurities results in enhancement of current density. Precipitated impurities affect the current density in a reproducible manner.<sup>1</sup>

The primary effect of nuclear radiation is the introduction in the lattice structure of simple defects which affect the critical supercurrent, the upper critical field and the critical temperature.

When irradiated at a temperature below transition value, low-current, high-field type II superconductors generally show an enhancement in their critical current density  $J_c$ ; high-current-density superconductors exhibit either no change or a reduction in their current-carrying capacity — e.g.,  $Nb_3Sn$  shows generally an improvement in  $J_c$  when irradiated, while irradiated  $NbTi$  exhibits a reduction in current-carrying capacity when irradiated at  $T < T_c$ .

---

\*Work supported by the U.S. Atomic Energy Commission.

1. H.T. Coffey et al., Phys. Rev. 155, 355 (1967).

Normal shunt materials (Cu, Al, Ag) become brittle. Their electrical resistivity is increased, thermal conductivity reduced.

Organic materials used to insulate conductors and coils show embrittlement and become crush sensitive. When insulation properties are degraded, interturn and inter-layer short circuits are produced, affecting over-all magnet charging time. If the short circuits are localized in one area, the magnet energy will be dissipated in case of a quench into this area, causing extensive damage to the magnet.

Liquid helium boil-off is generally enhanced. Even if the additional helium evaporation is moderate, in case of localized irradiation, isotopes, such as tritium, hydrogen, etc., are produced which, in frozen condition, may restrict coolant passages and affect operational reliability.

The study presented in this paper is at a very preliminary stage and is by no means complete. Considerably more work is needed to predict the lifetime of a magnet, operating in a radiation environment. However, the data presented should shed some light on this complex subject in order to determine the magnet degradation and predict operational stability.

## II. INDUCED RADIOACTIVITY

Induced activity exists in almost any accelerator. Radiation encountered includes fast and thermal neutrons, gammas, electrons and positrons, and protons. In electron accelerators, the electromagnetic shower develops in a short distance. Activation due to neutron capture reaction is less severe than in proton machines of equal power because of cross section for nuclear interaction. However, ionizing radiation fields are much larger.<sup>2</sup>

"Meson factories" produce a localized source of fast neutrons. High energy proton machines produce intense fast neutrons. But the shower is spread over large volumes and thus is less damaging.

In designing specific beam transport and septum magnets, dipole coils, etc., one important problem is the knowledge of the beam pattern throughout the system. In areas where the beam is deliberately absorbed, intense activation will exist. Penetration, scattering and "tails" of energy spectra are encountered around slits and collimators, as well as around targets. Activation due to beam absorbers exists in other locations of the system, endangering the long-term reliability of equipment and magnets.

Exact prediction of beam losses is difficult, but activity measurements in the early life of accelerators may reveal areas of high activation, where, if possible, appropriate measurements may be taken. Long-term continuous radiation measurements will yield undoubtedly the average integrated dose rates, which in turn are important to predict lifetime of equipment. Several systems of dosimeters are currently being utilized with good success in "danger" areas.<sup>3,4</sup>

To a certain extent, quantitative data on radiation properties of ferrous and non-ferrous materials, insulations, and superconductive type II materials are available at cryogenic temperatures. Although sketchy and not complete, they give a first-order

---

2. R.E. Taylor, IEEE Trans. Nucl. Sci. NS-12, No. 3, 846 (1965).

3. R. Sheldon, Rutherford High Energy Laboratory (1966).

4. M.H. Van de Voorde, Report CERN 67-14 (1967).

estimation of the average life expectancy of magnets. More information on material properties when irradiated at 2-10°K is urgently required, when superconducting magnets are introduced in vital areas of high-energy accelerators.

In order to present some quantitative data on beam losses, one may simulate the "deliberate" beam absorption by means of collimators, slits, or by accidental beam missteering in linear machines or beam switchyards by means of "thick target" studies, where the target length and radial extension exceed several radiation lengths. A charged particle, traversing the magnet, undergoes a large number of collisions, most of which produce small angular deflections. The particles lose energy by collision (pair production) and radiation. Exact estimates of the average dose rate are difficult and we use simplified models. Careful radiation mapping will give a good estimate of dose rates, specifically incident to beam entry direction and perpendicular to it.

Activation due to partial beam absorption by means of thin targets is also of importance.

In the following, we treat each case in more detail.

### 1. Thick Targets

Any obstacle in the path of the beam having dimensions of several radiation lengths in axial  $X_0$  (beam direction) and radial  $X_m$  directions (perpendicular to beam direction), being able to absorb most of the incident beam, can be considered as a thick target. Three types of particles are observed in conjunction with them:

a. Gammas. Measurements by DeStaebler et al.<sup>5</sup> indicate that induced dose rates for gammas are independent of the beam energy as first approximation (Fig. 1) and of the target material. For a cylindrical target having a length of  $17 X_0$  and a radius of  $3.6 X_m$ , Jenkins<sup>6</sup> measured for  $\theta = 0$  a dose rate of

$$2 \times 10^5 \frac{\text{rad}}{\text{h}} \cdot \frac{\text{m}^2}{\text{kW}}.$$

As seen from Fig. 2, the energy spread over  $4\pi$  sr is fairly isotropic. If we assume that 1% of the total energy escapes radially (Fig. 1), an average dose of

$$\bar{D} = 10^3 \frac{\text{rad}}{\text{h}} \cdot \frac{\text{m}^2}{\text{kW}}$$

can be calculated. To give an example, we assume that a coil is located 5 m from the thick target, where a beam power of 10 kW is absorbed. Generally the magnet dimensions are large enough that we can assume that all scattered particles may collide with the coil surface perpendicular to the incident beam direction.

A radiation dose rate  $D$  (rad/h) is equivalent to

$$\frac{D}{3.6 \times 10^8} \frac{\text{W}}{\text{g}}.$$

---

5. H. DeStaebler et al., The Stanford Two-Mile Accelerator (W.A. Benjamin Publishing Co., 1968), Chap. 26, p. 1029.

6. T.M. Jenkins, Report SLAC-PUB-432, to be published in Health Physics (1968).

The beam power induced by the scattered beam dissipated in a volume V of the magnet is given by

$$P_d = \frac{1}{3.6 \times 10^8} \int_V D \delta(V) dV \quad (W) \quad (1)$$

If the total dose rate D is absorbed by the coil and we estimate for the density  $\delta$  of the coil an average value of  $5 \text{ g/cm}^3$ , the power dissipated is

$$P_d = 1.388 \times 10^{-8} \bar{D} V$$

This additional power must be absorbed by the coolant. The integrated dose rate for this particular case can be calculated from:

$$d = 0.4 \times 10^3 \text{ rad/h}$$

b. Fast neutrons. Except in the forward direction, where production of muons becomes significant, neutrons with energies of 200-500 MeV dominate in high-energy accelerators. Higher energy neutrons are scarce because there are very few high-energy photons. Neutrons with lower energies have short attenuation distances and are more readily absorbed.

Neutron fluxes in the giant resonance region were measured at SLAC,<sup>6</sup> indicating that it is isotropic within a factor of 2.5 or better, if the effect of back-scatter is added. At an angle of  $90^\circ$  with respect to the incident beam, a neutron flux of  $1.25 \times 10^{12} \text{ n/sec/kW}$  could be measured. Assuming the flux distribution is isotropic, the flux at one-meter distance is expressed by

$$\phi = \frac{1.25 \times 10^{12}}{4\pi \times 10^4} \frac{\text{n}}{\text{sec} \cdot \text{kW}} \quad (2)$$

The neutron dose for 1 kW beam power at 1 m distance at 2-3 MeV peak neutron energies is given by:

$$\begin{aligned} \bar{D}_N &= \frac{1.25 \times 10^{12}}{4\pi \times 10^4} \times 6 \times 10^{-9} \times 3.6 \times 10^3 \\ &\cong 2.5 \times 10^2 \frac{\text{rad}}{\text{h}} \cdot \frac{\text{m}^2}{\text{kW}} \end{aligned}$$

(We use the conversion factor  $6 \times 10^{-9} \text{ rad/n/cm}^2$ .)

The integrated dose rate for  $r = 5 \text{ m}$  and  $P = 10 \text{ kW}$  gives the integrated dose rate of  $d = 10^2 \text{ rad/h}$ .

c. Muons. Muons lose energy by ionization and thus a unique range is associated with each energy. However, muons penetrate thick shielding of several meters in depth without appreciable energy loss. For electron and proton machines, high-energy muons are peaked predominantly in the forward direction. Transverse shielding is of no consequence. However, muons are still scattered up to angles of  $\pm 5^\circ - 8^\circ$  off the incident beam. Nelson<sup>7</sup> has measured muon peak dose rates without shielding of about

---

7. W.R. Nelson, Report SLAC-PUB-481, to be published in Nucl. Instr. and Methods (1968).

$$D_{\mu} = 10^2 \frac{\text{rad}}{h} \cdot \frac{\text{m}^2}{\text{kW}}$$

## 2. Thin Targets

Multiple scattering was studied by Molière<sup>8</sup> and recently by Marion and Zimmerman.<sup>9</sup> To determine the fraction of scattered electrons due to an incident electron beam of energy  $E_0$  passing through a thin target, data presented by Marion and Zimmerman and experimental results at SLAC<sup>6</sup> are used.

The angular distribution of scattered particles, concentrated at a forward angle, is approximately Gaussian, of the form

$$f(X) = e^{-(X/X_W)^2}$$

where  $X_W$  is the value of  $X$  at the  $1/e$  point. The differential angular distribution is a slowly varying function of the parameter  $B$ :

$$X_W^2 = 0.159 \frac{Z(Z+1)}{A} \cdot \frac{t}{(p\beta c)^2} \cdot B \quad (3)$$

where  $t$  = target thickness in  $(\text{g}/\text{cm}^2)$ ,  
 $Z$  = atomic number,  
 $A$  = atomic weight,  
 $(p\beta c)^2$  = relativistic particle energy  $\cong E_0$ .

At values of  $X$  larger than for the  $1/e$  point, the distribution falls more slowly due to wide-angle scattering contributions. The shape of the scattering distribution may be described by curves for various values of the parameter  $B$ . The differential distribution (function of  $X$ ) must be integrated over all angles to find the fractions of electrons  $G(X)$  that are scattered out of a cone of a given angle. This fraction is also a function of the parameter  $B$ .

For various target materials and thicknesses, Jenkins<sup>6</sup> has published  $B$  values. In Fig. 3, the calculated  $B$  value for copper is given. If the location of the target to a point in space, where activation must be determined, is known, we may calculate for various values of the scattering angle  $\theta$  the corresponding value  $\theta = X \cdot X_W$  and obtain from Fig. 3 the fraction of the scattered beam at the specific point in space. As an example, we use a copper target with

$$\begin{aligned} t &= 0.1 \text{ radiation length} \\ &= 0.1 \times 13.1 = 1.31 \text{ g/cm}^2 \\ Z &= 29 \\ A &= 63.54 \\ B &\cong 10 \end{aligned}$$

We calculate from Eq. (3)  $X_W \cong 5.35/E_0$  (with  $E_0$  in MeV).

---

8. G. Molière, Z. Naturforsch. 2a, 133 (1947); 3a, 78 (1948).

9. J.B. Marion and B.A. Zimmerman, Nucl. Instr. and Methods 51, 93 (1967).

For  $E = 10$  GeV, we calculate the radius  $r$  at which 0.1% of the energy scattered. From Fig. 3, for  $B = 10$ , we get  $X = 9.7$  and thus

$$\theta = 9.7 \times \frac{5.35}{10 \times 10^3} \cong 5.2 \text{ mrad} .$$

To determine the activation in superconducting coils, located at a certain distance from the thin target, the coil surface perpendicular to the incident beam direction may be subdivided into sections where  $\theta$  can be measured. With a given value of  $X_W$ , we calculate  $X$  and determine from Fig. 4 the fraction of the incident beam energy. To obtain the dissipated power due to radiation, one may use the method described for thick targets in Section II.1.

### 3. Maximum Expected Radiation Dose Inside Magnet Coils

For the buildup of showers inside coils, the variable collision loss is replaced by a constant collision loss  $\epsilon_0$ , called the "critical energy," which is the ionization loss per radiation length  $X_0$  expressed in g/cm<sup>2</sup>.

We confine the calculation to particle energies large compared to the critical energy. If the incident energy  $E_0$  is large, or:

$$E_0 \gg \frac{1}{\alpha} m_e \cdot c^2 Z^{-1/3} , \quad (4)$$

the shower may be described by "Approximation B," according to Rossi,<sup>10</sup> where:

$$\frac{1}{\alpha} = \frac{\hbar c}{e^2} = 137 \quad \text{structure constant}$$

$$m_e = 9.105 \times 10^{-28} \text{ g} \quad \text{electron rest mass}$$

$$Z = 29 \quad \text{atomic number for Cu} .$$

We use as an example the electron beam energy at SLAC:

$$E_i = 20 \text{ GeV} ,$$

and get

$$E_i = 20 \times 10^9 \text{ eV} \gg 2.286 \times 10^7 \text{ eV} .$$

For copper the radiation length is  $X_0 = 13.1 \text{ g/cm}^2$  and the critical energy

$$\epsilon_0 = 20.9 \times 10^6 \text{ eV} .$$

The average energy loss per particle per unit length (g/cm<sup>2</sup>) is calculated from:

$$\begin{aligned} - \frac{dE}{dX} &= \frac{\epsilon_0}{X_0} \\ &\cong 1.6 \text{ MeV/g} \quad (\text{for copper}) . \end{aligned} \quad (5)$$

---

10. B. Rossi, High Energy Particles (Prentice-Hall, New York, 1953).

The length where the shower maximum is reached is calculated according to Approximation B from:

$$\left( \frac{X}{X_0} \right)_{\max} = 1.01 \left[ \ln \frac{E_0}{\epsilon_0} - 1 \right] . \quad (6)$$

At the shower peak, the number of electrons is given by:

$$n_{\max} = n_0 \cdot \frac{0.31}{\left[ \ln \frac{E_0}{\epsilon_0} - 0.37 \right]^{\frac{1}{2}}} \cdot \frac{E_0}{\epsilon_0} , \quad (7)$$

where  $n_0$  is the incident number of electrons. Combining Eq. (5) and Eq. (7), we get:

$$- \frac{n_{\max}}{n_0} \frac{dE}{dX} = \frac{0.31}{\left[ \ln \frac{E_0}{\epsilon_0} - 0.37 \right]^{\frac{1}{2}}} \cdot \frac{E_0}{X_0} . \quad (8)$$

Equation (8), multiplied by the beam current density in  $A/cm^2$  gives the beam power absorbed by the coil in  $W/g$ .

If we assume as a first-order approximation that the whole beam energy of SLAC ( $20 \times 10^9$  eV) is concentrated in a beam with the radius  $r = 0.3$  cm and an average current of  $25 \times 10^{-6}$  A passes through the magnet, we get from Eq. (8):

$$- \frac{n_m}{n_0} \cdot \frac{dE}{dX} = 1.6 \times 10^8 .$$

For the magnet with an average density of  $\delta = 5$  g/cm<sup>3</sup>, one obtains

$$X_0 = 15 \text{ g/cm}^2 .$$

The beam current density is

$$J_b = 1.06 \times 10^{-4} \text{ A/cm}^2 ,$$

and thus the power absorbed in the magnet:

$$p_a = - \frac{n_m}{n_0} \cdot \frac{dE}{dX} \cdot J_b = 1.6 \times 10^8 \times 1.06 \times 10^{-4} \cong 1.7 \times 10^4 \frac{W}{g} .$$

The calculation of power density for a point beam gives excessive values. In fact, the high-energy beam has a finite cross section and the above calculation must be modified for more realistic cases. The power density for a diffuse source is calculated by Guiragossian<sup>11</sup> using Monte Carlo computation. The result of his calculation for a thick copper target is illustrated in Fig. 5. The radial extension of shower is estimated from  $2\pi$  revolution of the Gaussian beam distribution. The incident beam power of 1 MW/cm is modified in Curves 2 and 3 to determine the power density in

---

11. Z. Guiragossian, Technical Note SLAC-TN-63-85 (1963).



W/g in Curve 3. The beam radius at  $L = 0$  is 0.52 cm.<sup>11</sup> For the incident beam power of 1 MW, the power density at shower maximum is  $9.3 \times 10^3$  W/g.

If the beam is missteered and may hit the coil for only one second before the interlock may interrupt the beam, the energy of  $9.3 \times 10^3$  J/g is absorbed by the coil at shower maximum, corresponding to  $9.3 \times 10^8$  rad. In this case, the coil heating is more intensive than the ionization effect due to irradiation. If the magnet is protected by means of collimators and only a fraction collides with the coil, Curve 3 in Fig. 5 can be modified accordingly in order to determine the absorbed beam power at shower maximum.

#### 4. Expected Average Radiation Dose in Magnet Coils

In order to calculate the expected long-term integrated radiation dose in a magnet coil, we assume that a magnet is located 5 m from a collimator and a beam power of 10 kW is passed to the coil. This part will be partly scattered, partly absorbed.

The intensity of the scattered part of the beam decreases with the deflection angle according to:

$$\frac{1}{I_0} \frac{dI}{d\Omega} = \begin{cases} \frac{1}{\pi (\theta^2)_{av}} & \text{for } \theta^2 < (\theta^2)_{av} \\ \frac{(\theta^2)_{av}}{\pi \theta^4} & \text{for } \theta^2 > (\theta^2)_{av} \end{cases}$$

We assume the radial distance of the coil is 5 cm from the beam axis; thus:

$$\theta = 10^{-2} .$$

Using mean square angle of deflection, we write according to Rossi<sup>10</sup>

$$(\theta^2)_{av} = \left( \frac{E_s}{E_0} \right)^2 \cdot \frac{X}{X_0} \quad (9)$$

with

$$\begin{aligned} E_s &= \left( \frac{4\pi}{\alpha} \right)^{\frac{1}{2}} \cdot m_e c^2 \\ &= 21 \text{ MeV} . \end{aligned} \quad (10)$$

For the particular case of SLAC with  $E_0 = 20 \times 10^9$  eV, we get:

$$(\theta)_{av} = 1.05 \times 10^{-3} \left( \frac{X}{X_0} \right) .$$

For  $X = X_0$ , we have

$$(\theta^2)_{av} = 1.1 \times 10^{-6} < \theta^2 = 10^{-4}$$

and thus:

$$\frac{1}{I_0} \frac{dI}{d\Omega} = \frac{(\theta^2)_{av}}{\pi \theta^4} = \frac{1.1 \times 10^{-6}}{\pi \times 10^{-8}} = 3.5 \times 10^1 \text{ sr}^{-1}.$$

At 5 m distance, the current density of the scattered beam is:

$$J_{sc} = 3.5 \times 10^1 / 2.5 \times 10^5 = 1.4 \times 10^{-4} I_0 \text{ (A/cm}^2\text{)} \\ \approx I_0 / A_{eff},$$

which corresponds to an effective area of  $A_{eff} = 7.2 \times 10^3 \text{ cm}^2$ . For 10 kW beam power passed unaffected to the magnet, we get from Fig. 5

$$\frac{\partial P}{\partial W} = \frac{1}{\gamma A_X} \cdot \frac{\partial P}{\partial X} = 97 \text{ W/g}$$

at shower maximum, and

$$\frac{\partial P}{\partial W} = 11 \text{ W/g} \quad \text{at } X = X_0.$$

The power density at the magnet is decreased, because the effective beam area is increased, i.e.,

$$\left( \frac{\partial P}{\partial W} \right)_{coil} = \left( \frac{\partial P}{\partial W} \right)_{X=X_0} \cdot \frac{A_{X_0}}{A_{eff}} = 11 \cdot \frac{0.87}{7.2 \times 10^3} = 13.3 \times 10^{-4} \text{ W/g}.$$

The power density per unit volume is:

$$P_v = \delta \cdot \left( \frac{\partial P}{\partial W} \right)_{coil} = 5 \times 13.3 \times 10^{-4} = 6.65 \times 10^{-3} \text{ W/cm}^3.$$

The total dose rate is given by the simple relation:

$$D = \left( \frac{\partial P}{\partial W} \right)_{coil} \cdot t \cdot 10^7 \text{ (erg/g)}$$

with  $t$  in seconds.

### III. RADIATION EFFECTS ON TYPE II SUPERCONDUCTORS

When materials are irradiated, their properties are changed in a variety of ways, which are briefly summarized:

- a) Disordering effect of irradiation alters lattice irregularity (thermal and electrical conductivity).
- b) Mechanical properties are changed (hardness, elongation, ductility).
- c) Atomic displacements and associated phenomena.
- d) Ionization effects.

Production of defects is basically a cascade process, in which the incident irradiation interacts and displaces an atom with sufficient energy. This atom can initiate secondary, tertiary displacements, etc.

Once an atom has received enough energy to dislodge it from its equilibrium lattice site, it moves through the lattice losing its energy through further collisions with other atoms and individual electrons. If the atom is sufficiently energetic, it will be ionized and initially lose energy by ionizing collisions, occasionally displacing other atoms by coulomb scattering collisions.

However, the interactions produce a greater number of recoils. Displacement cross sections for fission neutrons are about  $10^{-21}$  cm<sup>2</sup>. Charged particles (protons, neutrons and alphas) are light and sufficiently energetic (~ 50 MeV). Their energy loss mechanism is primarily ionization (Rutherford scattering). Deuteron cross sections are about  $(3-4) \times 10^{-21}$  cm<sup>2</sup>.

Irradiation has at least four effects:

- 1) Exchange of atoms between sites.
- 2) Creation of interstitial vacancy pairs.
- 3) Clustering of vacancies.
- 4) Creation of new elements.

Of the four, the disorder caused by exchange of atoms is most important..

The proposed use of superconducting devices in a radiation environment has been accompanied by studies to determine the extent of radiation effects on such devices. Past and present experiments conducted have shed some light on the current-carrying capacity mechanism of superconducting type II materials. The important property here is creation of defect structures by cold working and irradiation. The importance of defect structures is particularly pertinent in ductile alloys such as NbZr and NbTi. It is recognized that gross radiation effects are similar to the effect of cold work. Both effects yield increase in hardness and tensile strength (indicating embrittlement). Both effects are annealed at approximately the same temperature.

Another important aspect concerns the thermal stability of radiation-induced defects. Many radiation effects anneal out at room temperature (some even at 10°K). Most promising experiments are those at liquid helium temperatures.

Information regarding irradiation effects on three widely used, commercially available superconducting type II materials is scattered in the literature. Details of measuring techniques, etc., are not presented here. We give quantitative data for a few of these materials, measured at temperatures below transition temperature.

#### a) Nb<sub>3</sub>Sn

Deuteron irradiation<sup>1</sup> doses up to  $10^{17}$  d/cm<sup>2</sup> reveal (Fig. 6) that at 5.7°K, the critical current density is increased for fields higher than 1 T and is not affected by annealing. At 10.9°K,  $J_c$  is reduced at all fields and tends toward annealed values. The increased current-carrying capacity is characterized by the Kim-Anderson model

$$J_c = \frac{\alpha}{H + B_0}$$

in the range of 1.... 4.5) T. Large departure from the model is observed at transverse fields higher than 4.5 T, where the  $H_{c2}$  values were changed. It was shown that the  $H_{c2}$  is of primary, the  $J_c$  of secondary importance.

Proton irradiation<sup>12</sup> shows an enhancement of the critical current density

$$\frac{\Delta J}{J_{c0}} = \frac{J_c^{\text{irr}} - J_{c0}}{J_{c0}}$$

in Fig. 7. The enhancement of  $J_c$  is independent at first approximation of external field  $H_a$  up to 5 T. The irradiated sample does not follow the Kim-Anderson model, although nonirradiated samples do. Similarity to heavily cold-worked  $\text{Nb}_3\text{Zr}$  alloys is evident at medium fields, where  $J_c$  is independent of  $H_a$ . The maximum value of  $\Delta J/J_{c0}$  is measured at a dose rate of  $N_p \approx 8 \times 10^{16}$  p/cm<sup>2</sup>. At higher irradiation doses,  $\Delta J$  decreases.

Neutron irradiation.<sup>13</sup> The critical current  $J_c$  and demagnetization factor  $\alpha$  of  $\text{Nb}_3\text{Sn}$  tubes placed in a reactor were enhanced up to 50%, after irradiation with a dose rate of  $2 \times 10^{18}$  fast neutrons/cm<sup>2</sup>. The magnetic field at the specimen was  $\sim 2$  T. The increase in  $\alpha$  (Anderson's model) and  $J_c$  are responsible, however, for a more unstable performance by exhibiting more flux jumping than the nonirradiated sample. Power dissipation (due to flux creep) increases exponentially with  $\alpha$  and leads to instabilities. Neutrons produce defect clusters with fluxoid pinning energies comparable to those already present in  $\text{Nb}_3\text{Sn}$  due to cold work. Measurements<sup>14</sup> at low fields ( $\sim 0.4$  T) indicate for diffusion-processed  $\text{Nb}_3\text{Sn}$  an enhancement in  $J_c$  by a factor of 2.7, while the critical temperature was decreased by 0.08°K. The radiation dose was  $10^{18}$  n/cm<sup>2</sup> and the preradiation current density  $10^5$  A/cm<sup>2</sup>. Unfortunately no neutron irradiation data at fields higher than 2 T are available at present.

#### b) $\text{Nb}_3\text{Zr}$ Alloys

Deuteron irradiation.<sup>1</sup> Copper-coated samples irradiated show a post-irradiation depression of the critical temperature of 0.2 ... 0.8°K. Samples not copper coated show little or no change in  $T_c$  ( $< 0.2^\circ\text{K}$ ). No great changes were observed in the critical current density except in the region near the upper critical field. Recovery at annealing was observed as in  $\text{Nb}_3\text{Sn}$  alloys. Measurements had been performed up to  $10^{17}$  (15 MeV) d/cm<sup>2</sup> (Fig. 8).

Neutron irradiation. Irradiation with fast neutrons up to  $10^{18}$  n/cm<sup>2</sup> did not reveal significant changes up to fields of 2 T. It is believed that near the upper critical field, the current density will again exhibit peak effects, as observed in the case of deuteron irradiation.

Proton irradiation. No detailed experiments have been reported.

#### c) $\text{Nb61\%Ti}$ Alloys

Deuteron irradiation.<sup>1</sup> As seen from Fig. 9, critical current density is reduced, specifically at fields between 4 and 5 T, indicating also a reduction of the upper critical field. Post-curing to 77°K restores

---

12. H.J. Bode and K. Wohleben, Phys. Letters 24A, 25 (1967).

13. P.S. Swartz et al., Appl. Phys. Letters 4, 71 (1964).

14. J.P. McEvory, Jr. et al., Appl. Phys. Letters 4, 43 (1964).

preirradiation properties. As no irradiation data above 5 T external fields are measured, it is not clear if peak effects observed for Nb25%Zr are repeated for NbTi.

Neutron and proton irradiation. No data are available at present.

#### IV. IRRADIATION EFFECT ON NONSUPERCONDUCTING METALS

Copper, aluminum, a few copper alloys, and silver are the few metals which are used extensively in conjunction with superconducting magnets. Irradiation properties of copper have been studied in detail and we report only properties pertinent to the stability of supermagnets.

##### 1. Mechanical Properties

Yield and tensile strengths of electric grade OFHC copper are given in Fig. 10, when subject to various dose rates of fast neutron irradiation. Both yield and tensile strengths are increased, indicating embrittlement. Examination by means of electron microscopes indicates that the high yield stress is caused by kinking of glide dislocations and the low rate of strain hardening is related to blocking free glide planes.

Bombardment by means of neutrons and electrons shows that irradiation causes a strengthening of copper. The decrease in internal friction is a result of pinning dislocations by irradiation. It was even suggested (decrease in internal friction is similar after neutron or gamma irradiation to a temperature quenching) that pinning sites are vacancies. After irradiation, many more defects could be observed, i.e., copper irradiated up to  $6.7 \times 10^{17}$  n/cm<sup>2</sup> at 35°C contains  $3 \times 10^{15}$  defects per cm<sup>3</sup> in the form of small strained regions. After increasing the radiation dose three orders of magnitude to  $14 \times 10^{20}$  n/cm<sup>2</sup>, many more defects, such as dislocation loops, were observed. The defect sizes were increased from 75 Å to about 150 Å. The loops grow by migration of vacancies or vacancy clusters.

##### 2. Electrical Resistivity

The atom-displacement type of damage in copper resulting from fast neutron irradiation causes lattice imperfections. This creates a residual disorder, specifically if irradiation temperature is low compared to the recovery temperature of the metal.

OFHC copper, irradiated at 78°K, shows an increase in resistivity of about 24%, electric grade Al even to 36%, when irradiated up to  $10^{19}$  nvt (integrated neutrons/cm<sup>2</sup>). High-purity copper, annealed at 90°C, shows an increase in resistivity of only 8%, when irradiated up to  $7 \times 10^{20}$  nvt.

Cooper et al.<sup>15</sup> measured a nearly linear change in resistivity of copper and silver with the number of deuterons bombarding the material at 10°K (10 MeV neutron irradiation). Further investigation shows that lower irradiation temperatures were necessary to immobilize defects produced. A portion of the change in physical properties is annealed and removed during continued irradiation at a given temperature. Room temperature radiation produces little permanent change because the effect of radiation anneals out at radiation temperature. Copper irradiated at 4°K shows some annealing already at 7°K. Nonlinear change in resistivity as a function of radiation dose is

---

15. H.G. Cooper et al., Phys. Rev. 97, 599 (1955).

attributed to annealing effects. The rate of increase in resistivity during neutron bombardment at 20°C is measured to be  $3.1 \times 10^{-11}$  for copper,  $7.9 \times 10^{-11}$  for aluminum, when bombarded with a neutron flux of  $7 \times 10^{11}$  n/cm<sup>2</sup>/sec. If annealing of induced defects is prevented, the increase in resistivity is assumed proportional to the number of defects produced in the metal. Annealing at elevated temperatures after irradiation reduces the resistivity to some proportion of the original preirradiation value. The damaging rate at 4.2°K in cold-worked copper is by far greater than for annealed copper.

The effect of neutron irradiation in low-alloy steels has been investigated by Porter.<sup>16</sup> Yield and tensile strengths are increased in the range of  $5 \times 10^{18}$  to  $10^{20}$  n/cm<sup>2</sup>, considered to be about  $7 \times 10^3$  kg/cm<sup>2</sup>. Up to  $10^{15}$  n/cm<sup>2</sup>, no changes could be measured (Fig. 11). Some measurements indicate that the rate of change in yield and ultimate tensile strengths decreases slightly after exposure of  $2 \times 10^{21}$  n/cm<sup>2</sup>.

The irradiation-induced hardening occurs to a greater extent in fully annealed materials than in steels purposely hardened prior to irradiation, or at cryogenic temperatures.

Magnetization properties of low-alloy steels have not been investigated as a function of irradiation dose.

## V. IRRADIATION EFFECTS ON INSULATIONS

Insulations in superconducting magnets are generally based on polyamides (Nomex, Nylon), polyethylenes (Mylar), polytetra fluoroethylene (Teflon), phenolic materials, epoxies, silicones, or glass filament epoxy complexes. Due to the cryogenic environment and the high electromagnetic stresses ( $> 10^4$  kg/cm<sup>2</sup>, compressive stress;  $> 2 \times 10^3$  kg/cm<sup>2</sup>, shear stress), requirements on mechanical and physical properties, specifically fatigue, and thermal expansion are enhanced.

The dielectric stress on the insulations is roughly the same as in water-cooled dc electromagnets, but in order to dissipate the electromagnetic field energy within a few seconds, into external water-cooled resistors, in order to prevent coils from damage after a quench and to preserve helium, voltages in excess of 5 kV may be necessary across the coil terminals. The transient voltage waveform produces voltage gradients between turns in the order of magnitude of several kV/cm. Internally, a few insulation breakdowns, leading to interturn short circuits or layer shorts, have several disconcerting effects:

- a) Current charging time is delayed.
- b) Occurrence of instabilities due to sudden changes of the coil inductance, indicating magnetic field rearrangement over the coil.
- c) Localized increase in ac resistivity in superconductors, producing local regions of normality.
- d) Increase of helium boil-off due to flux motion.
- e) Short circuits between turns and layers become more pronounced and extend over wider areas.
- f) Increased risk that a localized short circuit absorbs the magnet energy in case of a quench. This may produce melting and discontinuity of the conductor. The arc produced internally may destroy the coil.

---

16. L.F. Porter, Am. Soc. Testing Mater., Spec. Tech. Publ. No. 276.

Radiation properties of most organic insulations have been tested at room or elevated temperatures. Irradiation data at cryogenic temperatures specifically below 21°K are scarce. In the following, it is tried to correlate the existing data to mechanical and electrical properties expected at cryogenic temperatures. Irradiation effects on insulations can be summarized briefly as follows<sup>17</sup>:

- 1) Permanent changes. In appearance, color effects ( $< 10^5$  rad threshold damage).
- 2) Chemical changes. Double bond formation, cross linking, oxidative degradation, polymerization, depolymerization, gas evolution ( $10^6 - 5 \times 10^9$  rad).
- 3) Mechanical changes. Embrittlement, hardness, elongation, tensile and flexural stress, elastic modulus, flexibility ( $10^4 \dots 10^{12}$  rad).
- 4) Physical changes. Thermal conductivity, dielectric constant, volume resistivity, dissipation factor, heat distortion ( $10^5 \dots 10^{13}$  rad).

Several reactions may occur simultaneously. The initial effect is a curing process which improves tensile, flexural and shear stress by cross linking. The percentage elongation is reduced. The end result is always a structure highly cross-linked, fragile, and crush-sensitive.

At cryogenic environments, the irradiation effects are marked by low temperature effects. Tensile and elongation properties are enhanced considerably at low temperatures. The degradation of mechanical properties due to irradiation is again considerable, as in air at room or elevated temperatures, but they are vastly improved, compared to air radiation values. From the few available data<sup>18</sup> it is difficult to predict systematic changes of insulation materials, and thus materials are discussed in groups:

#### 1) Teflon TFE and FEP (films)

Material thickness and manufacturing procedure are probably the most important parameters in evaluation of irradiation properties. Thin films ( $5 \times 10^{-3}$  to  $10^{-2}$  cm) are more radiation resistant than thick films (0.1 cm thick). However, the data obtained are not systematic and the trend not predictable. Thickness and environmental effects reduce the ultimate elongation by a factor of 2 to 3.

Results obtained for 0.025 cm thick TFE film are summarized in Tables IA and IB.

At room temperature, evaluated elongation values for various thicknesses of Teflon FEP (Fluorinated Copolymer of Ethylene and Propylene) show one order of magnitude improvement in radiation dose, compared to Teflon TFE.

---

17. H. Brechna, Report SLAC 40 (1965).

18. E.E. Kerlin and E.T. Smith, General Dynamics, Fort Worth, Texas, Reports FZK 188-1 (1964), FZK 188-2 (1964), and FZK 290 (1966).

TABLE IA

Mechanical Properties of Teflon TFE (0.025 and 0.3 cm thick)

Average Temperature (°K)	Average Pressure (mm Hg)	γ Irradiation Dose (rad)	Ultimate Tensile Strength (kg/cm <sup>2</sup> )	Ultimate Elongation (%)
300 <sup>a</sup>	760	0	282 ± 70	270 ± 50
300 <sup>a</sup>	~ 10 <sup>-6</sup>	9 × 10 <sup>5</sup>	191 ± 14	180 ± 10
300 <sup>a</sup>	10 <sup>-6</sup>	5 × 10 <sup>7</sup>	91.7 ± 5	99 ± 3
78 <sup>b</sup>	760	0	705.0	5.2
78 <sup>b</sup>	760	10 <sup>7</sup>	564	2.15
21 <sup>b</sup>	760	0	820	3.2
21 <sup>b</sup>	760	7.5 × 10 <sup>6</sup>	800	2.45
21 <sup>b</sup>	760	4 × 10 <sup>9</sup>	785	1.95

a) 0.025 cm thick

b) 0.3 cm thick

TABLE IB

Electrical Properties of Teflon TFE (0.3 cm thick)

Average Temperature (°K)	Average Pressure (mm Hg)	γ Irradiation Dose (rad)	Dielectric Constant <sup>a</sup>	Dissipation Factor	Volume Resistivity (Ω·cm)
297	760	0	1	<2 × 10 <sup>-4</sup>	>5 × 10 <sup>17</sup>
89	5 × 10 <sup>-7</sup>	0	1.015	<2 × 10 <sup>-4</sup>	>5 × 10 <sup>17</sup>
297	760	9.5 × 10 <sup>7</sup>	0.9977	4.5 × 10 <sup>-3</sup>	2 × 10 <sup>14</sup>
88	3 × 10 <sup>-7</sup>	9.5 × 10 <sup>7</sup>	1.019	2.6 × 10 <sup>-3</sup>	>5 × 10 <sup>17</sup>

a) In the table, normalized dielectric constant is used to compare data. The true dielectric constant at room temperature and atmospheric pressure is 2.0.

2) Kynar 400\* (Halocarbon)

Fluorocarbon plastics, such as Kel F and some Teflons, are widely used in superconducting magnet systems. As seen, Teflon has poor radiation properties in air. The irradiation properties improve, however, if radiation and tests are performed in vacuum and at cryogenic temperatures. Kynar, used frequently in aerospace applications, may be useful for conductor insulations; it is a thermoplastic resin containing 59% Fluorine. It has improved irradiation stability, as seen from data for film specimens given in Tables IIA and IIB:

\*Trade name. Pensalt Chemical Corporation.



TABLE IIA

Electrical Properties of Kynar 400

Average Temperature (°K)	Average Pressure (mm Hg)	Gamma Dose (rad)	Dielectric Constant <sup>a</sup>	Dissipation Factor	Volume Resistivity (Ω·cm)
<u>Vacuum-Cryotemperature-Irradiation Tests</u>					
297.5	760	0	1.000	$4.2 \times 10^{-3}$	$4 \times 10^{15}$
81.0	$2 \times 10^{-6}$	0	0.5756	$1.4 \times 10^{-3}$	$>6 \times 10^{15}$
80.0	$2 \times 10^{-6}$	$6.6 \times 10^7$	0.5845	$7.5 \times 10^{-3}$	$>6 \times 10^{15}$
116.0	$2 \times 10^{-6}$	$1.7 \times 10^7$	0.6154 <sup>b</sup>	$2.51 \times 10^{-2b}$	$1 \times 10^{14}$
286	760	$6.6 \times 10^7$	0.9880	$1 \times 10^{-2}$	$5 \times 10^{13}$
<u>Air-Irradiation Tests</u>					
286	760	0	1.000	$3.8 \times 10^{-3}$	$8 \times 10^{14}$
291	760	$2.1 \times 10^8$	0.9994	$5.6 \times 10^{-3}$	$1 \times 10^{10}$

a) Normalized. Actual value at 300°K and 1 atm pressure is 4.

b) Values obtained during irradiation at highest dose rate.

TABLE IIB

Mechanical Properties of Kynar 400

Average Temperature (°K)	Average Pressure (mm Hg)	<u>Radiation Exposure</u>		<u>At Rupture</u>	
		Gamma Dose (rad)	Neutrons E>2.9 MeV (n/cm <sup>2</sup> )	Tensile Strength (kg/cm <sup>2</sup> )	Elongation (%)
297	760	0	0	325	91
333 <sup>a</sup>	760	$9.7 \times 10^7$	$2 \times 10^{15}$	520	7
366	760	$1.7 \times 10^9$	$2.5 \times 10^{16}$	354	4.2
333 <sup>b</sup>	$2 \times 10^{-6}$	$8.5 \times 10^7$	$1.7 \times 10^{15}$	565	19.2
333 <sup>c</sup>	$2 \times 10^{-6}$	$9.2 \times 10^7$	$1.5 \times 10^{15}$	290	6.2
77 <sup>d</sup>	760	0	0	1460	1.75
77 <sup>e</sup>	760	$7.8 \times 10^7$	$1.4 \times 10^{15}$	920	1.42
21 <sup>f</sup>	760	0	0	1425	2.15
21 <sup>g</sup>	760	$7.9 \times 10^7$	$1.4 \times 10^{15}$	940	1.44

a) Tested in air, measured in air.

b) Irradiated in vacuum, tested in air.

c) Irradiated and tested in vacuum.

d) Tested in liquid nitrogen.

e) Irradiated and tested in liquid nitrogen.

f) Tested in liquid hydrogen.

g) Irradiated and tested in liquid hydrogen.

### 3) Kepton (H-Film)

Kepton is a polyamid film and has a unique blend of physical, electrical and mechanical properties. Its dielectric constant is invariable in the range of 298°K to 473°K. It shows excellent irradiation properties up to  $8.8 \times 10^7$  rad; its contraction coefficient is best compatible to stainless steel and thus it is used frequently as a barrier in glass filament-epoxy structures against diffusion of gases and cryogenic liquids. It is used only in limited applications in superconducting magnets. Specimens of  $5 \times 10^{-3}$  cm thick films tested in air at room temperature, exhibit a change in tensile strength and break at  $3.3 \times 10^8$  rad, and a noticeable damage at  $1.7 \times 10^9$  rad. The initial value of elongation (109%) changed to 66% at  $3.3 \times 10^8$  rad, and to 98% at  $1.7 \times 10^9$  rad. There were no apparent color changes during test.

Presently, no data on irradiation properties of H-Films at cryogenic temperatures are available.

### 4) Lexan\*

Lexan is a polycarbonate plastic and is used in some high-energy superconducting magnets. Its room temperature properties are excellent. At  $10^8$  rad, Lexan changes color and becomes dark; however, it retains its transparency. Threshold value for embrittlement is  $10^8$  rad. At  $10^9$  rad, gamma irradiation caused swelling, severe embrittlement, and general disintegration.

Electrical properties of Lexan are given in Table IIIA. Room temperature mechanical properties are presented in Table IIIB. No mechanical tests at cryogenic temperature vs irradiation dose are reported.

TABLE IIIA  
Electrical Properties of Lexan

Average Temperature (°K)	Average Pressure (mm Hg)	γ Irradiation Dose (rad)	Dielectric Constant <sup>a</sup>	Dissipation Factor	Volume Resistivity (Ω·cm)
297	760	0	1	$1.2 \times 10^{-3}$	$6 \times 10^{15}$
286	760	$6.6 \times 10^7$	0.982	$1.4 \times 10^{-3}$	$7 \times 10^{14}$
77	$2 \times 10^{-6}$	$6.6 \times 10^7$	0.9612	$1.9 \times 10^{-3}$	$5 \times 10^{17}$
<u>Tests in air</u>					
286	760	0	1	$1.5 \times 10^{-3}$	$2 \times 10^{15}$
290	760	$2.1 \times 10^8$	0.997	$1.9 \times 10^{-3}$	$3 \times 10^{12}$

a) The values given in Table IIIA are normalized. The true dielectric constant of Lexan at room temperature and atmospheric pressure is 3.0.

\*Trade name. General Electric Company.

TABLE IIIB

Room Temperature Mechanical Properties of Lexan

Average Temperature (°K)	Average Pressure (mm Hg)	Radiation Exposure		Ultimate Tensile Strength (kg/cm <sup>2</sup> )	Ultimate Elongation (%)
		Gammas (rad)	Neutrons E>2.9 MeV (n/cm <sup>2</sup> )		
297	760	0	0	685	5
333 <sup>a</sup>	760	$9.7 \times 10^7$	$2 \times 10^{15}$	250	1.7
364 <sup>a</sup>	760	$1.7 \times 10^9$	$2.5 \times 10^{16}$	too brittle to test	
333	$2 \times 10^{-6}$	$8.5 \times 10^7$	$1.7 \times 10^{15}$	466	8

a) Irradiated in air, tested in air.

b) Irradiated under vacuum, tested in air.

5) Mylar

Mylar, a polyethylene terephthalate, is quite commonly used in superconducting magnets for interturn and interlayer insulation. As seen from Table IV, at a dose of  $5.7 \times 10^6$  rad, mechanical properties are improved. Degradation starts before  $9.7 \times 10^7$  rad and at  $1.6 \times 10^9$  rad, the samples were too brittle to permit testing. Vacuum-irradiated samples behaved similarly. No data at cryogenic temperatures are available.

TABLE IV

Room Temperature Mechanical Properties of Mylar

Average Temperature (°K)	Average Pressure (mm Hg)	Radiation Exposure		Rupture Tensile Strength (kg/cm <sup>2</sup> )	Rupture Elongation (%)
		Gammas (rad)	> 2.9 MeV Neutrons (n/cm <sup>2</sup> )		
297 <sup>a</sup>	760	0	0	1700	80
297 <sup>a</sup>	760	$5.7 \times 10^6$	$1.4 \times 10^{14}$	1700	91
311 <sup>a</sup>	760	$5.2 \times 10^7$	$1.1 \times 10^{15}$	1610	100
333 <sup>a</sup>	760	$9.7 \times 10^7$	$2 \times 10^{15}$	1280	65
350 <sup>a</sup>	760	$3.3 \times 10^8$	$5.4 \times 10^{15}$	too brittle to test	
300 <sup>b</sup>	$5 \times 10^{-7}$	$2.4 \times 10^6$	$4.4 \times 10^{13}$	1750	89
311 <sup>b</sup>	$2 \times 10^{-6}$	$8.5 \times 10^7$	$1.7 \times 10^{15}$	1370	87
300 <sup>c</sup>	$5 \times 10^{-7}$	$2.4 \times 10^6$	$4.4 \times 10^{13}$	1470	167
325 <sup>c</sup>	$9 \times 10^{-7}$	$5.3 \times 10^7$	$9.7 \times 10^{14}$	1100	44

a) Irradiated in air, tested in air.

b) Irradiated under vacuum, tested in air.

c) Irradiated under vacuum, tested in vacuum.

## 6) Thermoset Laminates

Glass fiber epoxy laminates are widely used as spacers, structural supports, pancake insulation for radial cooling, etc., in cryogenic magnets. Ample data on irradiation properties are available at room temperature<sup>19</sup> but test results at cryogenic temperatures are scarce.

Extensive data for Lamicoid 6038E (melamine-fiberglass) are presented by Kerlin and Smith<sup>18</sup> and Tables VA and VB reflect their measurements. These data are representative for glass fiber epoxy structures as well, and may be used to determine irradiation damage in interlayer and interturn insulations.

TABLE VA

### Electrical Properties of Melamine-Fiberglass Lamicoid

Average Temperature (°K)	Average Pressure (mm Hg)	γ Irradiation Dose (rad)	Dielectric Constant <sup>a</sup>	Dissipation Factor	Volume Resistivity (Ω·cm)
<u>Vacuum-Cryotemperature-Irradiation Tests</u>					
297	760	0	1	$1.9 \times 10^{-3}$	$7 \times 10^{14}$
86	$2 \times 10^{-6}$	0	0.86	$1.3 \times 10^{-3}$	$3 \times 10^{15}$
287	760	$6.6 \times 10^7$	0.99	$1.7 \times 10^{-3}$	$1 \times 10^{15}$
79	$2 \times 10^{-6}$	$6.6 \times 10^7$	0.866	$1.8 \times 10^{-3}$	$>5 \times 10^{15}$
<u>Air-Irradiation Tests</u>					
286	760	0	1	$2.6 \times 10^{-3}$	$6 \times 10^{14}$
340	760	$2.1 \times 10^7$	1.025	$2.8 \times 10^{-3}$	$2 \times 10^{14}$
290	760	$2.1 \times 10^7$	0.999	$3.2 \times 10^{-3}$	$2 \times 10^{12}$

a) Normalized dielectric constant. True value of melamine-fiberglass at room temperature and atmospheric pressure is 6.6.

19. M.H. Van de Voorde and G. Pluym, Report CERN MPS/Int Co., 66-25 and 66-27 (1966).

TABLE VB

Mechanical Properties of Melamine-Fiberglass

Average Temperature (°K)	Average Pressure (mm Hg)	<u>Radiation Exposure</u>		Rupture Tensile Strength (kg/cm <sup>2</sup> )	Rupture Elongation (%)
		$\gamma$ Irradiation (rad)	Neutrons (n/cm <sup>2</sup> )		
297	760	0	0	4060	2.18
366 <sup>a</sup>	760	$1.7 \times 10^9$	$2.5 \times 10^{16}$	3830	2.09
333 <sup>b</sup>	$2 \times 10^{-6}$	$9.7 \times 10^7$	$2.0 \times 10^{15}$	3520	1.63
333 <sup>c</sup>	$2 \times 10^{-6}$	$9.7 \times 10^7$	$2.0 \times 10^{15}$	4200	4.38
116 <sup>d</sup>	0.2 - 0.02	0	0	9000	7.15
94 <sup>e</sup>	0.13 - 0.07	$1.2 \times 10^8$	$9.4 \times 10^{14}$	7680	7.36
21 <sup>f</sup>	760	0	0	8000	8.5
21 <sup>g</sup>	760	$6.2 \times 10^7$	$1.1 \times 10^{15}$	8300	7.53
21 <sup>g</sup>	760	$2.3 \times 10^8$	$4.1 \times 10^{15}$	7750	7.42

- a) Tested and irradiated in air.  
b) Irradiated in vacuum, tested in air.  
c) Irradiated and tested in vacuum.  
d) Tested at LN<sub>2</sub> temperature.  
e) Irradiated and tested at LN<sub>2</sub> temperature.  
f) Tested at LH<sub>2</sub> temperature.  
g) Irradiated and tested at LH<sub>2</sub> temperature.

As expected, the glass fiber tapes or cloth impregnated with melamines, epoxies or silicones are radiation resistive up to dose rates of  $10^{10}$  rad in air. The radiation resistance is improved considerably at cryogenic temperatures. The radiation dosage for the above tests should be extended to  $10^{12}$  rad at liquid helium temperature (4.2°K) in order to make predictions about the performance of insulations for superconducting magnets.

Chemical Reactions

It is known that irradiation causes formation of H<sub>2</sub> and N<sub>2</sub> gases and produces radioactive isotopes (e.g., tritium). At cryogenic temperatures, no measurements of gas evolution are reported. Presumably gas evolution is reduced at liquid helium temperature. It is hoped that most gases produced, freeze inside the insulation material prior to penetration into liquid helium.

Data on gas evolution at room temperature are given below:

<u>Teflon TFE</u>	0.022 ml/g at $4 \times 10^6$ rad	(threshold $10^4$ rad)
	9.0 ml/g at $9 \times 10^8$ rad	
<u>Mylar (PT)</u>	1.2 ml/g at $3.3 \times 10^8$ rad	(threshold $6 \times 10^7$ rad)
<u>Phenolic Fabrics</u>	4.7 ml/g at $3.7 \times 10^8$ rad	(threshold $10^8$ rad)
<u>Polyethylene Films</u>	38 ml/g at $6.4 \times 10^8$ rad	(threshold $10^8$ rad)
<u>Glass-filament-epoxy structures</u>	Traces up to $10^{10}$ rad	(threshold $2 \times 10^{10}$ rad)

## VI. IRRADIATION EFFECTS ON HELIUM

Scattered parts of the beam have to traverse the liquid helium bath, or during shower development, fractions of the beam energy are absorbed by helium. The most interesting phenomena are power absorption and hydrogen evolution from photoreactions.

### 1. Power Absorption

For processes connected with the passage of electrons and photons of high energy through matter, when energy losses are essentially due to bremsstrahlung and photo-production, respectively, the range is expressed in terms of the radiation length  $X_0$ . For helium,  $^{20}X_0 = 93.1 \text{ g/cm}^2$ ; for a typical magnet,  $X_0 \approx 15 \text{ g/cm}^2$ . The density of saturated liquid helium at  $4.2^\circ\text{K}$  is  $0.126 \text{ g/cm}^3$ , and for the magnet, we assume an average density of  $\delta_m = 5 \text{ g/cm}^3$ . One centimeter of helium corresponds to  $1.35 \times 10^{-3} X_0$  and 1 cm depth of the magnet to  $0.333 X_0$ .

When the beam passes first through a relatively thin layer of helium, no shower is developed. We neglect shower buildup when the beam passes through the Dewar walls with  $\Delta \ll X_0$ , but we can determine shower buildup when the beam passes through structural parts and through the magnet. This shower buildup will add to the integrated irradiation dose generated in helium. The power absorbed in the helium bath with the magnet immersed in it must be calculated for the various sections of the magnet and Dewar system separately. By assuming that the particles traversing through the magnet-and-Dewar system have essentially the same energy as the incident beam, then, according to Fig. 5, about nine times more reactions are expected at shower maximum within the coil as would occur by passing through helium alone.

The average energy loss per particle by collision per unit length ( $\text{g/cm}^2$ ) was obtained from

$$-\frac{dE}{dX} = \frac{\epsilon_0}{X_0} \quad (5)$$

For liquid helium, the critical energy

$$\epsilon_0 \approx 250 \text{ MeV}$$

and thus

$$-\frac{dE}{dX} = 2.7 \text{ MeV/g/cm}^2$$

which corresponds to:

$$\begin{aligned} -\frac{dE}{dX} &= 2.7 \left( \frac{\text{MeV}}{\text{g/cm}^2} \right) \cdot 93.1 \left( \frac{\text{g}}{\text{cm}^2} \right) \cdot \frac{1}{X_0} \\ &= 250 \frac{\text{MeV}}{X_0} \end{aligned}$$

The fraction of energy absorbed in one radiation length depends on the incident beam energy; e.g., for  $E_0 = 20 \text{ GeV}$  (SLAC), one gets:

$$-\frac{dE}{dX} = \frac{250}{20} \times 10^{-3} = 1.25 \times 10^{-2} \text{ per radiation length.}$$

---

20. O.I. Dovzhenko and A.A. Pomanskiĭ, Soviet Phys. JETP 18, 187 (1964).

For one centimeter of helium, corresponding to  $1.35 \times 10^{-3} X_0$ , the absorbed beam power is:

$$\frac{\Delta P_{\text{abs}}}{\Delta P_{\text{inc}}} = 1.25 \times 10^{-2} \times 1.35 \times 10^{-3} = 1.7 \times 10^{-5} \frac{W_{\text{abs}}}{W_{\text{inc}}} / 1 \text{ cm He} .$$

Inside the magnet, due to shower production, we estimate the absorbed power from Fig. 5:

$$\frac{\Delta P_{\text{abs}}}{\Delta P_{\text{inc}}} = 9 \times 1.7 \times 10^{-5} = 1.53 \times 10^{-4} \frac{W_{\text{abs}}}{W_{\text{inc}}} / 1 \text{ cm He} .$$

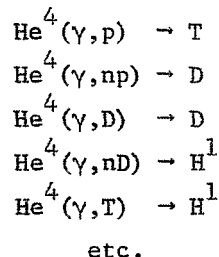
Taking into account shower development in structural parts and thin target type beam absorption in Dewar walls, we estimate a total power absorption of

$$\sim 2 \times 10^{-4} \frac{W_{\text{abs}}}{W_{\text{inc}}}$$

in one centimeter of the depth in the beam direction.

## 2. Photoreactions

Photoreactions in  $\text{He}^4$  lead to various forms of hydrogen, such as  $\text{H}^1$ ,  $\text{H}^2$ ,  $\text{H}^3$ , etc. The photo disintegration of  $\text{He}^4$  can be of the form:



It seems feasible to combine all the reaction products, such as (T, D,  $\text{H}^1$  ...) as hydrogen gas. Cross sections for the above reactions are listed up to 150 MeV by Ferguson.<sup>21</sup> The measurements are made by detecting the number of neutrons released. The number of neutrons are measured from  $(\gamma, n)$ ,  $(\gamma, 2n)$ , as well as  $(\gamma, np)$  and  $(\gamma, nD)$  reactions.

We make the assumption that there is an equality in the following cross sections:

$$\begin{aligned} (\gamma, p) \text{ cross section} &\cong (\gamma, n) \text{ cross section} \\ (\gamma, D) \text{ cross section} &\cong (\gamma, np) \text{ cross section} \\ (\gamma, T) \text{ cross section} &\cong (\gamma, 2n, 2p) \text{ cross section} \end{aligned}$$

Thus measuring neutrons from the  $(\gamma, n)$ ,  $(\gamma, np)$  and  $(\gamma, 2n, 2p)$  reactions is equivalent to measuring neutrons from  $(\gamma, p)$ ,  $(\gamma, D)$  and  $(\gamma, T)$  reactions.

---

21. G.A. Ferguson et al., Phys. Rev. 95, 776 (1954).

If the reaction cross sections were large, one could approximate

$$\frac{\int \sigma dk}{k_0^2} \text{ by } \frac{\int \sigma dk}{k_0^2} \quad (k_0 = 25 \text{ MeV}) .$$

Using cross section values obtained by integration of  $\int \sigma dk$  by Costa et al.,<sup>22</sup> we have, for a photon energy of 50 MeV:

$$50 \text{ MeV} \rightarrow 72 \text{ mb} \cdot \text{MeV}$$

and thus:

$$\frac{\int \sigma dk}{k_0^2} = \frac{72 \text{ mb} \times \text{MeV}}{(25)^2 (\text{MeV})^2} = \frac{110 \text{ } \mu\text{b}}{\text{MeV}}$$

which is a conservative estimate of the D, T, and H yield.

According to DeStaebler,<sup>23</sup> the differential photon track length (Approximation A) from the absorption of an electron with energy  $E_0$  is:

$$\frac{dN}{dk} = 0.57 \frac{E_0}{k^2} X_0 . \quad (11)$$

Accordingly, for the absorption of a beam current  $I$ , one may write:

$$\begin{aligned} R &= fI \int 0.57 \left( E_0 \cdot \frac{dk}{k^2} X_0 \right) g \cdot \frac{N_0}{A} \sigma(k) \\ &\cong 0.57 f (IE_0) g \cdot \frac{X_0 N_0}{A} \int_0^{E_0} \frac{\sigma(k)}{k^2} dk \end{aligned} \quad (12)$$

where

$IE_0$  = total beam power,

$fIE_0$  = fraction of beam power absorbed,

$g$  = atomic abundance of parent nucleide  $\cong 1$ ,

$N_0$  = Avogadro number,

$A$  = atomic weight,

$\sigma(k)$  = cross sections.

For 100 kW beam power, we have:

$$IE_0 = 6.25 \times 10^{17} \text{ MeV/sec} .$$

22. S. Costa et al., Il Nuovo Cimento 42B, 382 (1966).

23. H. DeStaebler, Technical Note SLAC-TN-62-10 (1962).



In Section VI.1, we calculated for one watt of incident beam power the absorbed power value of  $2 \times 10^{-4}$  W in one centimeter of helium. For  $10^5$  W of incident beam power, one gets, from Eq. (12):

$$R = 6.25 \times 10^{17} \times 2 \times 10^{-4} \times 1 \times \frac{93.1 \times 6 \times 10^{23}}{4} \cdot 1.1 \times 10^{-28} \text{ atoms/sec}$$

$$= 3.2 \times 10^{10} \text{ atoms/sec}$$

of hydrogen evolved per 100 kW of electron beam power. This is equivalent to  $6 \times 10^{-13}$  liter/sec in one centimeter of helium. These gases may freeze in the coolant passages of the magnet, or contaminate the refrigeration system.

## VII. CONCLUSION

Activation due to beam absorbers endangers long-time reliability of magnets more than particle beam missteering, which generates heat, but if the beam current can be interrupted fast enough, the generated heat in magnets can be absorbed.

The effects of nuclear irradiation in various materials are diverse and should be treated separately:

### 1) Superconducting type II materials

Changes in critical current density are different for various types of superconductors.  $\text{Nb}_3\text{Sn}$  exhibits at low initial  $J_c$  a marked enhancement in  $J_c$  and  $\alpha$ , making the conductor more flux jump sensitive. In  $\text{NbTi}$  and  $\text{NbZr}$  alloys,  $J_c$  is either reduced or is unchanged, with the exception of peak effect near the  $H_{c2}$  region, indicating production of new defects.  $H_{c2}$  is generally reduced in all three types of type II superconductors, as well as  $T_c$ .

Annealing to room temperature recovers initial conditions to a large extent.

### 2) Normal metals

At low integrated dose rates  $< 10^8$  rad, no major changes in physical properties are encountered. Material embrittlement is primarily due to cryogenic environment rather than induced activity. At higher dose rates, the resistivity of coppers, Al, and Ag is increased markedly. Thermal conductivity is reduced. Ultimate tensile strength is increased and elongation reduced. At very high dose rates, ultimate tensile strength is decreased subsequently.

### 3) Insulation materials

Irradiation tests on organic insulations (thermoplastic films and thermosetting compounds) are carried down only to liquid hydrogen temperatures. The irradiation effects are generally masked by the cryogenic environment. However, marked improvements against radiation damage are measured in mechanical properties, while electrical properties are less affected. Ionization effects measured during air radiation are reduced. Improvement in irradiation properties is in most insulations one order of magnitude, in some others even two orders of magnitude, compared to room temperature values. Gas evolution is markedly reduced. It is believed that generated isotopes freeze within the insulation matrix and may cause internal damage to the matrix structure before penetrating into the coolant.

The most dangerous effect is production of internal short circuits inside the coil between turns and layers which increase the current charging time constant, produce additional ac losses, or, in case of quenches, may lead to a melting of the conductor and destruction of the coil due to energy dissipation in the short circuit area. No safety precautions can be foreseen for internal failures.

#### 4) Helium

Helium evaporation is enhanced, but is in most cases less alarming. Production of isotopes, even in small quantities, inside the coil body in coolant passages is of concern, which in frozen condition may impair cooling or contaminate the refrigeration system.

Generally speaking, there is a considerable lack of irradiation data at liquid helium temperature. Specifically, a broad-range testing program is needed to determine the performance of insulation materials and normal shunt materials at liquid helium temperature. Tests on type II superconductors are required up to high fields, even, if possible, up to  $H_{c2}$  values, to correlate observations reported in the literature and in this paper. Evaluation of fatigue properties of insulations and superconductors is required.

Prior to any wide-range applications of superconducting magnets for beam transport and accelerators, it is imperative that test magnets should be placed and operated in high-irradiation environments in order to predict long-time coil performance.

#### ACKNOWLEDGMENT

Mr. T.M. Jenkins (SLAC) has been most helpful in compiling data, discussing many aspects of irradiation damage, and providing necessary information for induced activity. It is a pleasure to acknowledge his assistance.

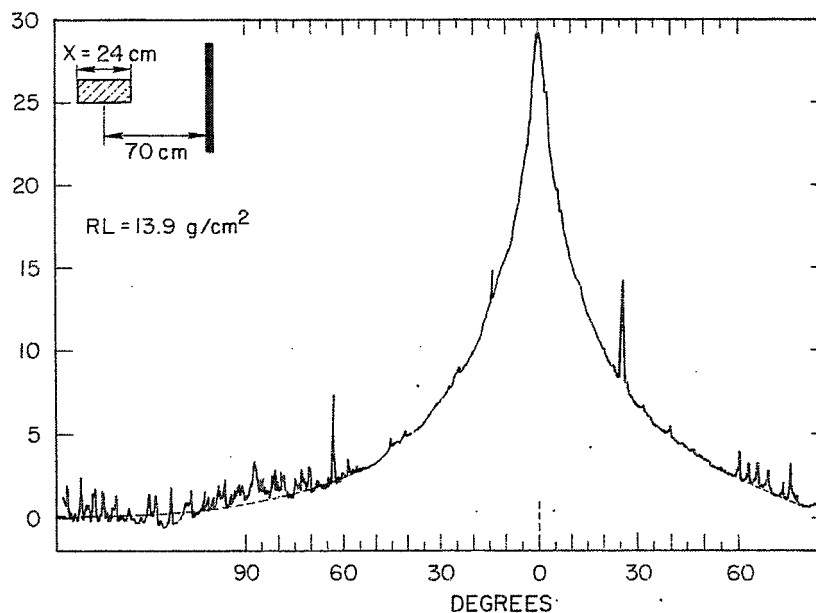


Fig. 1. Angular distribution of gamma dose rate from a typical beam absorber.

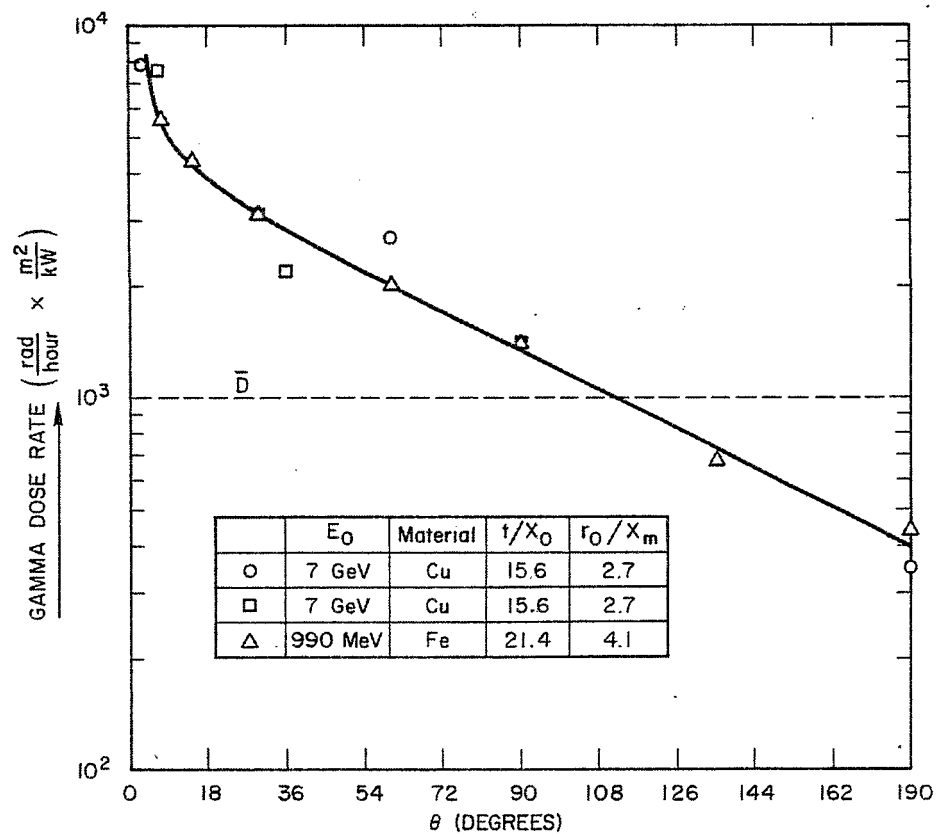


Fig. 2. Gamma dose rate from typical beam absorbers as a function of the angle from the incident beam direction, normalized to 1 kW of beam power and to a source to detector distance of 1 m.

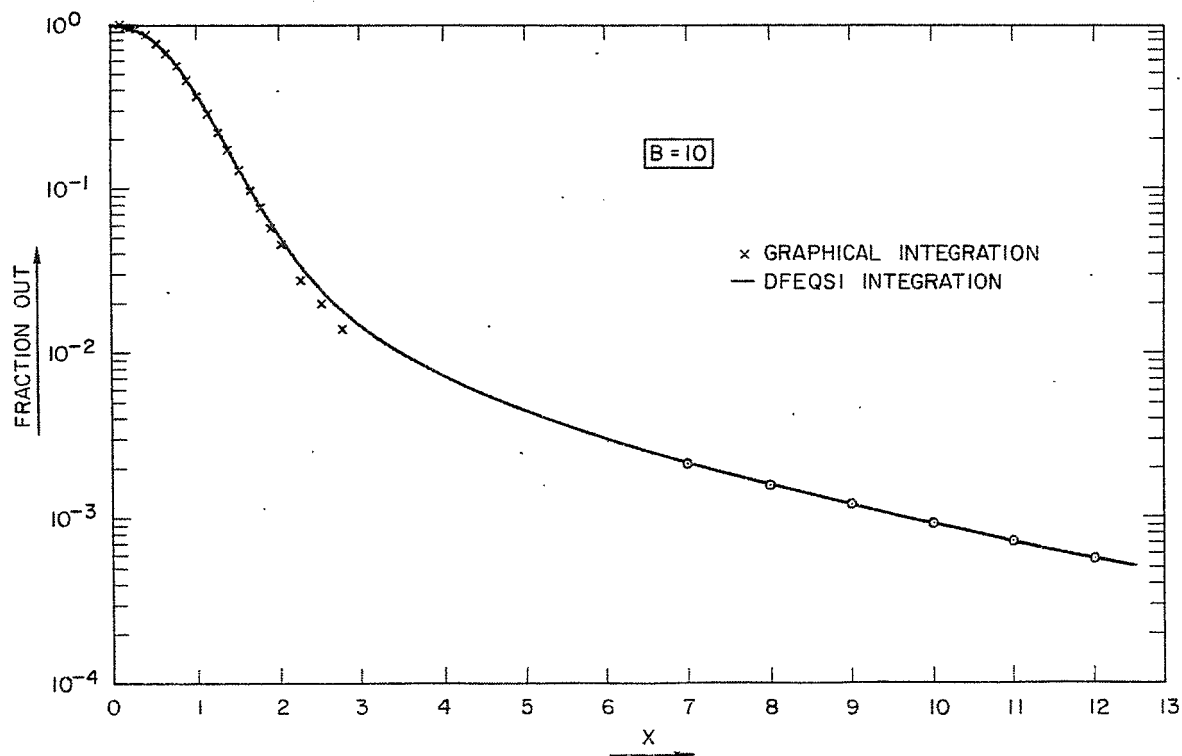


Fig. 3. The fraction of electrons that escape a cone with a space angle  $X = \theta/(X_B \sqrt{B})$  vs  $X$  for  $B = 10$  (copper).

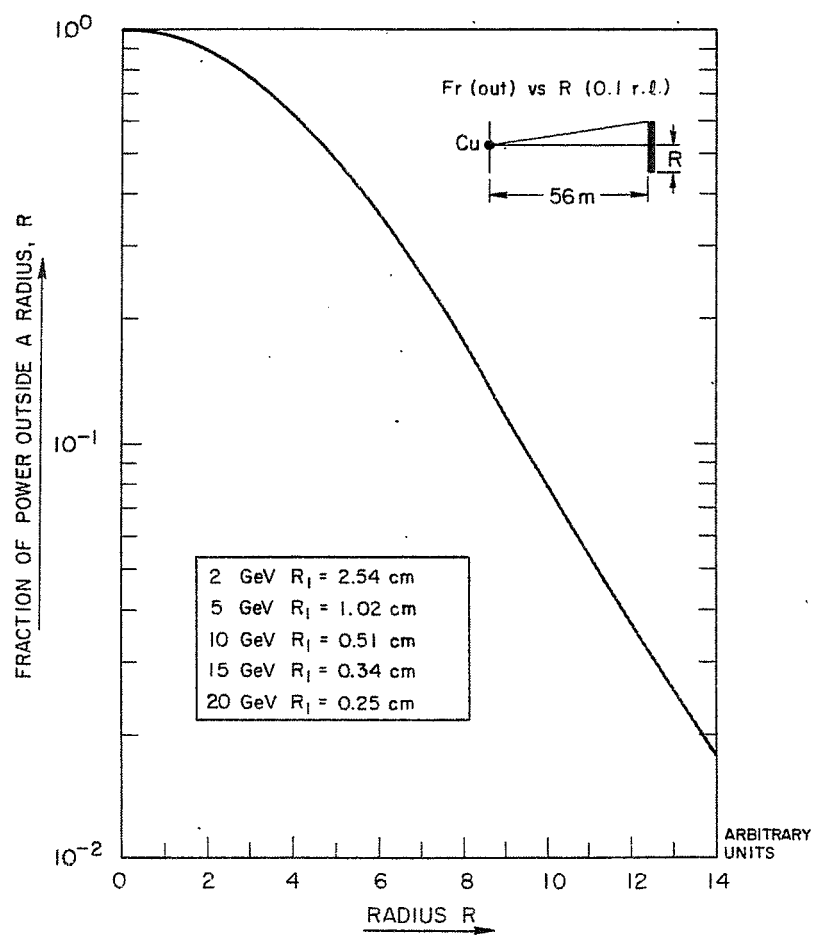


Fig. 4. Fraction of the incident energy that escapes from a thin target.

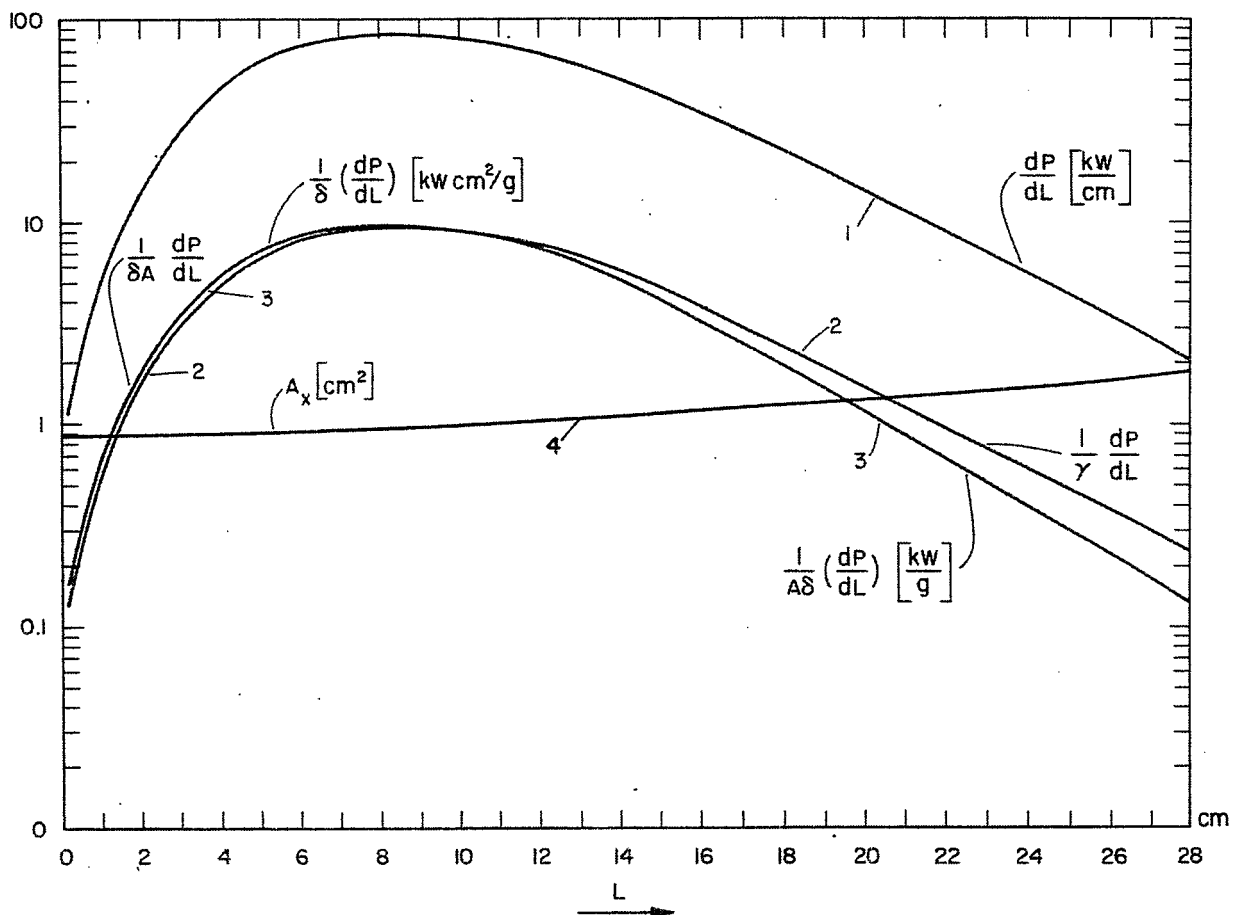


Fig. 5. Longitudinal electron beam power distribution in a shower initiated by electrons of incident energy  $E_0$  in copper.

1.  $dP/dL$  (kW/cm) for 1 MW incident beam power.
2.  $1/\gamma \frac{dP}{dL}$  (kW cm<sup>2</sup>/g) for 1 MW incident beam power.
3.  $1/\gamma A \frac{dP}{dL}$  (kW/g) for 1 MW incident beam power.
4. Beam cross section  $A_x$  in cm<sup>2</sup>.

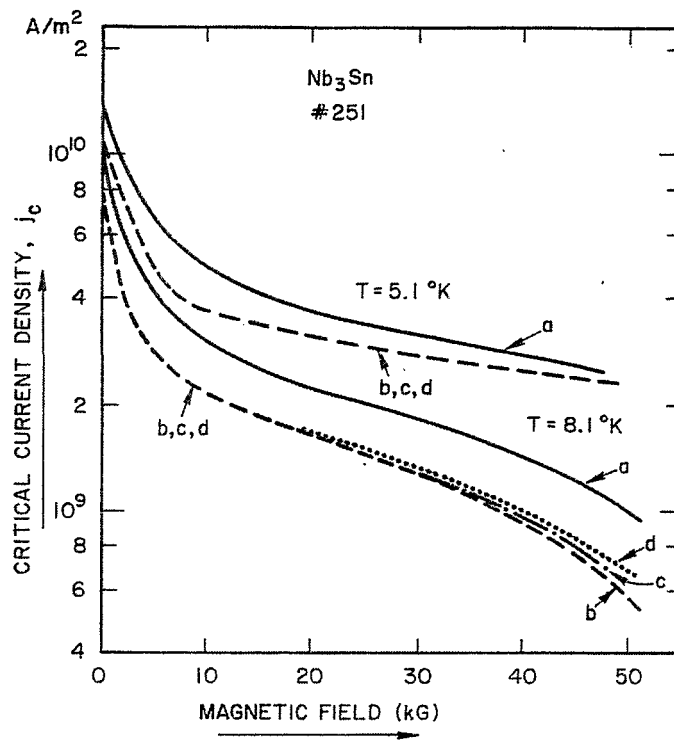


Fig. 6. Critical current density of  $\text{Nb}_3\text{Sn}$  vs applied transverse magnetic field.

- a. Preirradiation.
- b. Irradiated with  $10^{17}$  (15 MeV)  $\text{d}/\text{cm}^2$ .
- c. Post curing,  $77^\circ\text{K}$ .
- d. Post curing,  $300^\circ\text{K}$ .

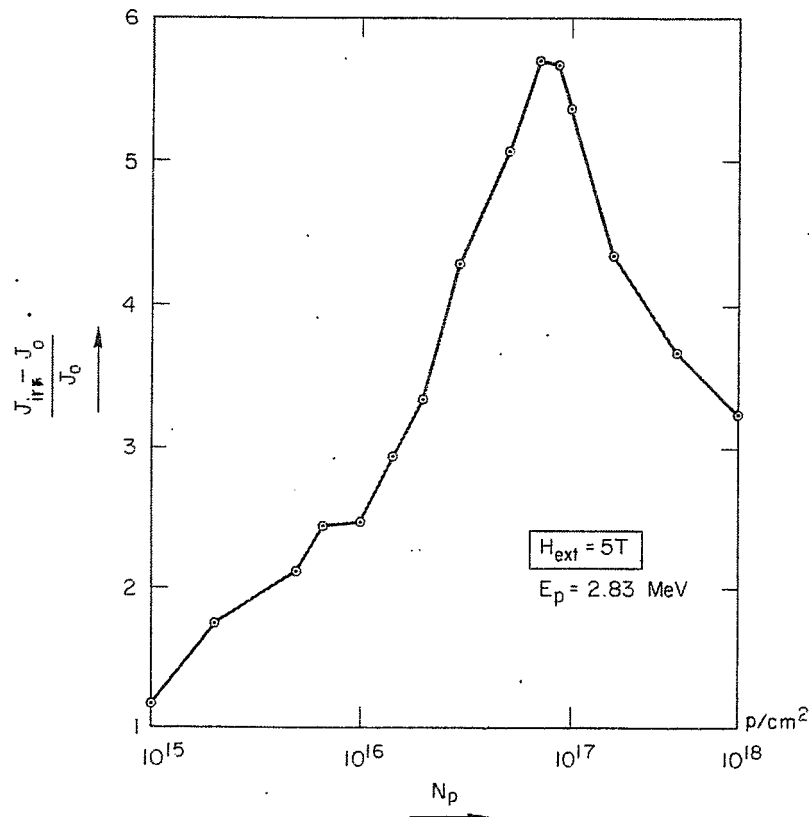


Fig. 7. Enhancement of critical current density for  $\text{Nb}_3\text{Sn}$  diffusion layers as a function of the integrated proton flux  $N_p/\text{cm}^2$ . Mean proton energy 2.83 MeV.

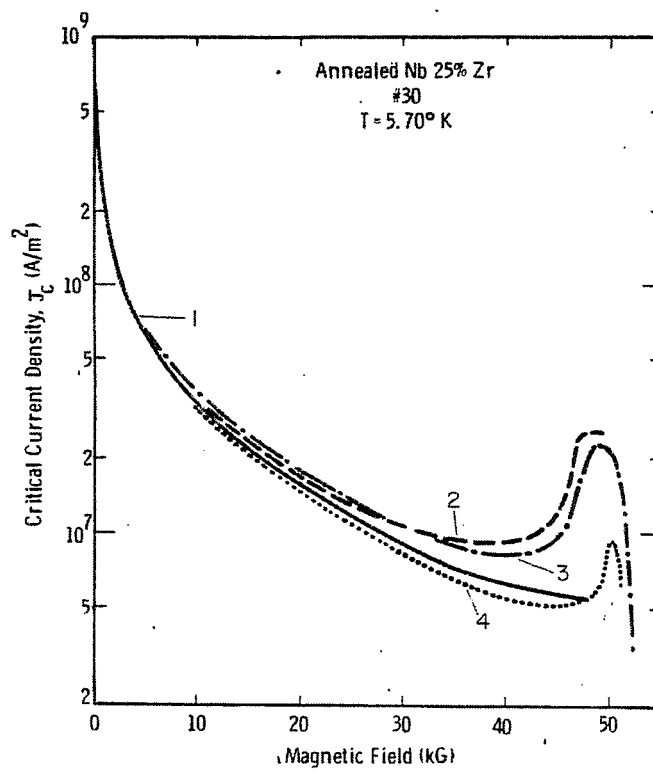


Fig. 8. Critical current density of Nb25%Zr vs applied transverse magnetic field.

1. Preirradiation.
2. Irradiated with  $10^{17}$  (15 MeV) d/cm<sup>2</sup>.
3. Post curing, 77°K.
4. Post curing, 300°K.

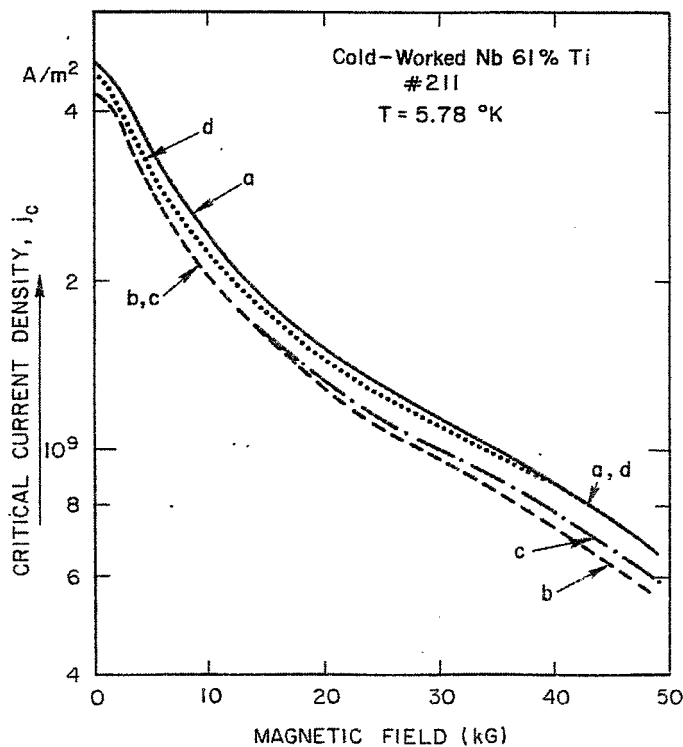


Fig. 9. Critical current density of Nb61%Ti vs applied transverse magnetic field.

- a. Preirradiation.
- b. Irradiated with  $10^{17}$  (15 MeV) d/cm<sup>2</sup>.
- c. Post curing, 77°K.
- d. Post curing, 300°K.

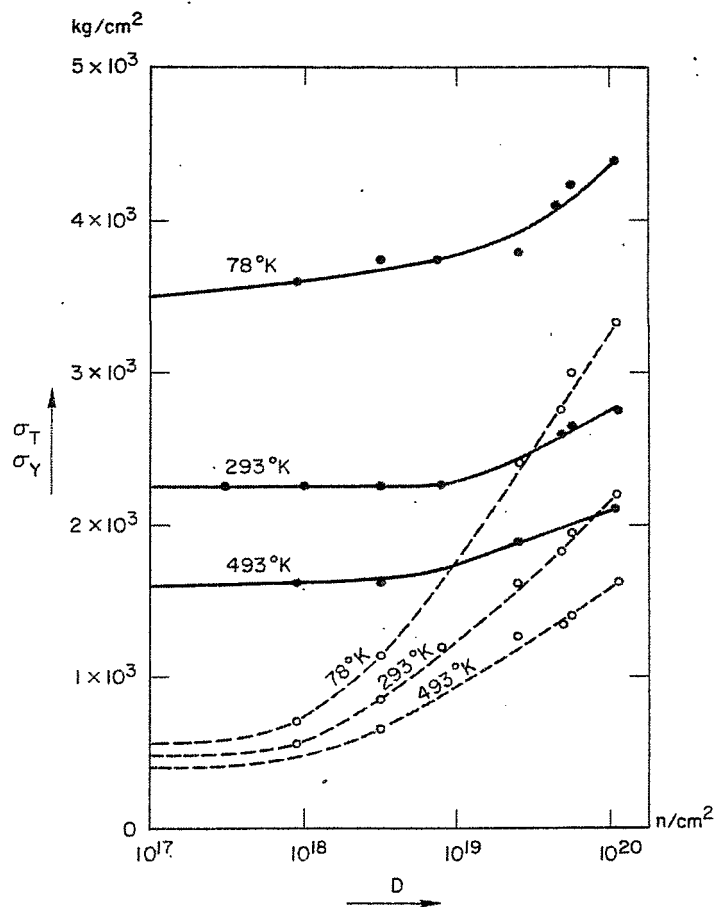


Fig. 10. Ultimate tensile and yield strengths of OFHC copper vs neutron irradiation dose ( $n/cm^2$ ).

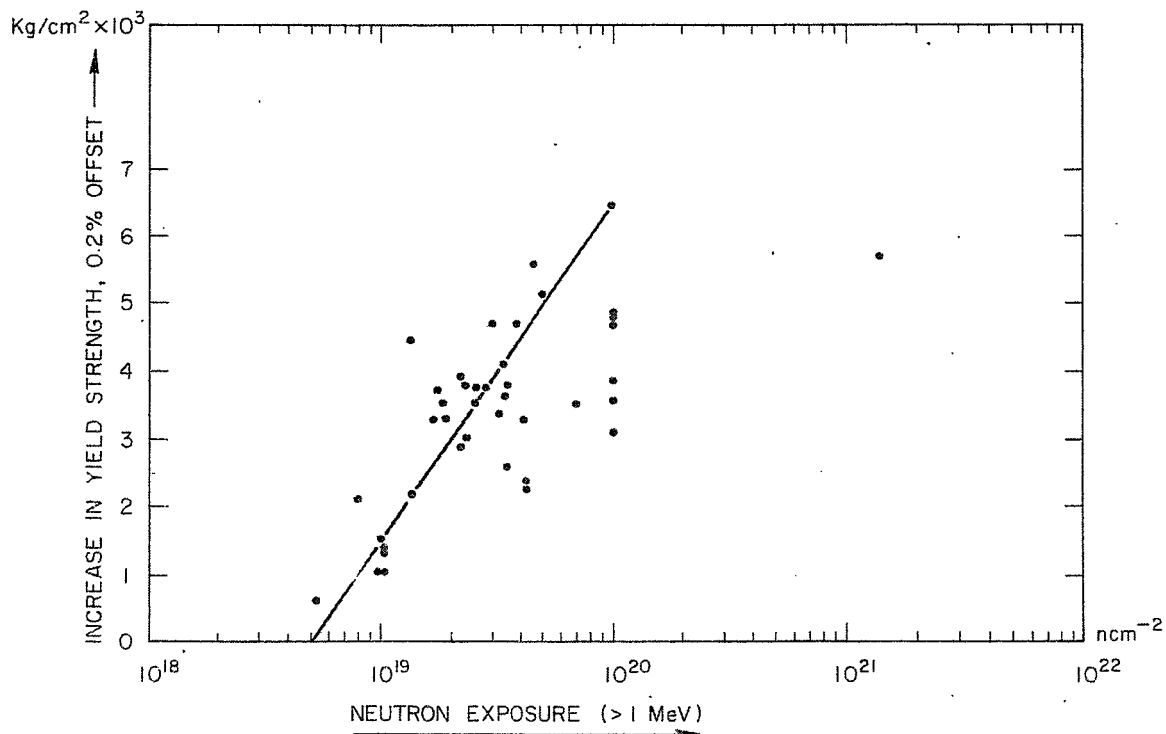


Fig. 11. Effect of neutron irradiation on the yield strength of low-carbon steel (irradiation temperature  $< 100^\circ C$ ).



# IRON SHIELDING FOR AIR CORE MAGNETS\*

J.P. Blewett  
Brookhaven National Laboratory  
Upton, New York

## INTRODUCTION

Air core magnets, whether superconducting or cryogenic, have high external fields which, in practical applications, can be troublesome. These can be removed either by additional windings (which decrease the useful field) or by using iron (which increases the useful field). This paper is on the consequences of the latter procedure.

## COILS OF INFINITESIMAL THICKNESS

The problem of distribution of fields around a multipole air core magnet surrounded by iron has been solved by Beth.<sup>1</sup> It has been treated also by Meuser.<sup>2</sup> The configuration studied by these authors is shown in Fig. 1. Region (1) of radius  $a_1$  is surrounded by a winding of infinitesimal thickness ( $a_2$  in Fig. 1 is assumed equal to  $a_1$ ) bearing a current normal to the paper of

$$I = I_0 \cos n\theta.$$

The region (3) beyond radius  $r = b$  is filled with iron of permeability  $\mu$ .

For the present purpose we assume  $\mu$  to be infinitely large and write Beth's solution in the form:

$$\text{In region (1): } B_r = 2\pi \mu_0 I_0 (r/a)^{n-1} \left\{ 1 + (a/b)^{2n} \right\} \sin n\theta$$
$$B_\theta = 2\pi \mu_0 I_0 (r/a)^{n-1} \left\{ 1 + (a/b)^{2n} \right\} \cos n\theta. \quad (1)$$

$$\text{In region (2): } B_r = 2\pi \mu_0 I_0 a^{n+1} \left\{ \frac{r^{n-1}}{b^{2n}} + \frac{1}{r^{n+1}} \right\} \sin n\theta$$
$$B_\theta = 2\pi \mu_0 I_0 a^{n+1} \left\{ \frac{r^{n-1}}{b^{2n}} - \frac{1}{r^{n+1}} \right\} \cos n\theta. \quad (2)$$

This solution gives zero azimuthal field at  $r = b$ . The maximum normal field is

$$B_{\max} = 4\pi \mu_0 I_0 (a/b)^{n+1}. \quad (3)$$

---

\*Work performed under the auspices of the U.S. Atomic Energy Commission.

1. R.A. Beth, Brookhaven National Laboratory, Accelerator Dept. Report AADD-119 (1966).
2. R.B. Meuser, Lawrence Radiation Laboratory Report UCRL-18318 (1968).

For the case where  $B_{\max}$  is assigned a specific value  $B_0$  (to avoid saturation, for example), the expression (3) defines  $b$  in terms of  $B_{\max}$  and the other parameters.

In Eqs. (1), the term  $(a/b)^{2n}$  represents the increase in field inside the magnet due to the presence of the iron. From (1) and (3) the field amplitude is

$$2\pi \mu_0 I_0 (r/a)^{n-1} \left\{ 1 + \left( \frac{B_0}{4\pi \mu_0 I_0} \right)^{2n/n+1} \right\}.$$

The second term is the increase due to the iron shield. For a dipole, ( $n = 1$ ), the increase is simply  $B_0/2$ . If fields as high as 20 kG are allowed at  $r = b$ , the iron will add 10 kG to whatever field is set up inside the magnet. For a quadrupole, ( $n = 2$ ), the additional term in the bracket is

$$\left( \frac{B_0}{4\pi \mu_0 I_0} \right)^{4/3}.$$

If, for example,  $I_0$  is such as to give 60 kG "pole-tip fields" without iron and  $B_0$  is chosen to be 20 kG, the increase in pole-tip field due to the iron will be about 5600 G.

The radius  $b$  for a 60 kG dipole with 20 kG at  $r = b$  will be given approximately by

$$b = 2a.$$

The radius  $b$  for a 60 kG pole-tip quadrupole with 20 kG at  $r = b$  will be given approximately by

$$b = 1.7a.$$

#### COILS OF FINITE THICKNESS

To obtain the fields for coils of finite thickness we merely replace  $I_0$  in Eqs. (1) and (2) by  $I_0 da$  and integrate from an inner radius  $a_1$  to an outer radius  $a_2$ . For radii  $r < a_1$  it is necessary only to integrate Eqs. (1) to obtain

$$\begin{aligned} B_r &= 2\pi \mu_0 I_0 r^{n-1} \left\{ \frac{1}{2-n} \left( a_2^{2-n} - a_1^{2-n} \right) + \frac{1}{(n+2)b^{2n}} \left( a_2^{n+2} - a_1^{n+2} \right) \right\} \sin n\theta \\ B_\theta &= 2\pi \mu_0 I_0 r^{n-1} \left\{ \frac{1}{2-n} \left( a_2^{2-n} - a_1^{2-n} \right) + \frac{1}{(n+2)b^{2n}} \left( a_2^{n+2} - a_1^{n+2} \right) \right\} \cos n\theta. \end{aligned} \quad (4)$$

For radii  $r > a_2$  we integrate Eqs. (2) to obtain:

$$\begin{aligned} B_r &= 2\pi \mu_0 I_0 \left( \frac{r^{n-1}}{b^{2n}} + \frac{1}{r^{n+1}} \right) \left( \frac{1}{n+2} \right) \left( a_2^{n+2} - a_1^{n+2} \right) \sin n\theta \\ B_\theta &= 2\pi \mu_0 I_0 \left( \frac{r^{n-1}}{b^{2n}} - \frac{1}{r^{n+1}} \right) \left( \frac{1}{n+2} \right) \left( a_2^{n+2} - a_1^{n+2} \right) \cos n\theta. \end{aligned} \quad (5)$$

Inside the coil, for  $a_2 > r > a_1$ , the solution is a combination of solutions of types (4) and (5):

$$B_r = 2\pi \mu_o I_o \left[ r^{n-1} \left\{ \frac{a_2^{2-n}}{2-n} + \frac{1}{(n+2)b^{2n}} \left( a_2^{n+2} - a_1^{n+2} \right) \right\} - \frac{a_1^{n+2}}{(n+2)r^{n+1}} + \frac{2nr}{n^2-4} \right] \sin n\theta$$

$$B_\theta = 2\pi \mu_o I_o \left[ r^{n-1} \left\{ \frac{a_2^{2-n}}{2-n} + \frac{1}{(n+2)b^{2n}} \left( a_2^{n+2} - a_1^{n+2} \right) \right\} + \frac{a_1^{n+2}}{(n+2)r^{n+1}} + \frac{4r}{n^2-4} \right] \cos n\theta .$$
(6)

The vector potentials in the three regions are:

for  $r < a_1$

$$A_z = -2\pi \mu_o I_o \frac{r^n}{n} \left\{ \frac{1}{2-n} \left( a_2^{2-n} - a_1^{2-n} \right) + \frac{1}{(n+2)b^{2n}} \left( a_2^{n+2} - a_1^{n+2} \right) \right\} \cos n\theta ,$$
(7)

for  $r > a_2$

$$A_z = -\frac{2\pi \mu_o I_o}{n(n+2)} \left( a_2^{n+2} - a_1^{n+2} \right) \left( \frac{r^n}{b^{2n}} + \frac{1}{r^n} \right) \cos n\theta ,$$
(8)

for  $a_2 > r > a_1$

$$A_z = -2\pi \mu_o I_o \left[ \frac{r^n}{n} \left\{ \frac{a_2^{2-n}}{2-n} + \frac{1}{(n+2)b^{2n}} \left( a_2^{n+2} - a_1^{n+2} \right) \right\} - \frac{a_1^{n+2}}{n(n+2)r^n} + \frac{2r^2}{n^2-4} \right] \cos n\theta .$$
(9)

#### DIPOLE FIELDS

For a dipole, the field patterns are:

for  $r < a_1$

$$B_r = 2\pi \mu_o I_o \left\{ \left( a_2 - a_1 \right) + \frac{1}{3b^2} \left( a_2^3 - a_1^3 \right) \right\} \sin \theta$$

$$B_\theta = 2\pi \mu_o I_o \left\{ \left( a_2 - a_1 \right) + \frac{1}{3b^2} \left( a_2^3 - a_1^3 \right) \right\} \cos \theta ,$$
(10)

for  $r > a_2$

$$B_r = (2/3)\pi \mu_o I_o \left( \frac{1}{b^2} + \frac{1}{r^2} \right) \left( a_2^3 - a_1^3 \right) \sin \theta$$

$$B_\theta = (2/3)\pi \mu_o I_o \left( \frac{1}{b^2} - \frac{1}{r^2} \right) \left( a_2^3 - a_1^3 \right) \cos \theta ,$$
(11)

for  $a_2 > r > a_1$

$$\begin{aligned} B_r &= 2\pi \mu_o I_o \left\{ a_2 + \frac{1}{3b^2} \left( a_2^3 - a_1^3 \right) - \frac{a_1^3}{3r^2} - \frac{2}{3} r \right\} \sin \theta \\ B_\theta &= 2\pi \mu_o I_o \left\{ a_2 + \frac{1}{3b^2} \left( a_2^3 - a_1^3 \right) + \frac{a_1^3}{3r^2} - \frac{4}{3} r \right\} \cos \theta \end{aligned} \quad (12)$$

The vector potential for a dipole is:

for  $r < a_2$

$$A_z = - 2\pi \mu_o I_o r \left\{ \left( a_2 - a_1 \right) + \frac{1}{3b^2} \left\{ a_2^3 - a_1^3 \right\} \right\} \cos \theta \quad , \quad (13)$$

for  $r > a_2$

$$A_z = - \frac{2}{3} \pi \mu_o I_o r \left( \frac{1}{b^2} + \frac{1}{r^2} \right) \left( a_2^3 - a_1^3 \right) \cos \theta \quad , \quad (14)$$

for  $a_2 > r > a_1$

$$A_z = - 2\pi \mu_o I_o r \left\{ a_2 + \frac{1}{3b^2} \left( a_2^3 - a_1^3 \right) - \frac{a_1^3}{3r^2} - \frac{2}{3} r \right\} \cos \theta \quad . \quad (15)$$

The field patterns for two possible dipoles are shown in Figs. 2 and 3. Figure 2 represents a dipole for 40 kG in an aperture of 5 cm radius. The coil is 1 cm in thickness and is surrounded by an iron shield of 10 cm radius. The maximum flux density entering the iron is 20 kG. To carry this flux at an average density of 16 kG the iron should be about 13 cm thick. Current density in the coil has a maximum value of about  $6 \times 10^4$  A/cm<sup>2</sup>.

Figure 3 represents a 60 kG magnet of the same aperture. The thickness of the coil is 1.5 cm, which results in about the same peak current density ( $6 \times 10^4$  A/cm<sup>2</sup>) as the coil of Fig. 2. The iron shield has an inner radius of 12.9 cm and a peak entering flux density of 20 kG. To carry the return flux at an average density of 16 kG, the iron should be about 16 cm thick. The weight of this shield would be slightly less than 2 tons per meter of length.

#### QUADRUPOLE FIELDS

When  $n$  is set equal to 2 in Eqs. (4)-(9), the reader may be disturbed by the appearance of  $2-n$  in the denominator of several terms. This, however, appears in terms of the form

$$\frac{1}{2-n} \left( a_2^{2-n} - a_1^{2-n} \right) \quad .$$

As  $n$  approaches 2, set  $n = 2 - \Delta$ . The term now becomes

$$\frac{1}{\Delta} \left( a_2^\Delta - a_1^\Delta \right) = \frac{1}{\Delta} \left( e^{\Delta \ln a_2} - e^{\Delta \ln a_1} \right) \quad .$$

As  $\Delta \rightarrow 0$ , this term becomes  $\ln (a_2/a_1)$ . Similar treatment removes the apparent singularity wherever it appears.

The vector potential for a quadrupole is:

for  $r < a_1$

$$A_z = -\pi \mu_o I_o r^2 \left\{ \ln (a_2/a_1) + \frac{1}{4b^4} (a_2^4 - a_1^4) \right\} \cos 2\theta ,$$

for  $r > a_2$

$$A_z = -\frac{\pi \mu_o I_o}{4} (a_2^4 - a_1^4) \left( \frac{r^2}{b^4} + \frac{1}{r^2} \right) \cos 2\theta ,$$

for  $a_2 > r > a_1$

$$A_z = -\pi \mu_o I_o r^2 \left\{ \ln (a_2/r) + \frac{1}{4b^4} (a_2^4 - a_1^4) - \frac{a_1^4}{4r^4} + \frac{1}{4} \right\} \cos 2\theta .$$

Figure 4 shows the field patterns for a quadrupole with 60 kG "pole-tip fields" surrounded by an iron shield whose maximum entering flux density is 20 kG. For an aperture of 5 cm radius, the coil thickness is 1.5 cm. The coil, as before, carries a  $\cos 2\theta$  current distribution of maximum density of about  $6 \times 10^4$  A/cm<sup>2</sup>. The inner radius of the iron shield is 10.7 cm. To carry the flux at an average density of 16 kG the iron should be about 7 cm thick.

#### IRON CROSS SECTION

Numerical examples thus far have used the case where the flux density of the iron ring is 20 kG (2 T). In this section it will be shown that less iron can be used if lower fields are chosen at the iron surface. This will result in less increase in the fields in the multipole due to the presence of iron, but it may nevertheless have economic advantages.

From Eqs. (5) the normal field at the surface of the iron is

$$B_r = \frac{4\pi \mu_o I_o}{n+2} \frac{1}{b^{n+1}} (a_2^{n+2} - a_1^{n+2}) \sin n\theta .$$

If  $b_2$  is the iron inner radius for which a maximum normal field of 2 T is set up, then

$$2 = \frac{4\pi \mu_o I_o}{n+2} \frac{1}{b_2^{n+1}} (a_2^{n+2} - a_1^{n+2})$$

and

$$B_r = 2 \left( \frac{b_2}{b} \right)^{n+1} \sin n\theta .$$

The total flux that must be carried by the iron is that entering between  $\theta = 0$  and  $\theta = \pi/2n$ , and is

$$\int_0^{\pi/2n} B_r b d\theta = \frac{2b_2}{n} \left( \frac{b_2}{b} \right)^n .$$

If the flux returns in the iron with an average flux density  $B_1$  and the iron ring has an outer diameter  $c$ , then

$$(c - b) B_1 = \frac{2b_2}{n} \left( \frac{b_2}{b} \right)^n$$

and

$$c = \frac{2b_2}{nB_1} \left( \frac{b_2}{b} \right)^n + b .$$

The cross-sectional area of the iron is

$$\pi (c^2 - b^2) = \frac{4\pi b_2^2}{nB_1} \left( \frac{b_2}{b} \right)^{n-1} \left\{ \frac{1}{nB_1} \left( \frac{b_2}{b} \right)^{n+1} + 1 \right\} .$$

For a dipole the area is

$$\frac{4\pi b_2^2}{B_1} \left\{ \frac{1}{B_1} \left( \frac{b_2}{b} \right)^2 + 1 \right\} .$$

For large  $b$ 's the iron area approaches a constant value of  $4\pi b_2^2/B_1$ . If  $B_1$  is 16 kG (1.6 T) as we have assumed in our previous examples, the maximum reduction in iron area possible below that necessary for 20 kG entering field is  $[(1/1.6) + 1]:1$  or about 1.6:1.

For a quadrupole, the iron area is

$$\frac{4\pi b_2^3}{2B_1 b} \left\{ \frac{b_2^3}{2B_1 b^3} + 1 \right\} .$$

Evidently, by reducing the entering field, the necessary iron for shielding a quadrupole can be reduced as far as desired.

#### DISTRIBUTION OF STORED ENERGY

For an evaluation of stored energy in the various regions, an approximate method will be used. It will be assumed that the thickness of the coil is small compared with the aperture dimensions. The following notation will be used:

$$a_2 = a_1 + \Delta$$

$$r = a_1 + x \text{ (within the winding)}$$

$$2\pi \mu_o I_o \Delta [1 + (a_1/b)^{2n}] = B_o .$$

The approximation will be carried only to the first order.

Equations (4) to (6) can now be written:

for  $r < a_1$

$$B_r = B_o (r/a_1)^{n-1} \sin n\theta$$

$$B_\theta = B_o (r/a_1)^{n-1} \cos n\theta ,$$

for  $a_1 < r < a_2$

$$B_r = B_o \sin n\theta$$

$$B_\theta = B_o \left\{ 1 - \frac{2x/\Delta}{1 + (a_1/b)^{2n}} \right\} \cos n\theta ,$$

for  $r > a_2$

$$B_r = \frac{B_o}{1 + (a_1/b)^{2n}} (a_1/r)^{n+1} \left[ 1 + (r/b)^{2n} \right] \sin n\theta$$

$$B_\theta = \frac{-B_o}{1 + (a_1/b)^{2n}} (a_1/r)^{n+1} \left[ 1 - (r/b)^{2n} \right] \cos n\theta .$$

Using these expressions the stored energy  $E$  in the various regions can easily be evaluated:

for  $r < a_1$

$$E = \frac{B_o^2 a_1^2}{8n \mu_o} ,$$

for  $a_1 < r < a_2$

$$E = \frac{B_o^2 a_1 \Delta}{4\mu_o} \left\{ \frac{2/3 + (a_1/b)^{2n} + (a_1/b)^{4n}}{\left[ 1 + (a_1/b)^{2n} \right]^2} \right\} ,$$

for  $r > a_2$

$$E = \frac{B_o^2 a_1^{2n+2}}{8n \mu_o a_2^{2n}} \left\{ \frac{1 - (a_2/b)^{4n}}{\left[ 1 + (a_1/b)^{2n} \right]^2} \right\} .$$

If  $(a_1/b)^{2n}$  is small, and  $a_2 \cong a_1$ , then the energy stored outside the coil is approximately the same as that stored in the useful aperture.

The average energy density in the aperture is

$$\frac{B_o^2}{8n \pi \mu_o}$$

In the coil it is

$$\frac{B_o^2}{8\pi \mu_o} \left\{ \frac{2/3 + (a_1/b)^{2n} + (a_1/b)^{4n}}{\left[ 1 + (a_1/b)^{2n} \right]^2} \right\}$$

For the particular case where  $b = 2a_1$ , the ratio of energy density in the coil to energy density in the useful aperture is

for a dipole: 0.63

for a quadrupole: 1.29 .

For cases of the type discussed above where  $\Delta = 0.3 a_1$  the ratio of the total energy stored in the coil to the total energy stored in the useful aperture will be

for a dipole: 0.44

for a quadrupole: 0.89 .

Hence for a dipole the total energy stored in the coil (for the dimensions quoted) is a little more than 20% of the total energy stored in the dipole system. For a quadrupole of similar dimensions the energy stored in the coil is about 45% of the total energy stored in the system.



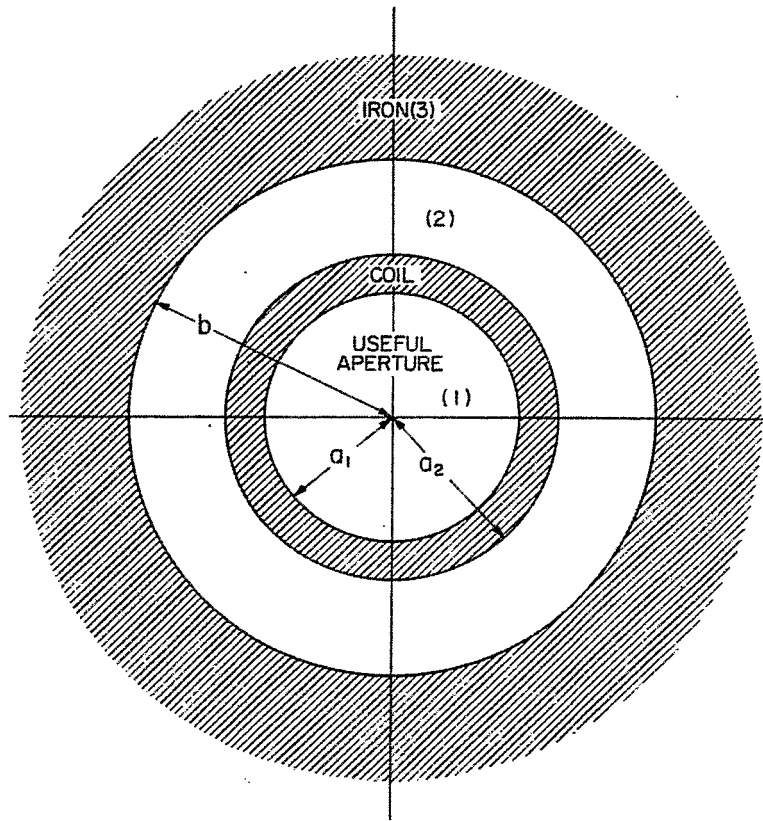


Fig. 1. Geometry of multipole winding and iron shield.

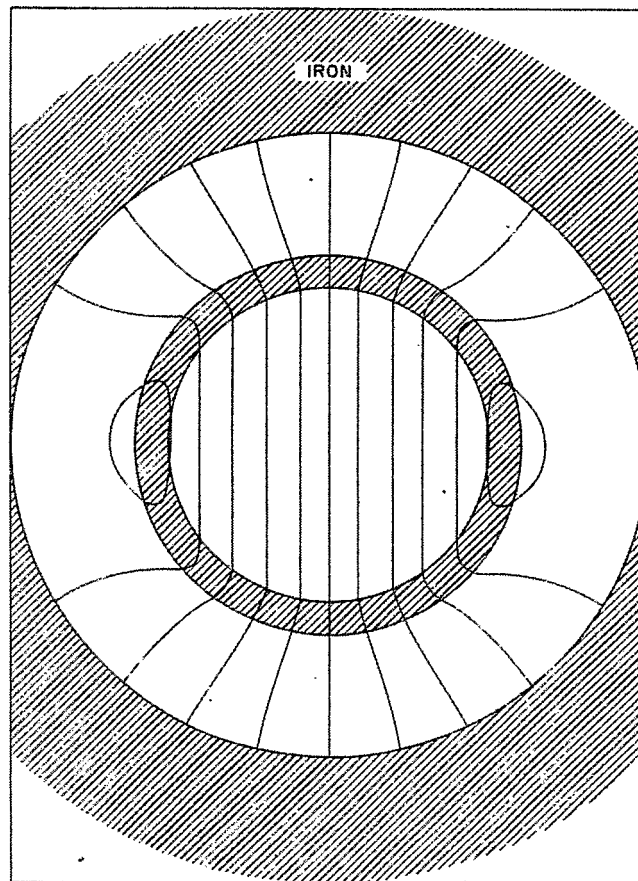


Fig. 2. Field pattern for 40 kG dipole.

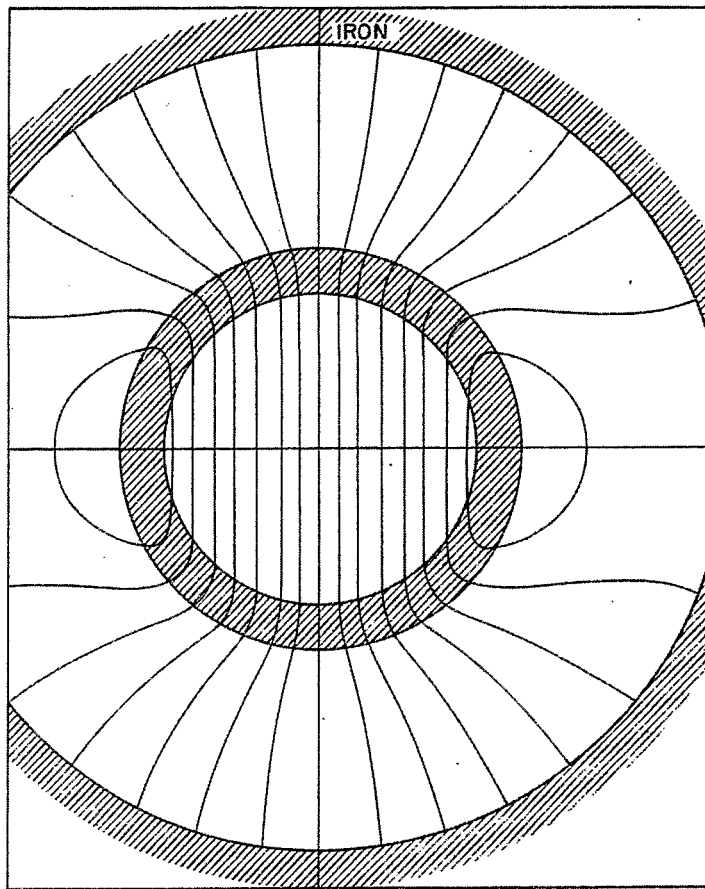


Fig. 3. Field pattern for 60 kG dipole.

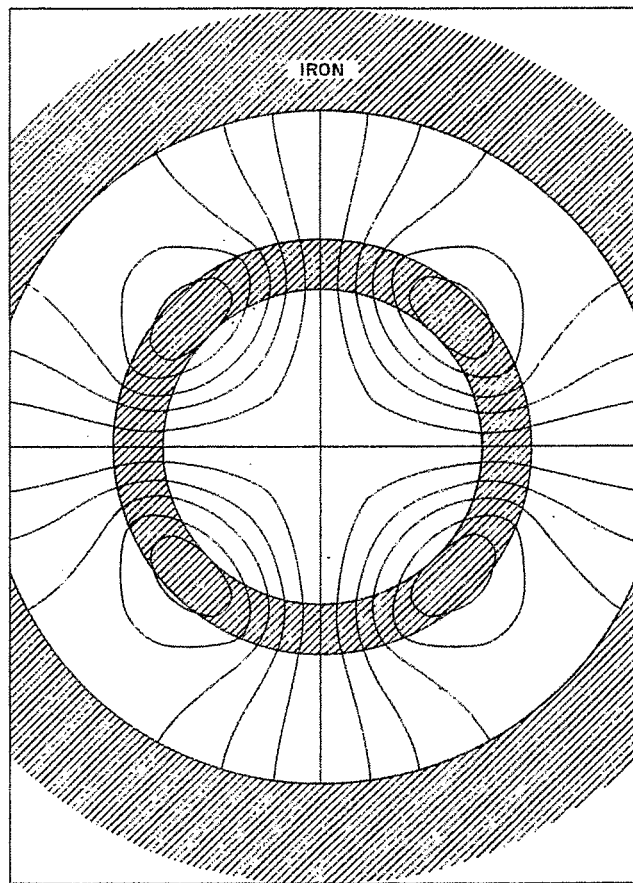


Fig. 4. Field pattern for quadrupole with 60 kG pole-tip field.

# SUPERCONDUCTING FFAG ACCELERATORS\*

G. Parzen  
Brookhaven National Laboratory  
Upton, New York

## I. INTRODUCTION

The possibility of superconducting high field magnets makes a nonpulsed accelerator like the FFAG (Fixed Field Alternating Gradient) seem attractive. It seems worthwhile to point out some characteristics of the FFAG which pertain to the possible use of this accelerator in the current state of the accelerator field.

One difficulty with the FFAG as it was conceived by the MURA group<sup>1</sup> was the large radial aperture required. This difficulty is to some extent ameliorated today for several reasons. One reason is that some accelerators being considered today have a low momentum ratio  $p_f/p_i$ , where  $p_f$  and  $p_i$  are the final and injection momenta of the particles. Some examples are:

- a) A 200 MeV to 1 GeV booster,  $p_f/p_i \approx 3$ .
- b) A high energy second stage, 300 GeV to 1000 GeV,  $p_f/p_i \approx 3$ .

The momentum swing of  $p_f/p_i = 3$  in the above two examples is small enough to be achievable in an aperture of about 15 cm.

A second reason is that the extraction from one accelerator followed by injection into a second accelerator now seems more feasible. Experience with extraction over the past years has increased one's confidence in being able to extract and inject. Thus, rather than build one FFAG accelerator with a very large aperture, it appears possible to build an FFAG having several stages, each with a moderate aperture, where the beam is extracted from one stage and injected into the following stage. An example of such a multistage FFAG would be an accelerator to go from 30 GeV to 800 GeV in three stages, each stage having a  $p_f/p_i = 3$ . The three stages would be

$$30 \rightarrow 90, 90 \rightarrow 270, 270 \rightarrow 810 .$$

One interesting result is that the radial aperture of each of the three stages would be the same. This result follows from the energy scaling properties of the FFAG and is discussed below. An aperture of about 15 cm in each stage may be satisfactory.

## II. CHOICE OF PARAMETERS

The horizontal aperture required for the accelerator depends on how large one can make the magnetic field gradient. However, the magnetic field gradient is limited by its effect on the stability limits for the betatron oscillations. The higher the gradient, the smaller the stability limits will be.

It is worth noting here that the FFAG is a high repetition rate machine, which means it can go through its acceleration cycle many times per second. A repetition

---

\*Work performed under the auspices of the U.S. Atomic Energy Commission.

1. MURA Proposal for a 10 GeV Accelerator, 1962.

rate of 30/sec to 60/sec seems reasonable.<sup>1</sup> Thus, the stability limits can be quite small for the three examples mentioned in the Introduction.

A stability limit of  $A_r = 1$  cm has been assumed in this paper. This choice should be reconsidered for the particular accelerator being designed. Further considerations on the stability limit and repetition rate are given in Section III.

The manner in which the accelerator parameters vary with the particle energy or the accelerator radius,  $R$ , follows from a consideration of the stability limits. It is shown in the Appendix that the radial aperture is energy independent for a given momentum swing  $p_f/p_i$  and is given by

$$\Delta R = 7.53 \frac{A_r}{f} \log (p_f/p_i) , \quad (1)$$

when  $f$  is the azimuthal flutter in the magnetic field. We find  $\Delta R = 8.26$  cm for  $A_r = 1$  cm,  $f = 1$  and  $p_f/p_i = 3$ . If we allow room for betatron oscillations, synchrotron oscillation and central orbit errors, assuming rather arbitrarily 1 cm for each, and allowing 0.3 cm for central orbit scalloping, we get  $\Delta R = 15$  cm.

The various parameters of several accelerators having different final energies are given in Table I. The maximum field in the median plane was assumed to be 50 kG, and a circumference factor of 2 was assumed. The median plane magnetic field varies according to

$$H_z = B_0 (r/r_0)^k \left[ 1 + f \cos \left( N\theta - P \log (r/r_0) \right) \right] . \quad (2)$$

Equation (2) indicates the meaning of the parameters  $k$ ,  $P$ ,  $N$ ,  $f$ . The parameter  $P$  determines the spiral of the magnetic field. The azimuthal periodicity is given by  $2\pi/N$ .  $f$  is the flutter of the field in the radial direction.  $k$  determines how rapidly the field rises in the radial direction.  $f$  was assumed to be 1. The choice of parameters given in Table I was found using the results listed in the Appendix.

TABLE I. A table of parameters of various accelerators having a final energy  $E_{\max}$  ranging from 0.2 to 800 GeV. Each accelerator has a maximum median plane field of 50 kG, a circumference factor of 2 and a momentum swing of 3.  $\Delta R$  is the good field radial aperture.

$E_{\max}$ (GeV)	0.2	1	30	90	270	800
$E_{\text{inj}}$ (GeV)	0.05	0.2	10	30	90	267
$R$ (m)	0.86	0.26	41.26	121	361	1069
$N$	18	30	124	212	366	632
$v_r$	3.6	6.2	24.8	42.4	73.2	126.4
$v_z$	2.5	4.2	17.5	2.90	51.6	89.1
$k$	11.4	30	543	1614	4807	14 218
$P$	73	192.1	3509	10 334	30 779	91 038
$f$	1	1	1	1	1	1
$\Delta R$ (cm)	15	15	15	15	15	15

### III. MATCHING OF BEAM INTENSITY AND PHASE SPACE

At this time there is interest in using a superconducting FFAG in connection with existing conventional accelerators. This raises the question as to whether the relatively small radius of the superconducting accelerator will give rise to problems as regards space-charge limits and in the matching of the emittance and acceptance of the accelerators.

To illustrate the problems that arise, an example will be considered which is the use of a superconducting FFAG booster to raise the injection energy of the 200 MeV linac to 1 GeV for injection into the Brookhaven AGS. The following arguments and calculations are very rough and are meant only to be indicative of the kind of solutions available.

In this example there are three aspects to be considered. These are: 1) space-charge limitations, 2) injection into the booster from the 200 MeV linac, and 3) extraction from the booster into the AGS at 1 GeV.

#### Space-Charge Limitations

The question here is whether the FFAG with a radius of 2.26 m and a stability limit of about 1 cm can contain enough charge to inject into the AGS at 1 GeV.

The incoherent space-charge limit is given very roughly by

$$N \cong \frac{a(a+b)}{R} \nu \cdot \Delta\nu \gamma\beta^2, \quad (3)$$

where a more conservative  $\gamma\beta^2$  dependence is used instead of  $\gamma^3\beta^2$ .  $a$  and  $b$  are the horizontal and vertical apertures respectively.  $\nu$  is the betatron oscillation frequency and  $\Delta\nu$  is the allowable shift in  $\nu$  due to space charge.  $R$  is the radius of the accelerator.  $\gamma$  and  $\beta$  are the particle energy  $E/mc^2$ , and the particle velocity  $v/c$ .

If we assume that the AGS at 200 MeV has the space-charge limit of  $N(\text{AGS}, 200 \text{ MeV}) = 1.0 \times 10^{13}$  protons, then Eq. (3) indicates that at 1 GeV,  $N(\text{AGS}, 1 \text{ GeV}) = 4.0 \times 10^{13}$  protons.

The injection space-charge limit of the FFAG may be found by comparison with the AGS at 200 MeV and using Eq. (3). The FFAG space-charge limit when compared with the AGS space-charge limit is larger by the radius factor  $120/2.26 = 53$ , is smaller by the aperture factor  $5(5 + 2.5)/1(1.0 + 1.0) = 18.7$ , and is smaller by the  $\nu$  factor  $8.25/4.2 = 2.08$ . Thus we find

$$N(\text{FFAG}, 200 \text{ MeV}) = 1.36 N(\text{AGS}, 200 \text{ MeV}),$$

$$N(\text{FFAG}, 200 \text{ MeV}) = 1.36 \times 10^{13} \text{ protons}.$$

The  $4 \times 10^{13}$  protons required by the AGS at 1 GeV can be obtained if the repetition rate of the FFAG is larger than 3/sec.

#### Injection into the FFAG

The 200 MeV linac has difficulty injecting enough protons into the FFAG because of the small time/turn due to the small radius. The time/turn at 200 MeV for the FFAG is  $\tau = 0.084 \mu\text{sec}$ . If the linac is assumed to deliver 50 mA, then it can inject  $2.5 \times 10^{10}$  protons per turn.

The number of turns that can be accepted is determined by the acceptance of the FFAG, which we will assume given by the rough formula

$$\text{Acceptance} \cong \frac{\nu a^2}{R} \quad (4)$$

Using  $a = 1$  cm,  $\nu = 6.2$ , we find the FFAG horizontal acceptance at 200 MeV,

$$\text{AC (FFAG, 200 MeV)} = \pi 27.4 \times 10^{-3} \text{ cm}\cdot\text{rad}$$

If we assume the emittance of the linac is  $\pi 1 \times 10^{-3}$  cm·rad, then we have room for 27 turns, or  $6.75 \times 10^{11}$  protons can be injected in 27 turns.

Thus in order to be able to inject the  $4 \times 10^{13}$  protons required by the AGS at 1 GeV, it is necessary for the FFAG to have a repetition rate of 60/sec.

An alternative to the repetition rate of 60/sec is to increase the stability limit to perhaps 1.4 cm, which would allow a repetition rate of 30/sec.

One may note that at the present time the Brookhaven 200 MeV linac is designed with a repetition rate of 10/sec.

#### Extraction from the FFAG into the AGS at 1 GeV

First let us compare the emittance of the FFAG at 1 GeV with the acceptance of the AGS at 1 GeV.

Because the momentum swing of the FFAG is  $p_f/p_i = 3$ , the emittance at 1 GeV is one-third the acceptance at 200 MeV or the emittance is

$$\text{EM (FFAG, 1 GeV)} = \pi 9.1 \times 10^{-3} \text{ cm}\cdot\text{rad}$$

The acceptance of the AGS at 1 GeV can be compared with the emittance of the FFAG at 1 GeV using Eq. (3). It is larger by the aperture factor  $(5\sqrt{3})^2 = 75$ , smaller by the radius factor  $120/2.26 = 53$ , and larger by the  $\nu$  factor  $9/6 = 1.5$ . We find that

$$\text{AC (AGS, 1 GeV)} = 2.1 \times \text{EM (FFAG, 1 GeV)}$$

One may note that the matching of the phase spaces is due to the cancellation of the radius factor by the aperture factor, which seems to require the stability limit of the FFAG to be relatively small or the emittance of the FFAG will become too large for injection into the AGS.

The transfer of the charge between the FFAG and the AGS is complicated by the radius factor of 53. A distance of  $2\pi \times 2.26$  m in the AGS can only contain 1/53 of the space-charge limit of  $4 \times 10^{13}$  protons.

One possible method is to inject 60 times/sec into the FFAG and to stack the 60 pulses at 1 GeV. The stacked beam, containing roughly  $4 \times 10^{13}$  protons, can be extracted over 53 turns in the FFAG and injected over the entire circumference of the AGS. Needless to say, there are many problems to be solved in such a scheme.

A second method would be to extract each of the 60 pulses in the FFAG after it is accelerated to 1 GeV and inject it over  $2\pi \times 2.26$  m in the AGS. If the transfer of charge is asynchronous, the process is likely to be less efficient.

In conclusion, it would seem that using a high repetition rate and a small aperture or stability limit with the small radius superconducting accelerator can produce a satisfactory match with a conventional accelerator. The above discussion should apply also to a superconducting pulsed AGS.

#### IV. A 200 MeV TO 1 GeV BOOSTER

A better idea of the magnetic field configuration in a superconducting FFAG may be obtained by considering a particular accelerator in more detail. For this purpose, let us consider a 200 MeV to 1 GeV FFAG booster which might be used in conjunction with the Brookhaven AGS.

A possible set of parameters for this booster are the following:

Inside radius, R	250 cm
Good field aperture, $\Delta R$	17 cm
Periodicity, N	24
$v_r$	4.8
$v_z$	3.3
Radial gradient, k	20.5
Spiral gradient, P	131
Spiral angle, $\alpha$	$10^\circ$
Flutter, f	1
Maximum field	50 kG
Injection field	13 kG
Horizontal stability limit, $A_x$	$\pm 1.62$ cm
Vertical stability limit, $A_y$	$\pm 0.46$ cm
Vertical aperture	$\pm 3$ cm

The above parameters are somewhat different from those given in Table I, and they are a little more on the conservative side. The stability limits  $A_x$ ,  $A_y$  are given at the azimuth where the horizontal  $\beta$  has a maximum.

#### Median Plane Magnetic Field

The magnetic field in the median plane is indicated in Fig. 1. The crosshatched areas indicate the regions of high field, the blank areas the regions of zero field. The region which will be crossed by protons is bounded by the dashed circles.

A possible magnet arrangement is shown in Fig. 1. In this arrangement the magnet edges are along radii to the center of the machine, and within each magnet the spirals may possibly be replaced by straight lines.

An alternate arrangement for a small accelerator is to use long spiral magnets whose shapes would be similar to the crosshatched areas in Fig. 1.

#### V. POSSIBLE PROBLEMS OF THE SUPERCONDUCTING FFAG

One aspect of the FFAG that may prove a serious problem has to do with the ratio of the maximum magnetic field at the current-carrying coils to the magnetic field on the median plane. If this ratio is too large, then the superconducting FFAG loses its advantage as the field at the coils is limited to some value of the order of 100 kG. This field ratio tends to get larger when the field has a rapid radial variation as is required in the FFAG.

Some other problems include that of determining the current distribution to obtain the desired median plane magnetic field, and the problem of putting radial straight sections in the FFAG. Some further considerations of particular magnets and machine design are reported elsewhere.<sup>2</sup>

#### ACKNOWLEDGEMENTS

The contents of this paper benefited from discussions with J.P. Blewett, D.D. Jacobus and P.G. Kruger.

#### APPENDIX

Some handy formulas are available for estimating the parameters of the FFAG.

The stability limits at some optimized operating point are related to the parameters by<sup>3</sup>

$$A_r/R = 3.74 f/N^2 \quad (A.1)$$

$$A_z/R = 5.12 f/N^2$$

$$k/N^2 = 0.03559 \quad (A.2)$$

$$fP/N^2 = 0.2279$$

$$v_r/N = 0.2007 \quad (A.3)$$

$$v_z/N = 0.1410$$

The radial aperture is given by

$$\Delta R = \frac{R}{k+1} \log (p_f/p_i), \quad (A.4)$$

where  $p_f$  and  $p_i$  are the final and initial momenta.

Rough formulas for  $v_r$  and  $v_z$  are

$$v_r^2 = k + 1 \quad (A.5)$$

$$v_z^2 = \frac{f^2 p^2}{N^2} - k + \frac{f^2}{2}$$

For a given operating point  $v_r/N$  and  $v_z/N$ , the stability limits are proportional to  $R/N^2$ , where  $2\pi/N$  is the periodicity of the accelerator. If one assumes that each

- 
2. P.G. Kruger and J.N. Snyder, University of Illinois Internal Report, Sept. 1966.
  3. G. Parzen and P. Morton, Rev. Sci. Instr. 34, 1323 (1963).



stage of the accelerator is to have the same stability limits, it follows that the periodicity parameter  $N$  varies with the radius according to

$$N \sim \sqrt{R} \quad . \quad (A.6)$$

Since for an accelerator with a given operating point  $v_r/N$ ,  $v_z/N$ , one must have  $k/N^2 = \text{constant}$ , where the field goes like  $r^k$ ; one finds that the field gradient parameter  $k$  varies with radius according to

$$k \approx R \quad . \quad (A.7)$$

The radial aperture,  $\Delta R$ , of the accelerator is given by Eq. (A.4).

Thus, for a given momentum swing  $p_f/p_i$ , the radial aperture varies like  $R/(k+1)$ , since  $k \approx R$  is independent of  $R$  for large  $k$ . This establishes the result, mentioned in Section I, that the radial aperture is the same for each stage of the accelerator. Combining Eqs. (A.1), (A.2) and (A.4) gives the result for the radial aperture

$$\Delta R = 7.53 \frac{A}{f} \log (p_f/p_i) \quad . \quad (A.8)$$

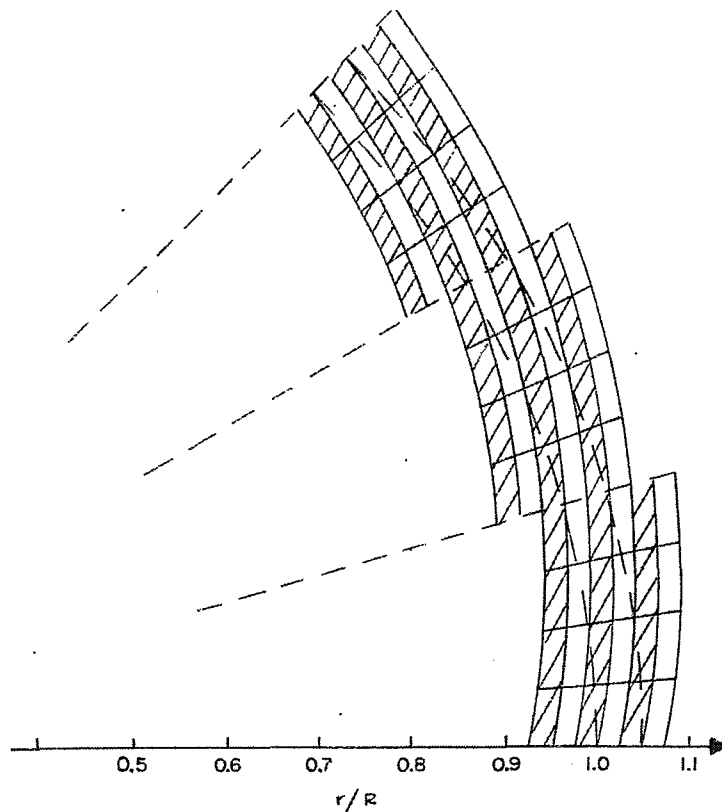


Fig. 1. The magnetic field in the median plane of an FFAG accelerator. Crosshatched areas indicate regions of high field. The period  $2\pi/N$  is  $15^\circ$  and the accelerator radius is 2.5 m.

## CALCULATIONS CONCERNING SUPERCONDUCTING ACCELERATORS

P. Gerald Kruger  
Physics Department, University of Illinois  
Urbana, Illinois

and

J.N. Snyder  
Department of Computer Science, University of Illinois  
Urbana, Illinois

### INTRODUCTION

Part I of this paper considers the number and positioning of Nb<sub>3</sub>Sn superconducting ribbons to produce the magnetic field necessary for an FFAG (fixed-field alternating-gradient) separated-sector spiral-ridge accelerator. It also considers the necessary flux biasing so that the field between peaks, as the radius increases, does not become negative. The net field (biased field) for several values of  $\theta$  (the azimuthal angle with respect to the center of the accelerator) is given. The field index,  $k$ , is found to be satisfactorily constant from  $R = 239$  cm to  $R = 261$  cm. This means that a model FFAG accelerator built to these specifications should be able to accept 50 MeV protons which are injected and accelerate them to about 1.2 GeV. It would be an interesting model to build with the Nb<sub>3</sub>Sn now available.

Part II considers a separated-function pulsed superconducting accelerator for 30 to 300 GeV. The necessary magnetic dipoles and quadrupoles can be built from Nb<sub>3</sub>Sn now available. One disadvantage of this type of accelerator is that the pulsing produces heating which must be removed by the refrigerating system and this is costly. But some members of this Summer Study believe that the cost will be reduced in the future so that it is not a serious inhibition to this type of accelerator.

A second disadvantage is that the pulsing demands a motor generator power source (or some similar equipment) so that the magnet may change the magnetic field from zero to a maximum magnetic field every 2 or 3 sec. Such capital equipment is costly and the operating cost for the many megawatts of power which are necessary to operate the magnets is a major item. Otherwise, these are interesting accelerators.

Part III concerns some parameters and properties of a superconducting FFAG accelerator for 30 to 300 GeV. Such an accelerator is feasible now with the Nb<sub>3</sub>Sn available and has the advantage that there is no heating owing to pulsing and thus no large expense is necessary for the refrigerating equipment. Secondly, no large and costly motor generator sets to run the magnet are necessary. It does have a small disadvantage owing to a circumference factor of 2 whereas the circumference factor for the pulsed accelerator is about 1.3 or 1.4.

Part IV compares, on a relative basis, the estimated costs of some components of the pulsed superconducting accelerators with an FFAG superconducting accelerator. It appears that at the present time the FFAG accelerator is much less expensive than the pulsed accelerator. However if, in the future, the heating owing to pulsing can be reduced by a factor of 5 and if the cost of refrigerating equipment were to be reduced by a factor of 4 (a total factor of cost reduction of 20) then the estimated cost of these critical items would be about the same for the two systems. At that time the remaining disadvantage of the pulsed accelerator would be the large power bill in the operating cost.

## I. THE BROOKHAVEN FFAG MODEL

Parzen has discussed superconducting FFAG accelerators at this Summer Study and elsewhere.<sup>1</sup> Consequently, and in accordance with those ideas, a model of an FFAG accelerator has been under discussion at Brookhaven National Laboratory for some time. It is a separated-sector spiral-ridge accelerator and consists of 24 sectors ( $N = 24$ ), each with eight subsections as shown in Fig. 1. Additional details of a spiral sector are given in Fig. 2 where, however, the number of turns per each subsection and the radii of the semicircular ends of the subsections are different from those used in the calculations described below.

While the general features of the Brookhaven model as given by Parzen and as drawn by D. Jacobus are maintained in these calculations, it is well known from the calculations done for the M4-24Q quadrupole<sup>2</sup> that it is necessary to make detailed magnetic field calculations using the actual currents in the (Nb<sub>3</sub>Sn) ribbon, if one is to have a good idea of the number of turns of ribbon necessary in the subsections, to produce a given magnetic field and a given field gradient (i.e., a specified field index,  $k$ ). Accordingly, Part I of this discussion deals with the magnetic field calculations for the model and the coil parameters deduced therefrom.

Preliminary field calculations<sup>3</sup> for this model include a description of the method by which the magnetic field is calculated in the median plane of the accelerator. (It is perpendicular to the major axis of the ellipse in Fig. 5.) In these preliminary calculations all subsections were rectangular and had their axes along the same straight line. In the present calculations the various subsections of the spiral have axes which are tangent to the real spiral and straight sides parallel to the axes. The ends of the subsections approximate a semicircle with four tangent straight sections. This geometry is shown in Fig. 3 and represents the geometry used in these calculations. The approximations are thought to be a reasonably good approximation to a real spiral FFAG ridge. Table I gives some physical data for one spiral and such a spiral is repeated every 15° around the accelerator.

TABLE I  
Pertinent spiral coil data which with the data  
in Fig. 3 specify one separated FFAG ridge

Subcoil number	Number of turns per subsection	Length between subsection centers (cm)	Inside radius of end turns of subsection (cm)
1	188	21.2725	1.763
2	140	16.8275	2.024
3	100	16.8275	2.237
4	79	16.8275	2.413
5	79	16.8275	2.555
6	60	16.8275	2.674
7	44	16.8275	2.770
8	32	20.9550	2.857

1. G. Parzen, Brookhaven National Laboratory, Accelerator Dept. Report AADD-138 (1967); G. Parzen and P. Morton, Rev. Sci. Instr. 34, 1323 (1963).
2. P.G. Kruger and J.N. Snyder, in Proc. 6th Intern. Conf. High Energy Accelerators, Cambridge, 1967, p. 391.
3. P.G. Kruger and J.N. Snyder, University of Illinois Report (1968).

Other pertinent data are:

- 1) The current in the ribbon is assumed to be 2000 A.
- 2) The ribbon is  $\frac{1}{2}$  in. wide Nb<sub>3</sub>Sn, 0.00625 in. thick.
- 3) For the calculations the current is assumed to be in eight wires uniformly spaced in the ribbon rather than in a uniform current sheet.

The magnetic field resulting from this current distribution has been calculated for a system of three spirals and for a system of five spirals but not for 24 spirals which make a complete accelerator. There is no significant difference in the results for the two cases and thus all data below are for a system of three spirals. The field has been calculated along R from R = 230 cm to 270 cm in steps of  $\Delta R = 1$  cm and at various angles of  $\theta$  where  $\theta = 0$  is the angular coordinate for the small end of one spiral which then ends at  $\theta = 32.872^\circ$ .

Figure 4 shows the results of the calculations for  $\theta = 30.5^\circ$ . It is noted in Fig. 4a that as R increases the field becomes negative between the peaks. This is undesirable and may be eliminated by flux biasing from current strips on an elliptical coil whose cross section is shown in Fig. 5. The necessary turns distribution for such flux biasing<sup>3</sup> is given in Table II and the calculated net biasing field for the above case is given in Fig. 4b. Figure 4c gives the net flux-biased field, i.e., the sum of the fields in Figs. 4a and 4b.

TABLE II

Necessary Turns Distribution for Flux Biasing

(Note the  $\pm$  signs denote the relative direction of the current in the strip.)

$\Delta\theta$ (degrees)	Number of turns per $\Delta\theta$
0 - 2.5	+ 0
2.5 - 5	+ 35
5 - 7.5	+ 30
7.5 - 10	+ 25
10 - 20	+ 42
20 - 30	+ 12
30 - 40	0
40 - 50	- 2
50 - 60	- 3
60 - 70	- 4
70 - 80	- 4
80 - 90	- 5
90 - 100	- 5
100 - 110	- 6
110 - 120	- 7
120 - 130	- 8
130 - 140	- 11
140 - 150	- 16
150 - 160	- 23
160 - 170	- 29
170 - 172.5	- 7
172.5 - 175	- 7
175 - 177.5	- 7
177.5 - 180	0

In Fig. 5 there is shown a schematic cross section of the vacuum chamber and the coil structure along a radius (the major axis of the ellipse). The spiral coils of Figs. 1 and 2 are represented by the open boxes above and below the major axis of the ellipse a distance  $Z$  (here  $Z = 1.1$  in. = 2.8 cm). The elliptical structure encloses the whole spiral-ridge-field coils and also supports the biasing field coils listed in Table II. The turns are placed in the angular sections shown in the outer ellipse of Fig. 5 and which are  $\Delta\theta = 2.5^\circ$  out to  $\theta = 10^\circ$  and then  $\Delta\theta = 10^\circ$  out to  $90^\circ$ . The turns wound in the  $\Delta\theta$  angle intervals to the left of the posts would have the current in one direction whereas to the right it would be in the opposite direction.

Figure 6 gives the calculated magnetic field (biased) as a function of the radius for four values of  $\theta$ .

From these it is possible to construct Fig. 7 which shows the peak value of the magnetic field at its corresponding radius. From these data it is possible to calculate an average value of  $k$  (the field index). From  $R = 239$  cm to  $R = 260$  cm,  $k = 20.44 (+ 0.27$  or  $- 0.36)$ . It may be possible to improve further the turn distribution so that  $k$  is even more constant. Also by a slight adjustment in the turn distribution  $k$  may be reduced in magnitude so that  $v_z$  (Table III) is larger than 3.5.

Other pertinent parameters for the model are calculated<sup>4</sup> in the usual way and are given in Table III. These appear to represent an interesting FFAG model accelerator which could be built with the superconducting  $\text{Nb}_3\text{Sn}$  ribbon now available.

TABLE III  
Pertinent Model Parameters

	<u>Initial</u>	<u>Final</u>
Energy (MeV)	50	1230
BR (kG·cm)	$1.03 \times 10^3$	$6.52 \times 10^3$
R accelerator (in.)	94.1	102.7
R accelerator (cm)	239	260.7
B peak accelerator (kG)	8.62	50
B average accelerator (kG)	4.31	25
$\beta$	0.31406	0.9
Rotational frequency ( $\text{sec}^{-1}$ )	$6.28 \times 10^6$	$16.5 \times 10^6$
$v_x = \sqrt{k+1}$	4.63	
$v_z^2 = -k + f^2 \tan^2 \xi + (f^2/2)$	3.50	
$f = 1$ (flutter)		
$\xi$ (degrees)	80.11	

4. K.R. Symon, D.W. Kerst, L.W. Jones, L.J. Laslett, and K.M. Terwilliger, Phys. Rev. 103, 1837 (1956).

## II. NOTES, COMMENTS AND CALCULATIONS CONCERNING A PULSED SUPERCONDUCTING ACCELERATOR

### 1. Introduction

Because of the success of the MURA<sup>5</sup> separated function storage ring and the design of the Weston 200 GeV accelerator as a separated function accelerator, there is much interest in the separated function superconducting accelerators. Furthermore, it is now well known that one can build superconducting quadrupoles<sup>2</sup> and dipoles almost any size which one may want and of elliptic or circular cross section. These make ideal components for a separated function accelerator provided that the losses in the superconductor owing to pulsing are not so large as to obviate the other advantages of the superconductor. These general ideas are considered in these notes.

### 2. Components for a 30 to 300 GeV Accelerator

Dipoles. Consideration will be given to dipoles with a circular cross section and a length of about 6 m. This length is arbitrarily chosen and seems like a reasonable length from an engineering standpoint: for a magnetic field of 60 kG and for 300 GeV protons where  $H\rho = 1.0038 \times 10^6$  kG·cm,  $\rho = 166.7$  m and thus there would be 175 six-meter-long magnetic dipoles in the circumference of the accelerator.

The diameter of the circular cross section of the dipole is specified by considering the sagitta for a chord of 6 m in length and a radius of 167 m. This calculates to be 2.7 cm. To this must be added about  $\pm 2$  cm for betatron oscillations and some small amount (say 2.3 cm) for design clearance, in which liquid helium may flow, and wall thickness of the chamber. Thus the inside diameter of the magnetic field is taken to be 9.0 cm or about 3.5 in.

Accordingly, under these conditions and assumptions, the total stored energy in the magnetic field will be about  $1.8 \times 10^5$  J/m so that

$$E_{\text{total, stored}} = 1.9 \times 10^8 \text{ J} .$$

The necessary turn distribution of 0.5 in. Nb<sub>3</sub>Sn on a 3.5 in. diameter dipole can be estimated from the data in an earlier report<sup>6</sup> wherein a 3 in. diameter dipole (M3-15D) was considered. From these data it is expected that the 60 kG field would be attained (conservatively) from the same turns distribution as that in Table VI of that report and that the field would be flat to about  $\pm 0.1\%$  over the requisite diameter.

The total length of Nb<sub>3</sub>Sn ribbons which are necessary is a minimum of  $1.22 \times 10^6$  m for the dipoles.

Quadrupoles. The M4-24Q quadrupoles<sup>2</sup> already built and tested at Brookhaven surely are more than adequate for this separated function accelerator. Since the focal lengths of a pair of quadrupoles are inversely proportional to the square of the field gradient and since the gradient in M4-24Q is about 16 kG/in. a quadrupole, M4-160 (i.e., 16 in. long instead of 24 in. long) will suffice. M4-24Q has 1280 turns which at 50 cm per turn (conservative) give 640 m of Nb<sub>3</sub>Sn ribbon necessary for each quadrupole.

---

5. E.M. Rowe and F.E. Mills, University of Wisconsin Physical Sciences Laboratory, private communication.

6. P.G. Kruger and J.N. Snyder, University of Illinois Report (1967).

It is estimated that for the M3.5-240D dipoles one needs 318 quadrupoles and consequently  $2.04 \times 10^5$  m of Nb<sub>3</sub>Sn ribbon.

About  $10^7$  J will be the total stored energy in the magnetic field of the quadrupoles. These data are summarized in Table IV.

TABLE IV

Summary of Some Parameters for a Pulsed Superconducting  
Separated Function Accelerator

Maximum proton energy (GeV)	300
H <sub>p</sub> (kG·cm)	$1.0038 \times 10^6$
Average dipole field (kG)	60
Length of dipole magnet sections (m)	6
Number of dipole magnet sections	175
$\rho$ , protons path radius in the magnetic field (m)	166
$2\pi\rho$ , magnetic field path in accelerator (m)	1047
Diameter of dipole cross section (in.)	3.5
Length of 0.5 in. ribbon Nb <sub>3</sub> Sn for dipoles (m)	$1.22 \times 10^6$
Length of 0.5 in. ribbon Nb <sub>3</sub> Sn for quadrupoles (m)	$0.2 \times 10^6$
Total length of Nb <sub>3</sub> Sn (m)	$1.45 \times 10^6$
Total stored energy dipoles and quadrupoles (J)	$2.0 \times 10^8$

III. PARAMETERS AND PROPERTIES OF A SUPERCONDUCTING FFAG ACCELERATOR  
30 TO 300 GeV PROTONS

1. Introduction

Many of the ideas expressed or used in Part III of this paper are based on those developed by Parzen.<sup>1</sup> These, together with the superconducting properties of Nb<sub>3</sub>Sn, make it feasible and reasonable to consider the construction of superconducting accelerators in the region of 30 to 300 GeV as well as in the region of 300 GeV to 3 TeV. Some of the notations used in Table V, where some parameters for a 30 GeV to 300 GeV accelerator are listed, are those of Symon et al.<sup>4</sup>

As mentioned by Parzen<sup>1</sup> two of the most important reasons for again considering FFAG structures for accelerators are:

- a) Nb<sub>3</sub>Sn makes large constant magnetic fields practical.
- b) The small  $\Delta R$  and large  $k$  now realizable make the structure economical and practical.

However, rather than limit  $\Delta R$  to about 15 cm and  $p_f/p_i$  to about<sup>1</sup> 3 which would necessitate many extractions and injections from ring to ring of successive accelerators, it will be considered here that  $p_f/p_i \cong 10$  and that  $\Delta R \cong 60$  cm (see Table V). This leads to a structure which has a reasonable engineering size and saves on extraction and injection. The circumference factor will be 2 and the flutter 1. Moreover,

the inside clearance between coils is assumed to be  $2Z = 2.2$  in. so that  $Z = 1.1$  in.  $= 2.8$  cm  $= A_r$ .<sup>1</sup>

## 2. Determination of Constants (see Table V)

- a) Choice of the magnetic field: The maximum magnetic field at the median plane of the FFAG structure is chosen to be 50 kG. This makes the estimated field at an Nb<sub>3</sub>Sn ribbon in a coil about 87 kG and according to the RCA superconductivity properties of the 0.5 in. wide ribbon, the critical current at this field is 1525 A.
- b) The field index  $k$ : This is given by the usual expression  $(B/B_0) = (R/R_0)^k$  which yields  $k = 1515$ .
- c) The radial betatron frequency: This is given by  $\sqrt{k+1} = 38.9$ .
- d) Now, the vertical betatron frequency is given by<sup>4</sup>  
 $v_z^2 = -k + f^2 \tan^2 \xi + f^2/2$  and this is satisfied by:  $v_z = 26.8$ ,  
 $\tan \xi = 47.35$ ,  $\xi = 88^\circ 47'$ . It is considered feasible to construct a spiral sector with  $\xi = 88^\circ 47'$ .
- e) Next  $\Delta R$  can be calculated from Parzen,<sup>1</sup> Eq. (A.4). This gives the value listed in Table V.
- f) Finally, the radial separation between points of maximum magnetic field is calculated to be  $\Delta r = R\lambda = 23.04$  cm  $= 9.08$  in.
- g) The lengths of a spiral sector are 28.16 m.

TABLE V  
Some Parameters for a 30 to 300 GeV FFAG Accelerator

	<u>Initial</u>	<u>Final</u>
Energy (GeV)	30	300
HR (kG·cm)	$1.0315 \times 10^5$	$1.0038 \times 10^6$
H(av) (kG)	2.58262	25
H(max) (kG)	5.16524	50
R (cm)	$3.994 \times 10^4$	$4 \times 10^4$
R (m)	399.4	400
$\Delta R$ (cm) (assumed)	60	
N	230	
k	1515	
$p = (1/w) = N \tan \xi = (2\pi/\lambda)$	$1.09 \times 10^4$	
$\tan \xi$	47.35	
$\xi$	$88^\circ 47'$	
$\lambda = (2\pi/p)$	$5.76 \times 10^{-4}$	
$\Delta r = [R\lambda \equiv 9.08 \text{ in.}]$ (cm)	23.04	
$v_x$	38.9	
$v_z$	26.8	



### 3. Some Details of Coil Construction

Based on the model design (Part I) and the field calculations for the model, it is possible to extrapolate those data to give preliminary constants for the spiral sector coils for the 30 GeV to 300 GeV FFAG accelerator. Accordingly, it will be considered that the spiral coils are 28.16 m long, have 12 subsections, that each subsection is 2.34 m in length and that each spiral sector is separated from its neighbor by 10.92 m along the circumference. These details are depicted in Fig. 8.

### IV. A COST COMPARISON OF SOME COMPONENTS OF SUPERCONDUCTING ACCELERATORS

The purpose of this part of the discussion is to present a comparison of the estimates of the costs of certain critical items for a pulsed and for an FFAG accelerator. It should be clearly understood that these are not estimated costs for an accelerator and that they are not accurately estimated costs but that the relative costs should be reasonably realistic.

For example, the cost of Nb<sub>3</sub>Sn for the two different types of accelerator is larger for the FFAG than for the pulsed accelerator. This is owing to the fact that the vacuum chamber (i.e., the magnetic field volume) is larger for the FFAG than for the pulsed machine. On the other hand, the costs for refrigeration to remove the heat produced by pulsing are large in the pulsed machine whereas they are nil for the FFAG machine. Correspondingly, the cost for a motor generator set or other similar equipment to provide the pulsed energy at the proper time interval (a few seconds) for the pulsed accelerator is large whereas for the FFAG accelerator it is negligible. Other costs as presented in Table VI are somewhat in favor of the pulsed accelerator, owing to the larger circumference factor for the FFAG machine.

The cost of the superconducting Nb<sub>3</sub>Sn ribbon is based on an estimated cost for the future and for a large quantity of the superconductor. It seems like a realistic price. (See notes on cost items.) In any case the amount of the needed superconducting ribbon is reasonably accurately estimated so that even if the absolute cost were in error the relative cost would be quite good.

The largest uncertainty in these cost estimates is that owing to the refrigeration necessary to remove the heat developed by pulsing the superconductor. This cost differs by about a factor of 20 from the present to the optimistic future cost which some people envision. At the present time the FFAG accelerator surely has a large cost advantage and even in the future would break even unless the present losses owing to pulsing are greatly reduced and concurrently the cost of refrigerating equipment is greatly reduced.

For larger accelerators the cost should scale approximately with the radius.

No rf costs are listed in Table VI.

Another disadvantage to the pulsed accelerator is that during operation many megawatts of power will be consumed by the magnetic structure and will need to be purchased. For the FFAG accelerator this operating cost is negligible.

Other possible disadvantages and advantages:

a) The pulsing of present accelerators has been responsible for some mechanical failure, problems, and difficulties. At the larger magnetic fields envisioned here the corresponding magnetic pressure may be 15 to 20 times larger than in present

machines since the pressure is proportional to  $B^2$ . Thus, one should not be surprised if it should be necessary to design to only 40% of the tensile strength of materials for the pulsed machine compared to 80% for the FFAG accelerator. It might also be that material fracture would result from pulsing at such high fields.

b) Possibly one might get larger beam currents from an FFAG accelerator than from a pulsed machine if one used the beam stacking techniques developed by MURA but, of course, one cannot extract more beam than is injected. Also, the power supply for the rf system will be relatively more costly for larger beam currents.

TABLE VI

A Cost Comparison for some Critical Items for Superconducting Accelerators  
with an Initial Energy of 30 GeV to a Final Energy of 300 GeV

(Estimated cost in millions of dollars)

	Pulsed Cost		FFAG Cost
	Present	Future Optimistic	Present
1. Cost of Nb <sub>3</sub> Sn for magnets			
a. Unbiased magnetic field coil			5.5
b. Biasing magnetic field coil			4.2
c. For dipoles	3.7	Same	
d. For quadrupoles	0.6	Same	
2. Cryogenic costs: refrigeration			
a. Owing to ordinary heat leaks	2.9	Same	5.0
b. Owing to pulsing the stored energy in the dipoles and quadrupoles			
i. At present prices	100		
ii. At optimistic future prices		5	
3. Magnet power supply	30	15	0.02
4. Housing for magnet power supply and primary and secondary power lines	2.0	Same	Nil
5. Vacuum system	0.55	Same	1.3
6. Ring building for the magnet	4.1	Same	7.5
7. Miscellaneous engineering costs	6.8	Same	12.5
Total relative estimated cost for these critical items	150.7	40	36

## Notes on Cost Items

- 1a. From Part III: (for spiral sectors)  
(4000 m per sector) 2 (230 sectors) \$3.00/m (Ref. 7) =  $5.52 \times 10^6$
- 1b. From Part III: (for flux biasing)  
(2mp) [552 turns] \$3.00/m =  $4.16 \times 10^6$
- 1c. From Part II:  
( $1.22 \times 10^6$  m) \$3.00/m (for dipoles) =  $3.66 \times 10^6$
- 1d. From Part II:  
( $2 \times 10^5$  m) \$3.00/m (for quadrupoles) =  $0.6 \times 10^6$
- 2a. Cryogenic cost owing to ordinary heat leaks will be that for an ordinary Dewar and is estimated to be about \$2000/m of circumference.  
For the pulsed accelerator =  $2\pi r$  (circumference factor) \$2000  
=  $2\pi r$  (1.4) \$2000 =  $2.9 \times 10^6$   
For the FFAG accelerator =  $2\pi r$  (2) \$2000 =  $5 \times 10^6$
- 2b. At present it is observed<sup>8</sup> that the energy loss owing to pulsing superconductors is given by:  
Energy loss (J/cycle)  $\approx 0.5\%$  of the maximum stored energy in the system.  
Also, it might be possible in the future to reduce this loss by a factor of 5 so that to be optimistic the future loss would be only 0.1%.  
Also note that at the present time refrigerating equipment costs about \$400/W at 500 W and at 4°K. In the future, according to the consensus of this Summer Study, this might be reduced to \$100/W.  
For these calculations it is assumed that the accelerator magnets will be pulsed once in 4 sec. Consequently the cost  
i. Present =  $100 \times 10^6$   
ii. Future =  $5 \times 10^6$ .  
This gives such a wide spread in cost that no reliable conclusion can be made. However, for the next few years an average value of the present and future price may not be far wrong.
3. This is based on the present cost for the new Brookhaven generator which is  $2 \times 10^6$  to handle  $12 \times 10^6$  J of stored energy. Then for the  $2 \times 10^8$  J to be stored here the scaled cost is  $30 \times 10^6$ . But P.F. Smith<sup>9</sup> at this Summer Study has expressed the belief that a superconducting power supply could be made in the future for about one-half of the present cost. Much engineering and development needs to be done before this is accomplished.

- 
7. A private communication estimates the future cost of 1.0 in. wide ribbon at 4000 A as \$6.00/m in quantities of two million meters or more for delivery over 1 to 2 years. This is equivalent to 0.5 in. ribbon at \$3.00/m.
8. W.B. Sampson, private communication.
9. P.F. Smith, these Proceedings, p. 1002.

5. The vacuum envelope can be just a stainless-steel tube or the equivalent (it is cooled to  $4^{\circ}\text{K}$ ) and so with pumps, valves, controls, etc. may cost \$400 or \$500/m.
6. The ring housing (tunnel) for the magnet is assumed to cost about \$3000/m.
7. Miscellaneous engineering costs: coil windings, structural support, outer shell, etc. Guess \$500/m.

#### ACKNOWLEDGEMENT

The writers wish to express their appreciation to D. Jacobus of Brookhaven National Laboratory for supplying Figs. 1 and 2 and for valuable conversations with him and G. Parzen of Brookhaven.

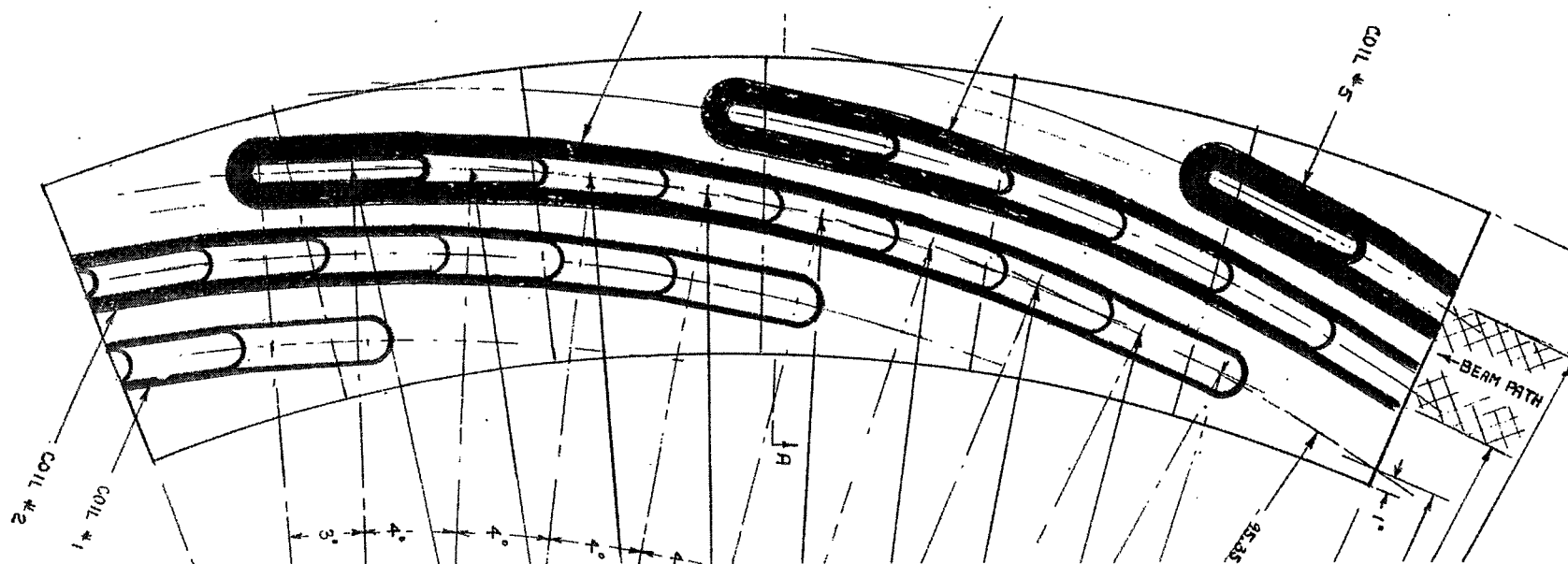


Fig. 1. Spiral-separated sectors for an FFAG model accelerator at Brookhaven, drawn by D. Jacobus of Brookhaven. The dimensions are somewhat different from those used in the text but all essential features are as Parzen originally outlined them.

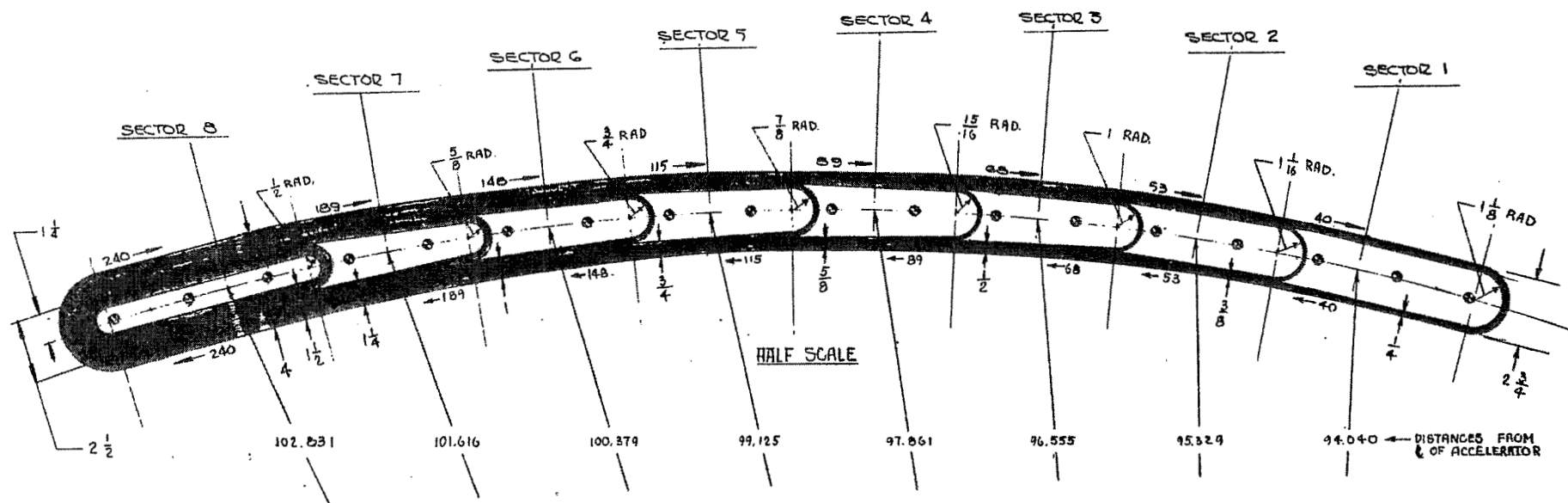


Fig. 2. Details of one spiral sector as drawn by D. Jacobus of Brookhaven. The number of turns of 0.5 in. wide  $\text{Nb}_3\text{Sn}$  per subsection is different from that used in the text, as are the radii of the semicircular ends (see Table I). However, the general features of the construction are maintained and are pertinent.

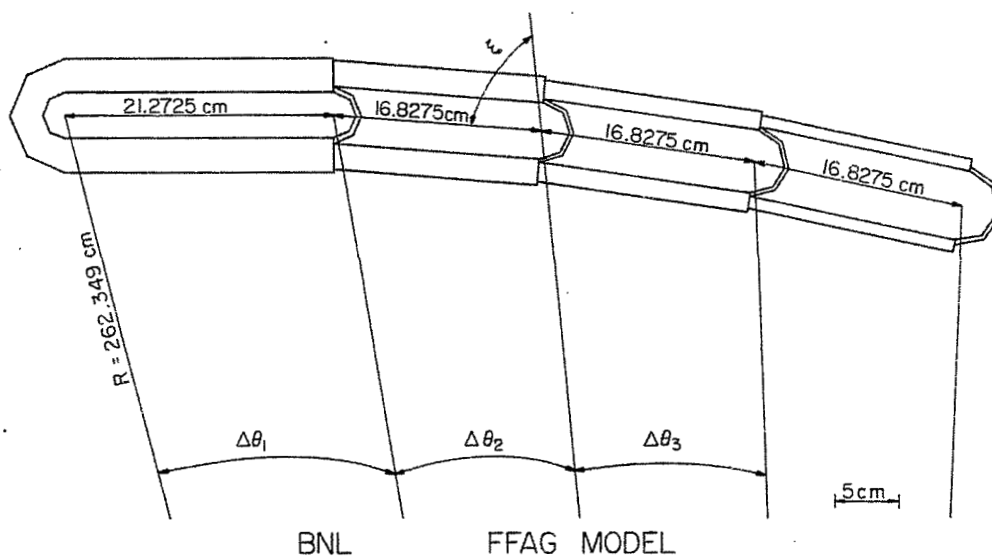


Fig. 3. Schematic coil construction to simulate actual coils such as those in Figs. 1 and 2. This geometry is assumed in the magnetic field calculations.

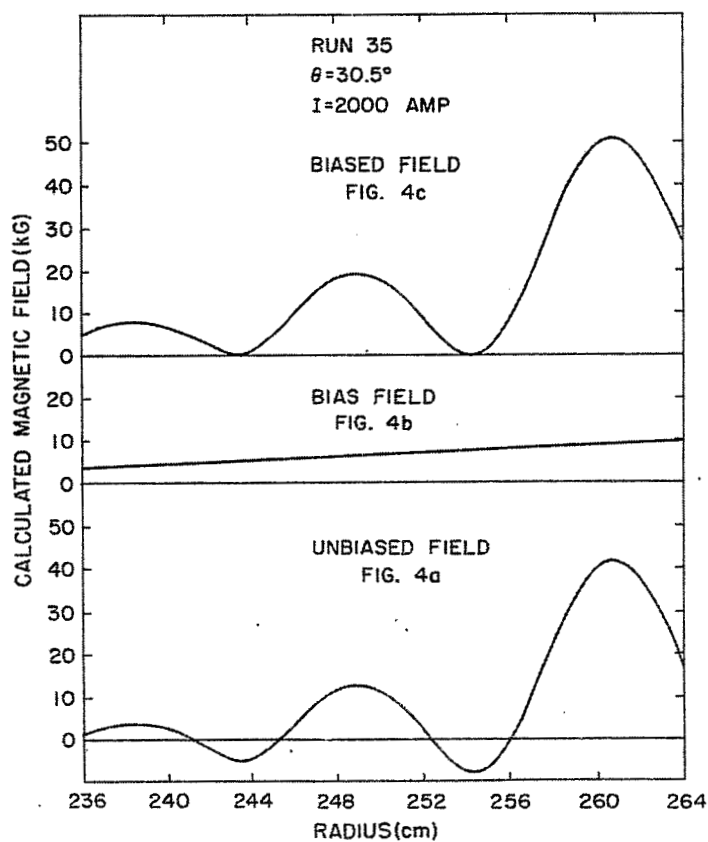


Fig. 4. Calculated  $B$  (kG) vs  $R$  (cm) at  $\theta = 30.5^\circ$ . The current in the 0.5 in. wide  $\text{Nb}_3\text{Sn}$  ribbon is assumed to be 2000 A. Figure 4a shows the unbiased field; Fig. 4b shows the biasing field; Fig. 4c shows the net biased field, i.e., the sum of the unbiased and biasing field.

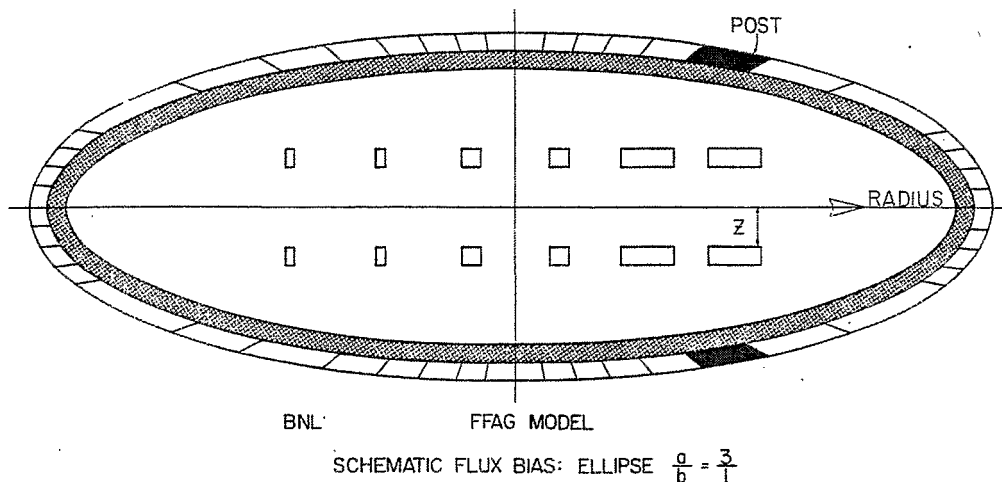


Fig. 5. Schematic flux biasing coils. The flux biasing coils are placed on an elliptical cross section which surrounds the main field coils. The net biased field is perpendicular to the median plane of the accelerator and vacuum chamber (see text).

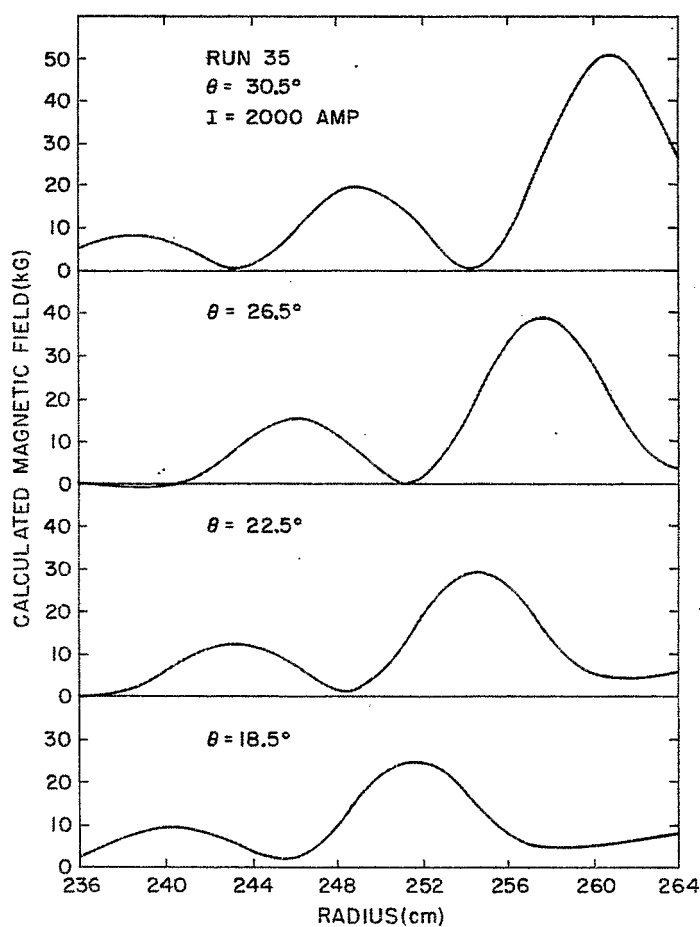


Fig. 6. Magnetic field (kG) plotted vs the radius (cm) of the accelerator for four values of  $\theta$ . The peaks of magnetic field owing to the spiral ridges are clearly resolved and appear at successively larger radii as they should in a good FFAG accelerator.



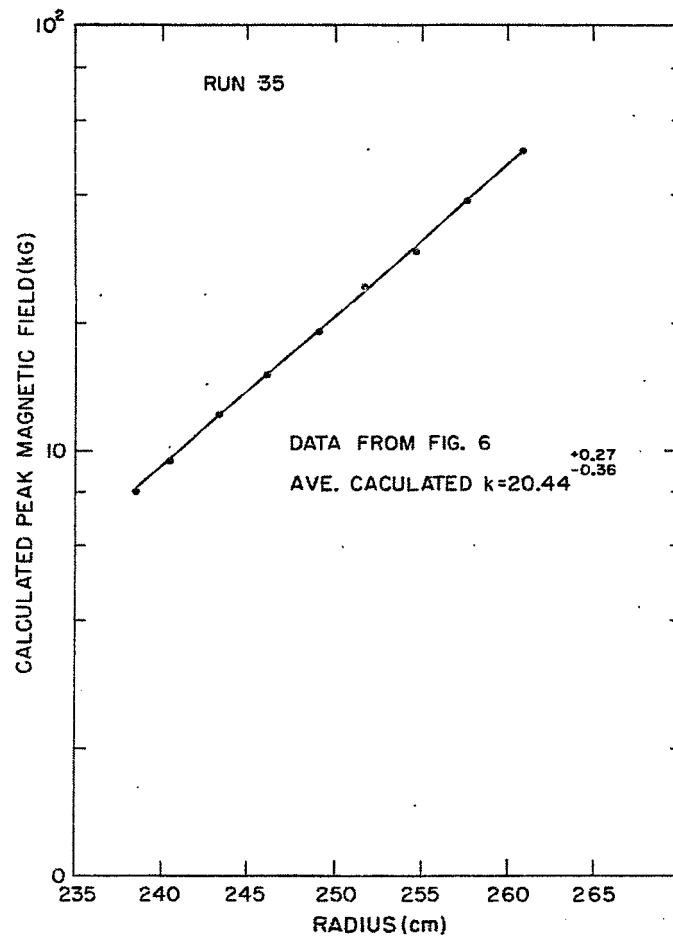


Fig. 7. Log of B vs R. Data used to calculate k, the field index, from R = 239 cm to R = 261 cm.

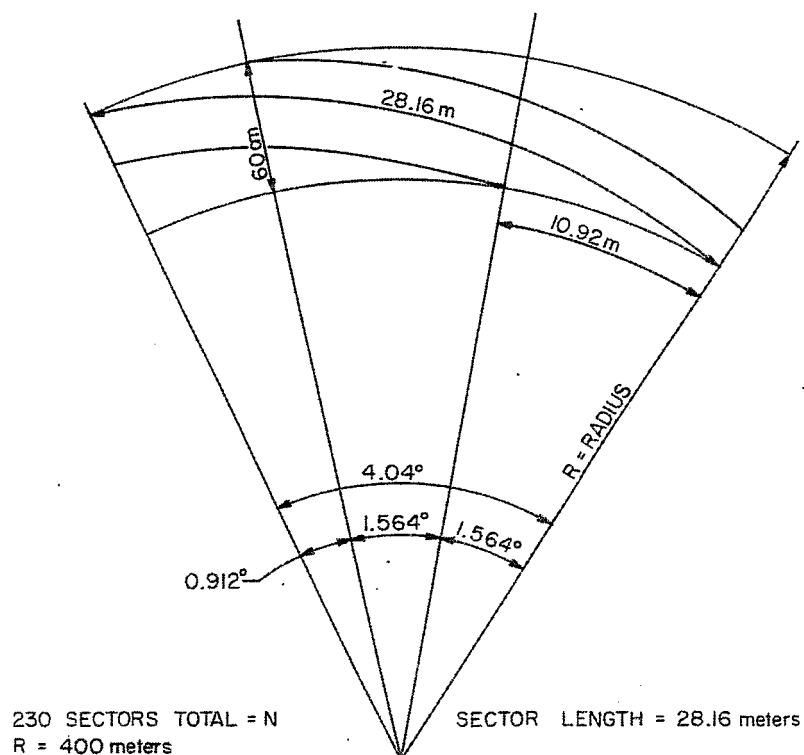


Fig. 8. Schematic details of a spiral sector for an FFAG superconducting 300 GeV accelerator (not to scale).

# PRELIMINARY STEPS FOR APPLYING SUPERCONDUCTORS TO FFAG ACCELERATORS\*

G. del Castillo, R.J. Lari, and L.O. Oswald  
Argonne National Laboratory  
Argonne, Illinois

## INTRODUCTION

In our effort to see the possibility of applying superconductors to accelerators, using magnetic guide fields, we came up with several questions. For some of them we have an answer, for others we see probable solutions, but there are still several for which we do not see a workable solution. Although this is our present situation, our answers and doubts are presented in this paper.

Some general considerations will be made on the problem of building a superconducting ring for an accelerator. These considerations will apply only to the guide field; problems related to injection and extraction or rf acceleration, although very important, are not discussed in this paper. Rather than presenting a detailed study of a cryogenic system with optimum performance, emphasis is placed on those problems where clear solutions are needed if one thinks seriously of building an accelerator.

Without talking specifically of a particular type of accelerator (pulsed or dc), we will discuss in general the problems of accuracy in field measurements, in positioning and alignment of a magnet set subject to thermal contraction and strong magnetic forces.

In what follows, three possible ways of building an accelerator magnet ring are presented.

- (A). The whole accelerator is in a vacuum chamber which serves as a cryogenic enclosure. This scheme is shown in Fig. 1. This design will apply to small machines, perhaps not more than 4 m diam; beyond this size this design is not economical.

If the magnets, forming the ring, have no obstructions in the median plane (open midplane), field measuring and positioning can be made inside of the enclosure at 4.2°K. It is required to have a support for the field measuring instruments and a boom that can move radially and azimuthally. The field mapping will be in polar coordinates.

One can conceive ways of "zeroing" the measuring scales at 4.2°K before starting to take magnetic measurements. A proper design may allow the field measuring devices to remain inside of the enclosure for future checking of the fields. Notice that this can be accomplished easily as there is no vacuum chamber in the field region.

For closed mid-plane magnets, the previous procedure will not apply. Magnetic measurements need to be carried out on a separate cryogenic measuring chamber (see Fig. 12); once a magnet is "measured" it takes its place in the ring. One very important point in this operation is that positioning a magnet requires reference marks that are related to magnetic measurements; the operation

---

\*Work performed under the auspices of the U.S. Atomic Energy Commission.

of the magnets is at  $4.2^{\circ}\text{K}$ ; thus, to minimize errors, a correspondence between field values and coordinates should be established at such a temperature. We will come back to discuss this point further.

- (B). The second alternative corresponds to the case of an accelerator having all the magnets in the ring sharing a common vacuum-cryogenic chamber as well as the same mechanical support. This case is illustrated in Fig. 2. This design will be suitable for large machines.

One can visualize at least two possible ways for field measuring and positioning of the magnets.

- (i). Using a cryogenic measuring chamber as mentioned above, regardless of whether the mid-plane is open or closed.— After measuring each magnet it is transferred into the ring. The final alignment of all magnets should be made at  $4.2^{\circ}\text{K}$ ; thus, it is essential to have access to reference marks or targets through the cryogenic enclosure. Azimuthal positioning can be done by normal surveying techniques and radial positioning by laser interferometry.
- (ii). Using a field measuring machine that can be part of the ring.— A magnet (and modular vacuum-cryogenic chamber) can be roughly positioned in the ring, the enclosure evacuated, cooled down, field measurements taken, and the reference marks established for future accurate positioning. In this case, as before, the reference marks should be accessible, through a window, from outside of the enclosure. Successive magnets will be accommodated in the ring until closed. Although this procedure may have some advantages, a detailed economic study will be needed to decide its applicability.

Versions A and B are also attractive from the point of view that, having the vacuum chamber at  $4.2^{\circ}\text{K}$ , ideal conditions against gas scattering will be obtained.

- (C). The field region of the magnet is at room temperature, each magnet being a separate unit (see Fig. 3). This design may be suitable for a very large machine, where each magnet is far away from its neighbor. In this last option, the minimum separation between two adjacent magnets is determined by the magnitude of the magnetic force that can be tolerated without producing misalignments.

The advantage of this design is that the magnetic fields can be measured, using well-known techniques, at room temperature; however, positioning reference marks should be located in the magnet, not in the shell of the cryogenic enclosure that, by definition, cannot be rigidly attached to the magnet.

This design may require a separate vacuum chamber, whereas in the two previous ones the cryogenic enclosure provides the vacuum needed for thermal insulation as well as for the beam. As mentioned before, the absence of a vacuum chamber may allow us to measure magnetic fields, at least in some spots, when the whole magnet ring is already assembled. This was a practice followed in the past for FFAG accelerators using iron magnets.

The previous examples illustrate the types of problems that will be encountered in this field. Neither of these designs presents a complete picture of the situation, as many details have been omitted for simplicity. Satisfactory solutions require the development of a new technology to meet tight tolerances in an environment at  $4.2^{\circ}\text{K}$ . A possible way to find some solutions will be outlined in this paper.

# PRELIMINARY STEPS FOR APPLYING SUPERCONDUCTORS TO FFAG ACCELERATORS\*

G. del Castillo, R.J. Lari, and L.O. Oswald  
Argonne National Laboratory  
Argonne, Illinois

## INTRODUCTION

In our effort to see the possibility of applying superconductors to accelerators, using magnetic guide fields, we came up with several questions. For some of them we have an answer, for others we see probable solutions, but there are still several for which we do not see a workable solution. Although this is our present situation, our answers and doubts are presented in this paper.

Some general considerations will be made on the problem of building a superconducting ring for an accelerator. These considerations will apply only to the guide field; problems related to injection and extraction or rf acceleration, although very important, are not discussed in this paper. Rather than presenting a detailed study of a cryogenic system with optimum performance, emphasis is placed on those problems where clear solutions are needed if one thinks seriously of building an accelerator.

Without talking specifically of a particular type of accelerator (pulsed or dc), we will discuss in general the problems of accuracy in field measurements, in positioning and alignment of a magnet set subject to thermal contraction and strong magnetic forces.

In what follows, three possible ways of building an accelerator magnet ring are presented.

- (A). The whole accelerator is in a vacuum chamber which serves as a cryogenic enclosure. This scheme is shown in Fig. 1. This design will apply to small machines, perhaps not more than 4 m diam; beyond this size this design is not economical.

If the magnets, forming the ring, have no obstructions in the median plane (open midplane), field measuring and positioning can be made inside of the enclosure at 4.2°K. It is required to have a support for the field measuring instruments and a boom that can move radially and azimuthally. The field mapping will be in polar coordinates.

One can conceive ways of "zeroing" the measuring scales at 4.2°K before starting to take magnetic measurements. A proper design may allow the field measuring devices to remain inside of the enclosure for future checking of the fields. Notice that this can be accomplished easily as there is no vacuum chamber in the field region.

For closed mid-plane magnets, the previous procedure will not apply. Magnetic measurements need to be carried out on a separate cryogenic measuring chamber (see Fig. 12); once a magnet is "measured" it takes its place in the ring. One very important point in this operation is that positioning a magnet requires reference marks that are related to magnetic measurements; the operation

---

\*Work performed under the auspices of the U.S. Atomic Energy Commission.

of the magnets is at  $4.2^{\circ}\text{K}$ ; thus, to minimize errors, a correspondence between field values and coordinates should be established at such a temperature. We will come back to discuss this point further.

- (B). The second alternative corresponds to the case of an accelerator having all the magnets in the ring sharing a common vacuum-cryogenic chamber as well as the same mechanical support. This case is illustrated in Fig. 2. This design will be suitable for large machines.

One can visualize at least two possible ways for field measuring and positioning of the magnets.

- (i). Using a cryogenic measuring chamber as mentioned above, regardless of whether the mid-plane is open or closed.— After measuring each magnet it is transferred into the ring. The final alignment of all magnets should be made at  $4.2^{\circ}\text{K}$ ; thus, it is essential to have access to reference marks or targets through the cryogenic enclosure. Azimuthal positioning can be done by normal surveying techniques and radial positioning by laser interferometry.
- (ii). Using a field measuring machine that can be part of the ring.— A magnet (and modular vacuum-cryogenic chamber) can be roughly positioned in the ring, the enclosure evacuated, cooled down, field measurements taken, and the reference marks established for future accurate positioning. In this case, as before, the reference marks should be accessible, through a window, from outside of the enclosure. Successive magnets will be accommodated in the ring until closed. Although this procedure may have some advantages, a detailed economic study will be needed to decide its applicability.

Versions A and B are also attractive from the point of view that, having the vacuum chamber at  $4.2^{\circ}\text{K}$ , ideal conditions against gas scattering will be obtained.

- (C). The field region of the magnet is at room temperature, each magnet being a separate unit (see Fig. 3). This design may be suitable for a very large machine, where each magnet is far away from its neighbor. In this last option, the minimum separation between two adjacent magnets is determined by the magnitude of the magnetic force that can be tolerated without producing misalignments.

The advantage of this design is that the magnetic fields can be measured, using well-known techniques, at room temperature; however, positioning reference marks should be located in the magnet, not in the shell of the cryogenic enclosure that, by definition, cannot be rigidly attached to the magnet.

This design may require a separate vacuum chamber, whereas in the two previous ones the cryogenic enclosure provides the vacuum needed for thermal insulation as well as for the beam. As mentioned before, the absence of a vacuum chamber may allow us to measure magnetic fields, at least in some spots, when the whole magnet ring is already assembled. This was a practice followed in the past for FFAG accelerators using iron magnets.

The previous examples illustrate the types of problems that will be encountered in this field. Neither of these designs presents a complete picture of the situation, as many details have been omitted for simplicity. Satisfactory solutions require the development of a new technology to meet tight tolerances in an environment at  $4.2^{\circ}\text{K}$ . A possible way to find some solutions will be outlined in this paper.

## THE FFAG ACCELERATOR

The application of superconductors to accelerators seems to be most probable in the case of machines using time independent magnetic fields. The FFAG accelerator is an attractive candidate. It has, however, a clear disadvantage, namely, the complexity of the magnetic field; it is, nevertheless, the type of machine that we will consider in what follows.

Among the two types of FFAG accelerators, we are interested in the spiral sector type<sup>1</sup> in which the field in the median plane is given by the well-known expression\*

$$B_z = B_0 (r/r_0)^k \left\{ 1 + f \cos \left[ N\theta - K \ln (r/r_0) \right] \right\} .$$

In a very small accelerator, one can produce this field by a current distribution running along a spiral from the inner to the outer radius of the machine.<sup>2\*\*</sup> Acceleration can be obtained by betatron action. However, if rf acceleration is used as in the case of a large machine, continuity within the spirals is no longer possible and the accelerator guide field needs to be interrupted by short straight sections. Furthermore, if each unit (between two straight sections) needs to be kept within a reasonable size, further division of the unit will be necessary. The spirals will then be broken into many pieces as illustrated in Fig. 4.<sup>3</sup> By assigning the required magnetic potential at the reference radius, the corresponding potentials (or ampere-turns) can be calculated along the different blocks forming the spiral. The change in potential per sector, i.e., between adjacent coils in any block, determines the ampere-turns required to excite each pole. Figure 4 shows these coils in an iron yoke. For simplicity in the calculations, the iron poles can be considered as magnetic equipotentials. For an air core magnet the required field may be obtained by some form of current distribution; our problem consists in selecting the distribution that satisfies both magnetic and mechanical requirements; the latter is related to deformations resulting from forces and thermal effects. The current distribution, from the geometrical point of view, should also conform with the shape of the superconductor, as mechanical stability in superconducting coils cannot be obtained through operations like vacuum impregnation or epoxying.

Taking these points into consideration together with the fact that the radial aperture in an FFAG machine is somewhat large, we believe that the block configuration of Fig. 4 may satisfy all requirements, at least in the first approximation.

A simple way to obtain a current distribution that may satisfy the field requirements was proposed by Blewett.<sup>4</sup> Given the scaling condition between sectors, the ampere-turns required for excitation are found for the successive poles located along a radius and for a given azimuth. This yields the field patterns already shown in Parzen's and Kruger's papers. The presence of negative fields is undesirable because

---

\* See G. Parzen's second article in these Proceedings, p. 1052.

\*\* This is discussed by P.G. Kruger in these Proceedings, p. 1059, although not in connection with small accelerators.

1. K.R. Symon et al., Phys. Rev. 103, 1837 (1956).
2. D.W. Kerst et al., Rev. Sci. Instr. 31, 1076 (1960).
3. Proposal for a High Intensity Accelerator, MURA, September 1963.
4. J.P. Blewett, Brookhaven National Laboratory, Accelerator Dept., AADD Technical Note No. 30 (1967).

they cause an increase in the circumference factor of the accelerator. The problem then consisted in finding the currents that will satisfy the scaling condition plus the condition that  $B = 0$  at the minima. This yielded five equations with five unknowns from which the currents were determined.

To see the practical difficulties that one may encounter in producing such a field when dealing with finite size coils and to study edge effects, which are difficult to calculate, a small copper model was built. The same three coil configurations used by Blewett were studied. A schematic view of the magnet appears in Fig. 5. The dimensions were determined experimentally to give the best fit to the calculated values, and the winding scheme was obtained from Blewett's note.

A comparison of our results to the calculated field can be seen in Fig. 6. The accuracy in the field measurement is about 0.5%. The results presented here were obtained after many trials where conditions were changed, and although there is still some discrepancy between the two curves, we believe that more work could yield better results. This, however, was not attempted as we are now interested in developing computer programs for calculating the fields in a realistic configuration involving finite size coils also satisfying the requirements needed in an accelerator.

### THE SUPERCONDUCTING MAGNET

Before one can think about using superconductors for magnetic guides in FFAG accelerators, one should have clear answers to the following questions, all related to an environment at  $4.2^{\circ}\text{K}$ .

- 1) Can one measure magnetic fields with accuracies of the order of 0.01%?
- 2) Is it possible to establish reproducible correlations between currents and fields compatible with the above accuracy?
- 3) In an FFAG magnet, how can one solve the problem of "low field superconductivity"?

There are also questions of an engineering nature, namely, can reference marks, related to field measurements, be established and extrapolated outside of the cryogenic enclosure maintaining accuracies of a few parts in  $10^5$  (in 100 in. length)?

These and other questions related to rf acceleration, injection and extraction at low temperatures are important to the accelerator builder.

A simple magnet configuration as illustrated in Fig. 7, having rectangular coils, may be a step in the right direction. The geometry is simple enough to facilitate calculations and interpretation of results. If one wants to be realistic, the dimensions and fields must be consistent with the parameters that may be used in an accelerator.

A possible field value of about 50 kG may be obtained in such a magnet using coils having about a 4 in.  $\times$  4 in. cross section and 18 in. long with a 6 in. separation between the centers of the coils. The expected variation of the  $B_y$  component of the field is shown in Fig. 8. The results of the calculation indicated that field uniformity of one part in  $10^4$  should be expected in a cylinder of 1 in. diameter and about 2 in. long. Each of these coils can be made using a conductor having 15 strands of superconducting NbTi in a copper matrix of a rectangular cross section 0.055 in.  $\times$  0.115 in. with a copper-to-superconductor ratio of 3.5:1. This conductor should carry at least 500 A at 50 kG.

In the absence of diamagnetic effects, the equigauss plot in the cross section

of the coil should be as shown in Fig. 9. This indicates the regions in the coil that one should protect against low field instabilities.<sup>5</sup>

Magnetic forces can be a serious problem in these coils as can easily be seen from Figs. 10 and 11. The expected total attractive force between the upper and lower coil is about 210 tons.

It would be naive to think that a coil subject to thermal contractions and large magnetic forces can maintain the dimensions as imposed by field tolerances, i.e., a displacement of the center of the coil bundle of 0.002 in. will produce a field change of about 0.01%. Thus, most likely correction coils need to be used; presumably these should be made of copper.

The first tests of this magnet can be carried out in a Dewar, the magnet standing in the vertical direction. Dimensional changes due to thermal contraction and magnetic forces may be observed and measured through a window in the Dewar. The field measurements can be made with an NMR probe (bore at room temperature) which will serve as a primary standard. Other magnetic measuring instruments, flip coil, rotating coil, and bismuth probe can then be calibrated both at 300°K and 4.2°K.

The final tests should be conducted in a cryogenic enclosure as shown in Fig. 12. This can be used for field mapping and establishing reference marks for future alignment. Provisions should be made for positioning the magnet with respect to the same coordinate system used for the magnetic field measuring instruments.

The enclosure essentially consists of two coaxial cylinders - the inner one at 77°K serves as a radiation shield between the magnet at 4.2°K, and the outer shell is at room temperature. Initially, liquid helium can be used in the reservoir designed for such a purpose; in the future a refrigerator may take the place of the helium reservoir. Many details have been omitted in this figure for clarity, but the final design contains the power connections, helium transfer and liquid level controller, plus instrumentation required for operating the enclosure and the magnet. The side windows will be used for alignment of the magnet.

Several mechanisms are now under study to select the most appropriate one for performing operations like rotations, displacements, etc., as required by the positioning devices and field measuring equipment.

The chamber is of a modular type; thus, combinations of magnets can be studied by adding a module of the size required to accommodate as many magnets as needed.

It is our hope that these steps will help us to better understand the problems in this field and look for the appropriate solutions.

We are grateful to Dr. T. Khoe for many illuminating discussions on the general subject of magnetic fields, and to Dr. E. Crosbie for his interest and support of this project.

Thanks are also due to Mr. E. Berrill who is developing the technology for measuring fields at low temperature.

---

5. G. del Castillo and L.O. Oswald, these Proceedings, p. 601.



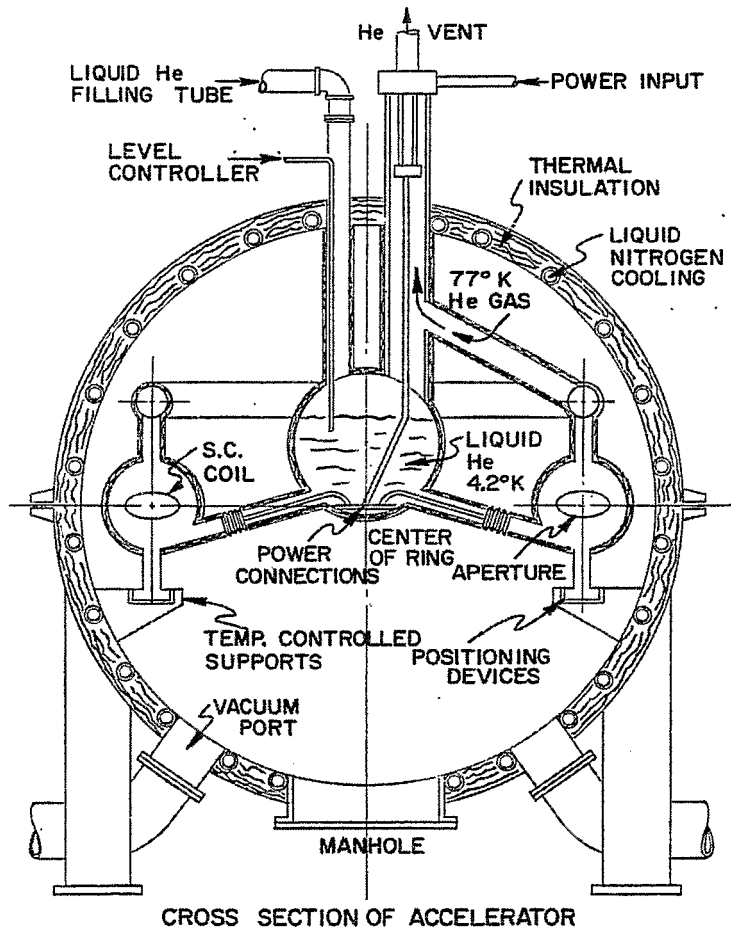


Fig. 1. Simplified version of a "superconducting" accelerator inside of a common vacuum chamber and cryogenic enclosure. The elliptical areas represent the magnetic field region. The beam circulates in a plane normal to the paper. The center of the machine coincides with the center of the spherical enclosure. This version offers optimum cryogenic conditions. For simplicity the use of liquid helium is illustrated; however, in this as well as the following cases, a refrigerator should be used.

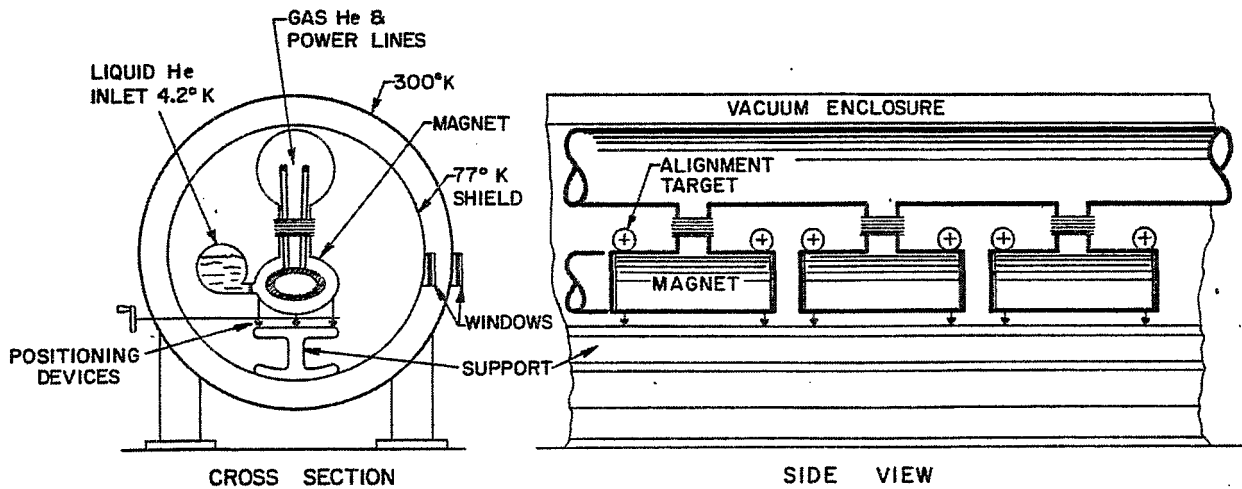


Fig. 2. Version of an accelerator using a common vacuum-cryogenic chamber and magnet support. Notice that windows for magnet alignment as well as manipulators for fine adjustment are required.

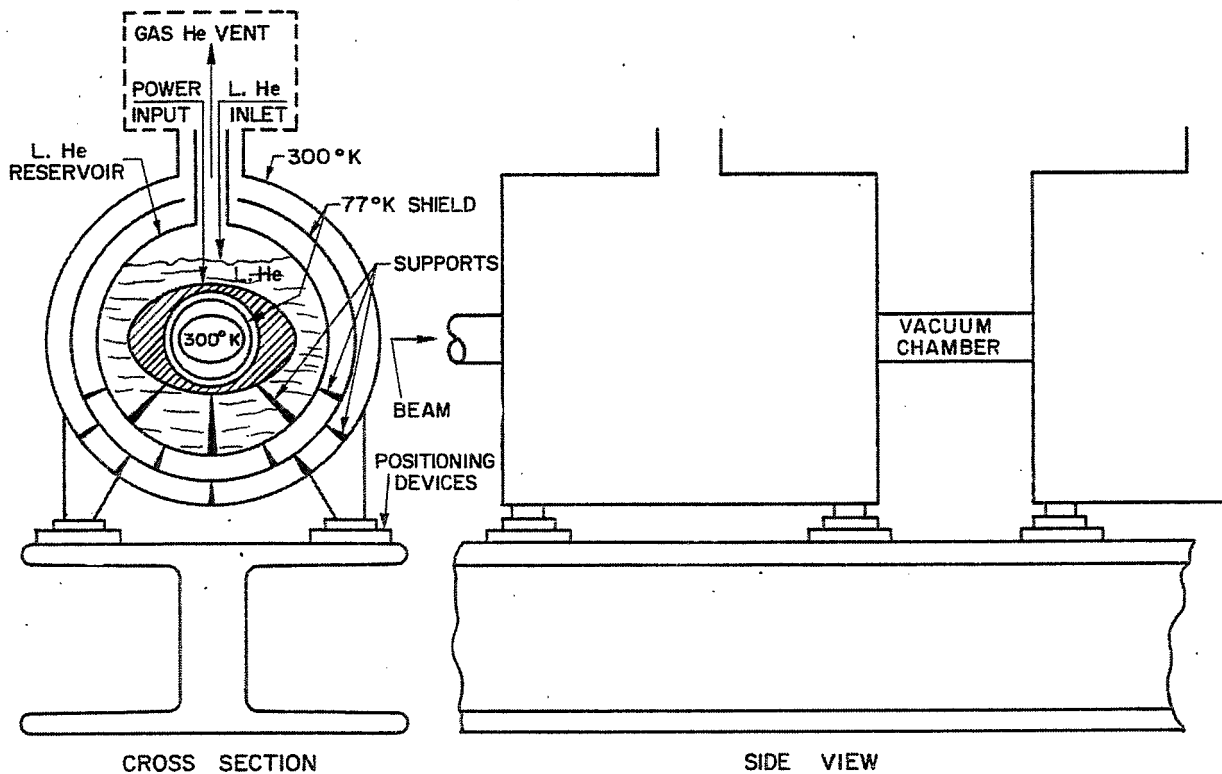


Fig. 3. Accelerator version using superconducting magnets with bore at room temperature. This design will be suitable for a large size machine or beam transport system. No alignment targets are included, as it is unlikely that after cool-down the targets located in the outer enclosure will remain unchanged relative to the magnet. Positioning of these magnets should follow other techniques different from triangulation.

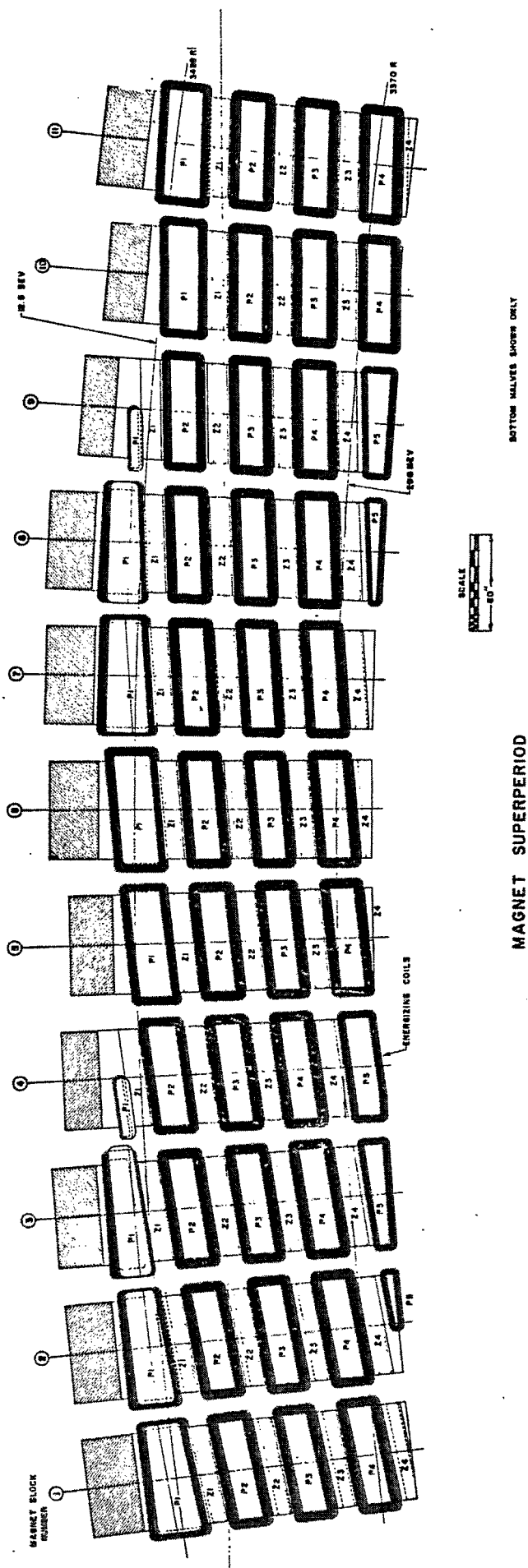


Fig. 4. Superperiod of a large FFAG accelerator using iron magnets (MURA Proposal, 1963).

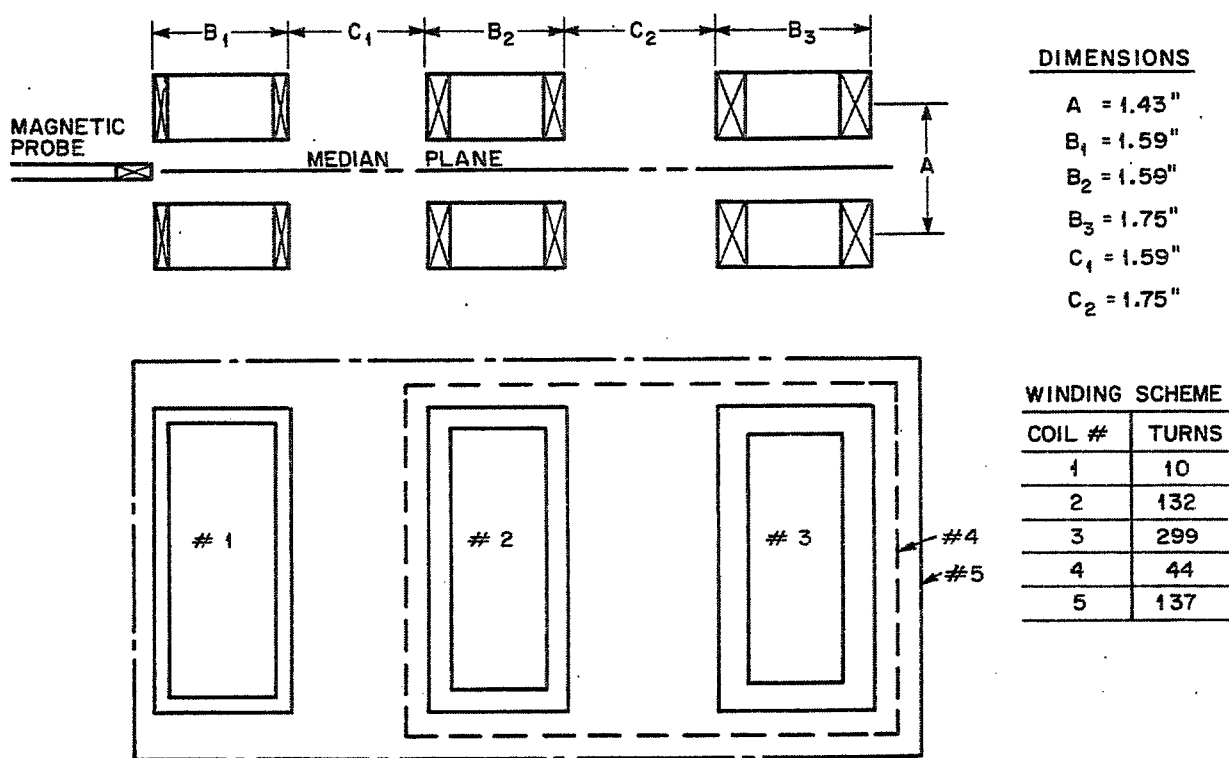


Fig. 5. Practical realization of J. Blewett's scheme. The two-dimensional calculation was used to build this magnet. The  $A = B = C$  condition used by Blewett was corrected, as indicated, to take into account finite size coils and end effects.

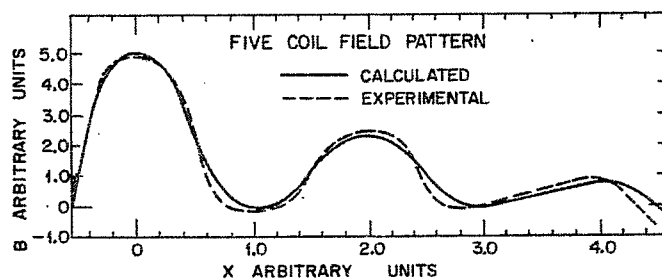


Fig. 6. Comparison between the results of magnetic measurements made in the model magnet and the two-dimensional calculation.

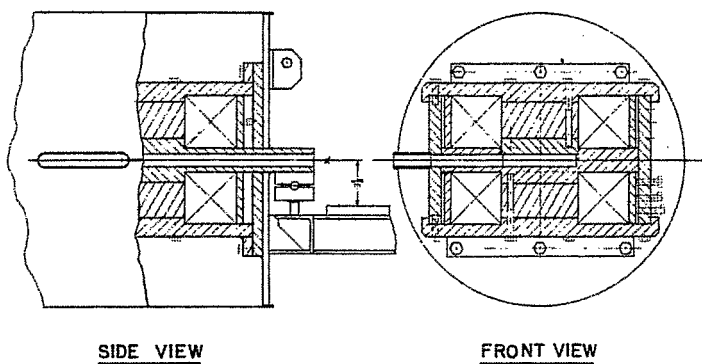


Fig. 7. 50 kG superconducting magnet. The stainless-steel structure surrounding the coils is needed to minimize dimensional changes due to magnetic forces. Two windows each 1 in.  $\times$  5 in. are provided along two perpendicular axes for magnetic measurements. The magnet is surrounded by an enclosure to be used in conjunction with the field measuring chamber (see Fig. 12).

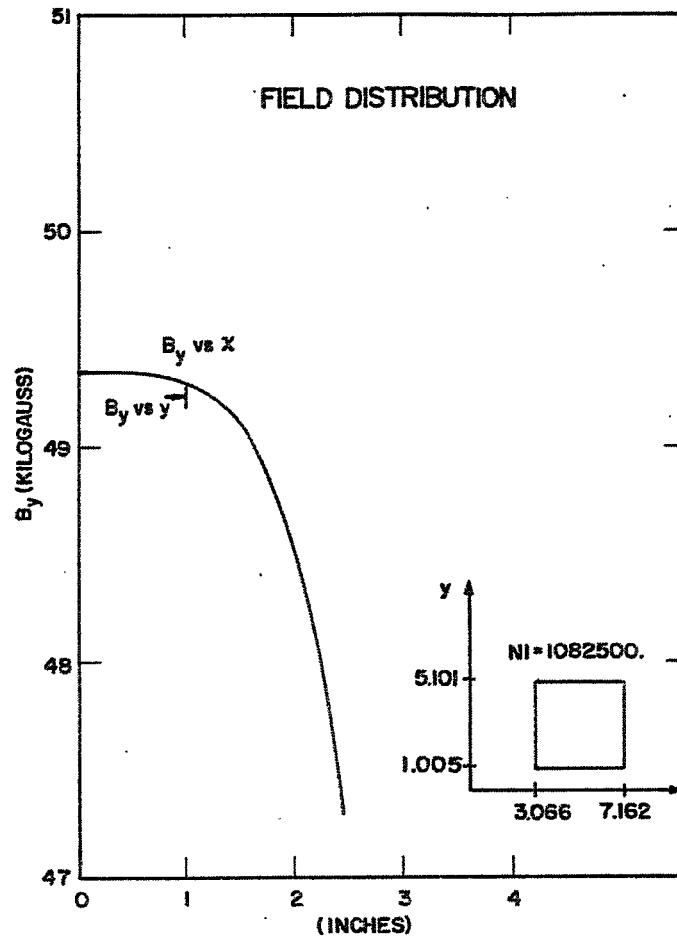


Fig. 8. Variation of  $B_y$  component of the field with respect to coordinates  $X$  and  $Y$ . The expected field uniformity is of one part in  $10^4$  in a cylinder 1 in. diam and 2 in. long.

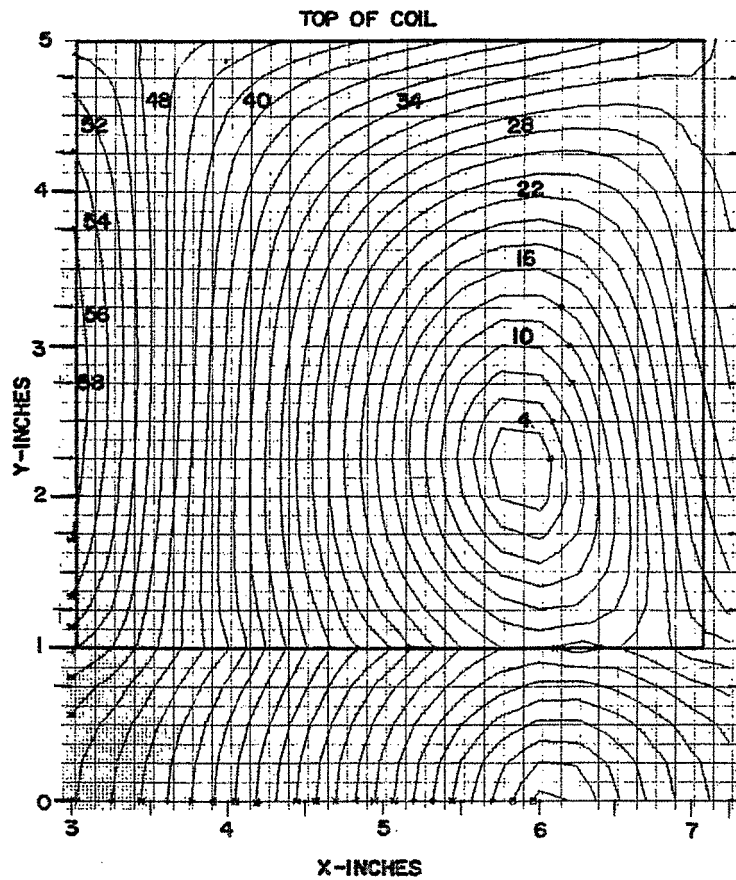


Fig. 9. Equigauss plot in the cross section of the coil shown in the insert of Fig. 8. No diamagnetic effects are considered in this calculation.

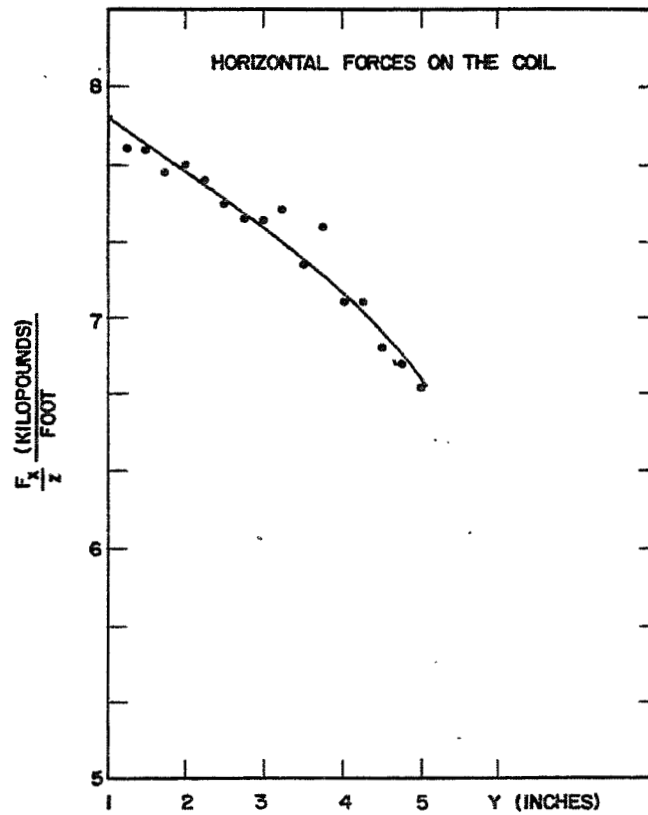


Fig. 10. Horizontal force distribution in the cross section of the coil.

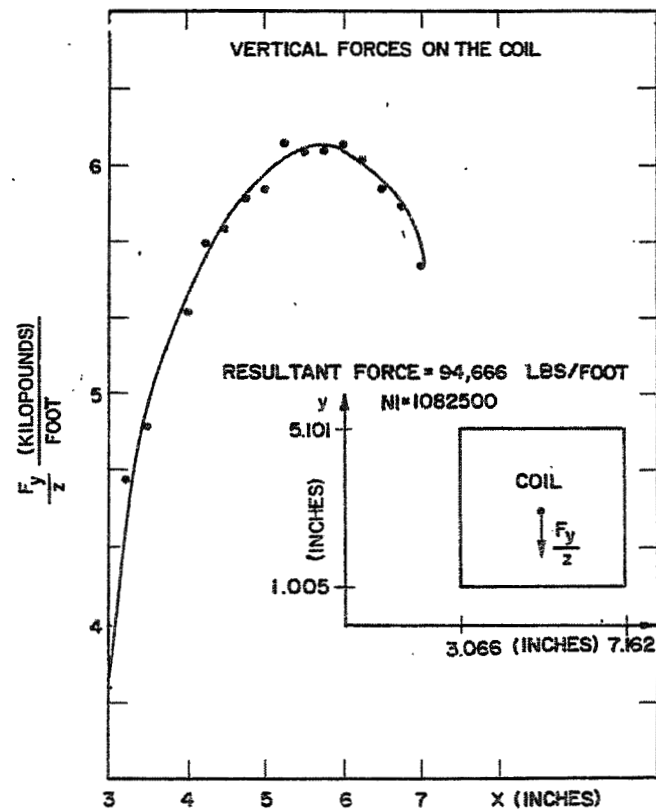


Fig. 11. Vertical force distribution in the cross section of the coil.



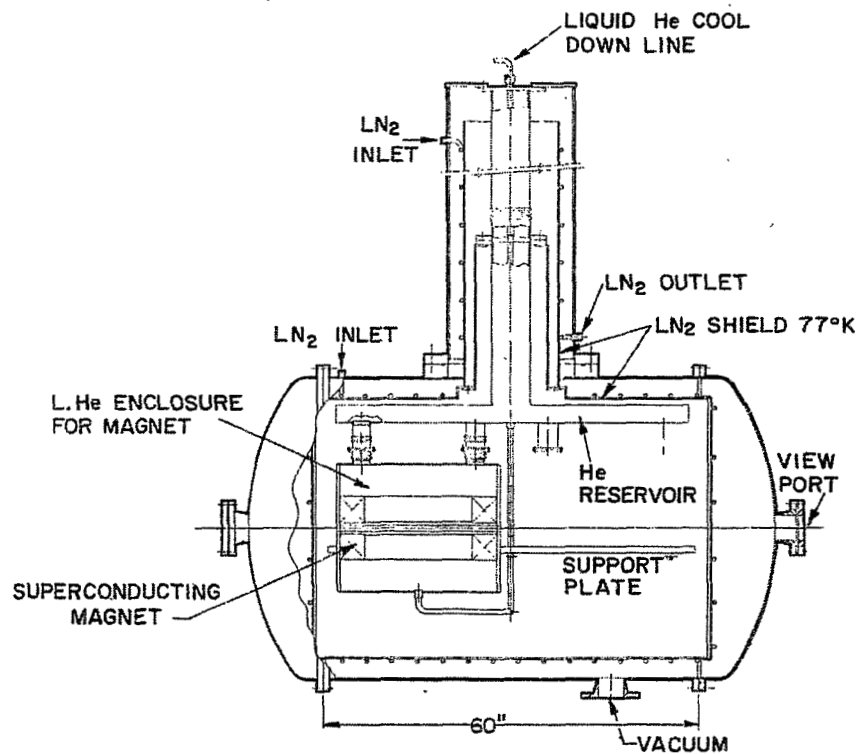


Fig. 12. Cryogenic field measuring chamber. The design is based on Fig. 1. The magnet, surrounded by its liquid helium enclosure, is shown near the end of the chamber. The other end is used for the field measuring instruments (not shown in the figure). For clarity many other details have been omitted. The diameter and length of the outer cylinder are 4 ft and 5 ft, respectively.

# A SUPERCONDUCTING SLAC WITH A RECIRCULATING BEAM\*

W.B. Herrmannsfeldt  
Stanford Linear Accelerator Center  
Stanford University, Stanford, California

## I. INTRODUCTION

The old idea of recirculating the beam in a linear accelerator becomes more interesting with the introduction of the superconducting accelerator. The long duty cycle makes it possible for the beam to go around several times. In fact, if the superconducting accelerator is operated cw, the recirculating beam could also be continuous.

The purpose of this note is to examine the practical limitations involved in recirculating a beam at SLAC in order to get the highest possible energy.

A nominal goal of 100 GeV has been chosen as a value worthy of an extensive rebuilding of the SLAC accelerator, yet low enough that good use can be made of the beam within the confines of the SLAC boundaries. Earlier in this Summer Study, Neal<sup>1</sup> reported on the tentative parameters of a 100 GeV superconducting accelerator, 3000 m long. It was noted that this requires an energy gradient of 33 MeV/m, a value which has yet to be demonstrated in a superconducting accelerator structure.

Interest in a recirculating beam stems from the need for an alternative way of obtaining high energy if for any reason it proves impossible or unfeasible to achieve the 33 MeV/m energy gradient. In passing, it should be noted that, although 33 MeV/m is theoretically possible for a traveling wave design in a niobium structure, there are at least two practical limitations which have not been resolved as of the date of this Summer Study. One limitation is the rf magnetic field limit,  $H_{c1}$ , at which the type II superconductor starts to go normal. The latest results, reported by Schwettman<sup>2</sup> at this Summer Study, in excess of 500 G for  $H_{c1}$ , are reasonably close to the approximately 750 G required for a TW structure at 33 MeV/m.

The second limitation is the onset of field emission for electrons from the walls of the structure. Rf energy is lost to such electrons which then strike the walls, converting the energy to heat which must be removed by the refrigeration system. An accelerator structure operating at a high energy gradient must have very low field emission or else the refrigeration demand becomes excessive. Until a structure can be operated in the accelerator mode at high enough field levels, it is essentially impossible to predict at what field level field emission could become important. Although the Fowler-Nordheim theory appears to apply,<sup>3</sup> field enhancement due to sharp projections or foreign matter on the surface may cause field emission at fields lower than predicted from rf field calculations.

---

\* Work supported by the U.S. Atomic Energy Commission.

1. R.B. Neal, these Proceedings, p. 101.
2. H.A. Schwettman, these Proceedings, p. 1.
3. H.A. Schwettman, J.P. Turneure, W.M. Fairbank, T.I. Smith, M.S. McAshan, P.B. Wilson, and E.E. Chambers, IEEE Trans. Nucl. Sci. NS-14, No. 3, 336 (1967).

## II. SYNCHROTRON RADIATION

The limitation on the energy of a circular electron accelerator is the loss of energy of the beam due to synchrotron radiation. Synchrotron radiation is the name given to the band of light and X-rays emitted by a beam of electrons which are being accelerated in an electromagnetic field. In the case in which the beam is caused to go in a circle, the energy loss per revolution is given by<sup>4</sup>

$$U = 8.85 \times 10^{-32} E^4 / r \quad (\text{eV/revolution}) \quad , \quad (1)$$

where  $r$  is the radius of curvature in meters and  $E$  is the beam energy in electron volts.

Figure 1 is a view of the SLAC site with the proposed recirculating beam superimposed using a 225 m radius for the loops. The choice of the radius is quite arbitrary, but the effect of changing it by less than a factor of two is essentially negligible for the purpose of this note. The long straight line for the return path is, of course, very simple and could be made by a tunnel-digging machine.<sup>5</sup> It would contain only an ordinary vacuum pipe and some steering and focusing magnets. The magnet rings are assumed to consist of a suitable lattice of separated function bending and focusing magnets. Figure 2 shows the topographic cross section on the beam path.

The fact that the synchrotron radiation limit is reached so quickly appears to favor a separate return path rather than one which uses the accelerator tunnel. Even though the beam can be accelerated on the return path in a standing wave accelerator, the bigger, more complicated magnet rings add to the cost without apparently adding any capability.

In an earlier note<sup>6</sup> on which this work is based, it was assumed that as many as three separated orbit return loops could be used. Subsequent consideration of the promise of superconducting rf structures, as described in Ref. 1, make it seem more realistic to assume that at least 50 or 60 GeV can be achieved in a single pass through the 3000 m long accelerator housing. Then only one return loop would be required to obtain 100 GeV.

Due to the high rate of synchrotron radiation, the beam energy is changing significantly within the magnet rings. Thus it is necessary to integrate the energy loss to calculate the remaining energy. From Eq. (1), the energy lost per radian is

$$\frac{dE}{d\theta} = - \frac{8.85 \times 10^{-32}}{2\pi} \frac{E^4}{r} \quad (\text{eV/rad}) \quad , \quad (2)$$

where  $r$  is a constant. Integrating Eq. (2) over  $2\pi$  radians results in

$$\left( \frac{1}{E} \right)^3 = \left( \frac{1}{E_0} \right)^3 + \frac{3 \times 8.85 \times 10^{-32}}{r} \quad , \quad (3)$$

where  $E$  is the energy after the beam has gone through both rings and is back at the injection end.  $E_0$  is the energy the beam had as it entered the magnet ring.

---

4. M.S. Livingston and J.P. Blewett, Particle Accelerators (McGraw-Hill, New York, 1962).

5. T.E. Howard, Scientific American 217, No. 11, 74 (1967).

6. W.B. Herrmannsfeldt, Stanford Linear Accelerator Center Technical Note TN-68-8 (1968).

The characteristic energy of the photon spectrum of the synchrotron radiation is given by<sup>7</sup>

$$E_c = \frac{3hc}{4\pi r} \gamma^3, \quad (4)$$

where  $h$  is Planck's constant,  $c$  is the velocity of light,  $r$  is the effective bending radius and  $\gamma$  is the beam energy in units of  $mc^2$ . An estimate for the statistical fluctuation of the emitted radiation can be found by assuming that the lost energy,  $E_0 - E = nE_c$ , where  $n$  is the number of photons emitted in a bend of  $2\pi$  radians. The standard deviation of the emitted radiation is thus

$$\Delta E = \sqrt{nE_c^2} = \sqrt{(E_0 - E) E_c}. \quad (5)$$

The resulting spread in the beam energy is  $\Delta E/E_0$ . The use of  $E_0$  rather than  $E$  is an acceptable approximation if  $E_0$  is used in Eq. (4) to calculate  $\gamma$ .

Using Eqs. (3) and (5) and the parameters assumed above, it is now possible to obtain a list of parameters for a recirculating beam facility (see Table I).

TABLE I

Parameters for a Single Loop, Recirculated Beam Accelerator

Length = 3000 m

Energy gain per pass = 60 GeV

Energy gradient = 20 MeV/m

Effective radius of loop = 200 m<sup>(a)</sup>

Energy lost to synchrotron radiation = 4.8 GeV (360° bend)

Final energy after two passes =  $2 \times 60 - 4.8 \approx 115$  GeV<sup>(b)</sup>

Characteristic energy of synchrotron photons = 2.5 MeV

Number of characteristic photons per electron = 1920

Quantum statistical energy spread = 109 MeV

One-loop percentage energy spread =  $0.109/55.2 = \pm 0.2\%$ <sup>(c)</sup>

Final percentage energy spread =  $\pm 0.1\%$ <sup>(c)</sup>

- 
- (a) Effective Radius: The effective radius is defined as the actual bending radius in the bending magnet. It was chosen as about 10% less than the radius of the beam line to permit insertion of suitable focusing magnets and drift lengths.
- (b) Final Energy: Assuming 60 GeV per pass, the final energy is somewhat higher than 100 GeV. Note that the maximum possible energy of electrons which can be bent through the 200 m loops, found by setting  $E_0$  to infinity in Eq. (3), is only 91 GeV (if we ignore quantum fluctuations).
- (c) Energy Spread: At the injector end, after the first loop, the spread is  $\pm 0.2\%$ . After the second pass through the accelerator, the spread due just to synchrotron radiation is  $\pm 0.1\%$ , which is probably comparable to the spread due to all other causes combined.
- 

7. J. Schwinger, Phys. Rev. 75, 1912 (1949).

### III. MAGNET LOOPS

At this time, only enough is known about the magnet loops to permit some general remarks.

It is expected that the magnets would be dc excited for economy and stability. If conventional magnets are used, the power costs would be considerable. Attention is thereby drawn to superconducting magnets or to aluminum wire cryogenic magnets such as described by Danby.<sup>8</sup> The latter would be ideally suited since the fields required are only about 10 kG.

The magnetic transport system must be both achromatic and isochronous. The isochronous (constant time) condition is required to preserve the bunched characteristic of the beam. Debunching due to velocity spread is negligible at these energies. It appears desirable to have the shortest possible focusing (betatron) wavelength in order to minimize debunching in each  $180^\circ$  bend. A small ( $\sim 6^\circ$ ) reverse bend, on the long straight return path, can be used to restore the bunch structure if necessary.

The effect on transverse phase space of the emission of synchrotron radiation is to cause an increase, particularly in the horizontal plane, which will be difficult to transport through the accelerator. The accelerator steering and focusing will be constrained by the requirement that two beams will be transported simultaneously. How much can be gained by damping with the magnetic focusing system has not been determined.

This proposal has been described as "4 miles of BBU." If a transverse instability develops it may, in fact, be possible to use a feedback scheme. Such a scheme is indicated because of the cw operation and the fact that the beam takes a longer path than the signal cable from pickup cavity to amplifier.

For the beam to be accelerated on the second pass, it must have traveled an integral number of rf wavelengths. The requirement for phasing to  $\lambda/100$  (about  $4^\circ$  of phase) requires that the path length tolerance is  $\lambda/100$ . In an isochronous system, the zero order path length is determined by the position of the focusing elements. The correct phase can be obtained by remotely moving some of the quadrupole lenses.

### IV. CONCLUSION

The problems discussed above make it clear that it would be much preferred if the 100 GeV beam can be generated without resorting to a recirculating scheme. However, it does appear that, if necessary, a recirculating beam facility could help boost the energy to about 100 GeV. That 100 GeV is nearly the upper limit is also fairly apparent.

### ACKNOWLEDGMENT

It is a pleasure to acknowledge helpful discussions with M.A. Allen, R.H. Helm, R.H. Miller, and M. Sands. R.S. Gould kindly supplied the topographic cross section.

---

8. G.T. Danby, these Proceedings, p. 1115.



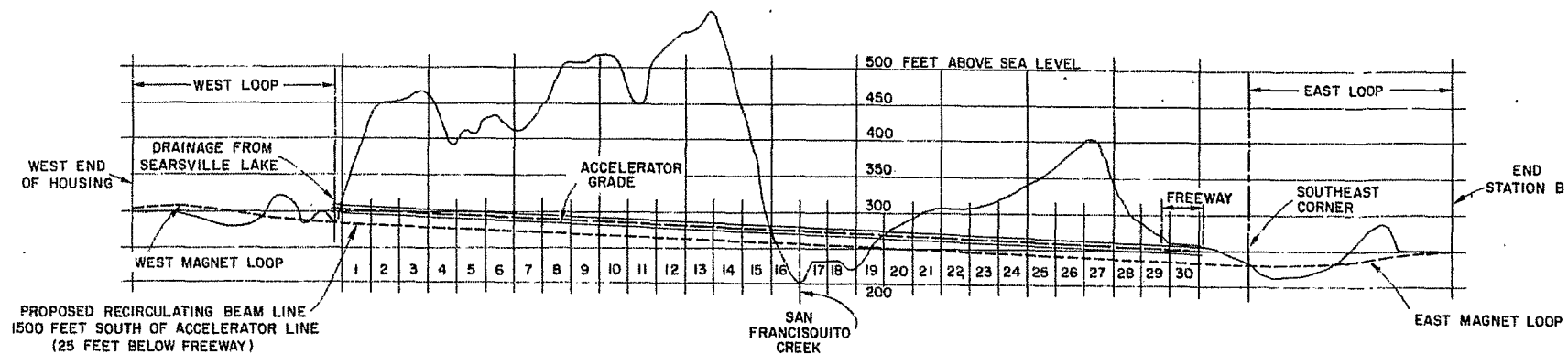


Fig. 2. Contour cross section showing the recirculating beam line from Fig. 1. Note that the loops are shown as a projection which makes the beam elevation appear to undulate.

# PROPERTIES AND PREPARATION OF HIGH-PURITY ALUMINUM\*

V. Arp  
Cryogenics Division, Institute for Basic Standards  
National Bureau of Standards  
Boulder, Colorado

## I. INTRODUCTION

The potential economy of using aluminum magnets operating at low temperatures was suggested by Post and Taylor<sup>1</sup> in 1959, before the advent of high field superconductivity. A liquid-hydrogen-cooled aluminum magnet was built and operated not long thereafter,<sup>2</sup> but by that time superconducting magnets seemed to be generally more attractive. Nevertheless, a small effort was carried on, since, for some low duty cycle conditions, aluminum appears to be more attractive than superconductors.<sup>3,4</sup> We have continued a study of the properties of aluminum which are related to this type of application, and a major part of this paper summarizes this study and knowledge in a tutorial fashion. The final and minor section of the paper reports the current status on the availability of high-purity aluminum in technologically useful quantities.

## II. PROPERTIES OF HIGH-PURITY ALUMINUM

In this, the major portion of the paper, electrical and thermal conductivities of metal are discussed, and data relevant to high-purity aluminum are presented. The analysis starts with a summary of various contributions to the dc resistivity. It then goes on to demonstrate the quantitative relationship between the electrical and thermal conductivities. Finally, it considers the response of metals under ac conditions.

### 1. The dc Resistivity of Metals

The customary approximation used in the discussion of the resistivity of metals is Mathiessen's rule

$$\rho \approx \sum_i \rho_i, \quad (1)$$

where  $\rho_i$  is the "partial" resistivity due to any one mechanism which inhibits the flow of electrons through the metal. In the next approximation, one can find deviation terms to be added to the right side of Eq. (1)<sup>5</sup>; however, they will not be considered in this paper. Equation (1), then, forms the basis for separate discussions of various contributions to the total electrical resistivity of a metal.

Data on the electrical resistivity of aluminum as a function of temperature are summarized in Fig. 1.<sup>6</sup> Starting at low temperature, samples of different purity are seen to have different resistivities, independent of temperature. This is the region where localized imperfections in the atomic lattice dominate the total resistivity; various types of imperfections, and the separate contributions to the total resistivity are discussed in Section 1.A. As the sample temperature is raised, the resistivity of all samples finally begins to rise, following a common or universal curve for this

---

\*This work was carried out at the National Bureau of Standards under the sponsorship of the Department of the Army and the Department of the Air Force.



# PROPERTIES AND PREPARATION OF HIGH-PURITY ALUMINUM\*

V. Arp  
Cryogenics Division, Institute for Basic Standards  
National Bureau of Standards  
Boulder, Colorado

## I. INTRODUCTION

The potential economy of using aluminum magnets operating at low temperatures was suggested by Post and Taylor<sup>1</sup> in 1959, before the advent of high field superconductivity. A liquid-hydrogen-cooled aluminum magnet was built and operated not long thereafter,<sup>2</sup> but by that time superconducting magnets seemed to be generally more attractive. Nevertheless, a small effort was carried on, since, for some low duty cycle conditions, aluminum appears to be more attractive than superconductors.<sup>3,4</sup> We have continued a study of the properties of aluminum which are related to this type of application, and a major part of this paper summarizes this study and knowledge in a tutorial fashion. The final and minor section of the paper reports the current status on the availability of high-purity aluminum in technologically useful quantities.

## II. PROPERTIES OF HIGH-PURITY ALUMINUM

In this, the major portion of the paper, electrical and thermal conductivities of metal are discussed, and data relevant to high-purity aluminum are presented. The analysis starts with a summary of various contributions to the dc resistivity. It then goes on to demonstrate the quantitative relationship between the electrical and thermal conductivities. Finally, it considers the response of metals under ac conditions.

### 1. The dc Resistivity of Metals

The customary approximation used in the discussion of the resistivity of metals is Mathiessen's rule

$$\rho \approx \sum_i \rho_i, \quad (1)$$

where  $\rho_i$  is the "partial" resistivity due to any one mechanism which inhibits the flow of electrons through the metal. In the next approximation, one can find deviation terms to be added to the right side of Eq. (1)<sup>5</sup>; however, they will not be considered in this paper. Equation (1), then, forms the basis for separate discussions of various contributions to the total electrical resistivity of a metal.

Data on the electrical resistivity of aluminum as a function of temperature are summarized in Fig. 1.<sup>6</sup> Starting at low temperature, samples of different purity are seen to have different resistivities, independent of temperature. This is the region where localized imperfections in the atomic lattice dominate the total resistivity; various types of imperfections, and the separate contributions to the total resistivity are discussed in Section 1.A. As the sample temperature is raised, the resistivity of all samples finally begins to rise, following a common or universal curve for this

---

\*This work was carried out at the National Bureau of Standards under the sponsorship of the Department of the Army and the Department of the Air Force.

element. The temperature dependent resistivity is due to lattice vibrations, and is discussed in Section 1.B. The increase in resistivity for small sample sizes, not illustrated in Fig. 1, is discussed in Section 1.C.

### 1.A. Imperfection Resistivity

Imperfections in a metal can be divided into two general classes: impurities, which are discussed in 1.A.1., and lattice defects, which are discussed in 1.A.2. Lattice defects are further subdivided into (a) vacancies, (b) dislocations, and (c) grain boundaries.

1.A.1. Impurity resistivity. In close analogy with Eq. (1), the impurity resistivity can be written

$$\rho_{\text{impurities}} = \sum_i (\rho/c)_i c_i \quad (2)$$

where  $(\rho/c)_i$  is a measure of the electron scattering by an isolated impurity atom of species  $i$  when substituted for a host atom in the lattice, and  $c_i$  is the concentration of the  $i$  atoms. Table I gives experimentally determined values of  $\rho/c$  for a variety of impurity atoms in aluminum.<sup>7-10</sup> It must be emphasized that these data cannot be used at high concentrations or where the sample treatment has caused precipitation, segregation, or clustering of the impurity atoms.

TABLE I  
Impurity Resistivity in Aluminum

Impurity	$\rho/c$ ( $10^{-12} \Omega \cdot \text{m/ppm}$ )	"Partial resistivity ratio" for 1 ppm of impurity
Cr	8	3 300
Mo	7.5	3 500
Mn, V, W, Zr	7	3 800
Fe	6.5	4 100
Ti	6	4 400
Sc	5	5 300
Co	3.5	7 500
Ni	1.8	15 000
Ge, Ag, Cu, Pb, Li, Sb, Sn, Sb	$\approx 1$	$\approx 26\ 000$
Si, Zn As, Be, Mg	$\leq 0.7$	$\geq 38\ 000$

In practice, for all reasonably pure metals except mercury, the impurity resistivity is much larger than any other contribution to the total resistivity in the liquid helium range. Thus, the resistivity at 4°K is a direct measure of the total impurity content of the metal. It has become customary, however, to cite the "residual resistance ratio," (usually called just the "resistance ratio," or just "ratio") which is

$$\text{Residual resistance ratio} = \frac{R(20^\circ\text{C})}{R(4^\circ\text{K})} \quad ,$$

where  $R$  is a measured sample resistance, rather than  $\rho(4^\circ\text{K})$  as a measure of the sample purity. The last column of Table I gives the resistance ratio which would result from 1 ppm of the stated impurity in aluminum. We have been using  $\rho(20^\circ\text{C}) = 2.64 \mu\Omega\cdot\text{cm} = 2.64 \times 10^{-8} \Omega\cdot\text{m}$ .

For samples having resistance ratios in the range 1000 to 10 000, we have found excellent agreement (within 20%) between the measured resistivities and resistivities calculated using Eq. (2), Table I, and quantitative mass spectroscopic analysis. At higher resistivity ratios (higher purities), the calculated resistivities tend to be systematically higher than the measured resistivities, the disagreement being a factor of two for a 24 000-ratio sample. This certainly is due in part to the great difficulty of doing accurate mass spectrographic impurity analyses at less than 1 ppm total impurity concentration. We feel, however, that the systematic trend may be evidence for segregation of a fraction of impurities at grain boundaries where they would have less effect on the total resistivity than they would if randomly distributed throughout the sample. This will be discussed more carefully in Section 1.A.2.

A recent study on copper<sup>11</sup> contains evidence for the major effect which clustering of impurities can have on the resistivity ratio. By a suitable oxygenation technique they have been able to increase the resistivity ratio of copper from 2500 to 42 000 without removing the impurity atoms. They suggest that this is probably due to solute atom clustering or precipitation of impurity oxides, but neither has been verified. If the impurity oxide precipitation is responsible, however, the analogous procedure for aluminum would probably be ineffective, since aluminum oxide has a higher heat of formation than do the oxides of any expected impurities in aluminum. We have found no difference between aluminum annealed in air and aluminum annealed in a vacuum.

1.A.2. The lattice defect resistivity. A number of defects may occur in the atomic lattice arrangement of a metal. For the purposes of this paper, we may group them into three classes: (a) vacancies and/or interstitial atoms, (b) dislocations, which are linear regions where the atomic layers exhibit a slight misfit, and (c) grain boundaries, which separate regions (crystals) having completely different lattice orientations. Impurity atoms are often attracted to these defects, and so must be considered in certain aspects of the study.

Vacancies are formed spontaneously in a metal when it is heated to near its melting temperature, but a substantial portion will be retained at low temperatures only if the metal is quenched rather than being allowed to cool slowly. They are also formed at any temperature when the metal is strained beyond its elastic region. For aluminum, the vacancy resistivity is<sup>12</sup>:

$$\rho/c = 1.4 \times 10^{-12} \Omega\cdot\text{m/ppm} . .$$

We have found that vacancy concentration reaches equilibrium in high-purity aluminum at room temperature in just a few hours.

The resistivity due to dislocation structures in metals is a subject of active study at the present time,<sup>13-15</sup> particularly in trying to find agreement between theory and experiment. The results depend to some extent on the type of dislocation and other factors which are beyond the scope of this paper. A reasonable estimate for aluminum comes from Rider and Foxon<sup>16</sup>:

$$\rho/n = 3 \times 10^{-25} \Omega\cdot\text{m}^3 ,$$

where  $n$  is the number of dislocation lines per square meter in the sample. We may reasonably expect no more than  $10^{10}$  or  $10^{11}$  dislocations/ $\text{m}^2$  in an annealed pure metal sample. After heavy deformation, this rises to a saturation value of roughly  $10^{16}/\text{m}^2$  for most metals.

As with vacancies, dislocations are formed when a metal is strained beyond its elastic limit. Large uncertainties exist in trying to predict theoretically the number of vacancies or dislocations which are formed by a given strain.<sup>17</sup> We have studied a portion of this problem with measurements on high-purity aluminum at low temperature. Samples were carefully prepared and annealed so as to be truly polycrystalline, since dislocation formation and structure are strongly dependent upon the relative orientation of the individual grains and the applied stress. Results obtained at 4°K on samples of about 2000 resistivity ratio are shown in Fig. 2, where the increase in resistivity is plotted against the strain  $\epsilon$  which produced that resistivity.

These results are described approximately by the equation

$$\Delta\rho (10^{-11} \Omega\cdot\text{cm}) = 110 \epsilon^{1.19}$$

It is reasonable to assume that minor changes in temperature or purity in the range of interest for cryogenic coils will not significantly change the numbers in this equation. Subsequent annealing of the samples at room temperature for a day or more results in the disappearance of about two-thirds of the strain-induced resistivity. We believe this is due to removal of vacancies and dislocation rearrangement. A much higher temperature, probably 300 to 400°C for one hour, would be necessary to eliminate the dislocations which are formed during straining.

Figure 3 shows the stress-strain curves which were taken simultaneously with the data of Fig. 2. It is difficult to estimate how the yield stress (about 3000 psi in these samples) would vary with purity in this high-purity range. It is, in fact, probably more strongly dependent upon grain size and orientation than on impurity content per se. The yield stress for annealed samples of 10<sup>3</sup> higher impurity content (commercial 1100 aluminum) is only 2 to 3 times higher than that of these samples, so that a dramatic decrease in yield stress would not be expected as the resistivity ratio is increased from 2000 to the limit of available material. We will be making experimental measurements in this range in the near future. Fatigue life at stress levels below the yield stress would be very high, probably well into the 10<sup>6</sup> to 10<sup>7</sup> cycle range.

The resistivity due to grain boundaries has not been studied in much detail, and its direct effect is probably rather small, especially in high-purity metals where the grain size may be very large. However, impurities are in general attracted toward grain boundaries and may thus be removed from solid solution where they have maximum contribution to the sample resistivity. If we make the assumption that the saturation concentration of impurities at the grain boundaries corresponds to one atomic layer,<sup>18</sup> this impurity trapping could become important when

$$(\text{impurity concentration in ppm}) \times (\text{grain diameter in mm}) \leq 2.$$

In practice, for a well-annealed sample, the grain size tends to increase as the purity increases, so that this inequality is not so easily satisfied. Much depends in this respect on details of sample preparation, annealing sequences, etc.

We have initiated a study of grain size vs resistivity in high-purity aluminum. Some of the preliminary results are shown in Fig. 4 which is a plot of sample resistivity as a function of grain boundary area per unit sample volume. The increase in resistivity at low values of grain boundary area/unit sample volume, S/V (large grain sizes), is tentatively interpreted as release of impurities from grain boundaries which have become saturated at the minima of the curves. This is in qualitative agreement with Fig. 3 of Maimoni's paper<sup>19</sup> where a minimum in aluminum resistivity is seen as a function of annealing temperature; he does not report the corresponding grain sizes. It is also similar to a resistivity minimum found in copper<sup>20</sup> and one in platinum<sup>21</sup> as a function of annealing temperature. None of these authors have suggested an explanation of the effect.

Extrapolation of these grain-size data to other purities, cold-work and annealing sequences, etc., is complex, and we cannot yet do this with confidence. The minimum in resistivity at less than maximum annealing conditions is of considerable importance, and should influence the design and fabrication of aluminum coils.

### 1.B. The Lattice Resistivity

In principle there would be no resistance to the motion of conduction electrons through a perfectly regular atomic lattice if the individual atoms were rigidly fixed in position. However, rather than being fixed in position, the atoms are vibrating about their equilibrium lattice positions with an amplitude and frequency which increases as the temperature rises, and as a result there is increasing resistance to the motion of conduction electrons through the lattice. This is the cause for the rise in resistivity seen in Fig. 1 as the temperature rises above the residual resistance region.

The theory for the lattice resistivity was worked out by Grüneisen, and is covered in many texts. For a given lattice, the Debye temperature  $\theta$  is an approximate characterization of the modes of vibration. Grüneisen theory predicts that

$$\begin{aligned} \rho &\propto T^5 & \text{when } T \ll \theta, \\ \text{and} \\ \rho &\propto T & \text{when } T > \theta. \end{aligned}$$

For most metals, the Debye temperature is in the neighborhood of 300°K. The Debye temperature of aluminum is a little higher than most, about 400°K.<sup>22,23</sup> (One must be careful to distinguish between the Debye  $\theta$  evaluated from resistivity measurements and Grüneisen theory and the Debye  $\theta$  evaluated from heat capacities or neutron spectroscopy. These are numerically close, but not identical.)

Numerous experiments on metals have verified that the Grüneisen theory is essentially correct, though the low temperature exponent on  $T$  is often closer to 4.5 than to 5. Several reports have shown that the lattice resistivity of aluminum at 20.4°K is about 0.64 mΩ·cm.<sup>10,24-26</sup> Of these, Pawleck and Rogalla<sup>26</sup> show that the resistivity is quite accurately proportional to  $T^5$  from 20°K up to about 50°K, while Alexandrov and d'Yakov<sup>25</sup> obtain 4.6 as the exponent on  $T$  in this range. In the neighborhood of room temperature, the exponent on  $T$  has fallen to about 1.27.

Below 20°K, available data for aluminum by Willott,<sup>27</sup> Holwech and Jeppeson,<sup>28</sup> Alexandrov and d'Yakov,<sup>25</sup> Revel,<sup>10</sup> and Chiang and Eremenko<sup>29</sup> are in major disagreement with extrapolation of the  $T^5$  law as well as being generally inconsistent among each other. It happens, though, that both Revel<sup>10</sup> and Willott<sup>27</sup> obtain a value of about  $1.3 \times 10^{-13}$  Ω·m at 4.2°K. Chiang and Eremenko<sup>29</sup> mention an unpublished suggestion of Alexandrov that there is a  $T^2$  contribution to the resistivity which is making itself felt below 20°K. Such a term has been found in transition metals and explained on the basis of electron-electron interactions,<sup>30</sup> but it is not expected to be measurable for aluminum in this purity range. A theoretical calculation by Kagan and Zhernov<sup>31</sup> shows that impurities may contribute a temperature dependent resistivity. At low temperatures they calculate terms proportional to  $T^2$ ,  $T^4$ , and  $T^5$ , but the magnitudes of the terms are not known. At present there are no clear correlations of theory to available experimental data. We will be making resistivity measurements in this range in the near future.

Figure 5 is a graphical summary of available data on the lattice resistivity of aluminum.

### 1.C. The Size Effect

When an electron strikes the surface of a sample, it is reflected back into the metal in a manner which depends primarily upon its angle of incidence and the microscopic surface roughness. A certain fraction of these reflections, in particular those near grazing incidence, will be specular and have no effect on the resistivity. More generally, however, these collisions with the surface will be diffuse and add to the resistivity in the same way that collisions with impurities do. When the sample size is reduced to the point that electron collisions with the surface become comparable in frequency with other types of collisions, the resistance of the sample rises. This is called the size effect.

The natural parameter to use in evaluation of the size effect is the ratio of the sample dimension,  $d$  (thickness of plate, or diameter of wire), to the electron mean free path,  $\ell$ , which would be observed in a large sized sample of the same percent impurity and imperfection, and at the same temperature. To evaluate  $\ell$ , it is most convenient to make use of the equation

$$\rho \times \ell \approx \text{constant} \equiv (\rho \ell)_{\infty} , \quad (3)$$

which is approximately true for a bulk sample independent of temperature and impurity. The constant  $(\rho \ell)_{\infty}$  is a measure of the area of the Fermi surface of the metal, again within a certain approximation. For aluminum, a reasonable average of reported values in the helium range is<sup>32</sup>

$$(\rho \ell)_{\infty} \approx 0.7 \times 10^{-15} \Omega \cdot \text{m}^2 .$$

The increase in resistivity with decreasing  $d/\ell$  was first calculated by Fuchs<sup>33</sup> and later Sondheimer,<sup>34</sup> on the assumption that there is no specular reflection at the surface. More recently Parrott,<sup>35</sup> and Brandli and Cotti<sup>36</sup> have extended the calculations on the assumption that electrons incident to the surface at less than some angle  $\theta$  will be specularly reflected, while those incident at greater angle (more nearly normal incidence) will be diffusely reflected; the angle  $\theta$  becomes an additional adjustable parameter. A yet more recent study by Soffer<sup>37</sup> relates statistical measures of surface roughness to the electron scattering process. He finds that the fractional specular reflection is angle-dependent, and that the diffuse reflection is anisotropic. The qualitative behavior of the resistivity as predicted by these theories as a function of sample thickness is shown in Fig. 6. Except for the unrealistic case of pure specular reflection, the theories are in pretty good quantitative agreement for thicknesses down to  $d/\ell \approx 1$  or 2. Quantitative corrections based on Fuchs' theory for flat plates and round wires, for both dc and eddy current measurements, are given in Fig. 7. The coordinates are chosen so that a measured resistivity can conveniently be corrected to a theoretical bulk resistivity. The eddy current correction for round wires has been evaluated from an unpublished calculation provided by Dr. Cotti. For rough calculation, the size effect resistivity  $\rho_{SE}$  to be added to the bulk resistivity  $\rho_B$  is

$$\rho_{SE} \approx \frac{(\rho \ell)_{\infty}}{d} ,$$

provided  $\rho_{SE} \ll \rho_B$ .

### 2. Magnetoresistivity

The statistical link between the macroscopic electrical resistivity and the parameters describing the microscopic electron collision processes is the Boltzman equation. Its various ramifications and approximations have been the subject of much study, and

the interested reader should consult a good text if he wishes to pursue this. The point to be made here is that the presence of a magnetic field enters the Boltzman equation in such a way as to affect all the electron collision processes (except for certain special cases and approximations of no importance here). Hence the change in resistivity of a sample as a function of applied magnetic field is more generally a multiplicative factor rather than an additive factor as with Matthiessen's rule; the only exception is the size effect resistivity, as will be explained later.

The general Boltzman equation including a magnetic field is not susceptible to simple analysis. However, with certain approximations, one can obtain Kohler's rule<sup>38</sup> which is useful for engineering study:

$$\frac{\rho(H,T)}{\rho(0,T)} = f \left( \frac{H}{\rho(0,T)}, \varphi \right),$$

where  $\varphi$  is the angle between the field  $H$  and the measuring current. The function  $f$  is unique for a given polycrystalline metal, i.e., it is independent of small variations in purity for a nominally pure metal.

Magnetoresistance data for aluminum have been summarized by Corruccini.<sup>24</sup> For transverse magnetoresistance (field perpendicular to current), he gives an empirical equation for  $f$  which fits most available data within about  $\pm 20\%$ :

$$\frac{\rho(H)}{\rho(0)} - 1 = \frac{h^2 (1 + 0.00177 h)}{1.8 + 1.6 h + 0.53 h^2},$$

where

$$h \equiv H \text{ (Oe)} \times \frac{\rho_{\text{ref}}}{\rho(0)} \times 10^{-3},$$

and

$$\rho_{\text{ref}} = 2.75 \times 10^{-8} \Omega \cdot \text{m}.$$

This equation is plotted in Fig. 8. It is important to note, however, that data taken at 20°K on aluminum of 10 000 to 20 000 ratio<sup>39</sup> are in major disagreement with this curve, and show a saturation magnetoresistivity of about 7 times the zero field value, rather than the approximate value of 3 from Fig. 8. This may be an indication of temperature dependent anisotropy in the electron scattering processes, a phenomenon which was assumed not to occur in deriving Kohler's rule.

Also shown in Fig. 8 is a curve summarizing available data on the magnetoresistivity of copper.<sup>40-43</sup> The linearity with field in the high field region is evident. This is related to immutable electronic properties of copper, and is the primary basis for choosing aluminum over copper for high field service.

When a sample thin enough to show the zero-field size effect is placed in an increasing magnetic field, two effects operate simultaneously: (1) The bulk resistivity begins rising as would be expected from Kohler's rule, and (2) the radius of the helical motion of the electrons decreases and for most geometries the electrons collide less often with the surface. Combination of these two effects may give resistance-field curves of unusual shape, especially in the low field region, which depend strongly on orientation.<sup>44,45</sup> At sufficiently high fields the size effect resistivity often disappears.

### 3.A. Thermal Conductivity

The conduction of heat through a metal is governed by much the same processes which govern the flow of electric current. It turns out, in fact, that the thermal conductivity  $K$  and the electrical resistivity are quantitatively related by the Wiedemann-Franz equation

$$K \cdot \rho = L \cdot T, \quad (4)$$

where  $L$  is known as the Lorenz number. Detailed theory<sup>46</sup> shows that in the residual resistance region at low temperatures, and at temperatures above the Debye temperature, the Lorenz number has the constant value

$$L = 2.44 \times 10^{-8} \text{ W}\Omega/\text{°K}^2$$

for any metal or alloy in which heat transport by lattice vibrations (phonons) is negligible, i.e., for any nominally pure metal or dilute alloy. This is a very powerful result, for it allows a prediction of thermal conductivity in these two temperature ranges from much simpler measurements of electrical resistivity on the same metal.

Over the intermediate temperature range there is no simple rule, but qualitative guides can be given. Consider Eq. (4) to be exact, so that a temperature dependent Lorenz number  $L(T)$  can be evaluated knowing  $K(T)$  and  $\rho(T)$ . Generally  $L(T)$  tends to drop below the theoretical value as  $T$  increases, and may exhibit less understandable bumps and dips before leveling off again at the theoretical value of  $T \gg \theta$ . This is illustrated in Fig. 9 (Powell, Hall, and Roder<sup>47</sup>; these data are slightly in error at low temperatures where corrected data converge to the theoretical Lorenz number within experimental error) and Fig. 10 (Hust and Powell<sup>48</sup>) for several aluminum alloys. Note that in no case does  $L(T)$  dip below 50% of the theoretical value. It is reasonable to expect that the deviations from the theoretical value will be of this order of magnitude for other dilute alloys.

In a heavily alloyed (highly impure) sample, or in one containing many dislocations or defect structures, resistance to the motion of conduction electrons may be so high that a significant portion of the heat is carried by lattice vibrations or phonons, as with an electrical insulator. In this case, the  $L(T)$  curve will rise above the theoretical value, at least initially. This is illustrated in Fig. 11 for A-110AT titanium.<sup>48</sup> Serious errors could occur in trying to estimate such a curve without much more knowledge than is available now.

Unfortunately there have been very few evaluations of  $L(T)$  in the literature, and no detailed correlations of such curves have been made. Studies along this line have begun in our laboratory.

### 3.B. Thermal Conductivity in a Magnetic Field

Just as a magnetic field inhibits the flow of electric current through a metal, it also inhibits the transfer of thermal energy by the (same) conduction electrons. In a nominally pure metal or dilute alloy, where most of the heat is carried by the conduction electrons, we thus might reasonably expect that the thermal conductivity would scale with the electrical conductivity in a magnetic field. In other terms, the Lorenz number would be relatively independent of magnetic field. This topic has not been studied theoretically to my knowledge, and I have not found experimental measurements which relate directly to this suggestion, though decreasing thermal conductivity in a magnetic field has been reported.<sup>49</sup> This might be a deterrent to the use of copper as a thermal conductor in a high field at low temperature, because of its high magnetoresistivity.



#### 4. Ac Effects

The response of a conductor to alternating electromagnetic fields may be typified by the relative magnitudes of three length parameters. These are:

The classical skin depth,  $\delta = \left( \frac{2\rho}{\mu_0 \omega} \right)^{\frac{1}{2}}$ ,

The electron mean free path,  $\ell$ ,

The sample dimension (thickness or diameter),  $d$ .

In the equation for the skin depth,  $\rho$  is the dc resistivity of a large sample of the conductor having the same percentage impurities,  $\mu_0 = 4\pi \times 10^{-7}$  H/m, and  $\omega$  is  $2\pi$  times the frequency. If response to a pulse rather than a continuous wave is being analyzed, it will be necessary to consider the Fourier components of the pulse in order to estimate the appropriate  $\omega$  and  $\delta$ ; however, in some situations it may be less complicated to use other mathematical techniques which do not explicitly involve the Fourier components. Classification of the types of response is outlined in Table II and discussed below.

TABLE II  
Frequency and Size Effects

$\delta > d > \ell$	dc circuit theory
$\delta > \ell > d$	dc size effect
$\ell > \delta > d$	dc size effect
$d > \delta > \ell$	classical skin effect
$d > \ell > \delta$	anomalous skin effect
$\ell > d > \delta$	"anomalous size effect"

At low frequencies  $\delta > d$ , current distribution is essentially uniform throughout the sample, and dc theory is applicable. If  $\ell > d$ , a size effect correction must be made.

When  $d > \delta > \ell$ , the theory of the classical skin effect applies. The current is confined to a thin surface layer, resulting in higher circuit resistance than in the dc case. The effective resistance of the surface layer is

$$Z = \left( \frac{\mu_0 \omega \rho}{2} \right)^{\frac{1}{2}}.$$

When  $d > \ell > \delta$ , the theory of the anomalous skin effect must be used. Analysis of this situation is much more complex than that of the classical skin effect. Here the electric field sensed by an electron changes significantly over the space of one mean free path. This means that instead of using the ordinary Ohm's law  $J(r) \times \rho = E(r)$  ( $J$  is the current density and  $E$  is the electric field) as was done in the classical skin effect calculation, one must in essence use an effective  $E$  averaged over the mean free path. The calculations are quite complex, and the resulting integro-differential equations have not been solved in full generality.<sup>46,50,51</sup> When  $\ell \gg \delta$  the resulting expression for the surface resistance is

$$Z = \left( \frac{\sqrt{3} \mu_0^2 \omega^2}{16\pi} (\rho \ell)_\infty \right)^{1/3}, \quad (5)$$

where  $(\rho \ell)_\infty$  is the same fundamental parameter which arose earlier in the discussion of the dc size effect. This expression assumes 100% diffuse reflection of the electrons at the sample surface, but it is multiplied only by a factor of 8/9 if 100% specular reflection occurs. It is worth noting that in this limit the surface impedance is independent of the sample purity. The surface resistivity will be higher than that calculated from the classical skin effect, since the current density falls off more sharply with distance than in the classical case (or following Pippard's reasoning, only a fraction  $\delta/\ell$  of the electrons contribute to the effective current).

The importance of using the anomalous skin effect theory for high-purity metals can be emphasized by calculating the frequency at which the electron mean free path  $\ell$  is equal to the classical skin depth  $\delta$ . Calling this frequency  $\omega_c$ , we find

$$\omega_c = \frac{2\rho^3}{\mu_0 (\rho \ell)_\infty^2}.$$

For aluminum this turns out to be a frequency

$$f_c \text{ (Hz)} = \frac{\omega_c}{2\pi} \approx \frac{10}{\left( \frac{\text{r.r.}}{10^4} \right)^3},$$

where r.r. is the resistivity ratio,  $2.64 \mu\Omega \cdot \text{cm}/\rho$ . Aluminum can be purchased at the present time in large ingots of about 14 000 resistivity ratio. With this material at helium temperatures, the anomalous skin effect theory would be necessary above about 4 Hz; with the most pure aluminum obtained in the laboratory (45 000 ratio), the anomalous skin effect theory would be used above 0.1 Hz.

When  $\ell > d > \delta$ , the theory of the anomalous skin effect must be combined with the size effect calculation. This subject has been discussed in the literature (Gantmakher<sup>52</sup> and references cited therein), though with particular application to various cyclotron-like resonances which occur in single crystals in a large static magnetic field. The analysis is not particularly applicable to systems in the absence of a magnetic field, and it is not clear what modification would be necessary in Eq. (5), for example. Cotti's eddy-current size effect correction illustrated in Fig. 7 is somewhat related to this problem, but his analysis was made in terms of response to a step function and did not treat individual Fourier components.

## 5. Summary

Through the analysis of Section 1, the complete resistivity-temperature curve for aluminum may be constructed by adding the residual resistivity to the "lattice" resistivity. The residual resistivity may be determined by direct measurement, or estimated from knowledge of impurity content, grain size, and state of lattice strain. The "lattice" resistivity below 20°K is not known accurately, but the curve in Fig. 5 labeled "Alexandrov" is probably the best estimate at the present time. The resistivity in a magnetic field at any temperature may then be calculated from the Kohler plot in Fig. 8; the important discrepancy between this curve and the data of Borovik, Volotskaya, and Fogel<sup>39</sup> for aluminum of the highest purity around 20°K is unresolved at present.

The thermal conductivity at any temperature may then be estimated from the Wiedemann-Franz relationship, Eq. (4), knowing the resistivity and assuming that the Lorenz number is roughly constant. More accurate assumptions on the Lorenz number are possible, in keeping with the curves of Figs. 9 and 10, but insufficient data exist to establish a truly reliable  $L(T)$  curve for high purity aluminum. Though the derivation of the Lorenz number assumed the absence of a magnetic field, it is postulated that in the first approximation the Lorenz number would be independent of magnetic field. Thus the thermal conductivity should decrease as the electrical resistivity increases.

The response of a conductor to alternating electromagnetic fields is discussed in terms of the skin depth  $\delta$ , the electron mean free path  $\ell$ , and the sample dimension  $d$ . The importance of the anomalous skin effect theory for high purity metals at low temperatures is emphasized. Calculations based on this theory are very complex, and have not been carried out except for the limiting case  $d \gg \ell \gg \delta$ , in which case the surface resistivity becomes independent of sample purity. In any case the surface resistivity will be higher than that calculated by the classical skin effect theory, since (in one sense) not all the electrons can effectively respond to the applied field.

### III. PREPARATION OF HIGH-PURITY ALUMINUM

Since the first separation of the metal from its ore, aluminum has been prepared by electrolytic reduction of molten aluminum oxide. Ishihara and Mukai<sup>53</sup> have suggested that residual impurities in the aluminum produced by this process may be strongly influenced by contaminants in the carbon electrodes, as well as the impurities in the original ore. With very careful selection, it is possible to obtain multikilogram quantities refined by only this technique having resistivity ratios in the range 1000 to 2000.

To obtain additional purity, zone refining is performed on the nominally pure metal. This process is usually found only on the laboratory scale, producing at most perhaps one-kilogram ingots at a low rate. Recently, however, a commercial source of zone refined ingots weighing up to about 40 kg has become available. The best 20 kg of these ingots are apparently of reasonably uniform high purity, having resistivity ratios in the 13 000 to 17 000 range. This seems to open the door to possible technological use in large-scale applications. We have found that this material can be handled and shaped, on a laboratory scale at least, without measurable contamination.

The success of zone refining depends on the increased solubility of impurity atoms in the molten metal as compared to their solubility in the solid. It turns out for aluminum<sup>54</sup> that Mn has close to the same solubility in the solid as in the liquid, while Ti, V, Cr, Zr, Nb, Mo, Ta, and W are less soluble in the liquid than in the solid. These are the impurities, then, which are not easily removed by zone refining, so that the final purity is significantly limited by the initial presence of these particular elements.

It seems clear that careful selection, probably including the source of the ore, may measurably improve the final product. Research groups in Norway, France, and Russia have reported zone refined aluminum, presumably in small quantities, having resistivity ratios in the 22 000 to 29 000 range.<sup>39,55,56</sup> Dr. Bratsberg has indicated to us (private correspondence) that the choice of starting material is of great importance.

The French group<sup>57,58</sup> has carried this line of reasoning one step further. They have obtained small quantities of aluminum prepared by an "organic refining" process involving the electrolytic reduction of  $\text{Al}(\text{C}_2\text{H}_5)_3$  and/or related compounds. This produces aluminum of 8000 to 10 000 ratio. With subsequent zone refining of this material,

Revel has obtained a resistivity ratio of 39 000 on a 5 mm diameter sample; correcting for the size effect, this corresponds to a resistivity ratio of about 47 000 for a bulk specimen. We likewise have obtained a small quantity of the organically-refined aluminum, had it zone refined, and obtained a resistivity ratio of about 45 000; correcting for the size effect in our sample brings this to 47 000, in remarkable agreement with the ratio obtained by Dr. Revel. We speculate that this organic refining method happens to be relatively effective in removing the transition metals which cannot easily be extracted by zone refining. We are having mass spectroscopic analyses made to cover this point, but do not yet have the results.

The availability of commercial quantities of this "organically-refined" aluminum seems remote at this time. The process is slow, and the high-purity anode decomposes at a relatively fast rate. Aluminum triethylene reacts vigorously or explodes on contact with oxygen, hydrogen, phenol, alcohol, acids, and water, and explodes spontaneously above 180°C. The reactivity can be lessened somewhat by addition of related organic compounds, but apparently this involves compensating disadvantages in the refining process.

At this time, then, it seems that for design purposes one can count on availability of about 15 000-ratio aluminum in ingots of about 20 kg. For laboratory measurements, one can obtain small quantities of about 45 000-ratio aluminum, but a major technological development would be required to obtain this on a commercial scale.

#### ACKNOWLEDGEMENTS

M.B. Kasen and R.P. Reed have contributed significantly to the collection and analysis of stress, strain, grain size, and annealing temperature effects in aluminum. More complete data and analysis will be published elsewhere. R.H. Kropschot has given valuable encouragement and advice, particularly with reference to possible technological usage. The work has been supported in part by contract LB523801A308 with the Army Missile Command, and in part by contract F33615-68-M-5000 with Wright-Patterson Air Force Base.

#### REFERENCES

1. R.F. Post and C.E. Taylor, in Advances in Cryogenic Engineering (Plenum Press, 1959), Vol. 5, p. 13.
2. J.R. Purcell and E.G. Payne, Rev. Sci. Instr. 34, 893 (1963).
3. V. Arp, in Proc. Intern. Symposium Magnet Technology, Stanford, 1965, p. 625.
4. C.E. Oberly and R.R. Barthelemy, in Proc. 12th Intern. Congress on Refrigeration, Madrid, Spain, 1967, Paper No. I.27.
5. R.L. Powell, H.M. Roder, and W.J. Hall, Phys. Rev. 115, 314 (1959).
6. L.A. Hall, National Bureau of Standards Technical Note 365 (1968).
7. C.R. Vassel, J. Phys. Chem. Solids 7, 90 (1958).
8. E. Kovacs-Csetenyi, C.R. Vassel, and I. Kovacs, Phys. Stat. Sol. 17, 123 (1966).
9. G. Boato, M. Bugo, and C. Rizzuto, Nuovo Cimento 45, 226 (1966).
10. G. Revel, Mem. Sci. Rev. Met. 65, 181 (1968).
11. J.J. Gniewek and A.F. Clark, J. Appl. Phys. 36, 3358 (1965).
12. R.M.J. Cotterill, Phil. Mag. 8, 1937 (1963).
13. Z.S. Basinski and S. Saimoto, Can. J. Phys. 45, 1161 (1967).

14. V. Ya. Kravchenko, Soviet Phys. — Solid State 9, 653 (1967).
15. H. Maeta, J. Phys. Soc. Japan 24, 757 (1968).
16. J.G. Rider and C.T.B. Foxon, Phil. Mag. 13, 289 (1966).
17. H.G. Van Bueren, Imperfections in Crystals (North-Holland Publishing Co., 1960).
18. D. McLean, Grain Boundaries in Metals (Clarendon Press, 1957).
19. A. Maimoni, Cryogenics 2, 217 (1962).
20. P.V. Andrews, Phys. Letters 19, 558 (1965).
21. K. Misec, Czech J. Phys. B17, 647 (1967).
22. V.P. Varshni and R.C. Shukula, J. Chem. Phys. 43, 3966 (1965).
23. R. Stedman, L. Almquist, and G. Nilsson, Phys. Rev. 162, 549 (1967).
24. R.J. Corruccini, National Bureau of Standards Technical Note No. 218 (1964).
25. B.N. Aleksandrov and I.G. d'Yakov, Soviet Phys. — JETP 16, 603 (1963).
26. F. Pawleck and D. Rogalla, Metall. und Tech. 20, 949 (1966).
27. W.B. Willott, Phil. Mag. 16, 691 (1967).
28. I. Holwech and J. Jeppesen, Phil. Mag. 15, 217 (1967).
29. Yu. N. Chiang and V.V. Eremenko, Soviet Phys. — JETP Letters 3, 293 (1966).
30. M.J. Rice, Phys. Rev. Letters 20, 1439 (1968).
31. Yu. Kagan and A.P. Zhernov, Soviet Phys. — JETP 23, 737 (1966).
32. P. Cotti, E.M. Fryer, and J.L. Olsen, Helv. Phys. Acta 37, 585 (1964).
33. K. Fuchs, Proc. Cambridge Phil. Soc. 34, 100 (1938).
34. E.H. Sondheimer, Advan. Phys. 1, 1 (1952).
35. J.E. Parrott, Proc. Phys. Soc. (London) 85, 1143 (1965).
36. G. Brandli and P. Cotti, Helv. Phys. Acta 38, 801 (1965).
37. S.B. Soffer, J. Appl. Phys. 38, 1710 (1967).
38. M. Kohler, Ann. Physik 32, 211 (1938).
39. E.S. Borovik, V.G. Volotskaya, and N. Ya. Fogel, Soviet Phys. — JETP 18, 34 (1964).
40. International Copper Research Association, unpublished, 1968.
41. G. Yntema, Phys. Rev. 91, 1953).
42. T.G. Berlincourt, Phys. Rev. 112, 381 (1958).
43. B. Luthi, Helv. Phys. Acta 33, 161 (1960).
44. B.N. Aleksandrov, Soviet Phys. — JETP 16, 286 (1963).
45. K. Forsvoll and I. Holwech, J. Appl. Phys. 34, 2230 (1963).
46. J.M. Ziman, Electrons and Phonons (Clarendon Press, 1960).
47. R.L. Powell, W.J. Hall, and H.M. Roder, J. Appl. Phys. 31, 496 (1960).
48. J.G. Hust and R.L. Powell, private communication (1968).
49. T. Amundsen and T. Olsen, Phys. Letters 4, 304 (1963).
50. A.B. Pippard, Rept. Progr. Phys. 22, 176 (1960).
51. G.E. Smith, in The Fermi Surface, edited by W.A. Harrison and M.B. Webb (J. Wiley & Sons, 1960).

52. V.F. Gantmakher, in Progress in Low Temperature Physics, edited by C.J. Gorter (North-Holland Publishing Co., 1967), Vol. 5, p. 181.
53. M. Ishihara and K. Mukai, Trans. AIME 236, 192 (1966).
54. G. Revel, Thesis (unpublished), 1965.
55. F. Montariol and R. Reich, Compt. Rend. 254, 3535 (1962).
56. H. Bratsberg, D. Foss, and O.H. Herbjornsen, Rev. Sci. Instr. 34, 777 (1963).
57. J. Bonmarin, Rev. Aluminum 330, 455 (1965).
58. G. Revel, Ann. Chim. (Paris) 1, 37 (1966).

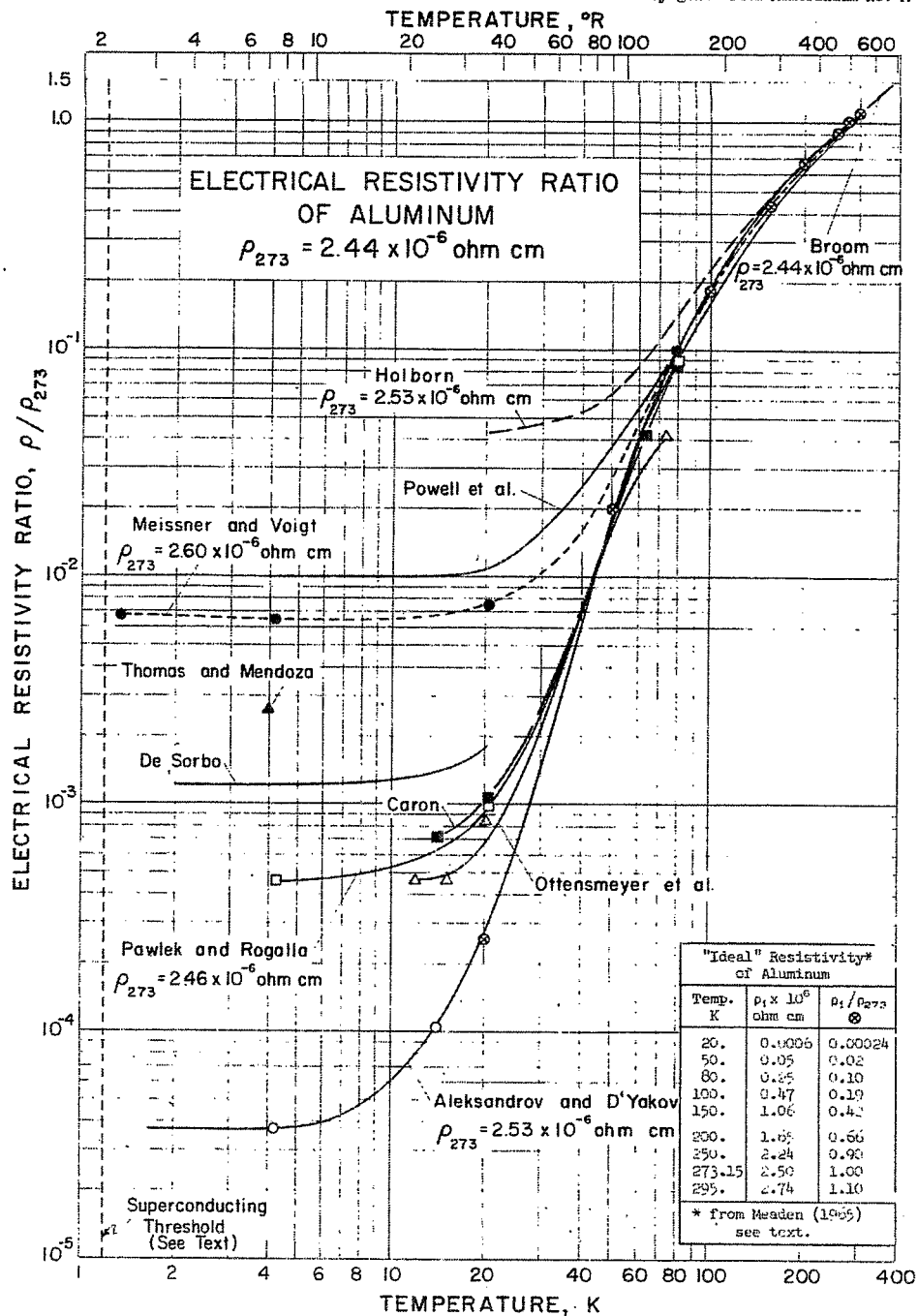


Fig. 1. Compilation of electrical resistivity measurements on aluminum.

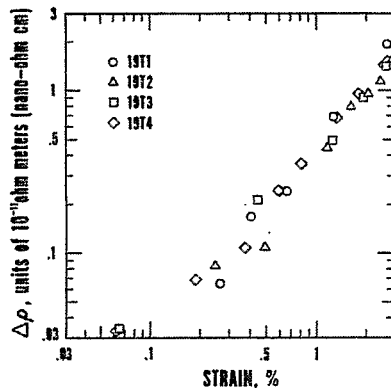


Fig. 2. Strain-induced resistivity in 2000-ratio aluminum at 4°K.

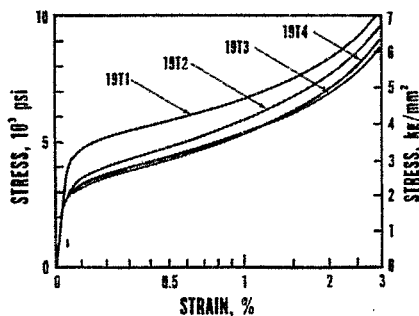


Fig. 3. Stress as a function of strain in polycrystalline 2000-ratio aluminum at 4°K. Data taken simultaneously with that of Fig. 2.

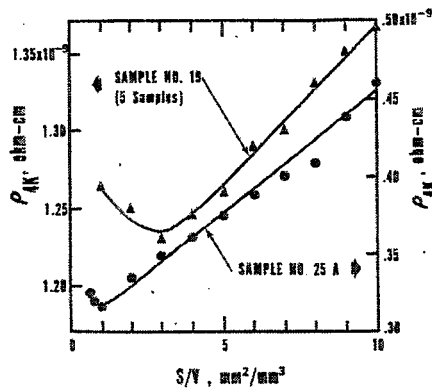


Fig. 4. Resistivity at 4°K as a function of grain boundary area per unit sample volume for two different sample purities. All five of the No. 19 samples had very close to the same purity.



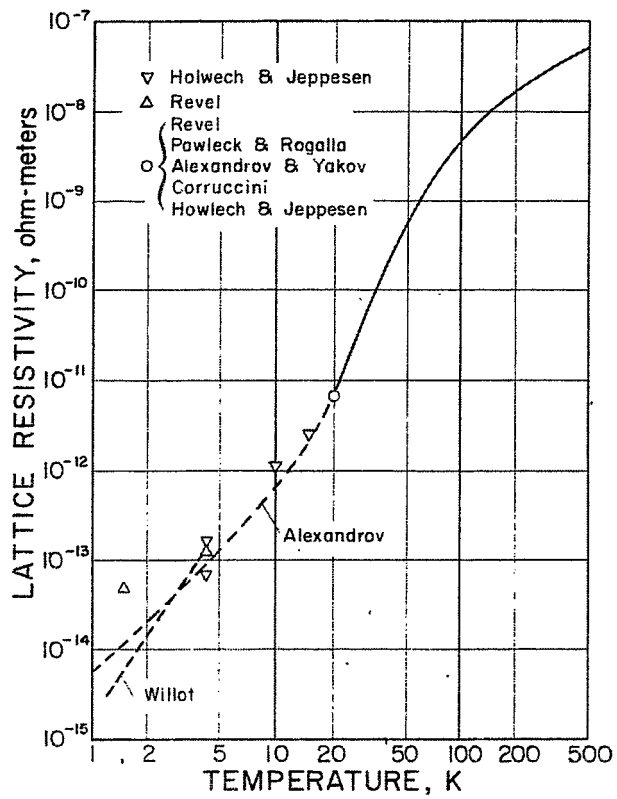


Fig. 5. Lattice resistivity of aluminum as a function of temperature.

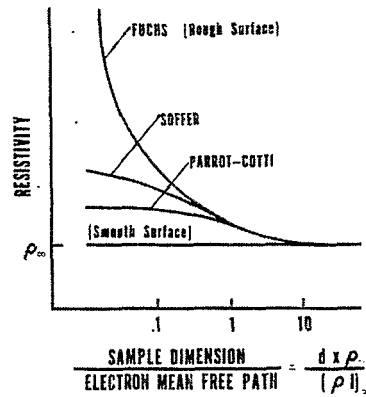


Fig. 6. Qualitative behavior of the resistivity as a function of (sample size/electron mean free path), according to various size effect theories.

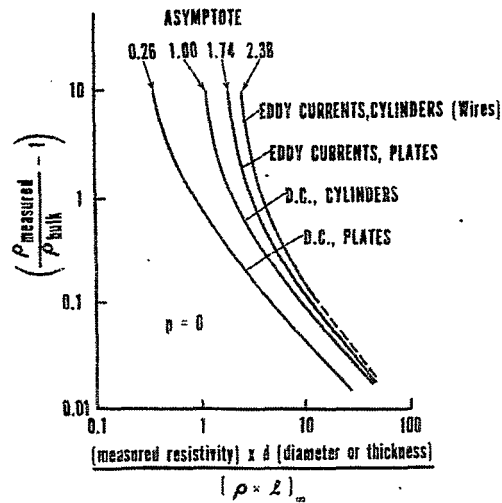


Fig. 7. The size effect correction assuming 100% diffuse reflection of electrons at the sample surface. These are equivalent to the "Fuchs" curve in Fig. 6.

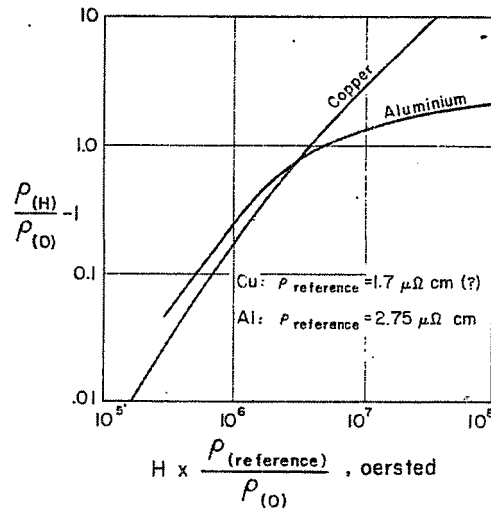


Fig. 8. Kohler plot giving transverse magnetoresistance of copper and aluminum.

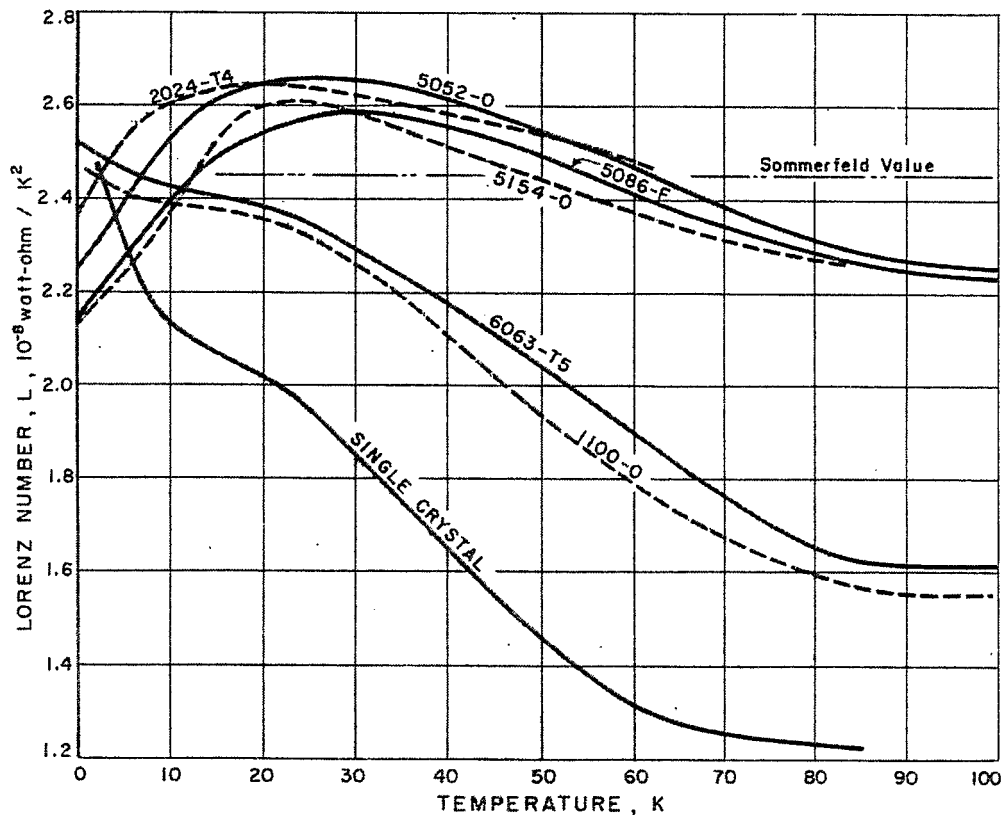


Fig. 9. Lorenz number as a function of temperature for several aluminum alloys. (The data actually converge the theoretical value  $2.44 \times 10^{-8}$  as  $T \rightarrow 0$ ; the graph is slightly in error due to a calibration error.)

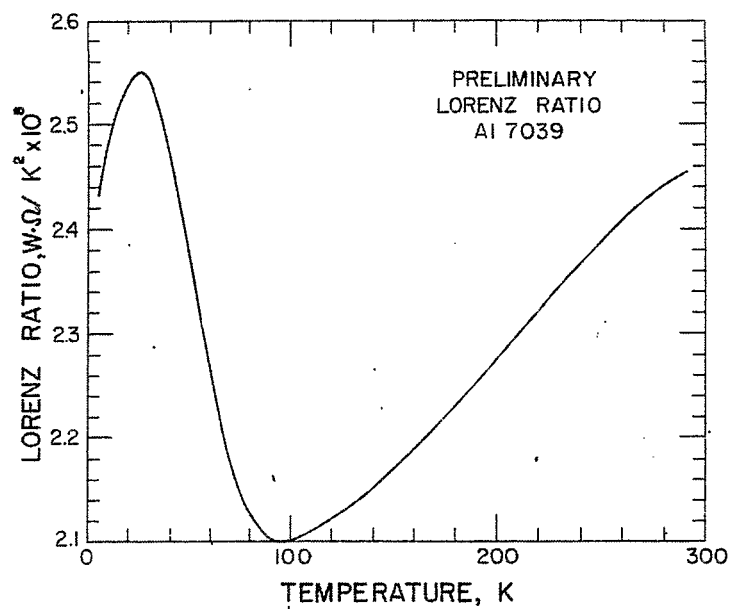


Fig. 10. Lorenz number as a function of temperature for 7039 aluminum.

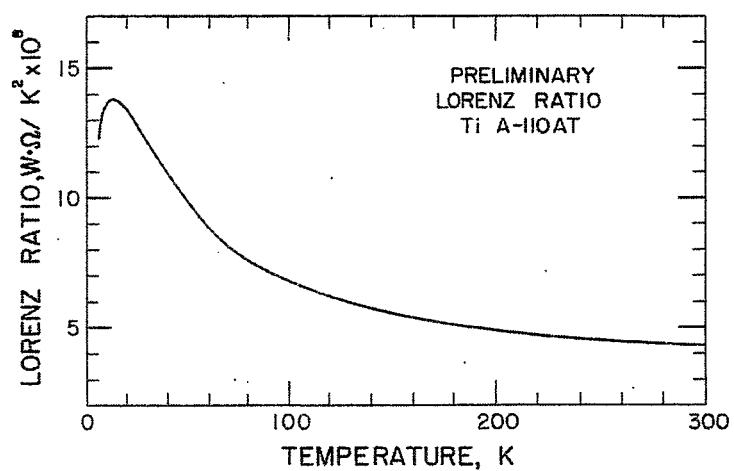


Fig. 11. Lorenz number as a function of temperature for A-110AT titanium alloy.

# SYNCHROTRON MAGNETS WITH CRYOGENIC EXCITING COILS\*

G.T. Danby, J.E. Allinger, and J.W. Jackson  
Brookhaven National Laboratory  
Upton, New York

## I. INTRODUCTION

By suitable choice of magnet parameters it is practical to excite iron magnets of the window frame type to fields exceeding 40 kG while retaining useful field properties.

High field performance is obtained by employing excitation current density values intermediate between normal 300°K practice and the very high current densities required for moderately thin shell air core magnets of small cross section.

Cryogenic aluminum exciting coils are competitive with superconducting coils from an ac loss point of view and appear to have many practical advantages.

In this paper a brief description of high current density iron magnet performance is given together with a summary of some parameters as applied to a 2 TeV (2000 GeV) machine lattice.

## II. STUDIES ON EXCITATION OF HIGH CURRENT DENSITY WINDOW FRAME DIPOLES

Various papers have been written by the authors on the subject of a separated function magnet lattice for large synchrotrons.<sup>1-3</sup> In addition to the advantages in flexible operation and control of an operating accelerator, and in flexibility and economy in constructing an expandable machine, it was recognized that efficient operation at high fields is limited by the low current densities practical at 300°K. It was stated that with superconducting or cryogenic exciting coils of about five times smaller cross section than are typical at 300°K, useful fields would be obtained to about 30 kG. This work has been pursued further.

For very large machines, various factors lead one to the conclusion that the vertical aperture can usefully be at least as large as the horizontal, i.e., a circular vacuum pipe would be quite satisfactory. Typically the vertical aperture has been one-half to one-third of the horizontal. Scaling up the aspect ratio of the vertical to horizontal aperture dimensions leads to equivalent levels of saturation and of harmful aberrations setting in at significantly higher values of the field.

A modeling program has been carried out. A flexible "kit" magnet was constructed in which the side yokes and pole plates are separate structures so that the basic

---

\* Work performed under the auspices of the U.S. Atomic Energy Commission.

1. G.T. Danby, J.E. Allinger, and J.W. Jackson, Brookhaven National Laboratory, Accelerator Dept. Report AADD-115 (1966).
2. G.T. Danby, J.E. Allinger, and J.W. Jackson, IEEE Trans. Nucl. Sci. NS-14, No. 3, 431 (1967).
3. G.T. Danby, J.E. Allinger, and J.W. Jackson, in Proc. 2nd Intern. Conf. Magnet Technology, Oxford, 1967, p. 87.

aperture parameters can be easily changed. The steel is M-36 silicon steel sheet left over from the AGS construction.

Figure 1 shows an assembly containing a matrix of search coils inserted in the aperture. The entire structure is simply immersed in liquid nitrogen.

Figure 2 illustrates schematically the type of construction. The top and bottom yokes (12 in. x 12 in. x 4 in.) are always used, and various side yokes, pole pieces, and coils are employed.

Figure 3 shows the effect on saturation of increasing the vertical gap dimension for a constant coil thickness of 1 in. and a constant aperture width of 1.8 in.

The slope of the saturation curve is inversely proportional to the vertical aperture; the aberrations similarly diminish with increasing vertical aperture. One is approaching more closely the uniform field between two parallel current sheets of infinite extent. For a synchrotron (or general beam transport) one can expand the field in multipolarities about its center and ask what terms are present over the necessary high field aperture.

For the present geometry, the field aberrations are predominantly sextupole. On the horizontal and vertical mid-planes the 10-pole term is quite small even at full aperture in the case of an approximately square aperture. At maximum extent on the  $45^\circ$  axes, i.e., in the corners, the 10-pole term is four times larger. However, experimentally at  $\sim 90\%$  of the way to the corner the fit is still good to sextupole and 10-pole terms, and in agreement with the horizontal mid-plane data. Practically speaking, an inserted vacuum pipe would be roughly circular, and the 10-pole field aberration at the vacuum pipe at all angles would have the same magnitude as on the mid-plane at full aperture. Figure 4 shows aberrations on the horizontal mid-plane for a 2.4 in. version.

It can be seen from Figs. 3 and 4 that the 2.4 in. gap model has about 20% saturation of the B vs I curve at 41 kG, and about 3.7% sextupole. This aberration can be corrected with properly distributed exciting coils in the magnet. Figure 5 illustrates a partial correction with a three-turn pole face winding. However, passive improvement with crenulations or pole shaping is very attractive. It should be borne in mind that a synchrotron should have sextupole control in each half cell in any case for beam manipulation and high intensity operation, even for "perfect" magnets with zero aberrations. As a result, reducing the above aberrations by about a factor of two is sufficient to keep combined control and aberration correction sextupole elements to modest proportions.

Tests to further improve magnet performance are in progress. This interacts with broader considerations of economically and operationally optimum current densities for a given application.

In summary, practical iron dipole magnets of  $> 40$  kG peak excitation have been demonstrated. The flux density in the yoke is of normal magnitude, and saturation occurs only in the pole regions adjacent to the aperture. In principle, small cross section insertions in this region of either high field magnet steel ( $\sim 3$  kG improvement) or of low temperature ferromagnetic rare earths could further enhance performance.

These magnets are very compact because of the high current density. This leads to a structure of small over-all cross section. The ratio of useful aperture stored energy to total stored energy is very large.

### III. CHOICE OF IRON CORE MAGNETS

Since this is not primarily an accelerator meeting no attempt is made to justify in detail the use of window frame iron dipoles in preference to air core cylindrical current distributions.

In the present design to a very good approximation the field is everywhere parallel to the plane of the current sheets both inside and outside the conductor. Pressures on the turns are almost uniformly outward, and modest in magnitude (the coil pressure is  $\sim 1200$  psi at 40 kG). Window frame dipole magnet coils are not "pole face windings" except in a quite weak sense. With good but common tolerances on the inner turns (which are wound first in a coil) aberrations due to coil locational errors are very small.

High current density air core magnets of small bore can have, in principle, negligible two-dimensional aberrations. However, they require high mechanical and electromagnetic stability of the current elements in the presence of complex forces of large magnitude.

In practice, for air core current distributions, an iron sheath may be attractive as a shield and to enhance somewhat the field, unless workable magnets can be made with much higher field-current density ( $B_j$  product) material than is presently contemplated. However, the multipolarities generated by the current distribution still largely determine the field properties, so the basic advantages and disadvantages of such thin shell cylindrical air core magnets are not greatly affected by concentric shields.

In this paper we concentrate on dipole magnets. Figure 6 shows reasonable lattice parameters for a 2 TeV synchrotron of 40 kG peak field, with  $v$  values of  $\sim 20$ . With a half cell length of  $\sim 185$  ft, only an  $\sim 8$  ft length of room temperature quadrupoles would be required. Quadrupoles are a minor consideration at this stage. However, one could also use cryogenically excited quadrupoles for compactness. As with the dipoles, higher current density coils will lead to considerably higher gradients being practical.

TABLE I  
Coefficients of Nonlinear Terms in a Typical  
Brookhaven 3-in. Quadrupole

Ratio of Coefficients	$B_{\text{tip}} = 7.1 \text{ kG}$	$B_{\text{tip}} = 13.5 \text{ kG}$	$B_{\text{tip}} = 16.3 \text{ kG}$
40/20	0.025%	0.048%	0.068%
60/20	+0.052 $-16^{\circ}39'$	+0.057 $-16^{\circ}40'$	+0.160 $-16^{\circ}30'$
100/20	-0.415 $-8^{\circ}19'$	-0.372 $-7^{\circ}47'$	-0.286 $-6^{\circ}22'$
140/20	+1.096 $-8^{\circ}09'$	+1.059 $-8^{\circ}15'$	+0.925 $-8^{\circ}26'$
30/20	0.03	0.05	0.07
50/20	0.01	0.03	0.05
70/20	0.02	0.02	0.02

Table I lists the amplitudes of aberrations measured almost touching the iron poles in a 3-in. diam Brookhaven quadrupole. The aberration multipolarities are given as a percentage of the quadrupole field at the measurement radius, which is  $\sim 0.025$  in.

from the iron. The true quadrupole aberration terms are 60, 100, and 140; these depend on the details of the particular design. For the magnet concerned, 60 can be made arbitrarily small, and all vary slowly with excitation. However these terms vary in amplitude with very rapidly increasing powers of radius, so that over a useful aperture of 80-90% of the pole aperture these effects can be made completely negligible. The 30, 40, 50, and 70 terms represent "noise" either due to structural asymmetry or to errors in the measurements. These results are typical and illustrate the high stability of such iron magnets.

#### IV. PROPERTIES OF LOW TEMPERATURE PURE ALUMINUM COILS

Magnet coils of pure metals operating at cryogenic temperatures have been considered for a long time.<sup>4</sup> Large stored energy magnets have been built, but, in general, have been overshadowed by the advantages of superconductors for such devices. Air core cryogenic synchrotron magnets have also been considered by several groups, but, unless a quite low duty factor was assumed, the high current density required for efficient small bore magnets has led to formidable refrigerator requirements. Considerable interest exists in the USA and other countries in various power frequency systems using either cryogenic or superconducting conductors.

The great promise of superconductivity has perhaps overshadowed too greatly considerations of pure metals. In the paper by Arp in these Proceedings,<sup>5</sup> it appears that very high resistivity ratio aluminum could be made available by large-scale commercial processes. As a result, even at the very low temperatures associated with superconductivity, aluminum may be very attractive for many applications.

For the present application it appears that the refrigerator requirements for the resistive losses in aluminum coils of existing material may be about the same as for optimistic superconductor ac losses. The aluminum coil system seems fairly straightforward. It is our judgment that, in addition, there are great practical operational and over-all cost advantages for Dewars, transfer lines, etc., by operating at higher temperatures (18-27°K). As a result, we arbitrarily concentrate the discussion in this range, although very low resistance appears practical at the helium temperatures associated with superconductors.

We now very briefly summarize some resistance properties, for which we are principally indebted to Arp.<sup>5</sup>

The resistivity, for no magnetic field present, is given by

$$\rho = \rho_0 + \rho_i(T)$$

The term  $\rho_i(T)$  represents the lattice resistivity and varies approximately as the cube of the temperature below 20°K. Above 20°K it approaches the fifth power law with temperature. The term  $\rho_0$  is due to impurities and lattice defects. In practice the resistivity ratio  $\rho(300^\circ\text{K})/\rho(4^\circ\text{K})$  gives  $\rho_0$ , since  $\rho_i(4^\circ\text{K})$  is extremely small.

For aluminum in a magnetic field  $\rho_H$  saturates at  $\sim 2.8\rho$ . The saturation occurs at lower fields as  $\rho$  decreases. In the present case, saturation occurs at a few kilogauss.

---

4. R.F. Post and C.E. Taylor, in Advances in Cryogenic Engineering (Plenum Press, 1959), Vol. 5, p. 13.

5. V. Arp, these Proceedings, p. 1095.



Anomalous resistive behavior occurs for thin material when the electron mean free path becomes appreciable compared to the thickness. However, in a magnetic field, the cyclotron radius reduces this effect.

For our case where we consider 0.015 in. tape coils and an effective resistivity of  $2.75 \times 10^{-9} \Omega \cdot \text{cm}$ , anomalous effects are very small.

Strain also increases  $\rho$ . The effect commences to be noticeable at 3000 psi and becomes quite appreciable about 10 000 psi. For the present coils, the pressures at 40 kG are only 1200 psi, so strain is not a problem.

In summary, for the coils considered herein, which are  $\sim 0.015 \text{ in.} \times 1.000 \text{ in.}$  tape, operating in the 18-27°K range, the resistivity is effectively the bulk resistivity.

We define a constant resistivity for the magnet coil ( $\rho \text{ eff.}$ ) which gives the correct dissipation for the assumed magnet cycle. Actually, the field in the coil varies with time and with location, so the effect of magnetic field should be somewhat below saturation. We assume  $\langle \rho \text{ eff.} \rangle = 2.75 \times 10^{-9} \Omega \cdot \text{cm}$  at an operating temperature T.

Assuming effectively pure aluminum,  $\rho_i(T)$  at  $T \sim 25^\circ\text{K}$  is  $\sim 2000$  times less than at  $300^\circ\text{K}$ . As a result, the resistivity ratio of the material should be a number large compared with 2000 to give this almost ideal aluminum behavior (i.e., perhaps 10 000).

Assume a power duty factor of 40% to 40 kG. This corresponds, for example, to a 1 sec dwell time, 1 sec rise time, 1 sec flat-top, and a 1 sec invert. (These equal time intervals can be changed from 1 sec without affecting the heat load.) This corresponds to a 25% flat-top duty factor. For a 2.25 in. magnet gap and a coil cross section of  $5.33 \text{ in.}^2$  of aluminum the dissipation is 60 W/ft.

#### Additional Losses (all for 1 sec rise time):

- (1) Vacuum chamber eddy currents. Assume a 0.020 in. cylinder of 2 in. diam and of  $\rho = 10 \times 10^{-6}$ . This gives 0.8 W/ft.
- (2) 0.015 in. aluminum tape coil eddy currents: 2 W/ft.
- (3) Iron eddy currents (0.025 in. steel): 2 W/ft.
- (4) Hysteresis in iron: 6 W/ft.
- (5) Dewar and transfer line losses: 1 or 2 W/ft.

### V. REFRIGERATION REQUIREMENTS

The over-all dissipative load is about 70 W/ft. This is approximately independent of rise rate, the dominant loss being resistive. For a given magnet design the dissipation is invariant with absolute scaling of aperture, if the same relative cross-sectional dimensions are maintained.

There are, however, several mechanisms by which this load can be varied by large amounts.

#### 1. Refrigerant

For  $27^\circ\text{K}$  (neon), the dissipation should be increased by about 50% (this is a lumped correction which includes both the higher  $\langle \rho \text{ eff.} \rangle$  at  $27^\circ\text{K}$  and the higher refrigerator temperature, since refrigerator efficiency is considered at  $20^\circ\text{K}$ ).

For 20°K (hydrogen), the dissipation would be reduced to two-thirds of the 70 W/ft.

At 18°K, the dissipative loads would be reduced to one-half of the 70 W/ft. (At 10°K, and with very pure Al, i.e., ~ 50 000 resistance ratio, the resistive dissipation goes down an order of magnitude; the other factors become more significant.)

## 2. Coil Area and Saturation

The dissipation was computed for a comparatively large coil of 5.33 in.<sup>2</sup> of actual conductor. It now seems more probable that one would use a coil of ~ 4 in.<sup>2</sup> over-all cross section, which could be made with a very high packing factor. This would increase the dissipation by about 35%. Magnet saturation also was not included, and prolonged operation at peak field with long flat-tops would increase the power by about 50%.

## 3. Duty Factor

Sixty percent of the dissipation is in the flat-top, and only 40% in the rise and fall of field. With saturation included almost all the excess is in the flat-top. Present large synchrotrons do not have such long flat-tops (and it is not certain that one could use them effectively if they were available). Furthermore, the power supply and rf costs and problems of a 1 sec rise time are formidable and it is probable that for 2 TeV operation, at least 2 or 3 sec of rise time will be used. A 2 or 3 sec flat-top at top energy is luxurious.

## 4. Energy Storage

One great advantage to the flexibility of cryogenic (or superconducting) accelerators is that the major electrical dissipation is transferred from the power supplies to the refrigerant. The heat of vaporization is so large for neon or even hydrogen that it would take hours of running to vaporize most of the refrigerant, even with the refrigerator off. (For neon 100 kW evaporates 1 liter/sec.)

A 300°K synchrotron has about a 1 sec time constant, so that unless a very large machine is pulsed formidably fast the power supply sees a very dissipative load. This greatly increases power supply cost and power consumption. A fast cycle requires a massive power supply (and rf system).

With a time constant of ~ 1000 sec, one has complete freedom to trade off the power supply cost and complexity, assuming an adequate flywheel, and the rf and refrigerator capacity. In the cryogenic case, one could, for example, have alternate pulses to 2 TeV and to 1 TeV and thereby cut the dissipation almost in half. (The 1 TeV load goes down by more than the  $\frac{1}{2}$  factor due to  $B^2$ .)

In summary, the figure of 70 W/ft refrigeration capacity is a conservative one, and a machine of high performance could be constructed with refrigerator capacities two or three times lower than this.

As an illustration of a large refrigerator plant, a 33 000 hp hydrogen plant at Sacramento, California, manufactured by Linde, would produce 530 kW at 20°K, operating as a refrigerator. This is a conversion ratio of 50 for input power to 20°K power. Responsible designs at 20°K for large systems give a range of conversion ratios from 35 to 50. By comparison, at 4°K the range of conversion ratios is 300 to 500. For comparison to superconductors a dissipation of 50 W/ft at 20°K is about equivalent to 5 W/ft at 4°K.

Figure 7 shows a magnet and Dewar cross section. Neither the magnet nor the Dewar design or refrigerant capacity are meant to be taken as more than an illustration.

Figure 8 illustrates a type of assembly of the ends of magnets and Dewars.

#### CONCLUSION

It appears that cryogenically powered magnets of the type described can be constructed with existing purity commercial aluminum and be competitive with projected superconductor coil ac losses. The compactness and high efficiency of stored energy actually in the useful region, plus the inherent flexibility of a system with a very long time constant will be very beneficial to over-all accelerator design.

#### ACKNOWLEDGEMENTS

We wish to thank the Senior Staff of the Accelerator Department at Brookhaven for their support of this activity.

We wish also to thank the Senior Staff of the Bubble Chamber Group and the Accelerator Department's Cryogenics Group for their assistance and the offering of their experience in large cryogenic systems.

We are also indebted to V. Arp of NBS for his knowledge and assistance in the properties of pure aluminum.

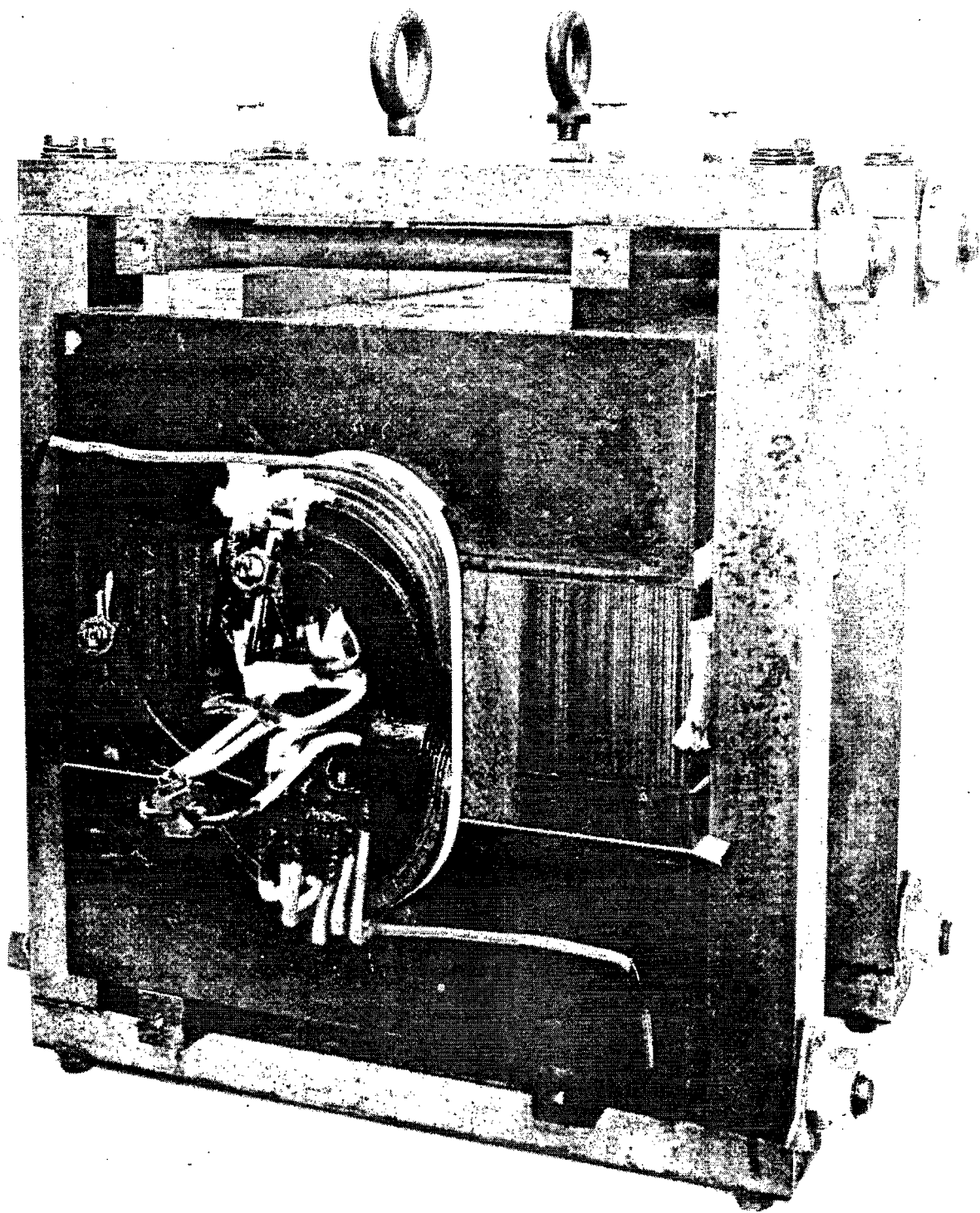


Fig. 1. Magnet model.

## 2 D 12-H MODEL MAGNET

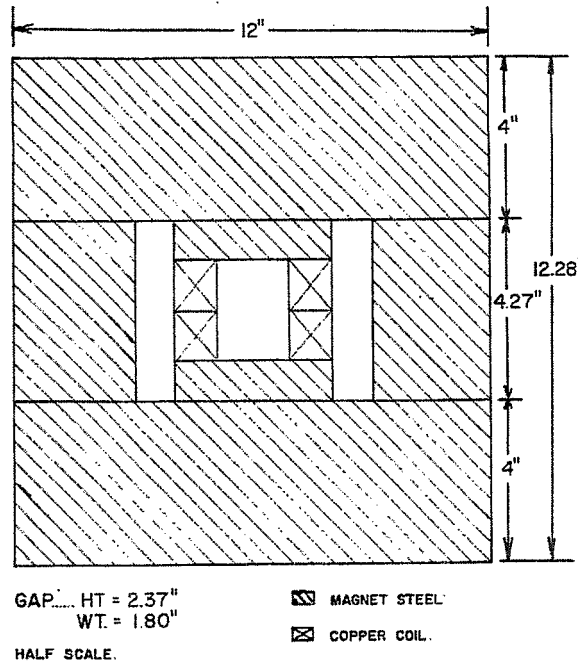


Fig. 2. Schematic assembly drawing of "kit" magnet.

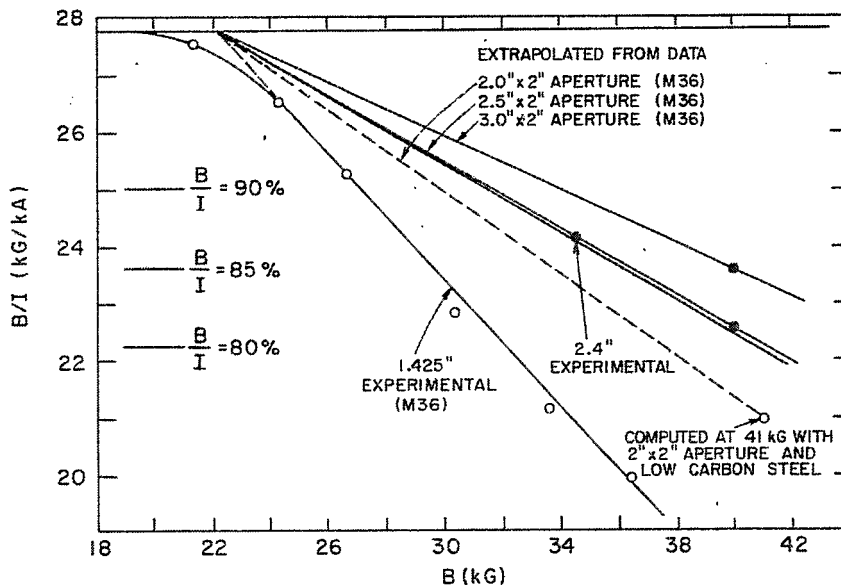


Fig. 3. Saturation effects for various magnet geometries.

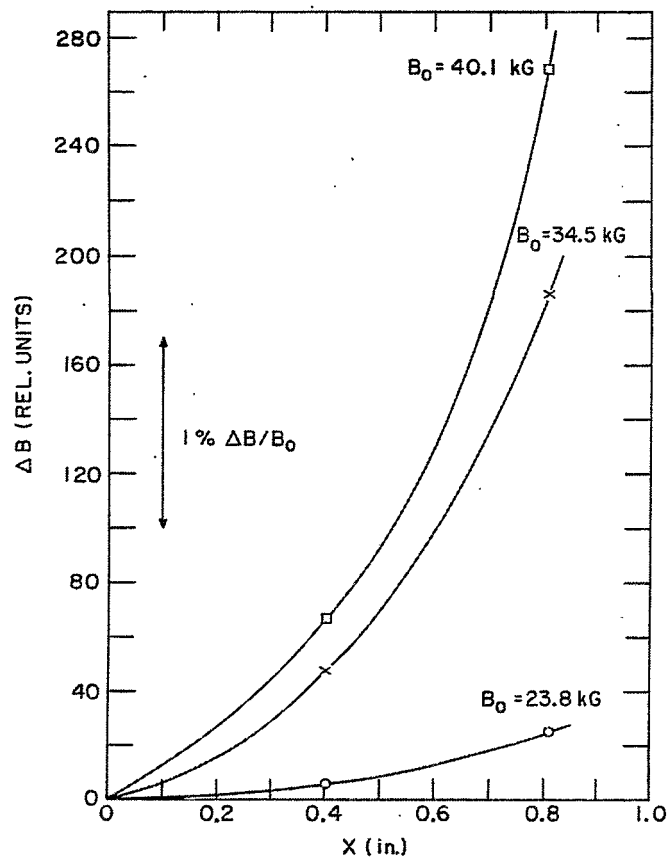


Fig. 4. Aberrations in 2.4 in. model.

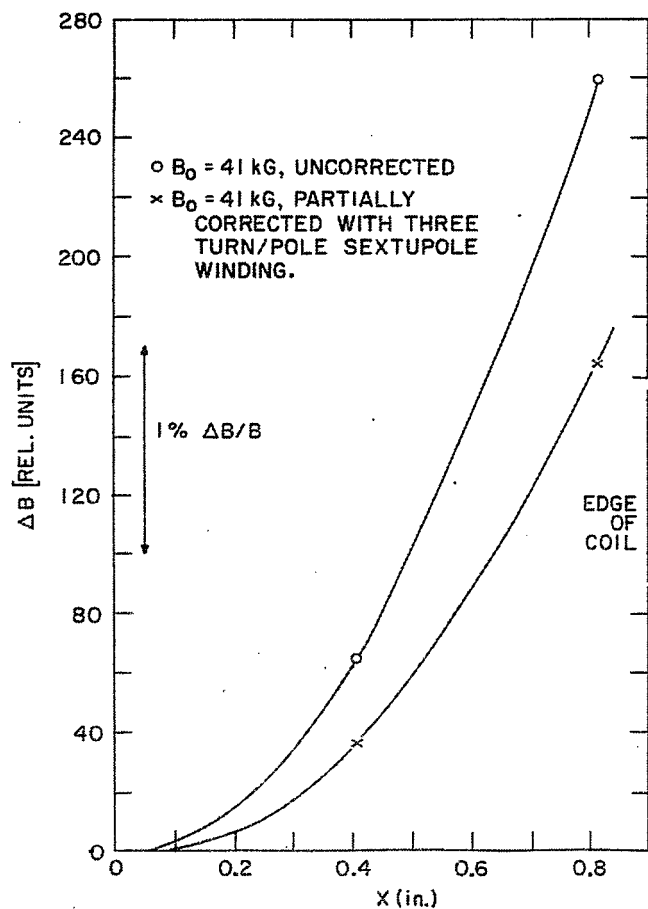


Fig. 5. Sextupole aberration partially corrected by pole face windings.

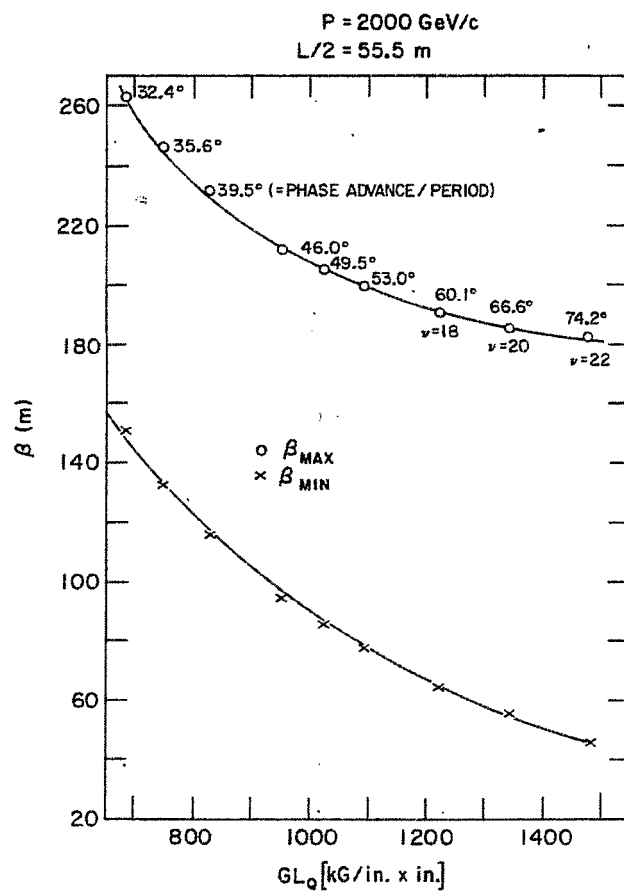


Fig. 6. Typical lattice parameters for 2 TeV synchrotron.

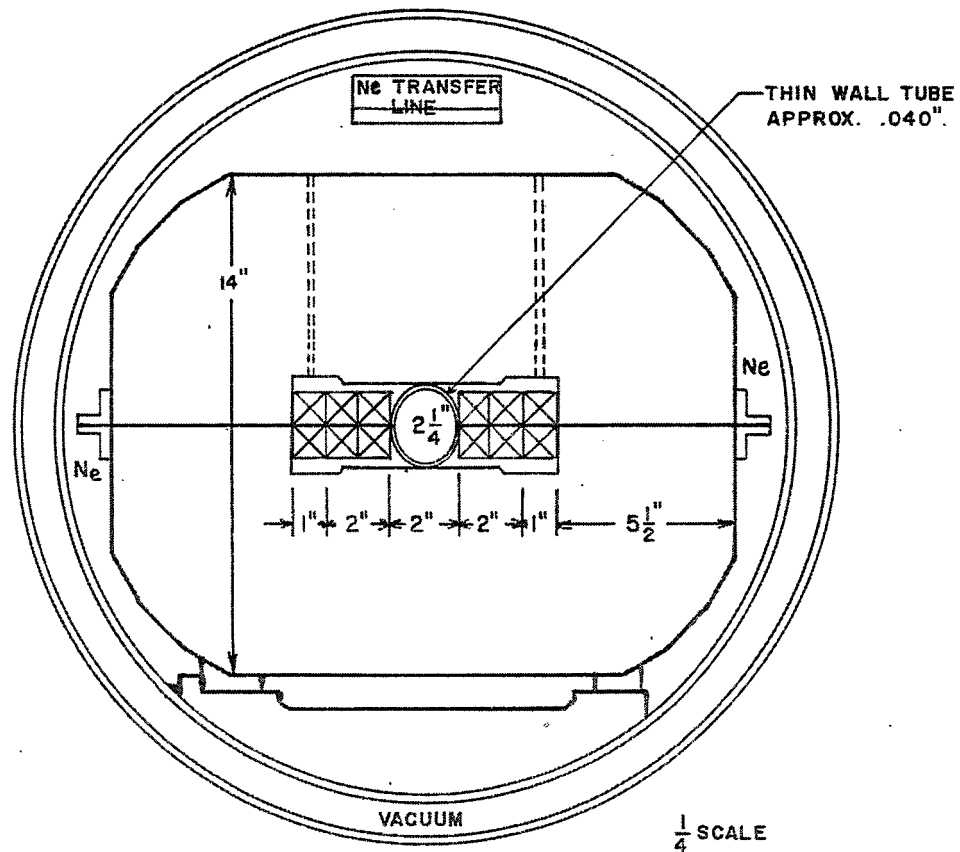


Fig. 7. Cross section of cryogenic magnet and Dewar (representative only).

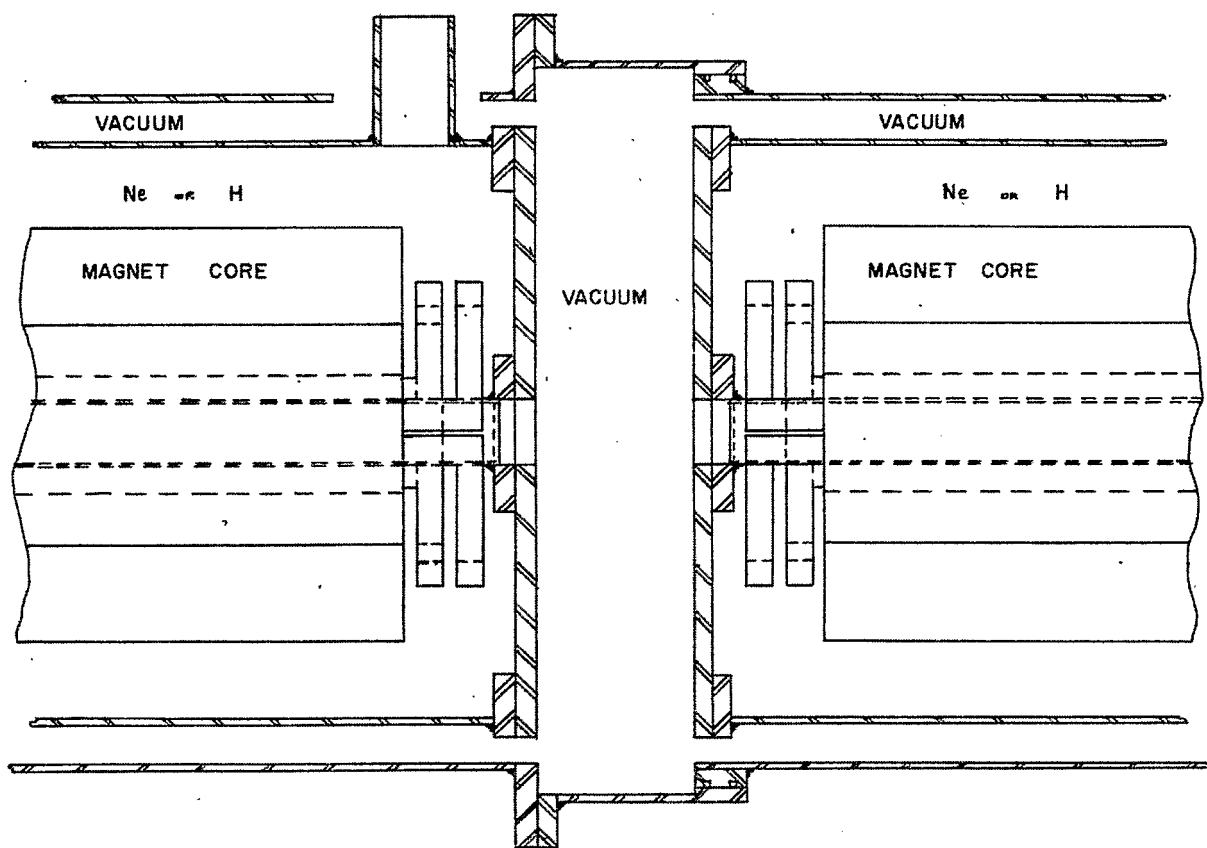


Fig. 8. Possible end section of magnets and Dewars.



## SUMMARY OF SIXTH WEEK OF 1968 SUMMER STUDY

J.P. Blewett  
Brookhaven National Laboratory  
Upton, New York

The topic of the sixth and last week of the 1968 Summer Study was "Accelerators and Storage Rings using Superconducting or Cryogenic Magnets." The first two days and a small part of the third day were devoted to design studies and cost estimates for accelerators using superconducting magnets. Storage rings were mentioned in passing but it soon became evident that there has been virtually no serious work on superconducting storage rings. The third day was "FFAG day" when Brookhaven and Argonne design work on superconducting FFAG machines was presented. On the fourth and last day of this session cryogenic magnets using pure, but not superconducting, metals were introduced.

### SUPERCONDUCTING SYNCHROTRONS

The week began with a discussion by Peter Smith of the Rutherford Laboratory on superconducting proton synchrotrons. His presentation was divided into four parts. The first was on costs, a subject which he considered in a paper in Nuclear Instruments and Methods last year. There he had shown that the cost of a superconducting 300 GeV machine could be 10-20% lower than that of a conventional, room-temperature machine. Optimum bending fields appear to be of the order of 60 kG. The main change in the picture since last year is the imminent solution of the problem of high losses in superconductors. This led into the second part of the lecture which was on ac losses and was a summary of a presentation by Smith given in the preceding week. At that time he described the design of a superconducting cable that consists of a large number of 1 mil or 2 mil strands of NbTi embedded in a high resistance alloy. Smith and others have shown that, if this cable is twisted around its axis at a rate of about one turn per inch, it should be free of flux jumps and should also have very low ac losses. This conductor has been fabricated in a variety of combinations and dimensions by IMI and is just now under test at the Rutherford Laboratory. Although the tests are not complete, the results to date seem to bear out the theoretical predictions and so are very encouraging. This probably is one of the most important revelations of the Summer Study. It should open the field of ac and power applications to low temperature operation.

The third part of Smith's presentation was devoted to design problems, of which there appear to be many. The straightforward problems of coil design, choice of aperture, magnet length, etc. involve educated choices from available techniques. Heating effects and removal of heat are more difficult. Heat may be generated by ac losses, eddy currents, or particle beam loss. Probably the cryostat must be nonconducting. Stray fields outside of the coil probably must be shielded.

The magnet power supply might consist of units rated at about 3000 A, 5000 V distributed around the ring. In a separate talk, Smith described some ingenious ideas for storing energy in superconducting coils. He showed that energy can be transferred from one inductance to another by making mechanical changes in the coupling coefficient and finally he described a rotating system in which energy could be transferred from a superconducting energy storage coil to a superconducting synchrotron without introduction of any external energy source.

Finally Smith described a few projects that are under consideration at the Rutherford Laboratory. These include conversion of the 7 GeV Nimrod accelerator to 40 GeV by replacement of Nimrod's room-temperature magnets with superconducting magnets. Another project involves a more modest increase in Nimrod's energy to about 25 GeV at which energy it would serve as a booster injector for a 100-200 GeV ring. In Smith's words "the costs are so low as to be unbelievable."

Some of the theoretical analyses presented by Smith were not followed completely by all members of the audience so when this presentation was completed, John Lawson, also of the Rutherford Laboratory, attempted to revive the sagging confidence of those who had been left behind. He wrote Maxwell's equations in appropriate form on the blackboard and showed how simple is the fundamental approach. As he said it is "the sort of thing you can do on the platform while you are waiting for trains." Later, it was said that nothing is involved but Ohm's law; it was stated that "Ohm's law is all you need to know, but you must know it very well." This statement was referred to more than once during the week.

A second paper primarily on costs of superconducting synchrotrons was presented by Michael Green of the Lawrence Radiation Laboratory. This was a carefully considered study of the consequences of redoing the original LRL 200 GeV study using superconducting magnets distributed around the LRL circle of 690 m radius. He made a number of rather conservative assumptions and used a computer to look for optimum parameters. These assumptions essentially concerned parameters that were close to the present state of the art. His first conclusions included the following:

- The push to high field may not be justified; the economic considerations seem to point to lower than maximum fields.
- High current density is important.
- Elliptical beam geometry may well change to circular geometry for superconducting systems.
- The cost of superconducting machines probably will decrease with time.

Green then proceeded to a cost study of a "bare-bones" 100 GeV machine, a machine which included no experimental facilities; indeed, it did not even include an injector.

A number of pertinent conclusions emerged from this study. The cost of the magnets, using present superconductor costs, was 70-85% accounted for by the cost of the superconducting ribbon or wire. At low fields NbTi is cheaper but, at about 100 kG, Nb<sub>3</sub>Sn was cheaper. Power supplies were estimated on conventional systems "bad as they are." Cryostats were to be of simple design with high heat leak but of high reliability. No liquid nitrogen shielding was included. Cost was estimated at \$2000-\$3000 per meter.

Refrigerators would be large units since cost of refrigeration seems to vary with about the two-thirds power of the refrigeration power required.

Other systems would be conventional with the exception of the vacuum system, which would use cryopumping.

Green's conclusions were somewhat surprising. For a 2 sec cycle his economic optimum occurred at a peak field of 25 kG (slightly higher for Nb<sub>3</sub>Sn superconductors). For a 10 sec cycle the optimum is at 35-40 kG.

Perhaps the main impact of Green's presentation came from the conclusion that, even at such modest increases in field, the cost of a superconducting synchrotron would be about half of that of a conventional machine for the same energy.

Sampson of Brookhaven then presented a combined paper. Under his chairmanship the previous week's session on superconducting magnets was so crowded that he postponed a paper of his own on pulsed superconducting magnets which was now coalesced with a study on superconducting synchrotrons.

Sampson and his associates have shown experimentally that:

- Loss per cycle is independent of frequency.
- Loss correlates with total field swing regardless of bias.
- Loss correlates even better with the rms value of field normal to the tape surface ( $\text{Nb}_3\text{Sn}$  tape was used in all cases).
- For the same change in field, loss is independent of current.
- Loss is proportional to the  $\text{Nb}_3\text{Sn}$  content of the tape used.
- Loss is influenced by the winding density.

Sampson emphasized a point made earlier in the session by Howard Hart of General Electric that attempts to increase current carrying capacity by increasing the thickness of a layer of  $\text{Nb}_3\text{Sn}$  can be self-frustrating since, from our experimental results, the low thermal conductivity of  $\text{Nb}_3\text{Sn}$  can make it impossible to remove the heat generated in ac losses in a thick layer of this superconductor.

Sampson then presented a few cost estimates for a modest accelerator of 2000 GeV using superconducting magnets. This is to be a machine of 1.5 km radius with a peak field of 60 kG. The aperture is assumed to be 6 cm in diameter. About 80% of the ring will be full of magnets. Stored energy in the ring has a peak value of about 750 MJ. Injection would be at 30 GeV, which happens to be available from Brookhaven's AGS.

From Brookhaven's ac measurements it seems that a ratio of stored energy to loss per cycle of about 200 is presently achievable. Sampson assumed that this can be increased to about 1000, an assumption that, in view of Smith's work, seems pessimistic. He then made cost estimates that were even more encouraging than those of Michael Green.

#### STORAGE OF ENERGY IN SUPERCONDUCTING MAGNETS

Smith's proposals for power supplies for superconducting synchrotrons already have been mentioned. Another energy storage project in progress in France was reported by G. Bronca of Saclay. In an attempt to simulate conditions encountered by satellites on re-entry into the atmosphere, the ONERA laboratory in France is planning storage of about 50 MJ in superconducting coils for release in 20-50 msec. Pilot tests for this experiment are in progress at Saclay.

#### AC LOSSES IN SUPERCONDUCTORS

LRL work on this topic was presented during the fourth week by F. Voelker. New work since that date was described by W.S. Gilbert, also of LRL. For those who did not hear Voelker's paper the earlier results were reviewed. New results on pancake coils of 0.5 in.  $\text{Nb}_3\text{Sn}$  ribbon were presented. The rather high losses observed precipitated a discussion of the significance of short circuits in test coils.

In conclusion Gilbert expressed considerable optimism about the possibility of operating at high over-all current densities.

## IRON SHIELDING FOR SUPERCONDUCTING MAGNETS

A short paper was presented by the writer on iron shielding for cosine wound circular dipoles and quadrupoles. Analytic expressions were written for a coil of finite thickness surrounded by a cylindrical shield of inner diameter large enough so that the external field of the magnet has fallen below the saturation value for iron. It was shown that such a shield will not distort the field in the useful aperture but that its value will be increased to some extent. In the case of dipoles the dipole field can be increased by about 10 kG for no change in current.

## RADIATION EFFECTS ON SUPERCONDUCTING MAGNETS

This subject was attacked by H. Brechna of SLAC who, in typical Brechna fashion, injected a few stimulating introductory remarks. These remarks were aimed at the general attitudes toward superconducting devices. He drew a picture of a classical scales. One pan of the scales included a package of "uncertainty about superconducting magnets + room temperature magnets." The other pan was filled with "experiments + optimism." It was his feeling that, in the present atmosphere, the former pan might move rapidly downward.

Brechna emphasized a few of the problems facing the designer of high field magnets - fatigue, for example, about which at this early state of knowledge little is known.

On the question of radiation effects, this talk was divided into five sections. These sections fell, very logically, into the following categories:

- Induced radioactivity. As an example, figures were presented for a magnet 5 m downstream from a target at SLAC. This magnet would receive 3 W of gamma rays, 1 W of neutrons, and 0.4 W of protons.
- Radiation effects on type II superconductors. The usual effects of radiation - lattice distortions, changes in mechanical properties, ionization effects, etc. can be expected. For  $\text{Nb}_3\text{Sn}$  changes of critical current in either direction can result. It should be noted that an increase in critical current, although apparently desirable, may make a stable superconductor unstable.  $\text{NbTi}$  and  $\text{NbZr}$  can both be expected to deteriorate slightly in their superconducting properties as a result of radiation.
- Radiation effects on nonsuperconducting metals. The usual metals used for stabilization - copper, silver or aluminum - can be expected to lose mechanical strength and to increase in electrical resistivity under intense radiation.
- Radiation effects on insulation. These also are uniformly bad. Insulation can be expected to become conducting and so to deteriorate the flux jump pattern. Many insulators evolve large quantities of gas. For example, teflon at  $9 \times 10^8$  rad gives off 9 mg per gram of material. The gas is predominantly fluorine.
- Radiation effects on helium. Here, offhand, one does not expect serious difficulty. But, of course, the three isotopes of hydrogen will be produced and could freeze and obstruct the cooling system. At SLAC in intense radiation areas hydrogen can be produced from helium at a rate of one liter every three hours.

Wednesday was FFAG day. The topic was introduced by George Parzen of Brookhaven. Parzen described the procedures for choosing parameters in an FFAG accelerator. At MURA, because of the very large range of momentum to be included, the proposed machine had an enormous (4 m) radial aperture. But if the momentum range could be held to a factor of three (for example, 200 MeV to 1 GeV or 300 GeV to 1000 GeV) the radial aperture could be held to 15 cm regardless of the energy level. Vertical apertures would be about 2 cm.

Problems with the FFAG mentioned by Parzen included:

- The field ratio between the useful field in the median plane and the maximum field at the windings. This could approach a factor of two. If a maximum field of 60 kG is tolerable at the windings the maximum usable field would be 30 kG.
- Magnet design, which at best is very complicated. End effects of return windings may be troublesome and are barely calculable.
- Field-free, straight sections of any appreciable length cannot be tolerated in an FFAG machine. Thus injection, ejection and rf acceleration systems become very difficult to design.

The design of a magnet for an FFAG accelerator was described by P. Gerald Kruger of the University of Illinois. Kruger has been for many years a consultant to Brookhaven. Using the computer at the Urbana campus Kruger has shown that air-core superconducting coils can be designed to provide the fields required for a superconducting accelerator. The structures that he described, although complicated, appeared to be quite feasible. Kruger presented a comparison between cost estimates for a pulsed synchrotron and an FFAG machine indicating that the dc operation of the FFAG accelerator might make it somewhat cheaper.

G. del Castillo of Argonne presented design ideas evolved at ANL and emphasized a number of mechanical problems that remain unsolved for FFAG and, indeed, for all types of superconducting machines. He emphasized the problems of aligning structures in cryostats at 4°K and of measuring magnetic fields at low temperature with the high precision required. He presented three possible cryostat designs, including means for making the necessary measurements, but it cannot be said that he appeared confident that any of his designs was completely satisfactory.

del Castillo then discussed plans for FFAG developments at Argonne. Room-temperature tests of a coil configuration proposed at Brookhaven indicated that such a configuration might be useful. Kruger pointed out the fact that this configuration, although initially intriguing, had very bad end effects.

Plans at Argonne include construction of a superconducting coil which would represent an element of an FFAG system. Attempts will be made with this coil to measure fields to 0.01% to check detailed computations of field patterns. The relation between field and current will be checked and the effects of field induced forces up to 200 tons will be observed.

A paper not in the program was introduced on Wednesday by W. Herrmannsfeldt of SLAC. After a few pungent remarks about cost estimates, Herrmannsfeldt discussed the possibility of converting the two-mile linear accelerator to a superconducting machine yielding 100 GeV. This would require acceleration rates of 10 MeV per foot which is somewhat above current acceleration rates. If this could not be achieved, SLAC proposes that the electron beam should be magnetically deflected back to the injection end of the machine and reaccelerated. A couple of intriguing problems raise their heads. The geometry of the return path is adversely affected by a new Freeway which

is under construction and which crosses the two-mile machine on a bridge. The second problem is that of energy loss by radiation in the curved sections of the returned beam. Here it is quite possible to lose half of the energy in the accelerated beam. These rather formidable problems do not appear to have frightened the indefatigable group at SLAC.

The last day of this week's session was a departure from superconductivity to a consideration of nonsuperconducting metals at cryogenic temperatures. Here pure aluminum appears to be the most promising material. It can be operated in the temperature range between 4° and 30°K. The properties of very pure aluminum were outlined by Vincent Arp of the Bureau of Standards at Boulder. The resistance of aluminum is made up of a sum of components due to impurities, lattice defects, grain boundaries, lattice vibrations, etc. The larger are these components the higher will be the value of the temperature at which a sample reaches an asymptotic value of resistance when cooled — further reduction of temperature will cause no further decrease in resistance. By removing impurities, the ratio of resistivity at room temperature to that at 4°K can be increased to values as high as 45 000. Values as high as 15 000 are commercially available — these samples are purified by zone refining. This process, however, leaves traces of transition metals. A new German process is now available which involves electrolytic deposition of aluminum from aluminum triethylene, a very inflammable and explosive substance. The electrolyzed aluminum has many impurities but does not include transition metals. It can then be zone refined to produce the highest purity yet attained.

The resistivity of aluminum rises sharply if it is strained beyond its yield point. The low value can be restored, however, if the sample is annealed at room temperature or at a somewhat higher temperature.

A desirable property of aluminum is a relatively low value of magnetoresistance. At about 10 kG the resistivity reaches a value approaching about three times its zero field value, but at higher fields the resistivity shows no further increase.

Aluminum samples show a variety of size effects when used in ac applications. These size effects depend on the relative magnitudes of the sample diameter, the classical skin depth, and the electron mean free path.

The possible use of aluminum in cryogenic accelerator or beam transport magnets was discussed by Gordon Danby of Brookhaven. Danby pointed out the fact that "picture frame magnets" for very high flux densities suffer from the relatively low current density attainable in copper in conventional room-temperature magnets. For fields much above 20 kG the winding becomes absurdly large. But for materially higher current densities Danby has shown that fields in iron core magnets can be pushed to 40 kG and above. Field distortions of sextupole or higher order become surprisingly low if the magnet gap is increased to be of the same order as the separation between the windings. The models thus far have included copper windings cooled by liquid nitrogen but Danby will soon have obtained some aluminum strip with a resistance ratio of 15 000. With this he hopes to attain current densities of the order of 10 000 A/cm<sup>2</sup>.

Danby then turned to consideration of a 2000 GeV accelerator using cryogenic magnets, operated at 40 kG. He would propose operation at 27°K using liquid neon as a coolant, although in the subsequent discussion it appeared that operation as low as 10°K might be advantageous. At 27°K resistive losses would amount to about 60 W/ft. Eddy current and hysteresis losses would increase the total loss to about 66 W/ft.

At this early stage it is not at all obvious whether cryogenic or superconducting magnets will be preferable for use in synchrotrons. Very preliminary cost estimates give comparable results for the two cases. They do, however, indicate that major savings should be possible for the super-energy synchrotrons of the future.

**PROCEEDINGS OF THE 1968 SUMMER STUDY  
ON SUPERCONDUCTING DEVICES AND ACCELERATORS  
Part I (pp. 1-376)**

**BROOKHAVEN NATIONAL LABORATORY**

**June 10 - July 19, 1968**

**Organizing Committee: JOHN P. BLEWETT, Chairman  
HARALD HAHN  
ARTHUR PASKIN  
ALBERT G. PRODELL  
WILLIAM B. SAMPSON**

**BROOKHAVEN NATIONAL LABORATORY  
UPTON, NEW YORK 11973**

Help and suggestions from Animesh Jain, David McChesney, Diana Votrubá, Peter Wanderer, Donna Zadow and Photography and Graphics Arts Division in putting these proceedings in electronic form are appreciated.

-Ramesh Gupta

[gupta@bnl.gov](mailto:gupta@bnl.gov)

---

**[Return to 1968 Proceedings Home Page](#)**

[Click here to e-mail comments, corrections, etc. on these Proceedings on the Web](#)

[Click Here to Visit Superconducting Magnet Division Home Page at BNL](#)

[Click Here to Visit Ramesh Gupta's Home Page at BNL](#)



# AUTHOR INDEX

## -A-

Allen, M.A.	34
Allinger, J.E.	1115
Altorfer, R.	567
Arp, V.	1095
Asner, A.	866
Autler, S.H.	49

## -B-

Barnes, C.	230
Bergmann, W.H.	681, 926
Beth, R.A.	843
Biquard, F.	171
Blewett, J.P.	544, 1042, 1127
Brady, B.G.	165
Brechna, H.	477, 1011
Britton, R.B.	449, 679, 893
Brown, D.P.	794
Brown, H.N.	136
Burgess, R.W.	794

## -C-

Caimi, F.	567
Carne, A.	165
Chambers, E.E.	79
Clee, P.T.M.	815
Cody, G.	405
Coffey, D.L.	929
Collins, S.C.	59
Coombs, G.P.	293
Cornish, D.N.	880
Cullen, G.W.	437

## -D-

Dahl, P.F.	559
Danby, G.T.	1115
del Castillo, G.	601, 1075

## -E-

Efferson, K.R.	667
----------------	-----

## -F-

Foster, E.H.	13
--------------	----

## -G-

Gauster, W.F.	929, 944
Gilbert, W.S.	1007
Green, M.A.	293, 981

## -H-

Haden, C.R.	40
Hahn, H.	13, 18
Halama, H.J.	13, 150
Hanson, A.O.	169
Hart, H.R.	571
Hassenzahl, W.V.	886
Henning, C.D.	304
Herrmannsfeldt, W.B.	1089
Hogg, H.A.	34
Hurlich, A.	311

## -J-

Jackson, J.W.	1115
Jüngst, W.	127

## -K-

Kilb, R.W.	714
Kruger, P.G.	1059

## -L-

Laquer, H.	673, 886
Lari, R.J.	1075
Lawson, J.D.	888
Leupold, M.J.	727
Lewin, J.D.	839, 913
Livingston, J.D.	377
Lubell, M.S.	667
Lyneis, C.M.	52

## -M-

Marston, P.G.	709
McAshan, M.S.	52
McInturff, A.D.	465, 612
Meuser, R.B.	946
Meyerhoff, R.W.	23
Miller, J.M.	18
Montgomery, D.B.	727
Morgan, G.H.	559
Morpurgo, M.	953
Mowers, R.	326
Mulholland, G.T.	794

## -N-

Nahman, N.S.	622
Neal, R.B.	101, 111
Newman, M.J.	165
Nguyen Tuong Viet	171
Novak, J.K.	886

-O-

Oswald, L.O. .... 601,1075

-P-

Parzen, G. .... 860,1052  
 Perry, J.L. .... 293  
 Pierce, N.T. .... 727  
 Prast, G. .... 205  
 Prodell, A.G. .... 786  
 Purcell, J.R. .... 765

-R-

Rayroux, J.M. .... 567  
 Rhodenizer, R.L. .... 654  
 Rogers, J.D. .... 886

-S-

Sampson, W.B. .... 908, 962, 998  
 Schwettman, H.A. .... 1, 52, 187  
 Septier, A. .... 171  
 Smith, P.F. .... 839, 913, 967,1002  
 Smith, R.V. .... 249  
 Snyder, J.N. .... 1059  
 Stekly, Z.J.J. .... 748  
 Stovold, R.V. .... 888  
 Strauss, B. .... 748  
 Strobridge, T.R. .... 193, 368  
 Suelzle, L.R. .... 67  
 Sutton, D.C. .... 169

-T-

Takano, N. .... 628  
 Taylor, C.E. .... 920  
 Thomas, D.B. .... 815  
 Thome, R. .... 748  
 Trowbridge, C.W. .... 815

-V-

Voelker, F. .... 550

-W-

Walters, C.R. .... 913  
 Webb, W.W. .... 396  
 Weggel, R. .... 727  
 Weissman, I. .... 32  
 Westendorp, W.F. .... 714  
 Williams, J.E.C. .... 727  
 Wilson, M.N. .... 839, 888, 913  
 Wipf, S.L. .... 393, 511, 619, 632, 683  
 Wittgenstein, F. .... 828

-Z-

Zabetakis, M.G. .... 229

AUTHOR INDEX

[A](#) [B](#) [C](#) [D](#) [E](#) [F](#) [G](#) [H](#) [I](#) [J](#) [K](#) [L](#) [M](#) [N](#) [O](#) [P](#) [Q](#) [R](#) [S](#) [T](#) [U](#) [V](#) [W](#) [X](#) [Y](#) [Z](#)

[Go to Subject Index](#)    [Return to 1968 Proceeding Home Page](#)

-A-

Allen, M.A.	.....	<a href="#">34</a>
Allinger, J.E.	.....	<a href="#">1115</a>
Altorfer, R.	.....	<a href="#">567</a>
Arp, V.	.....	<a href="#">1095</a>
Asner, A.	.....	<a href="#">866</a>
Autler, S.H.	.....	<a href="#">49</a>

-B-

Barnes, C.	.....	<a href="#">230</a>
Bergmann, W.H.	.....	<a href="#">681</a> , <a href="#">926</a>
Beth, R.A.	.....	<a href="#">843</a>
Biquard, F.	.....	<a href="#">171</a>
Blewett, J.P.	.....	<a href="#">544</a> , <a href="#">1042</a> , <a href="#">1127</a>
Brady, B.G.	.....	<a href="#">165</a>
Brechna, H.	.....	<a href="#">478</a> , <a href="#">1011</a>
Britton, R.B.	.....	<a href="#">449</a> , <a href="#">679</a> , <a href="#">893</a>
Brown, D.P.	.....	<a href="#">794</a>
Brown, H.N.	.....	<a href="#">136</a>
Burgess, R.W.	.....	<a href="#">794</a>

-C-

Caimi, F.	.....	<a href="#">567</a>
Carne, A.	.....	<a href="#">165</a>
Chambers, E.E.	.....	<a href="#">79</a>
Clee, P.T.M.	.....	<a href="#">815</a>
Cody, G.	.....	<a href="#">405</a>
Coffey, D.L.	.....	<a href="#">929</a>
Collins, S.C.	.....	<a href="#">59</a>
Coombs, G.P.	.....	<a href="#">293</a>
Cornish, D.N.	.....	<a href="#">880</a>
Cullen, G.W.	.....	<a href="#">437</a>

-D-

Dahl, P.F.	.....	<a href="#">559</a>
Danby, G.T.	.....	<a href="#">1115</a>
del Castillo, G.	.....	<a href="#">601</a> , <a href="#">1075</a>

-E-

Efferson, K.R. .... [667](#)

**-F-**

Foster, E.H. .... [13](#)

**-G-**

Gauster, W.F. .... [929](#), [944](#)

Gilbert, W.S. .... [1007](#)

Green, M.A. .... [293](#), [981](#)

**-H-**

Haden, C.R. .... [40](#)

Hahn, H. .... [13](#), [18](#)

Halama, H.J. .... [13](#), [150](#)

Hanson, A.O. .... [169](#)

Hart, H.R. .... [571](#)

Hassenzahl, W.V. .... [886](#)

Henning, C.D. .... [304](#)

Herrmannsfeldt, W.B. .... [1089](#)

Hogg, H.A. .... [34](#)

Hurlich, A. .... [311](#)

**-J-**

Jackson, J.W. .... [1115](#)

Jungst, W. .... [127](#)

**-K-**

Kilb, R.W. .... [714](#)

Kruger, P.G. .... [1059](#)

**-L-**

Laquer, H. .... [673](#), [886](#)

Lari, R.J. .... [1075](#)

Lawson, J.D. .... [888](#)

Leupold, M.J. .... [727](#)

Lewin, J.D. .... [839](#), [913](#)

Livingston, J.D. .... [377](#)

Lubell, M.S. .... [667](#)

Lyneis, C.M. .... [52](#)

**-M-**

Marston, P.G.	.....	<a href="#">709</a>
McAshan, M.S.	.....	<a href="#">52</a>
McInturff, A.D.	.....	<a href="#">465</a> , <a href="#">612</a>
Meuser, R.B.	.....	<a href="#">946</a>
Meyerhoff, R.W.	.....	<a href="#">23</a>
Miller, J.M.	.....	<a href="#">18</a>
Montgomery, D.B.	.....	<a href="#">727</a>
Morgan, G.H.	.....	<a href="#">559</a>
Morpurgo, M.	.....	<a href="#">953</a>
Mowers, R.	.....	<a href="#">326</a>
Mulholland, G.T.	.....	<a href="#">794</a>

**-N-**

Nahman, N.S.	.....	<a href="#">622</a>
Neal, R.B.	.....	<a href="#">101</a> , <a href="#">111</a>
Newman, M.J.	.....	<a href="#">165</a>
Nguyen Tuong Viet	.....	<a href="#">171</a>
Novak, J.K.	.....	<a href="#">886</a>

**-O-**

Oswald, L.O.	.....	<a href="#">601</a> , <a href="#">1075</a>
--------------	-------	--------------------------------------------

**-P-**

Parzen, G.	.....	<a href="#">860</a> , <a href="#">1052</a>
Perry, J.L.	.....	<a href="#">293</a>
Pierce, N.T.	.....	<a href="#">727</a>
Prast, G.	.....	<a href="#">205</a>
Prodell, A.G.	.....	<a href="#">786</a>
Purcell, J.R.	.....	<a href="#">765</a>

**-R-**

Rayroux, J.M.	.....	<a href="#">567</a>
Rhodenizer, R.L.	.....	<a href="#">654</a>
Rogers, J.D.	.....	<a href="#">886</a>

**-S-**

Sampson, W.B.	.....	<a href="#">908</a> , <a href="#">962</a> , <a href="#">998</a>
Schwettman, H.A.	.....	<a href="#">1</a> , <a href="#">52</a> , <a href="#">187</a>
Septier, A.	.....	<a href="#">171</a>
Smith, P.F.	.....	<a href="#">839</a> , <a href="#">913</a> , <a href="#">967</a> , <a href="#">1002</a>
Smith, R.V.	.....	<a href="#">249</a>
Snyder, J.N.	.....	<a href="#">1059</a>

Stekly, Z.J.J.	.....	<a href="#">748</a>
Stovold, R.V.	.....	<a href="#">888</a>
Strauss, B.	.....	<a href="#">748</a>
Strobridge, T.R.	.....	<a href="#">193</a> , <a href="#">368</a>
Suelzle, L.R.	.....	<a href="#">67</a>
Sutton, D.C.	.....	<a href="#">169</a>

**-T-**

Takano, N.	.....	<a href="#">628</a>
Taylor, C.E.	.....	<a href="#">920</a>
Thomas, D.B.	.....	<a href="#">815</a>
Thome, R.	.....	<a href="#">748</a>
Trowbridge, C.W.	.....	<a href="#">815</a>

**-V-**

Voelker, R.	.....	<a href="#">550</a>
-------------	-------	---------------------

**-W-**

Walters, C.R.	.....	<a href="#">913</a>
Webb, W.W.	.....	<a href="#">396</a>
Weggel, R.	.....	<a href="#">727</a>
Weissman, I.	.....	<a href="#">32</a>
Westendorp. W.F.	.....	<a href="#">714</a>
Williams, J.E.C.	.....	<a href="#">727</a>
Wilson, M.N.	.....	<a href="#">839</a> , <a href="#">888</a> , <a href="#">913</a>
Wipf, S.L.	.....	<a href="#">393</a> , <a href="#">511</a> , <a href="#">619</a> , <a href="#">632</a> , <a href="#">683</a>
Wittgenstein, F.	.....	<a href="#">828</a>

**-Z-**

Zabetakis, M.G.	.....	<a href="#">229</a>
-----------------	-------	---------------------

[A](#) [B](#) [C](#) [D](#) [E](#) [F](#) [G](#) [H](#) [I](#) [J](#) [K](#) [L](#) [M](#) [N](#) [O](#) [P](#) [Q](#) [R](#) [S](#) [T](#) [U](#) [V](#) [W](#) [X](#) [Y](#) [Z](#)

[Author Index as appeared in the original publication](#)

[Go to Subject Index](#)

[Return to 1968 Proceeding Home Page](#)

[Table of contents as they appeared in the original proceedings](#)

[Return to 1968 Proceedings Home Page](#)

**Directly Jump to**   [1st Week](#)   [2nd Week](#)   [3rd Week](#)   [4th Week](#)   [5th Week](#)   [6th Week](#)

[Author Index](#)

---

<a href="#">Introductory Remarks – Maurice Goldhaber, Director, Brookhaven National Laboratory</a>	<a href="#">iii</a>
<a href="#">Editor's Preface – Albert G. Prodell, Brookhaven National Laboratory</a>	<a href="#">iv</a>
<a href="#">Introduction – John P. Blewett, Brookhaven National Laboratory</a>	<a href="#">v</a>

## **FIRST WEEK – SUPERCONDUCTING RF CAVITIES AND LINACS**

**Chairman: H.A. Schwettman, Stanford University**

[\(Photos\)](#)

<a href="#">The Development of Low Temperature Technology at Stanford and its Relevance to High Energy Physics</a>	<a href="#">1</a>
H. Alan Schwettman, Stanford University	
<a href="#">Q Measurements on Superconducting Cavities at S-Band</a>	<a href="#">13</a>
H. Hahn, H.J. Halama, and E.H. Foster, Brookhaven National Laboratory	
<a href="#">Coupling Losses in Superconducting Cavities</a>	<a href="#">18</a>
H. Hahn and J. Miller, Brookhaven National Laboratory	
<a href="#">Fabrication of Niobium Rf Cavities</a>	<a href="#">23</a>
R.W. Meyerhoff, Union Carbide Corporation	
<a href="#">Fabrication of High Q Superconducting Niobium Cavities</a>	<a href="#">32</a>
I. Weissman, Varian Associates	
<a href="#">Materials Investigation for a Two-Mile Superconducting Accelerator</a>	<a href="#">34</a>
M.A. Allen and H.A. Hogg, Stanford Linear Accelerator Center	
<a href="#">Characterization of Residual Rf Losses in Superconductors</a>	<a href="#">40</a>
C.R. Haden, University of Oklahoma	
<a href="#">Technetium as a Material for ac Superconductivity Applications</a>	<a href="#">49</a>
S.H. Autler, NASA Electronics Research Center	
<a href="#">Applications of the Fountain Effect in Superfluid Helium</a>	<a href="#">52</a>
C.M. Lyneis, M.S. McAshan, and H.A. Schwettman, Stanford University	
<a href="#">Refrigeration at Temperatures Below the Boiling Point of Helium</a>	<a href="#">59</a>
S.C. Collins, 500 Incorporated	
<a href="#">Rf Amplitude and Phase Stabilization for a Superconducting Linear Accelerator by Feedback Stabilization Techniques</a>	<a href="#">67</a>
L.R. Suelzle, Stanford University	
<a href="#">Particle Motion in a Standing Wave Linear Accelerator</a>	<a href="#">79</a>
E.E. Chambers, Stanford University	

<a href="#">Sample Parameters of a Two-Mile Superconducting Accelerator</a>	<a href="#">101</a>
R.B. Neal, Stanford Linear Accelerator Center	
<a href="#">Consideration of the Use of Feedback in a Traveling-Wave Superconducting Accelerator</a>	<a href="#">111</a>
R.B. Neal, Stanford Linear Accelerator Center	
<a href="#">Summary of Recent Investigations of the Karlsruhe Group on Rf Properties of Superconductors and on Applications</a>	<a href="#">127</a>
W. Jungst, Kernforschungszentrum Karlsruhe	
<a href="#">An Enriched Particle Beam Using Superconducting Rf Deflectors</a>	<a href="#">136</a>
H.N. Brown, Brookhaven National Laboratory	
<a href="#">Design Problems in Superconducting Rf Beam Separators</a>	<a href="#">150</a>
H.J. Halama, Brookhaven National Laboratory	
<a href="#">Superconducting Rf Separator Research at the Rutherford Laboratory</a>	<a href="#">165</a>
A. Carne, B.G. Brady, and M.J. Newman, Rutherford Laboratory	
<a href="#">Beam Optics Design for a 600 MeV Microtron</a>	<a href="#">169</a>
D.C. Sutton and A.O. Hanson, University of Illinois	
<a href="#">High Stability UHF Oscillators using a Superconducting Cavity</a>	<a href="#">171</a>
F. Biquard, Nguyen Tuong Viet, and A. Septier, Institut d'Electronique, Orsay	
<a href="#">Summary of First week of Summer Study</a>	<a href="#">187</a>
H. Alan Schwettman, Stanford University	
<b>SECOND WEEK - CRYOGENICS</b>	
<b>Chairman: T.R. Strobridge, NBS, Boulder</b>	
<a href="#">(Photos)</a>	
<a href="#">Refrigeration at 4 <sup>0</sup>K</a>	<a href="#">193</a>
T.R. Strobridge, National Bureau of Standards, Boulder	
<a href="#">European State of the Art in Cryogenics</a>	<a href="#">205</a>
G. Prast, Philips Research Laboratories	
<a href="#">Cryogenic Safety</a>	<a href="#">229</a>
M.G. Zabetakis, Bureau of Mines	
<a href="#">Cryopumping</a>	<a href="#">230</a>
C. Barnes, CVI Corporation	
<a href="#">Review of Heat Transfer to Helium I</a>	<a href="#">249</a>
R.V. Smith, National Bureau of Standards, Boulder	
<a href="#">An Examination of a Liquid Helium Refrigeration System for Superconducting Magnets in the 200 GeV Experimental Area</a>	<a href="#">293</a>
M.A. Green, Lawrence Radiation Laboratory, Berkeley, and G.P. Coombs and J.L. Perry, 500 Incorporated	



<a href="#">Cryogenic Electrical Leads</a>	<a href="#">304</a>
C.D. Henning, Lawrence Radiation Laboratory, Livermore	
<a href="#">Low Temperature Metals</a>	<a href="#">311</a>
A. Hurlich, General Dynamics/Astronautics	
<a href="#">Properties of Nonmetallic Materials at Cryogenic Temperatures</a>	<a href="#">326</a>
R. Mowers, Rocketdyne	
<a href="#">Review of the Cryogenics Session – Second Week of the Summer Study</a>	<a href="#">368</a>
T.R. Strobridge, National Bureau of Standards, Boulder	

### **THIRD WEEK – SUPERCONDUCTING MATERIALS**

**Chairman: A. Paskin, Brookhaven National Laboratory**

[\(Photos\)](#)

<a href="#">Structure and Properties of High-Field Superconductors</a>	<a href="#">377</a>
J.D. Livingston, General Electric Company	
<a href="#">Instability Comments</a>	<a href="#">393</a>
S.L. Wipf, Atomics International	
<a href="#">Critical Current Behavior of Hard Superconductors</a>	<a href="#">396</a>
W.W. Webb, Cornell University	
<a href="#">Critical Fields of Type II Superconductors</a>	<a href="#">405</a>
G. Cody, RCA Laboratories	
<a href="#">The Effect of Radiation on the Properties of Superconducting Materials</a>	<a href="#">437</a>
G.W. Cullen, RCA Laboratories	
<a href="#">Niobium Tin and Related Superconductors</a>	<a href="#">449</a>
R.B. Britton, Brookhaven National Laboratory	
<a href="#">Composite Materials</a>	<a href="#">465</a>
A.D. McInturff, Brookhaven National Laboratory	
<a href="#">Materials and Conductor Configurations in Superconducting Magnets</a>	<a href="#">478</a>
H. Brechna, Stanford Linear Accelerator Center	

### **FOURTH WEEK – AC EFFECTS AND FLUX PUMPS**

**Chairman: S.L. Wipf, Atomics International**

[\(Photos\)](#)

<a href="#">Ac Losses in Superconductors</a>	<a href="#">511</a>
S.L. Wipf, Atomics International	
<a href="#">Use of Superconductors in High Energy Physics</a>	<a href="#">544</a>
J.P. Blewett, Brookhaven National Laboratory	
<a href="#">Electrical Loss Measurements in a NbTi Magnet</a>	<a href="#">550</a>
F. Voelker, Lawrence Radiation Laboratory, Berkeley	

<a href="#">Ac Losses in Magnets made of Nb<sub>3</sub>Sn Ribbon</a>	<a href="#">559</a>
G.H. Morgan and P.F. Dahl, Brookhaven National Laboratory	
<a href="#">Dynamic Resistivity of Hard Superconductors in a Perpendicular Time Varying Field</a>	<a href="#">567</a>
A. Altorfer, F. Caimi, and J.M. Rayroux, Oerlikon Engineering Company	
<a href="#">Magnetic Instabilities and Solenoid Performance: Applications of the Critical State Model</a>	<a href="#">571</a>
H.R. Hart, Jr., General Electric Company	
<a href="#">Magnetic and Thermal Instabilities Observed to Commercial Nb<sub>3</sub>Sn Superconductors</a>	<a href="#">601</a>
G. del Castillo and L.O. Oswald, Argonne National Laboratory	
<a href="#">Observations of Flux Jump Behavior Related to Various Changes of Geometry, and Thermal and Electrical Environment</a>	<a href="#">612</a>
A.D. McInturff, Brookhaven National Laboratory	
<a href="#">Instabilities and Flux Annihilation</a>	<a href="#">619</a>
S.L. Wipf, Atomics International	
<a href="#">Superconducting Transmission Lines – Communication and Power</a>	<a href="#">622</a>
N.S. Nahman, National Bureau of Standards, Boulder	
<a href="#">Recent Developments in Superconductivity in Japan</a>	<a href="#">628</a>
Presented by N. Takano, Tokyo Shibaura Electric Company	
<a href="#">The Case for Flux Pumps and Some of Their Uses</a>	<a href="#">632</a>
S.L. Wipf, Atomics International	
<a href="#">Design Principles and Characteristics of the G.E. Flux Pump</a>	<a href="#">654</a>
R.L. Rhodenizer, General Electric Company	
<a href="#">Flux Pumps as Power Supplies in Comparison with Alternatives</a>	<a href="#">667</a>
M.S. Lubell and K.R. Efferson, Oak Ridge National Laboratory	
<a href="#">Flux Pump Work at Los Alamos</a>	<a href="#">673</a>
H. Laquer, Los Alamos Scientific Laboratory	
<a href="#">60 Hz Flux Pumps</a>	<a href="#">679</a>
R.B. Britton, Brookhaven National Laboratory	
<a href="#">Proposal for a Flux Pump Utilizing the Inverse Ettingshausen Effect in Hard Type II Superconductors in the Mixed State</a>	<a href="#">681</a>
W.H. Bergmann, Argonne National Laboratory	
<a href="#">Summary of the Fourth Week – Ac Losses, Instability and Flux Pumps</a>	<a href="#">683</a>
S.L. Wipf, Atomics International	

## **FIFTH WEEK – SUPERCONDUCTING MAGNETS**

**Chairman: W.B. Sampson, Brookhaven National Laboratory**

[\(Photos\)](#)

<a href="#">Stress Problems Associated with Superconducting and Cryogenic Magnets</a>	<a href="#">709</a>
---------------------------------------------------------------------------------------	---------------------

P.G. Marston, Magnetic Engineering Associates

<a href="#">Stresses in Magnetic Field Coils</a>	<a href="#">714</a>
W.F. Westendorp and R.W. Kilb, General Electric Company	
<a href="#">Very High Field Hybrid Magnet Systems</a>	<a href="#">727</a>
D. Bruce Montgomery, J.E.C. Williams, N.T. Pierce, R. Weggel, and M.J. Leupold, Francis Bitter National Magnet Laboratory	
<a href="#">Principles of Stability in Cooled Superconducting Magnets</a>	<a href="#">748</a>
Z.J.J. Stekly, R. Thome, and B. Strauss, Avco Everette Research Laboratory	
<a href="#">The 1.8 Tesla, 4.8 m i.d. Bubble Chamber Magnet</a>	<a href="#">765</a>
J.R. Purcell, Argonne National Laboratory	
<a href="#">The Superconducting Magnet for the Proposed 25-foot Cryogenic Bubble Chamber</a>	<a href="#">786</a>
A.G. Prodel, Brookhaven National Laboratory	
<a href="#">The Superconducting Magnet for the Brookhaven National Laboratory 7-foot Bubble chamber</a>	<a href="#">794</a>
D.P. Brown, R.W. Burgess, and G.T. Mulholland, Brookhaven National Laboratory	
<a href="#">A 70 kilogauss Magnet for the Proposed Rutherford Laboratory 1.5 m Diameter Hydrogen Bubble Chamber</a>	<a href="#">815</a>
P.T.M. Clee, D.B. Thomas, and C.W. Trowbridge, Rutherford Laboratory	
<a href="#">Development Program for the Magnet of the European 3.7 m Bubble Chamber</a>	<a href="#">828</a>
Presented by F. Wittgenstein, CERN	
<a href="#">A Possible Source of Instability in “Fully Stabilized” Magnets</a>	<a href="#">839</a>
P.F. Smith, M.N. Wilson, and J.D. Lewin, Rutherford Laboratory	
<a href="#">Analytical Design of Superconducting Multipolar Magnets</a>	<a href="#">843</a>
Richard A. Beth, Brookhaven National Laboratory	
<a href="#">Superconducting Magnetic Dipoles</a>	<a href="#">860</a>
G. Parzen, Brookhaven National Laboratory	
<a href="#">Superconducting Quadrupole Focusing Lens – Part I: Analytical Design and Full-Scale Copper-Wound Pole</a>	<a href="#">866</a>
A. Asner, CERN	
<a href="#">Superconducting Quadrupole Focusing Lens – Part II: Construction and Preliminary Tests</a>	<a href="#">880</a>
D.N. Cornish, Culham Laboratory	
<a href="#">Quadrupole Focusing Magnet</a>	<a href="#">886</a>
J.D. Rogers, W.V. Hassenzahl, H.L. Laquer, and J. K. Novak, Los Alamos National Laboratory	
<a href="#">The Rutherford Laboratory Bending Magnet</a>	<a href="#">888</a>
M.N. Wilson, R.V. Stovold, and J.D. Lawson, Rutherford Laboratory	
<a href="#">Brookhaven Superconducting dc Beam Magnets</a>	<a href="#">893</a>
R.B. Britton, Brookhaven National Laboratory	

<a href="#">Pulsed Superconducting Magnets</a>	908
W.B. Sampson, Brookhaven National Laboratory	
<a href="#">Intrinsically Stable Conductors</a>	913
P.F. Smith, M.N. Wilson, C.R. Walters, and J.D. Lewin, Rutherford Laboratory	
<a href="#">Superconducting Magnets for Controlled Thermonuclear Research</a>	920
C.E. Taylor, Lawrence Radiation Laboratory, Livermore	
<a href="#">On Helium II Microstabilization of Nb<sub>3</sub>Sn</a>	926
W.H. Bergmann, Argonne National Laboratory	
<a href="#">Progress on the IMP Facility</a>	929
D.L. Coffey and W.F. Gauster, Oak Ridge National Laboratory	
<a href="#">Standardized Tests for Superconducting Materials</a>	944
W.F. Gauster, Oak Ridge National Laboratory	
<a href="#">Superconducting Magnets for the 200 GeV Accelerator Experimental Areas</a>	946
R.B. Meuser, Lawrence Radiation Laboratory, Berkeley	
<a href="#">Construction of a Superconducting Test Coil Cooled by Helium Forced Circulation</a>	953
M. Morpurgo, CERN	
<a href="#">Summary of Fifth Week of Summer Study</a>	962
W.B. Sampson, Brookhaven National Laboratory	
 <b>SIXTH WEEK – ACCELERATORS AND STORAGE RINGS USING SUPERCONDUCTING OR CRYOGENIC MAGNETS</b> <b>Chairman: J.P. Blewett, Brookhaven National Laboratory</b> <a href="#">(Photos)</a>	
<a href="#">Superconducting Synchrotrons</a>	967
P.F. Smith, Rutherford Laboratory	
<a href="#">Economic Factors Involved in the Design of a Proton Synchrotron or Storage Ring with a Superconducting Guide Field</a>	981
M.A. Green, Lawrence Radiation Laboratory, Berkeley	
<a href="#">A 2000 GeV Superconducting Synchrotron</a>	998
W.B. Sampson, Brookhaven National Laboratory	
<a href="#">Synchrotron Power Supplies using Superconducting Energy Storage</a>	1002
P.F. Smith, Rutherford Laboratory	
<a href="#">Some ac Loss Determinations by an Electric Multiplier Method</a>	1007
W.S. Gilbert, Lawrence Radiation Laboratory, Berkeley	
<a href="#">Radiation Effects on Superconducting Magnets</a>	1011
H. Brechna, Stanford Linear Accelerator Center	

<a href="#">Iron Shielding for Air Core Magnets</a>	<a href="#">1042</a>
J.P. Blewett, Brookhaven National Laboratory	
<a href="#">Superconducting EFAG Accelerators</a>	<a href="#">1052</a>
G. Parzen, Brookhaven National Laboratory	
<a href="#">Calculations Concerning Superconducting Accelerators</a>	<a href="#">1059</a>
P. Gerald Kruger and J.N. Snyder, University of Illinois	
<a href="#">Preliminary Steps for Applying Superconductors to FFAG Accelerators</a>	<a href="#">1075</a>
G. del Castillo, R.J. Lari, and L.O. Oswald, Argonne National Laboratory	
<a href="#">A Superconducting SLAC with a Recirculating Beam</a>	<a href="#">1089</a>
W.B. Herrmannsfeldt, Stanford Linear Accelerator Center	
<a href="#">Properties and Preparation of High-Purity Aluminum</a>	<a href="#">1095</a>
V. Arp, National Bureau of Standards, Boulder	
<a href="#">Synchrotron Magnets with Cryogenic Exciting Coils</a>	<a href="#">1115</a>
G.T. Danby, J.E. Allinger, and J. W. Jackson, Brookhaven National Laboratory	
<a href="#">Summary of Sixth Week of Summer Study</a>	<a href="#">1127</a>
J.P. Blewett, Brookhaven National Laboratory	

**Directly Jump to**    [1st Week](#)    [2nd Week](#)    [3rd Week](#)    [4th Week](#)    [5th Week](#)    [6th Week](#)

[Author Index](#)

---

[Table of contents as they appeared in the original proceedings.](#)

[Return to 1968 Proceedings Home Page](#)

## TABLE OF CONTENTS

Introductory Remarks — Maurice Goldhaber, Director, Brookhaven National Laboratory	iii
Editor's Preface — Albert G. Prodell, Brookhaven National Laboratory	iv
Introduction — John P. Blewett, Brookhaven National Laboratory	v

### FIRST WEEK — SUPERCONDUCTING RF CAVITIES AND LINACS

Chairman: H.A. Schwettman, Stanford University

The Development of Low Temperature Technology at Stanford and its Relevance to High Energy Physics . . . . .	1
H. Alan Schwettman, Stanford University	
Q Measurements on Superconducting Cavities at S-Band . . . . .	13
H. Hahn, H.J. Halama, and E.H. Foster, Brookhaven National Laboratory	
Coupling Losses in Superconducting Cavities . . . . .	18
H. Hahn and J.M. Miller, Brookhaven National Laboratory	
Fabrication of Niobium Rf Cavities . . . . .	23
R.W. Meyerhoff, Union Carbide Corporation	
Fabrication of High Q Superconducting Niobium Cavities . . . . .	32
I. Weissman, Varian Associates	
Materials Investigation for a Two-Mile Superconducting Accelerator . . . . .	34
M.A. Allen and H.A. Hogg, Stanford Linear Accelerator Center	
Characterization of Residual Rf Losses in Superconductors . . . . .	40
C.R. Haden, University of Oklahoma	
Technetium as a Material for ac Superconductivity Applications . . . . .	49
S.H. Autler, NASA Electronics Research Center	
Applications of the Fountain Effect in Superfluid Helium . . . . .	52
C.M. Lyneis, M.S. McAshan, and H.A. Schwettman, Stanford University	
Refrigeration at Temperatures Below the Boiling Point of Helium . . . . .	59
S.C. Collins, 500 Incorporated	
Rf Amplitude and Phase Stabilization for a Superconducting Linear Accelerator by Feedback Stabilization Techniques . . . . .	67
L.R. Suelzle, Stanford University	
Particle Motion in a Standing Wave Linear Accelerator . . . . .	79
E.E. Chambers, Stanford University	
Sample Parameters of a Two-Mile Superconducting Accelerator . . . . .	101
R.B. Neal, Stanford Linear Accelerator Center	
Consideration of the Use of Feedback in a Traveling-Wave Superconducting Accelerator . . . . .	111
R.B. Neal, Stanford Linear Accelerator Center	
Summary of Recent Investigations of the Karlsruhe Group on Rf Properties of Superconductors and on Applications . . . . .	127
W. Jüngst, Kernforschungszentrum Karlsruhe	

An Enriched Particle Beam using Superconducting Rf Deflectors . . . . .	136
H.N. Brown, Brookhaven National Laboratory	
Design Problems in Superconducting Rf Beam Separators . . . . .	150
H.J. Halama, Brookhaven National Laboratory	
Superconducting Rf Separator Research at the Rutherford Laboratory . . . . .	165
A. Carne, B.G. Brady, and M.J. Newman, Rutherford Laboratory	
Beam Optics Design for a 600 MeV Microtron . . . . .	169
D.C. Sutton and A.O. Hanson, University of Illinois	
High Stability UHF Oscillators using a Superconducting Cavity . . . . .	171
F. Biquard, Nguyen Tuong Viet, and A. Septier, Institut d'Electronique Fondamentale, Orsay	
Summary of First Week of Summer Study . . . . .	187
H. Alan Schwettman, Stanford University	

SECOND WEEK - CRYOGENICS  
Chairman: T.R. Strobridge, NBS, Boulder

Refrigeration at 4°K . . . . .	193
T.R. Strobridge, National Bureau of Standards, Boulder	
European State of the Art in Cryogenics . . . . .	205
G. Prast, Philips Research Laboratories	
Cryogenic Safety . . . . .	229
M.G. Zabetakis, Bureau of Mines	
Cryopumping . . . . .	230
C. Barnes, CVI Corporation	
Review of Heat Transfer to Helium I . . . . .	249
R.V. Smith, National Bureau of Standards, Boulder	
An Examination of a Liquid Helium Refrigeration System for Superconducting Magnets in the 200 GeV Experimental Area . . . . .	293
M.A. Green, Lawrence Radiation Laboratory, Berkeley, and G.P. Coombs and J.L. Perry, 500 Incorporated	
Cryogenic Electrical Leads . . . . .	304
C.D. Henning, Lawrence Radiation Laboratory, Livermore	
Low Temperature Metals . . . . .	311
A. Hurlich, General Dynamics/Astronautics	
Properties of Nonmetallic Materials at Cryogenic Temperatures . . . . .	326
R. Mowers, Rocketdyne	
Review of the Cryogenics Session - Second Week of the Summer Study . . . . .	368
T.R. Strobridge, National Bureau of Standards, Boulder	

THIRD WEEK - SUPERCONDUCTING MATERIALS  
Chairman: A. Paskin, Brookhaven National Laboratory

Structure and Properties of High-Field Superconductors . . . . .	377
J.D. Livingston, General Electric Company	
Instability Comments . . . . .	393
S.L. Wipf, Atomics International	
Critical Current Behavior of Hard Superconductors . . . . .	396
W.W. Webb, Cornell University	
Critical Fields of Type II Superconductors . . . . .	405
G. Cody, RCA Laboratories	
The Effect of Radiation on the Properties of Superconducting Materials . . . . .	437
G.W. Cullen, RCA Laboratories	
Niobium Tin and Related Superconductors . . . . .	449
R.B. Britton, Brookhaven National Laboratory	
Composite Materials . . . . .	465
A.D. McInturff, Brookhaven National Laboratory	
Materials and Conductor Configurations in Superconducting Magnets . . . . .	477
H. Brechna, Stanford Linear Accelerator Center	

FOURTH WEEK - AC EFFECTS AND FLUX PUMPS  
Chairman: S.L. Wipf, Atomics International

Ac Losses in Superconductors . . . . .	511
S.L. Wipf, Atomics International	
Use of Superconductors in High Energy Physics . . . . .	544
J.P. Blewett, Brookhaven National Laboratory	
Electrical Loss Measurements in a NbTi Magnet . . . . .	550
F. Voelker, Lawrence Radiation Laboratory, Berkeley	
Ac Losses in Magnets made of Nb <sub>3</sub> Sn Ribbon . . . . .	559
G.H. Morgan and P.F. Dahl, Brookhaven National Laboratory	
Dynamic Resistivity of Hard Superconductors in a Perpendicular Time Varying Field . . . . .	567
R. Altorfer, F. Caimi, and J.M. Rayroux, Oerlikon Engineering Company	
Magnetic Instabilities and Solenoid Performance: Applications of the Critical State Model . . . . .	571
H.R. Hart, Jr., General Electric Company	
Magnetic and Thermal Instabilities Observed in Commercial Nb <sub>3</sub> Sn Superconductors . . . . .	601
G. del Castillo and L.O. Oswald, Argonne National Laboratory	



Observations of Flux Jump Behavior Related to Various Changes of Geometry, and Thermal and Electrical Environment . . . . .	612
A.D. McInturff, Brookhaven National Laboratory	
Instabilities and Flux Annihilation . . . . .	619
S.L. Wipf, Atomics International	
Superconducting Transmission Lines - Communication and Power . . . . .	622
N.S. Nahman, National Bureau of Standards, Boulder	
Recent Developments in Superconductivity in Japan . . . . .	628
Presented by N. Takano, Tokyo Shibaura Electric Company	
The Case for Flux Pumps and Some of Their Uses . . . . .	632
S.L. Wipf, Atomics International	
Design Principles and Characteristics of the G.E. Flux Pump . . . . .	654
R.L. Rhodenizer, General Electric Company	
Flux Pumps as Power Supplies in Comparison with Alternatives . . . . .	667
M.S. Lubell and K.R. Efferson, Oak Ridge National Laboratory	
Flux Pump Work at Los Alamos . . . . .	673
H. Laquer, Los Alamos Scientific Laboratory	
60 Hz Flux Pumps . . . . .	679
R.B. Britton, Brookhaven National Laboratory	
Proposal for a Flux Pump Utilizing the Inverse Ettingshausen Effect in Hard Type II Superconductors in the Mixed State . . . . .	681
W.H. Bergmann, Argonne National Laboratory	
Summary of the Fourth Week - Ac Losses, Instability and Flux Pumps . . . . .	683
S.L. Wipf, Atomics International	

#### FIFTH WEEK - SUPERCONDUCTING MAGNETS

Chairman: W.B. Sampson, Brookhaven National Laboratory

Stress Problems Associated with Superconducting and Cryogenic Magnets . . . . .	709
P.G. Marston, Magnetic Engineering Associates	
Stresses in Magnetic Field Coils . . . . .	714
W.F. Westendorp and R.W. Kilb, General Electric Company	
Very High Field Hybrid Magnet Systems . . . . .	727
D. Bruce Montgomery, J.E.C. Williams, N.T. Pierce, R. Weggel, and M.J. Leupold, Francis Bitter National Magnet Laboratory	
Principles of Stability in Cooled Superconducting Magnets . . . . .	748
Z.J.J. Stekly, R. Thome, and B. Strauss, Avco Everett Research Laboratory	
The 1.8 Tesla, 4.8 m i.d. Bubble Chamber Magnet . . . . .	765
J.R. Purcell, Argonne National Laboratory	

The Superconducting Magnet for the Proposed 25-foot Cryogenic Bubble Chamber . . . . .	786
A.G. Prodel, Brookhaven National Laboratory	
The Superconducting Magnet for the Brookhaven National Laboratory 7-foot Bubble Chamber . . . . .	794
D.P. Brown, R.W. Burgess, and G.T. Mulholland, Brookhaven National Laboratory	
A 70 Kilogauss Magnet for the Proposed Rutherford Laboratory 1.5 m Diameter Hydrogen Bubble Chamber . . . . .	815
P.T.M. Clee, D.B. Thomas, and C.W. Trowbridge, Rutherford Laboratory	
Development Program for the Magnet of the European 3.7 m Bubble Chamber . . . . .	828
Presented by F. Wittgenstein, CERN	
A Possible Source of Instability in "Fully Stabilized" Magnets . . . . .	839
P.F. Smith, M.N. Wilson, and J.D. Lewin, Rutherford Laboratory	
Analytical Design of Superconducting Multipolar Magnets . . . . .	843
Richard A. Beth, Brookhaven National Laboratory	
Superconducting Magnetic Dipoles . . . . .	860
G. Parzen, Brookhaven National Laboratory	
Superconducting Quadrupole Focusing Lens - Part I: Analytical Design and Full-Scale Copper-Wound Pole . . . . .	866
A. Asner, CERN	
Superconducting Quadrupole Focusing Lens - Part II: Construction and Preliminary Tests . . . . .	880
D.N. Cornish, Culham Laboratory	
Quadrupole Focusing Magnet . . . . .	886
J.D. Rogers, W.V. Hassenzahl, H.L. Laquer, and J.K. Novak Los Alamos Scientific Laboratory	
The Rutherford Laboratory Bending Magnet . . . . .	888
M.N. Wilson, R.V. Stovold, and J.D. Lawson, Rutherford Laboratory	
Brookhaven Superconducting dc Beam Magnets . . . . .	893
R.B. Britton, Brookhaven National Laboratory	
Pulsed Superconducting Magnets . . . . .	908
W.B. Sampson, Brookhaven National Laboratory	
Intrinsically Stable Conductors . . . . .	913
P.F. Smith, M.N. Wilson, C.R. Walters, and J.D. Lewin, Rutherford Laboratory	
Superconducting Magnets for Controlled Thermonuclear Research . . . . .	920
C.E. Taylor, Lawrence Radiation Laboratory, Livermore	
On Helium II Microstabilization of Nb <sub>3</sub> Sn . . . . .	926
W.H. Bergmann, Argonne National Laboratory	
Progress on the IMP Facility . . . . .	929
D.L. Coffey and W.F. Gauster, Oak Ridge National Laboratory	

Standardized Tests for Superconducting Materials . . . . .	944
W.F. Gauster, Oak Ridge National Laboratory	
Superconducting Magnets for the 200 GeV Accelerator Experimental Areas . . . . .	946
R.B. Meuser, Lawrence Radiation Laboratory, Berkeley	
Construction of a Superconducting Test Coil Cooled by Helium Forced Circulation. .	953
M. Morpurgo, CERN	
Summary of Fifth Week of Summer Study . . . . .	962
W.B. Sampson, Brookhaven National Laboratory	
SIXTH WEEK - ACCELERATORS AND STORAGE RINGS USING SUPERCONDUCTING OR CRYOGENIC MAGNETS	
Chairman: J.P. Blewett, Brookhaven National Laboratory	
Superconducting Synchrotrons . . . . .	967
P.F. Smith, Rutherford Laboratory	
Economic Factors Involved in the Design of a Proton Synchrotron or Storage Ring with a Superconducting Guide Field . . . . .	981
M.A. Green, Lawrence Radiation Laboratory, Berkeley	
A 2000 GeV Superconducting Synchrotron . . . . .	998
W.B. Sampson, Brookhaven National Laboratory	
Synchrotron Power Supplies using Superconducting Energy Storage . . . . .	1002
P.F. Smith, Rutherford Laboratory	
Some ac Loss Determinations by an Electrical Multiplier Method . . . . .	1007
W.S. Gilbert, Lawrence Radiation Laboratory, Berkeley	
Radiation Effects on Superconducting Magnets . . . . .	1011
H. Brechna, Stanford Linear Accelerator Center	
Iron Shielding for Air Core Magnets . . . . .	1042
J.P. Blewett, Brookhaven National Laboratory	
Superconducting FFAG Accelerators . . . . .	1052
G. Parzen, Brookhaven National Laboratory	
Calculations Concerning Superconducting Accelerators . . . . .	1059
P. Gerald Kruger and J.N. Snyder, University of Illinois	
Preliminary Steps for Applying Superconductors to FFAG Accelerators . . . . .	1075
G. del Castillo, R.J. Lari, and L.O. Oswald, Argonne National Laboratory	
A Superconducting SLAC with a Recirculating Beam . . . . .	1089
W.B. Herrmannsfeldt, Stanford Linear Accelerator Center	
Properties and Preparation of High-Purity Aluminum . . . . .	1095
V. Arp, National Bureau of Standards, Boulder	
Synchrotron Magnets with Cryogenic Exciting Coils . . . . .	1115
G.T. Danby, J.E. Allinger, and J.W. Jackson, Brookhaven National Laboratory	
Summary of Sixth Week of Summer Study . . . . .	1127
J.P. Blewett, Brookhaven National Laboratory	

**PROCEEDINGS OF THE 1968 SUMMER STUDY  
ON SUPERCONDUCTING DEVICES AND ACCELERATORS  
Part I (pp. 1-376)**

**BROOKHAVEN NATIONAL LABORATORY**

**June 10 - July 19, 1968**



**BROOKHAVEN NATIONAL LABORATORY  
ASSOCIATED UNIVERSITIES, INC.**

**under contract with the  
UNITED STATES ATOMIC ENERGY COMMISSION**

## **EDITOR' S PREFACE**

**Albert G. Prodel**  
**Brookhaven National Laboratory**  
**Upton, New York**

These proceedings consist of papers based on formal talks given by participants of the Summer Study on Superconducting Devices and Accelerators. Wherever possible, edited drafts of these papers were returned to the authors for review and the papers as published include all corrections and changes.

In an attempt to maintain an open and informal atmosphere during the meetings, no records were made of the round-table discussions or of the discussion after each talk. These proceedings do not include any such discussions, and their contents, therefore, may be preserved only in the memories of the participants.

The task of editing these papers has been shared with Dr. H. Hahn and Dr. J.P. Blewett. The Photography and Graphic Arts Division has given useful advice and has been most diligent and cooperative in reproducing this report in its final form.

In any undertaking such as this, a major share of the effort is borne by one or two individuals who coordinate the activities of authors, editors, and publishers, who direct the flow of manuscripts and attend to innumerable details, and who with great competence organize and type vast amounts of written material. Our sincere appreciation is expressed to Mrs. Yvonne Winterbottom who has cheerfully and ably fulfilled all these functions with patience and understanding.

---

[Editor's Preface as it appeared in the original proceedings](#)

[Return to 1968 Proceedings Home Page](#)

## EDITOR'S PREFACE

Albert G. Prodell  
Brookhaven National Laboratory  
Upton, New York

These proceedings consist of papers based on formal talks given by participants of the Summer Study on Superconducting Devices and Accelerators. Wherever possible, edited drafts of these papers were returned to the authors for review and the papers as published include all corrections and changes.

In an attempt to maintain an open and informal atmosphere during the meetings, no records were made of the round-table discussions or of the discussion after each talk. These proceedings do not include any such discussions, and their contents, therefore, may be preserved only in the memories of the participants.

The task of editing these papers has been shared with Dr. H. Hahn and Dr. J.P. Blewett. The Photography and Graphic Arts Division has given useful advice and has been most diligent and cooperative in reproducing this report in its final form.

In any undertaking such as this, a major share of the effort is borne by one or two individuals who coordinate the activities of authors, editors, and publishers, who direct the flow of manuscripts and attend to innumerable details, and who with great competence organize and type vast amounts of written material. Our sincere appreciation is expressed to Mrs. Yvonne Winterbottom who has cheerfully and ably fulfilled all these functions with patience and understanding.

[paper@bel.ge](mailto:paper@bel.ge)

## **PROCEEDINGS OF THE 1968 SUMMER STUDY ON SUPERCONDUCTING DEVICES AND ACCELERATORS**

### **Brookhaven National Laboratory**

**June 10 - July 19, 1968**

1968 summer study on superconducting devices and accelerators at Brookhaven National Laboratory is considered as one of the most important and defining meeting that led to the application of superconductivity in modern particle accelerators and storage rings. One must admire that bold vision, and years of persistent and hard work of number of scientists, engineers and technicians which turned that vision in to reality. Moreover, the research work presented then, serves as a good reference material even today. Given its historical and scientific importance, the entire proceedings of this six week study is made available now on the web for easy and wide access. A [PDF viewer](#) is required to see most articles.

[Author Index](#)

[Subject \(Weekly\) Index](#)

[Table of Contents](#)

[Memorable Photographs](#)

[Other Information Pages](#)

---

[Cover Page As it Appeared in the Original Proceedings.](#)

[Go to the Workshops Page of the Superconducting Magnet Division at BNL.](#)

[Please e-mail comments, corrections, etc. to Ramesh Gupta at gupta@bnl.gov.](#)



[First Page of the Proceedings](#)

[Second Page \(Legal notice\)](#)

[Introductory Remarks -- Maurice Goldhaber, Director, Brookhaven National Laboratory](#)

[Editor's Preface -- Albert G. Prodell, Brookhaven National Laboratory](#)

[Introduction -- John P. Blewett, Brookhaven National Laboratory](#)

[Table of Contents As They Appeared in The Original Publication \(NO LINKS\)](#)

[Subject \(Weekly\) Index](#)

[Author Index](#)

[Memorable Photographs](#)

---

[Acknowledgments](#)

**[Return to 1968 Proceedings Home Page](#)**

[Click here to e-mail comments, corrections, etc. on these Proceeding on the Web](#)

[Click Here to Visit Superconducting Magnet Division Home Page at BNL](#)

[Click Here to Visit Ramesh Gupta's Home Page at BNL](#)

## **INTRODUCTION**

**John P; Blewett**  
**Brookhaven National Laboratory**  
**Upton, New York**

The 1968 Summer Study had as its objective a comprehensive survey of the field of superconducting devices and accelerators. The six weeks allotted to it seemed a reasonable period for a study that was to be relaxed though not leisurely, intensive but not concentrated like a five-day conference. On the whole these goals were achieved; we at Brookhaven learned a great deal and it is our hope that our visitors were equally happy.

Almost 200 visitors attended the study for varying periods. Of the attendees about half came from American or Canadian national laboratories and universities. About one-third of the visitors represented some twenty-seven American and Canadian companies involved in superconductivity or cryogenics. The remaining one-sixth of the study group came from foreign laboratories in England, France, Germany, Holland, Switzerland and Japan. It was particularly pleasant to welcome eleven representatives of our sister laboratory CERN.

Almost a hundred papers were presented during the study. Most of them are included in this volume which has been capably edited by Albert G. Prodell and Harald Hahn with the able assistance of Mrs. Yvonne Winterbottom.

The headquarters for the study was in Brookhaven's Accelerator Department but members of Brookhaven's Physics and Nuclear Engineering Departments, also were involved in the study's organization. Offices in an Accelerator Department annex were made available for the use of visitors, some of whom were able to join the study for several weeks.

The period of the study was divided into one-week sessions on various topics. Each session was organized by a "chairman for the week." The first week on "Superconducting Rf Cavities and Linacs" was organized by H.A. Schwettman of Stanford. T.R. Strobridge of the National Bureau of Standards in Boulder planned the second week on "Cryogenics." The third week on "Superconducting Materials" was under the direction of A. Paskin of Brookhaven. The fourth week was cut short by the Fourth of July holiday, most unfortunately since S.L. Wipf of Atomic International planned a very interesting program on "Ac Effects and Flux Pumps." The fifth week drew the largest attendance for a program on "Superconducting Magnets" arranged by W.B. Sampson of Brookhaven. The sixth, and final, week on "Accelerators and Storage Rings using Superconducting or Cryogenic Magnets" was organized by the writer. On the last day of the last week summaries of each session were presented by the various "chairmen of the week."

The organizing committee for the study included H. Hahn, A. Paskin, A.G. Prodell, W.B. Sampson, and the writer who acted as chairman.

It is a pleasure to acknowledge the assistance throughout the study period of Miss Barbara Pryor at the registration desk, of 3.R. Craig of Brookhaven's Instrumentation Department, of Mrs. Mariette Kuper and Mrs. Virginia Sayre of our Director's Office, of the staff of the Brookhaven Center, and of Brookhaven's Housing, Transportation and Travel Offices, all of whom provided unfailing and good-humored support for the program. Over-all supervision of the administrative details of the study was maintained by Mrs. Yvonne Winterbottom with her usual skill and efficiency.

---

[Introduction as it appeared in the original proceedings](#)

[Return to 1968 Proceedings Home Page](#)

## INTRODUCTION

John P. Blewett  
Brookhaven National Laboratory  
Upton, New York

The 1968 Summer Study had as its objective a comprehensive survey of the field of superconducting devices and accelerators. The six weeks allotted to it seemed a reasonable period for a study that was to be relaxed though not leisurely, intensive but not concentrated like a five-day conference. On the whole these goals were achieved; we at Brookhaven learned a great deal and it is our hope that our visitors were equally happy.

Almost 200 visitors attended the study for varying periods. Of the attendees about half came from American or Canadian national laboratories and universities. About one-third of the visitors represented some twenty-seven American and Canadian companies involved in superconductivity or cryogenics. The remaining one-sixth of the study group came from foreign laboratories in England, France, Germany, Holland, Switzerland and Japan. It was particularly pleasant to welcome eleven representatives of our sister laboratory CERN.

Almost a hundred papers were presented during the study. Most of them are included in this volume which has been capably edited by Albert G. Prodell and Harald Hahn with the able assistance of Mrs. Yvonne Winterbottom.

The headquarters for the study was in Brookhaven's Accelerator Department but members of Brookhaven's Physics and Nuclear Engineering Departments also were involved in the study's organization. Offices in an Accelerator Department annex were made available for the use of visitors, some of whom were able to join the study for several weeks.

The period of the study was divided into one-week sessions on various topics. Each session was organized by a "chairman for the week." The first week on "Superconducting Rf Cavities and Linacs" was organized by H.A. Schwettman of Stanford. T.R. Strobridge of the National Bureau of Standards in Boulder planned the second week on "Cryogenics." The third week on "Superconducting Materials" was under the direction of A. Paskin of Brookhaven. The fourth week was cut short by the Fourth of July holiday, most unfortunately since S.L. Wipf of Atomics International planned a very interesting program on "Ac Effects and Flux Pumps." The fifth week drew the largest attendance for a program on "Superconducting Magnets" arranged by W.B. Sampson of Brookhaven. The sixth, and final, week on "Accelerators and Storage Rings using Superconducting or Cryogenic Magnets" was organized by the writer. On the last day of the last week summaries of each session were presented by the various "chairmen of the week."

The organizing committee for the study included H. Hahn, A. Paskin, A.G. Prodell, W.B. Sampson, and the writer who acted as chairman.

It is a pleasure to acknowledge the assistance throughout the study period of Miss Barbara Pryor at the registration desk, of J.R. Craig of Brookhaven's Instrumentation Department, of Mrs. Mariette Kuper and Mrs. Virginia Sayre of our Director's Office, of the staff of the Brookhaven Center, and of Brookhaven's Housing, Transportation and Travel Offices, all of whom provided unfailing and good-humored support for the program. Over-all supervision of the administrative details of the study was maintained by Mrs. Yvonne Winterbottom with her usual skill and efficiency.

## INTRODUCTORY REMARKS

Maurice Goldhaber, Director  
Brookhaven National Laboratory  
Upton, New York

Superconductivity was discovered in the same year as the nucleus - 1911. I remember it well because I was born in the same year. Strangely, technology based on superconductivity is just coming to fruition, more than twenty years behind nuclear technology. This can probably be ascribed to the fact that superconductors for high fields were not discovered until a few years ago. The magic element is niobium, an element which has a single stable isotope, Nb<sup>93</sup>. Nuclear physicists have shown that it is just stable, but not by very much. The next odd Z element, technetium, did not quite make it, otherwise it would strongly compete with niobium. The interrelation of all physics progress is illustrated by the fact that the theory of superconductivity due to Bardeen, Cooper and Schrieffer has application also to the understanding of nuclei. The technology of dc superconducting magnets has been successfully developed for a number of years and you can see many examples of it here and elsewhere. I hope you will have a chance to see the new 7-ft bubble chamber test facility which has a very large superconducting magnet. Here at Brookhaven we have an important cooperative effort in superconductivity which involves the Accelerator, Nuclear Engineering, and Physics Departments. The big hope, especially of high energy physicists, is to build high field ac superconductors which will permit relatively cheap and relatively small, extremely high energy machines. Your Summer Study may prove to be an important contribution to this end. I wish you luck.

## **INTRODUCTORY REMARKS**

**Maurice Goldhaber, Director  
Brookhaven National Laboratory  
Upton, New York**

Superconductivity was discovered in the same year as the nucleus - 1911. I remember it well because I was born in the same year. Strangely, technology based on superconductivity is just coming to fruition, more than twenty years behind nuclear technology. This can probably be ascribed to the fact that superconductors for high fields were not discovered until a few years ago. The magic element is niobium, an element which has a single stable isotope, Nb93. Nuclear physicists have shown that it is just stable, but not by very much. The next odd 2 element, technetium, did not quite make it, otherwise it would strongly compete with niobium. The interrelation of all physics progress is illustrated by the fact that the theory of superconductivity due to Bardeen, Cooper and Schrieffer has application also to the understanding of nuclei. The technology of dc superconducting magnets has been successfully developed for a number of years and you can see many examples of it here and elsewhere. I hope you will have a chance to see the new 7-ft bubble chamber test facility which has a very large superconducting magnet. Here at Brookhaven we have an important cooperative effort in superconductivity which involves the Accelerator, Nuclear Engineering, and Physics Departments. The big hope, especially of high energy physicists, is to build high field ac superconductors which will permit relatively cheap and relatively small, extremely high energy machines. Your Summer Study may prove to be an important contribution to this end. I wish you luck.

---

[Introductory remarks as they appeared in the original proceedings](#)

[Return to 1968 Proceedings Home Page](#)

## LEGAL NOTICE

This report was prepared as an account of Government sponsored work. Neither the United States, nor the Commission, nor any person acting on behalf of the Commission:

A. Makes any warranty or representation, expressed or implied, with respect to the accuracy, completeness, or usefulness of the information contained in this report, or that the use of any information, apparatus, method, or process disclosed in this report may not infringe privately owned rights; or

B. Assumes any liabilities with respect to the use of, or for damages resulting from the use of any information, apparatus, method, or process disclosed in this report.

As used in the above, "person acting on behalf of the Commission" includes any employee or contractor of the Commission, or employee of such contractor, to the extent that such employee or contractor of the Commission, or employee of such contractor prepares, disseminates, or provides access to, any information pursuant to his employment or contract with the Commission, or his employment with such contractor.

Printed in the United States of America

Available from

Clearinghouse for Federal Scientific and Technical Information  
National Bureau of Standards, U.S. Department of Commerce  
Springfield, Virginia 22151

Price: Printed Copy \$3.00; Microfiche \$0.65

April 1969

1500 copies

PICTURES TAKEN AT  
THE 1968 BROOKHAVEN SUMMER STUDY ON  
**SUPERCONDUCTING DEVICES AND ACCELERATORS**

JUNE 10 - JULY 19, 1968

BROOKHAVEN NATIONAL LABORATORY  
ASSOCIATED UNIVERSITIES, INC.  
UPTON, NEW YORK

## FIRST WEEK - SUPERCONDUCTING RF CAVITIES AND LINACS

Chairman: H.A. SCHWETTMAN, Stanford University

The Summer Study began with a week on applications of superconducting surfaces at radio frequencies. Under the able leadership of Alan Schwettman, an easy and informal atmosphere was rapidly achieved and soon a free and vigorous interchange of information was in progress between exponents of various techniques and representatives of the manufacturers whose technology will be essential to progress in this field. The session was dominated by the energetic Stanford group who continually amazed the audience with the scope and daring of their plans.



Chairman H. Alan Schwettman with W.M. Fairbank and E. Jones, all of Stanford.

G.A. Loew and R.B. Neal of SLAC. In the background is H.J. Halama of Brookhaven.





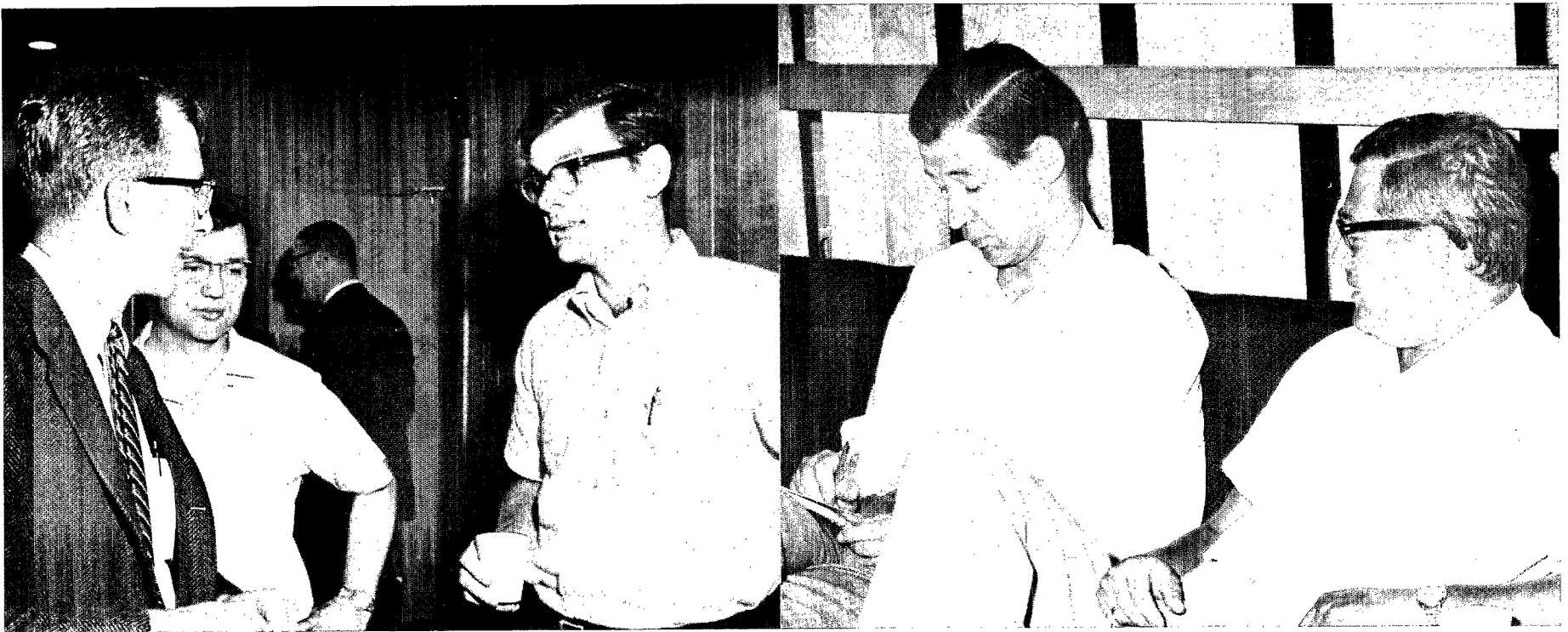
UPPER LEFT: J.P. Blewett of Brookhaven in a discussion with I. Weissman of Varian. UPPER RIGHT: J.E. Leiss of the Bureau of Standards in Washington with A.O. Hanson of the University of Illinois. LOWER LEFT: D. Leroy and

D. Gorié of CERN with C.R. Haden of the University of Oklahoma. LOWER RIGHT: A. Carne of the Rutherford Laboratory makes a point with H.J. Halama of Brookhaven.

## SECOND WEEK - CRYOGENICS

Chairman: T.R. STROBRIDGE, NBS, Boulder

A comprehensive survey of the esoteric mysteries of the field of cryogenics was arranged by Dick Strobridge. Enormously valuable papers were presented by Hurlich of General Dynamics and Mowers of Rocketdyne on the properties of materials at low temperatures; these papers will save many of us from making costly and dangerous mistakes. Papers on refrigeration and cryostat design provided a fine survey of the state of the art and of the directions in which further progress can be expected.



LEFT: Chairman T.R. Strobridge with W.H. Bergmann of Argonne and H.A. Schwettman of Stanford.

RIGHT: Two participants from European industry: G. Prast of Philips and G. Bogner of Siemens.



**UPPER LEFT:** H.M. Long and J. Notaro, both of Union Carbide, Linde Division, in Tonawanda, N.Y. **UPPER RIGHT:** In the foreground, B. Kirk of Air Reduction and J.L. Perry of 500 Inc.; in the background R. Jankowicz of the Princeton-Penn Accelerator and P. Chritchlow of Air Reduction. **LOWER**

**LEFT:** H. Kautsky of the Princeton-Penn Accelerator exchanging information with C.J. Kruse of SLAC. **LOWER RIGHT:** C.D. Henning of LRL, Livermore, with C.J. Walker of Air Reduction and G.K. Green, Chairman of Brookhaven's Accelerator Department.

### THIRD WEEK - SUPERCONDUCTING MATERIALS

Chairman: A. PASKIN, Brookhaven National Laboratory

Arthur Paskin arranged this week as a survey of presently available superconducting materials and a look into the future. Particularly interesting were two "Manufacturer-User round-tables," in which opinions were exchanged about what would be desirable in the realm of superconducting materials. The voice of common sense came from the representatives of industry who explained which user hopes were reasonable and which were not. Unfortunately for those who were not present, these sessions were not recorded; it had been agreed early in the Study that, in the interests of free discussion, nothing would be published that was not submitted to the Editors in writing.



Chairman Arthur Paskin listening to one of the presentations.



R.B. Britton of Brookhaven with H. Laquer of Los Alamos.





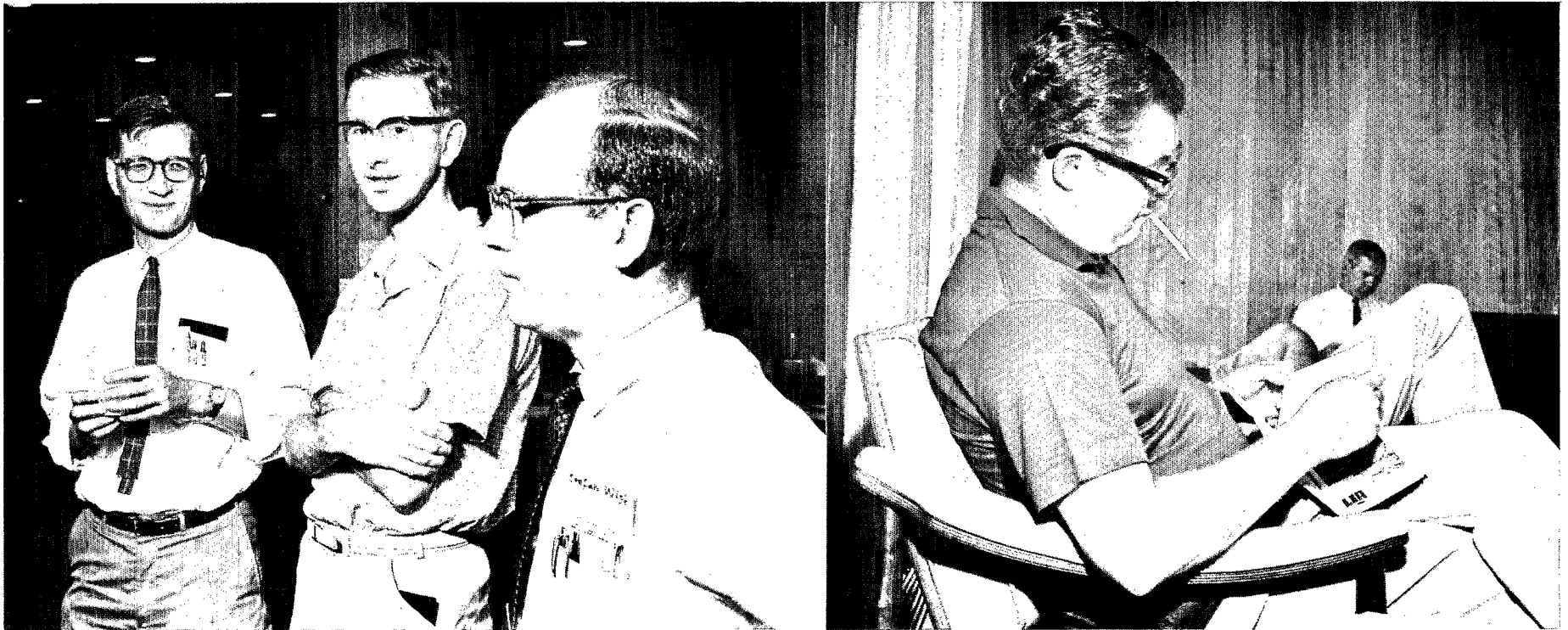
**UPPER LEFT:** M. Strongin of Brookhaven discussing a point with J.D. Livingston of G.E. **UPPER RIGHT:** J.R. Hale and Y. Iwasa of the Francis Bitter National Magnet Laboratory in Cambridge, Mass. **LOWER LEFT:** Sharing a coffee break – H. Brechna of SLAC, J.M. Rayroux of Oerlikon

in Zurich, Switzerland, and W.F. Gauster of Oak Ridge. **LOWER RIGHT:** One of the many informal "round-tables" – W.V. Hassenzahl (LASL), Y. Iwasa, J.M. Rayroux, H. Brechna, H. Laquer, and C.D. Graham and D.W. Lillie of G.E.

## FOURTH WEEK – AC EFFECTS AND FLUX PUMPS

Chairman: S.L. WIPF, Atomics International

Although the Fourth of July cut this week to three days, Stefan Wipf compressed into this period not only a brilliant survey of the problems of instabilities and ac effects in superconductors, but also a half-day review of the status of flux pumps. Particularly notable in the first category were the review papers by Hart of General Electric and by Chairman Wipf. Some very imaginative ideas in the field of superconducting transmission systems were outlined by Nahman of the Bureau of Standards who thinks not only of transmitting power but also of transmission in the same system of information and of cryogenic liquids.



C.D. Graham of G.E. and R. Hancox of the Culham Laboratory with Chairman S.L. Wipf.



G. Bogner of Siemens, Erlangen. In the background is R.L. Rhodenizer of G.E.



**UPPER LEFT:** M. Foss of the Carnegie Institute of Technology in a discussion with W.T. Beall of the Union Carbide Speedway Laboratories in Indianapolis. **UPPER RIGHT:** Waiting for the morning session to start – H. Brechna of SLAC, with R.L. Rhodenizer of G.E. in the background. **LOWER LEFT:** N.S.

Nahman and W.D. McCaa of the National Bureau of Standards in Boulder check in at the registration desk. **LOWER RIGHT:** R.L. Rhodenizer and G.W. Donaldson of G.E. Mr. Donaldson was on leave from the University of New South Wales in Sydney, Australia.

## FIFTH WEEK - SUPERCONDUCTING MAGNETS

Chairman: W.B. SAMPSON, Brookhaven National Laboratory

Bill Sampson's week on superconducting magnets was the most popular of the Summer Study. Superconducting magnets were described, from the huge affairs under construction for large bubble chambers to miniature units suitable for transport of particle beams. It was during this week that Peter Smith of the Rutherford Laboratory brought forward his suggestions for stabilizing superconducting magnets and for reducing ac losses. These ideas already have inspired programs in a number of laboratories; thus far Smith appears to have been correct in all of his predictions.



LEFT: Chairman W.B. Sampson with P.F. Smith of the Rutherford Laboratory. RIGHT: M. Morpurgo of CERN discusses a point with D. Bruce Montgomery of the Francis Bitter National Magnet Laboratory.





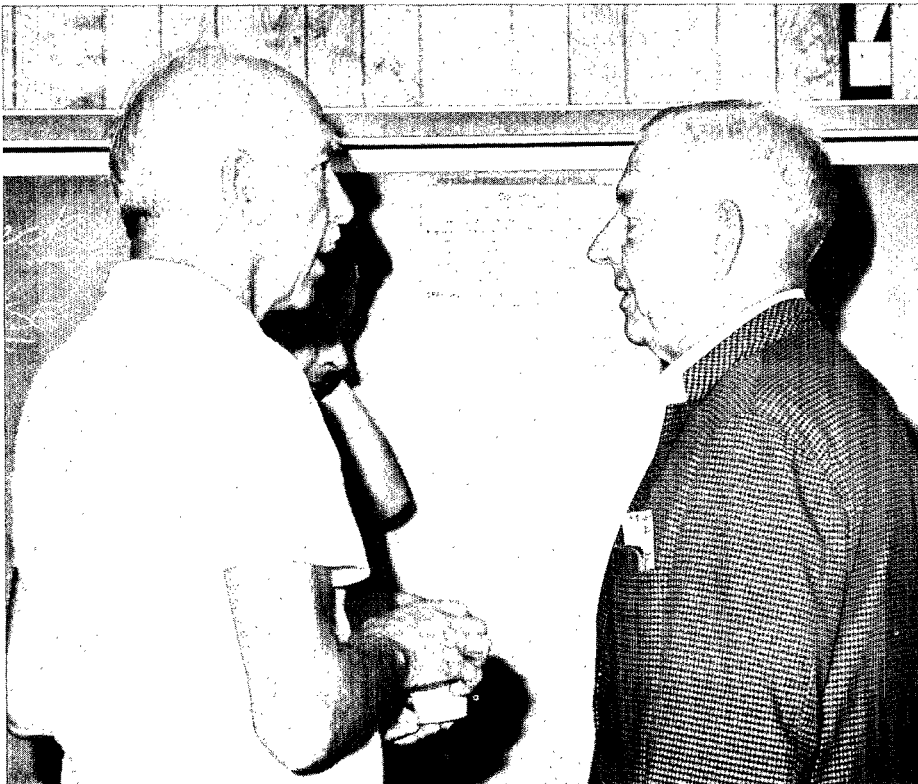
**UPPER LEFT:** A. Asner of CERN and D.N. Cornish of the Culham Laboratory reported on the CERN-Culham co-operative effort on a CERN superconducting quadrupole. **UPPER RIGHT:** P. Lazeyras and R. Wittgenstein of CERN; R.B. Meuser of LRL, Berkeley. **LOWER LEFT:** D. Bruce Montgomery of the National Magnet Laboratory and C.N. Whetstone of Cryomagnetics

exchange information; in the background are M. Morpurgo of CERN and H.M. Long of Union Carbide. **LOWER RIGHT:** J.D. Lawson of the Rutherford Laboratory, J. Alcorn of SLAC, R.B. Meuser of LRL, Berkeley, M. Snowdon of the Rutherford Laboratory listen to a point being made by J.P. Blewett of Brookhaven at a party given by Brookhaven's Director.

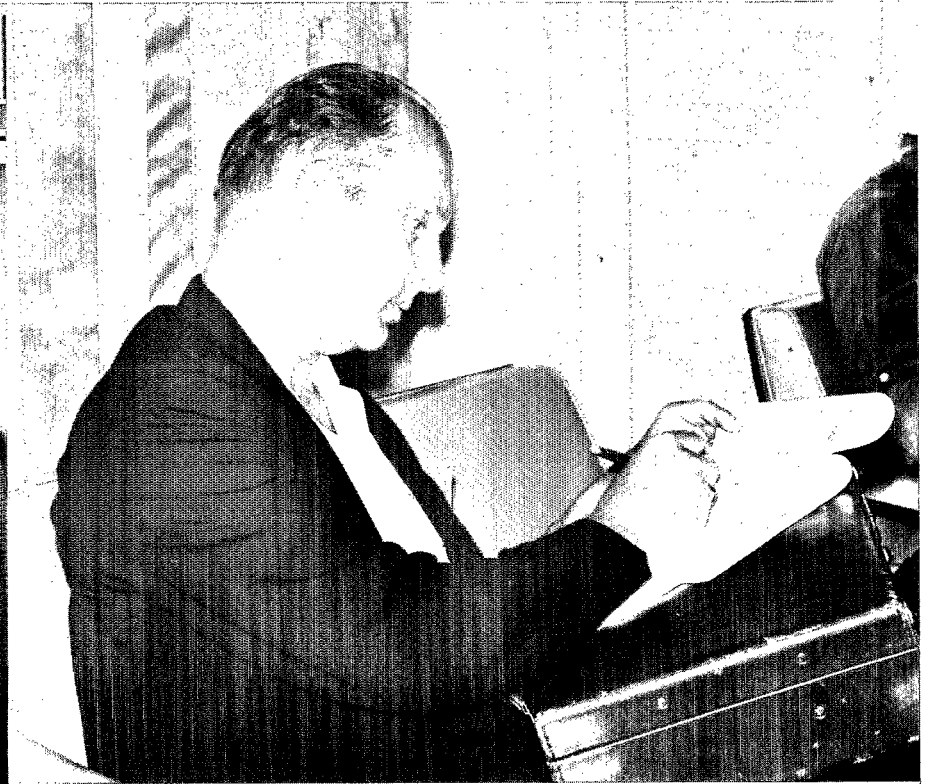
## SIXTH WEEK - ACCELERATORS AND STORAGE RINGS USING SUPERCONDUCTING OR CRYOGENIC MAGNETS

Chairman: J.P. BLEWETT, Brookhaven National Laboratory

The final week of the Summer Study, under John Blewett, was a speculative survey of the probable impact of superconducting magnets on the accelerator field. The atmosphere was generally confident and optimistic; superconducting accelerators are surely just over the horizon. A day during this week was devoted to an allied field, the use of pure, but not superconducting, metals at cryogenic temperatures. Here also the prospects appear to be bright. Finally, on the last day of the Study, the chairmen of all of the week-long sessions presented summaries of their weeks. The Study closed amid expressions of mutual admiration and self-satisfaction.



P. Gerald Kruger of the University of Illinois with D.D. Jacobus of Brookhaven.



W.C. Gough of the U.S. Atomic Energy Commission.



**UPPER LEFT:** W.S. Gilbert of LRL, Berkeley, preparing his presentation.  
**UPPER RIGHT:** M.A. Green of LRL, Berkeley, with C.J. Walker of Air Reduction.  
**LOWER LEFT:** A. Citron of Karlsruhe and Richard A. Beth of Brookhaven.  
**LOWER RIGHT:** Much discussion was held during the coffee breaks. Here are

W.B. Sampson of Brookhaven talking with P.F. Smith of the Rutherford Laboratory (with back to the camera) while A.D. McInturff and K.E. Robins of Brookhaven listen in.

## FIRST WEEK - SUPERCONDUCTING RF CAVITIES AND LINACS

Chairman: H.A. SCHWETTMAN, Stanford University

The Summer Study began with a week on applications of superconducting surfaces at radio frequencies. Under the able leadership of Alan Schwettman, an easy and informal atmosphere was rapidly achieved and soon a free and vigorous interchange of information was in progress between exponents of various techniques and representatives of the manufacturers whose technology will be essential to progress in this field. The session was dominated by the energetic Stanford group who continually amazed the audience with the scope and daring of their plans.



Chairman H. Alan Schwettman with W.M. Fairbank and E. Jones, all of Stanford.

G.A. Loew and R.B. Neal of SLAC. In the background is H.J. Halama of Brookhaven.





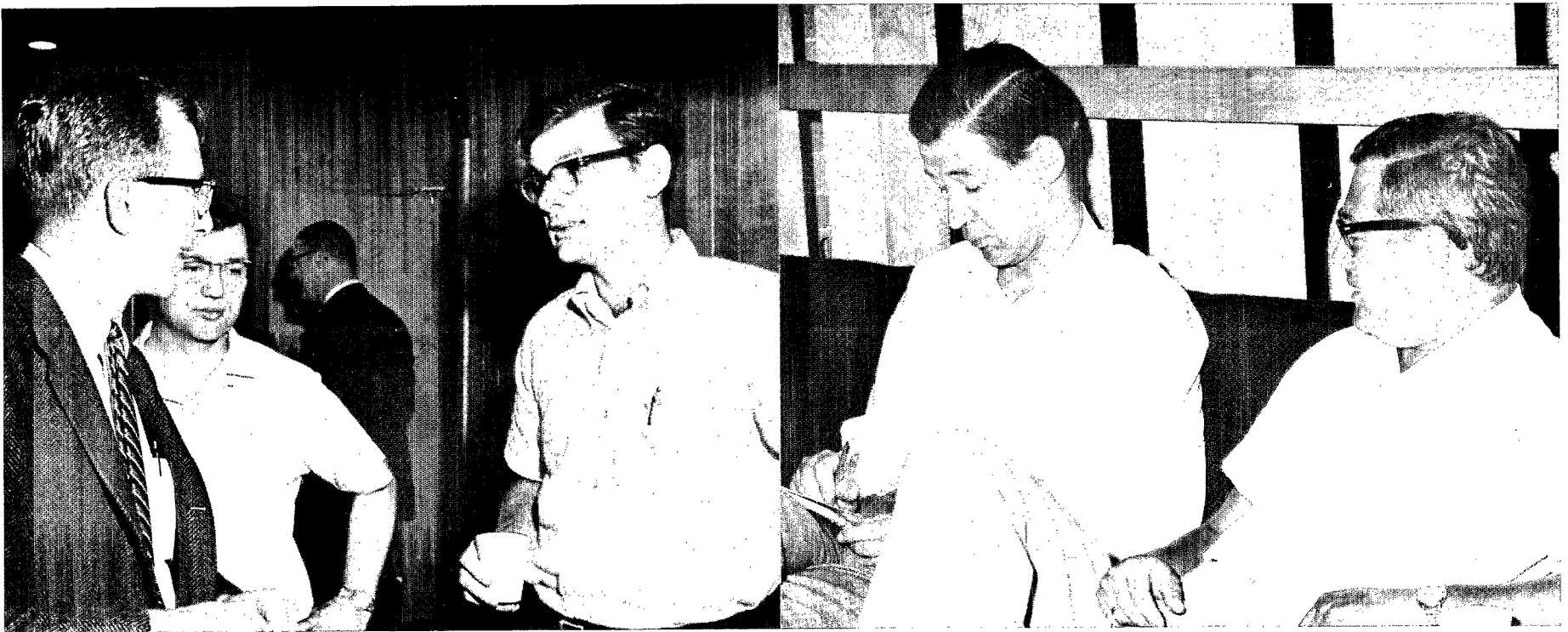
UPPER LEFT: J.P. Blewett of Brookhaven in a discussion with I. Weissman of Varian. UPPER RIGHT: J.E. Leiss of the Bureau of Standards in Washington with A.O. Hanson of the University of Illinois. LOWER LEFT: D. Leroy and

D. Gorlé of CERN with C.R. Haden of the University of Oklahoma. LOWER RIGHT: A. Carne of the Rutherford Laboratory makes a point with H.J. Halama of Brookhaven.

## SECOND WEEK - CRYOGENICS

Chairman: T.R. STROBRIDGE, NBS, Boulder

A comprehensive survey of the esoteric mysteries of the field of cryogenics was arranged by Dick Strobridge. Enormously valuable papers were presented by Hurlich of General Dynamics and Mowers of Rocketdyne on the properties of materials at low temperatures; these papers will save many of us from making costly and dangerous mistakes. Papers on refrigeration and cryostat design provided a fine survey of the state of the art and of the directions in which further progress can be expected.



LEFT: Chairman T.R. Strobridge with W.H. Bergmann of Argonne and H.A. Schwettman of Stanford.

RIGHT: Two participants from European industry: G. Prast of Philips and G. Bogner of Siemens.



**UPPER LEFT:** H.M. Long and J. Notaro, both of Union Carbide, Linde Division, in Tonawanda, N.Y. **UPPER RIGHT:** In the foreground, B. Kirk of Air Reduction and J.L. Perry of 500 Inc.; in the background R. Jankowicz of the Princeton-Penn Accelerator and P. Chritchlow of Air Reduction. **LOWER**

**LEFT:** H. Kautsky of the Princeton-Penn Accelerator exchanging information with C.J. Kruse of SLAC. **LOWER RIGHT:** C.D. Henning of LRL, Livermore, with C.J. Walker of Air Reduction and G.K. Green, Chairman of Brookhaven's Accelerator Department.

### THIRD WEEK - SUPERCONDUCTING MATERIALS

Chairman: A. PASKIN, Brookhaven National Laboratory

Arthur Paskin arranged this week as a survey of presently available superconducting materials and a look into the future. Particularly interesting were two "Manufacturer-User round-tables," in which opinions were exchanged about what would be desirable in the realm of superconducting materials. The voice of common sense came from the representatives of industry who explained which user hopes were reasonable and which were not. Unfortunately for those who were not present, these sessions were not recorded; it had been agreed early in the Study that, in the interests of free discussion, nothing would be published that was not submitted to the Editors in writing.



Chairman Arthur Paskin listening to one of the presentations.



R.B. Britton of Brookhaven with H. Laquer of Los Alamos.





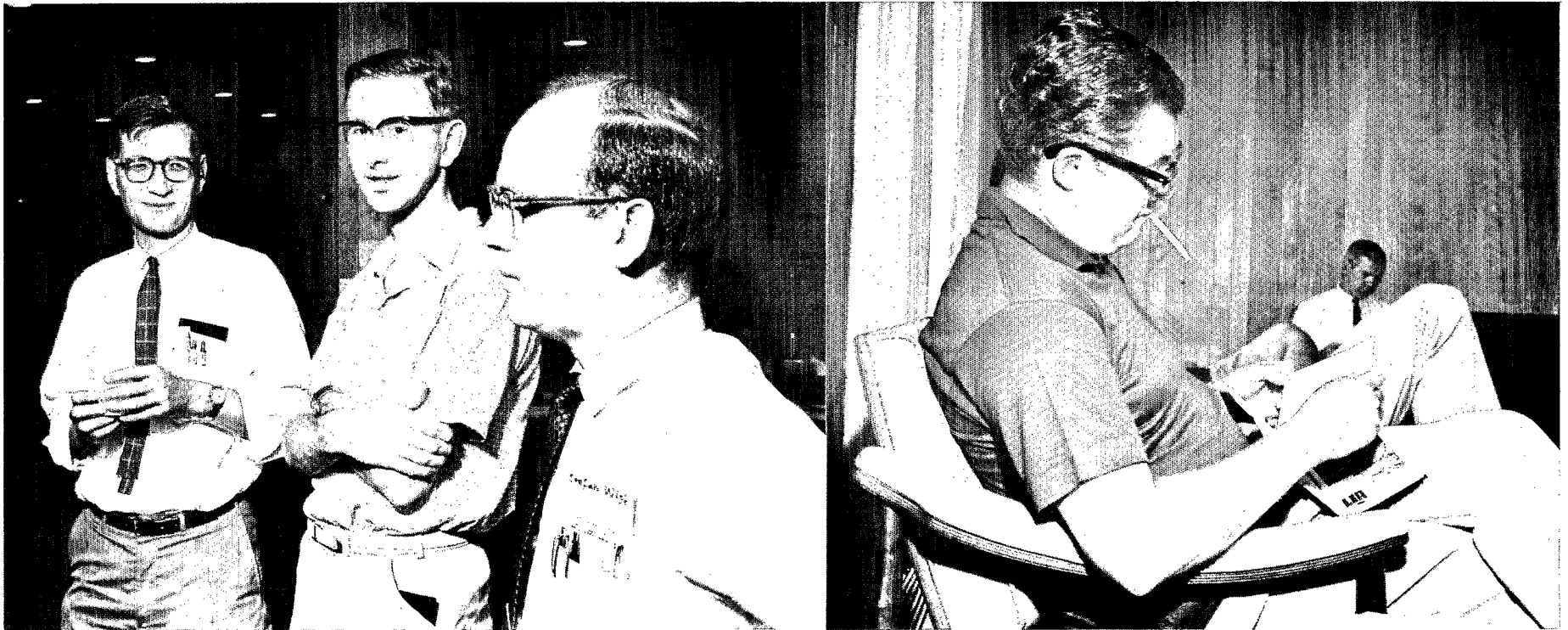
**UPPER LEFT:** M. Strongin of Brookhaven discussing a point with J.D. Livingston of G.E. **UPPER RIGHT:** J.R. Hale and Y. Iwasa of the Francis Bitter National Magnet Laboratory in Cambridge, Mass. **LOWER LEFT:** Sharing a coffee break – H. Brechna of SLAC, J.M. Rayroux of Oerlikon

in Zurich, Switzerland, and W.F. Gauster of Oak Ridge. **LOWER RIGHT:** One of the many informal "round-tables" – W.V. Hassenzahl (LASL), Y. Iwasa, J.M. Rayroux, H. Brechna, H. Laquer, and C.D. Graham and D.W. Lillie of G.E.

## FOURTH WEEK – AC EFFECTS AND FLUX PUMPS

Chairman: S.L. WIPF, Atomics International

Although the Fourth of July cut this week to three days, Stefan Wipf compressed into this period not only a brilliant survey of the problems of instabilities and ac effects in superconductors, but also a half-day review of the status of flux pumps. Particularly notable in the first category were the review papers by Hart of General Electric and by Chairman Wipf. Some very imaginative ideas in the field of superconducting transmission systems were outlined by Nahman of the Bureau of Standards who thinks not only of transmitting power but also of transmission in the same system of information and of cryogenic liquids.



C.D. Graham of G.E. and R. Hancox of the Culham Laboratory with Chairman S.L. Wipf.

G. Bogner of Siemens, Erlangen. In the background is R.L. Rhodenizer of G.E.



**UPPER LEFT:** M. Foss of the Carnegie Institute of Technology in a discussion with W.T. Beall of the Union Carbide Speedway Laboratories in Indianapolis. **UPPER RIGHT:** Waiting for the morning session to start – H. Brechna of SLAC, with R.L. Rhodenizer of G.E. in the background. **LOWER LEFT:** N.S.

Nahman and W.D. McCaa of the National Bureau of Standards in Boulder check in at the registration desk. **LOWER RIGHT:** R.L. Rhodenizer and G.W. Donaldson of G.E. Mr. Donaldson was on leave from the University of New South Wales in Sydney, Australia.

## FIFTH WEEK - SUPERCONDUCTING MAGNETS

Chairman: W.B. SAMPSON, Brookhaven National Laboratory

Bill Sampson's week on superconducting magnets was the most popular of the Summer Study. Superconducting magnets were described, from the huge affairs under construction for large bubble chambers to miniature units suitable for transport of particle beams. It was during this week that Peter Smith of the Rutherford Laboratory brought forward his suggestions for stabilizing superconducting magnets and for reducing ac losses. These ideas already have inspired programs in a number of laboratories; thus far Smith appears to have been correct in all of his predictions.



LEFT: Chairman W.B. Sampson with P.F. Smith of the Rutherford Laboratory. RIGHT: M. Morpurgo of CERN discusses a point with D. Bruce Montgomery of the Francis Bitter National Magnet Laboratory.





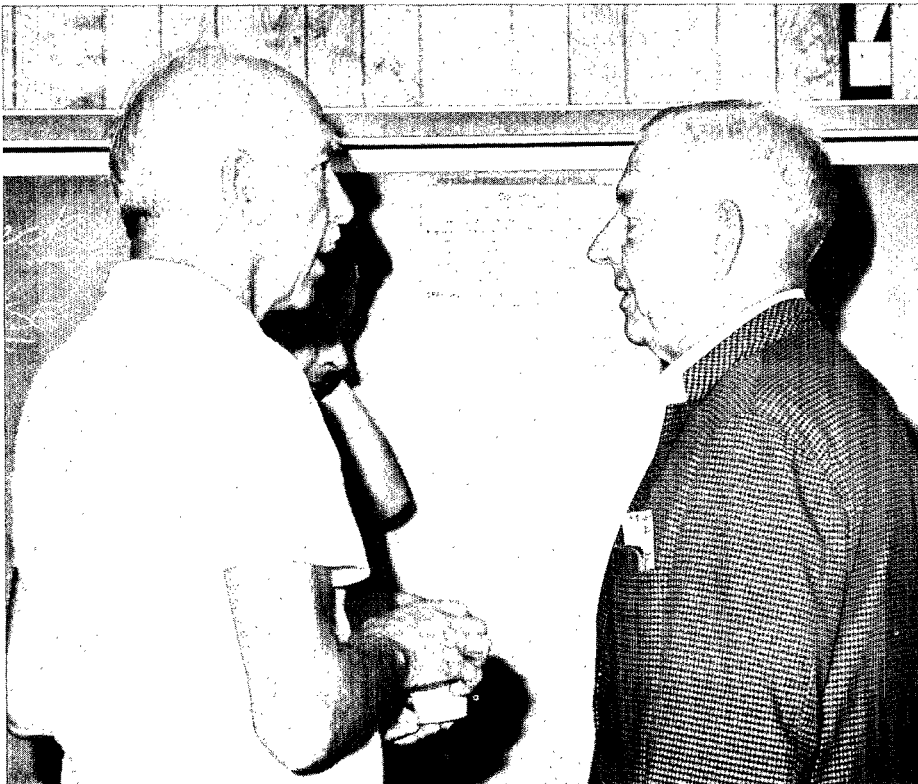
**UPPER LEFT:** A. Asner of CERN and D.N. Cornish of the Culham Laboratory reported on the CERN-Culham co-operative effort on a CERN superconducting quadrupole. **UPPER RIGHT:** P. Lazeyras and R. Wittgenstein of CERN; R.B. Meuser of LRL, Berkeley. **LOWER LEFT:** D. Bruce Montgomery of the National Magnet Laboratory and C.N. Whetstone of Cryomagnetics

exchange information; in the background are M. Morpurgo of CERN and H.M. Long of Union Carbide. **LOWER RIGHT:** J.D. Lawson of the Rutherford Laboratory, J. Alcorn of SLAC, R.B. Meuser of LRL, Berkeley, M. Snowdon of the Rutherford Laboratory listen to a point being made by J.P. Blewett of Brookhaven at a party given by Brookhaven's Director.

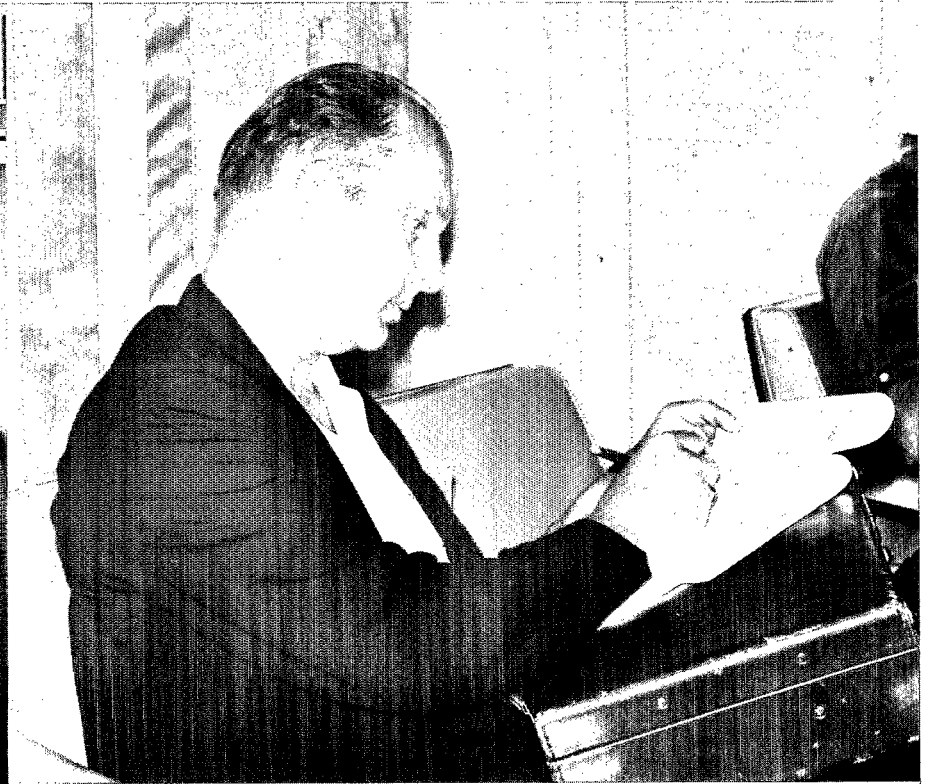
## SIXTH WEEK - ACCELERATORS AND STORAGE RINGS USING SUPERCONDUCTING OR CRYOGENIC MAGNETS

Chairman: J.P. BLEWETT, Brookhaven National Laboratory

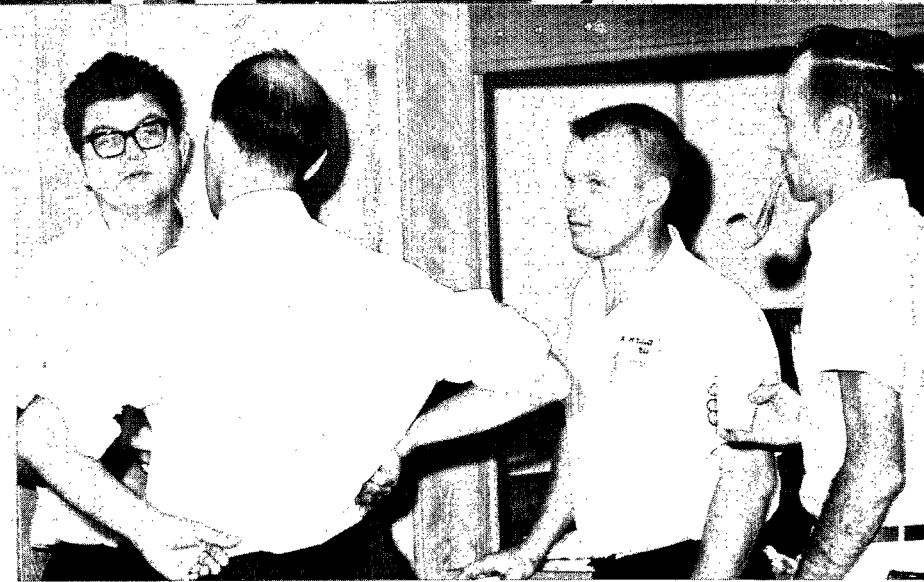
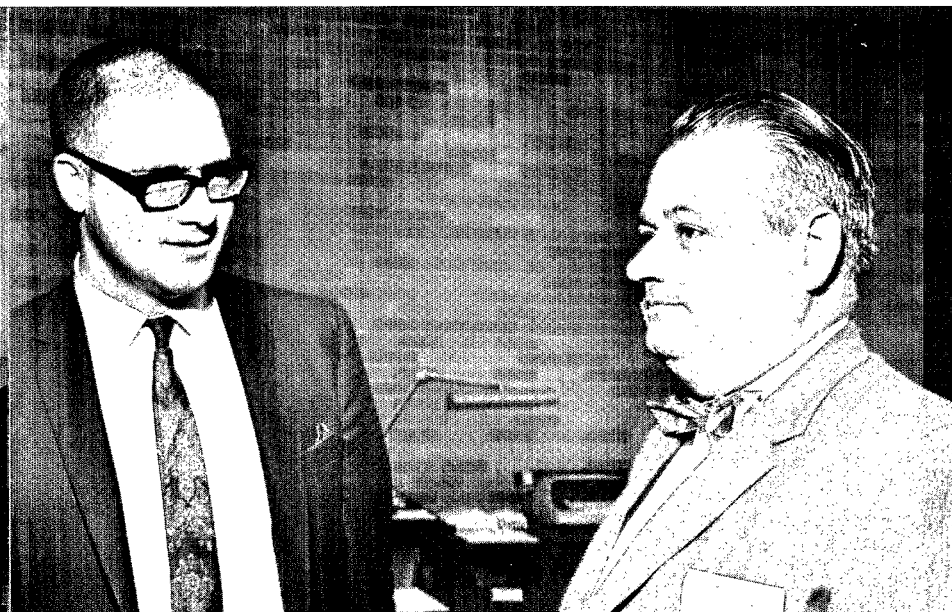
The final week of the Summer Study, under John Blewett, was a speculative survey of the probable impact of superconducting magnets on the accelerator field. The atmosphere was generally confident and optimistic; superconducting accelerators are surely just over the horizon. A day during this week was devoted to an allied field, the use of pure, but not superconducting, metals at cryogenic temperatures. Here also the prospects appear to be bright. Finally, on the last day of the Study, the chairmen of all of the week-long sessions presented summaries of their weeks. The Study closed amid expressions of mutual admiration and self-satisfaction.



P. Gerald Kruger of the University of Illinois with D.D. Jacobus of Brookhaven.



W.C. Gough of the U.S. Atomic Energy Commission.



**UPPER LEFT:** W.S. Gilbert of LRL, Berkeley, preparing his presentation.  
**UPPER RIGHT:** M.A. Green of LRL, Berkeley, with C.J. Walker of Air Reduction.  
**LOWER LEFT:** A. Citron of Karlsruhe and Richard A. Beth of Brookhaven.  
**LOWER RIGHT:** Much discussion was held during the coffee breaks. Here are

W.B. Sampson of Brookhaven talking with P.F. Smith of the Rutherford Laboratory (with back to the camera) while A.D. McInturff and K.E. Robins of Brookhaven listen in.

When you insert CD, the file index.htm should open automatically. This will help you navigate through the proceedings.

If it does not open automatically, then click on index.htm or open index.htm with your favorite web browser.



The Summer Study ran for six weeks, with each week covering an in-depth discussion on the subject listed below. Please follow the links for presentations, photos and other information.

1. [SUPERCONDUCTING RF CAVITIES AND LINACS \(First Week\)](#)
2. [CRYOGENICS \(Second Week\)](#)
3. [SUPERCONDUCTING MATERIALS \(Third Week\)](#)
4. [AC EFFECTS AND FLUX PUMPS \(Fourth Week\)](#)
5. [SUPERCONDUCTING MAGNETS \(Fifth Week\)](#)
6. [ACCELERATORS AND STORAGE RINGS USING SUPERCONDUCTING OR CRYOGENIC MAGNETS \(Sixth Week\)](#)

---

[Author Index](#)

[Return to 1968 Proceedings Home Page](#)

## **SUPERCONDUCTING RF CAVITIES AND LINACS**

**(First Week)**

**Chairman: H.A. Schwettman, Stanford University**

[\(Photos\)](#)

The Summer Study began with a week on applications of superconducting surfaces at radio frequencies. Under the able leadership of Alan Schwettman, an easy and informal atmosphere was rapidly achieved and soon a free and vigorous interchange of information was in progress between exponents of various techniques and representatives of the manufacturers whose technology will be essential to progress in this field. The session was dominated by the energetic Stanford group who continually amazed the audience with the scope and daring of their plans.

Following papers were submitted for publication:

[The Development of Low Temperature Technology at Stanford and its Relevance to High Energy Physics](#)

H. Alan Schwettman, Stanford University

[Q Measurements on Superconducting Cavities at S-Band](#)

H. Hahn, H.J. Halama, and E.H. Foster, Brookhaven National Laboratory

[Coupling Losses in Superconducting Cavities](#)

H. Hahn and J. Miller, Brookhaven National Laboratory

[Fabrication of Niobium Rf Cavities](#)

R.W. Meyerhoff, Union Carbide Corporation

[Fabrication of High Q Superconducting Niobium Cavities](#)

I. Weissman, Varian Associates

[Materials Investigation for a Two-Mile Superconducting Accelerator](#)

M.A. Allen and H.A. Hogg, Stanford Linear Accelerator Center

[Characterization of Residual Rf Losses in Superconductors](#)

C.R. Haden, University of Oklahoma

[Technetium as a Material for ac Superconductivity Applications](#)

S.H. Autler, NASA Electronics Research Center

[Applications of the Fountain Effect in Superfluid Helium](#)

C.M. Lyneis, M.S. McAshan, and H.A. Schwettman, Stanford University

[Refrigeration at Temperatures Below the Boiling Point of Helium](#)

S.C. Collins, 500 Incorporated

[Rf Amplitude and Phase Stabilization for a Superconducting Linear Accelerator by Feedback Stabilization Techniques](#)

L.R. Suelzle, Stanford University

[Particle Motion in a Standing Wave Linear Accelerator](#)

E.E. Chambers, Stanford University

[Sample Parameters of a Two-Mile Superconducting Accelerator](#)

R.B. Neal, Stanford Linear Accelerator Center

[Consideration of the Use of Feedback in a Traveling-Wave Superconducting Accelerator](#)

R.B. Neal, Stanford Linear Accelerator Center

[Summary of Recent Investigations of the Karlsruhe Group on Rf Properties of Superconductors and on Applications](#)

W. Jungst, Kernforschungszentrum Karlsruhe

[An Enriched Particle Beam Using Superconducting Rf Deflectors](#)

H.N. Brown, Brookhaven National Laboratory

[Design Problems in Superconducting Rf Beam Separators](#)

H.J. Halama, Brookhaven National Laboratory

[Superconducting Rf Separator Research at the Rutherford Laboratory](#)

A. Carne, B.G. Brady, and M.J. Newman, Rutherford Laboratory

[Beam Optics Design for a 600 MeV Microtron](#)

D.C. Sutton and A.O. Hanson, University of Illinois

[High Stability UHF Oscillators using a Superconducting Cavity](#)

F. Biquard, Nguyen Tuong Viet, and A. Septier, Institut d'Electronique, Orsay

[Summary of First week of Summer Study](#)

H. Alan Schwettman, Stanford University

---

[Table of contents as they appeared in the original proceedings.](#)

[Return to Subject Index](#)

[Go to Author Index](#)

[\*\*Return to 1968 Proceedings Home Page\*\*](#)

## **CRYOGENICS** **(Second Week)**

**Chairman: T.R. Strobridge, NBS, Boulder**  
[\(Photos\)](#)

A comprehensive survey of the esoteric mysteries of the field of cryogenics was arranged by Dick Strobridge. Enormously valuable papers were presented by Hurlich of General Dynamics and Mowers of Rocketdyne on the properties of materials at low temperatures; these papers will save many of us from making costly and dangerous mistakes. Papers on refrigeration and cryostat design provided a fine survey of the state of the art and of the directions in which further progress can be expected.

Following papers were submitted for publication:

### [Refrigeration at 4<sup>0</sup>K](#)

T.R. Strobridge, National Bureau of Standards, Boulder

### [European State of the Art in Cryogenics](#)

G. Prast, Philips Research Laboratories

### [Cryogenic Safety](#)

M.G. Zabetakis, Bureau of Mines

### [Cryopumping](#)

C. Barnes, CVI Corporation

### [Review of Heat Transfer to Helium I](#)

R.V. Smith, National Bureau of Standards, Boulder

### [An Examination of a Liquid Helium Refrigeration System for Superconducting Magnets in the 200 GeV Experimental Area](#)

M.A. Green, Lawrence Radiation Laboratory, Berkeley, and G.P. Coombs and J.L. Perry, 500 Incorporated

### [Cryogenic Electrical Leads](#)

C.D. Henning, Lawrence Radiation Laboratory, Livermore

### [Low Temperature Metals](#)

A. Hurlich, General Dynamics/Astronautics

### [Properties of Nonmetallic Materials at Cryogenic Temperatures](#)

R. Mowers, Rocketdyne

### [Review of the Cryogenics Session – Second Week of the Summer Study](#)

T.R. Strobridge, National Bureau of Standards, Boulder

---

[Table of contents as they appeared in the original proceedings.](#)

[Return to Subject Index](#)

[Go to Author Index](#)

[Return to 1968 Proceedings Home Page](#)

## **SUPERCONDUCTING MATERIALS**

**(Third Week)**

**Chairman: A. Paskin, Brookhaven National Laboratory**

[\(Photos\)](#)

Arthur Paskin arranged this week as a survey of presently available superconducting materials and a look into the future. Particularly interesting were two “Manufacturer-User round-tables,” in which opinions were exchanged about what would be desirable in the realm of superconducting materials. The voice of common sense came from the representatives of industry who explained which user hopes were reasonable and which were not. Unfortunately for those who were not present, these sessions were not recorded; it had been agreed early in the Study that, in the interests of free discussion, nothing would be published that was not submitted to the Editors in writing.

Following papers were submitted for publication:

[Structure and Properties of High-Field Superconductors](#)

J.D. Livingston, General Electric Company

[Instability Comments](#)

S.L. Wipf, Atomics International

[Critical Current Behavior of Hard Superconductors](#)

W.W. Webb, Cornell University

[Critical Fields of Type II Superconductors](#)

G. Cody, RCA Laboratories

[The Effect of Radiation on the Properties of Superconducting Materials](#)

G.W. Cullen, RCA Laboratories

[Niobium Tin and Related Superconductors](#)

R.B. Britton, Brookhaven National Laboratory

[Composite Materials](#)

A.D. McInturff, Brookhaven National Laboratory

[Materials and Conductor Configurations in Superconducting Magnets](#)

H. Brechna, Stanford Linear Accelerator Center

---

[Table of contents as they appeared in the original proceedings.](#)

[Return to Subject Index](#)

[Go to Author Index](#)

[Return to 1968 Proceedings Home Page](#)

## AC EFFECTS AND FLUX PUMPS

(Fourth Week)

Chairman: S.L. Wipf, Atomics International

[\(Photos\)](#)

Although the Fourth of July cut this week to three days, Stefan Wipf compressed into this period not only a brilliant survey of the problems of instabilities and at effects in superconductors, but also a half-day review of the status of flux pumps. Particularly notable in the first category were the review papers by Hart of General Electric and by Chairman Wipf. Some very imaginative ideas in the field of superconducting transmission systems were outlined by Nahman of the Bureau of Standards who thinks not only of transmitting power but also of transmission in the same system of information and of cryogenic liquids.

Following papers were submitted for publication:

[Ac Losses in Superconductors](#)

S.L. Wipf, Atomics International

[Use of Superconductors in High Energy Physics](#)

J.P. Blewett, Brookhaven National Laboratory

[Electrical Loss Measurements in a NbTi Magnet](#)

F. Voelker, Lawrence Radiation Laboratory, Berkeley

[Ac Losses in Magnets made of Nb<sub>3</sub>Sn Ribbon](#)

G.H. Morgan and P.F. Dahl, Brookhaven National Laboratory

[Dynamic Resistivity of Hard Superconductors in a Perpendicular Time Varying Field](#)

A. Altorfer, F. Caimi, and J.M. Rayroux, Oerlikon Engineering Company

[Magnetic Instabilities and Solenoid Performance: Applications of the Critical State Model](#)

H.R. Hart, Jr., General Electric Company

[Magnetic and Thermal Instabilities Observed to Commercial Nb<sub>3</sub>Sn Superconductors](#)

G. del Castillo and L.O. Oswald, Argonne National Laboratory

[Observations of Flux Jump Behavior Related to Various Changes of Geometry, and Thermal and Electrical Environment](#)

A.D. McInturff, Brookhaven National Laboratory

[Instabilities and Flux Annihilation](#)

S.L. Wipf, Atomics International

[Superconducting Transmission Lines – Communication and Power](#)

N.S. Nahman, National Bureau of Standards, Boulder

[Recent Developments in Superconductivity in Japan](#)

Presented by N. Takano, Tokyo Shibaura Electric Company

[The Case for Flux Pumps and Some of Their Uses](#)

S.L. Wipf, Atomics International

[Design Principles and Characteristics of the G.E. Flux Pump](#)

R.L. Rhodenizer, General Electric Company

[Flux Pumps as Power Supplies in Comparison with Alternatives](#)

M.S. Lubell and K.R. Efferson, Oak Ridge National Laboratory

[Flux Pump Work at Los Alamos](#)

H. Laquer, Los Alamos Scientific Laboratory

[60 Hz Flux Pumps](#)

R.B. Britton, Brookhaven National Laboratory

[Proposal for a Flux Pump Utilizing the Inverse Ettingshausen Effect in Hard Type II Superconductors in the Mixed State](#)

W.H. Bergmann, Argonne National Laboratory

[Summary of the Fourth Week – Ac Losses, Instability and Flux Pumps](#)

S.L. Wipf, Atomics International

---

[Table of contents as they appeared in the original proceedings.](#)

[Return to Subject Index](#)

[Go to Author Index](#)

[\*\*Return to 1968 Proceedings Home Page\*\*](#)

## **SUPERCONDUCTING MAGNETS**

**(Fifth Week)**

**Chairman: W.B. Sampson, Brookhaven National Laboratory**  
**[\(Photos\)](#)**

Bill Sampson's week on superconducting magnets was the most popular of the Summer Study. Superconducting magnets were described, from the huge affairs under construction for large bubble chambers to miniature units suitable for transport of particle beams. It was during this week that Peter Smith of the Rutherford laboratory brought forward his suggestions for stabilizing superconducting magnets and for reducing ac losses. These ideas already have inspired programs in a number of laboratories; thus far Smith appears to have been correct in all of his predictions.

Following papers were submitted for publication:

**[Stress Problems Associated with Superconducting and Cryogenic Magnets](#)**

P.G. Marston, Magnetic Engineering Associates

**[Stresses in Magnetic Field Coils](#)**

W.F. Westendorp and R.W. Kilb, General Electric Company

**[Very High Field Hybrid Magnet Systems](#)**

D. Bruce Montgomery, J.E.C. Williams, N.T. Pierce, R. Weggel, and M.J. Leupold,  
Francis Bitter National Magnet Laboratory

**[Principles of Stability in Cooled Superconducting Magnets](#)**

Z.J.J. Stekly, R. Thome, and B. Strauss, Avco Everette Research Laboratory

**[The 1.8 Tesla, 4.8 m i.d. Bubble Chamber Magnet](#)**

J.R. Purcell, Argonne National Laboratory

**[The Superconducting Magnet for the Proposed 25-foot Cryogenic Bubble Chamber](#)**

A.G. Prodell, Brookhaven National Laboratory

**[The Superconducting Magnet for the Brookhaven National Laboratory 7-foot Bubble chamber](#)**

D.P. Brown, R.W. Burgess, and G.T. Mulholland, Brookhaven National Laboratory

**[A 70 kilogauss Magnet for the Proposed Rutherford Laboratory 1.5 m Diameter Hydrogen Bubble Chamber](#)**

P.T.M. Clee, D.B. Thomas, and C.W. Trowbridge, Rutherford Laboratory

**[Development Program for the Magnet of the European 3.7 m Bubble Chamber](#)**

Presented by F. Wittgenstein, CERN

**[A Possible Source of Instability in "Fully Stabilized" Magnets](#)**

P.F. Smith, M.N. Wilson, and J.D. Lewin, Rutherford Laboratory

**[Analytical Design of Superconducting Multipolar Magnets](#)**

Richard A. Beth, Brookhaven National Laboratory

**[Superconducting Magnetic Dipoles](#)**

G. Parzen, Brookhaven National Laboratory

**[Superconducting Quadrupole Focusing Lens – Part I: Analytical Design and Full-Scale Copper-Wound Pole](#)**

A. Asner, CERN



[Superconducting Quadrupole Focusing Lens – Part II: Construction and Preliminary Tests](#)

D.N. Cornish, Culham Laboratory

[Quadrupole Focusing Magnet](#)

J.D. Rogers, W.V. Hassenzahl, H.L. Laquer, and J. K. Novak, Los Alamos National Laboratory

[The Rutherford Laboratory Bending Magnet](#)

M.N. Wilson, R.V. Stovold, and J.D. Lawson, Rutherford Laboratory

[Brookhaven Superconducting dc Beam Magnets](#)

R.B. Britton, Brookhaven National Laboratory

[Pulsed Superconducting Magnets](#)

W.B. Sampson, Brookhaven National Laboratory

[Intrinsically Stable Conductors](#)

P.F. Smith, M.N. Wilson, C.R. Walters, and J.D. Lewin, Rutherford Laboratory

[Superconducting Magnets for Controlled Thermonuclear Research](#)

C.E. Taylor, Lawrence Radiation Laboratory, Livermore

[On Helium II Microstabilization of Nb<sub>3</sub>Sn](#)

W.H. Bergmann, Argonne National Laboratory

[Progress on the IMP Facility](#)

D.L. Coffey and W.F. Gauster, Oak Ridge National Laboratory

[Standardized Tests for Superconducting Materials](#)

W.F. Gauster, Oak Ridge National Laboratory

[Superconducting Magnets for the 200 GeV Accelerator Experimental Areas](#)

R.B. Meuser, Lawrence Radiation Laboratory, Berkeley

[Construction of a Superconducting Test Coil Cooled by Helium Forced Circulation](#)

M. Morpurgo, CERN

[Summary of Fifth Week of Summer Study](#)

W.B. Sampson, Brookhaven National Laboratory

---

[Table of contents as they appeared in the original proceedings.](#)

[Return to Subject Index](#)

[Go to Author Index](#)

[Return to 1968 Proceedings Home Page](#)

## **ACCELERATORS AND STORAGE RINGS USING SUPERCONDUCTING OR CRYOGENIC MAGNETS (Sixth Week)**

**Chairman: J.P. Blewett, Brookhaven National Laboratory**  
[\(Photos\)](#)

The final week of the Summer Study, under John Blewett, was a speculative survey of the probable impact of superconducting magnets on the accelerator field. The atmosphere was generally confident and optimistic; superconducting accelerators are surely just over the horizon. A day during this week was devoted to an allied field, the use of pure, but not superconducting, metals at cryogenic temperature. Here also the prospects appear to be bright. Finally, the chairman of all of the week-long sessions presented summaries of their weeks. The study closed amid expressions of mutual admiration and self-satisfaction.

Following papers were submitted for publication:

[Superconducting Synchrotrons](#)

P.F. Smith, Rutherford Laboratory

[Economic Factors Involved in the Design of a Proton Synchrotron or Storage Ring with a Superconducting Guide Field](#)

M.A. Green, Lawrence Radiation Laboratory, Berkeley

[A 2000 GeV Superconducting Synchrotron](#)

W.B. Sampson, Brookhaven National Laboratory

[Synchrotron Power Supplies using Superconducting Energy Storage](#)

P.F. Smith, Rutherford Laboratory

[Some ac Loss Determinations by an Electric Multiplier Method](#)

W.S. Gilbert, Lawrence Radiation Laboratory, Berkeley

[Radiation Effects on Superconducting Magnets](#)

H. Brechna, Stanford Linear Accelerator Center

[Iron Shielding for Air Core Magnets](#)

J.P. Blewett, Brookhaven National Laboratory

[Superconducting EFAG Accelerators](#)

G. Parzen, Brookhaven National Laboratory

[Calculations Concerning Superconducting Accelerators](#)

P. Gerald Kruger and J.N. Snyder, University of Illinois

[Preliminary Steps for Applying Superconductors to FFAG Accelerators](#)

G. del Castillo, R.J. Lari, and L.O. Oswald, Argonne National Laboratory

[A Superconducting SLAC with a Recirculating Beam](#)

W.B. Herrmannsfeldt, Stanford Linear Accelerator Center

[Properties and Preparation of High-Purity Aluminum](#)

V. Arp, National Bureau of Standards, Boulder

[Synchrotron Magnets with Cryogenic Exciting Coils](#)

G.T. Danby, J.E. Allinger, and J. W. Jackson, Brookhaven National Laboratory

[Summary of Sixth Week of Summer Study](#)

J.P. Blewett, Brookhaven National Laboratory

---

[Table of contents as they appeared in the original proceedings.](#)

[Return to Subject Index](#)

[Go to Author Index](#)

[Return to 1968 Proceedings Home Page](#)